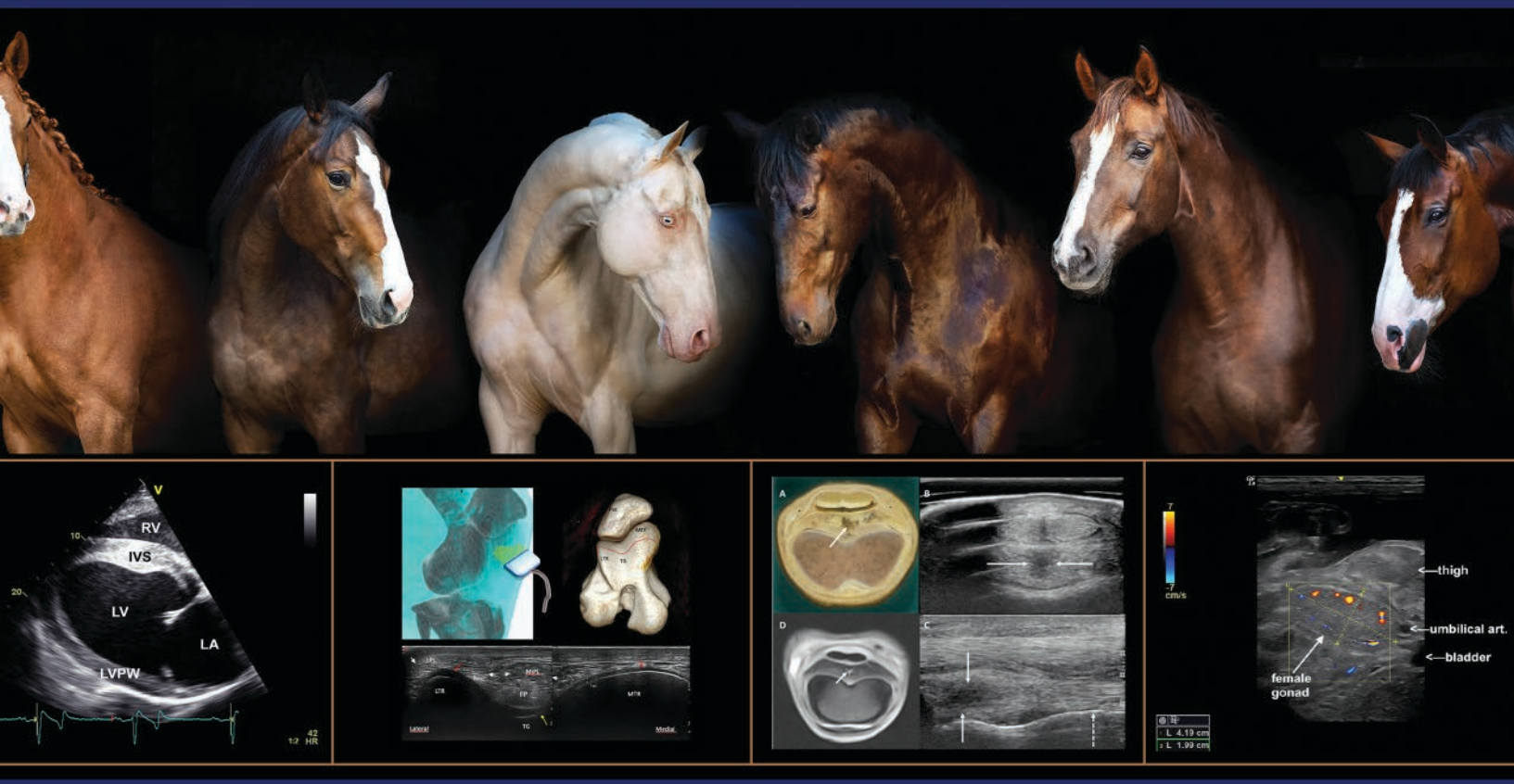
SECOND EDITION

ATLAS OF EQUINE ULTRASONOGRAPHY

EDITED BY

JESSICA A. KIDD · KRISTINA G. LU
MICHELE L. FRAZER



WILEY Blackwell

Atlas of Equine Ultrasonography

Atlas of Equine Ultrasonography

Edited by

Jessica A. Kidd, BA, DVM, CertES (Orth)
Diplomate ECVS, MRCVS
Oxfordshire, UK

Kristina G. Lu, VMD, Diplomate ACT
Hagyard Equine Medical Institute, Lexington, KY, USA

Michele L. Frazer, DVM, Diplomate ACVIM, ACVECC
Hagyard Equine Medical Institute, Lexington, KY, USA

Second Edition

WILEY Blackwell

This edition first published 2022
© 2022 John Wiley & Sons Ltd

Edition History
John Wiley & Sons Ltd (1e, 2014)

All rights reserved. No part of this publication may be reproduced, stored in a retrieval system, or transmitted, in any form or by any means, electronic, mechanical, photocopying, recording or otherwise, except as permitted by law. Advice on how to obtain permission to reuse material from this title is available at http://www.wiley.com/go/permissions.

The right of Jessica A. Kidd, Kristina G. Lu and Michele L. Frazer to be identified as the authors of the editorial material in this work has been asserted in accordance with law.

Registered Offices
John Wiley & Sons, Inc., 111 River Street, Hoboken, NJ 07030, USA
John Wiley & Sons Ltd, The Atrium, Southern Gate, Chichester, West Sussex, PO19 8SQ, UK

Editorial Office
9600 Garsington Road, Oxford, OX4 2DQ, UK

For details of our global editorial offices, customer services, and more information about Wiley products visit us at www.wiley.com.

Wiley also publishes its books in a variety of electronic formats and by print-on-demand. Some content that appears in standard print versions of this book may not be available in other formats.

Limit of Liability/Disclaimer of Warranty
The contents of this work are intended to further general scientific research, understanding, and discussion only and are not intended and should not be relied upon as recommending or promoting scientific method, diagnosis, or treatment by physicians for any particular patient. In view of ongoing research, equipment modifications, changes in governmental regulations, and the constant flow of information relating to the use of medicines, equipment, and devices, the reader is urged to review and evaluate the information provided in the package insert or instructions for each medicine, equipment, or device for, among other things, any changes in the instructions or indication of usage and for added warnings and precautions. While the publisher and authors have used their best efforts in preparing this work, they make no representations or warranties with respect to the accuracy or completeness of the contents of this work and specifically disclaim all warranties, including without limitation any implied warranties of merchantability or fitness for a particular purpose. No warranty may be created or extended by sales representatives, written sales materials or promotional statements for this work. The fact that an organization, website, or product is referred to in this work as a citation and/or potential source of further information does not mean that the publisher and authors endorse the information or services the organization, website, or product may provide or recommendations it may make. This work is sold with the understanding that the publisher is not engaged in rendering professional services. The advice and strategies contained herein may not be suitable for your situation. You should consult with a specialist where appropriate. Further, readers should be aware that websites listed in this work may have changed or disappeared between when this work was written and when it is read. Neither the publisher nor authors shall be liable for any loss of profit or any other commercial damages, including but not limited to special, incidental, consequential, or other damages.

A catalogue record for this book is available from the Library of Congress

Hardback ISBN: 9781119514725; ePub ISBN:9781119514688; ePDF ISBN:9781119514718; oBook ISBN: 9781119514671

Cover images: © Callipso88/Adobe Stock Photos, Courtesy of Michele L. Frazer, Eddy Cauvin, Roger Smith, Dr. Stefania Bucca DVM
Cover design by Wiley

Set in 10/12pt WarnockPro by Integra Software Services Pvt. Ltd, Pondicherry, India

Vet-ebooks.com

Michele L. Frazer:
To Oliver, Richard, Leah, and Gabrielle for their love and encouragement in this and all life's adventures.
To Lee for…everything.
In loving memory of my mother, Betty, for her support through the years, and, of course for tolerating all my dogs.

Jessica Kidd:
To Geoff Lane and Derek Knottenbelt for their ongoing support and friendship over the years.
And to Toby and Arthur.

Vet-ebooks.com

Vet-ebooks.com

Contents

About the Editors *x*
List of Contributors *xi*
About the Companion Website *xiii*

Introduction *1*
Kimberly Palgrave and Jessica Kidd

Section 1 Musculoskeletal *23*

1 **Ultrasonography of the Foot and Pastern** *25*
Ann Carstens and Roger K.W. Smith

2 **Ultrasonography of the Fetlock** *49*
Eddy R.J. Cauvin and Roger K.W. Smith

3 **Ultrasonography of the Metacarpus and Metatarsus** *85*
Roger K.W. Smith and Eddy R.J. Cauvin

4 **Ultrasonography of the Carpus** *128*
Ann Carstens and Sheelagh Higgerty

5 **Ultrasonography of the Elbow and Shoulder** *148*
Barbara Riccio

6 **Ultrasonography of the Hock** *173*
Katherine S. Garrett

7 **Ultrasonography of the Stifle** *189*
Eddy R.J. Cauvin

8 **Ultrasonography of the Pelvis** *229*
Marcus Head

9 **Ultrasonography of the Back and Neck** *243*
Marcus Head

10 **Ultrasonography of the Head** *255*
Debra Archer

Vet-ebooks.com

Section 2 Reproduction *267*

Section 2a Ultrasonography of the Stallion Reproductive Tract *269*

11 Ultrasonography of the Internal Reproductive Tract *271*
Malgorzata A. Pozor

12 Ultrasonography of the Penis *300*
Malgorzata A. Pozor

13 Ultrasonography of the Testes *310*
Charles Love

Section 2b Ultrasonography of the Mare Reproductive Tract *321*

14 Use of Ultrasonography in the Evaluation of the Non-Pregnant Mare *323*
Walter Zent

15 Use of Ultrasonography for Evaluation of Mare Reproductive Abnormalities *331*
Ryan A. Ferris and Kristina G. Lu

16 Transrectal Ultrasonography of Early Equine Gestation – the First 60 Days *347*
Chelsie A. Burden

17 Use of Early Gestation Ultrasonography in Twin Management *363*
Richard Holder

18 Use of Ultrasonography in Equine Fetal Sex Determination between 55 and 200 days of Gestation *370*
Richard Holder

19 Use of Ultrasonography in Fetal Development and Monitoring *383*
Stefania Bucca

Section 3 Internal Medicine *407*

20 Thoracic Ultrasonography, Non Cardiac *409*
Peter R. Morresey

21 Ultrasonography of the Heart *421*
Katharyn J. Mitchell and Colin C. Schwarzwald

22 Ultrasonography of the Liver, Spleen, Kidneys, Bladder, and Peritoneal Cavity *446*
Nathan Slovis

23 Ultrasonography of the Gastrointestinal Tract *465*
Rana Bozorgmanesh

24 Equine Ocular Ultrasonography *481*
Rodolfo Gialletti

Vet-ebooks.com

25 Ultrasonography of the Soft Structures of the Neck *510*
Massimo Magri

26 Ultrasonography of Vascular Structures *540*
Rana Bozorgmanesh

27 Umbilical Remnant Preparation and Scanning Technique *547*
Massimo Magri

28 Post Foaling Complications *558*
Peter R. Morresey

29 Neonatology *573*
J. Barry David

Index *580*

Vet-ebooks.com

About the Editors

Jessica A. Kidd is a board-certified equine surgeon based in Oxfordshire, England. She was born in England but raised in the United States. She attended veterinary school at Purdue University, followed by two years in mixed practice and an internship at a racehorse referral hospital in Florida before returning to the UK to undertake a surgical residency at the University of Bristol. She has worked in both academia and private practice in the UK and is currently an external surgical consultant to a number of clinics and hospitals for surgical and orthopaedic cases. In addition to being Editor in Chief of the *Atlas of Equine Ultrasonography*, she has also contributed book chapters to Auer's "Equine Surgery" and Henson's "Equine Neck and Back Pathology." She has given presentations at national and international meetings and has lectured in over 25 countries, often as part of the charity Vets with Horsepower which raises money to support equine and children's charities.

Michele L. Frazer attended the University of Kentucky for her undergraduate education before graduating from Auburn College of Veterinary Medicine in 1995. After working in a referral clinic in Birmingham, Alabama, she obtained board certification in internal medicine from Hagyard Equine Medical Institute in 1999. She then served as an equine clinician and instructor at Kansas State Veterinary College before returning to Lexington and establishing a solo practice. She joined Hagyard Equine Medical Institute as an Internal Medicine Specialist in 2004. In 2011, she obtained Diplomate status in the Veterinary College of Emergency and Critical Care Medicine as well as certification in equine acupuncture. Although Dr Frazer enjoys all aspects of equine internal medicine, she has a particular interest in protein losing enteropathies, neonatology, and critical care medicine. She regularly speaks at nationally recognized meetings including the AAEP and ACVIM forums, publishes in veterinary journals, and is co-editor of an ultrasound atlas.

Kristina G. Lu grew up in Philadelphia, Pennsylvania, USA. After obtaining a veterinary degree at the University of Pennsylvania she completed a large animal theriogenology residency at the New Bolton Center in Kennett Square, Pennsylvania, USA. She is currently in private practice at Hagyard Equine Medical Institute in Lexington, Kentucky, USA, where she focuses on advancing treatment and management of subfertility in mares and stallions.

Vet-ebooks.com

List of Contributors

Debra Archer, BVMS, PhD, CertES (soft tissue) DipECVS, MRCVS
Professor of Equine Surgery
Philip Leverhulme Equine Hospital
University of Liverpool
Wirral, UK

Sarah Boys Smith, MA VetMB, CertES (Orth) DipECVS, DipACVSMR MRCVS RCVS
and European Specialist in Equine Surgery
American Specialist in Veterinary Sports Medicine and Rehabilitation
Senior Orthopaedic Clinician
Rossdales Equine Hospital and Diagnostic Centre
Newmarket, UK

Rana Bozorgmanesh
Hagyard Equine Medical Institute
Lexington, KY, USA

Stefania Bucca, DVM
Senior Clinical Veterinarian-Reproduction/ Theriogenology
Equine Veterinary Medical Center
Doha, Qatar

Chelsie A. Burden, DVM, MS, DACT
Goulburn Valley Equine Hospital
Victoria, Australia

Ann Carstens, BVSc, MS, MMedVet (Large Animal Surgery) Diploma in Tertiary Education MMedVet (Diagnostic Imaging) DiplECVDI, MRCVS, PhD
Associate Professor Diagnostic Imaging
Professor Emeritus
Faculty of Veterinary Science
University of Pretoria
Onderstepoort, South Africa

Eddy R.J. Cauvin, DVM, MVM, PhD, HDR, DipECVS
Associate member ECVDI
Partner
AZURVET Referral Veterinary Centre
Saint-Laurent-due-Var, France

J. Barry David
Associate Veterinarian
Hagyard Equine Medical Institute
Lexington, KY, USA

Ryan A. Ferris, DVM, MS, DACT
Owner
Summit Equine
Gervais, OR, USA

Michele L. Frazer, DVM, DiplACVIM ACVECC
Associate Veterinarian
Hagyard Equine Medical Institute
Lexington, KY, USA

Katherine S. Garrett, DVM, DipACVS
Director of Diagnostic Imaging
Rood and Riddle Equine Hospital
Lexington, KY, USA

Rodolfo Gialletti, Med Vet, PhD
Department of Veterinary Medicine
University of Perugia
Via San Costanzo
Perugia, Italy

Vet-ebooks.com

Marcus Head, BVetMed, MRCVS
Leicestershire, UK

Sheelagh Higgerty, B.A (Natal), BVSc (Hons) (Pretoria)
Crowthorne Veterinary Clinic
Kyalami, South Africa

Richard Holder, DVM
Senior Partner
Hagyard Equine Medical Institute
Lexington, KY, USA

Jessica A. Kidd, BA, DVM, CertES (Orth), DipECVS
RCVS and EBVS Recognised Specialist in Equine Surgery
Oxfordshire, UK

Charles Love, DVM, DipACT
Associate Professor of Theriogenology
Texas A&M University College of Veterinary Medicine
College Station, TX, USA

Kristina G. Lu, VMD, DACT
Theriogenologist
Hagyard Equine Medical Institute
Lexington, KY, USA

Massimo Magri, DVM
Practice Owner
Clinic Veterinaria Spirano
Spirano (BG), Italy

Katharyn J. Mitchell
Assistant Professor, Large Animal Internal Medicine
Department of Clinical Sciences
College of Veterinary Medicine
Cornell University, USA

Peter R. Morresey, BVSc, MVM. MACVSc, DipACT DipACVIM (Large Animal), CVA
Internal Medicine Clinician
Rood and Riddle Equine Hospital
Lexington, KY, USA

Kimberly Palgrave, BS, BVM&S, GPCert (DI), MRCVS
Associate Veterinarian
Overland Animal Hospital
Denver, CO, USA

Malgorzata A. Pozor, DVM, PhD, DipACT
Clinical Assistant Professor
Department of Large Animal Clinical Sciences
College of Veterinary Medicine
University of Florida
Gainesville, FL, USA

Barbara Riccio, DVM, PhD ISELP Certified DipACVSMR, DipECVSMR
Via Montebello 15
Torino (TO), Italy

Colin C. Schwarzwald, Dr. med. vet., PhD Diplomate ACVIM & ECEIM
Director, Clinic for Equine Internal Medicine
Equine Department
University of Zurich
Zurich, Switzerland

Nathan Slovis, DVM, DipACVIM
CHT (Certified Hyperbaric Technologist)
Hagyard Equine Medical Institute
Director, McGee Medical and Critical Care Center
Lexington, KY, USA

Roger K.W. Smith, MA, VetMB, PhD, FHEA, DEO
Large Animal Imaging Associate of ECVDI
DipECVSMR, DipECVS
FRCVS
Professor of Equine Orthopaedics
Department of Clinical Sciences and Services
The Royal Veterinary College
North Mymms, Hatfield, UK

Walter Zent, DVM, DipACT (Hon)
Senior Partner
Hagyard Equine Medical Institute
Lexington, KY, USA

Vet-ebooks.com

About the Companion Website

This book is accompanied by companion website:

www.wiley.com/go/kidd/atlas

This website includes:

- Videos 1–82 were compiled by Sarah Boys Smith.
- 10 Videos relate to Chapter 16 of the book.

Vet-ebooks.com

Vet-ebooks.com

Introduction

Kimberly Palgrave[1] and Jessica Kidd[2]

[1] *VCA Central Park Animal Hospital, Denver, Colorado, USA*
[2] *Oxfordshire, UK*

Welcome to the second edition of the *Atlas of Equine Ultrasonography*. The second edition has been expanded from the first edition to include updated chapter text and inclusion of many more images. We hope you enjoy the new version.

The field of veterinary ultrasonography has blossomed in the last 40 years and the improvements in technology since its first use have been exponential. It is also now being used on structures and body systems that were not previously thought to be conducive to ultrasonography. Many vets in equine practice now have access to an ultrasound machine and along with radiography, ultrasonography has become a mainstay of equine diagnostic imaging. It has the advantages of being non-invasive and complementary to radiography. The purpose of this book is to encourage further use of ultrasonography in clinical cases and expansion of the clinical techniques of vets both in general practice and at the referral level.

Ultrasonography is an excellent diagnostic tool which has many applications in veterinary practice. When considered in conjunction with relevant clinical information such as patient history and physical examination findings, it can be an extremely useful aid in the clinical decision-making process. Developing the skills necessary to confidently acquire and interpret ultrasound images requires knowledge of normal equine anatomy and an understanding of the mechanisms displayed by individual body systems when reacting to various disease processes. We hope this book will help achieve this. A general appreciation of the physics of ultrasound is also necessary, as this enables the ultrasonographer to optimize the diagnostic quality of ultrasound images obtained by appropriately altering their technique and machine settings. The aim of this introductory chapter is to provide an overview of ultrasound technology and the fundamental principles of image evaluation with a focus on the applications of ultrasound within equine practice.

How to Use This book

The book is divided into three main sections: musculoskeletal, internal medicine, and reproduction. Each section is then further subdivided into chapters by anatomical region. Within each chapter is information on scanning technique for that area, a review of the normal anatomy, and discussion of some of the more common ultrasonographic abnormalities. This is then followed by the images to show normal and abnormal findings. The end of each chapter lists "Recommended Reading" for more extensive references relating to the chapter topics.

Physics of Ultrasound

Ultrasound physics is a vast and theoretically complex subject; however, a thorough understanding of this topic is not required for performing and utilizing diagnostic ultrasonography effectively in the clinical environment. Therefore, this text will cover the aspects of ultrasound physics which directly relate to the interaction of ultrasound waves with tissue and how these interactions translate to the displayed image. Additional sources covering this subject matter in greater detail are listed at the end of this chapter under "Recommended Reading,"

Atlas of Equine Ultrasonography, Second Edition. Edited by Jessica A. Kidd, Kristina G. Lu and Michele L. Frazer.
© 2022 John Wiley & Sons Ltd. Published 2022 by John Wiley & Sons Ltd.
Companion Website: www.wiley.com/go/kidd/atlas

Vet-ebooks.com

Features of Ultrasound Waves

Ultrasound waves have features in common with audible sound waves, although they have a higher frequency than audible sound and cannot be heard by the human ear; hence the term "ultrasound." They are both created through the vibration of an object resulting in movement of surrounding molecules. Ultrasound waves are produced through the application of an electric current to piezoelectric crystals within the transducer (probe), causing the crystals to vibrate. This vibration is transmitted through the surrounding tissues in the form of sound waves. These waves interact with the tissues along their path of travel in various ways, which may result in *attenuation* of the ultrasound beam.

Attenuation is defined as the progressive weakening in intensity of the ultrasound wave as it is transmitted through body tissues. Sound waves passing through tissues can either be *reflected*, *refracted*, *scattered*, or *absorbed*. These are the primary causes of attenuation of the ultrasound wave and these phenomena are ultimately responsible for the formation of an ultrasound image.

Reflection and Acoustic Impedance

As ultrasound waves travel through the body, they come into contact with structures which reflect a proportion of the waves directly back toward the piezoelectric crystals, while the remainder of the waves continue to travel deeper into the tissues. The force of the returning waves or echoes results in vibration of the crystals and this vibration is then translated into an electrical signal which is used to create the image displayed on the screen. Therefore, a unique feature of piezoelectric crystals is that they are capable of both emitting and receiving ultrasound waves.

It is important to realize that an ultrasound image is only produced when ultrasound waves are *reflected* back to the transducer. *Reflection* occurs when an ultrasound wave reaches an interface between two tissues as it is transmitted through the body and a portion of that wave is returned or "bounced back" to the probe while the remainder of the wave continues to travel deeper into the body. The strength of the returning wave and the length of time taken for that wave to travel through the tissues before returning to the probe is recognized and processed by the ultrasound machine in order to create the ultrasound image. These concepts will be later explored in the Section on B-Mode and Echogenicity.

The proportion of the emitted wave which is reflected back to the probe depends on the acoustic impedance of the interface between tissues and the angle at which the ultrasound wave strikes the interface. The acoustic impedance of a tissue is a product of the density of that tissue and the speed at which sounds waves travel through it. A dense tissue, such as bone, has a high acoustic impedance (7.8) compared to the relatively low acoustic impedance of air (0.0004), with soft tissues being in between (i.e., kidney – 1.62) (see Table I.1). However, it is the difference in acoustic impedance between tissue types that determines the reflective nature of a given tissue interface, not the acoustic impedance of a single tissue in isolation. For example, both a bone-soft tissue interface and an air-soft tissue interface have significant differences between the acoustic impedance values of the tissues at that interface, despite the fact that bone and air are at opposite ends of the acoustic impedance spectrum. Therefore, both bone-soft tissue and air-soft tissue interfaces are highly reflective, with the majority of the ultrasound waves being reflected back to the transducer in both scenarios. This also results in very little of the ultrasound wave remaining to penetrate into the deeper tissues beyond this highly reflective interface. By comparison, soft tissue–soft tissue interfaces (either between or within soft tissue structures) are less reflective due to the small differences between the acoustic impedances of these tissue types. Understanding this physical property of ultrasound wave propagation is essential to understanding how tissue variations translate into the ultrasound image appearance. This also justifies the need for appropriate patient preparation including clipping of the haircoat where possible and application of ultrasound coupling gel to minimize the amount of air at the probe–skin interface. Differences in acoustic impedance also contribute to artifact formation, which will be discussed later in the chapter.

The angle at which the ultrasound beam strikes the tissues is also integral to the degree of **reflection** of the ultrasound wave. Only ultrasound waves striking an interface which is perpendicular to the direction

Table I.1 Approximate acoustic impedance in commonly encountered tissues. Adapted from Curry, T.S. III *et al*. 1990.

Tissue	Acoustic Impedance (in Rayls)
Air	0.0004
Fat	1.38
Water (50°C)	1.54
Brain	1.58
Blood	1.61
Kidney	1.62
Liver	1.65
Muscle	1.70
Lens of eye	1.84
Bone (skull)	7.80

Vet-ebooks.com

in which the wave is traveling will result in reflection of the wave directly back to the probe. If the wave reaches the tissue interface at an angle, the waves will be reflected into adjacent tissues instead of back to the probe, resulting in a lack of direct information from that area of the body. Therefore, the true reflective nature of that particular tissue will not be accurately represented in the displayed ultrasound image. In practical terms, imaging a structure when the ultrasound beam is not directed perpendicular to the region of interest may result in a smaller proportion of the wave being reflected to the probe and the resulting ultrasound appearance of that structure may appear "patchy" or irregular, although this effect can be used to the ultrasonographer's advantage by allowing the margins of structures to be more easily recognized, for example.

Refraction, Scatter, and Absorption

In addition to reflection, other types of interaction between the ultrasound beam and tissues include *refraction*, *scatter*, and *absorption*. If an ultrasound wave reaches an interface between tissues of different acoustic impedances (i.e., the ultrasound wave travels at different speeds through the tissues) at an angle other than perpendicular, the beam will change direction while continuing to travel deeper within the tissues before ultimately being reflected back to the probe. This phenomenon, known as refraction, is commonly observed in association with curved structures (e.g., endometrial cysts, embryonic vesicles) and will be covered in the Section on Ultrasound Artifacts.

The appearance of parenchymatous organs on ultrasound examination is primarily attributable to *scatter* of the ultrasound waves. Scatter occurs when the beam encounters small, irregular interfaces with minimal differences in acoustic impedance within an organ, as is present within the liver. The result of this interaction is the *scattering* of waves throughout the tissues in all directions instead of direct reflection back to the transducer. The strength of individual reflected echoes from these interfaces is relatively weak, compared to the strength of echoes being returning to the transducer from highly reflective interfaces, such as bone/soft tissue (e.g., interface between suspensory ligament/metacarpal III). However, due to their abundant numbers, scattered waves contribute significantly to image formation of more homogenous tissues, such as the spleen.

Absorption is the only interaction between the ultrasound beam and tissues which directly results in a reduction in the energy of the waves. This form of attenuation occurs when the mechanical energy of the ultrasound wave is converted to heat which is then contained in the tissues. The heat generated within tissues from the use of diagnostic ultrasound is generally considered to be negligible.

B-Mode and Echogenicity

The production of an ultrasound image relies on information detailing the nature and location of structures within the region of interest being relayed effectively to the ultrasound machine. In real-time B-mode ("brightness" mode) imaging (Figure I.1), the strength of the signal received by the crystals within the probe correlates to the strength (amplitude) of ultrasound waves returning to the probe. These echoes are represented on the ultrasound screen by a series of dots on a black background. The brightness of each dot is determined by the strength of the returning echo that it represents. In practical terms, a strong returning echo will appear "brighter" (whiter) while a weaker echo appears "darker" (grey or black).

The terminology used when describing the ultrasonographic appearance of various tissues is referred to as the "echogenicity" of that tissue. Structures which do not reflect ultrasound waves appear black on the ultrasound image and are termed anechoic. Fluid filled structures such as ovarian follicles and the vitreous chamber of the eye are considered to be anechoic (Figure I.2).

The echogenicity of other tissues types must be considered in relation to one another. When comparing two tissues in an ultrasound image, the darker structure is referred to as being more hypoechoic while the brighter structure is termed hyperechoic. Soft tissue structures within the body may exhibit varying

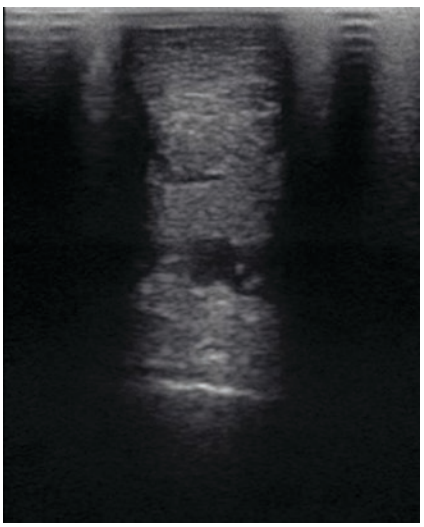


Figure I.1 B-mode, cross-sectional image of the soft tissue structures on the palmar aspect of the equine distal limb.

Vet-ebooks.com

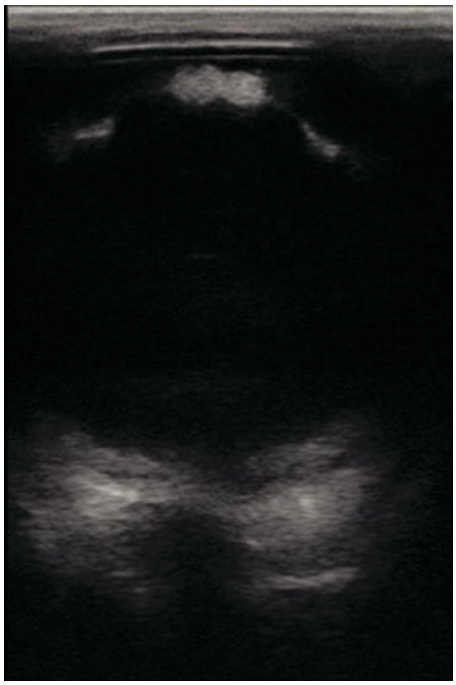


Figure I.2 Ultrasound image of the equine globe and orbit with anechoic fluid within the vitreous chamber.

echogenicities (Figure I.3), while the typical appearance of both a bone-soft–tissue interface (e.g., region of the suspensory ligament and metacarpal III) and an air-soft–tissue interface (e.g., parietal pleura and air-filled lung) is strongly hyperechoic (a bright-white line) (Figure I.4). If two tissues are represented by the same level of brightness in the ultrasound image, they are deemed to be isoechoic to one another.

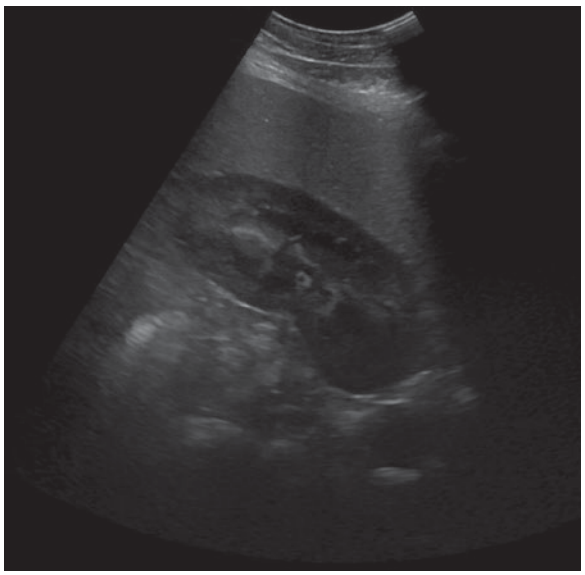


Figure I.3 Image of the equine spleen and left kidney demonstrating the mixed echogenic appearance of soft tissue structures; the spleen in the top of the image and in this image is hyperechoic compared to the kidney.

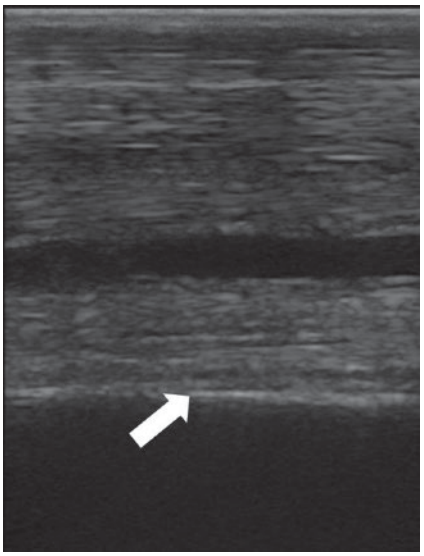


Figure I.4 Ultrasound image of the equine distal limb in the longitudinal plane demonstrating the appearance of the interface between the suspensory ligament and metacarpal III (bone-soft–tissue interface) as a hyperechoic line (arrow).

The location (i.e., depth) of a reflective tissue interface is determined by the length of time taken for the ultrasound wave to be emitted by the crystals within the probe, travel through tissues to the reflective structure, and finally be transmitted back to the probe. An ultrasound wave which takes longer to be reflected back and received by the crystals within the probe will be represented on the ultrasound image as a dot located farther away from the transducer. This signifies a reflective structure positioned at a greater depth within the tissues.

M-Mode

M-mode imaging displays the movement of structures along a narrow, user-defined region of the ultrasound image in relation to time. A common example is cardiac ultrasonography. First, an optimal B-mode image is obtained and M-mode imaging is then selected. A linear cursor is displayed which originates from the midpoint of the transducer contact area and runs through the superficial structures into the deeper tissues. Depending on the type of ultrasound machine in use, the user will have a varying ability to position this cursor in the ideal location. When M-mode imaging is activated, the movement of tissues along the cursor line is displayed as a function of time, with the horizontal axis representing time and the vertical axis representing tissue depth. As in B-mode imaging, the brightness of the displayed image correlates to the strength (amplitude) of returning echoes (Figure I.5). M-mode imaging enables the ultrasonographer to evaluate the relative movement of structures in a

Vet-ebooks.com

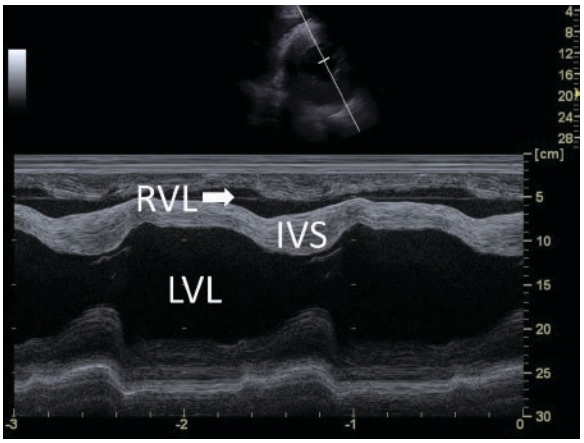


Figure I.5 M-mode image of the region of the equine mitral valve.

particular region of interest over time and perform relevant measurements/calculations relating to changes in dimensions of those structures. This imaging mode is particularly useful for cardiac applications such as evaluating relative changes in chamber sizes throughout the cardiac cycle.

Ultrasound Machine

Console

The ultrasound machine setup includes the console and the transducer. Both are essential to the production of a quality diagnostic ultrasound image. The console is responsible for activating the piezoelectric crystals within the transducer, functioning as the processing center for all information received by the crystals, providing the user with various controls necessary for optimizing the quality of the ultrasound image, and housing the screen which displays the final ultrasound image. Depending on the type of ultrasound machine being used, the console also provides the user with various image manipulation, storage, and file transfer options.

Transducer Frequency and Image Resolution

The primary function of the ultrasound transducer (probe) is to house the piezoelectric crystals which emit and receive ultrasound waves used in the production of a diagnostic image. The differences in transducer shape, size, and frequency options reflect the wide variety of ultrasound applications within equine practice and the requirement for specific probes which are most appropriate for particular uses (see section below on Types of Transducer).

The ability to emit ultrasound waves of varying frequencies is a feature which will greatly enhance the versatility of an ultrasound probe. Frequency is defined as the number of times a wave repeats over a given time period (cycles per second). As previously described, ultrasound waves are similar to audible sound waves; however, the frequency range of diagnostic ultrasound is much higher than that of audible sound. Diagnostic ultrasonography commonly utilizes frequencies in the range of 1–20 MHz compared to a range of 20–20,000 Hz for audible sound. The frequency of ultrasound waves passing through tissues has a significant impact on the quality of the ultrasound image produced. In particular, the resolution of a diagnostic image can be greatly enhanced through the use of an appropriate transducer frequency setting. This is largely due to the fact that as frequency increases, wavelength (the distance that a wave travels during a single cycle) decreases and the interaction of tissues with ultrasound waves of shorter wavelengths results in better ultrasound image resolution, although at the expense of depth of tissue penetration. Practically, this means that the higher the probe frequency, the higher the image resolution but the lower the penetration into the tissues.

Image resolution can be defined as the ability of the ultrasound wave to distinguish between two separate structures within the tissues. In practical terms, resolution relates to the clarity of the ultrasound image displayed. "Axial resolution" concerns structures which are parallel to the direction of the beam (along the path of travel), while "lateral resolution" relates to structures which are orientated perpendicular to the direction of the beam (Figure I.6). Lateral resolution is primarily a function of ultrasound beam width while axial resolution is related to the ultrasound pulse length (wavelength multiplied by the number of cycles per pulse). Both axial and lateral resolutions are improved by the use of a higher frequency ultrasound beam; however, increasing the frequency setting improves axial resolution to a greater degree.

When compared to lower frequency waves traveling to the same depth within the tissues, higher frequency ultrasound waves will interact with more structures along their path of travel. As ultrasound waves are physical pressure waves, they are attenuated by interactions with tissues and lose strength as a result of these interactions. In practical terms, ultrasound waves are stronger when they initially leave the transducer and arrive at superficial structures compared to when they have traveled deeper within the body tissues. Therefore, a balance must always be struck between image resolution and the ability of an ultrasound wave to penetrate to the required depth of tissue. In summary, a higher

Vet-ebooks.com

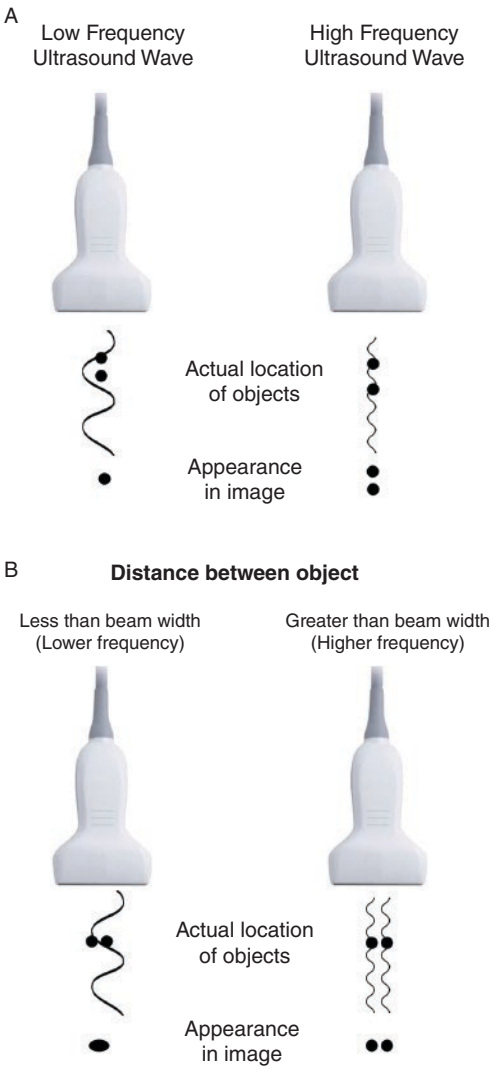


Figure I.6 Illustration of the relationship between frequency and image resolution: (A) axial resolution; (B) lateral resolution.

frequency setting will result in production of an image with better resolution but decreased ability to penetrate to the deeper structures. A lower frequency setting will enable the ultrasound wave to penetrate deeper into the tissues; however, image resolution will be diminished.

Types of Transducer

There are two broad categories of ultrasound transducer – mechanical and electronic. Mechanical probes are characterized by the presence of single or multiple piezoelectric crystals mounted within the probe head. The crystal apparatus oscillates or rotates within the probe while the external housing of the transducer is stationary. Mechanical probes have been largely superseded by electronic (array) transducers, as these probes do not have moving parts which are liable to fatigue and wear over time.

Electronic transducers have several stationary crystal elements arranged within the probe head. These crystals are electronically stimulated to vibrate in particular sequences to create waves for specific types of ultrasound examinations. Several types of electronic transducers are manufactured; however, the most common types found within equine practice are linear (rectal and musculoskeletal), convex, and phased-array.

Linear probes are most commonly used for evaluating the equine distal limb. They are also used for performing *per rectum* examination of the reproductive tract of the mare (Figure I.7). The crystal elements in linear probes are arranged along the scanning surface ("footprint") of the probe and these crystals are stimulated sequentially to emit ultrasound waves. This results in the formation of a rectangular ultrasound image. Linear probes usually emit ultrasound waves of higher frequency (7–13 MHz) and therefore provide images with enhanced resolution of superficial structures. However, they do not provide appropriate penetration for the evaluation of deeper structures and the





Figure I.7 Different forms of linear transducers for use in equine ultrasonography (rectal probe – left; musculoskeletal "tendon" probe – right).

Vet-ebooks.com

large footprint hampers contact in certain areas such as between the heel bulbs.

Curvilinear transducers are similar to linear probes; however, due to the crystal arrangement along a curved probe head, the resultant ultrasound image is sector ("pie")/wedge-shaped. These probes are often referred to as convex or micro-convex, depending on the size and frequency range (typically 2–5 MHz for convex and 4–10 MHz for micro-convex) of the individual transducer (Figure I.8). Convex probes are primarily used for abdominal imaging and for scanning the sacroiliac and stifle regions in the horse. Micro-convex probes may be used in ocular ultrasonography and in orthopaedic examinations in areas in which the footprint of a linear probe would hinder obtaining an image.

Phased-array probes are designed almost exclusively for use in cardiac ultrasound applications with a typical frequency range of 1–5 MHz. The crystals are stimulated nearly simultaneously (<1 μsec intervals), resulting in the formation of a sector-shaped image which is updated more rapidly compared to curvilinear or linear probes. This is particularly useful when evaluating more rapidly moving structures, such as the myocardium. Phased-array probes generally have a smaller "footprint" which enables the ultrasonographer to access the intercostal space more readily when performing an echocardiographic examination (Figure I.9).

Commercially manufactured standoffs are available from various suppliers. A *standoff* creates a physical separation between the probe and the tissues being imaged to allow the superficial tissues to be seen more clearly as they are not compressed into a smaller area of the image. These standoffs should be flexible to enable them to conform to the shape of the limb as well as the probe (generally manufactured for use with linear array transducers – either rectal or musculoskeletal configurations) (Figure I.10), have an acoustic impedance similar to soft tissue, be comfortable to use when scanning and easy to clean.

Ultrasound Machine Controls and Image Optimization

The ability of the ultrasonographer to optimize the quality of the displayed ultrasound image relies on several factors, including adequate patient preparation and appropriate adjustment of the machine controls/settings. The degree to which the ultrasonographer can alter the ultrasound wave characteristics and manipulate the image displayed is specific to each ultrasound manufacturer and model of machine. However, the fundamental controls used to optimize image quality are generally common to the vast majority of machines used throughout equine practice.

Machine Presets

Ultrasound machine presets enable the user to define a set of machine parameters which are generally





Figure I.8 Convex (left) and micro-convex (right) transducers.



Figure I.9 Phased-array transducer.

Vet-ebooks.com

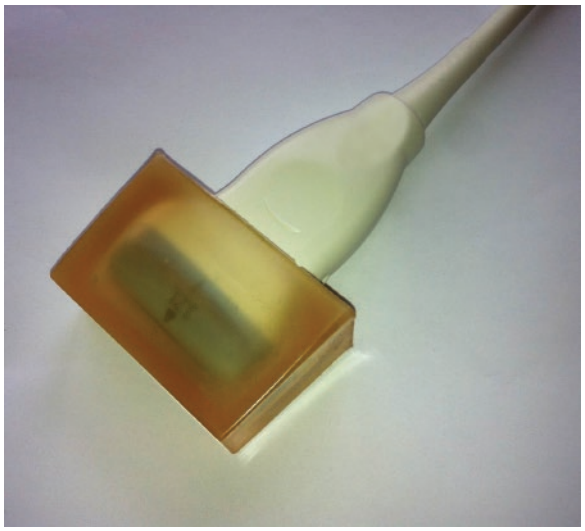


Figure I.10 Standoff for linear transducer (musculoskeletal "tendon").

suited to a specific type of ultrasound examination (e.g., abdominal, musculoskeletal, reproduction). Parameters that can be set within each preset include, but are not limited to, transducer frequency, gain, Time-Gain Compensation (TGC), and depth. The use of user-defined presets provides the ultrasonographer with an acceptable "starting point" for machine settings, so that only minor adjustments to the controls are required to optimize the appearance of the ultrasound image for individual patients.

Frequency

As previously stated, altering the frequency of the ultrasound waves produced by the transducer has a significant impact on image resolution. Therefore, choosing the correct frequency setting on a multi-frequency probe (mechanical or electronic) or selecting the most appropriate probe for a specific type of examination (if single frequency probes are used) is essential for optimizing image quality. In general, it is recommended to use the highest frequency setting available to enhance image resolution, but which retains sufficient ability to penetrate to the required depth for the region of interest.

Gain

The purpose of the gain control is to increase or decrease the brightness of the image displayed through uniform, non-selective amplification or reduction of all echoes returning to the transducer. Altering the gain control has a more profound effect on the diagnostic quality of the image than simply adjusting the brightness of the console monitor. Increasing the overall gain setting will result in the strength of all returning waves being amplified. Although the appropriate level of image brightness is subjective and based on user preference, it is important that the gain control is not set too high as this will result in overamplification of weaker echoes and tissue contrast and resolution will be compromised. Conversely, using a gain control setting which is too low may result in the loss of subtle tissue detail as weaker echoes are not translated into the displayed image.

Time–Gain Compensation

Due to the physical properties of ultrasound waves, their interactions with tissues along the path of travel results in attenuation of those waves at increasing tissue depths. Stated another way, as sound waves travel through the tissues, they lose strength and therefore echoes returning to the probe from greater depths will be weaker. If not compensated for, this results in an ultrasound image in which superficial structures nearer to the transducer appear brighter ("near-field"), whereas deeper structures farther from the probe appear darker ("far-field"). The Time-Gain Compensation (TGC) control enables the user to correct for this phenomenon by selectively amplifying returning echoes depending on their depth within the tissues, to create an image of uniform brightness (Figure I.11).

Depth

The region of interest should ideally occupy three-quarters of the displayed image. Altering the depth to the appropriate level for the structures being evaluated will also allow the user to make adjustments to the frequency settings to optimize image quality. For example, when imaging the equine distal limb, decreasing the depth such that the third metacarpal bone forms the far-field boundary of the image (approximately 4–6 cm depth depending on patient conformation) will enable a higher frequency transducer setting to be used as increased penetration ability of the ultrasound waves are not required. This will optimize the quality of the ultrasound image displayed by enhancing image resolution.

Focus

As a conventional, unfocused ultrasound beam leaves the transducer and enters the tissues, it naturally begins to diverge/widen as it travels deeper within the tissues. This results in decreased resolution of structures in the far-field as beam width has a significant impact on lateral resolution. Focusing the ultrasound beam acts to narrow the beam width at a particular location along its length (the "focal zone"), resulting in improved resolution of the structures in the focused region (Figure I.12). Depending on machine capabilities, single or multiple focal zones can be selected and placed at specific intervals along the length of the ultrasound beam to correspond to the regions of interest within the ultrasound

Vet-ebooks.com



Figure I.11 Time-Gain Compensation control on an ultrasound console (red box).

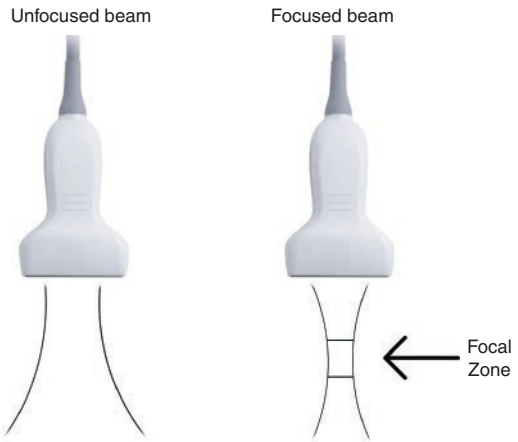


Figure I.12 Illustration of the effect of beam focusing on beam width.

image. However, selecting multiple focal zones can result in a decrease in frame rate and may therefore limit the ability to effectively image rapidly moving structures (e.g., foetal heartbeat).

Frame Rate

The frame rate of an image is the number of ultrasound images displayed per second. Essentially, it is how quickly the image is updated. With respect to array transducers, a single ultrasound beam which is created by stimulation of an individual crystal element within the probe must be emitted, travel through the tissues, and be reflected back to the probe prior to the next crystal element in the sequence being activated. Therefore, echoes traveling deeper within the tissues will take longer to return to the probe and the sequential stimulation of the crystal elements within the probe is delayed. Therefore, the frame rate decreases as the image depth increases and the length of the transducer surface or "footprint" increases. Higher frame rates are required to perform meaningful imaging studies of more rapidly moving structures, such as the heart.

Tissue Harmonic Imaging

Tissue harmonic imaging (THI) is an ultrasonographic technique utilizing the concept of harmonic frequencies to optimize both image resolution and penetration ability of the ultrasound beam. As described earlier in this chapter, conventional ultrasound imaging utilizes portions of the primary ultrasound beam which have been reflected back to the transducer to create the displayed image – the so called "fundamental frequencies." Throughout this process, additional waves are also being created which are returned to the probe alongside the fundamental frequency waves. These are referred to as *harmonic waves*. In conventional B-Mode imaging, these harmonic waves are ignored and only the reflections from the primary beam are utilized for image formation.

By comparison, THI ignores the fundamental frequency waves so that only the harmonic waves are used to create the ultrasound image. Compared to the fundamental beam, harmonic waves are of a higher frequency but lower intensity. Intensity of the ultrasound wave is defined as the rate at which energy from the ultrasound wave is transferred to surrounding structures in a specific area. Therefore, THI uses various signal processing techniques to filter out echoes resulting from reflection of the primary ultrasound beam. In other words, THI emits a lower frequency wave from

Vet-ebooks.com

the transducer but only "listens" to the higher frequency waves returning to the probe to form the ultrasound image. The purpose of this is to provide the improved resolution and image quality achieved when higher frequency ultrasound waves are used, while overcoming the limitation of decreased penetration at increasing depth (attenuation) which is also associated with the use of higher wave frequencies. Benefits of THI include increased resolution as the harmonic frequency beam is also narrower than the fundamental beam and a decrease in some artifacts.

Ultrasound Machine and Transducer Selection

There are various manufacturers and suppliers of ultrasound equipment for use in equine veterinary practice. The following are a few points which should be considered when acquiring new equipment and personal requirements should be discussed with the supplier who can help the user select the most appropriate machine:

1. Who will be using the equipment? – Is the machine in use for an equine only or a mixed practice? What is the user experience level? Will the machine be used for ambulatory work (i.e., a portable machine is needed) or will the machine be used in a practice setting and therefore be non-portable?
2. What types of ultrasound examination are to be performed? Will they be predominantly musculoskeletal, or will they be reproductive, abdominal, cardiac/thoracic, or ophthalmic? This will determine the number and types of transducers required.
3. How many scans are to be performed on a weekly or monthly basis?
4. What is the available budget? This should include purchase of the equipment and any maintenance/service fees.
5. What equipment features are required? Is a new machine necessary or is a refurbished machine suitable? Does the machine require color/doppler capability? Is a human machine acceptable or is there need for veterinary specific software/presets and hardware? What image storage capability is required (internal memory, storage to USB, printing of individual images, ability to network with practice management software/connect to PACS).
6. What post-purchase support is provided by the manufacturer/supplier? This is extremely important for support after the initial purchase and should be taken into consideration – warranties, breakdown support/equipment repair, maintenance/scheduled service costs, product training, clinical training, and provision of a loan machine while any servicing is performed.

Patient Preparation

Along with operator skill and the type of ultrasound equipment used for scanning, appropriate attention to patient preparation plays a key role in obtaining ultrasound images of diagnostic quality. Good preparation of the patient will greatly improve the images obtained. It is important that the patient be adequately restrained on a non-slip surface for the duration of the ultrasound examination, either by physical means (i.e., purpose-built stocks, assistant using a well-fitting headcollar or bridle, use of restraint aids such as a twitch) and/or through the use of chemical restraint (i.e., sedation) if necessary (ensuring adherence to competition regulations regarding usage of pharmaceuticals). Horses should stand squarely to load the soft tissue structures evenly throughout the examination.

One of the most significant contributors to poor image quality is the presence of air between the transducer and the skin surface. The haircoat traps air which will degrade image quality and therefore, ideally, the regions of interest should be clipped with fine bladed clippers prior to the application of coupling gel (Figure I.13). If the owner does not consent to clipping for aesthetic reasons, such as in an animal with a light haircoat, water may be applied to the regions to be scanned. However, the owner should be made aware that the possible reduction in image quality may result in an inability to adequately visualize and diagnose more subtle lesions. Improved images may be obtained without fully clipping if the clippers are used in the direction of the haircoat ("down the leg") to remove the ends of the hair coat. This decreases the amount of air in the coat and is difficult to detect visually.

In an animal with a greasy or dirty haircoat, in addition to clipping, the area may be washed with a very dilute chlorhexidine scrub solution to remove excessive organic matter. Some users choose to apply surgical spirit to the region to be scanned; however, if this practice is to be employed, caution should be taken to ensure that a sufficient amount of gel is used on the skin surface and that the probe is thoroughly cleaned following the ultrasound examination as surgical spirit may damage the transducer. Finally, ultrasound coupling gel should ideally be applied a few minutes prior to initiating the examination as this will significantly improve the quality of images produced. It is useful to apply the gel in a proximal to distal direction to avoid the introduction of air bubbles.

Cobs and heavy breeds of horse present their own particular challenges for ultrasonography. A useful technique is to prepare them well in advance by clipping and cleaning the area thoroughly, applying copious amounts of ultrasound gel, wrapping the legs in plastic foodwrap/cellophane, and applying an

Vet-ebooks.com



Figure I.13 Patient being prepared for an ultrasound examination of the proximal aspect of the distal hind limb. The haircoat has been removed from the caudal aspect of the distal limb in the regions of interest and extends a sufficient distance medially and laterally.

external bandage to hold the gel and plastic wrap in place. This results in much better penetration of the gel into the skin and improves image quality significantly. These horses can also be difficult to scan due to the presence of skin folds, particularly in the palmar/plantar pastern region, and scanning with the leg in a non-weightbearing position may be of benefit.

Ultrasound Artifacts

An *artifact* is defined as "something observed in a scientific investigation or experiment that is not naturally present but occurs as a result of the preparative or investigative procedure." In terms of ultrasonography, features of the ultrasound image which do not represent actual body tissues or misrepresent the relationship between tissues may be referred to as an artifact. The presence of these artifacts can significantly impede the user's ability to distinguish normal structures from pathological changes. However, understanding the cause of these artifacts enables the user to minimize them where possible, recognize and ignore the artifacts if they cannot be diminished, or even use them to their advantage by actively incorporating the artifact into the ultrasound exam.

Operator Error Artifacts

Artifacts in ultrasonography may be due to operator error or be directly related to the physics of ultrasonography. Common operator error artifacts include poor skin preparation/contact artifacts which are created when the transducer cannot make uniform contact with the skin due to dirt, scabs, hair, or other impediments. Air bubbles between the skin and the transducer also limit the ability of the ultrasound beam to effectively penetrate into the underlying tissues, resulting in artifact production. These artifacts are discussed in greater detail under the sections headed Reverberation Artifact and Acoustic Shadowing Artifact.

Incorrect gain, focal depth, or frequency settings will adversely affect image quality, as will scanning with the ultrasound beam being directed at an angle other than perpendicular to the tissue/region of interest (i.e., "off-incidence"). Optimal images are obtained when the ultrasound beam is at 90 degrees to the tissues being imaged, because this results in the most accurate representation of tissue location in the ultrasound image. If the ultrasound beam is not perpendicular to the tissues, a portion of the ultrasound beam will be reflected into surrounding tissues instead of back to the probe, resulting in fewer echoes returning to the transducer for image formation. For example, when imaging the distal limb in longitudinal section, the tendons will appear darker than normal (hypoechoic), although the borders will generally remain brighter (hyperechoic), which can give the misleading appearance of pathology. Being off incidence, even by a few degrees, can give rise to this artifact, although it can be utilized for diagnostic purposes as it can assist in the visualization and identification of structural margins.

If excessive pressure is applied to a region of the tissues containing either a discrete fluid-filled structure (e.g., ovarian follicle, embryonic vesicle,

Vet-ebooks.com

distended synovial structure) or "free" fluid (e.g., peritoneal effusion), the fluid may be displaced such that the true volume and location is distorted. This may result in the ultrasonographer being unable to detect small volumes of fluid or underestimating the total volume present. The application of excessive pressure can also cause soft tissue structures (e.g., tendons, vascular structures, anterior chamber of the globe) to be deformed, leading to inaccurate representation of margination and shape.

Other artifacts which are the direct result of the physics of ultrasonography are discussed in greater detail below.

Reverberation Artifact

Reverberation artifact is seen when imaging adjacent interfaces with high acoustic impedance (highly reflective interfaces). There are three primary types of reverberation artifact which are classified based on the location and type of structures involved in the production of the artifact: i) transducer and a reflective surface; ii) reflective surfaces which are closely spaced together within the tissues ("comet-tail" artifact); and ii) fluid trapped within a collection of small gas bubbles ("ring-down" artifact).

Regardless of the structures involved and therefore the individual classification of this artifact, reverberation is a result of the ultrasound beam encountering two highly reflective interfaces which are parallel to one another and subsequently being reflected back and forth between them. As the wave reaches the first interface, it is strongly reflected back toward the probe. However, in this scenario, as the wave reaches the second interface, it is then reflected away from the probe and back into the tissues once more. As this sequence takes place again and again, the ultrasound machine continues to receive strong echoes over regular, closely spaced intervals. As previously described, the ultrasound image is constructed by depicting the strength of the returning echo as the echogenicity (degree of brightness) and the length of time taken for the signal to be transmitted through the tissues and return to the probe as depth. Therefore, these numerous, strong echoes are depicted as hyperechoic bands at regular intervals extending into the deeper field of the ultrasound image. Therefore, reverberation artifact generally appears on the ultrasound image as a series of evenly spaced, hyperechoic lines.

For example, when scanning the equine distal limb, air trapped between the probe and the limb will act as a highly reflective interface. As the ultrasound wave leaves the probe and contacts air on the skin surface, the wave is reflected back toward the probe where it is registered and the skin surface is displayed as a hyperechoic line on the ultrasound image. However, some of the returning wave "bounces" off the surface of the probe and back toward the skin. This second wave encounters the highly reflective air–skin interface once more, returns to the probe, and a second hyperechoic line is represented on the image deep to the "true" image display. The process continues to repeat, resulting in a series of evenly spaced, hyperechoic lines appearing to extend into the deeper field of view, which represents the number of times the wave has traveled from skin surface to probe and back (Figure I.14). Therefore, poor contact between the probe and the body will result in reverberation artifact and a loss of visualization of the soft tissue structures of the limb. To minimize this artifact, the patient should be appropriately prepared and additional ultrasound coupling gel should be used throughout the examination. However, it is important to recognize that this artifact will inevitably be seen at the medial and lateral margins of the ultrasound image when scanning the limb in the transverse plane. This is a result of the curved shape of the limb and the fact that the ultrasound probe will likely not be fully in contact with the patient when scanning in this orientation (variable with probe selection and patient conformation). This artifact is also routinely encountered when scanning the equine thorax and *per rectum* imaging of the reproductive tract, as both the aerated lung and gas within the colon/rectum are highly reflective interfaces just below the surface of the transducer (Figure I.15).

When the ultrasound wave encounters two closely spaced, highly reflective surfaces, a portion of the wave

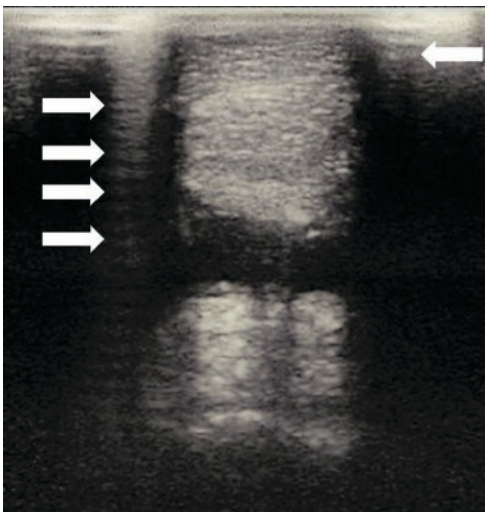


Figure I.14 Cross-sectional image of the equine distal limb with reverberation artifact (arrows) on the lateral and medial aspects of the image resulting from lack of contact between the transducer and the limb in these regions (transducer is wider than the surface of the leg in this scanning plane).

Vet-ebooks.com

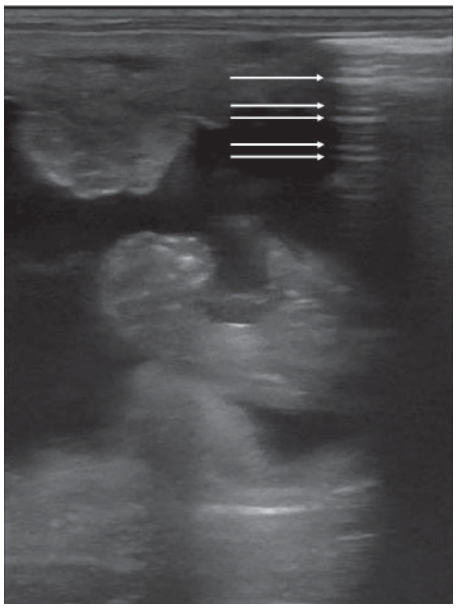


Figure I.15 Image of the equine foetus with reverberation artifact (arrows) resulting from the presence of gas within the rectum.

will become "trapped" between the reflective surfaces where it reverberates back and forth. With each reverberation, some of the wave "escapes" and returns to the probe where it is depicted on the image display as a hyperechoic line. Therefore, the collection of these returning waves has the appearance of a series of bright, white lines which decrease in intensity deep to the reflective surfaces. This is commonly referred to as "comet-tail" artifact. Specific objects which commonly produce comet-tail artifacts are metallic objects (e.g., needle, surgical staple, orthopaedic surgical implant), small calcifications, or crystalline structures.

A specific form of comet-tail artifact, more recently described in the literature as "lung comets," occurs within the thorax at the highly reflective interface of the parietal pleura and the visceral pleura of the physiologically aerated lung as it slides during respiration. When compared to other forms of reverberation artifact, these comet tails within the thorax diminish in intensity with increasing depth and also do not extend the entire depth of the image (they are "shorter" than other forms of reverberation artifact) (Figure I.16). These lung comets are artifacts which should be considered non-pathologic when visualized during ultrasound evaluation of the normal lung and indicate that the visceral and parietal pleura are in contact with one another. Therefore, the lack of lung comets observed in a region of lung indicates that a pathologic process, such as pneumothorax, is present which has resulted in separation of the pleural layers.

Another subcategory of reverberation artifacts is the "ring-down" artifact. If an ultrasound wave strikes a pocket of fluid trapped within a collection of gas bubbles such as in the gastrointestinal tract, the

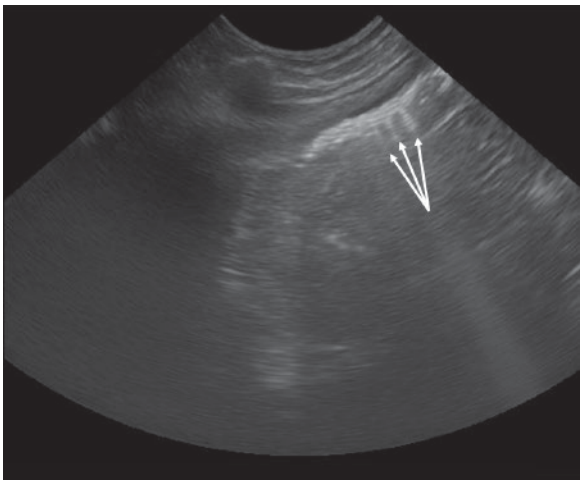


Figure I.16 Image of the thorax with visible "lung comets" (arrows), representing the ultrasound appearance of normal lung.

interface between the gas bubbles and the fluid is highly reflective. In this scenario, the ultrasound waves reverberate ("ring") inside the fluid, with a portion of the wave "escaping" with each reverberation and returning to the probe. These echoes are detected and displayed on the ultrasound image as either a continuous hyperechoic line or a series of parallel hyperechoic bands extending deep to the collection of gas. This specific type of reverberation artifact is commonly referred to as "ring-down" artifact. In comparison to the comet-tail artifact, when visualizing ring-down artifact, the hyperechoic bands do not diminish in intensity with increasing depth and they also extend to the deep edge of the ultrasound image.

When in association with thoracic ultrasonography, this specific type of ring-down artifact is referred to as "B-line" artifact. These B-lines originate at the pleural line and are seen to move in synchrony with respiration/lung sliding. B-line artifact in the thorax occurs in the presence of pathology, such as pulmonary oedema, due to the change in the pulmonary parenchyma that pathologic conditions create (Figure I.17). In abnormal lung, the presence of fluid, cellular infiltrate, or inflammatory cells increases the opportunity for the development of fluid trapping between a collection of gas bubbles which creates all forms of ring-down artifact. Therefore, the visualization of numerous B-lines within the thorax is indicative of a pathologic process. B-lines may also occasionally be observed when imaging healthy lung, but in fewer numbers per intercostal space than when pathology is present (typically greater than 3 B-lines per field of view is considered pathologic).

It is important to recognize that, in recent years, ultrasonographers have provided clarification regarding the nomenclature of specific types of reverberation artifact. In particular, what has historically been referred to as comet-tail artifacts in the thorax are actually B-lines, a form of ring-down artifact as

Vet-ebooks.com

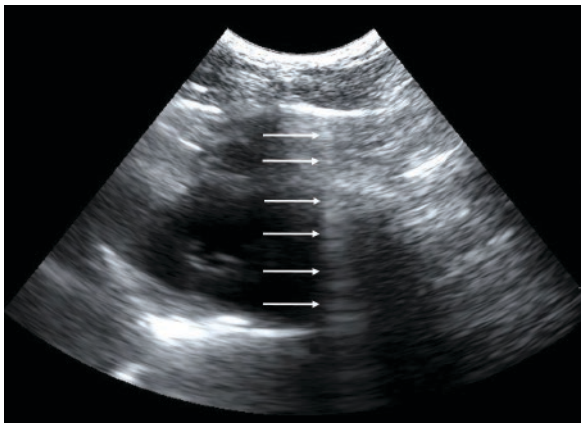


Figure I.17 Image of the equine thorax with "ring-down" artifact ("B-line") (arrows) due to the presence of pulmonary oedema.

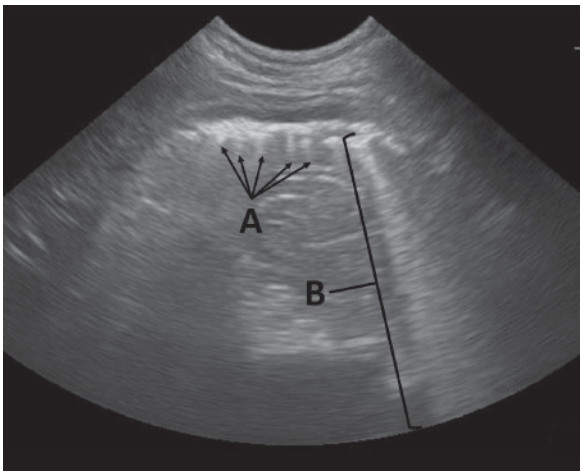


Figure I.18 The differing appearance of "comet-tails" (A) and "B-lines" (B) on ultrasound evaluation of the lung.

described above. To summarise, true comet-tail artifacts within the thorax are observed when imaging normal lung and are the result of the visceral and parietal pleura being in normal anatomical contact. Therefore, a decrease in the observance of comet-tails or synonymously, lung comets, is indicative of the presence of pathology. B-lines (which have previously been referred to as comet-tails), are most commonly identified when lung pathology is present and are, in fact, a form of ring-down artifact (Figure I.18).

Reverberation artifacts in the near-field may also be a result of the ultrasound beam itself as waves released from the piezoelectric crystals in the transducer require a short distance to coalesce into an organized wave. This distance varies primarily with the frequency capability of the probe, with higher frequency transducers producing less reverberation artifact in the near-field. If necessary, a "standoff" may be used to reduce the appearance of this artifact, particularly when evaluating superficial structures in the distal limb such as the superficial digital flexor tendon.

Acoustic Enhancement Artifact

Acoustic enhancement artifact is created when the ultrasound waves pass through a tissue causing minimal attenuation, such as fluid, and appears as an artifactual brightness of tissues deep to that fluid-filled structure. As previously described, ultrasound waves are attenuated as they pass through the body, resulting in a loss of strength of echoes returning to the probe from deeper tissues. Without the appropriate usage of the TGC controls, these deeper tissues (those farther away from the probe) would therefore appear artifactually less echogenic (hypoechoic) than more superficial structures. Conversely, if the ultrasound beam is not attenuated by more superficial structures (e.g., because they are fluid filled), the waves reaching

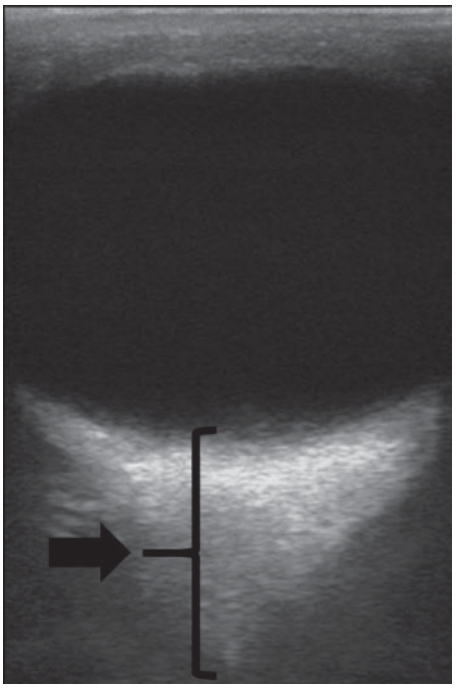


Figure I.19 Image of an equine globe and orbit with acoustic enhancement artifact (arrow) deep to the vitreous.

the deeper tissues will be relatively stronger than they should be at that given depth. Thus, the waves reflected back to the probe from these regions will also be stronger, resulting in an artifactual brightness (increased echogenicity or hyperechoic) of tissues deep to the fluid filled structure being displayed on the ultrasound image. This is referred to as **acoustic enhancement** and is commonly associated with ultrasonography of fluid-filled structures such as tendinous "core" lesions, cystic lesions, ovarian follicles, early embryonic vesicles, and the eye as ultrasound waves are not attenuated by fluid (Figure I.19). This can also be observed when imaging the distal limb as the

Vet-ebooks.com

metacarpal/tarsal vessels will not attenuate the ultrasound wave, thereby the underlying suspensory ligament will appear artifactually brighter (hyperechoic) when imaged through these vessels.

Acoustic enhancement may interfere with assessment of tissues deep to a fluid-filled structure as well as the deep margin/interface of the fluid and underlying soft tissue. The user may find it useful to decrease the degree of brightness in the far-field by adjusting the TGC controls for the areas deep to the fluid to minimize the appearance of this artifact. In other words, by decreasing the gain in the deeper field of view, the structures in the far-field (including the wall of the fluid-filled structure) may be evaluated more readily. It is important that the TGC is then reset for the remainder of the ultrasound examination.

Acoustic Shadowing Artifact

In contrast to acoustic enhancement, *acoustic shadowing artifact* results from the complete or near complete reflection of the ultrasound beam at a highly reflective interface.

As previously described, when an ultrasound wave reaches a highly reflective interface, such as mineral/soft tissue or gas/soft tissue, the vast majority of waves are reflected back to the probe resulting in a uniform, hyperechoic line being displayed for that corresponding depth. Therefore, the reflected ultrasound beam will not reach the structures deep to the highly reflective interface and that region will appear uniformly anechoic or hypoechoic as none/very few echoes are being received from that depth. This is termed *acoustic shadowing* and is observed in deep to bony structures such as the metacarpals/metatarsals, ribs (Figure I.20), sesamoid bones of the fetlock joint (Figure I.21), and pelvis, as well as gaseous structures such as aerated lung and loops of intestine. It should be noted that acoustic shadowing and reverberation artifact may both be present when imaging these types of structures.

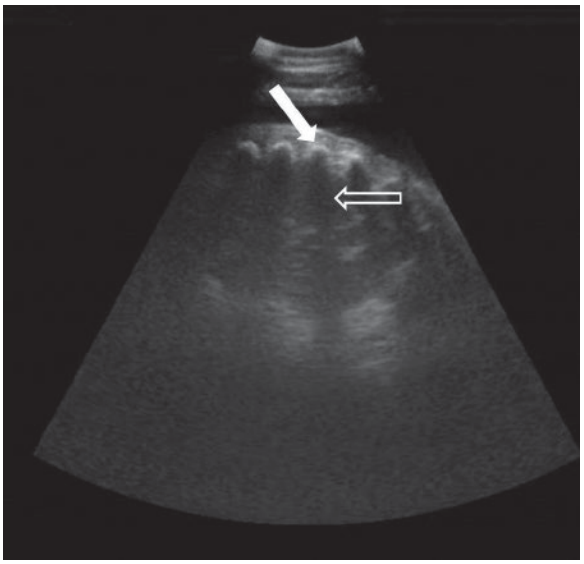


Figure I.20 Image of the equine foetus demonstrating acoustic shadowing artifact (open arrow) deep to the hyperechoic foetal rib (closed arrow).

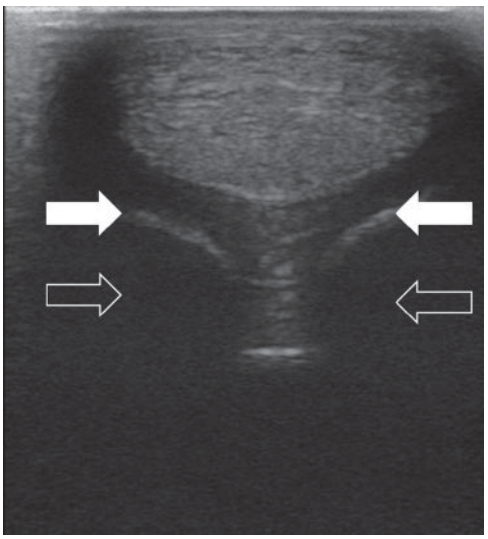


Figure I.21 Acoustic shadowing demonstrated in this cross-sectional image of the equine distal limb at the level of the sesamoid bones of the fetlock joint with anechoic regions (open arrows) deep to the hyperechoic cortex of the sesamoid bones (closed arrows).

Edge Shadowing Artifact

Edge shadowing, also known as edge refraction, occurs deep to a curvilinear interface and is caused by the ultrasound wave striking such an interface at an angle. The interaction of an ultrasound beam with the lateral margins of a spherical/curved structure can result in the wave being redirected or "bent" away from the structure and into the deeper tissues with no ultrasound waves being transmitted directly below the edges of that structure. Therefore, no echoes are returned to the probe from these areas and an anechoic line or "cone" originating at both edges of the structure and extending into the deeper tissues is displayed. This ultrasonographic appearance is known as the *edge shadowing artifact*. Uterine horns, ovarian follicles, ovaries, and the globe are all examples of structures causing edge shadowing artifact (Figure I.22). This can also commonly be seen when imaging the suspensory branches from the palmar/plantar aspect of the limb.

Slice-Thickness Artifact

Slice-thickness artifact is related to ultrasound beam width and is responsible for the artifactual appearance of soft tissue within a fluid-filled viscus

Vet-ebooks.com

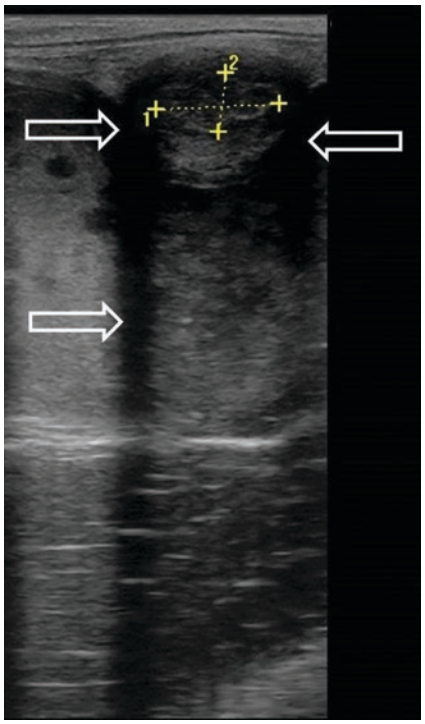


Figure I.22 Edge shadowing artifact is evident in this ultrasound image of the equine reproductive tract (open arrows). (*Source:* BCF Technology Ltd. Reproduced with permission).

("pseudo-sludge"). The relationship between beam width and the distance between two points in the tissues has previously been described under the topic of image resolution. In addition to the negative effect on lateral resolution, a beam that is wider ("thicker") than the distance between two defined points along its path ("slice") may also result in the production of an image artifact. This *slice-thickness artifact* is most appreciable when imaging near the periphery of a curved, fluid-filled structure. Depending on the cellularity of the fluid, these structures should appear on the ultrasound image as hypo/anechoic with a more hyperechoic margin representing the wall. If the orientation of the probe is such that the ultrasound wave is directed along the margin of a curved, the fluid-filled structure and the beam is wide, tissue reflectors from the wall and surrounding tissues will be detected and reflect a portion of the wave, while the remainder of the wave passes through the fluid unimpeded. Thus, instead of the fluid appearing anechoic, the additional tissue reflectors will be represented as more hyperechoic material within this region of the ultrasound image, thereby giving the fluid an artificially flocculent appearance. For example, slice-thickness artifact may mimic the presence of reflective material within the vitreous chamber or particulate material within a preovulatory follicle (Figure I.23).

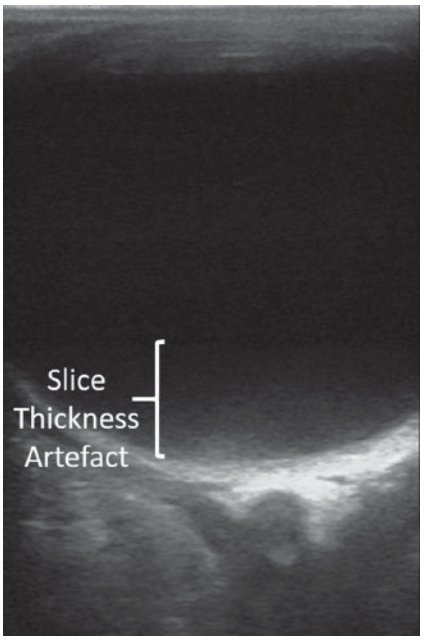


Figure I.23 Slice-thickness artifact (open arrow) is commonly observed when imaging curved, fluid filled structures such as this equine globe and orbit.

Distinguishing between fluid containing tissue reflectors and slice-thickness artifact can be achieved by changing the position of the probe or altering the width of the beam. Moving the probe in relation to the anatomical region of interest will change the path of the ultrasound wave such that it will contact the fluid-filled structure at various angles. This will cause the artifact to disappear or be diminished at different orientations of the beam while true sediment or particulate matter will have a more consistent ultrasonographic appearance. Narrowing of the beam also diminishes the presence of slice-thickness artifact and the user can accomplish this by focusing the beam in the region of the image where the artifact is observed. It may also be helpful to note the relationship of the fluid and the potential material within it. Artifactual sediment has a curved surface and true sediment/flocculent material generally has a flat surface and may be resuspended upon gentle agitation of the fluid-filled structure.

Side-Lobe Artifact

Side-lobe artifact occurs when accessory ultrasound waves contribute erroneous information regarding tissue location and echogenicity during image formation. The ultrasound beam emitted from the transducer is comprised of a primary beam which is directed perpendicular to its point of origin on the probe and the tissues below it. However, there are also accessory beams ("side-lobes") on either side of the primary beam which are weaker and do not travel

Vet-ebooks.com

perpendicularly to the underlying tissues. Due to their weak nature, interaction between these side-lobes and body tissues generally does not result in the production of echoes which will contribute to the displayed image. However, if a highly reflective interface is along the path of these accessory, non-perpendicular waves, the interaction may result in an echo of appreciable strength returning to the probe. The location of this structure will be correctly represented by the primary beam; however, it will also be represented as being located to the side of the actual structure. This side-lobe artifact will be less echogenic than the true structure appearance because it is originating from weaker echoes. This effect is most pronounced when a highly reflective structure is present within an anechoic region (e.g., the foetal skeleton within the foetal fluids) (Figure I.24).

Mirror-Image Artifact

Similar to reverberation artifact, a *mirror-image artifact* is caused by a disruption in the normal sequence of travel of an ultrasound wave as a result of an interaction with a highly reflective interface. A mirror-image artifact is characterized by a misrepresentation of a structure's location on both sides of the reflective interface. The "true" component of the image is created by the usual interaction of an ultrasound wave with a reflective structure within the tissues (echoes traveling from probe to tissue reflector and then directly back to the probe). The artifactual region of the image is produced by that portion of the beam which first contacts the highly reflective interface and is reflected into another area of the tissues instead of returning to the probe. The wave is then reflected back toward the interface and upon reaching the interface for a second time, is finally returned to the probe. The ultrasound machine is only able to interpret the time taken for this portion of the beam to return to the transducer, not the diverted path of travel. As this travel time is prolonged by the additional reflections, the ultrasound machine translates this as the tissue reflector being farther away from the ultrasound probe (e.g., at a greater depth). Therefore, the final image construction combines the "true" image on the appropriate side of the highly reflective interface (more superficial) with the "mirror" image on the opposite side of that interface (deeper).

This is commonly appreciated in ultrasonography of the cranial abdomen in small animals at the highly reflective interface of the lung-diaphragm interface (gas–soft tissue interface) and may also be appreciated in equine patients at this same location. Mirror-image artifact may also be observed on ultrasonography of the equine reproductive tract (duplication of ovary or foetus is possible if a highly reflective loop of intestine or muscle is present). It is important to consider the possible presence of this artifact if additional, unexpected structures are visualized on the ultrasound image, as these could otherwise be mistaken for pathology. Redirection of the transducer in different scanning angles/planes may diminish or completely eliminate this artifact, making it possible for the user to evaluate the actual region of interest more readily.

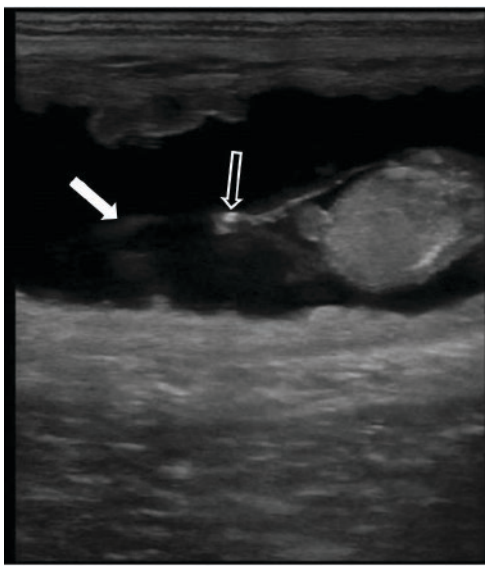


Figure I.24 Image of the equine foetus with the highly reflective bones of the distal limb causing reflection of side-lobes echoes and the inaccurate representation of the location of the limbs (closed arrow) adjacent to the actual location of the foetal limbs (open arrow).

Doppler Imaging

Doppler imaging enables the direction and velocity of blood flow within the patient to be determined and represented in an ultrasound image. The speed of ultrasound waves traveling in soft tissue is a known constant value. In addition, the frequency of the ultrasound wave being used is also known (dependent on the transducer frequency setting determined by the user). Using these two known values, the machine is able to calculate the movement of structures (e.g., red blood cells) relative to the ultrasound beam and display the speed and direction of this movement on the ultrasound image.

As the ultrasound wave strikes a moving object, the wave will be reflected and returned to the probe. The frequency of the wave will have been altered by the interaction with the moving object. An increase in the ultrasound wave frequency will occur if the object is moving toward the probe and is referred to as a "positive frequency shift." Conversely, the wave frequency will decrease if the object is moving away from the probe and is recognized as a "negative frequency shift."

Vet-ebooks.com

Therefore, the difference between the frequency of the wave transmitted from the probe and the frequency of the wave returning to the probe can be calculated and this difference in frequency is the "Doppler shift" (Figure I.25). Therefore, if an object, such as a red blood cell, is moving along the path of the ultrasound wave, the direction (away from or toward the probe) and the speed of the moving object can be determined by the ultrasound machine due to the change in the frequency of the returning ultrasound wave.

Doppler Modes

There are distinct Doppler modes which provide the user with additional information regarding tissue movement. More commonly available modes include spectral, color flow, and power Doppler.

Spectral Doppler

Spectral Doppler is useful for quantifying the velocity and direction of blood flow in relation to time. When the ultrasound machine is in spectral Doppler mode, the ultrasound probe receives the returning echo signal and the machine records the Doppler frequency shift in a graphical representation referred to as a "trace." Each spectral waveform is thus representing the velocity of blood flow over time. This is depicted by a sharp line bounding the area of each waveform on the spectral trace, and is often referred to as the "envelope." Areas of the spectral trace above the baseline represent blood flow toward the probe (Figure I.26), while those areas below the baseline represent blood flow away from the probe (Figure I.27).

The two main types of spectral Doppler are pulsed wave (PW) Doppler and continuous wave (CW) Doppler.

Pulsed Wave (PW) Doppler

In pulsed wave Doppler mode, the same crystal both sends and receives the ultrasound waves responsible for the Doppler display. While in B-mode, the region of interest is identified (e.g., blood vessel, valvular region)

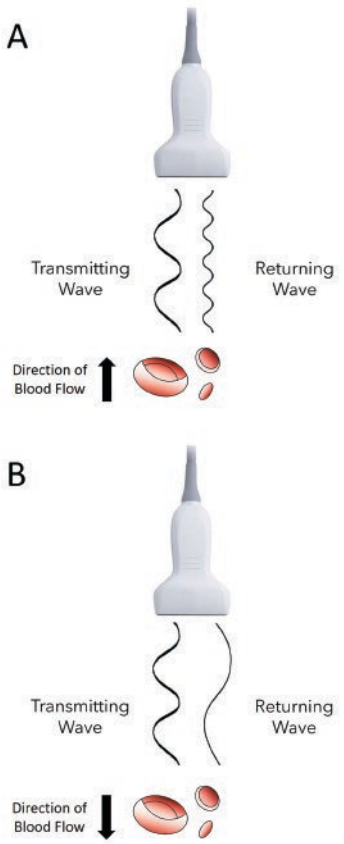


Figure I.25 Illustrations of Doppler shift: (A) positive Doppler shift when the flow of blood is toward the transducer and the returning wave is of a higher frequency than the transmitted wave; (B) negative Doppler shift when the flow of blood is away from the transducer and the returning wave is of a lower frequency than the transmitted wave.

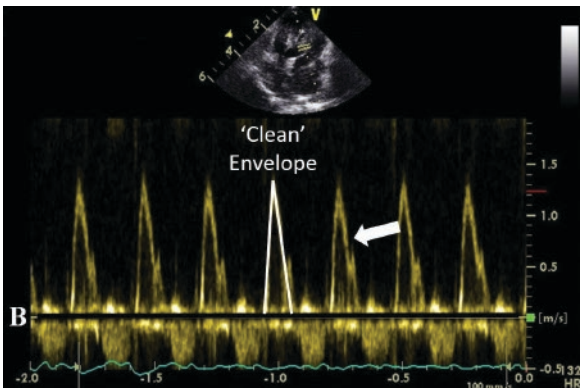


Figure I.26 Spectral Doppler trace with "envelopes" above the baseline (B) representing direction of bloodflow toward the probe (arrow).

FPO

Figure I.27 Spectral Doppler trace with envelopes below the baseline (B) representing direction of bloodflow away from the probe (arrow).

Vet-ebooks.com

and the view is optimized for Doppler investigation. Most importantly, it is imperative that the ultrasound beam be parallel to the line of blood flow for the most accurate velocity readings to be obtained. PW Doppler mode is selected and an electronic "gate" is displayed which is then used to specify the sampling region (e.g., the region of the valve leaflets). Only echoes retuning from this region will be displayed. Thus, PW Doppler is very specific for identifying velocity of blood flow in a discrete location.

In PW Doppler mode, the machine is also able to detect turbulence of flow which is helpful when investigating possible valvular disease. Smooth (laminar) flow will be displayed with a "clean" envelope as the red blood cells are traveling at a near-uniform velocity (Figure I.28). Turbulent flow (where the red blood cells are traveling at various velocities due to an obstruction which results in abnormal blood flow) will result in spectral broadening (display of low, medium, and high velocities) and possibly an increase in the peak (highest) velocity. Therefore, the envelope will not be "clean," as a wide range of velocities will be depicted.

The crystal sending the ultrasound wave must wait for the signal to return from the gated region before sending another wave. Therefore, if the red blood cells are traveling at a high velocity, they may overtake the returning ultrasound signal before it reaches the probe and the next ultrasound signal is emitted. Otherwise stated, the velocity of bloodflow is faster than the pulse repetition frequency. This results in aliasing, where the high frequency portion of the signal is displayed on the wrong side of the baseline ("wrapped around"), resulting in the true measurement of this high velocity flow being inaccurately represented on the spectral trace. Therefore, PW Doppler is unreliable when measuring high velocity blood flow.

Continuous Wave (CW) Doppler

In comparison to PW Doppler, CW Doppler is performed by two separate crystals housed within the transducer. One crystal continuously emits an ultrasound signal while the other crystal continuouly receives the ultrasound signal. Therefore, there is constant sampling of Doppler frequency shift along the length of the ultrasound beam. As a result, CW Doppler is highly accurate for measuring Doppler shift (high sensitivity) and higher velocity blood flow can be recorded compared to PW Doppler. However, as there are numerous velocities being recorded simultaneously, the envelope will not be "clean" and is referred to as being "filled-in." In other words, the spectral trace of a CW Doppler study will be displayed with the red blood cells traveling at the greatest velocity being on the outer edge of the trace and those at lower velocity being displayed in the space below that curved outline, "filling" it in. (Figure I.29).

Color Flow Doppler

Color flow Doppler is a variation on PW Doppler where a gate is used to identify the sampling region of interest. Instead of the velocity and direction of flow being plotted against time on a spectral trace, the direction and relative velocity of blood flow are characterized and displayed through the use of colur-coding (Figure I.30). The colors displayed are user defined; however, convention dictates that the direction of flow in relation to the transducer should follow the acronym BART – blue away, red toward. Turbulent flow is indicated by a mosaic of color, with green usually indicating non-laminar flow. The relative velocity of flow may be indicated by the brightness of hue (i.e., higher velocity, brighter hue). Aliasing can occur with high velocities as this form of Doppler is a variation on PW Doppler.

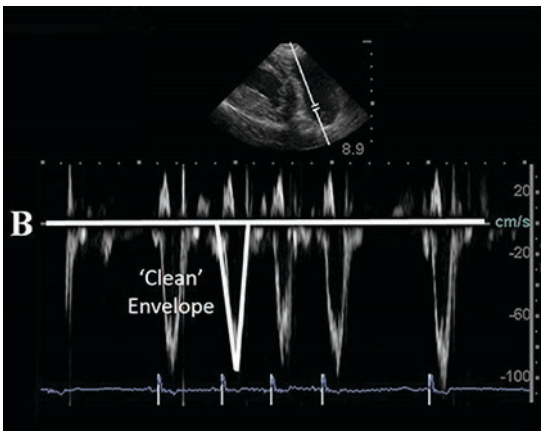


Figure I.28 Pulsed Wave (PW) Doppler study of blood flow through the pulmonic valve. Note the "clean" envelope indicating laminar flow and display below the baseline (B) indicating primary direction of blood flow away from the transducer.

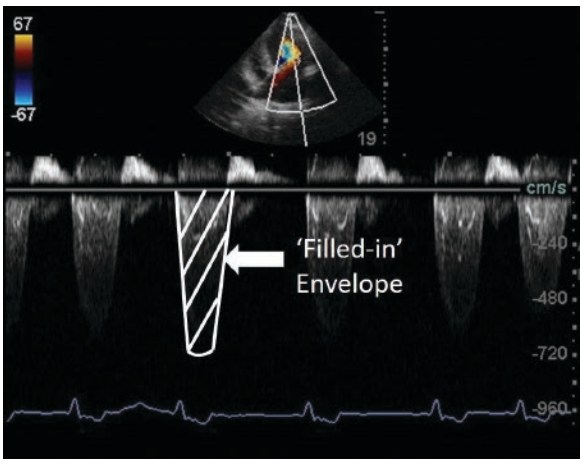


Figure I.29 Continuous wave (CW) Doppler trace exhibiting a 'filled-in' envelope (arrow).

Vet-ebooks.com

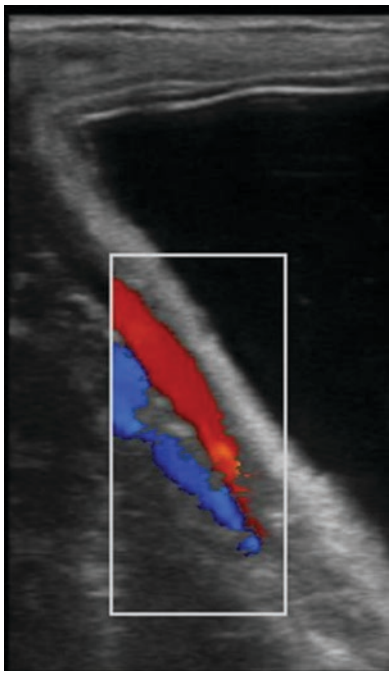


Figure I.30 Color flow Doppler image representing arterial and venous bloodflow in the region of the utero-placental unit.

Power Doppler

Power Doppler is a form of Doppler which analyzes the total strength of the returning echoes and ignores direction of flow. A color map of the Doppler frequency shift is created where the hue and brightness of the displayed color represent the power of the returning signal (superimposed on a B-mode image). When in Power Doppler mode, the machine is able to detect very low velocity blood flow and may be useful for identifying blood flow within a suspected lesion.

Summary/Conclusion

Ultrasonography is a versatile, powerful, and invaluable component of the equine veterinary diagnostic toolbox. In order to maximize the diagnostic quality of the information obtained during the ultrasound examination, a practical working knowledge of ultrasound physics is required. This will enable the clinician to fully optimize the machine settings, understand and interpret the image displayed, and also avoid the potential pitfalls associated with the appearance of artifacts on the ultrasound image. Finally, and perhaps most importantly, this knowledge will also enable the ultrasonographer to perform the examination with greater skill and confidence.

Recommended Reading

Choudhry, S., Gorman, B., Charboneau, J.W. et al. (2000). Comparison of tissue harmonic imaging with conventional US in abdominal disease. *Radiographics* 20: 1127–1135.

Curry, T.S. III, Dowdey, J.E., and Murray, R.C. Jr. (1990). *Christensen's Physics of Diagnostic Radiology*, 4th ed. Philadelphia: Lea & Febiger.

Dietrich, C.F., Mathis, G., Blaivas, M. et al. (2016). Lung B-line artifacts and their use. *Journal of Thoracic Disease* 8(6): 1356–1365.

Evans, D.H. and McDicken, W.N. (2000). *Doppler Ultrasound: Physics, Instrumentation, and Signal Processing*, 2nd ed. New York: Wiley.

Feldman, M.K., Katyal, S., and Blackwood, M.S. (2009). US artifacts. *Radiographics* 29: 1179–1189.

Ginther, O.J. (1996). *Ultrasonic Imaging and Animal Reproduction: Fundamentals, Book 1*. Cross Plains: Equiservices Publishing.

Goldstein, A. (1993). Overview of the physics of US. *Radiographics* 13: 701–704.

Kremkau, F.W. (2002). *Diagnostic Ultrasound: Principles and Instruments*, 6th ed. Philadelphia: W.B. Saunders Company.

Kristoffersen, M., Öhberg, L., Johnston, C. et al. (2005). Neovascularisation in chronic tendon injuries detected with colour Doppler ultrasound in horse and man: implications for research and treatment. *Knee Surgery, Sports Traumatology, Arthroscopy* 13: 505–508.

Lee, F.C.Y., Jenssen, C., and Dietrich, C.F. (2018). A common misunderstanding in lung ultrasound: The comet tail artifact. *Medical Ultrasonography* 20(3): 379–384.

Louvet, A. and Bourgeois, J.M. (2008). Lung ring-down artifact as a sign of pulmonary alveolar interstitial disease. *Veterinary Radiology and Ultrasound* 49(4): 374–377.

Matheson, J.S., O'Brien, R.T., and Delaney, F. (2003). Tissue harmonic ultrasound for imaging normal abdominal organs in dogs and cats. *Veterinary Radiology and Ultrasound* 44(2): 205–208.

Merritt, C.R.B. (1991). Doppler US: The basics. *Radiographics* 11: 109–119.

Penninck, D.G. (1995). Imaging artifacts in ultrasound. In: *Veterinary Diagnostic Ultrasound* (ed. T.G. Nyland and J.S. Mattoon). Philadelphia PA: W.B. Saunders Company.

Pozniak, M.A., Zagzebski, J.A., and Scanlan, K.A. (1992). Spectral and color Doppler artifacts. *Radiographics* 12: 35–44.

Reubin, J.M. (1994). Spectral Doppler US. *Radiographics* 14: 139–150.

Vet-ebooks.com

Scanlan, K.A. (1991). Sonographic artifacts and their origins. *American Journal of Roentgenology* 156: 1267–12272.

Shapiro, R.S., Wagreich, J., Parsons, R.B. et al. (1998). Tissue harmonic imaging sonography: Evaluation of image quality compared with conventional sonography. *American Journal of Roentgenology* 171: 1203–1206.

Tranquart, F., Grenier, N., Ader, V. et al. (1999). Clinical use of ultrasound tissue harmonic imaging. *Ultrasound in Medicine and Biology* 25(6): 889–894.

Zagzebski, J.A. (1996). *Essentials of Ultrasound Physics*. St Louis MO: Mosby, Inc.

Ziskin, M.C. (1993). Fundamental physics of ultrasound and its propagation in tissue. *Radiographics* 13: 705–709.

Vet-ebooks.com

Vet-ebooks.com

Section 1

Musculoskeletal

Vet-ebooks.com

Vet-ebooks.com

1

Ultrasonography of the Foot and Pastern

Ann Carstens[1] *and Roger K.W. Smith*[2]

[1] *University of Pretoria, Onderstepoort, South Africa*
[2] *The Royal Veterinary College, North Mymms, Hatfield, UK*

The Foot

Lameness associated with the foot is common and routinely evaluated using radiography. However, many causes of lameness are associated with soft tissue pathology where there are no or minimal radiographic changes. While magnetic resonance imaging (MRI) has become the imaging modality of choice for identifying such soft tissue causes, MRI is costly and not always available. Therefore, ultrasonography is a logical imaging modality to consider but its use is compromised by the presence of the hoof capsule, which precludes imaging through it. However, there are three ultrasonographic windows where images can be obtained of structures of the foot – proximal to the coronary band palmarly and dorsally, and transcuneally/transsolarly.

Ultrasonography Proximal to the Coronary Band

A number of structures within the foot extend proximal to the coronary band and so lend themselves to ultrasonographic examination.

Preparation

The hair should be clipped and cleaned as for other ultrasound examinations. Gel should be rubbed onto the area and left for a few minutes to improve contact as this is often limiting.

Technique

For the palmar aspect of the foot a small footprint transducer (ideally a microconvex transducer) can be placed longitudinally between the bulbs of the heel, with the foot placed on a wooden wedge, as used for foot radiography (Figure 1.1), so as to have the fetlock partially flexed and the foot extended. This allows the assessment of the deep digital flexor tendon (DDFT), the palmar pouch of the distal interphalangeal (DIP) joint, the collateral sesamoidean ligament ("T" ligament), and the navicular bursa distally to the level of the proximal border of the navicular bone (Figure 1.2). The small footprint of a microconvex transducer can also enable transverse images in this location. However, the DDFT is off-incidence to the ultrasound beam and hence is hypoechoic, and the imaging window incorporates only the middle portion of the DDFT, making identification of DDFT tears, most commonly present in the lobes, difficult unless there is fibrosis which results in retained echogenicity within an anechoic tendon.

A microconvex transducer can also be used in an oblique orientation to guide a spinal needle into the navicular bursa without going through the DDFT (Figures 1.2 and 1.3).

For the dorsal, medial, and lateral aspects, the transducer is positioned both transversely and longitudinally adjacent and directly over the coronary band where the ultrasonographic transmission properties are improved (Figure 1.4) and moved from the dorsal aspect to the dorsomedial and dorsolateral aspects where the dorsal joint capsule and collateral ligaments of the DIP joint (Figure 1.5) can be imaged immediately proximal to the coronary band. The collateral ligaments traverse the coronary band and so only the proximal third of the ligament are visible ultrasonographically. Care should be taken to ensure the transducer is on-incidence to the collateral

Atlas of Equine Ultrasonography, Second Edition. Edited by Jessica A. Kidd, Kristina G. Lu and Michele L. Frazer.
© 2022 John Wiley & Sons Ltd. Published 2022 by John Wiley & Sons Ltd.
Companion Website: www.wiley.com/go/kidd/atlas

Vet-ebooks.com



Figure 1.1 Positioning of either a curvilinear (A) or linear (B) transducer between the bulbs of the heels to image the palmar aspect of the foot.

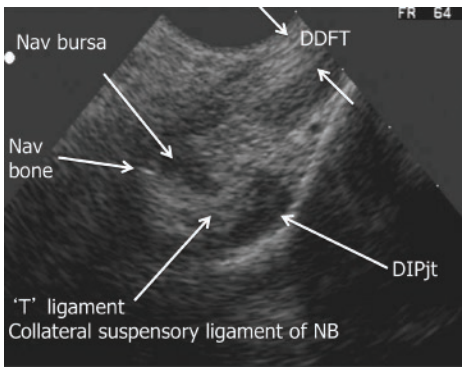


Figure 1.2 Normal sagittal ultrasonographic anatomy of the palmar foot. Proximal is to the right.

ligament as it is easy to generate off-incidence artifacts in the ligaments that can resemble pathology (Figure 1.6). Further caudally lie the collateral cartilages, which are hypoechoic but can show areas of ossification (and therefore acoustic shadowing).

Ultrasound Guided Injections of the Collateral Ligaments of the Distal Interphalangeal Joint

Injuries to the collateral ligaments are often associated with a guarded prognosis and hence there has been enthusiasm to perform intraligamentar injections of affected cases. Both radiographic, MRI, and, most recently, ultrasonographic guided injection techniques have been published. As most collateral ligament injuries involve the distal portions of the ligament, longitudinally guided injections are essential. The ultrasound technique involves inserting a 1.5-inch needle vertically downward approximately 2 cm proximal to the coronary band over the affected ligament in a location determined from a transverse ultrasound examination. Once the needle has been inserted through the skin, the transducer is swivelled 90 degrees into a longitudinal orientation over the ligament. The needle is then advanced under ultrasound guidance ensuring that the needle enters the ligament as abaxially as possible within the ultrasound window. The needle is then advanced until it hits bone. Concurrent radiographic assessment of its distal position can be helpful but it must be appreciated that even when using this guided technique there is a high risk of injecting the joint accidentally.

Ultrasonographic Abnormalities

Via the palmar window, distension of the palmar/plantar pouch of the distal interphalangeal joint and/or the proximal pouch of the navicular bursa, and chronic DDFT pathology, where there is retained echogenicity and/or mineralization within the off-incidence hypoechoic DDFT, can be visualized ultrasonographically (Figure 1.7). In some cases, DDFT

Vet-ebooks.com

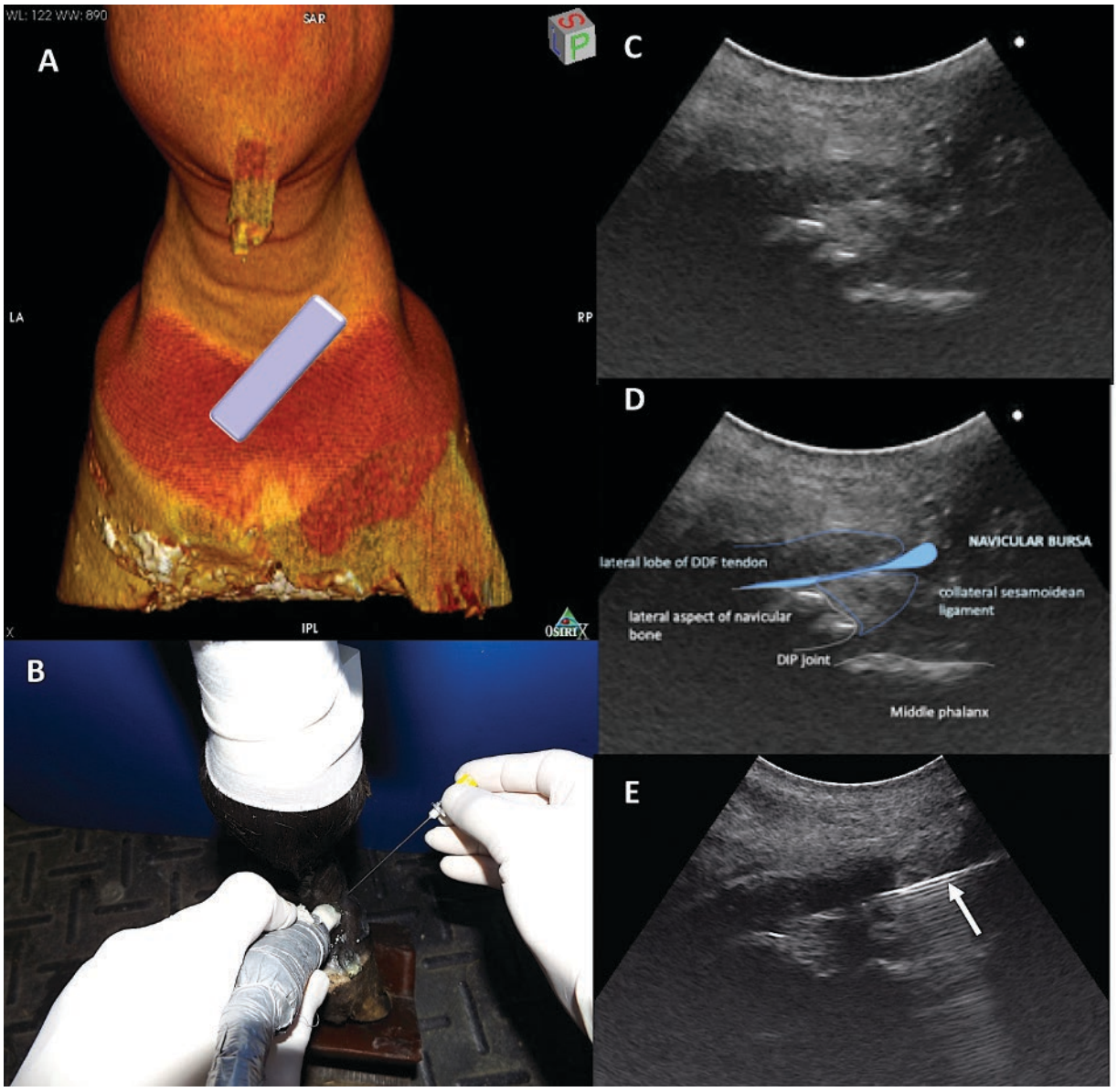


Figure 1.3 Ultrasound guided tendon sparing approach to the navicular bone [1]. (A) shows the orientation of the microconvex transducer between the bulbs of the heel. (B) shows the alignment of the spinal needle (introduced just proximal to the ipsi-axial collateral cartilage) to the microconvex transducer. (C) shows a representative image, which is annotated in (D). (E) shows the spinal needle being guided into the navicular bone deep to, and avoiding penetrating, the deep digital flexor tendon. (Images courtesy of Dr Michael Schramme).

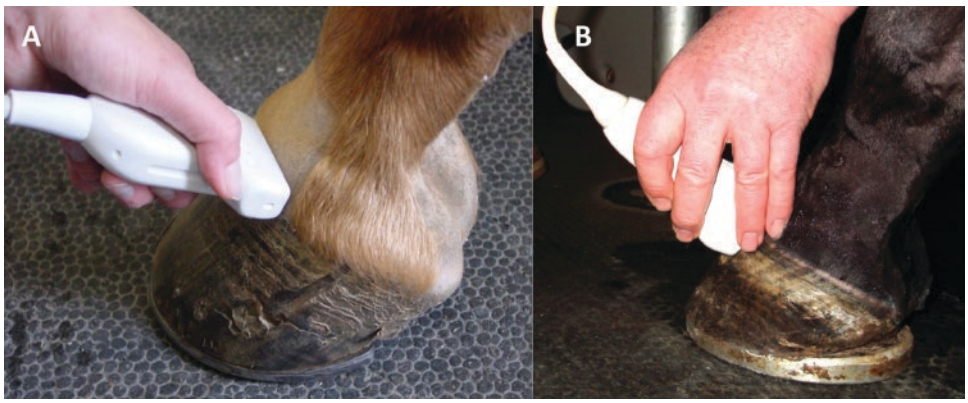


Figure 1.4 Linear transducer positioning to evaluate the dorsal and dorsolateral/dorsomedial aspects of the foot. Note the transducer spanning the coronary band in the longitudinal orientation.

Vet-ebooks.com

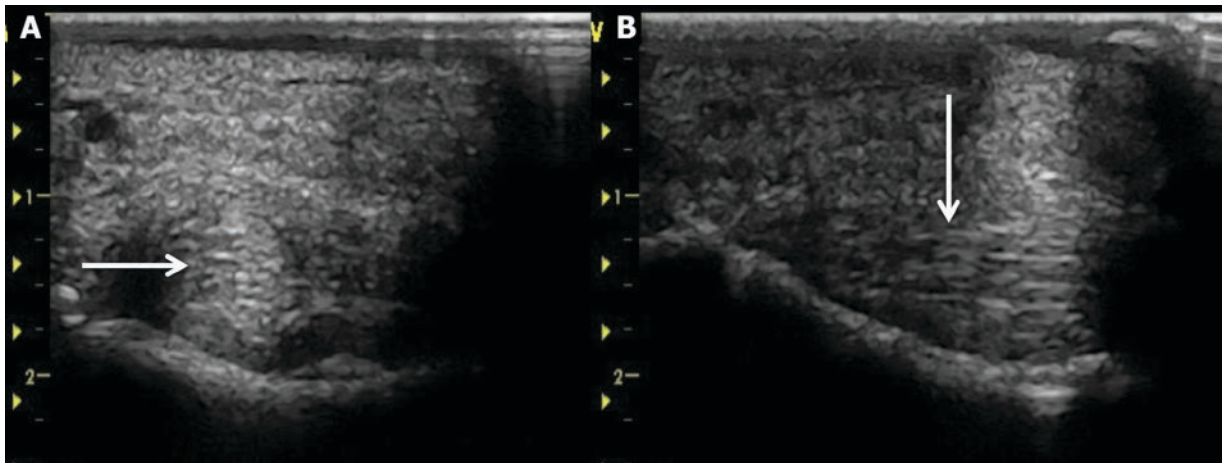


Figure 1.5 Normal ultrasonographic appearance of the distal interphalangeal joint collateral ligaments. (A) Transverse image: note the oval-shaped collateral ligament (arrow) lying in a depression in the underlying bony surface of the second phalanx. (B) Longitudinal image (proximal to the left): the longitudinal striations of the ligament are visible (arrow). Note the acoustic shadowing over the hoof capsule.

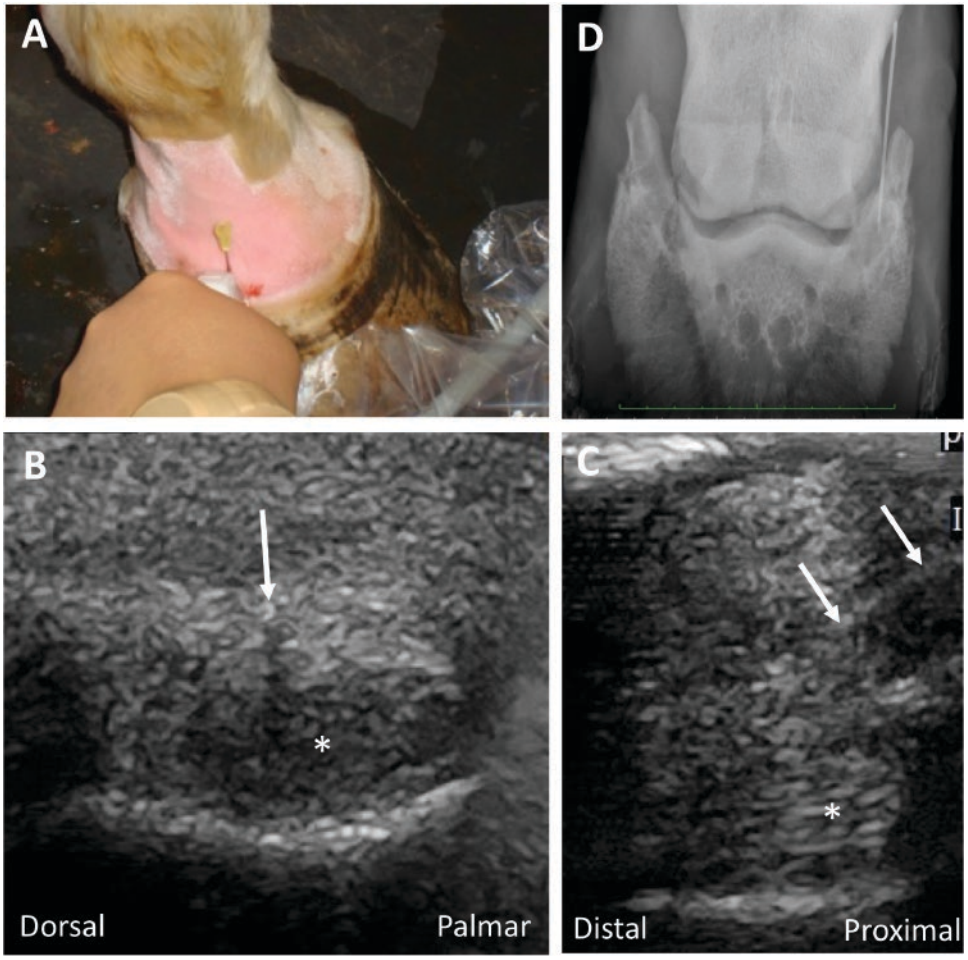


Figure 1.6 Ultrasound-guided injection of the distal interphalangeal joint collateral ligaments. (A) A 1.5- or 2-inch needle is inserted vertically downward in the standing limb approximately 2 cm proximal to the coronary band. Its position over the collateral ligament is identified using a transversely orientated view at the level of the coronary band (B). The needle is then advanced distally, entering the collateral ligament as superficially as possible, with in-plane targeting (C and A). The end of the needle is no longer visible once it disappears under the hoof capsule but it is advanced until in contact with bone. A radiograph can be obtained to determine the needle's accurate location in the fossa of insertion of the ligament onto the distal phalanx (D) but there is still a high risk of entering the distal interphalangeal joint [2].

Vet-ebooks.com

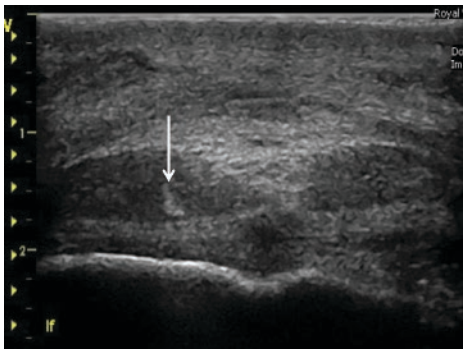


Figure 1.7 Transverse ultrasound scan obtained with a linear transucer directed distally from the distal palmar ultrasound "window" to the foot. There is retained echogenicity in an off-incidence transverse image of the distal deep digital flexor tendon consistent with chronic tendinopathy and/or mineralization.

pathology within the foot will extend sufficiently proximally to be visible in standard views within the distal pastern (see Chapter 2).

Abnormalities of the distal interphalangeal joint can result in changes to the dorsal pouch which are visible ultrasonographically – both distension and synovial thickening (Figure 1.8) as well as osteophytosis in cases of osteoarthritis (Figure 1.9). Where ultrasonography of this region carries the most useful imaging is for collateral ligament desmitis, although only when the proximal third of the ligament is involved. This is only in a minority of cases, as most pathology is distal within the foot and hence not identifiable ultrasonographically. The most appropriate cases to scan are those with palpable swelling in the region of the ligament (dorsomedially or dorsolaterally) at the level of the coronary band. Ultrasonographic abnormalities vary between enlargement to complete rupture characterized by an anechoic ligament (Figure 1.10). Careful comparison with the contra-axial and contralateral ligaments is essential to be confidant of a diagnosis.

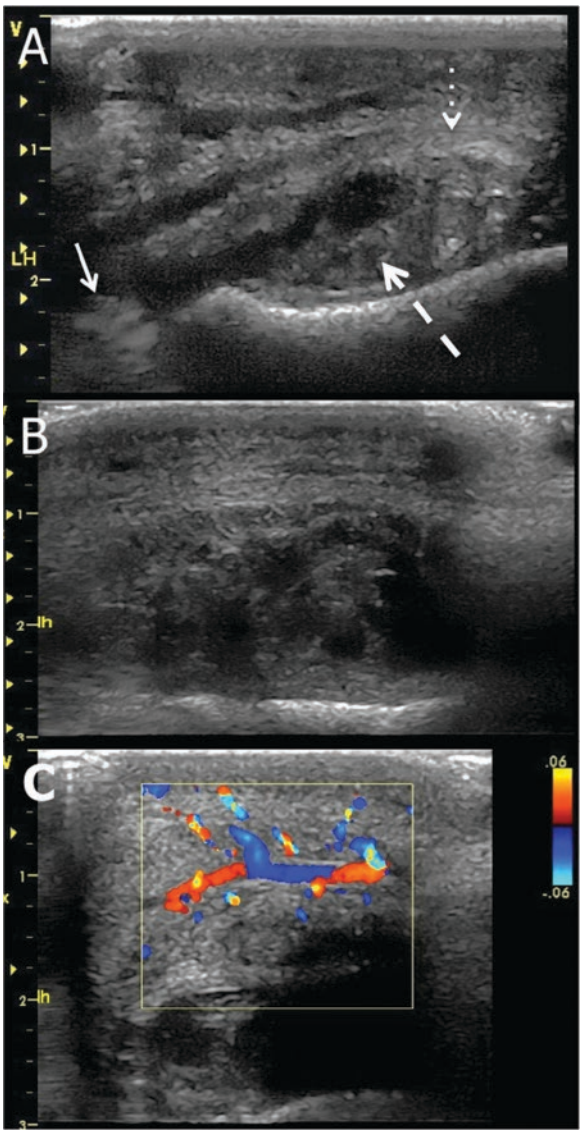


Figure 1.8 (A) Longitudinal image adjacent to the dorsal coronary band showing the extensor process of the distal phalanx (solid arrow), the digital extensor tendon (dotted arrow), and hypertrophied synovium (dashed arrow) together with a distended distal interphalangeal joint in a horse with distal interphalangeal joint sepsis (proximal to the right). (B) shows the corresponding transverse image and (C) the transverse image with Doppler imaging, showing the marked hyperemia of the joint capsule.

Transsolar and Transcuneal Ultrasonography

The third phalanx (P3), distal sesamoid bone (navicular bone) (DSB), navicular bursa (NB), implantation of the deep digital flexor tendon (DDFT), distal sesamoid impar ligament (DSBIL), and other suprasolar structures can be evaluated ultrasonographically transcuneally (through the frog) and transsolarly (through the sole). A 7.5 MHz transducer, preferably curvilinear, should be used, although lower multi-frequency transducers such as a 3.5 MHz transducer used at 6 MHz can also give adequate images.

Preparation

Since the frog and sole are relatively impenetrable to ultrasound waves, and loose solar and frog keratin can trap air, it is important to prepare them to optimize the image. The sole and frog should be trimmed to get rid of loose scaly keratin and then pared

Vet-ebooks.com

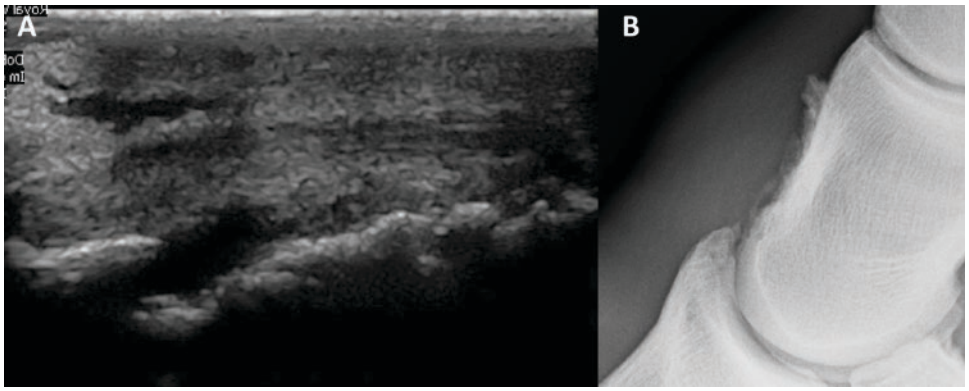


Figure 1.9 Distal interphalangeal joint osteoarthritis. Dorsal longitudinal ultrasonographic image (A) – proximal to the right), showing irregular new bone on the dorsal surface of the second phalanx, as seen radiographically (B).

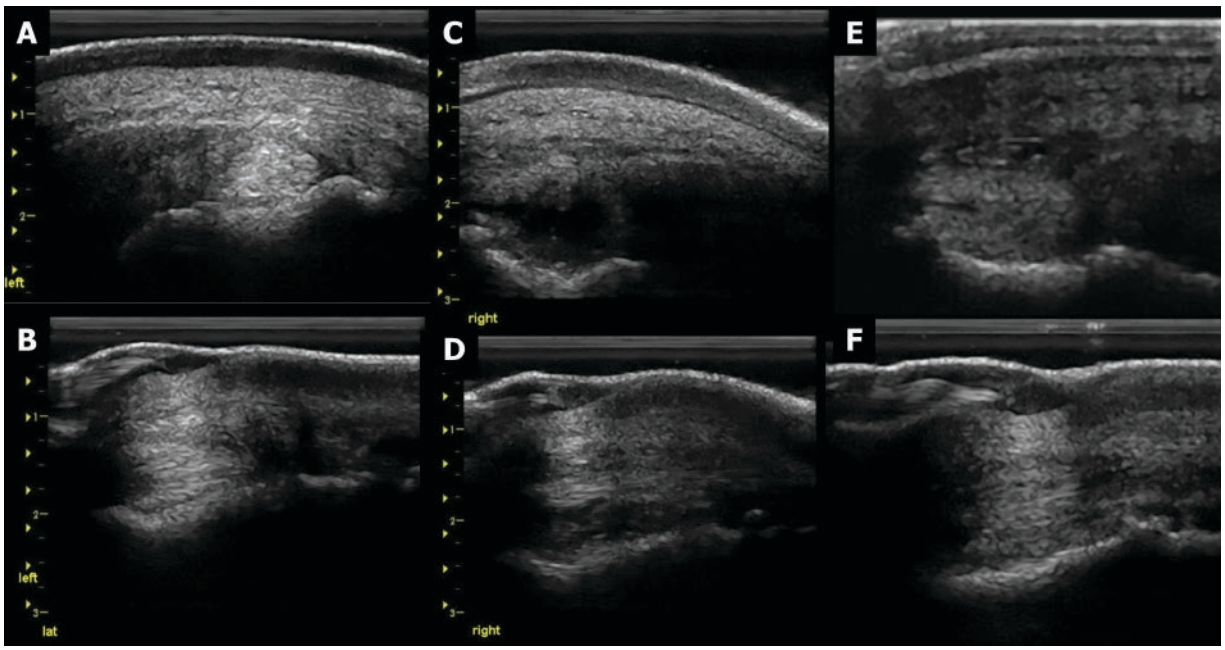


Figure 1.10 Ruptured collateral ligament of the distal interphalangeal joint. (A) and (B) show the transverse (A) and longitudinal (B) images of the normal contralateral medial collateral ligament. (C) and (D) show the corresponding ultrasonographic images of the ruptured ligament. Note the absence of any organized echogenic ligament tissue where the ligament should be. (E) and (F) show the "regeneration" of a new ligament after 2 months in a distal limb cast, indicating that these injuries, although seemingly severe, can heal satisfactorily when the joint is immobilized adequately.

smooth. The foot should then be soaked in bandages/a poultice for at least an hour in water. This may need to be prolonged to overnight soaking, if there is initially minimal softening of the sole or frog. Application of acoustic coupling gel (ACG) for 10–15 minutes prior to and during scanning also helps image visibility. Copious amounts of ACG that fill the collateral and central sulci of the frog also help to establish a clearer image with fewer artifacts and serve as a standoff medium. An assistant can hold the leg in a position so that the ultrasonographer can access the sole or the ultrasonographer may elect to hold the pastern between his/her knees with the sole facing upward.

Scanning Procedure

For the navicular bone and associated structures (Figure 1.11), the area over the frog is scanned in both transverse and sagittal planes; oblique parasagittal planes can also be evaluated. The proximal aspect of the DSB is approximately at the middle of the frog and the insertion of the DDFT on P3 is just proximal to the apex of the frog (Figure 1.12). Using this technique, the hyperechoic collateral ligament of the DSB

Vet-ebooks.com

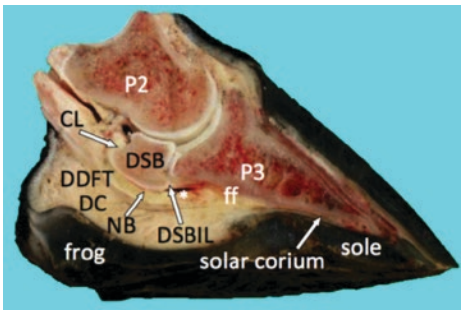


Figure 1.11 Anatomical structures in a sagittal section of the distal digit. P2: second phalanx; P3: third/distal phalanx; DSB: distal sesamoid bone; DDFT: deep digital flexor tendon; CL: collateral ligament of the DSB; NB: navicular bursa; DC: digital cushion; ff: *facies flexoria*; * distal recess of the NB.

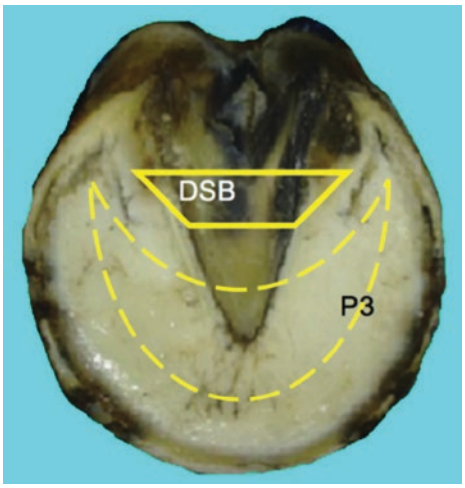


Figure 1.12 Diagrammatic illustration of the position of the DSB and P3 on a solar view of the foot. P3: third/distal phalanx; DSB: distal sesamoid bone.

can be seen indistinctly on the proximal aspect of the DSB. The DSB flexor surface and distal aspect can be seen as a hyperechoic surface. Palmar/plantar to this is the hypoechoic DSB fibrocartilage, then the navicular bursa followed by the fibers of the DDFT, which, when followed distally and dorsally, can be seen fanning out to implant on the semi-lunar *facies flexoria* of P3. Palmar/plantar and proximal to the DDFT and closely associated to it, is the very thin (hardly visible) distal digital annular ligament. From the distal aspect of the DSB, the 3–4 mm thick distal sesamoidean impar ligament (DSBIL) fibers can be seen extending distally to implant on P3 approximately halfway between the DDFT implantation (*facies flexoria)* and the palmar articulation surface of P3. The echogenicity of the DSBIL may vary, even in normal sound horses, but is usually slightly more echogenic than that of the DDFT. This also depends on the angle of insonation.

Between the DSBIL and the distal DSB is the hypo- to anechoic distal palmar recess of the distal interphalangeal joint (DIPJ). Between the DSBIL and the implantation of the DDFT is the distal recess of the navicular bursa, usually only a potential space. Between the DDFT and the sole is the inhomogeneously hyperechoic digital cushion, the most dorsal portion of which is hyperechoic and fibrous (Figures 1.13, 1.14, 1.15, and 1.16).

The entire solar surface of the distal two-thirds of P3 can be evaluated if a small end-on footprint curvilinear transducer is used. Again, the surface is evaluated both in the transverse and sagittal planes. The hyperechoic solar bone surface can be followed from centrally to its margin. A normal interruption can be seen at the tip of P3 if a crena is present. The overlying hypoechoic solar corium can be seen as well as the hyperechoic transitional line to the inhomogeneously hyperechoic keratinized epidermis of the sole (Figures 1.17, 1.18, 1.19, and 1.20). Similar ultrasonographic findings have been described in the foal.

Ultrasound-guided navicular bursocentesis can be performed by positioning the transducer in the sagittal plane over the DSB and placing the needle in the midline proximal to the bulbs of the heel and visualizing the tip of the needle when it reaches the proximal or flexor aspect of the DSB (Figure 1.21). Navicular bursa fluid can be aspirated or therapeutic or contrast agents can be deposited within the NB.

Ultrasonographic Abnormalities

Subsolar gas indicative of a solar abscess or penetrating foreign body will be seen as hyperechoic specks within the solar corium or at the corium–epidermis interface (Figure 1.22). Pedal osteitis changes (Figure 1.23) or marginal fractures of P3 (Figure 1.24) will be seen as an irregular P3 margin. In chronic laminitis (Figure 1.25), where capsular rotation of P3 or distal displacement of P3 relative to the hoof wall has taken place (sinking), the tip of P3 will be seen closer to the solar surface of P3 than normal (less than approximately 10.4 mm in the Thoroughbred). Abscessation or edema of the digital cushion will be seen as a change in its normal echogenicity.

Navicular bursitis with an effusion can be seen as an increase in fluid within the bursa and, depending on the nature of the fluid, will be more echoic if it is a modified transudate or exudate. Adhesions of the DDFT to the flexor surface of the DSB may be seen as increased echogenicity in this area and may be further evaluated dynamically while scanning by flexing and extending the tip of the foot while scanning in a longitudinal plane. If adhesions are present, the

Vet-ebooks.com

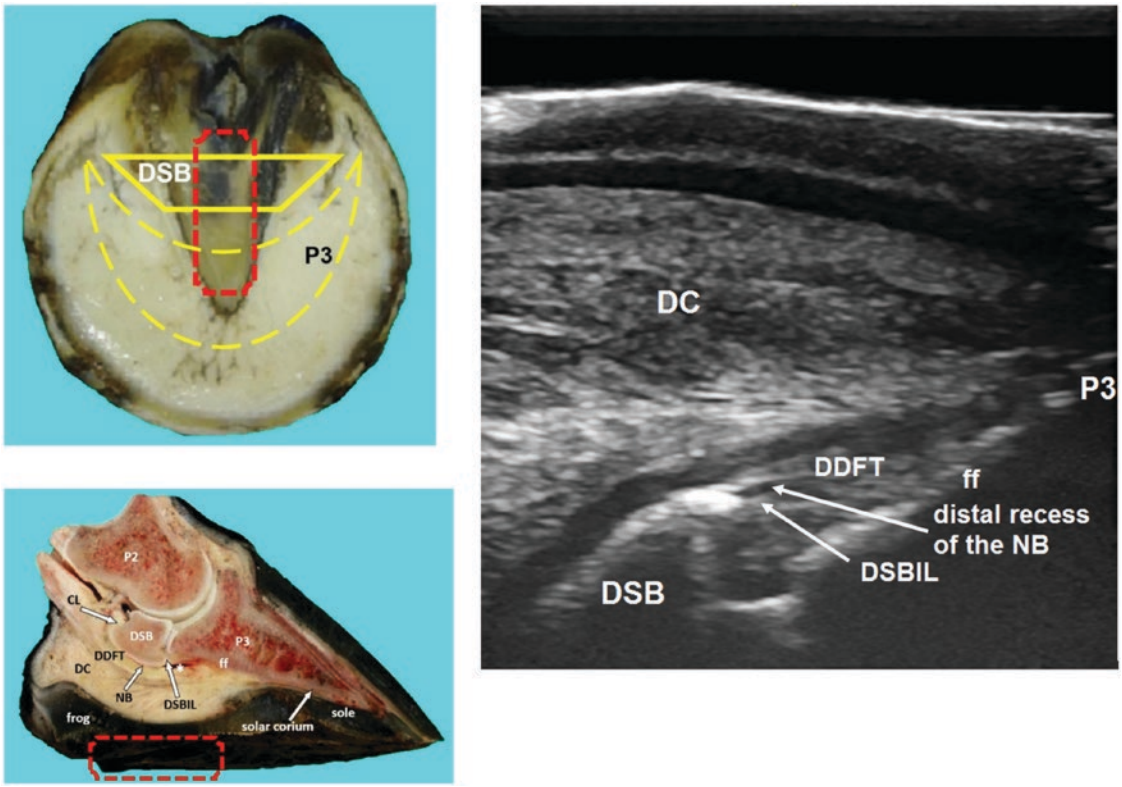


Figure 1.13 Sagittal transcuneal ultrasound image of the hyperechoic flexor cortical surface of the DSB and the solar surface of P3. DSB: distal sesamoid bone; P3: third/distal phalanx; DDFT: deep digital flexor tendon; DSBIL: distal sesamoidean impar ligament; NB: navicular bursa; ff = *facies flexoria* = DDFT insertion on P3; DC: digital cushion. Proximal is to the left and the solar surface is at the top of the image. The stippled red box in this, and all subsequent images in this chapter, indicates the transducer position.

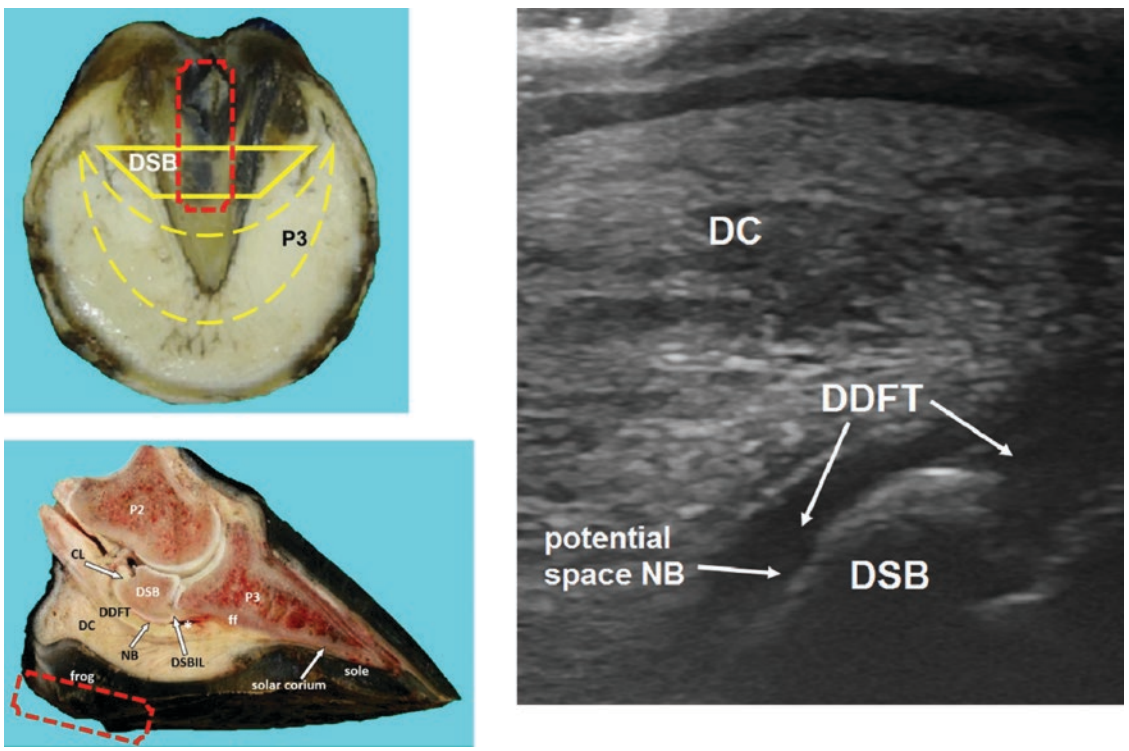


Figure 1.14 Sagittal transcuneal ultrasound image of the hyperechoic flexor cortical surface of the proximal DSB. Note the loss of image proximal to the DSB where transducer contact is poor and the DDFT is obliquely oriented to the angle of incidence of the ultrasound beam. DSB: distal sesamoid bone; DDFT: deep digital flexor tendon; NB: navicular bursa; DC: digital cushion. Proximal is to the left and the solar surface is at the top of the image.

Vet-ebooks.com

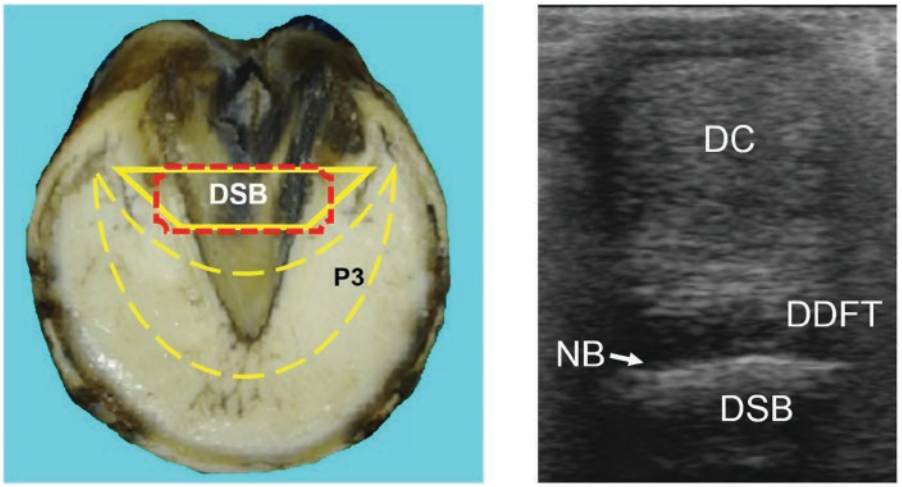


Figure 1.15 Transverse transcuneal ultrasound image of the hyperechoic flexor cortical surface mid-DSB. DSB: distal sesamoid bone; DDFT: deep digital flexor tendon; NB: navicular bursa; DC: digital cushion. The solar surface is at the top of the image.

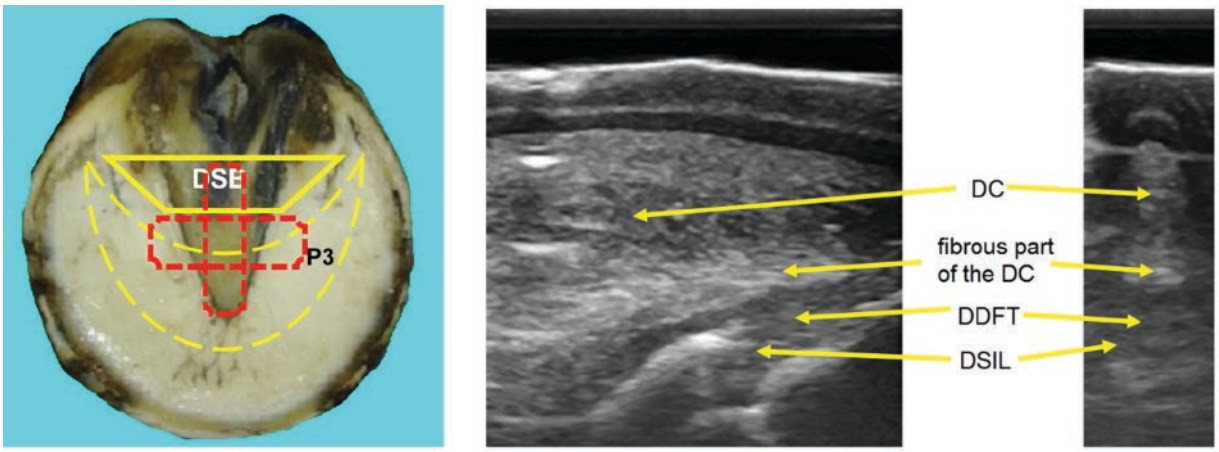


Figure 1.16 Sagittal (right) and transverse (left) transcuneal ultrasound images. The transverse image is taken immediately distal to the DSB. DSB: distal sesamoid bone; DDFT: deep digital flexor tendon; P3: third/distal phalanx; CD: digital cushion. The solar surface is at the top of both images and proximal is to the left on the sagittal image.

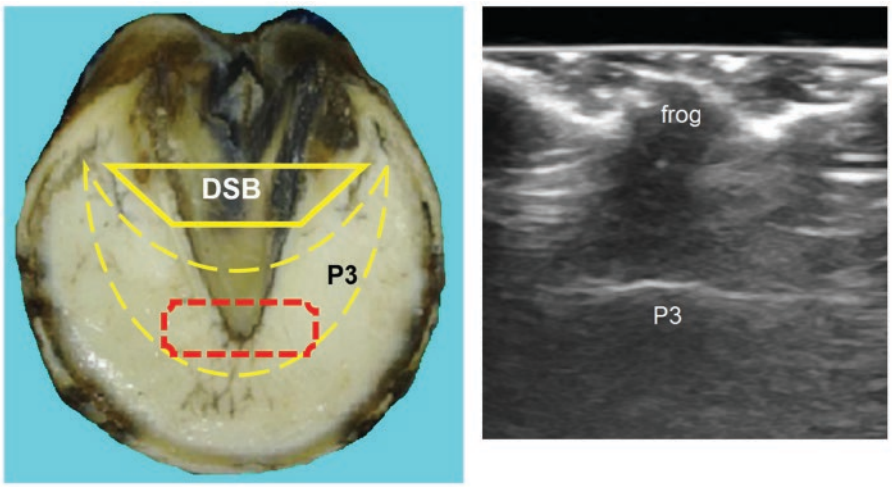


Figure 1.17 Transverse transsolar ultrasound image of P3 at the level of the frog apex. The solar corium is the hypoechoic structure above P3. DSB: distal sesamoid bone; P3: third/distal phalanx.

Vet-ebooks.com

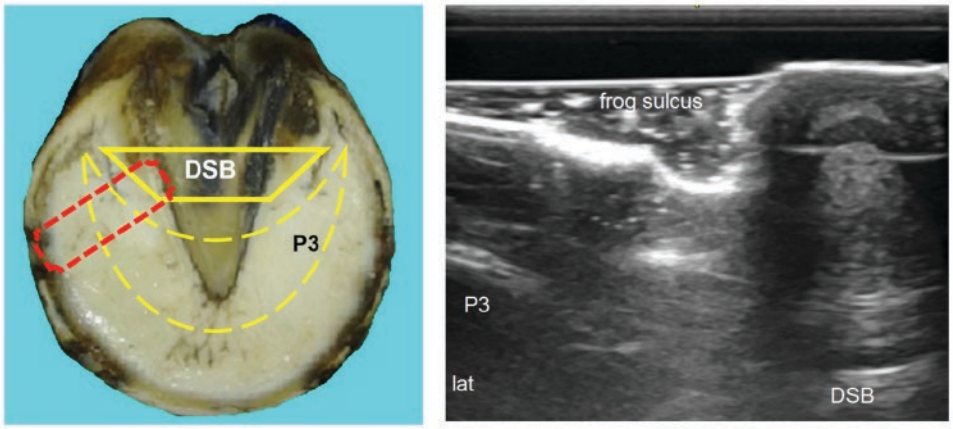


Figure 1.18 Oblique transverse transsolar/cuneal ultrasound image of the hyperechoic lateral solar surface of P3 with the DSB seen obliquely in the far field at the level of the distal third of the frog. DSB: distal sesamoid bone; P3: third/distal phalanx. Laterodistal is to the left.

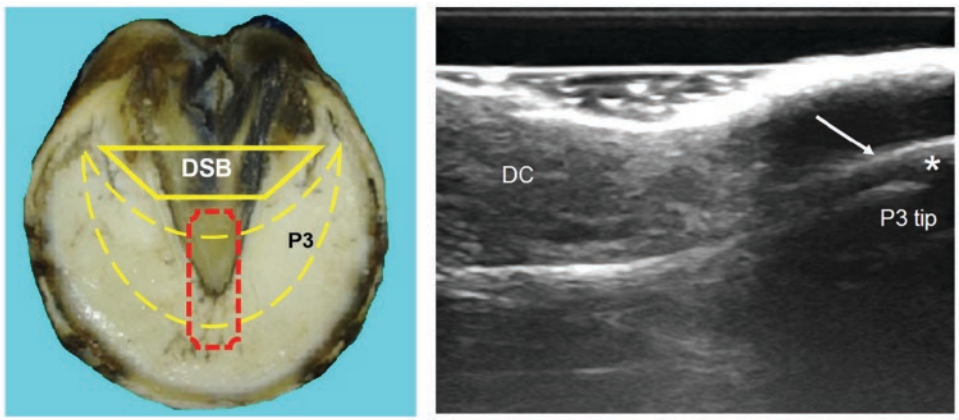


Figure 1.19 Sagittal transsolar ultrasound image of the hyperechoic solar tip of P3. Note the hypoechoic corium immediately solar to P3 (*) and the corium–solar keratinized epidermis interface (arrow). DSB: distal sesamoid bone; P3: third/distal phalanx. Proximal is to the left.

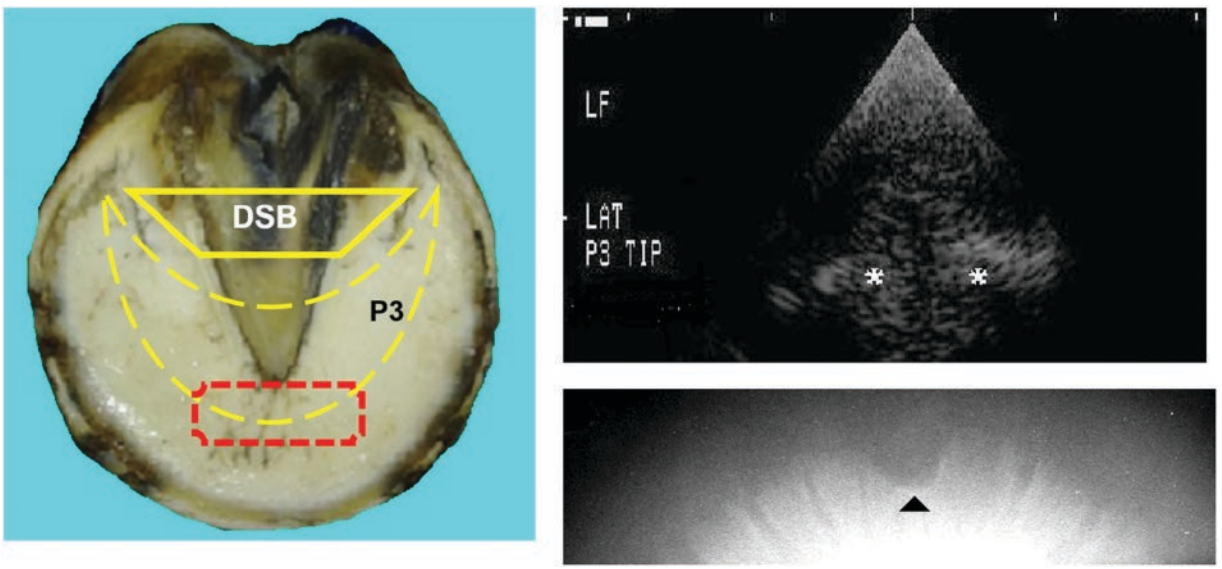


Figure 1.20 Transverse ultrasound image of the *crena marginis solearis* (crena) seen as a disruption of the hyperechoic margin of the tip of P3. Asterisks indicate the lateral and medial sides of the concavity. (Reprinted with permission from Figure 5B (p. 453) from [3].) Sixty-degree dorsopalmar oblique radiograph of the tip of the distal phalanx with a distinct *crena marginis solearis* (arrowhead); DSB: distal sesamoid bone; P3: third/distal phalanx. Lateral is to the left of the image. (Reprinted with permission from Figure 5A (p. 453) from [3]).

Vet-ebooks.com

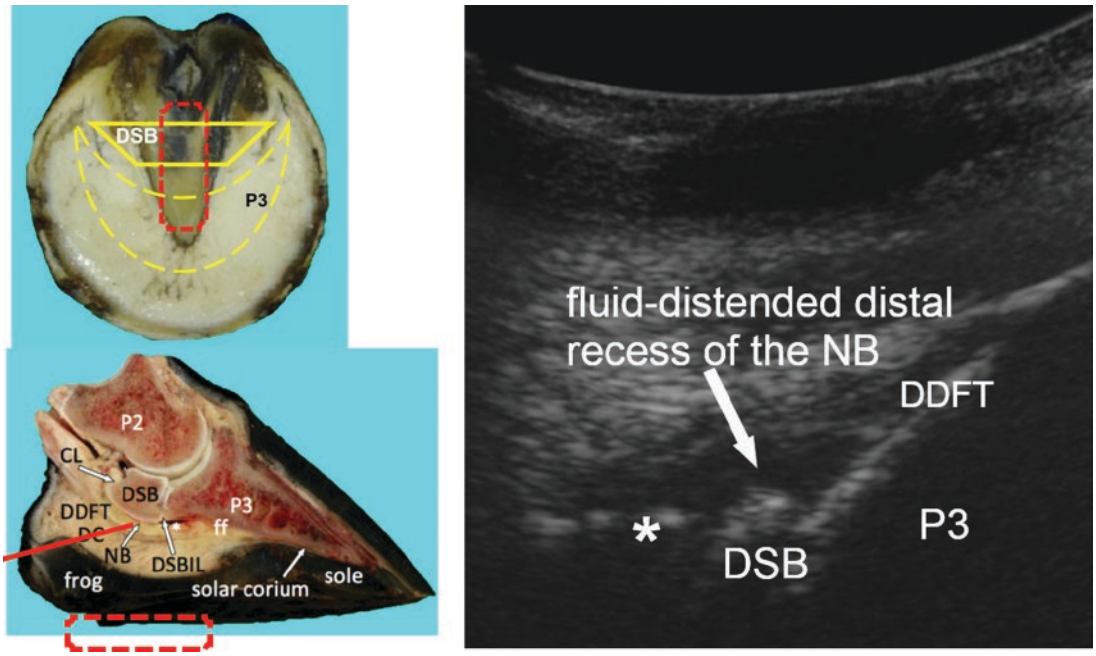


Figure 1.21 Ultrasound-guided injection of the navicular bursa. Sagittal image showing needle (red line) placement for NB arthrocentesis. Sagittal transcuneal ultrasound image showing the tip of the needle placement (*) to inject fluid into the NB. The distal recess of the bursa can be seen filled and distended with anechoic fluid depressing the DDFT solarly. Effusive navicular bursitis would appear similar with possible increase in echogenicity depending on nature of the fluid. DDFT: deep digital flexor tendon; NB: navicular bursa; DSB: distal sesamoid bone. Proximal is to the left.

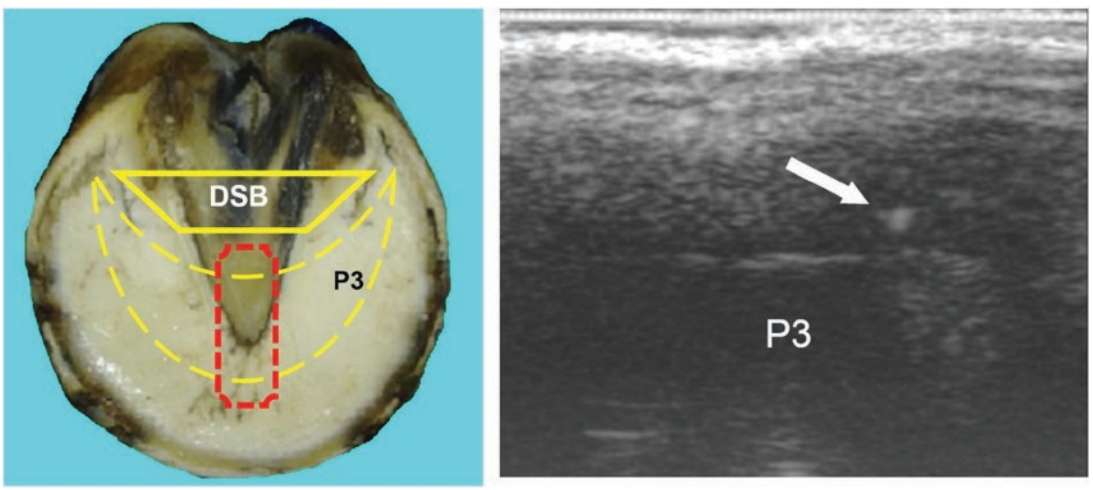


Figure 1.22 Subsolar abscess. Sagittal transsolar ultrasound image showing a focal hyperechoic area (arrow) immediately solar to the hyperechoic tip of P3, indicating subsolar gas. The adjacent dermis appears slightly thicker than normal and bulging slightly. P3: third/distal phalanx. Proximal is to the left.

normal gliding of the DDFT over the DSB will be impaired. Lesions of the DDFT can be seen as a thickening of the DDFT and, if acute or subacute (Figure 1.26), as a decreased echogenicity and loss of fiber alignment. A more chronic lesion will result in a more hyperechoic tendon. Rupture of the DDFT should be seen as an interruption of the normal fiber continuity, possibly with associated inhomogeneous echogenicities around and within it due to hemorrhage.

Fractures of the DSB and P3 can be seen as an interruption in the hyperechoic cortical line. Avulsion fractures of the DSB involving the DSBIL may result in a subluxation of the DSB and visualization of the underlying distal aspect of the second phalanx (P2). (Figures 1.27 and 1.28). Distal sesamoidean impar ligament (DSBIL) rupture may also result in proximal displacement of the DSB, allowing visualization of the distal condyle of P2 as well

Vet-ebooks.com

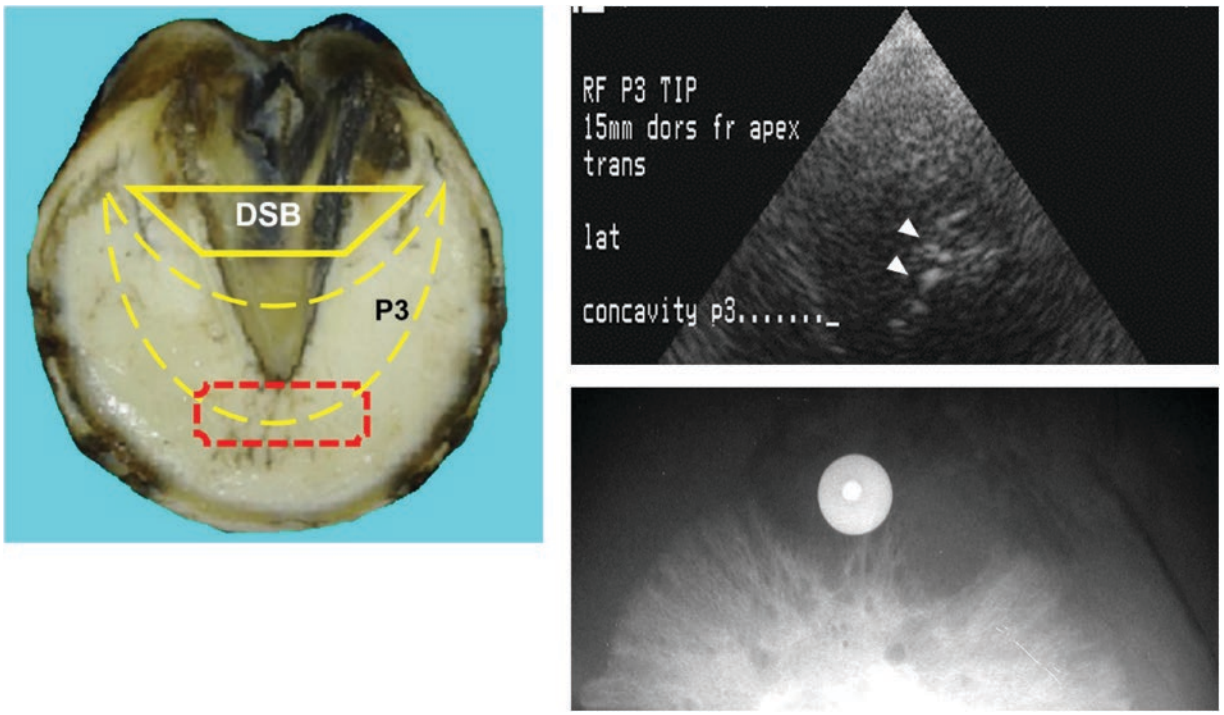


Figure 1.23 Septic pedal osteitis. Transverse ultrasound image of tip of P3; note the irregular hyperechoic areas (fragments – arrowheads) within the hypo- to anechoic fracture bed of the tip of P3. (Reprinted with permission from Figure 7B (p. 455) from [3].) Dorsoproximal–palmarodistal radiograph of the tip of P3 of a clinical case of septic pedal osteitis. Note the irregularly marginated W-shaped radiolucent concavities of the tip of P3; metallic opacity drawing pin present. (Reprinted with permission from Figure 6A (p. 454) from [3].) P3: third/distal phalanx.

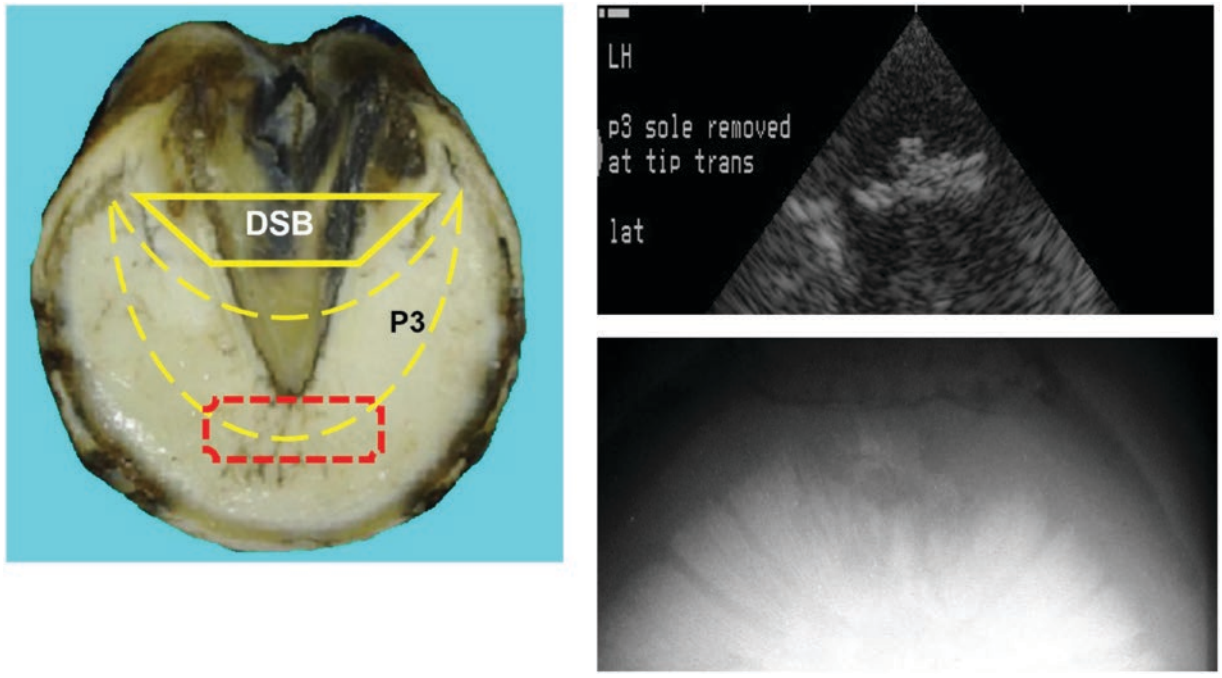


Figure 1.24 Pathological large marginal fracture of P3 secondary to a septic pedal osteitis. Transverse ultrasound image of tip of P3; note the irregular hyperechoic areas (fragments – arrowhead) within the hypo- to anechoic fracture bed of the tip of P3. (Reprinted with permission from Figure 7B (p. 455) from [3].) Dorsoproximal–palmarodistal radiograph of tip of P3 of a clinical case with a pathological large marginal fracture of P3 secondary to chronic subsolar abscessation; note the irregular radiolucency at the tip of the distal phalanx and the bony opacities disassociated from the parent bone. The toe of the sole has been pared away. (Reprinted with permission from Figure 7B (p. 455) from [3].) P3: third/distal phalanx.

Vet-ebooks.com

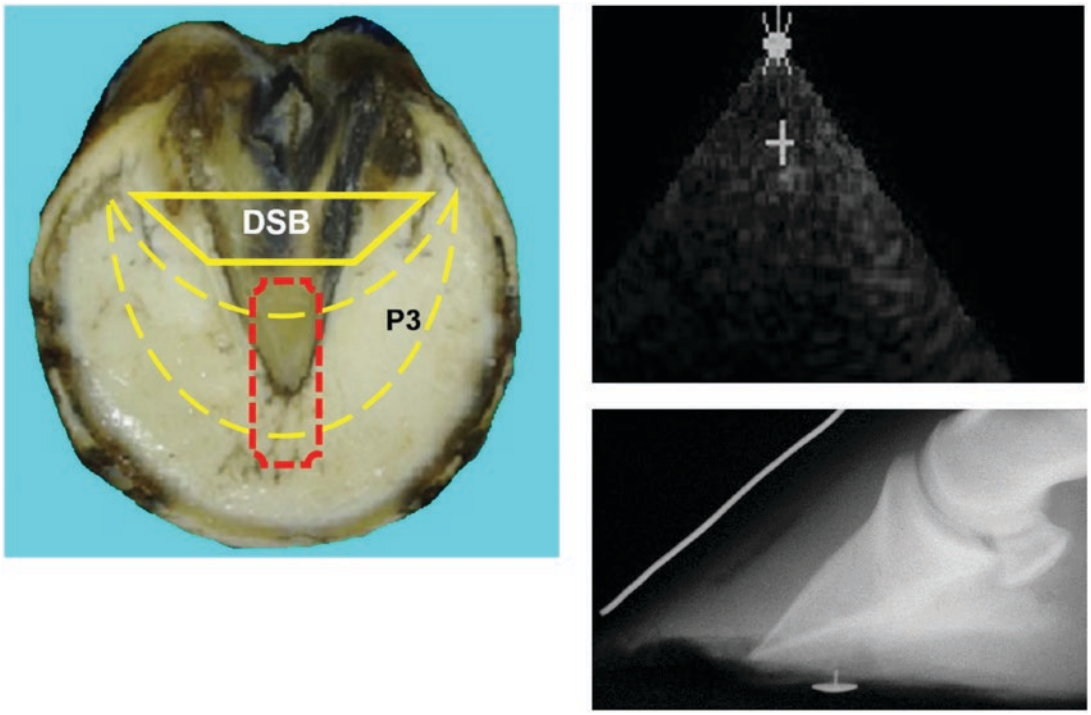


Figure 1.25 Chronic laminitis with capsular rotation of P3. Sagittal ultrasound transsolar image of distal tip of P3 (below cursor); the distance from the tip of the distal phalanx to the sole is 2.4 mm, indicating a marked decrease of the distance of the tip of P3 from the solar hoof surface. The normal distance in the Thoroughbred should not be less than 10.4 mm. (Reprinted with permission from Figure 8B (p. 456) from [3].) Lateromedial radiograph of P3, showing marked capsular rotation of P3; metallic linear marker indicates dorsum of hoof wall; the magnification corrected distance between the tip of the distal phalanx and the solar margin is 3 mm; metallic drawing pin indicates frog apex. (Reprinted with permission from Figure 8A (p. 456) from [3].) P3: third/distal phalanx.

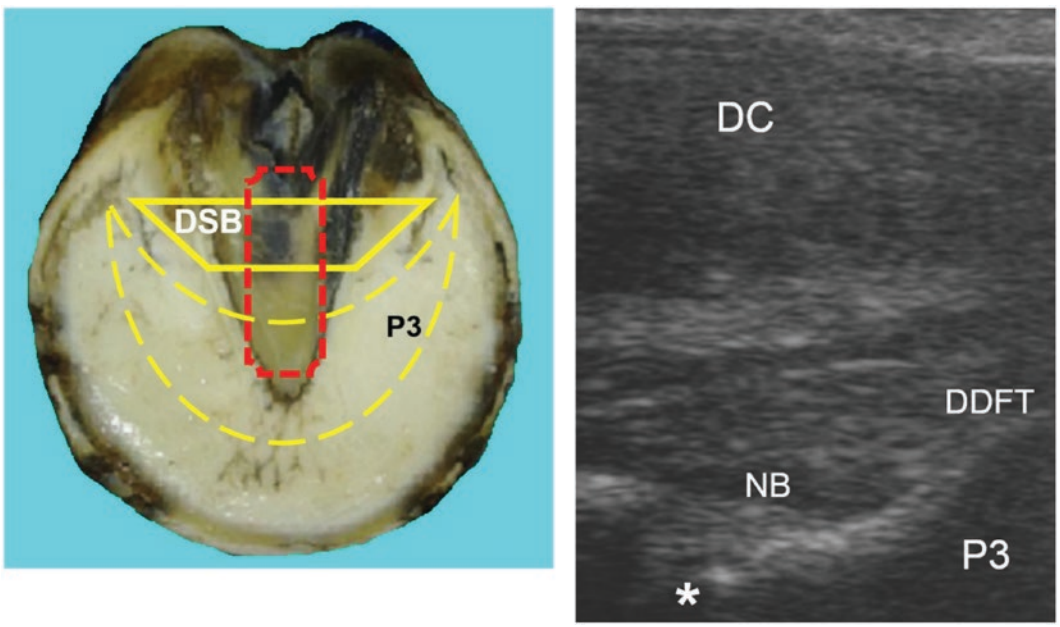


Figure 1.26 Implantational deep digital flexor tendinopathy. Sagittal transcuneal ultrasound image showing a thickening and bulging of the most distal aspect of the DDFT with decreased echogenicity and a decrease in the distinct fiber alignment as seen normally. There also appears to be an increase in the fluid within the distal recesses of the NB and DIPJ (*). P3: third/distal phalanx; DDFT: deep digital flexor tendon; NB: navicular bursa; DIPJ: distal interphalangeal joint. Proximal is to the left.

Vet-ebooks.com

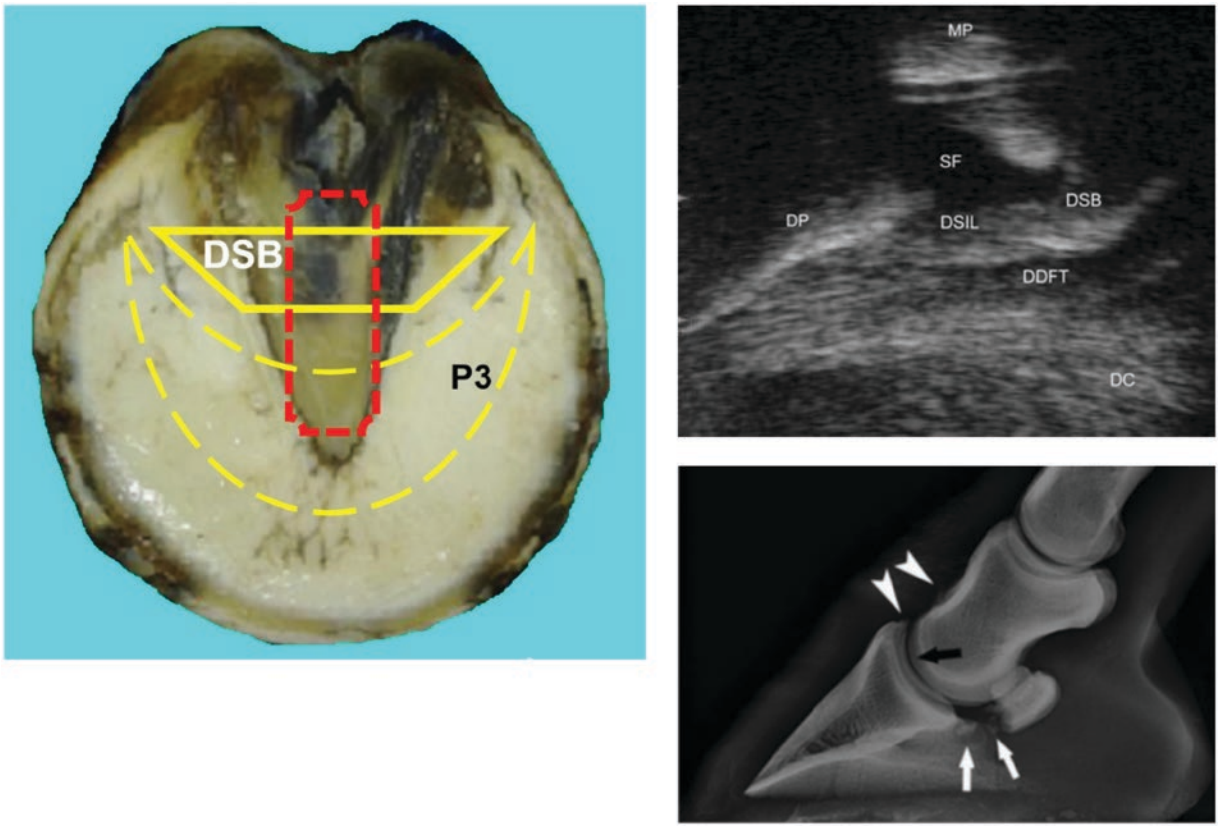


Figure 1.27 Distal sesamoid impar ligament rupture [4]. Sagittal ultrasound image; note the hypoechogenic appearance of the DSBIL with fiber disruption, proximal displacement of the DSB, and a large pocket of synovial fluid (SF). The proximal displacement of the DSB allows visualization of the distal condyle of the second/middle phalanx (MP). The DDFT looks slightly less echogenic than normal but it is within the normal range of size. The architecture and variation in imaging representation is related to the orientation of the probe. (Reprinted with permission from Figure 3B (p. 118) from [4].) LM radiograph of the right hind digit. Note several avulsion fracture fragments (white arrows) and the proximal displacement of the navicular bone as well as the dorsal periarticular remodeling of the DIPJ (arrowhead). The joint space is enlarged dorsally (black arrow) compared with the plantar aspect consistent with DIPJ instability. DIPJ: distal interphalangeal joint. (Reprinted with permission from Figure 1 (p. 117) from [4].) DSB: distal sesamoid bone; DP: third/distal phalanx; DDFT: deep digital flexor tendon; DSBIL: distal sesamoidean impar ligament; NB: navicular bursa; DC: digital cushion. Proximal is to the right and the solar surface is to the bottom of the image.

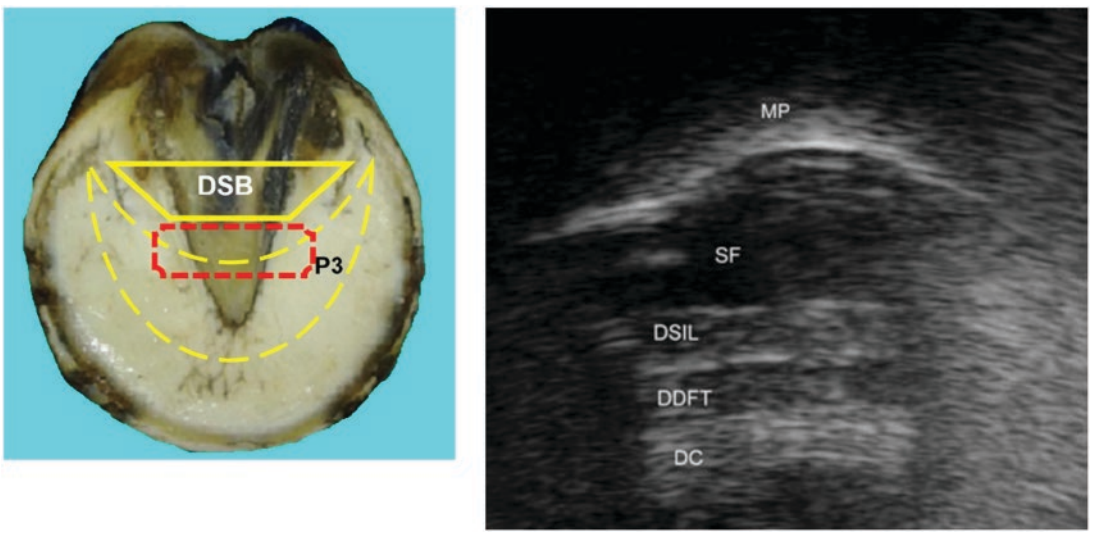


Figure 1.28 The same case as in Figure 1.27. Transverse ultrasound image. Proximal displacement of the DSB allows visualization of the distal condyle of the second/middle phalanx (MP) and of a large pocket of synovial fluid (SF). Note the hypoechogenic appearance of the DSBIL. The solar surface is to the bottom of the image. (Reprinted with permission from Figure 4B (p. 119) from [4].) DDFT: deep digital flexor tendon; DSIL/DSBIL: distal sesamoidean impar ligament; DC: digital cushion.

Vet-ebooks.com

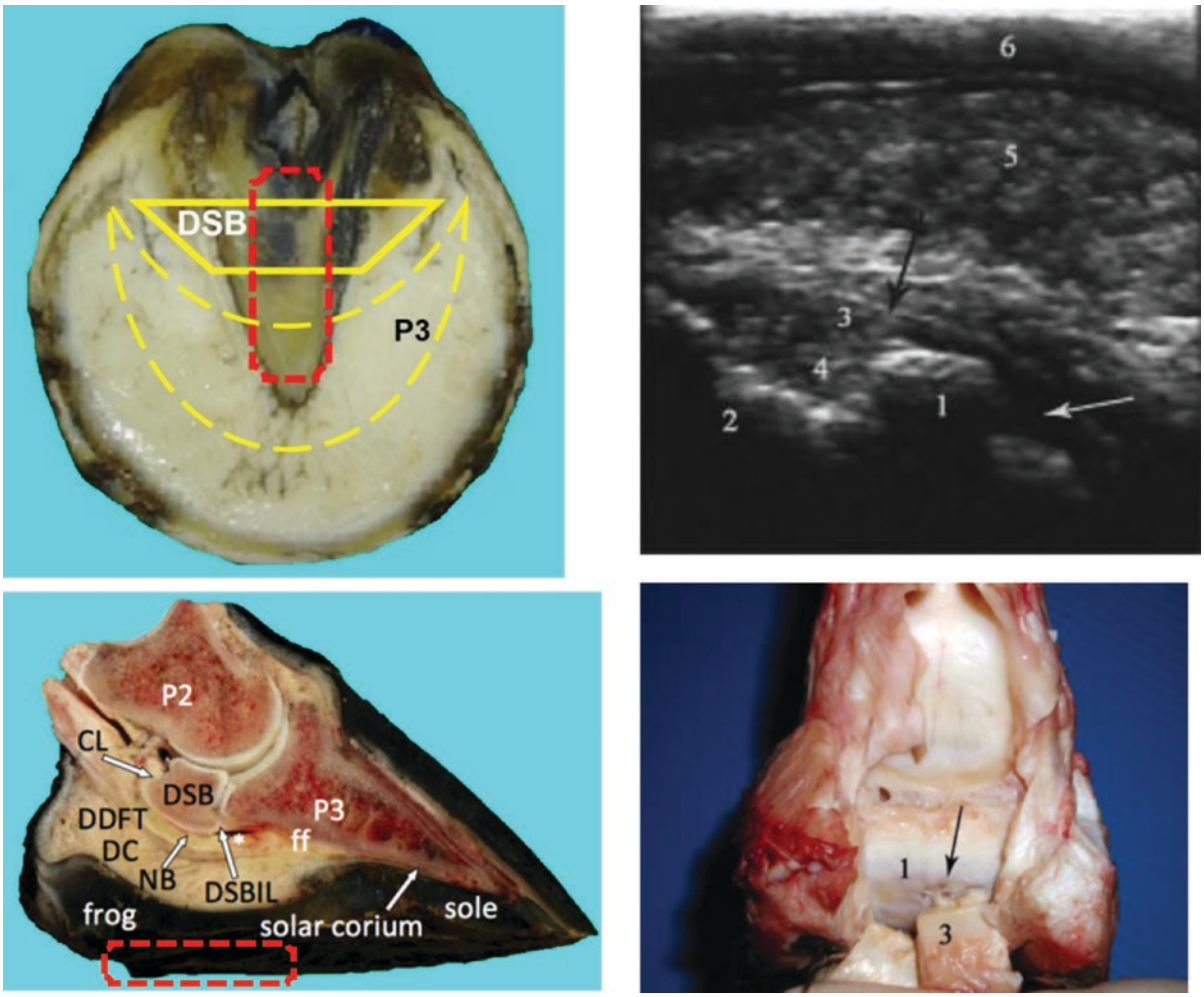


Figure 1.29 Severe fibrocartilage degeneration of the DSB. Sagittal transcuneal ultrasonographic image of left front foot. There is a defect in the flexor surface of the navicular bone (white arrow). The deep digital flexor tendon is modified in shape and echogenicity (black arrow). Post-mortem examination of left front foot (palmar view). The DDFT has been cut sagittally and reclined distally. There is an adhesion between the DDFT and the navicular bone (arrow). 1: navicular bone; 2: distal phalanx; 3: deep digital flexor tendon; 4: distal sesamoidean impar ligament; 5: digital cushion; 6: frog. DSB: distal sesamoid bone; DDFT: deep digital flexor tendon. Distal is to the left and the solar surface is at the top of the image. (*Source*: Ultrasound and post-mortem images [5]. Reproduced with permission of John Wiley & Sons Ltd).

as fiber disruption of the DSBIL. Damage to the flexor surface of the distal sesamoid bone can result in discontinuation of the hyperechoic surface with possible DDFT adhesion (Figures 1.29 and 1.30).

Doppler ultrasonography can indicate increased or decreased blood flow within the DDFT, DSBIL, or solar corium (Figures 1.31 and 1.32).

The Pastern

The use of ultrasonography to investigate lesions in this region of the distal limb is particularly applicable, as many injuries to the soft tissue structures on the palmar aspect of the limb result in non-specific subcutaneous fibrosis which can limit accurate digital palpation of the area. The area has complex anatomy but, with a little practice, can be evaluated very satisfactorily using the ultrasound machines and probes available in general practice. A variety of transducers can be used to examine these areas. Both microconvex and linear probes are applicable – the linear probe offers superior longitudinal images, while the microconvex transducer can scan further distally in the pastern region by placing it between the bulbs of the heels.

The fetlock and pastern regions are particularly complex in the arrangement of its ligament and tendons, many running in oblique directions which require a wider array of imaging planes for comprehensive evaluation. In addition, many primarily soft tissue abnormalities will also have bony lesions in this region of the limb and vice versa. Therefore the combination of ultrasonographic and radiographic techniques is frequently indicated. The most diagnostic information is usually obtained by performing a radiological appraisal *first*, followed by ultrasonography.

Vet-ebooks.com

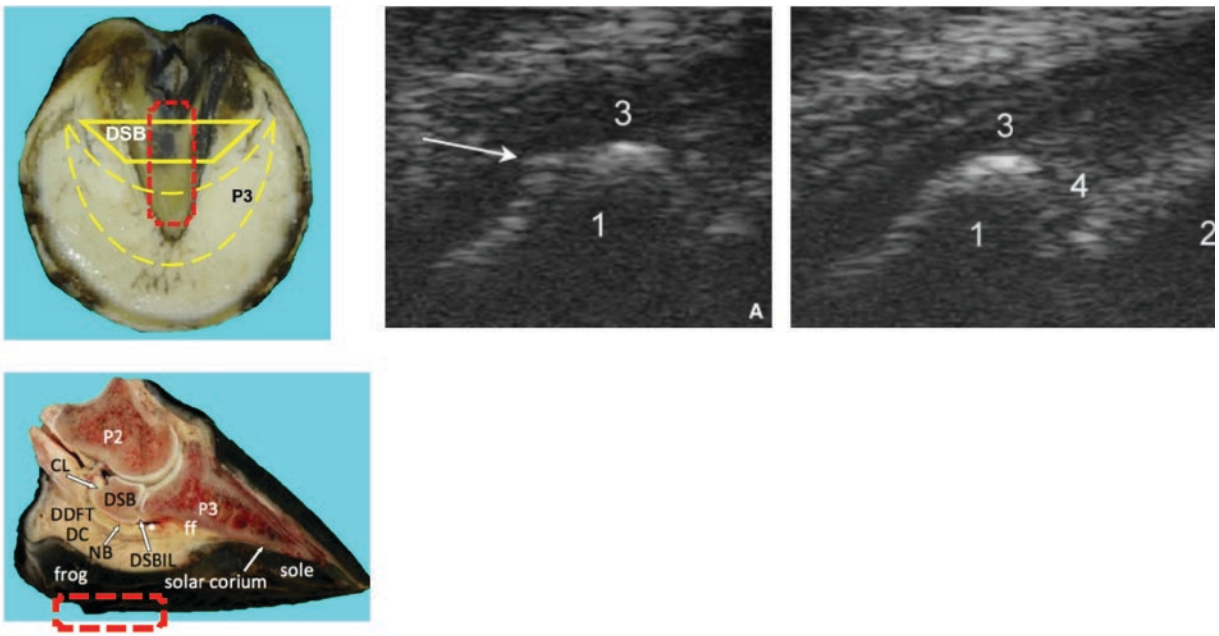


Figure 1.30 Abnormal navicular bone flexor surface. Sagittal transcuneal ultrasonographic image of the foot. Note the abnormal navicular bone flexor surface (left) in comparison to the normal contralateral navicular bone (right). There is slight roughening of the hyperechoic bone profile of the navicular bone associated with a small hyperechoic spur (arrow) visible in the lame limb (left). 1: navicular bone; 2: distal phalanx; 3: deep digital flexor tendon; 4: distal sesamoidean impar ligament. 5: digital cushion; 6: frog; DSB: distal sesamoid bone; DDFT: deep digital flexor tendon. Proximal is to the left and the solar surface is at the top of the image. (*Source*: Ultrasound images from [6]. Reproduced with permission of John Wiley & Sons Ltd).

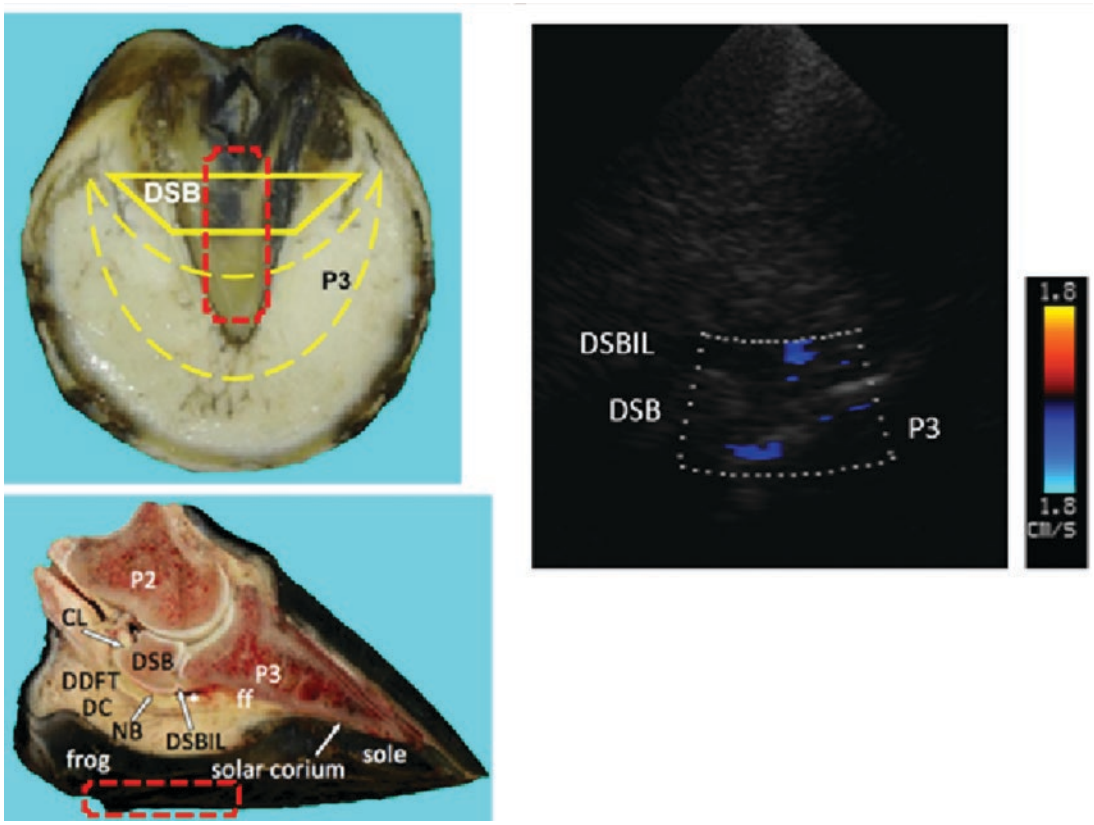


Figure 1.31 Sagittal transcuneal Doppler ultrasonographic image indicating blood flow away from the transducer dorsal to the DSBIL at approximately 1.8 cm/s in a normal horse. DSB: distal sesamoid bone; DSBIL: distal sesamoidean impar ligament; P3: third/distal phalanx. Proximal is to the left and the solar surface is at the top of the image.

Vet-ebooks.com

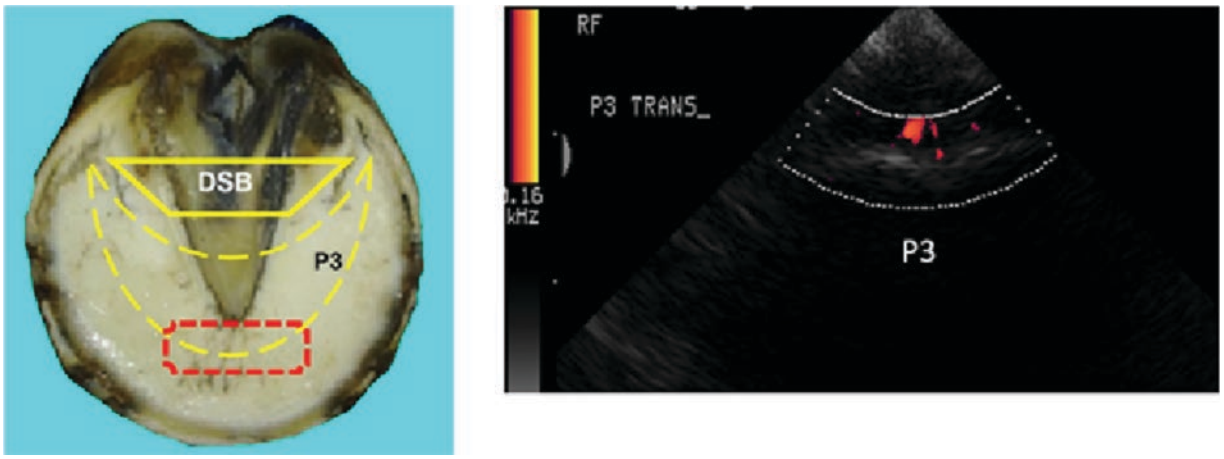


Figure 1.32 Transverse trans-solar Power Doppler ultrasonographic image indicating blood flow distal to the tip of P3 in the corium in a normal horse. DSB: distal sesamoid bone; P3: third/distal phalanx. Lateral is to the left and the solar surface is at the top of the image.

Preparation and Scanning Technique

The skin is prepared as for other areas and the probe applied using couplant gel and a standoff pad. The latter is usually used, as many of the structures being assessed are superficial. However, appreciable subcutaneous edema or fibrosis, common in this region, will provide a "natural" standoff and a separate standoff pad can be dispensed with in many cases.

The ultrasound examination is initially performed with the limb fully weightbearing and the horse standing square. Exceptions to this include placement of the limb further caudally to hyperextend the DIP joint to allow easier access to the palmar/plantar aspect of the pastern and to allow scanning further distally. Alternatively the foot can be elevated by placing it on a block to improve access and maneuverability of a large transducer.

Because many injuries to this region involve the digital sheath, an ultrasonographic examination of this area should stretch from the proximal limit of the digital sheath (mid-metacarpal) to the bulbs of the heels and hence this chapter should be read in conjunction with Chapter 2.

The palmar/plantar pastern region is also divided into a number of levels (1–3) or zones (P1a–c; P2a–b). The most accessible region covers the palmar/plantar aspect of the proximal phalanx from the base of the proximal seamoid bones to the level of the proximal interphalangeal joint. The distal two zones correspond to the more distal position that can be more easily achieved with a microconvex transducer between the bulbs of the heels, although a linear transducer can gain greater access if the limb is placed caudally so as to hyperextend the DIP joint. A single longitudinal level is usually achievable with a linear transducer, although a rectal probe may require reversing so that the lead is positioned proximally and does not contact the heels, compromising the required probe orientation.

As well as midline transverse and longitudinal images obtained from the palmar/plantar aspect of the pastern, oblique 45-degree transverse and longitudinal views should be included routinely for a complete examination because a number of structures pass obliquely across the first phalanx (oblique distal sesamoidean ligaments proximally; SDFT branches distally). Hence the skin should be clipped to the medial and lateral limits of the pastern when preparing the limb. The contralateral limb should be scanned as well, both for comparative purposes but also as non-traumatic soft tissue injuries in this region can be bilateral.

Line drawings of the normal anatomy are shown in Figure 1.33.

Ultrasonographic Anatomy

The most frequently affected structure in the palmar/plantar pastern is the digital flexor tendon sheath which contains the two digital flexor tendons but is also closely related to a number of other structures. This anatomy is covered in Chapter 2.

Dorsal to the digital sheath in the proximal pastern are the oblique (ODSL) and straight (SDSL) distal sesamoidean ligaments (DSLs), which can easily be identified ultrasonographically. The SDSL is a single mid-line structure and is the most echogenic structure within the pastern region and hence a useful landmark. The ODSLs, in contrast, are paired and run from abaxially proximally to axially distally and therefore require oblique views to image them adequately. There are additional DSLs, the paired short

Vet-ebooks.com

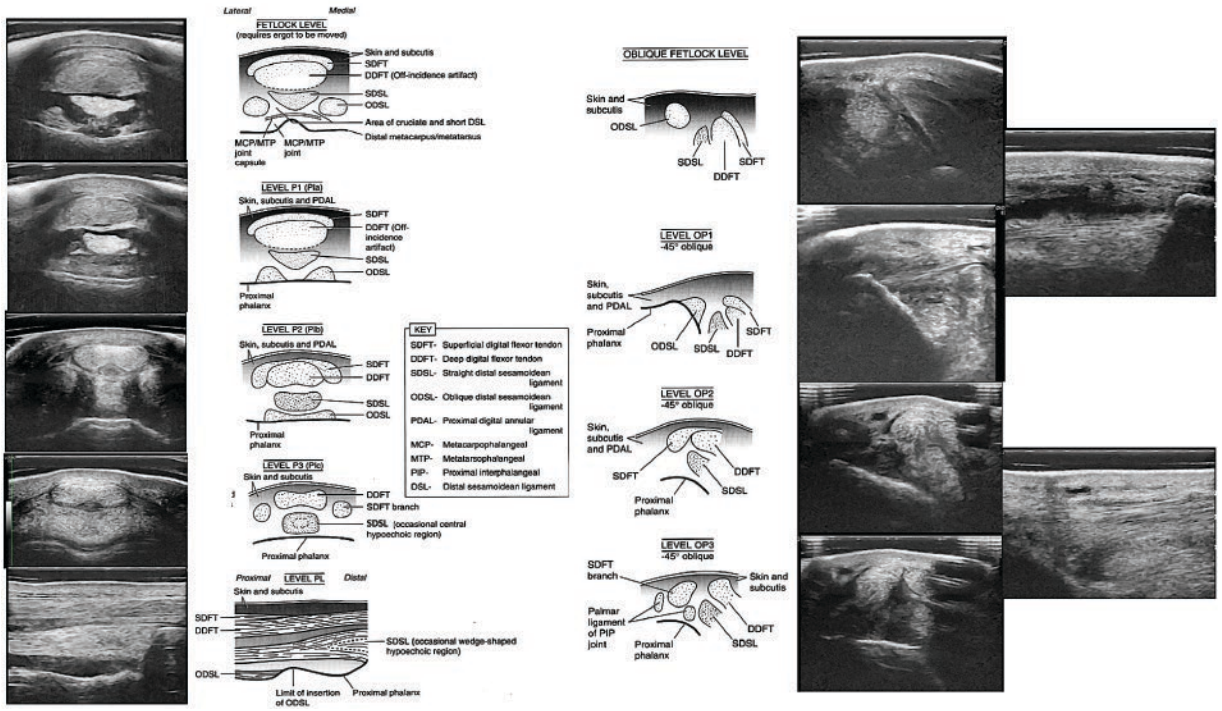


Figure 1.33 Diagrammatic representation of ultrasonographic anatomy of the pastern region (adapted from [5]).

and cruciate DSLs, which cannot easily be distinguished but can sometimes be identified adjacent to the joint capsule in oblique views of the palmar/plantar aspect of the fetlock joint.

Beware of the insertion of the SDSLs onto the middle scutum on the palmar/plantar aspect of the proximal interphalangeal joint (PIP) joint. This area will frequently have a hypoechoic "core" or "sandwich" in the transverse views (P3 only) and a hypoechoic "wedge" with its apex directly proximally in the longitudinal view (Figure 1.34). The hypoechoic region does not extend further proximally than the distal limit of insertion of the ODSL. This is a normal anatomic feature and should not be mistaken for pathology.

Both proximal and distal digital annular ligaments exist within the pastern; they cannot be easily visualized from the plamar/plantar aspect in the normal horse (they are usually less than 1 mm in thickness) but can be seen when enlarged. The proximal digital annular ligament can be identified proximal to the distal outpouching of the digital sheath, especially medially and laterally where they are more discrete structures grossly.

At the level of the proximal interphalangeal joint, there are abaxial and axial ligaments of the PIP joint which lie adjacent to the branch of the superficial digital flexor tendon. Hence, pathology of these structures can be easily confused and careful scanning using the oblique views are imperative to ensure an accurate diagnosis.

Ultrasonographic Abnormalities

Many soft tissue injuries to the pastern region are associated with the digital sheath, so Chapter 2, relating to this structure, should be consulted in conjunction with this section.

Distal Sesamoidean Ligament Abnormalities

Injury to these ligaments is relatively rare but affects either the single straight distal sesamoidean ligament (SDSL) or one of the paired oblique distal sesamoidean ligaments (ODSL). The changes identified ultrasonographically are similar to those seen in other strains involving other ligaments (enlargement, alterations in echogenicity, and loss of the normal striated pattern) (Figure 1.35). Because these are ligaments which naturally have off-incidence artifacts within them because their internal fibers run in different directions, improved confidence in diagnosis can be provided by the additional signs of periligamentar fibrosis and enthesiopathy at the ligament's insertion sites (especially the base of the proximal sesamoid bones).

Enlargement of the SDSL is manifested by occlusion of the space between the palmar/plantar surface of the first phalanx/ODSL and the SDSL, and between

Vet-ebooks.com

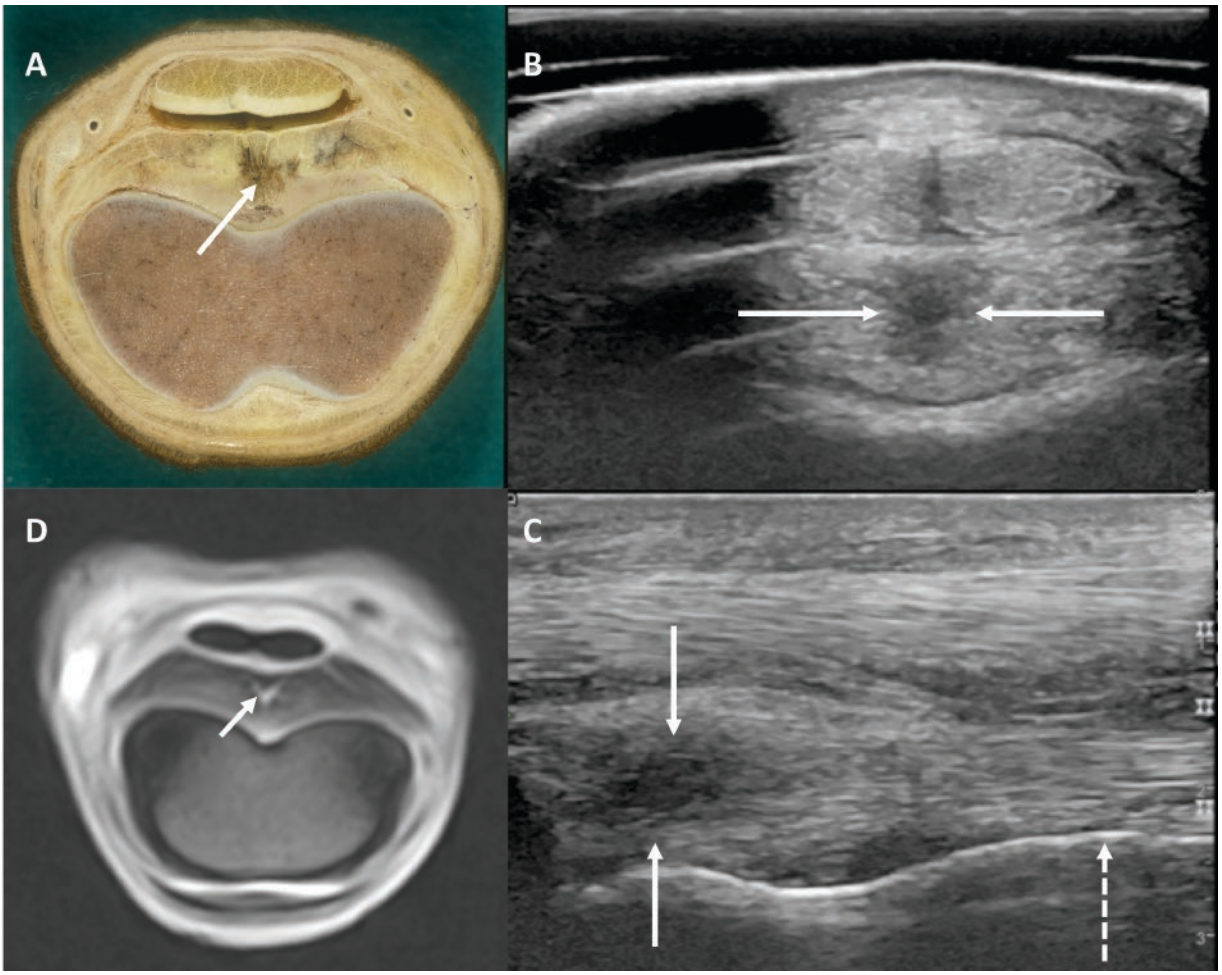


Figure 1.34 Appearance of the insertion site of the straight distal sesamoidean ligament (SDSL) via the middle scutum onto the proximal aspect of the middle phalanx. (A) Transverse ultrasound image. (B) Longitudinal image (proximal is to the right). Note the normal hypoechoic area with the distal SDSL/middle scutum (arrows) which should not be mistaken for SDSL desmitis. This hypoechoic area should not extend further than the limit of insertion of the oblique distal sesamoidean ligaments indicated by at bony prominence on the palmar/plantar aspect of the proximal phalanx (dashed arrow) on the longitudinal image.

the DDFT and the SDSL. Once again, subcutaneous fibrosis is a common concurrent finding. Some SDSL (and more rarely, ODSL) injuries can tear into the adjacent digital sheath resulting in digital sheath distension and can benefit from tenoscopic debridement. Ultrasonographic features consistent with this are anechoic lesions on the palmar/plantar surface of the ligaments with or without an opening into the sheath cavity. Contrast tenography can help confirm such communication (Figure 1.36). Severe disruption of the DSLs can result in proximal displacement of the proximal sesamoid bones (as opposed to severe SL disruption giving distal displacement).

Radiography can also be helpful in these cases, not only to identify entheseopathy, avulsion fractures, or proximal displacement of the proximal sesamoid bones, but also for subluxation of the PIP joint, which can result from severe damage to the SDSLs (or the branches of the superficial digital flexor tendon). It is equally useful to image the area ultrasonographically after the radiographic evaluation if osseous abnormalities are identified where the osseous changes can be linked to specific structures.ODSL injury can be difficult to identify ultrasonographically unless oblique ultrasonographic views are used, as a significant proportion of ODSL injuries occur within the proximal half of the ligament which is not visible from the palmar aspect of the limb. Injuries to these structures have been a relatively common diagnosis on magnetic resonance imaging (MRI), although care must be taken to avoid misinterpretation due to the magic angle artifact associated with the obliquity of these ligaments. Convincing changes on ultrasound include enlargement and altered longitudinal pattern, together with

Vet-ebooks.com

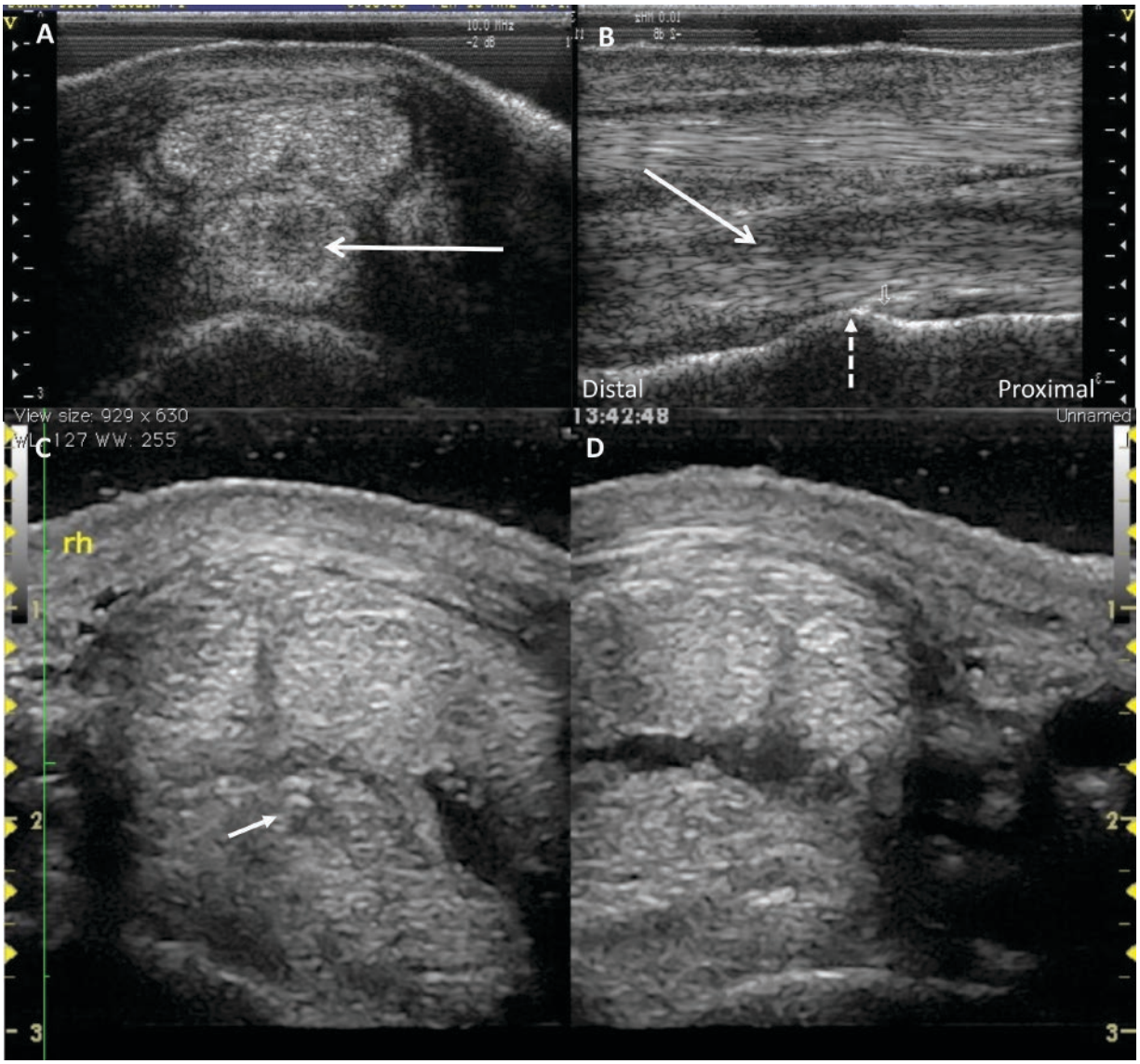


Figure 1.35 Straight distal sesamoidean ligament desmitis. Note the hypoechoic area seen in both transverse (A) and longitudinal images (B) extending further proximally than the limit of insertion of the oblique distal sesamoidean ligaments (dashed arrow). (C) An oblique transverse view of a different case with a more subtle lesion, possibly containing some mineralization is the medial border of the straight distal sesamoidean ligament. (D) shows the contra-axial oblique for comparison.

overlying subcutaneous fibrosis and enthesophytosis at the base of the proximal sesamoid bones (Figure 1.37).

Enthesophytosis associated with the insertion of the ODSL onto the palmar/plantar aspect of the proximal phalanx is characterized as an irregularity to the bone surface. Although this is a common finding at this site, it is rarely a cause of lameness and usually unassociated with significant ODSL pathology on ultrasound.

Digital Annular Ligaments

Digital annular ligaments are rarely a cause of lameness, but they have beenimplicated in constriction syndromes similar to the palmar/plantar digital annular ligament (PAL). In these situations, they appear as thickened structures in the subcutaneous space and can be traced to their attachments to the palmar/plantar aspect of the proximal phalanx. Like the PAL, the identification of such thickening does not confirm constriction, which probably is more reliably made on tenoscopic examination. These ligaments may also enlarge secondarily to many soft tissue conditions of the pastern region.A small number of cases have been seen where horses have been presented with acute lameness referable to the proximal pastern region. Both radiography and ultrasonography have shown the presence of avulsion fractures at the origin of the proximal digital annular ligament (Figure 1.38). As with many avulsion

Vet-ebooks.com

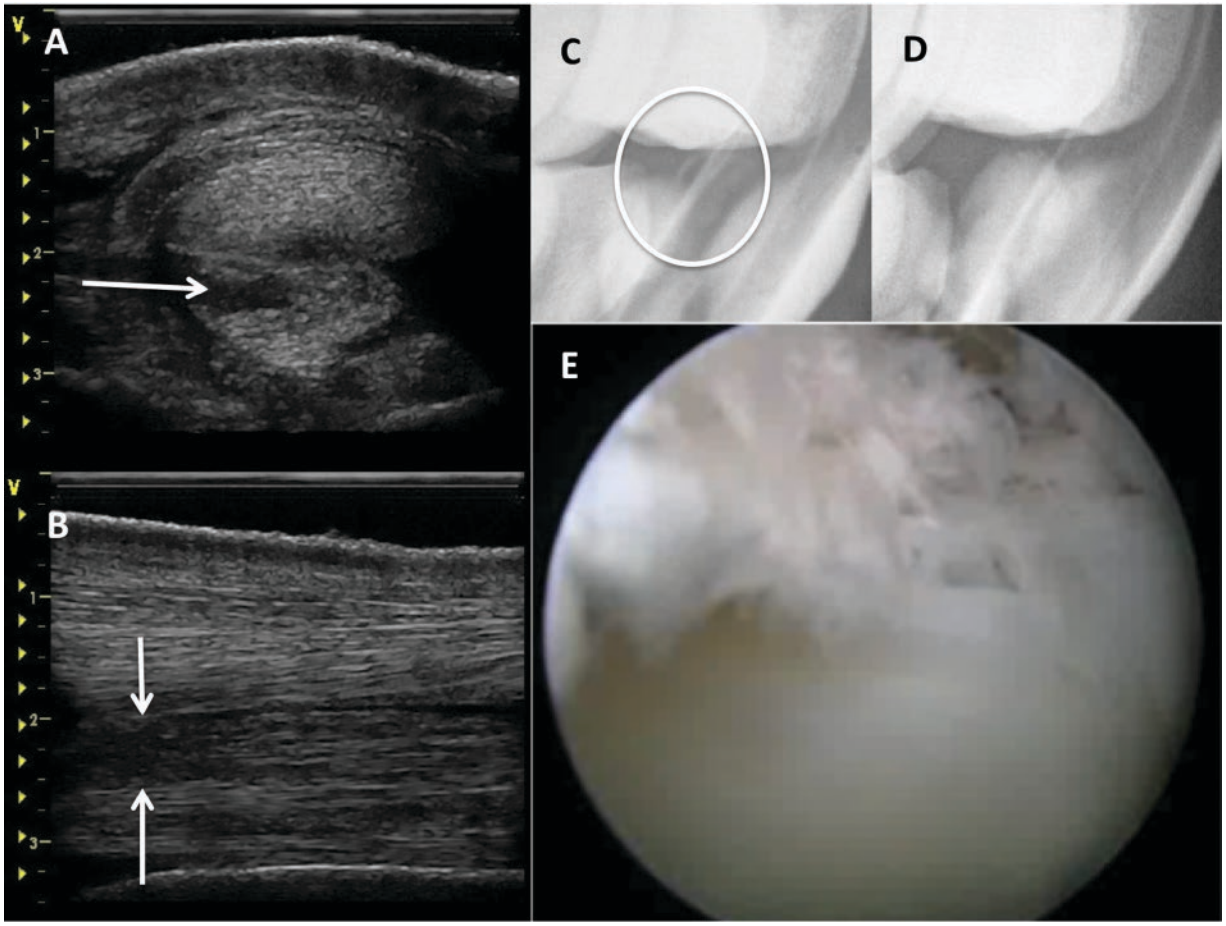


Figure 1.36 (A) and (B) are transverse and longitudinal ultrasound images showing an anechoic asymmetrical lesion in the proximal straight distal sesamoidean ligament (arrows). Its anechoic appearance in this location strongly suggests communication with the adjacent digital sheath, which was demonstrated in this case with contrast tenograms (C) circled; contralateral normal limb for comparison (D) and tenoscopically (E).

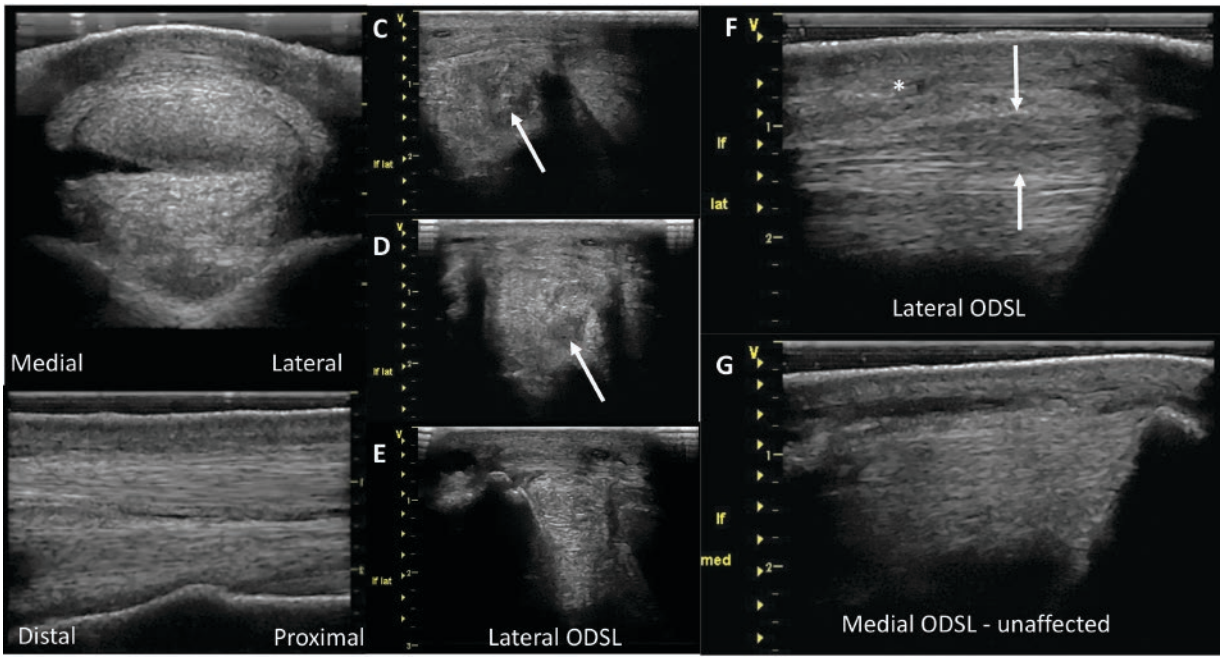


Figure 1.37 Transverse ultrasound image from the palmarolateral aspect of the proximal pastern region showing desmitis of the oblique distal sesamoidean ligament (arrow). This injury is invariably accompanied by subcutaneous fibrosis over the affected ligament (dashed arrow).

Vet-ebooks.com

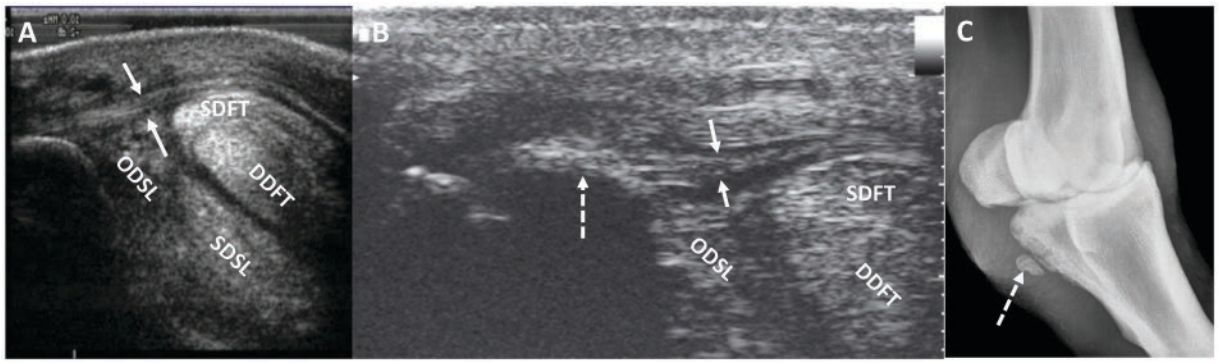


Figure 1.38 Avulsion of the proximal digital annular ligament (PDAL). This injury occurs in hind limbs. (A) The normal appearance of the PDAL between the solid arrows. (B) The association of the avulsion fragment (dashed arrow) with the PDAL (solid arrows). (C) The radiographic appearance (avulsion fragment indicated by the dashed arrow). DDFT: deep digital flexor tendon; SDSL: straight distal sesamoidean ligament; ODSL: oblique distal sesamoidean ligament.

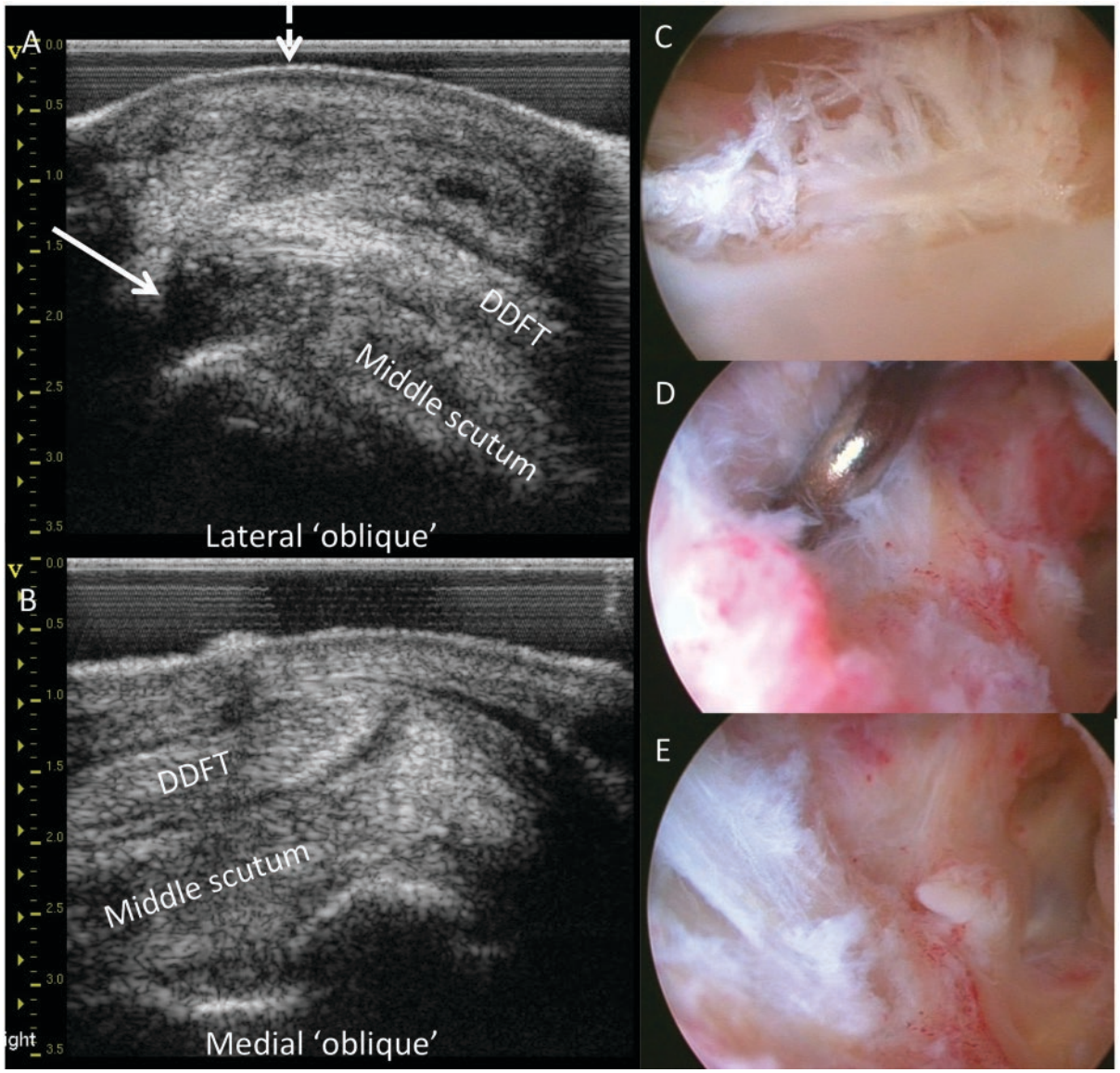


Figure 1.39 Desmitis of the lateral axial palmar ligament of the proximal interphalangeal (PIP) joint. Transverse ultrasound images obtained obliquely over the distal pastern region at the level of the proximal interphalangeal joint from the palmarolateral (A) and normal palmaromedial (B) aspects. The dashed arrow shows the subcutaneous fibrosis and the solid arrow the hypoechogenic palmar ligaments of the PIP joint. This disruption extended into the palmar pouch of the PIP joint, seen arthroscopically (C). An arthroscopic probe could be inserted into the damaged ligament (D). Image (E) shows the arthroscopic appearance of the ligament after debridement.

Vet-ebooks.com

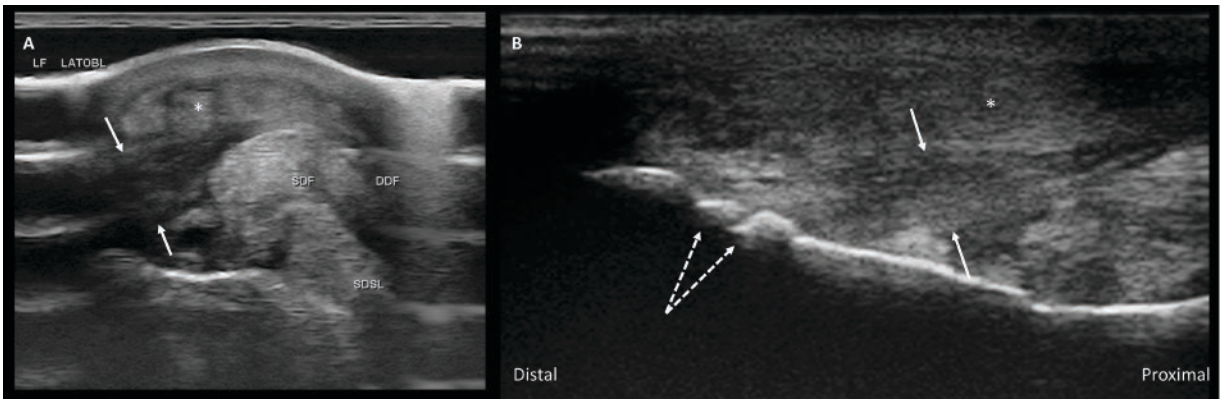


Figure 1.40 Desmitis of the palmar abaxial ligament of the proximal interphalangeal joint. (A) Transverse oblique image (palmarolateral aspect) and (B) longitudinal oblique image on the right (proximoaxial to distoabaxial). Note the substantial oedema (*). The damaged ligament is delineated by solid arrows while the enthesiopathy at their attachment site on the second phalanx is shown by the dashed arrows. Distal is to the left.

fractures, the ligaments themselves have been largely normal in appearance.

Proximal Interphalangeal Joint (PIP)

Abnormalities

Synovial effusion can be identified ultrasonographically during ultrasonographic evaluation of the distal palmar/plantar pastern as an anechoic region deep to the straight distal sesamoidean ligament. Dorsally, effusion can be identified deep to the common or long digital extensor tendon.With degenerative joint disease of the PIP joint, osteophytes and enthesophytes can be visualized ultrasonographically around the periphery of a joint by a roughened bone surface echo. Osteophytes can be imaged on the palmar surface at the limits of the anechoic synovial cavity when scanning longitudinally over the pastern.Osteoarthritis of the PIP joint can often be related to damage of the collateral. Acute injury to these ligaments can be identified by enlargement and hypoechogenicity of the ligaments and occasionally avulsions. More chronic pathology is manifest by osteoarthritis and enthesophytosis, which are best identified ultrasonographically when the transducer is oriented longitudinally and moved over the lateral and medial aspect of the PIP joint.

Injury can also occur to the palmar/plantar ligaments of the PIP joint (Figure 1.39). These injuries are rare but manifest as swelling in the distal pastern with pain on palpation in the region of the branches of the superficial digital flexor tendon. Ultrasonographic examination is the best way to distinguish the origin of the swelling from injury to the branches of the superficial digital flexor tendon. There is subcutaneous hypoechoic swelling (oedema) with hypoechogenicity around and deep to the branch of the superficial digital flexor tendon. Longitudinal oblique views in line with the ligament can demonstrate irregularity at the sites of attachments of the palmar/plantar ligaments abaxially on the surface of the distal proximal phalanx (Figure 1.40)

The articular cartilage of the PIP joint is very thin, which makes accurate identification of cartilage lesions difficult. Osteochondrotic lesions are usually identifiable by their bony changes (visible radiographically) rather than the articular cartilage changes per se. Ultrasound can be useful to differentiate some of the bony fragments on the palmar/plantar aspect of the fetlock joint, some of which are considered to be osteochondrotic in origin, while others are fractures or ossification within the DSLs.

Recommended Reading

Busoni, V. and Denoiz, J.-M. (2001). Ultrasonography of the podotrochlear apparatus in the horse using a transcuneal approach: Technique and reference images. *Veterinary Radiology & Ultrasound* 42: 534–540.

Chope, K. and García-López, J.M. (2013). Ultrasound and treatment of conditions affecting the navicular bursa. In: *Conference: Large Animal Proceedings*, North American Veterinary Conference: Orlando FL, 19–23 January 2013.

Dik, K.J., Boroffka, S., and Stolk, P. (1994), Ultrasonographic assessment of the proximal digital annular ligament in the equine forelimb. *Equine Veterinary Journal* 26: 59–64.

Dyson, S.J. (1992). Ultrasonographic examination of the pastern. *Equine Veterinary Education* 4: 254–256.

Grewal, J.S., McClure, S.R., Booth, L.C. et al. (2004). Assessment of the ultrasonographic characteristics of the podotrochlear apparatus in clinically normal horses

Vet-ebooks.com

and horses with navicular syndrome. *Journal of American Veterinary Medical Association*. 225: 1881–1888.

Gunkelman, M.A. and Hammer, C.J. (2017). A preliminary study examining the digital cushion in horses. *Journal of Equine Veterinary Science* 56: 6–8.

Hauser, M.L., Rantanen, N.W., and Modransky, P.D. (1982). Ultrasound examination of distal interphalangeal joint, navicular bursa, navicular bone and deep digital flexor tendon. *Equine Veterinary Science* 2: 95–97.

Heitzmann, A.G. and Denoix, J.-M. (2007). Rupture of the distal sesamoidean impar ligament with proximal displacement of the distal sesamoid bone in a steeplechaser. *First Published in Equine Veterinary Education* 19: 117–120.

Jacquet, S. and Denoix, J.-M. (2012). Ultrasonographic examination of the distal podotrochlear apparatus of the horse: A transcuneal approach. *Equine Veterinary Education* 24: 90–96.

Kristoffersen, M. and Thoefner, M.B. (2003). Ultrasonography of the navicular region in horses. *Equine Veterinary Education* 15: 150–157.

MacDonald, J.L., Richter, R.-A., and Wimer, C.L. (2018). Ultrasonographic variations are present in the distal sesamoidean impar ligament of clinically sound horses. *Veterinary Radiol & Ultrasound* 59: 607–612.

O'Brien, E.J.O., McAlpine, J.M., Schramme, M.C. et al. (2018). Avulsion of the proximal digital annular ligament in five hindlimbs. *Equine Veterinary Education* 30(8): 427–432.

Olivier-Carstens, A. (2004). Ultrasonography of the solar aspect of the distal phalanx in the horse. *Veterinary Radiology & Ultrasound* 45: 449–457.

Sage, A.M. and Turner, T.A. (2000). Ultrasonography in the horse with palmar foot pain: 13 cases. *Proceedings of the American Association of Equine Practitioners* 46: 380–381.

Sage, A.M. and Turner, T.A. (2002). Ultrasonography of the soft tissue structures of the equine foot. *Equine Veterinary Education* 14: 78–283.

Smith, M. and Smith, R. (2008). Diagnostic ultrasound of the limb joints, muscle and bone in horses. *In Practice* 30: 152–159.

Spriet, M. and Rossier, Y. (2005). Use of ultrasonography in differential diagnosis of chronic palmar foot pain: 3 cases. *Equine Veterinary Education* 17: 230–234.

Van Thielen, B., Murray, R., Willekens, I. et al. (2017). Ultrasonographic evaluation of the anatomy of the foal foot from 0 to 7 months. *Journal Equine Veterinary Science* 50: 33–43.

References

1 Nottrott, K., De Guio, C., Khairoun, A. et al. (2017). An ultrasound-guided, tendon-sparing, lateral approach to injection of the navicular bursa. *Equine Veterinary Journal* 49(5): 655–661.

2 Smith, R., Parsons, J., and Dixon, J. (2020). Risk of intra-articular injection with longitudinal ultrasound-guided injection of collateral ligaments of the equine distal interphalangeal joint. *Veterinary Radiologu & Ultrasound* 61(1): 67–76.

3 Olivier-Carstens A. (2004). Ultrasonography of the solar aspect of the distal phalanx in the horse. *Veterinary Radiology & Ultrasound* 45: 449–457.

4 Heitzmann AG and Denoix J-M. (2007). Rupture of the distal sesamoidean impar ligament with proximal displacement of the distal sesamoid bone in a steeplechaser. *First published in Equine Veterinary Education* 19: 117–120.

5 Spriet, M. and Rossier, Y. (2005). Use of ultrasonography in differential diagnosis of chronic palmar foot pain: 3 cases. *Equine Veterinary Education* 17: 230–234.

6 Rabba, S., Bolen, G., Verwilghen, D. et al. (2011). Ultrasonographic findings in horses with foot pain but without radiographically detectable osseous abnormalities. *Veterinary Radiology & Ultrasound* 52: 95–102.

Vet-ebooks.com

2

Ultrasonography of the Fetlock

Eddy R.J. Cauvin[1] *and Roger K.W. Smith*[2]

[1] *AZURVET Referral Veterinary Centre, Centre d'Imagerie, Saint-Laurent-du-Var, France*
[2] *The Royal Veterinary College, North Mymms, Hatfield, UK*

The Fetlock Joint

The fetlock region is one of the most common seats of conditions causing lameness in horses of all types and uses. It is a relatively "simple" diarthodial articulation and is probably the easiest starting point for anyone willing to learn to scan joints: most structures are directly accessible through the skin and can be imaged with standard equipment. Many ultrasonographic changes encountered in the fetlock joint may be extrapolated to any other joint or synovial structure throughout the equine body.

Preparation and Scanning Technique

High-frequency (7.5–18 MHz) linear array transducers provide optimal information in this area, although a micro-convex probe may occasionally be useful to image the distal aspect of the sesamoid bones. A standoff pad may be used to improve probe-to-skin contact and structure alignment. However, with copious amounts of coupling gel, placing the probe directly on the skin provides finer control of the pressure exerted on the skin and underlying structures. Excessive pressure may cause pain, alter the shape of structures examined, and displace an effusion or a mobile fragment, which may thus be overlooked.

The technique is fairly simple as most structures are close the skin surface and relatively perpendicular to the sound beam when the probe rests on the skin. Images obtained in a longitudinal plane, i.e., in a direction perpendicular to the joint space and parallel to the long axis of the limb, are easier to interpret, although both longitudinal and transverse planes should be used in combination. A standard examination protocol is presented in Figure 2.1. The joint is first examined with the horse weightbearing on the limb examined. Examination starts on the dorsal aspect of the joint in the sagittal plane, to visualize the sagittal ridge of the metacarpal/metatarsal condyle (MC3) (Figure 2.1A). By convention, the proximal aspect of the limb is placed to the left of the image. The probe is then moved laterally or medially, in parasagittal planes, in order to scan the whole width of the condylar surfaces and the dorsoproximal border of the proximal phalanx (P1) (Figure 2.1B). It is important that the probe remains perpendicular to the joint surface, i.e., in planes parallel to the sagittal plane, to obtain the brightest (most echogenic) and sharpest image of the subchondral bone interface. This applies to most structures to be evaluated. Once the whole dorsal articular surface has been examined in longitudinal views, the transducer is placed over the sagittal ridge and rotated 90 degrees so that the lateral aspect of the limb is to the left of the image (Figure 2.1C). The joint is then scanned in transverse planes from proximal to distal and from lateral to medial, including the entire joint, i.e., from the distal one-third of the metacarpus/metatarsus to the proximal third of P1.

Both abaxial aspects (i.e., lateral and medial aspects) are subsequently assessed, including the abaxial surface of the sesamoid bones. The examination is performed in both longitudinal (i.e., frontal) (Figure 2.1D) and transverse planes (Figure 2.1E), to image the collateral ligaments, epicondyles, joint space, abaxial aspect of the sesamoid bones, and the palmar/plantar joint pouch. Complete evaluation of the collateral ligaments will require slight rotation of

Atlas of Equine Ultrasonography, Second Edition. Edited by Jessica A. Kidd, Kristina G. Lu and Michele L. Frazer.
© 2022 John Wiley & Sons Ltd. Published 2022 by John Wiley & Sons Ltd.
Companion Website: www.wiley.com/go/kidd/atlas

Vet-ebooks.com

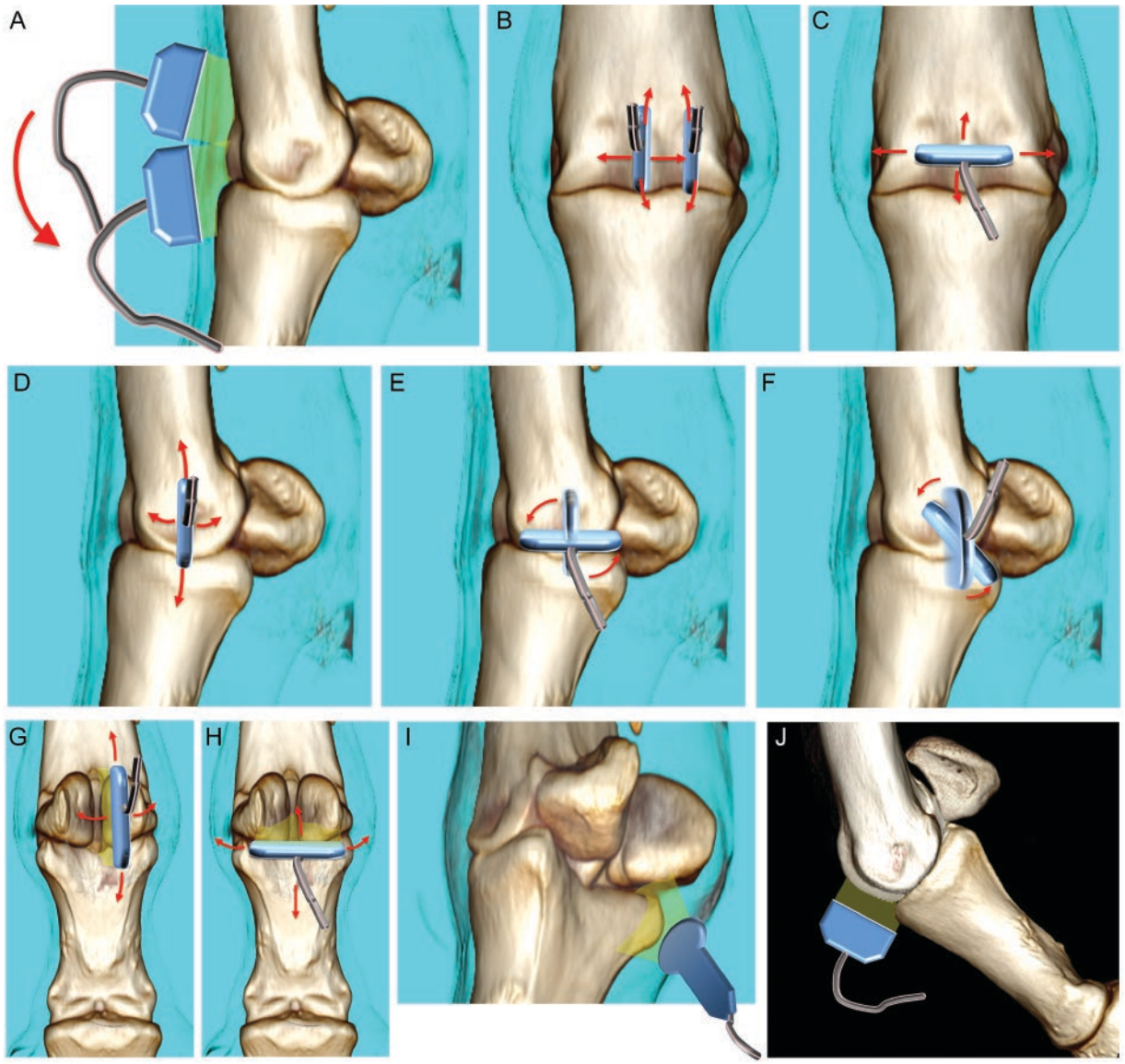


Figure 2.1 Schematic views showing the position of the transducer to examine the four quadrants of the fetlock. Each time the probe is rotated 90 degrees to obtain both longitudinal (A) and (B) and transverse plane (C) images. In between, oblique positions are often necessary to better visualize the various structures. (A) Sagittal plane scan images over the sagittal ridge of MC3. The probe is placed over the dorsal-most aspect of the joint and moved proximally and distally from distal metacarpus to proximal third of P1. (B) The probe is then moved abaxially to assess both medial and lateral MC3 condyles, the sound beam remaining parallel to the sagittal plane in order to remain perpendicular to the joint surfaces. (C) The examination of the dorsal joint region is repeated in a transverse plane. This time the probe plane must follow the curvature of the MC3 condyle and bone surfaces. This is achieved by constantly looking for the brightest bone interface. The probe must be moved both from proximal to distal and lateral to medial in order to scan the whole volume of the dorsal aspect of the joint. (D) and (E) both abaxial (i.e., lateral and medial) aspects of the joint are evaluated both in longitudinal and transverse planes in the same manner. In the transverse plane, the metacarpo-sesamoidean ligament (collateral ligament of the sesamoid) can be seen as a thin, striated structure caudal to the collateral ligament. Special attention is devoted to visualizing the collateral ligaments. To do so, the probe must be aligned to the ligament fibers by gentle rotation of the probe until the required image is obtained (F). The superficial branch is close to the frontal plane of the metacarpus, while the deeper branch is obliquely oriented, the metacarpal origin being dorsal to the long branch and the phalangeal insertion being palmar. (G) and (H) Finally the palmar aspect of the joint is visualized along with the structures of the digital flexor tendon sheath, abaxial surfaces of the proximal sesamoid bones and suspensory ligament structures (see below). Both transverse (H) and longitudinal (G) plane images must be obtained over the whole extent of the digital sheath from proximal to distal and from lateral to medial, including the abaxial surface of the sesamoid bones and P1. In order to image the oblique and short distal sesamoidean ligaments, the probe must be angled in order to align the beam with the ligament fibers. This requires thorough knowledge of the anatomy and some practice. (I) To image the short (deep) distal sesamoidean ligament, a microconvex transducer must be used and placed distoabaxial to the base of the sesamoid bones, in the space between the latter and the palmar processes of P1. It is angled upward and axially. (J) The examination is completed by flexing the joint and holding it off the ground or with the toe resting on a block, in order to expose the distal aspect of the metacarpal condyle. The examination is performed over this area as in (A) to (C).

Vet-ebooks.com

the probe in the long axis, in order to bring the superficial and deep branch fibers in alignment with the scan plane (i.e., align the ligament fibers across the image) (Figure 2.1F). The superficial branch is more or less parallel to the long axis of the metacarpus with the limb weightbearing. The deep branch crosses its superficial counterpart, so that the probe must be tilted counterclockwise laterally and clockwise medially (i.e., the proximal end of the probe is rotated dorsally and the distal end toward the palmar aspect of the limb).

Finally, the examination is continued over the palmar/plantar aspect of the fetlock to image the tendon sheath structures (see below) but also the sesamoid bone surfaces, inter-sesamoidean ligament, and distal sesamoidean ligaments for a comprehensive assessment of the fetlock area (Figures 2.1G and 2.1H). It may be useful to use a convex array transducer to image the space between the base of the sesamoid bones and the proximal palmar border of P1 and the short distal sesamoidean ligaments (Figure 2.1I). A small-footprint linear transducer may also be used. This will be described in the second part of this section.

The limb is eventually picked up and flexed as much as the horse will tolerate in order to evaluate the distal metacarpal/metatarsal joint surfaces (Figure 2.1J). This may be performed in both longitudinal and transverse planes.

Ultrasonographic Anatomy of the Normal Fetlock Joint

The gross morphology of the fetlock has been described in textbooks and the reader is encouraged to review the anatomy in detail in order to improve both the technique and ability to detect subtle anomalies. The main anatomical features to bear in mind will be reviewed here before addressing the normal ultrasonographic features.

The fetlock may be considered a typical condylar diarthrodial joint (Figure 2.2). As for all diarthodial articulations, the fetlock comprises the bone surfaces, the overlying hyaline cartilage, the joint capsule with an inner synovial membrane, and outer fibrous capsule (ligaments are local fibrous reinforcements of the fibrous capsule).

The pathology will therefore reflect this structure and many ultrasonographic alterations encountered in each joint tissue will be the same in the same tissue type for all diarthrodial joints.

The distal articular surface of the third metacarpus (MC3) or metatarsus (MT3) (referred to as metacarpal or metatarsal head in the *Nomina Anatomica Veterinaria*) forms a transversely arranged, cylindrical surface, separated into two condyles by a sagittal ridge. These parts of the metacarpal/metatarsal head fit into reciprocal depressions on the proximal

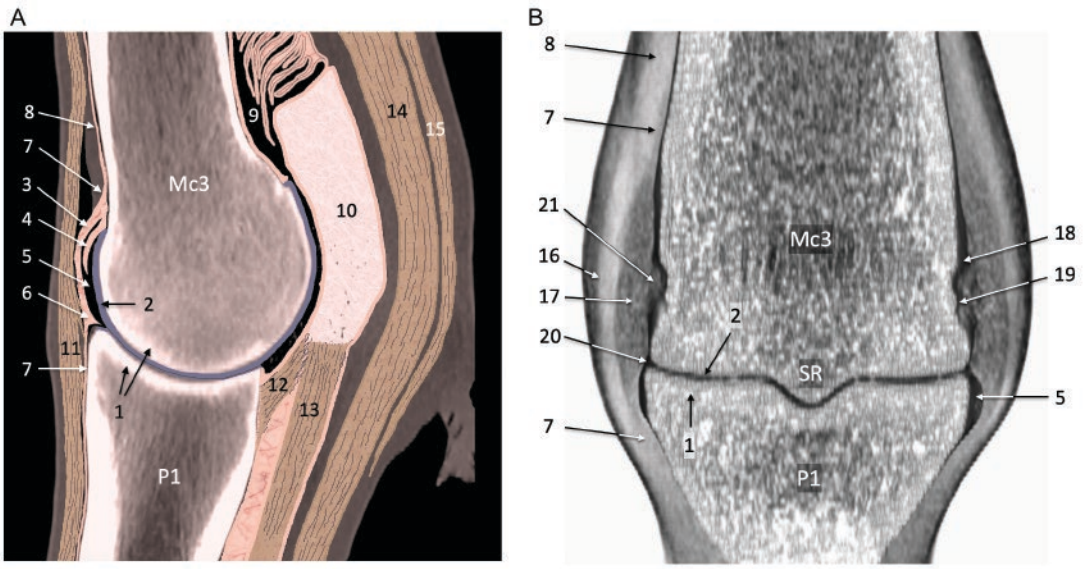


Figure 2.2 Schematic organization of the fetlock joint – Sagittal (A) and frontal (B) sections. MC3: third metacarpal/metatarsal bone; P1: proximal phalanx; SR: sagittal ridge of the metacarpal condyle; 1: subchondral bone; 2: hyaline cartilage; 3: joint capsule (fibrous with inner synovial lining); 4: dorsal proximal synovial fold; 5: joint fluid; 6: transverse fold; 7: enthesis (capsular/ligamentous insertions); 8: periosteum; 9: palmar joint pouch with villous synovial folds; 10: proximal scutum/intersesamoidean ligament; 11: common/long digital extensor tendon; 12: short distal sesamoidean ligament; 13: straight distal sesamoidean ligament; 14: deep digital flexor tendon; 15: superficial digital flexor tendon; 16: collateral ligament (superficial branch, continuous with periosteum); 17: collateral ligament (deep branch, obliquely transsected); 18: metacarpal epicondyle; 19: epicondylar fossa; 20: joint space.

Vet-ebooks.com

surface of the proximal phalanx (P1). This arrangement only allows for flexion and extension movements in the sagittal plane of the limb. The joint is encased in a single joint capsule, although this is functionally separated into dorsal and palmar/plantar compartments by the collateral ligaments medially and laterally. These are tightly pushed against the abaxial surfaces of the MC3 or MT3 head, although synovial membrane fills the space between the concave supracondylar fossa of the MC3/MT3 and the ligament, leaving only a very thin, slit-like passage for the synovial fluid between the two compartments. Fluid distension can therefore only occur dorsal or palmar/plantar to the collateral ligaments, unless these have ruptured. Dorsally, the capsule is quite redundant to allow for extension. It forms a wide and thin synovial fold dorsoproximally and a fibroelastic transverse ridge which fills the triangular space between the capsule, metacarpal head, and proximal P1. The digital extensor tendons are closely associated with the capsule, although there is a synovial bursa between these two structures dorsoproximally.

The proximal sesamoid bones are ossified structures developing within the palmar/plantar joint capsule. They are joined by a short and strong, transversely arranged intersesamoidean ligament. They are covered on the dorsal, articular surface by hyaline cartilage and on the palmar/plantar surface by fibrocartilage to sustain the pressure from the deep digital flexor tendon. This modified palmar/plantar capsule is refered to as proximal scutum (scutum proximale). It attaches to the palmar/plantar aspect of the proximal and middle phalanges by a series of strong distal sesamoidean ligaments, reinforcing the capsule (see below). Finally, each sesamoid bone has an ipsilateral collateral sesamoidean ligament whose transverse fibers blend into the capsule and superficial branch of the collateral ligaments.

The ultrasonographic anatomy of the fetlock has been described by Denoix (1996) [1]. The fetlock is grossly similar in the thoracic and pelvic limbs. "Metacarpus" and "palmar" will therefore be used for both "metacarpus"/"metatarsus," and "palmar"/"plantar" in the following text. The basic organization of the joint is schematically reviewed in Figure 2.2.

The distal metacarpus forms a smooth, cylindrical surface, transversally oriented and separated into two condyles (lateral and medial) by the sagittal ridge. The latter is perfectly round and smooth in longitudinal section and triangular in cross-section (Figure 2.3). The cartilage is anechogenic and regular in thickness. It is thickest over the sagittal ridge (usually 1–1.2 mm) and thinner over the condyles, typically less than 0.7 mm. The mineralized part of the cartilage and underlying subchondral bone cannot be differentiated; they form a smooth, hyperechogenic interface, producing shadowing and reverberation.

Proximal to the condyles and sagittal ridge, the cartilage is interrupted and there is often a small step between the edge of the cartilage and bare bone proximal to it. In this location, bone is actually covered by synovium up to the proximal insertion of the joint capsule. This area may be variable in shape, slightly irregular, or concave (Figure 2.4).

The dorsoproximal edge of the proximal phalanx (P1) is rounded and smooth and its proximal articular surface is not visible (Figure 2.3). The dorsomedial and dorsolateral eminences of P1 are slightly convex, the medial one being slightly more prominent. In normal joints, the capsule and synovium are tightly applied against the bone surfaces. With severe effusion, the capsule may be displaced away from the bone surfaces.

The joint capsule on the dorsal aspect of the joint is thick, fibrous (isoechogenic to the extensor tendons), and elastic (Figures 2.2 and 2.3). It inserts proximally on the metacarpus 3–4 cm proximal to the proximal limit of the condyles and distally on the dorsoproximal aspect of P1, approximately 2 cm distal to the proximal border. There, the capsule adheres to the common/long digital extensor tendon. The lateral digital extensor tendon blends broadly into the fibrous capsule.

Dorsally, the synovial membrane forms a transverse ridge, triangular in longitudinal section, which fills the space between the metacarpal condyles and P1. Proximally, the membrane reflects back to form a thin, flat, and transversely oriented fold or pad (also called the synovial plica), normally not visible unless there is marked thickening and/or effusion. No fluid is normally visible.

The thin (2–4 mm) common (or long) digital extensor tendon (CDE) is separated from the joint capsule by a small subtendinous bursa. The latter is virtual and rarely visible in normal horses (Figure 2.3).

Abaxially (laterally and medially), the medial (MCL) and lateral (LCL) collateral ligaments are mere focal thickening of the joint capsule (Figure 2.5). Their borders are therefore difficult to differentiate from the rest of the fibrous capsule in cross-sections. In longitudinal (frontal) planes, parallel striation similar to that of tendons is clearly identified. Each ligament is made out of two separated branches: a long, superficial part and a shorter, deep part. The superficial branch originates from the metacarpal epicondyle and blends into the periosteum some 3 cm proximal to it. It inserts distally on the abaxial border of P1,

Vet-ebooks.com

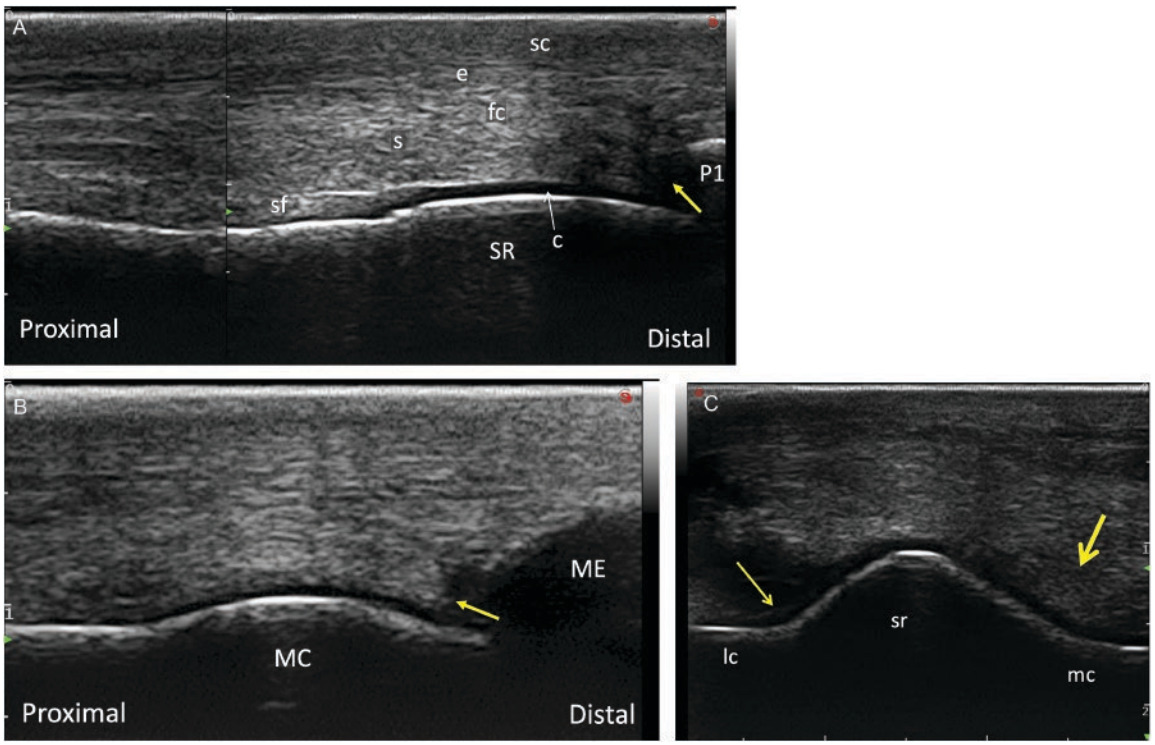


Figure 2.3 (A) Sagittal ultrasound scan over the sagittal ridge, showing the smooth sagittal ridge (SR) with overlying hyaline cartilage (c), the proximal dorsal aspect of P1 (p), synovial membrane (s), and common (or long) digital extensor tendon (e). Note the synovial pad reflection (dorsal synovial fold) in the proximal aspect of joint (sf). Little or no fluid is usually visible in the joint space. Sc: subcutaneous tissue; fc: fibrous capsule. The triangular, dorsal space between the joint surfaces (yellow arrow) is filled by a rigid synovial membrane extension, which forms a pointy transverse fold. (B) A parasagittal image obtained medial to the sagittal ridge shows the round medial metacarpal condyle (MC) and dorsomedial proximal eminence of P1 (ME). The cartilage is thinner than on the sagittal ridge. The transverse synovial fold may be surrounded by a small amount of joint fluid (arrow). (C) Transverse image over the dorsal aspect of the fetlock. The sagittal ridge (sr) and condyles (lateral [lc] and medial [mc]) are smooth and even. The cartilage is clearly visible, except over the sides of the sagittal ridge where it is off-incidence. The synovial membrane fills the space on either side of the ridge (thick arrow). A small amount of fluid may be seen on the side of the sagittal ridge, and a thin interface is seen between the anechogenic cartilage and the fluid (thin arrow).

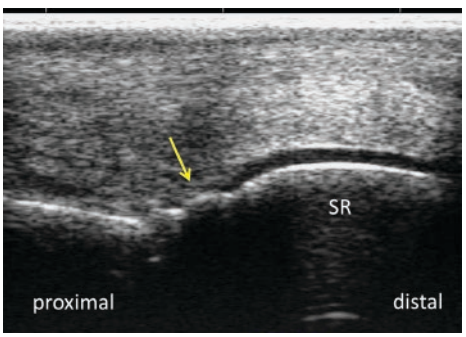


Figure 2.4 Sagittal view of the dorsoproximal aspect of the sagittal ridge, showing a common variation in the normal bony contour, proximal to the sagittal ridge (SR) where the cartilage thins out gradually at its edge. The bone surface proximal to it is lined by synovial membrane (arrow). The bone there may be irregular. Although this may be associated with joint disease, it is often encountered in clinically normal horses.

2–3 cm distal to the joint space. The deep branch originates dorsodistal to the epicondyle, crosses in a distopalmar direction under the superficial branch, and inserts on the edge of P1 close to the joint space. The collateral ligaments are therefore X-shaped and each branch must be examined separately (Figure 2.1). The transversely oriented collateral ligaments of the proximal sesamoid bones blend into the ipsilateral deep branch of the collateral ligament.

The palmar aspect of the joint is largely hidden by the proximal sesamoid bones (Figure 2.6). The sagittal ridge of the distal metacarpus is visible from the palmar aspect of the limb between them, through the transversely oriented intersesamoidean ligament and hypoechogenic proximal scutum.

The palmar synovial recess of the fetlock joint is a large synovial pouch located between the metacarpus, the apex of the sesamoid bones, the branches of the suspensory ligament, and the distal extremity ("button") of the splint bones (second and fourth

Vet-ebooks.com

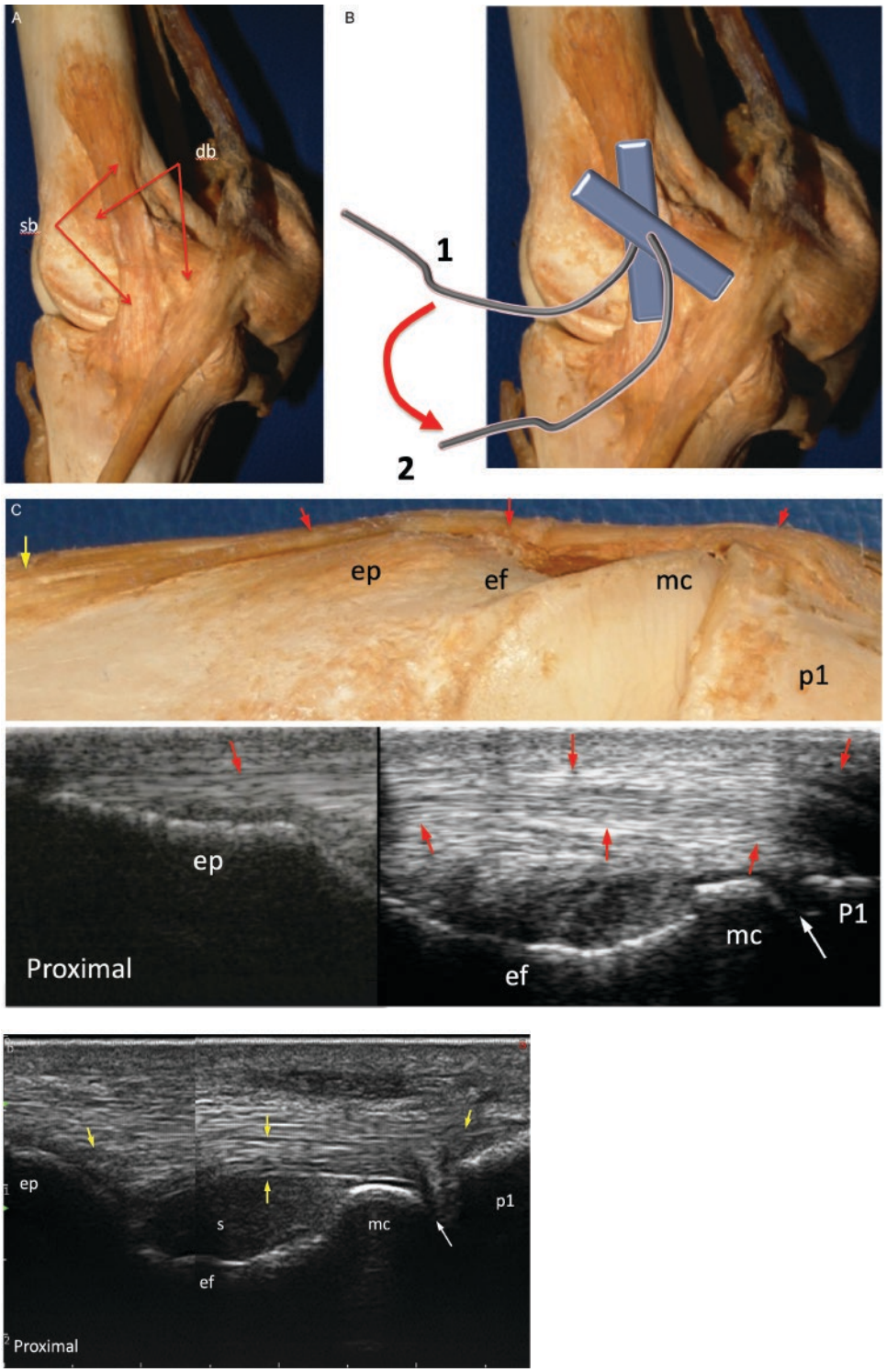


Figure 2.5 (A) Dissected specimen showing the structure of the collateral ligaments (sb: superficial branch; db: deep branch). (B) Positioning of the transducer, along the axis of the metacarpus to image the sb (1) and after an approximate 30-degree rotation to image the db (2). (C) Dissected specimen and ultrasonographic image obtained in a frontal plane (probe aligned with the metacarpus in position 1 showing the superficial branch of the collateral ligament (red arrows) extending from proximal to the epicondyle (ep) to the abaxial aspect of P1 (p1). The superficial branch blends into the periosteum (yellow arrow). The joint space is indicated by the white arrow. ef epicondylar fossa; mc metacarpal condyle. (D) Rotation of the probe according to position 2 will bring the deep branch into view (yellow arrows). Its extends from the distal aspect of the epicondyle (ep) to the proximal edge of P1, spanning the epicondylar fossa (ef). The space between the bone and ligament is filled with hypoechogenic synovial membrane (s). The white arrow points to the joint space.

Vet-ebooks.com

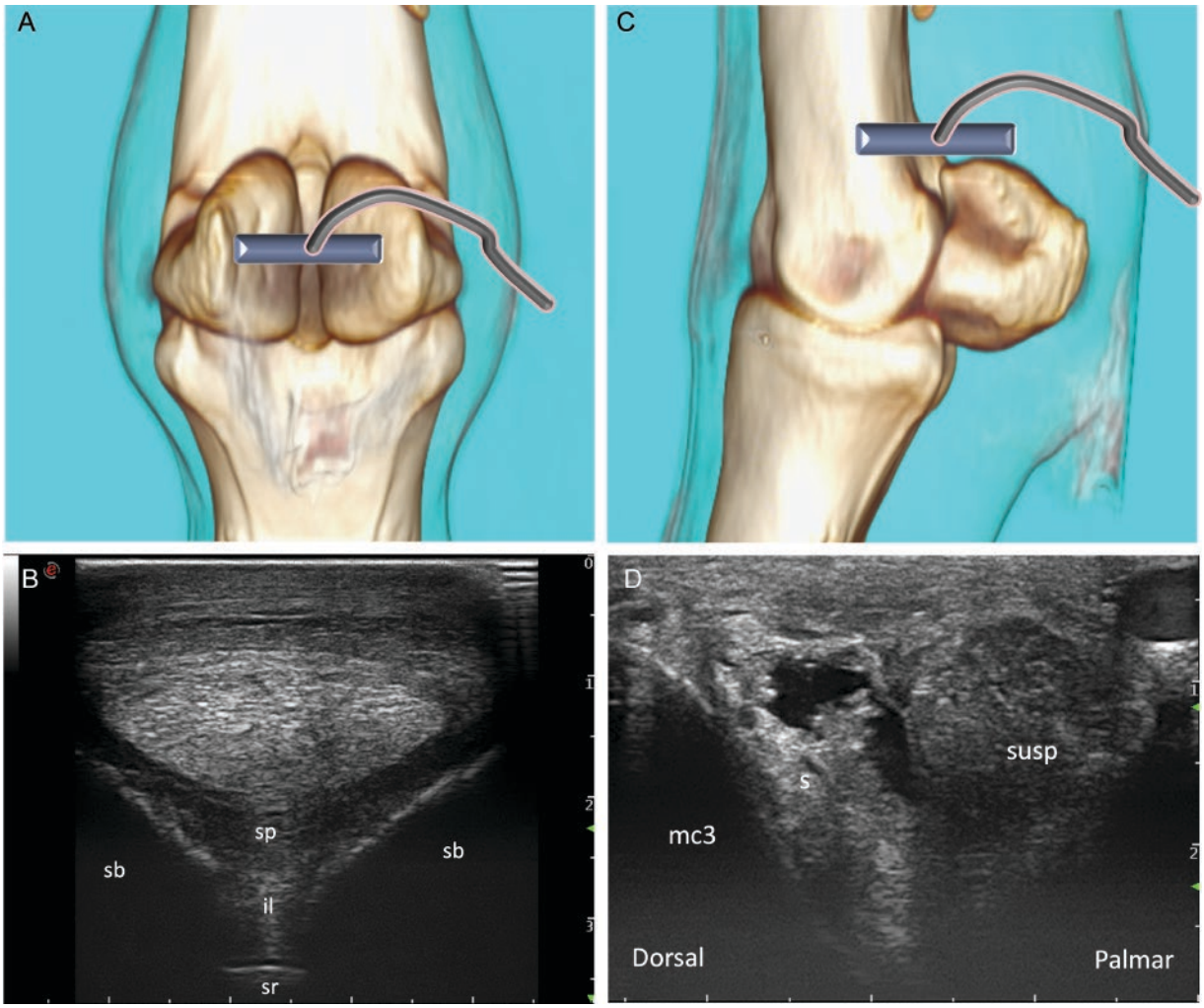


Figure 2.6 Imaging of the palmar aspect. (A) Position of the transducer. (B) Ultrasonographic image with the transducer as in (A). The scutum proximale (sp) forms a thick fibrocartilage, which encloses the sesamoid bones (sb). The intersesamoidean ligament (il) should be homogeneous and regular with a transverse fiber pattern. Only a small width of the sagittal ridge (sr) is visible between the two sesamoid bones. (C) The palmar recess of the metacarpophalangeal joint is imaged through a palmaroabaxial approach. (D) The palmar recess is located in a triangle between the metacarpus (MC3), proximal sesamoid bone, and branch of the suspensory ligament (susp). It is filled with synovial villi (s) with little fluid normally visible.

metacarpal bones). In normal horses, it is mostly filled by thick, highly vascularized synovial folds and contains little fluid. It can, however, fill up with a moderate amount of fluid in clinically normal horses.

Ultrasonographic Abnormalities of the Fetlock

Synovitis/Arthritis

Synovitis refers to inflammation of the synovial lining of the joint. It is a feature of most joint diseases but may occur as a primary entity, particularly in sports and racehorses. It should not be mistaken for a non-inflammatory joint effusion ("cold effusion"), where abnormal amounts of anechogenic fluid are present without any thickening of the synovium.

Acute synovitis is characterized by mild to severe thickening of the synovial layer of the capsule (this layer is not normally visible) because of edema, vascular hyperemia, and distension of the synovial pouches by joint fluid (Figure 2.7). The inflammation is most obvious dorsoproximally. The dorsal fold ("synovial pad or plica") is displaced away from the articular surface, and becomes hypoechogenic, mildly thickened, and clubbed (Figure 2.8). The palmar pouch contains large synovial villi that rapidly become hypertrophied and fill up the pouch within a matter of days. These form dense, amorphous, and highly vascularized masses.

Vet-ebooks.com

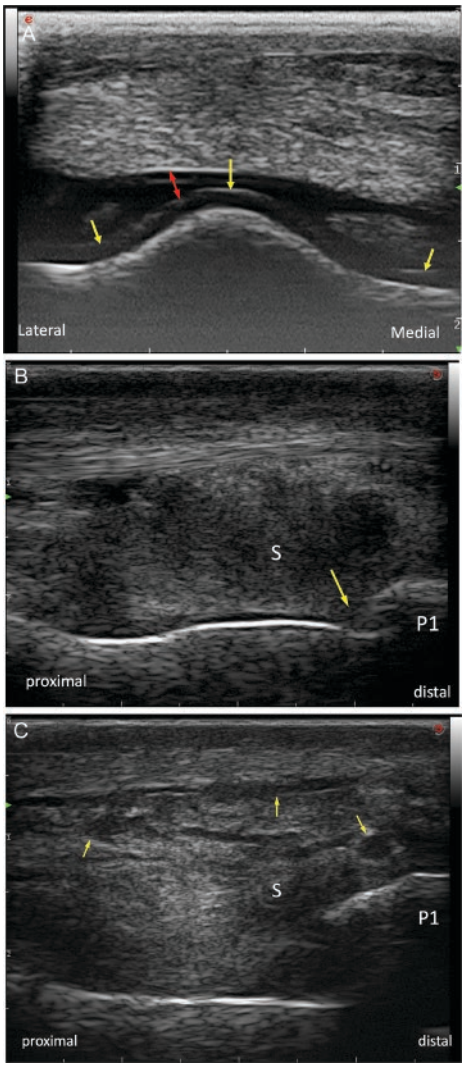


Figure 2.7 Acute synovitis. (A) Dorsal aspect, transverse plane: the dorsal pouch is filled with anechogenic fluid displacing the capsule and extensor tendon dorsally (double red arrow). The cartilage interface is visible (yellow arrows). (B) Dorsal aspect, sagittal plane: the synovial membrane (s) is hypoechogenic, and the transverse synovial ridge remains sharp and triangular (arrow). (C) Dorsomedial aspect, parasagittal plane: in severe cases, very enlarged capsular vessels are seen (arrows), and edema causes the synovium to appear heterogeneous (s).

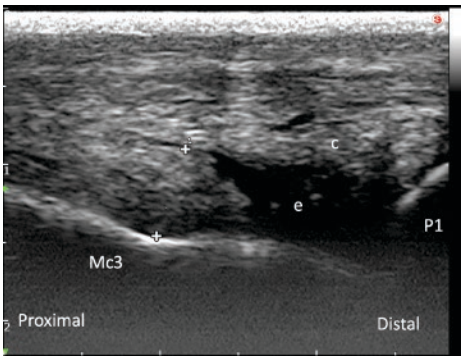


Figure 2.8 Within hours of injury, the proximal synovial pad thickens up and takes on a clubbed appearance (calipers), though remaining hypoechogenic (dorsomedial aspect, parasagittal plane). The capsule is thickened, heterogeneously hypoechogenic, and displaced by the synovial fluid effusion (e). MC3: distal metacarpus, c = joint capsule.

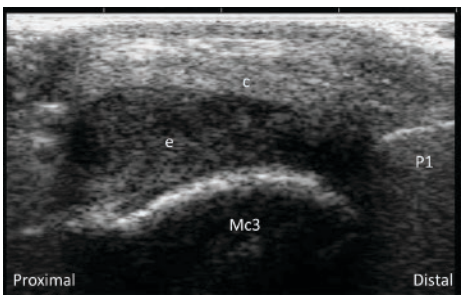


Figure 2.9 Hemarthrosis (dorsomedial aspect, parasagittal plane). The joint fluid (e) is abnormally echogenic and grainy. This may be indistinguishable ultrasonographically from purulent septic fluid. C: joint capsule.

The fluid is normally anechogenic. In early, acute stages, mildly echogenic, "cellular" and grainy fluid may be present (Figure 2.9). This is typical of hemarthrosis, although this appearance is very similar to that of septic exudate. Bleeding probably occurs through trauma and tearing of the capsule and synovium. The fluid rapidly becomes anechogenic unless recurrent bleeding or sepsis is present, although fibrin clots and pannus may remain, adhering to cartilage for several days to weeks (Figure 2.10).

Chronic synovitis may develop as a complication of nearly any fetlock joint pathology that has been left untreated for too long or has not responded to treatment. The echogenicity of the synovial membrane increases, mostly because of a cellular infiltrate and secondary fibroplasia. It becomes more homogeneous and isoechogenic relative to the fibrous capsule. Fibrosis and retraction lead to rounding of the synovial pads and ridges (Figure 2.11).

Assessment of the synovial fold on the dorsal aspect of the joint is usually used as a reference point to confirm chronic inflammatory changes. There currently is a lack of quantitative data regarding what tissue thickness should be regarded as abnormal. Denoix suggests that thickening of the dorsoproximal synovial fold over 2 mm in thickness is a sign of

Vet-ebooks.com

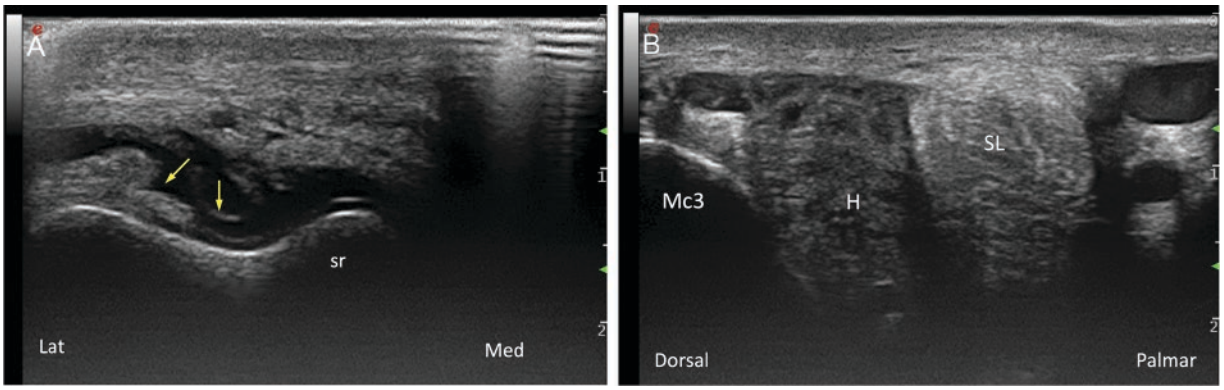


Figure 2.10 In the subacute stage, blood is removed but fibrin pannus or strands (arrows) may be visible. (A) Dorsal aspect transverse oblique plane), and an organizing hematoma (H) may become visible in the redundant palmar pouch. (B) Palmar lateral aspect, transverse plane). SR: sagittal ridge of MC3; SL: lateral suspensory ligament branch.

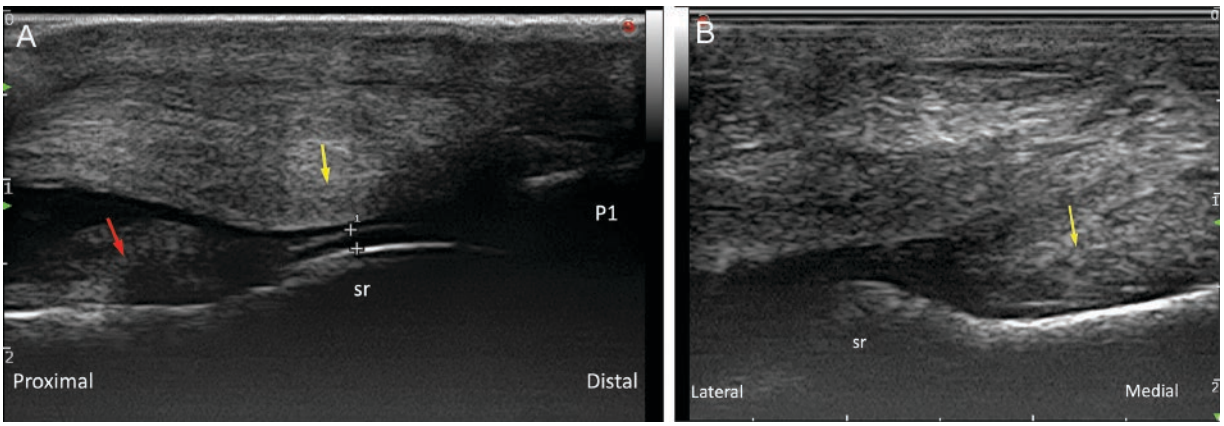


Figure 2.11 (A) Dorsal aspect, sagittal plane. In chronic synovitis, the synovial membrane becomes more echogenic and rounded (yellow arrow). Note the cartilage interface (calipers) over the sagittal ridge (sr) and clubbed, thickened proximal synovial fold (red arrow). (B) Dorsal aspect, transverse plane: The dorsoproximal synovial pad becomes rounded to club-shaped, forming a dense, mass-like structure most prominent abaxial to the sagittal ridge, immediately proximal to the medial and/or lateral condyles (arrow).

inflammation, while other authors use a cut-off thickness of 4 mm [1].

In the palmar pouch, hypertrophic villi may be clubbed or rounded or form localized, dense masses, which can eventually undergo fibrocartilaginous metaplasia or even become mineralized (thus producing hyperechoic acoustic shadowing artifacts).

Synovial hypertrophy and hyperplasia can form space-occupying lesions (Figure 2.12A). Initially referred to as villonodular synovitis**,** they are most frequently recognized in the dorsal proximal pouch, where a pressure-induced, smooth, and rounded defect is often observed on the dorsodistal aspect of the metacarpus on radiographs as on ultrasound images (Figure 2.12B)**.** Similar hyperplastic masses are also common in the palmar pouch (Figure 2.12C). This condition is purely inflammatory in horses and should therefore be referred to as chronic hypertrophic synovitis. In-between stages, spanning from mild proliferation to very large mass formation, are encountered.

Traumatic Cartilage/Subchondral Bone Injury

Traumatic arthritis of the fetlock can include bone contusion and various degrees of bone surface damage (subchondral bone or cartilage injuries, fragmentation, etc.). Although radiography, using specific oblique views, can show the presence of fragmentation or defects, radiographs are often non-diagnostic. Scintigraphy and magnetic resonance imaging (MRI) are the most sensitive techniques to confirm such lesions. Ultrasonography will often confirm the presence of subchondral bone defects or cartilage erosions (Figure 2.13). Lesions located on the palmar part of the metacarpal condyles are hidden from view by the sesamoid bones. Large lesions may, however, be identified with the joint fully flexed.

Vet-ebooks.com

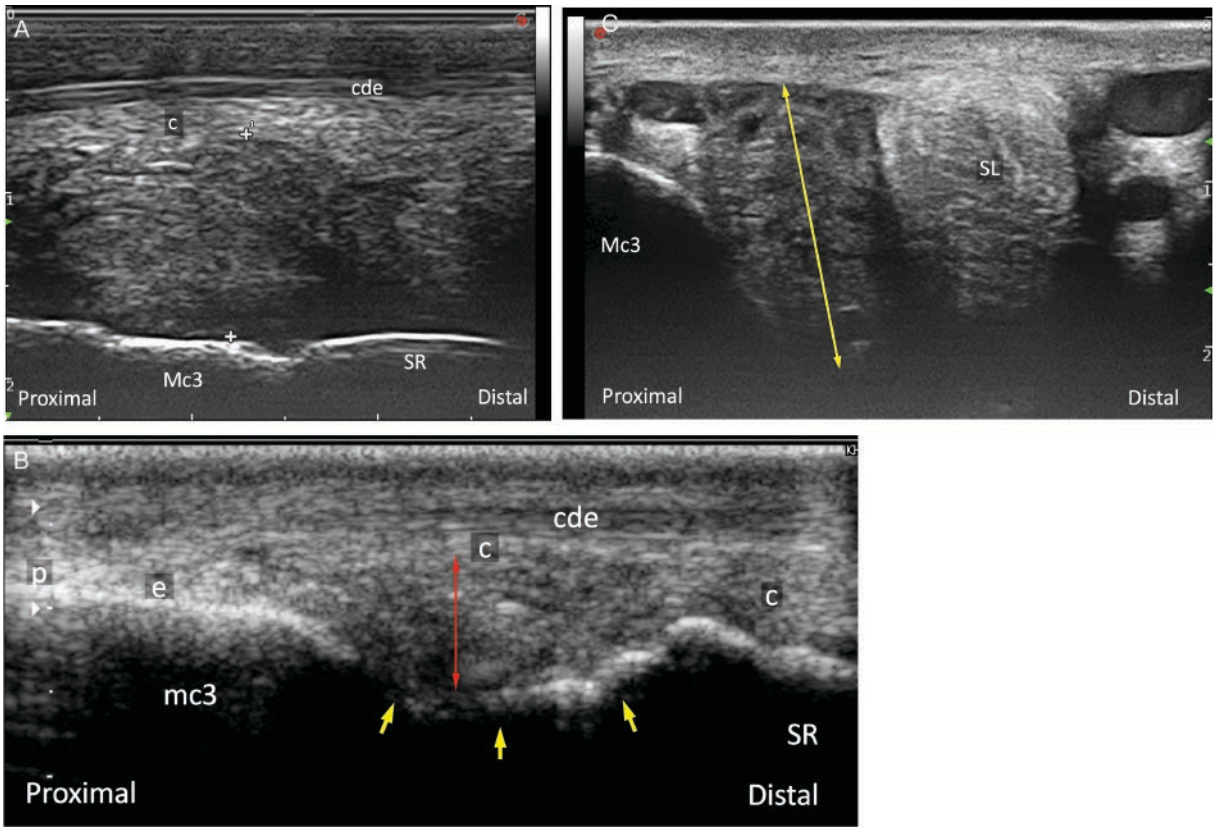


Figure 2.12 (A) Dorsal aspect of the fetlock, sagittal plane. Chronic hypertrophic synovitis can produce firm synovial masses (between calipers) filling the joint recesses and displacing the fibrous capsule (c) and extensor tendons, cde: common digital extensor tendon. (B) Same plane in a different animal. These synovial masses are space occupying and can eventually cause pressure remodeling of the underlying bone (double red arrow), especially prominent dorsoproximally, proximal to the sagittal ridge (SR) and condyles. (C) Transverse image over the palmar joint pouch showing a tissue mass (double yellow arrow) filling the space between the medial suspensory ligament branch (SL) and the palmar aspect of MC3. SR: sagittal ridge; MC3: third metacarpal bone; e: proximal capsular enthesis; p: periosteum.

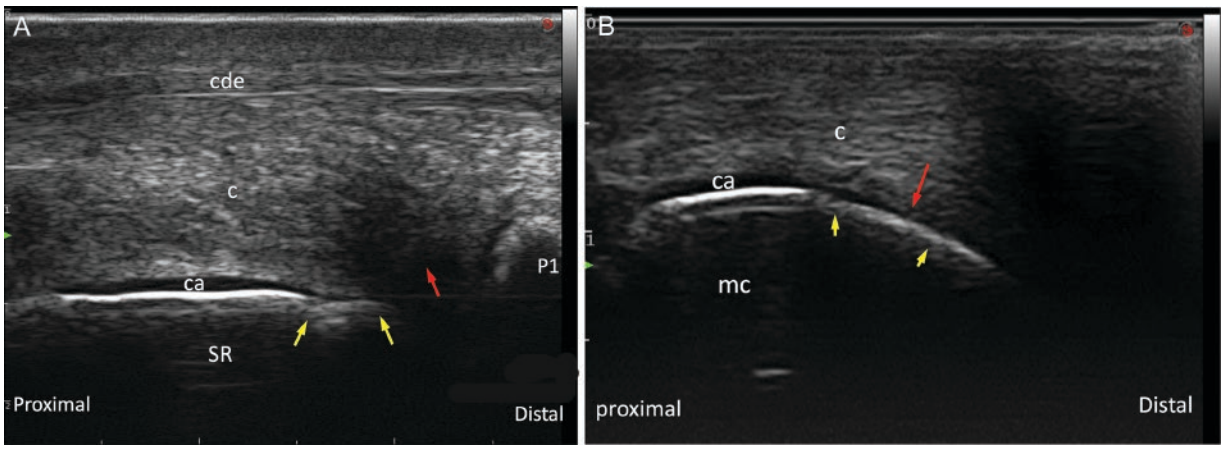


Figure 2.13 Trauma or concussion to the joint surface can cause focal destruction of the cartilage and erosion or chipping of the underlying subchondral bone. (A) A focal defect is seen on the subchondral bone of the sagittal ridge (yellow arrows), with loss of cartilage and direct contact between the synovium and exposed bone (dorsal aspect, sagittal plane, horse weightbearing). Subacute synovitis is present with synovial edema and effusion (red arrow). Similar images may be obtained with "kissing lesions." (B) Parasagittal view over the distal aspect of the metacarpus (lateral condyle) with the fetlock fully flexed (probe position as on Figure 2.1j), showing focal loss of cartilage, exposing the underlying subchondral bone (yellow arrows) which appears slightly irregular. The synovial membrane fills the defect (red arrow). mc: medial condyle; P1: proximal phalanx; SR: sagittal ridge; ca: hyaline cartilage; c: capsule; cde: common digital extensor tendon.

Vet-ebooks.com

Proximal P1 subchondral injuries are not amenable to ultrasonographic diagnosis. Further investigations may be indicated if there is ultrasonographic evidence of severe synovitis without specific lesions identified on either radiography or ultrasonography.

Osteoarthritis (OA)

Fetlock OA is extremely common. Radiographic signs are often subtle and occur late in the disease process, at a stage where cartilage damage has become irreversible. Ultrasonography provides much earlier signs of joint disease and permits identification of very subtle lesions or new bone production (Figure 2.14).

Typically, the earliest signs of OA include mild to severe synovitis and subtle cartilage changes, with focal or diffuse irregularity and discrete hyperechogenic foci. Thinning is most obvious on the sagittal ridge (although care should be taken not to misinterpret the incidental irregularity frequently seen at the dorsoproximal end of this ridge). Erosions may be visible on the distal aspect of the metacarpal condyles. In severe cases, there may be barely any visible cartilage left, the capsule coming into contact with the subchondral bone (Figure 2.14). Focal defects may result from contact ("kissing") lesions induced by osteochondral fragments (Figure 2.15). High-frequency probes (12–18 MHz) may be required to provide details of cartilage integrity.

Osteophytes are bony proliferations at the ends of the subchondral bone plate, where the synovial membrane replaces cartilage. True osteophytes form irregular to spiky, hyperechogenic interfaces that protrude into the joint (Figure 2.16). They are typically in alignment with the joint surface. They are most commonly encountered at the dorsoproximal border of P1, along the proximo-abaxial edges of P1 and the disto-abaxial edges of the metacarpal condyles, along the dorsoproximal margin of the cartilage-covered condyles and at the apex of the sesamoid bones. There may also be marked irregularity of the proximal extremity of the sagittal ridge.

Enthesophytes are bony new bone productions within the insertion of capsules (Figure 2.16C), ligaments, or tendons. They may be secondary to chronic inflammation, OA, primary capsulitis, or collateral desmitis (see below). They are encountered within the dorso-abaxial insertion of the capsule, and at the collateral ligament attachments on P1 and the metacarpus.

Chronic hypertrophic synovial hyperplasia is usually present in OA (Figure 2.14C), although repeat intra-articular medication with steroid drugs may prevent chronic inflammatory changes, especially in young racehorses, making the diagnosis more difficult to confirm on ultrasound examination.

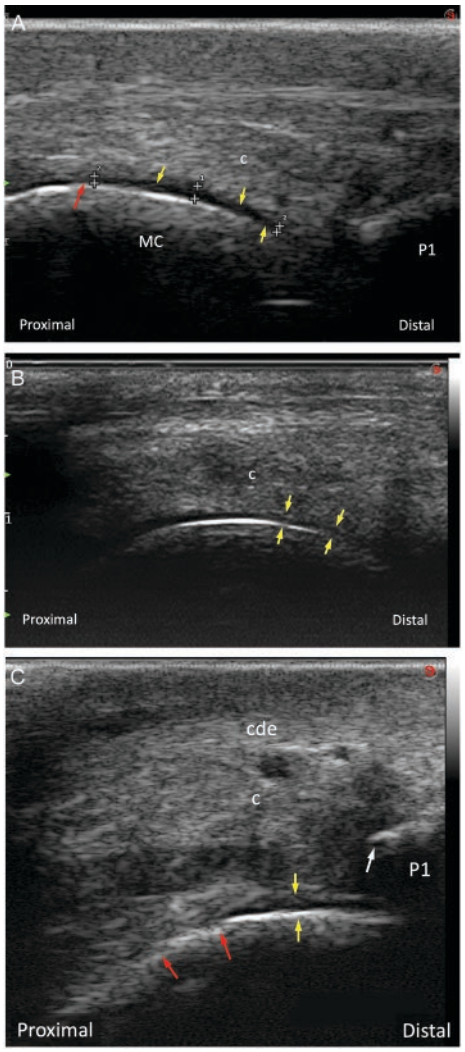


Figure 2.14 Standing, medial parasagittal image over the medial metacarpal condyle (MC). The cartilage is abnormally thin and very irregular in thickness (calipers). It is heterogeneously hyperechogenic (yellow arrows) and a focal chondral erosion is visible (red arrow).

Osteochondrosis and Cyst-Like Lesions

Subtle erosions or defects in the subchondral bone outline are more readily identified ultrasonographically

Vet-ebooks.com

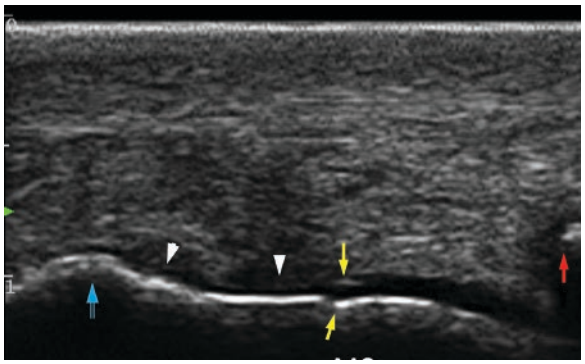


Figure 2.15 There is small, mineralized "chip" fragment at the dorsomedial proximal border of the proximal phalanx (red arrows). (A) A discrete defect (yellow arrows) is noted in the cartilage and subchondral bone on the medial condyle, at the area of contact of the fragment during hyperextension ("kissing lesion"). The cartilage proximal to the impact lesion is markedly thinned and heterogeneous (white arrow heads). Note an early osteophyte at the proximal extent of the subchondral bone interface (blue arrow). (B) Flexed parasagittal view over the dorsomedial aspect of the joint. The subchondral bone of the medial metacarpal condyle is smooth and even but there is diffuse thinning of the cartilage (arrows), which appears slightly hyperechogenic and heterogeneous. (C) Partially flexed, medial parasagittal view over the medial metacarpal condyle. There is severe, chronic synovitis with the capsule displacing the common digital extensor (CDE) tendon. The cartilage is very irregular and heterogeneously echogenic (yellow arrows) and there is widespread loss of cartilage, the synovial membrane coming into contact with the underlying bone interface (red arrows). Note the osteophytic bone spur on P1 (white arrow). C: capsule.

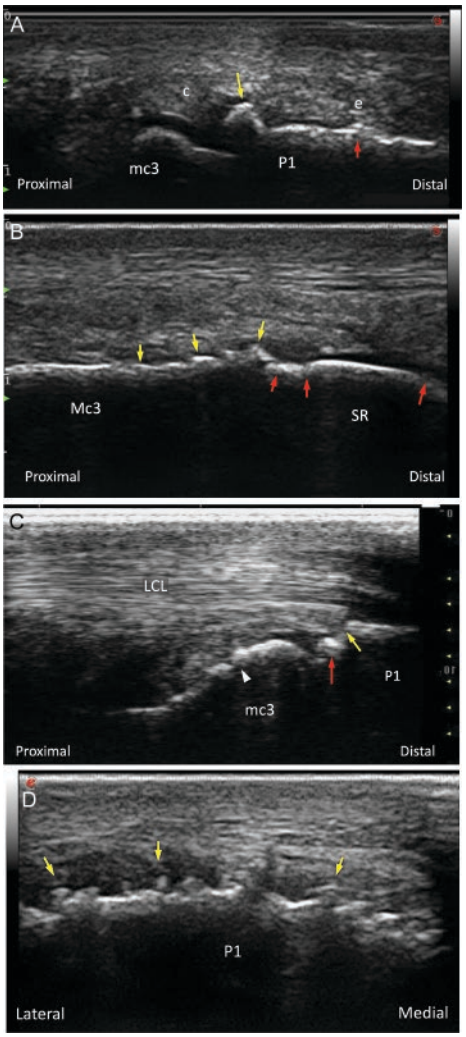


Figure 2.16 Various locations and appearances of osteophytes. (A) Spur-like exostosis (yellow arrow) at the dorso-medio-proximal border of P1 (medial dorsal eminence) (dorsal parasagittal image). Note the echogenic thickening of the capsule (c) and entheseous new bone remodeling (red arrow) at the capsular insertion on P1 (e). (B) More diffuse irregular new bone (yellow arrows) at the dorsoproximal aspect of the sagittal ridge (SR), with focal erosions and areas of hyperechogenicity of the hyaline cartilage (red arrows). (C) Spur-like new bone production at the lateral articular border of P1 (red arrow). Note this osteophytic bony spur is continuous with the articular surface of P1 and deep to the insertion of the collateral ligament (LCL). This must be differentiated from entheseophytes at the insertion of the deep branch of the ligament (yellow arrow). More diffuse, irregular osteophytic new bone is visible at the abaxial border of the metacarpal condyle (white arrow-head). (D) Long-standing, severe OA can lead to exuberant new bone productions (yellow arrows) at the articular margins, as here on P1 (transverse view over the dorsal aspect of the proximal P1).

than radiographically. The extent of the lesion in both longitudinal and transverse planes can be accurately established. Associated soft tissue inflammatory changes, cartilage thinning, and adhesions can also be detected. Depending on the stage of the lesion, it may be difficult to differentiate osteochondrosis from osseous cyst-like lesions, subchondral bone trauma, and erosions secondary to OA.

Osteochondrosis (OC) is common in the fetlock. The most common site is the dorsal aspect of the sagittal ridge where it can span from mild, usually clinically silent flattening of the ridge, to various degrees of subchondral bone defects (Figure 2.17). The thickness and echogenicity of the cartilage are both increased in OC, although thinning of the cartilage will eventually occur as a result of fragmentation and fibrillation of the damaged cartilage, and secondary OA. Ultrasonography provides useful information on cartilage dissection or fragmentation and on the extent and location of the lesions (Figure 2.18). Cartilage dissection (osteochondritis dissecans or OCD) may be identified by the formation of an interface between the cartilage and bone defect in some cases (Figure 2.18A). Hyperechogenic areas of mineralization may be seen within affected cartilage

Vet-ebooks.com

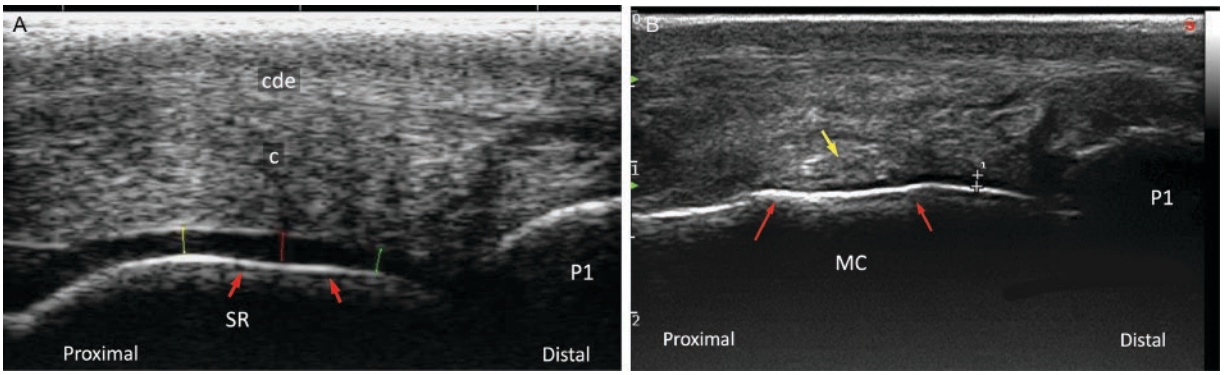


Figure 2.17 (A) Osteochondrosis lesion of the sagittal ridge (SR), with an abnormally flat to slightly concave shape of the subchondral bone (red arrows) and focal thickening of the overlying cartilage (calipers). The latter is regular and anechogenic, there is no sign of dissection. This is usually an incidental finding, although in this horse the capsule (c) is notably thickened and the common digital extensor tendon (cde) displaced. (B) There is a more severe OC lesion on the dorsal aspect of the medial condyle, immediately medial to the sagittal ridge (MC). The subchondral bone is irregular and concave, the overlying cartilage has partially sloughed off and appears irregular and heterogeneous (red arrows). The cartilage appears normal distal to the lesion (calipers). Thickened synovium adheres to the lesion (yellow arrow). Note the chronic synovitis.

(Figures 2.18B, 2.18C, and 2,18D) and loose cartilage or osteochondral fragments ("joint mice") may be identified within the joint space. Large fragments, usually lenticular (i.e., thin and oval shaped) may be encountered within, or attached to the dorsoproximal synovial fold (Figure 2.18E). These are often associated with large erosions on the lateral and/or medial condyle(s) but do not seem to arise from the hyaline cartilage. Although it is unclear what their origin may be, histological features suggest they probably represent articular chondromatosis (i.e., ectopic intrasynovial development of growth-cartilage fragments).

Osseous cyst-like lesions are rare in the fetlock and may occur either in the proximal P1, in which case they are not visible ultrasonographically, or in the distal metacarpal condyle (Figure 2.19). They appear as localized defects on the subchondral bone surface with associated defects or abnormalities of the overlying cartilage, which becomes thickened, echogenic, and irregular. They may be indistinguishable from subchondral bone injuries.

Osteochondral Fragments

Hyperechogenic fragments are most frequently encountered on the dorsal aspect of the metacarpophalangeal joint. It can be difficult to differentiate between fractures, osteochondrosis, and ectopic bone or mineralization on radiographs. Ultrasonography has been shown to be more sensitive and specific than radiography to identify and localize osteochondral fragments in the dorsal fetlock region. Furthermore, it can provide useful information regarding the clinical significance of such fragments, including secondary synovitis, OA, or associated cartilage injuries.

Chip fractures occur most commonly at the dorsomedio-proximal eminence of P1 (Figure 2.20), and occasionally the lateral eminence. They form hyperechoic, convex interfaces that cast an acoustic shadow, separated from the bone by a hypoechogenic gap. The fragment typically retains the dimensions and shape of the normal eminence with a sharp interruption of the bone interface at the fracture site. There is usually marked soft tissue thickening dorsal to the fracture and in chronic cases new bone formation usually develops around the fracture site, often in association with signs of OA.

The fragments may be loose within the joint space, moving freely when the joint is manipulated or if pressure is exerted on the capsule with the probe (Figure 2.21). Most fragments are, however, partially attached to the capsule or synovium. The extent of soft tissue attachment should be evaluated. These fragments may be embedded within the synovial membrane (Figure 2.22), which may have important repercussions on the decision for or against surgery and the favored technique for its removal.

Partially mineralized fragments may arise within the synovial membrane without obvious fragmentation or osteochondrosis. As previously described, they may result from idiopathic chondromatosis. Contrary to fracture fragments, these are usually very smooth and rounded, sometimes with a hypoechoic, superficial layer (Figures 2.18E). Some loose or synovial mineralized bodies may also occur from cartilaginous metaplasia or ectopic mineralization, possibly as a result of chronic inflammatory changes, corticosteroid injections, or hemarthrosis (Figure 2.23).

Vet-ebooks.com

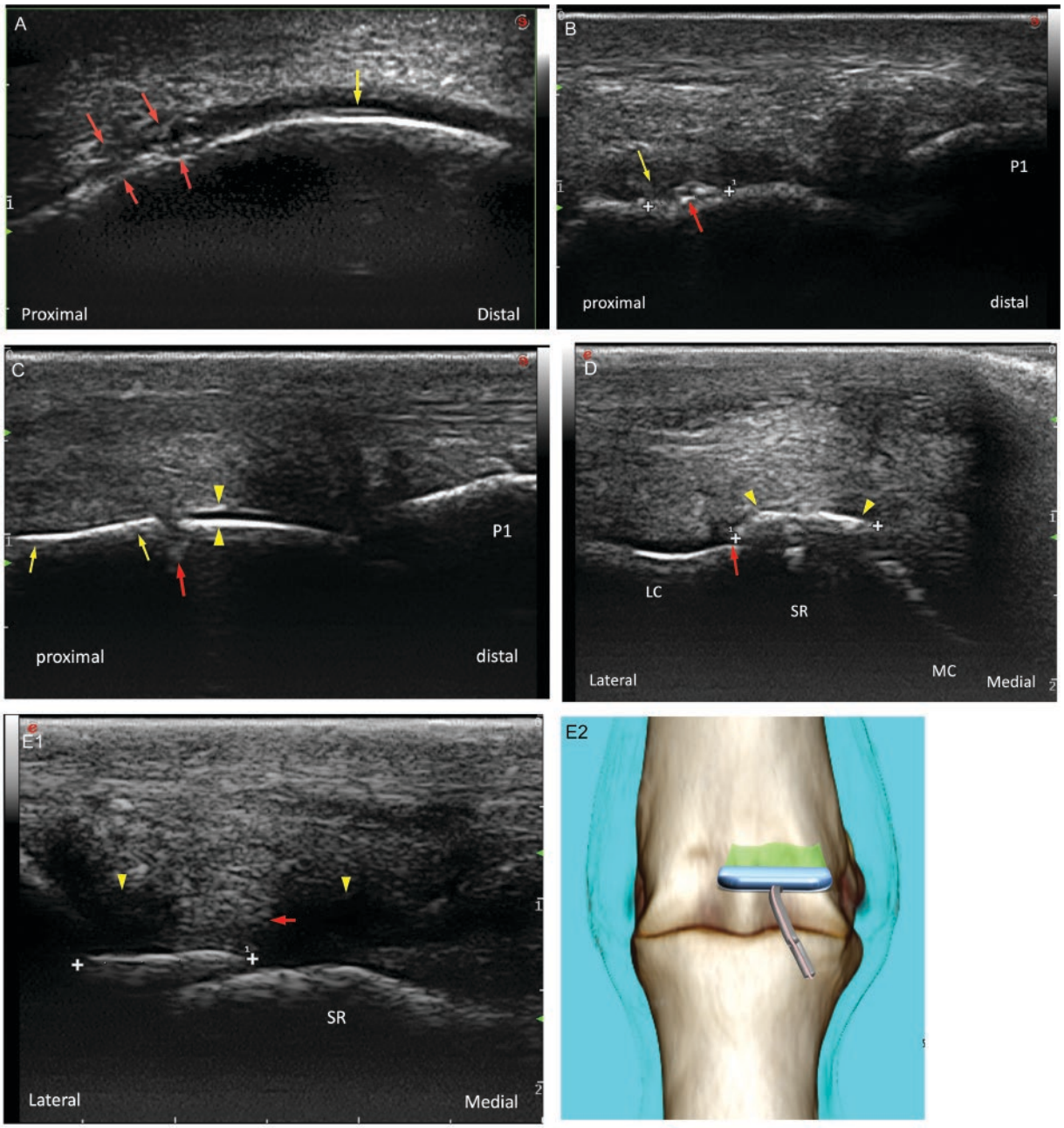


Figure 2.18 (A) Osteochondrosis of the dorsal aspect of the sagittal ridge. The subchondral bone is irregular proximally with thickened, echogenic, and heterogeneous cartilage (red arrows). (A) A linear interface (yellow arrow) is noted between the deep portion of the cartilage and a shallow subchondral bone defect, characteristic of cartilage dissection (OCD). The cartilage flap is thinned and heterogeneous. (B) Dorsal aspect of the medial condyle, parasagittal plane: OC lesion with an irregular subchondral bone defect (calipers). Mineralization of the abnormal cartilage is evidenced by hyperechogenic foci within the thickness of the cartilage (red arrow). The synovial membrane adheres to the defect (yellow arrow). (C) Large OCD lesions on the dorsal aspect of the sagittal ridge can give rise to large, smooth mineralized fragments sitting in place (yellow arrows). What looks like subchondral bone is actually an osteochondral fragment. A defect (red arrow) delineates the margin of the fragment. The remainder of the cartilage over the sagittal ridge is normal (arrow-heads) and there is no sign of synovitis or osteoarthritis at this stage (sagittal plane). (D) Transverse image over the dorsal aspect of the metacarpal condyle. An irregular, mineralized chondral fragment is visible on the tip of the sagittal ridge (callipers). The synovial membrane is in contact with the mineralized interface (yellow arrow-heads). The red arrow points to the margin of the fragment whose size can be precisely measured. SR: sagittal ridge; LC: lateral condyle. (E) Image obtained in a transverse plane, immediately proximal to the dorsal limit of the sagittal ridge and corresponding scanning position. A large, mineralized fragment (between the calipers) is embedded in the dorsoproximal synovial fold, lateral to the sagittal ridge and proximal to the lateral condyle. Effusion displaces the capsule away from the bone interface (yellow arrow-heads) but not from the fragment it adheres to (red arrow).

Vet-ebooks.com

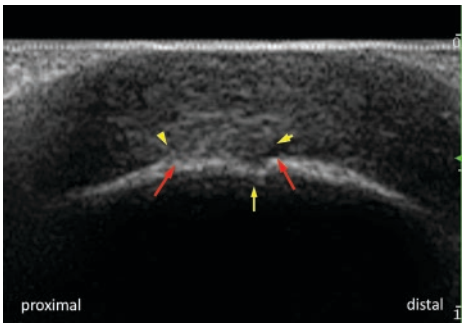


Figure 2.19 Flexed medial parasagittal image over the exposed distal medial metacarpal condyle. Osseous cyst-like lesion ("bone cyst") of the distal condyle. The ostium (yellow arrow) is very thin and surrounded by a crater-shaped defect in the subchondral bone (red arrows). Note the synovial membrane filling the osteochondral defect (arrow-heads).

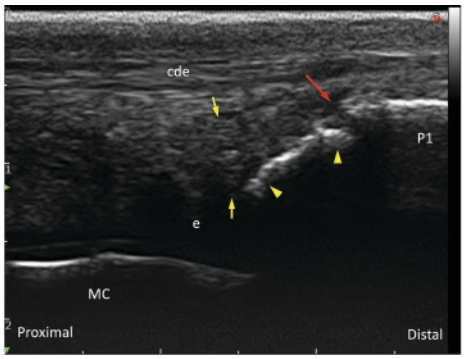


Figure 2.20 Dorsomedial parasagittal image over the medial metacarpal condyle showing a large bony fragment (arrow-heads) broken off the dorsomedial eminence of P1. The fracture line is visible with irregular new bone at the margins (red arrows). There is marked capsule thickening (yellow arrows) and anechogenic effusion (e). MC: medial condyle of MC3; cde: common digital extensor tendon.

These "bodies" may be difficult to differentiate and can be very large, with no corresponding defect being identified on radiographs. They are usually located within the synovium, especially in the dorsoproximal synovial fold (pad) or occasionally in the transverse fold or palmar pouch. They may be an incidental finding with no associated inflammatory changes, unless there is mechanical interference with the joint. Looking for secondary joint injury, particularly synovitis and cartilage erosions (kissing lesions), helps with establishing the prognosis and with making a decision for or against surgery.

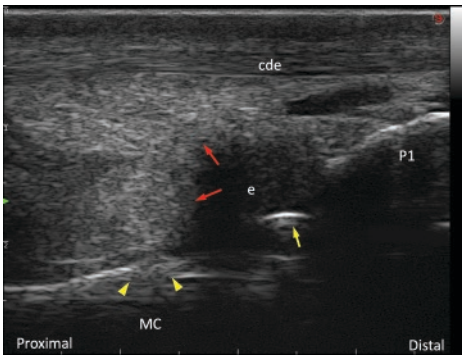


Figure 2.21 Bone fragment (yellow arrow) moving freely within the fluid-distended joint space (e). The capsule is markedly thickened and displaced (red arrows) and a focal "kissing lesion" is noted on the condylar surface (arrow heads) (dorsomedial aspect, parasagittal plane). cde: common digital extensor tendon.

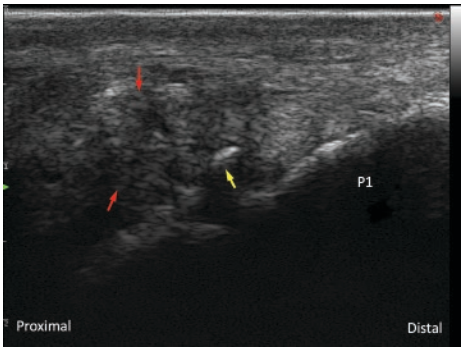


Figure 2.22 Small chip fragment (yellow arrows) arising from the dorsolateral eminence of P1, displaced but embedded in the thickened synovial membrane (red arrows), which completely surrounds the hyperechogenic interface. These fragments may be difficult to see arthroscopically (dorsolateral, parasagittal plane).

Developmental osteochondral fragments commonly arise at the dorsoproximal aspect of P1. These are often suspected to be a form of osteochondrosis, although there is controversy regarding their pathogenesis. These may be difficult to differentiate from chip fractures (Figure 2.24), unless located within the original defect in the subchondral bone (see Figure 2.19). No associated fracture bed is identified in P1, although a smooth, shallow underlying defect may be present. They may be hypoechogenic but most commonly become partially or fully mineralized. Loose osteochondral fragments may be free within the joint cavity. Most commonly, however, they are attached to

Vet-ebooks.com

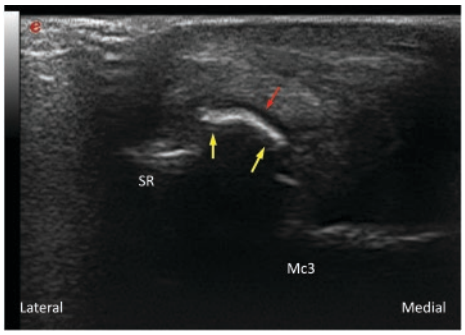


Figure 2.23 Large mineralized fragment (yellow arrows) embedded in the synovial membrane, on the dorso-medio-proximal aspect of the fetlock immediately medial to the proximal extent of the sagittal ridge (SR) (transverse plane). There is a thin, anechogenic layer around the fragment (red arrow). This may be suggestive of chondromatosis, although the irregular shape and significant thickness of this body may also suggest a displaced OC fragment secondarily embedded in synovium.

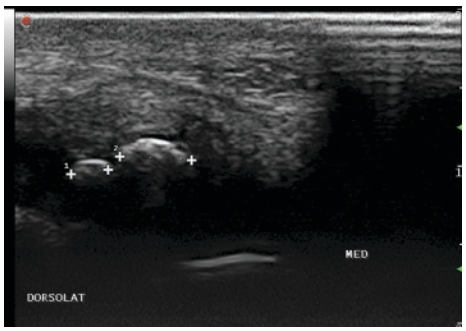


Figure 2.24 OCD fragments (calipers) are usually rounded and smooth and often attached to synovial membrane (transverse plane, dorsolateral aspect).

the capsule by fibrous adhesions or are completely surrounded by synovial membrane. They are often an incidental finding with no other associated sign of joint disease.

Collateral Ligament Desmopathy

Injured collateral ligaments present with features similar to those of injured tendons. Although there may be focal, hypoechoic areas ("core lesions"), the most common ultrasonographic changes include increase in size, diffuse decrease of echogenicity, loss of fiber pattern, and edema (hypoechoic halo) around the ligament (Figure 2.25). These changes may affect one or both branches of the affected ligament. The injuries can be subtle or discrete (Figure 2.26), so the ligaments should be compared with the contralateral limb. In less severe sprains, there is diffuse decrease of echogenicity of the ligament without obvious fiber disruption (Figure 2.27). Periligamentous swelling often forms a hypoechogenic halo around the ligament and there may be variable evidence of secondary synovitis in the joint. There is currently no published data regarding normal thickness for these ligaments.

Rupture may be partial (desmitis) or complete, with both deep and superficial branches being damaged in the majority of cases, although occasionally only one branch is affected or the severity of injury may differ between both branches. The lateral collateral ligament (LCL) was more frequently injured than the medial one (MCL) in Tenney and Whitcomb's review of 2008 [2]. In their study, rupture of both LCL and MCL was not observed but the contralateral ligament usually showed some thickening and heterogeneity, suggesting biaxial desmitis.

Complete rupture is evidenced by complete loss of fiber alignment and outline of the ligament. Often, the proximal and distal portions of the ligament are still visible, separated by mottled or honeycomb material, representing hematoma and necrosis initially, and granulation tissue and/or early fiboplasia in later stages (Figure 2.28). No longer under tension and crimped, the retracted ends appear hypoechoic and enlarged, with a faint linear fiber pattern. Avulsed pieces of bone may occasionally be seen.

Joint instability may be confirmed dynamically by imaging both separation of the ligament stumps and joint space widening while manipulating the joint (i.e., manually abducting and/or adducting P1).

Fibrous tissue gradually replaces the granulation tissue, with associated increase in echogenicity. Ligaments heal via scar tissue formation and rarely recover a normal linear pattern. However, unlike for flexor tendons, a less than optimal linear pattern is often functional for ligaments. Healing normally takes several months in optimal conditions (stability) and ultrasonography is by far the most accurate way to assess the progress of healing and determine if and when the horse may resume exercise.

As for tendon injuries, chronic desmitis can lead to chronic thickening, poor fiber orientation, and ectopic mineralization (Figure 2.29). Enthesophytes are seen as hyperechoic interfaces extending from the bone enthesis at the origin and/or insertion of the ligaments, or there may be an irregular bone-to-ligament transition (Figure 2.30). These are noticed much earlier than on radiographs and they tend to be more irregular and prominent than those secondary to chronic capsulitis or OA.

Vet-ebooks.com

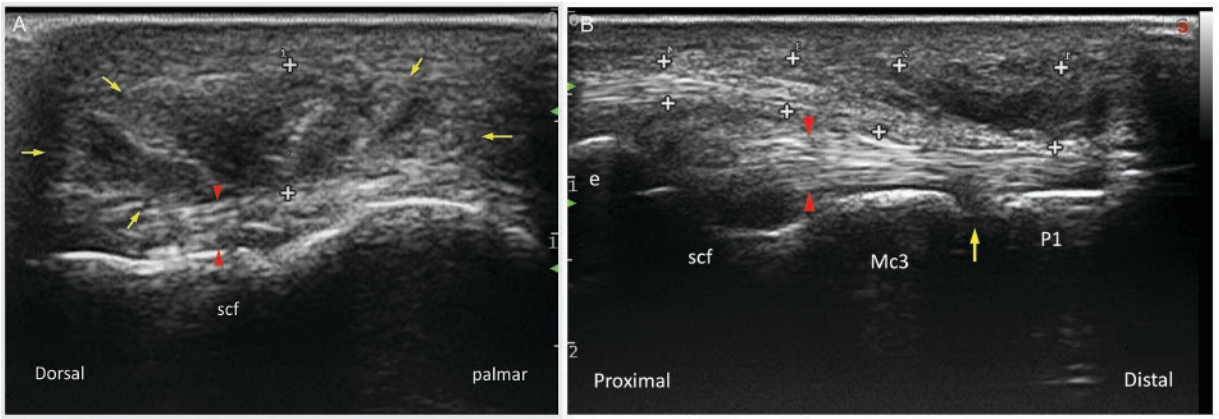


Figure 2.25 Severe collateral ligament injury in a horse. (A) A transverse plane over the supracondylar fossa of MC3 (scf) showing a large, diffuse, and hypoechogenic area in the superficial branch of the lateral collateral ligament (calipers and yellow arrows). The branch is enlarged with loss of contours. The deep branch (red arrow-heads) appears unaffected. (B) Frontal longitudinal plane: there is marked disruption in the fiber pattern of the superficial branch (calipers), while the deep branch presents with a regular striation (red arrow-heads). The yellow arrow points to the joint space. e: epicondyle of MC3; P1: proximal phalanx.

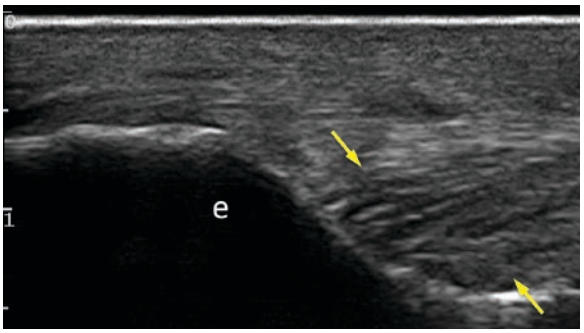


Figure 2.26 More discrete lesion affecting the metatarsal origin of the deep branch of the medial collateral ligament (arrows). e: lateral metacarpal epicondyle; scf: supracondylar fossa; LC: lateral metacarpal condyle.

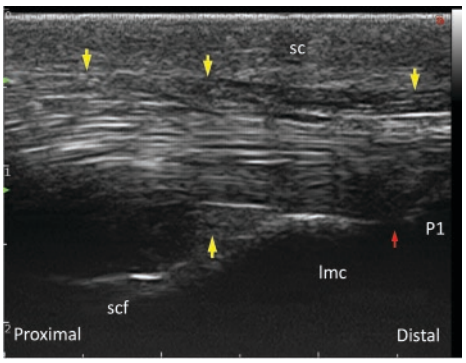


Figure 2.27 Diffuse collateral ligament injury with minimal fiber loss but with marked periligamentous swelling, creating a hypoechogenic halo around the ligament (yellow arrows). The red arrow points to the joint line. Scf: supracondylar fossa; lmc: lateral metacarpal condyle.

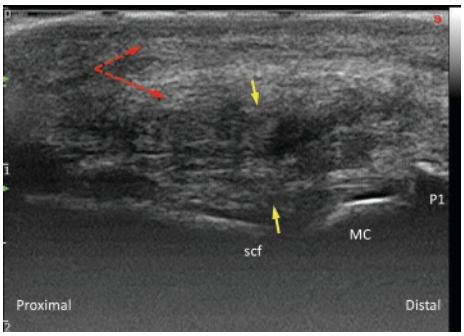


Figure 2.28 Longitudinal (frontal) plane image over the medial collateral ligament. The ligament has completely ruptured, appearing severely enlarged with total loss of the normal striation (yellow arrows). The amorphous, hypoechogenic pattern is due to hemorrhage. There is marked periligamentous swelling (red arrows). Scf: supracondylar fossa; mc: metacarpal condyle.

Desmitis of the Intersesamoidean Ligament (Palmar Metacarpophalangeal Ligament)

This condition is rare but causes severe lameness. Ultrasonography from a palmar approach shows ligament thickening, marked bone–ligament interface irregularity, loss of the normal transverse linear pattern, and hypoechogenic areas within the ligament (Figure 2.31). The space between the two proximal sesamoid bones (PSBs) may be slightly widened. Avulsed fragments are occasionally seen.

Vet-ebooks.com

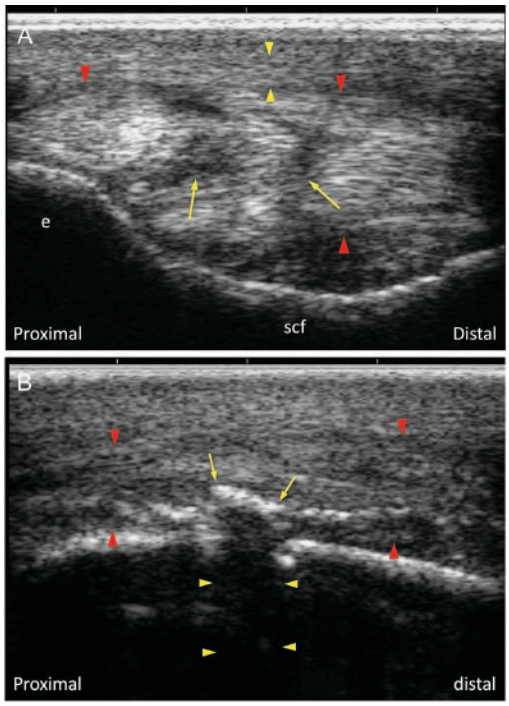


Figure 2.29 (A) Chronic collateral ligament desmitis, as for tendinitis, leads to a poorly organized, hyperechogenic, and thickened ligament parenchyma (red arrow-heads). The surrounding fascia is thickened and hyperechogenic (yellow arrow-heads). Irregular, hypoechogenic bands (yellow arrows) represent poorly organized tissue and possibly areas of chronic disruption and granulation (frontal plane image over the lateral aspect of the fetlock) Scf: supracondylar fossa. (B) Ectopic calcifications (yellow arrows) create discrete, hyperechogenic interfaces, casting acoustic shadowing (yellow arrow-heads), within the thickness of the ligament scar (red arrow-head) (longitudinal (fontal plane) image over the lateral metacarpal epicondyle).

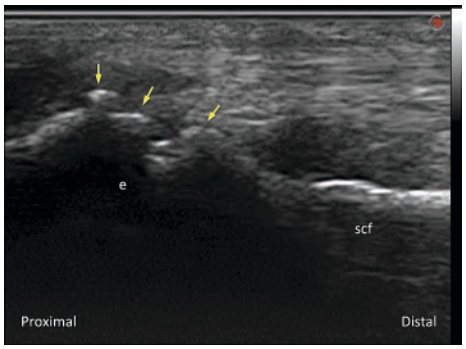


Figure 2.30 Longitudinal (frontal) plane image over the medial epicondyle (e). Spiky, entheseous new bone production is present at the origin of the long collateral ligament branch (arrows).

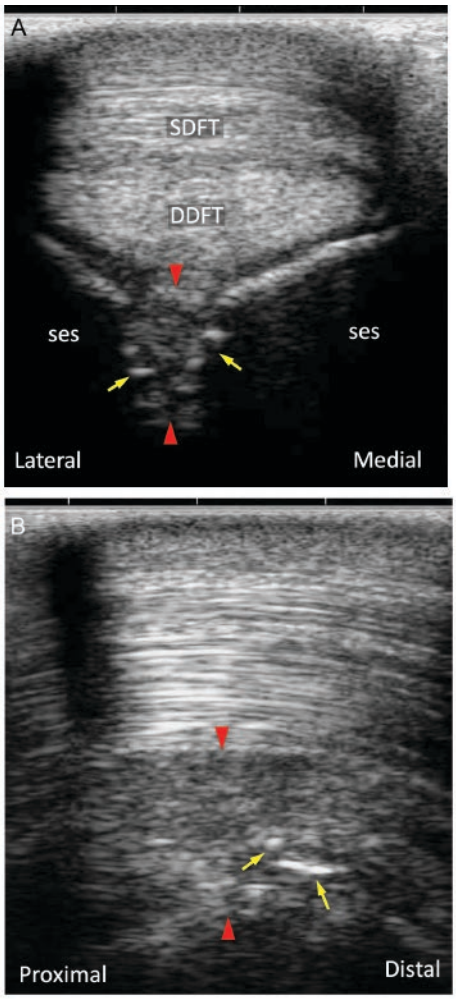


Figure 2.31 Transverse (A) and sagittal (B) plane images from the palmar aspect of the limb, showing severe desmopathy of the intersesamoidean ligament (red arrow-heads), with loss of the striated transverse pattern, heterogeneous decrease of echogenicity, and irregular, entheseous new bone (yellow arrows) at the insertions on the axial surface of the sesamoid bones (ses).

Insertional injuries are associated with osteitis of the axial aspect of the sesamoid bones. There may be radiographic evidence of erosion or irregular lucency on the axial borders of the proximal sesamoid bones, which should be differentiated from osteomyelitis, usually secondary to septic tenosynovitis.

Proximal Sesamoid Bone (PSB) Fractures

The PSBs are parts of the metacarpophalangeal joint, as they are entirely located within the palmar joint capsule. Fractures are readily identified on radiographs but careful ultrasonographic evaluation is often useful to assess the amount of joint damage, rule out or confirm the involvement of the suspensory ligament branches, and clarify the

Vet-ebooks.com

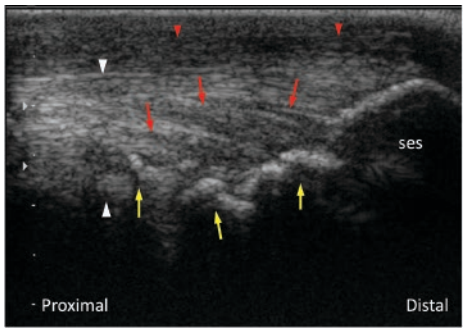


Figure 2.32 Longitudinal image over the abaxial aspect of the proximal sesamoid bone (ses): apical sesamoid bone fracture with several bone fragments (yellow arrows), tightly attached to the suspensory ligament branch (white arrow-heads). There is a focal, hypoechogenic lesion at the ligament insertion (red arrows) and marked, periligamentous swelling (red arrow-heads).

configuration of the fracture. Bony fragments may be loosely attached to the capsule (Figure 2.32) or may have large capsule or suspensory ligament attachments. Such details may be helpful for preoperative planning. Furthermore, associated joint surface damage and associated suspensory ligament branch injury have major repercussions on the postoperative prognosis.

Palmar/Plantar P1 Fragments

Type I (axial) palmar or plantar P1 fragments develop within the capsule between the base of the sesamoid bones and the proximopalmar articular border of the proximal phalanx. They are difficult to visualize ultrasonographically. The more abaxially located type II (*Birkeland*) fragments are commonly very large but rarely cause lameness. Their etiology is uncertain, although there is evidence that they may be fractures occurring at an early age, and they are often discovered incidentally on survey radiographs. They are extracapsular, usually located deep to the origin of the oblique distal sesamoidean ligaments and lateral to the deep distal sesamoidean ligaments without an obvious link to these structures (Figure 2.33). Ultrasonography may be useful when there is suspected pain associated with them, in order to evaluate the location of the fragment(s) in relation to the collateral ligaments, distal sesamoidean ligaments (DSL), and joint capsule. Occasionally these fragments may be observed incidentally in association with more significant lesions to peripheral structures, in particular the deep distal sesamoidean ligaments (DDSL) (Figures 2.33B and 2.33C).

Articular Long Bone Fractures

These injuries present as linear defects on the bone interface and ultrasound may be useful to establish the three-dimensional (3-D) configuration of a fracture and most importantly to provide information regarding associated cartilage damage, the presence of combined ligament or capsule injury, and potential fragmentation. It is also useful pre- or postoperatively to control adequate reduction of the articular fracture component.

Periarticular Injuries

Tendons, tendon sheaths, and bursae may be affected alone or in combination with joint disease. Ultrasonography is particularly useful to differentiate periarticular swelling (whether due to wounds, tenosynovitis, acquired bursae, abscesses, etc.) from joint diseases. Extensor tendinitis is common and is nearly always traumatic in origin (Figure 2.34). Complete rupture may be ascertained, especially in the case of deep wounds. Abscesses, hematomata, and foreign body granulomas are common in the fetlock region. There may also be acquired subcutaneous bursae, either septic or not, that develop over the dorsal aspect of the fetlock. Bursitis of the subtendinous extensor bursa is rare but may be occasionally recognized between the joint capsule and the extensor tendon (Figure 2.35).

Septic Arthritis

Articular contamination and infectious synovitis may be confirmed on ultrasound examination. Wounds and sinus tracts may be traced back to the joint (Figure 2.36). Occasionally, small, strongly hyperechogenic gas bubbles casting comet tail artifacts may be seen in the proximal recesses of the joint.

Initially, especially in foals, the joint fluid remains anechoic, but synovial membrane inflammation and edema are tremendous. As time goes on, the synovial membrane thickens and becomes more echogenic. The joint fluid rapidly becomes heterogeneous and echogenic, because of fibrin deposits and highly cellular, purulent exudate. When pressing with the probe on the joint pouch, the dense material can be seen to "float" in the fluid. It may be difficult in early cases to differentiate blood from exudate. In such cases, sample collection and cytological examination are warranted. Cartilage erosions and subchondral bone defects (osteomyelitis and osteitis) appear at a more advanced stage of infection.

Vet-ebooks.com

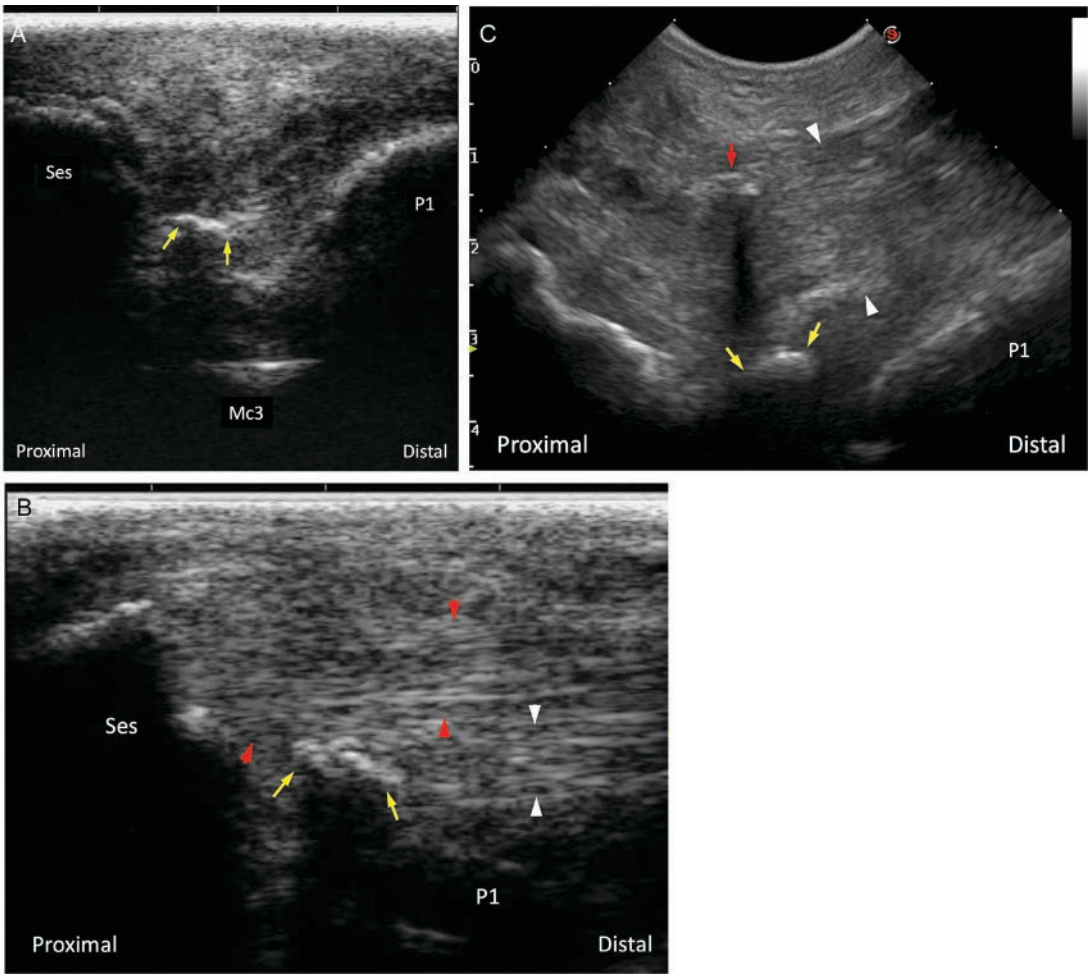


Figure 2.33 (A) image obtained in a longitudinal oblique plane, from the plantaro-abaxial aspect of the fetlock, distal to the base of the lateral sesamoid bone (ses), using a small linear-array probe angled slightly proximad (see Figure 2.1i). A smooth type II plantar P1 fragment (yellow arrows) is visible deep (dorso-abaxial) to the oblique distal sesamoidean ligament (ODSL, not visible in this section). (B) Similar approach over the ODSL. An avulsion fracture fragment (yellow arrows) is seen at the sesamoidean origin of a deep distal sesamoidean ligament (white arrow-heads), deep to the ODSL (red arrow-heads). The latter is thickened and heterogeneous. (C) The same approach, using a microconvex probe. The ODSL (white arrow-heads) is enlarged and ectopic mineralization is seen within its parenchyma (red arrow). A smooth bone interface (yellow arrow) is present in the space between the ODSL, deep DSL, sesamoid bone, and P1. This is probably an incidental finding (type II fragment), although concurrent avulsion of a deep DSL cannot be excluded.

Foreign bodies (thorns, needles, wires, etc.) may be found in the soft tissues, in or around the extensor tendons (Figure 2.35), within the joint capsule, or even in the joint space. These may cause septic inflammation or may be an incidental finding.

The Digital Flexor Tendon Sheath

The digital flexor tendon sheath lies on the palmar/plantar aspect of the fetlock and contains the digital flexor tendons. However, its anatomy is complex and is closely associated with a number of bony and ligamentous structures. It extends from the distal quarter of the metacarpal/metatarsal region to the foot, and so a full ultrasonographic examination should extend over this entire region.

The most appropriate transducer to use for this area is a linear one as it offers superior longitudinal images, while a microconvex transducer can scan further distally in the pastern region by placing it between the bulbs of the heels (see Chapter 1). The skin is prepared as for other areas and the probe applied using coupling gel and a standoff pad. The latter is usually used, as many of the structures being assessed are superficial. However, appreciable subcutaneous edema or fibrosis, common in this region, will provide a "natural" standoff and a separate standoff pad will not always be needed.

Vet-ebooks.com

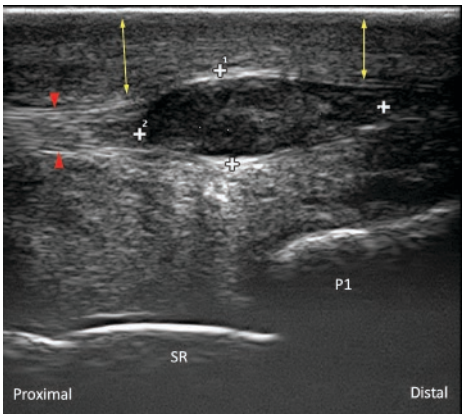


Figure 2.34 Focal extensor tendinitis (long digital extensor tendon) with focal rupture of the tendon (calipers) over the dorsal aspect of the fetlock (sagittal image). The distal end of the tendon has retracted distally and is not visible. Only the tendon tissue is replaced by hypoechogenic material (hemorrhage and granulation tissue/immature scar tissue). Note the marked peritendinous and subcutaneous swelling (double yellow arrows). The intact proximal stump of the tendon is frayed and widens out at the level of the rupture (red arrow heads).

Normal Ultrasonographic Anatomy of the Digital Sheath

The ultrasonographic anatomy of the digital sheath can be found in Figure 3.1 (proximal) and Figure 1.28 (pastern region). In the distal metacarpal and metacarpophalangeal joint regions, the deep digital flexor tendon (DDFT) is considerably larger than the superficial digital flexor tendon (SDFT), which has become a thinner structure superficial to the DDFT. In the hind limb, the dorsal surface of the DDFT usually has a well circumscribed hypoechoic region within it in the proximal limit of the digital sheath (Figure 2.37). This is a normal finding in a hind limb and should not be confused with pathology.

The proximal pouch of the digital sheath contains synovial plicae, consisting of two layers of synovium, which join the DDFT to the digital sheath wall both medially and laterally (Figure 2.38). The lateral synovial plica is usually more substantial and extends further distally than the medial one. In addition, the lateral part of the proximal pouch of the digital sheath is usually larger than the medial aspect and so the lateral plica is the most frequently identified. Although not normally visible in the non-distended sheath, they are easily identified with the improved contrast associated with sheath distension. The plicae should not be confused with adhesions, but they are useful structures with

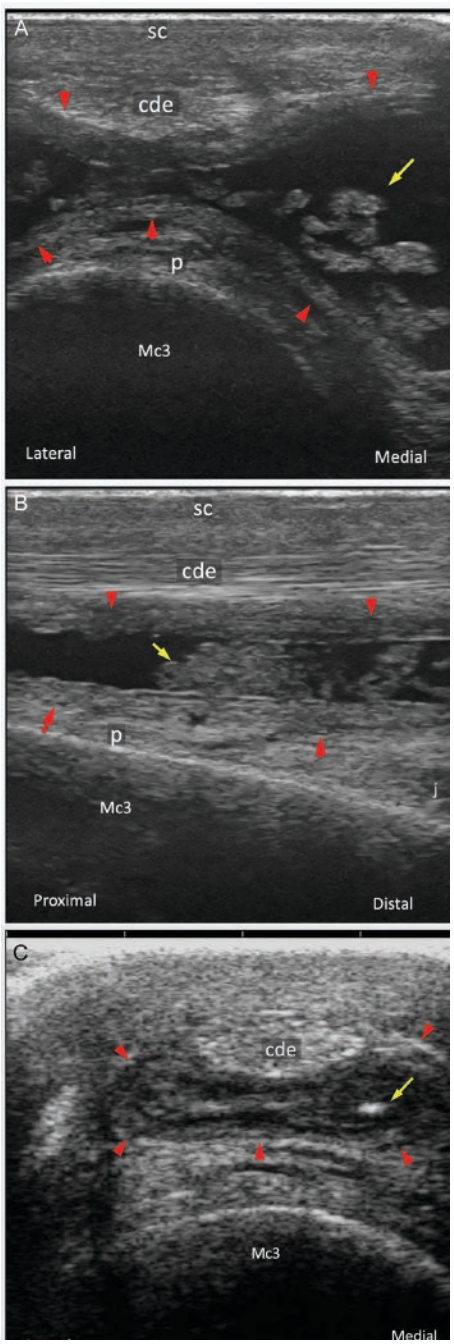


Figure 2.35 Transverse (A) and longitudinal (B) images on the dorsal aspect of the distal metacarpus (MC3) at the dorsoproximal extent of the fetlock of a sound horse presented for a fluctuant, non-painful swelling. The subtendinous bursa is distended by hypoechogenic fluid containing cauliflower-like echogenic material, representing either fibrinous material or synovial tissue proliferation (yellow arrow). The bursal lining (red arrow-heads) is markedly thickened. The extensor tendon (cde) appears normal. Note diffuse thickening of the subcutaneous tissue (sc), suggesting a previous trauma. P: periosteum; j: proximal dorsal recess of the metacarpophanalgeal joint. (Images courtesy of Jessica Kidd and Sara Dante). (C) Transverse view in the same location. Septic extensor bursitis due to a penetrating thorn (thick arrow). Note the thickened subtendinous bursa (thin arrows) containing echogenic, heterogeneous material.

Vet-ebooks.com

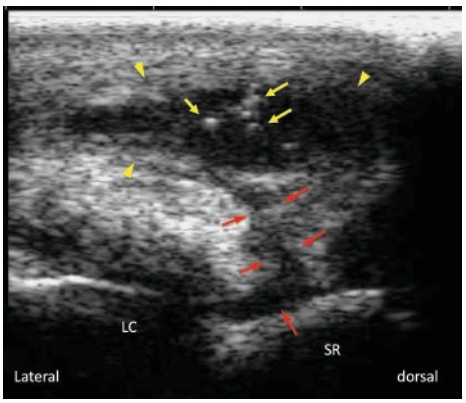


Figure 2.36 Dorsolateral aspect of the fetlock, transverse plane: a hypoechogenic cavity is present in the subcutaneous tissue (yellow arrow-heads), containing small gas bubbles (yellow arrows). A fistulous tract runs from the pouch into the joint through the joint capsule (red arrows). SR: sagittal ridge; LC: lateral metacarpal condyle.

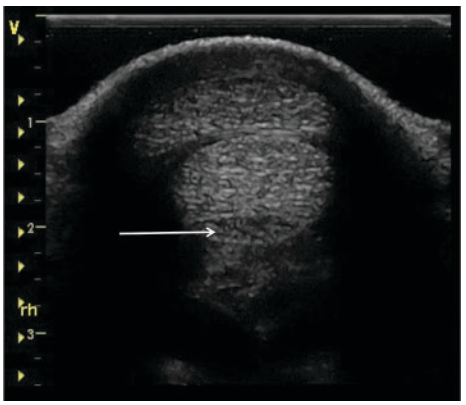


Figure 2.37 Transverse ultrasound image (lateral to the left) from the distal metatarsal region showing the normal dorsal hypoechoic region in the deep digital flexor tendon (arrow) at the proximal limit of the digital sheath. This should not be confused with pathology.

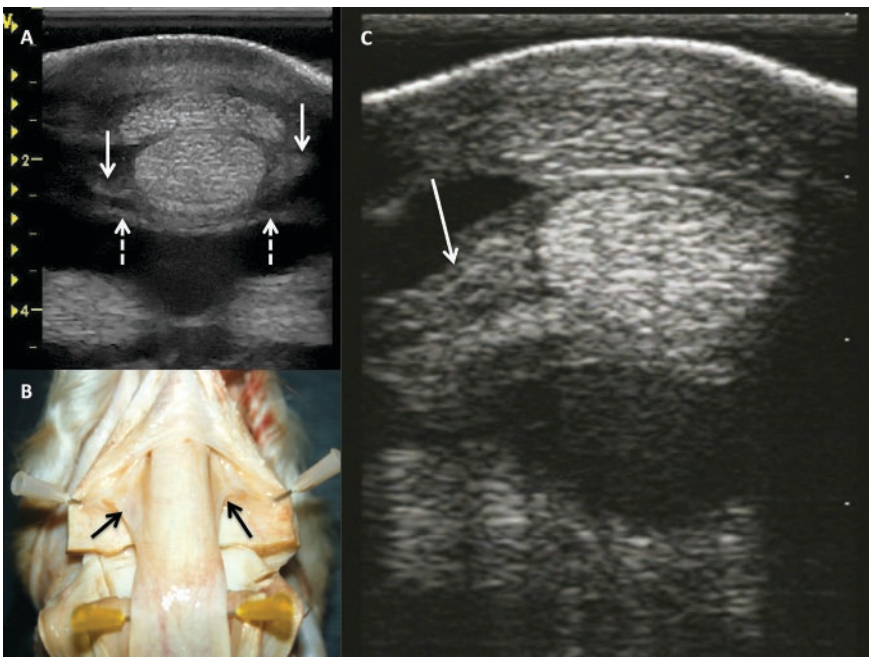


Figure 2.38 Synovial plica of the proximal digital sheath. (A) Transverse ultrasound image from a distended proximal digital sheath showing the medial and lateral plica attaching to the borders of the deep digital flexor tendon (solid arrows) and the dashed line refers to the synovial layer that attaches to the proximal border of the manica flexoria and divides the proximal digital flexor tendon sheath into two separate cavities. (B) Gross dissection of the proximal digital sheath showing the plica (black arrows). (C) Thickened plica in a chronically distended sheath with hypertrophied synovium.

which to assess the status of the synovial membrane (i.e., if hypertrophied, etc.) (Figure 2.38).

Immediately proximal to the fetlock joint, there is a loop of the superficial digital flexor tendon which surrounds the deep digital flexor tendon, known as the manica flexoria. Its free distal edge is very thin and enters the fetlock canal when the fetlock joint is extended. Attached to its proximal border is a layer of synovium that is attached to the proximal limit of the digital sheath, thereby dividing the proximal digital sheath into two separate cavities dorsal to the flexor tendons (see Figure 2.38). The manica flexoria can often be more easily evaluated using longitudinal views in the midline where it can be seen tightly opposed to the dorsal surface of the deep digital flexor tendon with its free tapering end distal to the apices of the proximal sesamoid bones abaxially, or the proximal limit of the sagittal ridge in the midline (Figure 2.39).

Vet-ebooks.com

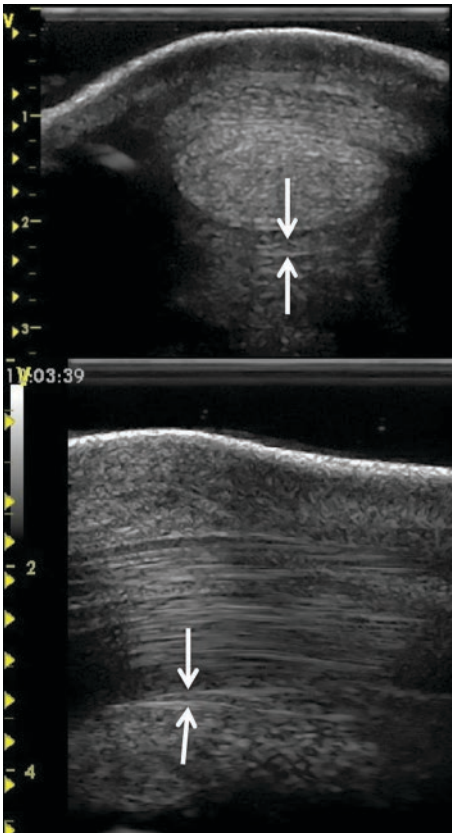


Figure 2.39 Transverse and longitudinal ultrasonographs (proximal is to the left) from the distal metacarpal region in the weightbearing limb showing the manica flexoria (arrows). Note the tapering of the manica flexoria in its normal position terminating distally at the level of the apex of the proximal sesamoid bone.

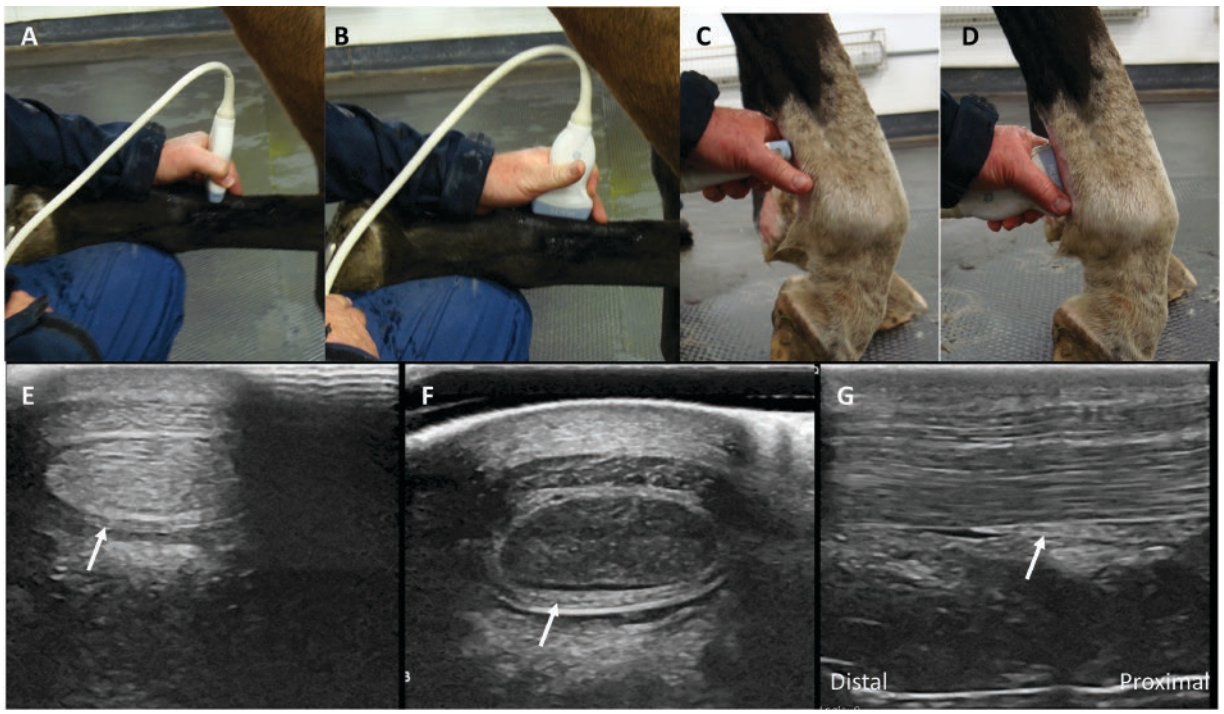


Figure 2.40 (A–D) show the positioning of the probe for evaluating the manica flexoria is a non-weightbearing limb. (A) and (C) transverse transducer position; (B) and (D) longitudinal transducer position. (A and B) – fore limb; (C) and (D) – hind limb. (E) Transverse image of the manica flexoria (arrow), which can be accentuated by tilting the transducer slightly to give an off-incidence artifact in the deep digital flexor tendon (F). Because the fibres of the manica are circumferential, they retain their echogenicity which highlights the manica. This "trick" can be used to increase the visibility of the manica in both weightbearing and non-weightbearing views. The manica is best identified in the longitudinal images (G; arrow). Note the tapering of the manica flexoria distally although, because of the flexion of the limb, it is normally displaced proximally compared to the weightbearing position but remains apposed to the deep digital flexor tendon.

Vet-ebooks.com

The manica flexoria can be made more visible in a non-weightbearing limb. The fore limb is lifted by an assistant or rested in a neutral position on the ultrasonographer leg in a quiet horse (see Figure 2.40). In hind limbs, horses can usually be persuaded to rest one hind limb to achieve a similar unloaded scan. The transducer is then positioned longitudinally and transversely in the midline to evaluate the manica flexoria which becomes positioned from proximally but still aligned to the deep surface of the deep digital flexor tendon. Effusion in the digital flexor tendon sheath improves its visibility further.

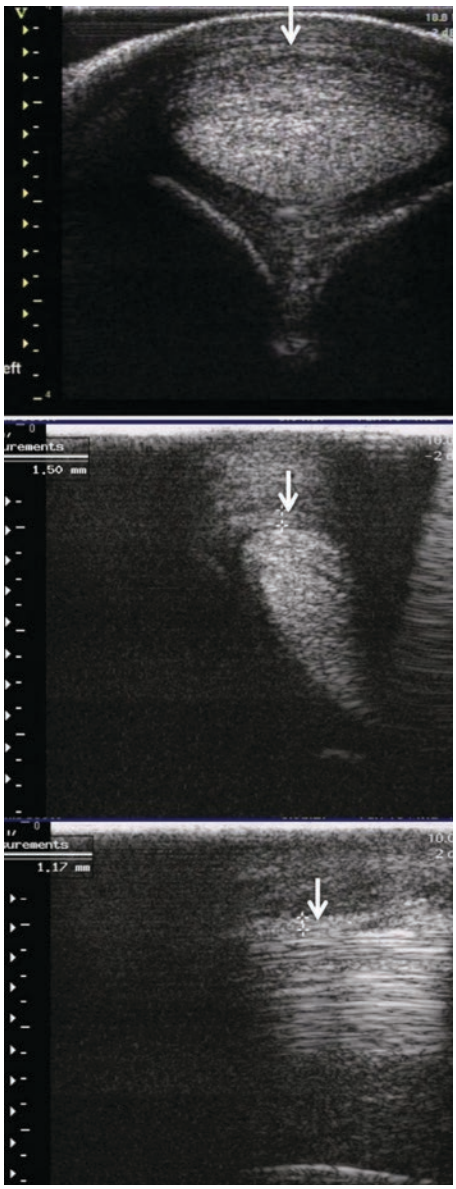


Figure 2.41 Imaging the palmar/plantar annular ligament (PAL). This can be achieved from the midline (top image), in an oblique image, where the attachment of the PAL to the respective proximal sesamoid bone can assist in its identification (middle image), and longitudinally, where the PAL has a stippled pattern due to the orientation of the fibers in contrast to the adjacent striated pattern of the tendons and often has an "upturned" proximal edge (bottom image).

Identification of the palmar/plantar annular ligament of the fetlock (PAL) in normal horses is difficult because of its size (only 1–2 mm in thickness). However, moving the probe medially or laterally away from the midline (where the PAL is attached to the superficial digital flexor tendon by a mesotenon, the vinculum) will improve definition of the ligament by the relatively hypoechogenic synovial lining (± synovial fluid) between it and the SDFT. If it still cannot be identified with confidence, the probe should be moved further medially or laterally to visualize its attachment to the very palmar/plantar border of the proximal sesamoid bones. Further confirmation can be provided by a longitudinally oriented scan (Figure 2.41).

Some authors prefer to assess the PAL by measuring the distance between the palmar/plantar surface of the SDFT and the skin surface, although this distance will include all the components of the "PAL complex" – the skin, subcutaneous tissues, PAL, and synovial membrane, all of which can be affected to a variable degree in the condition of annular ligament syndrome. A normal measurement of 3.6 ± 0.7 mm for the ligament alone has been quoted; hence, anything over 5 mm should be considered significant, although this can be considerably larger in normal cob-like horses.

The intersesamoidean ligament is situated between the proximal sesamoid bones. Longitudinal images are frequently more useful to evaluate this structure because of the curved contour of the fibers in the intersesamoidean ligament which results in off-incidence images abaxially when using a transversely orientated linear transducer. The axial margin of the proximal sesamoid bones can be irregular in normal horses. A fibrocartilagenous extension, known as the proximal scutum, extends proximally from the intersesamoidean ligament, on which the deep digital flexor tendon is apposed.

The ergot can result in a "blind" region at the base of the proximal sesamoid bones. To avoid missing localized pathology, the ergot can be moved medially/laterally or proximally/distally to minimize this blind spot.

Proximally in the pastern, the DDFT will frequently contain a central hypoechoic region, which is a normal finding and represents an off-incidence artifact resulting from the change in angle of the DDFT as it passes over the palmar/plantar aspect of the fetlock and its fibrocartilage-like phenotype in this region. Thus different orientations of the probe can be helpful to minimize this artifact. The DDFT is semi-circular in cross-section proximally but becomes bilobed as it runs distally. These lobes become larger in the distal pastern region.

The SDFT is a thin layer surrounding the palmar/plantar and abxial surfaces of the DDFT in the

Vet-ebooks.com

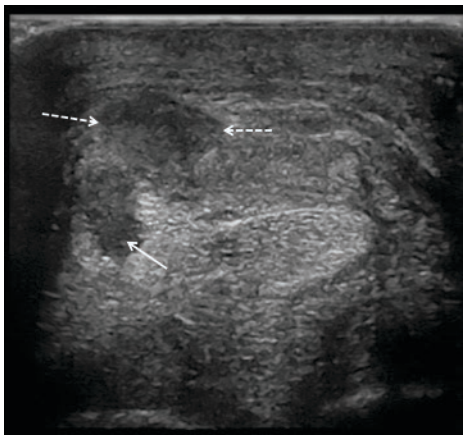


Figure 2.42 Percutaneous trauma to the deep digital flexor tendon in the distal pastern region. Because of the close proximity of the digital sheath and the DDFT to the palmar/plantar aspect of the pastern, injuries to this area are common and ultrasound is invaluable in identifying the nature of the damage to the tendons, especially when the pastern is swollen. This image is of a transverse ultrasonograph (medial to the left) from the distal pastern region showing a defect in the medial border of the DDFT (solid arrow) associated with a barbed wire injury. This had been missed on a previous ultrasound examination because the scan had not been continued sufficiently distally. Note also the marked synovial and subcutaneous thickening and the presence of a hypoechoic region adjacent to the tendon defect, which raises the suspicion of a developing abscess (dashed arrows). This was confirmed during surgery.

proximal pastern. As it runs distally it thins further in the midline as it divides into two branches which become larger as they run abaxially to insert via the middle scutum onto the proximal palmar/plantar aspect of the middle phalanx abaxially. The distal manica of the SDFT is usually visible deep to the DDFT in the mid-pastern region, although it is a thin structure and has minimal clinical significance. The distal palmar/plantar pouch of the digital sheath can be sometimes identified superficial to the DDFT as a thin anechoic region. Its size will vary depending on the amount of fluid within the sheath and frequently it is obliterated by the pressure applied with the probe. In the distal pastern region, synovial attachments are present between the dorsal surface of the DDFT and the dorsal wall of the digital sheath and, again, these should not be confused with adhesions.

The other soft tissue structures of the palmar/plantar pastern are covered in Chapter 1.

Ultrasonographic Abnormalities

Digital Sheath Abnormalities

Primary Tenosynovitis

Primary tenosynovitis of the digital sheath can be either non-septic or septic. Septic tenosynovitis is common because it is an area frequently subjected to trauma. Because of the close proximity of the digital sheath to the skin, puncture wounds, even though they may appear innocuous, are often associated with digital sheath penetration and underlying soft tissue trauma, which will frequently lead to septic tenosynovitis. Therefore, such wounds should always be imaged ultrasonographically. Large skin defects result in poor contact with the transducer, so that ultrasonography is less applicable in these wounds. Digital exploration and visualization of the damaged structures frequently offers sufficient information. However, as penetrating injuries can lacerate tendons when the metacarpophalangeal joint is hyperextended, the tendon laceration is frequently at a site variably distant from the wound. Therefore, not only is ultrasonographic evaluation of adjacent areas to the wound important, but the ultrasound examination should include evaluation of the entire digital sheath (Figure 2.42).

Sepsis of the digital sheath will produce ultrasonographic signs of marked considerable effusion within the sheath, which can range from anechoic to hypoechoic, dependent on the fibrin and cellular content of the fluid. The subcutaneous tissues and synovial membrane will be markedly thickened and edematous (hypoechogenic) and, depending on the duration of the sepsis, adhesions may be evident. The DDFT epitenon becomes thickened, giving rise to a hypoechoic halo around the tendon (Figure 2.43). These changes should be taken as strongly suggestive of digital sheath sepsis,

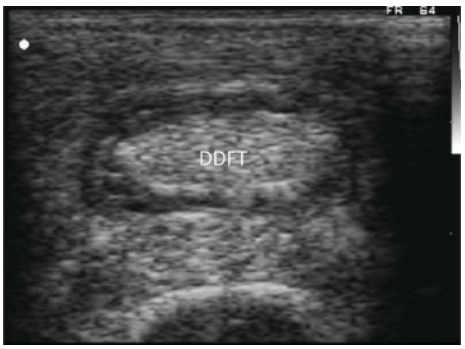


Figure 2.43 Characteristics of an infected digital sheath. The marked inflammation causes a hypoechogenic halo around the tendons (here demonstrated around the deep digital flexor tendon in the mid-pastern region).

Vet-ebooks.com

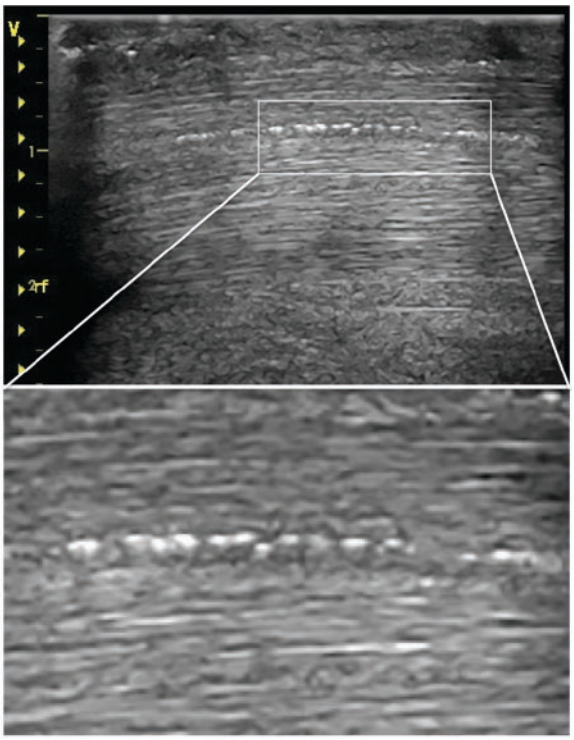


Figure 2.44 Percutaneous laceration in the distal metacarpal region showing a collection of air bubbles between the digital flexor tendons in this longitudinal ultrasound image. Note the presence of scattered hyperechoic foci with small central reverberation artifacts highly suggestive of gas/air and therefore confirming violation of the digital sheath.

although they are not pathognomonic; synovial fluid analysis is still needed to establish a positive diagnosis.

Foreign material can be introduced following traumatic injuries. Ultrasound is very sensitive at detecting foreign bodies, which are all hyperechogenic and cause variable amounts of acoustic shadowing. Radiolucent foreign bodies such as wood are easily detectable with ultrasonography. Some metal foreign bodies can produce a reverberation artifact depending on their shape and size. Air/gas can be present as a result of aspiration through an open wound (Figure 2.44), or it can be iatrogenically introduced (e.g., following nerve blocking), or it can be produced by gas-forming bacteria. Air will tend to be present as bubbles, which often collect at the more proximal limits of the digital flexor tendon sheath. The shape of the bubbles is responsible for the characteristic ultrasonographic appearance of air – a combination of acoustic shadowing and reverberation artifact.

Non-septic tenosynovitis will produce an effusion that is usually anechoic and is most easily identified, especially lateral and medial to the digital flexor tendons in the proximal pouch and palmar/plantar to the DDFT in the mid-pastern region. It need not be associated with lameness where it is usually bilaterally symmetrical and can be considered an incidental finding. Its presence will often improve the definition of the flexor tendons within the sheath and the digital sheath wall. Such improved definition can also be provided by scanning the area after injection of, for example, local anesthetic into the sheath. Care has to be taken, however, to avoid introducing air at the same time, as this will compromise the image because of the shadowing caused by the air.

Acute or chronic synovial inflammation is associated with synovial thickening. This can sometimes be appreciated as a thickening of the inner lining of the sheath wall which is usually slightly hypoechoic compared to the fibrous sheath wall. However, the best assessment of the synovial membrane is made in the proximal pouch region, from either the lateral and medial synovial plicae, or the synovial layer that attaches to the proximal margin of the manica flexoria and extends proximally to divide the sheath into two cavities on the dorsal side of the flexor tendons (see Figure 2.38). This synovial hypertrophy and/or accumulation of fibrinocellular conglomerate can be responsible for synovial "masses" within the sheath (Figure 2.45).

The sheath wall can become damaged which, in the acute stages, is difficult to identify ultrasonographically. Disruption of the sheath wall or the attachments of the synovial plica can sometimes be identified as suggestive of such tears but tenoscopy is the definitive way of confirming the injury where the synovial lining is disrupted and associated with focal hemorrhage and inflammation.

When trauma to the synovial wall results in leakage of synovial fluid into the subcutaneous space, it causes a significant fibrotic reaction which walls off the

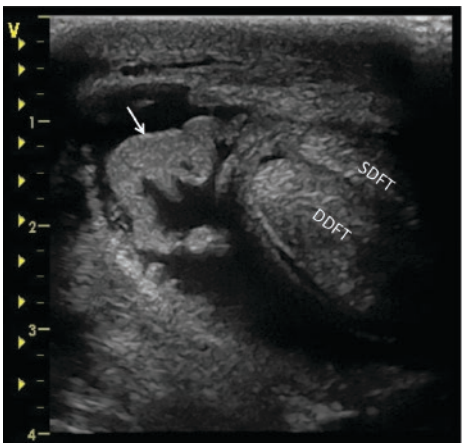


Figure 2.45 Oblique transverse ultrasound image from the palmarolateral aspect of the distal metacarpal region of a horse with marked inflammation of the digital sheath associated with tendon and sheath wall tear. Note the accumulation of fibrinocellular conglomerate within the cavity of the digital sheath (arrow).

Vet-ebooks.com

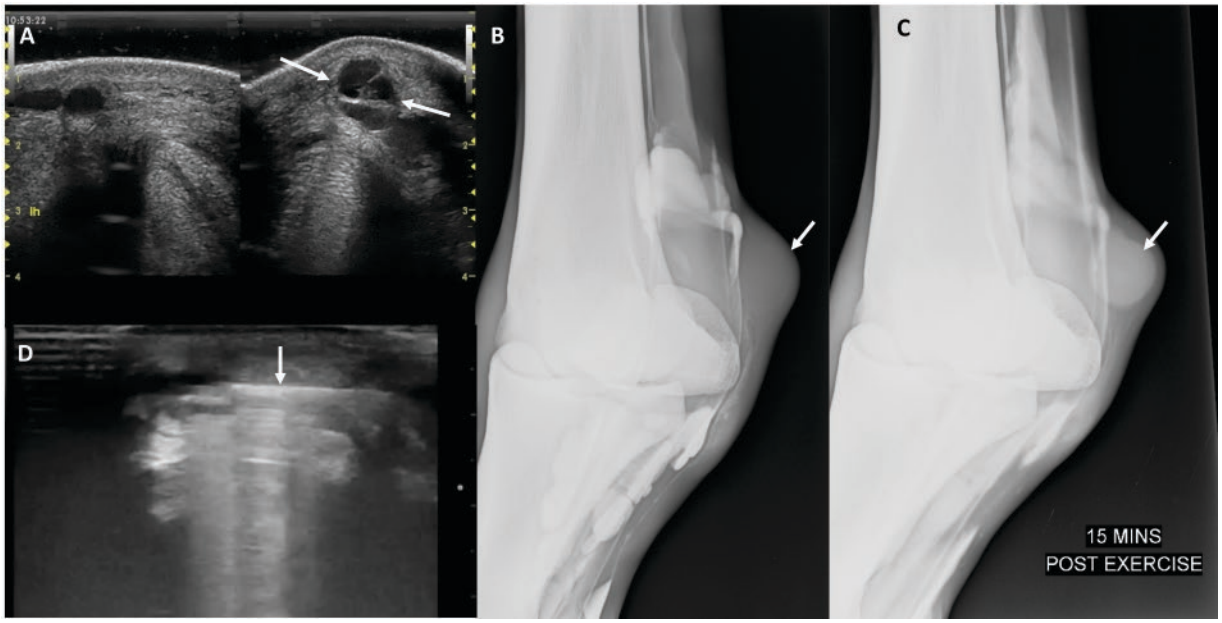


Figure 2.46 (A) Ultrasonographic appearance of a typical synoviocoele (right image) and a multiloculated anechoic cavity visible outside the digital flexor tendon sheath cavity (arrows) with the unaffected side of the limb on the left-hand side. (B) and (C) are contrast tenograms showing the synoviocoele (B; arrow) that becomes filled with contrast only after a period of exercise (C; arrow). (D) The use of intra-operative ultrasound to guide a synovial resector (arrow) into the cavity to enlarge the opening which is often not visible.

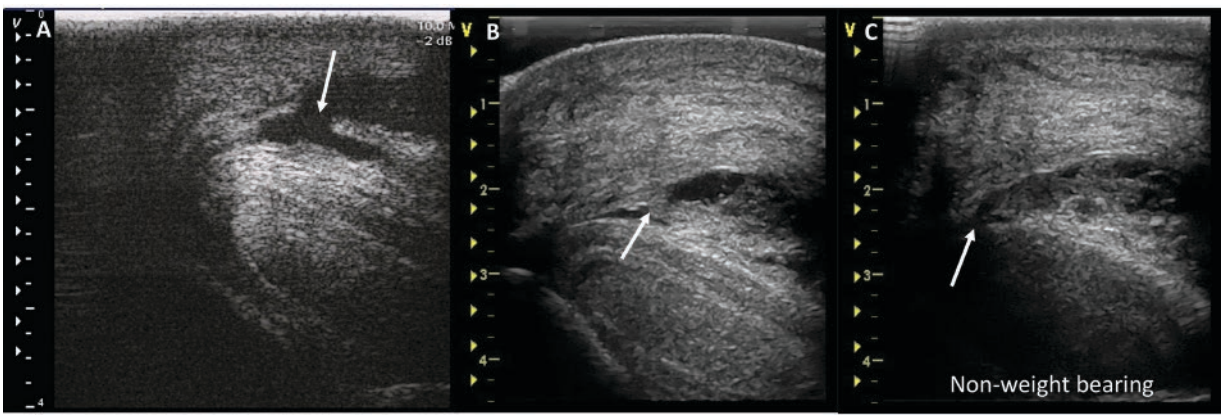


Figure 2.47 (A) A transverse image at the level of the fetlock showing a defect in the palmar annular ligament (arrow) through which anechoic synovial fluid is leaking. Note the pronounced fibrosis around the synovial fluid when outside a synovial cavity. (B) Recent trauma to the palmar annular ligament showing fluid outside the ligament and a defect (arrow) that does not appear to be open. However, when weight is taken off the limb (C), the defect becomes apparent (arrow).

synovial fluid and creates an outpouching, known as a synoviocoele. Although synoviocoeles can form adjacent to any synovial cavity, they are particularly common in the proximal digital flexor tendon sheath. Their clinical significance is highly variable and depends on the size of the communication with the main sheath cavity. Clinical significance is most likely when there is restricted communication between the two cavities, often described as a "one-way valve" so that synovial fluid can only enter the synoviocoele and not return, resulting in a hard swelling where the fluid under pressure is thought to give rise to pain. A simple, but not always reliable, test for this is to lift up the leg to see whether the synoviocoele deflates. Furthermore, pain on palpation, and response to intra-thecal analgesia, gives additional diagnostic information, although they can also be secondary to other intra-thecal pathology. For this reason a full ultrasonographioc examination of the digital flexor tendon sheath is important. Ultrasonographically, synoviocoeles appear as variably fluid-filled cavity outside the confines of the digital flexor tendon sheath, most commonly immediately

Vet-ebooks.com

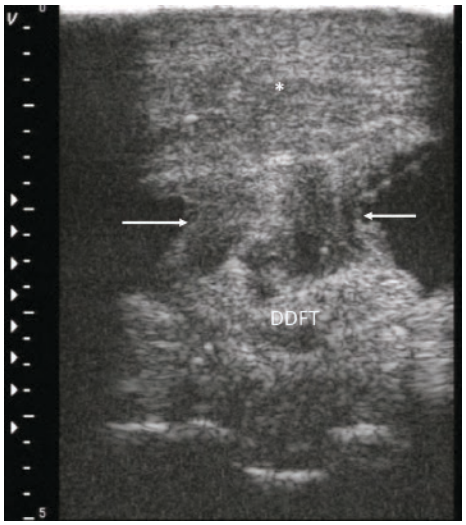


Figure 2.48 Blunt trauma to the deep digital flexor tendon (DDFT) in the distal pastern region showing marked distension of the distal digital sheath but also an adhesion between the damaged DDFT and the palmar sheath wall.

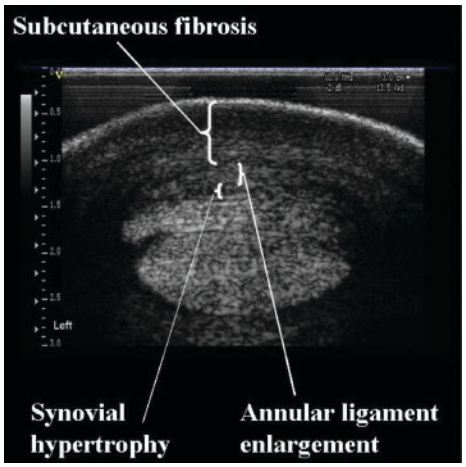


Figure 2.49 Transverse ultrasonography of the palmar/plantar fetlock region in a case of annular ligament syndrome. Thickening of the palmar/plantar annular ligament (PAL) is usually accompanied by variable amounts of synovial hypertrophy and subcutaneous fibrosis. True constriction is difficult to establish ultrasonographically, which requires either contrast tenography or tenoscopy for a more confident diagnosis.

proximal to the PAL (Figure 2.46). Occasionally they can form after tears in the PAL itself (Figure 2.47). Additional imaging appropriate for synoviocoeles include contrast tenography to assess communication with sheath cavity (Figure 2.46), although this may require exercise to demonstrate the communication when it is intermittent.

Adhesions can arise after any pathology to and within the digital flexor tendon sheath, usually requiring two apposing surfaces to be damaged to enable an adhesion to form between the two. Consequently, adhesions are often associated with a focal hypoechoic damage on the surface of the tendon to which they are attached, which may be the cause or the consequence of the adhesion (Figure 2.48). Accurate identification of adhesions can be challenging to the ultrasonographer. Caution is advised in the interpretation of indistinct borders of the flexor tendons being a sign of adhesions. This change more often reflects the degree of contrast supplied by the synovial fluid and membrane rather than adhesions per se. Adhesions can, however, be diagnosed with greater confidence if extra echogenic material can be identified within anechoic synovial fluid attached to both surfaces (Figure 2.48). Reducing pressure on the transducer can help identify these attachments, as can dynamic scans with the limb lifted and flexed repeatedly. Using a longitudinally aligned transducer over the palmar/plantar aspect of the limb, flexion of the fetlock (and not the distal interphalangeal joint) should result in both flexor tendons moving through the fetlock canal unimpeded. If one (usually the SDFT) is adhered to the sheath wall, the DDFT will move independent of the SDFT (as will happen if just the distal interphalangeal joint is flexed) and will result in kinking of the SDFT where gapping can occur between the two tendons (the latter can also happen after a manica flexoria tear – see below).

Digital sheath tenosynovitis is often secondary to other soft tissue pathology – either the flexor tendons lying within the sheath or immediately adjacent structures such as the palmar annular ligament (see next section). It is also possible that some tendon lesions can occur secondary to chronic inflammatory tenosynovitis.

Palmar/Plantar Annular Ligament (PAL) Syndrome

Annular ligament syndrome (ALS) is characterized by relative constriction of the digital flexor tendons within the PAL. It can be either primary, when it is thought to result from primary desmitis of the PAL following direct or indirect (repeated over-extension of the fetlock joint) trauma, or secondary to other pathology, such as tendinitis, digital sheath tenosynovitis, and septic tenosynovitis.

Changes seen ultrasonographically include variable amounts of thickening of the synovial membrane, PAL (which can be hypoechoic if active desmitis is present), and/or subcutaneous tissues (Figure 2.49). It remains to be seen if prognosis or treatment is altered by the preponderance of each component. Digital sheath tenosynovitis will also be present and if the annular ligament syndrome is secondary, the primary pathology may also be identifiable. Many chronic cases of ALS also have enthesophytosis at the insertion of the PAL which can be identified both

Vet-ebooks.com

radiographically and ultrasonographically (as a roughening to the palmar/plantar border of the proximal sesamoid bones, seen best with the probe positioned longitudinally over the palmar/plantar border). Calcification can also occur within the PAL where it will produce a bright hyperechoic reflection with acoustic shadowing deep to it. Contrast tenography can also provide some evidence for constriction based on the amount of contrast lying palmar/plantar to the SDFT in the fetlock canal (Figure 2.58).

The treatment for true constriction by the PAL is surgical transection of the PAL. However, it is often not clear if true constriction is present and PAL constriction is often secondary to other primary pathology.

Treatment is therefore probably more appropriately directed at the primary cause (if identified), and current studies evaluating outcome of different intrathecal pathologies treated with or without PAL transection have not been able to prove definitively if PAL is associated with an improved prognosis when primary pathology is present. Consequently, the authors believe that PAL transection should only be considered after evaluation of the digital sheath tenoscopically, when passage of the arthroscope through the fetlock canal can give the most convincing evidence for the degree of constriction and primary pathology can be identified.

Deep Digital Flexor Tendon (DDFT) Abnormalities

Over-Strain Midsubstance Injuries

Over-strain injuries of the DDFT invariably occur within the digital sheath or in the navicular bursa in the foot. The lesions vary widely in appearance from a considerably enlarged tendon containing multiple hypoechoic foci to more focal hypoechoic/anechoic lesions (Figure 2.50). Very anechoic lesions may represent communication of the lesion with the cavity of the digital sheath and non-weightbearing views may be helpful at demonstrating any communication more clearly.

As with any intra-sheath tendinitis, there will frequently be an accompanying tenosynovitis, often more evident in the region of the injury and also more severe if the lesion communicates with the digital sheath. Lameness is often severe and unremitting.

Mineralization/ossification is a frequent consequence of chronic injury in this tendon. This will show up as a brightly hyperechoic reflection which will cause a variable amount of acoustic shadowing, depending on its size and degree of mineralization/calcification (Figure 2.51). Not all mineralizations are significant but those associated with lameness often have a positive Doppler signal (Figure 2.51).

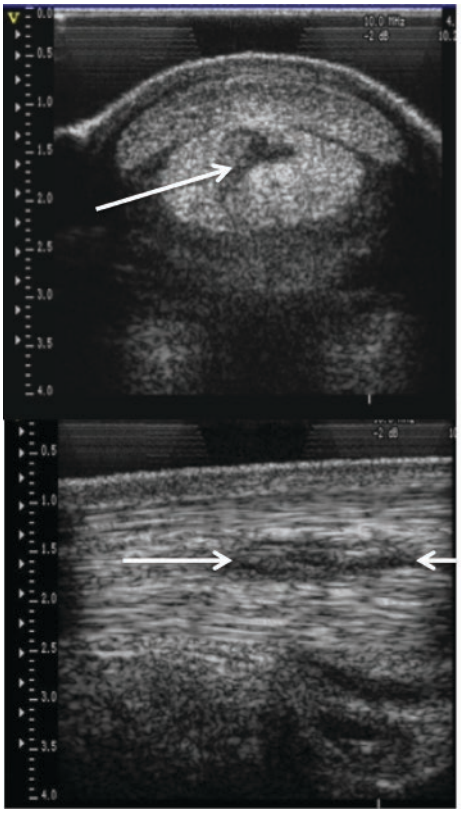


Figure 2.50 Deep digital flexor tendinopathy. Mid-substance tendinopathy of the deep digital flexor tendon (DDFT) can affect the DDFT in any part of the digital sheath (or distally within the foot) but is rare proximal to the digital sheath. These are transverse and longitudinal images from a case of deep digital flexor tendinopathy present in the proximal digital sheath (arrows). The location of the lesion can usually be identified clinically by a painful response to digital palpation and distension of the digital sheath, proportionately greater in the region of the lesion.

Vet-ebooks.com

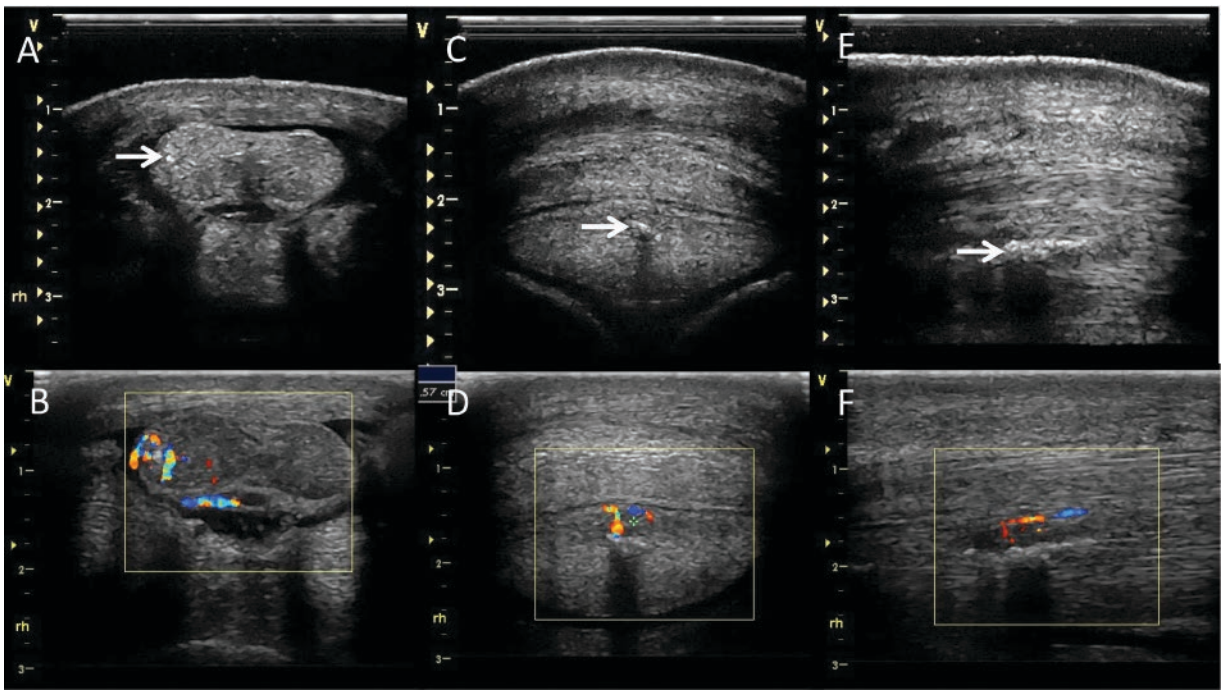


Figure 2.51 Chronic deep digital flexor tendinopathy characterized by mineralization of the tendon. (A) A transverse ultrasonograph from the distal pastern region where pin-point mineralization is difficult to identify (arrows). This can be improved by tilting the transducer (off-incidence artifact) or by the use of Doppler imaging for those cases with an active signal (B). Transverse (C) and longitudinal (E) images show mineralization in the deep digital flexor tendon at the level of the proximal sesamoid bones. While this lesion is very evident ultrasonographically, mineralization is not always clinically significant, although the concurrent presence of a Doppler signal ((D) and (F)) suggests greater significance.

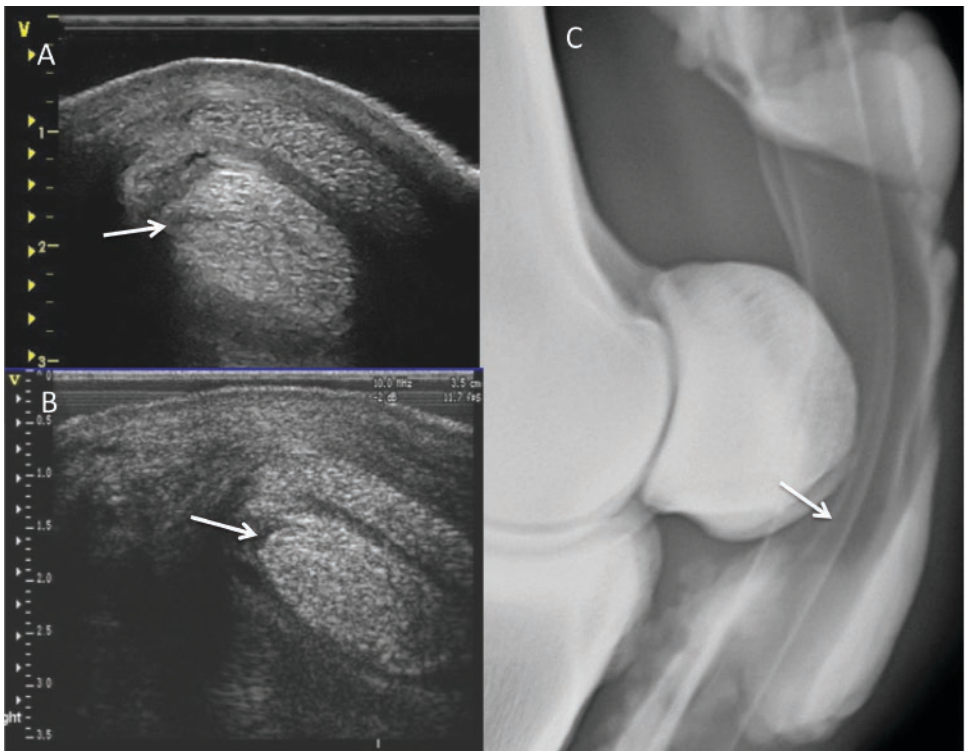


Figure 2.52 Marginal deep digital flexor tendon (DDFT) tears. (A) An oblique transverse image from the distal metacarpal region showing a deep longitudinal tear in the lateral margin of the DDFT (arrow). Deep tears are readily visible ultrasonographically. Less deep tears can be more difficult to identify ultrasonographically because the tension in the tendon under weightbearing load tends to close the defect. Greater sensitivity in detection can be provided by using non-weightbearing views proximal to the fetlock, oblique imaging (B), or contrast tenography where the tears are visible distal to the proximal sesamoid bones in the weightbearing limb (C – arrowed). This area should also be evaluated ultrasonographically to identify tears in the weightbearing limb – see Figure 2.53.

Vet-ebooks.com

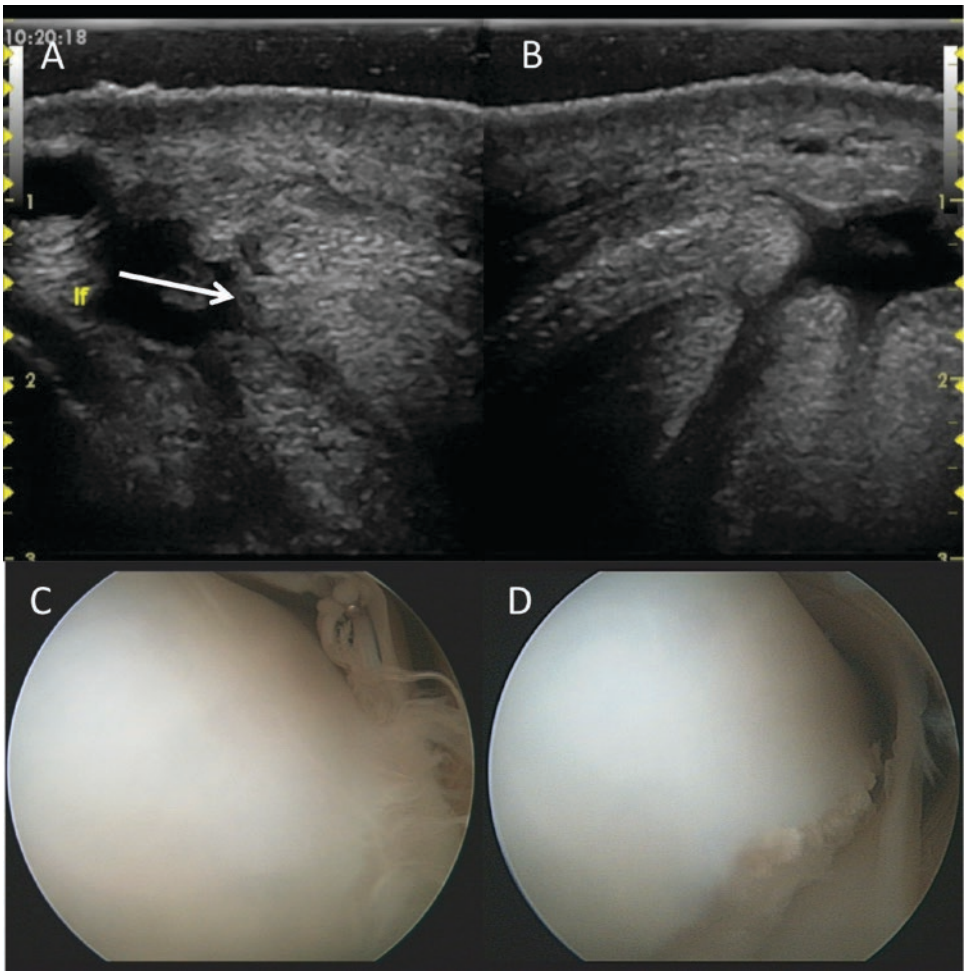


Figure 2.53 Detection of marginal tears of the deep digital flexor tendon (DDFT) using oblique transverse images immediately distal to the proximal sesamoid bones. (A) shows the "lateral" oblique with the transducer centered over the palmarolateral aspect of the proximal pastern where irregularity of the lateral margin of the DDFT is evident in contrast to the medial border (B). The corresponding tenoscopic images of the lateral aspect (lateral to the right) are shown before (C) and after (D) debridement.

Tears

Damage to the surface of the deep digital flexor tendon can occur as a variant of over-extension injury to the tendon. These most frequently occur on the abaxial borders of the deep digital flexor tendon in the region of the metacarpophalangeal joint (i.e., usually in the fore limb), presumably due to excessive forces during over-extension which compress the tendon and cause a pressure-induced rupture. Due to their intrasynovial location and being bathed in synovial fluid, healing frequently does not occur and these lesions will persist, relatively unaltered for months and years, being responsible for persistent digital sheath tenosynovitis and lameness. Most tears result in echogenic material adjacent to the DDFT but this is a non-specific finding for tenosynovitis and not specific for a DDFT tear. The larger of these tears are visible ultrasonographically as an irregular tendon border or defect within the tendon in the proximal digital sheath in the weightbearing limb. Visualization of the tear can be improved by using oblique images, non-weightbearing scans and Doppler imaging (Figure 2.52). However, many are difficult to identify and require high-quality machines and experienced operators. Even then, many lesions are focal and centered at the level of the ergot, which can be a "blind spot" on ultrasound scanning, and are actually best seen immediately distal to the proximal sesamoid bone using oblique views in the weightbearing limb (Figure 2.53). Hence a negative finding on ultrasound does not rule out the presence of a tear. Contrast tenography (undertaken at the same time as diagnostic analgesia) can demonstrate the presence of a tear in the same location immediately distal to the proximal sesamoid bones in the standing horse as a line of contrast overlying the space-filling lucency of the DDFT in a lateromedial view (Figure 2.52). However, tenoscopy is still the gold standard for

Vet-ebooks.com

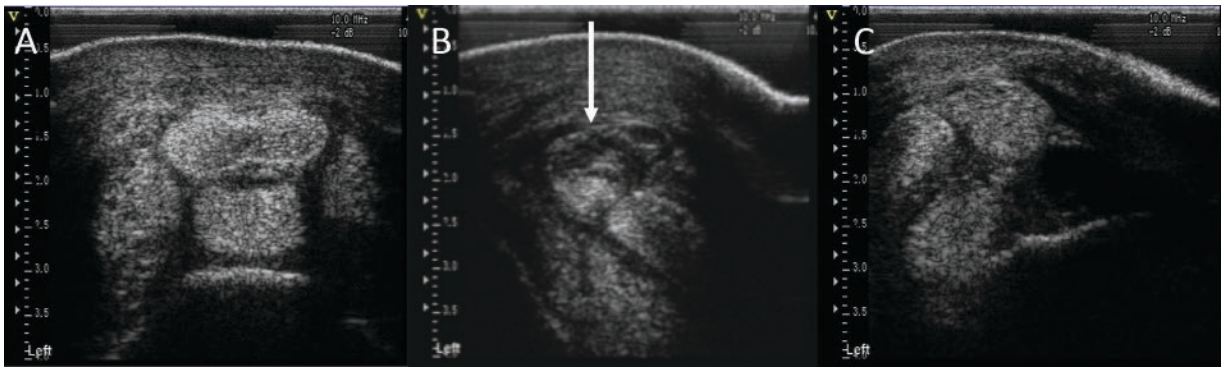


Figure 2.54 Tendinopathy of the lateral branch of the superficial digital flexor tendon (SDFT) in the pastern region. Because of the oblique angle of the branches, the lesion is not readily visible in midline transverse images (A – lateral to the left), although asymmetrical subcutaneous fibrosis is evident. Full visualization requires movement of the transducer to the palmarolateral aspect of the pastern (B), where the branch can be seen as hypoechoic (arrow) and covered with subcutaneous fibrosis in contrast to a normal medial branch (C).

evaluation of these tears and is recommended to identify occult tears. It should certainly be considered in those cases of tenosynovitis that have failed to respond or recurred after intrathecal medication.

Trauma

Penetrating injuries to the pastern are common and can have potentially disastrous consequences if the extent of the soft tissue pathology is not recognized early. The DDFT is commonly damaged with such injuries and the ultrasonographic abnormalities range from very subtle palmar/plantar defects to penetrations extending from the palmar/plantar surface dorsally (see Figure 2.42). The digital sheath may not necessarily develop sepsis as a consequence of either the penetrating body entering the DDFT without significantly contaminating the sheath, or blunt trauma damaging the DDFT without actually entering the sheath. Consequently, superficial wounds in the pastern region should be evaluated ultrasonographically, especially if the lameness is severe or persists. DDFT lesions may not always be visible ultrasonographically immediately after bruising, so follow-up examinations are recommended if lameness and/or digital sheath effusion persists.

Because apposing surfaces are frequently damaged with external trauma, adhesions can subsequently develop attaching to the tendon defects. Alternatively, appreciable tendon defects within the digital sheath may not show healing in the long term, with anechoic defects persisting.

The affected tendon can also become septic, although this is rare. In such cases the ultrasonographic characteristics are a rapidly destructive (hypoechoic/anechoic lesions) condition with minimal tendon enlargement.

Superficial Digital Flexor Tendon (SDFT) Abnormalities

The fetlock region of the SDFT is usually spared injury in equine superficial digital flexor tendinitis. However, severe cases of tendinitis or, more commonly re-injury, can result in tendinitis of the SDFT distal to the fetlock; either the thin layer of SDFT immediately proximal to the branches, or of the branches of the SDFT. Hence if SDFT tendinitis is identified ultrasonographically within the pastern region, the mid-metacarpal region should also be examined.

To image the branches satisfactorily, the probe needs to be moved to the medial and lateral aspects of the limb (45 degrees oblique) where the branches appear as comma-shaped structures which enlarge as their insertion point is approached. The ultrasonographic changes include enlargement, heterogeneous echogenicity, and peritendinous fibrosis (Figure 2.54). Estimation of size is made by comparing with the other branch of the same limb and with the branches on the contralateral limb, which has to be made at the same level on the limb because the branches increase in cross-sectional area in a proximodistal direction.

Partial or complete tearing of the attachments of the manica flexoria (the loop of tendon that surrounds the deep digital flexor tendon) to the medial and lateral borders of the SDFT most commonly occurs in the hind limbs and results in secondary tenosynovitis. The injury appears to disproportionately affect cob-like horses but can occur in any breed and discipline, although it is rare in racehorses. The original descriptions of this injury indicated ppor sensitivity of ultrasound to detect this injury. However, more recently,

Vet-ebooks.com

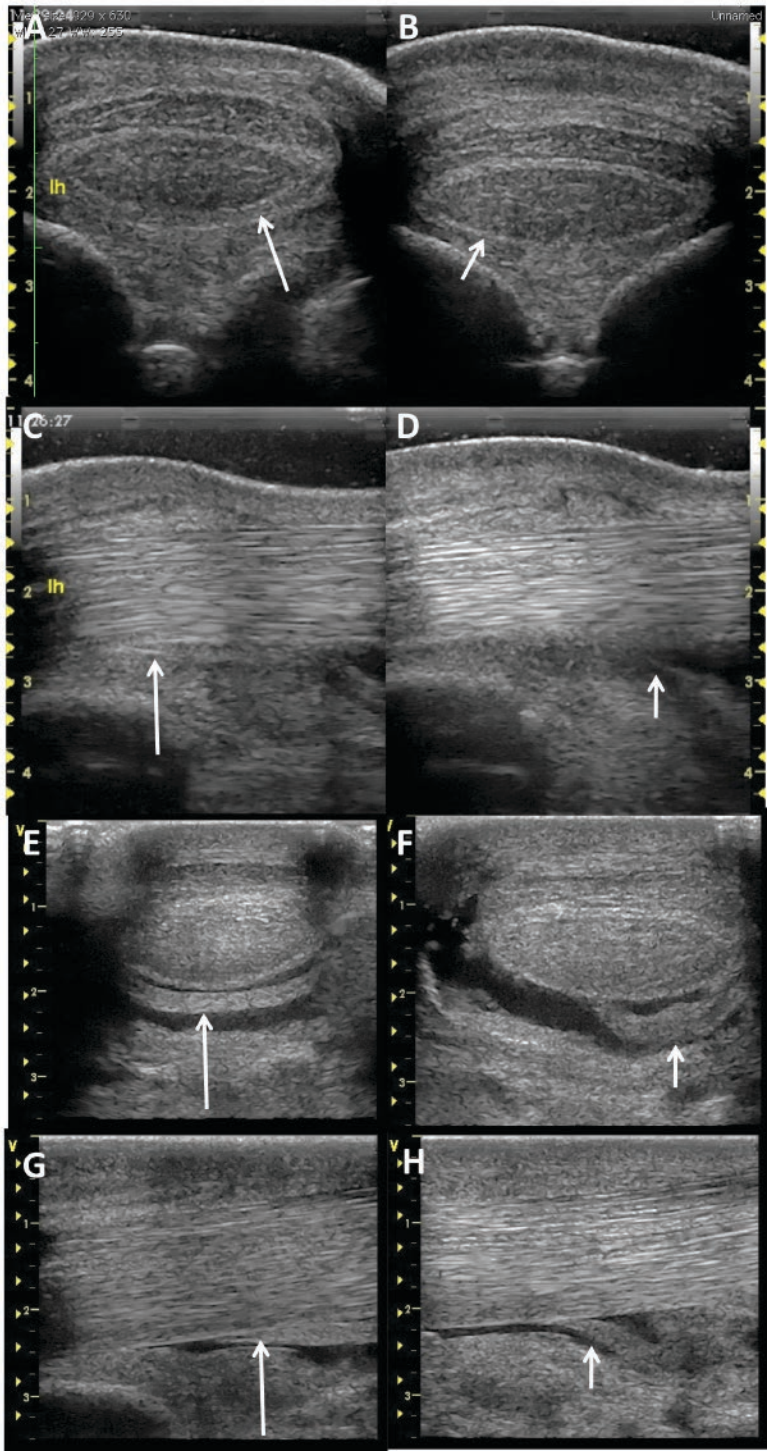


Figure 2.55 Tearing of the manica flexoria. (A), (C), (E), and (G) are from the unaffected limb. (B), (D), (F), and (H) are from the affected limb. (A–D) are weightbearing scans and (E–H) non-weightbearing scans. Medial (for transverse images) and distal (for longitudinal images) are to the left. The manica is indicated by the arrow. The manica is most reliably seen in longitudinal images, especially with the limb raised where the torn manica is displaced proximally and is often separated from the deep digital flexor tendon. With a complete tear, "gapping" between the superficial and deep digital flexor tendon can sometimes be seen with marked flexion. Other signs of a manica tear are thickening; comparing (E) and (F) and the torn side (usually medial) can often be best appreciated from non-weightbearing transverse scans.

Vet-ebooks.com

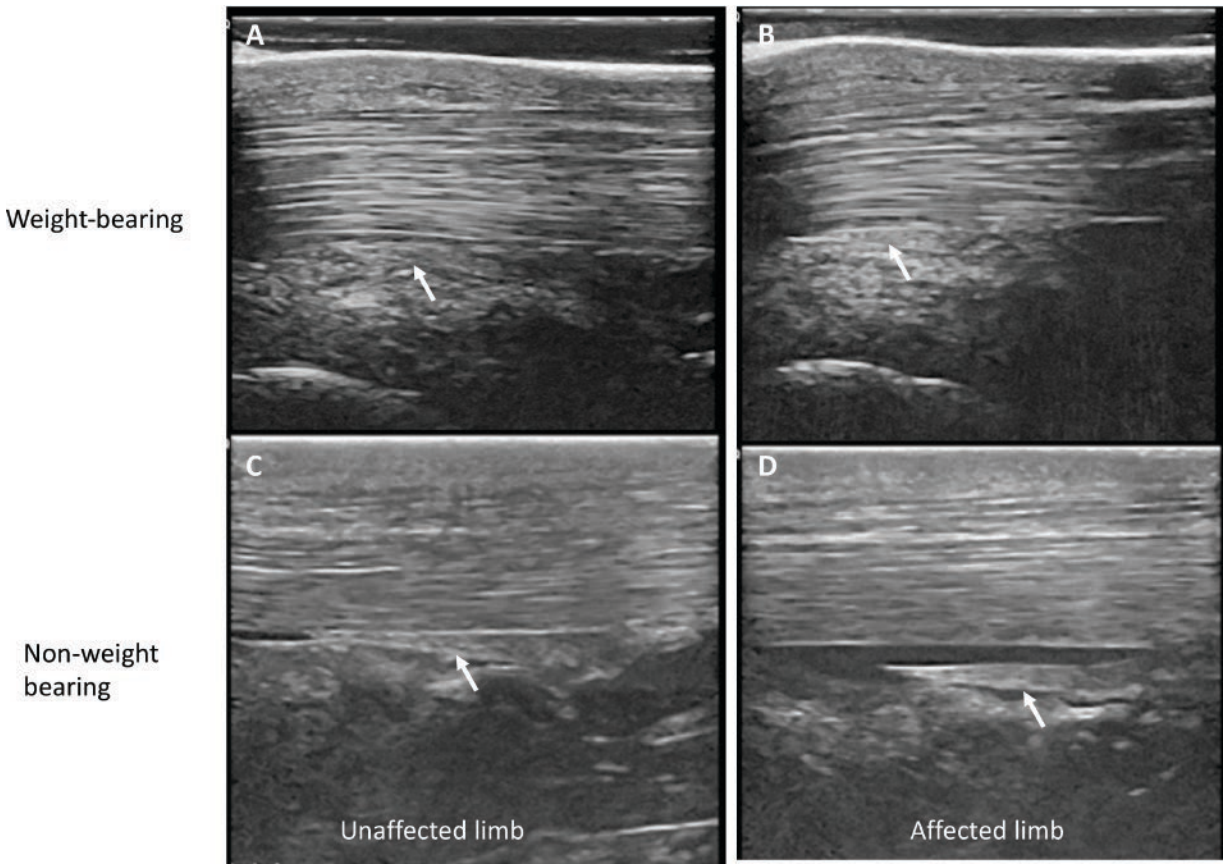


Figure 2.56 Midline longitudinal scans (weightbearing and non-weightbearing) of a more subtle case of tearing of the manica flexoria. (A) and (C) are from the unaffected limb and (B) and (D) are from the affected limb. The weightbearing scans show few abnormalities, while the non-weightbearing scans show proximal displacement of the manica (arrow) with separation from the deep digital flexor tendon.

techniques have been developed which has made the pre-operative diagnosis of manica tears much more reliable. For ultrasound detection, the transducer is positioned longitudinally in the midline just proximal to the level of the apices of the proximal sesamoid bones. This enables the manica to be identified as a thin structure apposed to the dorsal surface of the DDFT and tapering to a point distal to the level of the apices of the proximal sesamoid bones or the proximal limit of the sagittal ridge of the third metacarpus/metatarsus (Figure 2.55). Transverse images can identify the manica dorsal to the DDFT, although its thickness varies depending on where along the tapering end of the manica the transverse scan is orientated. Tilting the probe to create an off-incidence view of the DDFT can make the manica easier to identify as it tends to retain its echogenicity because its fibres run orthogonally to the DDFT.

Imaging the manica flexoria is, however, much easier when there is effusion (usually the case) and when the limb is non-weightbearing. The manica does displace slightly proximally but, if intact, remains apposed to the DDFT (Figure 2.56). Signs of tearing include more proximal displacement and thickening of the manica when compared to the contralateral limb, displacement from the deep surface of the DDFT, and gapping between the SDFT and DDFT when the tear is complete (Figure 2.55). Non-weightbearing views can also clarify which side of the manica is torn, although this is usually the medial attachment (Figure 2.57).

This technique has improved the reliability of ultrasonographic diagnosis of manica flexoria tears but this can also be enhanced with the use of contrast tenography which can be undertaken at the same time as diagnostic analgesia and where the manica is outlined very effectively by contrast as two parallel lines which taper to a point distal to the apices of the proximal sesamoid bones. Tearing results in proximal displacement while more subtle tearing may be associated with accumulations of contrast over the manica (Figure 2.58).

Intersesamoidean Ligament/Proximal Scutum Abnormalities

Injuries to this structure include small avulsion fractures from the axial borders of the proximal

Vet-ebooks.com

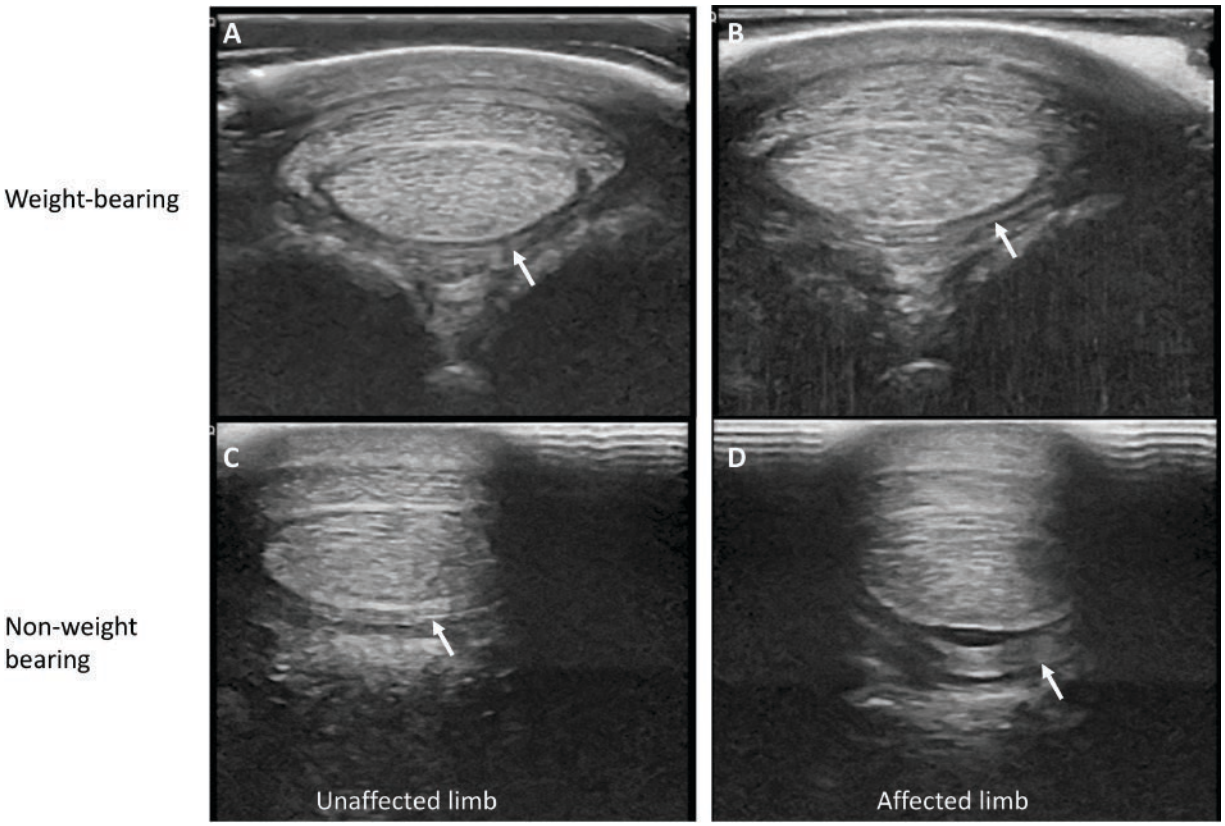


Figure 2.57 Transverse scans (weightbearing and non-weightbearing) of the same horse as in Figure 2.56. (A) and (C) are from the unaffected limb and (B) and (D) are from the affected limb. Note the thickening of the manica flexoria (arrow) most evident in the non-weightbearing scan.

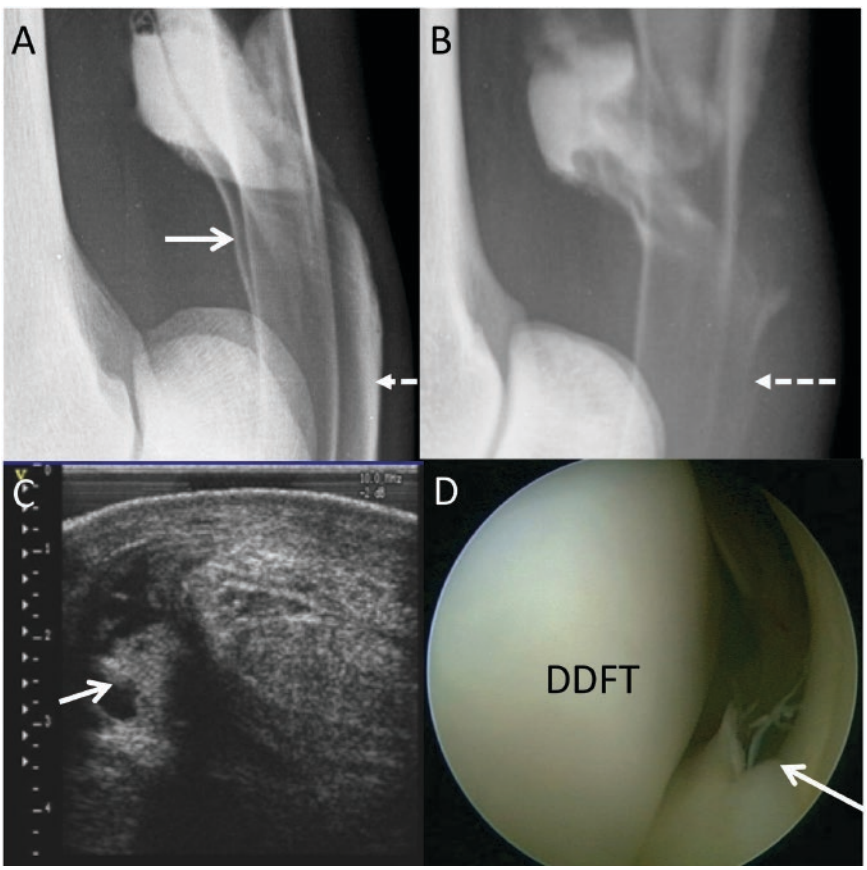


Figure 2.58 Tearing of the manica flexoria. (A and B) Contrast tenography where the contrast agent is introduced at the same time as diagnostic analgesia. A normal manica position is represented by parallel contrast columns tapering together at the level of the apex of the proximal sesamoid bones (A – arrow) in contrast to an absence of the columns in a fully displaced manica flexoria (B). Note also the absence of contrast within the fetlock canal in (B) compared with the normal contrast tenogram (A), suggestive of palmar/plantar annular ligament constriction (dashed arrows). (C) Oblique transverse image from the distal metatarsal region showing echogenic material lateral to the digital flexor tendons. This is a non-specific sign of digital sheath pathology. (D) shows the tenoscopic appearance of the torn margin of the superficial digital flexor tendon (arrows) in a case of a torn manica flexoria.

Vet-ebooks.com

sesamoid bone (often more easily identified ultrasonographically than radiographically because of the superimposition of the axial border on the distal metacarpus in most projections), and abscessation (localized hypoechogenicity) within the ligament (associated with septic osteitis of the axial border of the proximal sesamoid bones). Most injuries to the intersesamoidean ligament involve the articular surfaces but tearing of the proximal scutum communicating with the digital sheath has been described. Arthroscopy and tensocopy can also be used to evaluate the surfaces of the intersesamoidean ligament and the proximal scutum.

Recommended Reading

Barclay, W.P., Foerner, J.J., and Phillips, T.N. (1987). Lameness attributable to osteochondral fragmentation of the plantar aspect of the proximal phalanx in horses. *Journal of the American Veterinary Medical Association* 191: 855–857.

Barrett, E.J. and Rodgerson, D.H. (2014). Ultrasound assisted arthroscopic approach for removal of basilar sesamoid fragments of the proximal sesamoid bones in horses. *Veterinary Surgery* 43: 712–714.

Bastiani, G., De La Côrte, F., Brass, K. et al. (2014). Association of ultrasound and anatomopathologic findings of equine metacarpophalangeal lesions. *Journal of Equine Veterinary Science* 34: 1218–1225.

Carnicer, D., Coudry, V., and Denoix, J.-M. (2012). Ultrasonographic examination of the palmar aspect of the pastern of the horse: Sesamoidean ligaments. *Equine Veterinary Education* 25: 256–263.

Crawford, A., O'Donnell, M., Crowe, O. et al. (2011). Digital sheath synovial ganglion cysts in horses. *Veterinary Surgery* 40(1): 66–72.

Dabareiner, R.M., White, N.A., and Sullins, K.E. (1996). Metacarpophalangeal joint synovial pad fibrotic proliferation in 63 horses. *Veterinary Surgery* 25: 199–206.

Denoix, J.M. (2019). *Essentials in Clinical Anatomy of the Equine Locomotor System*. Boca Raton: Taylor & Francis,

Denoix, J.M. (2000). *The Equine Distal Limb: Atlas of Clinical Anatomy and Comparative Imaging*. Iowa: Iowa State University Press.

Dik, K.J., Dyson, S.J., and Vail, T.B. (1995). Aseptic tenosynovitis of digital flexor tendon sheath, fetlock, and pastern annular ligament constriction. *Veterinary Clinics of North America: Equine Practice* 11: 151–162.

Redding, W.R. (1993). Evaluation of the equine digital flexor tendon sheath using diagnostic ultrasound and contrast radiography. *Veterinary Radiology and Ultrasound* 34: 42–48.

Fiske-Jackson, A.R., Barker, W.H., Eliashar, E. et al. (2013). The use of intrathecal analgesia and contrast radiography as preoperative diagnostic methods for digital flexor tendon sheath pathology. *Equine Veterinary Journal* 45(1): 36–40.

Kent, A.V., Chesworth, M.J., Wells, G. et al. (2020). Improved diagnostic criteria for digital flexor tendon sheath pathology using contrast tenography. *Equine Veterinary Journal* 52(2): 205–212.

O'Brien E., McAlpine J.M., Schramme, M.C. et al. (2018). Avulsion of the proximal digital annular ligament in five hindlimbs. *Equine Veterinary Education* 30(8): 427–432.

Redding, W.R. (1993). Evaluation of the equine digital flexor tendon sheath using diagnostic ultrasound and contrast radiography. *Veterinary Radiology and Ultrasound*. 34: 42–48.

Smith, R., Parsons, J., and Dixon, J. (2020). Risk of intra-articular injection with longitudinal ultrasound-guided injection of collateral ligaments of the equine distal interphalangeal joint. *Veterinary Radiology Ultrasound* 61(1): 67–76.

Steyn, P.F., Schmidt, D., and Watkins J. (1989). The sonographic diagnosis of chronic proliferative synovitis in the metacarpophalangeal joints of a horse. *Veterinary Radiology* 30: 125–127.

Vanderperren, K., Gielen, I., Van Caelenberg, A. et al. (2012). Ultrasonographic appearance of bony abnormalities at the dorsal aspect of the fetlock joint in geriatric cadaver horses. *Veterinary Journal* 193: 129–134.

Vanderperren, K., Martens, A.M., Declercq, J. et al. (2009). Comparison of ultrasonography versus radiography for the diagnosis of dorsal fragmentation of the metacarpophalangeal or metatarsophalangeal joint in horses. *Journal of the American Veterinary Medical Association* 235: 70–75.

Weaver, J.C.B., Stover, S.M., and O'Brien, T.R. (1992). Radiographic anatomy of the soft tissue attachments in the equine metacarpophalangeal and proximal phalangeal region. *Equine Veterinary Journal* 24: 310–315.

Yamada, A., Pinheiro, M., Marsiglia, M.F. et al. (2020). Ultrasound and clinical findings in the metacarpophalangeal joint assessment of show jumping horses in training. *Journal of Veterinary Scienc*. 21: e21. https://doi.org/10.4142/jvs.2020.21.e21

References

1 Denoix, J.M., Jacot, S., Bousseau, B. et al. (1996). Ultrasonographic anatomy of the dorsal and abaxial aspects of the equine fetlock. *Equine Veterinary Journal* 28: 54–62.

2 Tenney, W.A. and Whitcomb, M.B. (2008). Rupture of collateral ligaments in metacarpophalangeal and metatarsophalangeal joints in horses: 17 cases (1999–2005). *Journal of the American Veterinary Medical Association* 233: 456–462.

Vet-ebooks.com

3

Ultrasonography of the Metacarpus and Metatarsus

Roger K.W. Smith[1] *and Eddy R.J. Cauvin*[2]

[1] *The Royal Veterinary College, North Mymms, Hatfield, UK*
[2] *AZURVET Referral Veterinary Centre, Saint-Laurent-de-Var, France*

Preparation and Scanning Technique

Careful preparation of the skin is paramount, including fine clipping, scrubbing of the limb to remove dirt and cut hairs, cleansing with surgical spirit (alcohol) to degrease the skin, and liberal application of coupling gel which should ideally be given time to soak in. The area to be clipped depends on the structures being imaged but for complete evaluation of all the palmar soft tissue structures in the metacarpal/metatarsal region, the skin should be clipped from the palmar carpal region, immediately distal to the accessory carpal bone, down to the ergot of the fetlock and over the whole palmar aspect of the metacarpus from the palmaromedial to the palmarolateral aspect of the third metacarpal bone. For the hind limb, clipping should involve the metatarsal region up to the chestnut. It is possible in some thin-haired horses to perform ultrasonography without clipping, but the image quality will usually be impaired and an acceptable image may not be obtained in all cases. If scanning without clipping, it is advised to dispense with the soap scrubbing as this generates air between the hairs, and just clean the limb with surgical spirit, with or without the application of contact gel.

High-frequency (7.5–16 MHz) linear array transducers are preferred. A micro-convex transducer may be useful to image the proximal aspect of the suspensory ligament in some horses. A standoff pad is recommended to widen the ultrasound window to permit imaging of the whole width of the tendons in one picture, move the superficial structures away from the emission artifact at the top of the screen, and also has the added value in protecting the surface of the transducer. However, some operators prefer to scan the limb without the use of a pad, particularly with high-frequency transducers, to improve penetration. In this case, the contact area will be reduced so it is important to image the limb from both palmar and palmaro-abaxial approaches to obtain a comprehensive assessment of the palmar limb structures.

The scanning protocol for the metacarpal region should consist of both weightbearing and non-weightbearing images. Tendinous structures are under tension when fully weightbearing, which minimizes artifacts; however, non-weightbearing scans can be useful to assess specific structures and some lesions that are more visible when the tendons are unloaded (such as marginal lesions), the motion of each tendon in relation to the others, and for Doppler evaluation (Table 3.1).

Images should be obtained in both transverse and longitudinal orientations in sagittal and, when appropriate, frontal planes. For reference purposes, several systems have been described to determine the level of the section on the limb. None of these has gained general acceptance. The most widely-used system consists of dividing the metacarpal region into three equal tiers (proximal, middle, and distal) from the carpometacarpal joint to the proximal extent of the fetlock palmar annular ligament, termed I to III from proximal to distal. The metatarsal region is divided into four zones (I–IV), with zone I extending from the tuber calcis to the tarsometatarsal joint. Each of these zones is further divided into two halves, named a and b. The palmar fetlock area (at the level of the palmar fetlock annular ligament) is usually referred to as IIIc area in the forelimb, and IVc in the hind limb. It may

Atlas of Equine Ultrasonography, Second Edition. Edited by Jessica A. Kidd, Kristina G. Lu and Michele L. Frazer.
© 2022 John Wiley & Sons Ltd. Published 2022 by John Wiley & Sons Ltd.
Companion Website: www.wiley.com/go/kidd/atlas

Vet-ebooks.com

Table 3.1 Scanning protocol for the metacarpal/metatarsal regions.

Step	Loading	Views
"Standard" views	Weightbearing	Transverse and longitudinal views from the palmar aspect
"Lesion-orientated" views	Weightbearing	"Close ups" (e.g., appropriate enlargement for superficial structures) Oblique images Off-incidence (for the assessment of chronic tendinopathy)
Flexed	Non-weightbearing	Off-incidence (proximal suspensory ligament) Specific structures (e.g., intra-thecal tendon tears) Doppler Tendon movement

be simplified further by dividing the distance from the level of the carpometacarpal joint to the distal sesamoid bones into seven regions (1–7) in both fore- and hind limbs along the length of the third metacarpal/metatarsal bone, although proximal extension of the examination over the palmar carpus and plantar calcaneus is advised for proximal lesions. This system has the advantage of not depending upon the animal's size but is based on specific anatomic features (Figure 3.1) and therefore permits not only comparisons in the same animal, but also between individuals. An alternative technique is to measure the distance from the distal palpable border of the accessory carpal bone or from the tuber calcis to the point at which the ultrasonographic section is obtained. Although this only allows comparisons in the same individual, it may be useful when greater objectivity of position is needed, such as for research purposes.

Typically, the examination is performed from proximal to distal, first in transverse and then in longitudinal planes from the palmar/plantar aspect, followed by any appropriate oblique views. The authors start by examining all the palmarly/plantarly located tendons and ligaments in both planes, then the specific structures of interest by altering the settings on the machine (e.g., enlarging the image to evaluate the superficial structures such as the superficial digital flexor tendon), and then finally the branches of the suspensory ligament from the lateral and medial aspects. The limb may then be picked up for non-weightbearing views. This is most easily achieved in the fore limb by maintaining the limb in a horizontal "neutral" position (straight limb; see Chapter 2, Figure 2.40). For the hind limb, horses frequently rest one hind limb during the examination, especially when sedated (Figure 2.40), and this position provides an easier opportunity to obtain non-weightbearing views without having to hold the limb or have an assistant hold the limb raised. The limbs have to be held for flexion and extension when evaluating relative motion of the tendons. It is important to flex both the distal interphalangeal joint and fetlock joint separately to evaluate tendon movement when assessing adhesion formation. The former will move the deep digital flexor tendon independently of the superficial digital flexor tendon, while the latter will move both tendons together through the fetlock canal. Flexing the distal interphalangeal joint alone while keeping the fetlock joint in the same position may prove difficult in some heavy-set horses but with careful manipulation, even a small range of movement between the tendons can be appreciated with ultrasound.

Ultrasonographic Anatomy

The anatomy of the equine "tendon" region has been reviewed in numerous texts (see Recommended Reading at the end of the chapter). It is fairly simple, although with improving imaging, subtle anatomic details may be evaluated.

General Appearance of Tendons and Ligaments (Figure 3.2)

In normal tendon, the fascicular pattern is characterized by multiple interrupted echoes in transverse images and a regular striated pattern in longitudinal scans. However, the fascicular pattern in equine tendon is complex with different sized fascicles grouped together [1]. The axial spatial resolution (i.e., the ability to differentiate two separate interfaces along a vertical line on the screen) depends mostly on the frequency of the transducer. For a 12 MHz probe, it is theoretically in the order of 0.13 mm. However, other factors, both machine and tissue related, limit the resolution, so that it is in the order of 0.5–1 mm for a broad-band (8–18 MHz), high frequency linear probe. Even when using the higher frequency ultrasound transducers available today, the ultrasonographic striations can only represent the higher-order organization of

Vet-ebooks.com

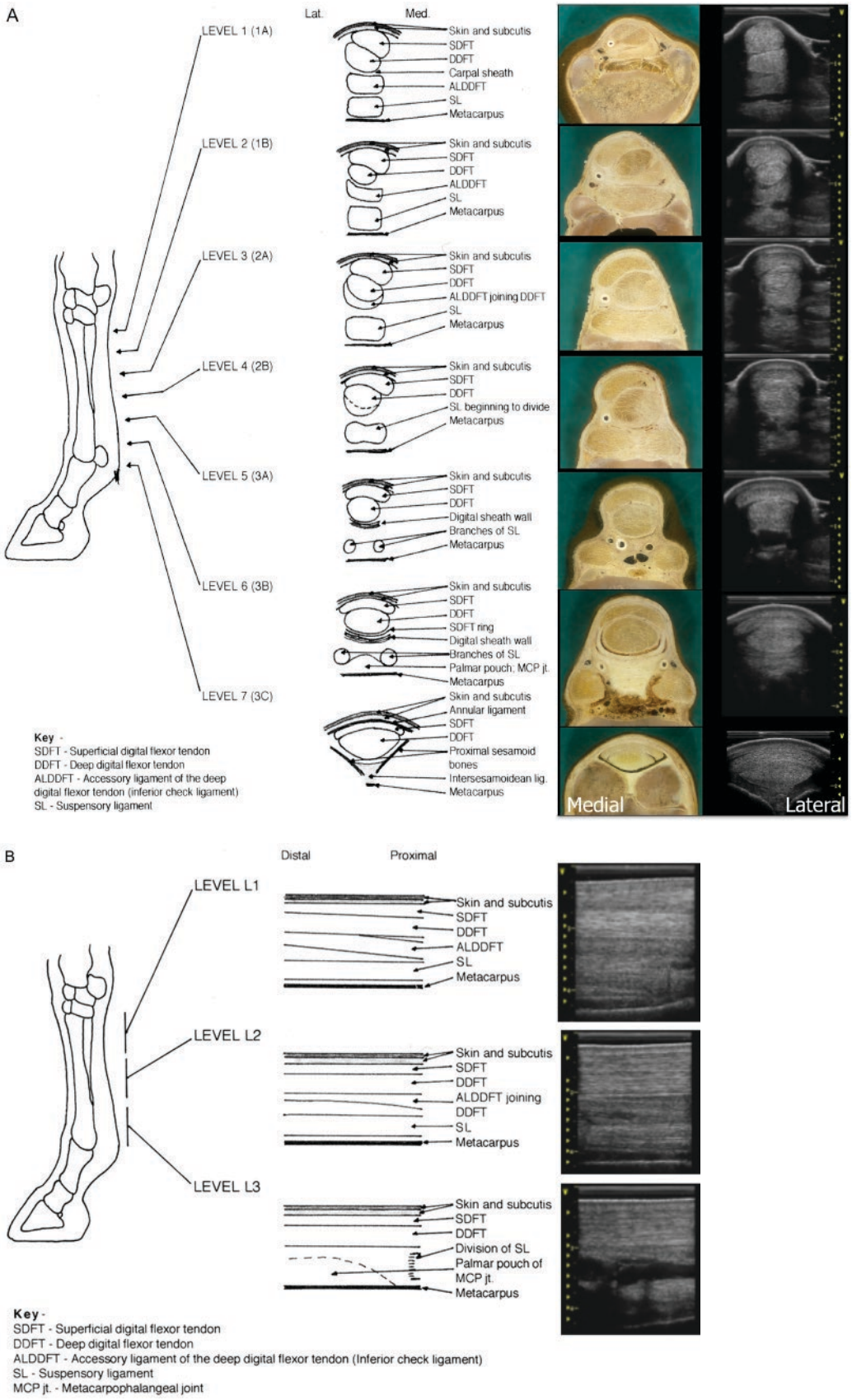


Figure 3.1 Normal ultrasonographic anatomy of the palmar aspect of the metacarpus. (A) Transverse ultrasonographic images are presented on the right side with comparative anatomy sections in the center and diagramatic representation of the location of the transverse images on the left side for the seven standard levels (labeled 1 (Ia) to 7 (IIIc)). The structure labeled "SDFT ring" is the manica flexoria. (B) Longitudinal midline sagittal images in the three thirds of the palmar metacarpus.

Vet-ebooks.com

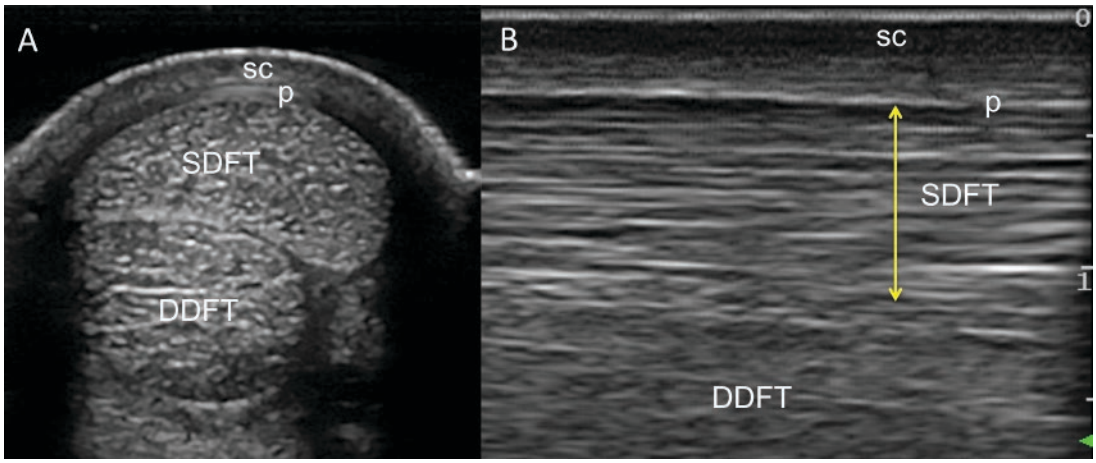


Figure 3.2 Ultrasonographic appearance of tendons and ligaments. (A) In transverse sectional images, the tendon parenchyma typically appears as a "granular" substance with densely packed echogenic dots. The subcutaneous tissue (sc) is hypoechogenic, while the paratenon and overlying fascia form a hyperechogenic interface (p). (B) The tendon parenchyma (SDFT) presents in the long-axis (longitudinal scans) as a series of coarse, transversely oriented hyperechogenic interfaces. These do not represent fibers as such, but rather discrete interfaces between fiber packets. They are separated by anechogenic spaces that represent endotenon (loose, vascularized connective tissue) but also non-resolvable (visible) fibers located before the next visible interface. See the key in Figure 3.1A for abbreviations.

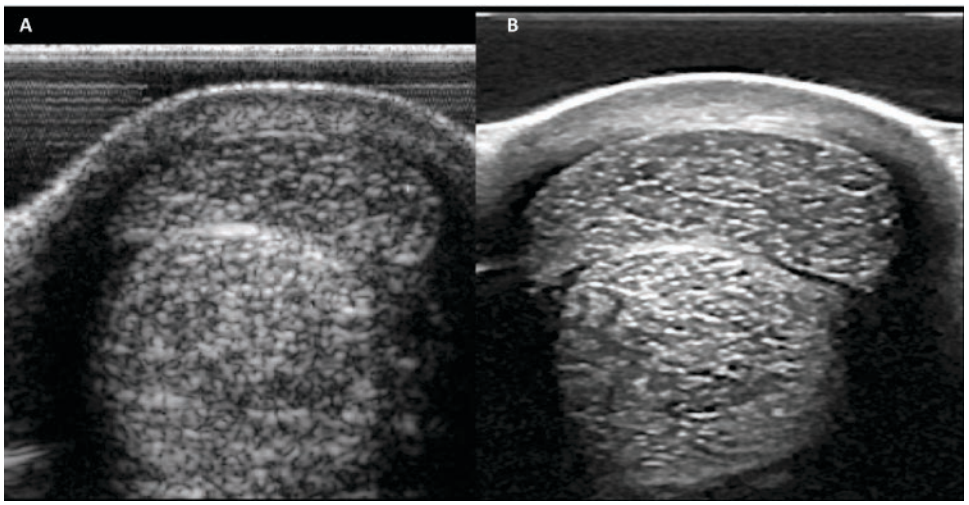


Figure 3.3 The improvement in detail seen in ultrasound quality over 15 years. (A) A transverse image of the superficial digital flexor tendon obtained in 2004 and (B) a similar image obtained in 2019. Note the extra detail of the fascicular architecture visible in the more recent scan. Thus, newer equipment can provide significantly more information on the structure of the superficial digital flexor tendon.

discrete interfaces between groups of fascicles and not individual bundles. Furthermore, echo formation depends on acoustic impedance differences at interfaces, so echoes may occur between many tissue types and may represent the surface of a vessel, a fiber bundle, connective tissue, or any irregularity in the parenchyma. Endotenon and the size of fiber bundles do therefore participate in the heterogeneity of tendon parenchyma and account in part for the differences in appearance between different tendons. Nevertheless, an even, regular striation aligned with the long axis of the tendon and that extends over the width of the image closely follows the underlying microstructure, and has been used to provide objective assessment of structure, so-called ultrasound tissue characterization [2]. The higher the frequency probes, the finer the assessment of fascicular structure (Figure 3.3)

Thoracic Limb

There are four tendons running over the palmar aspect of the metacarpus (Figure 3.1). Respectively, from palmar (superficial) to dorsal (deep), they are

Vet-ebooks.com

the superficial digital flexor tendon (SDFT), deep digital flexor tendon (DDFT), accessory ligament of the DDFT (ALDDFT) proximally, and tendon of the third interosseous muscle, more commonly referred to as the suspensory ligament (SL). These will be reviewed in turn.

Superficial Digital Flexor Tendon (SDFT)

The SDFT arises from the SDF muscle in the distal antebrachial area, 2–6 cm proximal to the accessory carpal bone. The musculotendinous junction extends from the distal quarter of the caudal antebrachium to the proximal edge of the accessory carpal bone (ACB). Hypoechogenic muscle strands can extend more distally in young horses, often well into the carpal canal. The appearance of the junction varies between individuals and depending on breed and age. However, it is usually bilaterally symmetrical. The accessory ("radial check" or "superior check") ligament of the SDFT (ALSDFT) lies dorsomedial to the SDFT close to the musculotendinous junction. This thick ligamentous structure derives from an atrophied radial head and runs obliquely from the caudomedial aspect of the radius just proximal to the chestnut, to join the SDFT proximal to the ACB.

Within the carpal and proximal metacarpal regions, the SDFT is oval to circular in cross-section and is located palmaromedial to the DDFT. Its dorsal aspect becomes concave as it runs distally, giving it a thick crescent shape, with thicker medial and thinner lateral borders, in zone II. It is located at the palmar aspect of the limb in this region. It becomes gradually thinner dorsopalmarly in the distal metacarpus and fetlock regions, with its dorsal surface tightly molded around the palmar contour of the DDFT. In zone IIIb (distal part of the metacarpus, within the digital flexor tendon sheath) it forms a thin membranous ring around the deep digital flexor tendon called the manica flexoria, which arises from the sharp lateral and medial edges of the SDFT. The SDFT eventually divides into two branches in the mid-pastern area, distal to the ergot, each branch blending abaxially into the middle scutum (a palmar fibrocartilaginous pad on the palmar aspect of the proximal interphalangeal joint) before inserting on the middle phalanx (P2). The SDFT is a very dense, echogenic tendon, although it is normally less echogenic than the DDFT and ALDDFT. Using high-frequency ultrasound transducers (>10 MHz), fiber fascicles can be differentiated within the parenchyma. In longitudinal sections the tendon has a regular, continuous striated pattern, characteristic of tendons.

Deep Digital Flexor Tendon

The DDFT also originates in the distal antebrachium from the reunion of three muscular heads (humeral, ulnar, accessory or radial), and its musculotendinous junction occurs at the same level as that of the SDFT. The muscle heads, along with that of the SDF, are indistinguishable ultrasonographically, although the radial head can sometimes be identified cranial to the other heads in the distal antebrachium [3]. The DDFT is initially dorsolateral to the SDFT in the carpal region, where it runs over the medial surface of the ACB. It lies dorsal to the superficial digital flexor tendon in the middle and distal thirds of the metacarpus. It is oval in shape throughout its path but flattens to form sharp medial and lateral borders within the fetlock canal. In the pastern area, it becomes slightly bilobed, with a "ski goggle" appearance on ultrasonographs. It becomes flatter in the foot over the palmar aspect of the navicular bone before inserting on the palmarodistal surface of the distal phalanx (P3).

Accessory Ligament of the Deep Digital Flexor Tendon (ALDDFT)

The ALDDFT ("inferior or distal check ligament") originates on the palmar aspect of the carpus as a distal continuation of the palmar carpal ligament. It joins the deep digital flexor tendon at the mid-metacarpal region (zone II). The junction is very gradual from IIb to IIIa. As the fibers of the ALDDF are oblique, this creates a hypoechogenic, off-incidence artifact within the dorsal aspect of the DDFT in this area (see zone 2A (level 4) in Figure 3.1). The ALDDFT is rectangular in cross-section in zones IA and B (levels 1 and 2); see Figure 3.1, then becomes crescent shaped in zone II (3 and 4), curving mostly around the lateral aspect of the DDFT. The carpal flexor tendon sheath lining forms a hypoechoic space between the deep digital flexor tendon and the ALDDFT down to their junction, and it occasionally contains some anechogenic fluid.

Suspensory Ligament (SL)

The SL is formed by the atrophied interosseous III muscle and its tendon. It is anatomically divided into three approximately equal portions: the proximal origin (3–5 cm long), the body (main portion down to the bifurcation), and the two branches (lateral and medial). The origin and body of the suspensory ligament are examined from the palmar aspect of the limb, whereas the branches should be examined in turn from the lateral and medial aspects. Some muscle fibers remain in young horses, giving the ligament a mottled, hypoechoic appearance. These may decrease with age. Most studies have showed that the heterogenous pattern of the proximal SL in normal horses is bilaterally symmetrical at any level. The SL originates from the proximal palmar cortex of

Vet-ebooks.com

the third metacarpal bone but has an additional component extending proximally to the carpus, blending into the joint capsule of the carpometacarpal joint and palmar carpal ligament. The origin and body of the SL are rectangular in cross-section, although usually only the middle half or two-thirds of the ligament is visible within the ultrasound window in a weight-bearing limb from a palmar approach. To evaluate the entire volume of the SL, it is necessary to rotate the probe from medial to lateral (It may be useful to use a convex probe in the proximal metacaparpus). The origin is divided into two lobes, sometimes visible as separated by hypoechogenic tissue. These two lobes are molded by the slightly concave surfaces on the palmar aspect of the third metacarpal bone, separated by a variably prominent, sagittal bony ridge. The body of the SL has a coarser, less echogenic appearance than the tendons. The SL divides in the distal third of the metacarpus into two branches (medial and lateral). Each inserts over the abaxial surface of the ipsilateral proximal sesamoid bone. The medial branch is slightly larger than the lateral, but both are pear- or tear-drop- shaped. As they insert they become triangular to crescent-shaped. The striated pattern is regular over the whole length of the SL, although it is not uncommon in adults and older horses to have a thinner or less marked striation at the proximal and body regions.

The SL branches are continued distodorsally by the extensor branches, which course dorsally and join in the distal pastern onto the common digital extensor tendon (CDET). The sesamoid bones are an integral part of the suspensory apparatus, as are their distal ligaments (see Chapter 1). Ideally, these should therefore be examined along with the SL, as combined injuries are fairly common.

Extensor Tendons

In the metacarpal area, the extensor tendons are easily identified over the dorsal aspect of the third metacarpal bone (Mc3). They have a less echogenic, coarser appearance than flexor tendons. They are very thin and flat in cross-section, located in the connective tissue between the skin and periosteum. The CDET is dorsolateral proximally and dorsal in the distal half of the metacarpus. The lateral digital extensor tendon (LDET) is much smaller, round in cross-section, and situated laterally in the proximal metacarpus. It runs obliquely to follow the lateral edge of the CDET in the distal third, where it becomes flatter and blends into the fetlock joint capsule.

Other Structures

The surface of the third metacarpal bone (Mc3) is round and forms a smooth, sharp, hyperechoic interface. The overlying periosteum is clearly visible as an echogenic, 2–3 mm thick, homogeneous layer overlying the bone. The splint bones (Mc2 and Mc4) can also be assessed; they are smooth and regular in long-axis scans and sharply rounded in cross-section. The interosseous ligament between the splint bones and the cannon bone forms an echogenic space between the bone interfaces, and it may become mineralized in older horses.

All tendons, except in sheathed areas, are surrounded by a thin connective tissue layer (the paratenon). This is less echogenic than the tendon parenchyma and contains numerous small vessels that are not visible in normal tendons. The carpal and digital flexor tendon sheaths are described in other sections of this text.

The neurovascular bundles are easily identified in this part of the limb (Figure 3.4). In the proximal and mid-metacarpal area, the medial palmar artery and nerve run together and are identified close to the skin surface but deep to the fascia, along the medial aspect of the DDFT, while their lateral counterpart is more deeply and dorsally located on the lateral aspect of the ALDDFT. The corresponding veins are larger and located slightly more dorsally in the looser connective tissue space dorso-abaxial to the ALDDFT. The lateral vein is more axially located. In the distal third of the metacarpus, the bundles run over the dorsoabaxial border of the DDFT/ALDDFT and then become more superficial, running over the abaxial aspect of the proximal sesamoid bones palmar to the SL branch insertions. The nerve is always palmar to the associated artery. The connecting branch between the two palmar nerves arises from the medial palmar nerve at the mid-metacarpal level and runs obliquely in a latero-distal direction over the palmar surface of the SFDT before joining onto

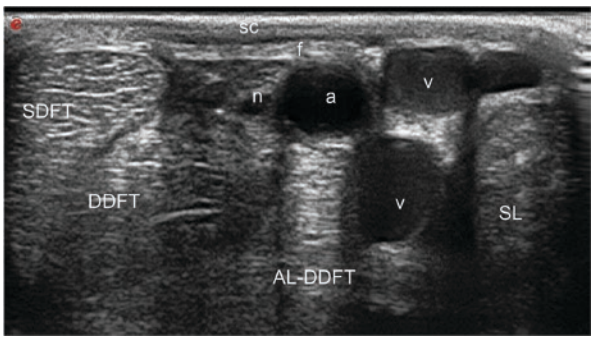


Figure 3.4 Transverse ultrasonograph from the mid-metacarpal region using a palmaromedial approach. Neurovascular structures are identified: the medial common palmar nerve (n) has coarse, grainy appearance; the associated artery (a) is round in section with a thick wall; the veins (v) are easily compressed due to the thin walls. Note the thick superficial fascia (f).

Vet-ebooks.com

the lateral palmar nerve 1 or 2 cm further distally. This may be felt and cause a slight elevation of the skin and probe in relation to the SDFT.

The nerves have a coarse striated pattern on long-axis scans and a coarse grainy appearance on cross-section.

The veins are anechogenic with thin, deformable walls, so that they may be easily obliterated by excessive probe pressure on the skin. Echogenic whorls of moving blood cells may be identified in the veins and larger arteries because of the slow flow in equine extremities. Venous valves can occasionally be identified and can be seen to open and close with flow. However, blood flow is often static in a horse standing still. The arteries are of much smaller caliber and have thicker walls, which gives rise to twin echoes on their superficial and deep surfaces. They are always round in cross-section and more difficult to compress. The arterial flow is laminar with poorly marked systolic surges in Doppler studies.

Pelvic Limb Differences

The overall arrangement is similar to that of the thoracic limb. It is virtually the same in the distal two-thirds of the metatarsus. Proximally, the SDFT is slightly flatter than in the fore limb, and is located plantarolateral to the DDFT as it runs over the plantar aspect of the tuber calcis of the fibular tarsal bone (calcaneus) and overlying long plantar ligament. The SDFT does not have any muscular body in the equine pelvic limb. The DDFT is formed by the fusion of two tendons: the lateral digital flexor tendon (LDFT) is the main part, running medial to the tuber calcis over the sustentaculum tali of the calcaneus and then plantar to the distal tarsal bones. The medial digital flexor tendon (MDFT) is a small, cylindrical, tendon that runs over the medial aspect of the tarsus, in a groove on the medial aspect of the tibial tarsal bone, closely associated with the medial collateral ligament of the tarsus, before joining onto the medial border of the LDFT in the proximal quarter of the metatarsus to form the DDFT. Both structures have their own tendon sheath in the tarsal area, although these sometimes communicate distally.

Contrary to what has been previously described in some anatomy textbooks, there is an ALDDFT in the hind limb. It is often rather thin and varies between individuals from a thin aponeurotic membrane to a fully developed ligament, similar but substantially smaller than that encountered in the thoracic limb. It arises from the short plantar ligament of the tarsus.

Finally, the SL has two, well differentiated heads in the hind limb, the lateral head being larger and tightly packed against the axial border of the fourth metatarsal bone (Mt4). It is more triangular to oval shaped than in the fore limb. The intercapital ridge on the plantar proximal metatarsus is rather less marked than in the fore limb. A strong, deep fascia can sometimes be identified plantar to the SL, running between the heads of the two splint bones and enclosing the proximal suspensory ligament in a canal. In the proximal part of the metatarsus, imaging the SL from a plantar approach can be limited, because of the prominent and axially concave head of the fourth metatarsus (lateral splint bone). It is therefore useful to use a plantaromedial approach, the so-called "medial window," because the second metatarsal (medial splint) bone is considerably smaller than its lateral counterpart. In some horses, the use of a micro-convex array transducer can be very useful to image the origin of the ligament as the pie-shaped beam easily encompasses the whole cross-section of the SL from a plantaromedial to plantar entry point.

Quantitative Assessment of Flexor Tendon and SL Size

Reference measurements for the SDFT have a wide range because of a greater than two-fold variation in tendon size between normal individuals, and because of variations between breeds or type of horses. Cross-sectional areas (CSA) of the SDFT in Thoroughbreds in the United States has been given as 0.8–1.2 cm^2, while a larger range (0.72–1.93 cm^2) has been reported as the normal range for Thoroughbreds in Great Britain, with 0.77–1.39 cm^2 in level 4 (zone IIb; mid-metacarpal region) in National Hunt horses [4]. Tendon CSA varies with breed and size, and is smaller in Arabian-type horses (0.6–0.8 cm^2) and in ponies. In contrast, Smith et al. (1994) did not find a significant difference between Thoroughbreds and Irish Draughts [5]. The CSA varies with the anatomic level; it is smallest in the mid-metacarpal area and largest in the fetlock region. It may vary somewhat with age and training. The lateromedial dimension varies between 1 and 3 cm, depending on the location. The dorsopalmar thickness has been reported to be 0.7–0.8 cm proximally, decreasing to approximately 0.4 cm distally. but these measurements are less accurate for determining enlargement compared to measuring the CSA. DDFT CSAs vary from 1.35–2.2cm^2 [5], with its smallest CSA immediately proximal to the insertion of the accessory ligament of the deep digital flexor tendon [5].

For the SL in racing Thoroughbreds and Standardbreds in the United States, the cross-sectional area ranges from 1.0–1.5 cm^2, with most horses having a cross-sectional area of 1.0–1.2 cm^2 for the suspensory body. It is slightly larger in the pelvic limb (1.2–1.75 cm^2). The branches measure 0.6–0.8 cm^2 proximally to

Vet-ebooks.com

1–1.2 cm^2 distally. Measuring the dorsopalmar/plantar thickness of the ligament is probably of greater clinical interest than for the SDFT, especially in the origin and proximal body area, as it is difficult to image the entire SL in one image necessary for CSA measurement. It is normally less than 1 cm in average-sized horses (0.8–0.9 cm in Thoroughbreds). The branches are less than 1 cm thick in a dorsopalmar direction.

Ultrasonographic Abnormalities

Tendinopathy/Desmopathy

General Ultrasonographic Changes

Tendinitis/desmitis refers to spontaneous loss of structural integrity of the fibrous parenchyma of tendons and ligaments respectively. The complex pathogenesis of this condition has been reviewed elsewhere and will not be reviewed here [6]. Tendinopathy/desmopathy is the more appropriate term to cover all types of tendon injury, although tendinitis/desmitis remains more widely used.

Ultrasonography allows us to detect variations in gross anatomy (size and shape of the tendon or ligament) but also in the overall structure of the parenchyma (refer to the Section on Ultrasonographic Anatomy). Acute damage is associated with several changes in the ultrasonographic appearance of the tendon – an increase in size, a reduction in echogenicity with loss of the normal striated pattern, often affecting the central area of the tendon, and changes in shape, margination, and position. Immediately after the injury, the lesion fills with blood and debris, which are variably echogenic (hypo- to hyperechogenic) and heterogeneous. The lesion in the first few days may be subtle or even missed, as matrix debris and clots may have similar echogenicity to that of the normal parenchyma (Figure 3.5). The acute lesion is usually poorly defined and heterogeneous but long-axis images will confirm loss of fiber alignment (Figure 3.6).

Edema leads to increased water content and decreased echogenicity in the surrounding tendon, paratenon, and subcutaneous tissues (Figure 3.6). The tendon may be swollen, although this is variable initially, but peritendinous and subcutaneous edema should be detectable. Comparison with the contralateral limb (which may not be completely normal with many overstrain injuries) may help confirm increased tendon size. After a few days, an organized hematoma and early, immature granulation tissue fill in the

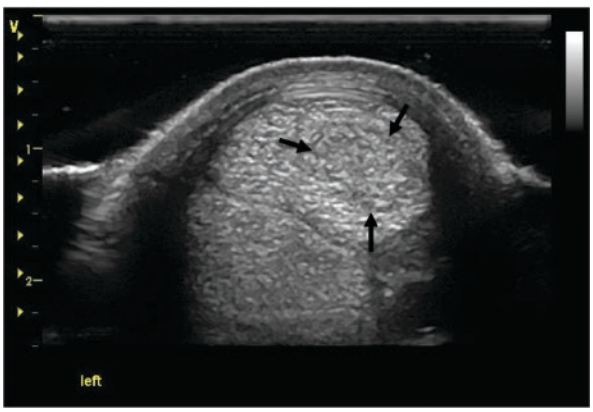


Figure 3.5 Transverse ultrasound scan image at level 1 showing a poorly defined area within the SDFT that is grossly isoechogenic to the remaining parenchyma but with altered echotexture. More subtle lesions are easily missed at this early, acute stage.

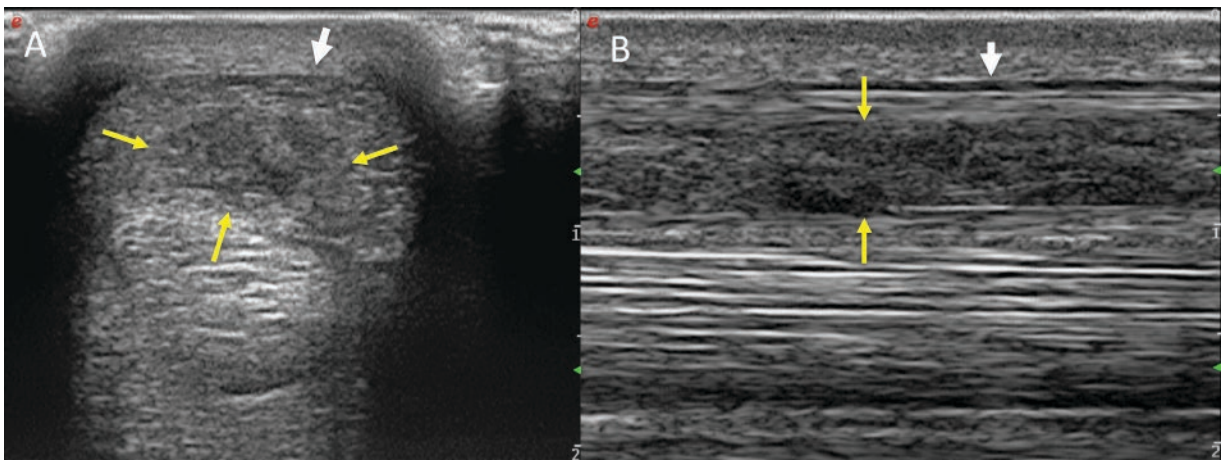


Figure 3.6 Transverse (A) and longitudinal (B) ultrasound scan images showing a poorly defined, heterogeneous, and slightly hypoechogenic area in the transverse plane within the SDF tendon (yellow arrows). The sagittal plane image shows severe fiber disruption and decreased echogenicity. Note the increased cross-sectional area of the SDFT and peripheral swelling of the paratenon (white arrow).

Vet-ebooks.com

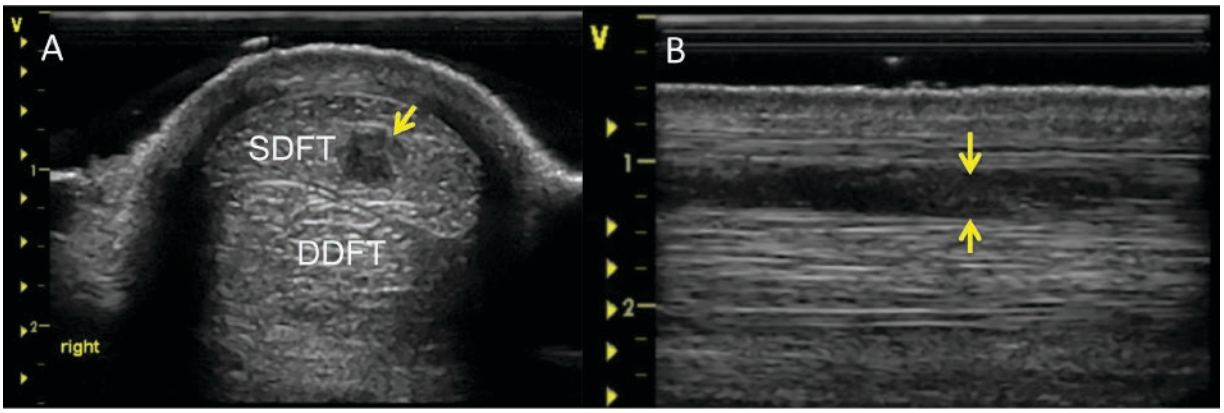


Figure 3.7 Transverse (A) and longitudinal (B) ultrasound scan images of the palmar mid-metacarpal region (level 3). A well defined, hypoechogenic "core" lesion is present in the central part of the tendon. This appearance is related to early granulation tissue which appears homogeneously hypoechogenic.

lesion. They are hypoechogenic and provide the typical, discrete appearance of many tendinitis lesions (Figure 3.7).

The lesion may increase in size for several days after injury, because of repeat bleeding and local release of degrading enzymes by invading inflammatory cells, usually making the lesion more evident after several days. Therefore, to establish a baseline severity scan, lesions are best examined ultrasonographically at 7–10 days after injury: this is usually the stage when the lesion is largest and most obvious. If any doubt persists, the animals should remain box-rested and be re-evaluated 2 weeks later.

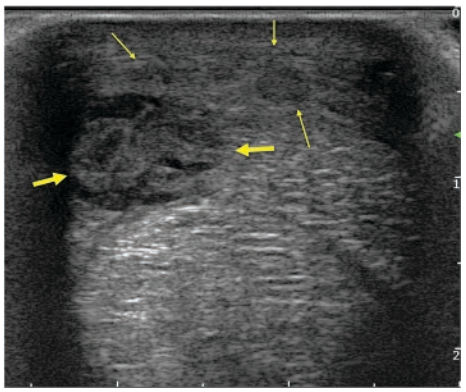


Figure 3.8 Transverse image obtained at level 4, showing an acute, hypoechogenic lesion with a honeycomb pattern, typical of organized hematoma. It distorts the lateral aspect of the SDFT (thick arrows). The paratenon is markedly thickened (thin arrows) around the lesion, extending around the SDFT.

SDF Tendinopathy

A common manifestation of acute SDFT injury is a discrete hypoechoic lesion visible in the central region of the tendon (hence the usual term, "core lesion;" Figure 3.7). It is most commonly centered in the mid-metacarpal region (usually zone 4/IIb). Lesions can also occur more eccentrically within the tendon (Figure 3.8). Lesions occurring at the periphery of the tendon are often associated with extension of the hematoma into the paratenon or even peritendinous tissues. These may be traumatic in origin (see Section on Local Trauma). Such lesions often alter the shape of the tendon. There is also an increase in tendon cross-sectional area, which is highly variable between lesions. The size of the lesion is relative to the cross-sectional area of the tendon, but its proximodistal length should also be ascertained to aid in prognostication (see Section on Semi-Objective Assessment of Severity) and for future reference.

Diffuse lesions are more challenging to visualize: the tendon becomes enlarged, hypoechogenic, and heterogeneous (Figure 3.9). Sagittal ultrasound scans confirm diffuse loss of striation. Enlargement and diffuse hypoechogenicity is sometimes seen in young Thoroughbreds without other clinical signs (so-called "juvenile tendinitis"). The aetiology is unclear and affected horses often recover without significantly increased risk of re-injury.

Tendon enlargement can be measured objectively by measuring the cross-sectional area (CSA) of the tendon on transverse images. Injured tendons have a CSA greater than normal (see Section on Quantitative Assessment of Flexor Tendon and SL Size), although this can be difficult to ascertain, given the large variation in normal cross-sectional areas. If previous scans are available, a greater than 10% increase in cross-sectional area is usually significant or, if

Vet-ebooks.com

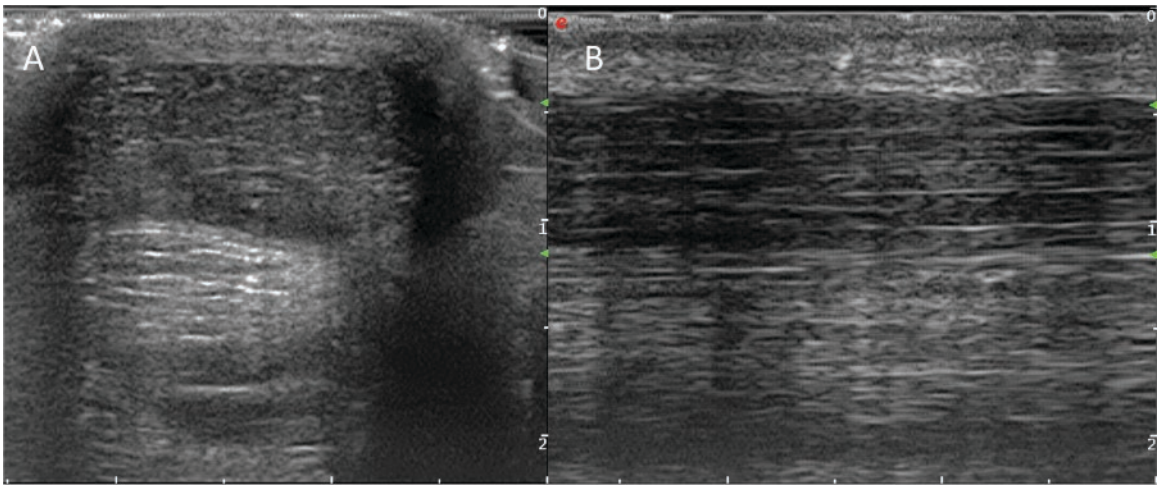


Figure 3.9 Diffuse tendinopathy similar to that seen in young horses ("juvenile tendinitis"). Transverse (A) and longitudinal (B) ultrasound scan images of the palmar mid-metacarpal region (zone 3). The SDFT is generally enlarged, hypoechogenic without a discrete lesion being visible. The striation is poorly organized and uneven on the longitudinal scan.

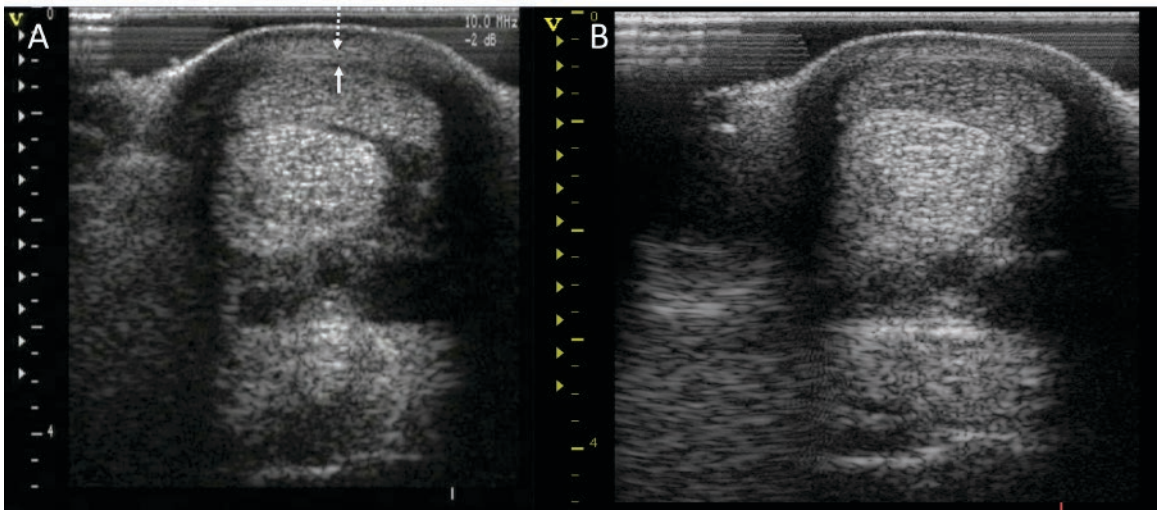


Figure 3.10 Transverse ultrasonographs from the mid-metacarpal region (level 4) showing thickening of the paratenon (solid arrow) and subcutaneous tissues (dashed arrow) associated with peritendinous edema but without any tendon enlargement (A) when compared to the contralateral limb (B). This can either be a sign of mild local trauma or early overstrain injury. The limb should be re-examined ultrasonographically if the edema does not spontaneously resolve within a few days.

comparing with the contralateral limb, a greater than 20% difference would be considered significant [5], although this may not be the case if both limbs are affected or there is a previous injury.

In very subtle cases, often the only finding can be enlargement and/or change in shape of the tendon. This can be accompanied by peritendinous edema, which is not specific for tendinitis and can also result from local trauma (Figure 3.10) or any other inflammatory condition in the limb. Providing there is no evidence of tendon injury and the edema disappears, work can be resumed after a short period of rest. If edema persists, however, the presence of tendinitis should be suspected and repeat examinations are warranted.

There is some controversy as to the ability to detect subclinical or preclinical lesions with ultrasound. Certainly, gradual degeneration as observed biochemically or histologically is at a level that cannot be detected by the resolution of ultrasound, and recent studies have failed to identify prodromal changes ultrasonographically [4], even though some subtle heterogeneity is sometimes interpreted as signs of aging change (Figure 3.11). However, the detection of

Vet-ebooks.com

previous injury, which may have been missed clinically, is a recognized risk for re-injury. Therefore, with increasing use of ultrasonography as a preventive means, the identification of chronic pathology or mild injuries will increase. Subclinical tears or degeneration are represented by small hypoechogenic foci or diffuse areas, and an altered longitudinal pattern, without overt signs of enlargement and inflammation (Figure 3.12).

Injury can also occur to the SDFT either proximally or distally and should not be overlooked. Distally in the fetlock ("low bow") and pastern regions, they can be associated with variable amounts of digital sheath effusion. These injuries are addressed in Chapters 1 and 2. However, occasionally lesions may occur in the distal metacarpal area and extend into the sheathed portion of the tendon without concurrent sheath effusion or inflammation. There is usually secondary subcutaneous fibrosis with these injuries, in contrast to those affecting the SDFT more proximally. Proximal SDFT tendinitis can extend to within the carpal sheath region, again with or without associated tenosynovitis (Figure 3.13). All injuries occurring within an intrathecal portion of the tendon tend to carry a graver prognosis because of the absence of a paratenon within these regions. If the lesion is confluent with the cavity of the tendon sheath, synovial fluid inhibits tendon healing and subsequent adhesions can prevent restoration of normal function [7]. Often these are recurring injuries occurring distal or proximal to the previous scar. One should therefore look for evidence of previous injury to the mid-metacarpal region.

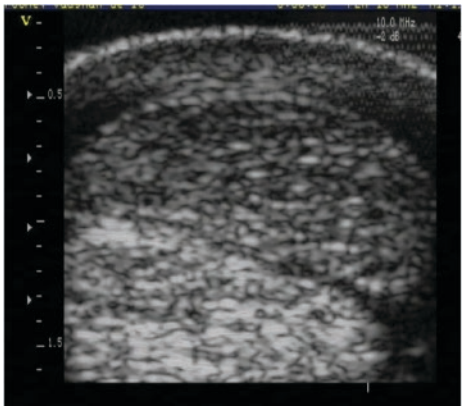


Figure 3.11 Transverse ultrasonograph from the proximal metacarpal region showing scattered hyperechoic foci within the superficial digital flexor tendon, characteristic of aging degeneration but not always associated with active or chronic clinical tendon disease. This tendon had a normal longitudinal striated pattern.

Complete rupture of the SDFT is the most severe extreme of an over-strain injury and often results in an almost totally anechoic region of the SDFT surrounded by a thin echogenic line (the paratenon, which usually remains intact unless the injury has been caused by percutaneous trauma) (Figure 3.14). Evidence of damage will also be apparent proximal and distal to the rupture. If the tendon ends have retracted, the outline of the paratenon at the site of the rupture may not be particularly enlarged but bunched-up; retracted fibers will be identifiable proximal and distal to the rupture site, giving the tendon a "cauliflower"-like appearance. The SDFT also becomes medially displaced because of lengthening of the tendon. Subcutaneous thickening is usually marked in these cases. Complete rupture of the SDFT may occur spontaneously in older horses (Figure 3.15).

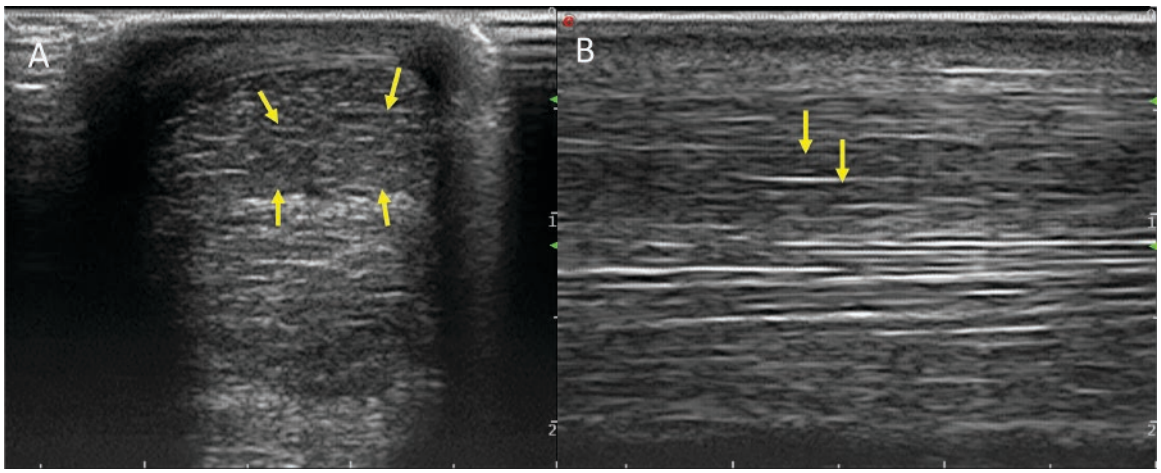


Figure 3.12 Transverse (A) and longitudinal (B) ultrasound scan images of the palmar metacarpal region (zone 3). Despite this horse having no known history of previous or current tendon injury, the SDFT is heterogeneous with iso- to hypoechogenic areas within the tendon and a disrupted fascicular pattern (yellow arrows). On longitudinal images, these areas present with finer, less organized striation and decreased echogenicity (yellow arrows). These were interpreted as subclinical, chronic lesions.

Vet-ebooks.com

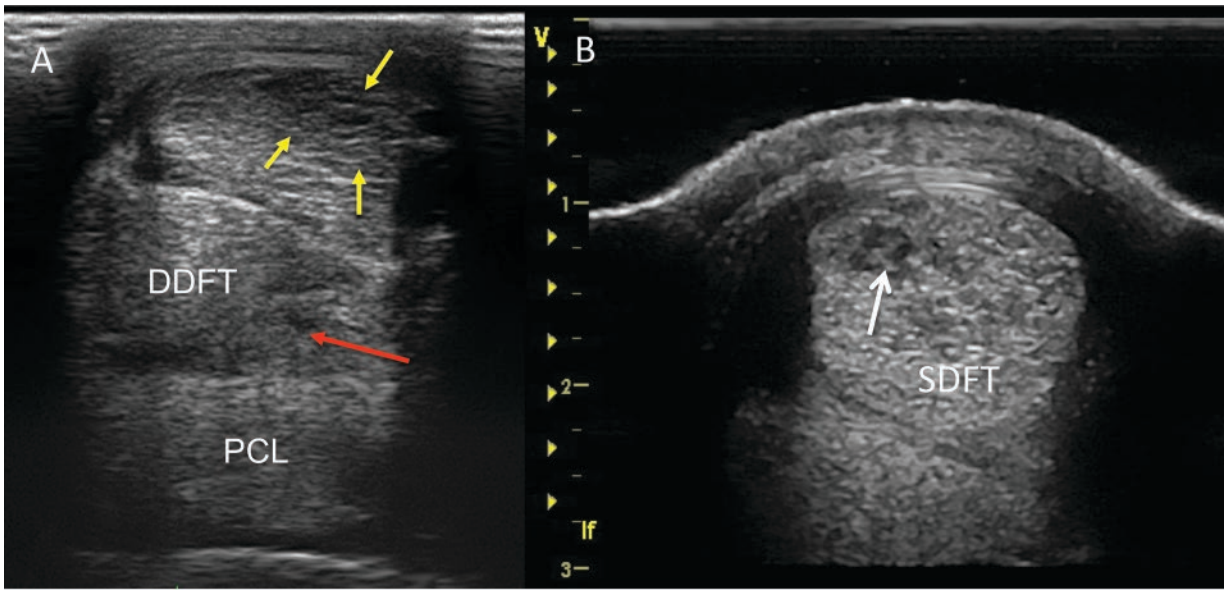


Figure 3.13 Proximal metacarpal superficial digital flexor tendinopathy. (A) Transverse image obtained palmar to the proximal metacarpal area. There is a diffuse hypoechogenic lesion in the palmaromedial aspect of the superficial digital flexor tendon (SDFT; yellow arrows) associated with diffuse thickening of the carpal flexor tendon sheath synovial membrane (red arrow), a sign of tenosynovitis. The lesion extended proximad from a metacarpal SDFT tear. PCL: palmar carpal ligaments. (B) Transverse image obtained at the level of carpometacarpal joint showing a hypoechogenic "core" lesion that spans the carpal and metacarpal regions. This lesion did not communicate with the carpal sheath and there was minimal associated tenosynovitis. While marked distension of the tendon sheath occurs when the lesion communicates with the tendon sheath cavity, its presence is not unique to surface disruption.

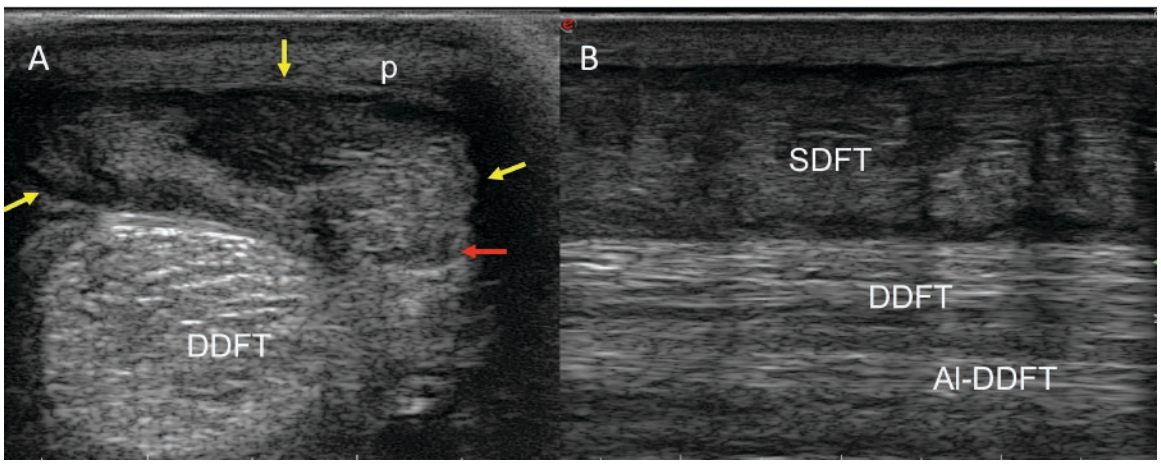


Figure 3.14 Transverse (A) and longitudinal (B) ultrasound images of the palmar metacarpal region (zone 4). The superficial digital flexor tendon (SDFT) is very enlarged and hypoechogenic with no evidence of normal striations over most of its cross-section (yellow arrows). Some remaining fibers are seen medially (red arrow), and amorphous tissue strands are mixed with the hypoechogenic material. This was an acute, spontaneous rupture following recurrence of a severe tendinitis lesion in a French trotter racehorse. p: paratenon; ALDDFT: accessory ligament of the deep digital flexor tendon.

Semi-Objective Assessment of Severity

Objective measurements potentially allow better determination of prognosis and assessment of healing. The percentage ratio of the damaged tendon can be calculated for discrete lesions by summing the CSA for the focal lesion relative to the total tendon CSA at each individual level for all seven zones (Ia to IIIc) to give an approximation of the "volume" ratio of the lesion over the whole tendon (Figure 3.16). This has been used to objectively assess severity: injuries are considered to be mild if the ratio is in the 0–15% range, moderate for 16–25% ratios, and severe if more than 25%. An alternative and simpler method is to consider the maximum injury zone only: mild injuries involve less than 10% of the cross-sectional area; moderate 10–40%; and severe > 40%. This obviously does not take into account the length of the lesion, although even with short, discrete lesions, the pathology usually extends further than the visible lesion, usually throughout most of the metacarpal region. These

Vet-ebooks.com

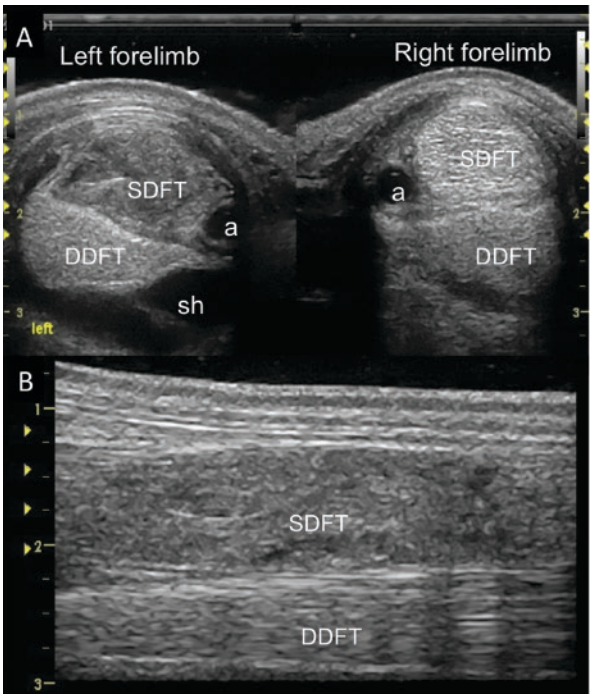


Figure 3.15 Transverse (A) images obtained at the level of the carpal canal with comparison between left and right transverse plane images. The left superficial digital flexor tendon (SDFT) is minimally enlarged but hypoechogenic and devoid of any normal longitudinal striation because the tendon fascicles have been pulled apart. This appearance is typical of spontaneous rupture where the tendon parenchyma is replaced by hemorrhage and granulation tissue, contained within the visceral synovial layer. The common medial palmar arteries (a) are normal in this case, and there is marked carpal sheath effusion (sh). The right fore limb is normal. (B) Longitudinal image of the left fore limb. SDFT: superficial digital flexor tendon; DDFT: deep digital flexor tendon.

different assessments of severity all result in characterization of pathology into mild, moderate, and severe categories [8]. It is generally recognized that the severity of the lesion is related to the prognosis for return to work at the same level; the larger the lesion, the greater the loss of alignment and the lower the echogenicity of the lesion, the poorer the chances for return to work at the same level as prior to injury.

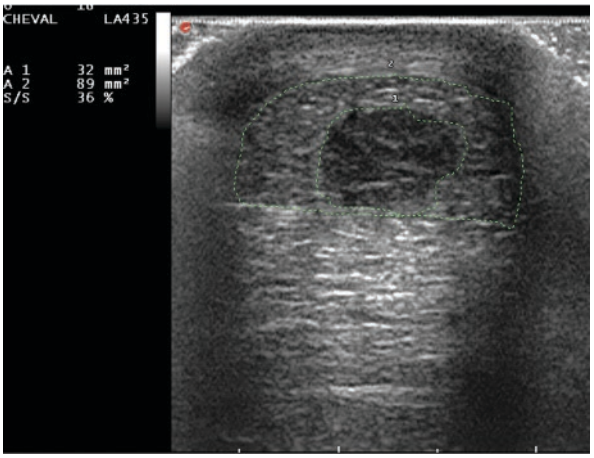


Figure 3.16 Transverse image at level 3, showing trace measurements of the ratio of the lesion to total cross-sectional area of the superficial digital flexor tendon (SDFT). This is repeated at each standard level from proximal to distal and either the greatest ratio, or the average of all measured ratios is used to assess severity.

This, together with the fiber alignment at the time the horse returns to work provides the best assessment of prognosis, although the relationship is not strong and outcome is still variable. Thus, small lesions can fail to heal adequately, while larger lesions can heal well.

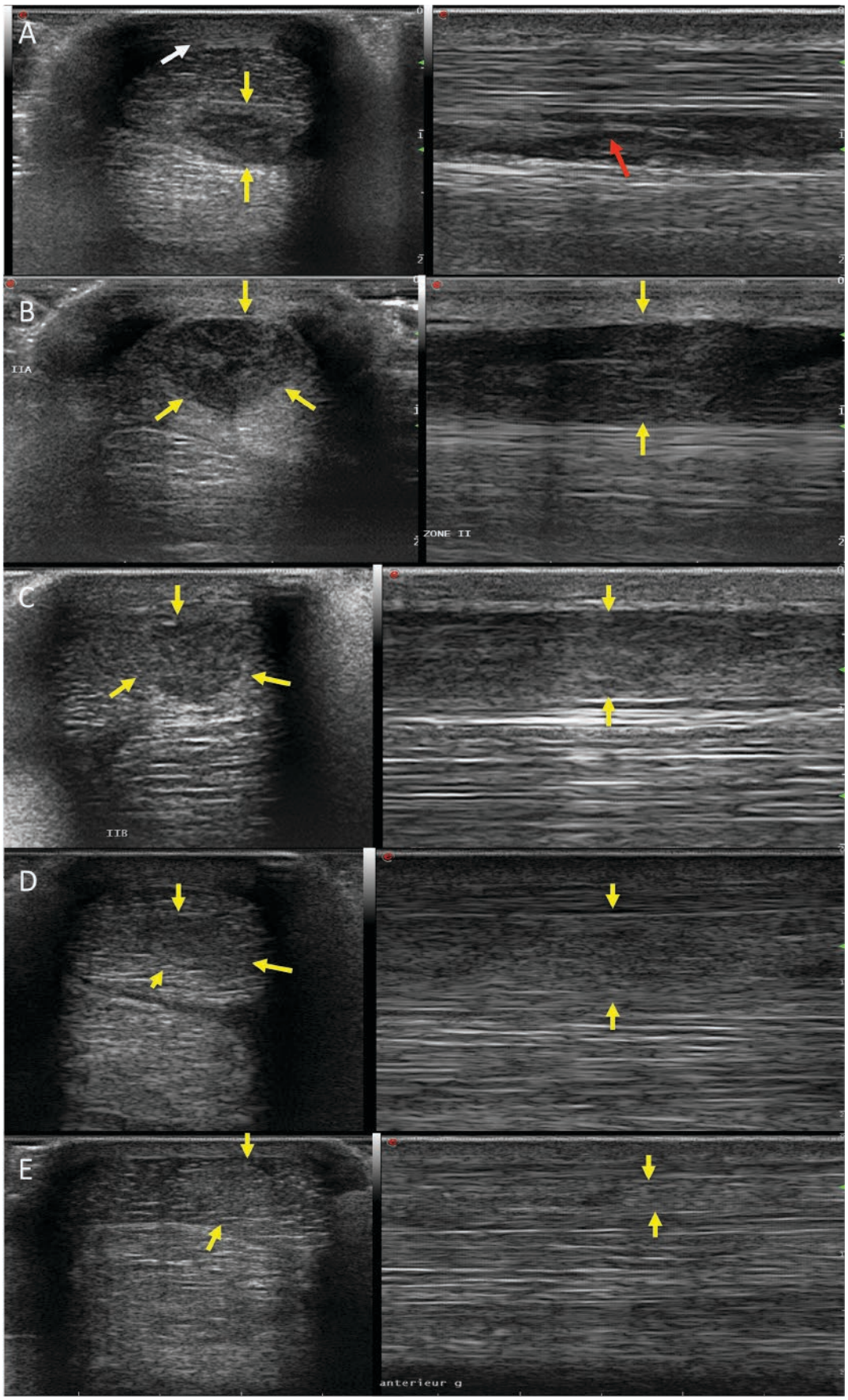
Assessment of Healing

Evaluating the progression of healing over time requires experience and is somewhat subjective. There is a lot of variation depending on many factors, including severity of the initial lesion, variation in healing rate between horses, occurrence of re-injury, etc. However, it is generally accepted that ultrasonography will help monitor the progress and quality of the healing process to some extent (Figure 3.17). There is a relatively poor correlation between the ultrasonographic image and molecular composition but there are definite features that are believed to relate to histological stages of healing. Initial hypoechogenicity is induced by a mixture of fluid infiltration (hemorrhage and edema) and cellular infiltrates that decrease the number of detectable interfaces. Both the initial thrombus and early granulation tissue contain cells,

Figure 3.17 Combined evaluation of transverse and longitudinal plane images allows us to subjectively assess the stage and quality of healing. (A) At the acute stage (the first few days), fibrinous clots and debris fill the lesion creating a heterogeneous, poorly defined, and variably hypoechogenic area, with a more echogenic halo often visible (yellow arrows). Longitudinal images show loss of fiber continuity, with normal fibers being visible at the extremities of the lesion (red arrow). Note the marked peritendinous soft tissue swelling (white arrow). (B) After a few days, the clot becomes invaded by cellular infiltrates and eventually immature granulation tissue. In the absence of organized fibers creating interfaces, this tissue is very hypoechogenic, although remaining matrix may create slightly more echogenic foci. (C) During the fibroblastic stage (2 weeks until 3–6 months) the lesion gradually increases in echogenicity and decreases in cross-sectional area. The overall tendon surface area decreases slightly and the peritendinous swelling resolves. (D) With time and tissue remodeling, the lesion regains an echogenicity similar to that of normal tendon tissue on transverse scans; however, long-axis images still show a lack of adequate fiber realignment. Horses may resume training at this stage but should still be monitored closely for re-injury. (E) The tendon can be considered to be healed and sufficiently remodeled to sustain return to exercise when its cross-section has reduced to near its original size, the lesion is isoechogenic to the rest of the parenchyma, and a linear pattern can be seen within it. The tendon, however, will never return to normal, with an abnormally short, coarse pattern usually noted in the scar tissue.

Vet-ebooks.com

Figure 3.17 (*Continued*)



Vet-ebooks.com

microscopic debris, poorly organized matrix, and microvascular structures, all of which are below the definition of ultrasound. They therefore appear hypoechogenic.

Gradual increase in echogenicity occurs because newly formed collagen fibers aggregate to form more organized bundles and thus create detectable interfaces. Peritendinous swelling resolves after a few weeks. With time, in the absence of recurrence or chronic evolution, the immature scar tissue is gradually replaced by more mature parenchyma, which usually manifests itself as a more echogenic and homogeneous tissue, containing finely striated longitudinal interfaces. These initially form dots or small dashes, giving the scar an even, grainy appearance. As fibers form larger bundles, linear interfaces become visible but until these are longitudinally aligned the striation is irregular and very short. An adequately remodeled scar forms a rough striated pattern in longitudinal scans and a fairly homogeneous, grainy image on transverse ultrasound scans.

All tendon injuries should ideally be monitored ultrasonographically regularly at up to 3-monthly intervals or less, and particularly after any change in the exercise level. At each examination, the following factors indicate good progress:

1. A stable or decreasing cross-sectional area: sequential CSA measurements provide the most sensitive indicator of adequacy or mismatch between exercise intensity and tendon healing during the rehabilitation phase. If the CSA at any level increases by more than 10% compared to the previous examination, it is advisable to lower the exercise level.
2. An increase in the lesion echogenicity and an increasingly homogeneous texture. A subjective type score of the relative echogenicity of the lesion has been proposed compared to that of the surrounding, intact parenchyma (Figure 3.18): type 1 lesions are only slightly hypoechoic (more white

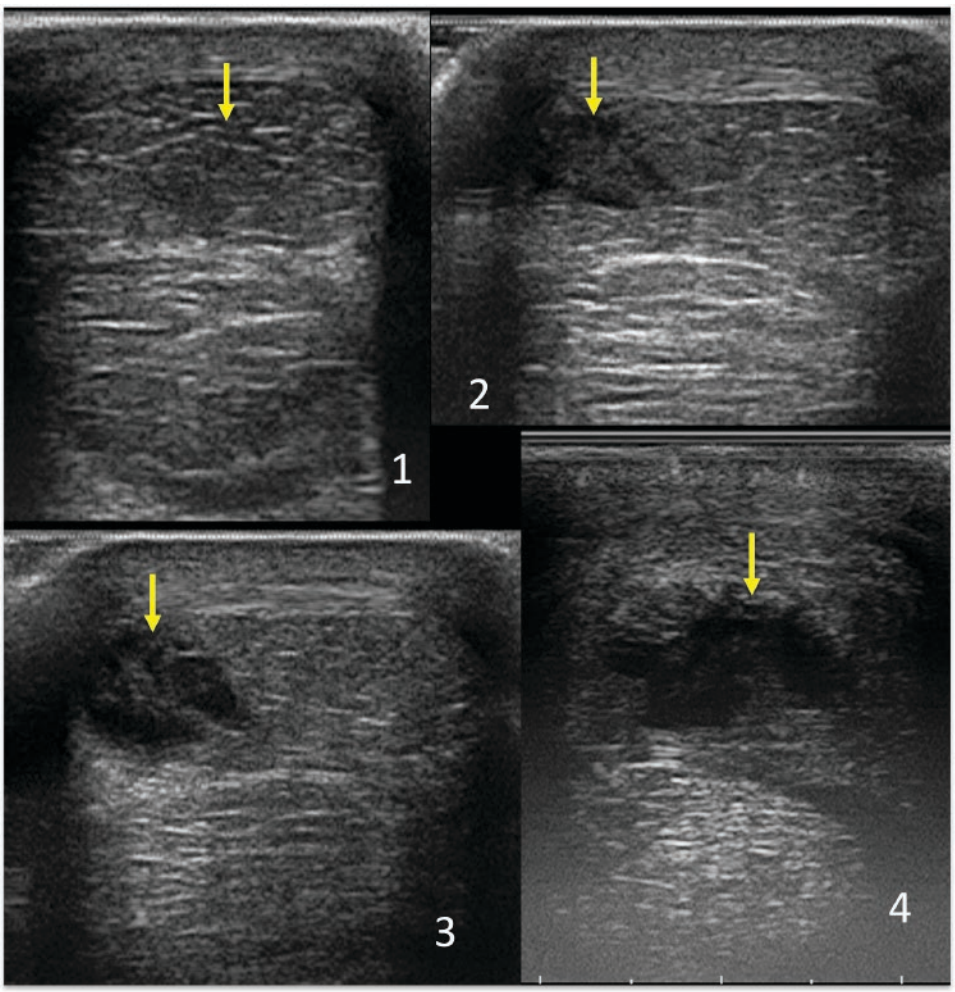


Figure 3.18 Subjective echogenicity score: depending on the echogenicity of the lesion relative to the normal parenchyma, the lesion may be subjectively graded from 1 (slight hypoechogenicity) to 4 (anechogenic). However, echogenicity cannot be quantified as it dvepends on many factors including beam frequency, gain, contrast and brightness settings, and subjective factors such as "echogenicity" of the skin and tissues.

Vet-ebooks.com

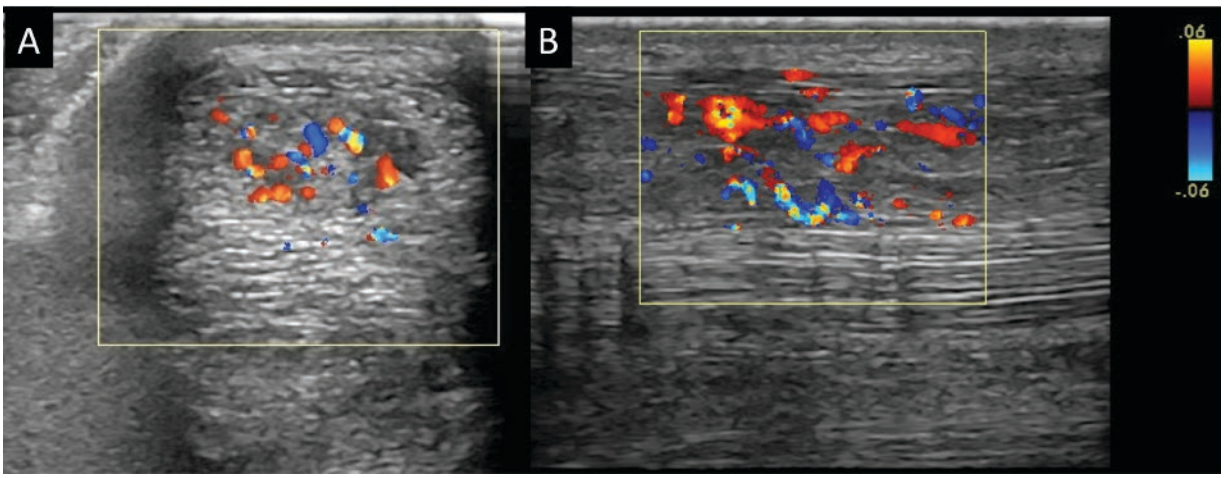


Figure 3.19 Transverse (A) and longitudinal (B) images obtained from a subacute case of superficial digital flexor tendinopathy. These images are obtained in the non-weightbearing limb and the presence of a positive Doppler signal, while subjective, is indicative of an active healing lesion (normal tendon has no Doppler signal). The reappearance of a positive Doppler signal after it has disappeared during the chronic stages of healing is strongly suggestive of re-injury.

than black); type 2 lesions are moderately hypoechoic (same amounts of white and black); type 3 lesions are very hypoechoic (more black than white); and type 4 lesions are anechoic (totally black).

3. An improvement in the striated pattern seen longitudinally (Figure 3.17). A subjective fiber alignment score can be used to monitor the improvement in the longitudinally aligned interfaces in the lesion on sagittal or frontal plane images – varying from 0 (76–100% parallel fibers considered normal) to 3 (0–25% of parallel fibers).
4. Absence of peritendinous fibrosis and adhesions.
5. Decreasing blood flow. Increased blood flow within healing digital flexor tendons can be identified using color flow Doppler imaging but this requires the limb to be non-weightbearing, as weightbearing load increases the pressure inside the tendon and prevents blood flow being visualized. Normal digital flexor tendons have minimal discernible blood flow while, after injury, a pronounced vascular pattern is usually visible (Figure 3.19). Hypervascularity is normal in the healing process but should subside as healing progresses (highly variable but normally between 3 and 6 months after injury) and its re-appearance can be an indication of re-injury.

Chronic Tendinopathy

Horses suffering from tendinitis are constantly at risk of re-injury. Complete healing, determined histologically, takes at least 15–18 months. The mean interval between injury and return to training in racehorses is dependent on the severity of the initial injury and varies between 9 and 18 months. Sports horses may be able to return to full work in a shorter time but even the mildest ultrasonographically detectable injuries should entail at least 6 months off work. Occasionally horses are successfully returned to full work prior to full resolution of the ultrasonographic lesion; however, this success may be due to the horse being capable of sustaining work in spite of the presence of a tendon injury.

Chronic tendinitis refers to either an end-stage tendinopathy or recurring and/or ongoing tearing and inflammation, generally caused by poor healing of the initial, acute injury or premature return to work before the scar tissue has sufficiently matured.

Ultrasonographic characteristics of chronic tendinopathy are variable and can be subtle. The tendon is often enlarged (Figure 3.20). Its echogenicity varies from hypoechogenic through normoechogenic to hyperechogenic, depending on the severity of the initial injury and the degree of fibrosis that has occurred. The parenchymal pattern is usually coarser, heterogeneous, with a lack of striations in longitudinal images. In some cases, the outline of the original core lesion can still be seen (the so-called "onion-ring lesion"). Mineralization is rare in the SDFT compared to the DDFT, but if present, causes discrete, hyperechoic interfaces casting acoustic shadowing. If calcification is florid, previous intratendinous injection of depot corticosteroids should be suspected. Off-incidence transducer orientation can help to define areas of disorganized scar tissue in chronic injury, because it retains its echogenicity at greater transducer angles than normal tendon (Figure 3.21).

Vet-ebooks.com

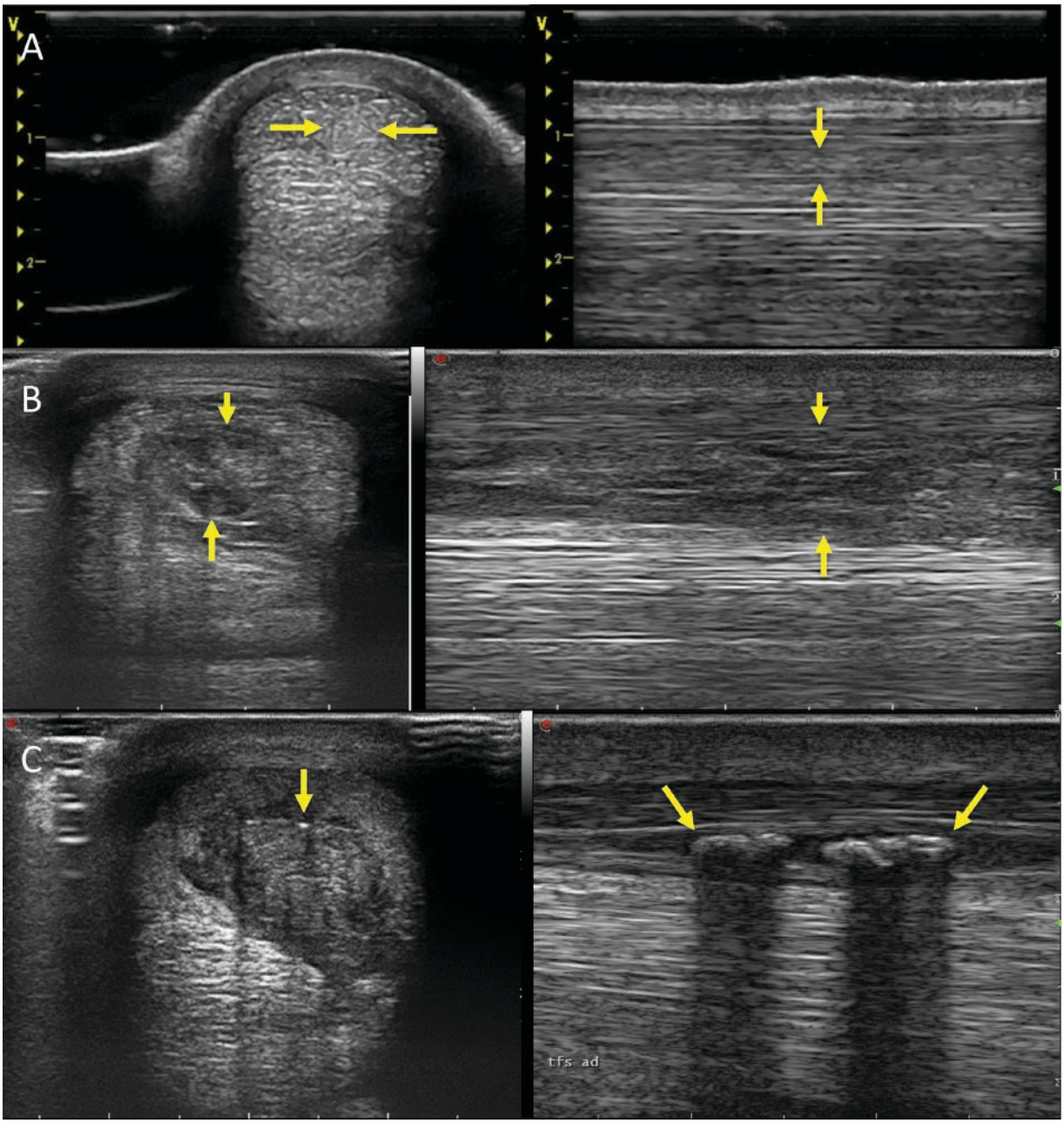


Figure 3.20 Chronic superficial digital flexor tendinopathy showing different qualities of healing. (A) A well healed lesion (yellow arrows) showing good incorporation of the scar tissue within the tendon. Note the persistent poor longitudinal pattern that remains. (B) Chronic tendinopathy characterized by a heterogeneous tissue (yellow arrows) with mixtures of echogenic scar tissue and hypoechogenic areas representing either recurring tears or amorphous connective tissue. (C) Calcification (yellow arrows) is rare in the superficial digital flexor tendon (SDFT), being more common in the DDFT. It may be subtle as in the left transverse image, or more florid as in the right longitudinal image. The latter had received previous intratendinous injections with neat bone marrow.

Persistent "active" pathology is characterized by a persistent Doppler signal.

Recurrence is common after tendon injury and should be differentiated from chronic tendinopathy. The presentation is very variable, from a mottled, diffuse hypoechogenicity superimposed on the repair tissue, to discrete tearing elsewhere in the tendon. The most common site of re-injury is one extremity of the scar. In this case, the scar seems to be detached from the rest of the tendon by a conical hypoechogenic area (Figure 3.22).

Vet-ebooks.com

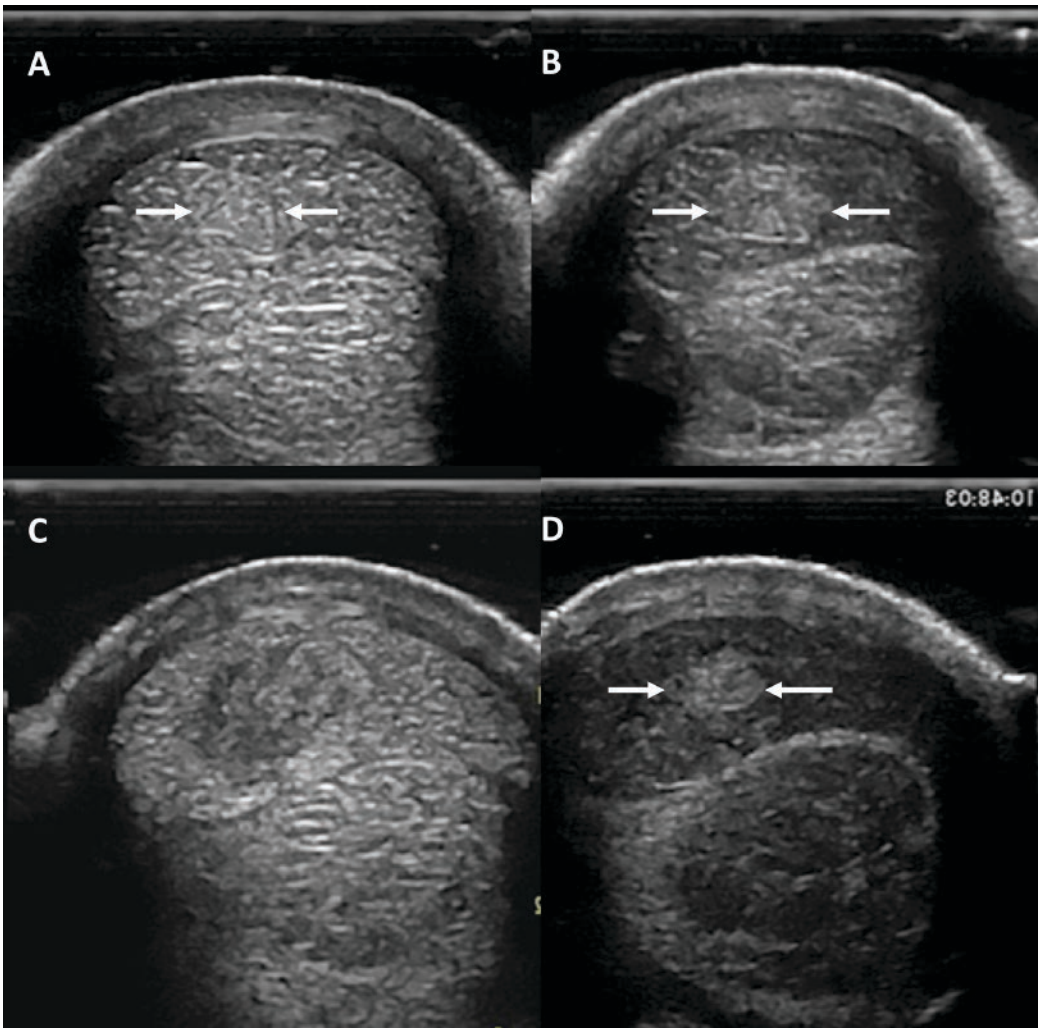


Figure 3.21 Using an off-incidence (non-orthogonal) imaging artifact can help highlight poorly organized tissue within a tendon. (A) is an on-incidence view where the faint outline of a healed lesion is visible (arrows), largely because of the loss in fascicular pattern. (B) shows the same tendon with the transducer tilted by about 10 degrees. The normal parenchyma will become hypoechogenic, whereas the scar tissue, being devoid of longitudinal arrangement, usually remains echogenic and is therefore more visible. (C) shows a transverse scan on a recently damaged superficial digital flexor tendon (SDFT). Some of the fascicles have been torn and are retracted inside a core lesion. The off-incidence view (D) shows the same retained echogenicity (arrows), but this time due to disorganized torn fascicles rather than fibrous scar tissue.

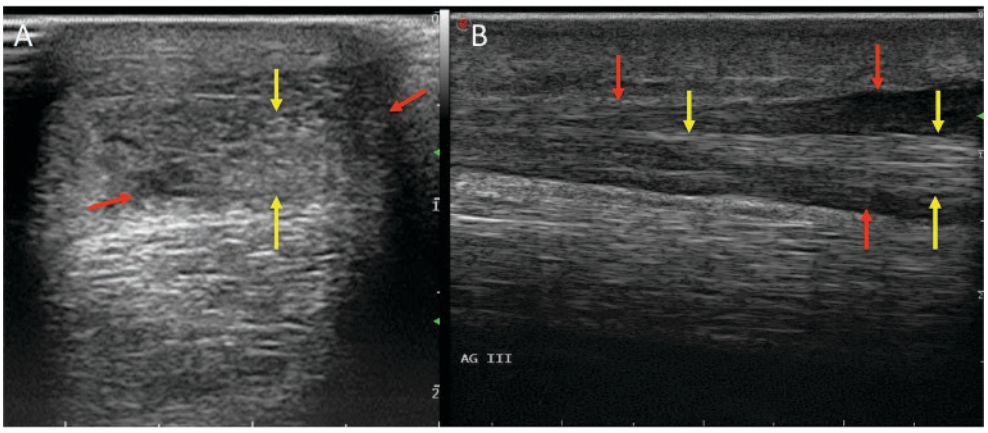


Figure 3.22 Recurrence often occurs at the extremity of the scar tissue (yellow arrows), which becomes separated from the normal tendon tissue by an ill defined, hypoechogenic area (red arrows).

Vet-ebooks.com

Local Trauma

Spontaneous, over-strain injuries need to be distinguished from local trauma. These injuries may be caused by a slipped or over-tight bandage ("bandage bow"), hitting obstacles or loose objects, or percutaneous trauma (particularly from interference with another limb, most frequently a hind foot). If trauma occurs through bandages or boots, the skin may not be breached or damaged, and contusion and bleeding occur deeper, at the tendon interface. The effects of local trauma can vary from localized subcutaneous or peritendinous edema, and later fibrosis, with no evidence of intratendinous damage, through localized hypoechoic/anechoic lesions on the palmar surface of the tendon, to partial or complete transection of the SDFT (Figure 3.23), sometimes extending to the

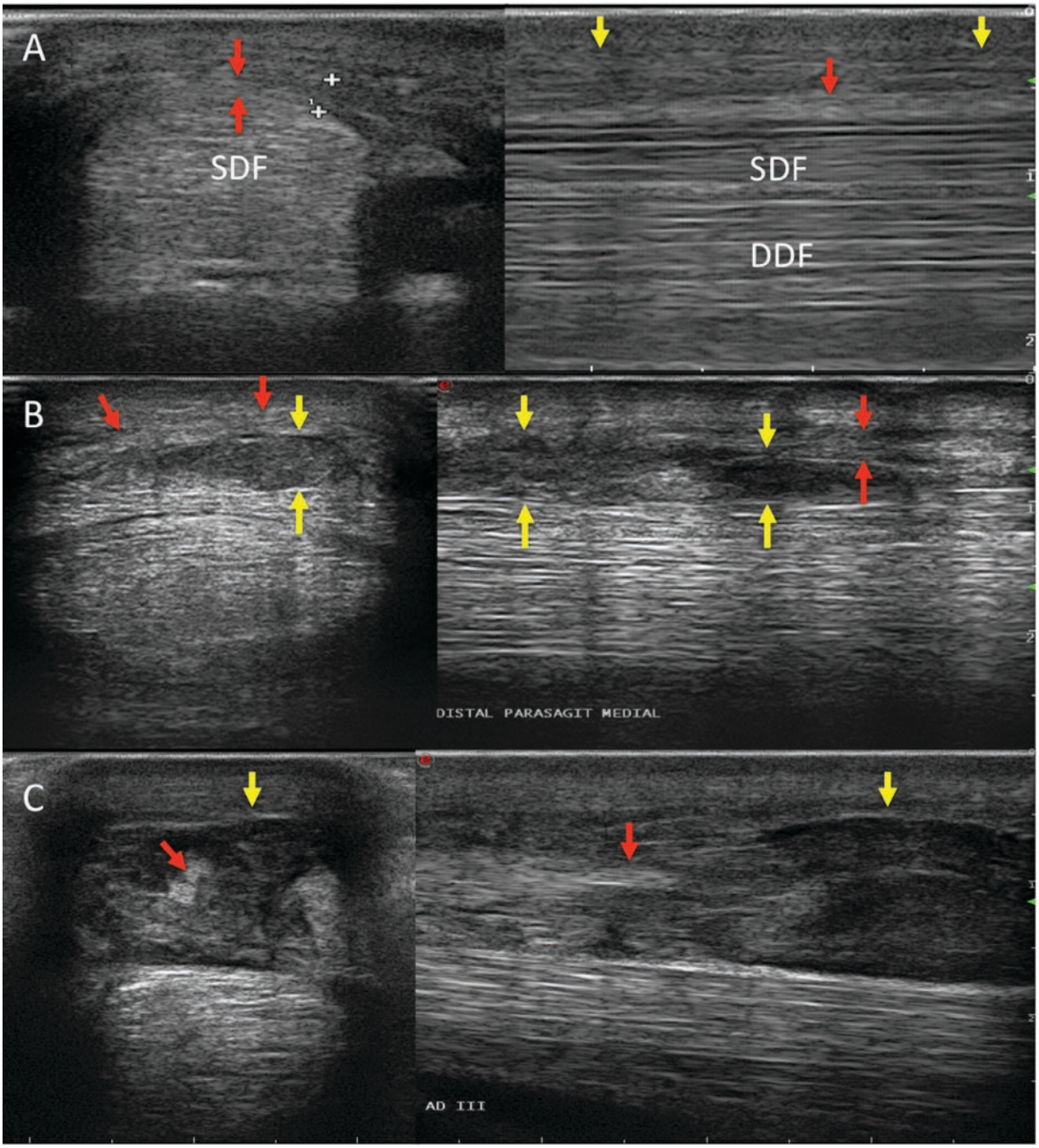


Figure 3.23 Trauma to the palmar aspect of the metacarpus can lead to varying degrees of injury. A superficial contusion (A) extends to the subcutaneous and peritendinous tissue (yellow arrow), with thickening of the paratenon (red arrow). In some cases (B), the contusion will affect the palmar surface of the tendon, causing a hypoechogenic, superficial lesion (yellow arrows) and elevating the paratenon (red arrow). When the skin is breached, the lesion may extend any distance down to the bone. (C) Transection of the SDFT will cause the torn ends to retract proximally and distally (red arrows). The gap becomes filled with hemorrhage and debris (yellow arrow).

Vet-ebooks.com

deeper tendons. Local traumatic injuries are, at least in the acute stage, very localized. They rarely extend far proximodistally. However, partial lacerations can be associated with longitudinal splits in the tendon, extending proximally or distally, and resulting from shear stresses (Figure 3.24). Tendon trauma can be easily missed if the examination is restricted to the site of the wound as they often occur when the tendon is fully loaded, so that the site of injury moves more proximally in the resting limb. Ultrasound is therefore very useful to identify these sites of injuries not visible through the wound.

Sepsis following a penetrating injury (or occasionally, hematogenous spread) of the SDFT is rare and usually gives an anechoic lesion, often with a communicating tract to the periphery of the tendon (Figure 3.25). It may occasionally be very extensive and diffuse. Aspiration of the lesion will yield an exudate containing large numbers of degenerate neutrophils. These lesions do not usually cause gross enlargement of the affected tendon and change rapidly in time in comparison to core lesions in a tendon strain. If the lesion is present within a tendon sheath, there will invariably be an accompanying septic tenosynovitis. Occasionally, foreign bodies can be deposited inside the tendon where they can cause local tissue disruption (Figure 3.26), but are not always associated with tendon sepsis.

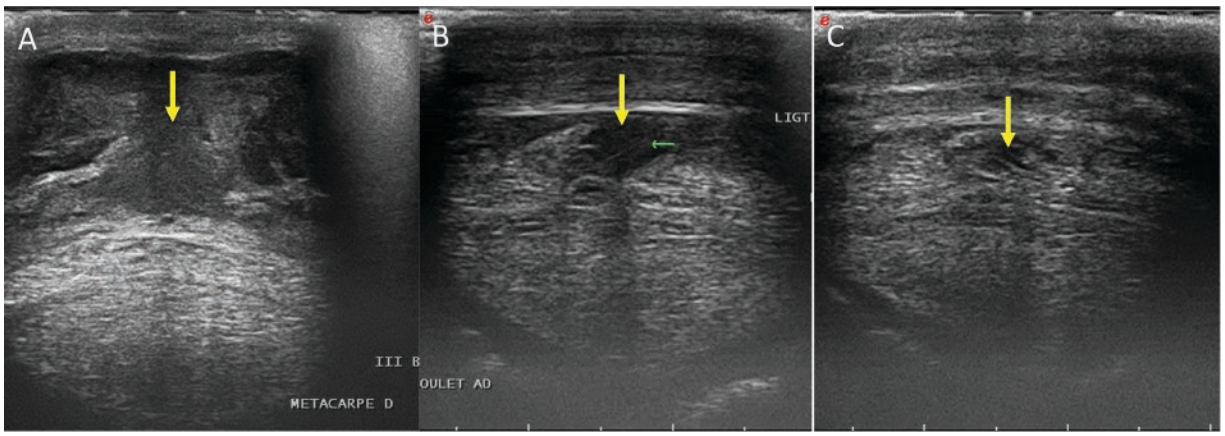


Figure 3.24 (A) This horse sustained a laceration proximal to the palmar annular ligament (zone 6). (B and C) Although fairly superficial at the level of the wound, a longitudinal tear extended distally into the parenchyma (arrows).

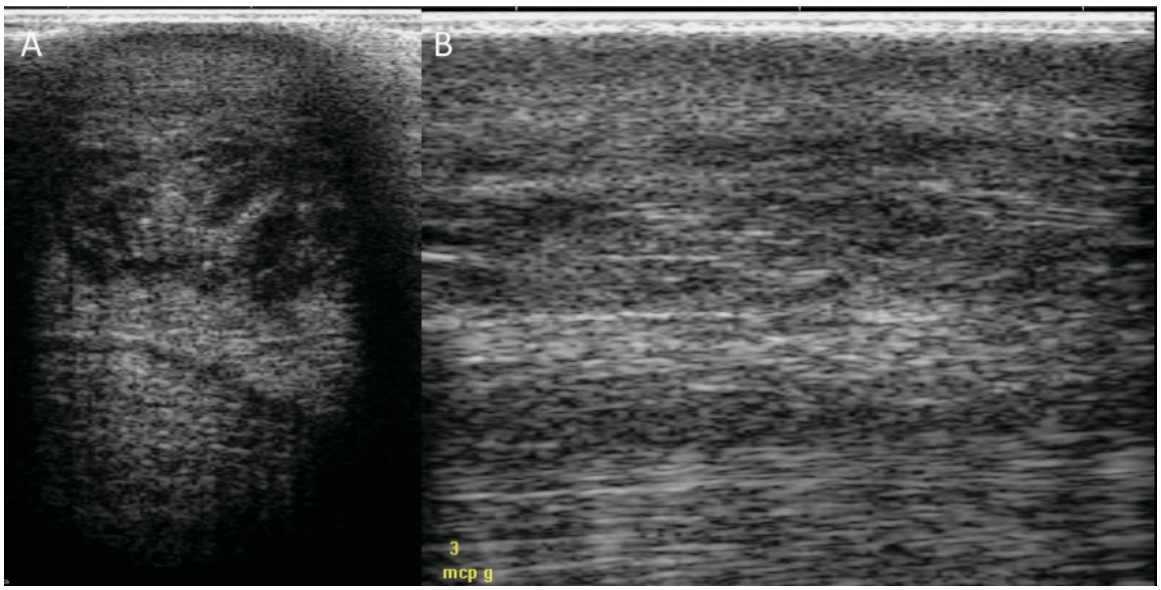


Figure 3.25 Septic tendinitis secondary to a penetrating injury. Note the mottled, moth-eaten appearance of the superficial digital flexor tendon (SDFT) and severe, peritendinous swelling.

Vet-ebooks.com

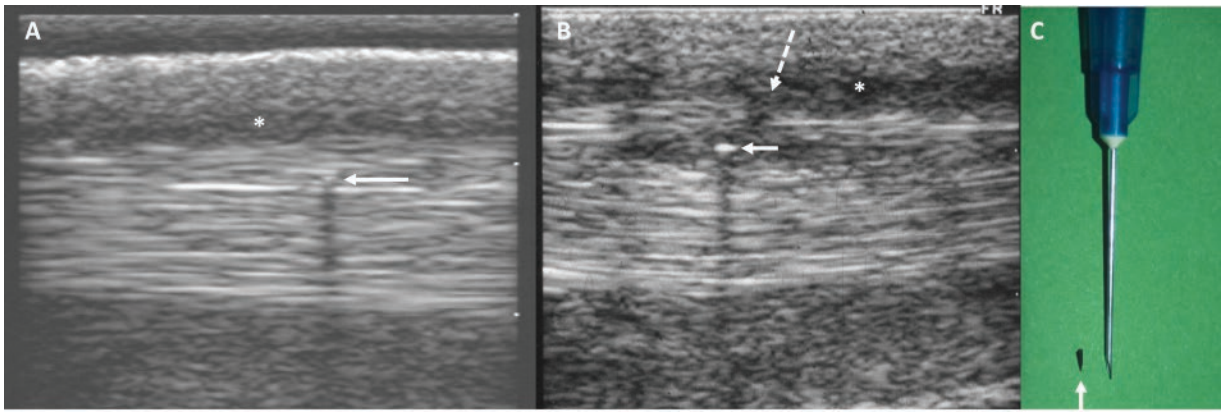


Figure 3.26 (A) Longitudinal scan over the SDFT showing a focal hyperechogenicity casting an acoustic shadow within the SDFT (arrow). (B) shows the same tendon when non-weightbearing. This now shows the entry site for the foreign body (dashed arrow) which is sitting inside a cavity. The tendon is surrounded by oedema (*). The foreign body was a small piece of thorn (C; arrow) which was removed using a minimally invasive technique under ultrasound guidance to minimize damage to the tendon.

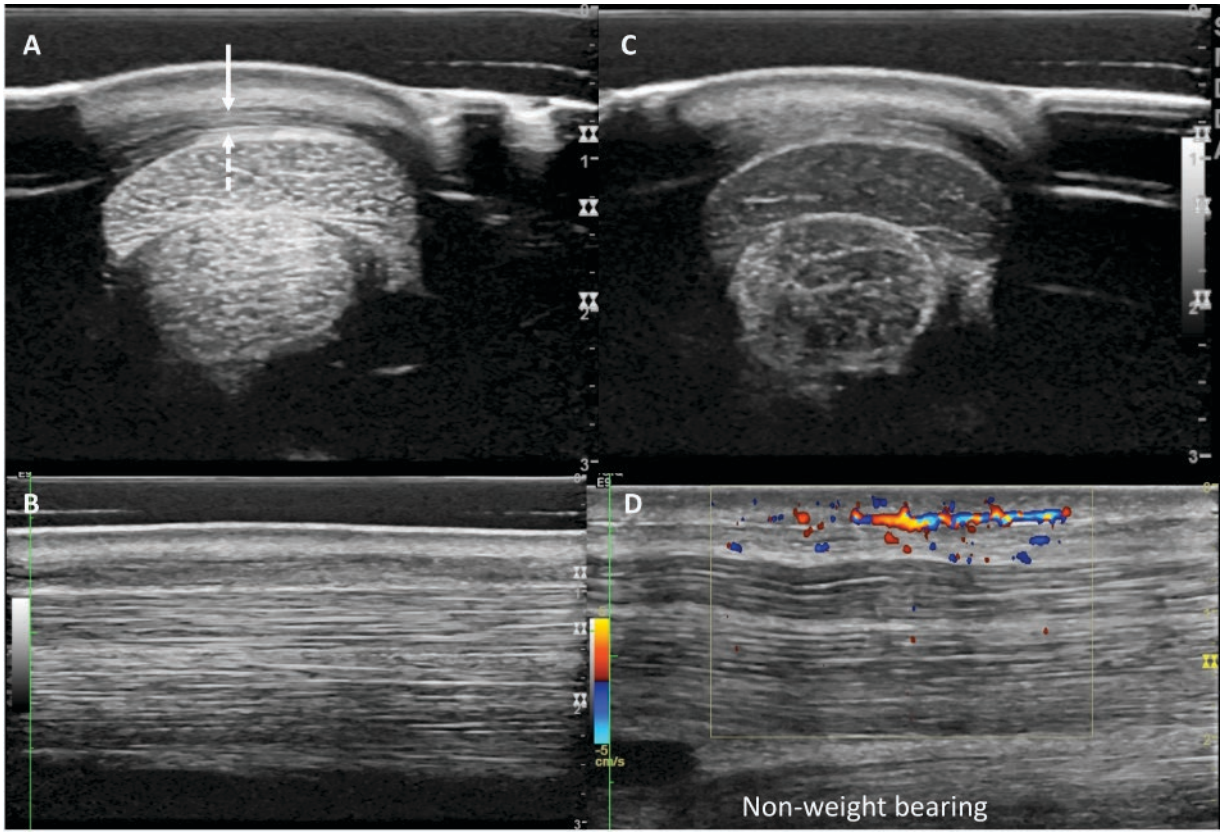


Figure 3.27 Bandage bow over a superficial digital flexor tendon (SDFT). (A) shows the thickening of the paratenon (between arrows), together with subcutaneous oedema but without any tendon damage. The longitudinal view in (B) and the off-incidence view in (C) helps outline the border of the tendon and can be useful in identifying subtle damage on the surface of the tendon. Doppler imaging in the non-weightbearing limb (D) shows only a signal in the subcutaneous tissues and not in the tendon. Even though there is no evidence of damage at this examination, it is worth checking again after 7–10 days when the oedema should have resolved.

"Bandage bows" may be subtle with only focal thickening of the skin, subcutaneous tissue, and paratenon, but can involve the underlying tendon if severe. (Figure 3.27) Ultrasound is therefore very helpful to identify the presence of tendon injury, although this may not be immediately apparent. All bandage bows should therefore be evaluated ultrasonographically. If only the paratenon is involved, the condition should really be termed paratendinitis. Typically, this richly vascularized tissue surrounding

Vet-ebooks.com

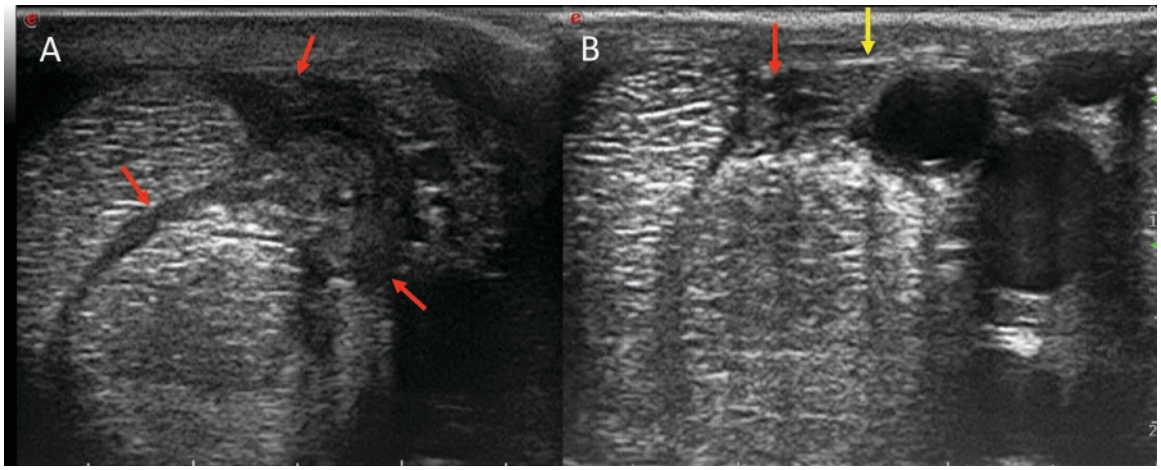


Figure 3.28 Percutaneous injury can cause peritendinous bleeding (arrows) with the hematoma spreading around and between the tendons. Although usually benign, these lesions can be painful, especially when associated with palmar nerve compression.

the tendon is slightly hypoechogenic to the parenchyma and measures 1–2 mm. Injury will present either as diffuse thickening with decreased echogenicity, or as focal hypo- to hyperechogenic tissue lifting the paratenon and overlying fascia. This represents hemorrhage, often with a fusiform appearance in longitudinal scans, dissecting the virtual space between the tendon and the paratenon. Blood collection is most often seen at the lateral or medial borders of the tendon, in the space between the edges of the SDFT and DDFT or between the DDFT and ALDDFT (Figure 3.28). The lesion occasionally extends over the whole length of the metacarpus/metatarsus. It should be noted that the majority of curb deformities of the plantar aspect of the hock are due to focal contusion and thickening of the paratenon (paratendinitis) and subcutaneous tissues (Figure 3.29), although a small number may be the result of plantar ligament desmitis (Figure 3.30).

In some cases, the lesion extends into the periphery of the tendon, forming variably large, discrete, and hypoechogenic peripheral lesions with a large base facing eccentrically toward the paratenon. Although these may be caused by the initial trauma, they are often seen to occur gradually over sequential examinations. They may be due to the release of collagenase induced by the initial hemorrhage.

Paratendinitis rarely affects the integrity of the tendon parenchyma and therefore carries a better prognosis than tendinitis. However, the owners should be warned that resolution may take 3–12 weeks and that recurrent bleeding can create severe tendon defects that carry a poorer prognosis (E. Cauvin personal data).

Deep Digital Flexor Tendinopathy

Deep digital flexor tendon injuries are extremely rare in the extrathecal regions of the metacarpus, as they nearly always occur within the confines of the digital sheath or navicular bursa (i.e., intrathecally). They will therefore be addressed in the Section on the Pastern. They have also been described associated with ALDDFT injuries in both fore- and hind limbs. Care should be taken to avoid confusing DDF tendinopathy and desmitis of the ALDDFT, especially in the hind limb, which appear very similar.

Suspensory Desmopathy

"Suspensory desmitis" should in fact be called "tendinopathy," since the suspensory ligament (SL) is actually the tendon of the interosseous III muscle. However, the term "desmitis" is more generally accepted because of the relative scarcity of muscular tissue in this structure. It is the second-most common site for injury in the metacarpal/metatarsal region. Although it is encountered in all breeds, it is most common in the fore limbs of Thoroughbred racehorses and in the fore- and hind limbs of Standardbreds and other trotters. The etiology is believed to be similar to that of SDF tendinitis. Proximal suspensory desmitis is a very common diagnosis in the hind limbs of sports horses, but may not always involve the ligament as the primary pathology and hence should probably be regarded as a syndrome.

The features differ depending on the level of the lesion. Desmitis is therefore divided into proximal desmitis, desmopathy of the body, and desmopathy of the branches.

Vet-ebooks.com

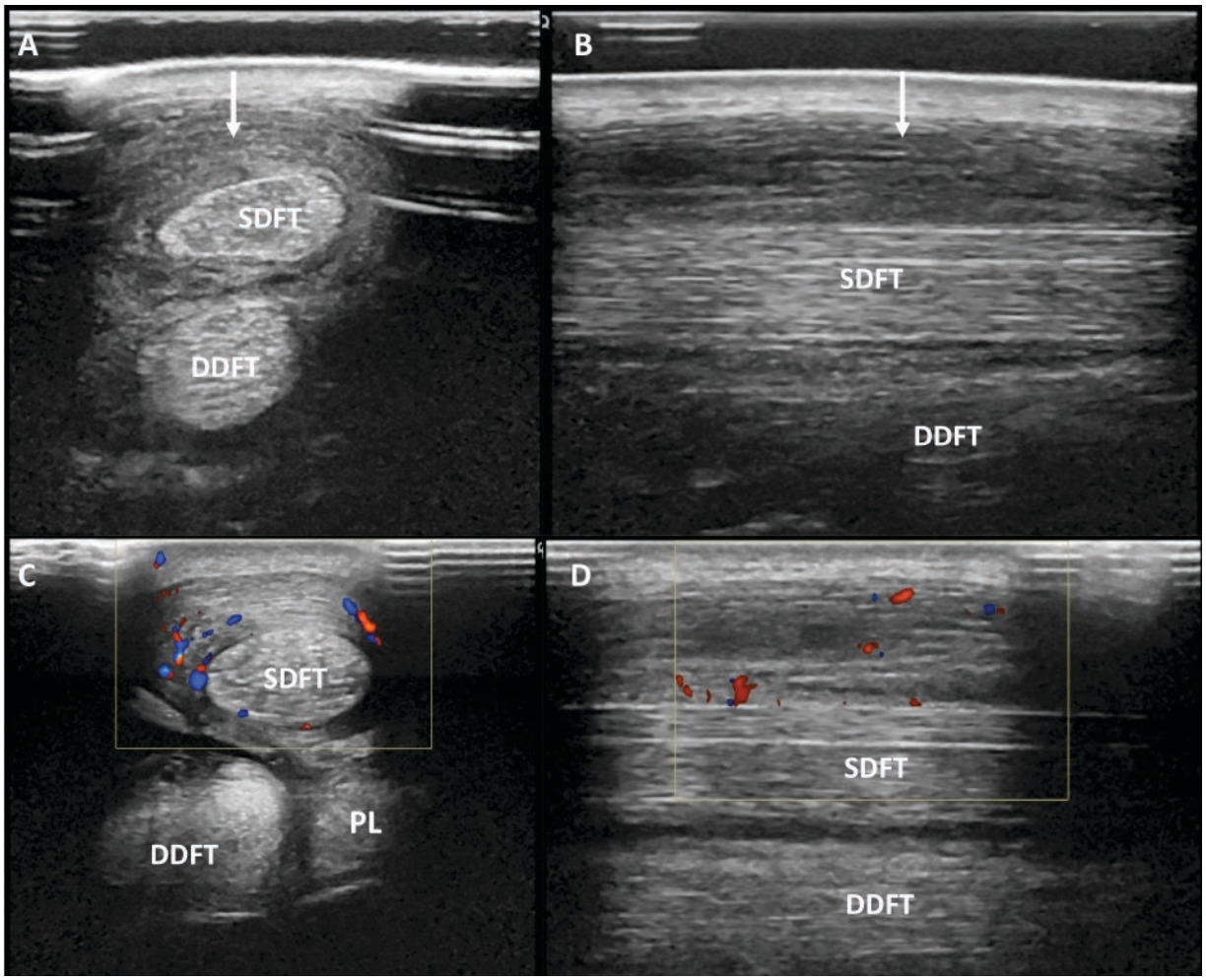


Figure 3.29 Paratendinitis of the superficial digital flexor tendon (SDFT), thought to be due to external trauma, which is a common cause of a "curb" on the plantar aspect of the proximal metatarsal region. (A) shows the transverse image (medial to the left) with oedema and fibrosis surrounding the SDFT (arrow). (B) is a longitudinal image (distal to the left) from the same area showing the hypoechogenic oedema (arrow). (C) and (D) are the equivalent images in a non-weightbearing limb showing the inflammation (signified by the positive Doppler signal) only in the peritendinous tissues. SDFT: superficial digital flexor tendon; DDFT: deep digital flexor tendon; PL: plantar ligament.

Proximal Suspensory Desmitis

Also called "high suspensory disease," this refers to injury to the origin, or proximal enthesis, of the SL. It is encountered in most breeds but is particularly prominent in the fore- and hind limbs of trotters and Standardbreds and in the hind limbs of dressage, eventing, and show jumping horses. Horses with straight hock and low metatarsophalangeal joint (hyperextension) conformations may be predisposed to SL injuries, particularly proximal desmitis. Conversely, this deformity may be a consequence of severe SL injury.

The ultrasonographic appearance of this injury has considerable overlap with that of the normal ligament because of the physiological heterogeneity of this region. The ultrasonographic features must therefore be interpreted with great caution. The appearance of the SL at any given level is usually bilaterally symmetrical in normal horses and so comparison between right and left limbs is recommended to assist with diagnosis. Bear in mind, however, that SL injuries are also commonly bilateral, although the lesions are rarely symmetrical. More than for any other condition, proximal SL ultrasonography must be interpreted in the light of clinical findings (swelling, pain on palpation) and diagnostic local analgesia. The use of other diagnostic techniques, including radiography, scintigraphy, and magnetic resonance imaging (MRI), may be useful in some cases but is beyond the scope of this chapter. However, it is highly recommended that a good-quality radiographic examination be performed to look for plantar fissure fractures,

Vet-ebooks.com

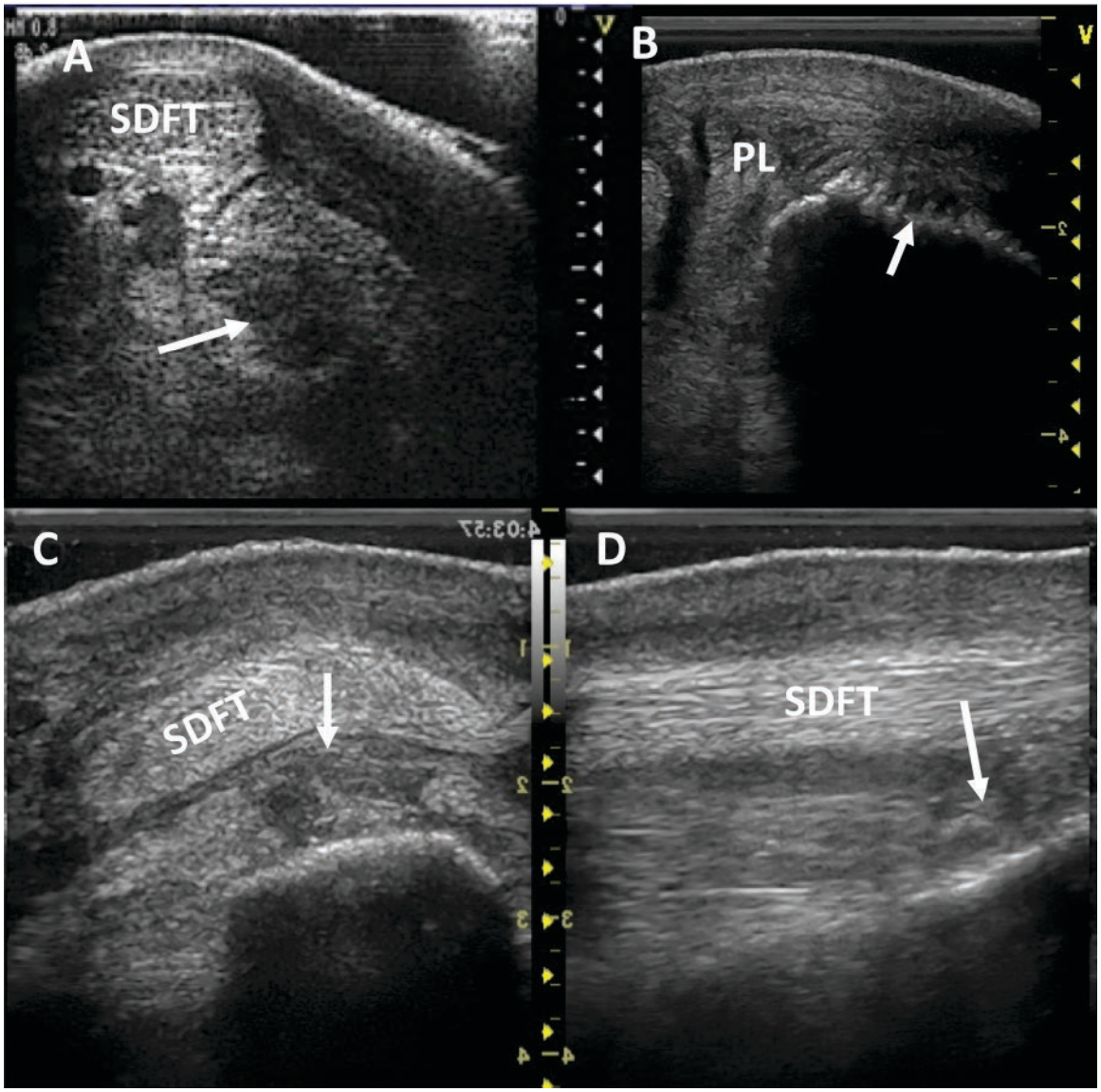


Figure 3.30 Desmitis of the long plantar ligament of the tarsus is a less common cause of a "curb" deformity. (A) and (B) are lateral oblique images. (A) shows a large core lesion in the body of the plantar ligament (arrow). (B) shows a distal entheseopathy on the proximal margin of the fourth metatarsal bone (arrow). (C) and (D) are transverse and longitudinal images respectively of a proximal injury to the plantar ligament at its origin at the proximal end of the calcaneus (arrow). SDFT: superficial digital flexor tendon; PL: plantar ligament.

avulsion fragments, injury to the splint bones, and sclerosis of the proximopalmar/plantar third metacarpus/metatarsus.

Ultrasonographic features of proximal SL injury are similar to those of other tendons but may be very subtle. Changes are usually more easily identified in the fore limbs. Diffuse enlargement of the suspensory ligament is common but may be difficult to ascertain, unless severe. On long-axis scans, the palmar or plantar border of the ligament may appear convex. However, sagittal images can be difficult to obtain in the hind limb and obliquity can influence the thickness of the SL. A consistent feature is poor definition to the margins of the SL, in both transverse and longitudinal images, especially dorsal, which seems to blend into the peripheral inflammatory tissue and the space between the dorsal surface of the proximal suspensory ligament and the palmar/plantar aspect of the metacarpus/metatarsus is lost (Figure 3.31). The deep fascia becomes indistinguishable from the ligament and may be pushed palmarly/plantarly until the SL, fascia, and accessory ligament of the DDFT, and DDFT are difficult to differentiate. In the acute stage, this is caused by hypoechogenic edema and bleeding in and around the ligament.

Vet-ebooks.com

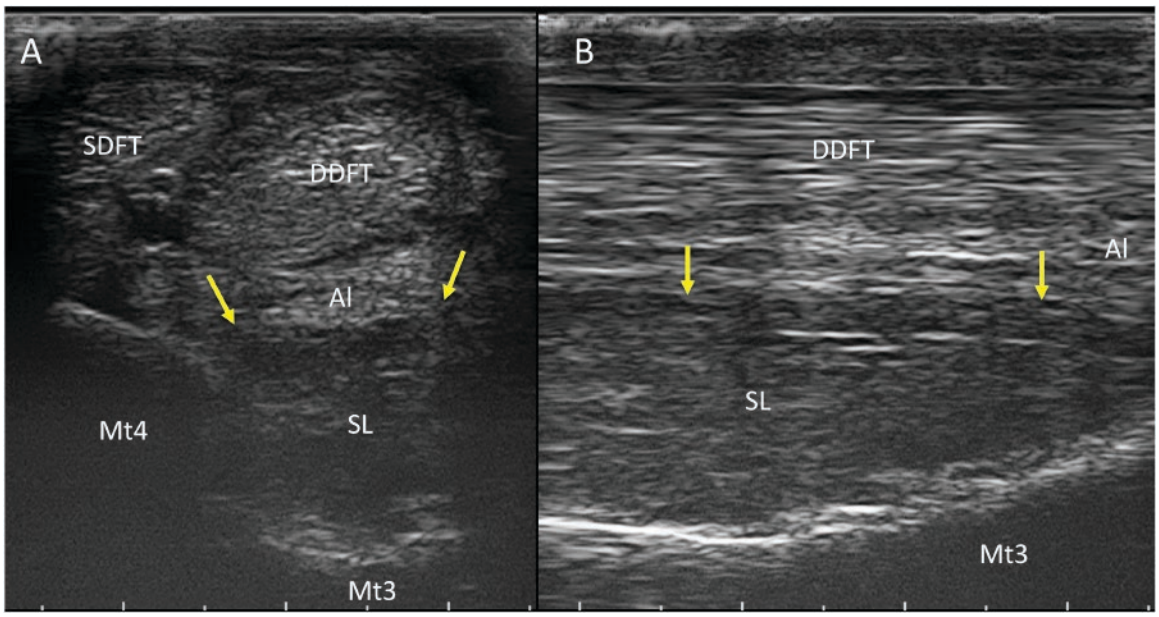


Figure 3.31 Severe, proximal suspensory desmitis in the hind limb of a French trotter racehorse. A common feature is loss of the sharp margins of the ligament: the suspensory ligament (SL) is thickened, bulging plantarly, and displacing the soft tissue structures (arrows), here the deep digital flexor tendon (DDFT) and its accessory ligament (AL). There is diffuse thickening of the peritendinous and periligamentous tissues, and the outline of the SL is poorly defined, especially dorsally. Mt4: fourth metatarsal bone; Mt3: third metatarsal bone.

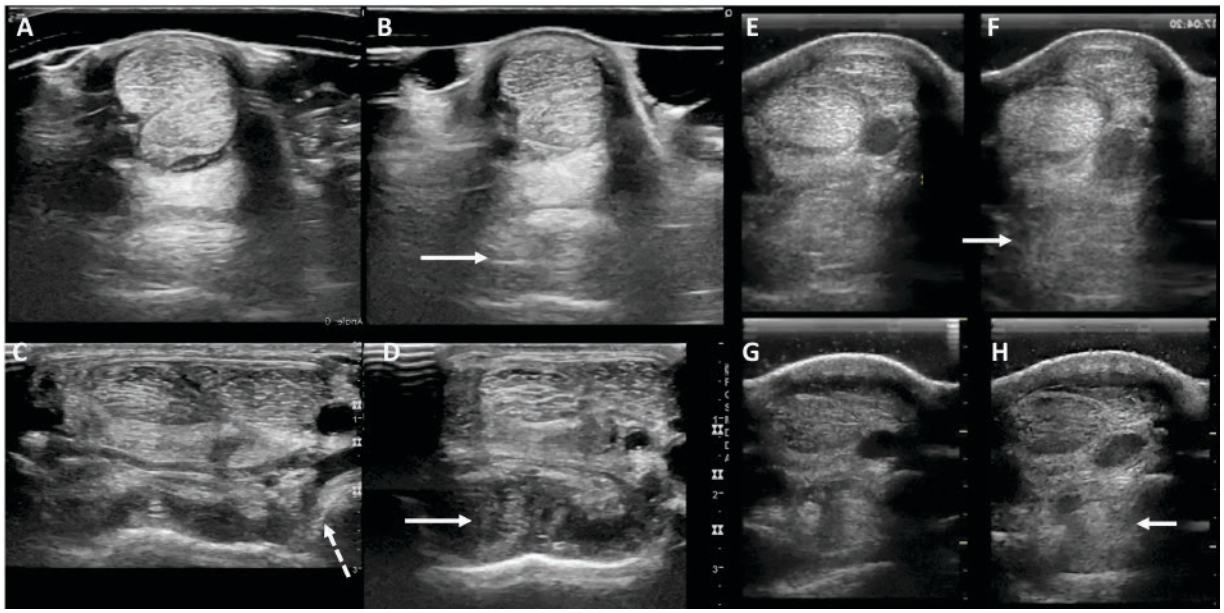


Figure 3.32 The use of the non-weightbearing off-incidence view for the diagnosis of proximal suspensory desmitis. (A–D) are from the fore limb; (E–H) are from a hind limb. The upper row of images (A, B, E, and F) are transverse weightbearing images (medial to the left), while the lower row of images (C, D, G, and H) are non-weightbearing off-incidence views (medial to the left). In each set of four views, the left side two images are from the contralateral normal limb (A, C, E, and G). The arrows show the enlarged proximal suspensory ligament with a hypoechoic dorsal part of the ligament. Note in the non-weightbearing view more of the ligament is visible and the echogenic connective tissue component of the proximal suspensory ligament is displaced palmarly. Note also how this view enables the axial margin of the splint to be identified (dashed arrow). In the hind limb, the connective tissue bundles are less well defined but increased enlargement (F; arrow) and echogenicity (H; arrow) can be identified.

In chronic cases, periligamentar and interligamentar fibrous tissue is isoechogenic to the injured ligament. Non-weightbearing off-incidence views (Figure 3.32) allow the differentiation of the linear ligament fibers from the connective tissue and the distortion or displacement of the connective tissue components may help to identify pathology in this region [9] (Figure 3.33).

Vet-ebooks.com

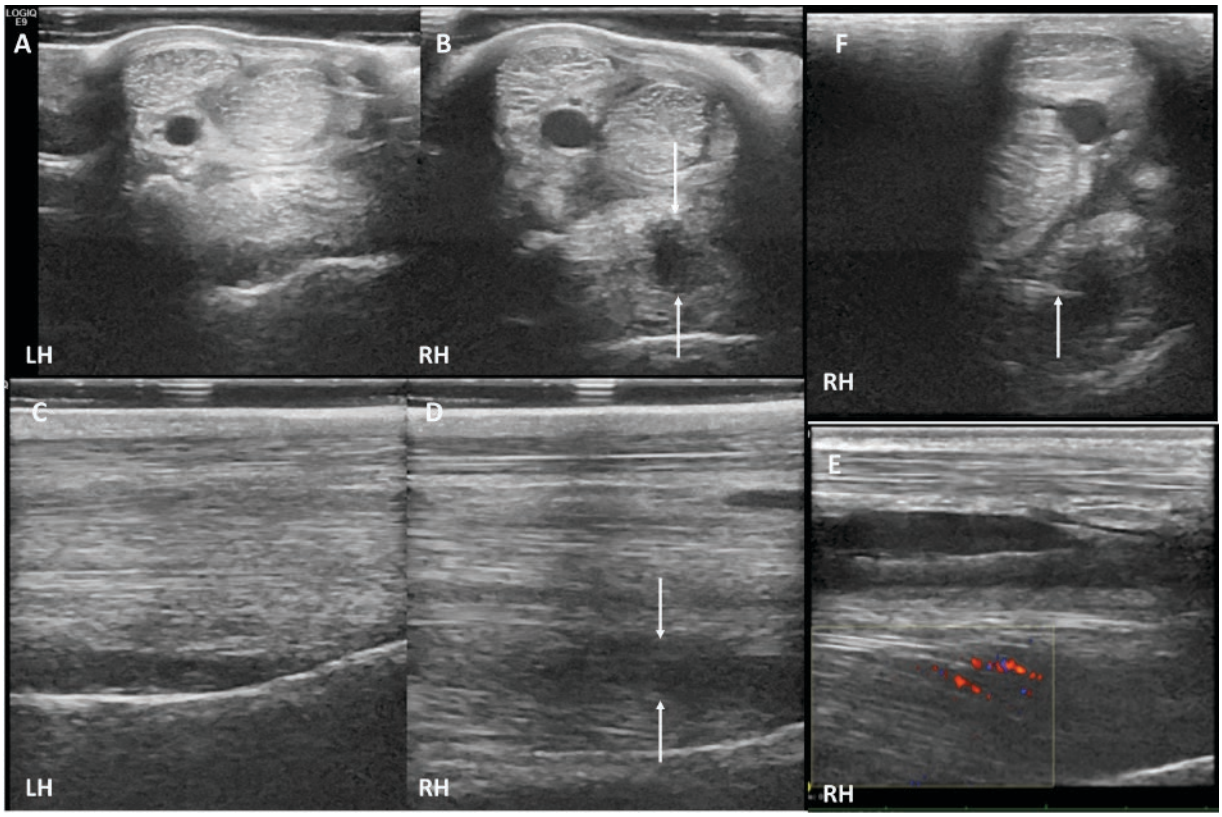


Figure 3.33 Transverse (A) and (B) images showing a focal lesion in the proximal suspensory ligament of the right hind limb (arrows). (C) and (D) longitudinal images showing the focal central defect (arrows) which is, unusually for many proximal suspensory ligament injuries, positive for a Doppler signal (red areas in (E). Note the significant swelling denoted by the depth of the plantar surface of the third metatarsus in the affected limb in both transverse and longitudinal images. (F) shows an oblique transverse image during an ultrasound-guided injection of the proximal lesion. The needle can be identified in the middle of the lesion (arrow). This lesion was injected with PRP (platelet-rich plasma), but consideration should be given to possibly increasing the size of the proximal suspensory ligament which may exacerbate compressive neuropathy of the deep branch of the lateral plantar nerve and contribute to lameness.

Discrete, hypoechogenic core lesions are unusual in proximal SL injuries (Figure 3.27C) unless they extend from more distal body injuries (especially in Standardbreds). Single or multiple, poorly defined focal areas of hypoechogenicity, or diffuse, mottled hypoechogenicity, are more frequent features (Figure 3.34), whose identification can be improved in the hind limb by moving the transducer medially to avoid the large head of the lateral splint bone (Figure 3.35). In chronic cases, the ligament appears more diffusely enlarged and heterogeneous but remains fairly echogenic (Figure 3.36). Ectopic mineralizations are extremely rare in this area unless intralesional injections have been previously performed. Sagittal/parasagittal plane images typically show a diffuse loss of longitudinally arranged striation at any stage; in chronic or long-standing cases, the long-axis sections show a granular, either mottled or densely packed appearance with ill defined, hyperechogenic areas (Figure 3.37).

Irregularity of the palmar/plantar surface of the proximal metacarpus/metatarsus is indicative of enthesophytosis or simply bony reaction to chronic inflammation. It gives a spiky or irregular appearance to the normally smooth bone surface (Figure 3.37). Larger enthesophytes can mimic "avulsion" fragments; radiography can be used to confirm avulsion fragments.

Avulsed fragments of the palmar/plantar cortex occur at the SL origin, usually 1–3 cm distal to the carpometacarpal or tarsometatarsal joint but they may be displaced 1 cm (or more) distally. The fragments may be quite large but never seem to involve the whole enthesis. They appear as a flat, discrete hyperechogenic interface, casting a strong acoustic shadow. They are slightly elevated (1–3 mm) from the rest of the palmar/plantar cortical interface of the third metacarpal/metatarsal bone (Figure 3.38) and there may be a shallow defect in the latter at the proximal border of the fragment. Fibers are seen in

Vet-ebooks.com

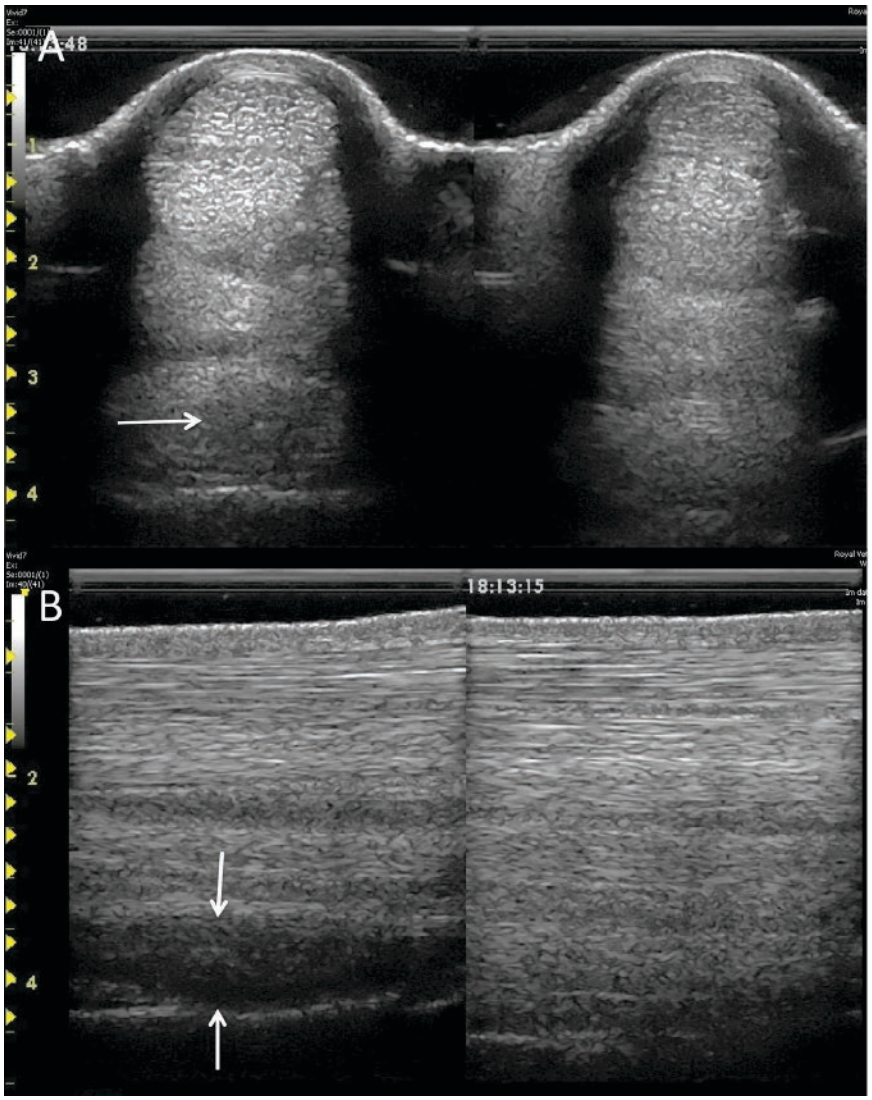


Figure 3.34 Proximal suspensory desmitis of the fore limb. Desmitis of the proximal suspensory ligament is more readily identified in the fore limb than its counterpart in the hind limb. (A) Transverse ultrasonographs from the left and right fore limbs showing a lesion in the proximal suspensory ligament of the left fore limb (arrow). The lesion can be seen as a corresponding hypoechoic area (arrows) in the longitudinal images (B).

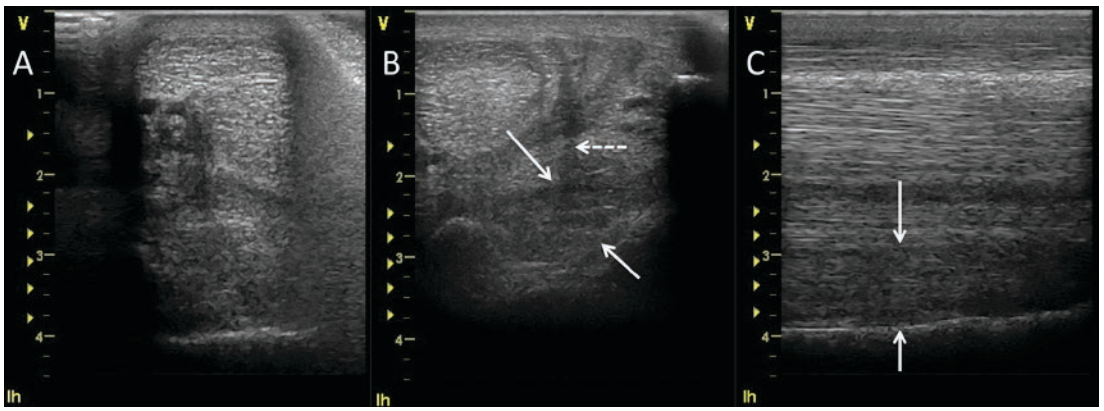


Figure 3.35 Proximal suspensory desmitis of the hind limb. (A) shows the standard transverse image from the plantar aspect of the limb showing diffuse hypoechogenicity of the proximal suspensory ligament. The lesion is more clearly observed (arrows) by moving the probe to the plantaromedial aspect (B), utilizing the "medial window" associated with the smaller head of the medial splint bone. Note, however, that edge refraction artifacts from the tendon borders and blood vessels can still compromise the image (dashed arrow) and so longitudinal views (C) should always be used in conjunction to confirm the presence of pathology (arrows).

Vet-ebooks.com

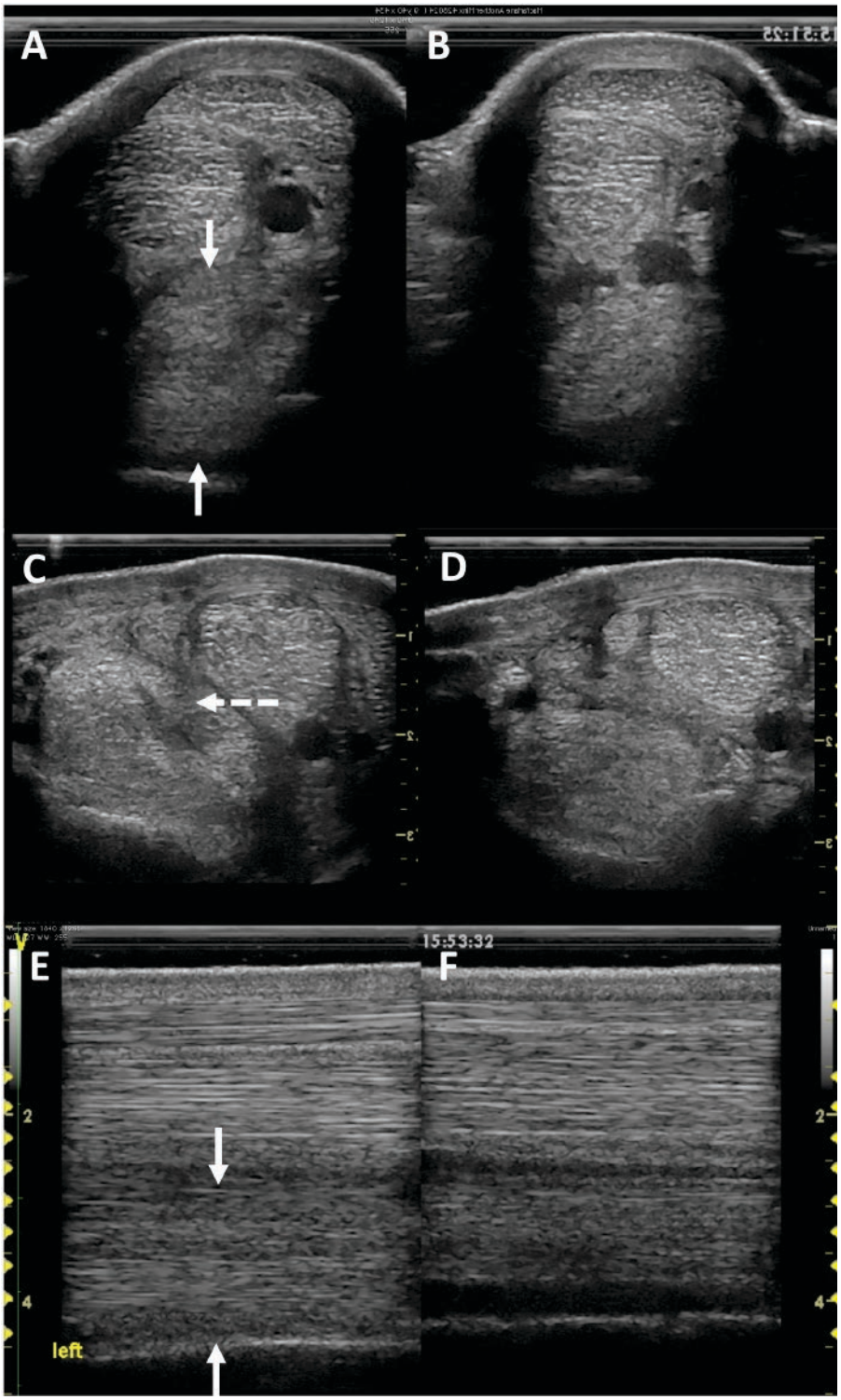


Figure 3.36 Transverse (A) and (B) images from a case of chronic proximal suspensory desmitis in the left hind limb (medial to the left). The left hind limb images are on the left and the right hind limb images on the right. Note the enlarged ligament on the left (arrows). The lesion can be seen more easily from the "medial window" (C) and (D), although an acoustic shadow (dashed arrow) is cast through the proximal suspensory ligament. Longitudinal images (E) and (F) show the enlarged ligament but normal echogenicity (arrows). A disrupted fiber pattern characteristic of fibrosis is less apparent in chronic suspensory desmopathy because the normal longitudinal striated pattern in a suspensory ligament is not as well defined as in a flexor tendon.

Vet-ebooks.com

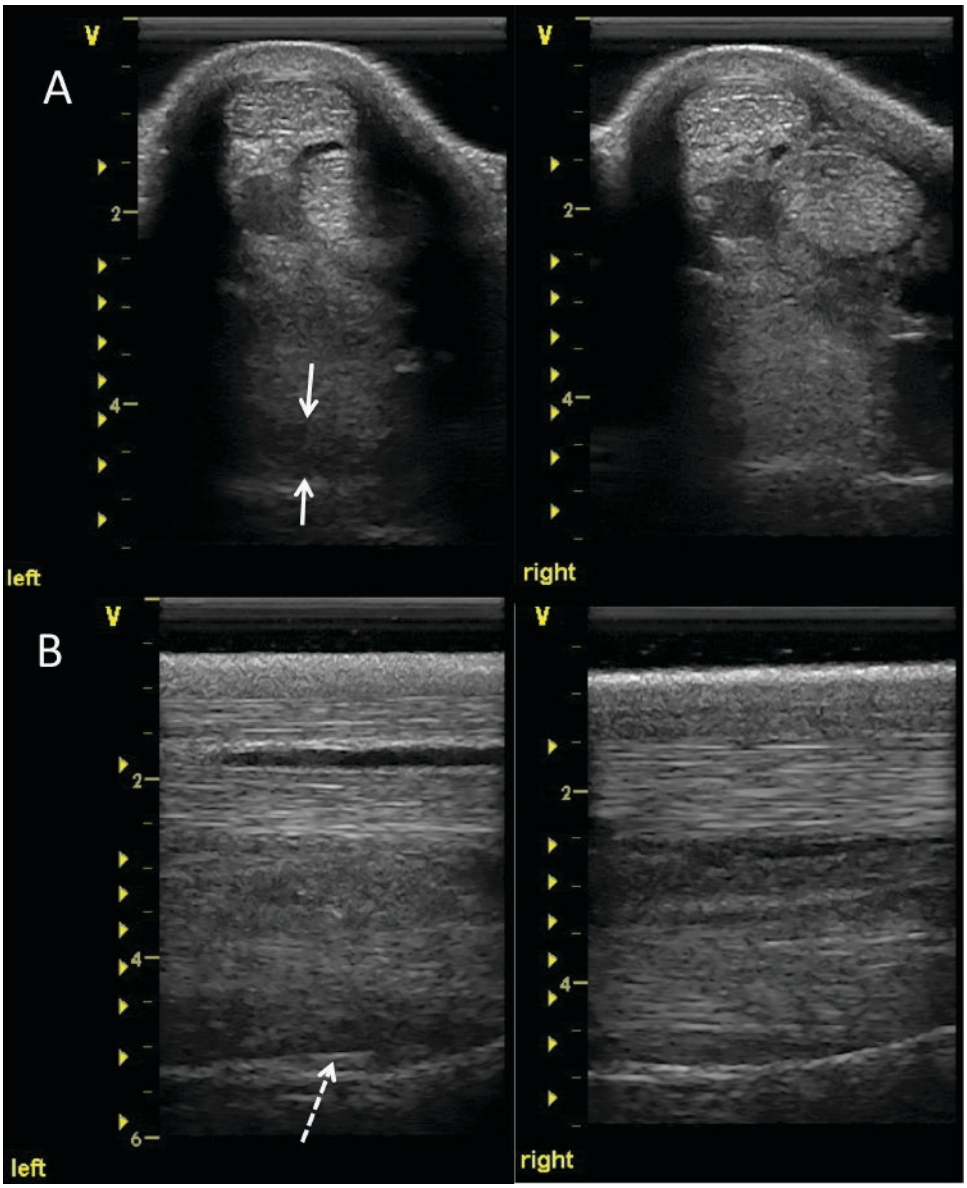


Figure 3.37 Transverse (A) and longitudinal (B) images from a case of chronic bilateral proximal suspensory desmitis in both hind limbs, but with the left hind limb more severely affected than the right. Note the more hypoechoic dorsal border of the left proximal suspensory ligament (arrows), although both ligaments are enlarged with a "ground glass" texture. There is also evidence of enthesopathy (dashed arrow). Left hind limb is on the left and right hind limb is on the right.

continuity with the ligament and there is usually a hypoechogenic area of ligament disruption around the lesion, with focal to more diffuse desmitis usually present. Avulsions appear to be most common in racehorses, particularly Standardbreds. The lesion may be more clearly visible on longitudinal images.

Spontaneous, non-displaced unicortical fatigue fractures of the palmar or plantar cortex may be seen on ultrasound scans as a focal, longitudinal defect in the palmar/plantar cortex of the third metacarpus/metatarsus (Figure 3.39). There is usually no evidence of SL desmitis, and there does not seem to be a direct link between these conditions. Focal hypoechogenic reaction is occasionally noted between the dorsal surface of the SL and the bone around the lesion, representing hematoma, granulation tissue, or early callus. In more chronic cases, irregular new bone is visible. Radiography remains the technique of choice to visualize these, although scintigraphy and MRI may be useful in some cases.

Desmitis of the Body of the SL

Injuries to the body portion of the SL usually present with generalized hypoechogenicity and enlargement

Vet-ebooks.com

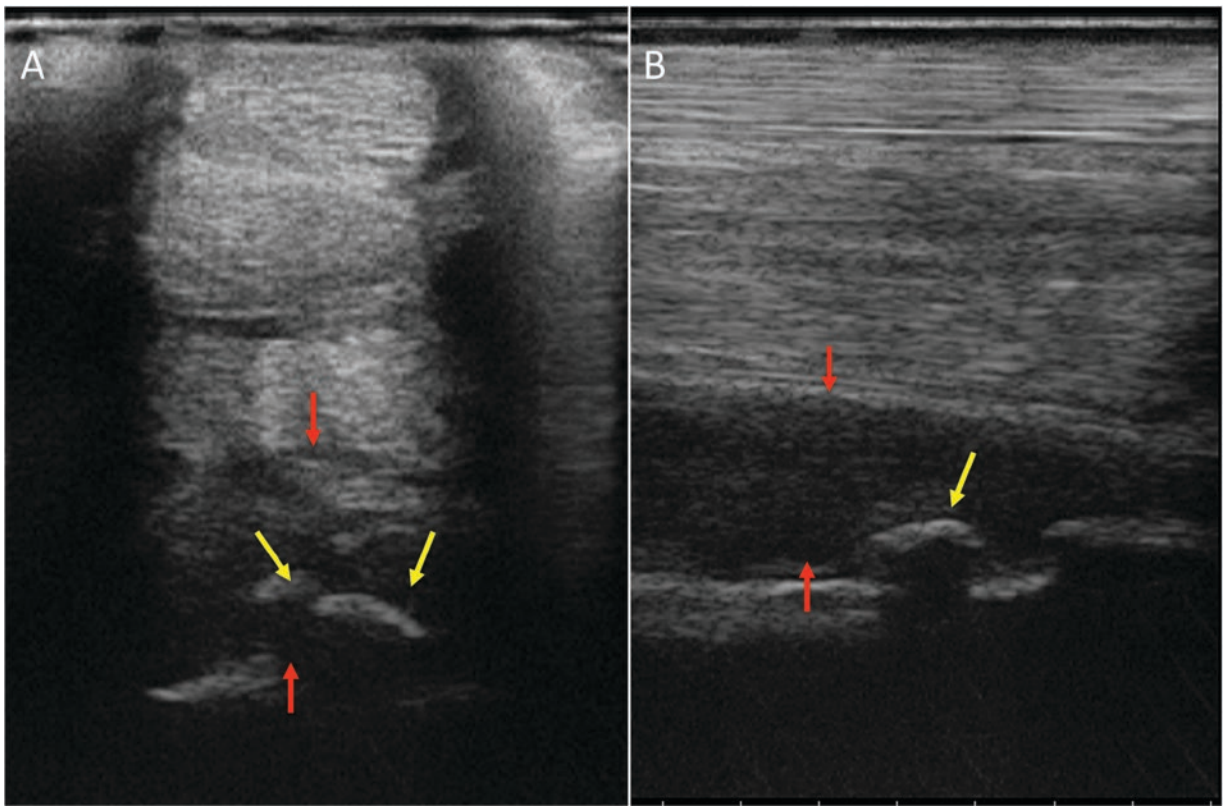


Figure 3.38 (A) Avulsion of the origin of the suspensory ligament (SL). The SL is very enlarged, hypoechogenic, and devoid of normal linear striation on the sagittal image (red arrows). (B) A hyperechogenic interface, casting a strong acoustic shadow is visible within the dorsal portion of the SL and represents an avulsed fragment of the palmar cortex of the third metacarpal bone (yellow arrow). This injury appears to be more common in Standardbreds.

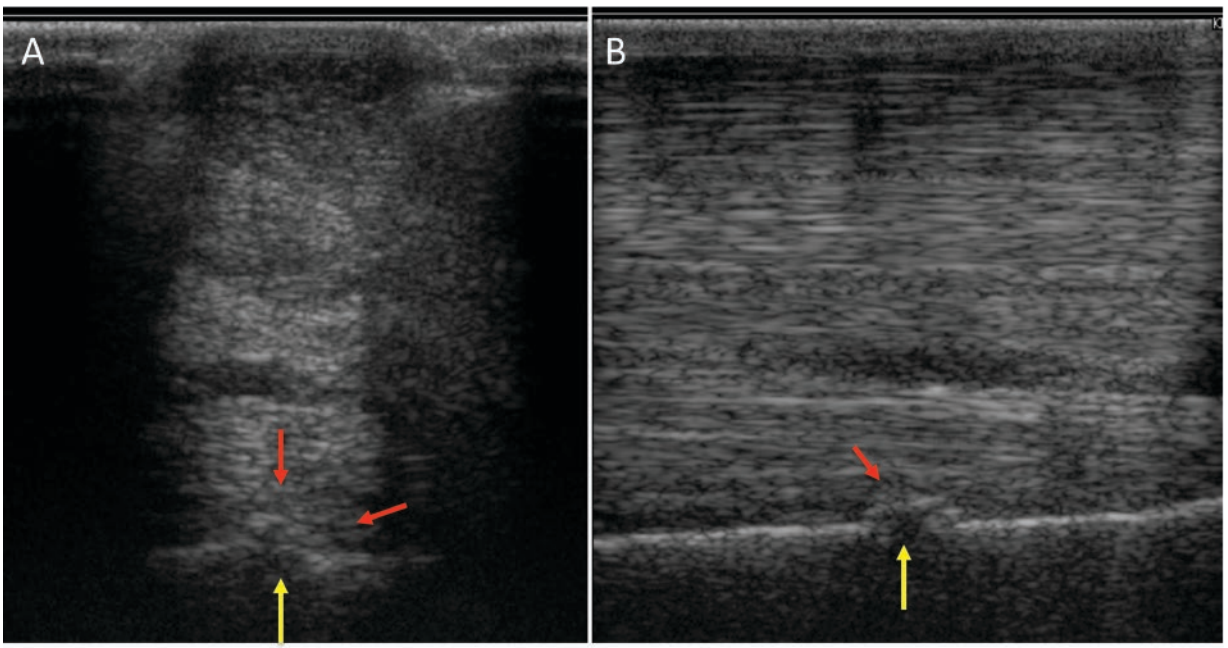


Figure 3.39 Unicortical "fissure" fractures of the palmar cortex of the third metacarpal bone are a rare condition usually unrelated to suspensory ligament (SL) desmitis. Ultrasonographically, focal irregularity of the palmar cortex interface (yellow arrow) represents new bone formation around the fracture line. There is no obvious damage to the SL, except a slight hypoechogenic halo at the interface between the bone spikes and the ligament (red arrows).

Vet-ebooks.com

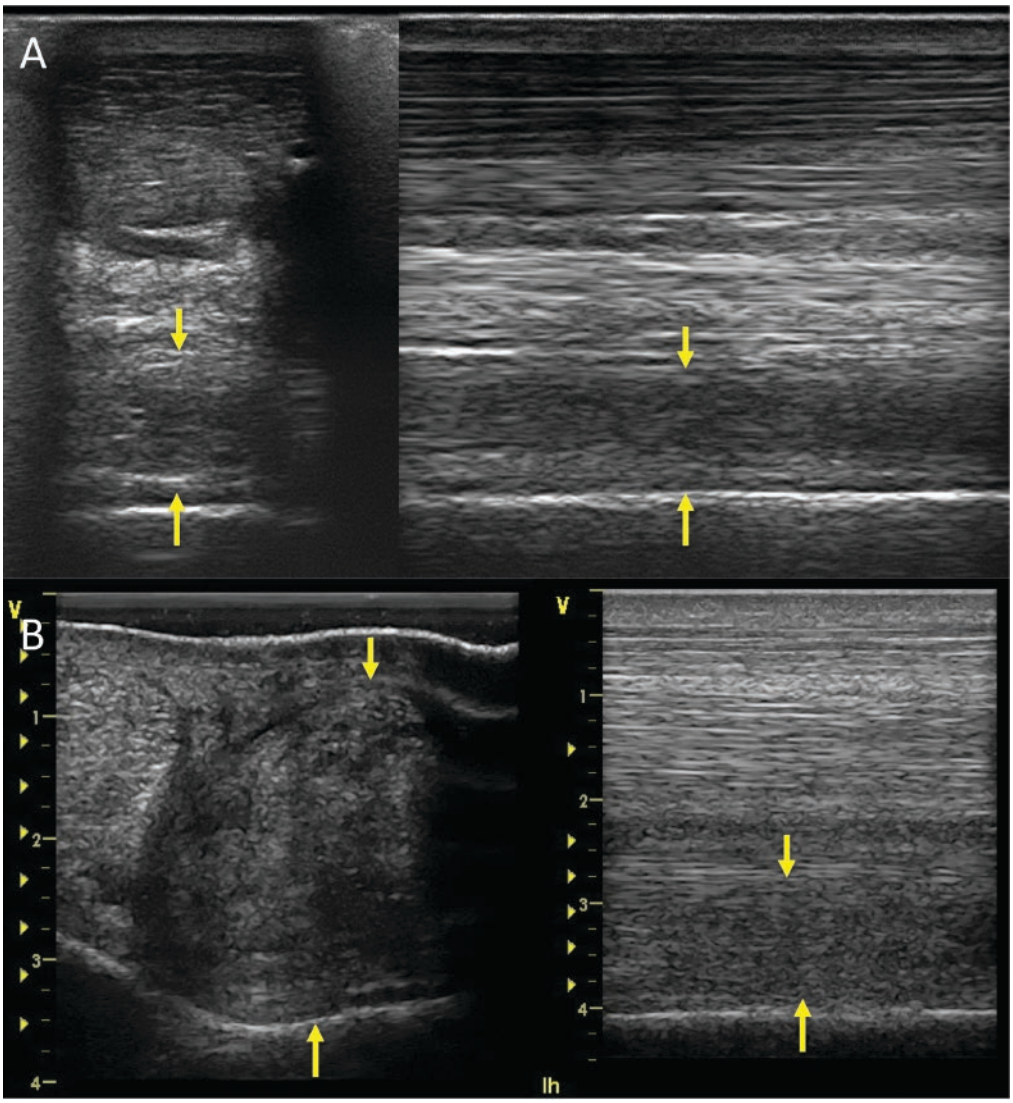


Figure 3.40 (A) Diffuse, subacute lesion in the body of the suspensory ligament (SL) in a 3-year-old French trotter: the SL body (arrows) is moderately enlarged with poorly defined contours and a mottled, hypoechogenic parenchyma. There is obvious loss of striation on the sagittal image. (B) In this horse, the lesion is very mottled and diffuse, with severe enlargement of the ligament.

of the ligament (Figure 3.40). Although diffuse lesions are most frequent, core lesions are also encountered and may extend proximally to the origin and distally into one or both branches (Figure 3.41). As an isolated lesion, it is rare in disciplines other than racehorses, especially in Standardbreds. Chronic desmitis is common because of recurrent injury and leads to very marked enlargement and periligamentous fibrosis. Recurrence can occasionally lead to severe, diffuse ligament disruption and near-rupture of the SL body. Percutaneous trauma can damage the borders of the body of the ligament while the proximal part of the ligament is protected by the splint bones. Such trauma is best identified with an abaxially positioned transducer (Figure 3.42). Intraparenchymal, ectopic mineralization, forming discrete hyperechogenic foci casting an acoustic shadow, may rarely be observed in long-standing cases. Previous intralesional injections have been incriminated.

Body SL desmitis may be associated with second and fourth metacarpal/metatarsal bone periostitis ("splints") and fractures. There is some controversy over the link between these two conditions. Aggressive exostoses may mechanically impinge on the SL and cause focal, hypoechogenic lesions centered on the new bone (Figure 3.43). This, however, probably occurs in only the minority of cases. Most exostoses grow abaxially into the fascia, rather than into the SL. Nevertheless, splints are often associated with focal or more diffuse SL body or branch injuries. Careful assessment by oblique positioning of the ultrasound

Vet-ebooks.com

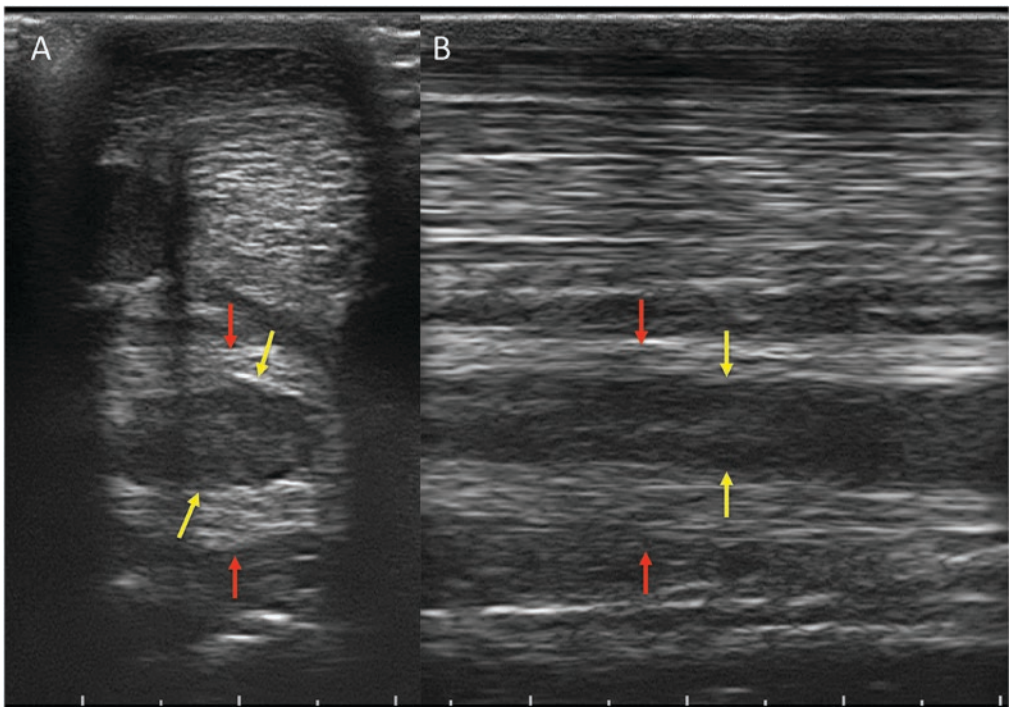


Figure 3.41 Acute SL body desmitis in a French trotter: a discrete "core" lesion (yellow arrows) is present in the center of the body of the SL. The SL is only slightly enlarged at this stage (red arrows). This presentation is more frequently encountered in racehorses.

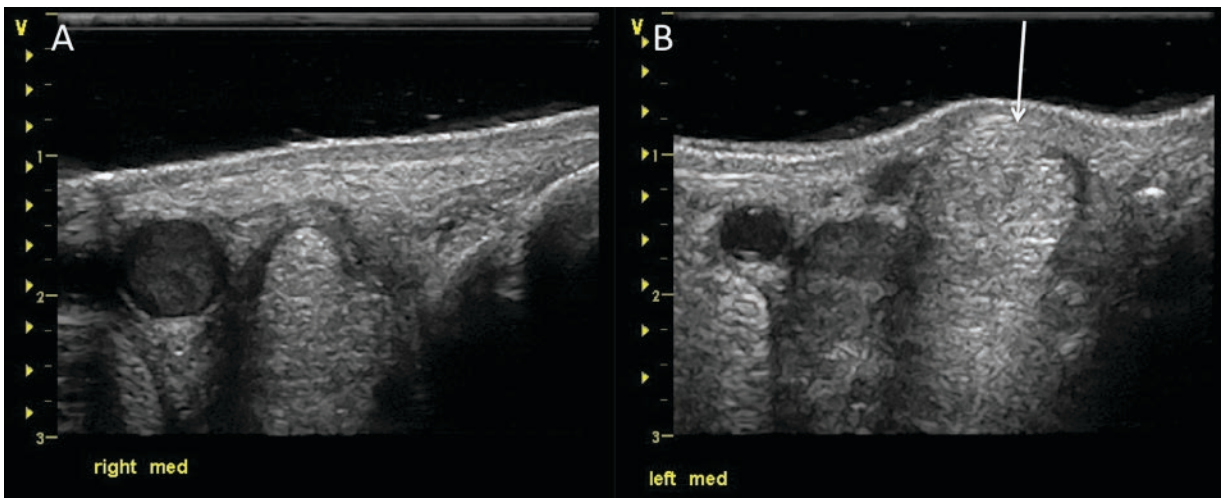


Figure 3.42 Transverse ultrasonographs from the medial aspect of the right (A) and left (B) fore limbs in a horse which has suffered trauma to the medial aspect of the left suspensory ligament body, characterized by enlargement and altered skin contour (arrow).

Vet-ebooks.com

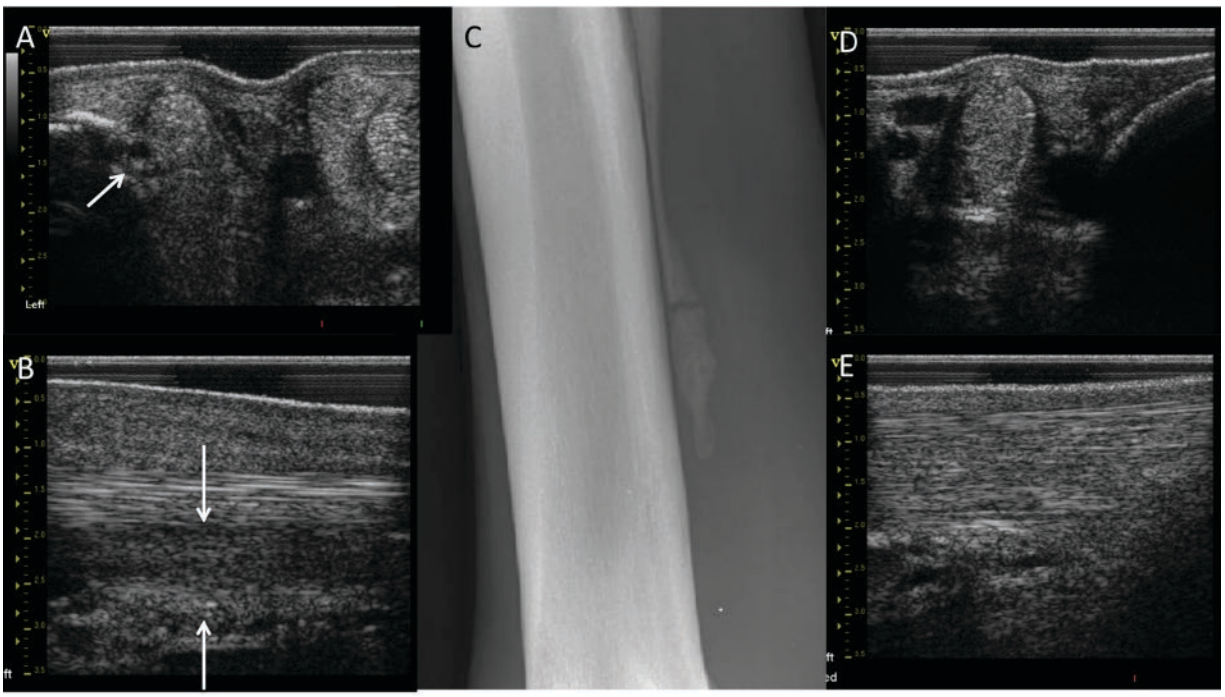


Figure 3.43 Damage to the adjacent suspensory ligament branch caused by a fractured splint. Most splint bone fractures do not cause irritation of the adjacent suspensory ligament but in this case the fracture (seen radiographically in (C)) has resulted in callus that is impinging on the suspensory ligament branch (A; arrow) and causing disruption of the branch seen in the longitudinal view (B; arrows) compared to the contralateral limb (D) and (E).

transducer from the opposite side of the limb can help to visualize focal SL lesions. A curved array probe occasionally improves imaging. The encroachment may be better assessed in non-weightbearing views as this widens the ultrasound window and enables identification of the axial margins of the splint bones from the palmar/plantar aspect of the limb. Adhesions between the fibrous tissue and periosteum may thus be visualized. Pre-existing desmitis may lead to splints because of adhesion formation or increased tension on the fascia that attaches to the palmar/plantar surface of the splint bone by the enlarged ligament. The distal third of the splint bones is anatomically related to the suspensory apparatus, as there are ligamentous connections to the sesamoid bones and the periosteum blends into the deep fascia that is tightly adherent to the SL paratenon. Thus distal fractures are frequently seen with suspensory body and branch desmitis.

Desmitis of the Suspensory Ligament Branches

This is the most common SL injury in sports and pleasure horses but it is encountered in all breeds and is also very common in racehorses. It occurs in both fore- and hind limbs, affecting any of the branches or both. The prognosis appears to be significantly worse when both branches are affected. In all cases, injury to associated structures of the suspensory apparatus, including the distal sesamoidean ligaments, should be ruled out. A core lesion or generalized involvement of the branch together with very marked enlargement are seen ultrasonographically (Figure 3.44). Longitudinal images from the abaxial aspect ("ski jump" image) give an excellent assessment of the abaxial surface of the proximal sesamoid bones, where associated enthesopathy ("sesamoiditis") or avulsion fractures are demonstrated by spikes or steps in the S-shaped surface of the bone, extending into or between the ligament fibers (Figure 3.45). Lesions that are on the joint side of the branch close to their insertion onto the proximal sesamoid bone (Figure 3.44) can rupture into the fetlock joint because the branches are subsynovial. These injuries cause persistent lameness and joint effusion and are slow to heal because of the adverse effect of communication with the synovial cavity. They are candidates for arthroscopic debridement.

Desmitis is associated with enlargement, and the size of the suspensory ligament branches should be compared with both contra-axial and contralateral branches at the same level. One of the most sensitive indicators of suspensory branch desmitis is

Vet-ebooks.com

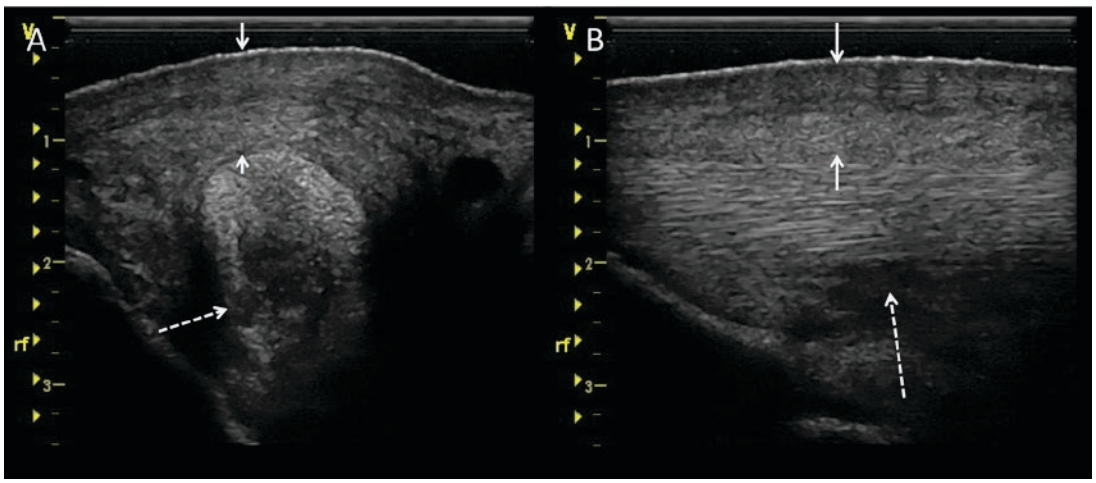


Figure 3.44 Desmitis of the medial suspensory ligament branch. Note the hypoechoic lesion seen in both the transverse (A) and longitudinal (B) images which appears to have a defect at its articular margin (dashed arrow). It is not uncommon for such suspensory branch lesions to tear into the palmar pouch of the metacarpophalangeal joint, thereby causing an inflamed joint, justifying arthroscopic debridement. Note also the periligamentar fibrosis which commonly accompanies these injuries (solid arrows).

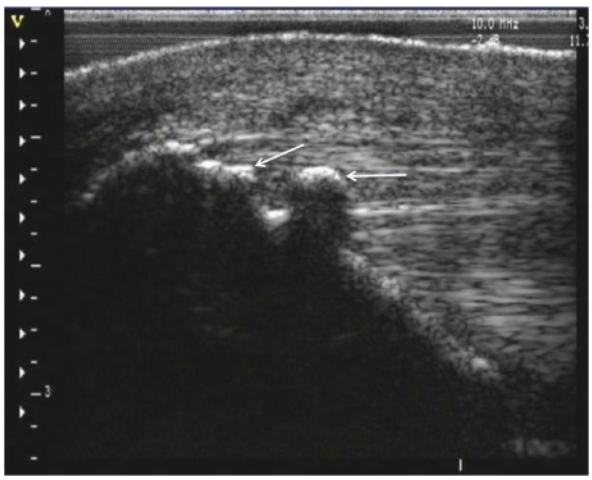


Figure 3.45 Longitudinal ultrasonograph directly over the insertion of the suspensory branch onto the abaxial surface of the proximal sesamoid bone. There is enthesophytosis at the attachment site characterized by irregular bone protruding along the suspensory ligament fibers (arrows).

periligamentar fibrosis, common after all ligament injuries, although rarer with tendon pathology. This has the effect of displacing the abaxial surface of the suspensory ligament branch away from the skin surface (Figure 3.44). It forms a diffuse, hypo- to hyperechogenic, amorphous halo around the ligament.

SL branch injuries usually heal with a shorter (6–9 months) time course than for SDFT injuries, but this healing is less reliable and can result in persistent lesions which can remained painful and cause long-term lameness (chronic desmitis) (Figure 3.46). New lesions often occur proximal or distal to the previous scar, creating overlapping areas of hyperechogenic and hypoechogenic areas. Ectopic mineralization foci may also be encountered in the branches in chronic cases and can occasionally be very prominent and extensive. The recurrence rate is high for these injuries.

It should be noted that irregular, mottled, or heterogeneous areas are occasionally seen within the SL branches in horses that are apparently sound and without clinical evidence of focal pain or swelling. The ligament may be of normal size or slightly enlarged and longitudinal images show core-like areas devoid of normal fiber alignment. Some of these horses will also present with enthesophyte formation on the sesamoidean insertion site. The significance of these is unclear but they may represent subclinical lesions that may or may not evolve to overt strain injury or previous "healed" SL branch lesions.

Another feature that is occasionally observed as an incidental finding in horses, especially trotters, is diffuse soft tissue thickening over the abaxial aspect of the distal branch, often extending over the abaxial aspect of the sesamoid bone distal to the SL insertion. There may be mild, irregular new bone formation on the sesamoid bone palmar or distal to the enthesis. This is currently of unclear significance, as many of these horses do not seem to be affected in their gait or performance.

Desmitis of the Accessory Ligament of the Deep Digital Flexor Tendon (ALDDFT)

The ALDDFT can suffer a variety of ultrasonographic pathologies – from generalized enlargement and hypoechogenicity of the whole ligament (Figure 3.47) to, less commonly, more focal areas of

Vet-ebooks.com

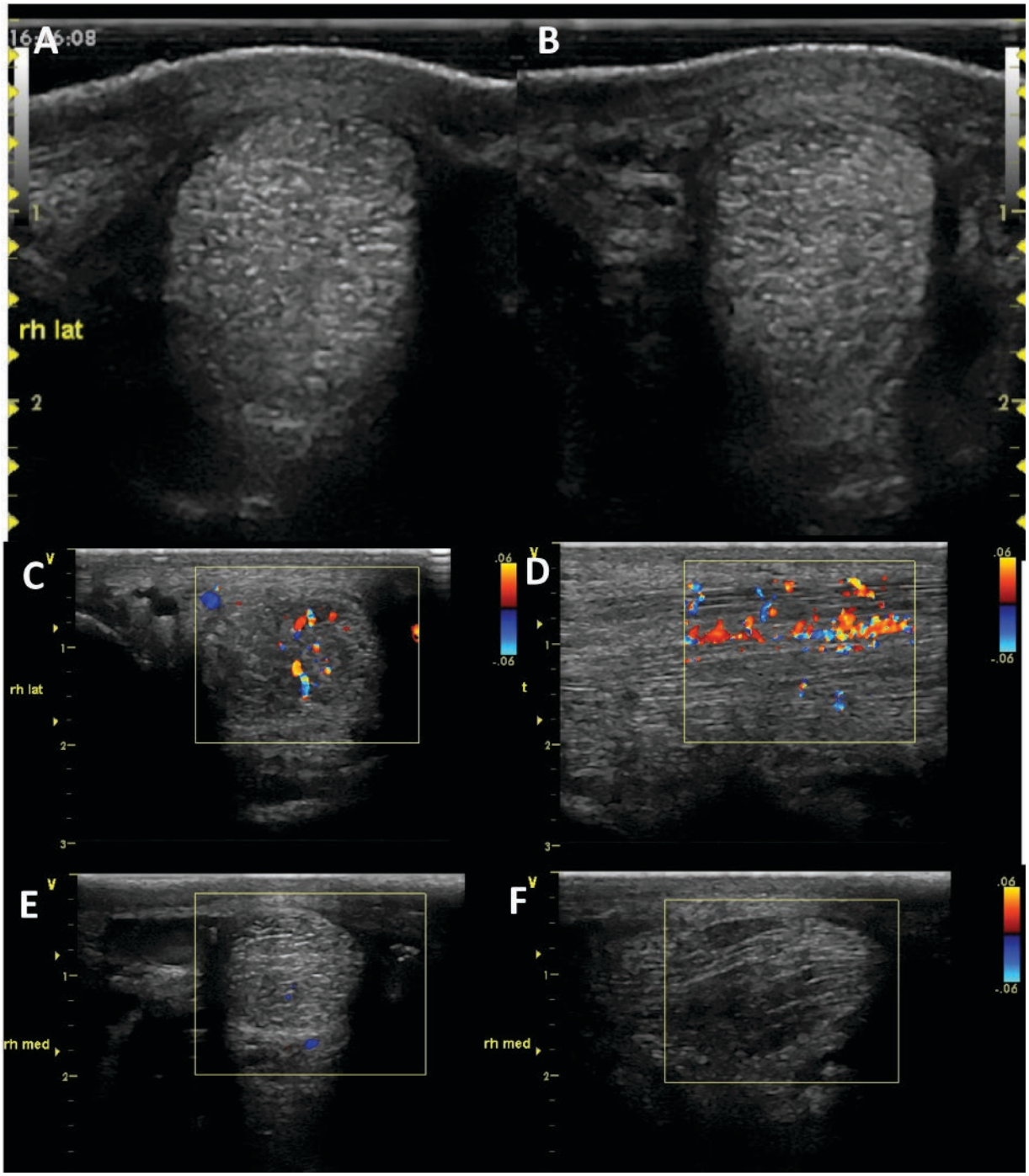


Figure 3.46 Transverse ultrasonographs of the lateral (A) and (C) and medial (B) and (E) suspensory ligament branches of a horse exhibiting right hind limb lameness and pain on palpation over the lateral suspensory ligament. Longitudinal images are shown in (D) (lateral branch) and (F) (medial branch). Both branches show signs of chronic desmitis characterized by branch enlargement and periligamentous fibrosis, but only the lateral one shows a positive Doppler signal on non-weightbearing scans (C) and (D).

Vet-ebooks.com

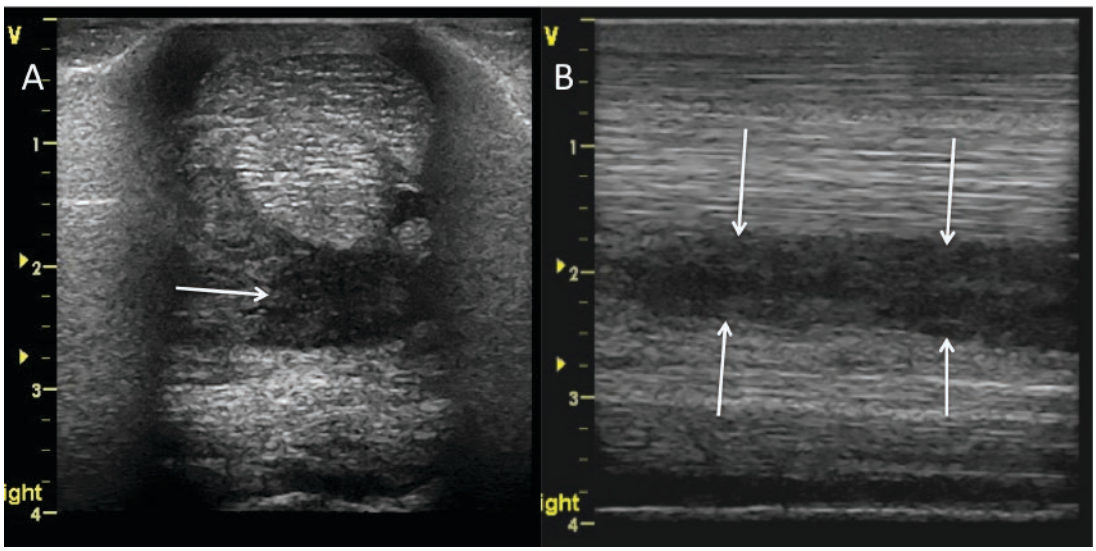


Figure 3.47 Transverse (A) and longitudinal (B) ultrasound images of desmitis of the accessory ligament of the deep digital flexor tendon. Note that the hypoechoic ligament (arrows) fills the space between the flexor tendons and the suspensory ligament.

involvement (Figure 3.48). The swelling of the ligament results in obliteration of the space between the ALDDFT and the underlying suspensory ligament. Some focal lesions, including those rare cases caused by percutaneous trauma to the lateral aspect of the metacarpal region, will only be visible if the transducer is moved over the palmarolateral aspect of the limb (Figure 3.48). This action is also important to detect adhesion formation between the lateral (usually) and medial (less commonly) borders of the ALDDFT and the SDFT, which can be responsible for flexural deformities and persistent lameness in chronic, unresponsive cases. Careful concurrent assessment of the SDFT should also be performed because concurrent injuries to the SDFT are not uncommon in horses [10]. Desmitis of the ALDDFT alone is the most common palmar metacarpal soft tissue injury in ponies

Distal lesions can be difficult to differentiate from the normal hypoechoic area where the fibers of the ALDDFT merge with those of the DDFT. The use of obliques and Doppler can help to confirm the presence of these lesions (Figure 3.49). Ultrasonographic assessment should extend proximally over the palmar aspect of the carpus to avoid missing very proximal lesions (Figure 3.50) [11].

These can occasionally affect part or all of the palmar carpal ligament and may be associated with carpal flexor tendon sheath tenosynovitis. In ALDDFT desmopathy, the distal synovial recess of the carpal sheath may be obliterated by ligament enlargement and adhesions and slight to moderate fluid distension of the sheath may occur.

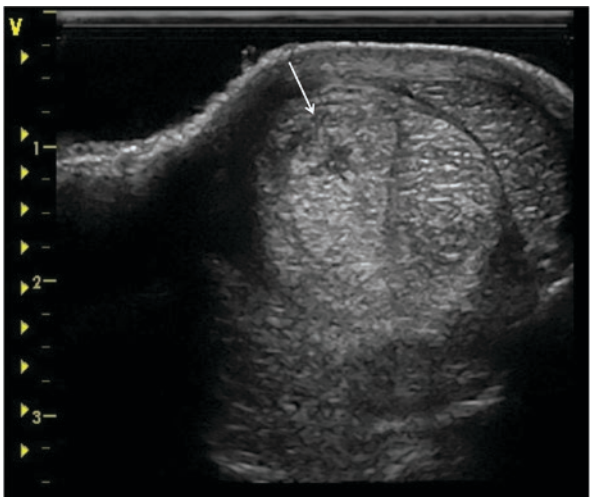


Figure 3.48 Transverse ultrasonograph over the lateral aspect of the proximal metacarpal region showing a focal lesion (arrow) in the accessory ligament of the deep digital flexor tendon, not visible from a standard palmar view.

ALDDFT Desmitis of the Hind Limb

The equivalent ALDDFT in the hind limb, the subtarsal check ligament, is a thin structure lying on the dorsal surface of the distal limit of the tarsal sheath. In normal animals it is poorly visible although always present and it can sometimes be better defined by orienting the transducer toward the medial aspect of the limb (Figure 3.31). Desmitis of this ligament can manifest in two forms – as an acute desmitis causing lameness or as chronic disease in adults with a distal interphalangeal joint flexural deformity [12]. In all

Vet-ebooks.com

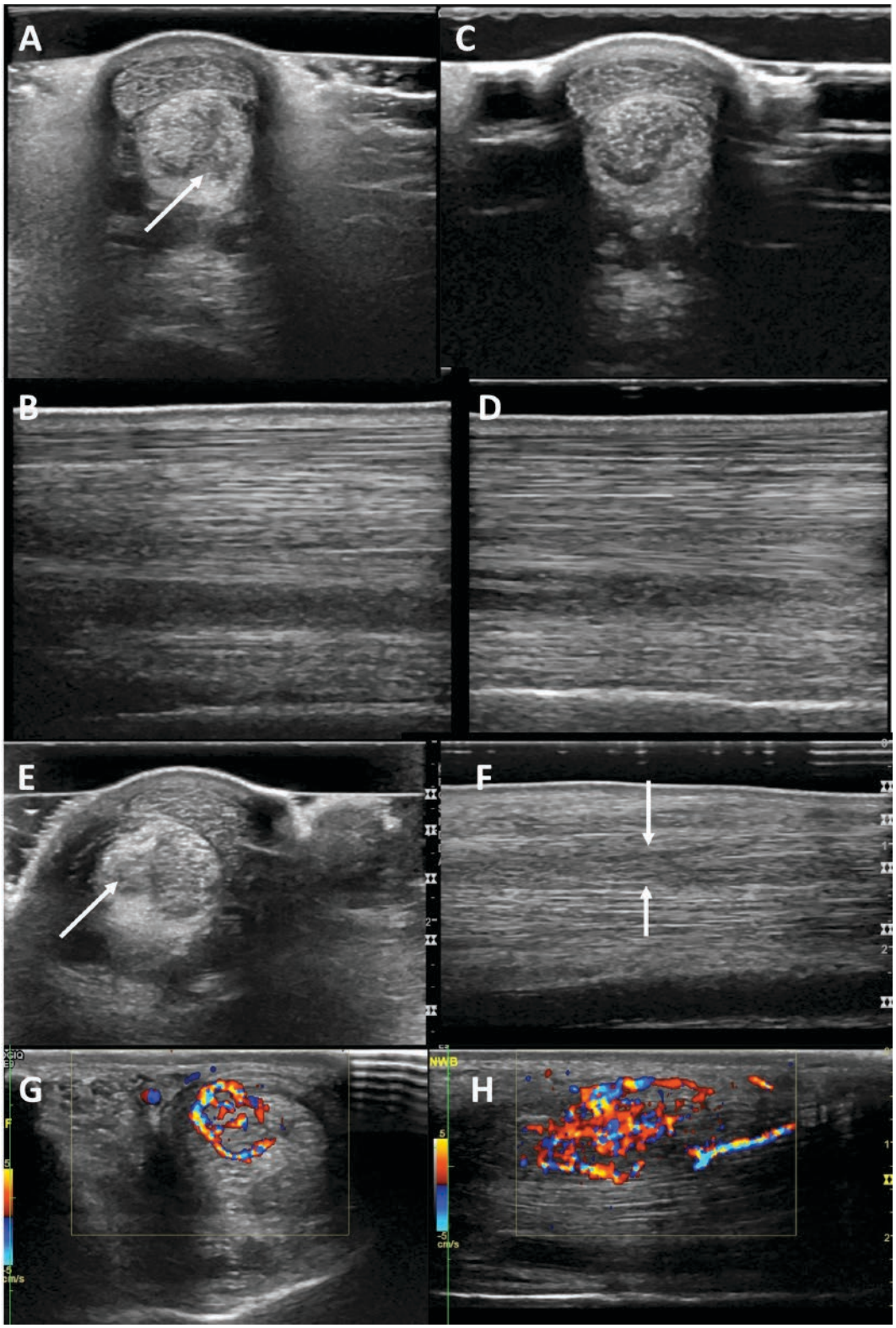


Figure 3.49 Distal insertional desmopathy of the ALDDFT. (A) and (B) are transverse and longitudinal images respectively from the affected limb showing the increased and less well defined hypoechoic area between the fibers of the deep digital flexor tendon and the ALDDFT compared to the contralateral limb (C). However, because the lesion is off the midline it is not apparent in the midline longitudinal images (B) which is similar to the contralateral limb (D). (E) and (F) are lateral oblique transverse and longitudinal images showing the lesion more clearly (arrows). Further confirmation is achieved with Doppler imaging in the non-weightbearing affected limb (G); transverse and (H); longitudinal).

Vet-ebooks.com

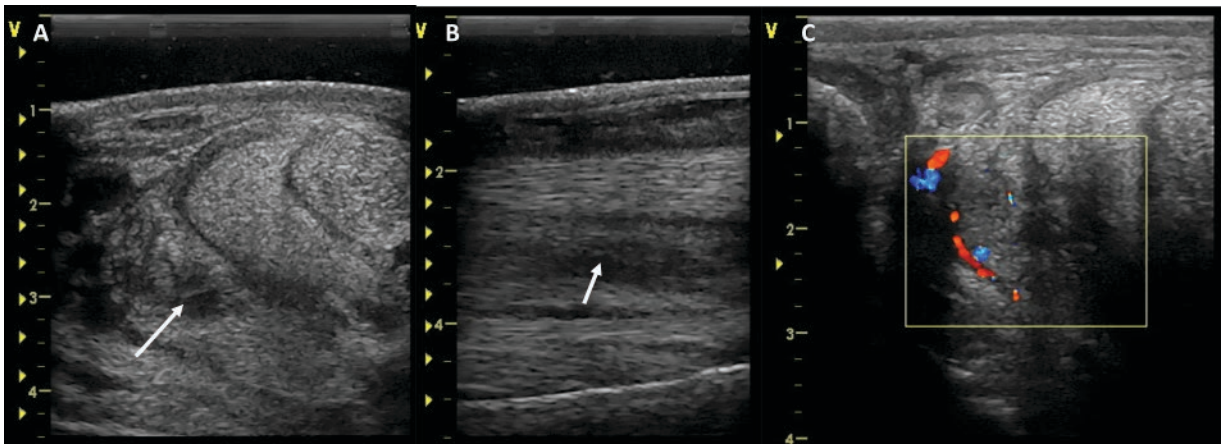


Figure 3.50 Proximal desmitis of the fore limb ALDDFT. These lesions can be easily missed in standard views from the palmar aspect of the limb. (A) transverse) and (B) longitudinal) images are from the palmarolateral aspect of the limb. The arrows show the lesion which may communicate with the carpal sheath. The Doppler signal in the non-weightbearing limb (C) confirms that the lesion is "active".

these cases, the ligament has been grossly enlarged, resembling a fore limb ALDDFT (Figure 3.51). Interestingly, while most cases of fore limb ALDDFT desmitis are unilateral, these cases have been invariably bilateral.

Extensor Tendons

Percutaneous extensor tendon injuries are common, especially in the hind limb as a result of kick injuries, interference with the other limbs, or hitting fixed objects. They may occur through wounds to the dorsal aspect of the limb or as a result of blunt contusion to the soft tissues. However, they can occasionally be due to over-strain injuries (Figure 3.52). Even significant damage can be clinically insignificant in terms of lameness (Figure 3.53).

Although the diagnosis is usually obtained through clinical evaluation, and treatment usually unnecessary, ultrasonography can provide valuable information, such as the extent of the wound, involvement of part of the tendon or complete transection, and involvement of the tendon sheaths. The periosteum should be also assessed to look for evidence of severe stripping which may lead to sequestrum formation.

Spontaneous rupture of the common or long digital extensor tendon over the dorsal aspect of the carpus is observed in foals and can cause severe longitudinal swelling of the accompanying tendon sheath over the distolateral radius. In the acute stage, mottled, hypoechogenic tissue represents hematoma formation. The retracted ends of the torn tendon are seen proximal and distal to the rupture site, sometimes at a surprising distance.

Bony Injuries

While metacarpal bone fractures are most readily assessed radiographically, ultrasonography can occasionally provide additional useful information. The configuration of complex third metacarpal/metatarsal bone fractures may be difficult to ascertain radiographically. Ultrasonographic evaluation can help to localize more accurately the position of the fracture line around the bone (Figure 3.54). Associated periosteal lifting and hemorrhage can help to detect the fracture line.

Periostitis and fracture of the second and fourth metacarpal/metatarsal (splint) bones may not be visible radiographically initially. These can occur from trauma to the splint bones, to the third metacarpus/metatarsus or both, with the medial aspect being most commonly involved. The horses are generally very lame but focal swelling may be subtle or, on the contrary, masked by diffuse edema. Ultrasonography is very useful to confirm the injury: the periosteum is thickened and hypoechogenic; subperiosteal hemorrhage is seen as a spindle-shaped, hypoechogenic tissue separating the hyperechoic bone interface from the lifted periosteum (Figure 3.55). In the subacute stage, early new bone

Vet-ebooks.com

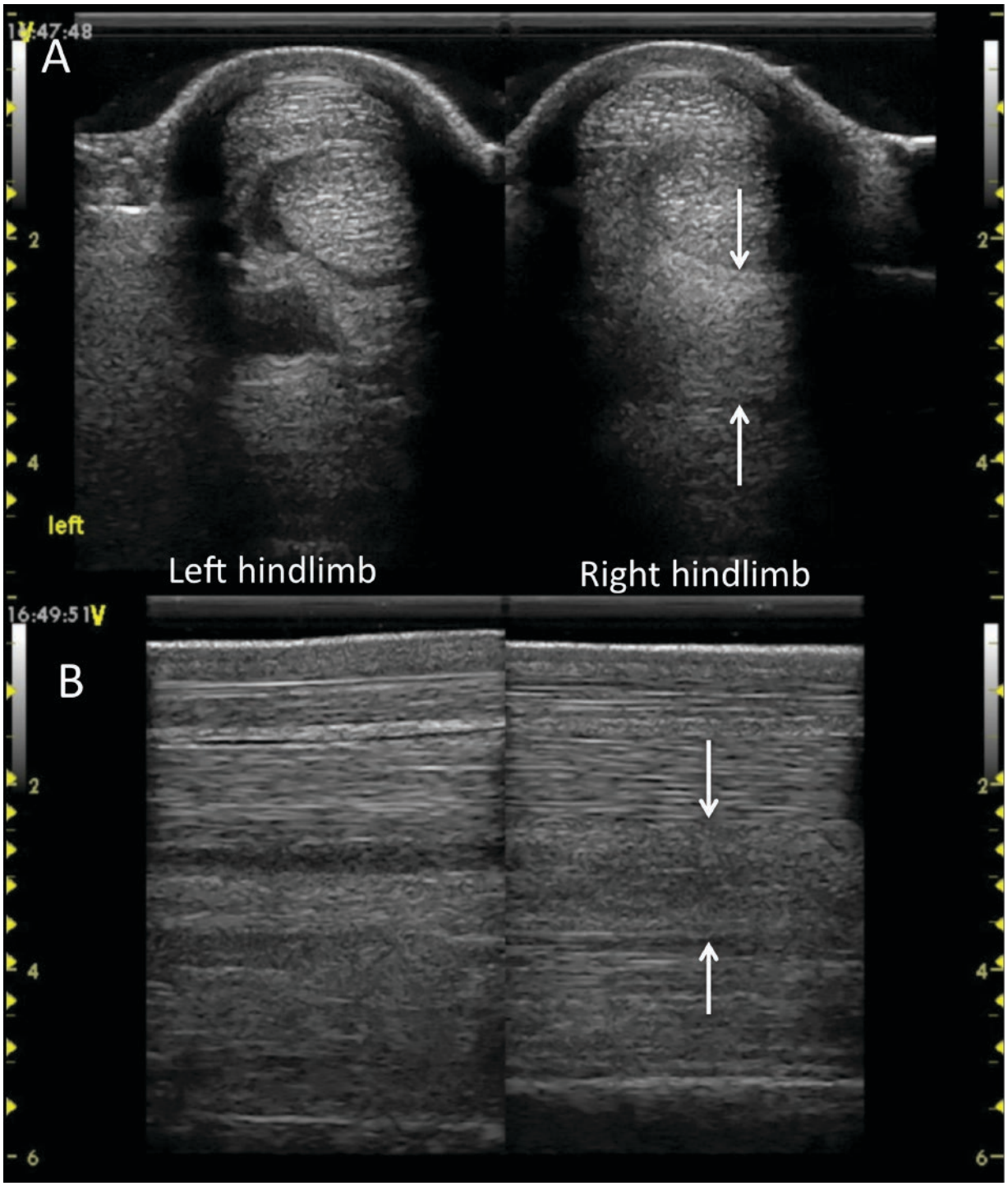


Figure 3.51 Desmitis of the accessory ligament of the deep digital flexor tendon in the right hind limb. Note the enlargement of the ligament on the dorsal surface of the deep digital flexor tendon in both transverse (A) and longitudinal (B) images (arrows).

Vet-ebooks.com

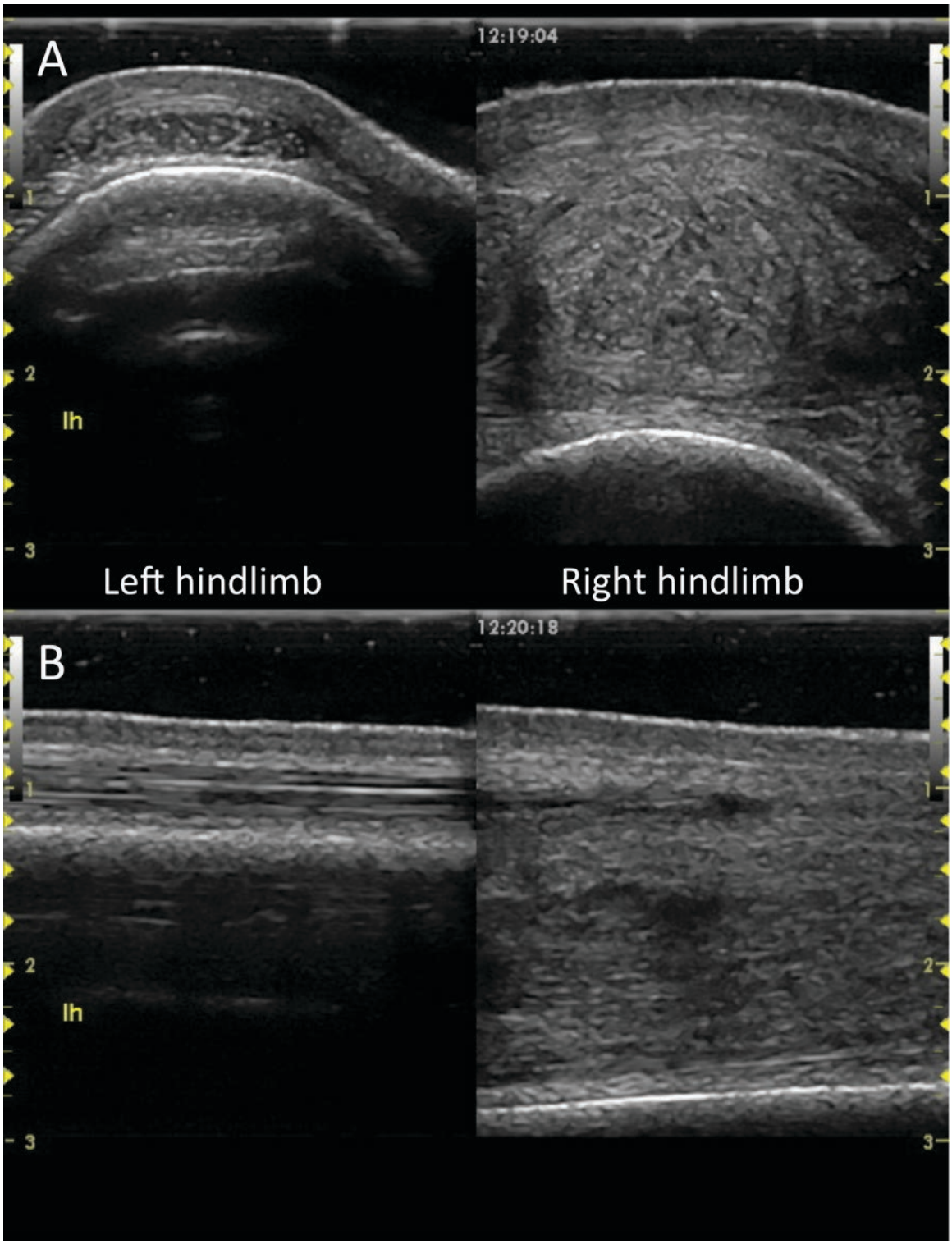


Figure 3.52 Long digital extensor tendinopathy. Transverse (A) and longitudinal (B) images of both the normal left hind limb and affected right hind limb. Note the considerable enlargement of the tendon with a completely disrupted longitudinal pattern. In spite of the severity of the pathology, these injuries rarely cause long-term problems.

Vet-ebooks.com

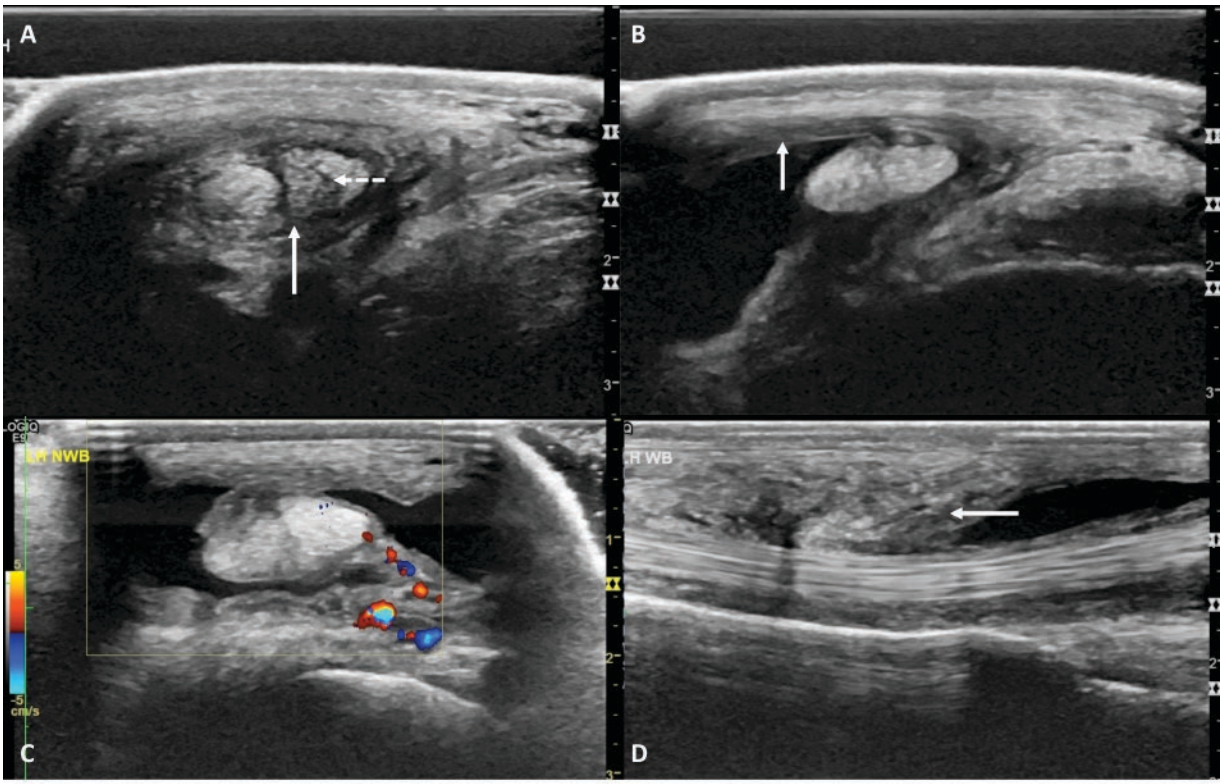


Figure 3.53 Lateral digital flexor tendinopathy with tenosynovitis over the dorsal aspect of the hock. (A) and (B) are transverse ultrasonographs over the dorsodistal aspect of the hock showing a split in the lateral digital extensor tendon (arrow in (A)) with mineralization causing shadowing (dashed arrow in (A)). There is associated significant thickening of the synovial lining (arrow in (B), but no increased blood flow within the tendon (C). (D) is the longitudinal image showing significant synovial proliferation. In spite of all these ultrasonographic changes, the left hind limb lameness was not associated with this pathology and its appearance remained unaltered over time.

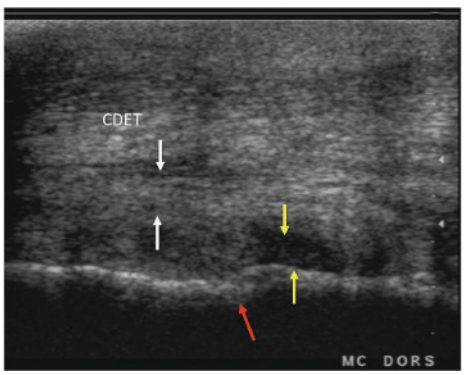


Figure 3.54 Transverse ultrasonographic image obtained over the dorsal aspect of the mid-metacarpus. The periosteum (white arrows) is thickened, hypoechogenic, and lifted from the cortical bone interface by hypoechogenic tissue (yellow arrows: edema and hemorrhage). An ill defined, focal irregularity, and loss of continuity of the cortical surface is caused by a non-displaced longitudinal fracture. CDET: common digital extensor tendon.

formation can give a spiky or sunburst appearance on ultrasonography, despite being barely visible on radiographs (Figure 3.56). Finally, ultrasonography can be useful for monitoring the progression of bony fragments in terms of sequestrum formation. This is characterized by a thin but strongly echogenic bone interface casting a shadow, lying in a depression in the underlying bone and surrounded by anechoic material (Figure 3.57). Ultrasonography may help to locate and follow fistulous tracts between the breached skin and a sequestrum or infected bone fracture, sometimes over surprisingly long distances.

The metacarpal/metatarsal region represents the most common site for an ultrasound examination because of the high frequency of overstrain and percutaneous injuries affecting the tendon and ligaments in this region of the limb. However, this area is also particularly well suited to ultrasound examination and quality diagnostic images can be obtained with relatively little practice.

Vet-ebooks.com

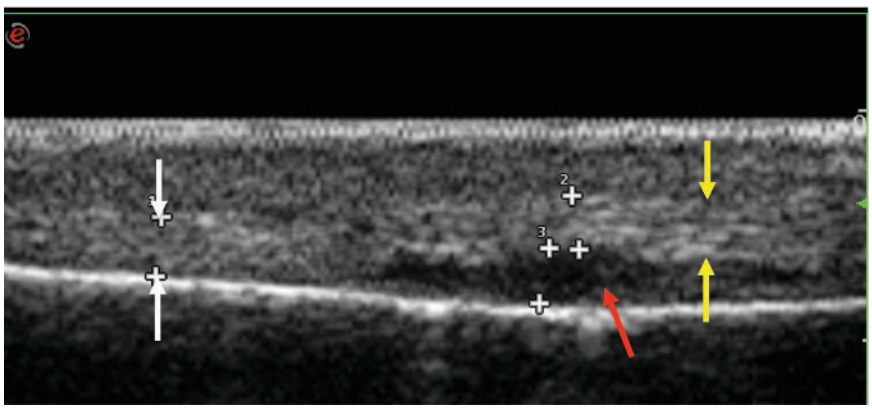


Figure 3.55 Acute trauma over the metacarpal bones can cause subperiosteal hemorrhage. This is characterized ultrasonographically (longitudinal/frontal plane image obtained over the second metacarpal bone) by lifting of the periosteum (yellow arrows) from the cortical bone interface by a spindle-shaped layer of hypoechoic material (blood) (red arrow). The surrounding, attached periosteum is abnormally thickened (white arrows).

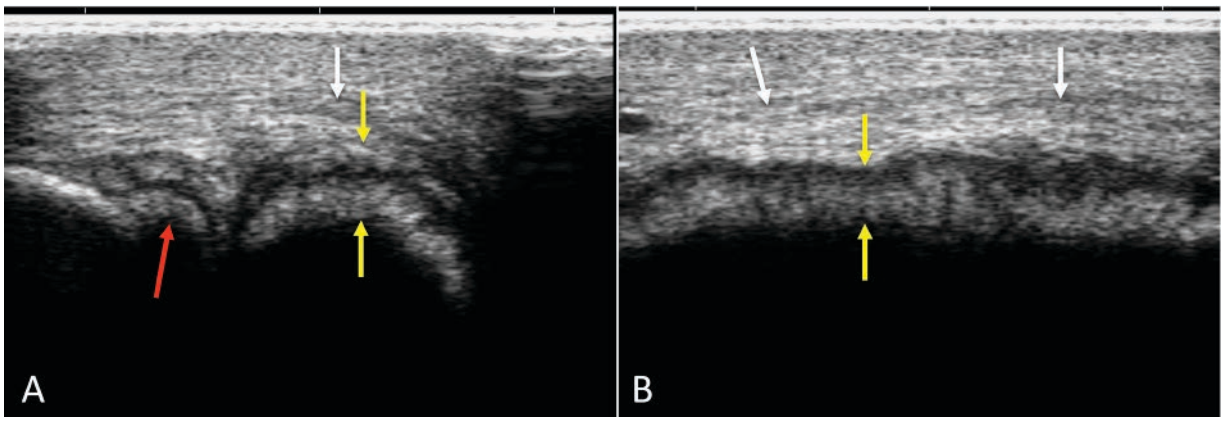


Figure 3.56 Transverse and longitudinal (frontal plane) images over the second metacarpal bone. Subacute periostitis has a typical appearance: the bone interface is irregular and spiky, with a "sunburst" appearance highlighted by an ill defined hypoechogenic halo (yellow arrows). The fibrous layer of the periosteum is thickened and lifted, and poorly visualized because of peripheral soft tissue reaction (white arrows). This appearance is that of early periosteal new bone formation. Note the new bone production from the third metacarpal bone in the interosseous space (red arrow).

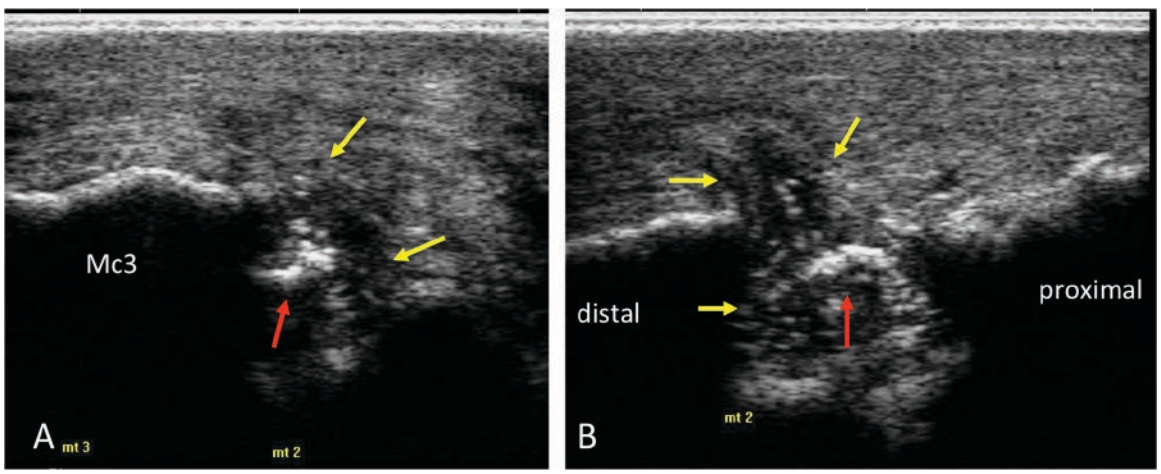


Figure 3.57 Transverse and longitudinal images obtained over the medial mid-metacarpal region. A fluid- and gas-filled fistula is seen (yellow arrows) to penetrate an irregular defect in the surface of the second metacarpal bone. A hyperechogenic, irregular interface represents a bony fragment sitting in the defect (red arrow). The fragment, surrounded by fluid, is most likely to be necrotic (sequestrum).

Vet-ebooks.com

Recommended Reading

Avella, C.S., Ely, E.R., Verheyen, K.L. et al. (2009b). Ultrasonographic assessment of the superficial digital flexor tendons of National Hunt racehorses in training over two racing seasons. *Equine Veterinary Journal* 41: 449–454.

References

1 Ali, O.J., Comerford, E.J., Clegg, P.D. et al. (2018). Variations during ageing in the three-dimensional anatomical arrangement of fascicles within the equine superficial digital flexor tendon. *European Cells & Materials* 35: 87–102.

2 Van Schie, H.T., Bakker, E.M. et al. (2003). Computerized ultrasonographic tissue characterization of equine superficial digital flexor tendons by means of stability quantification of echo patterns in contiguous transverse ultrasonographic images. *American Journal of Veterinary Research* 64: 366–375.

3 Minshall, G.J. and Wright, I.M. (2012). Tenosynovitis of the carpal sheath of the digital flexor tendons associated with tears of the radial head of the deep digital flexor: Observations in 11 horses. *Equine Veterinary Journal* 44: 76–80.

4 Avella, C.S., Ely, E.R., Verheyen, K.L. et al. (2009a). Ultrasonographic assessment of the superficial digital flexor tendons of National Hunt racehorses in training over two racing seasons. *Equine Veterinary Journal* 41: 449–454.

5 Smith, R.K., Jones, R., and Webbon, P.M. (1994). The cross-sectional areas of normal equine digital flexor tendons determined ultrasonographically. *Equine Veterinary Journal* 26: 460–465.

6 Kuemmerle, J., Theiss, F., and Smith, R.K.W. (2018). Diagnosis and management of tendon and ligament disorders. In: *Equine Surgery*, 5th edn (ed. J. Auer and S. Ja), Chapter 83. St Louis MO: Elsevier.

7 Garvican, E.R., Salavati, M., Smith, R.K.W. et al. (2016). Exposure of a tendon extracellular matrix to synovial fluid triggers endogenous and engrafted cell death: A mechanism for failed healing of intrathecal tendon injuries. *Connect Tissue Research* 1–9.

8 Smith, R.K. and Mcilwraith, C.W. (2012). Consensus on equine tendon disease: Building on the 2007 Havemeyer symposium. *Equine Vetinary Journal* 44: 2–6.

9 Werpy, N.M., Denoix, J.M., Mcilwraith, C.W. et al. (2013). Comparison between standard ultrasonography, angle contrast ultrasonography, and magnetic resonance imaging characteristics of the normal equine proximal suspensory ligament. *Veterinary Radiology Ultrasound* 54: 536–547.

10 Dyson, S.J. (1991). Desmitis of the accessory ligament of the deep digital flexor tendon: 27 cases (1986–1990). *Equine Veterinary Journal* 23: 438–444.

11 Dyson, S. (2012). Proximal injuries of the accessory ligament of the deep digital flexor tendon in forelimbs and hindlimbs: 12 horses (2006–2010). *Equine Veterinary Education* 24: 134–142.

12 Eliashar, E., Dyson, S.J., Archer, R.M. et al. (2005). Two clinical manifestations of desmopathy of the accessory ligament of the deep digital flexor tendon in the hindlimb of 23 horses. *Equine Veterinary Journal* 37: 495–500.

Vet-ebooks.com

4

Ultrasonography of the Carpus

Ann Carstens[1] *and Sheelagh Higgerty*[2]

[1] *University of Pretoria, Onderstepoort, South Africa*
[2] *Crowthorne Veterinary Clinic, Kyalami, South Africa*

Introduction

Radiography is the modality most often used to evaluate the equine carpus, since most lesions in this area are bony in nature; however, radiologically evident soft tissue swelling is often associated with, and secondary to, bony carpal pathology, i.e., a middle carpal joint effusion secondary to a distal radiocarpal chip fracture. Additionally, there is also often no radiological evidence of bony changes in the carpus, and ultrasonography lends itself to evaluate soft tissue changes. Cortical abnormalities are also amenable to ultrasonographic evaluation and particularly useful as a preliminary evaluation if radiological equipment is not to hand.

Inspection, palpation, and flexion of the carpus are usually adequate to determine the anatomic structure/s affected in the presence of a pericarpal swelling, but perineural or intra-articular blocks may be required if the above are negative or equivocal. The carpus is a complex joint with multiple bones, ligaments, tendons, tendon sheaths, bursae, and three joints with recesses. To scan the entire carpus may be time-consuming, and it is suggested that the area or areas identified clinically or with other modalities, such as radiography or scintigraphy, be ultrasonographically evaluated in detail and the rest of the carpus scanned in a more cursory manner if time is not available.

Carpal anatomy should be revised prior to ultrasonographic evaluation, if the ultrasonographer is unfamiliar with the area to be scanned. It is also advisable to have a mounted bone specimen available to assist in determining precisely where one is scanning.

A 7.5–13 MHz linear transducer is advised for evaluating the carpus, with or without a standoff pad, depending on the depth of the area to be evaluated. A split screen or C-scape modality can be used to make a composite image on the screen. The figures in this chapter include either a bony specimen or a radiograph to show where the transducer is positioned.

Anatomy and Scanning Technique

Dorsal Carpus

The transducer is placed sagittally at the distal aspect of the radius cranially and moved distally, respectively evaluating the bones and superficial structures of the distal radius, the antebrachiocarpal joint (ACJ), the proximal row of carpal bones, the middle carpal joint (MCJ), the distal row of carpal bones, the carpometacarpal joint (CMCJ), and the proximal aspect of metacarpus 3 (MC3) (Figure 4.1). The surface of the bones should be smooth hyperechoic lines with elevations at the dorsal tubercles at implantation of the dorsal intercarpal ligaments. The hyperechoic cortical line will have a distinct interruption where the joint margin starts; angling the transducer will allow visualization of the most dorsal part of the articular surface. The approximately 1 mm thick dorsal intercarpal ligaments can be noted, running transversely immediately deep to the skin surface. Hereafter the transducer can be moved again to the distal aspect of the radius laterally or medially and the movement repeated until the entire dorsum is scanned. This is then repeated with the transducer held in a transverse plane. In this way the distal cranial radius, dorsal aspect of the radial (RCB), intermediate (ICB), ulnar (UCB),

Atlas of Equine Ultrasonography, Second Edition. Edited by Jessica A. Kidd, Kristina G. Lu and Michele L. Frazer.
© 2022 John Wiley & Sons Ltd. Published 2022 by John Wiley & Sons Ltd.
Companion Website: www.wiley.com/go/kidd/atlas

Vet-ebooks.com

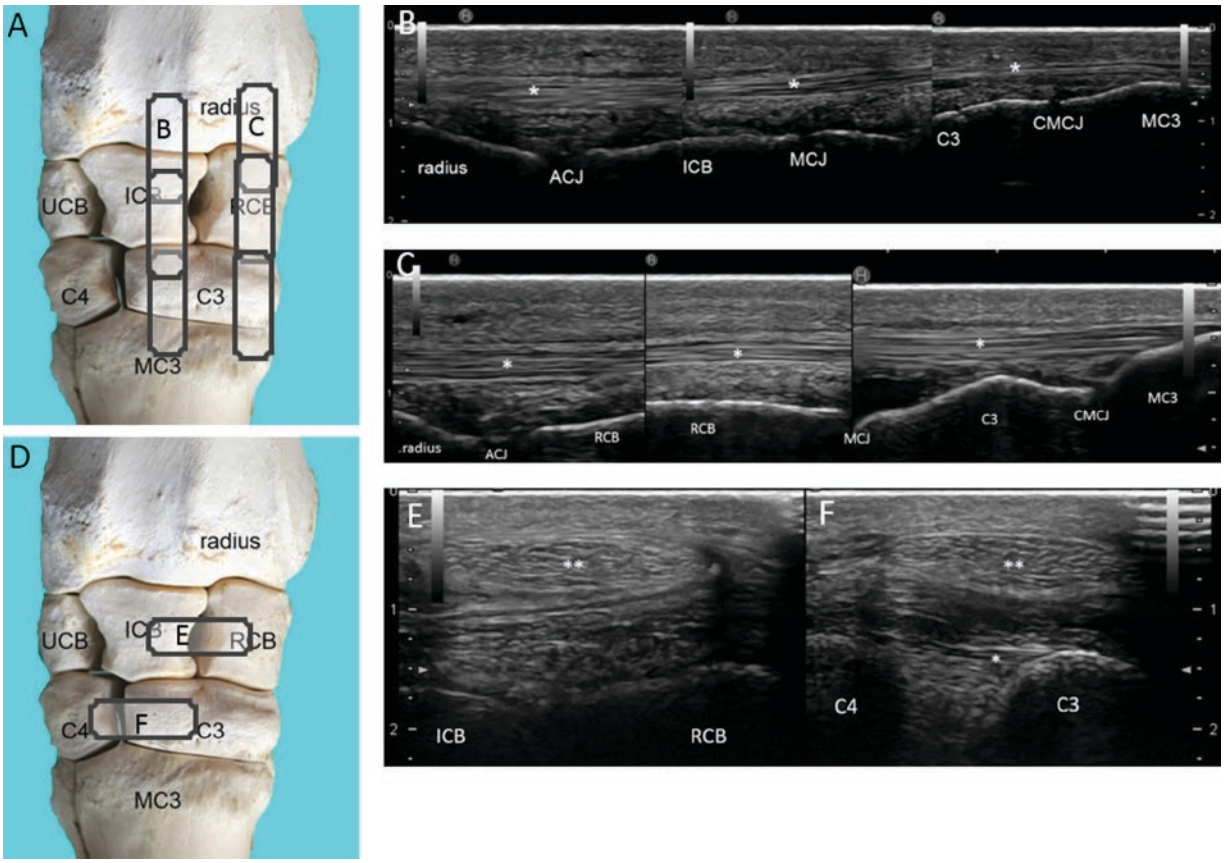


Figure 4.1 Dorsal carpus illustrating the surface of the dorsal joint spaces and tendons of the common digital extensor and extensor carpi radialis muscles. Longitudinal split screen composite image of the dorsal mid-carpus showing the antebrachiocarpal joint (ACJ), the middle carpal joint (MCJ), the carpometacarpal joint (CMCJ), and the tendon of the common digital extensor (CDE)(*). Proximal is to the left. (C) Longitudinal split screen composite image of the dorsal mid-medial aspect of the carpus showing the ACJ, the MCJ, and the CMCJ, and the tendon of the extensor carpi radialis (ECR)(*) attaching to the medial tuberosity of the proximal MC3; note the hypoechoic villous structures within the ACJ and the anechoic fluid within the MCJ. Proximal is to the left. (E) Transverse images showing the dorsal hyperechoic surfaces of the intermediate carpal bone (ICB) and the radiocarpal bone (RCB) and transverse section through the ECR tendon (ECRT)(**). Lateral is to the left. (F) Transverse image showing the dorsal hyperechoic surfaces of fourth and third carpal bones (C4 and C3) and transverse section through the CDET(**); note the intercarpal ligament between C4 and C3 (*). Lateral is to the left.

second (C2), third (C3), and fourth (C4) carpal bones, the third metacarpal bone (MC3) and the three joints can be visualized. The tendons of the common digital extensor (CDET) and the extensor carpi radialis (ECRT) must also be examined, noting the size, echogenicity, and fiber alignment. A bursa of the extensor carpi radialis (ECRB) is present under the implantation of the ECRT, but usually only visible when more than normal synovial fluid is present within. The tendon sheaths and joints are evaluated for the presence, echogenicity, and amount of fluid within and the joint capsule, the synovial membrane, and sheaths themselves are evaluated for thickening, abnormal echogenicity, or abnormal growths. The abductor digiti 1 longus (ADL) body and insertion can be visualized, but has not been described to be of clinical significance.

If pathology in a specific structure, such as a single tendon and its sheath, is suspected, it should be evaluated in full. For example, for a tendon and its sheath, noting the muscular portion as well as the implantation is advised.

Lateral Carpus

Again using a sequential sagittal and transverse scanning technique, starting slightly dorsolaterally, the lateral aspect of the carpus is evaluated, identifying the lateral styloid process, and the lateral aspects of the ACJ, C4, MCJ, UCB, CMCJ, and MC4 (Figure 4.2). The hypoechoic cartilaginous or partially mineralized C5 may be noted, although uncommonly seen. Further palmarly, the lateral collateral ligament provides passage for the lateral digital extensor (LDET), between its long superficial and short deep parts (Figure 4.2).

Some of the ligaments associated with the accessory carpal bone can also be visualized scanning

Vet-ebooks.com

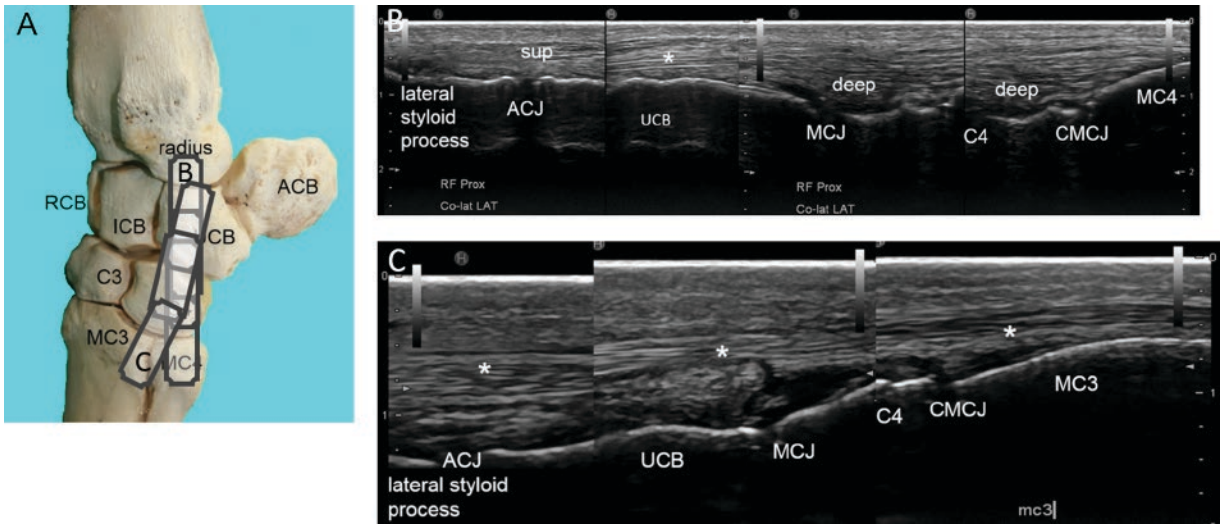


Figure 4.2 Lateral carpus illustrating the surface of the lateral joint spaces, the lateral collateral ligament, and the tendon of the lateral digital extensor muscle. (A) Anatomical specimen indicating transducer placement. (B) Longitudinal combined split screen images of the lateral carpus with the superficial (sup) and deep parts of the lateral collateral ligament and the lateral digital extensor tendon (LDET) (*) between them. Proximal is to the left. (C) Obliquely orientated longitudinal split screen image of the lateral to dorsolateral carpus of the LDET (*) to just before it joins the common digital extensor tendon between them. Proximal is to the left. ACJ: antebrachiocarpal joint; C4: fourth carpal bone; CMCJ: carpometacarpal joint; MCJ: middle carpal joint; RCB: radiocarpal bone; UCB: ulnar carpal bone.

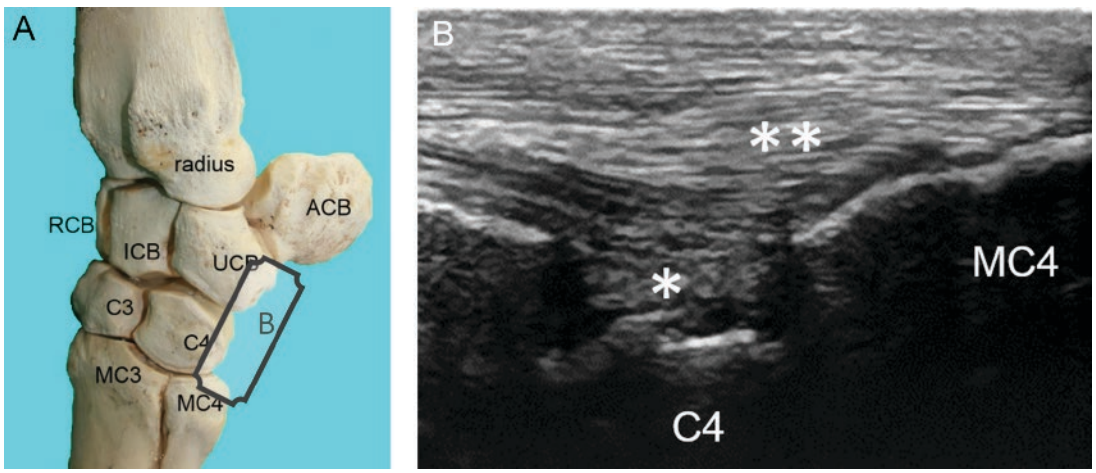


Figure 4.3 Lateral carpus illustrating two ligaments associated with of the accessory carpal bone. (A) Anatomical specimen indicating transducer placement. (B) Longitudinal image of the lateral carpus showing the accessorioquartal ligament extending from the ACB to C4 (*) and the more superficial accessoriometacarpal ligament extending from the ACB to MC4 (**). Proximopalmar is to the left. C4: fourth carpal bone; MC4: fourth metacarpal bone.

palmarolaterally from the accessory carpal bone to C4 and MC4. (Figure 4.3)

Whereas the main insertion of the ulnaris lateralis tendon (ULT) is on the proximal aspect of the accessory carpal bone (ACB), its extension (long part) can be visualized where it inserts on proximal MC4 after running through a groove on the lateral part of the ACB (Figure 4.4).

Again the size, echogenicity, and fiber alignment and sheaths of the tendons are examined. Further palmarly and proximal to the ACB, the musculotendinous junction of the deep digital flexor tendon (DDFT) can be seen next to the distocaudal radius. If there is an effusion in the palmar recess of the ACJ or very marked effusion in the carpal canal (CC), this may be seen between the radius and the DDFT.

Medial Carpus

While again using a sequential sagittal and transverse scanning technique, starting slightly dorsomedially, the medial aspect of the carpus is evaluated, identifying the medial styloid process, the medial aspects of the ACJ, RCB, MCJ, C2

Vet-ebooks.com

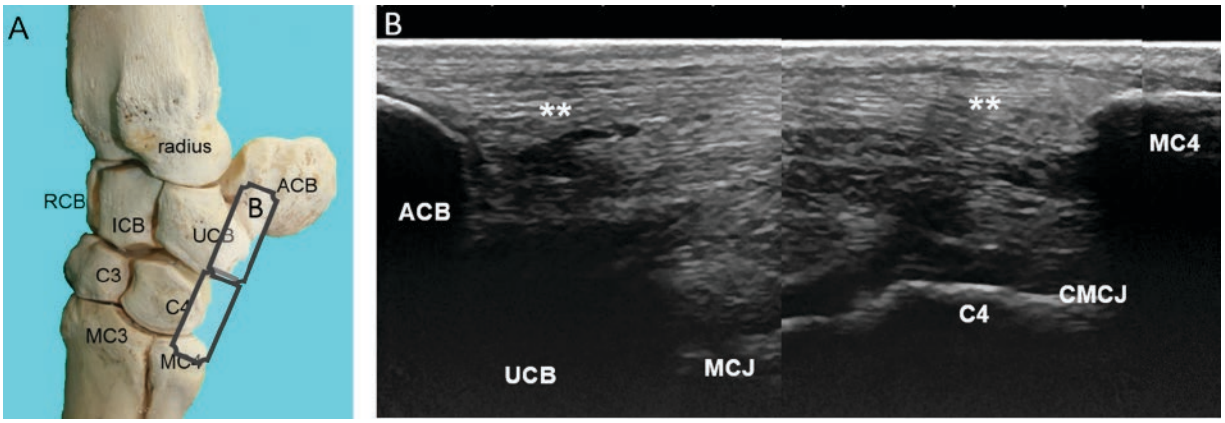


Figure 4.4 Lateral carpus illustrating the ulnaris lateralis tendon. (A) Anatomical specimen indicating transducer placement. (B) Longitudinal split screen image of the lateral carpus indicating the extension of the long part of the ulnaris lateralis tendon (ULT) (**) from the groove on the lateral aspect of the ACB distally to its distal insertion on MC4. Proximal is to the left. ACB: accessory carpal bone; C4: fourth carpal bone; CMCJ: carpometacarpal joint; MCJ: middle carpal joint; RCB: radiocarpal bone; UCB: ulnar carpal bone.

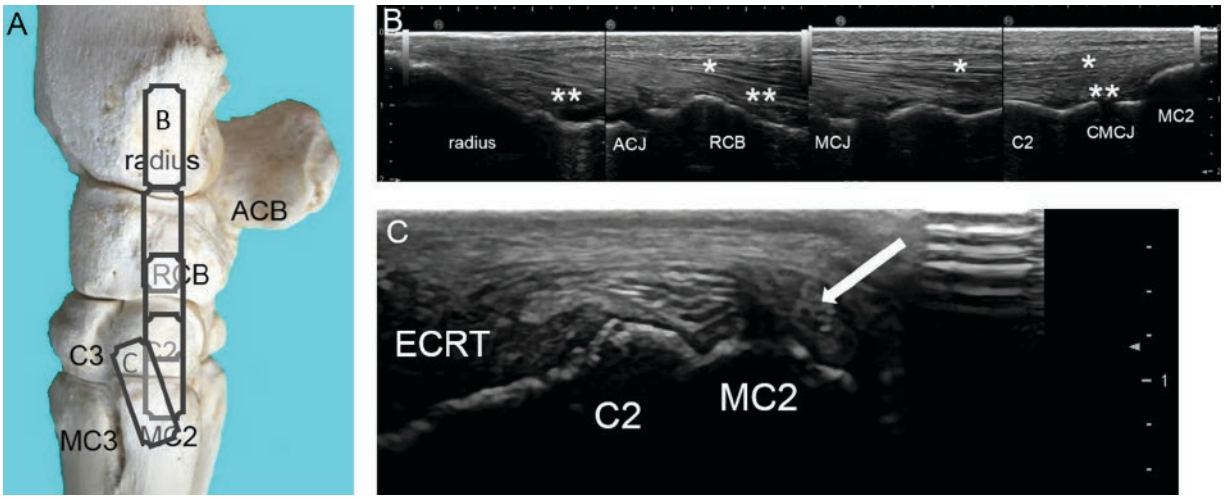


Figure 4.5 Medial carpus illustrating the medial collateral ligament and the abductor digiti 1 longus tendon. (A) Anatomical specimen indicating transducer placement. (B) Longitudinal split screen image of the medial carpus illustrating the medial collateral ligament in its entirety; note the long (superficial) fibers (*) extending to MC2 and the short (deeper) fibers (**) attaching to the RCB and C2. Proximal is to the left of the image. (C) Longitudinal scan of the dorsomedial aspect of the carpometacarpal joint, showing the insertion of the obliquely scanned abductor digiti 1 longus tendon (arrow) on the head of the MC2, which has an irregular periosteal reaction thereon, as has the dorsum of C2. Proximal is to the left. ACJ: antebrachiocarpal joint; C2: second carpal bone; ECRT: extensor carpi radialis tendon; MC2: second metacarpal bone; RCB: radiocarpal bone; CMCJ: carpometacarpal joint; MCJ: middle carpal joint; RCB: radiocarpal bone.

(possibly also C1), CMCJ, MC2, both the long and short segments of the medial collateral ligament (MCL), and insertion of the obliquely scanned abductor digiti 1 longus tendon on the head of the MC2 after passing over the tendon of the extensor carpi radialis tendon (ECRT) (Figure 4.5).

The muscle bellies and tendons of the superficial digital flexor muscle (tendon – SDFT) and DDFT can be best seen on the palmar view. The palmar proximal recess of the ACJ as well as the carpal canal may be visualized adjacent to the distal medial radius caudally if there is synovial distension.

Palmar Carpus

This aspect is actually approached as the mediopalmar to palmar aspect since the ACB curves around on the most lateropalmar aspect of the carpus providing the lateral border of the carpal canal (CC) and partially providing the insertion of the retinaculum of the carpus (RetC). The CC extends from approximately 20 cm proximal to the ACJ to approximately 10 cm distal to the CMJ. The ULT can be viewed inserting on the proximal aspect of the accessory carpal bone (ACB). Within

Vet-ebooks.com

the carpal canal the muscular bodies of the tendons of the DDFT and SDFT are visualized from the level of the chestnut where they start becoming tendinous. Immediately proximal to the carpus, the median artery (MA) sends off the distal radial artery (DRA) and then enters the carpal canal, seen as an anechoic tubular structure. The accessory ligament of the SDFT (AL-SDFT) is seen as an homogeneous hyperechoic trapezoid structure (in the transverse plane) originating from the caudomediodistal aspect of the radius dorsomedial to the SDFT, thinning further distally and fusing to the SDFT tendon. The AL-SDFT is bordered medially by the FCRT, and palmaromedially by the MA, vein, and nerve. Mediopalmar to the MA and the AL-SDFT is the flexor carpi ulnaris muscle (FCU). Medially to the SDFT is the muscle belly of the ulnar carpal flexor (flexor carpi ulnaris tendon – FCUT) and caudolaterally to the DDFT is the UL muscle. The cephalic vein (CV) is situated medial to the RetC. The palmar carpal canal should be evaluated transversely and longitudinally (see Figures 4.6, 4.7, 4.8, and 4.9).

The palmar aspects of all the carpal bones can be visualized to a greater or lesser degree; again use a sequential approach to evaluate them from either medially to laterally or vice versa from proximally to distally. Proximally, the distal radial condyle is divided into the lateral ulnar facet (UF), the more medial intermediate facet (IF), and the medial radial facet

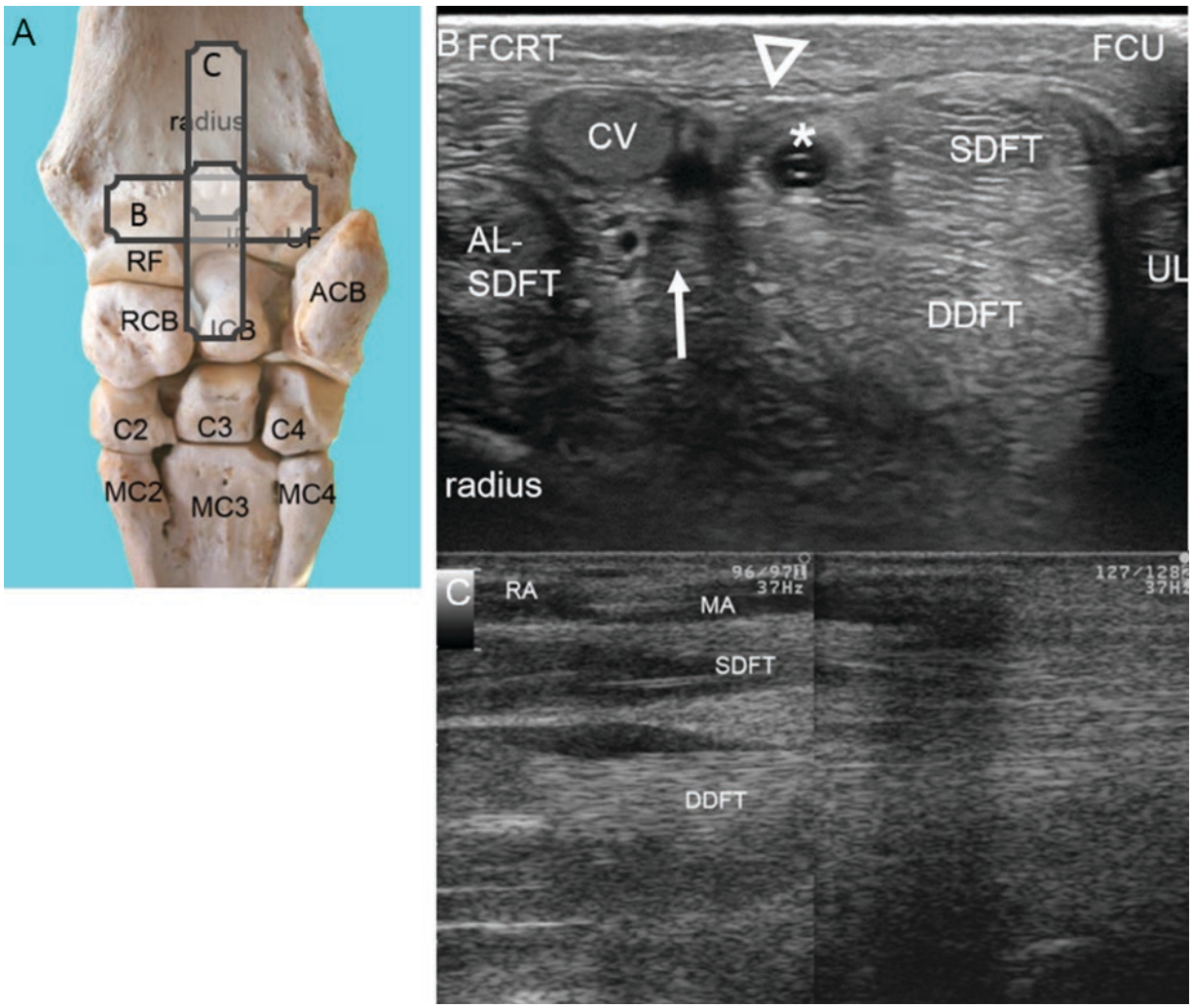


Figure 4.6 Caudal distal radius and proximal palmar carpus illustrating the carpal canal. (A) Anatomical specimen indicating transducer placement. (B) Caudal transverse ultrasound image at level of distal radius; note the median artery (*), the retinaculum of the carpal canal (open arrow head), and the median nerve (white arrow). Medial is to the left. (C) Palmaromedial longitudinal split screen ultrasound image showing superficial and deep digital flexor tendon musculotendinous junctions immediately proximal to the accessory carpal bone (ACB). Proximal is to the left. AL-SDFT: accessory ligament of the superficial digital flexor tendon; CV: cephalic vein; DDFT: deep digital flexor tendon; SDFT: superficial digital flexor tendon; MA: median artery; FCU: flexor carpi ulnaris; RA: radial artery; UL: ulnaris lateralis.

Vet-ebooks.com

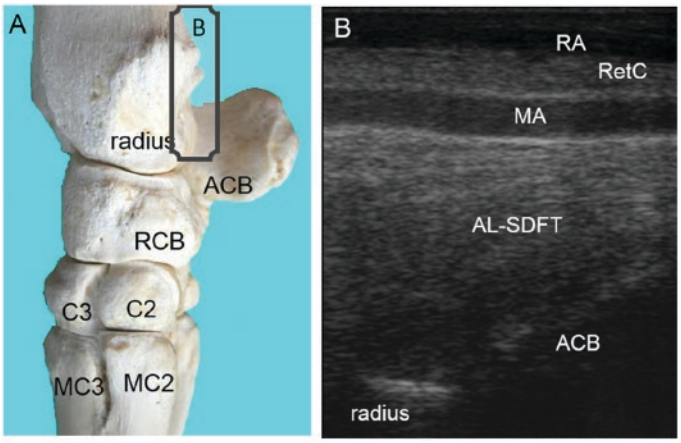


Figure 4.7 Carpal canal over the caudomedial distal radius illustrating the accessory ligament of the superficial digital flexor tendon. (A) Anatomical specimen indicating transducer placement (angled slightly craniolaterally). (B) Medial longitudinal ultrasound image showing the median artery and accessory ligament of the superficial digital flexor tendon (AL-SDFT). Proximal is to the left. ACB: accessory carpal bone; MA: median artery; RA: radial artery; RetC: retinaculum of the carpal canal.

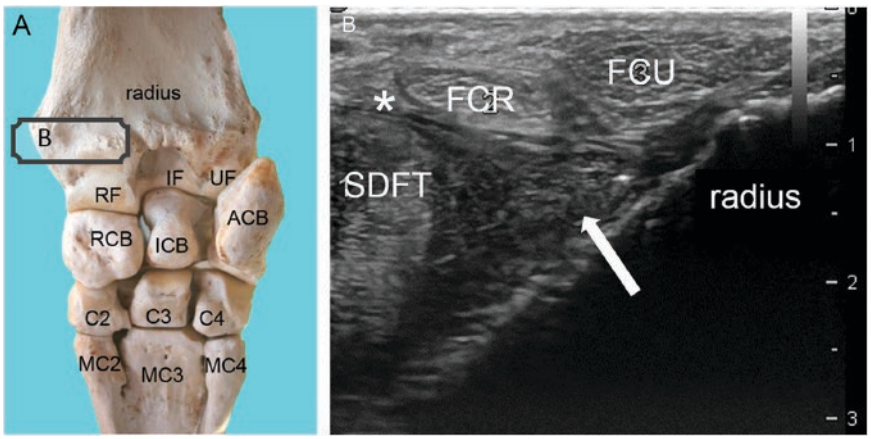


Figure 4.8 Caudomedial distal radius illustrating the tendons of the SDFT, FCR, FCU, and the AL-SDFT. (A) Anatomical specimen indicating transducer placement (angled slightly craniolaterally). (B) Transverse scan of the caudomedial aspect of the distal radius, showing the tendons of the SDFT, FCR, FCU, and the AL-SDFT (arrow); in this region, the FCU tendon starts to blend with the carpal retinaculum (*). Medial is to the left. AL-SDFT: accessory ligament to the superficial digital flexor tendon; FCR: flexor carpi radialis; FCU: flexor carpi ulnaris; SDFT: superficial digital flexor tendon.

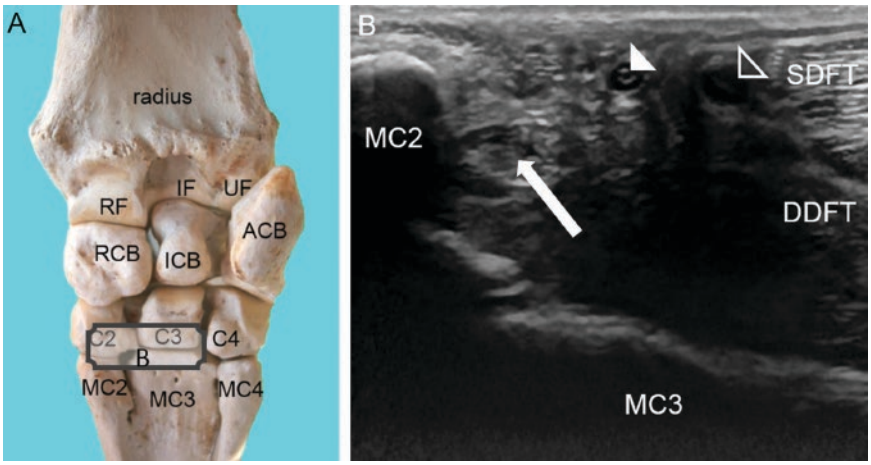


Figure 4.9 Palmarodistal aspect of the medial carpus illustrating the flexor carpi radialis tendon insertion. (A) Anatomical specimen indicating transducer placement. (B) Palmar transverse scan of the proximal metacarpal area medially, showing the tendon of the flexor carpi radialis attaching to the axial aspect of the MC2 (arrow); radial artery (white closed arrowhead); medial palmar artery (open white arrowhead). Medial is to the left. MC2: metacarpus 2; MC3: metacarpus 3.

Vet-ebooks.com

(RF). Similarly. the palmar aspect of the carpal joint spaces can be seen (Figures 4.10 and 4.11).

Joints and Bone

Higher-frequency transducers can optimize evaluation of the articular cartilage and subchondral bone. Normal cartilage should be anechoic, with a smooth surface and in the case of the carpus, be approximately 1 mm thick. The subchondral bone of the adult horse should be relatively smooth. Flexing the joint and using a curvilinear or micro-convex transducer will allow visualization of the deeper (more palmar) joint surfaces. Interarticular ligaments, such as the medial palmar intercarpal ligament (MPaICL), extending from between palmar C2 and RCB distally extending to palmar proximally, have been described and other intercarpal ligaments may also be visualized (see Recommended Reading at the end of this chapter). Ultrasonography of the intercarpal ligaments such as the medial palmar intercarpal ligament is performed with the carpus in flexion and the MCJ imaged through the ECRT (Figure 4.12).

In the immature horse, the distal radial epiphysis can be seen as a disruption of the distal radius cortex. In young foals, the carpal bones have a thicker anechoic cartilage with the underlying mineralized bone having a slightly less regular surface. In the premature animal, the cartilage is particularly thick and the hyperechoic bony center small or absent (Figure 4.13B). In Figure 4.13C, a 100 ml of saline was injected into the

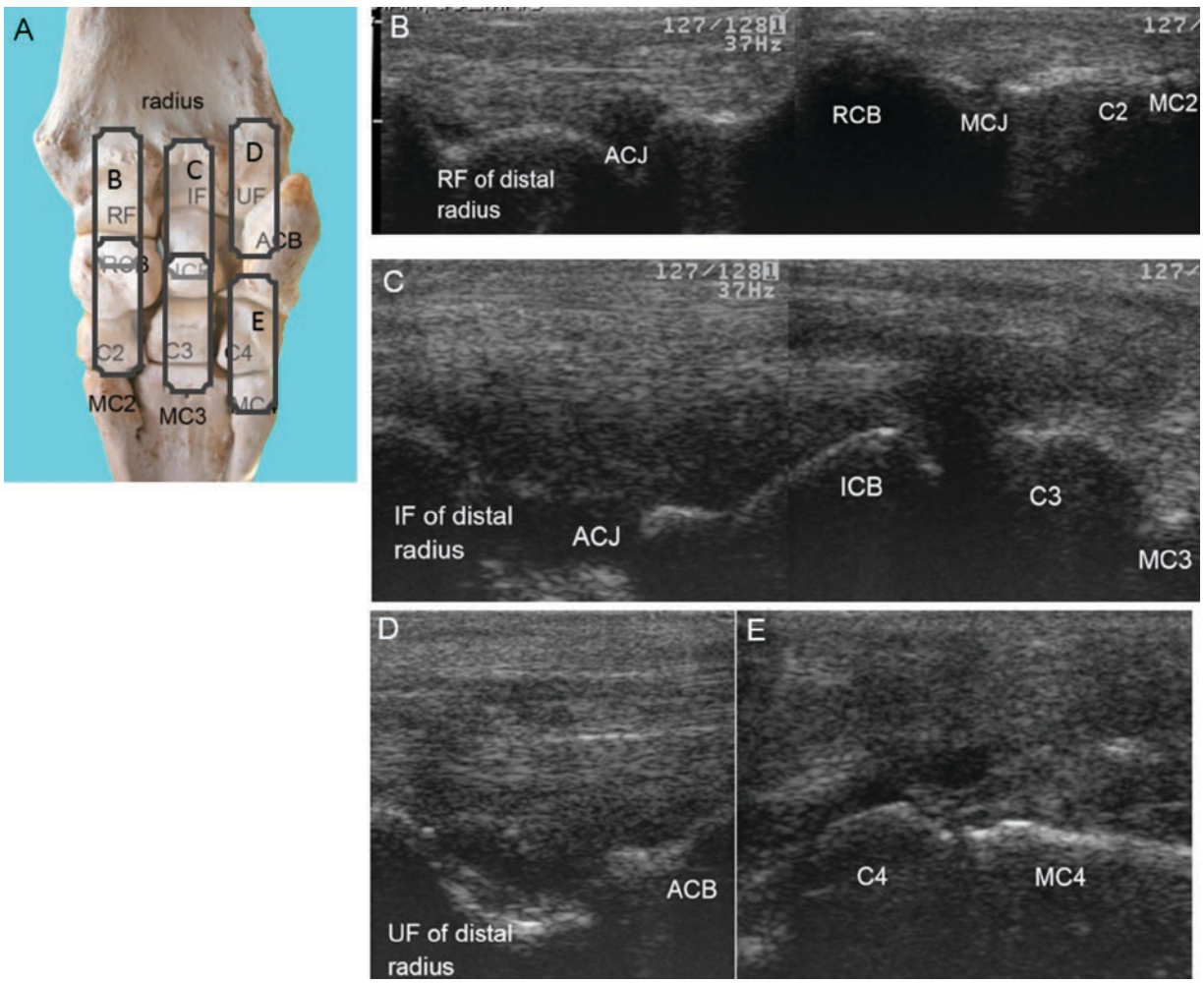


Figure 4.10 Longitudinal evaluation of palmar carpus illustrating the palmar surface of the carpal bones and joint spaces. (A) Anatomical specimen indicating transducer placement. (B, C, D, and E) Longitudinal split screen composite image of the palmar aspect of the right carpus showing the hyperechoic palmar surfaces of the carpal and metacarpal bones and the palmar aspect of the carpal joint spaces. Proximal is to the left. ACB: accessory carpal bone; ACJ: antebrachiocarpal joint; ICB: intermediate carpal bone; MCJ: middle carpal joint; RCB: radiocarpal bone; UCB: ulnar carpal bone; RF: radial facet; IF: intermediate facet; UF: ulnar facet.

Vet-ebooks.com

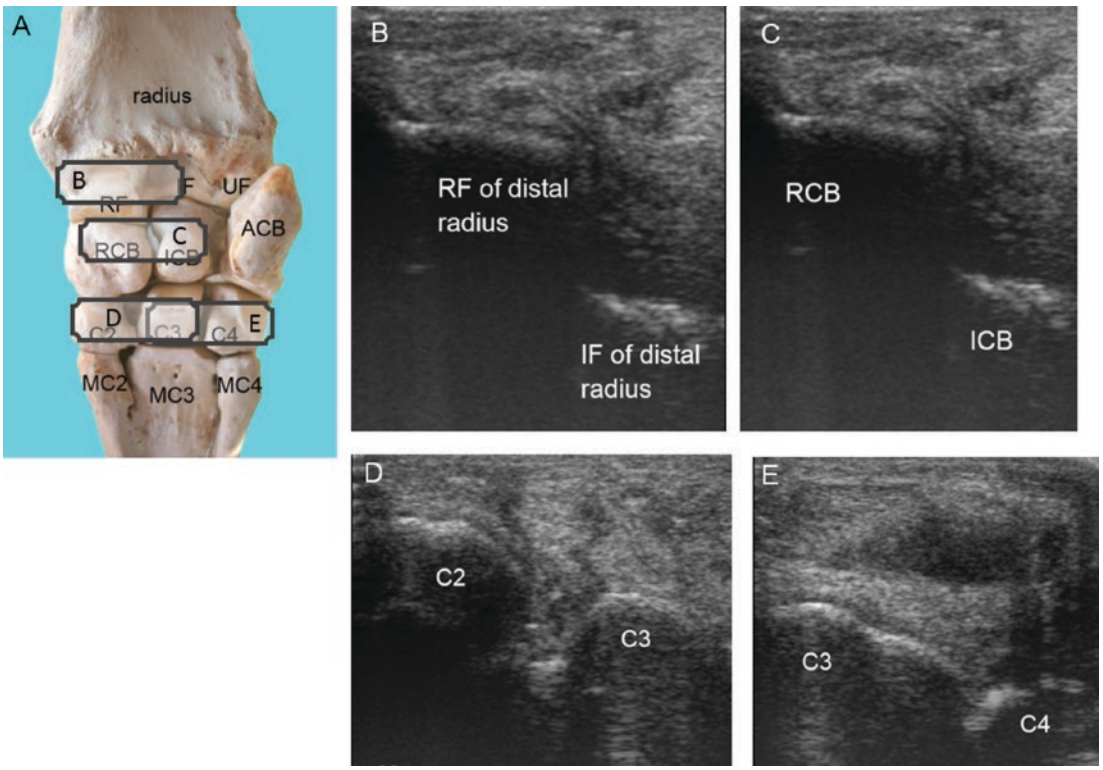


Figure 4.11 Transverse evaluation of palmar carpus illustrating the palmar surface of the carpal bones and joint spaces. (A) Anatomical specimen indicating transducer placement. (B, C, D, and E) Transverse images of the palmar aspect of the right carpus showing the hyperechoic palmar surfaces of the carpal bones and the palmar aspect of the carpal joint spaces. Medial is to the left. ACB: accessory carpal bone; ACJ: antebrachiocarpal joint; ICB: intermediate carpal bone; MCJ: middle carpal joint; RCB: radiocarpal bone; UCB: ulnar carpal bone; RF: radial facet; IF: intermediate facet; UF: ulnar facet.

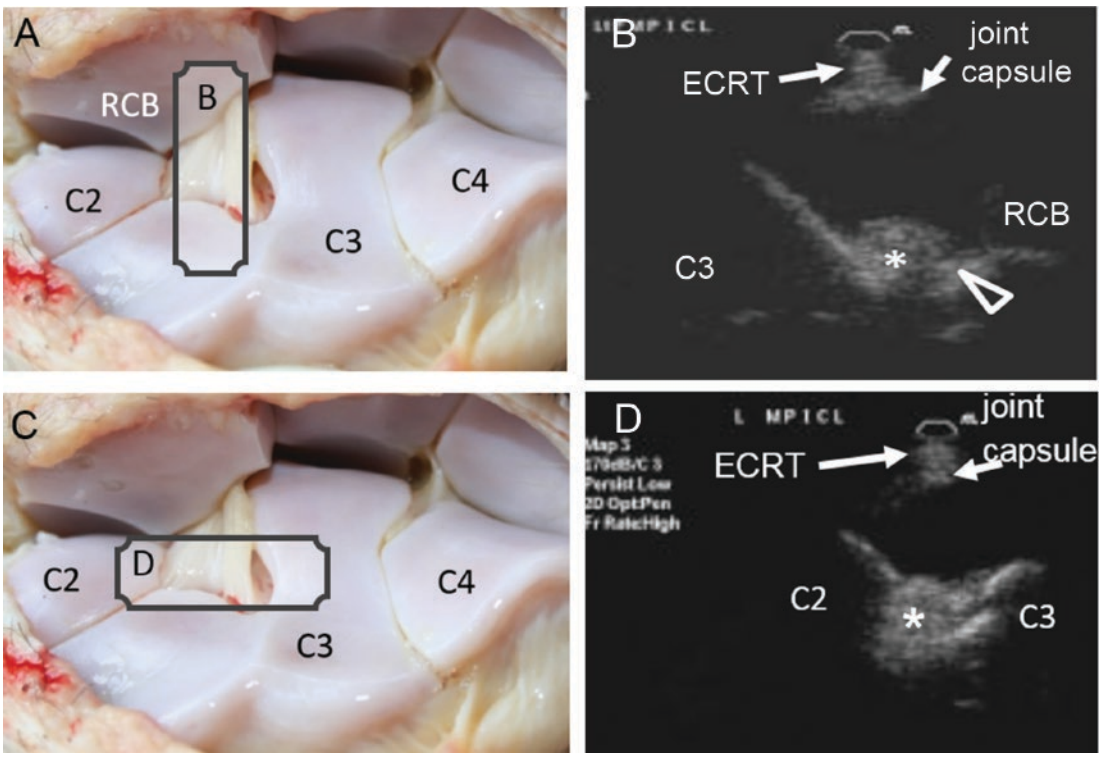


Figure 4.12 Postmortem and ultrasonographic images illustrating the medial palmar intercarpal ligament. (A and C) Anatomical specimens indicating transducer placement. (B) Sagittal and (D) transverse images of the medial palmar intercarpal ligament (MPICL) (*); these images were obtained with the carpus in flexion, and a 7.5 MHz small footprint transducer placed over the ECRT, enabling visualization of the deep aspect of the middle carpal joint through the tendon; arrow head: mirror image artifact of the MPICL. (B) Proximal is to the right. (C and D) Medial is to the left. C2: second carpal bone; C3: third carpal bone; ECRT: extensor carpi radialis tendon; RCB: radiocarpal bone. (*Source*: Parts B and D – Adapted from Driver, E.J. et al. (2004). Reproduced with permission of John Wiley & Sons Ltd.).

Vet-ebooks.com

ACJ and CMCJ of a 4-day-old foal normal cadaver carpus for purposes of extending the joint capsule to illustrate carpal joint effusion ultrasonographically.

Ultrasonographic Abnormalities

Ultrasonographically, pathology can be suspected when the normal ultrasonographic anatomy is not appreciated. Comparison with the opposite limb is encouraged to compare between the pathological limb and the normal limb. Be aware, however, that the contralateral limb may itself have ultrasonographically visible pathology, particularly since some injuries may occur simultaneously bilaterally. See Figures 4.14, 4.15, 4.16, 4.17, 4.18, 4.19, 4.20, 4.21, 4.22, 4.23, 4.24, 4.25, 4.26, 4.27, 4.28, 4.29, and 4.30.

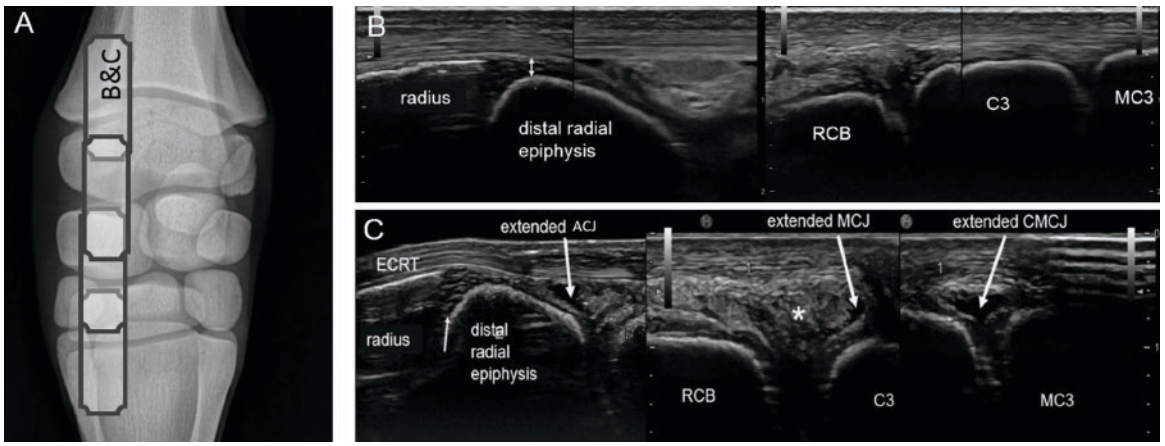


Figure 4.13 Normal neonate dorsal carpus illustrating normal degree of incomplete cartilage ossification. (A) Dorsopalmar radiograph indicating transducer placement. (B) Longitudinal composite split screen image of the dorsum of the medial aspect of the carpus of a normal 4-day-old foal, with a skeletal ossification index Grade 4 [1]. Note the cartilage that still needs to ossify (double headed arrow) and the rounded edges of the carpal bones. (C) Longitudinal composite split screen scan of the dorsum of a 4-day-old foal normal cadaver carpus into which 100 ml of saline was injected into the ACJ and CMCJ for purposes of extending the joint capsule to illustrate carpal joint effusion ultrasonographically. Note the distension of all three joints by anechoic fluid (arrows) with hyperechoic synovium suspended within (*). Proximal is to the left. ACJ: antebracheocarpal joint; CMCJ: carpometacarpal joint; C3: third carpal bone; MC3: third metacarpal bone; MCJ: middle carpal joint; RCB: radial carpal bone.

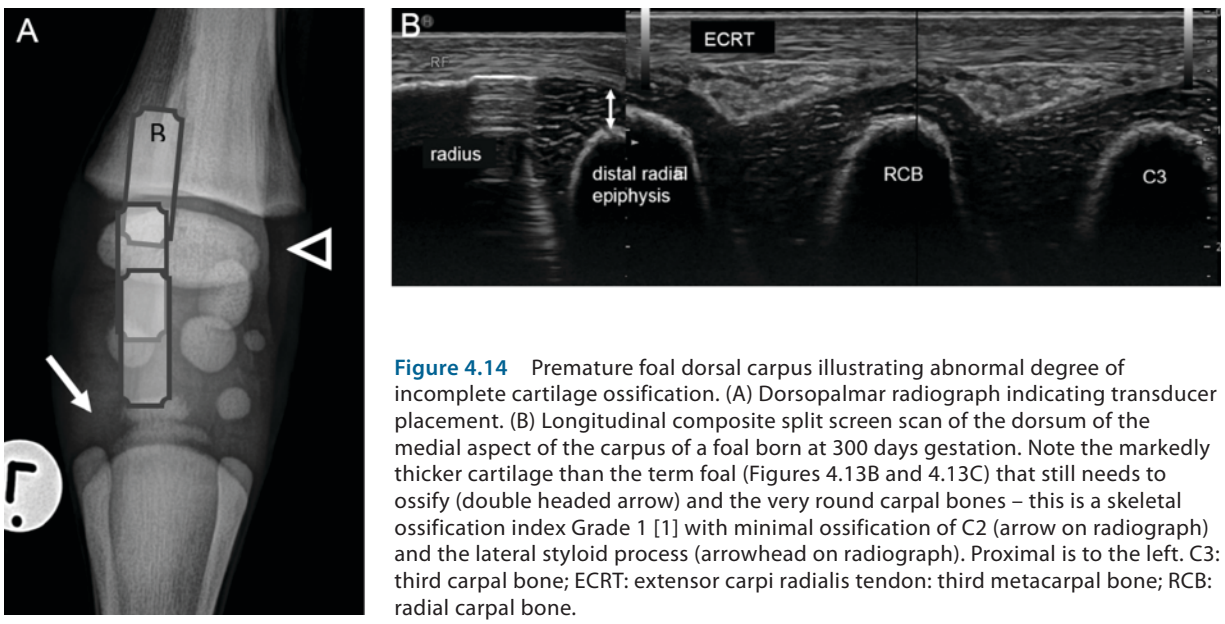


Figure 4.14 Premature foal dorsal carpus illustrating abnormal degree of incomplete cartilage ossification. (A) Dorsopalmar radiograph indicating transducer placement. (B) Longitudinal composite split screen scan of the dorsum of the medial aspect of the carpus of a foal born at 300 days gestation. Note the markedly thicker cartilage than the term foal (Figures 4.13B and 4.13C) that still needs to ossify (double headed arrow) and the very round carpal bones – this is a skeletal ossification index Grade 1 [1] with minimal ossification of C2 (arrow on radiograph) and the lateral styloid process (arrowhead on radiograph). Proximal is to the left. C3: third carpal bone; ECRT: extensor carpi radialis tendon: third metacarpal bone; RCB: radial carpal bone.

Vet-ebooks.com

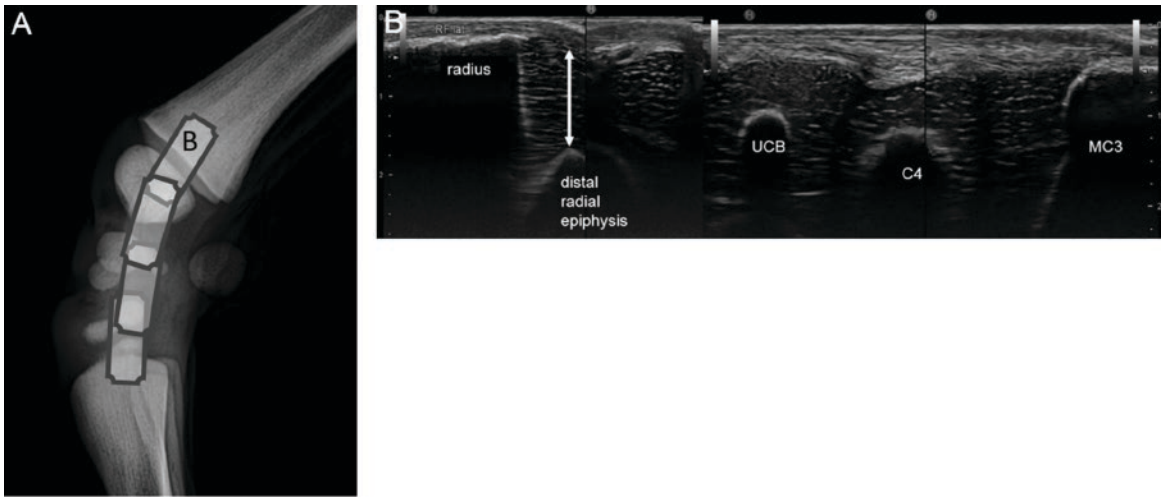


Figure 4.15 Premature foal lateral carpus illustrating abnormal degree of incomplete cartilage ossification. (A) Flexed lateromedial radiograph indicating transducer placement. (B) Longitudinal composite split screen scan of the lateral aspect of the carpus of a foal born at 300 days gestation. Note the absence of the lateral styloid process ultrasonographically seen as a cartilage template that still needs to ossify (double headed arrow) and the small very rounded carpal bones. Proximal is to the left. C4: fourth carpal bone; MC3: third metacarpal bone; UCB: ulnar carpal bone.

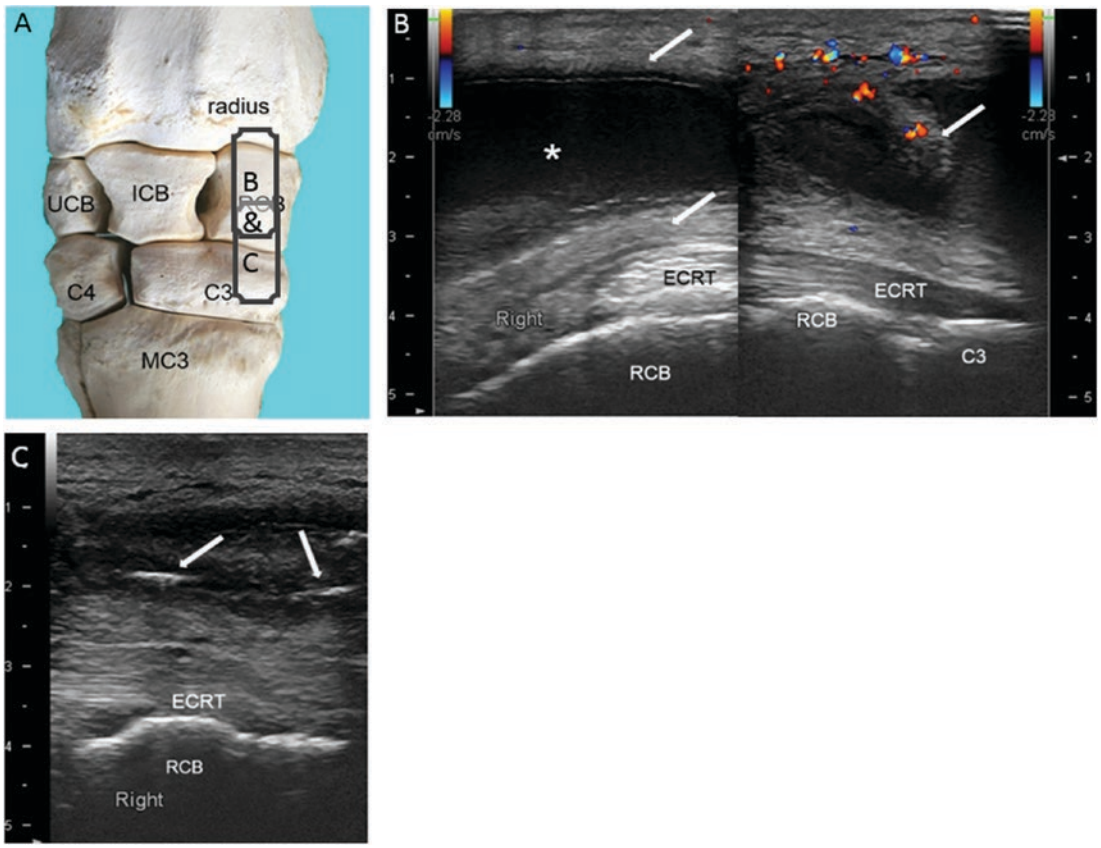


Figure 4.16 Abscess dorsal carpus. (A) Anatomical specimen indicating transducer placement. (B) Longitudinal split screen scan of the dorsal right fore carpus of a 24-year-old Thoroughbred gelding with a history of banging the stable door with his front legs and subsequent chronic thickening of both dorsal carpi. The horse presented with a temperature, and a hot painful swelling on the dorsal right carpus. (B) Note the hypoechoic (*) well-encapsulated (proximal two arrows) abscess dorsal to the ECRT. The distal image of B's color flow Doppler image shows the vascularity of the capsule as well as that of a hyperechoic septum extending into the abscess lumen (distal arrow). Drainage of the abscess revealed a thick yellow purulent fluid. It was flushed with sterile saline and a subsequent image obtained. (C) This longitudinal scan shows collapse of the fluid pocket and residual gas hyperechogenicities (arrows). A pure growth of *Strep. Epidermidis* was cultured. Proximal is to the left. C3: third carpal bone; ECRT: extensor carpi radialis tendon; RCB: radiocarpal bone.

Vet-ebooks.com

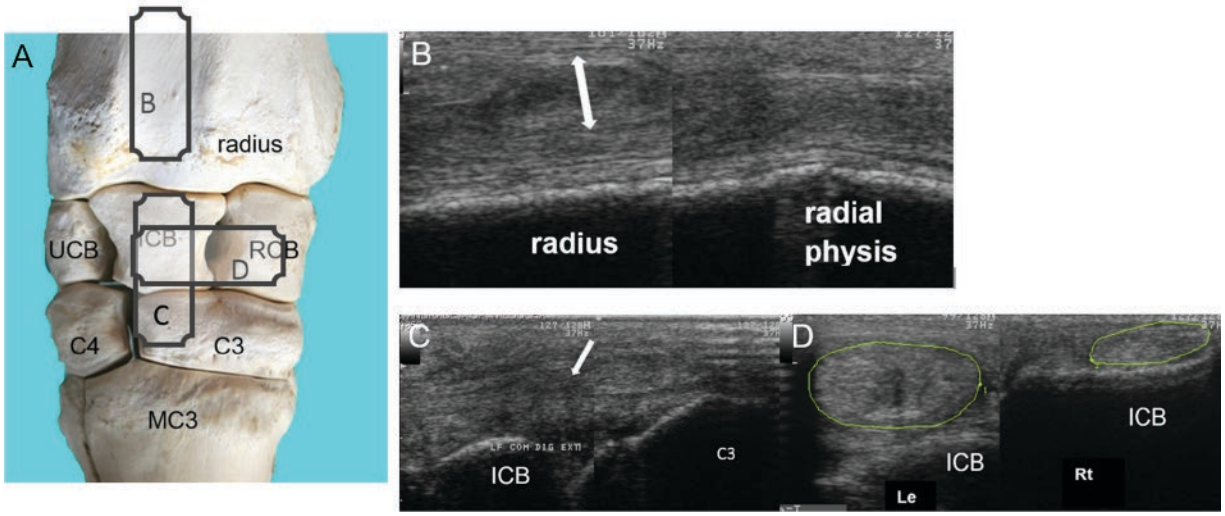


Figure 4.17 Common digital extensor tendon (CDET) rupture. (A) Anatomical specimen indicating transducer placement. Longitudinal (B and C) and transverse (D) images of the dorsal aspect of the left carpus showing partial rupture of the CDE tendon. (B) Split screen image with mildly thickened subcutaneous tissues and marked disruption of the tendon fibers of the CDET (double headed arrow) with focal hypoechoic areas within. Proximal is to the left. (C) Split screen composite image with mildly thickened subcutaneous tissues and marked disruption of the tendon fibers of the CDE (arrow) with hypoechoic striations within and mild amount of hypoechoic fluid within the tendon sheath. Proximal is to the left. (D) Split screen composite image of abnormal left and comparative normal right carpus showing marked enlargement and inhomogeneously hypoechoic left CDE tendon and increased distance between the skin surface and underlying bone. Medial of the left carpus is to the right. ICB: intermediate carpal bone; RCB: radiocarpal bone; UCB: ulnar carpal bone.

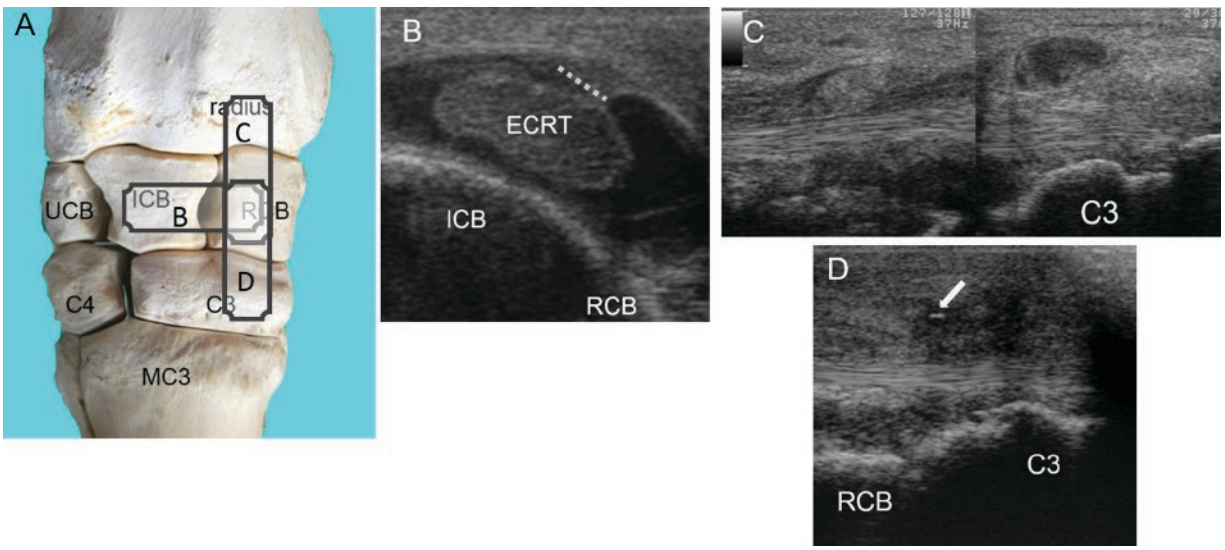


Figure 4.18 Septic extensor carpi radialis tenosynovitis. (A) Anatomical specimen indicating transducer placement. Transverse (B) and longitudinal (C composite and D) images of the dorsal aspect of the carpus showing a septic extensor carpi radialis (ECR) tenosynovitis as the result of a penetrating foreign body. (B) Marked distension of the ECR sheath with anechoic as well as hypoechoic fluid therein with a few criss-crossing hyperechoic fibrin-like bands. The tendon itself appears slightly swollen and more hypoechoic than normal. Note the widened hypoechoic mesotendon (stippled line). Medial is to the right. (C) Marked distension of the ECR sheath with hypoechoic and hyperechoic fluid therein with a few hyperechoic fibrin-like bands and formation of some inhomogeneous pockets of fluid. The ECR tendon is slightly swollen with some decrease in fiber alignment. Proximal is to the left. (D) Thickened subcutaneous tissues with a focal poorly marginated hypoechoic area with a hyperechoic structure (arrow) within this with mild acoustic shadowing distally, consistent with a foreign body. The ECRT periphery is irregular. Note the irregular cortical margin of C3. Proximal is to the left. ICB: intermediate carpal bone; RCB: radiocarpal bone; UCB: ulnar carpal bone.

Vet-ebooks.com

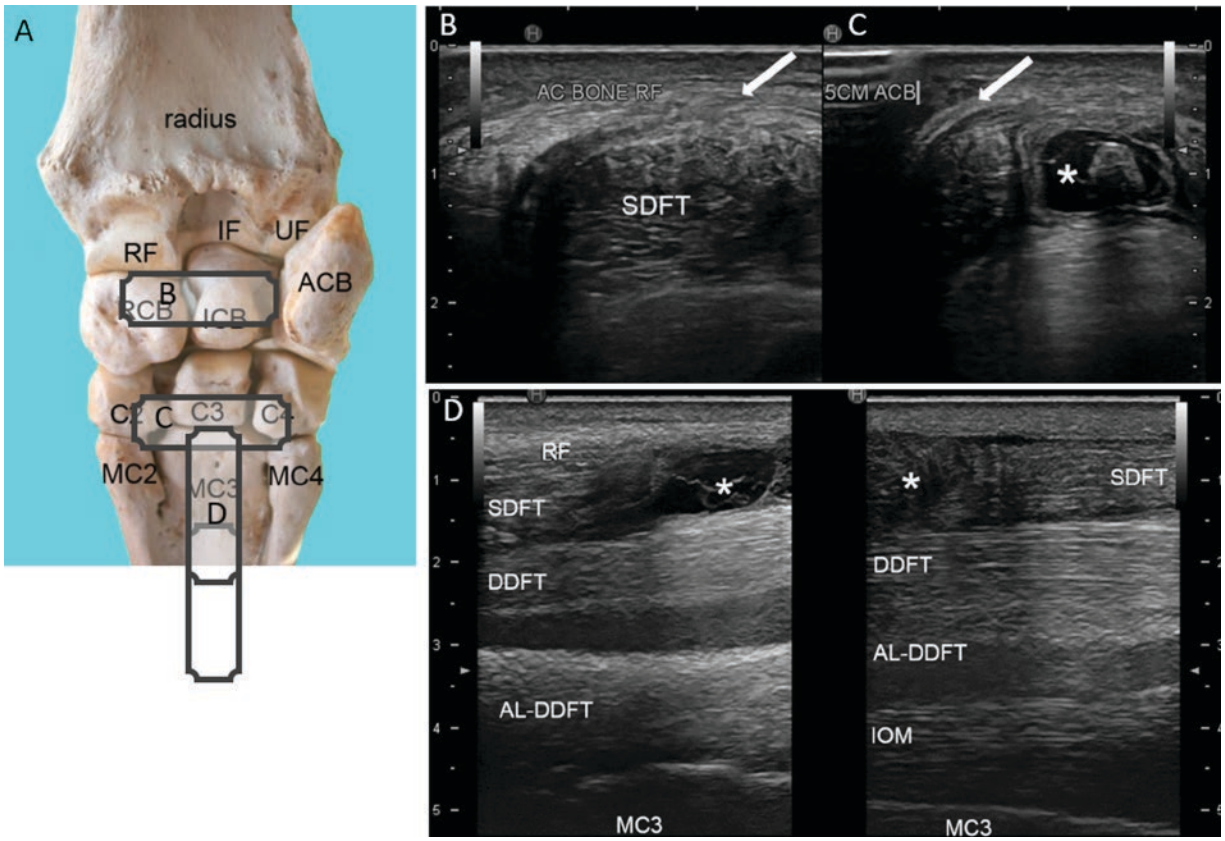


Figure 4.19 Superficial digital flexor tendon rupture. (A) Anatomical specimen indicating transducer placement. (B and C) Transverse scan of the carpal canal at (B), the level of the ACB, and (C) at 5 cm distal to the ACB; note the relative hypoechoic appearance of the SDFT in (B) and the absence of the SDFT in (C) with only anechoic fluid and a central hyperechoic structure, likely fibrin within (*). The arrow indicates the carpal retinaculum. Lateral is to the left. (D) Longitudinal composite split screen scan of the proximal flexor tendons showing a total rupture of the SDFT with a 5 cm anechoic gap with some hyperechoic fibrin strands within (*). The fibers at both ends of the SDFT are hypoechoic and appear to have a mild wavy appearance. Proximal is to the left. ACB: accessory carpal bone; AL-DDFT: accessory ligament to the deep digital flexor tendon; DDFT: deep digital flexor tendon; IOM: interosseous medius; MC3: third metacarpal bone; RF: right fore; SDFT: superficial digital flexor tendon.

Vet-ebooks.com

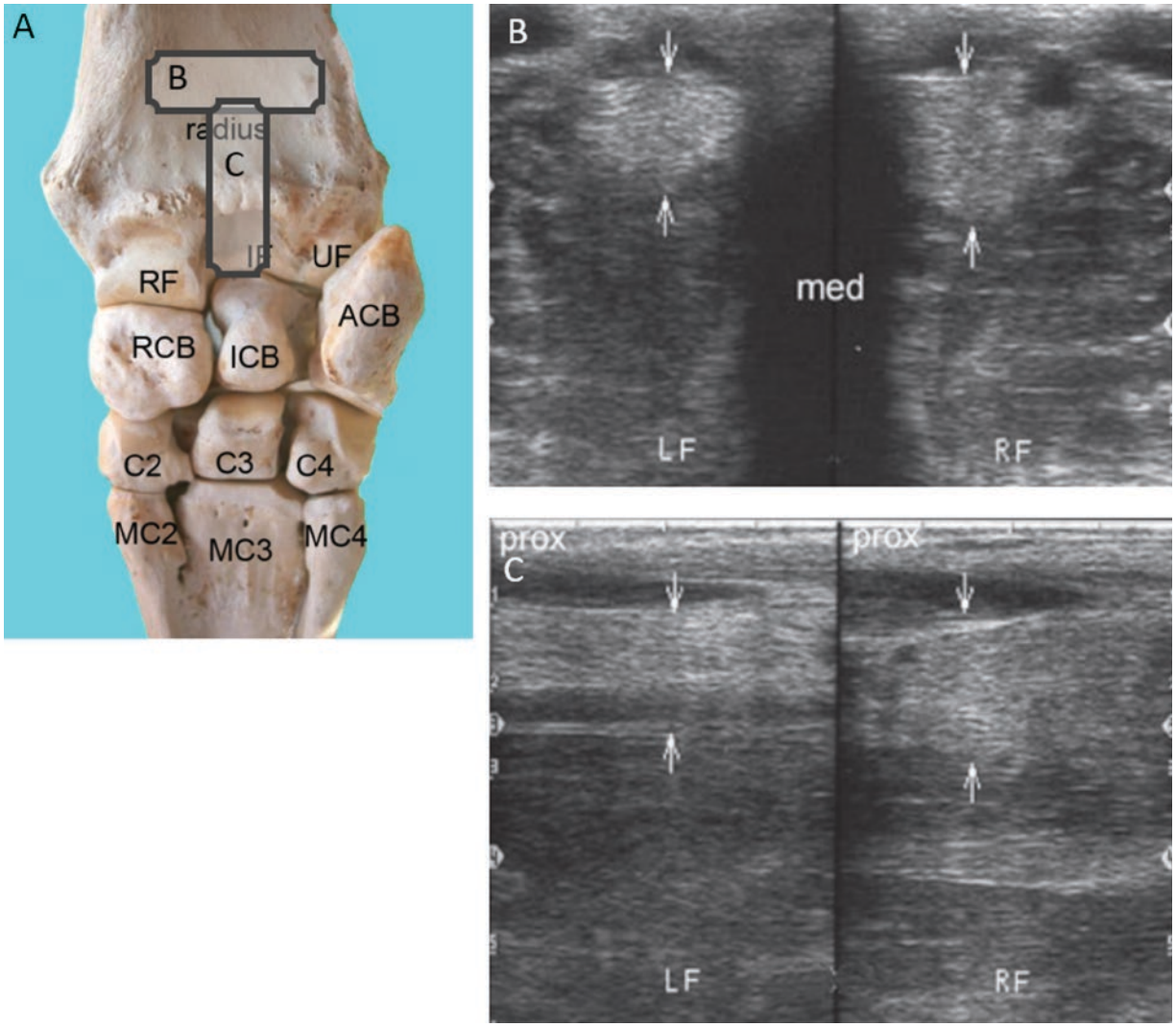


Figure 4.20 Desmitis of the right accessory ligament of the superficial digital flexor tendon (AL-SDFT). (A) Anatomical specimen indicating transducer placement. (B) Transverse images of the AL-SDFT of the left (LF) and right fore limbs (RF). An injury to the RF AL-SDFT at level 2A (~9–11 cm proximal to the accessory carpal bone (ACB)) is present (arrows), illustrating enlargement and decreased echogenicity; medial sides of each limb marked (med). (C) Longitudinal image of the enlarged and inhomogenously hypoechoic AL-SDFT (arrows). ICB: intermediate carpal bone; RCB: radiocarpal bone; UCB: ulnar carpal bone; RF: radial facet; IF: intermediate facet; UF: ulnar facet. (*Source*: Parts B and C – Adapted from Jorgensen, J.S. et al. (2010) [3] Reproduced with permission of John Wiley & Sons Ltd.).

Vet-ebooks.com

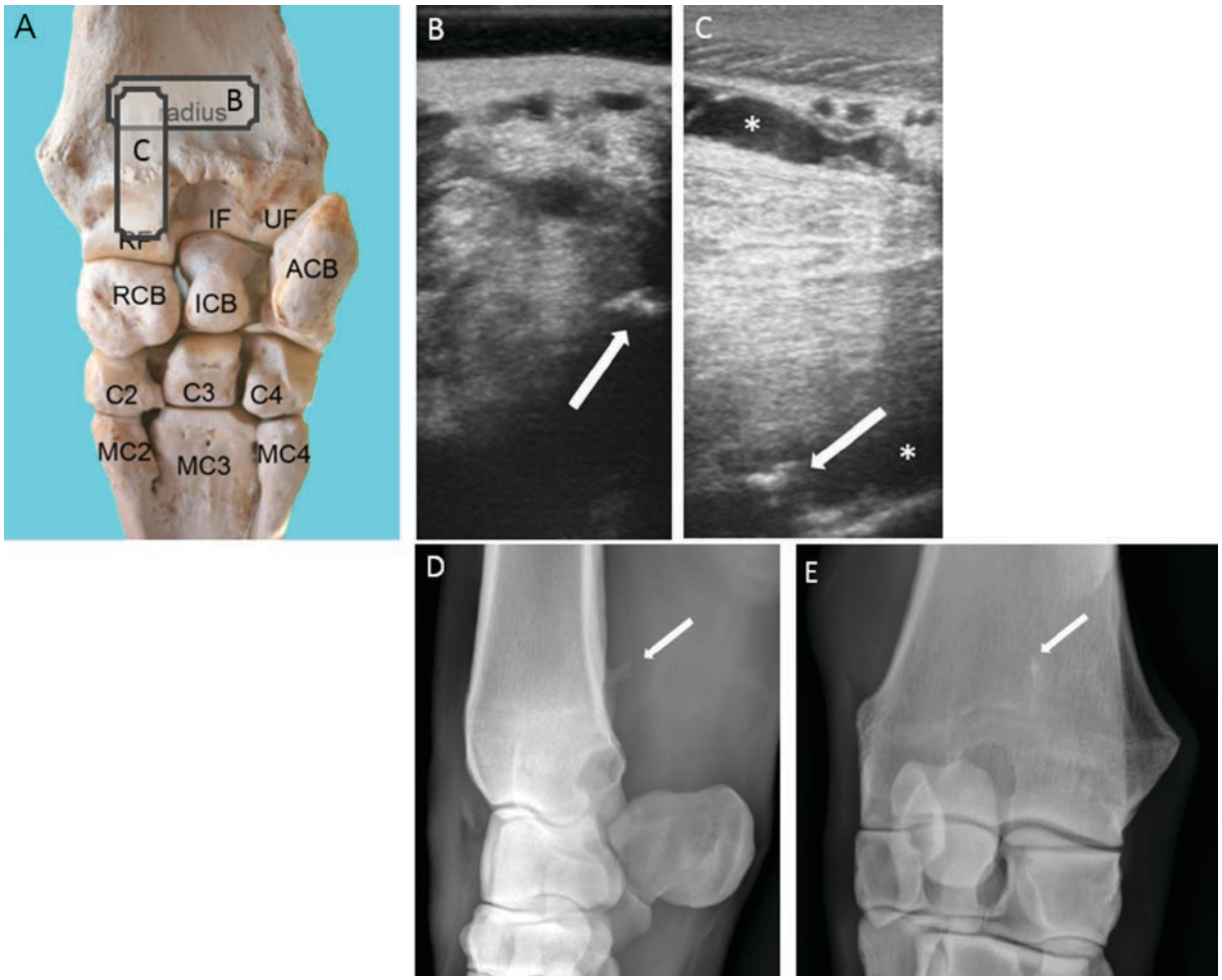


Figure 4.21 (A) Osteochondroma distocaudomedial radius. (B) Transverse image of the distal radial metaphysis. Note the hyperechoic acoustic shadow-casting structure in the depth of the field (arrow). (C) Longitudinal image distal metaphysis radius. The irregular hyperechoic acoustic shadow-casting structure (arrow) is in the depth nearly adjacent to the radius. Note the anechoic fluid with a few hyperechoic fibrin-like strands in the near and far field within the carpal canal (*). Proximal is to the left. (D) Lateromedial radiograph of the carpus. Note the mineralized spike extending from the caudodistal radius (arrow). There is also marked soft tissue swelling associated with carpal canal effusion. (E) Dorsopalmar radiograph of the same case: note the focal mineralized opacity superimposed over the caudodistal radius slightly medially. There is also marked soft tissue swelling associated with carpal canal effusion. ACB: accessory carpal bone; ICB: intermediate carpal bone; RCB: radiocarpal bone; UCB: ulnar carpal bone; RF: radial facet; IF: intermediate facet; UF: ulnar facet; SDFT: superficial digital flexor tendon; DDFT: deep digital flexor tendon. (Acknowledged with thanks Drs Baker and McVeigh and Associates. Summerveld, South Africa).

Vet-ebooks.com

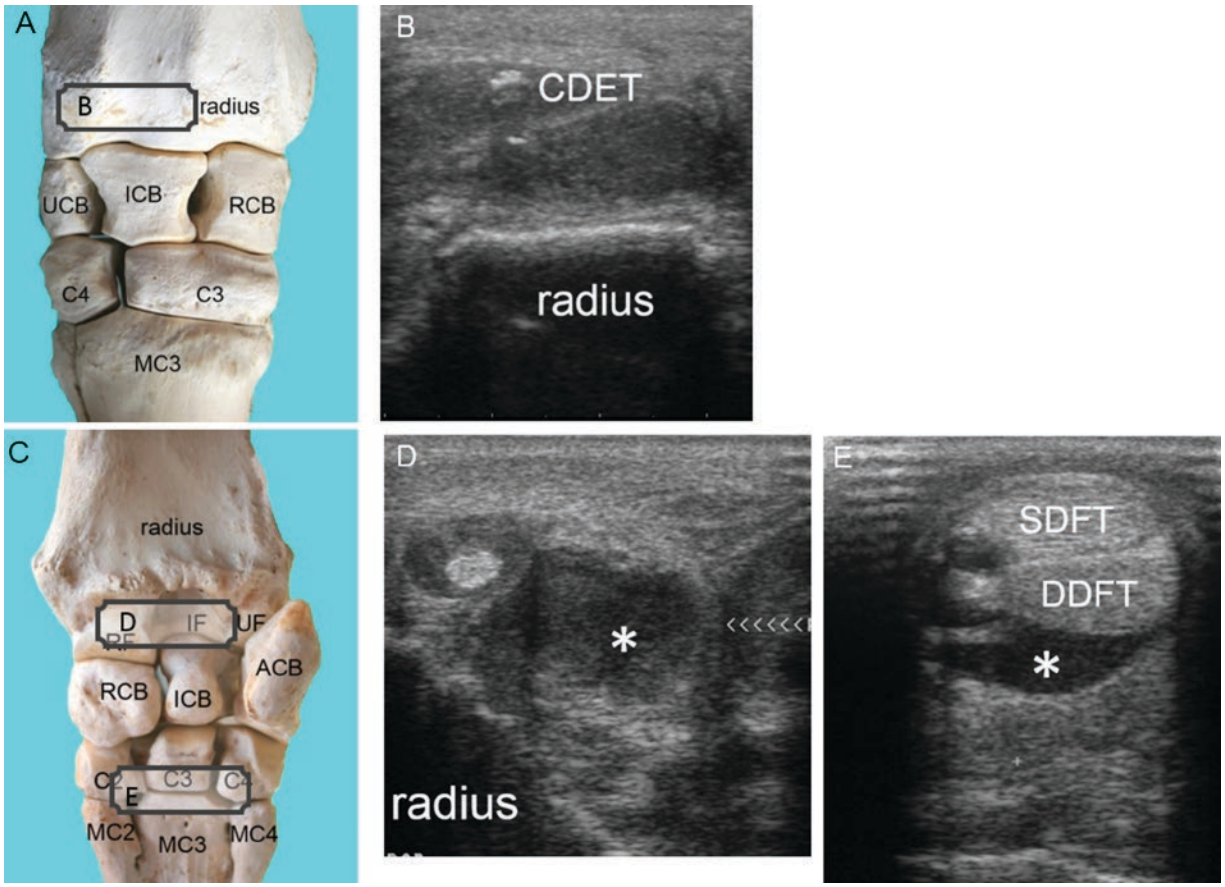


Figure 4.22 Pericarpal abscessation, septic common digital extensor tendon (CDET), and carpal canal tenosynovitis. (A) and (C) Anatomical specimens indicating transducer placement. (B) Transverse image of right dorsal distal radius area with marked distension of the CDET sheath with hypoechoic speckled fluid. Note the hyperechoic specks casting dirty acoustic shadows – likely gas within the most non-dependant part of the sheath. Medial is to the left. (D) Transverse image of the carpal canal: hyperechoic fluid within right carpal sheath at level of distal radius (*). Normal anatomic structures poorly visible. Medial is to the left. (E) Transverse image of right carpal canal with distension with hypoechoic speckled fluid at level of proximal metacarpus 3 (*). Medial is to the left. Note the oval hypoechoic median artery to the left of the image. DDFT: deep digital flexor tendon; SDFT: superficial digital flexor tendon.

Vet-ebooks.com

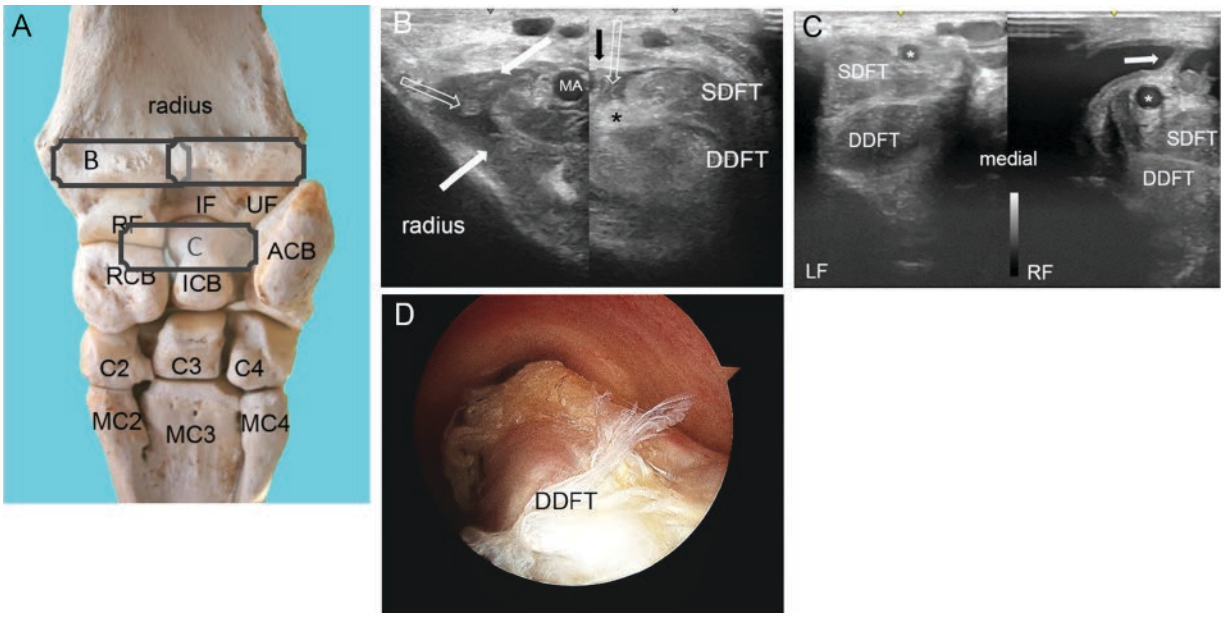


Figure 4.23 Septic carpal canal and deep digital flexor tendonitis. (A) Anatomical specimen indicating transducer placement. (B) Transverse composite split screen scan of the carpal sheath area just proximal to the accessory carpal bone (the 2 images are not quite on the same plane). There is a moderate amount of inhomogenously hypoechoic carpal sheath effusion with hyperechoic strands of fibrin-like material within (open white arrows); the synovial membrane is also thickened (closed arrows). The DDFT has an indistinct hypoechoic area in its center extending caudally; note the increased visibility of the attachment of the AL-SDFT (*) due to the presence of the effusion; carpal retinaculum: black arrow; medial is to the left. (C) comparative transverse scan between the normal LF and abnormal RF carpal sheath at the level of the accessory carpal bone after antibiotic therapy; note the thickening of the synovial membrane and the mesotendon of the RF carpal sheath (arrow), visible as a result of the surrounding anechoic fluid; note also the relatively larger size of the RF MA (*); medial is to the right on the LF and to the left on the RF. (D) Tenoscopic image of the severely damaged DDFT as the result of an axial chip fracture of the accessory carpal bone, subsequently resulting in a septic tenosynovitis of the carpal sheath. AL-SDFT: accessory ligament to the superficial digital flexor tendon; DDFT: deep digital flexor tendon; LF: left fore; MA: median artery; RF: right fore. (*Source*: Image (B) courtesy of Dr T Ovendale, Equine-Librium College, Plettenberg Bay, South Africa; images (C) and (D) courtesy of Dr A Gray, Vetscape Referrals – Equine. Paarl, South Africa).

Superficial Soft Tissues

Skin may be thicker than normal due to fibrosis (hyperechoic), granulomatous (hypoechoic), or neoplastic (mixed echogenicity) tissue, e.g., sarcoids or squamous cell carcinoma. Subcutanous tissue may be deeper than normal due to edema, hemorrhage, or contusion which often gives a heterogeneous hypoechoic appearance.

Tendons and Ligaments

Inflammation or partial tearing of these structures is seen as enlargement with loss of echogenicity and loss of normal fiber alignment. Complete disruption of the structure is seen as a complete loss of anatomic detail in the affected area with intervening heterogeneous echogenicities consistent with the stage of the condition, whether acute, subacute, or chronic. Healed tendons/ligaments are usually hyperechoic and fiber alignment is usually haphazard.

Tendon Sheaths, Bursae, Joint Spaces

Usually there is little to no free fluid within tendon sheaths and bursae, and little in the joints, and if present, as in cases of stable edema of the carpal canal, is anechoic in nature. If fluid is excessive and anechoic it is usually a transudate and unlikely to be of major concern. If fluid is excessive and hypo- to hyperchoic, increased cellularity and increased protein content is likely, and a modified transudate or exudate should be suspected. The latter is often indicative of a septic process. If there are also very hyperechoic multifocal single specks that tend to move non-dependently within the fluid, the presence of gas is likely and indicative of an open wound and/or gas-producing bacteria.

Bones

If the normal smooth hyperechoic cortex is disrupted, a fracture should be considered. New bone can be seen as irregular hyperechoic extensions of the subchondral

Vet-ebooks.com

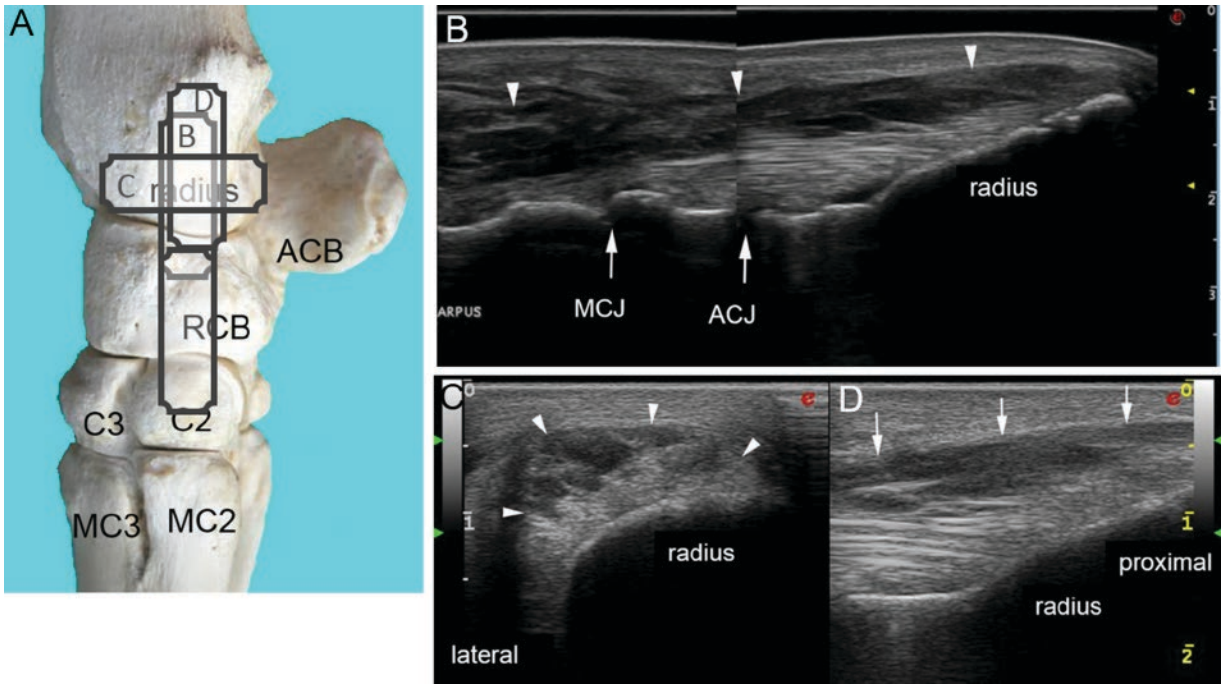


Figure 4.24 Medial collateral ligament strain/desmitis. (A) Anatomical specimen indicating transducer placement. (B) Composite split screen longitudinal image of a severe medial collateral ligament (MCL) injury in an adult horse that developed acute lameness and carpal swelling after a fall. There is diffuse tearing of the superficial portion of the MCL (arrowheads) as it extends over the antebrachiocarpal joint (ACJ) and middle carpal joint (MCJ). Proximal is to the right. (C and D) Severe injury of the MCL origin at the radius in a 15-year-old Quarter Horse cutting horse of unknown cause. There is a large, nearly anechoic area involving the abaxial half of the ligament on the transverse image (arrowheads) with corresponding fiber disruption visible on the longitudinal image (arrows); lateral is to the left on the transverse image. Proximal is to the right on the longitudinal image. (*Source*: Images (B), (C), and (D) courtesy of Prof Mary Beth Whitcomb, School of Veterinary Medicine, University of California, Davis, CA 95616, USA.)

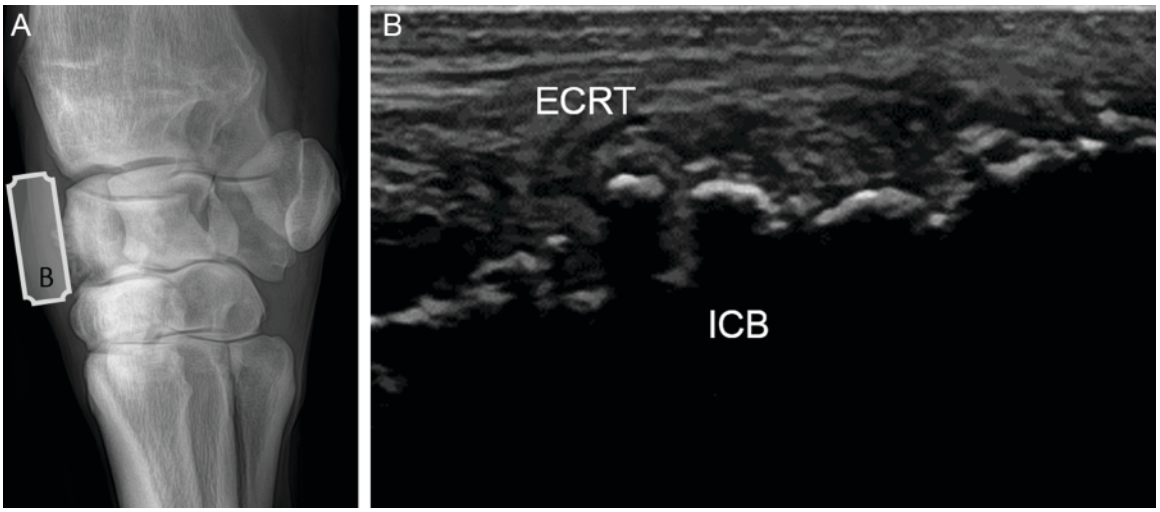


Figure 4.25 Periosteal / enthesophytic new bone formation. (A) Dorsolateral-palmaromedial oblique radiographic view indicating transducer placement. (B) Longitudinal image of the dorsal aspect of the ICB showing an irregular hyperechoic surface indicative of the periosteal / enthesophytic new bone as seen radiographically. Proximal is to the left. ECRT: extensor carpi radialis tendon; ICB: intermediate carpal bone.

Vet-ebooks.com

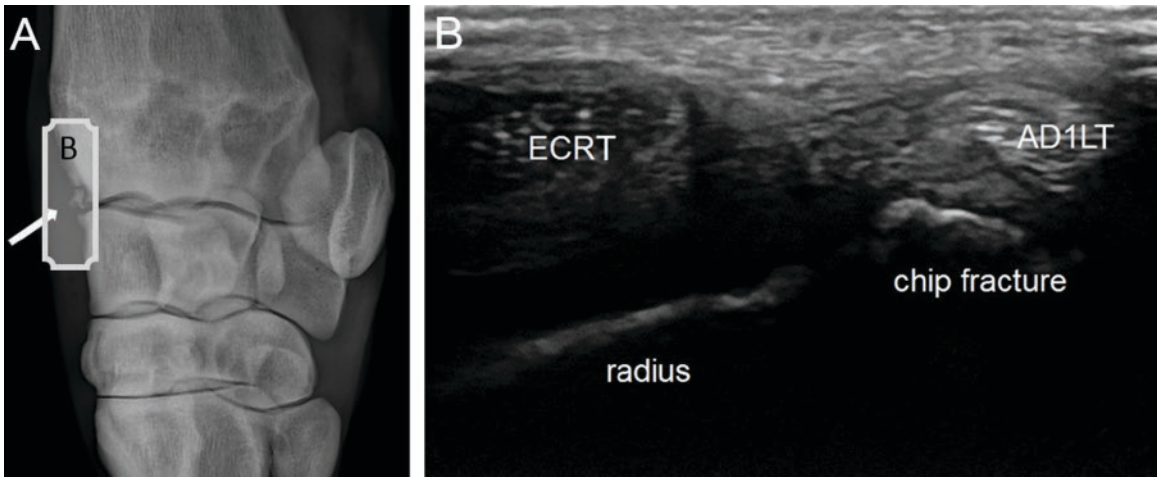


Figure 4.26 Chip fracture distal craniomedial radius. (A) Craniolateral-caudomedial oblique radiographic view indicating transducer placement, illustrating an irregularly marginated chip fracture off the distal craniomedial aspect of the radius as well as two associated osteophytes. (B) Transverse ultrasonographic image of the distal craniomedial aspect of the radius, illustrating the hypoechoic gap between the distal radius parent bone and a chip fracture; the latter lies immediately caudal to the tendon of the abductor digiti 1 longus; craniomedial is to the left. AD1LT: abductor digiti 1 longus tendon; ECRT: extensor carpi radialis tendon.

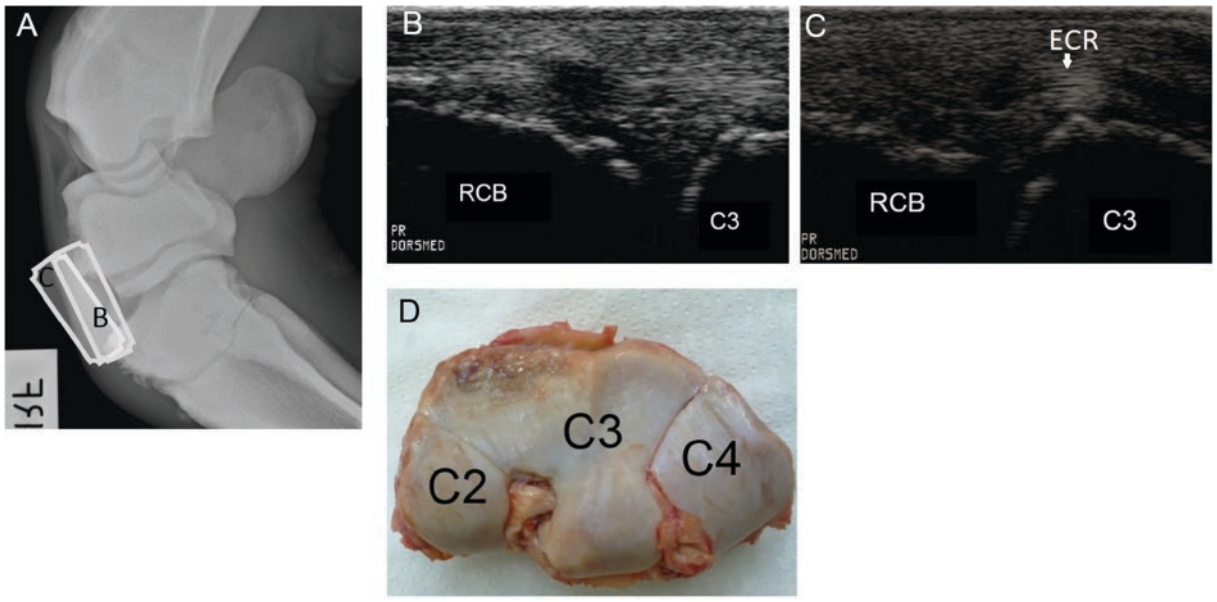


Figure 4.27 Osteochondral fragmentation. (A) Lateromedial flexed radiographic view indicating transducer placement. (B) Longitudinal image of the dorsum of the carpus with marked irregular cortical margins of the radiocarpal bone (RCB), consistent with chip fracture/osteophyte, and (C) Longitudinal image of the dorsum of the carpus with mildly irregular proximodorsal margin of C3. Note the extensor carpi radialis (ECR) superficially with focal loss of echogenicity due to off-incidence artifact. Proximal is to the left. (D) Macerated postmortem specimen of proximal joint surfaces of C2, C3, and C4. Note the marked articular cartilage destruction of dorsoproximal C3. Medial is to the left. C2, C3, and C4: respectively second, third, and fourth carpal bones; RCB: radio carpal bone.

Vet-ebooks.com

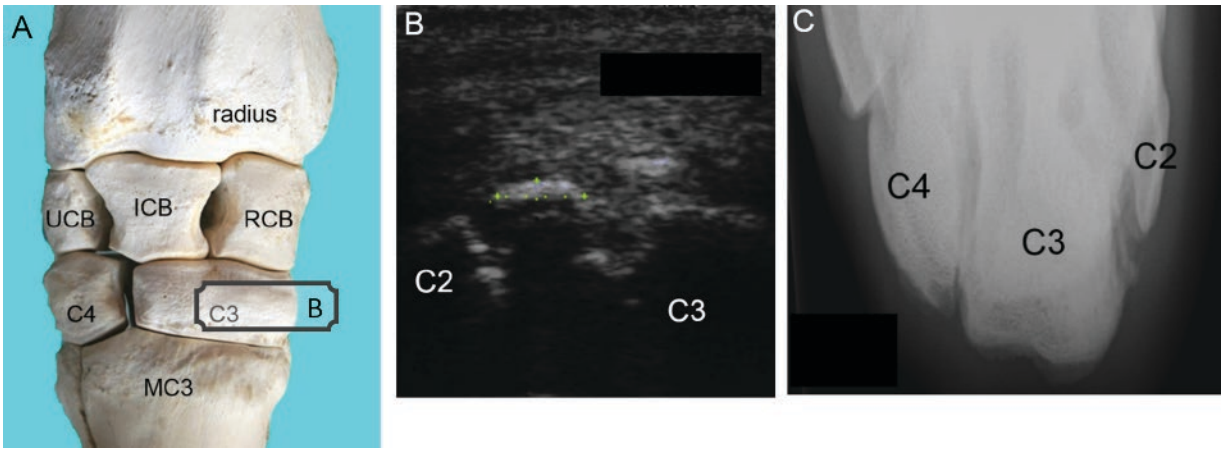


Figure 4.28 Sagittal slab fracture of C3. (A) Anatomical specimen indicating transducer placement. (B) Transverse image of the dorsum of C3 and C2 (transducer positioned more obliquely dorsomedially than depicted in guide image). A 5.4 mm wide hyperechoic structure with distal acoustic shadowing is depicted separate from and slightly dorsal to the parent C3 with a few smaller hyperechoic structures in the vicinity. Medial is to the left. (C) D35ºPrDDiO radiographic view of the carpus, showing a focal area of multiple fragments off the medial aspect of the radial facet of C3. C2, C3, C4: second, third and fourth carpal bones, respectively.

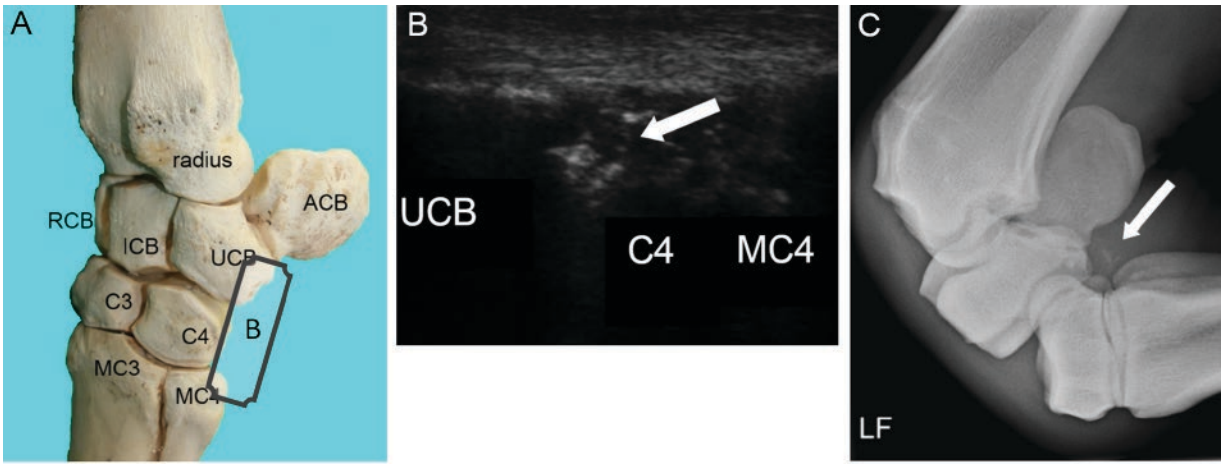


Figure 4.29 Multiple palmar chip fractures from the palmar distal aspects of the proximal row of carpal bones and/or the palmar proximal aspect of the distal row of carpal bones. (A) Anatomical specimen indicating transducer placement. (B) Longitudinal image, palmarolateral ulnar carpal bone (UCB), C4 and fourth metacarpal bone (MC4). Overlying the slightly recessed C4 there are multiple irregular small hyperechoic fragments consistent with small bony chip fractures (arrow). Proximal is to the left. (C) Flexed lateromedial view of the carpus illustrating several mineralized fragments in the palmar recess of the middle carpal joint (arrow). ACB: accessory carpal bone; ICB: intermediate carpal bone; RCB: radiocarpal bone; UCB: ulnar carpal bone.

bone (osteophytic), or source or implantations of ligaments, tendons, or joint capsules (enthesophytic), or on the bone surface (periosteal). Hypo- to anechoic fluid accumulation between the periosteum and cortical bone is highly indicative of osteomyelitis.

Joint Surfaces

Although challenging, and more clearly visualized by means of computed tomography, specific MRI sequences, contrast arthrography, with arthroscopy being the gold standard, the keen ultrasonographer may be able to evaluate the joint surface for irregular thinned cartilage and irregular subchondral bone, indicative of possible osteoarthritis or developmental orthopedic disease.

Surgery

Ultrasound-guided surgical procedures of the carpus have been described, such as removal of osteochondral fragments of carpal bones and foreign bodies and is perhaps an underutilized surgical tool.

Vet-ebooks.com

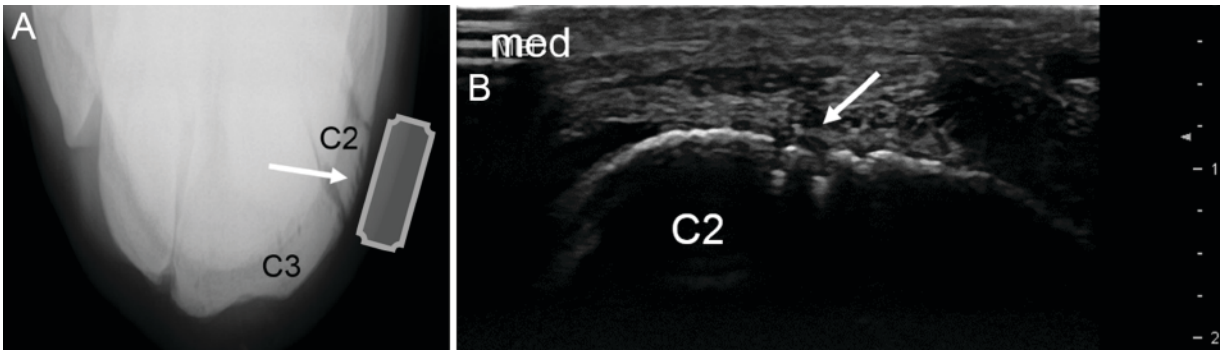


Figure 4.30 Osseous cyst-like lesions C2. (A) D35ºPrDDiO radiographic view of the carpus of a 19-year-old Thoroughbred mare presented for a right fore limb lameness, which was isolated to the carpus, indicating transducer placement. (B) Transverse image of the dorsum of C2, illustrating several cortical interruptions (arrow); radiographically these appear to be several osseous cyst-like lesions. Medial is to the left of the image. C2: second carpal bone; C3: third carpal bone.

Recommended Reading

Denoix, J.-M. and Yousfi, S. (1996). Spontaneous injury of the accessory ligament of the superficial digital flexor tendon (proximal check ligament): A new ultrasonographic diagnosis. *Journal of Equine Veterinary Science* 16: 191–194.

Denoix, J.M. and Busoni, V. (1999). Ultrasonographic anatomy of the accessory ligament of the superficial digital flexor tendon in horses. *Equine Veterinary Journal* 31: 186–191.

Desmaizieres, L.M. and Cauvin, E.R. (2005). Carpal collateral ligament desmopathy in three horses. *Veterinary Record* 157: 197–201.

Driver, A.J., Barr, F.J., Fuller, C.J. et al. (2004). Ultrasonography of the medial palmar intercarpal ligament in the Thoroughbred: Technique and normal appearance. *Equine Veterinary Journal* 36: 402–408.

Jorgensen, J.S., Stewart, A.A., Stewart, M.C. et al. (2010). Ultrasonographic examination of the caudal structures of the distal antebrachium in the horse. *Equine Veterinary Education* 22: 146–155.

Jorgensen, J.S., Genovese, R.L., Dörte D. et al. (2015). Musculoskeletal lesions and lameness in 121 horses with carpal sheath effusion (1999–2010). *Veterinary Radiology Ultrasound* 56: 307–316.

Minshall, G.J. and Wright, I.M. (2012). Tenosynovitis of the carpal sheath of the digital flexor tendons associated with tears of the radial head of the deep digital flexor: Observations in 11 horses *Equine Veterinary Journal* 44: 2 76–80.

Minshall, G.J. and Wright, I.M. (2014). Frontal plane fractures of the accessory carpal bone and implications for the carpal sheath of the digital flexor tendons. *Equine Veterinary Journal* 46: 579–584.

Minshall, G.J. and Wright, I.M. (2015). Diagnosis and treatment of intrathecal tears of the accessory ligament of the superficial digital flexor. *Equine Veterinary Journal* 47: 48–53.

Piccot-Crezollet, C. and Cauvin, E.R. (2005). Treatment of a second carpal bone fracture by removal under ultrasonographic guidance in a horse. *Veterinary Surgery* 34: 662–667

Probst, A., Macher, R., Hinterhofer, C. et al. (2008). Anatomical features of the carpal flexor retinaculum of the horse. *Anatomy, Histology, Embryology* 37: 415–417.

Reef, V.R. (1998). *Equine Diagnostic Ultrasound*. Philadelphia: W.B. Saunders & Co.

Reef, V.R., Whittier, M., and Allam, L.G. (2004). Joint ultrasonography. *Clinical Techniques in Equine Practice* 3: 256–267.

Shields, G.E., Barrett, M.F. and Johnson, S. (2015). How to ultrasound the carpal canal and caudal antebrachium. *Proceedings of the AAEP Annual Convention*, Las Vegas NV, 5–9 December, 439–447.

Smith, M. and Smith, R. (2008). Diagnostic ultrasound of the limb joints, muscle and bone in horses. *In Practice* 30: 152–159.

Tnibar, M., Kaser-Hotz, B., and Auer, J.A. (1993). Ultrasonography of the dorsal and lateral aspects of the equine carpus: Technique and normal appearance. *Veterinary Radiology and Ultrasound* 34: 413–425.

References

1 Adams, R. and Poulos, P. (1988). A skeletal ossification index for neonatal foals. *Veterinary Radiology* 29: 217–222.

2 Driver, A.J., Barr, F.J., Fuller, C.J. et al. (2004). Ultrasonography of the medial palmar intercarpal ligament in the Thoroughbred: Technique and normal appearance. *Equine Veterinary Journal* 36: 402–408.

3 Jorgensen, J.S., Stewart, A.A., Stewart, M.C. et al. (2010). Ultrasonographic examination of the caudal structures of the distal antebrachium in the horse. *Equine Veterinary Education* 22(3): 146–155.

Vet-ebooks.com

5

Ultrasonography of the Elbow and Shoulder

Barbara Riccio

Via Montebello 15, Torino (TO), Italy

Introduction

Ultrasonographic examination of the elbow and shoulder yields information about the soft tissue structures of elbow and shoulder joints, complementing the information that is obtained through radiography and nuclear scintigraphy. These areas have been traditionally difficult to examine properly in the field with radiography, and ultrasonographic examination can be helpful for the practitioner to obtain diagnostic information about conditions related to these areas. An upper limb lameness, a history of trauma, a swelling or local deformation, a hematoma, an abscess, a draining tract, or a lameness localized to the joint are all common indications for ultrasonography of the shoulder and elbow. In cases in which the lameness is localized to the elbow, ultrasonography is considered more sensitive than radiography for detection of early bone remodeling that is usually associated with osteoarthritis. As an ultrasound examination of the shoulder and the elbow is less commonly performed than in other regions, it is recommended to prepare both limbs in order to use the opposite limb for comparison. Sedation is usually not needed in adults, while young animals usually require a low dose of sedation.

Elbow

Preparation and Scanning Technique

Routine skin preparation is used. Diagnostic images can be obtained with high-frequency linear transducers (5–10 MHz), but a convex probe can be useful at the cranial aspect of the elbow to study the distal insertion of the biceps brachii tendon. In cases of ultrasound-guided injections, a micro-convex probe is suitable. A standoff pad is required to improve contact with the lateral aspect of the elbow during examination of the lateral collateral ligament of the elbow joint.

The elbow joint can be scanned from cranial, lateral, and medial approaches. Ultrasonography of the elbow is performed in the weightbearing position, but the evaluation of the medial aspect of the elbow joint is limited in this position. To allow better positioning of the transducer in this area the limb should be pulled forward, but nevertheless medial access in not easy.

A complete sonographic examination of the elbow should involve the lateral and medial collateral ligaments, the triceps brachii tendon, the proximal tendon of the ulnaris lateralis, the distal biceps brachii tendon, the joint space, and the articular cartilage. Examination of the lateral collateral ligament, the triceps brachii tendon, the proximal tendon of the ulnaris lateralis, and the articular cartilage of the humeral trochlea is straightforward. The medial collateral ligament and the distal biceps brachii tendon require more expertise to assess.

Ultrasonographic Anatomy and Ultrasonographic Abnormalities

Elbow Joint

The elbow joint is formed by the articulation of the distal humerus with the radius and ulna. The distal humerus has two condyles that are unequal in size, with the medial condyle being significantly larger.

Atlas of Equine Ultrasonography, Second Edition. Edited by Jessica A. Kidd, Kristina G. Lu and Michele L. Frazer.
© 2022 John Wiley & Sons Ltd. Published 2022 by John Wiley & Sons Ltd.
Companion Website: www.wiley.com/go/kidd/atlas

Vet-ebooks.com

They are separated by a groove that sometimes contains a synovial fossa (Figure 5.1). The epicondyles sit proximal and caudal to the condyles, and between the epicondyles is the olecranon fossa which interdigitates with the anconeal process of the ulna. The joint is supported medially and laterally by collateral ligaments and dorsally by a thick dorsal capsule, which includes the attachment of the proximal tendon of the extensor carpi radialis. At this level on the dorsal aspect, the humeral condyle is covered by three muscles (from medial to lateral): the biceps brachii muscle belly and distal tendon, the brachialis muscle, and the extensor carpi radialis muscle. The biceps brachii tendon and the brachialis muscles may appear hypoechoic as a function of the orientation of the probe. In a normal joint, no synovial fluid is present on the cranial aspect of the joint. The amount of synovial fluid and the articular margins are better evaluated on the lateral aspect at the level of the collateral lateral ligament. In the lateral recess of normal horses, it is possible to find a small amount of synovial fluid. The best site to perform an ultrasound-guided injection is at the level of the joint space, immediately caudal to the lateral collateral ligament, with the probe in transverse section.

Abnormalities of the elbow joint other than septic arthritis are uncommon and septic arthritis is the most common abnormality seen. Septic arthritis is most common in foals, but occasionally is seen in older horses in association with trauma. The humerus, other than the deltoid tuberosity, is largely protected from the effects of direct trauma by muscles, but the olecranon of the ulna and the lateral aspect of the elbow are covered with minimal soft tissues and are therefore much more susceptible. With trauma to the lateral aspect of the elbow joint, wounds may easily extend into the elbow joint and sepsis should be considered. Ultrasonographically, this condition is characterized by a large amount of synovial fluid, which can appear hypoechogenic or echogenic due to an increased cellularity and/or the presence of fibrin (Figure 5.2).

In horses, osteoarthritis of the elbow joint is relatively unusual but can be seen in older sport horses, often with a history of trauma. Osteoarthritis can also be secondary to collateral ligament desmitis, osseous cyst-like lesions of the proximal aspect of the radius, olecranon fractures, post-sepsis, or some other primary insult to the joint. Periarticular bone modeling, osteophytes, and an increased amount of synovial fluid with echogenic spots consistent with fibrin are the most likely ultrasonographic findings (Figure 5.3).

Collateral Ligaments of the Elbow Joint

The lateral collateral ligament of the elbow joint is short; it originates from the lateral humeral condyle and inserts distally on the lateral tuberosity of the radius just distal to the joint margin. The lateral collateral ligament is a strong ligament compared to the medial, which is thinner and weaker. The lateral collateral ligament is easily

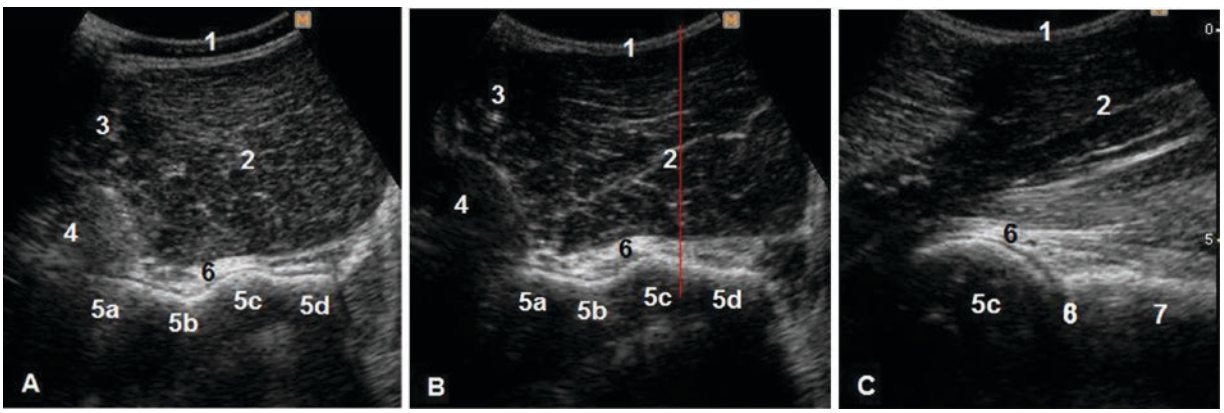


Figure 5.1 Normal images of the dorsal aspect of the elbow joint in transverse (A and B) (medial is to the left) and longitudinal (C) (proximal is to the left) sections. (A and B) The dorsal aspect of the elbow joint is characterized by a strong articular capsule with the attachment of the extensor carpi radialis tendon. By slightly changing the orientation of the probe, we can better visualize the articular cartilage and the biceps brachii becomes more echogenic as seen in (A). (C) Longitudinal section corresponding to the red line in Figure 5.1B. 1: skin; 2: extensor carpi radialis muscle; 3: brachialis muscle; 4: biceps brachii muscle; 5: dorsal aspect of the humeral condyle; 5a: medial ridge of the trochlea; 5b: groove; 5c: lateral ridge of the trochlea; 5d: capitulum; 6: dorsal articular capsule; 7: dorsal aspect of the proximal radius; 8: joint space.

Vet-ebooks.com

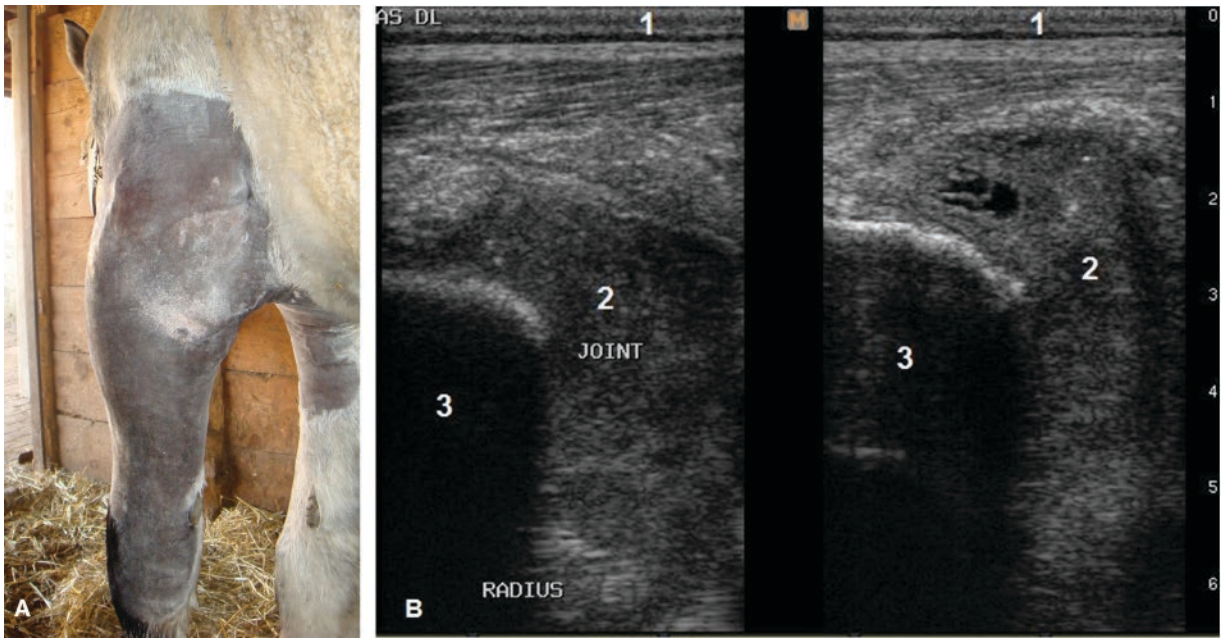


Figure 5.2 Septic arthritis of the elbow joint. (A) A 5-year-old draft horse with a severe swelling of the left elbow region caused by septic arthritis of the joint secondary to trauma. (B) Ultrasonogram of the lateral aspect of the left elbow. The lateral recess of the elbow joint is filled with a large amount of echogenic synovial fluid consistent with septic arthritis. The diagnosis was confirmed by synovial fluid analysis. 1: skin; 2: lateral recess of the elbow joint; 3: radius.

imaged under the lateral head of the triceps brachii muscle. This ligament is slightly heterogeneous because of its spiral fibers. The ligament has two portions with different fiber orientation: the deep portion which is shorter and travels obliquely in a disto-caudal direction and is less echoic, and a superficial portion which is longer and almost vertical. In a transverse section, it is possible to obtain three different images of the collateral ligament: at its proximal humeral enthesis, at the joint space, and at its distal radial insertion. The proximal part of this ligament appears ovoid/elliptic shaped and appears less homogeneous than distally (Figures 5.4 and 5.5).

Compared to the lateral collateral ligament, the medial collateral ligament is longer and thinner so its ultrasonographic examination is more challenging. The muscular mass of the pectoralis muscles make its visualization more complicated. Pulling the limb forward and pushing back the pectoralis muscles may help in the examination of this area. The medial collateral ligament originates proximally from an eminence on the medial humeral epicondyle, and consists of a long superficial portion and a short deeper portion. The deep part inserts on the radial tuberosity; the longer branch ends more distally on the medial border of the radius, just distal to the interosseous space between the radius and the ulna. Figure 5.6 shows the medial collateral ligament at its proximal insertion and at the level of the joint space. The distal insertion can be more difficult to identify. The medial aspect of the radius is often irregular without clinical significance, and care should be taken in interpreting these findings. At the medial aspect of the elbow joint, superficially and adjacent to the medial collateral ligament, there are large neurovascular structures: the median arteries and veins, and the median nerve (Figure 5.7).

Collateral ligament injuries are uncommon and usually the result of trauma. Lesions to the collateral ligaments result in an enlarged hypoechoic collateral ligament with disruption of the normal fiber pattern. Sometimes avulsion fractures of the collateral ligaments from the humeral condyle or the distal radial insertion are seen, or periosteal new bone can be associated with collateral ligament desmitis. Figure 5.8 shows an example of chronic enthesopathy of the lateral collateral ligament.

Ulnaris Lateralis Muscle

The ulnaris lateralis muscle originates proximal to the lateral epicondyle of the distal humerus, caudal and deep to the lateral collateral ligament; its tendon then courses caudal to the lateral collateral

Vet-ebooks.com

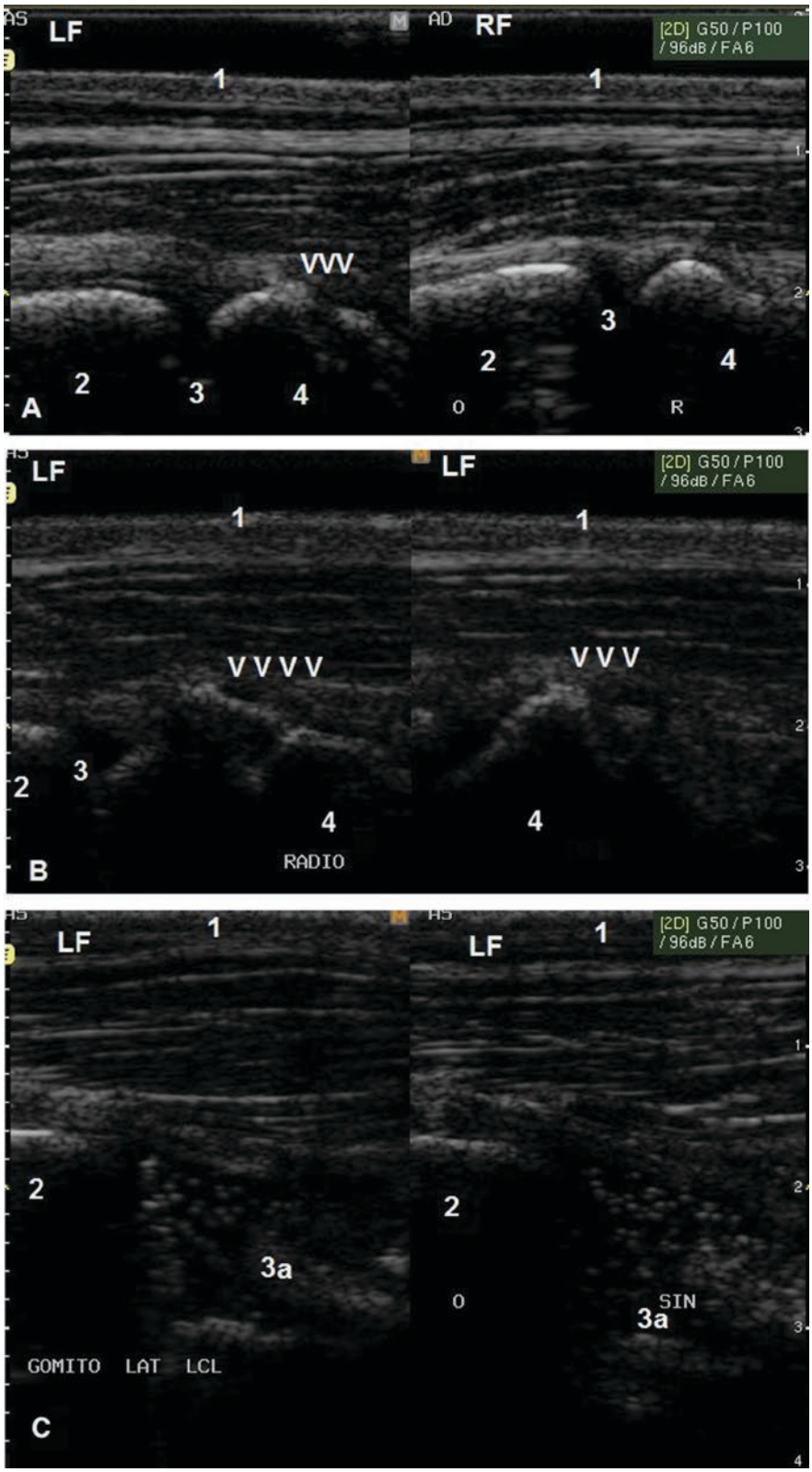


Figure 5.3 Osteoarthritis of the elbow joint. Ultrasonogram of the lateral aspect of the left elbow of a 10-year-old show jumper horse with a chronic intermittent left fore limb lameness. (A) Longitudinal sections of the joint slightly cranial to the lateral collateral ligament. The bone surface of the lateral aspect of the affected left radial condyle (LF) is irregular (arrows) compared to the unaffected contralateral right limb (RF). (B) Two longitudinal sections of the affected left fore limb showing similar abnormal findings to (A). (C) Two transverse images of the lateral recess of the elbow joint which is markedly distended. The synovial fluid contains multiple echogenic "spots," consistent with fibrin. These findings are indicative of osteoarthritis with chronic synovitis. 1: skin; 2: lateral humeral condyle; 3: joint space; 3a: lateral recess of the elbow joint; 4: lateral radial condyle.

Vet-ebooks.com

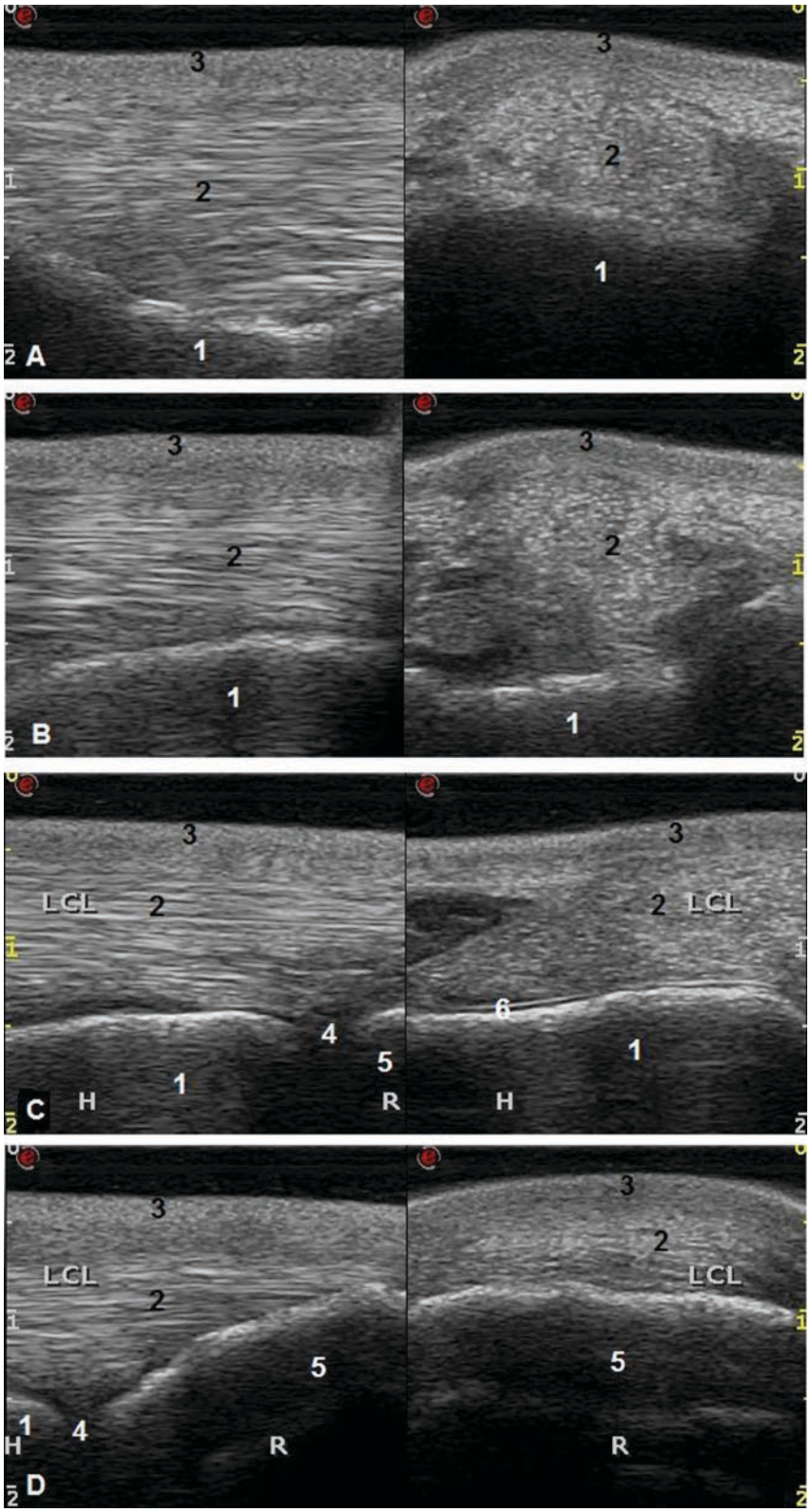


Figure 5.4 Normal longitudinal (left) and transverse (right) ultrasound scans of the lateral collateral ligament (LCL) of the elbow joint from its origin (A), just proximal to the joint space (B), at the level of the joint space (C), and at its distal insertion (D). The shape of the LCL is ovoid proximally and becomes more flat distally. In the transverse scan at the level of the joint space (C), it is possible to appreciate the articular cartilage layer (6). Longitudinal section: proximal is to the left, lateral is to top. Transverse section: cranial is to the left, lateral is to top. 1: lateral humeral condyle; 2: lateral collateral ligament; 3: skin; 4: joint space; 5: lateral radial tuberosity; 6: articular cartilage; R: radius.

Vet-ebooks.com

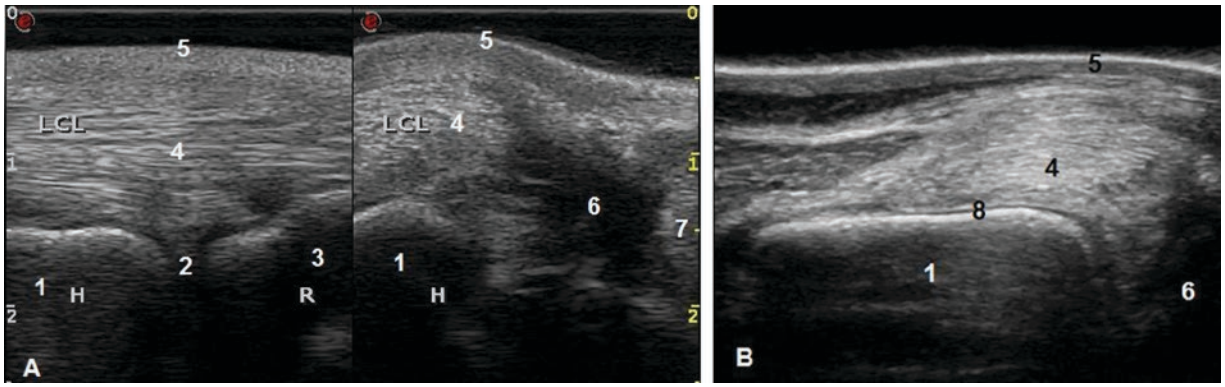


Figure 5.5 Normal longitudinal (left) and transverse (right) ultrasound scans of the lateral collateral ligament (LCL) of the elbow joint at the level of the joint space. (A) Longitudinal section (proximal is to the left, lateral is to top) and transverse section (cranial is to the left, lateral is to top). (B) Transverse section (cranial is to the left, lateral is to top). In transverse section, caudally to the LCL, there is the lateral recess of the elbow joint which shows a small amount of anechoic synovial fluid. 1: lateral humeral condyle; 2: joint space; 3: lateral radial tuberosity; 4: lateral collateral ligament; 5: skin; 6: synovial fluid in the lateral recess of the elbow joint; 7: ulnaris lateralis tendon; 8: articular cartilage.

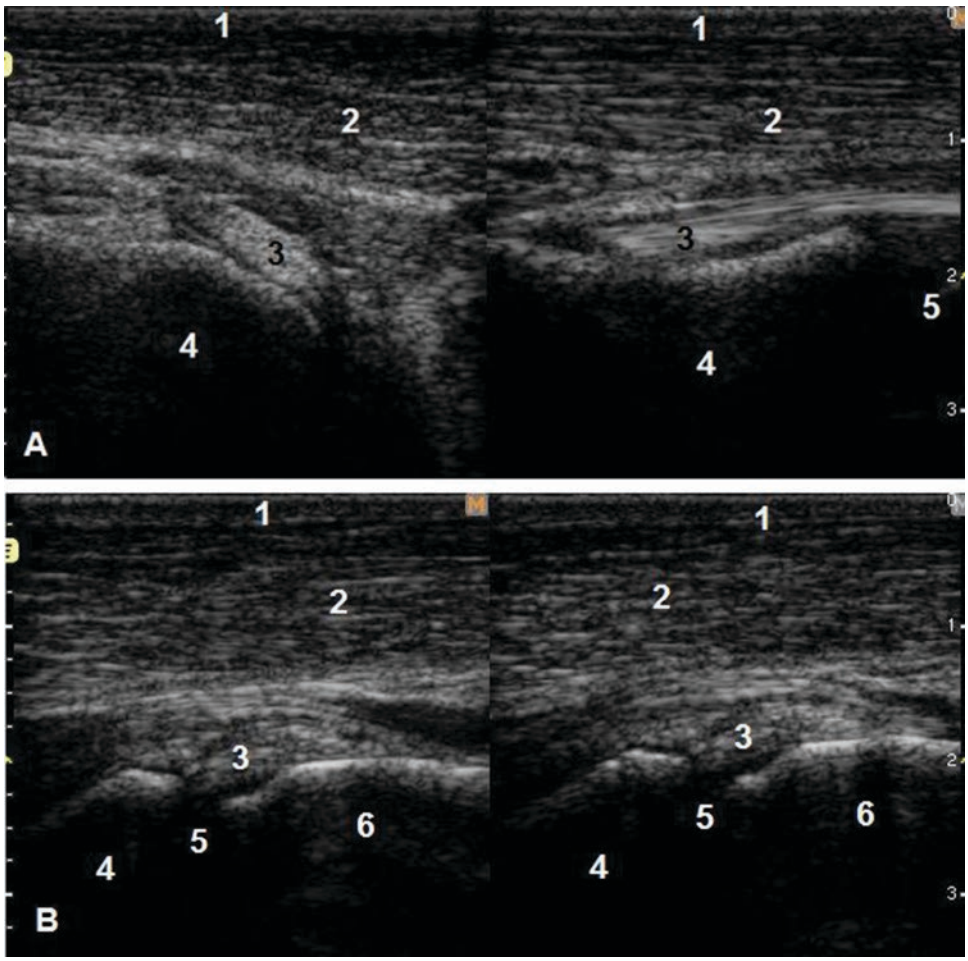


Figure 5.6 Normal transverse ultrasound scan of the medial collateral ligament (MCL) of the elbow joint at the level of the joint space. When the transducer is perpendicular to the ligament fibers in transverse scans, the MCL looks homogeneous and echogenic. In longitudinal section, the MCL can appear more or less flat, depending on the position of the probe in the craniocaudal plane. Cranial is to the left, medial is to the top. 1: skin; 2: pectoralis transversus muscle; 3: MCL; 4: medial humeral condyle; 5: joint space; 6: medial aspect of the proximal radius.

Vet-ebooks.com

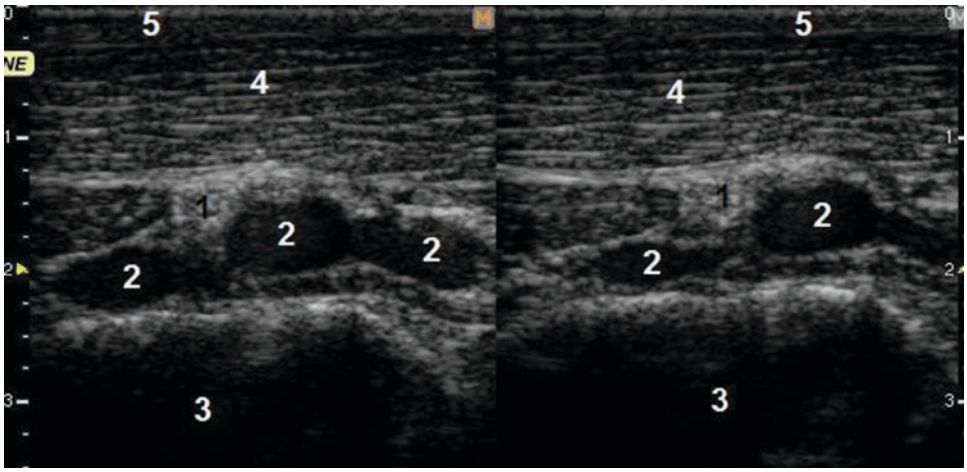


Figure 5.7 Normal transverse ultrasound scan of the medial aspect of the elbow joint at the level of the medial radial condyle showing the vessels and the median nerve. The irregularity of the radial bone surface is normal. 1: median nerve; 2: median arteries and veins; 3: medial radial condyle; 4: pectoralis transversus muscle; 5: antebrachial fascia.

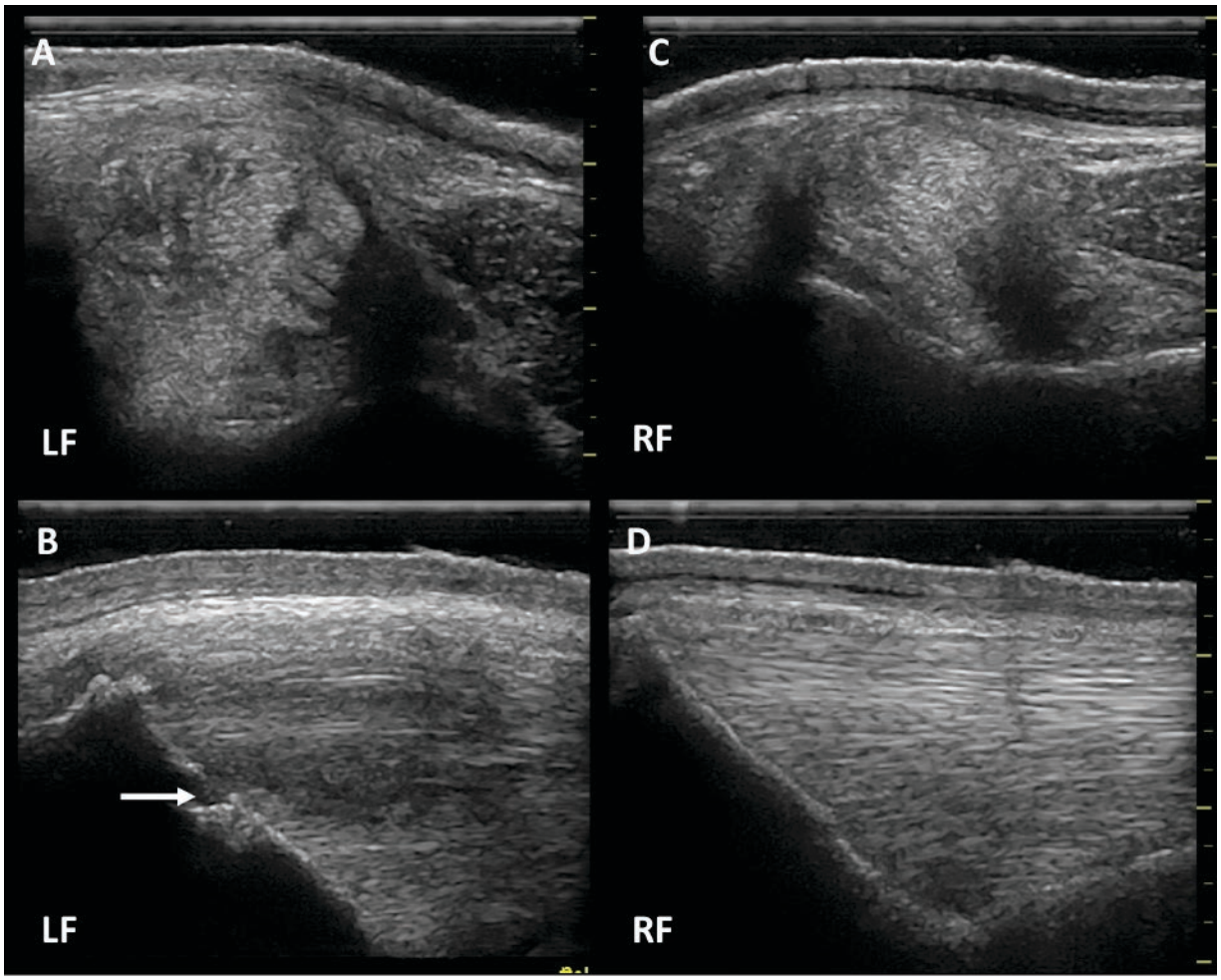


Figure 5.8 Proximal insertional desmitis of the lateral collateral ligament (LCL) of the elbow joint. The left LCL is enlarged and shows disrupted fiber pattern on transverse and longitudinal section (A and B). The bone surface of the left lateral humeral condyle is irregular (arrow) compared to the normal contralateral right fore limb (B and D). Transverse section (cranial is to the left, lateral is to top). Longitudinal section (proximal is to left, lateral is to top). (*Source*: Courtesy: Dr Roger Smith).

Vet-ebooks.com

ligament. For this reason, an ultrasound examination of the ulnaris lateralis is easier if it begins with the transverse section of the lateral collateral ligament just proximal to the joint space, and then the probe is moved slightly caudally (Figure 5.9). In cases with synovial distension of this lateral articular recess, the ulnaris lateralis tendon is separated from the lateral collateral ligament by a synovial fold.

Figure 5.10 shows a rare case of avulsion of the ulnaris lateralis muscle following a fall over a fence.

Distal Insertion of the Biceps Brachii

In horses, the biceps brachii muscle is characterized by an intramuscular tendon continuing to its distal tendon. Because of the concave shape of this anatomical area, it is easier to examine the distal insertion of the biceps brachii with a convex transducer. To identify the biceps brachii enthesis, it is useful to begin with longitudinal scanning on the dorsal aspect of the elbow joint (see Figure 5.1) and then move the probe slightly medially to identify the insertion located at the craniomedial aspect of the elbow (Figure 5.11).

Enthesopathy of the biceps brachii insertion is caused by a tearing of its distal attachment on the cranioproximal aspect of the radius. In chronic cases, radiographic and ultrasonographic examination may identify periosteal new bone on the cranial tuberosity of the radius at the site of the insertion of the biceps brachii. Pathology of the biceps brachii is much more common in the shoulder region and will be discussed in the section on the shoulder.

Triceps Brachii Muscle and Distal Tendon

Situated at the caudolateral aspect of the elbow region, the triceps brachii muscle is one of the principal extensors of the elbow joint and inserts on the olecranon tuberosity of the ulna. Figure 5.12 shows the normal appearance of the distal triceps brachii tendon.

The muscle can be affected by a post-anesthetic myopathy. Sonographic findings of post-anesthetic myopathy consist of loss of normal muscle striations and an overall increased muscle echogenicity. Sometimes, an affected triceps brachii muscle can return to a normal ultrasonographic appearance, but in most cases it remains abnormal. A rare condition is a tendinopathy of the distal tendon of the triceps brachii muscle. In these cases, the tendon is enlarged and becomes heterogeneous; if there is also damage to the enthesis, it is possible to find modeling of the olecranon surface with new bone formation.

Shoulder

Scanning Technique

A standoff pad is usually not necessary because most anatomic structures are positioned relatively deeply, except at the point of the shoulder where a standoff is useful to improve the contact between the skin and the probe. The shoulder should be scanned from cranial to caudal with the horse fully weightbearing on the limb to avoid hypoechogenic artifacts. Diagnostic images are best obtained with medium- to high-frequency linear or curved transducers (5–10 MHz). Anatomic structures close to the skin surface are visualized with a high-frequency linear probe, but this can be inadequate to examine the scapulohumeral joint in large horses. The advantage of a convex probe is a larger acoustic window which is useful to visualize the entire biceps brachii tendon at the level of the humeral tubercles. A 5–7.5 MHz micro-convex transducer is useful in case of ultrasound-guided injection.

A complete sonographic examination of the shoulder should include the scapula, the supraglenoid tubercle, the biceps brachii tendon, the bicipital bursa, the humeral tubercles, the intertubercular groove, the supraspinatus and infraspinatus tendons, and the scapulohumeral joint.

Ultrasonographic Anatomy and Ultrasonographic Abnormalities

Scapula and Supraglenoid Tubercle

The equine shoulder is characterized by a simple scapulohumeral joint without collateral ligaments and a remarkable muscle mass providing stability to the joint. An ultrasound study of the scapula begins proximally at the level of the scapular cartilage, which is very superficial and covered by the trapezius muscle. This muscle appears hypoechogenic and attaches to the scapular spine. The scapula consists of a scapular spine and two fossae; the spine is identified as a regular hyperechoic line generating acoustic shadowing. The scapular spine becomes taller around the mid part of the scapula. At this level, the fossae are easily identified. The supraspinatus fossa is cranial to the scapular spine and houses the supraspinatus muscle (Figure 5.13). Caudally, the infraspinatus fossa, larger than the supraspinatus fossa, accommodates the origin of the infraspinatus muscle covered with the deltoideus muscle (Figure 5.13).

Fractures of the body of the scapula may be difficult to identify with a radiographic examination but they are more easily detected ultrasonographically. A fracture line appears as a hypoechoic to anechoic line through the cortical bone, allowing

Vet-ebooks.com

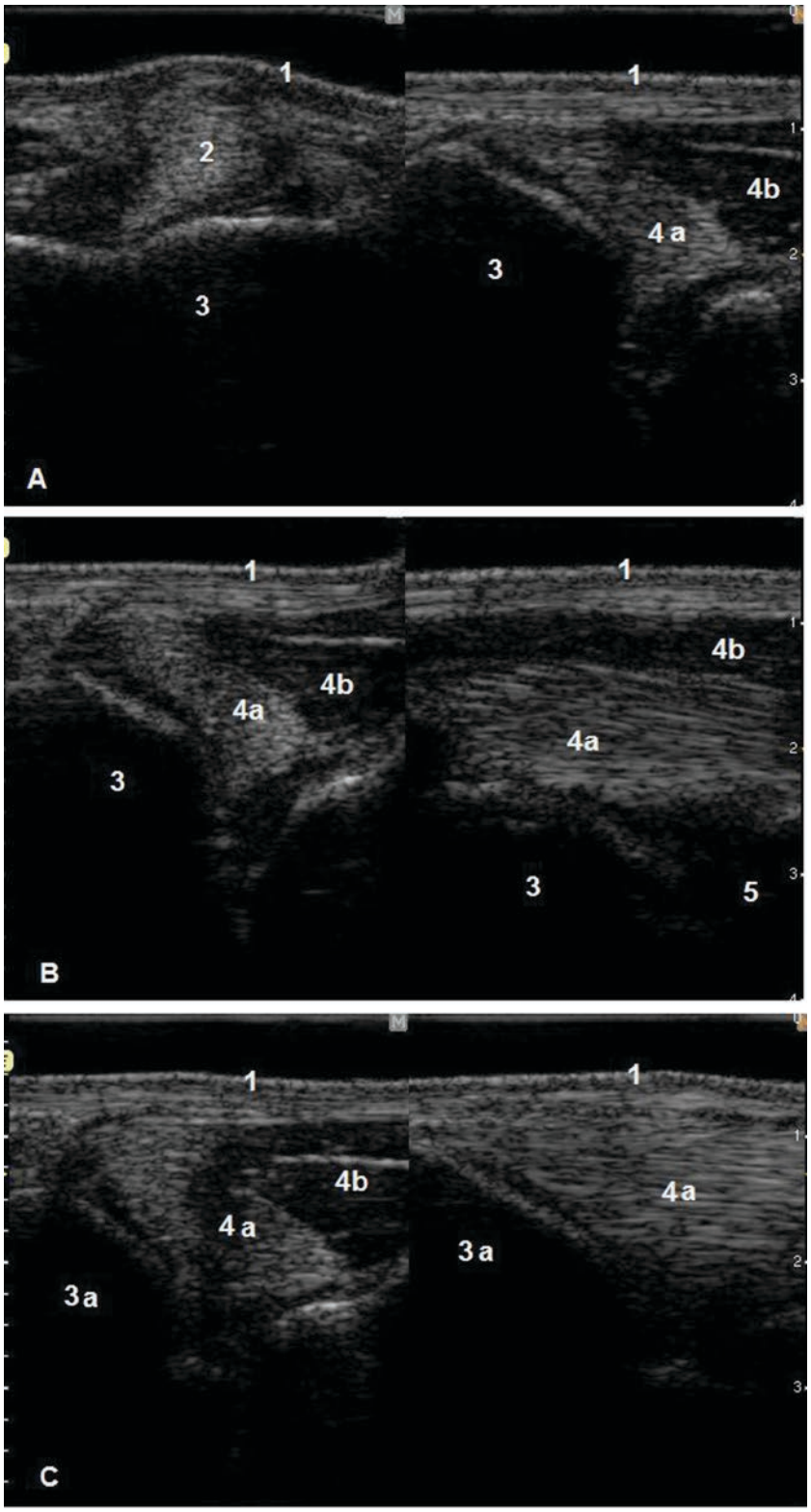


Figure 5.9 Normal ultrasound scans of the ulnaris lateralis (UL) at the lateral aspect of the elbow. (A) Transverse section of the lateral collateral ligament (left) and ulnaris lateralis tendon (right). (B) Transverse (left) and longitudinal (right) sections of the UL tendon. (C) Transverse (left) and longitudinal (right) sections of the UL tendon at the level of its enthesis on the lateral epicondyle. Longitudinal section: proximal is to the left, medial is to top. Transverse section: cranial is to the left, medial is to top. 1: skin; 2: lateral collateral ligament; 3: lateral aspect of the humerus; 3a: lateral humeral epicondyle; 4: ulnaris lateralis: 4a: tendon,; 4b: muscle; 5: lateral recess of the cubital joint with a small amount of synovial fluid.

Vet-ebooks.com

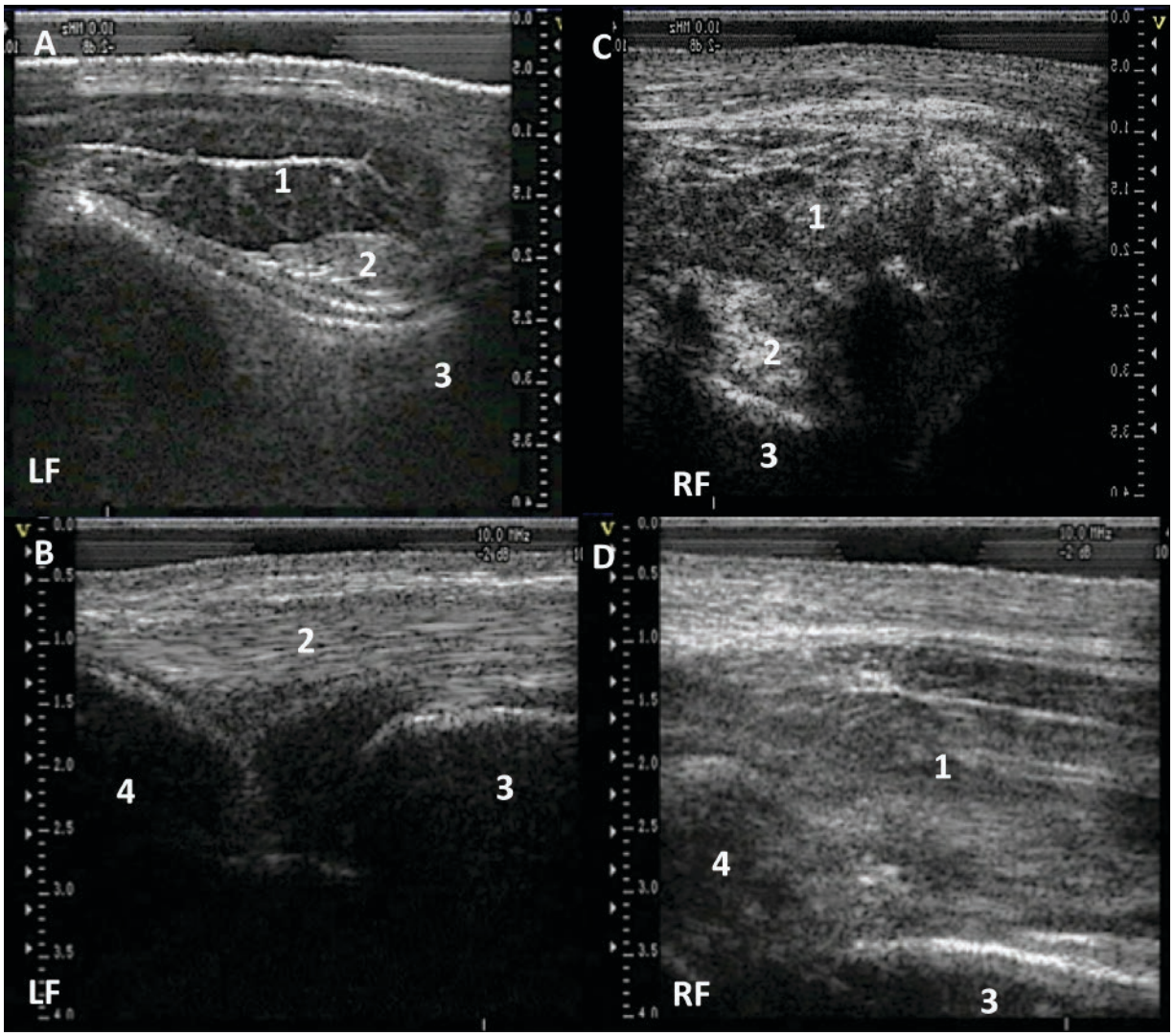


Figure 5.10 Avulsion of the ulnaris lateralis (UL) muscle following a fall over a fence. The abnormal right ulnaris lateralis muscle is severely swollen with a clear abnormal fiber pattern in transverse (C) and longitudinal (D) sections when compared to the normal UL on the left (A and B). On transverse section of the RF, it is difficult to identify the tendon and some bony avulsion fragments are present. (A) Transverse section (cranial is to the left, lateral is to top). Longitudinal section (proximal is to left, lateral is to top). 1: UL muscle belly; 2: UL tendon; 3: Lateral aspect proximal radius; 4: Lateral humeral epicondyle. *Source*: Courtesy: Dr Roger Smith

the ultrasound beam to penetrate through the bone for a certain distance. Distraction of the fracture fragment from the parent portion may occur and should be detected in two mutually perpendicular planes. In cases of chronic scapular fractures, ultrasonographic findings show an irregular bone surface consistent with a bone callus (Figure 5.14).

Fractures of the scapula most commonly involve the supraglenoid tubercle. Figure 5.15 shows the normal ultrasonographic appearance of the supraglenoid tubercle. These fractures are one of most common shoulder injuries, particularly in young horses. The fracture may be simple or comminuted and there is often an intra-articular component. In these cases, ultrasonographic findings are characterized by an irregular bone surface of the neck of the scapula with an irregular defect in the hyperechogenic bone line and distal displacement of the bony fragment, as the fracture is distracted by the pull of the biceps brachii tendon (Figure 5.16). This lesion is therefore often associated with relaxation of the proximal insertion of the biceps brachii muscle along with scapulohumeral synovitis and bicipital bursitis.

Intertubercular Sulcus and Humeral Tubercles

In a normal horse, the single intertubercular sulcus (also called the intertubercular groove) is divided into two grooves by the intermediate tubercule. The bone

Vet-ebooks.com

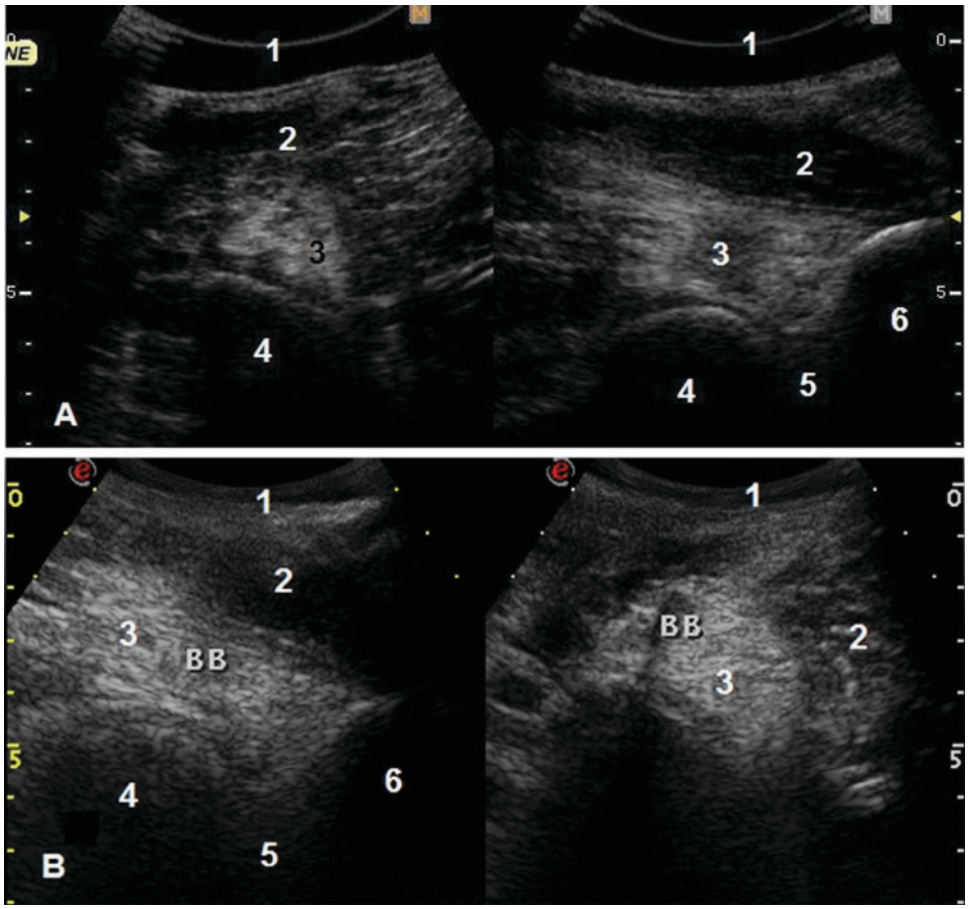


Figure 5.11 Normal ultrasonograms of the distal insertion of the biceps brachii tendon on the craniomedial aspect of the elbow. (A) Transverse (left: medial is to the left) and longitudinal (right: proximal is to the left) sections of the distal biceps brachii tendon. The hypoechoic area inside of the tendon in both scans is normal and it is due to the presence of hypoechoic muscle fibers. (B) Longitudinal (left: proximal is to the left) and transverse (right: medial is to the left) sections of the distal biceps brachii tendon. The shape of the distal tendon on transverse scans appears different according to the level of the section. 1: skin; 2: extensor carpi radialis muscle; 3: distal tendon of biceps brachii muscle; 4: dorsomedial aspect of the humeral condyle; 5: joint space; 6: radial tuberosity.

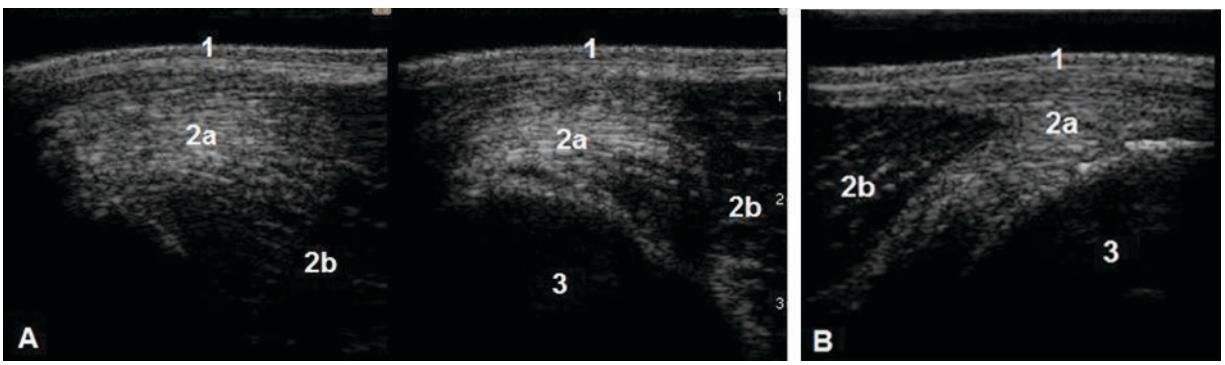


Figure 5.12 Normal ultrasonogram of the distal insertion of the triceps brachii tendon on the olecranon tuberosity of the ulna. (A) Transverse (medial is to the left) sections of the distal triceps brachii tendon just proximal to the olecranon tuberosity (left) and at the level of the olecranon (right). (B) Longitudinal (proximal is to the left) section of the distal enthesis of the triceps brachii tendon. The hypoechoic tissue proximal to the tendon is the muscle belly of the triceps brachii. 1: skin; 2: triceps brachii: 2a: distal tendon of triceps brachii muscle; 2b: triceps brachii muscle; 3: olecranon tuberosity.

Vet-ebooks.com

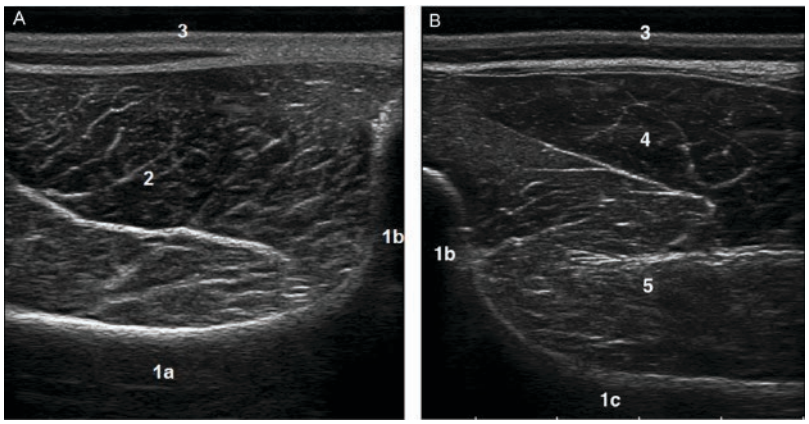


Figure 5.13 Normal transverse ultrasound scans of the mid-scapular spine (cranial to the left, caudal to the right). (A) The supraspinatus muscle originates from the supraspinatus fossa. (B) At this level, in the infraspinatus fossa the infraspinatus muscle is deep to the deltoideus muscle; 1: scapula; 1a: supraspinatus fossa; 1b: capular spine; 1c: infraspinatus fossa; 2: supraspinatus muscle; 3: skin; 4: deltoideus muscle; 5: infraspinatus muscle.

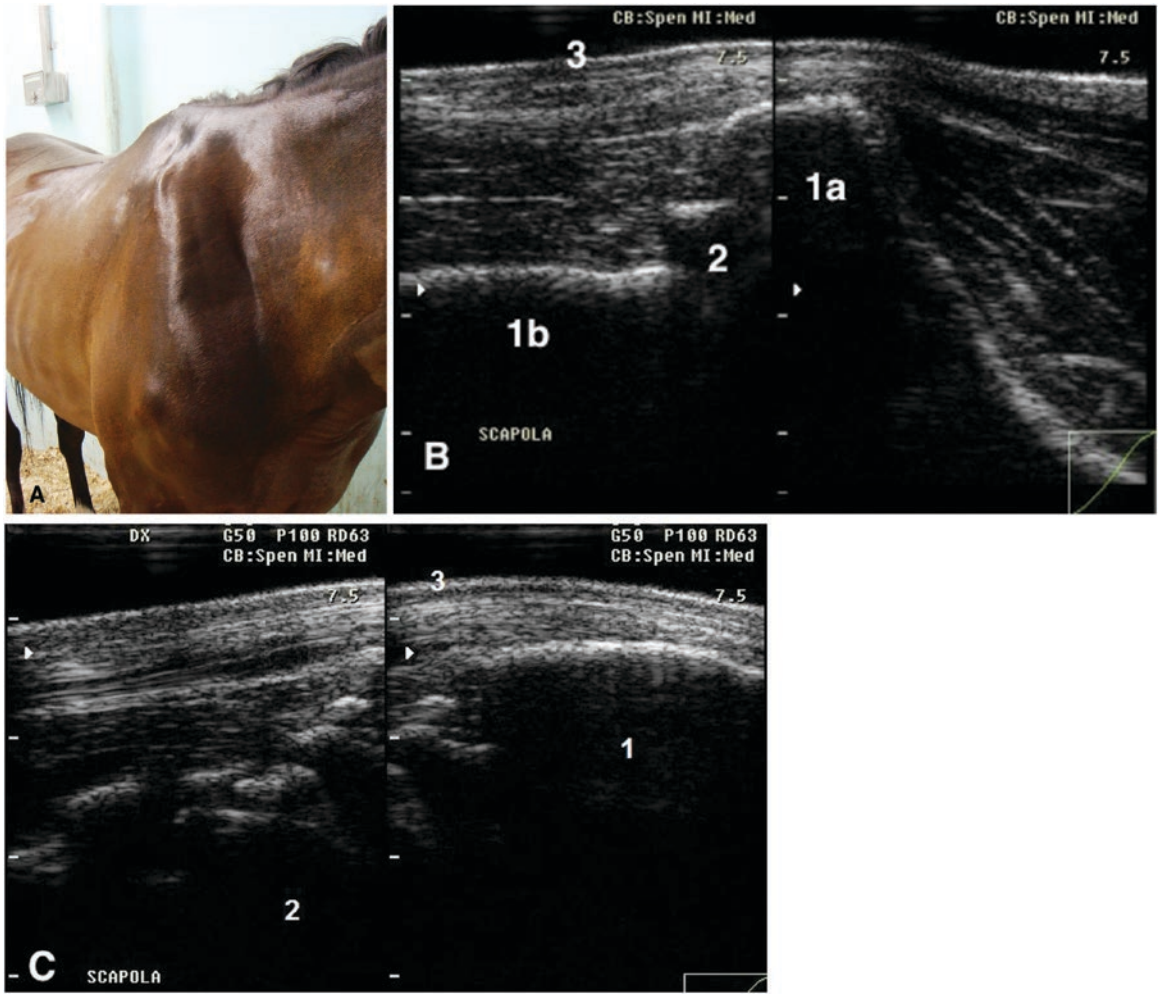


Figure 5.14 Chronic scapular fracture. (A) A 7-year-old Thoroughbred gelding with severe deformation of the right shoulder region caused by an old fracture of the body of the scapula. (B) Transverse scan of the right scapula (cranial is to the left). The scapular spine appears irregular in shape and enlarged. The suprascapular fossa also shows an abnormal convex shape. (C) Longitudinal scan of the right scapula. Bone remodeling is present at the cranial aspect of the scapular body. 1: scapula; 1a: scapular spine; 1b: suprascapular fossa; 2: bone remodeling; 3: skin.

Vet-ebooks.com

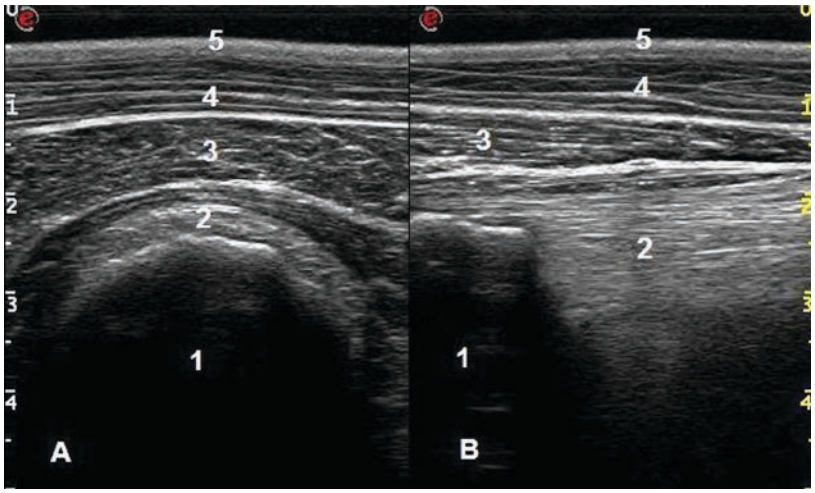


Figure 5.15 Normal origin of the biceps brachii tendon. Transverse (A) (medial is to the left) and longitudinal (B) (proximal is to the left) ultrasound scans of the origin of the biceps brachii tendon on the supraglenoid tubercle of the scapula. The tendon looks homogeneously echogenic in both sections. The bone surface of the supraglenoid tubercle should be smooth and regularly hyperechoic in both sections. 1: supraglenoid tubercle; 2: proximal tendon of the biceps brachii; 3: supraspinatus muscle; 4: brachiocephalicus muscle; 5: skin.

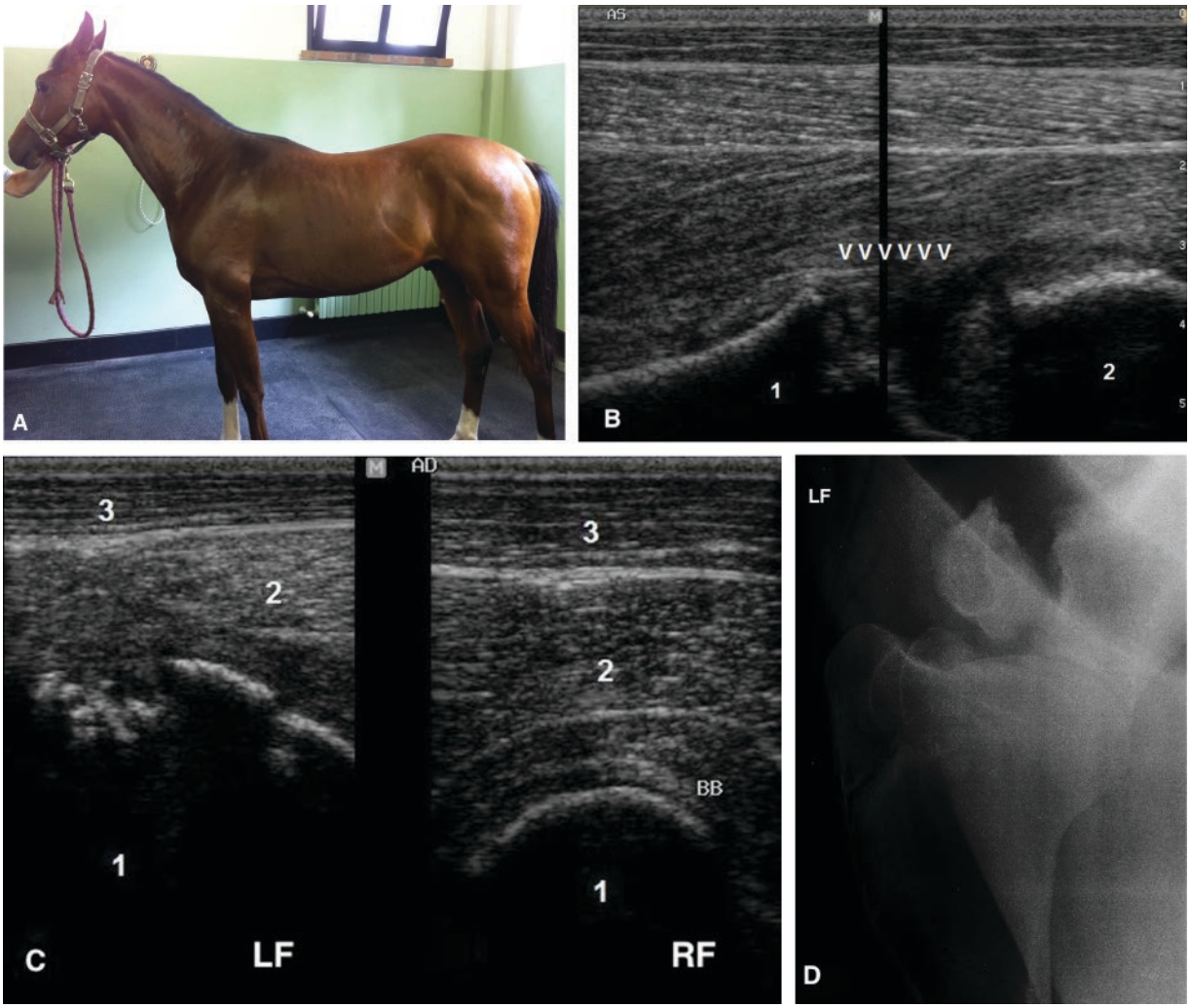


Figure 5.16 Supraglenoid tubercle fracture. (A) An Arabian yearling with an acute-onset severe left fore limb lameness caused by a fracture of the supraglenoid tubercle (photo). (B) Longitudinal ultrasound scan of the scapular neck. The bony fragment (2) is displaced distally and a large anechoic space (arrows) is visible between the fragment and the scapular neck (1) (proximal is to the left). (C) Transverse (medial is to the left) ultrasound scans of the supraglenoid tubercle in the same horse showing the fracture of the supraglenoid tubercle (LF) compared with the normal opposite limb (RF). The fracture fragment shows extensive bone remodeling. (D) Mediolateral radiographic view of the left scapulohumeral joint confirming the intra-articular fracture of the supraglenoid tubercle with distal displacement of the bony fragment. 1: supraglenoid tubercle of the scapula; 2: supraspinatus muscle; 3: brachiocephalicus muscle; BB: proximal biceps brachii tendon.

Vet-ebooks.com

surface of the intertubercular sulcus is visualized as a smooth hyperechoic W-shaped line, with the convex portions corresponding to the medial (lesser), intermediate, and lateral (greater) humeral tubercles (Figure 5.17). The greater tubercle has two eminences: cranial (the point of the shoulder) and caudal. Between these two landmarks is the site for intra-articular injection of the shoulder joint. In foals, there are two separate centers of ossification of the proximal humeral epiphysis: one for the greater tubercle and one for the humeral head and lesser tubercle. The cartilage skeleton of the tubercles is still very large and anechoic and should not be mistaken for fluid (Figure 5.18). In yearlings, because of the on-going ossification process, the intermediate tubercle has an irregular contour which is normal in this age group (Figure 5.19). The proximal humeral physis closes between 24 and 36 months of age. In some mature horses, a notch over the intermediate tubercle can be seen as a result of incomplete ossification and represents a normal variant. The contour of demarcation between cartilage and subchondral bone in the intermediate tubercule can normally be quite irregular.

Osseous lesions, including osteomyelitis, osseous cyst-like lesions, and penetrating tracts can involve these structures. In most cases of osseous lesions there is a cortical defect with underlying abnormal architecture of the subchondral bone. It is often useful to examine the opposite limb to determine if a lesion truly exists. Malformation of the intertubercular sulcus has been reported in four adult horses and in a Welsh pony.

Biceps Brachii Tendon

Bicipital tendinitis and bursitis are uncommon but, nonetheless, pathology in these structures is a significant cause of lameness referable to the shoulder. The biceps brachii tendon should be scanned in transverse and longitudinal sections from its origin on the supraglenoid tubercle of the scapula (Figure 5.15) to its distal insertion on the proximal tuberosity of the radius (see the section on the elbow). In a normal horse, the origin of the tendon of the biceps brachii appears as an echogenic crescent-shaped convex structure in cross-sectional scans. Just proximal to the intertubercular sulcus, the tendon becomes bilobed and shows a linear fibrillar echogenic pattern with a thin hypoechoic layer over its

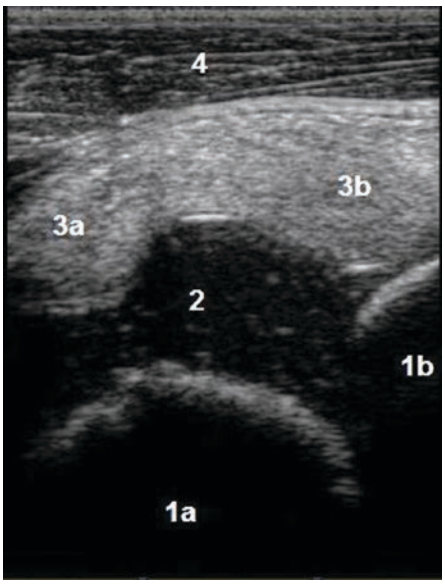


Figure 5.18 Normal point of the shoulder in a foal. Transverse ultrasound scan (medial is to the left) of the cranial aspect of the point of the shoulder in a normal foal. Because of the age of the subject, in this image the separation between the two ossification centers (1a and 1b) is still visible. 1: intertubercular humeral sulcus; 1a: intermediate tubercle; 1b: greater tubercle; 2: cartilage; 3: proximal tendon of the biceps brachii; 3a: medial lobe; 3b: lateral lobe; 4: brachiocephalicus muscle.

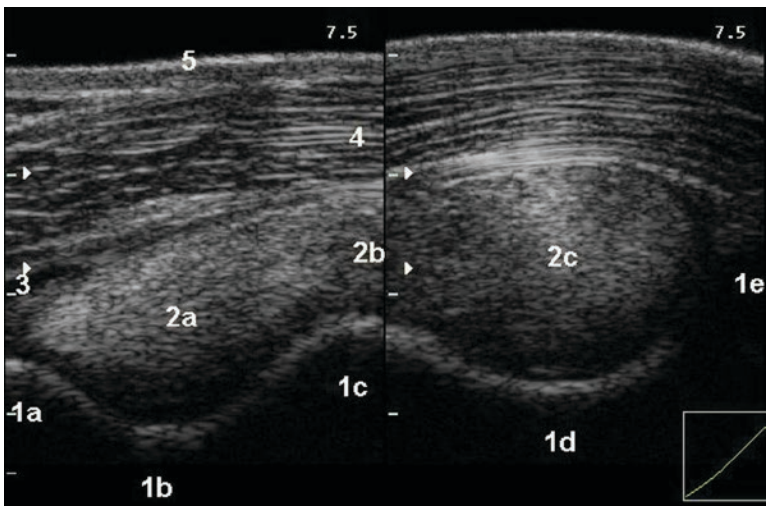


Figure 5.17 Normal proximal biceps brachii tendon. Transverse ultrasound scans (medial is to the left) of the proximal tendon of the biceps brachii over the intertubercular sulcus in a normal horse. The bicipital bursa lies between the tendon and the intertubercular sulcus. Normally the bicipital bursa is a virtual cavity and no fluid is visible. 1: intertubercular humeral sulcus; 1a: lesser tubercle; 1b: medial groove; 1c: intermediate tubercle; 1d: lateral groove; 1e: greater tubercle; 2: proximal tendon of the biceps brachii: 2a: medial lobe; 2b: isthmus; 2c: lateral lobe; 3: upraspinatus muscle; 4: brachiocephalicus muscle; 5: skin.

Vet-ebooks.com

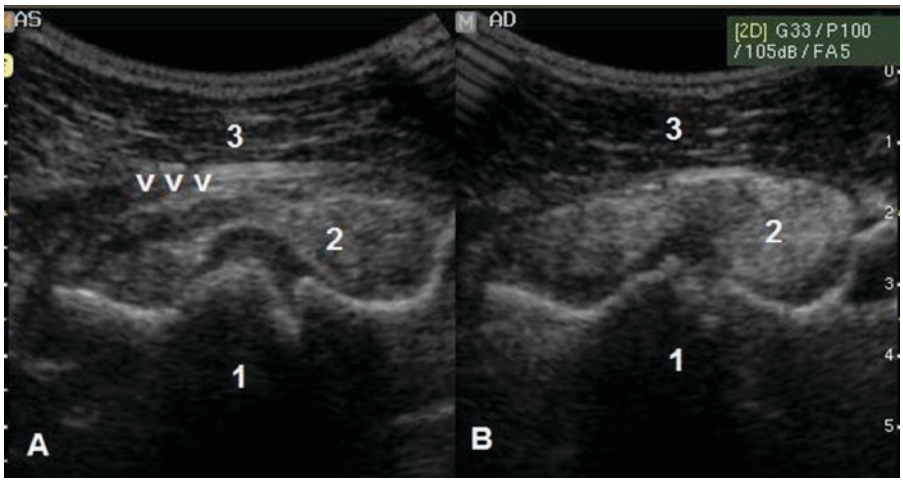


Figure 5.19 Acute tendinitis of biceps brachii tendon in a yearling. Transverse (medial is to the left) ultrasound scans, obtained with a convex probe, of the proximal biceps brachii tendon at the level of the intertubercular sulcus in a yearling. (A) The medial lobe has a large anechoic lesion (arrows) without enlargement of the tendon. This image is indicative of an acute tendinitis of the biceps brachii tendon. This yearling had a supraglenoid tubercle fracture the month before. The irregularity of the contour of the intermediate tubercle present in both limbs is normal. At this age there is a partial degree of ossification of the two ossification centers. (B) Normal opposite limb. 1: intermediate tubercle; 2: proximal tendon of the biceps brachii (lateral lobe); 3: brachiocephalicus muscle; arrows: lesion of the medial lobe of the biceps brachii tendon.

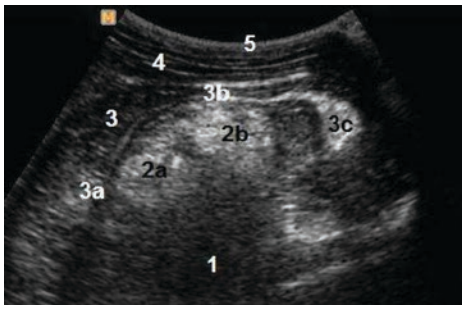


Figure 5.20 Normal transverse image (medial is to the left) of the cranial aspect of the shoulder, just distal to the supraglenoid tubercle and proximal to the intertubercular sulcus. 1: scapulohumeral fat pad; 2: proximal biceps brachii tendon: 2a: medial lobe; 2b: lateral lobe; 3: supraspinatus muscle; 3a: medial tendon; 3b: aponeurosis of the supraspinatus muscle; 3c: lateral tendon; 4: brachiocephalicus muscle; 5: skin.

cranial border, corresponding to the muscular fibers of the biceps brachii (Figure 5.20). Coursing distally, the tendon becomes irregularly elliptic in shape and heterogeneous because it is infiltrated by hypoechogenic fatty connective tissue (Figure 5.21). Some of these muscular fibers are sometimes also visible at the level of the intertubercular sulcus (Figure 5.22). Over the point of the shoulder, the tendon is molded to the intertubercular sulcus, which is covered with fibrocartilage; the bicipital bursa is interposed between the bone surface and the tendon (Figure 5.17). The tendon is bilobed in shape, with a larger lateral lobe and a smaller medial lobe connected by an isthmus. The isthmus lies cranial to the intermediate humeral tubercle. The lateral lobe runs in the intertubercular groove between the greater and the intermediate tubercles of the humerus, and the medial between the intermediate and the lesser humeral tubercles. At this level, the tendon is so large that it is almost impossible to visualize the entire tendon in one transverse image using most linear transducers. A convex probe can provide a better representation of the entire tendon on a transverse scan. When using a linear transducer, an independent evaluation of each lobe is often required. Figure 5.23 shows a longitudinal scan of the proximal bicipital tendon from its origin; the probe should be moved medially and laterally to examine the medial and lateral lobes. Distal to the intertubercular groove, the proximal tendon of the biceps brachii merges progressively into the muscle belly. On a transverse section, the tendon is now oval and heterogeneous, due to the presence of hypoechogenic striated fibers in its center. The distal recess of the bicipital bursa and fat are interposed between the biceps brachii tendon and the proximal humerus.

Injuries of the biceps brachii tendon itself consist of enlargement of the tendon, presence of hypoechoic–anechoic areas, and loss of the normal fiber pattern. Artifactual hypoechoic areas in the bicipital tendon are easily created because its fibers do not lie all in the same scan plane due to its curved contour. Changing the orientation of the probe is useful and lesions should be identified in both the transverse and longitudinal scan to be sure that the hypoechoic area is not an artifact (Figures 5.19 and 5.24). In chronic cases, dystrophic mineralization or calcification of the biceps brachii tendon may occur. A case of rupture of

Vet-ebooks.com

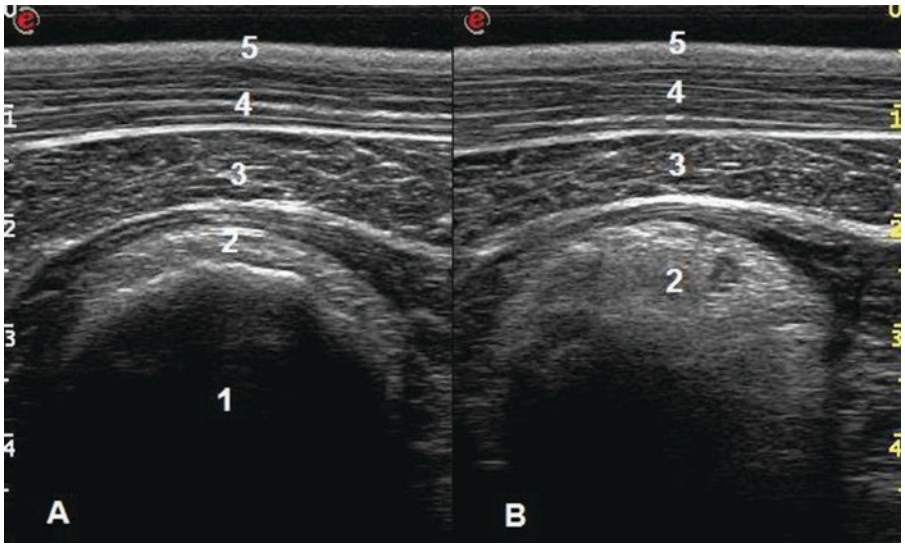


Figure 5.21 Normal transverse ultrasound images of the proximal biceps brachii tendon (medial is to the left). (A) At the level of the supraglenoid tubercle, the tendon is homogeneously echogenic. (B) Just distal to the supraglenoid tubercle, the tendon has a heterogeneous echogenicity because of the presence of fat connective tissue areas. 1: supraglenoid tubercle; 2: proximal tendon of the biceps brachii; 3: supraspinatus muscle; 4: brachiocephalicus muscle; 5: skin.

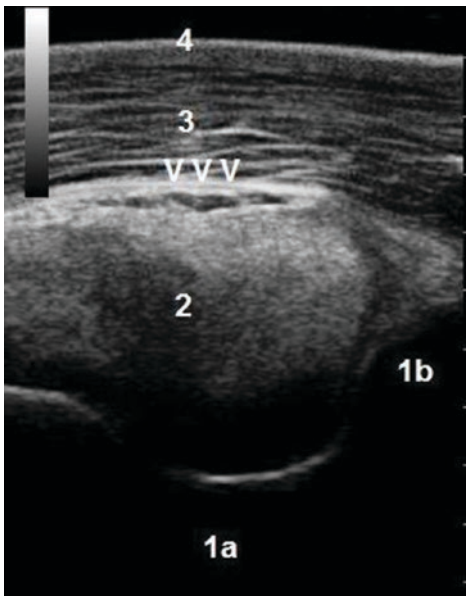


Figure 5.22 Normal transverse (medial is to the left) ultrasound scan of the lateral lobe of the proximal tendon of the biceps brachii over the intertubercular sulcus in a normal horse. 1: intertubercular sulcus: 1a: lateral groove; 1b: greater tubercle; 2: lateral lobe of proximal bicipital tendon; 3: brachiocephalicus muscle; 4: skin; arrows: cranial muscle fibers of the biceps brachii.

the biceps tendon in a Thoroughbred steeplechaser has also been described.

Bicipital Bursa

The bicipital bursa is a potential space between the biceps brachii tendon and the proximal humerus. In normal horses, this bursa is not clearly visible because no or very little fluid is discernible (Figure 5.17). The small anechoic space between the humeral tubercles and the biceps brachii tendon is fibrocartilage and should not be confused with fluid. Bicipital bursitis can be found alone or secondary to bony lesions or bicipital tendinitis. Distension of the bicipital bursa is seen as fluid accumulation around the medial and lateral sides of the biceps brachii tendon (Figure 5.25). In normal horses, a small amount of synovial fluid can be found at the lateral aspect of the bicipital bursa slightly distal to the greater tubercle. However, when the distension is severe, anechoic synovial fluid causes cranial protrusion of the tendon and the mesotendon becomes visible. In most chronic cases of bicipital bursitis, sonographic findings include an increased volume of hypoechoic fluid, and fibrin and synovial proliferation within the bursa (Figure 5.26). In most cases of septic bursitis, the synovial fluid becomes echogenic, although when anechoic synovial fluid distension is seen, a recent-onset septic process cannot be ruled out without bursocentesis. The underlying bone should also be carefully examined for lytic areas of the intertubercular groove, particularly in cases of septic bursitis. Figure 5.27 shows a case of proximal humeral osteitis associated with bicipital bursitis.

Supraspinatus Muscle and Tendons

The supraspinatus muscle originates from the homonymous fossa of the scapula (Figure 5.28) and splits at the neck of the scapula into two branches each with an intramuscular tendon. The tendons can be identified as echogenic structures within the less echoic supraspinatus muscle. They run superficially, one laterally and the other medially, to the biceps

Vet-ebooks.com

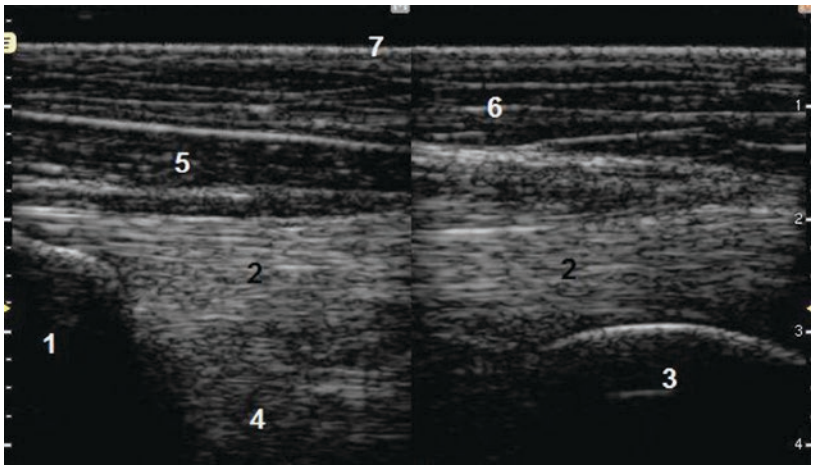


Figure 5.23 Normal sagittal (proximal is to the left) ultrasound scans of the proximal tendon of the biceps brachii from the supraglenoid tubercle to the intertubercular sulcus. The tendon shows parallel echogenic fibers deep to the supraspinatus and brachiocephalicus muscles. 1: supraglenoid tubercle of the scapula; 2: proximal tendon of the biceps brachii; 3: intertubercular sulcus (sagittal ridge); 4: fat; 5: supraspinatus muscle; 6: brachiocephalicus muscle; 7: skin.

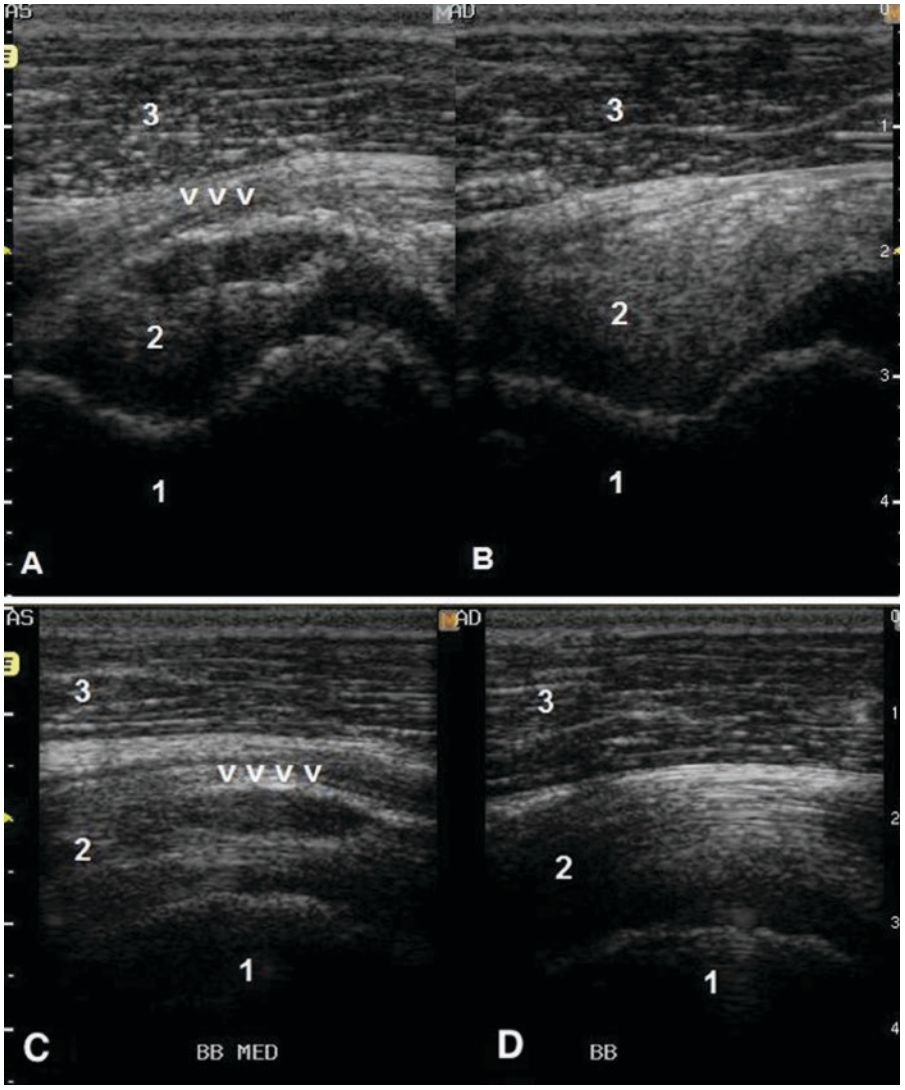


Figure 5.24 Acute tendinitis of the biceps brachii tendon in a yearling associated with a recent fracture of the supraglenoid tubercle. Transverse (A and B, medial is to the left) and longitudinal (C and D, proximal is to the left) ultrasound scans of the medial lobe of the proximal biceps brachii tendon. (A) The medial lobe (2) is not enlarged compared to the opposite limb but a large oval anechoic lesion (arrows) is present within the tendon. (B) Normal medial lobe on the opposite limb. (C) A large oval anechoic lesion (arrows) is present within the medial lobe of the biceps brachii tendon. This image, also visualized in cross-section, is typical of an acute tendinitis. (D) Normal medial lobe on the opposite limb. 1: medial groove of the intertubercular sulcus; 2: medial lobe of the proximal tendon of the biceps brachii muscle; 3: brachiocephalicus muscle.

Vet-ebooks.com

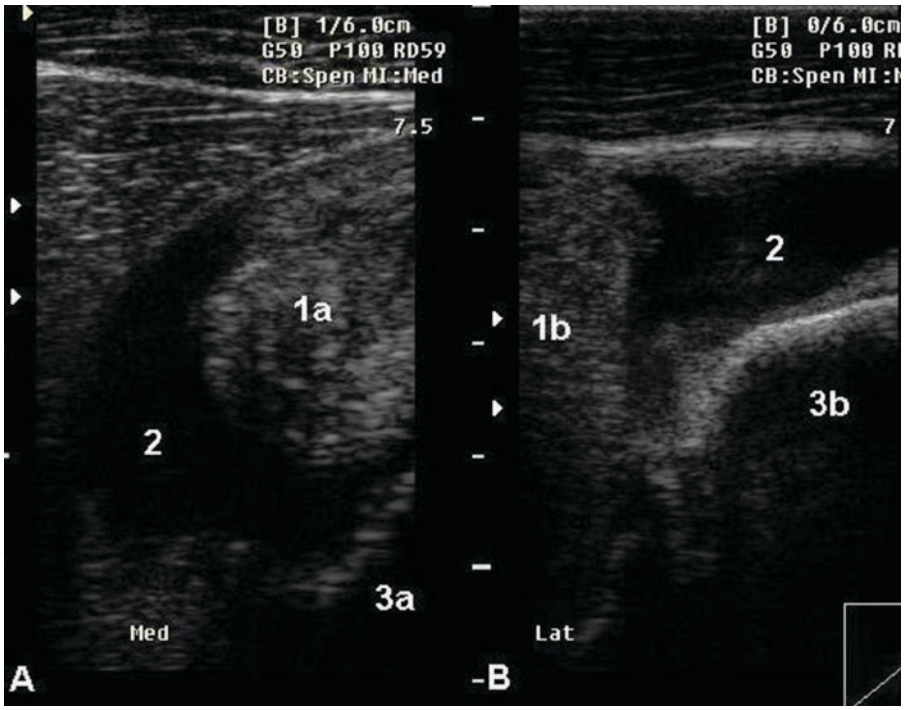


Figure 5.25 Chronic bicipital bursitis secondary to a supraglenoid tubercle fracture. Transverse (medial is to the left) ultrasound scans of the cranial aspect of the shoulder in a young horse. (A) The medial lobe of the bicipital tendon (1a) looks hypoechoic and is surrounded by an anechoic space (2) compatible with a fluid effusion. (B) On the lateral side of the biceps brachii tendon (1b) there is anechogenic fluid distension (2). These abnormal findings are consistent with a chronic bicipital bursitis. 1: proximal tendon of the biceps brachii; 1a: medial lobe of the proximal tendon of the biceps brachii; 1b: lateral lobe of the proximal tendon of the biceps brachii; 2: synovial distension of the bicipital bursa; 3: intertuberculus humeral sulcus; 3a: medial groove; 3b: greater tubercle.

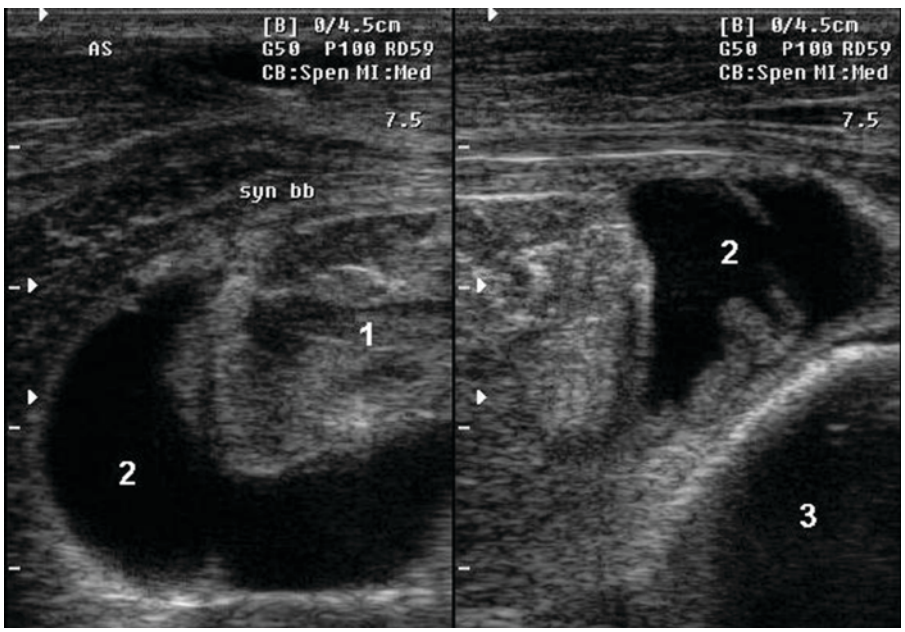


Figure 5.26 Chronic bicipital bursitis. Transverse (medial is to the left) ultrasound scans of the cranial aspect of the shoulder in a colt with a chronic left fore limb lameness. The probe is slightly distal to the point of the shoulder. The biceps brachii tendon (1) is imaged just distal to the intertubercular sulcus. Its heterogeneous pattern is due to a tendon lesion but also the presence of hypoechogenic striated fibers of the muscle body. The distal recess of the bicipital bursa (2) is well visualized because of the extensive synovial fluid distension. Synovial membrane thickening and proliferation are also seen. 1: proximal tendon of the biceps brachii; 2: synovial distension of the bicipital bursa; 3: proximal humerus.

Vet-ebooks.com

brachii tendon. The two tendons are connected by an aponeurosis of the supraspinatus muscle (Figure 5.20). The lateral tendon, bigger and roughly triangular in shape, is easier to identify and follow to its insertion on the cranial part of the greater humeral tubercle, where it is in close proximity to the lateral lobe of the biceps brachii tendon (Figure 5.29). The medial tendon, smaller and flatter, is more difficult to scan (Figure 5.20). It attaches on the cranial part of the lesser tubercle of the humerus in a position close to the medial lobe of the biceps brachii tendon. The bicipital bursa is interposed between these two structures. At this level, the lateral tendon is covered with the hypoechoic brachiocephalicus muscle.

Infraspinatus Muscle and Tendon

At the lateral aspect of the shoulder, the infraspinatus muscle originates from the infraspinatus fossa of the scapula (Figure 5.30).The intramuscular tendon looks echoic within the infraspinatus muscle (Figure 5.31).

Its distal tendon slides over the convexity of the greater tubercle of the humerus and inserts on the caudal eminence of this tubercle. Distally, as it approaches its humeral insertion, it becomes wider and heterogeneous because of its lobulated structure. In fact, over the caudal part of the greater tubercle, it appears as first three and then further distally two superimposed portions. There is an infraspinatus bursa located

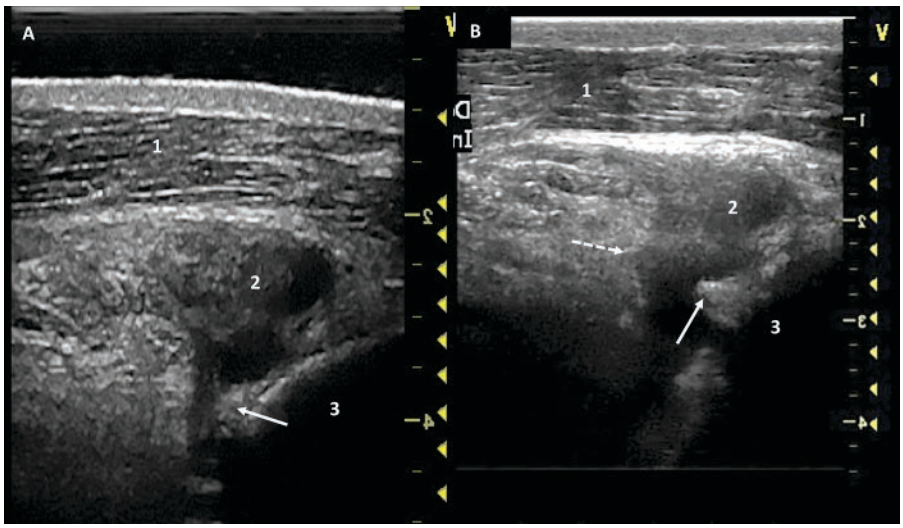


Figure 5.27 Proximal humeral osteitis and bicipital bursitis. Transverse section of the lateral lobe of the bicipital tendon showing chronic bicipital bursitis and bone irregularity of the greater tubercle. Medial is to the left, lateral is to the right. (A) is in the weightbearing limb and (B) in the non-weightbearing limb. Note the osseous irregularity on the axial margin of the greater tubercle (solid arrow) and the indentation in the opposing surface of the biceps tendon (dashed arrow) only visible in the non-weightbearing image. 1: brachiocephalicus muscle; 2: distended bicipital bursa with inflamed synovium; 3: greater tubercle of humerus. (*Source*: Courtesy: Dr Roger Smith.)

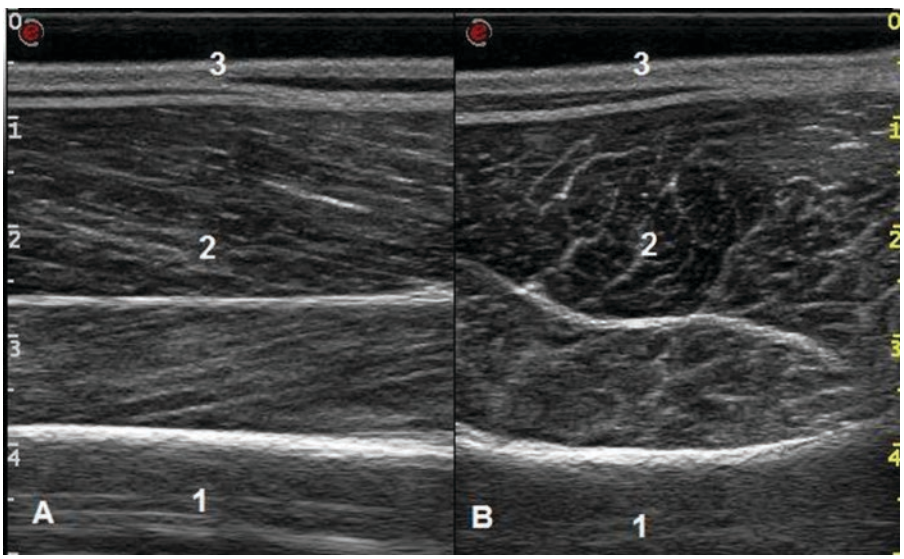


Figure 5.28 Normal images of the supraspinatus muscle at the level of the supraspinatus fossa. Longitudinal (A) and transverse (B) ultrasound scans. 1: supraspinatus fossa; 2: supraspinatus muscle; 3: skin.

Vet-ebooks.com

between this tendon and the caudal part of the greater humeral tubercle, which can be visualized as an anechoic space deep to the infraspinatus tendon. A small amount of synovial fluid in the infraspinatus bursa is also visible in normal horses (Figure 5.32).

Traumatic injury of the lateral aspect of the shoulder can cause infraspinatus bursitis, associated with fracture of the greater tubercle. In horses with suprascapular nerve paralysis, the infraspinatus muscle is more echogenic than normal as the muscle atrophies leaving the connective tissue surrounding the muscle fascicles, and consequently its tendon becomes less visible (Figure 5.33)

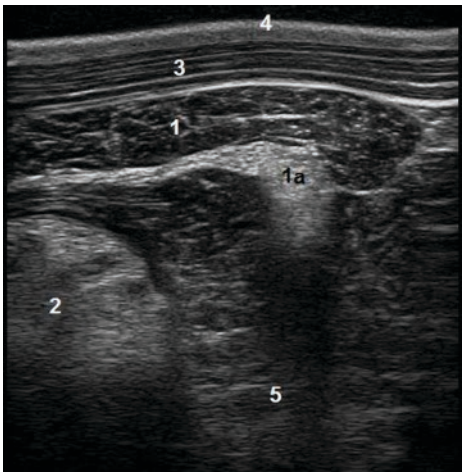


Figure 5.29 Normal lateral supraspinatus tendon at the level of the scapulohumeral joint. Transverse (medial is to the left) ultrasound scan proximal to the intertubercular sulcus. 1: supraspinatus muscle; 1a: lateral supraspinatus tendon; 2: biceps brachii tendon; 3: brachiocephalicus muscle; 4: skin; 5: scapulohumeral fat pad.

Scapulohumeral Joint

The scapulohumeral joint is composed of two bones: the distal end of the scapula (glenoid cavity) and the proximal humerus (humeral head). Because no collateral ligaments are present, the thick surrounding musculature provides stability to the joint. The glenoid labrum sits around the margins of the glenoid cavity and is a fibrous pad which enlarges the contact between the two articular surfaces. A large portion of the scapulohumeral joint space is hidden from view. Only the craniolateral, lateral, and caudolateral aspects of the shoulder joint can be scanned in a longitudinal plane using a linear or convex 5–7.5 MHz probe without a standoff pad. All three approaches to the scapulohumeral joint in longitudinal section allow detection of the presence of a synovial effusion and periarticular bony proliferation. Conversely, ultrasound can only provide a limited examination of the humeral head using a caudolateral approach. A normal joint has smooth articular margins and little or no synovial fluid (Figures 5.34 and 5.35). Transverse images are more useful in cases of ultrasonographic-guided injection of this joint.

In adult horses, synovial fluid distension and articular margin modeling are indicative of osteoarthrosis of the scapulohumeral joint. In young horses, a diagnosis of scapulohumeral osteochondrosis, with osteochondral fragmentation of the humeral head, may be made with a caudolateral approach. Septic synovitis of the shoulder joint occurs more frequently in foals than in adults. In yearlings and adults, injuries to this joint are infrequent and are more likely to occur secondary to trauma such as a fracture of the supraglenoid tubercle (Figures 5.36 and 5.37). In cases of supraglenoid tubercle fractures, ultrasonographically there is synovial fluid distension causing

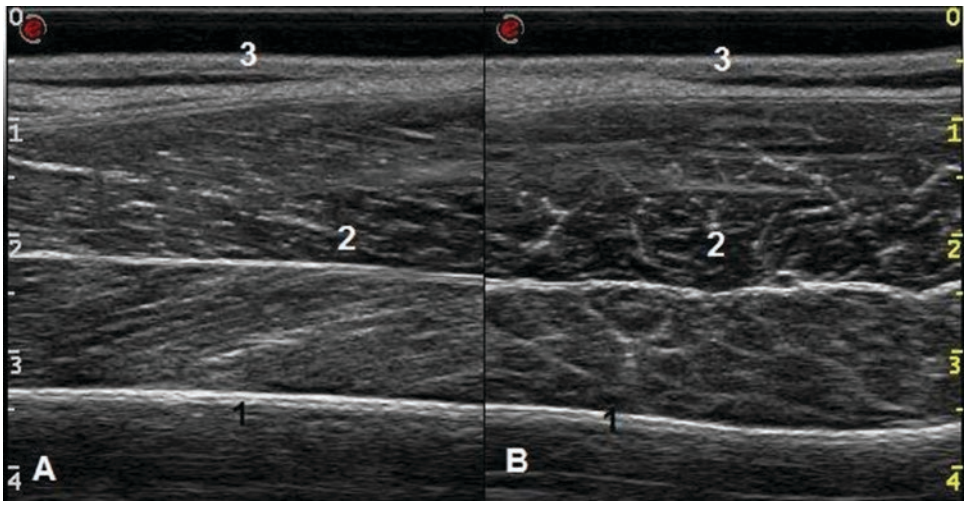


Figure 5.30 Normal infraspinatus muscle. Longitudinal (A) and transverse (B) ultrasound scans of the infraspinatus muscle at the level of the infraspinatus fossa. 1: infraspinatus fossa; 2: infraspinatus muscle; 3: skin.

Vet-ebooks.com

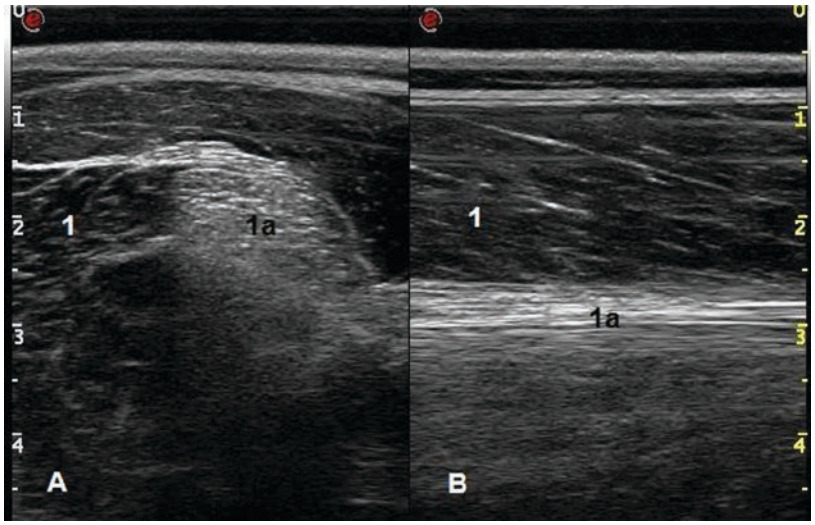


Figure 5.31 Normal infraspinatus tendon within the infraspinatus muscle. Transverse (A) and longitudinal (B) ultrasound scans of the infraspinatus muscle at the lateral aspect of the shoulder distal to the infraspinatus fossa. 1: infraspinatus muscle; 2: infraspinatus tendon.

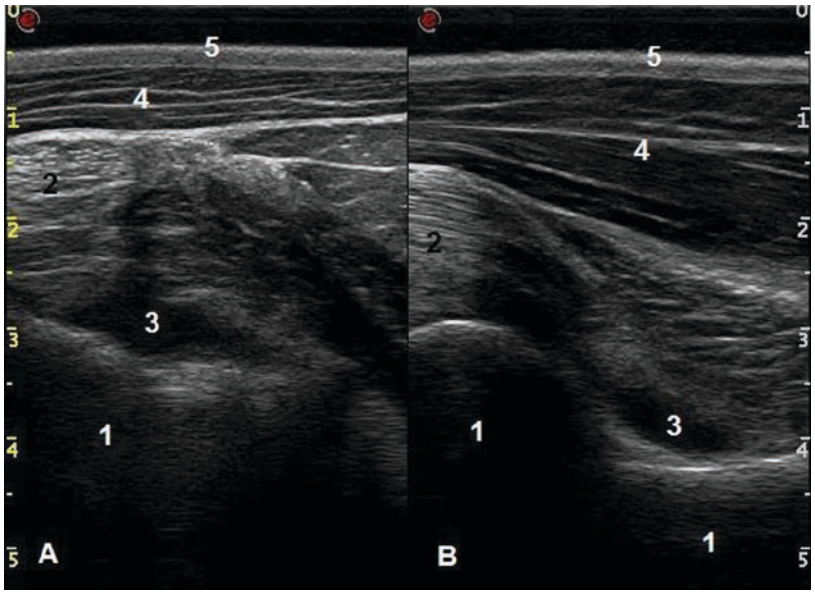


Figure 5.32 The infraspinatus bursa containing a small amount of synovial fluid. (A) Transverse ultrasound scan (cranial is to the left); (B) Longitudinal ultrasound scan (proximal is to the left). 1: caudal part (crest) of the major humeral tubercle; 2: infraspinatus tendon; 3: infraspinatus bursa (mild synovial distension); 4: omotransverse muscle; 5: skin.

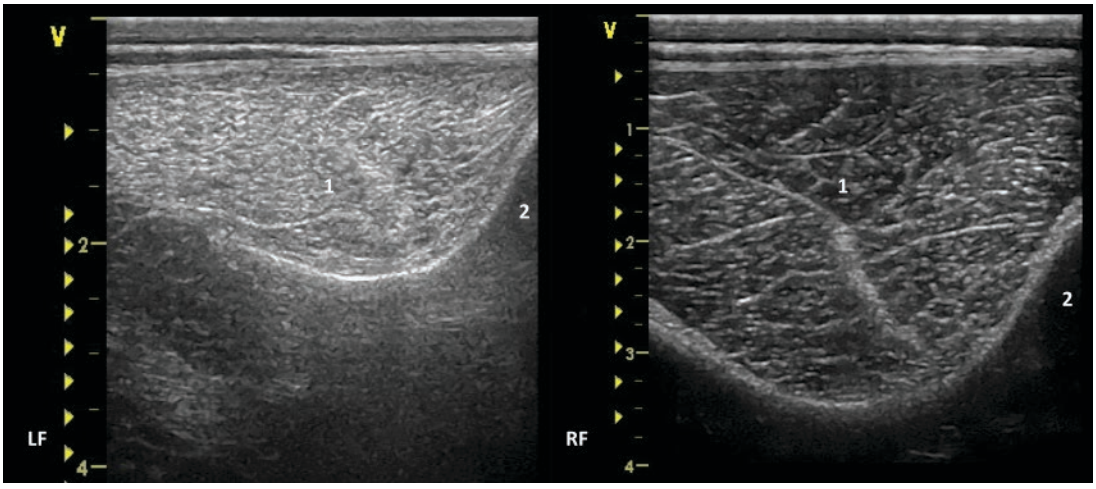


Figure 5.33 Transverse ultrasound images (caudal to the left; cranial to the right) of neurogenic infraspinatus muscle atrophy (Sweeny). The abnormal left infraspinatus muscle is smaller and more echogenic compared to the normal right: the ratio of "muscle fibers/connective tissue" is now in favor of the latter with a greater proportion of connective tissue to muscle fibers on the right. 1: infraspinatus muscle; 2: scapula spine. *Source*: Courtesy: Dr Roger Smith.

Vet-ebooks.com

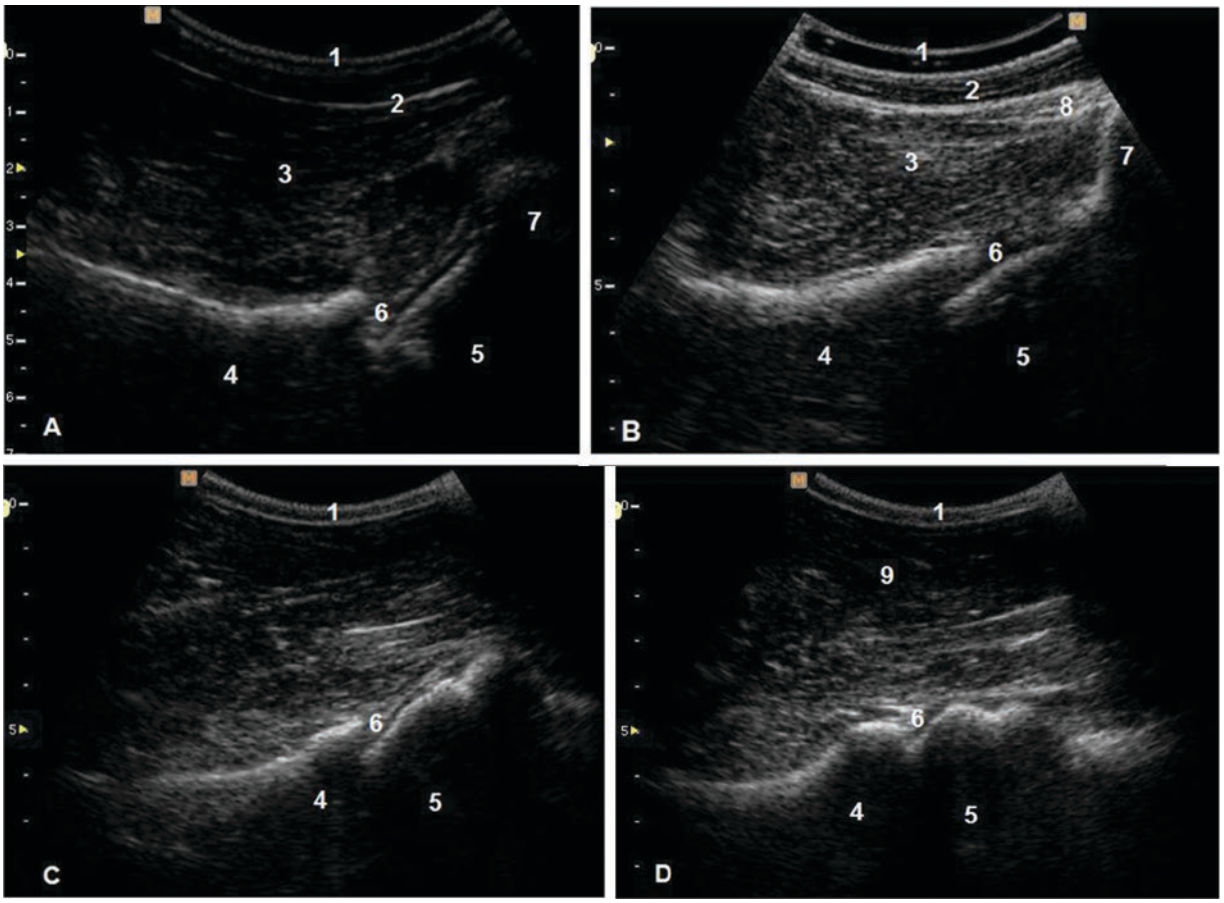


Figure 5.34 Normal proximodistal ultrasound scans of the scapulohumeral joint (SHJ) (proximal is to the left). The convex probe is held vertically and moved cranial to caudal. (A) Craniolateral aspect of the SHJ: the probe is positioned between the supraspinatus and infraspinatus muscles. (B) Lateral aspect of the SHJ: the probe is positioned at the level of the infraspinatus intramuscular tendon. (C and D) Caudolateral aspect of the SHJ: the probe is positioned caudal to the infraspinatus tendon. The humeral head always has a bilobed shape. 1: skin; 2: omotransverse muscle; 3: infraspinatus muscle; 4: scapula; 5: humeral head; 6: joint space; 7: major tubercle; 8: infraspinatus tendon; 9: triceps brachii muscle.

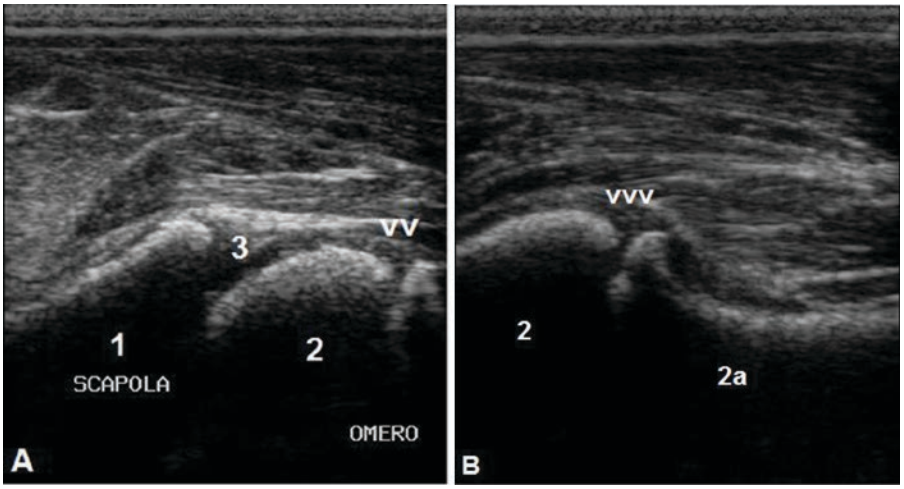


Figure 5.35 Normal proximodistal ultrasound scans of the scapulohumeral joint (A) and the proximal aspect of the humerus (B) in a 7-month-old foal (proximal is to the left). At this age, the proximal humeral epiphysis (arrows) is not closed and should not be mistaken for a fracture line. 1: scapula; 2: humeral head; 2a: humeral neck; 3: joint space.

Vet-ebooks.com

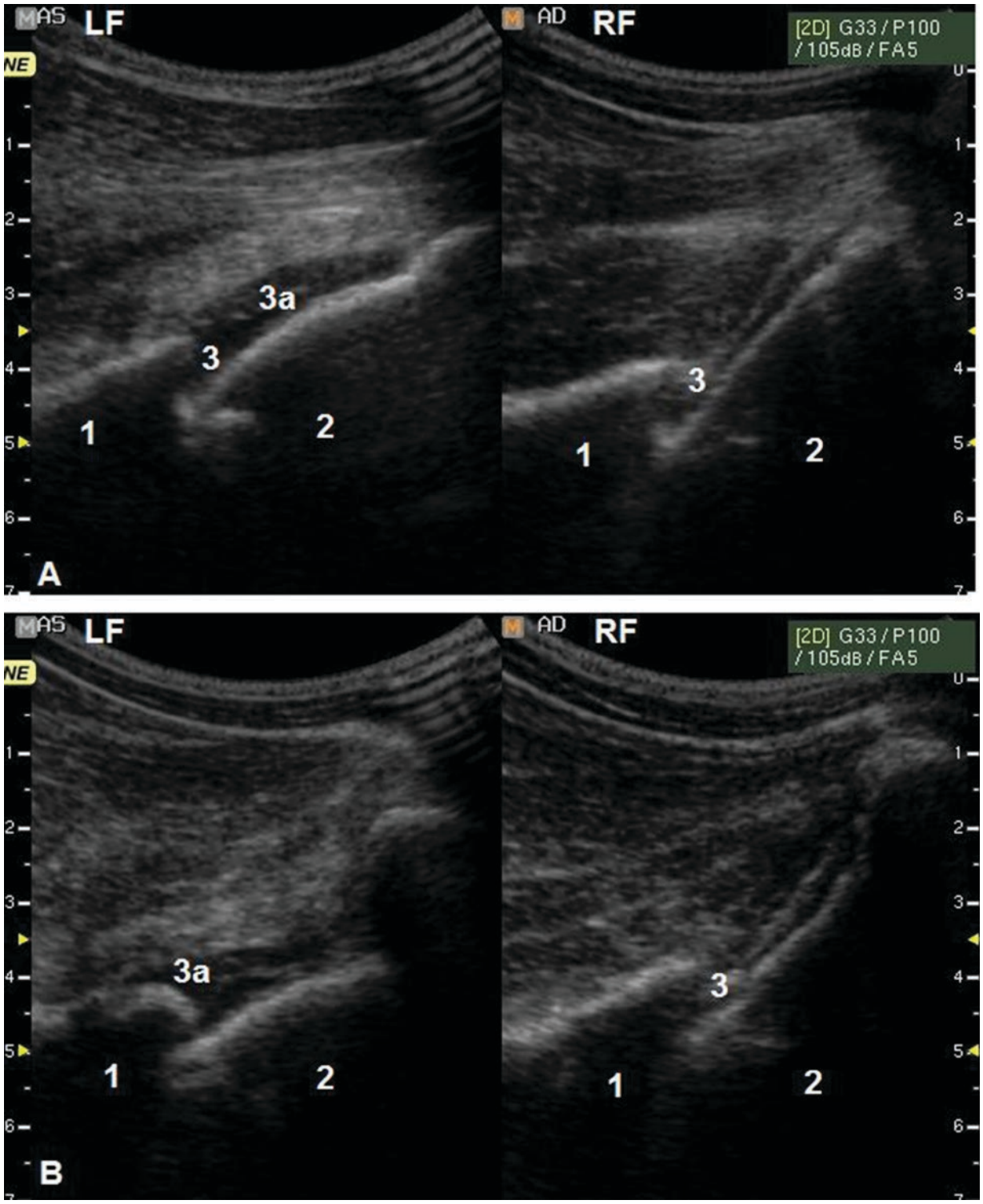


Figure 5.36 Ultrasound scans of the left (LF) and right (RF) scapulohumeral joints (SHJ) of an Arabian yearling who suffered an acute intra-articular supraglenoid fracture of the left shoulder (Figure 5.16). These scans have been obtained with a convex probe. In both images (A and B) the left SHJ has synovial fluid distension which is raising the articular capsule. The echogenicity of the synovial fluid is increased because of the presence of fibrin. There is no synovial fluid evident in the contralateral SHJ (RF). 1: scapula; 2: humeral head; 3: HJ space; 3a: synovial fluid.

Vet-ebooks.com

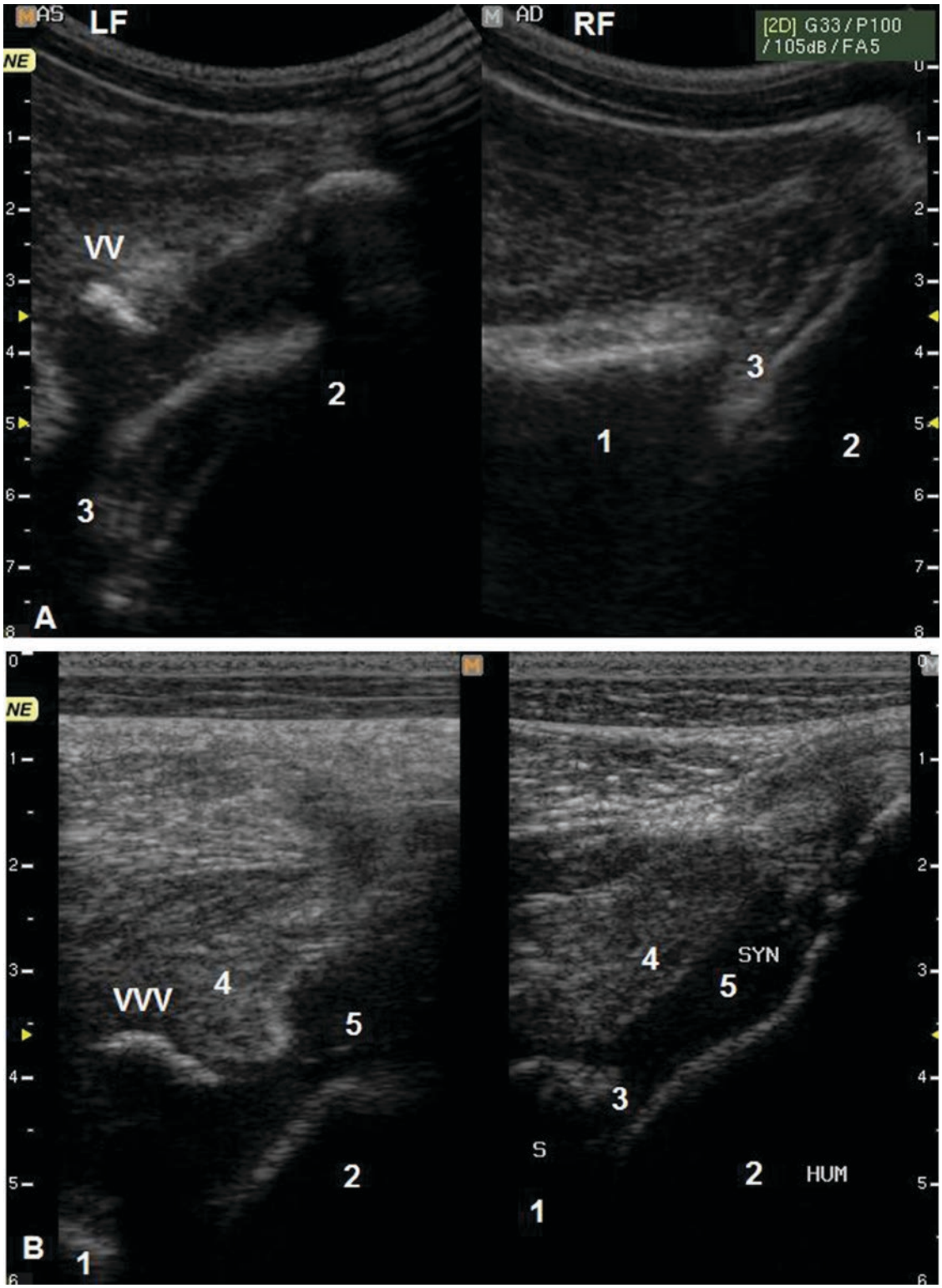


Figure 5.37 Ultrasound scans of the left (LF) and right (RF) scapulohumeral joints (SHJ) of the same Arabian yearling in Figures 5.14 and 5.32. (A) On the abnormal left fore limb, the synovial recess is markedly distended and a bony fragment (arrows) is present in the synovial fluid. There is no synovial fluid evident in the contralateral normal SHJ (RF). (B) The same images as (A) obtained with a linear transducer. The images obtained with a convex probe (A) show a larger view of the SHJ but with less detail. In (B) it is possible to appreciate the thickening and the heterogeneous pattern of the synovial membrane, which are underestimated in (A). 1: scapula; 2: humeral head; 3: SHJ space; 4: synovial membrane; 5: synovial fluid.

Vet-ebooks.com

the joint capsule to bulge. The echogenicity of the synovial fluid may be increased because of the presence of blood or fibrin.

Recommended Readings

Carnicer, D., Coudry, V., and Denoix, J.-M. (2008). Ultrasonographic guided injection of the scapulohumeral joint in horses. *Equine Veterinary Education* 20(2): 103–106.

Cauvin, E.R.J. (1998). Soft tissue injuries of the equine shoulder region: A systematic approach to differential diagnosis. *Equine Veterinary Education* 10(2): 70–74.

Coudry, V., Allen, A.K., and Denoix, J.-M. (2005). Congenital abnormalities of the bicipital apparatus in four mature horses. *Equine Veterinary Journal* 37(3): 272–275.

Gough, M.R. and McDiarmid, A.M. (1998). Septic intertuberal (bicipital) bursitis in a horse. *Equine Veterinary Education* 10(2): 66–69.

Little, D., Redding, W.R., and Gerard, M.P. (2009). Osseous cyst-like lesions of the lateral intertubercular groove of the proximal humerus: A report of 5 cases. *Equine Veterinary Education* 21(2): 60–66.

McDiarmid, A.M. (1999). The equine bicipital apparatus: Review of anatomy, function, diagnostic investigative techniques and clinical conditions. *Equine Veterinary Education* 11(2): 63–68.

Pasquet, H., Coudry, V., and Denoix, J.-M. (2008). Ultrasonographic examination of the proximal tendon of the *biceps brachii*: Technique and reference images. *Equine Veterinary Education* 20(6): 331–336.

Redding, W.R. and Pease, A.P. (2010). Imaging of the shoulder. *Equine Veterinary Education* 22(4): 199–209.

Tnibar, M.A., Auer, J.A., and Bakkali, S. (1999). Ultrasonography of the equine shoulder: Technique and normal appearance. *Veterinary Radiology & Ultrasound* 40(1): 44–57.

Tnibar, M.A., Auer, J.A., and Bakkali, S. (2001). Ultrasonography of the equine elbow: Technique and normal appearance. *Journal of Equine Veterinary Science* 21(4): 177–187.

Vet-ebooks.com

6

Ultrasonography of the Hock

Katherine S. Garrett

Rood and Riddle Equine Hospital, Lexington, KY, USA

Introduction

Ultrasonography of the tarsus can be challenging, but it is an important part of a complete diagnostic evaluation of tarsal disease. As with other body regions, a thorough understanding of normal anatomy is essential. Comparison with magnetic resonance, computed tomographic, and/or radiographic images, and dissected specimens can be helpful in understanding the anatomic relationships and the precise locations and paths of the tendinous and ligamentous structures.

Excellent reviews of scanning techniques for the tarsal region have been published. Regardless of the particular approach chosen, a systematic method for evaluation of this complex structure is helpful. The structures to be examined include the tendons and ligaments, the synovial structures, the bony surfaces, and the subcutis. Comparison with the opposite limb can be extremely helpful in determining if an unusual abnormality is present or in cases of mild disease.

A linear transducer (8–12 MHz) is generally most useful, but a micro-convex transducer (7–10 MHz) can be helpful in some situations. Sedation is often necessary to ensure patient compliance and sonographer safety. If the hair in the area can be clipped, image quality will be improved. Scanning the contralateral or unaffected hock can be useful for comparison.

Tendons and Ligaments

The tarsal region contains many tendons and ligaments, some of which have complex attachments or insertions distant from the tarsus itself.

Collateral Ligaments

The lateral and medial collateral ligaments both have two major components, a long superficial component and a short deeper component. The long portion of the lateral collateral ligament originates on the caudal portion of the lateral malleolus of the distal tibia and has insertions on the calcaneus, fourth tarsal bone, and third and fourth metatarsal bone. The tripartite short portion originates on the cranial portion of the lateral malleolus and extends in a nearly horizontal plane to the lateral aspect of the talus and calcaneus. The lateral collateral ligament is less distinct than the medial collateral ligament.

The long medial collateral ligament originates on the medial malleolus of the distal tibia and extends distally, inserting on the distal talus, central, fused first and second, and third tarsal bones, and second and third metatarsal bones. The short portion of the ligament originates on the medial malleolus and has three subsections that travel in a more horizontal plane than the long portion and insert on the proximal medial talus and the sustentaculum tali.

During ultrasonographic examination, the lateral and medial collateral ligaments can be located most easily in the longitudinal plane. As the short components lie in a more transverse plane than the long components, an image in the transverse plane can then be obtained by rotating the transducer by 90 degrees. In addition, some of the short portions are in partial relaxation when the horse is weightbearing, so imaging these ligaments while the horse is not fully weightbearing (and the ligament is more taut) may aid in evaluation of the ligament.

Atlas of Equine Ultrasonography, Second Edition. Edited by Jessica A. Kidd, Kristina G. Lu and Michele L. Frazer.
© 2022 John Wiley & Sons Ltd. Published 2022 by John Wiley & Sons Ltd.
Companion Website: www.wiley.com/go/kidd/atlas

Vet-ebooks.com

Desmitis of any of the collateral ligaments can occur, but is more commonly seen in the long medial collateral ligament. Ultrasonographic signs of desmitis are similar to those in any ligament and include increased size, decreased echogenicity, and abnormal fiber pattern (Figures 6.1 and 6.2). If the insertion of the ligament is involved, bony irregularity or avulsion fragments may be imaged (Figure 6.3). Horses with collateral ligament desmitis typically also have synovial effusion and synovial membrane thickening due to an intra-articular component.

The short lateral collateral ligament is invariably involved in fractures of the lateral malleolus of the distal tibia, while the long lateral collateral ligament is less commonly affected (Figure 6.4). These fractures are usually caused by external trauma. Ultrasonography can be useful to assess the degree of involvement of the collateral ligaments and potential for instability of the joint.

Plantar Aspect

The common calcaneal tendon/gastrocnemius tendon, superficial digital flexor tendon, and long plantar ligament are found on the plantar aspect of the tarsus. The gastrocnemius tendon inserts on the proximal surface of the tuber calcanei. The long plantar ligament originates on the plantar surface of the proximal tuber calcanei and inserts on the fourth tarsal and fourth metatarsal bones. The superficial digital flexor tendon largely passes over the surface of the tuber calcanei, but the medial and lateral aspects insert on the proximal aspect of this bone via a retinaculum.

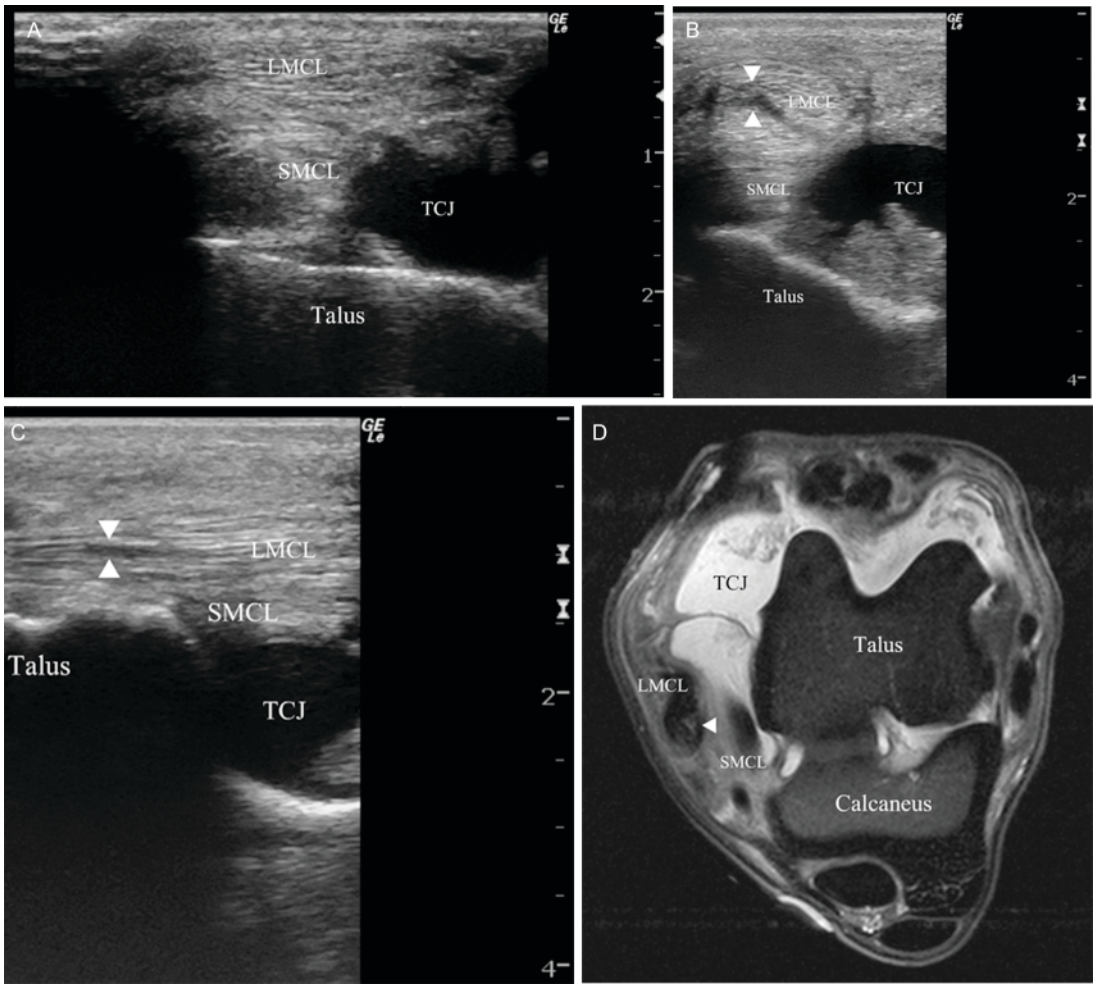


Figure 6.1 (A) Longitudinal image of a normal long medial collateral ligament (LMCL) and short medial collateral ligament (SMCL). TCJ: tarsocrural joint. Proximal is to the right of the image. Transverse (B) and longitudinal (C) plane images of an abnormal LMCL. The ligament is enlarged with a focal region of marked hypoechogenicity and fiber disruption (arrowheads). Synovial effusion is present in the TCJ. Dorsal and proximal are to the right of the images. (D) Transverse plane magnetic resonance image of the same horse. Note the marked synovial effusion in the TCJ and focal region of increased signal (arrowhead) in the LMCL. Dorsal is to the top of the image, medial is to the left of the image.

Vet-ebooks.com

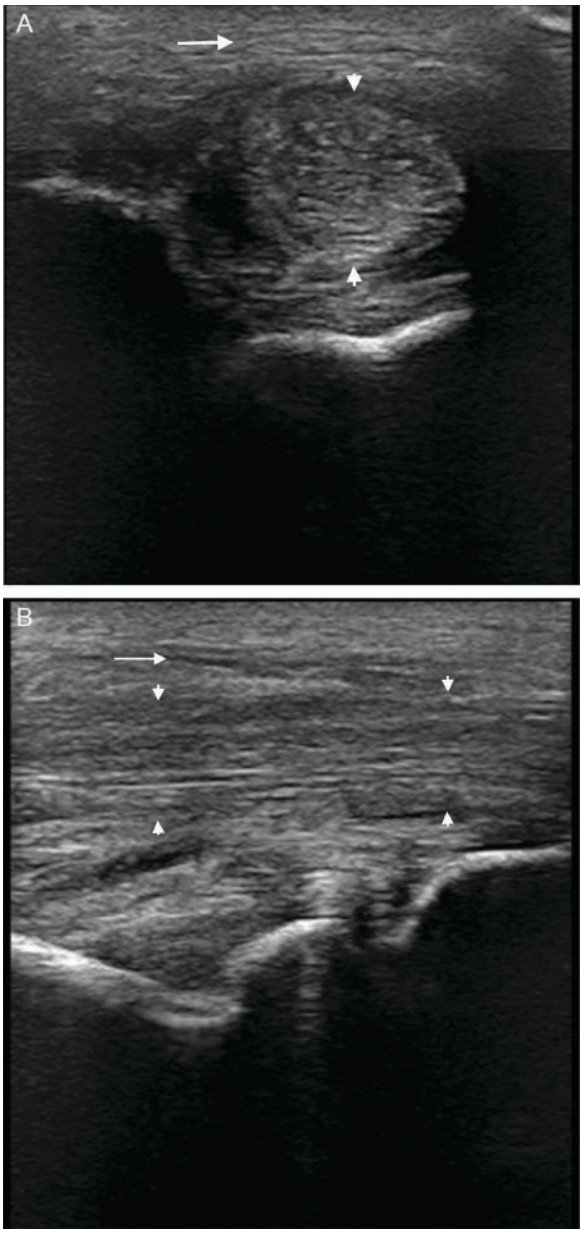


Figure 6.2 Transverse (A) and longitudinal (B) images of the long portion of the lateral collateral ligament. Dorsal (A) and proximal (B) are to the right of the images. The ligament is enlarged with decreased echogenicity diffusely (arrowheads). There is thickening of the subcutaneous tissues as well (arrow).

Soft tissue swelling of the plantar aspect of the tarsus ("curb") may be caused by injury to the long plantar ligament or superficial digital flexor tendon. Subcutaneous edema or thickening may give a similar external appearance and seems to be more common than tendon or ligament injuries. Desmitis of the long plantar ligament is characterized by enlargement and hypoechogenicity of the ligament (Figure 6.5).

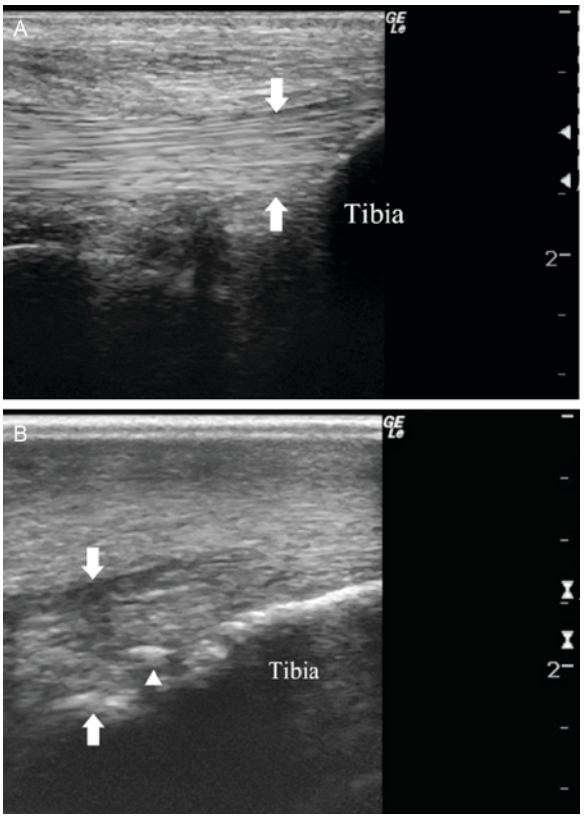


Figure 6.3 Longitudinal plane images of the proximal insertion on the medial malleolus of a normal (A) and abnormal (B) medial collateral ligament (arrows). In (B) there are areas of hypoechogenicity within the ligament as well as small avulsion fragments (arrowhead) and thickening of the subcutaneous space. Proximal is to the right of the images.

Plantaromedial Aspect

The lateral deep digital flexor tendon is located on the plantaromedial aspect of the tarsus, passing over the sustentaculum tali within the tarsal sheath. The smaller medial deep digital flexor tendon is contained within its own synovial sheath located dorsomedial to the lateral deep digital flexor tendon. The medial tendon joins the lateral tendon in the proximal metatarsal region. While scanning the tarsal sheath, the transducer should be positioned in a caudomedial/plantaromedial location in the distal crus and tarsal regions and rotate toward the plantar aspect of the limb as it is moved distally. This region of the tarsus has irregular contours in the normal horse, which can make maintaining good transducer contact challenging. As a result, images of the lateral deep digital flexor tendon can often be more easily obtained by using a standoff pad with a linear probe or by using a micro-convex probe due to its smaller footprint. When soft tissue swelling is present in this area, it tends to smooth the surface contours of the limb and facilitate good transducer contact.

Vet-ebooks.com

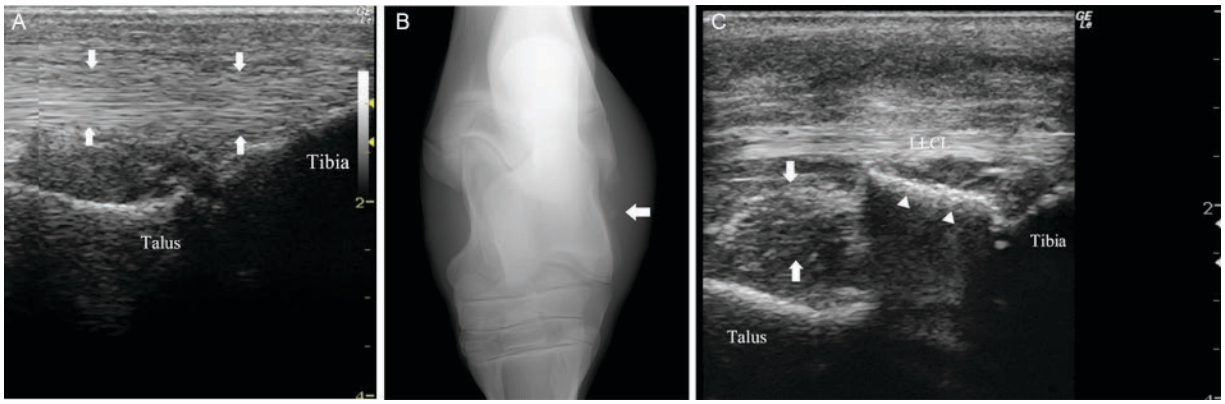


Figure 6.4 (A) Longitudinal plane image of a normal short lateral collateral ligament (SLCL); (arrows) origin on the lateral malleolus. Proximal is to the right of the image. (B) Dorsoplantar radiographic image of a horse with a lateral malleolus fracture (arrow). Note the distal displacement of the fragment. Lateral is to the right of the image. (C) Longitudinal plane image of the lateral malleolus fragment (arrowheads) and involvement of the SLCL (arrows) of the horse in (B). The fragment has displaced distally and plantarly along the course of the SLCL to lie deep to the long lateral collateral ligament (LLCL). Short collateral ligament association with the fragment was confirmed arthroscopically. Thickening of the subcutaneous tissue is evident. Proximal is to the right of the image.

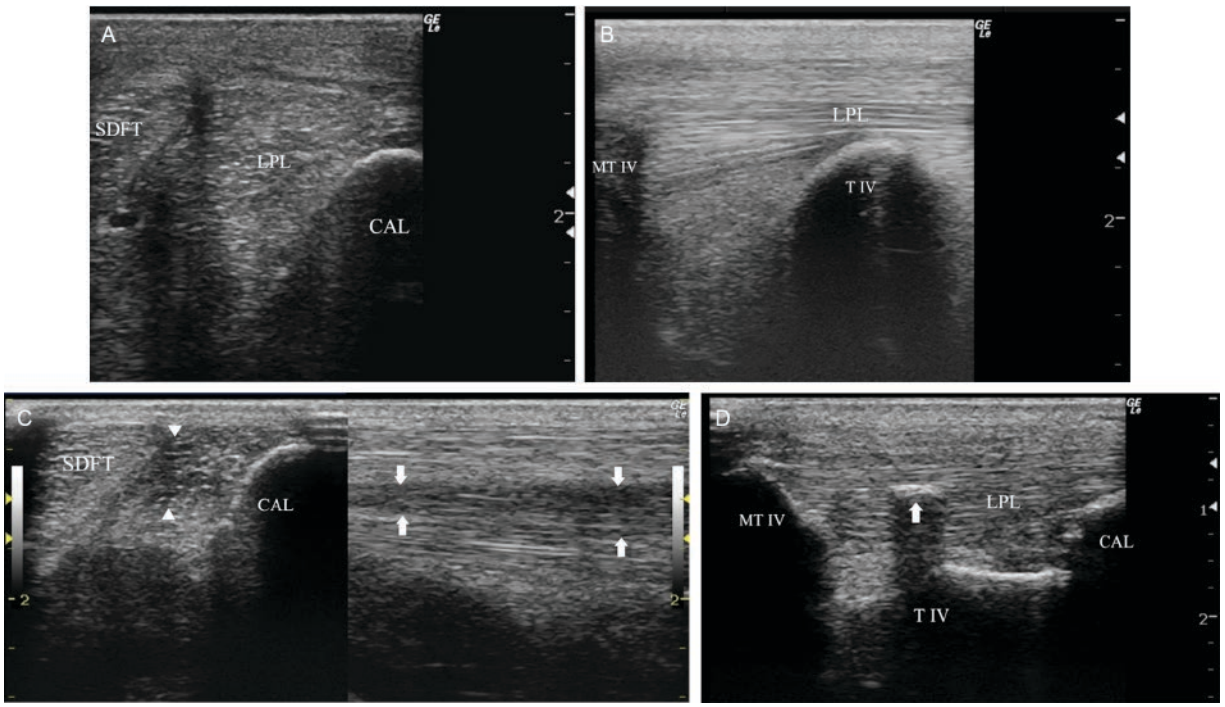


Figure 6.5 (A) Transverse plane image of a normal long plantar ligament (LPL). CAL: calcaneus; SDFT: superficial digital flexor tendon. Lateral is to the right of the image. (B) Longitudinal plane image of the LPL distal insertion on the fourth tarsal bone (T IV) and fourth metatarsal bone (MT IV). Proximal is to the right of the image. (C) Transverse (left image) and longitudinal (right image) images of a horse with LPL desmitis. Hypoechogenicity of the ligament is apparent (arrowheads and arrows). SDFT: superficial digital flexor tendon. Lateral and proximal are to the right of the images. (D) Longitudinal plane image of an LPL with focal mineralization within the ligament (arrow). Proximal is to the right of the image.

Vet-ebooks.com

Ultrasonographic examination of the lateral deep digital flexor tendon within the tarsal sheath is complicated by multiple factors. The musculotendinous junction generally extends distally to within the proximal aspect of the tarsal sheath and its heterogeneous pattern can be confused with tendonitis. The normal curvature of the tendon as it passes over the sustentaculum tali can also introduce hypoechogenic artifacts (Figure 6.6). Although tendonitis of the deep digital flexor tendon is uncommon, it can be a source of lameness. Ultrasonographic signs are similar to those seen with tendonitis in general (hypoechogenicity, irregular fiber pattern, and/or enlargement), along with an effusion of the tarsal sheath.

Dorsal Aspect

The peroneus tertius and the tendons of the cranial tibial muscle have complex insertions on the dorsal aspect of the distal tarsal region. The distal peroneus tertius forms a tunnel through which the distal cranial tibial tendon emerges. The peroneus tertius is the most echogenic structure on the dorsal tibia, making it easier to identify. The dorsal tendon of the peroneus tertius then inserts on the central and third tarsal and third metatarsal bones. The lateral tendon inserts on the fourth tarsal bone and the distolateral calcaneus and talus. The dorsal tendon of insertion of the cranial tibial muscle inserts on the third tarsal and third metatarsal bones. The cunean tendon is the medial tendon of insertion of the cranial tibial muscle. It passes medially across the central tarsal bone, inserting on the fused first and second tarsal bone, central tarsal bone, and second metatarsal bone. The tendons of insertion of the cranial tibial and peroneus tertius can be identified by following each of the tendons individually from their origins in the distal tibia.

Diagnosis of peroneus tertius rupture can generally be made on physical examination by extending the tarsus while the stifle is flexed. Ultrasonography shows a discontinuity in the tendon with edema and disrupted muscle architecture of the cranial tibial muscle (Figure 6.7).

Two extensor tendons cross the tarsal region, both within separate synovial sheaths. The long digital extensor tendon is located on the dorsolateral aspect of the limb. The lateral digital extensor tendon is located on the lateral aspect of the tarsus and in close proximity to the long portion of the lateral collateral ligament. Tendinitis of these structures is characterized by enlargement, hypoechogenicity, and abnormal fiber pattern of the tendons with effusion of the synovial sheath or bursa (Figure 6.8).

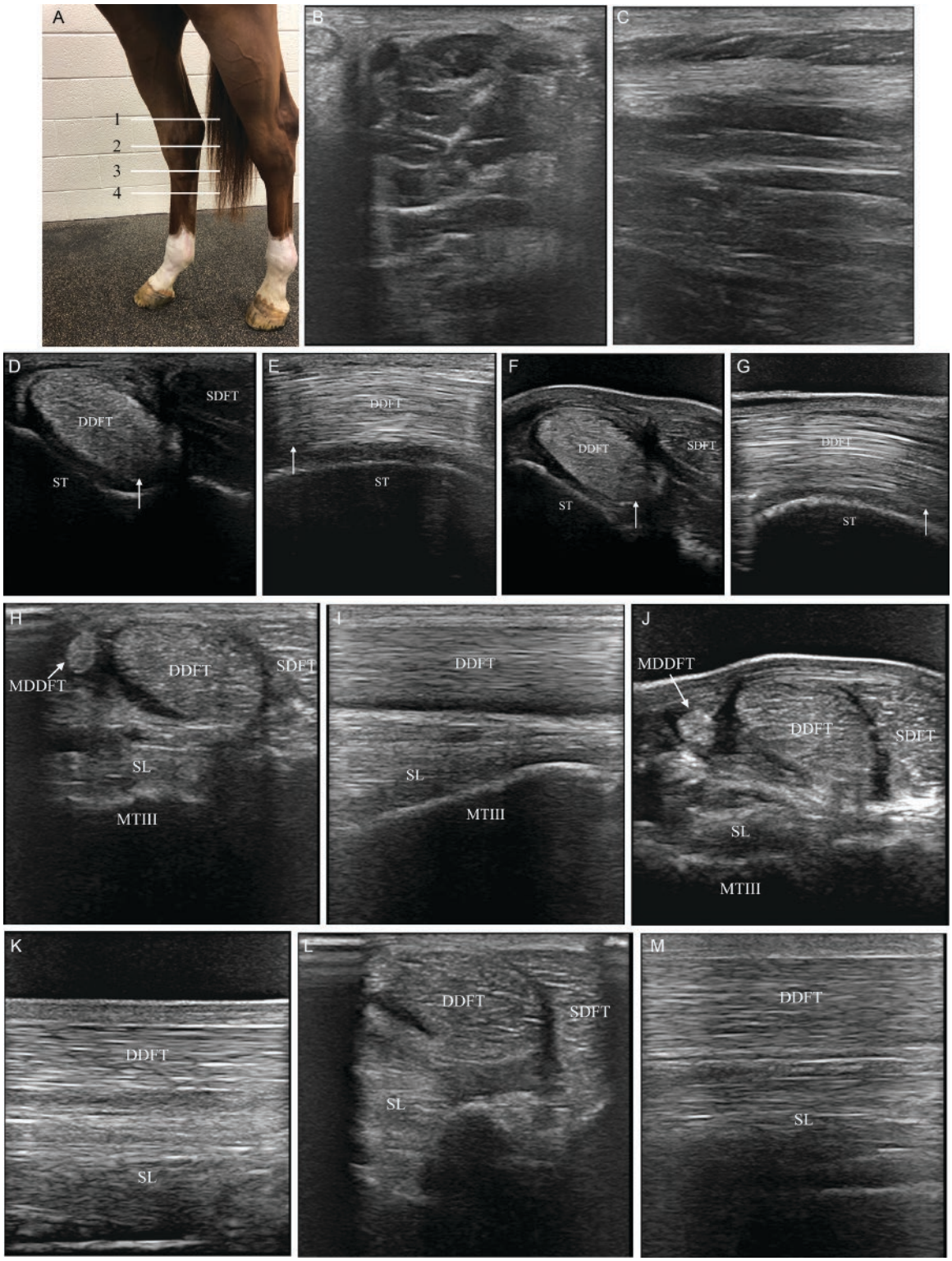
Synovial Structures

The tarsus contains multiple synovial structures, including joints, bursae, and tendon sheaths. Ultrasonography is useful in differentiating potential causes of tarsal region swelling, allowing differentiation of cellulitis, synovitis, or abscessation. In cases of synovitis or bursitis, ultrasonography can assist with determination of which synovial structures may be involved. Penetrating wound tracts can also be followed to assess possible synovial structure involvement. Ultrasonography can also be very useful to determine the best location for synoviocentesis.

In general, the synovial structures should be evaluated for the amount and character of the synovial fluid and synovial membrane thickness. Normal synovial fluid is anechogenic. In cases of synovitis, the synovial fluid may appear more echogenic than normal and may contain hyperechogenic strands or clumps consistent with fibrin accumulation. The synovial membrane may be thickened, especially in cases of septic synovitis (Figure 6.9). While assessment of the character of the synovial fluid may provide some information on the degree of cellularity of the fluid, it is important to note that ultrasonography

Figure 6.6 Images of the normal tarsal sheath. The anatomic locations of these images are indicated by the horizontal lines on the limb of the horse in (A). Transverse (B) and longitudinal (C) images of the lateral deep digital flexor tendon in the proximal tarsal sheath at the musculotendinous junction (level 1 in (A)). The normal heterogeneous pattern of the muscle is apparent. (D to G): Transverse (D and F) and longitudinal (E and G) images at the level of the sustentaculum tali (level 2 in (A)). In (F) and (G), a standoff pad is used to improve image quality, but artifactual areas of hypoechogenicity remain in all four images (arrows) and the margin of the DDFT artifactually appears irregular. These artifacts are due to small differences in tendon fiber orientation as the tendon follows a curved path over the sustentaculum tali. Slight changes in transducer position and angle can be used to assess these different fiber orientations in real time. (H to K) Transverse (H and J) and longitudinal (I and K) images at the level of the proximal metatarsus (level 3 in (A)). In (J) and (K), a standoff pad is used to improve image quality. (L and M) Transverse (L) and longitudinal (M) images at the level of the distal tarsal sheath (level 4 in (A)). At this level, the smaller medial deep digital flexor tendon has joined the larger lateral deep digital flexor tendon. Proximal or lateral is to the right of the images. DDFT: lateral deep digital flexor tendon; MDDFT : medial deep digital flexor tendon; MTIII: third metatarsal bone; SDFT: superficial digital flexor tendon; SL: suspensory ligament; ST: sustentaculum tali.

Vet-ebooks.com



Vet-ebooks.com

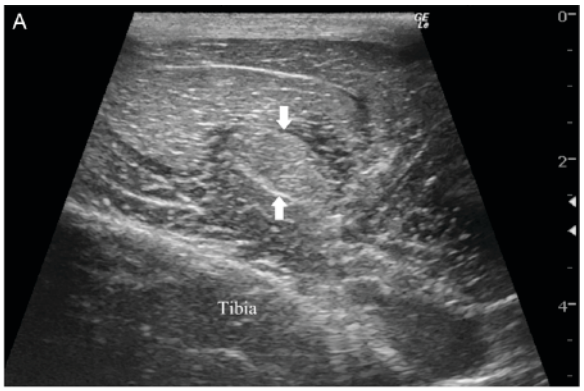


Figure 6.7 (A) Transverse plane image of normal peroneus tertius tendon (arrows) surrounded by muscle. (B) Transverse plane image of disrupted peroneus tertius tendon showing loss of the normal muscle and tendon architecture. Lateral is to the right of the images. These images are at the level of the mid-tibia.

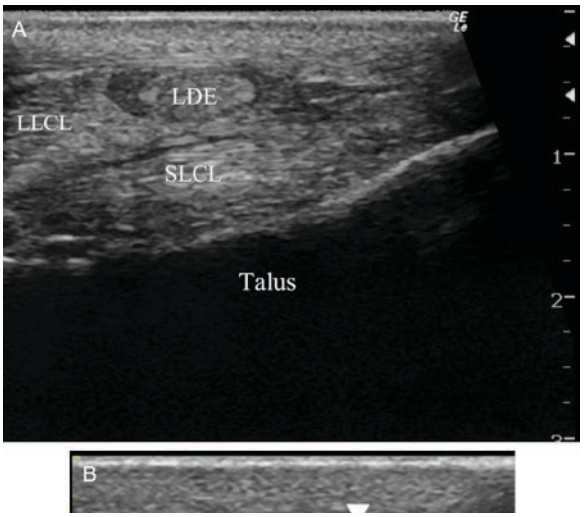


Figure 6.8 (A) Transverse plane image at the lateral aspect of the tarsus. The lateral digital extensor tendon (LDET) is immediately dorsal to the long lateral collateral ligament (LLCL) and superficial to the short lateral collateral ligament (SLCL). (B) Tendinitis of the LDET (arrowheads). Note enlargement of the tendon and heterogeneous echogenicity. Dorsal is to the right of the images.

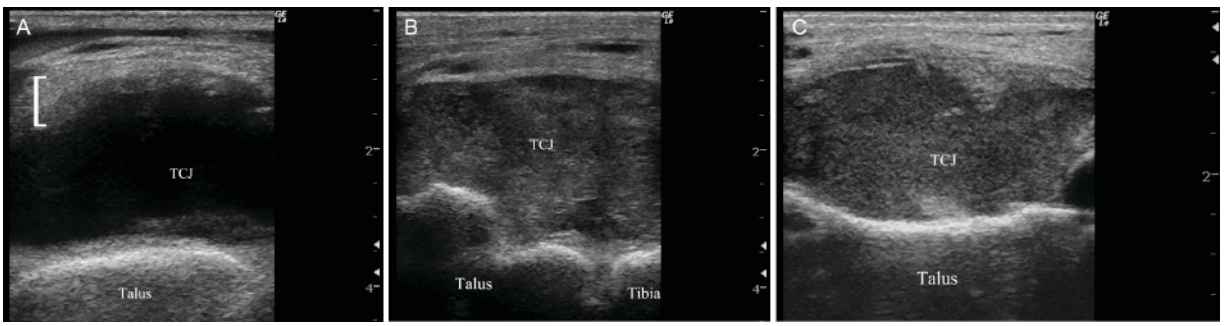


Figure 6.9 Dorsomedial pouch of the tarsocrural joint (TCJ). (A) Anechogenic effusion of the TCJ with synovial membrane thickening (bracket). The synovial fluid analysis of this joint was within normal limits. (B and C) Similar appearance of heterogeneous echogenic effusions of the TCJ. The horse in (B) was confirmed to have septic arthritis of the TCJ, while the horse in (C) had a non-septic hemarthrosis. Proximal is to the right of the images.

Vet-ebooks.com

is not a substitute for synoviocentesis and fluid analysis when determining the nature of an effusion.

The tarsus is composed of four joints: the communicating tarsocrural and proximal intertarsal joints, the distal intertarsal joint, and the tarsometatarsal joint. The dorsolateral, dorsomedial, plantarolateral, and plantaromedial portions of the tarsocrural joint should all be examined, as they may contain varying amounts of synovial fluid, fibrin, or synovial membrane proliferation. This information can assist in determining an appropriate site for arthrocentesis of the tarsocrural joint. The distal intertarsal joint is most easily assessed on the medial and dorsal aspects of the joint (Figure 6.10), while the tarsometatarsal joint is most easily assessed on the plantarolateral aspect of the joint in the typical site for arthrocentesis (Figure 6.11).

There are two consistent bursae present on the plantar aspect of the proximal tarsus: the gastrocnemius bursa, deep to the distal aspect of the gastrocnemius tendon, and the calcaneal bursa, between the gastrocnemius tendon and the superficial digital flexor tendon (Figure 6.12). A subcutaneous bursa ("capped hock") may be present between the superficial digital flexor tendon and the skin in some horses. This bursa may develop in response to local trauma and can be quite large in the initial stages (Figure 6.13). When evaluating penetrating wounds or potentially septic bursitis, it should be kept in mind that the gastrocnemius bursa and the calcaneal bursa consistently communicate and communication between the subcutaneous bursa and calcaneal bursa is present in approximately 40% of horses. The cunean bursa is deep to the cunean tendon on the dorsomedial aspect of the limb and is generally not imaged unless it is distended (Figure 6.14).

Multiple synovial sheaths surround tendons and ligaments of the tarsal region, the largest of which is the tarsal sheath, which will be considered separately. They should be assessed for abnormalities as described for other synovial structures. As these sheaths may be small in volume, the ultrasonographer should be mindful that pressure applied by the transducer may displace effusion. Additional evaluation of these structures with a minimal amount of pressure applied to the transducer can be helpful in these situations. If abnormalities of these tendon sheaths (e.g., increased synovial fluid) are present, the tendon within the sheath should be carefully assessed for abnormalities.

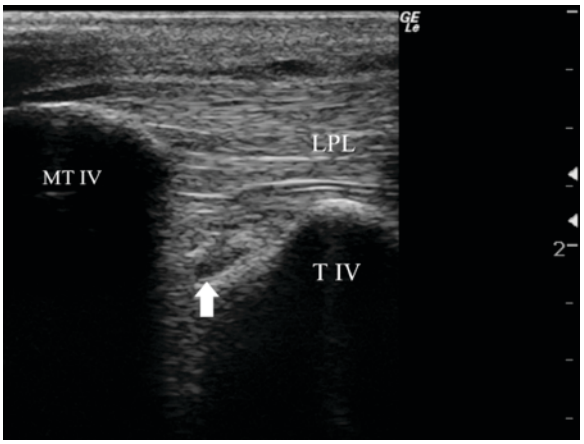


Figure 6.11 Normal tarsometatarsal joint (TMTJ) (arrow) imaged from the plantarolateral aspect of the tarsus. LPL: long plantar ligament; T IV: fourth tarsal bone; MT IV: fourth metatarsal bone. Proximal is to the right of the image.

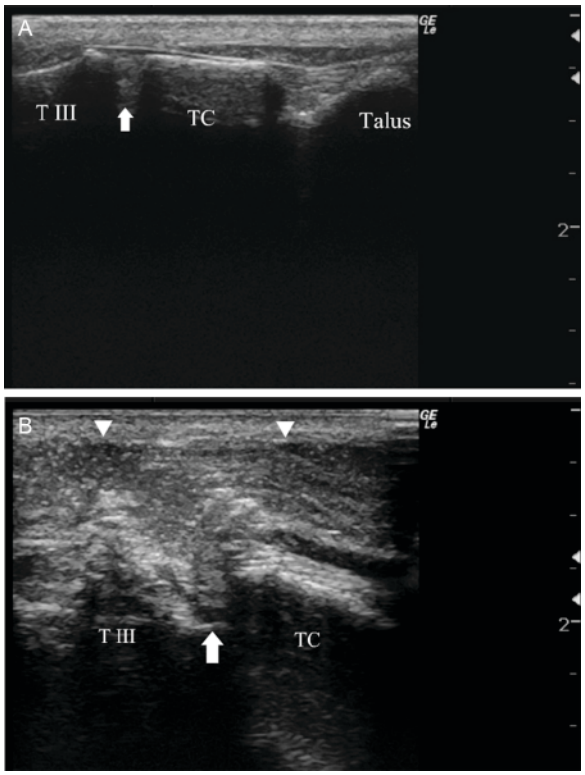


Figure 6.10 Normal (A) and abnormal (B) distal intertarsal joint (arrow) imaged from the medial aspect of the tarsus. The horse in (B) has a marked echogenic effusion of the joint (arrowheads) as well as irregularity of the third tarsal bone (T III) consistent with osteomyelitis. Purulent material was obtained from this joint. TC: entral tarsal bone. Proximal is to the right of the images.

Tarsal Sheath

The tarsal sheath is extensive in size, extending from the distal tibial region to the proximal metatarsal region. It contains the lateral deep digital flexor tendon, while the medial deep digital flexor tendon is contained within its own sheath located dorsomedial to the tarsal sheath. The sheath of the medial deep

Vet-ebooks.com

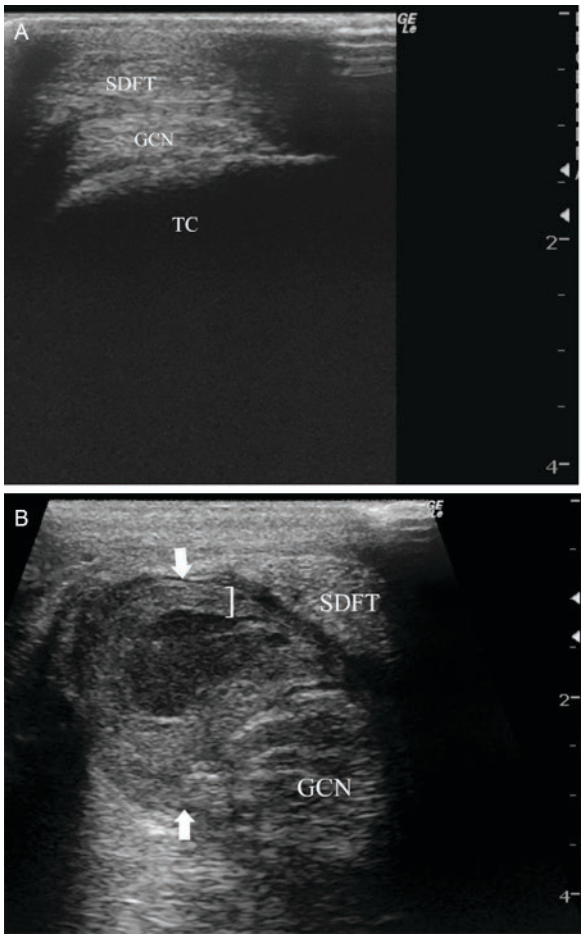


Figure 6.12 (A) Transverse plane image of a normal superficial digital flexor tendon (SDFT) and gastrocnemius tendon (GCN) at the proximal aspect of the tuber calcanei (TC) obtained from the plantar aspect of the limb. (B) Effusion of the calcaneal bursa (arrows) imaged from a slightly plantaromedial aspect immediately proximal to the TC. Note the degree of synovial membrane thickening (bracket). This horse was confirmed to have septic synovitis of the calcaneal bursa. Lateral is to the right of the images.

digital flexor tendon generally does not communicate with the tarsal sheath.

Effusion of the tarsal sheath ("thoroughpin") may be confused with effusion of the plantar pouches of the tarsocrural joint, as they are in close proximity to one another. The tarsal sheath is also susceptible to septic tenosynovitis, due to its superficial location on the plantaromedial hock where it is susceptible to kicks and trauma, which should be suspected if moderate–severe lameness, tarsal sheath effusion, synovial membrane thickening, and fibrin accumulation are present and particularly if a wound is present. In more severe cases, regions of hypoechogenicity may be seen within the deep digital flexor tendon itself and the bony contour of the sustentaculum tali may be irregular, suggestive of osteomyelitis (Figures 6.15 and 6.16). The medial head of the deep digital flexor tendon and its sheath may be affected as well (Figure 6.17). Confusingly, similar ultrasonographic findings (effusion, synovial membrane thickening, and fibrin accumulation) combined with moderate-severe lameness may be seen in a non-septic "sympathetic" synovitis, for example when sepsis is present in an anatomic location close to the tarsal sheath but the sheath itself is not involved and ultrasound guided synoviocentesis can aid a definitive diagnosis (Figure 6.18).

Bony Structures

The bony structures of the tarsal region should be evaluated critically because ultrasonography may reveal subtle bony surface changes at an earlier stage than radiography. Assessment can be challenging due to the many contours of the tarsal bones, particularly the talus, calcaneus, and distal tibia. Bony margins should be smooth and regular. Areas of irregularity may

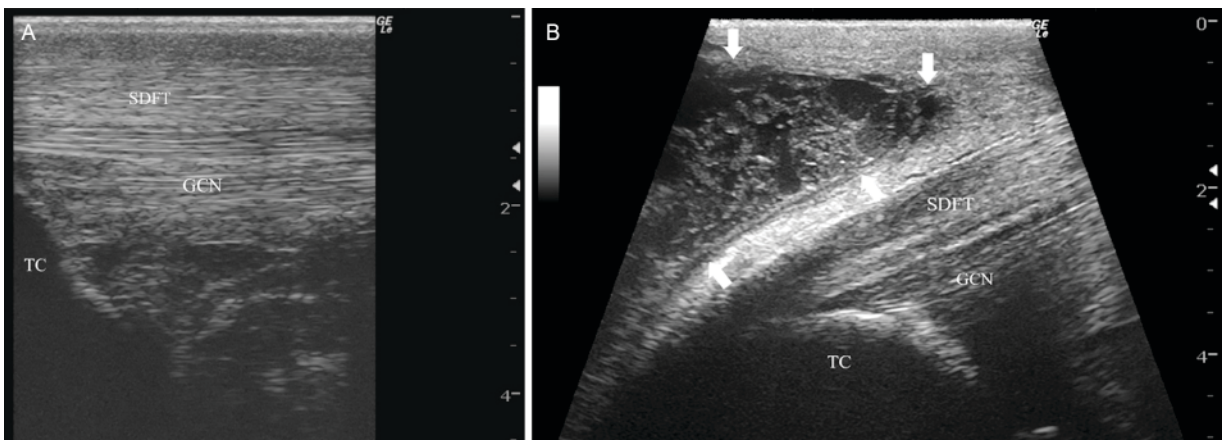


Figure 6.13 Normal longitudinal images of the superficial digital flexor tendon (SDFT) and gastrocnemius tendon (GCN) at the insertion of the GCN on the tuber calcanei (TC). The horse in (B) has a large heterogeneous mass in the subcutaneous space (arrows) consistent with subcutaneous bursitis. Relaxation artifact is present in the SDFT and GCN. Proximal is to the right of the images.

Vet-ebooks.com

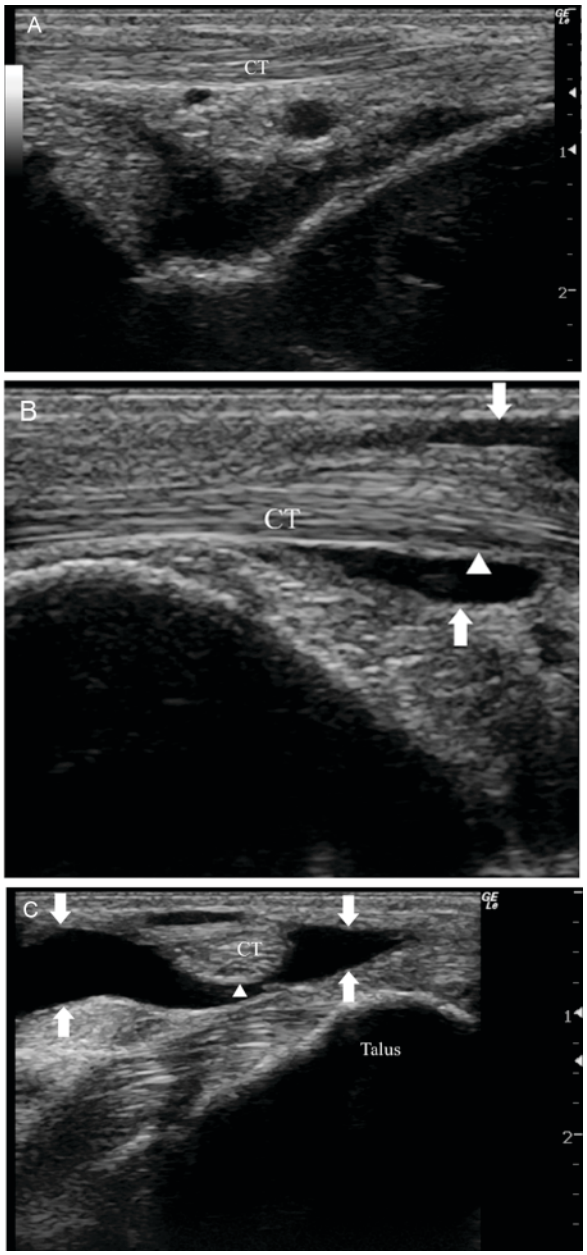


Figure 6.14 (A) Longitudinal image of a normal cunean tendon (CT). The cunean bursa surrounding the cunean tendon is not imaged distinctly due to the small amount of fluid in the normal bursa. Dorsoproximal is to the right of the image. (B) Longitudinal image of the cunean tendon in a horse with cunean bursitis and cunean tendonitis. There is an increase in anechogenic fluid (arrows) within the cunean bursa as well as hypoechogenicity in the cunean tendon on the right side of the image (arrowhead). Dorsoproximal is to the right of the image. (C) Transverse image of the CT and effusion of the cunean bursa (arrows) of the same horse as in (B). The area of hypoechogenicity in the deep aspect of the cunean tendon is visible (arrowheads). Plantaroproximal is to the right of the image. This image is obtained on the dorsomedial aspect of the tibia at the level of distal talus.

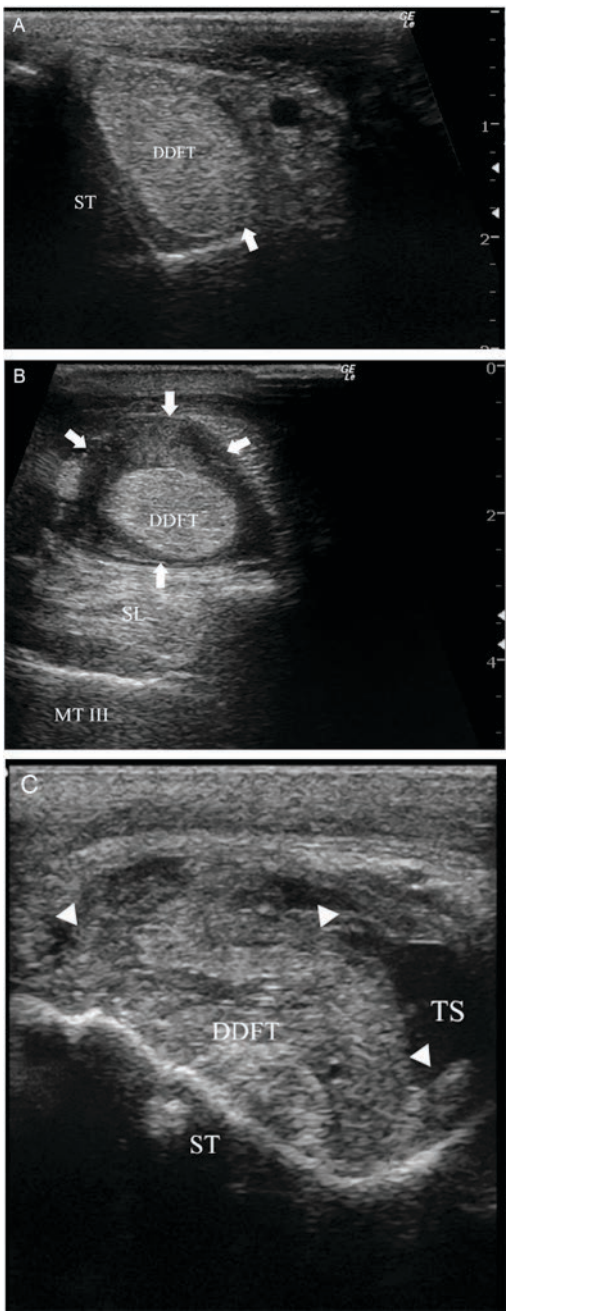


Figure 6.15 (A) Transverse image of the deep digital flexor tendon (DDFT) within the tarsal sheath at the level of the sustentaculum tali (ST) in a normal horse. Due to the DDFT curving over the ST, some fibers of the DDFT appear hypoechogenic to the remainder of the tendon (arrow). (B) Echogenic effusion of the tarsal sheath (arrows) surrounding the DDFT in the proximal metatarsal region in a horse with septic synovitis of the tarsal sheath, distal to the sustentaculum tali. SL: suspensory ligament; MT III: third metatarsal bone. (C) DDFT within the tarsal sheath at the level of the ST (at the same level as the image in (A) in a horse with septic tenosynovitis. The tendon has decreased echogenicity and its margins are irregular and difficult to define (arrowheads). Mild irregularity of the ST margin is present. Lateral is to the right of the images.

Vet-ebooks.com

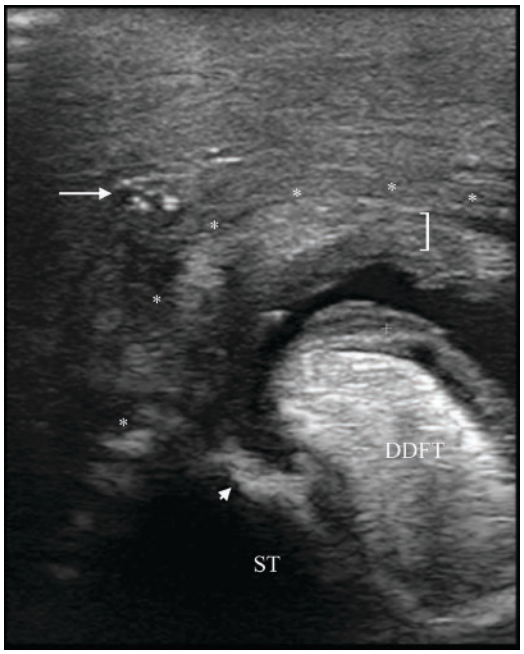


Figure 6.16 Transverse image of the tarsal sheath at the level of the sustentaculum tali (ST). Lateral is to the right of the image. This horse had evidence of a wound at this level. The sustentaculum tali is irregular (arrowhead) and echogenic material consistent with synovial membrane proliferation (]) and fibrin deposition (+) is present within the tarsal sheath. Additionally, there is marked subcutaneous soft tissue thickening with small hyperechogenic foci consistent with gas (arrow) consistent with a penetrating wound. The boundaries of the tarsal sheath are indicated with asterixis (*).

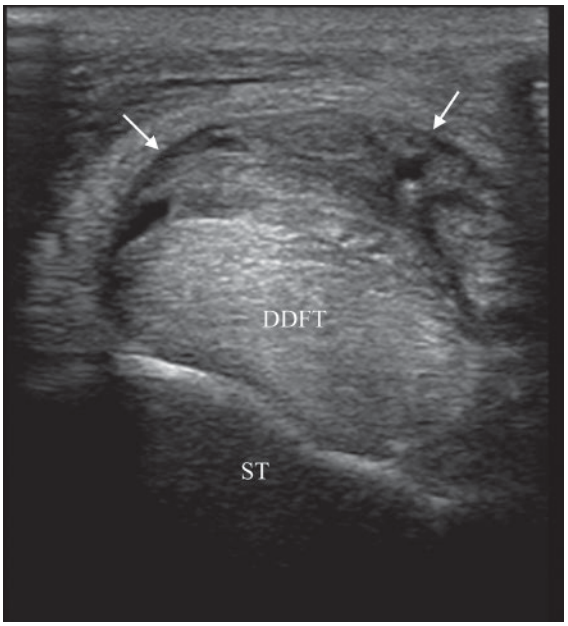


Figure 6.18 Transverse image of the tarsal sheath at the level of the sustentaculum tali. Lateral is to the right of the image. There is echogenic material (synovial membrane thickening and fibrin) present within the tarsal sheath (arrows). Synovial fluid analysis showed that this inflammation was non-septic in nature. This horse had a subcutaneous abscess in the proximal metatarsal region which was suspected to be the source of the regional inflammation. Note the similarity in ultrasonographic appearance between this horse with non-septic inflammation and the horse in Figure 6.15C with septic inflammation.

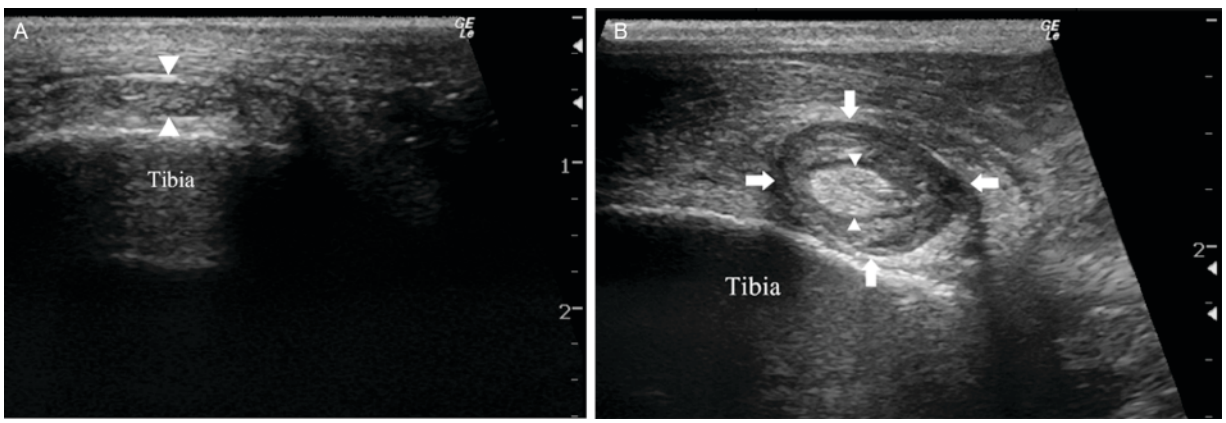


Figure 6.17 Transverse images of the medial head of the deep digital flexor tendon (DDFT) (arrowheads) in its synovial sheath at the level of the distal tibia in a normal horse (A) and in a horse with septic tenosynovitis (B). In (B), an echogenic effusion (arrows) is present within the sheath and mild irregularity of the tendon margin is present. Plantar is to the right of the images. These images were obtained at the level of the tuber calcanei immediately plantar to the medial malleolus of the tibia.

represent sites of osteomyelitis, osteophyte formation, fracture, osteochondrosis, or sequestrum formation.

Osteochondrosis and osteochondrosis dessicans are typically diagnosed using radiography. However, ultrasonography has been shown to be more sensitive than radiography for lesions of the medial malleolus and distal intermediate tibial ridge (Figure 6.19). Areas of abnormal bony contour consistent with osteitis, osteomyelitis, or sequestrum formation can be identified using ultrasonography (Figures 6.20 and 6.21).

In young horses, the physes of the distal tibia and the tuber calcanei should be examined. The physis is normally a thin structure with well defined, crisp margins. Widening, irregularity, or increased echogenicity of the physeal region are indicative of septic or traumatic physitis (Figure 6.22).

Vet-ebooks.com

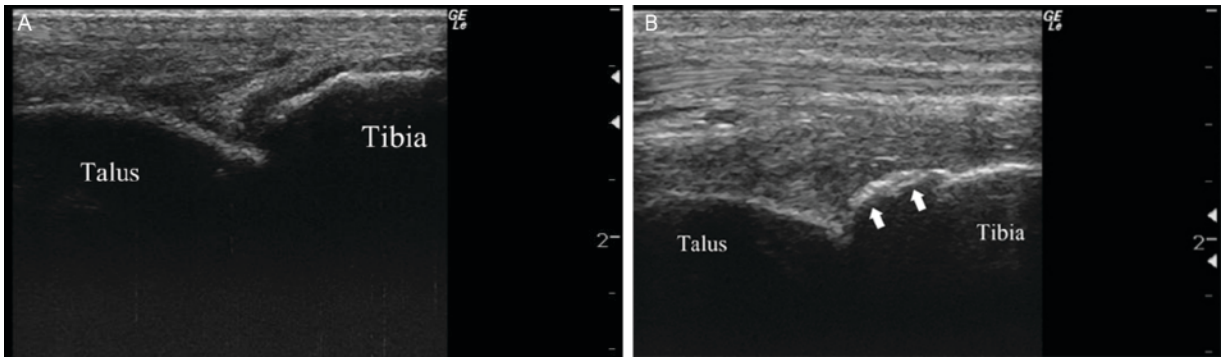


Figure 6.19 Longitudinal image of the distal intermediate ridge of the tibia in a normal horse (A) and in a horse with an osteochondrosis fragment (arrows) (B) and synovial membrane thickening. This fragment was removed arthroscopically. Proximal is to the right of the images.

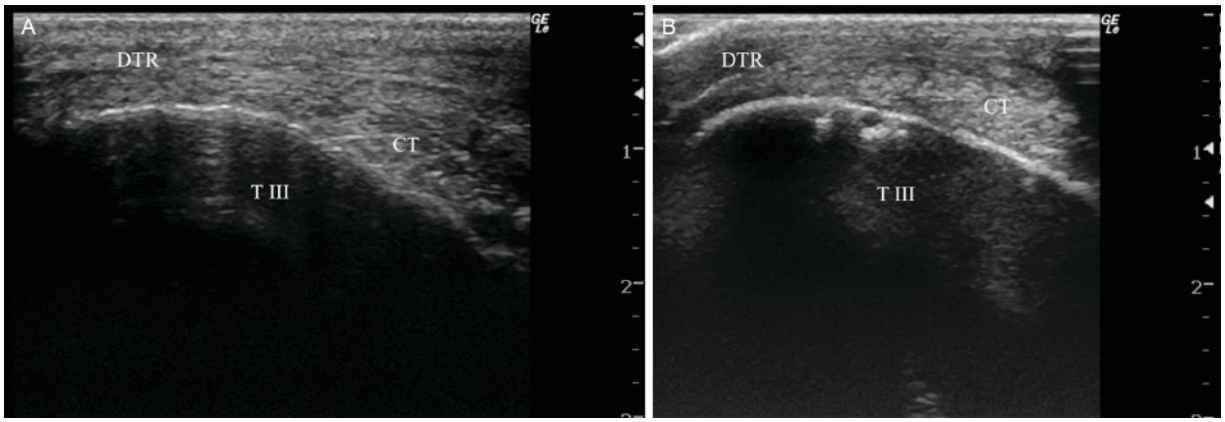


Figure 6.20 Transverse plane image of the dorsal aspect of the third tarsal bone (T III) in a normal horse (A) and in a horse with osteomyelitis (B) where irregularity of the bony margin is present. Lateral is to the right of the images. DTR: dorsal tarsal retinaculum; CT: metatarsal branch of the cranial tibial tendon.

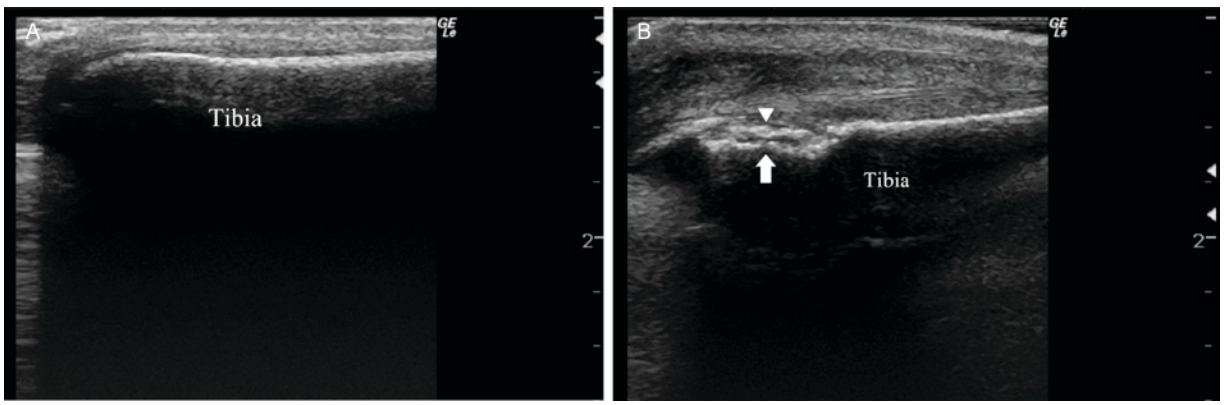


Figure 6.21 Longitudinal images of the distal medial tibia in a normal horse (A) and in a horse with a draining tract (B). A sequestrum is indicated by the arrowhead and the involucrum is indicated by the arrow. Subcutaneous thickening and edema are present. Proximal is to the right of the images.

Vet-ebooks.com

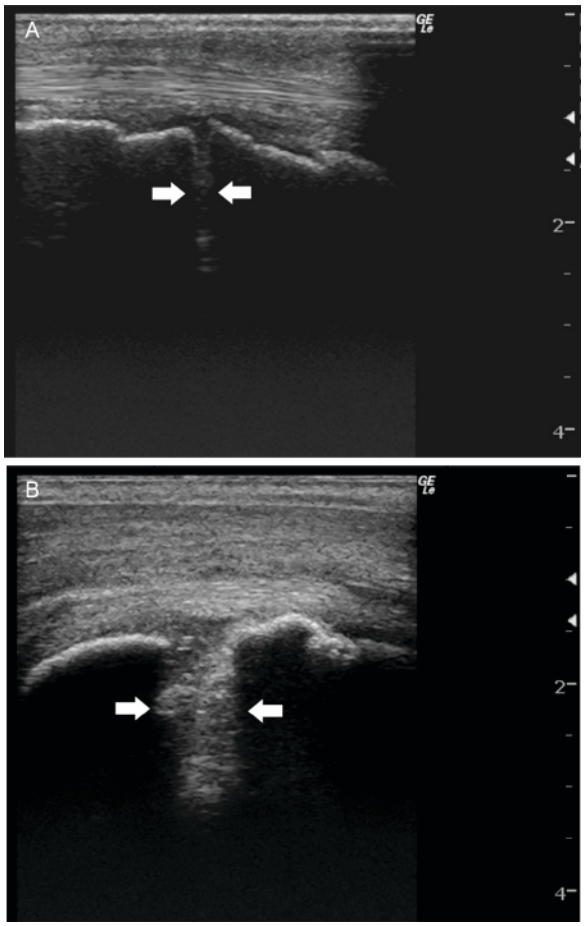


Figure 6.22 Longitudinal images of the distal tibial physis (arrows) in a normal horse (A) and in a horse with septic tibial physitis (B) with widening and irregularity of the physis as well as subcutaneous thickening.

Subcutis

In cases with profound soft tissue swelling of the tarsal region, it can be difficult to determine the nature and location of the swelling or effusion. Ultrasonography can assist with differentiation of cellulitis or abscessation from synovial sepsis (Figure 6.23). In the author's experience, cellulitis associated with the dorsal aspect of the tarsal region can result in abscessation very quickly, and serial examinations are very helpful (Figure 6.24).

Intra-Arterial Perfusion

As regenerative medicine has grown in popularity, a variety of delivery methods for these treatments have been used. One such method is intra-arterial perfusion of the cranial tibial artery. This artery can be accessed on the dorsal-dorsolateral aspect of the distal tarsus in the standing, sedated horse as well as in horses under general anesthesia. Regional anesthesia (peroneal nerve block and/or local line block proximal to the needle insertion site) is recommended for operator safety as well as to minimize horse movement during the procedure. The artery can be identified by its thicker wall as compared to the veins in the area and an appropriate location for ultrasound-guided injection (where the artery is relatively superficial) can be determined (Figure 6.25).

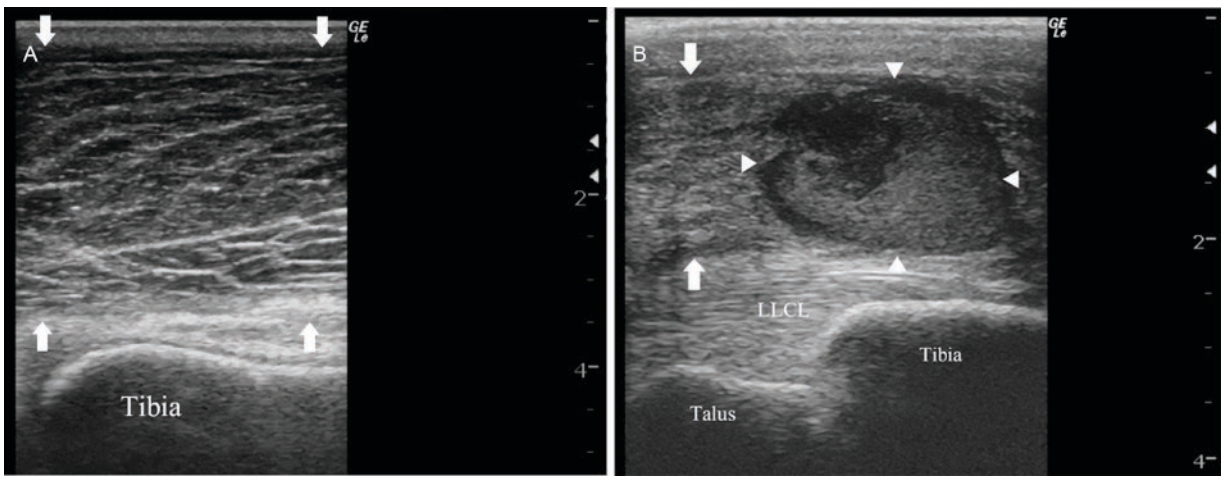


Figure 6.23 Longitudinal images of the lateral distal tibia and proximal tarsus. (A) A horse with subcutaneous cellulitis. The thickened, edematous subcutaneous tissues are indicated by the arrows. (B) A horse with a subcutaneous abscess and cellulitis. The abscess is indicated by the arrowheads and the thickened subcutaneous tissues are indicated by the arrows. LLCL: long lateral collateral ligament.

Vet-ebooks.com

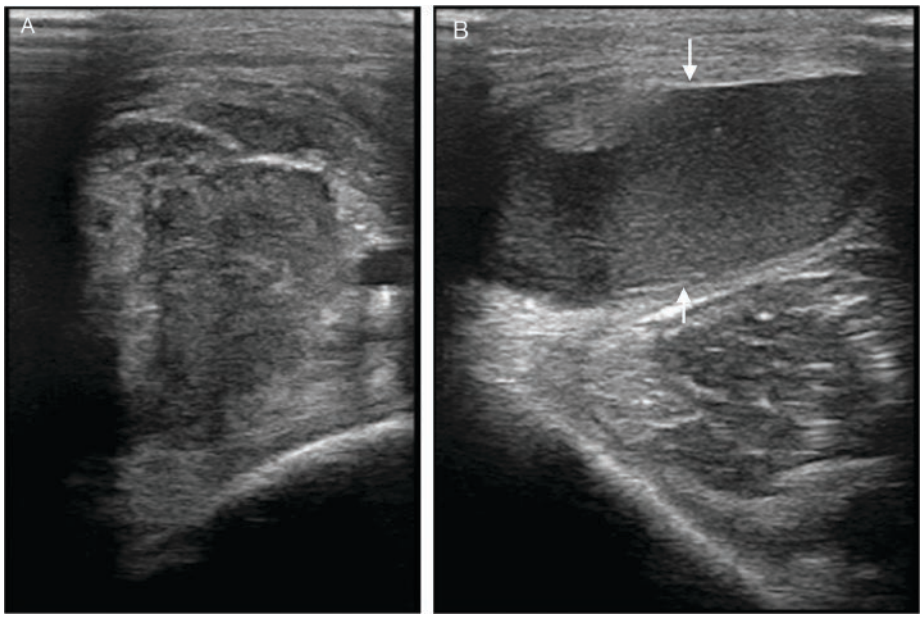


Figure 6.24 Transverse images of the dorsal aspect of the tarsal region. Lateral is to the right of the images. The image in (A) was obtained at initial presentation. There is a large amount of heterogeneous material present, but no distinct fluid pocket was identified. One day later (B), a distinct pocket had formed due to focal peritarsal cellulitis (arrows).

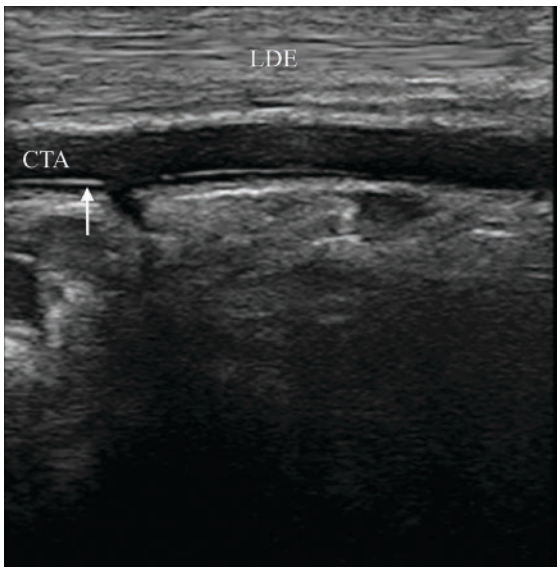


Figure 6.25 Longitudinal image of the cranial tibial artery (CTA) at the dorsal-dorsolateral aspect of the tarsus. Proximal is to the right of the image. The artery is identified by its thicker wall (arrow) as compared to the veins in the area. The long digital extensor tendon (LDE) is superficial to the artery at this location.

Foals

In lame foals, prompt diagnosis (especially determining if the lameness is a result of a septic process) is crucial in order to institute appropriate treatment as soon as possible. Sepsis may be suspected based on the presence of a fever, abnormal white blood cell count, or elevated fibrinogen/serum amyloid A, but the absence of these findings does not rule out a septic process. The tarsus may be suspected as the anatomic location of the problem based upon a combination of physical examination findings (e.g., the presence of soft tissue swelling, pain on palpation or flexion) and results of diagnostic analgesia. Ultrasonography can be particularly useful in evaluation of the tarsus in these cases. Common findings in foals include trauma (Figure 6.26), subcutaneous abscess, subcutaneous cellulitis, septic physitis, osteomyelitis (Figure 6.27), and septic synovitis (Figure 6.28) (tarsocrural/proximal intertarsal joints more commonly than the distal intertarsal and tarsometatarsal joints, the tarsal sheath, or regional bursae). Repeated ultrasonographic examination after 1–2 days allows monitoring of lesions as well as identification of additional abnormalities as the ultrasonographic appearance can change rapidly in foals.

Conclusion

Although the tarsus region is anatomically challenging, ultrasonography provides important information that assists with prompt diagnosis and institution of appropriate treatment. A multimodality approach is often helpful for both clinical cases as well as increasing the skill of the operator.

Vet-ebooks.com

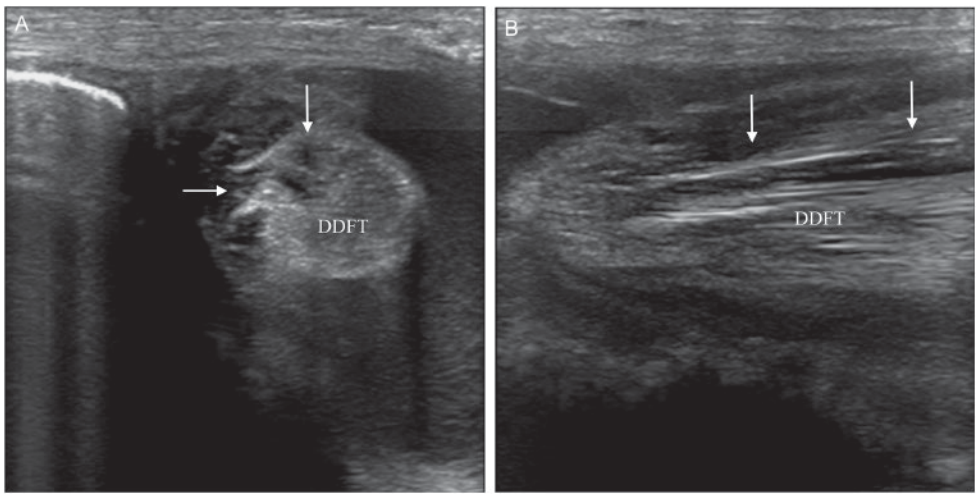


Figure 6.26 Transverse (A) and longitundinal (B) images of the deep digital flexor tendon proximal to the sustentaculum tali in a foal. Proximal or lateral are to the right of the images. The margin of the tendon is irregular and there are areas of anechogenicity in the tendon (arrows). Analysis of a fluid sample from the tarsal sheath was not supportive of a septic process, suggesting this was a traumatic tendon lesion.

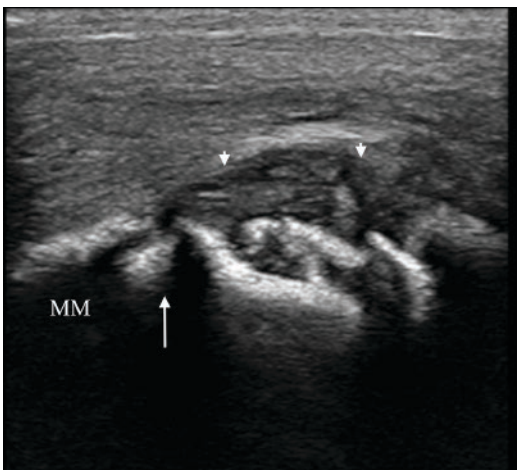


Figure 6.27 Longitudinal image of the distomedial tibia at the medial malleolus (MM) of a foal. Proximal is to the right of the image. The location of the physis is indicated by the arrow. There is irregularity of the bony margin at the physis that extends proximally along the bone consistent with physitis/osteomyelitis. There is a heterogeneous pocket superficial to the irregularity (arrowheads). An ultrasound-guided aspirate of the heterogeneous pocket revealed purulent material that cultured Rhodococcus equi.

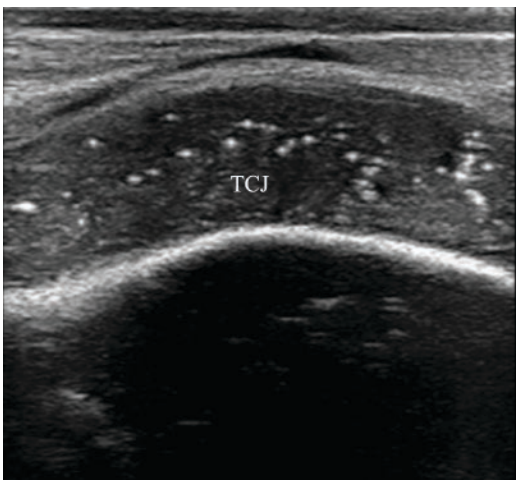


Figure 6.28 Longitudinal image of the dorsal aspect of the tarsocrural joint (TCJ). Proximal is to the right of the image. The synovial fluid is markedly echogenic and heterogeneous. Frank pus was obtained from a joint aspirate of the joint.

Recommended Reading

Cauvin, E.R. (1999). Endoscopic examination of the tarsal sheath of the lateral digital flexor tendon in horses. *Equine Veterinary Journal* 31: 219–227.

Davis, W., Caniglia, C.J., Lustgarden, M. et al. (2014). Clinical and diagnostic imaging characteristics of lateral digital flexor tendinitis within the tarsal sheath in four horses. *Veterinary Radiology and Ultrasound* 55: 166–173.

Dik, K.J. (1993). Ultrasonography of the equine tarsus. *Veterinary Radiology* 34: 36–43.

Pilsworth, R.C. and Head, M.J. (2001). A study of ten cases of focal peritarsal infection as a cause of severe lameness in the Thoroughbred racehorse: Clinical signs, differential diagnosis, treatment and outcome. *Equine Veterinary Journal* 33(4): 366–370.

Post, E.M., Singer, E.R., and Clegg, P.D. (2007). An anatomic study of the calcaneal bursae in the horse. *Veterinary Surgery* 36: 3–9.

Vet-ebooks.com

Raes, E.V., Vanderperren, K., Pille, F. et al. (2010). Ultrasonographic findings in 100 horses with tarsal region disorders. *Veterinary Journal* 186: 201–209.

Relave, F., Meulyzer, M., Alexander, K. et al. (2009). Comparison of radiography and ultrasonography to detect osteochondrosis lesions in the tarsocrural joint: A prospective study. *Equine Veterinary Journal* 41: 34–40.

Smith, M.R.W. and Wright, I.M. (2010). Arthroscopic treatment of fractures of the lateral malleolus of the tibia: 26 cases. *Equine Veterinary Journal* 43: 280–287.

Torrent, A., Spriet, M., Espinosa-Mur, P. et al. (2019). Ultrasound-guided injection of the cranial tibia arter for stem cell administration in horses. *Equine Veterinary Journal* epub ahead of print.

Updike, S.J. (1984). Functional anatomy of the equine tarsocrural collateral ligaments. *American Journal of Veterinary Research* 45: 867–874.

Vanderperren, K., Raes, E., Bree, H.V. et al. (2009a). Diagnostic imaging of the equine tarsal region using radiography and ultrasonography. Part 2: Bony disorders. *Veterinary Journal* 179: 188–196.

Vanderperren, K., Raes, E., Hoegaerts, M. et al. (2009b). Diagnostic imaging of the equine tarsal region using radiography and ultrasonography. Part 1: The soft tissues. *Veterinary Journal* 179: 179–187.

Whitcomb, M.B. (2006). Ultrasonography of the equine tarsus. *Proceedings of the American Association of Equine Practitioners*, 52: 13–30.

Young, A., Whitcomb, M.B., Vaughan, B. et al. (2010). Ultrasonographic features of septic synovial structures in 62 horses (2004–2009). *Proceedings of the American Association of Equine Practitioners*, 56: 238.

Vet-ebooks.com

7

Ultrasonography of the Stifle

Eddy R.J. Cauvin

AZURVET Referral Veterinary Centre, Saint-Laurent-du-Var, France

Stifle injuries are increasingly recognized as a major cause of hind limb lameness. Ultrasonography is well suited to image the stifle and has gained popularity as it is easily available, may be used in the standing patient, and will provide access to most parts of this joint. It has tremendously improved our ability to confirm or rule out stifle lesions, which, in most cases, primarily involve soft tissue structures.

Radiography may be useful to detect bony lesion such as fractures, osteochondrosis, cyst-like lesions, etc., but most frequently, only late degenerative changes will be recognized. Magnetic resonance imaging (MRI) and computed tomography (CT) are increasingly used for the diagnosis of stifle conditions in horses but access to these modalities remains limited. CT-arthrography (images acquired after intra-articular injection of iodinated contrast medium) of the stifle has been described in recent years. It procures useful information on joint surfaces and the outlines of menisci and ligaments. However, the parenchyma is poorly visualized and the presence of synovial thickening can alter the appearance of intra-articular structures. MRI has been little used so far because of difficulties placing the stifle in most magnets and long acquisition times, although it may be increasingly used in coming years.

The equine stifle is a large, complex region and its ultrasonographic examination requires a thorough knowledge of the anatomy. A comprehensive, standardized approach is recommended. A systematic approach to the joints is paramount to avoid overlooking subtle changes, which may have strong clinical repercussions, in particular meniscal tears or focal cartilage or subchondral trauma. Many artifacts can impair the sensitivity and specificity of the examination, so it is particularly important to acquire experience and a thorough knowledge of the gross and ultrasonographic anatomy in order to optimize stifle ultrasonography.

Preparation and Scanning Technique

The stifle region should be finely clipped from distal to the tibial tuberosity up to the stifle skin fold, and all around the limb, then prepared as usual. Most of the examination is performed with the limb weightbearing, although, in very lame horses, examination can be adequately performed with the limb partially flexed. To scan the cranial aspect of the femorotibial joints, however, the limb must be flexed in order to expose the joint surfaces and intra-articular structures. It may be useful to use a wooden block to stabilize the foot. It is not necessary to achieve full flexion, which is often not tolerated by the injured horse. Intra-articular analgesia will dramatically interfere with evaluation of the joint, as it causes hemorrhage, inflammation, and effusion, and because air may be introduced into the joint space or periarticular soft tissues. Gas can persist in the joint for up to 2 weeks; it is therefore preferable to perform an ultrasonographic examination prior to diagnostic intra-articular analgesia whenever possible.

A high-frequency (8–15 MHz) linear probe is best to evaluate the femoropatellar joint and the medial aspect of the stifle. A standoff pad may be used but can be fiddly and is not usually necessary. To examine the cranial, lateral, and caudal aspects of the stifle, 4–10 MHz convex to micro-convex, curved array transducers are preferred, as they are easier to align to deeper structures not parallel to the skin.

Atlas of Equine Ultrasonography, Second Edition. Edited by Jessica A. Kidd, Kristina G. Lu and Michele L. Frazer.
© 2022 John Wiley & Sons Ltd. Published 2022 by John Wiley & Sons Ltd.
Companion Website: www.wiley.com/go/kidd/atlas

Vet-ebooks.com

Comprehensive examination of the stifle may be time-consuming, although with experience it may be performed in under 15 minutes. Typically, it is performed in 5 stages (Figure 7.1).

1) Starting with the limb extended and weightbearing (if the horse allows), the femoropatellar articulation is examined with a linear transducer from a cranial approach, using both transverse and longitudinal sections of the limb and spanning the area from the fold of the stifle proximally to the tibial tuberosity distally and half of the circumference of the femur from medial to lateral (Figures 7.1a).
2) The examination is continued, with the limb in the same extended position, over the medial femorotibial joint region with the same probe. The

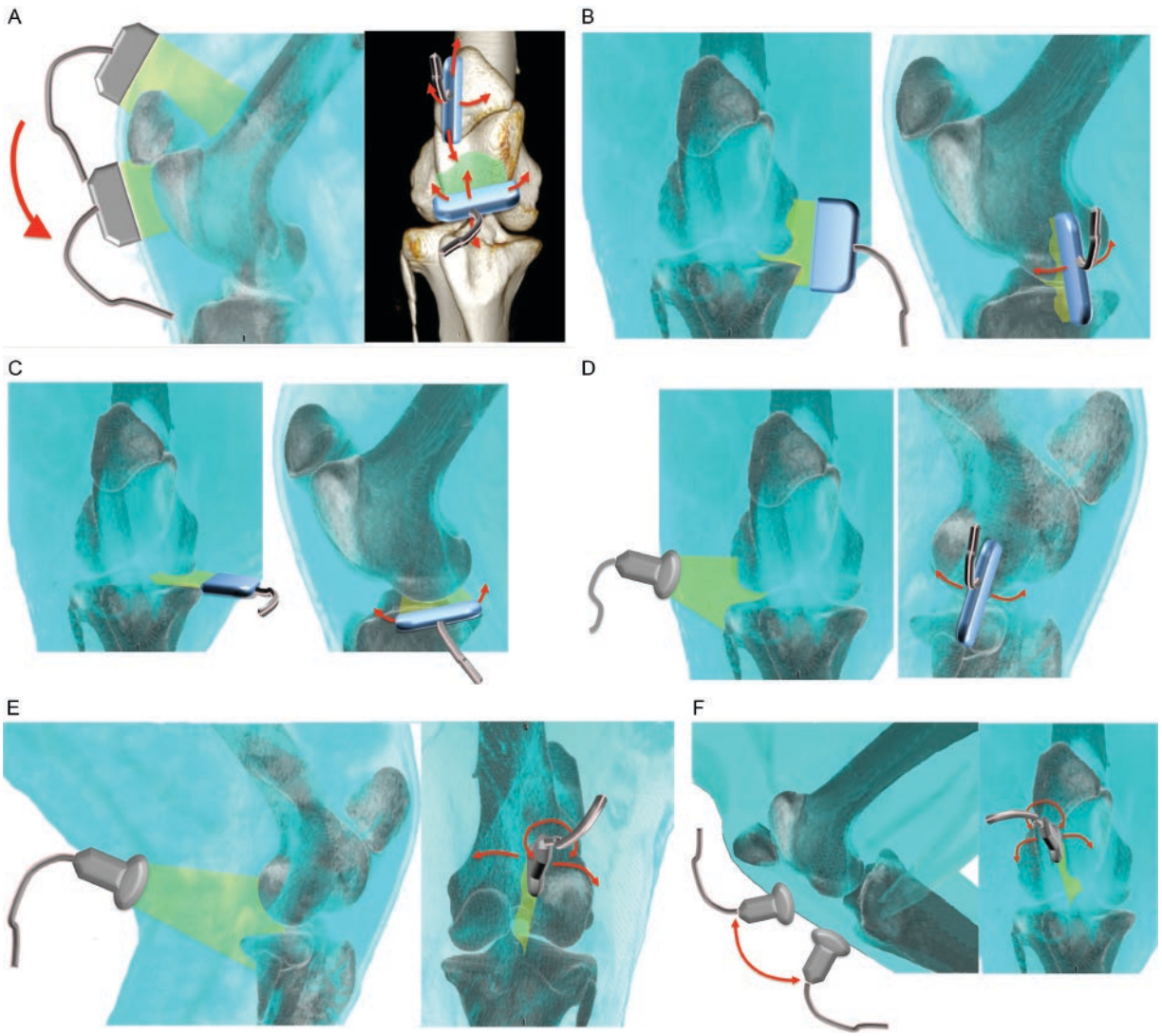


Figure 7.1 5-stage protocol for the ultrasonographic examination of the stifle. (1a) the femoropatellar articulation is examined with a linear transducer from a cranial approach with the limb extended and weightbearing, in both transverse and longitudinal planes. The transducer is moved from proximal to distal and from lateral to medial over the cranial one half of the stifle. (1b) and (1c) The medial femorotibial articulation is then examined with the limb weightbearing or flexed, first in a frontal plane from craniomedial to caudomedial over the joint space (1b). It is important to follow the curvature of the stifle, i.e., in a craniomedial position the probe must be aimed slightly caudally, and at the caudomedial aspect it must be tilted slightly cranially. Transverse section images are obtained by placing the probe horizontally directly over the edge of the meniscus which is found proximal to the palpable edge of the medial tibial condyle (1c). (1d) The lateral femorotibial articulation is approached in a similar manner, using a linear probe and, if necessary, a convex or microconvex probe. It may be necessary to slightly tilt the probe downward to improve the images (Figure 7.1d). (1e) The caudal aspect of the stifle is assessed with the limb weightbearing, using a convex transducer. It may be approached through the semitendinosus or semimembranosus muscles, pushing the probe into the muscles either at the caudal angle of the stifle or 10 cm proximally, slightly tilting the probe downward. (1f) To image the cranial aspect of the femorotibial joints and intercondylar space, the limb is partially flexed (~45 degrees). A convex or microconvex transducer must be used from a cranial approach. The technique requires accurate knowledge of the 3-D arrangement of each structure and will be detailed later in this chapter.

Vet-ebooks.com

examination is easiest using longitudinal sections (i.e., with the probe placed in a frontal plane, perpendicular to the tibial plateau (Figure 7.1b)). Transverse section images may be useful to evaluate the meniscal parenchyma over their whole width, notably to look for vertical tears (Figure 7.1c).

3) The lateral aspect of the joint is approached with a linear probe and, if necessary, with a convex or microconvex probe. Longitudinal (frontal) plane images are preferred and it may be necessary to slightly tilt the probe downward to improve the images (Figure 7.1d).
4) The caudal aspect of the stifle is assessed through the caudal thigh muscles using a convex transducer (Figure 7.1e).
5) Finally the limb is flexed (~45 degrees) and the cranial aspect of the femorotibial articulations is examined using a convex or microconvex transducer (Figure 7.1f). Each structure is imaged in both longitudinal and transverse planes, which requires an accurate knowledge of the topography of each anatomical structure (i.e., joint surfaces, tendons, and ligaments)

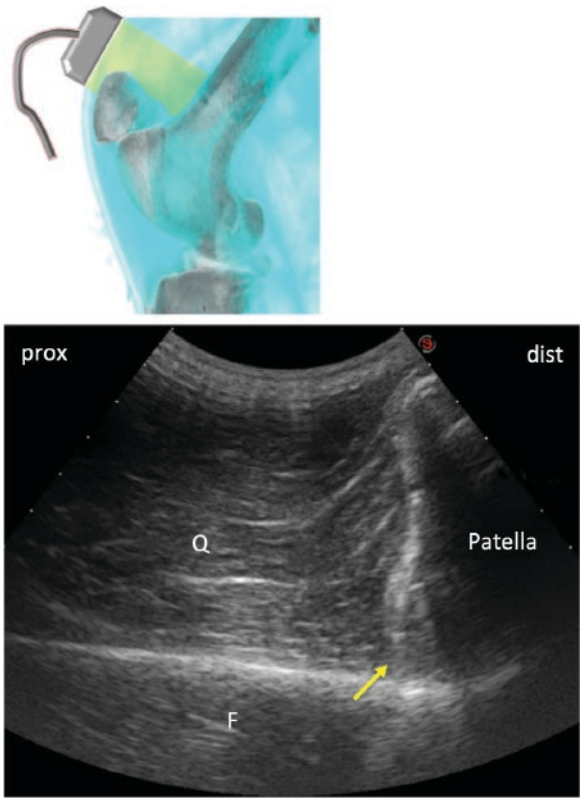


Figure 7.2 Imaging of the proximal recess of the femoropatellar joint (arrow) in a longitudinal (sagittal) plane proximal to the patella. The synovial recess is virtual unless distended and extends between the quadriceps muscle (Q) and the cranial surface of the femur (F). Proximal is to the left of the image.

Ultrasonographic Anatomy

The anatomy of the stifle region has been described elsewhere and the reader is encouraged to study anatomy texts in detail to better understand the 3-D arrangement of this complex joint.

Femoropatellar Joint

The femoropatellar joint is best imaged with the joint extended, as most of the trochlea is hidden by the patella when the limb is flexed. In the extended position the patella points craniolaterally, and the large medial trochlear ridge is palpable under the skin cranially. Starting in transverse planes, the probe is placed cranioproximally over the quadriceps muscles and examination is continued from proximal to distal, down to the tibial tuberosity. The quadriceps muscle is relatively homogeneous with a typical hypoechogenic muscular pattern. There is no insertion tendon as such, so that there is a sharp interface between the muscle belly and the proximal outline of the patella (Figure 7.2). The cranial surface of the patella forms a sharp, smooth hyperechogenic interface. Distally, it forms a shallow groove at the origin of the middle patellar ligament (PL) (see below). Medially, it is prolonged by the hypoechogenic, crescent-shaped parapatellar fibrocartilage, which curves around the medial trochlear ridge and terminates via the thin medial collateral patellar ligament (Figure 7.3). It also gives rise to the medial PL (see below).

Distal to the apex of the patella, the trochlear groove appears as a wide, U-shaped bone interface covered by anechogenic cartilage (Figures 7.4 and 7.5). In many horses, the latter is irregular in the center of the groove, but this is considered to be a normal feature. The medial trochlear ridge is broad, smooth, and rounded, and is covered by relatively thin cartilage (0.8–1 mm thickness). This becomes irregular medially. The lateral trochlear ridge is much narrower and triangular in cross-section. Its cartilage is thicker (2–4 mm). In longitudinal sections (parasagittal), the trochlear ridges form a smooth, convex bone interface, topped by anechogenic cartilage, which should be perfectly regular in thickness. The lateral PL is seen as a striated structure lying directly over the cartilage of the lateral ridge. The capsule is tightly applied against the cartilage surface, and no fluid is normally visible over the trochlea.

Anatomically, the patellar ligaments actually correspond to the quadriceps tendon and they are, therefore, similar in appearance to digital flexor

Vet-ebooks.com

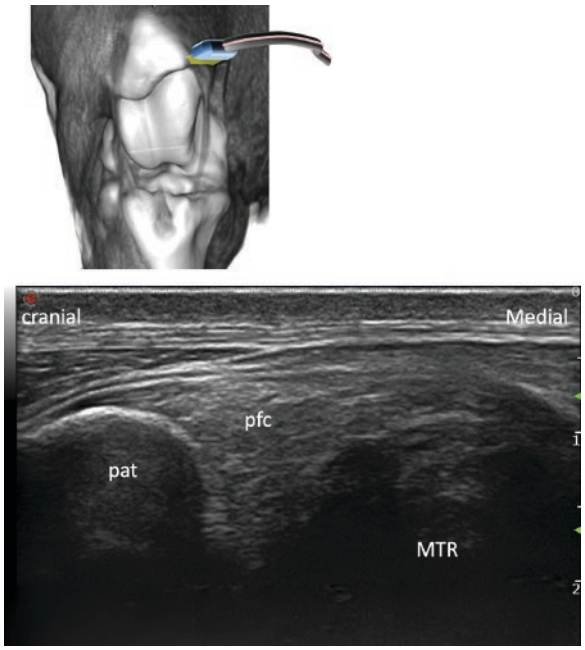


Figure 7.3 In transverse planes the cranial surface of the patella (pat) appears as a smooth, curved, hyperechogenic interface. Medially, the medial collateral patellar ligament forms a large fibrocartilaginous pad (parapatellar fibrocartilage (pfc)), which curves around the medial trochlear ridge (MTR) and terminates via the thin medial collateral patellar ligament.

tendons (Figure 7.6). Their borders are, however, ill defined due to poor contrast with the surrounding, hyperechogenic infrapatellar fat pad (see Figure 7.4). The middle PL is round to oval in cross-section and is the largest of the three PLs. It runs from the apex of the patella to the cranial-most part of the tibial tuberosity, within the fat pad and in the center of the trochlear groove (Figure 7.6). Distally, it becomes more triangular in section and always contains thin, hypoechogenic lines, giving it a webbed appearance. This should not be mistaken for a tear. Tilting of the probe to create an off-incidence artifact will cause the ligament to become hypoechogenic, enhancing its outline within the fat pad (Figure 7.7). The medial PL is triangular in cross-section and, in the extended limb, lies over the medial aspect of the medial trochlear ridge, 4 or 5 cm caudal to the apex of the ridge (Figure 7.8). Proximally, it becomes more heterogeneous as its fibers spread out into the parapatellar fibrocartilage (Figure 7.9). Distally, it inserts on the medial aspect of the tibial tuberosity, approximately 2 cm medial to the middle PL and

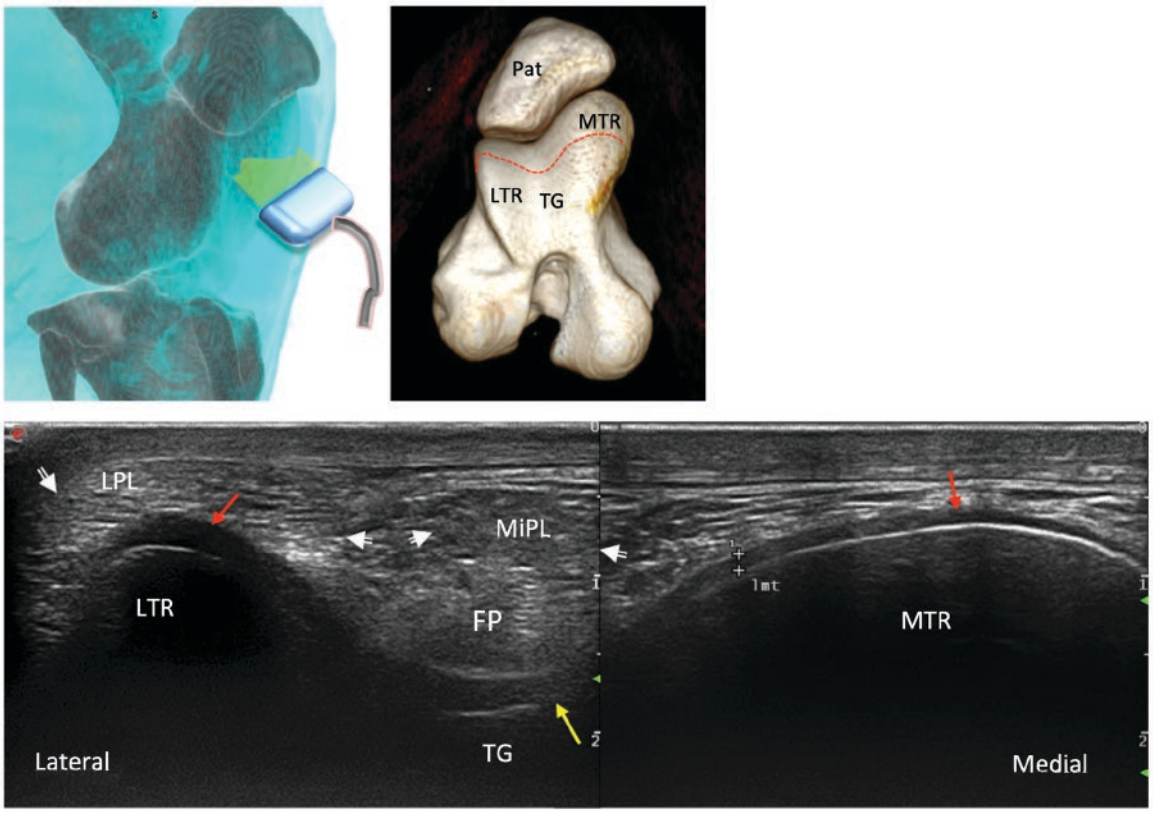


Figure 7.4 Transverse plane image of the right femoral trochlea 4 cm distal to the patellar apex (pat). The probe is place over the trochlea, i.e., over the craniolateral aspect of the stifle. The trochlear groove (TG) forms a concave trough, the lateral trochlear ridge (LTR) a narrow, sharply convex surface, and the medial trochlear ridge (MTR) a wide, rounded surface. The cartilage is thickest over the LTR and thinnest over the MTR (red arrows). The bone surface and cartilage may be irregular in the center of the groove (yellow arrow). The lateral (LPL) and middle (MiPL) patellar ligaments are recognized because of the regular, grainy appearance (double white arrows) but contrast poorly with the surrounding infrapatellar fat pad tissue (FP). Note that the joint capsule is tightly applied against the cartilages with no visible fluid.

Vet-ebooks.com

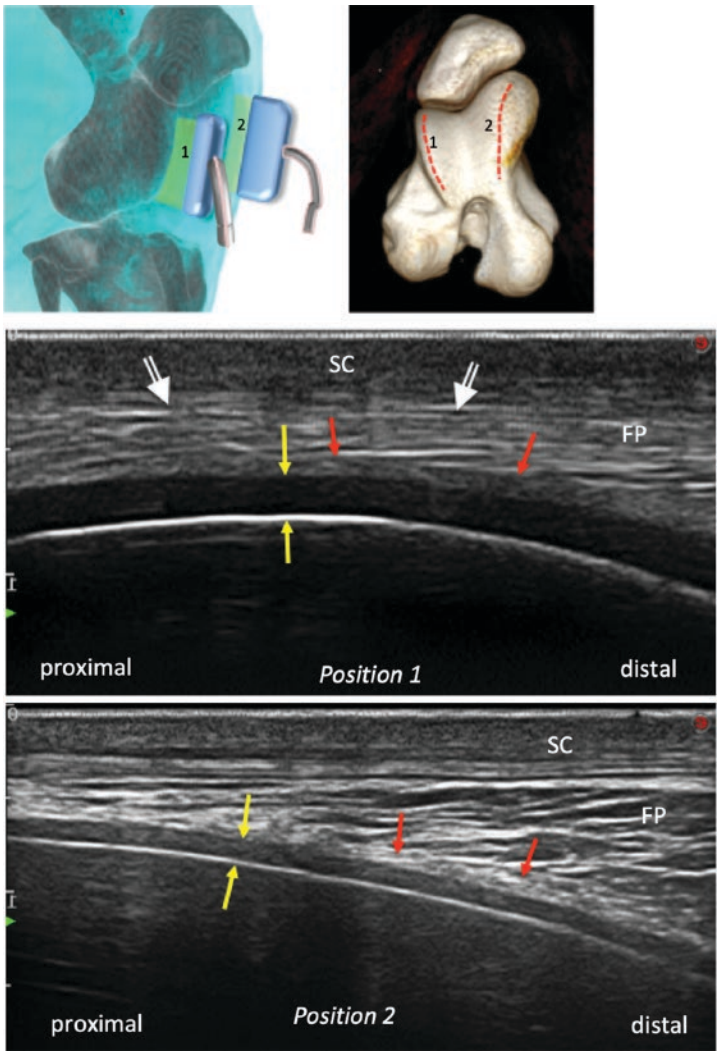


Figure 7.5 Rotating the probe by 90 degrees into a parasagittal plane from a cranial approach, the whole trochlea is evaluated from lateral, over the LTR (position 1) all the way to the MTR (position 2). The cartilage (yellow arrows) forms a hypoechogenic, homogeneous tissue between the smooth, hyperechogenic subchondral bone interface and the echogenic joint capsule (red arrows). Laterally, the thin lateral patellar ligament forms a regular striated pattern (double white arrows). SC: subcutaneous tissue.

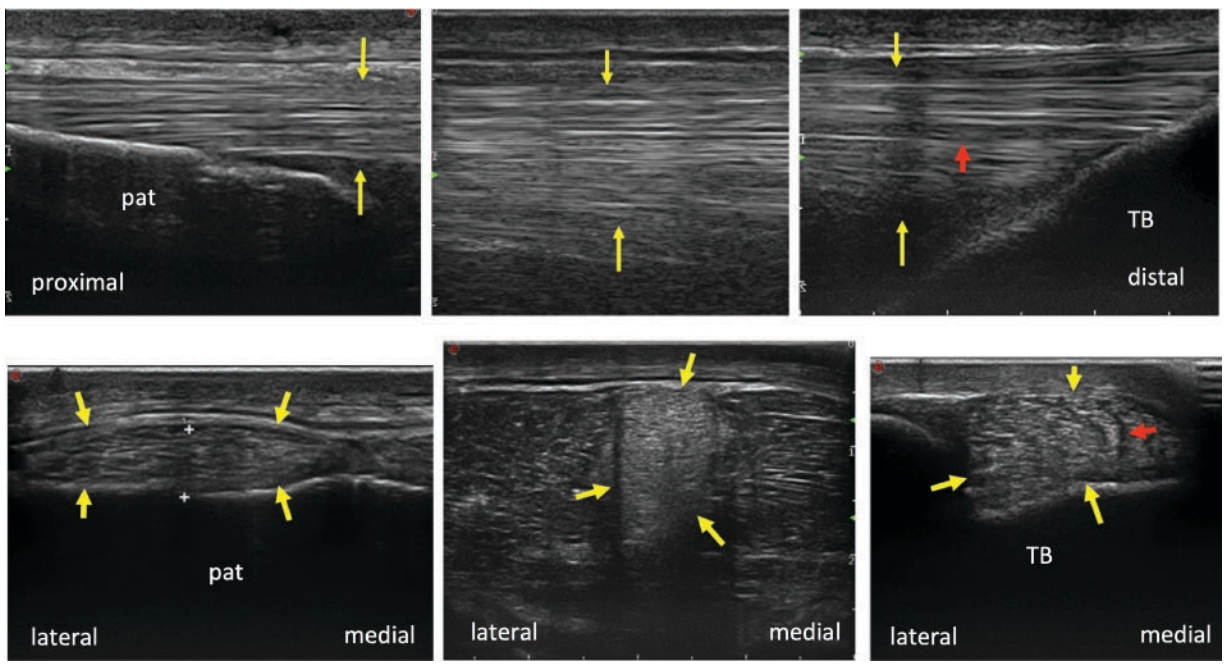


Figure 7.6 Longitudinal (top images) and transverse plane (bottom images) of the middle patellar ligament from proximal (left) to distal (right). The outline of the ligament is indicated by yellow arrows. Proximally, the MiPL originates from a curved groove on the distal surface of the patella (pat), before continuing its course within the fat pad. The section is oval proximally, then rectangular to round in the middle third, and triangular distally. In the distal third of the ligament, endoligamentar connective tissue forms hypoechogenic linear areas on longitudinal plane images and a reticulated webbed pattern on transverse plane images (red arrows). TB: tibia.

Vet-ebooks.com

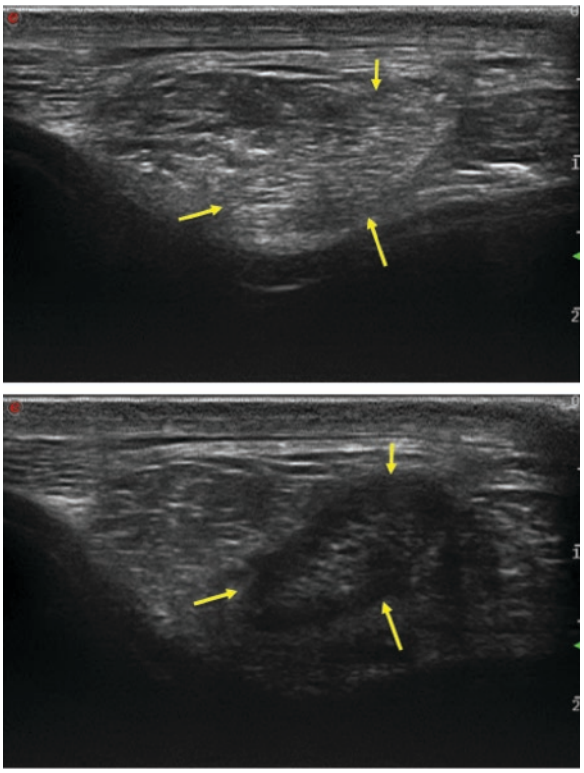


Figure 7.7 The patellar ligaments are of a similar echogenicity to that of the fat pad, so that their edges may be difficult to delineate (yellow arrows). Creating an off-incidence artifact (bottom image) can help to better delineate the ligament contours because their aligned fibers will become hypoechogenic, while the non-aligned adipo-elastic tissue will remain hyperechogenic in all planes. The middle patellar ligament is shown in these images.

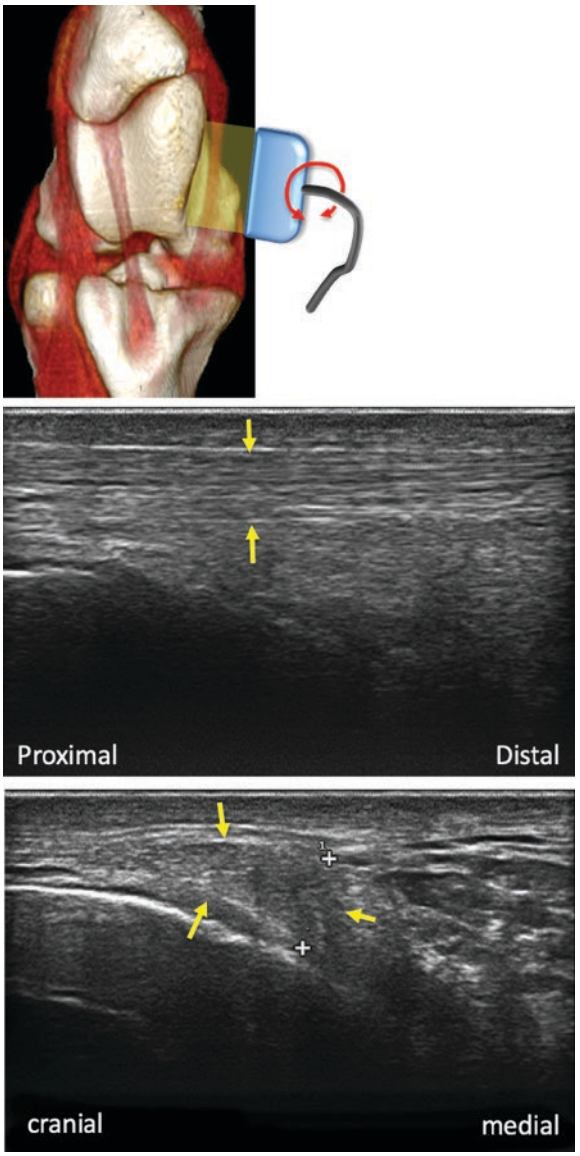


Figure 7.8 Longitudinal (frontal) plane image of the medial patellar ligament obtained caudomedial to the edge of the medial trochlear ridge (MTR) (top image). The ligament has a regular striated pattern (yellow arrows). Rotating the probe by 90 degrees to obtain a transverse plane image (bottom image), the ligament is triangular in shape and poorly defined from the surrounding fascia and joint capsule (yellow arrows).

receives a tendinous branch from the sartorius muscle. The lateral PL is thinner, flatter, and crescent-shaped in cross-section (Figure 7.4). It caps the apex of the lateral trochlear ridge, outlining the cartilage (Figure 7.5). It inserts on the tibial tuberosity, immediately lateral to the middle PL's insertion. There is often a small to moderate amount of anechogenic synovial fluid in the lateral femoropatellar joint recess, caudal to the LPL, and over the lateral surface of the lateral trochlear ridge. A small amount of fluid may be present caudal to the medial PL, although this is less prominent.

Medial Femorotibial Joint: Medial Aspect

A linear transducer is best suited, as the joint surfaces lie very close to the skin. The topography of the medial aspect of the joint and organization of the medial meniscus are reviewed in Figure 7.10. The proximal edge of the tibial condyle and the round, smooth surface of the medial femoral condyle form a triangular space filled by the echogenic medial meniscus (Figure 7.11). The latter is separated from the condyles by thin, hypoechogenic cartilage. Linear, anechogenic artifacts running perpendicular to the probe interface through the meniscal parenchyma are caused by refraction at the insertion of the capsule on the outer surface of the meniscus. These are easily mistaken for tears but they should remain perpendicular to the probe when the latter is tilted. The capsule inserts over the whole abaxial aspect of the meniscus, so that fluid can only

Vet-ebooks.com

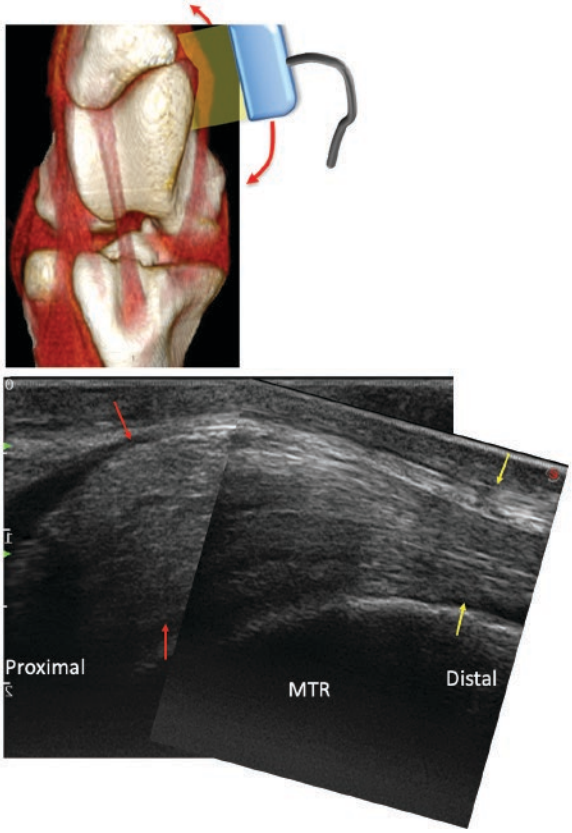


Figure 7.9 Longitudinal (frontal) plane image of the origin of the medial patellar ligament (yellow arrows). The ligament has a typical striated pattern and runs over the medial aspect of the medial femoral trochlear ridge (MTR). It arises as a continuation of the medial parapatellar fibrocartilage (red arrows), which is hypoechogenic and devoid of striation.

accumulate proximal to it, over the abaxial surface of the medial femoral condyle. Discrete distension of the joint is common cranial to the collateral ligament but the synovial membrane should remain thin. Small villi may be seen in the pouch in normal horses. Occasionally, very small gas bubbles, forming multiple, punctate hyperechogenic interfaces casting strong acoustic shadows, may be seen within the joint fluid. These represent nitrogen released by articular depression (vacuum phenomena). This is a normal, physiological occurrence. Transverse plane images of the menisci are obtained by rotating the probe by 90 degrees. The scan plane should be parallel to the edge of the tibial plateau. These images are useful to better evaluate the configuration of certain tears.

The medial collateral ligament (MCL) is a strong, flattened structure, approximately 5–6 mm in thickness. As in most joints, it is made up of two poorly differentiated branches (Figure 7.10). It is necessary to rotate the probe to image each branch individually, as they run obliquely to each other, crossing over the meniscus. The superficial branch runs vertically; it originates on the femoral epicondyle several centimeters proximal to the joint, and inserts on the abaxial surface of the tibia (Figure 7.12). It receives part of the insertion of the adductor muscle proximally. The deep branch originates caudal to it, and runs in a craniodistal direction to insert on the tibia, cranial to the superficial branch. It is strongly adherent to the abaxial surface of the meniscus.

Lateral Femorotibial Joint: Lateral Aspect

As for its medial counterpart, the general topography is presented in Figure 7.13. The joint is covered by a thicker layer of muscle and the bone surfaces are very oblique to the skin. It is consequently difficult to obtain sharp images using a linear transducer. Convex or micro-convex probes, allowing the beam to be angled relative to the skin, may provide better images. Craniolaterally, the tendon of origin of the long digital extensor and peroneus tertius muscles originates on the lateral femoral epicondyle and runs within the extensor groove of the proximal tibia (Figure 7.14). The groove is covered by cartilage and a synovial recess extends from the lateral femorotibial joint (LFT), between the bone surface and the tendon. Similarly to the MCL, the lateral collateral ligament (LCL) is divided into two branches, superficial and deep, although they are more difficult to tell apart. They insert respectively on the tibia and the fibular head. The popliteal tendon originates from a small depression on the lateral femoral epicondyle, immediately cranial to the LCL and caudal to the long digital extensor tendon. It runs obliquely in a caudodistal direction, passing over the meniscus and underneath the LCL. Because of its oblique course, it will be located proximal to the meniscus at the level of the collateral ligament and directly adjacent (abaxial) to the meniscus caudolaterally. It is triangular in cross-section at the level of the collateral ligament and should not be mistaken for a torn portion of the meniscus. It becomes rectangular in shape over the caudal horn. The tendon runs within the joint space cranially and in the capsule caudally. Its hypoechogenic muscle belly fans out over the caudal proximal tibia. Fluid may be seen proximal to the meniscus and cranial or caudal to the collateral ligament, but this is less common than in the medial compartment.

Vet-ebooks.com

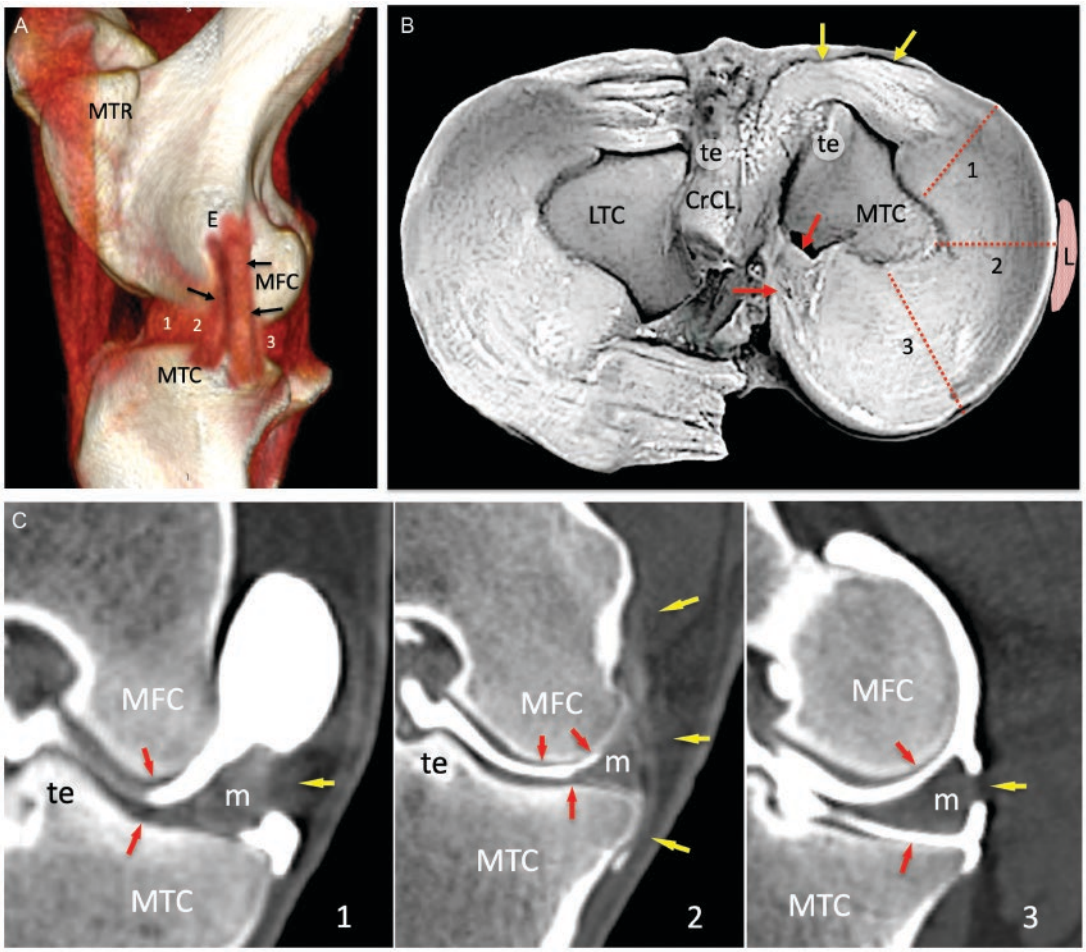


Figure 7.10 (A) Computed tomography (CT) scan three-dimensional (3-D) reconstruct of the stifle showing the topography of the medial femorotibial joint. The medial femoral condyle (MFC) and medial tibial condyle (MTC) are separated by the wedge-shaped meniscus. The latter is topographically divided into body (2), at the level of the medial collateral ligament (black arrows), and cranial (1) and caudal (3) horns. The medial collateral ligament (MCL) is flat but strong and extends from the medial femoral epicondyle (E) to the medial aspect of the MTC and is divided into two distinct branches. MTR: medial trochlear ridge. (B) Schematic view of the menisci (proximal view after removal of the femur) indicating the topographic division of the medial meniscus. The middle third is the body (2), deep to the medial collateral ligament (L). The cranial horn (1) is prolonged by the cranial meniscotibial ligament (yellow arrows), which attaches to the cranial surface of the medial tibial protuberance of the tibial eminence (te). The caudal horn (3), the largest and thickest portion, inserts on the tibia via a short caudal meniscotibial ligament (red arrows). CrCL: cranial cruciate ligament. Cranial is at the top of the image. (C) CT arthrography reconstructions help to understand the ultrasonographic anatomy of the menisci. The three sections correspond to the red dotted lines on Figure 7.10B. The hyperattenuating contrast medium appears white and indicates the joint space and synovial recesses, the largest bulging proximal to the cranial and caudal horns of the meniscus (m). The joint capsule and medial collateral ligament (central image) (yellow arrows) adhere to the abaxial surface of the meniscus. The red arrows point to the cartilage (dark, hypoattenuating rim along the condylar surfaces) showing that it is thinnest at the contact points with the meniscus and thickest around the tibial eminence. MFC: medial femoral condyle; MTC: medial tibial condyle.

Vet-ebooks.com

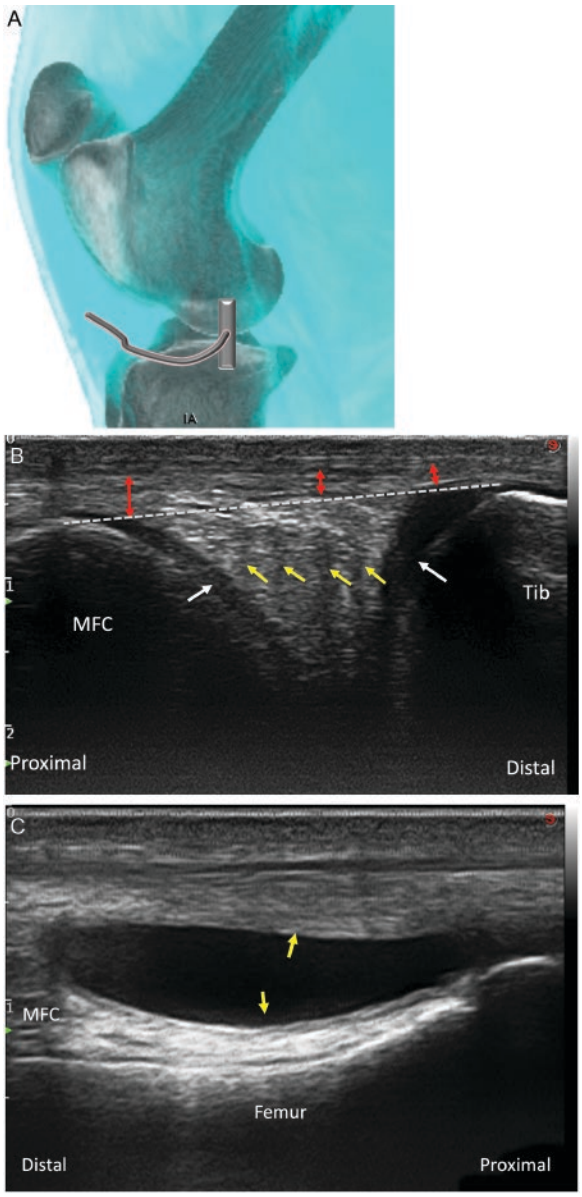


Figure 7.11 (A) Position of the transducer over the medial aspect of the medial femorotibial joint. (B) Longitudinal (frontal) plane ultrasonographic image obtained cranial to the collateral ligament. The meniscus is echogenic, wedge-shaped, and amorphous. It sits axial to an imaginary line drawn between the edges of the condyles (dotted line). The underlying cartilage is smooth and even (white arrows) and the fibrous capsule (red double arrows) inserts over its abaxial border. Note the hypoechogenic artifacts running perpendicular to the transducer (yellow arrows). (C) Image obtained proximal to that in (B). Note the mild distension of the joint pouch by anechogenic fluid. No fluid is seen over the meniscus (B). The membrane is thin and even (yellow arrows) in the absence of inflammation. MFC: medial femoral condyle; Tib: tibia.

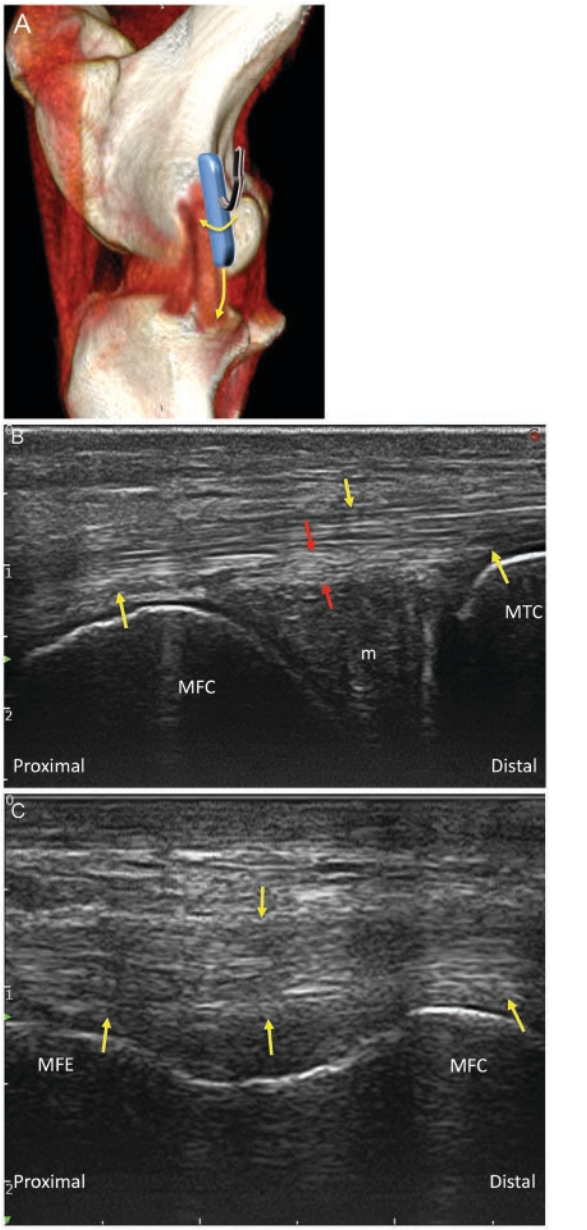


Figure 7.12 (A) Position of the transducer over the medial aspect of the stifle to image the medial collateral ligament. (B and C) Longitudinal (frontal) plane ultrasonographic images over the medial aspect of the stifle showing the superficial branch of the collateral ligament (yellow arrows), recognized by its striated pattern. It runs from the medial femoral epicondyle (MFE) over the medial meniscus and abaxial borders of the medial femoral condyle (MFC) and medial tibial condyle (MTC). The deep branch (red arrows) runs obliquely to it, hence a grainier pattern as the fibers are not aligned with the transducer. It separates the superficial branch from the meniscus to which it adheres. Note that the ligaments are poorly distinguished from the rest of the fibrous capsule.

Vet-ebooks.com

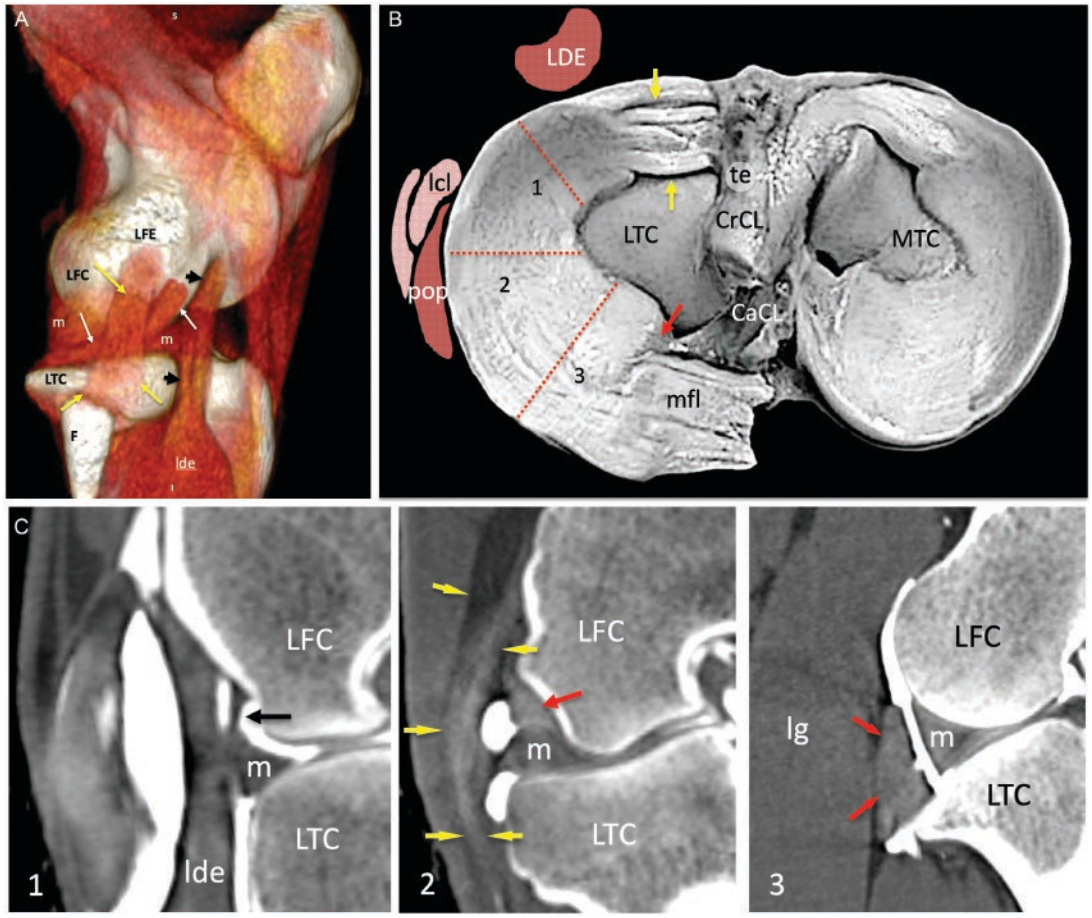


Figure 7.13 (A) CT scan 3-D reconstruct showing the topography of the lateral femorotibial joint. The lateral femoral (LFC) and tibial (LTC) condyles are separated by the lateral meniscus (m). The lateral collateral ligament (yellow arrows) is made up of two closely related branches originating from the lateral femoral epicondyle (LFE). Both insert on the tibia and fibula (yellow arrows). The common tendon of origin (black arrowheads) of the peroneus tertius and long digital extensor muscles (lde) originates from the abaxial aspect of the lateral trochlear ridge and runs over the cranial horn of the meniscus, within the extensor fossa of the tibia. The tendon of origin of the popliteus muscle (white arrows) originates from the femoral epicondyle, cranial to the collateral ligament and runs between the latter and the lateral meniscus, in a caudodistal direction. F: fibula. (B) Same schematic as in Figure 7.10B indicating the topographic division into three segments for the lateral meniscus. The lateral cranial meniscotibial ligament (yellow arrows) is similar to its medial counterpart. The caudal ligament is much slighter (red arrow). The meniscofemoral ligament (mfl) is a strong ligament arising from the caudal horn. The long digital extensor (LDE) tendon runs over the cranial meniscal horn. The popliteal tendon (pop) runs freely between the lateral collateral ligament (lcl) and the abaxial border of the meniscal body then follows the caudal horn. CrCL cranial and CaCL caudal cruciate ligaments. (C) CT-arthrography multiplanar reconstruction (MPR) reconstructions along the three planes indicated in (B). The hyperattenuating (white) contrast medium highlights the joint recesses of the lateral femorotibial articulation. On the craniolateral aspect (1) the LDE tendon runs within a synovial pouch over the abaxial border of the meniscus (m). A thin synovial fold partially separates the tendon from the rest of the joint (black arrow). Moving caudally to the lateral aspect of the joint (2), the lcl appears hyperattenuating but receives less attenuating (darker) aponeurotic fibers from the lateral thigh muscles (yellow arrows). The origin of the popliteal tendon (red arrow) has a triangular section. Finally, on the caudolateral aspect (3), the popliteal tendon (red arrows) becomes wider and blends into the joint capsule. The caudal meniscal horn (m) has a more triangular section. Lg: lateral gastrocnemius muscle.

Vet-ebooks.com

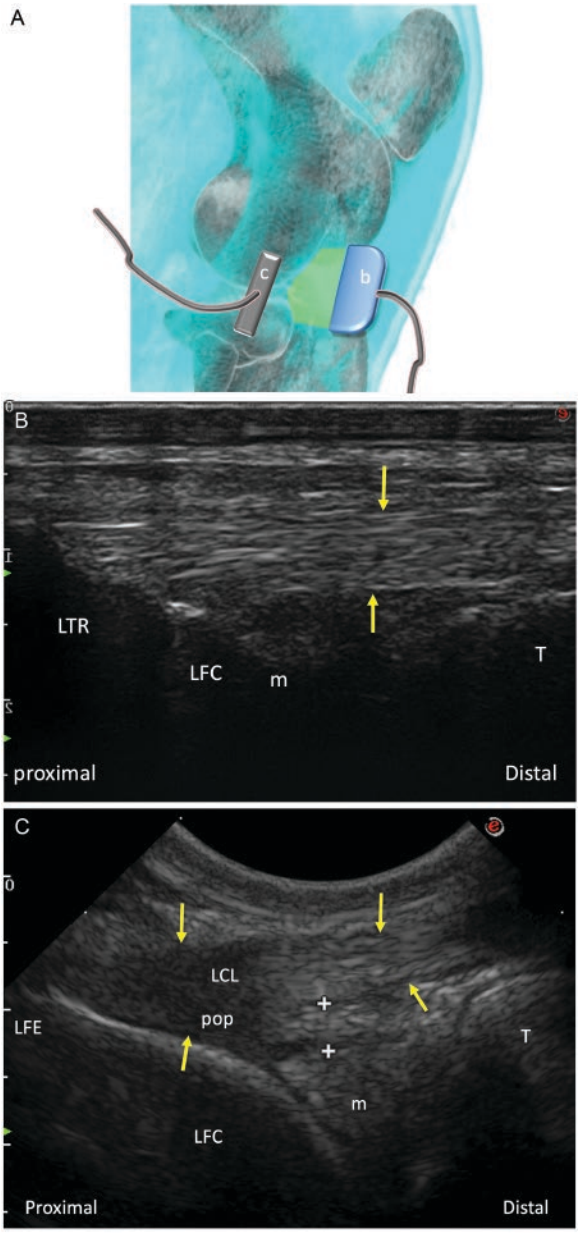


Figure 7.14 (A) 3-D reconstruct showing the position of the transducer in the two positions (B and C) corresponding to the ultrasound images over the extensor groove of the tibia (B) and lateral aspect of the lateral femorotibial joint (C). Compare to Figures 7.7, 13C1, and 13C2. (B) Longitudinal (frontal) plane ultrasonographic image showing the common tendon of origin of the peroneus tertius and long digital extensor muscles (arrows) coming off the abaxial aspect of the lateral trochlear ridge (LTR) and running over the extensor groove of the tibia (T). (C) Longitudinal (frontal) plane ultrasonographic image showing the lateral collateral ligament (LCL, yellow arrows). The striation is lost proximally because of the use of a curved array transducer inducing an off-incidence artifact. The hypoechogenic artifact helps to better see the ligament contours. At this level the popliteus tendon (pop: calipers) is flat and located between the meniscus (m) and LCL. LFE: lateral femoral epicondyle.

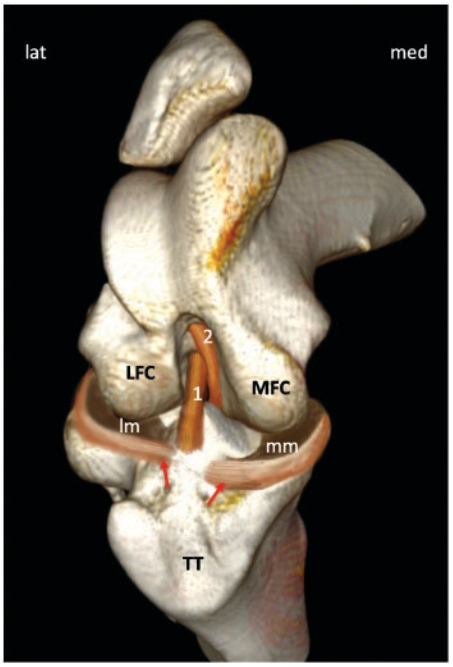


Figure 7.15 3-D CT-scan reconstruct showing the topographic anatomy of the cranial aspect of the femorotibial articulation. The stifle is partially flexed to expose the intercondylar space. Full flexion will expose most of the articular surfaces of the femoral condyles but the cruciate ligaments will flatten out against the tibial eminence. A 30–45-degree flexion is sufficient to image the cranial meniscal attachments and cruciate ligaments. The ligaments have been drawn to show their general topography. The cranial cruciate ligament (1) runs in a caudoproximolateral to distocraniomedial direction, between the axial surface of the lateral femoral condyle (LFC) and the tibial eminence; the caudal cruciate ligament (2) runs in the sagittal plane, in a cranioproximal to caudodistal direction, crossing its cranial counterpart medially between the two condyles. It originates distal to the trochlea and inserts on the caudal aspect of the tibial plateau; the two arrows indicate the cranial meniscotibial ligaments. MFC: medial femoral condyle; lm: lateral meniscus; mm: medial meniscus; TT: tibial tuberosity.

Cranial Aspect of the Femorotibial Joints

Imaging the cranial aspect of the femorotibial articulation requires that the stifle be flexed, in order to expose the femoral condyles, cranial horn of both menisci, intercondylar space, and the cruciate ligaments (Figure 7.15). Full flexion will expose most of the articular surfaces of the femoral condyles but the cruciate ligaments will flatten out against the tibial eminence and horses with stifle disease may resent this degree of flexion unless sufficient analgesia is provided. A 30–45-degree flexion is sufficient to image the cranial meniscal attachments and cruciate ligaments. A convex array or

Vet-ebooks.com

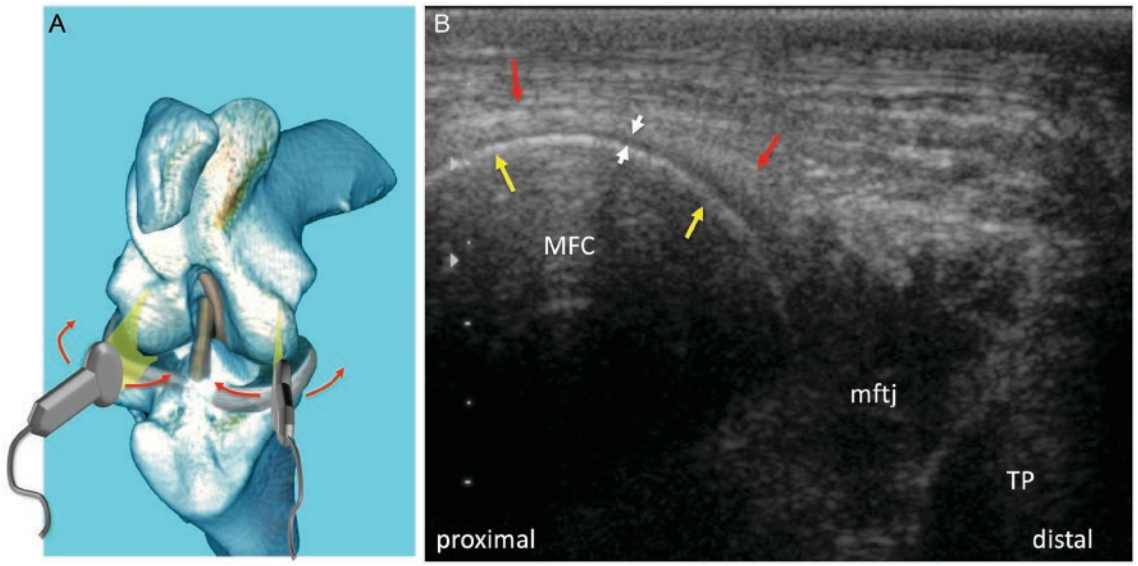


Figure 7.16 (A) Position of the transducer to image the lateral femoral condyle and cranial aspect of the lateral femorotibial joint compartment (left) and the medial condyles and medial femotibial joint (right). A linear transducer may be used but a convex or micrconvex probe will allow for some angling of the beam. The stifle is flexed as much as the horse will allow to expose the femoral condylar surfaces. The beam must be kept perpendicular to the bone surface while scanning from medial to lateral (red arrows). (B) Longitudinal (parasagittal) scan image over the cranial aspect of the medial femoral condyle (MFC). With full flexion, a large portion of the latter is exposed. Note the perfectly smooth and round surface of the calcified cartilage/subchondral bone layer (yellow arrows) and overlying, hypoechogenic hyaline cartilage (white arrows). The fibrous joint capsule (red arrows) is tightly applied over the cartilage, unless there is marked joint distension. Very mild joint distension of the medial femorotibial joint pouch is visible (mftj) between the MFC and tibial plateau (TP).

micro-convex transducer must be used to allow for angulation of the beam in relation to the skin. The surface of the femoral condyles, overlying cartilage, and cranial horns of the menisci are easily visualized dorsomedially (medial femoral condyle) or laterally (lateral femoral condyle), deep to the infrapatellar fat pad. The round surfaces of the condyles can be assessed for cartilage or subchondral defects as flexion exposes their distal-most aspect (Figure 7.16).

To image the cranial cruciate ligament (CrX), the ultrasound beam must be aligned perpendicular to the ligament fibers (Figure 7.17): the probe is placed immediately distal to the patella, over or medial to the middle PL. The probe is angled downward in the sagittal plane to image the surface of the tibial eminence. The beam is then rotated 15–20 degrees clockwise in the left limb and anticlockwise in the right limb until the linear pattern of the ligament is recognized. The CrX originates caudally on the axial (medial) aspect of the lateral femoral condyle, and inserts in a dip between the medial and lateral prominences of the tibial eminence. It may be useful to approach the joint immediately medial to the middle PL and point the probe slightly toward the lateral side to image the axial (medial) surface of the lateral femoral condyle, before rotating very slightly toward the intercondylar space to find the ligament, which curves around the condyle. Cross-sectional images can be obtained by rotating the probe 90 degrees in the same position. The CrX is hyperechogenic with a regular striated pattern. As the ligament curves around the caudal cruciate ligament, it is difficult to image its entire length on one scan image. Cross-sections may be obtained but as the ligament is surrounded by connective tissue and fat, its margins are ill-defined and the ligament contrasts poorly with intercondylar tissue.

The cranial (femoral) origin of the caudal cruciate ligament (CaX) is visualized by directing the beam upward, with the probe placed between the lateral and middle PLs, or directly over the latter, immediately proximal to the tibial tuberosity (Figure 7.18). The surface of the intercondylar space of the femur is identified between the condyles and distal to the trochlear groove. The CaX runs distocaudally in the sagittal plane, directly over the bone surface of the femur between the condyles. It crosses over the medial aspect of the cranial cruciate ligament within the intercondylar fossa. The ligaments are slightly curved, so that it is difficult to obtain perfect alignment of the fibers throughout their lengths and both ligaments are often visible on the same scan image (Figure 7.19).

Vet-ebooks.com

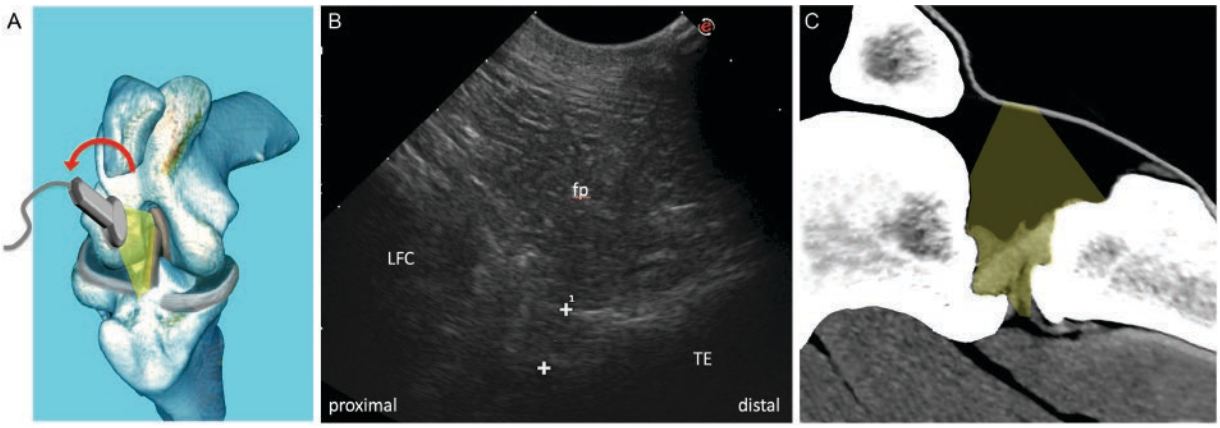


Figure 7.17 (A) Position of the transducer to image the cranial cruciate ligament; the stifle is partially flexed. The probe is placed 1 or 2 cm distal to the patella, pushing it into the skin, and angled downward 20–30 degrees in the sagittal plane; it is rotated anticlockwise (right stifle) to align the beam to the ligament fibers. (B) Corresponding longitudinal (sagittal) plane ultrasonographic image showing the cranial cruciate ligament (calipers) between the axial aspect of the lateral femoral condyle (LFC) and tibial eminence (TE). fp: fat pad. (C) Corresponding 3-D multiplanar reconstruction (MPR) CT image (soft tissue window) showing the relationship of the scan beam to bone surfaces on the section plane.

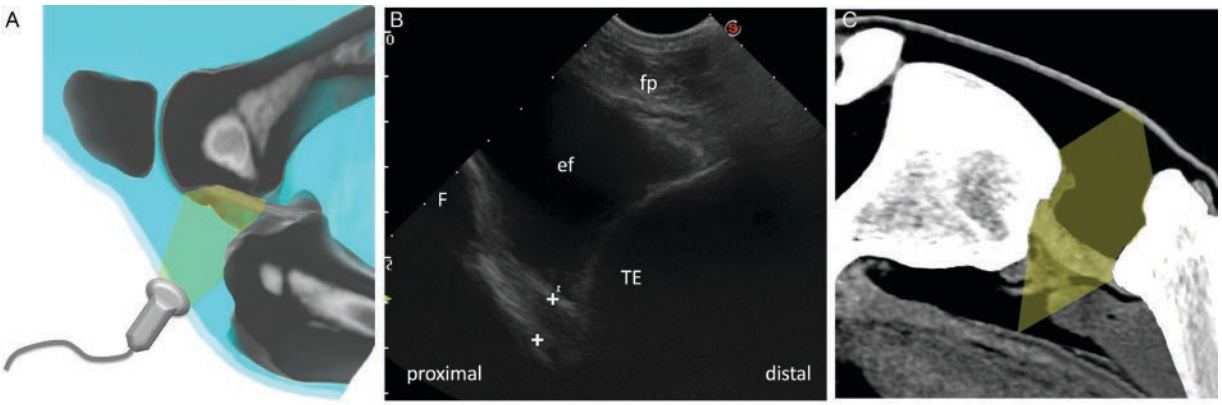
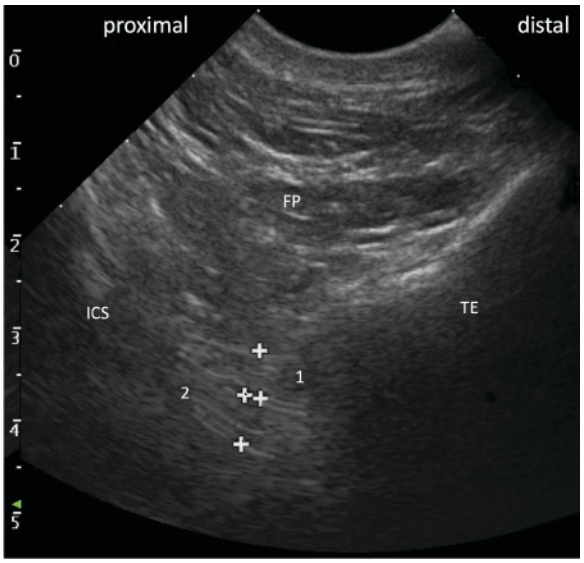


Figure 7.18 (A) Position of the transducer to image the femoral origin of the caudal cruciate ligament from a cranial approach. The stifle is partially flexed. The probe is placed distally close to the tibial tuberosity, and the beam is directed in the sagittal plane, proximally, to visualize the intercondylar fossa of the femur. (B) Corresponding longitudinal (sagittal) plane ultrasonographic image showing the caudal cruciate ligament (calipers) running from just distal to the femoral trochlea (F) to the caudal aspect of the proximal tibia. TE: tibial eminence. Medial femorotibial effusion (ef) in this horse enhances the normal appearing ligament. fp: fat pad. (C) (optional) Corresponding 3-D MPR CT image (soft tissue window) showing the extent of the scan beam.

Figure 7.19 Slightly oblique view obtained half-way between those in Figures 7.11B and 7.12B, showing the crossing point between the cranial (calipers 1) and caudal (calipers 2) cruciate ligaments. As the two ligaments are slightly curving around each other, it is common that both appear within the same scan plane. TE: tibial eminence; FP: fat pad; ICS: intercondylar eminence.



Vet-ebooks.com

Finally, the cranial tibial insertions of the menisci (cranial meniscotibial ligaments – CMTL) are imaged from the craniolateral and craniomedial aspects respectively. The cranial horn of the meniscus is visualized as a wedge-shaped structure between the femoral and tibial condyles cranioabaxially. Each meniscus is followed cranially by following the curved contour of the ipsilateral femoral condyle and then along the cranial aspect of the tibial eminence. To visualize the ligaments, the probe must be angled downward to keep the proximal surface of the tibia perpendicular to the beam (Figure 7.20). Both longitudinal and transverse images of the ligaments may be obtained from this position by rotating the transducer by 90 degrees, revealing a regularly striated, echogenic structure running between the cranial meniscal horn and the cranial aspect of the tibial eminence. This requires some practice but reproducible images of the CMTL and cranial meniscal horn can easily be obtained.

Caudal Aspect of the Femorotibial Joints

The topography is reviewed in Figure 7.21. The leg is examined extended and weightbearing. Because of the large caudal muscle mass, the depth of the joint varies from 5–12 cm. For this reason, lower frequency (e.g., 5–9 MHz) transducers may be necessary.

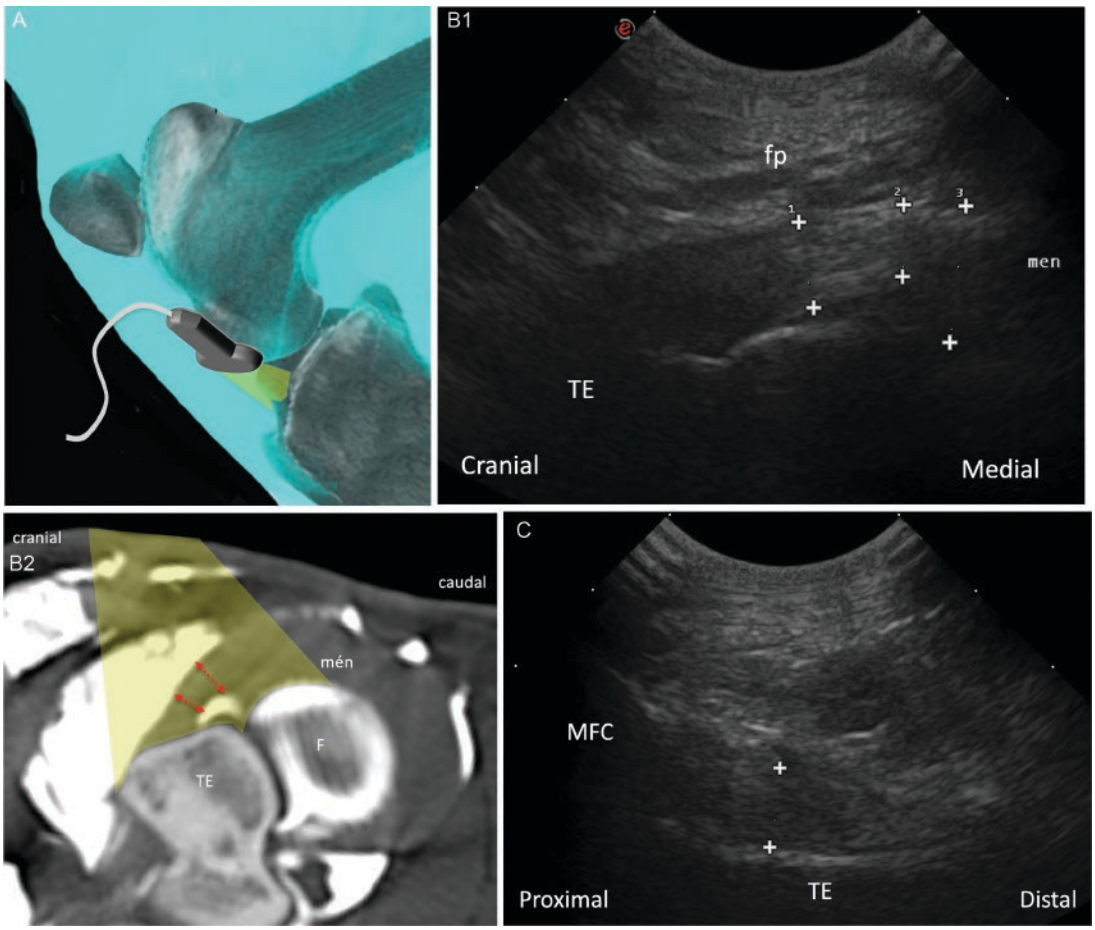


Figure 7.20 Imaging the cranial meniscotibial ligaments may be challenging. This is, however, a common site of pathology. (A) The stifle should be partially flexed and the probe placed cranial to the corresponding meniscus (craniomedially for the medial meniscus). A longitudinal scan image of the ligament is obtained by placing the probe half-way between the patella and tibial tuberosity, and orienting the beam transversely across the limb and tilting the probe downward, in order to be more or less perpendicular to the tibial plateau. (B) Corresponding scan image. The regularly striated ligament is visible (calipers marked 1 and 2) between the cranial horn of the meniscus (calipers marked 3) and the craniomedial border of the tibial eminence. This view may be obtained with a curved or linear array transducer. (B2) (optional) Corresponding 3-D MPR CT arthrography image (soft tissue window) showing relationship of scan beam to the bone surfaces and ligament on a transverse section plane. (C) A transverse ultrasonographic image of the ligament is obtained by rotating the beam by 90 degrees. The calipers mark the extent of the cranial meniscotibial ligament.

Vet-ebooks.com

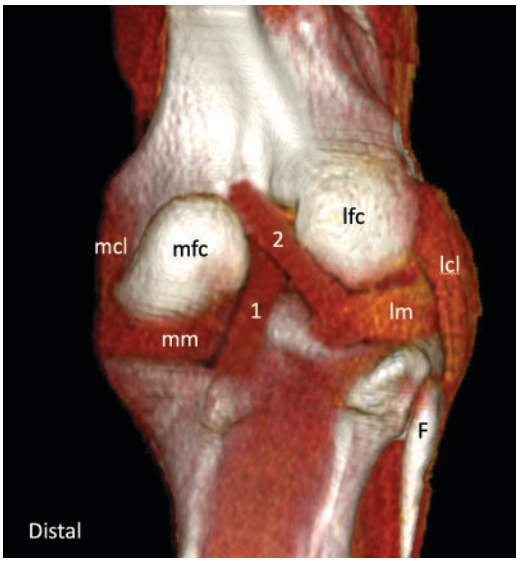


Figure 7.21 CT 3-D reconstruct showing the topographic anatomy of the caudal aspect of the femorotibial articulation. mfc: medial femoral condyles; lfc: lateral femoral condyles; mm: medial meniscus, lm: lateral meniscus; mcl: medial collateral ligament; lcl: lateral collateral ligament; F: fibular head; 1: caudal cruciate ligament inserting on a sharp tibial tubercle on the caudal aspect of the tibial plateau; 2: meniscofemoral ligament.

Convex or micro-convex probes are used to angle the probe up or down in relation to the skin to image the various ligaments. Adequate images of the caudal cruciate ligament are obtained with the transducer placed on the caudal aspect of the distal thigh muscles, 10–15 cm proximal to the junction thigh/leg. The probe is pushed into the semimembranosus/semitendinosus muscle mass and angled downward at 15–30 degrees (i.e., perpendicular to the tibia) (Figure 7.1e). From a caudal approach, the femoral condyles are round and smooth with an even anechoic cartilage. The caudal meniscal horns are wedge-shaped and curve around the caudal aspect of each condyle (Figure 7.22). The joint capsule is only obvious when highlighted by a joint effusion which may be voluminous in the caudal aspect of the stifle.

The CaX is imaged in the sagittal plane (Figures 7.23A and 7.23B). It runs from the intercondylar fossa of the femur, between the condyles, in a caudodistal direction and inserts on a sharp bony prominence on the caudal proximal border of the tibia, axial (medial) to the medial meniscus. The probe must be oriented downward by 30 degrees. From this position, the transducer can then be rotated anticlockwise in the right stifle, clockwise in the left limb, by 30–40 degrees to the axial plane, to image the lateral meniscofemoral ligament, which links the caudal horn of the lateral meniscus to the femur immediately proximal to the medial condyle (Figure 7.23C).

Ultrasonographic Abnormalities

General principles applying to ultrasonographic signs of joint disorders are reviewed in detail in Chapter 2. The same basic signs should be looked for in the stifle, including inflammatory changes in the synovial membrane and capsule, cartilage, and subchondral bone defects, fragmentation, etc. More specific conditions are reviewed here.

Femoropatellar Joint

Effusion

Synovial effusion is the most common finding in the femoropatellar joint. It is most prominent in the abaxial recesses, lateral and medial to the trochlea and trochlear ridges. It may be encountered in many sound horses without synovial thickening ("cold effusion"), with a variable amount of fluid present (Figure 7.24). *Inflammatory changes* (*synovitis*) are characterized by synovial thickening (Figure 7.25) and may be observed without identifiable causes. However, a potential primary lesion should always be suspected or ruled out. In acute inflammation, the synovium is typically moderately thickened and hypoechogenic because of edema and hyperaemia (Figure 7.25A). With chronic synovitis, fibrosis will cause the synovial membrane and joint capsule to become more echogenic and rounded (Figure 7.25B). Villous proliferation may be seen as lollipop- or polyp-shaped images in the abaxial recesses (Figure 7.25C), and synovial masses (fibrous hyperplasia or fibrocartilaginous metaplasia) are occasionally observed (Figure 7.25C). Large amounts of anechogenic fluid may be present, displacing the capsule and overlying muscles. Normally, the tension in the quadriceps muscle pushes the patella and patellar ligaments tightly against the trochlear surfaces. Only in the most severe cases will the fluid pressure become substantial enough to displace the patella and patellar ligaments away from the femur (Figure 7.26). Signs of hemorrhage may be

Vet-ebooks.com

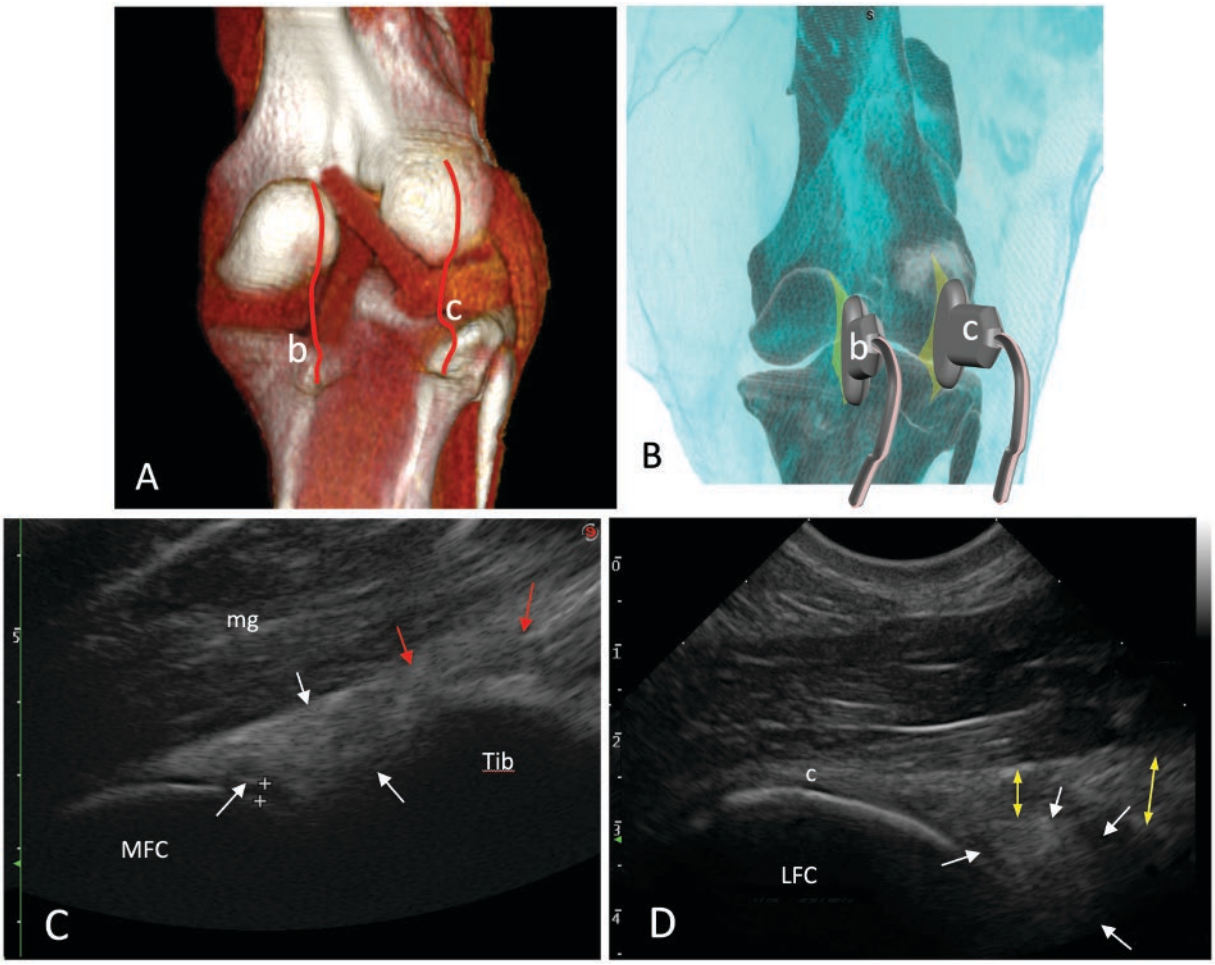


Figure 7.22 (A) and (B) CT 3-D reconstructs showing the position of the ultrasound transducers used to image the caudal horn of the medial meniscus and caudal aspect of the medial femoral condyle (position b) and the caudal horn of the lateral meniscus and caudal aspect of the lateral femoral condyle (position c). (C) Longitudinal (parasagittal) plane image corresponding to position b. The medial meniscus (white arrows) is brightly echogenic and wedge-shaped. Its caudal meniscotibial insertion (red arrows) forms a thin ligament inserting on the caudal aspect of the tibial plateau (Tib). The medial femoral condyle (MFC) is very smooth and rounded with regular hypoechogenic cartilage (calipers) overlying the smooth subchondral bone surface. The medial gastrocnemius (mg) muscle belly is superficial to the capsule. (D) The lateral femoral condyle (LFC) is similar to the MFC. The caudal horn of the meniscus (white arrows) lies below the thin popliteal tendon (yellow double arrows) which extends distally over the caudal surface of the tibia (off incidence). Note the thick joint capsule overlying the cartilage (c).

noted, although this appears to be rare in the stifle and is usually associated with trauma (Figure 7.27). Osteoarthritis may be very subtle in this joint, with increased cartilage echogenicity only visible with high-resolution images (Figure 7.28A). Significant, generalized cartilage thinning may be found in severe, long-standing cases. Osteophytes are visible at the apex of the patella and at the abaxial edges of the trochlear ridges (Figure 7.28B).

Patellar Ligament Injuries

Patellar ligament injuries have been increasingly recognized. They may be due to direct trauma in many cases, although progressive degeneration through repeated strain injuries might be incriminated as for digital flexor tendons. The middle PL is most commonly affected (Figures 7.29, 7.30, and 7.31). A recent review of 42 cases [1] showed that the lesions are most common in the middle one-third of the ligament and that in most cases these injuries occur in combination with other stifle conditions. The medial PL may be primarily injured, particularly in trotters (Figure 7.31). This should not be mistaken for previous desmotomy of the medial PL, which can give rise to a very thickened, heterogeneous or hyperechogenic ligament. The lateral PL is less commonly affected alone but it may be damaged in complex traumatic injuries, in combination with other lesions, or in association with direct trauma and wounds over the lateral trochlear ridge.

Vet-ebooks.com

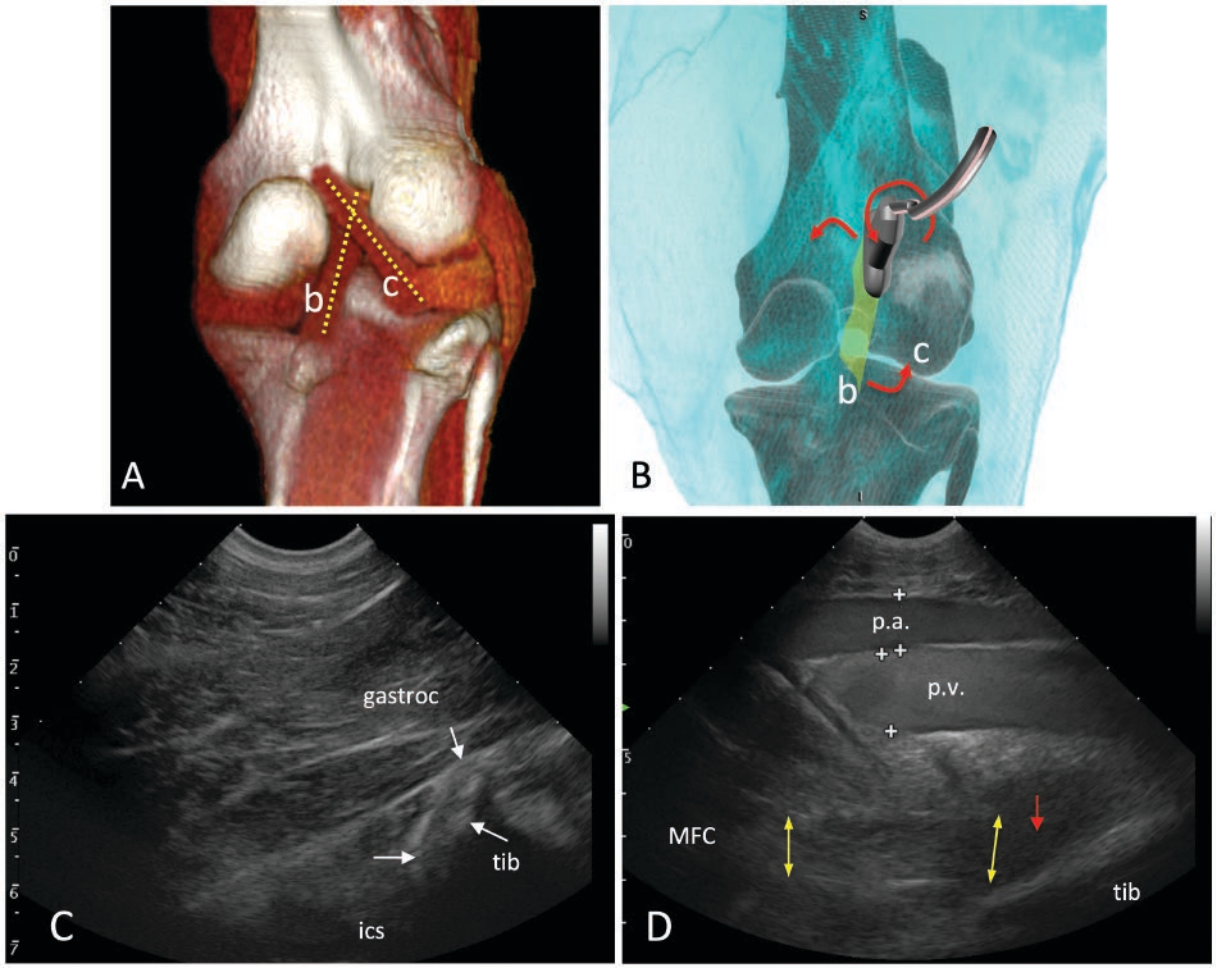


Figure 7.23 (A) and (B) CT 3-D reconstructs showing the position of the ultrasound transducer used to image the tibial insertion of the caudal cruciate ligament (position b) and the meniscofemoral ligament (position c). (C) Sagittal plane ultrasonographic image corresponding to position b. The tibial insertion (tib) of the caudal cruciate ligament is very pointy. The ligament itself is echogenic and well circumscribed (white arrows). Its femoral origin is rarely seen within the intercondylar space (ics). The gastrocnemius muscle mass (gastroc) overlies the joint capsule. (D) A 30-degree rotation of the beam creates a very oblique section but provides a longitudinal image of the meniscofemoral ligament (yellow double arrows). The red arrow points to the caudal horn of the lateral meniscus, in close contact with the tibial plateau (tib). Proximally, the ligament originates from the surface of the femur, just proximal to the medial femoral condyle (MFC). Depending on the position of the probe, the scan plane may cross the path of the popliteal artery (p.a.) and vein (p.v.).

"Core lesions," similar to those in the superficial digital flexor tendon, can occur, associated with enlargement and decreased echogenicity of the ligament (Figure 7.29). In most cases, however, diffuse or reticulated anechoic areas are visible in the enlarged ligament (Figure 7.30). Severe ligament tears cause them to appear grossly enlarged and poorly defined with a diffuse, hypoechogenic, and mottled appearance (Figure 7.31). The boundaries of the ligament may become indistinguishable from the surrounding, echogenic fat. Spontaneous rupture or avulsion of the patellar origin or tibial insertion occur occasionally (Figure 7.32). Severe, complex PL injuries may be encountered, due in particular to high-speed falls or road traffic accidents: these may be associated with patellar fracture or dislocation. PL injury may also occur in combination with avulsion fractures of the tibial tuberosity. This may have important repercussions when assessing the postoperative recovery risk or long-term prognosis.

Although ultrasonographic examination is often requested by trainers and veterinarians in cases of upward fixation of the patella, it is very unusual to observe any abnormality of the patellar ligaments in these cases. Desmitis of the medial PL usually occurs in combination with middle PL injury, although the author has encountered it as a primary entity in trotters, either as a result of previous surgery (longitudinal desmotomy, intraligamentous injections) or as a spontaneous injury (Figure 7.33). Ultrasonography may be useful in such cases, however, in order to rule out associated synovitis and trochlear or secondary patellar

Vet-ebooks.com

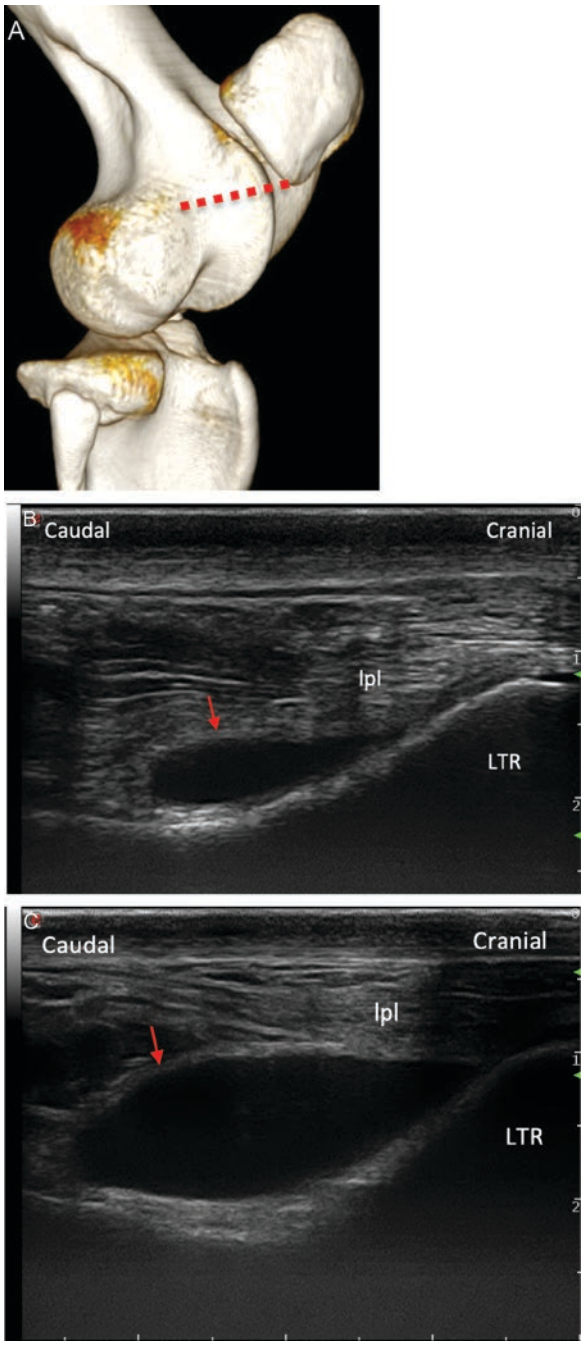


Figure 7.24 Idiopathic non-inflammatory effusion of the femoropatellar joint is common in horses and is most commonly encountered lateral to the lateral trochlear ridge (LTR) and caudal to the overlying lateral patellar ligament (lpl). (A) shows the level and position of the sound beam. Typically the distended joint pouch (red arrow) is filled with anechogenic fluid and lined by a thin echogenic capsule. The amount of fluid may be slight (B) or occasionally voluminous (C) and may vary with time in the same animal.

injuries. Fragmentation of the distal articular border of the patella, secondary to medial PL desmotomy, may be associated with significant remodeling, mineralization, and damage to the origin of the middle PL.

Osteochondrosis

Ultrasonography is more sensitive than radiography to detect osteochondrosis (OC), especially of the trochlear ridges. In one study comparing ultrasound with radiography and arthroscopy [2], ultrasonography provided a 94% sensitivity and 100% specificity. A recent, prospective study showed that ultrasound was superior to radiography for early detection of trochlear ridge OC in foals [3]. It is particularly helpful for accurately determining the extent of OC lesions, which has been closely related to the prognosis after surgery. OC lesions of the trochlear ridges have been graded in relation to their proximodistal extent [4]: grade I lesions are less than 2 cm in length, grade II measure 2–4 cm, and grade III lesions are greater than 4 cm. The prognosis is closely related to the lesion size, with grade I, II, and III lesions carrying a 78, 63, and 54% chance of returning to the intended use, respectively.

In trochlear ridge OC, the subchondral bone is flattened or irregular, forming a discrete defect (Figure 7.34). The overlying cartilage is increased and irregular in thickness (Figure 7.34). It is often heterogeneous, with moderately to strongly echogenic areas. Amorphous, heterogeneous, and echogenic material may be visible in the depth of the defect, underneath the cartilage, representing necrotic cartilage and pannus (fibrous material) (Figure 7.34B). The overlying cartilage may be lifted, forming a flap, and eventually sloughs off (dissecting lesion or "osteochondrosis dissecans," OCD) (Figure 7.34C). In most cases, smooth, hyperechogenic fragments casting an acoustic shadow represent mineralized flaps or fragments (Figure 7.35). Both the proximodistal and lateromedial extent of the lesion should be evaluated as this may have important repercussions on the prognosis and surgical approach. Irregular areas in the center of the trochlear groove should be considered as a normal feature. Ultrasound is also useful to confirm, prior to surgery, the location of free osteochondral fragments, which may detach and migrate proximally into the suprapatellar pouch, abaxially or distally into the corresponding joint recesses (Figure 7.36). Many fragments are enclosed in the synovial membrane and may therefore be more difficult to locate arthroscopically. OC of the patella is usually not visible ultrasonographically.

OC lesions may be detected at an early age in foals. However, many lesions will resolve spontaneously before the age of 5–8 months, so that early detection warrants regular recheck examinations. The trochlea of new-born or dysmature foals may not be completely ossified, so that the subchondral bone can appear very irregular, and the cartilage very thick with echogenic radially arranged striations (Figure 7.37A).

Vet-ebooks.com

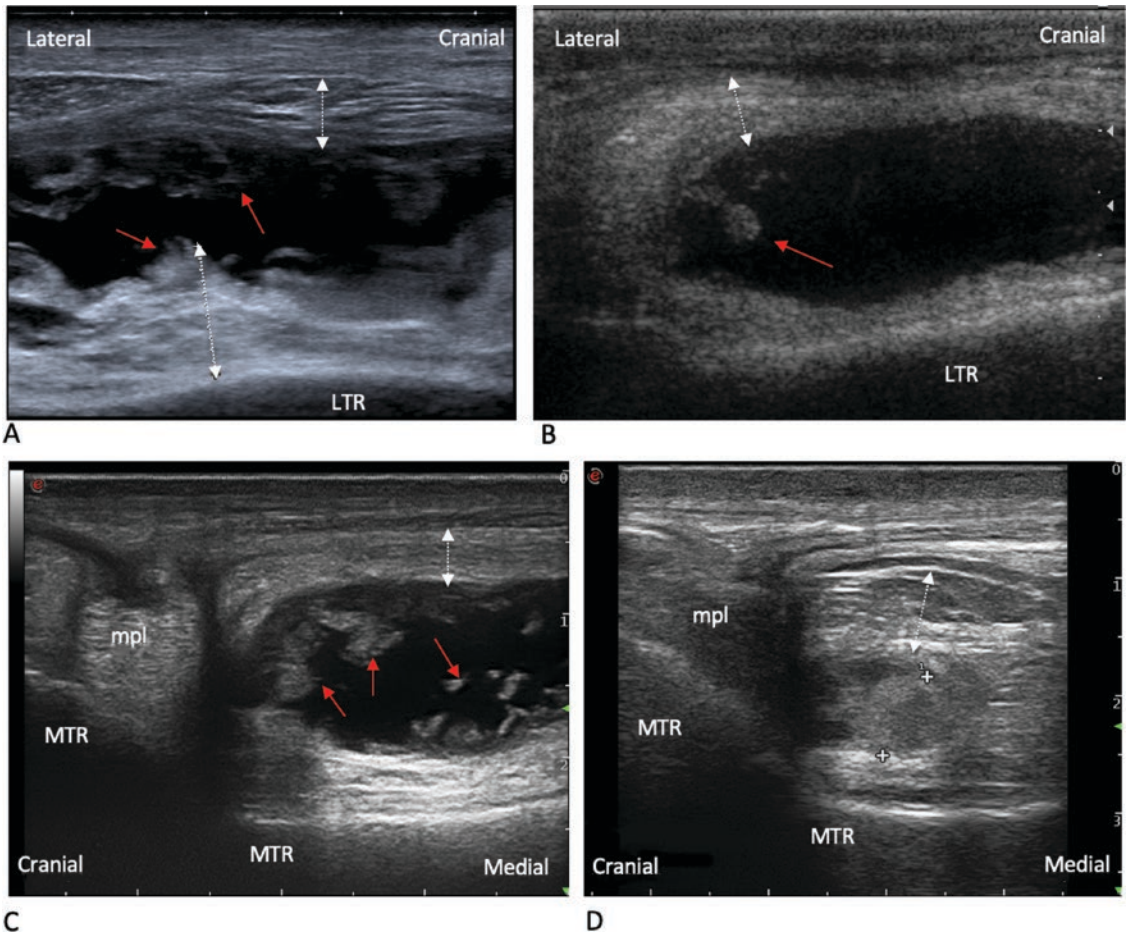
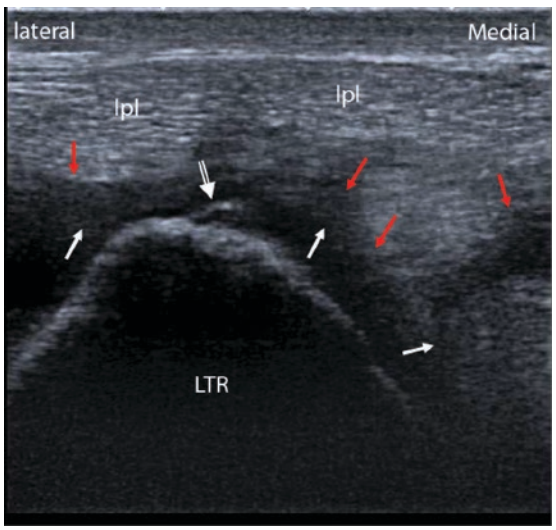


Figure 7.25 Inflammatory changes in the femoropatellar joint capsule. (A) and (B) Transverse ultrasound images obtained lateral to the lateral trochlear ridge (LTR) and caudal to the lateral patellar ligament. (A) Acute inflammation involves edema and vascular dilation, with diffuse fluid infiltration of the capsular tissues giving them a layered, "puff-pastry" appearance (double white arrows). The synovial lining is irregularly thickened, hypoechogenic with thickening of the villous folds (red arrows). (B) With chronicity, fibrosis will cause the capsule and synovium to become more echogenic, with smooth contours (double white arrows) and clubbing of the hypertrophied villi (red arrows). (C) and (D) Transverse ultrasound images obtained caudomedial to the medial trochlear ridge (MTR) and caudal to the medial patellar ligament (mpl). (C) Chronic villous hypertrophy (red arrows) may be very marked, largely filling the distended pouch bound by thickened capsule (double white arrow). (D) Chronic thickening of the capsule can be dramatic (double white arrow), leading to mechanical impairment of limb flexion, and intrasynovial masses may develop from metaplastic, fibrous villous hypertrophy (between calipers).

Figure 7.26 In some chronic or severe cases, the amount of fluid effusion may be such that the pressure becomes greater than the tension on the quadriceps muscle, so that the fluid may physically displace the patella and patellar ligaments cranially, away from the trochlear surfaces. Here the lateral patellar ligament (lpl) is separated from the lateral trochlear ridge (LTR) by hypoechogenic fluid and the thickened synovial membrane (red arrows). The latter is irregularly hypertrophied (white arrows). Note the irregular joint surface with focally sloughing mineralized cartilage due a long-standing osteochondrosis lesion (double arrow).



Vet-ebooks.com

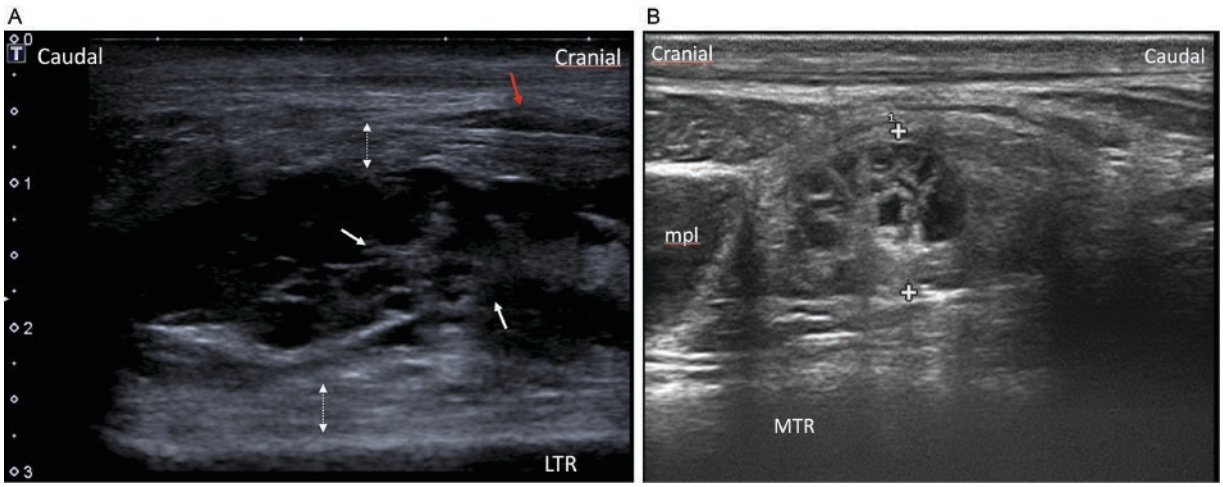


Figure 7.27 Hemorrhage may occur either from acute trauma, synoviocentesis, or because of intra-articular tearing of an inflamed synovium (e.g., because of cartilage fragment displacement or tearing of adhesions). (A) With recent hemarthrosis, strands of fibrin clots form an irregular reticulated, echogenic pattern within the lateral femoropatellar joint pouch (white arrows). In very early cases, the synovial fluid may appear echogenic and granular. This is acute injury on a chronically inflamed joint as showed by the echogenic, thickened capsule (double white arrows). Note the presence of pericapsular edema (red arrow). (B) More chronic hemorrhage may cause cavitary masses within the synovial membrane (organized hematomata). Image obtained on the medial aspect of the stifle.

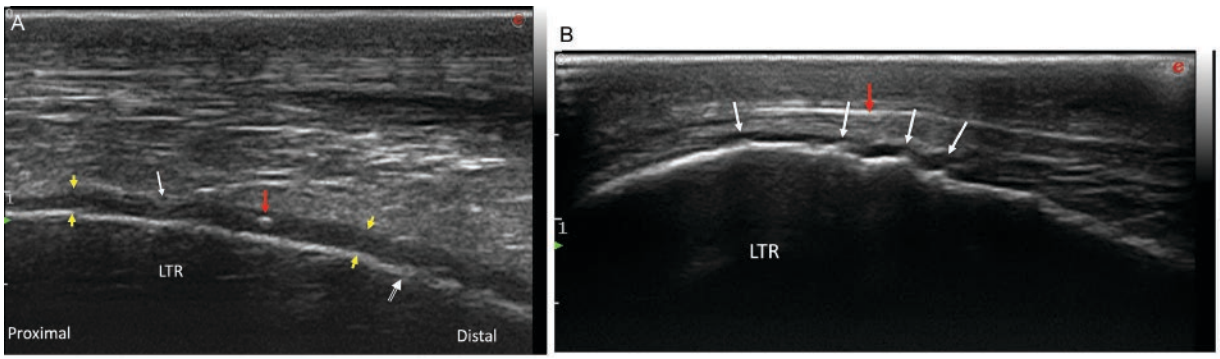


Figure 7.28 Degenerative joint disease (osteoarthritis) of the femoropatellar joint may be very subtle. (A) The main changes consist of cartilage degeneration. On the lateral trochlear ridge (LTR) of this horse, the cartilage (between yellow arrow-heads) is uneven in thickness, abnormally echogenic, with multifocal areas of superficial erosion (white arrow) and hyperechogenic foci (red arrow) representing partial mineralization or fibrosis (there is no acoustic shadowing). The underlying subchondral bone may be irregular (double arrow). (B) Moving slightly abaxially from the position in (A), shows periarticular new bone (osteophytes) forming spiky interfaces at the periphery of the cartilage (white arrows). Note moderate capsular thickening (red arrow) but an absence of fluid distension.

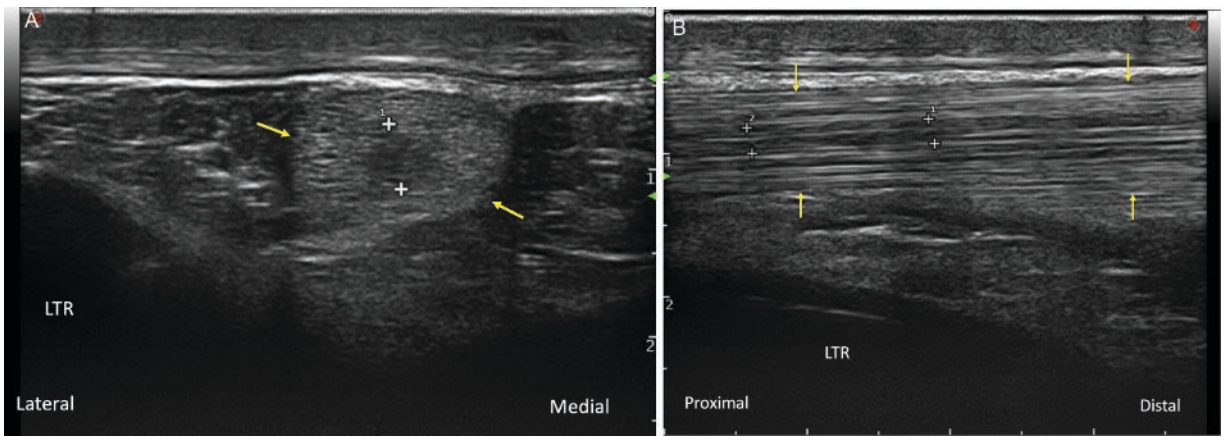


Figure 7.29 Transverse (A) and sagittal (B) images of the middle patellar ligament and trochlea. Although the ligament is little enlarged (yellow arrows), there is a discrete, hypoechogenic core lesion in the center (calipers).

Vet-ebooks.com

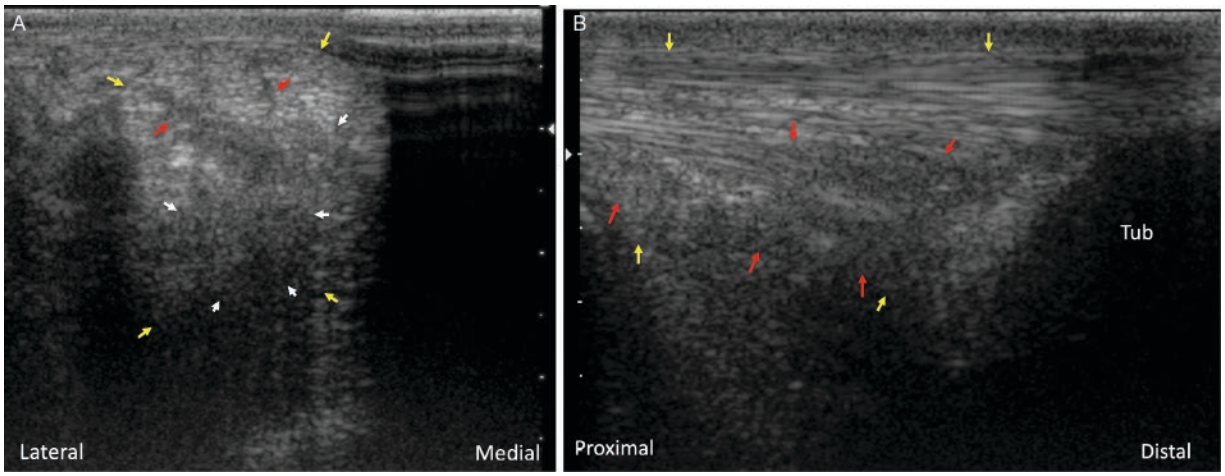


Figure 7.30 (A) Transverse image in the distal third of the middle patellar ligament. The ligament is diffusely enlarged (yellow arrows). There is diffuse fiber disruption of its caudal portion (white arrow heads), with loss of the caudal margin. The hypoechogenic lesion is ill-defined and extends into the rest of the parenchyma as narrow tears (red arrows). (B) The longitudinal section shows marked enlargement of the distal one-third of the ligament, proximal to its insertion on the tibial tuberosity (Tub). There is severe loss of fiber alignment (red arrows).

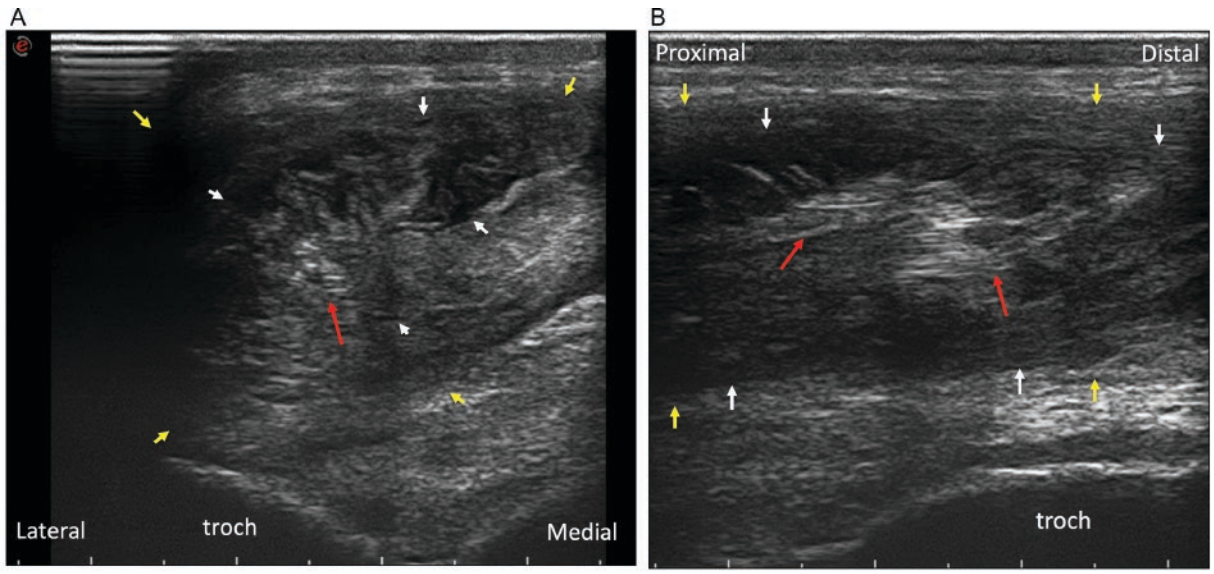


Figure 7.31 Transverse (A) and sagittal (B) images of the middle patellar ligament showing gross enlargement of the ligament (yellow arrows) with a diffuse hypoechogenic, poorly-defined lesion (white arrows), with complete loss of fiber pattern. Torn remaining fibers (red arrows) are surrounded by hypoechogenic hemorrhagic tissue. Troch: trochlear groove.

However, ossification is all but complete by 6 weeks and any irregularity of the subchondral bone after that age should be considered abnormal (Figure 7.37B).

Patellar Fractures

Patellar fractures, sometimes difficult to visualize on radiographs, can often be seen ultrasonographically as loss of continuity of the bone interface. Fragments may be visible and the fracture line(s) can usually be followed to assess its configuration (Figure 7.38). In early cases, large hematomas are usually present over the patella and within the quadriceps. In more chronic cases, a hyperechoic callus may be visible and irregular new bone is present around the fracture site. Joint involvement (articular fractures) leads to severe synovitis, and hemarthrosis (echogenic, granular fluid distension) may be obvious in the acute stage. Severe effusion, synovial thickening, and signs of osteoarthritis may be

Vet-ebooks.com

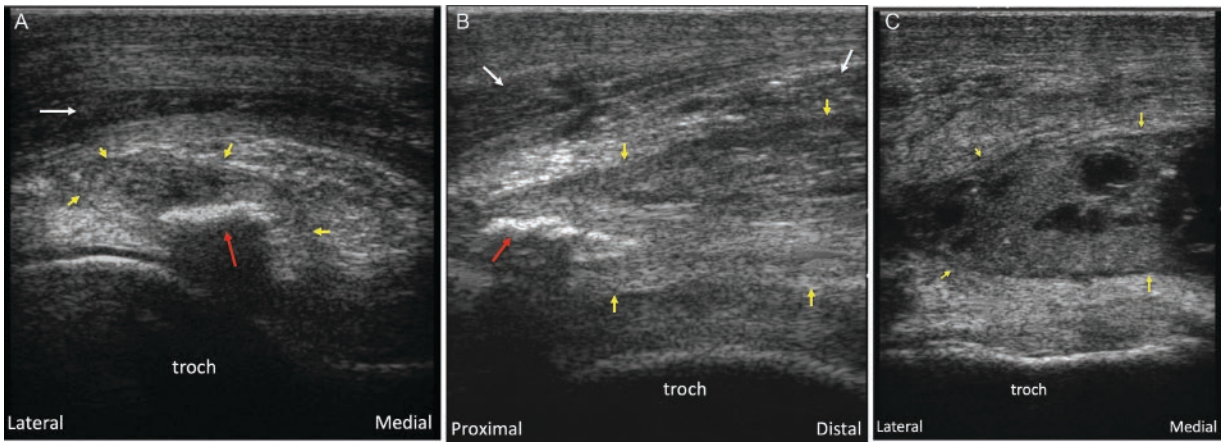


Figure 7.32 Transverse (A) and sagittal (B) images of the middle patellar ligament avulsed from the patella. A bone fragment (red arrow) is displaced distally with the untorn ligament within the fat pad. The latter shows marked oedema (white arrows). As it is no longer under tension, the ligament (yellow arrows) appears hypoechogenic and devoid of fiber pattern, although there is probably associated, diffuse parenchymal injury. (C) Between the avulsed ligament and distal patella, the path left by the displaced ligament contains an organizing hematoma with fluid filled cavities (yellow arrows). Troch: trochlea.

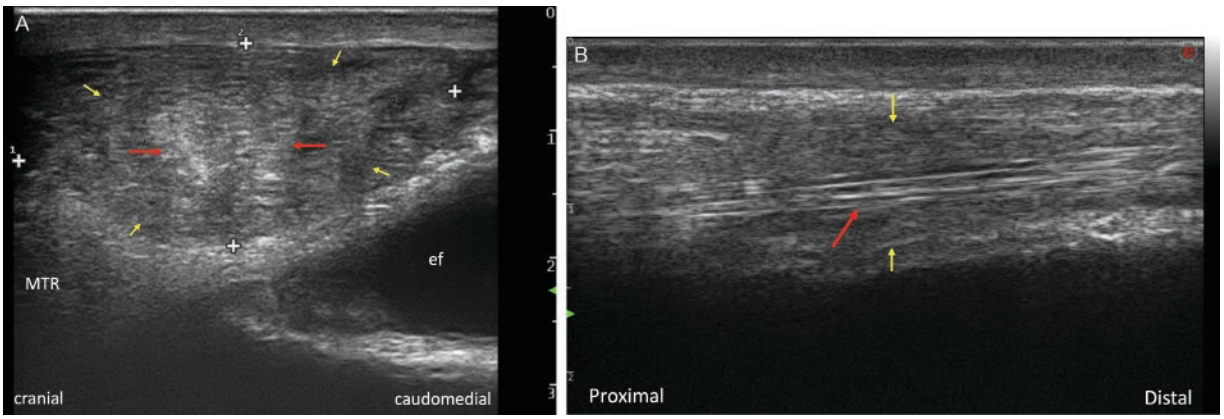


Figure 7.33 Transverse (A) and longitudinal (B) ultrasonographic image of the medial patellar ligament obtained medial to the media trochlear ridge (MTR): the ligament (calipers) is severely enlarged and diffusely hypoechogenic (yellow arrows). Marked joint effusion is visible caudal to the ligament (ef). Intact fibers remain in the center (red arrows). These appear echogenic on the transverse image and with a regular striation on the longitudinal image, while the rest of the parenchyma is devoid of aligned fibers.

prominent in more chronic cases. Sagittal fracture of the medial aspect of the patella is a common occurrence with trauma and has been associated with concurrent lateral collateral ligament injury, and a comprehensive evaluation of the whole stifle should therefore be carried out.

Apical osteochondral patellar fragmentation has been referred to as *chondromalacia patellae*, although the condition differs significantly from that described in humans. Medial PL desmotomy has been showed to be a major cause of fragmentation. The author has observed fragmentation in a group of French trotters (Standardbreds) a few months after MPL desmotomy, whereas this condition is extremely rare as a spontaneous occurrence in this breed. Typically the apex of the patella is truncated and shortened, immediately distal to the origin of the middle patellar ligament and multiple fragments are visible within a moderately echogenic tissue which extends to the joint surface (Figure 7.39). Effusion and chronic synovitis are generally prominent. The origin of the middle PL may be enlarged, hypoechogenic with loss of fiber alignment, and there may be mineralized foci within the ligament, although the significance of this is unclear.

Vet-ebooks.com

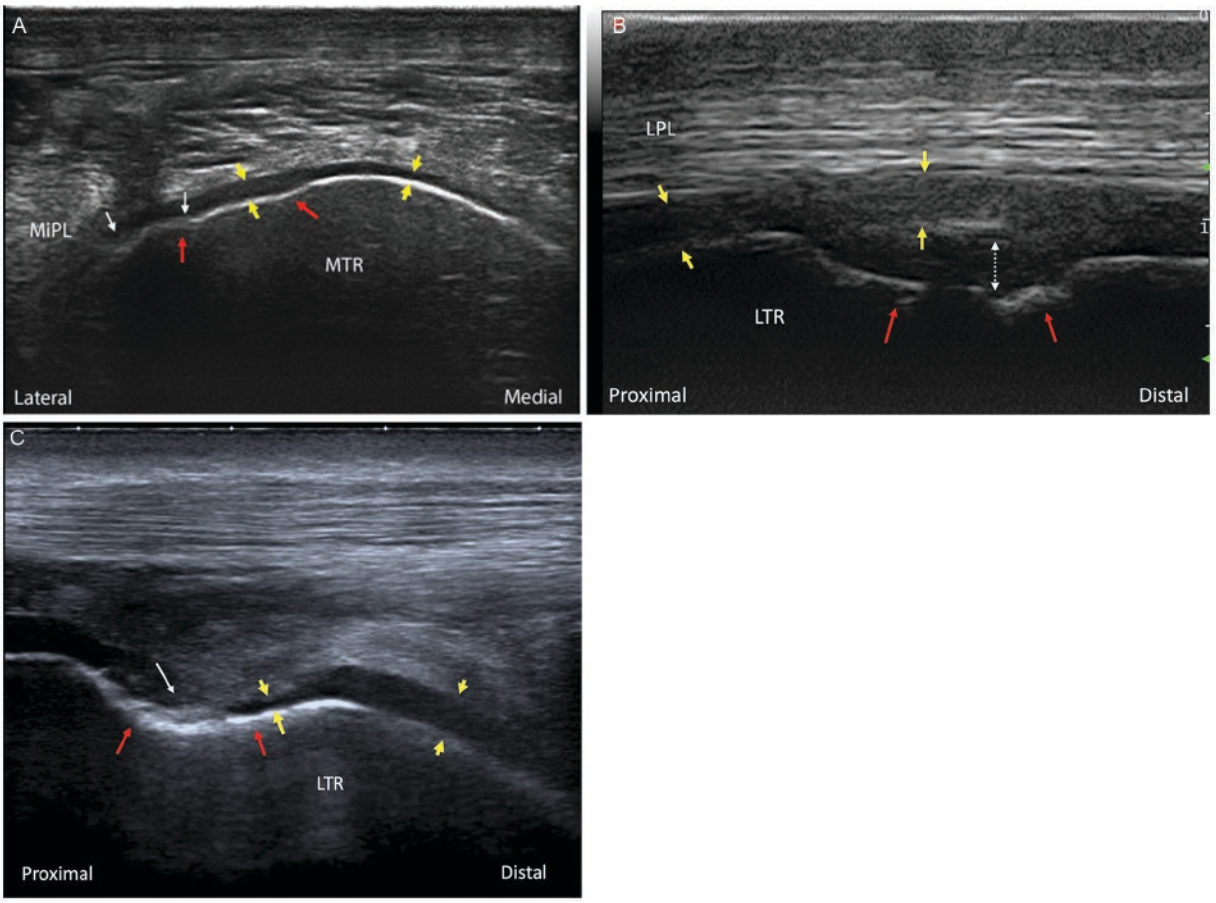


Figure 7.34 (A) Transverse ultrasonographic image of the medial trochlear ridge (MTR): the subchondral bone outline is flattened and slightly irregular (red arrows). The overlying cartilage is abnormally thick and echogenic within the lesion compared with the cartilage overlying normal subchondral bone (yellow arrows). This is pathognomonic of osteochondrosis. There is no major cartilage dissection in this lesion, although the cartilage is thinning with a thin hyperechogenic line between the cartilage and subchondral bone axially, deep to the middle patellar ligament (MiPL). This may represent early dissection (white arrows). (B) Longitudinal image over the lateral trochlear ridge (LTR). There is a discrete defect within the subchondral bone (red arrows) underneath the lateral patellar ligament (LPL). The hyaline cartilage (yellow arrows) is echogenic and mottled and separated from the mineralized tissue interface by a hypoechogenic area (double white arrow) representing necrotic tissue. This is a typical OCD lesion. (C) Longitudinal image over the LTR. A focal subchondral bone defect is present. The cartilage is thinned and irregular at the lesion margins (yellow arrows) and absent in its center, where hyperechogenic fibrous tissue adheres both to the bone and hypertrophied synovial membrane (white arrow). This suggests that the cartilage flap has separated and migrated elsewhere within the joint pouch.

Hematomas and Abscesses

Hematomas and abscesses are relatively common over the cranial stifle. Abscesses (Figure 7.40) are characterized by echogenic, grainy, and heterogeneous fluid. They contain irregular echogenic clots and are surrounded by a thick, hyperechogenic capsule. Air or gas may be present if there is an associated wound (Figure 7.40C). There is usually marked peripheral edema. Most abscesses occur either within the fat pad or in the subcutaneous tissues but hematogeneous infection may lead to muscular or bone sepsis. Large hematomas are frequently encountered in the stifle region, especially over the quadriceps muscle or on the medial aspect of the joint, directly adjacent to the synovial membrane (Figure 7.41). They present with a honeycomb pattern, characteristic of organized hematomata, although they may initially present as poorly defined hypoechogenic areas, in the acute or subacute stages. They are often very painful initially and eventually form large fluid-filled pouches that can persist (seroma). The latter form anechogenic fluid-filled sacs with an obvious capsule. Quadriceps muscle tears are occasionally encountered. They are caused either by overstrain injury,

Vet-ebooks.com

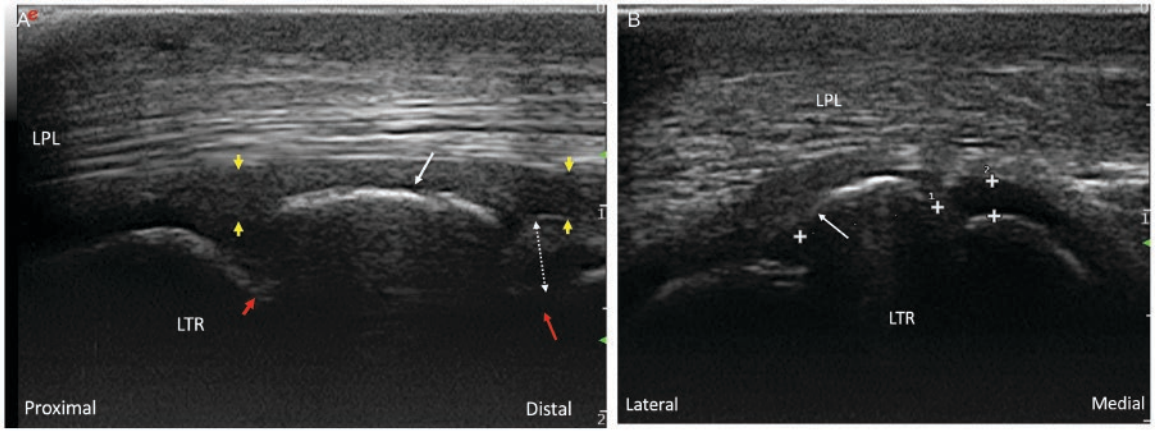


Figure 7.35 (A) Longitudinal image over the LTR at the level of the lateral patellar ligament (LPL). A smooth, hyperechogenic interface (white arrow) casting a shadow is present within a subchondral bone defect (red arrows), indicating an undisplaced, mineralized OC fragment. The defect and fragment are covered by a layer of echogenic cartilage (yellow arrows) and some non-mineralized necrotic material is visible at the periphery of the mineralized tissue (double white arrow). (B) Transverse image in the same animal. The mineralized fragment (callipers labeled 1) can be measured in all directions. Note the thickened cartilage (callipers labeled 2) and focal adhesion between the lesion and synovial membrane (arrow).

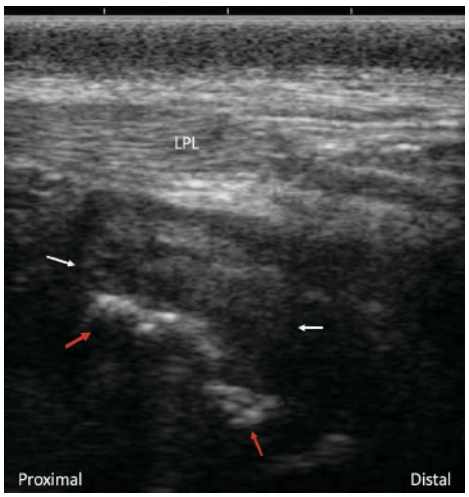


Figure 7.36 Longitudinal image obtained at the distal aspect of the LTR, directly over the distal one-third of the LPL. A very irregular, partially mineralized fragment (red arrows) is present within the hypertrophied synovial tissue (white arrows) in the distal recess of the femoropatellar joint pouch. Ultrasound in combination with radiography is useful to locate such joint "mice" prior to surgical intervention.

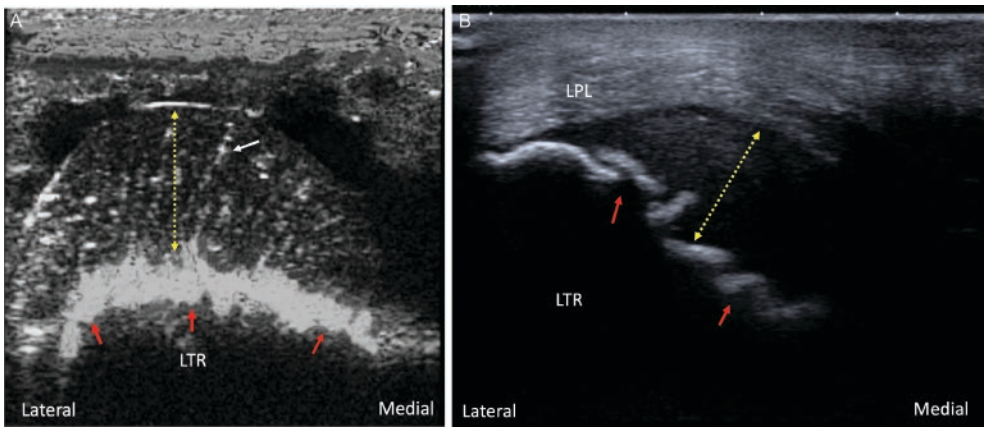


Figure 7.37 (A) Transverse image of the lateral trochlear ridge of a 1- week-old foal presented for stifle effusion (image from the Royal Veterinary College, University of London). The ridge is incompletely ossified, giving the typical ultrasonographic appearance of endochondral ossification: the mineralizing front (red arrows) is hyperechogenic but thick and very irregular. The cartilage is very thick and echogenic, with smooth contours (double yellow arrow). Note the hyperechogenic, centrifugal striations radiating from the ossifying front (white arrow). (B) Transverse image of the LTR in an 8-week-old foal. Unlike in the normal ossifying cartilage, the cartilage here is very thick (double yellow arrow) but hypoechogenic with no radiating striations. The subchondral bone is extremely irregular (red arrows). Although the cartilage in foals is thicker than in mature animals, this image represents an OC lesion.

Vet-ebooks.com

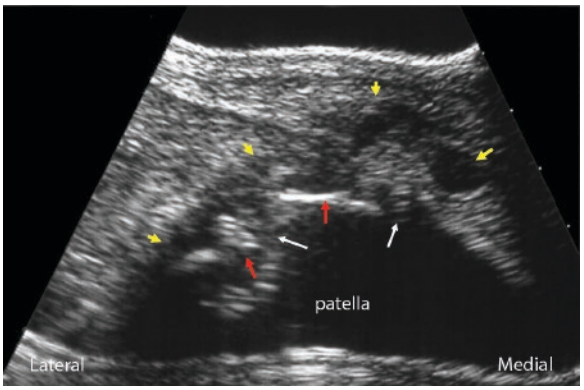


Figure 7.38 Transverse image over the cranial aspect of the patella. Several, irregular bony fragments are present (red arrows) separated by multiple hypoechogenic fracture lines (white arrows). The fracture is surrounded by hypoechogenic tissue representing hemorrhage (yellow arrows).

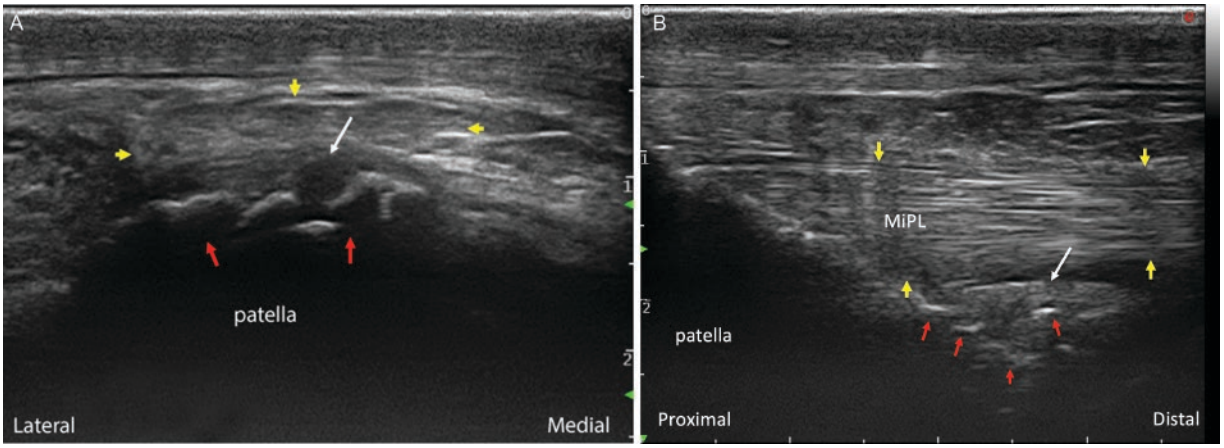


Figure 7.39 Transverse (A) and longitudinal (B) ultrasonographic images on the distal patella: multiple hyperechogenic fragments, casting acoustic shadows, are present at the distal end of the patella (red arrows), deep to the origin of the MiPL (yellow arrows). The latter is hypoechogenic and slightly enlarged. Amorphous, hypoechogenic tissue (inflammatory/fibrocartilaginous metaplasia) is visible around the fragments (white arrows).

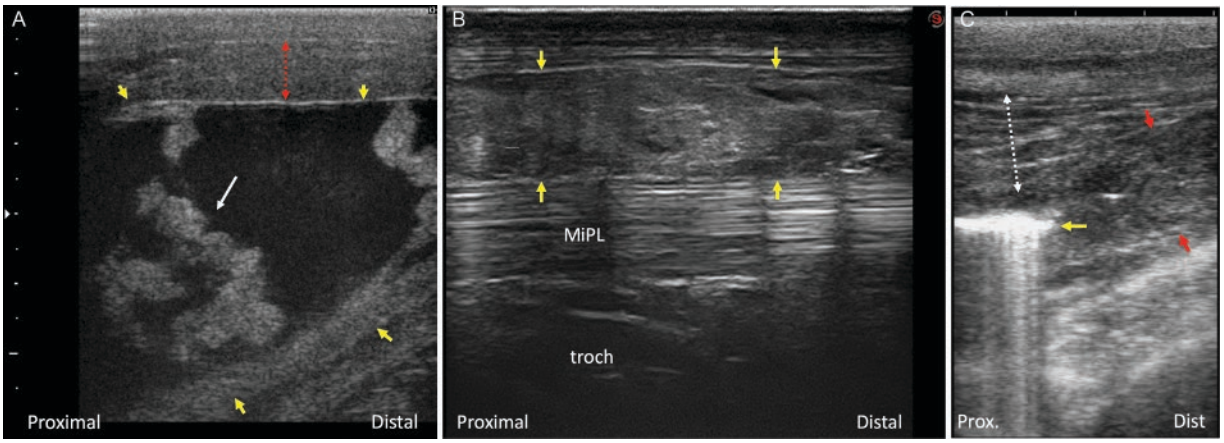


Figure 7.40 Various presentations of stifle abscesses. (A) In a typical abscess (here within the quadriceps muscle), granular ("cellular") fluid accumulates within a pouch (yellow arrows) bound by a thick, echogenic capsule (red double arrow). Strands of fibrin and debris float within the exudate (white arrow). (B) In this abscess (yellow arrows) located within the fat pad between the middle patellar ligament and superficial fascia, dense, inspissated material appears echogenic. This is due to fat necrosis and haemorrhage. Troch: trochlear ridge. (C) In the presence of an open wound or after a puncture, air or gas can accumulate proximally, forming hyperechogenic interfaces casting strong acoustic shadowing and comet tail artifacts (yellow arrow). This must not be mistaken for foreign bodies. The thick fibrinous exudate forms a poorly circumscribed cavity (red arrows) surrounded by oedematous fat or steatisis (double, white dotted arrow).

Vet-ebooks.com

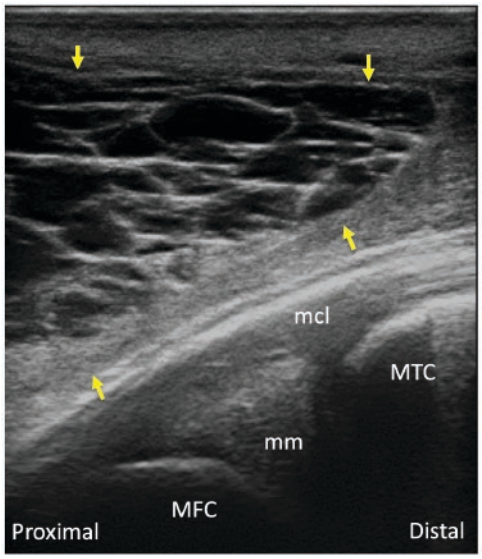


Figure 7.41 Longitudinal (frontal plane) image over the medial aspect of the stifle. A large, soft cavity is filled with anechogenic fluid separated into geometric cavities by thin, echogenic trabeculae. This is the typical appearance of an organized hematoma. Here the blood has accumulated over the stifle through gravity, flowing into the space between the muscles and fascia but the trauma occurred in the proximal thigh. The medial femorotibial joint with medial meniscus (mm), medial collateral ligament (mcl), medial femoral (MFC), and tibial (MTC) condyles have a normal appearance.

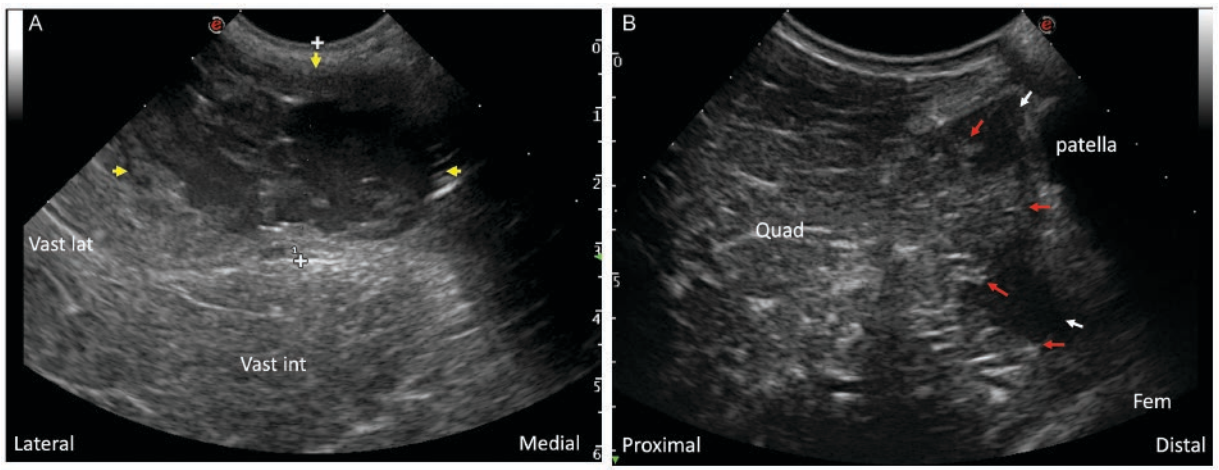


Figure 7.42 Quadriceps muscle tears are relatively common in horses. (A) Transverse plane image over the distal cranial thigh, 10 cm proximal to the patella. The rectus femoris muscle has ruptured and the muscle belly has retracted proximally, leaving an empty cavity (callipers) filled with a hematoma (yellow arrows).The underlying vastus intermedius (vast int) and lateralis (vast lat) muscles are intact (as was the vastus medialis muscle). (B) Sagittal image over the distal cranial thigh and patella. More severe, acute quadriceps (Quad) tear due to a fall over an obstacle during hurdle racing. There is diffuse, hypoechogenic fluid representing non-organized hemorrhage (white arrows) and loss of continuity between the vastus intermedius and rectus femoris muscles proximally (quad), and the patella distally. The red arrows point to the frayed muscle tissues retracted away from their patellar insertion (musculo-aponeurotic tear). Fem: femur.

especially secondary to falls, or direct trauma through kicks, hitting fixed obstacles, or being hit by a vehicle or other animal. They can give rise to diffuse swelling or hematoma formation (Figure 7.42). They can cause persistent, severe lameness because of fibrosis and muscle retraction and should be ruled out in the presence of a cranial thigh or stifle hematoma.

Femorotibial Joints

Ultrasonography is particularly valuable in the assessment of the lateral and medial femorotibial joints (LFT and MFT, respectively). Radiography is often disappointing because most injuries affect the soft tissues and because the large dimensions and complexity of the bone structures cause superimposition, which can mask potential changes.

Fluid effusion, visible as large, fluid-filled (anechogenic) pockets bulging proximal to the menisci, and both cranial and caudal to the collateral ligaments, is a very common, fortuitous finding. Even marked distension may be encountered in clinically normal horses (see Figure 7.11C). It is therefore important to look for signs of synovial inflammation, such as

Vet-ebooks.com

synovial thickening and villous hypertrophy (for principles, see Chapter 2) or concurrent pathology and interpret the sonograms in the light of clinical findings.

Collateral Ligament (CL) Desmitis and Tears

CL lesions are rare in the author's experience and are most commonly combined with injury to other stifle structures (meniscal tears, bone fractures, cruciate ligament damage, avulsion of the femoral origin of the long digital extensor muscle). They can therefore be associated with severe joint instability and should not be overlooked, particularly in severe trauma cases.

Partial CL tears may be due to falls or a spontaneous strain injury. They often evolve chronically after the initial injury, causing moderate to severe chronic lameness. Most partial CL tears present with concurrent meniscal injury, supposedly because of the associated instability. Both lateral and medial CLs may be involved; however, the medial CL appears to be more commonly affected. Milder cases present with swelling around the ligament, thus forming a hypoechogenic halo, without obvious structural changes within the ligament. Most stifle CL tears, however, are associated with marked fiber disruption (Figure 7.43A). CL tears occasionally present as well-defined, hypoechogenic "core" lesions within the ligament, representing fiber tearing and hemorrhage (Figure 7.43B). In most cases, however, the affected ligament is enlarged with a diffuse, heterogeneous decrease in echogenicity and loss of fiber pattern in long-axis planes (Figure 7.43C). There is often marked periligamentous thickening. Most commonly, both superficial and deep branches are involved, although occasionally only one of them is affected (Figure 7.43D).

In complete rupture, the affected CL is interrupted, with frayed tissue remaining at the insertion sites (Figure 7.44). The ligament is usually replaced by a heterogeneous, hypoechogenic tissue or an organized hematoma. In chronic cases, organized fibrous tissue replaces the ligament and some partial fiber realignment may become evident after several months (Figure 7.45). Marked entheseous new bone is often visible at the insertion sites on the femoral epicondyle and/or the tibial enthesis and these may develop early on (Figures 7.43C and 7.46). There may also be mineralization or fibrosis within and around the ligament.

The prognosis with stifle CL injuries is generally poor because of the associated instability, involvement of other structures, and secondary degenerative joint disease.

Meniscal Injuries

Meniscal tears have been increasingly recognized since the advent of arthroscopy and ultrasonography. The first technique reveals fraying and linear tears at the cranial horn of the menisci and their tibial attachment (cranial meniscotibial ligaments: CMTL). However, only a very small portion of the cranial portion of the meniscus is visible through standard cranial portals. A caudal arthroscopic approach will improve visualization of lesions in the caudal horn. MRI has become the technique of choice to evaluate the menisci in humans and dogs but there are currently few descriptions of MR findings for the equine stifle. Ultrasonography is currently the technique of choice to examine the entire meniscus. Some experience will help to improve ultrasonographic approaches to the cranial and caudal horns, which can be challenging at first. Care must also be taken not to over-interpret the numerous artifacts that occur within the menisci. Recent reviews suggest that meniscal injuries are a common cause of stifle lameness and probably the most common femorotibial abnormality encountered. The cause is unclear and is most likely due to progressive degeneration associated with repeated trauma and shearing rather than a single traumatic event.

The configuration of meniscal tears is subject to some debate at the present time. Cranial meniscotibial ligament (CMTL) tears have been well documented, based on arthroscopic findings. These are longitudinal tears along the long axis of the CMTL that usually extend some distance into the meniscal parenchyma. They have been classified by J. Walmsley into 3 grades (Figure 7.47A): grade I tears extend for a short distance into the cranial horn without separation of the tissues; grade II tears extend to the axial edge of the cranial horn of the meniscus, creating an axial fragment attached to the frayed ligament; grade III tears are defined as CMTL tears extending caudally into the meniscus beyond the limits of the arthroscopic field of view. Since CMTL tears are the only ones objectively visualized at surgery, other types of tears have not been clearly described and it is often considered that they are all grade III tears. A major bias is that unlike in humans or dogs, it is impossible to observe the body and most of the caudal horn at surgery.

Conversely, tears of the body and caudal horn are more frequently described with ultrasound, but no postmortem study confirming their configuration is available in horses at the present time and there is clear lack of pathological data available. In other species, six types of tears are described (Figure 7.47B), although many are complex (multiple components), especially when degenerative. Most tears in humans or dogs are "longitudinal" and occur in a more or less parasagittal plane, separating the meniscus into an axial sliver and larger abaxial fragment. The latter

Vet-ebooks.com

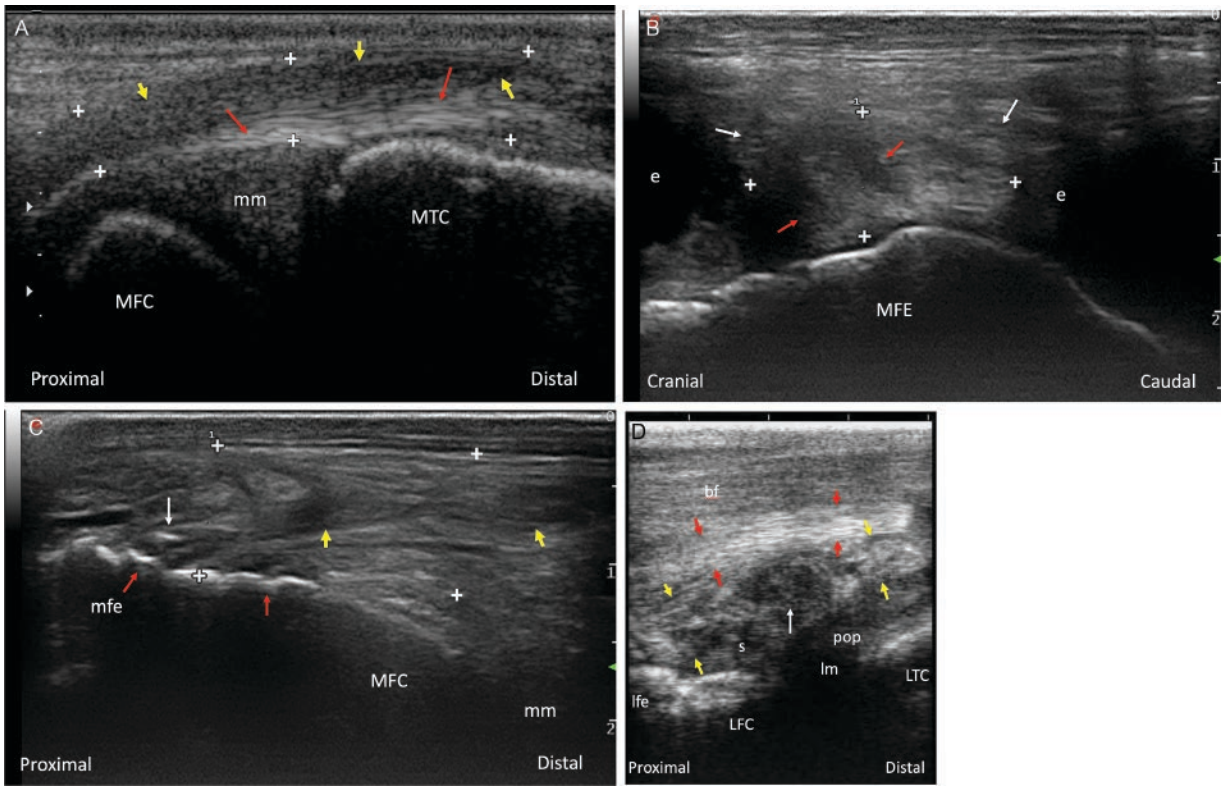


Figure 7.43 (A) Longitudinal (frontal plane) image over the medial aspect of the femorotibial joint. The medial collateral ligament is enlarged (white callipers). Most of the ligament has lost its normal striated pattern and appears diffusely hypoechogenic (yellow arrows), although there remain some intact fibers in the deep branch (red arrows). The medial meniscus (mm) is hypoechogenic and slightly displaced away from the medial femoral (MFC) and tibial (FTC) condylar surfaces, suggesting a possible concomitant meniscal injury. (B) Transverse image over the medial femorotibial joint, immediately proximal to the meniscus. The medial collateral ligament (white callipers) is very enlarged and heterogeneous with an irregular, hypoechogenic core lesion (red arrows). There is thickening and decreased echogenicity of the capsule (white arrows) and marked joint effusion cranial and caudal to the ligament (e). These are signs of an acute injury. MFE: medial femoral epicondyle. (C) Longitudinal (frontal plane) image over the medial femorotibial joint. The medial collateral ligament is enlarged (white callipers) and severely disrupted at its origin on the medial femoral epicondyle (mfe), with a diffuse hypoechogenic area representing fluid and haemorrhage (yellow arrow). The ligament is devoid of any linear arrangement. Although this is a recent injury, there is already some entheous new bone formation (red arrows) and a sharp, hyper-reverberating interface (white arrow), suggesting either an avulsed fragment of bone or early soft tissue mineralization. (D) Longitudinal (frontal plane) image over the lateral femorotibial joint. Complete rupture of the deep branch of the lateral collateral ligament leaves a hypoechogenic space filled with amorphous echogenic debris (white arrow). There is marked soft tissue fraying around the lesion (yellow arrows). The superficial branch is intact with a regular linear arrangement (red arrows), although it appears heterogeneous. Marked synovial hypertrophy is present (s). The lateral meniscus (lm) and popliteal tendon (pop) appear anechogenic because of an off-incidence artifact. Bf: biceps femoris muscle and aponeurosis; lfe: lateral femoral epicondyle.

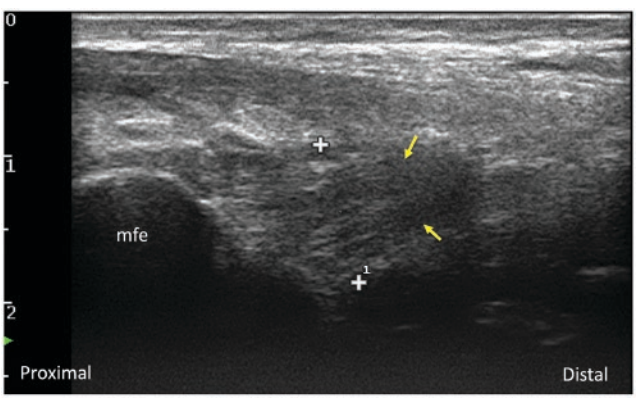


Figure 7.44 Longitudinal image over the medial femoral epicondyle (mfe). The medial collateral ligament is completely ruptured close to its femoral origin. The remaining stump (white callipers) is enlarged and hypoechogenic with loss of definition of the frayed end (yellow arrows).

Vet-ebooks.com

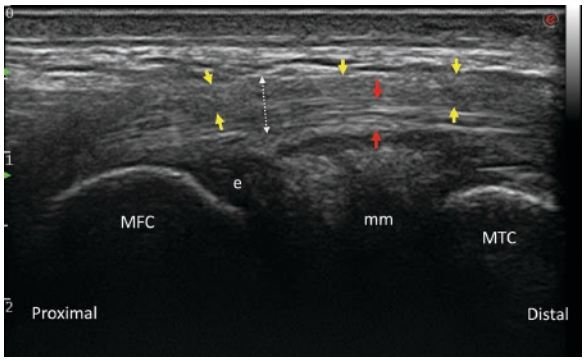


Figure 7.45 Chronic medial collateral ligament injury. The ligament is enlarged (double white arrow). There is diffuse loss of linear arrangement of most of the ligament (yellow arrows) replaced by granular echogenic tissue. Little periligamentous inflammation is visible. Irregular striation is still visible in the deep part of the ligament (red arrows). The medial meniscus (mm) is heterogeneous and is abnormally demarcated from the ligament by a hypoechogenic area representing previous capsular tearing. Some joint effusion (e) remains.

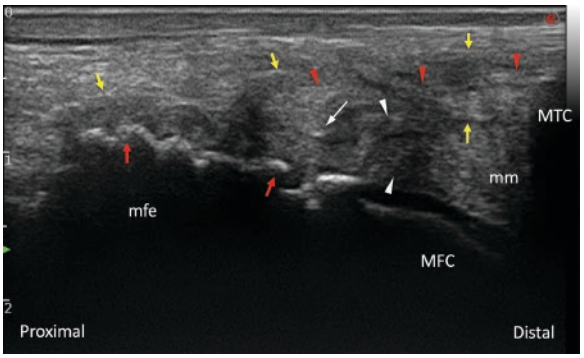


Figure 7.46 Severe medial collateral ligament injury with an acute on chronic evolution. The ligament is ill-defined, devoid of a normal striation, and very heterogeneous, with an amorphous, "cotton-like" echogenic appearance (red arrow-heads) and marked entheous new bone formation (red arrows). A focus of intraligamentous mineralization is visible (thin, white arrow). Although these are indicative of a chronic lesion, hypoechogenic periligamentous thickening (yellow arrows) suggests an active "subacute" episode. Note severe fraying (white arrowheads) of the capsular attachment to the medial meniscus (mm).

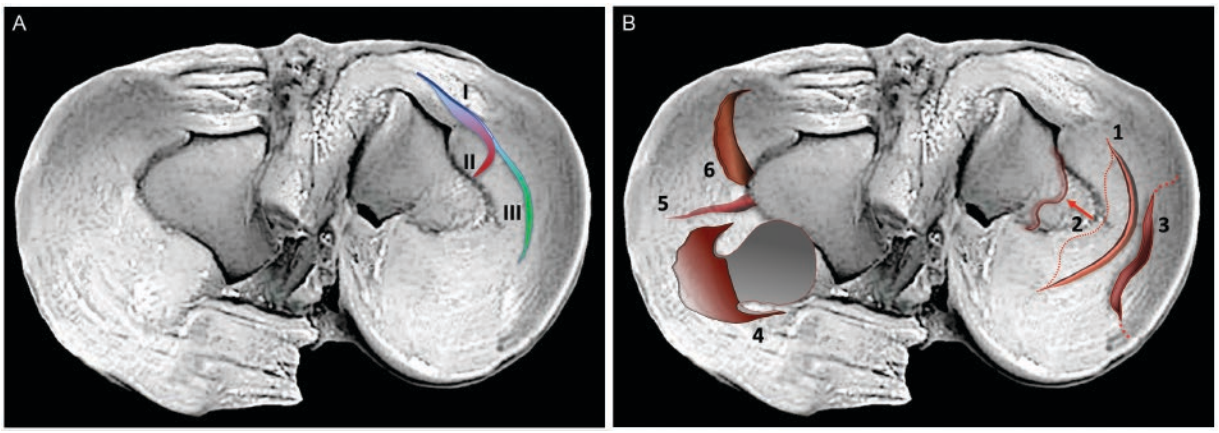


Figure 7.47 (A) Schematic drawing of the menisci illustrating the grading system proposed by J. Walmsley for cranial meniscal and meniscotibial ligament tears. Grade I (blue line) are partial or complete longitudinal (vertical) tears through the ligament, extending into the cranial horn but not exiting and without separation of the two sides of the tear. Grade II tears (red) are open tears, usually exiting through the axial border of the cranial horn, thus delimiting an unstable axial fragment attached to the axial part of the ligament. Grade III tears (green) extend caudally under the femoral condyle and their extent cannot be determined through a standard cranial arthroscopic portal. They may be complete or partial and sometimes extend as far as the caudal horn. They can exit through the proximal (femoral), distal (tibial), axial, or abaxial borders of the meniscus and tend to have a poorer prognosis. (B) Using the same drawing, the six types of meniscal tears described in humans and in dogs are: i) longitudinal tears with vertical or oblique clefts following the collagen fibers from cranial to caudal. These can eventually exit at one extremity to form a free axial flap of meniscus (combined type 1 and 6 tear); ii) repeated shearing of a grade 1 tear can lead to the axial segment of meniscus becoming displaced axially toward the tibial eminence, leaving a large defect in the center of the meniscus. The femoral condyle passes through the defect and comes into direct contact with the tibial surface. This is referred to as "bucket-handle" tear; iii) horizontal tears are parallel with the tibial joint surface and usually exit through the femoral (proximo-axial) surface of the meniscus, less commonly through the tibial (distal) surface; iv) type 3 tears can create flaps of tissue that eventually slough off the meniscus or can fold back cranially or abaxially (type 4 tear). These typically cause a "locking" syndrome in humans as in dogs; v) radial or transverse tears seem to be rare in horses but have been encountered. They run across the short axis of the meniscus and partially separate a cranial and caudal fragments. If the defect is large enough, the condyles come into contact and the fragments move abaxially and away from each other; and vi) type II or III CMTL tears but also radial or longitudinal tears can curve and exit at the axial border of the meniscus, forming a "parrot-beak"-shaped axial fragment.

Vet-ebooks.com

may become displaced abaxially, forming a "bucket-handle shaped tear." "Radial tears" correspond to frontal plane lesions, thus partially separating the meniscus into cranial and caudal fragments. Usually the abaxial part of the meniscus remains intact. Oblique radial tears are named "parrot-beak tears." Finally, "horizontal tears" create a flap of tissue on the proximal (femoral) surface of the meniscus and can lead to fraying or axial displacement of the free flap. McIlwraith et al. (2015) have suggested that longitudinal tears are probably type 3 CMTL tears and that radial and horizontal tears occur less commonly [4]. Some experimental data suggest that the cranial horn of the medial meniscus is subjected to greater tensile forces than the rest of the meniscus or the lateral meniscus [5].

The ultrasonographic appearance of most meniscal tears in equids suggests that they would likely correspond to either horizontal tears or longitudinal tears as described in humans, although radial tears probably also occur occasionally. It is the author's subjective impression that CMTL tears and more caudal tears may often be two separate conditions, as most mid-body tears identified with ultrasound rarely extend toward the cranial horn and are often not identified arthroscopically. A recent study based on MRI would suggest the latter may be degenerative lesions [6]. McIlwraith et al. (2015) have also observed caudal horn and bucket-handle-shaped tears [4]. The medial meniscus is most commonly affected, although the lateral meniscus and, occasionally both menisci, may also be affected. The prognosis associated with most body and caudal horn injuries is generally poor as surgical access for debridement or repair is often difficult or impossible. The prognosis is therefore considered to be good for type I CMTL tears, moderate for type II CMTL tears, and poor for grade III CMTL tears and more caudal lesions. Identifying the type of tear, with the exception of types I and II CMTL lesions, may therefore not significantly alter the prognosis at present, the extent and location of the lesion being more important. Ultrasound will also help to detect concurrent lesions, in particular of the collateral ligaments, cartilage, or cruciate ligaments.

Meniscal lesions in horses are variable in ultrasonographic appearance (Figure 7.48). Actual tears appear as thick, hypoechogenic tracts or lines running through the thickness of the meniscus. Partial thickness lesions appear as hypoechogenic areas (Figure 7.48A). Tears often run horizontally or obliquely across the thickness of the meniscus (i.e., perpendicular to the skin surface). These lesions should not be mistaken for the common anechogenic artifacts described previously, that form thin, regular anechogenic lines in the same direction. Real tears are often irregular and remain in the same position within the meniscal parenchyma when the probe is slightly tilted. Longitudinal tears may run in a vertical plane but are most commonly very oblique with both vertical and horizontal components (Figures 7.48B and 7.28C). Caudal horn tears can form an axial fragment which can fold back cranially or axially (Figure 7.48D). A large hypoechogenic area may develop within the thickness of the meniscus, with the abaxial fragment moving out of the joint space (Figure 7.48D). These probably correspond to bucket-handle or parrot-beak tears. Tears should be imaged over the entire circumference of the meniscus to ascertain their configuration and extent.

CMTL tears are visible ultrasonographically, using a flexed, cranial approach, as described above (Figures 7.16 and 7.20). These tears can be diffusely hypoechogenic (Figure 7.49A) or form irregular, hypoechogenic areas within the striated ligament (Figure 7.49B). There may be irregular new bone formation at the ligament insertion on the tibia (enthesophytes). Synovial proliferation and fraying of the ligament may be prominent, forming echogenic strands extending into the distended joint pouch(es). The tears may be followed up into the cranial horn of the meniscus (grades II and III tears). Avulsion of the CMTL from the tibial eminence is occasionally observed, especially on the lateral meniscus (Figure 7.49C).

Hypoechogenic areas or focal mottling within the meniscus likely represent degeneration secondary to degenerative joint disease, aging, and/or cyclic trauma. The meniscus may be distorted in shape and outline, protruding outward of the joint space (Figure 7.50A). Normal menisci are bound by the capsule and should not extend more than 1 or 2 mm beyond a line drawn between the edges of the tibial and femoral condyles. The capsule often appears to be torn off the medial meniscus with frayed echogenic structures floating in the distended joint pouch. Obvious collapse of the meniscus and joint space occur in most severe cases and direct contact between the joints surfaces of tibial and femoral condyles may be visualized (Figure 7.50B). In such cases, the meniscus may become markedly hypoechogenic and appear like chewed gum extruded along the abaxial edge of the joint.

Mineralization of a meniscal fragment is uncommon but can be extensive (Figure 7.50C). Occasionally, cyst-like anechogenic structures develop within a damaged meniscus, resembling meniscal cysts described in humans (Figure 7.50D). These have been described in horses [7] and appear to always be associated with meniscal tear. They are space occupying

Vet-ebooks.com

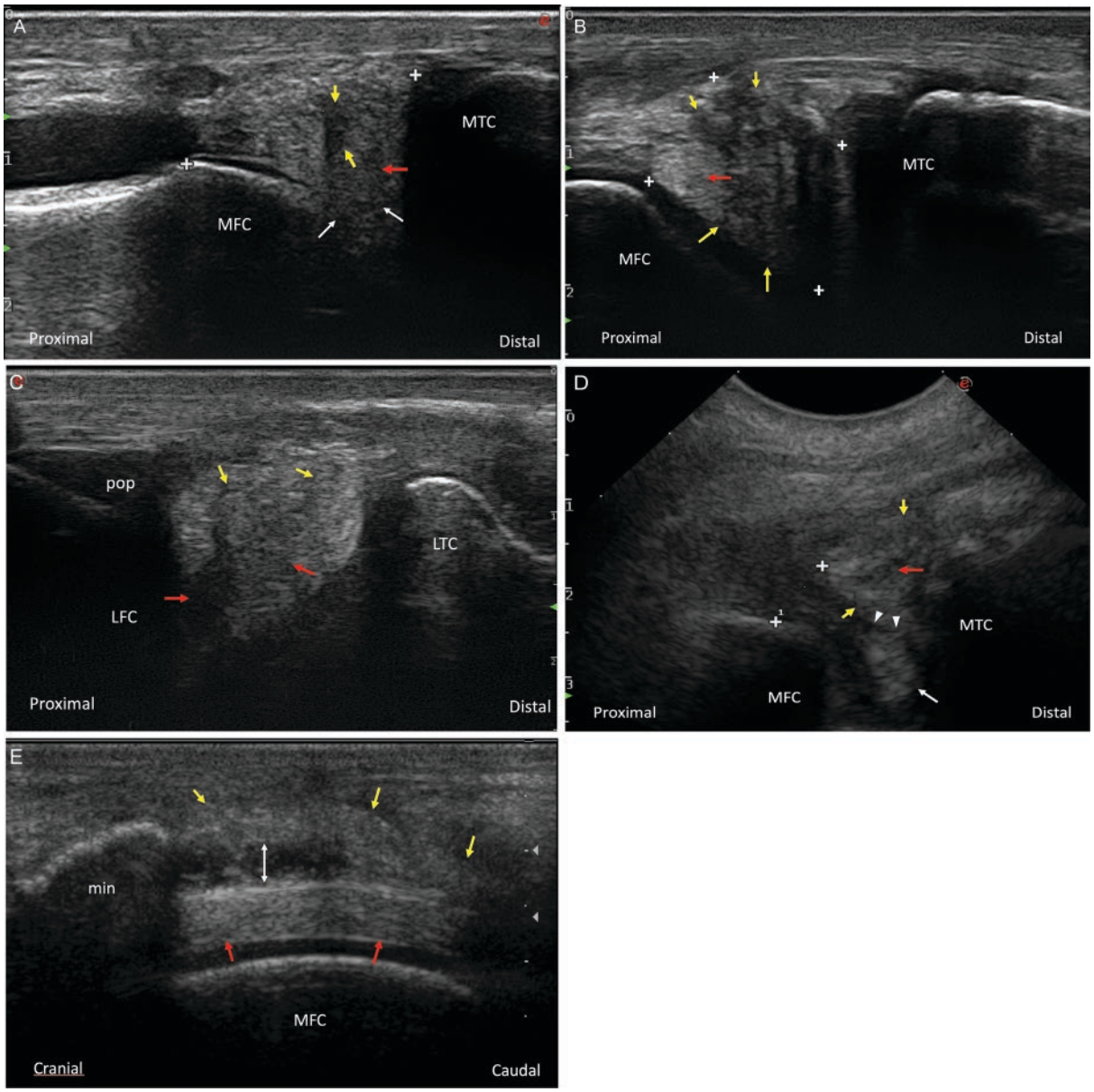


Figure 7.48 (A) Longitudinal image over the medial aspect of the stifle. The medial meniscus is slightly swollen, bulging abaxially (beyond a dotted line between callipers). A discrete hypoechogenic tear is present in the center of the meniscal body (yellow arrows). The rest of the meniscus is hypoechogenic (red arrow) with thin reticulated lines (white arrows) probably representing fissures. (B) More severe tear extending from the abaxial border to the femoral surface in a horizontal plane (yellow arrows). The meniscus is severely swollen (callipers) and unstable as evidenced by the increased space between it and the tibial condyle (MTC). A flap of intact tissue is present on the femoro-abaxial surface (red arrow). (C) Diffuse longitudinal tear starting from the femoral surface of the meniscus (red arrows) with hypoechogenic tracts extending horizontally and obliquely to the abaxial surface (yellow arrows). These mixed components are common in chronic cases, probably because of tissue degeneration. LFC : lateral femoral condyle; LTC: lateral tibial condyle; pop: popliteal tendon. (D) Caudal horn tear (medial meniscus) (white arrow-heads). The abaxial portion of the meniscus (yellow arrows) is heterogeneous with abnormally hypoechogenic tissue (red arrow), and it is deformed and displaced caudomedially away from the joint space (callipers). A flap of frayed tissue has folded cranially into the joint space (white arrow). Though common in humans or dogs, this presentation is unusual in horses. This can be addressed arthroscopically through a caudal approach. (E) Transverse plane image of the medial meniscus obtained with a horizontal beam (parallel with the tibial articular surface). A large, hypoechogenic tear (double white arrow) has formed between the medially displaced abaxial fragment (yellow arrows) still attached to the capsule, and the axial fragment (red arrows) sitting on the cartilage of the medial femoral condyle (MFC). This configuration is typical of bucket-handle vertical tears. The torn cranial horn has formed a large mineralized body (min).

Vet-ebooks.com

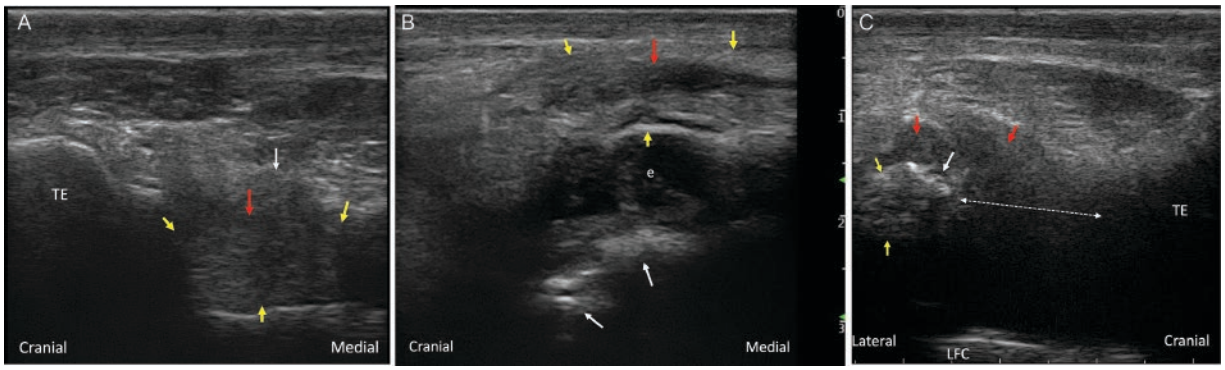


Figure 7.49 (A) Transverse (horizontal) plane image from a craniomedial approach with the stifle flexed. The cranial meniscotibial ligament (CMTL) of the medial meniscus is swollen, hypoechogenic with loss of the normal striation (yellow arrows). The abaxial border shows frayed echogenic tissue (red arrow) and there is marked synovial thickening (white arrow). This is a grade I injury. (B) Severe grade II injury. The cranial meniscotibial ligament (CMTL) (yellow arrows) is enlarged with a thick, hypoechogenic longitudinal lesion (red arrow). There is irregular new bone formation along the tibial eminence (white arrows) and severe effusion and synovial thickening (e). (C) Avulsion of the lateral cranial meniscotibial ligament (CMTL). A bony fragment (white arrow) has come off the tibial eminence (TE) along with the heterogeneous CMTL (yellow arrows), leaving a gap (double dotted arrow) filled with synovial tissue. Note the marked effusion between the ligament and lateral femoral condyle (LFC) and synovial hypertrophy (red arrows).

and can cause persistent lameness, especially when in close contact with the joint surfaces. They can, however, be found incidentally when protruding into a loose synovial pouch.

Cruciate Ligament Injuries

Damage to the cruciate ligaments (XL) is reportedly rare in horses, although partial fraying and degenerative changes may not be unusual in animals with meniscal injury or with other articular lesions (bone cysts, osteoarthritis, etc.). Complete rupture is very uncommon. In a series of ten horses with a diagnosis of XL rupture, six had concurrent fractures of the tibial eminence and all of them had associated injury to other stifle structures, especially the menisci and collateral ligaments. Comprehensive examination of the whole joint is therefore mandatory. XL injury may be difficult to confirm. Injured ligaments are enlarged, heterogeneous, and generally hypoechogenic (Figures 7.51A and 7.51B). Fraying of the ligaments is usually obvious as strands of tissue floating in the joint pouch cranially (Figure 7.51C). It is commonly accompanied by marked joint distension and thickening of the synovial membrane. Complete rupture is rare, but is evidenced by the inability to image the ligament (Figure 7.52). It is possible to observe a "cranial drawer" instability in anesthetized animals but this is virtually impossible in standings horses. The torn ends are visible at the insertion sites and often form cauliflower-like masses (Figure 7.52A). Avulsion of either insertion or fracture of the tibial eminence is commonly encountered and is evidenced as large, hyperechogenic fragments protruding into the intercondylar space (Figure 7.52B). Flexing the joint can be painful with cruciate ligament injury, so adequate analgesia and tranquilization is warranted. The prognosis is usually considered to be very poor, although this may be due more to the concurrent damage to other articular structures and associated osteoarthritis, as a severed cranial cruciate ligament alone does nor appear to cause significant joint instability (P. Clegg, personal communication).

Osseous Cyst-Like Lesions

Subchondral cyst-like lesions are usually fairly obvious on radiographs. Ultrasonography, however, is useful to determine more precisely the extent of the articular defect, to look for the presence of a communication between the cyst cavity and joint space, and to allow standing, ultrasound-guided injection of the cyst (Figure 7.53). This is achieved from a cranial distal approach with the stifle in full flexion. Associated cartilage and soft tissue damage and osteoarthritis should be evaluated.

Osteoarthritis

Joint disease is characterized by chronic synovial changes (membrane thickening, effusion, villous hypertrophy) and remodeling of the bone edges. Radiography is very insensitive to look for osteoarthritic changes in the stifle and ultrasonography will frequently reveal marked changes in radiologically normal joints (Figure 7.54). Periarticular new bone (osteophytes) causes spiked or spur-like deformity of

Vet-ebooks.com

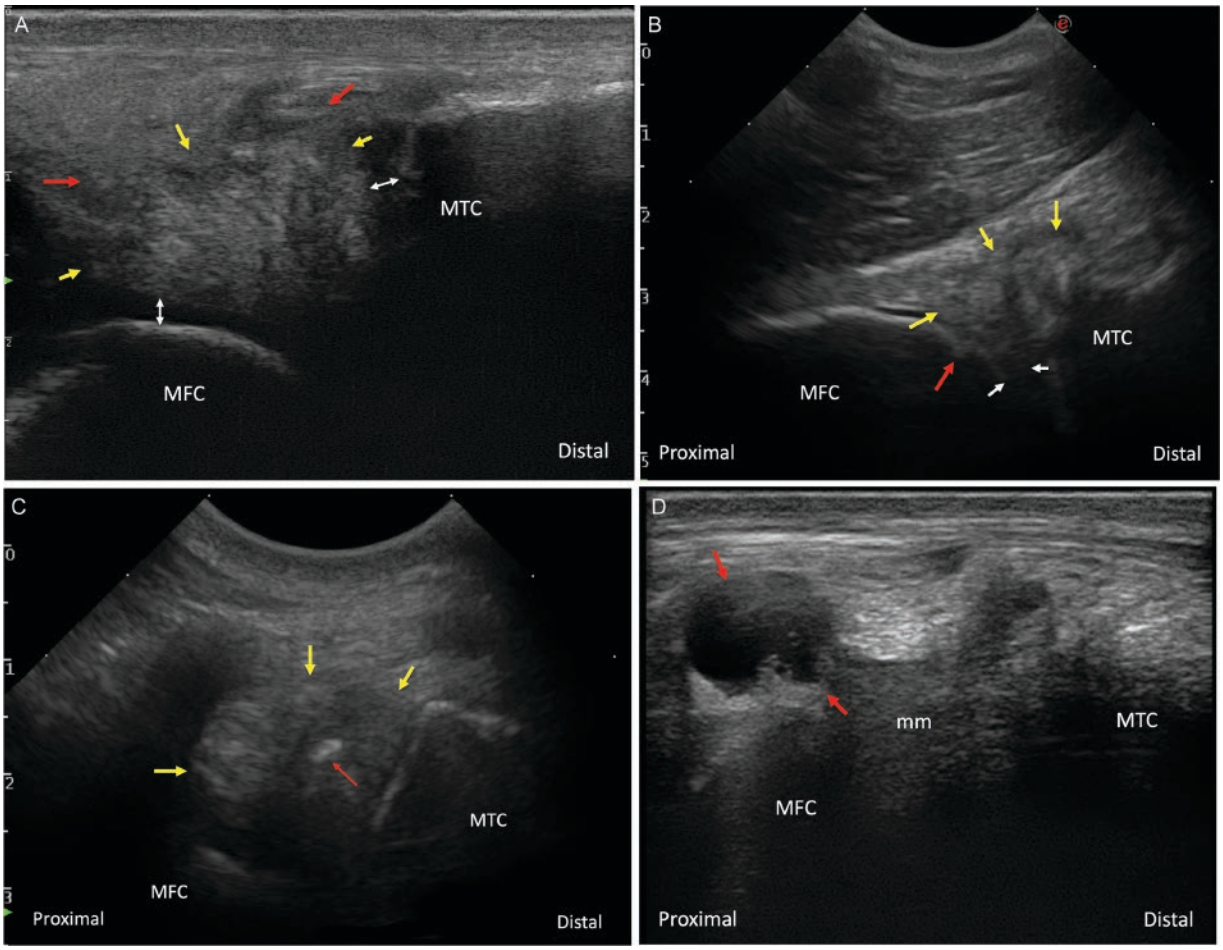


Figure 7.50 (A) Chronic degenerative changes in the medial meniscus lead to a heterogeneous, mottled appearance with marked deformity and swelling of the meniscus (yellow arrows). The meniscus protrudes abnormally out of the joint space with widening of the distance from the cartilage surfaces (double arrows). Note fraying of the capsular attachments and synovial proliferation (red arrows). MFC : medial femoral condyle; MTC: medial tibial condyle. (B) This caudal medial meniscal horn shows a horizontal tear but also marked heterogeneity of the whole parenchyma. The meniscus is deformed abaxially and displaced away from the joint space (yellow arrows). The joint surfaces are coming into contact (white arrows) and there is marked irregularity of the subchondral bone surface with thinning of the cartilage (red arrow) due to osteoarthritis. MFC: medial femoral condyle; MTC: medial tibial condyle. (C) Mineralized foci (red arrow) may occur secondary to meniscal degeneration (yellow arrows). These have been associated with a poorer prognosis. MFC: medial femoral condyle; MTC: medial tibial condyle. (D) Meniscal cysts have been described as a rare entity in horses in association with meniscal tears. They typically appear as anechogenic fluid-filled cavities bound a relatively thin membrane (red arrows) and continuous with the meniscal tissue (mm). Their origin remains unclear. MFC: medial femoral condyle; MTC: medial tibial condyle.

the abaxial borders of the femoral and tibial condyles, and enthesophytes produce irregular bone productions at the insertions of the capsule and collateral ligaments. Cartilage damage may be visible in advanced cases as irregular, echogenic areas (Figure 7.50). Osteoarthritis is most often a consequence of chronic instability, as in meniscal tears and complex ligament injuries, or osteochondrosis. However, osteoarthritis may be encountered without other primary lesions detectable, both in older animals and in sports horses, presumably as a result of overuse, cyclic trauma, and/or age-related degeneration.

Septic Arthritis

The stifle may be infected through hematogenous spread in foals, or in adult horses via puncture wounds or iatrogenically as a complication of intra-articular medication or joint surgery.

The joint fluid can remain fairly anechoic, especially in foals with hematogenous infectious arthritis. However, in most cases, debris, hemorrhage, and exudate cause the joint fluid to become echogenic and granular in appearance within hours of injury (Figure 7.55A). Severe synovial proliferation is always present and fibrin clots may form strands or

Vet-ebooks.com

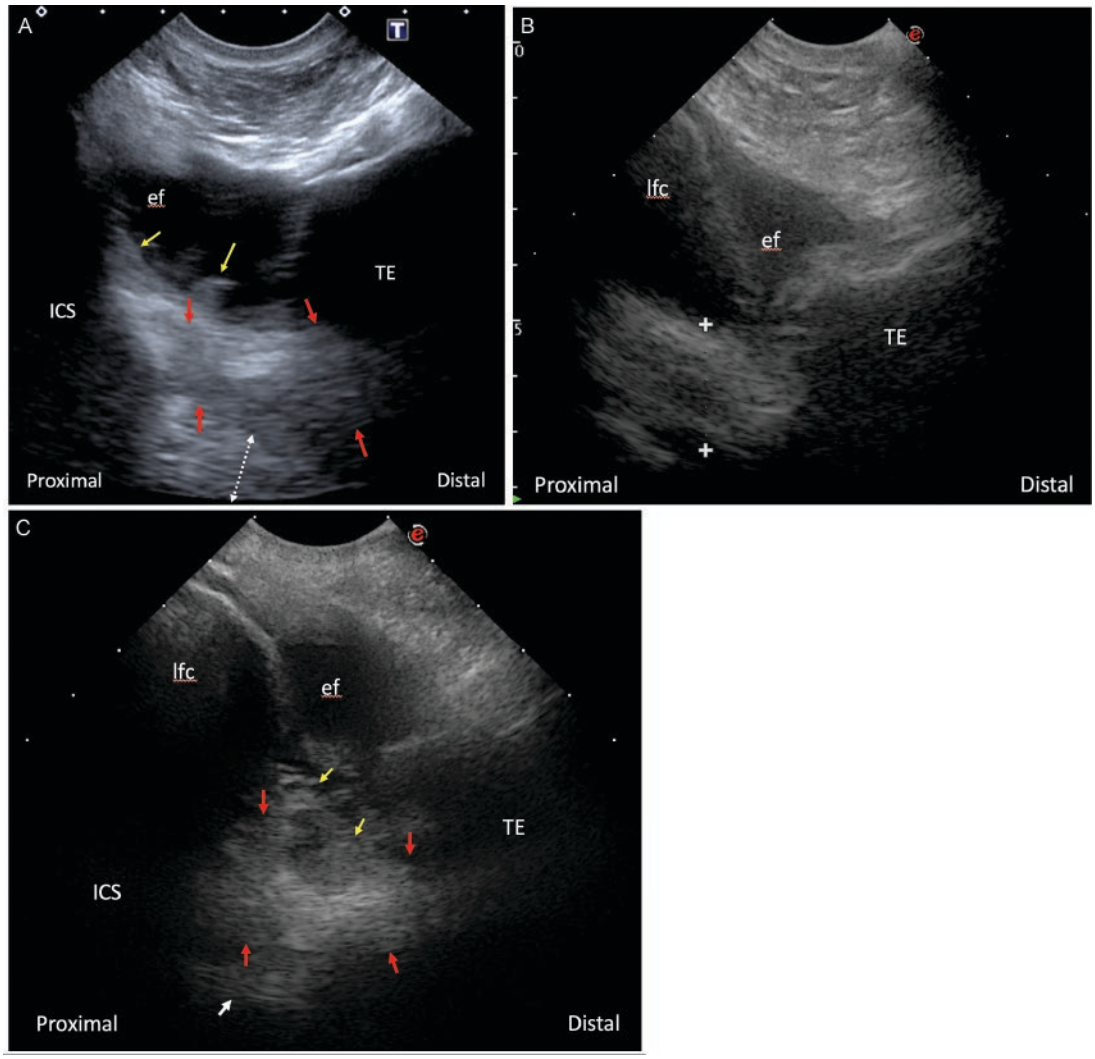


Figure 7.51 (A) Longitudinal image using a flexed, cranial approach. The cranial cruciate ligament (red arrows) is seen between the tibial eminence (TE) and intercondylar space (ICS). The linear striation is partially lost and the ligament abnormally heterogeneous and hypoechogenic. Spiky echogenic tissue representing synovial proliferation and/or parenchymal fibrillation (yellow arrows) protrude into the distended cranial pouch (ef). Note the normal caudal cruciate ligament (white double arrow). (B) Chronic cranial cruciate ligament desmopathy is characterized by thickening and heterogeneity of the ligament (callipers). Irregular new bone is present on the tibial eminence (TE). Effusion is moderate, with an echogenic appearance due to filling by thickened synovium. Note the partial volume artifact with the axial border of the lateral femoral condyle (lfc) imprinted on the image without creating an acoustic shadow (related to the slice thickness). Partial volume thickness artifact; an ultrasound section is actually a slab. It has a certain thickness. If some tissue does not occupy the entire thickness of the slab, sound can move past it and collect information distal to it even though its interface should be hyperechoic, or on the contrary not show at all on this slice. This is called a partial volume or partial volume averaging artifact. The thinner the slice, the less these artifacts occur.) (C) Similar view in a horse with a partial tear of the cranial cruciate ligament. The ligament (red arrows) is enlarged and there is a focal hypoechogenic lesion with frayed fibers (yellow arrows) floating in the distended cranial recess (ef). Note the cranial border of the intact caudal cruciate ligament (white arrow). TE: tibial eminence; ICS: intercondylar space.

Vet-ebooks.com

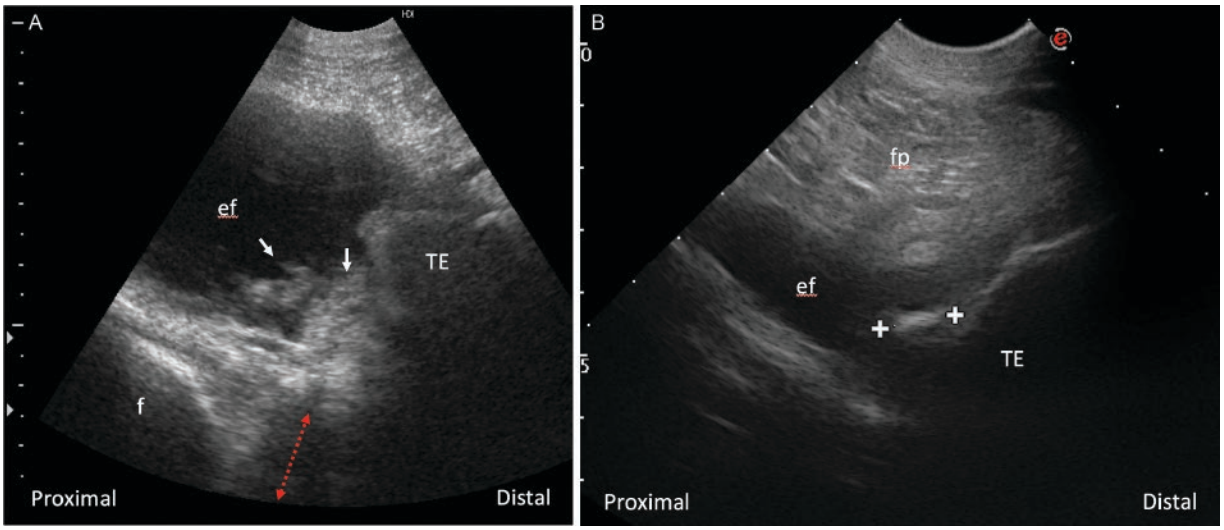


Figure 7.52 (A) Complete rupture of the cranial cruciate ligament. The caudal cruciate ligament (double red arrow) is clearly seen at its origin on the femur between the condyles (f). It is surrounded by hyperechogenic fibrous tissue. The cranial cruciate ligament is not visible within the effusion (ef) and frayed fibers form an amorphous mass at its insertion on the tibial eminence (te, white arrow). (B) Avulsion fragments are common in cruciate ligament injuries. Here a discrete fragment is seen at the tibial insertion of the cranial cruciate ligament. FP: infrapatellar fat pad; ef: effusion; TE: tibial eminence.

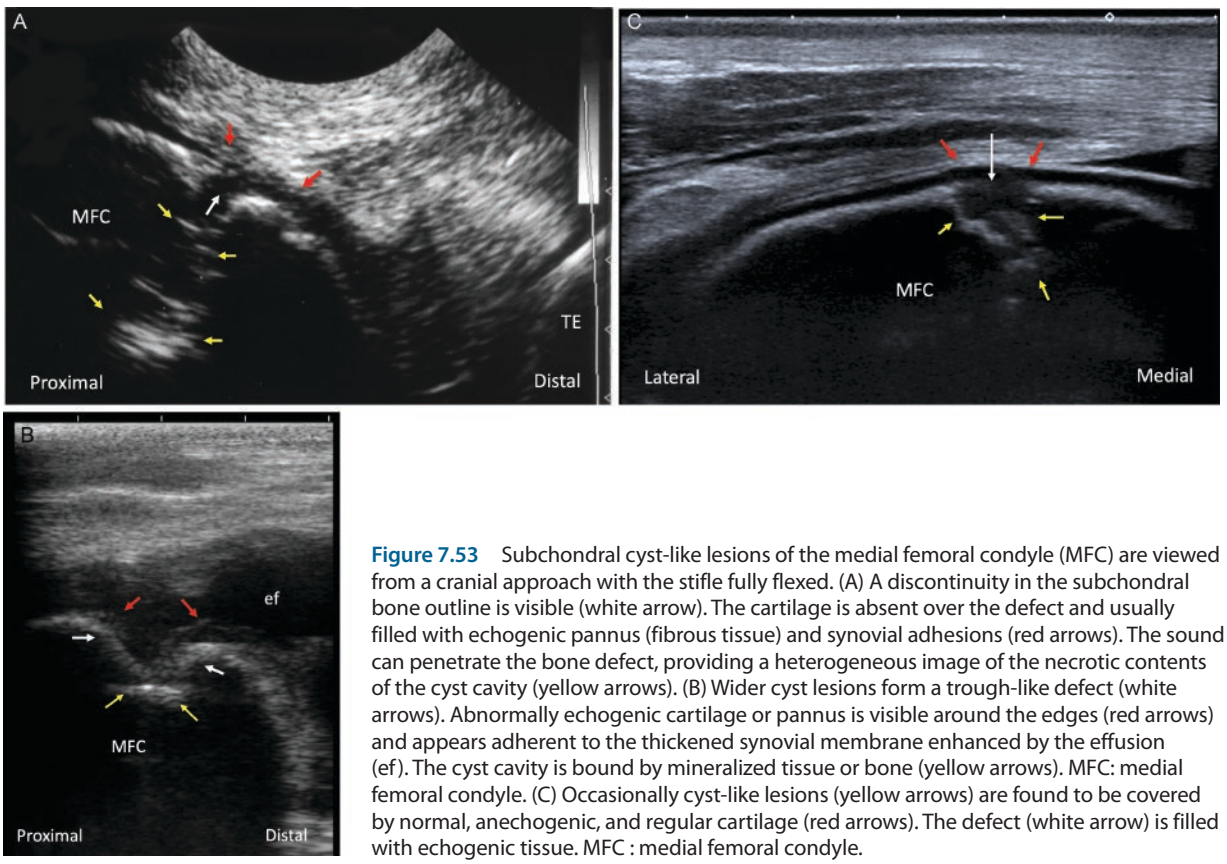


Figure 7.53 Subchondral cyst-like lesions of the medial femoral condyle (MFC) are viewed from a cranial approach with the stifle fully flexed. (A) A discontinuity in the subchondral bone outline is visible (white arrow). The cartilage is absent over the defect and usually filled with echogenic pannus (fibrous tissue) and synovial adhesions (red arrows). The sound can penetrate the bone defect, providing a heterogeneous image of the necrotic contents of the cyst cavity (yellow arrows). (B) Wider cyst lesions form a trough-like defect (white arrows). Abnormally echogenic cartilage or pannus is visible around the edges (red arrows) and appears adherent to the thickened synovial membrane enhanced by the effusion (ef). The cyst cavity is bound by mineralized tissue or bone (yellow arrows). MFC: medial femoral condyle. (C) Occasionally cyst-like lesions (yellow arrows) are found to be covered by normal, anechogenic, and regular cartilage (red arrows). The defect (white arrow) is filled with echogenic tissue. MFC : medial femoral condyle.

Vet-ebooks.com

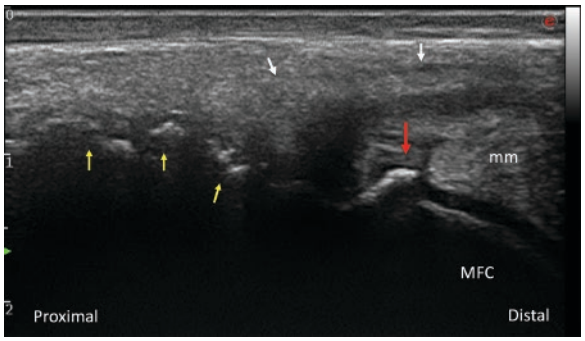


Figure 7.54 Longitudinal (frontal) plane image of the medial femorotibial joint. Periarticular new bone is visible in the form of an osteophyte at the immediate periphery of the cartilage covered joint surface of the medial femoral condyle (MFC, red arrow) and enthesophytes (yellow arrows) at the origin of the joint capsule (white arrows). The medial meniscus (mm) is in place and has a normal shape but appears heterogeneous, suggesting possible degenerative changes.

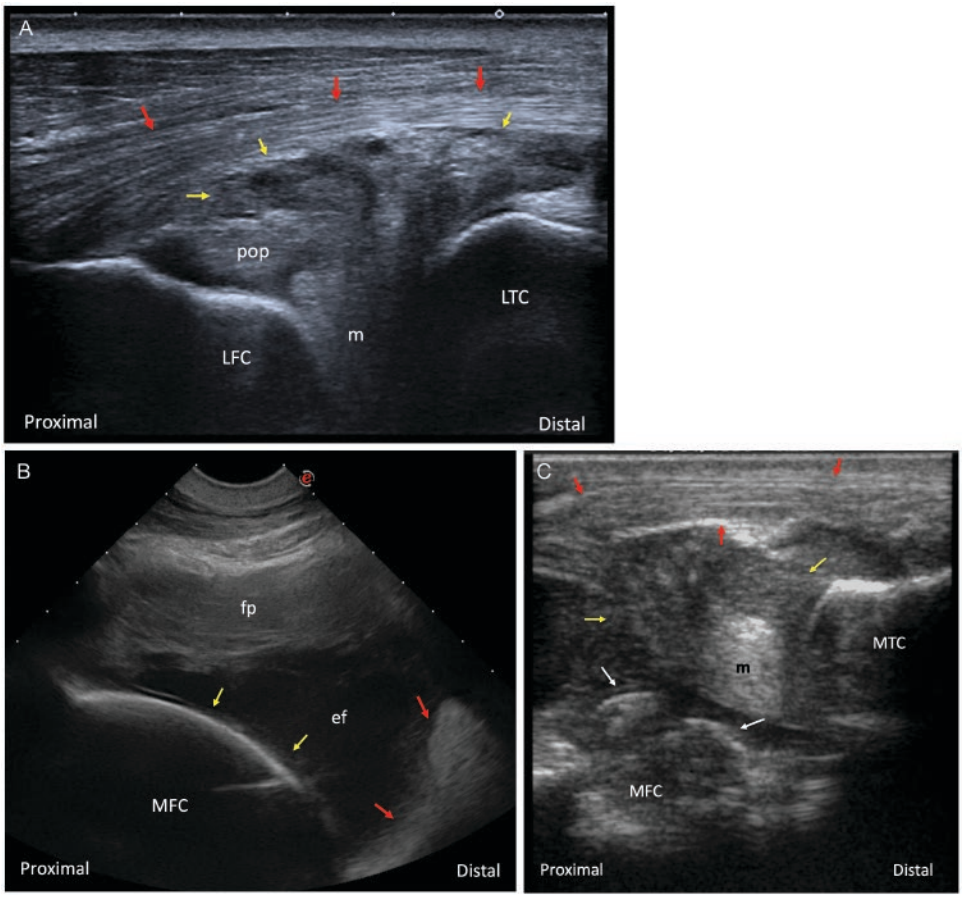


Figure 7.55 (A) Lateral aspect of the stifle in a Standardbred with iatrogenic septic arthritis. The synovial cavity is markedly distended by very echogenic (fibrinous) material, mixed with severely thickened synovium (yellow arrows) isoechogenic to the lateral meniscus (m) and popliteal tendon (pop). The lateral collateral ligament (red arrows) is displaced abaxially. LFC: lateral femoral condyle; LTC: lateral tibial condyle. (B) Cranial aspect of the flexed stifle. Infectious arthritis secondary to a penetrating wound. The joint is markedly distended by hypoechogenic, granular fluid (ef) bound by a thickened synovial membrane. Homogeneous echogenic (fibrinous) material has sedimented in the dependant part of the joint (red arrows). The cartilage covering the medial femoral condyle is thinned and irregular and replaced in areas by echogenic fibrin (yellow arrows). MFC: medial femoral condyle; fp: femoropatellar fat pad. (C) Hematogenous septic arthritis in a 3-month-old foal (medial aspect of the stifle). The medial meniscus (m) is displaced abaxially. The joint fluid is abnormally echogenic and difficult to differentiate from the hypertrophic synovial tissue (yellow arrows). The collateral ligament is thickened and displaced (red arrows). The medial femoral condyle (MFC) is fragmented into several portions (white arrows) with abnormal transmission of the sound beam through the lytic epiphyseal bone. The joint is irreversibly damaged. MTC = medial tibial condyle.

Vet-ebooks.com

whorl-like masses in the fluid (Figure 7.55B). Fibrin often clings to the joint surface to form an echogenic tissue overlying the cartilage ("pannus"). Cartilage or subchondral bone defects may develop, sometimes after a few days, over the condyles and trochlear ridges (Figure 7.55B) and bone, meniscus, or cartilage fragments may be visible in the joint recesses.

Wounds over the stifle area should be examined thoroughly to look for evidence of joint sepsis or overt communications with the joint before the joint is tapped for synovial fluid analysis, in order to avoid inserting a needle through septic material into a non-infected joint.

In normal young foals, less than 8 months old, the hyaline cartilage is very thick and the immature subchondral bone may be very irregular. The incompletely mineralized trochlear ridges have a "sunburst" appearance, due to centripetal ossification of the trochlear ridge ossification centers (Figure 7.37A). This should not be mistaken for infection. In these animals, however, the bone is very soft and prone to early defect formation or even joint surface destruction (Figure 7.55C).

Avulsion of the Tendon of Origin of the Long Digital Extensor Muscle and Peroneus Tertius Tendon

This is a rare condition which may, however, lead to significant joint swelling and should therefore be included in the differential diagnosis. The common tendon of origin of the fibularis tertius (peroneus tertius) tendon and long digital extensor muscle arises from the craniolateral aspect of the lateral femoral condyle, cranial to the epicondyle (lateral CL origin) and caudodistal to the lateral trochlear ridge. It runs in the extensor groove of the tibia where it is lined by an extention of the lateral femorotibial joint synovial pouch. Injuries to this structure therefore lead to synovitis. Furthermore, trauma may lead to concurrent injury to other structures, including the cruciate ligaments or menisci. In a series of 27 horses with signs of ruptured peroneus tertius tendon, only 2 had a lesion located at the origin of the tendon [8].

Miscellaneous

Various additional conditions may occur in the stifle region. Ultrasonography may be useful to assess unusual conditions and deformities.

Capsular rupture is a rare occurrence and may be a result of trauma or severe joint distension (probably combined with trauma). It is always described as acute in humans. The author has encountered one case in an equine stifle, although it may occur more commonly in other joints. The synovial membrane herniates through the capsular tear, forming an abnormal fluid pouch in the overlying soft tissues (Figure 7.56).

Patellar luxation may be conveniently imaged with ultrasound. The patella is found displaced laterally or medially. The trochlear groove is found to be empty and therefore abnormally visible. There is usually marked joint effusion and, in traumatic cases, there may be hemorrhage and tissue damage, in particular the torn patellar collateral ligament and joint capsule may appear as echogenic, frayed fibrous tissue at the

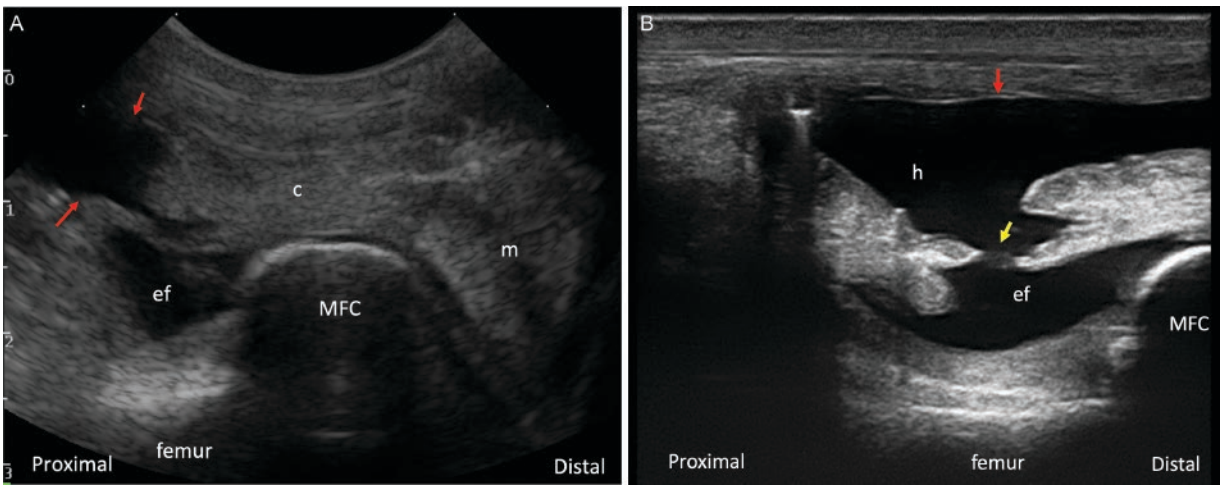


Figure 7.56 Medial aspect of the stifle in a Standardbred injured in a fall during harness racing. (A) The joint is moderately distended (ef) and an abnormal pouch (red arrows) is visible abaxial to the capsule (c) under the fascia consistent with a joint capsule rupture. The meniscus (m) is intact. MFC: medial femoral condyle. (B) Detail showing the rupture in the echogenic capsule (yellow arrow) and synovial herniation through the tear (h). ef: effusion; MFC: medial femoral condyle.

Vet-ebooks.com

torn side (opposite the luxation). The latter is important to assess for surgical planning. Ultrasound may also help to identify trochlear ridge hypoplasia in congenital cases (seen in miniature breeds), trochlear ridge fragmentation, and/or patellar fracture in traumatic cases.

Calcinosis circumscripta is a rare occurrence in horses but the lateral aspect of the stifle is a predilection site. Ultrasound is of limited use as the mineralized mass does not transmit the sound beam and only the abaxial surface will be visible. It helps, however, to rule out other mineralized masses or concurrent injury to surrounding structures.

Tumors are unusual in equine limbs but various types may be encountered. Ultrasound is particularly useful to image soft tissue masses, to assess their exact location, association with specific tissues (muscle, subcutaneous tissue, bone, synovial membrane, etc.). Color-flow Doppler ultrasound may be helpful to give an insight into aggressiveness and to help for surgical planning. Finally, ultrasound-guided fine-needle aspiration or needle-biopsy are nearly always indicated to obtain a histological diagnosis. This is paramount to guide further investigations and staging, for prognosis determination and treatment recommendations.

Recommended Reading

Adrian, A.M., Barrett, M.F., Werpy, N.M. et al. (2017). A comparison of arthroscopy to ultrasonography for identification of pathology of the equine stifle. *Equine Veterinary Journal* 49: 314–321. 10.1111/evj.12541. Epub 25 February 2016.

Aldrich, E.D., Goodrich, L.R., Contino, E.K. et al. (2019). Usefulness of caudomedial-craniolateral oblique radiographic views for the diagnosis of injury to the origin of the cranial cruciate ligament in two horses. *Journal of the American Veterinary Medical Association* 15(254): 508–511. 10.2460/javma.254.4.508.

Barrett, M.F., Frisbie, D.D., McIlwraith, C.W. et al. (2012). The arthroscopic and ultrasonographic boundaries of the equine femorotibial joints. *Equine Veterinary Journal* 44: 57–63. 10.1111/j.2042-3306.2011.00369.x. Epub 8 June 2011.

Beccati, F., Chalmers, H.J., Dante, S. et al. (2013). Diagnostic sensitivity and interobserver agreement of radiography and ultrasonography for detecting trochlear ridge osteochondrosis lesions in the equine stifle. *Veterinary Radiology & Ultrasound* 54: 176–184. 10.1111/vru.12004. Epub 26 December 2012.

Budras, K.D., Sack, W.O., and Roes, S. (2009). *Anatomy of the Horse*, 5th revised edn, 200. Hanover: Schlütersche Verlagsgesellschaft.

Busschers, E. (2009). Patellar luxation in horses: Treatment and prognosis. *Equine Veterinary Education* 21: 464–466. 10.2746/095777309X468122.

Cauvin, E.R.J., Munroe, G.A., Boyd, J.S. et al. (1996). Ultrasonographic examination of the femorotibial articulation in horses: Imaging of the cranial and caudal aspects. *Equine Veterinary Journal* 28: 285–296.

Cuevas-Ramos, G., Cova, M., Arguelles, D. et al. (2019). Anatomical variations of the equine popliteal tendon. *Journal of Veterinary Science* 20: e36. 10.4142/jvs.2019.20.e36.

Daglish, J., Frisbie, D.D., Selberg, K.T. et al. (2018). High field magnetic resonance imaging is comparable with gross anatomy for description of the normal appearance of soft tissues in the equine stifle. *Veterinary Radiology & Ultrasound* 59: 721–736. 10.1111/vru.12674. Epub 22 August 2018.

Denoix, J.-M.and and Coudry, V. (2018). Ultrasonographic examination of the quadriceps femoris muscle: Normal images and findings. *Equine Veterinary Education* 31: 478–482.

Denoix, J.M., Crevier, N., Perrot, P. et al. (1994). Ultrasound examination of the femorotibial joint in horses. *Proceedings of the American Association of Equine Practitioners*, 41: 57–58.

Dubuc, J., Girard, C., Richard, H. et al. (2018). Equine meniscal degeneration is associated with medial femorotibial osteoarthritis. *Equine Veterinary Journal* 50: 133–140. 10.1111/evj.12716. Epub 12 August 2017.

Dyson, S.J. (2002). Normal ultrasonographic anatomy and injury of the patellar ligaments in the horse. *Equine Veterinary Journal* 34: 258–264.

Ebling, A.J., Slack, J., and Reef, V.B. (2008). Imaging diagnosis: Avulsion of the origin of the popliteal tendon in a horse. *Veterinary Radiology & Ultrasound* 49: 567–569.

Edwards, R.B., IIIand Nixon, A.J. (1996). Avulsion of the cranial cruciate ligament insertion in a horse. *Equine Veterinary Journal* 28: 334–336.

Flynn, K.A. and Whitcomb, M.B. (2002). Equine meniscal injuries: A retrospective study. *Proceedings of the American Association of Equine Practitioners*, 48: 249–254.

Gibson, K.T., McIlwraith, C.W., Park, R.D. et al. (1989). Production of patellar lesions by medial patellar desmotomy in normal horses. *Veterinary Surgery* 18: 466–471.

Vet-ebooks.com

Gottlieb, R., Whitcomb, M.B., Vaughan, B. et al. (2016). Ultrasonographic appearance of normal and injured lateral patellar ligaments in the equine stifle. *Equine Veterinary Journal* 48: 299–306. 10.1111/evj.12444. Epub 29 May 2015.

Hoegaerts, M., Nicaise, M., Van Bree, H. et al. (2005). Cross-sectional anatomy and comparative ultrasonography of the equine medial femorotibial joint and its related structures. *Equine Veterinary Journal* 37: 520–529.

Judy, C. (2011). Chapter 18: The stifle. In: *Equine MRI* (ed. R.C. Murray), Chapter 18, 451–466. Chichester, UK: Wiley-Blackwell.

Koneberg, D.G. and Edinger, J. (2007). Three-dimensional ultrasonographic *in vitro* imaging of lesions of the meniscus and femoral trochlea in the equine stifle. *Veterinary Radiology & Ultrasound* 48: 350–356.

Labens, R., Busoni, V., Peters, F. et al. (2005). Ultrasonographic and radiographic diagnosis of patellar fragmentation secondary to bilateral medial patellar ligament desmotomy in a Warmblood gelding. *Equine Veterinary Education* 17(4): 201–206.

McIlwraith, C.W. (1990). Osteochondral fragmentation of the distal aspect of the patella in horses. *Equine Veterinary Journal* 22: 157–163.

McIlwraith, C.W. and Martin, G.S. (2008). Arthroscopic surgery for the treatment of osteochondritis dissecans in the equine femoropatellar joint. *Veterinary Surgery* 14: 105–116.

McIlwraith, C.W., Nixon, J., and Wright, I.M. (2015). Diagnostic and surgical arthroscopy of the femoropatellar and femorotibial joints. In: *Diagnostic and Surgical Arthroscopy in the Horse*, 4th edn (ed. C.W. McIlwraith, I.M. Wright, and J. Nixon), 175–242. Saint Louis, MO: Mosby.

McLellan, J., Plevin, S., and Taylor, E. (2012). Concurrent patellar fracture and lateral collateral ligament avulsion as a result of trauma in 3 horses. *Journal of the American Veterinary Medical Association* 240: 1218–1222. 10.2460/javma.240.10.1218. PMID: 22559112.

Nelson, B.B., Kawcak, C.E., Goodrich, L.R. et al. (2016). Comparison between computed tomographic arthrography, radiography, ultrasonography, and arthroscopy for the diagnosis of femorotibial joint disease in western performance horses: Comparative imaging of equine stifle joints. *Veterinary Radiology & Ultrasound* 57: 387–402. 10.1111/vru.12366. Epub 12 May 2016.

Penninck, D.G., Nyland, T.G., O'Brien, T.R. et al. (1990). Ultrasonography of the equine stifle. *Veterinary Radiology* 31: 293–298.

Prades, M., Grant, B.D., Turner, T.A. et al. (1989). Injuries to the cranial cruciate ligament and associated structures: Summary of clinical, radiographic, arthroscopic and pathological findings from 10 horses. *Equine Veterinary Journal* 21: 354–357. PubMed PMID: 2776722.

Rose, P.L., Graham, J.P., Moore, I. et al. (2001). Imaging diagnosis-caudal cruciate ligament avulsion in a horse. *Veterinary Radiology & Ultrasound* 42: 414–416.

Rubio-Martínez, L.M., Redding, W.R., Bladon, B. et al. (2018). Fracture of the medial intercondylar eminence of the tibia in horses treated by arthroscopic fragment removal (21 horses). *Equine Veterinary Journal* 50: 60–64. 10.1111/evj.12720. Epub 15 August 2017.

Sanders-Shamis, M., Bukowiecki, C.F. et al. (1998). Cruciate and collateral ligament failure in the equine stifle: Seven cases (1975–1985). *Journal of the American Veterinary Medical Association* 193: 573–576.

Vekens, E.V., Bergman, E.H., Vanderperren, K. et al. (2011). Computed tomographic anatomy of the equine stifle joint. *American Journal of Veterinary Research* 72: 512–521. 10.2460/ajvr.72.4.512.

Walmsley, J.P. (2005). Diagnosis and treatment of ligamentous and meniscal injuries in the equine stifle. *Veterinary Clinics of North America: Equine Practice* 21: 651–672.

Walmsley, J.P. (2011). The stifle. In: *Diagnosis and Management of Lameness in the Horse*, 2nd edn (ed. M.W. Ross and S.J. Dyson), Chapter 46, 532–549. Saint Louis, MO: Elsevier-Saunders. 10.1016/B978-1-4160-6069-7.00046-8.

References

1 Hoaglund, E.L., Barrett, M.F., Daglish, J. et al. (2019). Intermediate patellar ligament desmopathy often occurs in conjunction with other stifle abnormalities. *Veterinary Radiology & Ultrasound* 60: 416–422. 10.1111/vru.12760. Epub 21 May 2019.

2 Bourzac, C., Alexander, K., Rossier, Y. et al. (2009). Comparison of radiography and ultrasonography for the diagnosis of osteochondritis dissecans in the equine femoropatellar joint. *Equine Veterinary Journal* 41: 685–692.

3 Martel, G., Crowley, D., Olive, J. et al. (2018). Ultrasonographic screening for subclinical osteochondrosis of the femoral trochlea in foals (28–166 days old): A prospective farm study. *Equine Veterinary Journal* 50: 312–320. 10.1111/evj.12772. Epub 9 November 2017.

Vet-ebooks.com

4 McIlwraith & Martin 1985.
5 Fowlie, J.G., Arnoczky, S.P., Lavagnino, M. et al. (2012). Stifle extension results in differential tensile forces developing between abaxial and axial components of the cranial meniscotibial ligament of the equine medial meniscus: A mechanistic explanation for meniscal tear patterns. *Equine Veterinary Journal* 44: 554–558.
6 Waselau, M., McKnight, A., and Kasparek, A. (2020). Magnetic resonance imaging of equine stifles: Technique and observations in 76 clinical cases. *Equine Veterinary Education* 32(S10): 85–91. 10.1111/eve.13248.
7 Sparks, H.D., Nixon, A.J., Boening, K.J. et al. (2011). Arthroscopic treatment of meniscal cysts in the horse. *Equine Veterinary Journal* 43: 669–675. 10.1111/j.2042-3306.2010.00348.x. Epub 15 March 2011.
8 Koenig, J., Cruz, A., Genovese, R. et al. (2005). Rupture of the peroneus tertius tendon in 27 horses. *Canadian Veterinary Journal* 46: 503–506. PMID: 16048009; PMCID: PMC1140395.

Vet-ebooks.com

8

Ultrasonography of the Pelvis

Marcus Head

Ultrasonography is an extremely useful tool in the diagnosis and management of a number of conditions affecting the pelvis of horses, augmenting and, in some instances, replacing the established techniques of radiography and scintigraphy. The pelvis can be imaged percutaneously from the dorsal aspect, but also *per rectum*. Ultrasonographic assessment is useful in a wide variety of investigations, from subtle performance-limiting problems in sports horses to severe lameness in racehorses.

Equipment

Clipping is often necessary, although not in fine coated horses. A high-frequency linear probe is the most useful for superficial structures but imaging the pelvis also requires a lower-frequency curvilinear or sector probe. Imaging can be difficult in patients with significant subcutaneous fat or thick skin. A rectal probe is necessary for internal examinations.

Indications

Reasons for performing an ultrasound assessment of the pelvis are varied but the commonest indication in non-Thoroughbred practice is evaluation of reduced performance. As for examination of the back and neck, these investigations can be time-consuming and frustrating, but the use of ultrasonography enables a greater number of differential diagnoses to be considered. Other indications include lameness suspected to arise from the upper limb that has eluded diagnosis by distal anesthesia or is known to have been associated with a fall or other trauma. In Thoroughbred racehorses, indications also include evaluation of stress fractures known to occur in the pelvis.

The main areas of interest in the pelvis are:

- Ilial wings and shafts
- *Tubera sacrale*, *tubera ischii*, third trochanters, and *tubera coxae*
- Hip joints
- The lumbosacral, sacroiliac, and intertransverse joints (*per rectum)*
- Internal bony structures (*per rectum)*

The Ilium

The most important reason for imaging the ilium is for the detection of fractures. In racehorses, these occur most frequently as fatigue injuries (stress fractures) caused by the accumulation of damage with cyclical loading and the vast majority originate on the caudal aspect of the ilial wing, close to the sacroiliac joint and the junction of the wing and shaft of the ilium. As they are caused by cumulative damage, horses often show extensive signs of injury on ultrasound by the time they are presented for lameness examination or poor performance. However, while ultrasound is very useful in the detection of these injuries, a normal ultrasound does not rule out injury to this region; some horses have "hotspots" on a bone scan that have no abnormalities ultrasonographically. In other types of horse, the

Atlas of Equine Ultrasonography, Second Edition. Edited by Jessica A. Kidd, Kristina G. Lu and Michele L. Frazer.
© 2022 John Wiley & Sons Ltd. Published 2022 by John Wiley & Sons Ltd.
Companion Website: www.wiley.com/go/kidd/atlas

Vet-ebooks.com

most common reason for imaging the ilium is because of lameness thought to be caused by trauma to the pelvis; displacement of the *tuber coxa* or "knocked down hip" being the most common.

Figure 8.1 shows the technique described by Shepherd and Pilsworth to map the ilial wing by imagining four lines superimposed on the pelvis. The transducer is placed just off midline, holding the probe at 90 degrees to midline on the side of interest, and moved toward the *tuber coxa* slowly while maintaining the image of the bone surface as a smooth, continuous echogenic line (Figure 8.2). It appears as a sweeping curve running from the *tuber sacrale* to the *tuber coxa*. It is important that the examination should cover the entire surface of the ilial wing, as stress fractures may produce pathology in a localized region (typically the caudal aspect), so that a single image may miss these injuries. The operator must ensure that, particularly at the cranial and caudal sites (lines 1 and 3 in the illustration), the edges of the bone are imaged. This can be achieved by tilting the probe forward and backward so that the bone surface temporarily disappears from view at these sites. By following a systematic approach, incomplete fractures will not be missed. Be aware of edge artifacts produced by the many large vessels and fascial planes between the muscles; these can give the impression that there is discontinuity in the surface of the bone. Subtle injuries may present with only minor changes to the contour of the bone surface (Figure 8.3) and in some cases it is possible to identify pathology of different ages; recent, sharply defined fracture lines cranially and more longstanding callus caudally (Figure 8.4). Immature callus will appear irregular and allow some of the ultrasound beam to pass through. Mature callus is smooth and of equal echogenicity to the adjacent, normal bone. As fractures heal, the development of callus can be followed, as its contour changes from convex to concave and it becomes more echogenic with maturation. This is useful as fractures are monitored during recuperation.

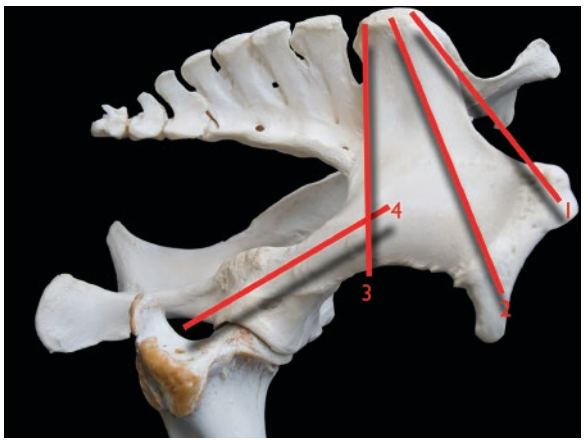


Figure 8.1 Systematic and complete ultrasonographic assessment of the ilium is best achieved by visualizing four planes: three running from the *tuber sacrale* to the *tuber coxa* and one following the ilial shaft.

Rotating the probe to image the ilial wing in a parasagittal plane is sometimes interesting, but its main use is to identify the ilial shaft easily. The smooth caudal edge of the wing becomes the long smooth surface of the shaft and can be followed down to the hip joint. Ilial shaft fractures can be difficult to diagnose unless they are complete; unlike ilial wing fractures, early changes to the bone that precede complete failure are rarely detected. When complete, the normal linear contour to the bone surface that is visualized by running the transducer from cranial to caudal is interrupted, often with a step in the surface evident. This is frequently accompanied by significant hemorrhage. Young animals can suffer "green stick" fractures of the ilial shaft.

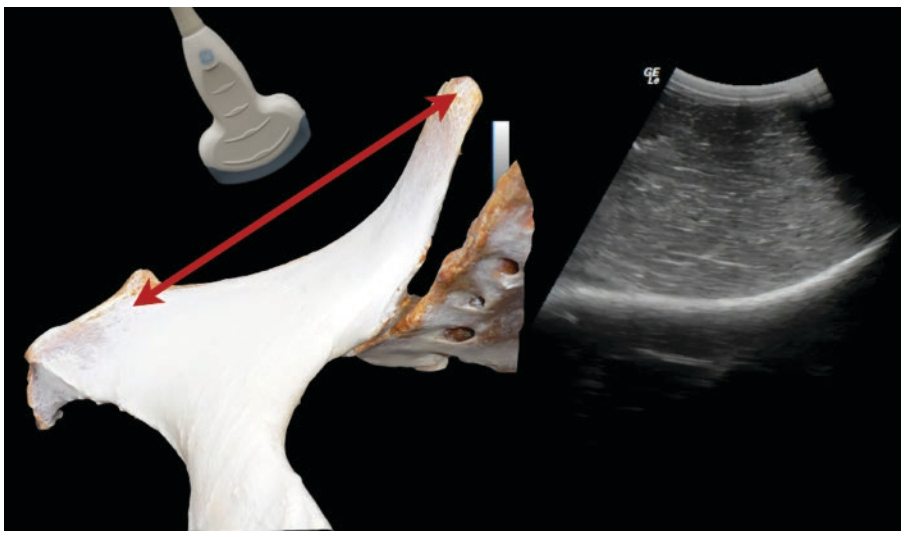


Figure 8.2 The transducer is moved slowly from midline outward along each of the imaginary lines running from the *tuber sacrale* to the *tuber coxa*, imaging the smooth concave surface of the ilial wing.

Vet-ebooks.com

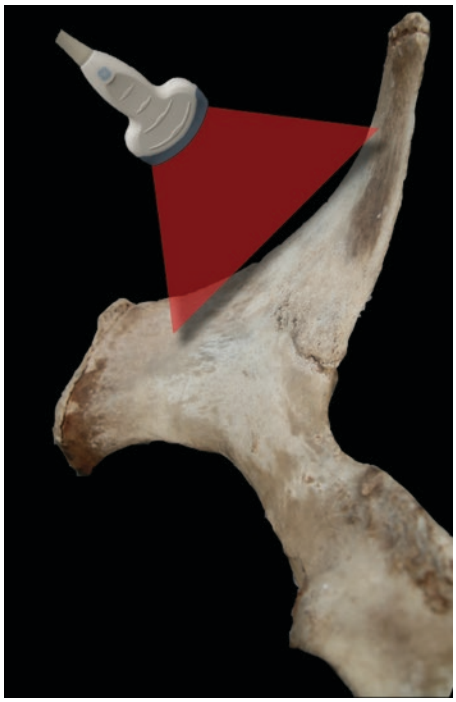


Figure 8.3 For the identification of stress fractures in racehorses (the commonest indication for this technique) care should be taken to assess the full width of the bone; almost all injuries of this kind begin caudally and propagate cranially, perhaps over a period of weeks. In this specimen, the cranial edge of the ilium would appear normal, while pathology can be seen clearly at the caudal aspect.

Tubera Sacrale, Ischii, and *Coxae*

Imaging the bony prominences of the pelvis is best done with a combination of linear high-frequency and lower-frequency curvilinear transducers.

The *tubera sacrale* can be identified, along with the dorsal parts of the dorsal sacroiliac ligaments, in transverse and longitudinal planes. Asymmetry of these structures is quite common and does not correlate well with clinical disease.

Serving as the attachment for the large biceps femoris, semimembranosus and semitendinosus muscles (all of which can be imaged), the *tuber ischium* can be injured as a result of direct trauma (frequently a fall) or as an avulsion injury in athletic horses. The bony prominences are easily palpated either side of the tail head and can be imaged horizontally and vertically. Although they have a certain degree of roughening in normal horses, they present a continuous surface readily amenable to ultrasound imaging. Careful comparison with the opposite side is useful as most injuries seem to involve displacement of bone, so roughening is rarely the only sign. Injury usually results in significant disruption to the normal bone contour and in some cases clear fragmentation (Figure 8.5).

Fractures to the *tuber coxa* also occur as a result of direct trauma or as an exercise-induced

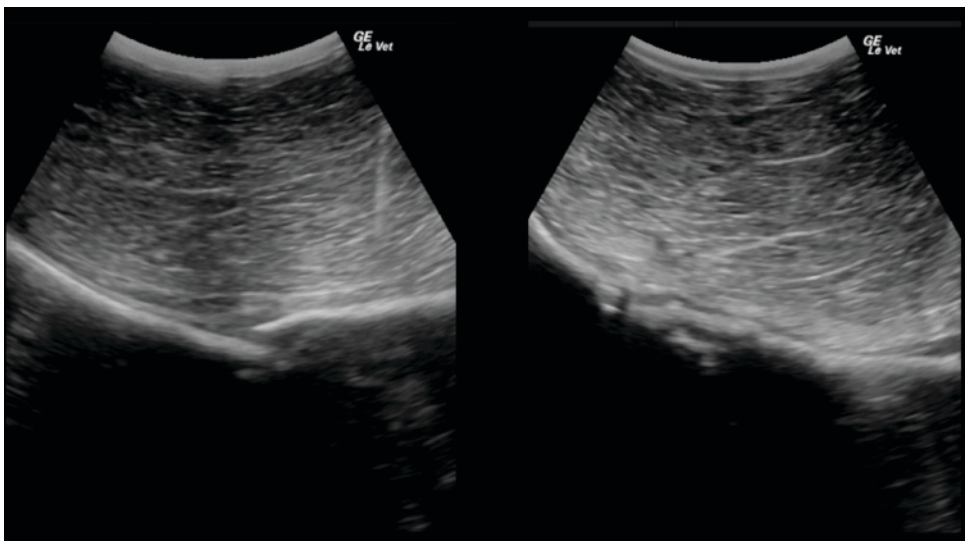


Figure 8.4 In some horses, different stages of fracture development and repair can be seen in the same ilial wing. The image on the left was obtained cranially (line 1 in Figure 8.9) while the image on the right was obtained caudally (line 3). The cranial image shows acute changes with separation of the fracture and relatively sharp bone edges. Caudally, however, there is clear evidence of callus formation with incompletely mineralized bone only partially attenuating the ultrasound beam.

Vet-ebooks.com

avulsion injury. They result in the typical "knocked down hip" appearance and the sharp edge of the parent bone may, rarely, erode through the skin. Although not usually a challenge to diagnose clinically, information regarding fracture configuration can be obtained through ultrasonography (Figures 8.6 and 8.7). It is also useful to scan from the fracture toward midline and attempt to reconstruct a mental map of the fracture configuration, particularly as to whether the injury affects the shaft of the ilium. Some racehorses will suffer severe lameness caused by avulsion injury of the *tuber coxa*, but the typical clinical appearance associated with displacement of the fragment may not become evident for several days after the onset of lameness.



Figure 8.5 Images demonstrating the appearance of the normal (on the left) and injured *tuber ishium*, superimposed on a normal specimen.

Third Trochanter

A much more common site of injury than is widely recognized, the third trochanter serves as the insertion for the superficial gluteal and its tendon, which is easily visualized attaching to this bony prominence in the upper femur. Injuries typically occur in a fall but sometimes present as an avulsion. The area is easily palpated and amenable to percutaneous ultrasonography, so do not forget to include this when assessing sudden onset "upper limb" lameness (Figures 8.8). Once again, the structure can be imaged in orthogonal planes (Figure 8.9). Damage may consist of roughening or proceed to fracture, with or without displacement of the trochanter under the pull of the tendon (Figure 8.10).

Note that the ultrasonographic appearance of third trochanter, *tuber coxa*, and *tuber ischium* injuries may not alter significantly with time and it can be very difficult to date the lesion. This makes ultrasound less useful in following these injuries during the healing process and may lead to false positives if a horse has sustained an injury to these areas previously that may no longer be relevant clinically.

The Dorsal Sacroiliac Ligaments

Divided into dorsal and ventral parts, the dorsal ligaments connect the *tubera sacrale* to the sacrum. They are thin and crescent-shaped cranially, becoming more "apostrophe-shaped" caudally. The two separate parts of each left and right ligament can be appreciated in transverse and longitudinal images (Figure 8.11). The position of these parts relative to each other varies slightly from horse to horse and even from side to side in the same horse (often associated with clinically



Figure 8.6 Anatomical specimen (A) and ultrasonographs (B) of "knocked down hip." In this injury, the *tuber coxa* is fractured and usually displaces cranioventrally. The normal smooth surface of the bone appears as a sharp point when damaged in this way (bottom right of (B)).

Vet-ebooks.com

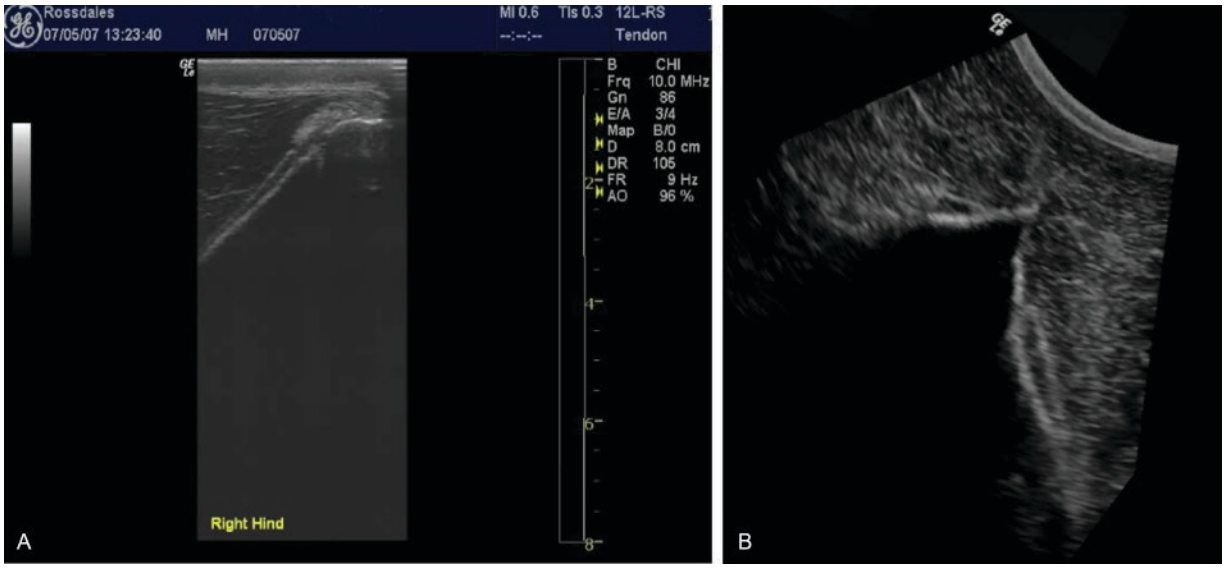


Figure 8.7 Fractures of the *tuber coxa* with a non-displaced fracture seen in (A) and a complete fracture leaving a sharp bone point in (B).

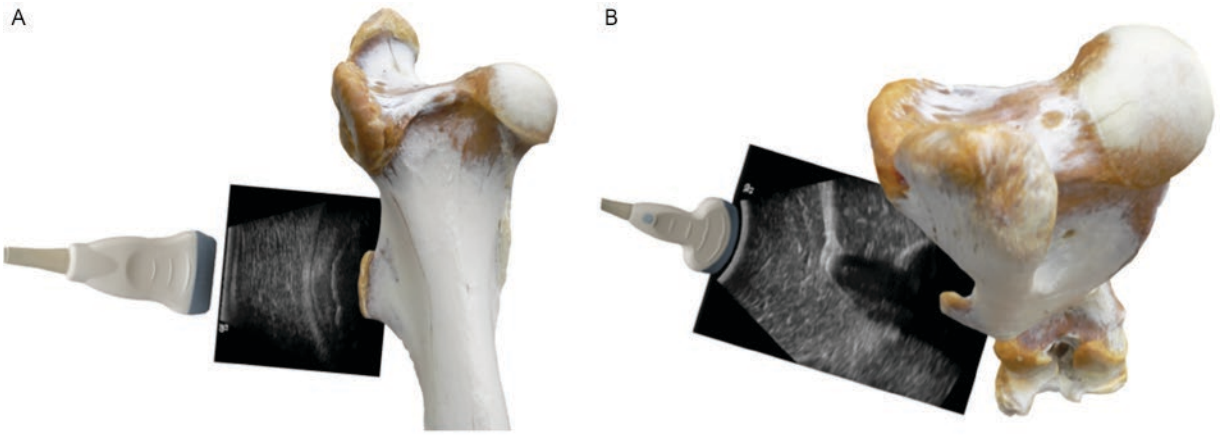


Figure 8.8 Longitudinal (A) and transverse (B) scans of a normal third trochanter superimposed on an anatomical specimen.

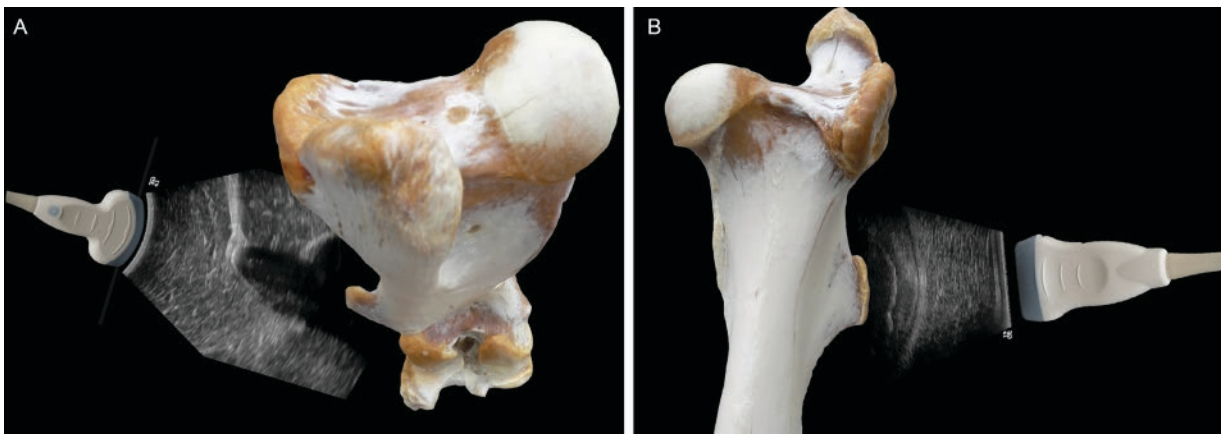


Figure 8.9 Transverse (A) and longitudinal (B) ultrasonographs of a normal third trochanter (note the tendon of insertion of the superficial gluteal evident in (A) and the use of both linear and curvilinear transducers).

Vet-ebooks.com

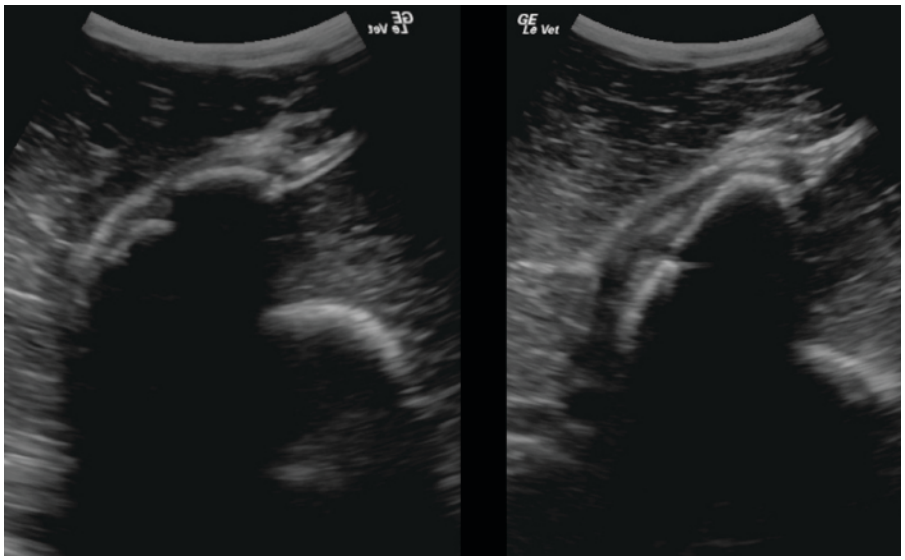


Figure 8.10 Two examples of injury to the third trochanter. In both, a fracture gap is visible on the caudal aspect of the bone surface. In the image on the right, the normal orientation of the trochanter to the femoral diaphysis is maintained, but in the image on the left the trochanter appears to have "fallen over," indicating displacement of the fracture.

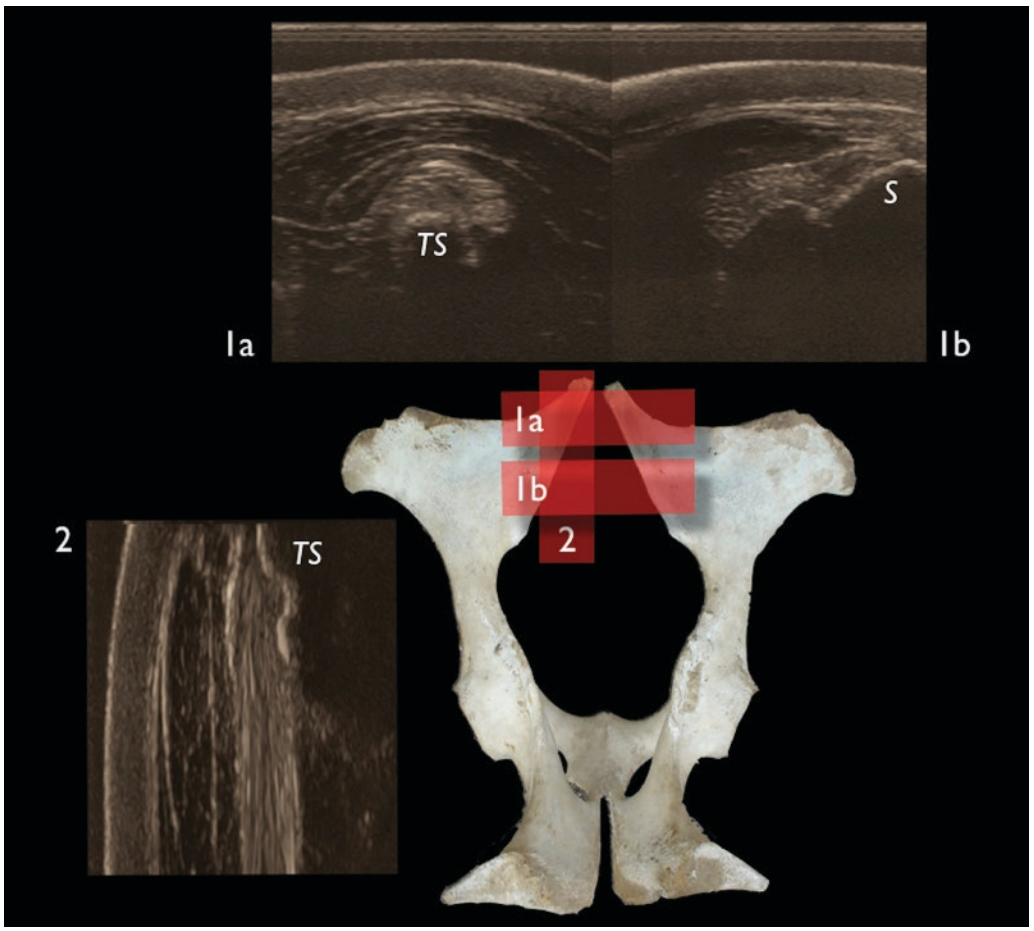


Figure 8.11 The normal appearance of the dorsal sacroiliac ligaments. TS: *tuber sacrale*; S: sacral spine.

Vet-ebooks.com

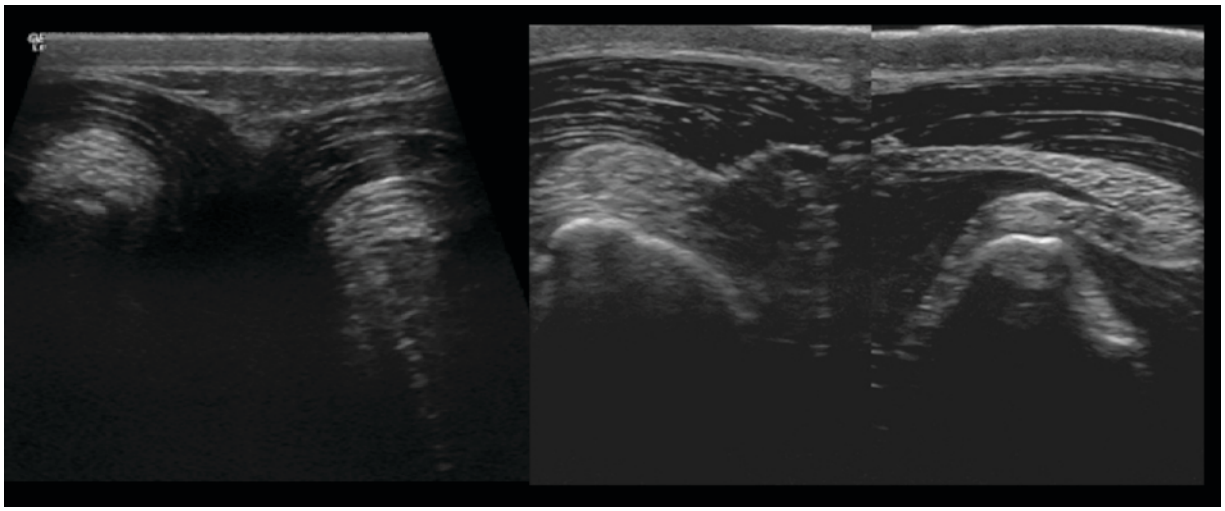


Figure 8.12 Asymmetry of the *tubera sacrale* is a common incidental finding (left of image) and normal variations in the appearance of the dorsal sacroiliac ligaments should not be interpreted as lesions (right of image).

insignificant asymmetry of the *tubera sacrale*) so these "changes" need to be interpreted carefully (Figure 8.12). Care should be taken in interpretation as, like the supraspinous ligament (SSpL: Chapter 9), hypoechogenic areas can be seen in normal horses (Figure 8.13). Long-axis scans allow evaluation of longitudinal fiber pattern and assessment of the integrity of the entheses. As with the SSpL, a degree of off-incidence artifact and age-related change can cause false positives. Interpret changes with care, as injury here is rare and artifact more common.

The ventral parts of the dorsal sacroiliac ligaments can be imaged through a small acoustic window between the *tubera sacrale* but they rarely appear to be affected clinically.

Hip Joints

The hip joint is identified most easily by following the ilial shaft in a caudoventral direction. The transducer can then be rotated slowly to improve the image and identify the curved acetabulum, the smooth, convex femoral head, and the large greater trochanter (Figures 8.14A and 8.14C). By rocking the transducer backward and forward, it should be possible to appreciate the relation between the closely apposed bone surfaces of the acetabulum and femoral head, and gain information regarding the health of the joint (Figure 8.14). Altering the orientation of the probe allows evaluation of the joint edges more easily. In a normal horse, the acetabulum and femoral head have a smooth appearance and there is only a narrow "gap" between them. In younger horses, the edges of the acetabulum are often rounded and the joint space is wider (Figure 8.15). The presence of the symphysis between the bones that form the acetabulum (ilii, ischii, and pubis) could be misinterpreted as a fracture. This fuses at approximately one year of age, and up to this time the appearance of the hip joint changes considerably, so comparisons with the contralateral limb are invaluable.

In foals, the joint space also appears wider because of the increased thickness of articular cartilage. The normal discontinuity seen in foals should not be mistaken for a



Figure 8.13 Central hypoechogenic regions within the dorsal sacroiliac ligaments should be interpreted with care, particularly when not accompanied by other signs such as an increase in cross-sectional area, as they are frequently artifactual.

Vet-ebooks.com

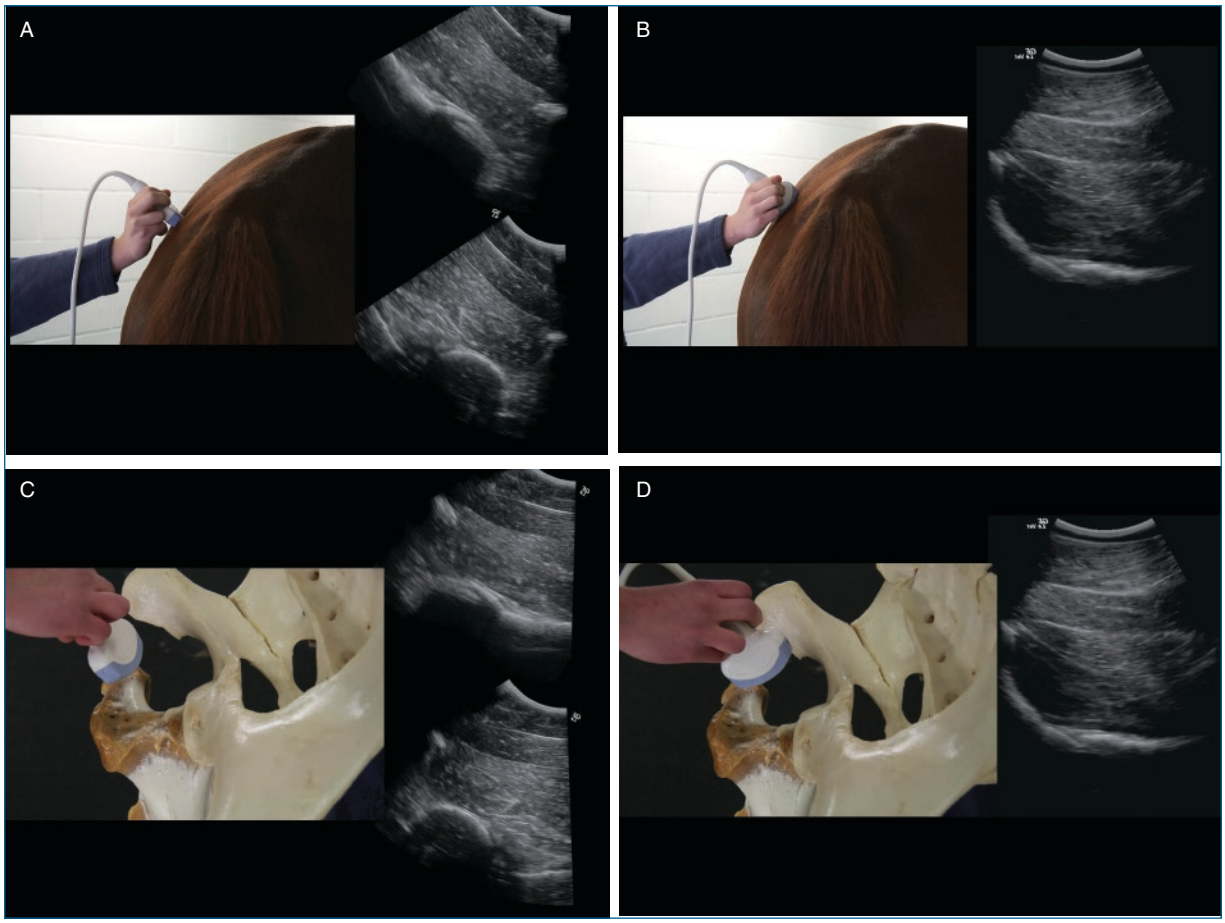


Figure 8.14 (A) The initial position of the transducer for imaging of the coxofemoral joint, having followed the line of the ilial shaft caudally [1]. By tilting the probe, it is possible to image the acetabulum (top right) and the femoral head (bottom right). (B) The transducer is rotated to evaluate the edge of the acetabulum, the joint capsule, and the femoral head. (C) The transducer and anatomical specimen illustrating the orientation of the transducer in (A). (D) The transducer and anatomical specimen illustrating the orientation of the transducer in (B).

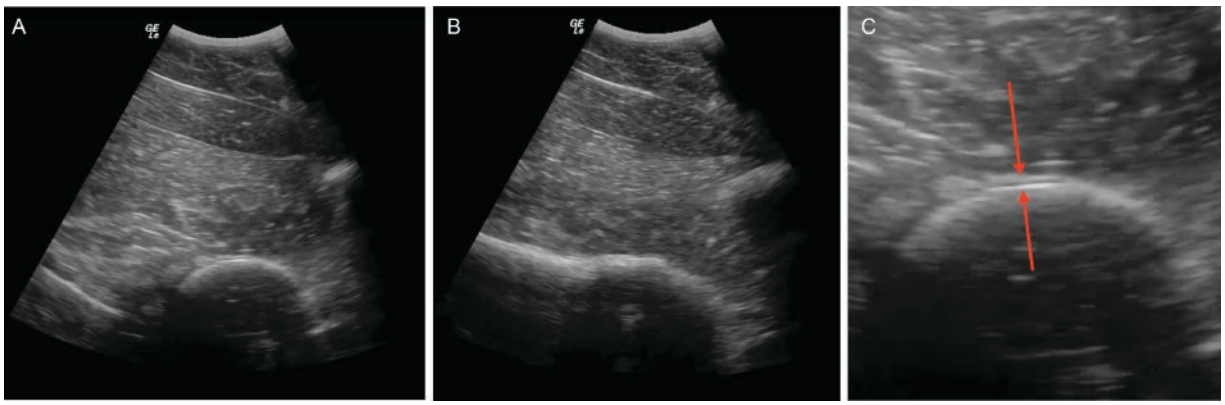


Figure 8.15 Hip joint: normal appearance of the femoral head (A) and acetabulum (B). Note that it is not possible to image both simultaneously; the transducer must be tilted back and forth to appreciate both structures separately. In some horses, the thickness of the articular cartilage on the femoral head can be assessed (C).

fracture, although it can be a site for injury (Figure 8.16). Again, comparison with the contralateral joint is useful.

Additional information can be obtained by rotating the probe through ninety degrees so that the transducer is perpendicular to the edge of the acetabulum (Figures 8.14B and 8.14D). This approach allows further evaluation of the acetabulum, in particular, which should appear as a sharp, clearly delineated edge. The joint capsule can also be identified, permitting assessment of distension and the

Vet-ebooks.com



Figure 8.16 The physes forming the acetabulum close at around one year of age. Before then, disruption can occur through them. The image bottom left shows the normal appearance in a young foal while the image on the right shows a displaced fracture. A normal anatomical specimen is also seen, for reference.

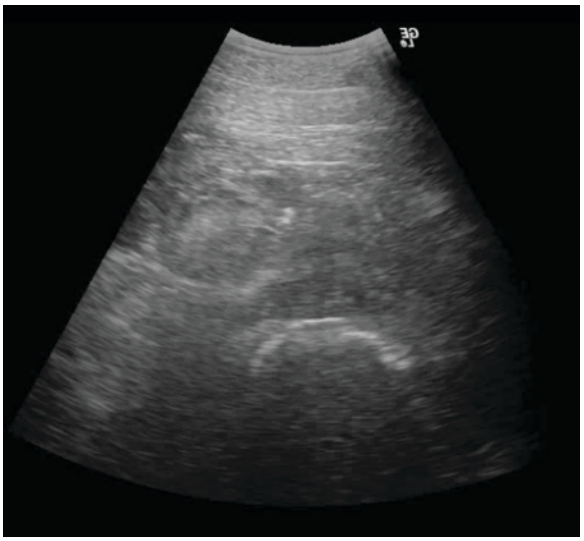


Figure 8.17 Ultrasonograph from a horse with chronic hip joint OA. The contour of the femoral head is irregular and roughened.

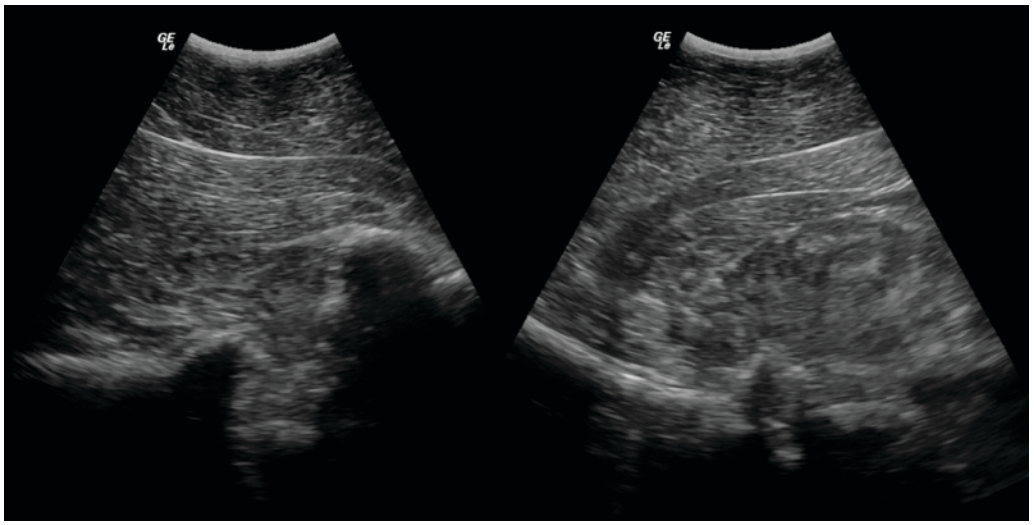


Figure 8.18 In these examples, from a horse that sustained a fracture of the femoral neck, the normal architecture of the joint has been severely disrupted. Note the abnormal proximity of the greater trochanter to the acetabulum (left image) and the hemorrhage into the periarticular tissues along with fragmentation seen around the hip joint (right image).

congruity of the joint. This is also the view that is used when performing ultrasound-guided injection of the hip joint [1].

It is fair to say that the assessment of the hip is limited because only a small portion of the joint can be imaged and pathology must be advanced or severe to be appreciated. However, although hip joint injury is uncommon, it is frequently advanced when cases do present for investigation and ultrasonography can play a very useful role as an adjunct to the clinical assessment, radiography, and scintigraphy.

Osteoarthritis (OA) will cause new bone production around the joint and roughening of the bone surfaces. This can be subtle, or more obvious if the inciting cause of OA was more dramatic (Figure 8.17). Through a dynamic assessment of the joint, by rocking the transducer back and forth, it may be possible to confirm flattening of the femoral head and incongruity of the normally narrow joint space. Be aware that the joint space will appear wider in a horse that is not weightbearing properly, possibly leading to the false impression of subluxation.

Vet-ebooks.com

In some cases of severe trauma, the normal alignment of the joint will be completely destroyed. Figure 8.18 shows images from a horse that suffered a complete fracture of the femoral neck. Although the primary injury could not be identified accurately, it was clear immediately that the normal joint architecture had been severely compromised.

Per Rectum Evaluation

Assessment of the internal surface of the pelvic bones is an important part of the examination, particularly in sudden onset severe lameness thought to be originating from the proximal limb. Palpation should be performed first, without ultrasound, but lack of abnormalities during palpation should not preclude scanning. Fractures or callus can be missed with palpation alone and in some acute or subacute cases, hemorrhage can make direct manipulation of bone surfaces impossible. When palpated in acute injuries there may a feeling that there is swelling of the region, when compared to the other side. This often gives way to a sense that the bone is much more prominent, because muscle atrophy occurs, during the subacute and chronic stages.

Figure 8.19 highlights the common sites for injury that can be diagnosed during *per rectum* scanning. The normal medial acetabulum can be imaged with a linear rectal probe and seen as a smooth contour. Early in the injury this may become stepped or fragmented. Callus appears during the later stages (Figure 8.20). In some cases, the only findings are soft tissue swelling and hemorrhage and a definitive bone injury cannot be identified. This is still highly significant. In other cases, a step in the bone surface can be seen, but might only be appreciated with careful placement of the probe (Figure 8.21): a slow methodical approach is required. In cases with more longstanding pathology, callus may be evident as the injury repairs. In acute cases, particularly ones in which hemorrhage could be seen but no primary bone injury, the ultrasound examination should be repeated 10–14 days later as the damage may become more evident with time.

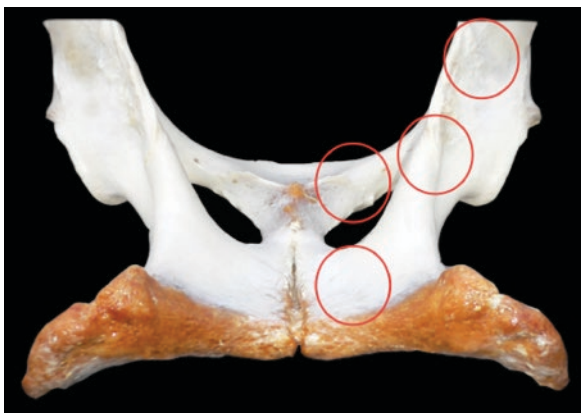


Figure 8.19 *Per rectum* palpation and ultrasonography can be very useful for detection of pelvic fractures. The sites circled on the right of the image are the areas injured most frequently, usually by trauma.

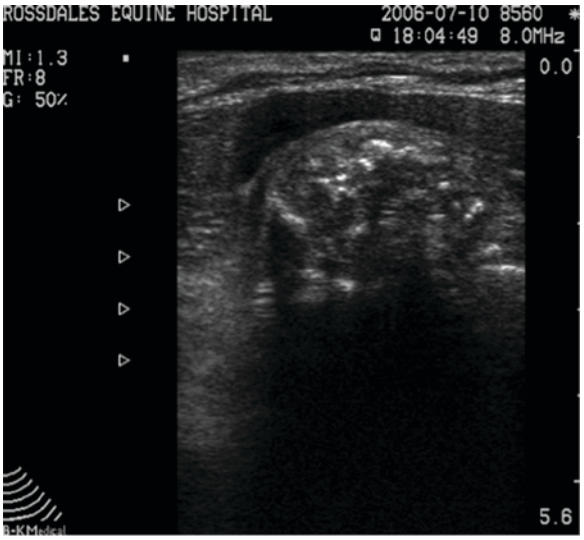


Figure 8.20 Callus indicating a chronic acetabular fracture.

The Lumbosacral, Sacroiliac, and Lumbar Intertransverse Joints

Much of the information we have on the imaging of these areas comes from the work of Jean-Marie Denoix and it is a region that we are still learning much about. Ultrasonography of this area must be interpreted with caution and with the knowledge that, although we can document several new disease processes, our view is restricted and the correlation with clinical syndromes is still, in some cases, vague.

Lumbosacral Joints

The junction between the last lumbar vertebra and the sacrum contains a large fibrocartilaginous disc, which experiences significant movement during exercise. Almost all of the flexion/extension of the caudal spine occurs at the lumbosacral junction and damage to the disc in this region can be associated with discomfort and performance limiting problems. Although horses do not suffer from disc disease in the same way that humans and other species do, there is evidence that this disc can suffer degeneration and cause problems.

Vet-ebooks.com

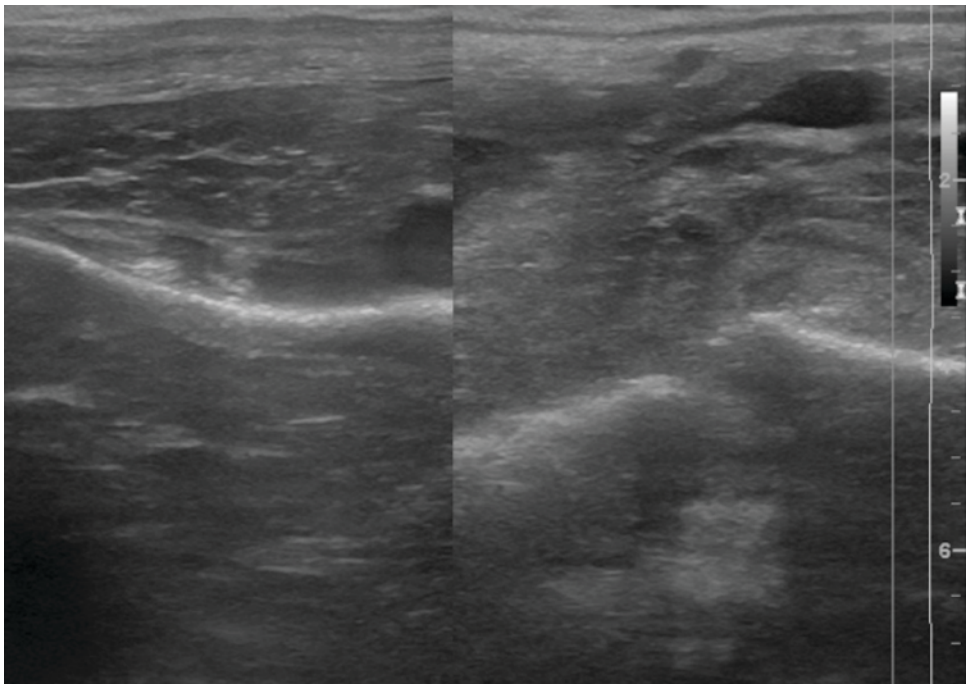


Figure 8.21 Ultrasonographs from a horse that had recently sustained a fracture of the pubis (*per rectum* examination; normal on the left, injured on the right). Note the discontinuity of the bone surface associated with soft tissue swelling and hemorrhage.

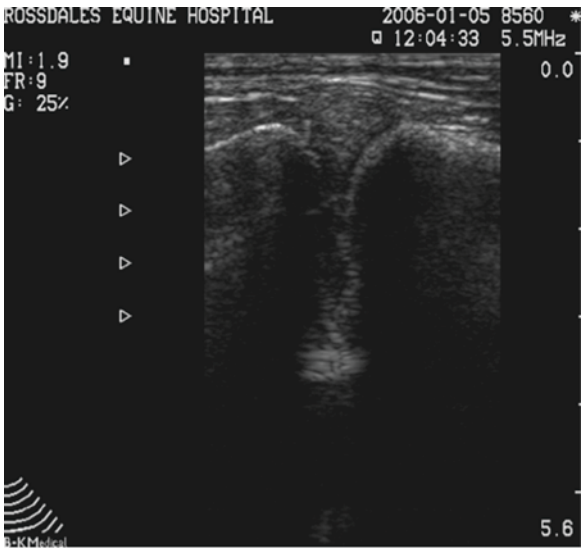


Figure 8.22 A normal lumbosacral junction obtained by scanning *per rectum*.

It is easily located by palpating the ventral spine *per rectum*: the joint is the prominent ventral midline bulge felt caudal to the terminal aorta and branching vessels when the fingers are run cranial to caudal along the underside of the caudal spine.

The lumbosacral junction can be imaged *per rectum* and is easily recognized, being larger than the adjacent intervertebral spaces (Figure 8.22). A linear rectal probe is placed midline and faced upward, so that the ventral aspect of the joint is seen. The disc should not bulge out past the limits of the adjacent bone, the space should be even, and it should be possible to visualize the disc for its full depth, although sacralization may prevent this and does not necessarily indicate pathology. Ultrasonographically, it appears not dissimilar to the medial meniscus of the stifle (Figure 8.23). By examining further cranially, the next junction between L5/6 can be seen. Again, occasionally sacralization may occur so that the L6/S1 disc is reduced in size or absent, with the L5/6 disc often larger to compensate: this is considered a normal variant. As well as being an important structure in its own right, the lumbosacral joint provides the main anatomical landmark to locate the other adjacent joints. In young horses, the irregularity caused by the presence of open physes in the vertebral bodies should not be confused with new bone formation.

Extreme pathology can be observed (Figure 8.24) and is likely to be significant if clinical evidence and the results of other techniques confirm this conclusion. Minor pathology in the form of uneven echogenicity or changes in shape of the disc require cautious interpretation.

Vet-ebooks.com

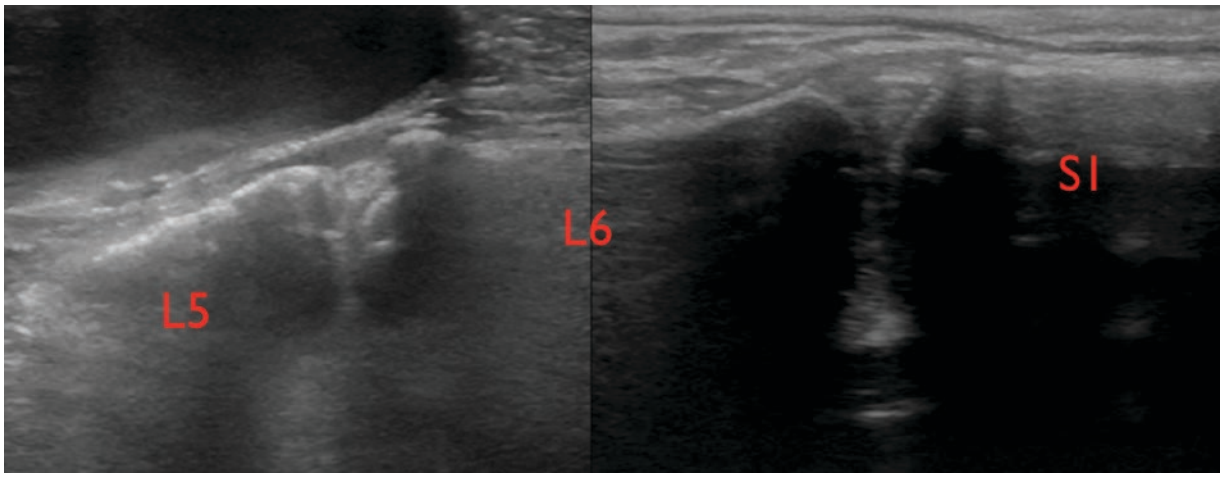


Figure 8.23 Composite *per rectum* ultrasonograph of the lumbosacral region. The transducer is imaging the ventral aspect of the caudal spine. The large intervertebral disc between L6 and S1 can be seen (lumbosacral junction) and the smaller disc between L5/6. The entire depth of the L6/S1 disc can be viewed down to the vertebral canal.

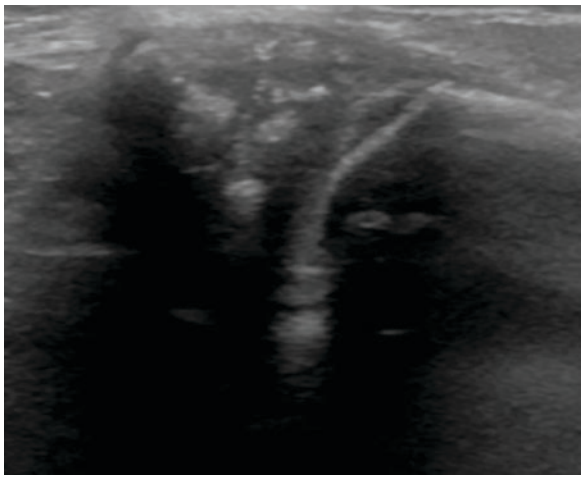


Figure 8.24 Image of a diseased LSJ disc showing severe disruption to the substance of the disc, the overlying ligament, and irregularity of the caudal aspect of L6.

Sacroiliac Joints

Only a very small part of the sacroiliac joint can be imaged *per rectum* and this is an important limitation of the technique. It is also unclear in many cases just how significant changes in this area are. The joint can be visualized by starting from the lumbosacral joint, moving caudally one sacral vertebra's length and then swinging the transducer to the left, or right. In normal horses, a clear space can be identified (Figure 8.25). New bone production is seen in some horses. Widening of the sacroiliac joint is considered a normal variation, particularly in geldings.

Lumbar Intertransverse Joints

The horse is unusual in having normal articulations between the transverse processes of the last lumbar and first sacral vertebrae. They are easily identified by locating the lumbosacral joint and moving the probe a short distance to the left or right (Figure 8.26). The normal intratransverse joints present a sharp, clearly demarcated joint space. Although disease of these joints can cause discomfort or reduced mobility, it is their proximity to the lumbosacral nerves that may be more important. New bone formation and soft tissue swelling may cause impingement of the lumbosacral nerve roots (especially that of L6) causing neuralgia and lower motor nerve signs (Figure 8.27). The author has seen several cases of what appeared to be equine "sciatica," responsive to anti-inflammatory medication of the region.

Sacrum

The ventral aspect of the sacrum can be assessed *per rectum*, simply by following the smooth bony surface caudally from the lumbosacral joint (Figure 8.28). Pathology needs to be extreme to be easily identified as complete fractures in racehorses may occur as the end stage of fatigue injuries or may be the result of trauma in all types of horses. In such cases, a step in the bone contour can be seen where the fracture displaces, often associated with significant hemorrhage (Figure 8.29).

Vet-ebooks.com

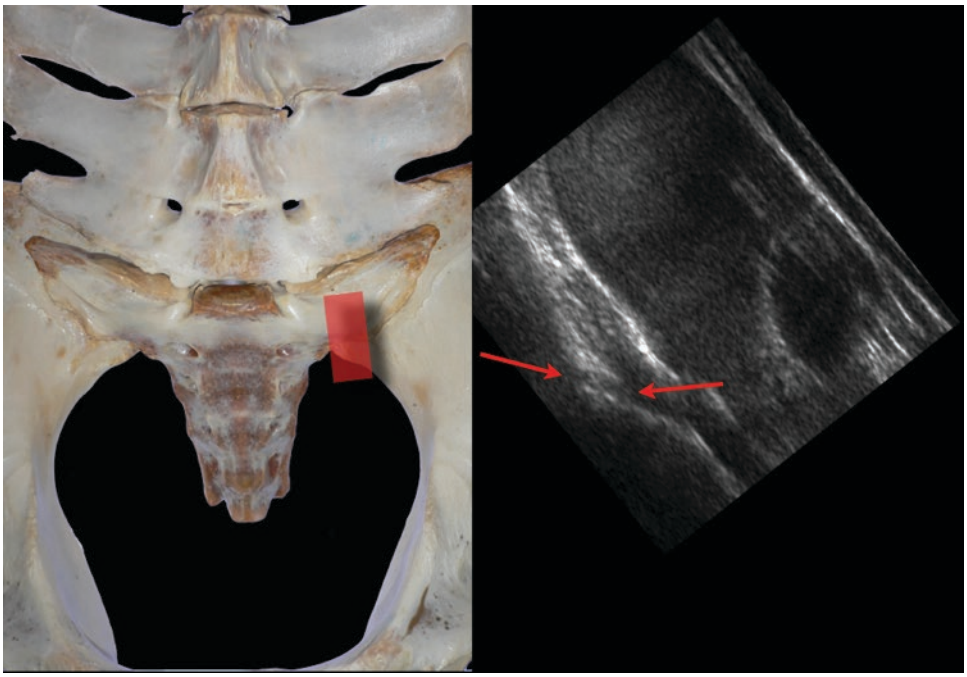


Figure 8.25 The caudal aspect of the sacroiliac joint imaged *per rectum*.

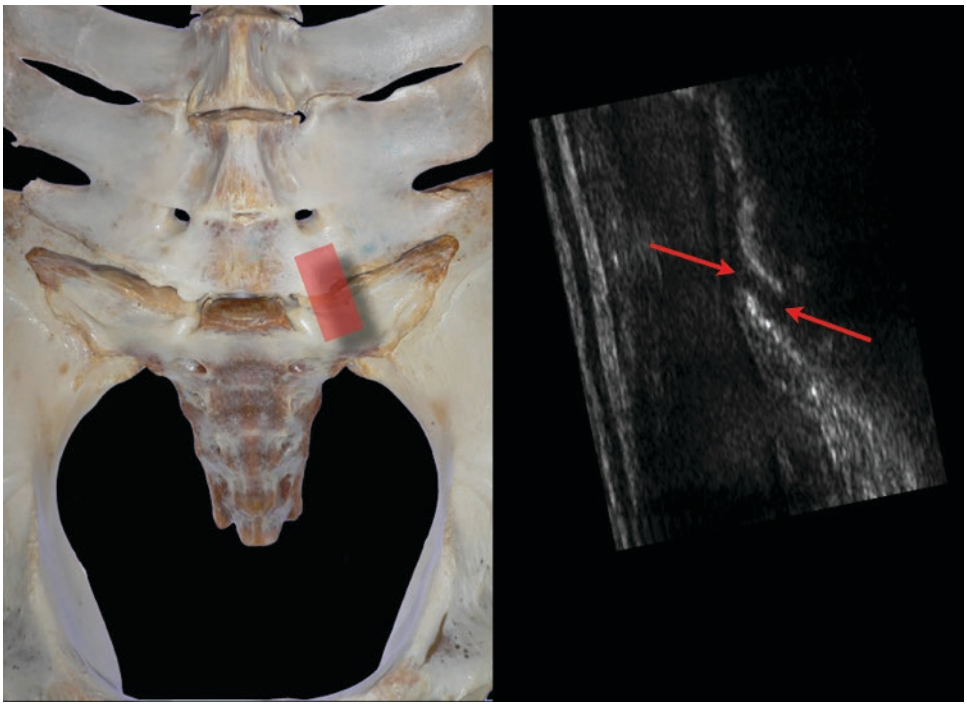


Figure 8.26 Imaging the normal intertransverse joint *per rectum*. The red area superimposed on the specimen demonstrates the position of the transducer to obtain this image.

Vet-ebooks.com

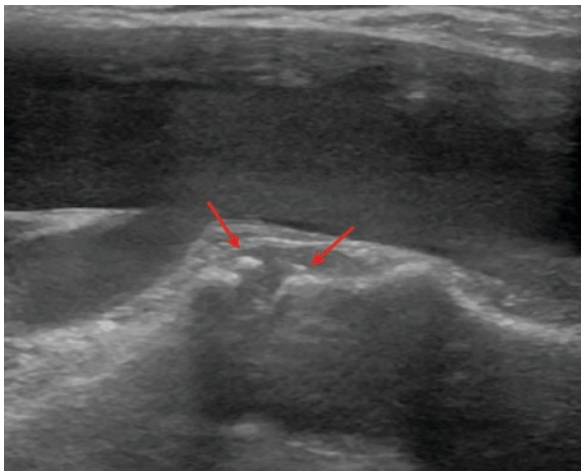


Figure 8.27 Irregular new bone formation around the intertransverse joint. Abnormalities in this region can cause discomfort and neurological signs if there is impingement on the L6 nerve root.



Figure 8.28 Position of the transducer to image the ventral sacrum *per rectum*. Note that this is a specimen from a young horse where fusion of the vertebral bodies is incomplete; however, the ventral aspect presents a relatively flat surface.

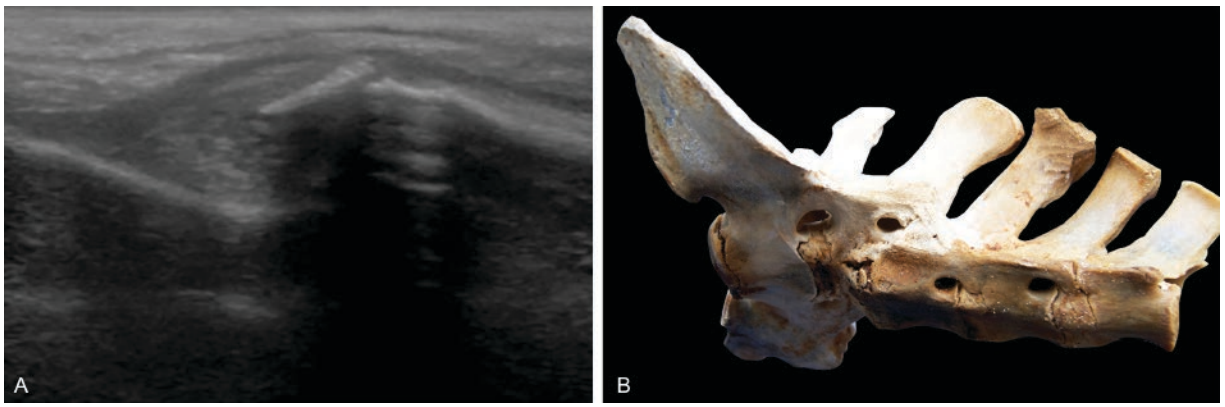


Figure 8.29 Ultrasonograph (A) and isolated sacrum (B) from a horse that had suffered a complete fracture through the caudal part of S2. (A) note the displacement and comminution evident; this image was obtained soon after injury, before signs of repair such as new bone production became evident. (B) The repair process is more advanced.

Recommended Reading

Powell, S. (2011). Equine practice: Investigation of pelvic problems in horses. *In Practice*, 33: 518–524.

Shepherd, M. and Pilsworth, R. (1994). The use of ultrasound in the diagnosis of pelvic fractures. *Equine Veterinary Education*, 6(4): 223–227.

Reference

1 David, F., Rougier, M., Alexander, K. et al. (2007) Ultrasound-guided coxofemoral arthrocentesis in horses. *Equine Veterinary Journa*, 39: 79–83.

Vet-ebooks.com

9

Ultrasonography of the Back and Neck

Marcus Head

Ultrasonographic assessment of the back and neck has added significantly to our ability to clinically evaluate these areas and provides imaging of the axial skeleton which complements radiography and scintigraphy. It also has the advantage that, in the axial skeleton, ultrasonography can be accomplished with most if not all ultrasound machines, compared to scintigraphy and the majority of axial skeleton radiography which can only be accomplished in a hospital setting. Although ultrasound examination of the back is limited to the epaxial structures, ultrasonographic assessment is useful in a wide variety of investigations, from trauma to poor performance.

Indications

Reasons for performing ultrasound assessment of the back and neck are varied but the commonest indication in non-Thoroughbred practice is evaluation of reduced performance due to suspected back or neck pain. These investigations can be time-consuming and frustrating, but the use of ultrasonography enables a greater number of differential diagnoses to be considered. Lower motor nerve signs, such as muscle atrophy or abnormal "stringhalt-like"| gaits, which may be caused by lumbosacral nerve compression, can also be evaluated. In Thoroughbred racehorses, indications also include evaluation of stress fractures known to occur in the back.

Equipment

Clipping is often necessary, although not in fine coated horses – a 5 cm wide strip extending from the withers to behind the *tubera sacrale* should be prepared. It should be widened over the caudal thoracic and lumbar regions to allow imaging of the facet joints.

A high-frequency linear probe is the most useful for superficial structures but imaging the facet joints requires a lower-frequency curvilinear or sector probe. Imaging can be difficult in patients with significant subcutaneous fat or thick skin.

Back

The main areas that can be imaged are:

- Supraspinous (SSpL) and interspinous ligaments along with the dorsal aspects of the spinous processes
- Sacroiliac ligaments
- Caudal thoracic and lumbar intervertebral (facet) joints
- Epaxial musculature

Supraspinous and Interspinous Ligaments

The tough, fibrous SSpL connects the summits of the dorsal spinous processes and is easily visualized using a linear transducer. Its appearance is similar to other ligaments or tendons, with a striated fiber pattern evident when viewed longitudinally. The ligament lies in close

Atlas of Equine Ultrasonography, Second Edition. Edited by Jessica A. Kidd, Kristina G. Lu and Michele L. Frazer.
© 2022 John Wiley & Sons Ltd. Published 2022 by John Wiley & Sons Ltd.
Companion Website: www.wiley.com/go/kidd/atlas

Vet-ebooks.com

apposition to the interspinous ligaments, whose fibers may run at a different angle, and this can cause off-incidence artifacts if care is not taken. The correct technique involves dynamic assessment of the ligament, tilting the probe forward and backward along its long axis to appreciate the slight curve/angle change of the fibers as they insert onto the DSPs (a standoff pad is therefore very useful). In addition, care should be taken that it is the SSpL being imaged, as the strong aponeurosis of the longissimus muscle has a prominent tendon-like appearance just to the left and right of midline (Figure 9.1). Transverse images of the ligament can be obtained simply by rotating the probe and are useful to corroborate potential injury identified longitudinally.

The supraspinous ligament often appears hyperechogenic relative to the interspinous ligament and this can lead to errors in concluding that there is damage to the SSpL, when in fact it is normal interspinous ligament tissue. As well as this, the fibers of the SSpL alter their angle of orientation slightly as they insert upon the oblique dorsal surfaces of the DSPs. This can lead to misinterpretation due to off-incidence artifacts. The SSpL is larger and more fibrous as it progresses caudally; images in the lumbar region are generally more consistent between individuals but there is a wide variation in "normal" appearance. This may be due to operator factors, anatomical idiosyncrasy, or previous but currently insignificant injury.

Interpretation of potential lesions follows the same basic principles as with other ligaments or tendons, with attention paid to size, echogenicity, and fiber pattern particularly (Figure 9.2). A certain degree of caution needs to be exercised when interpreting the appearance of the SSpL: it seems that a degree of dystrophic, possibly age-related change, is evident in some horses and not necessarily indicative of disease. In addition, sites of injury rarely recover a normal appearance and regions of hypoechogenicity may not relate to current pathology. In almost all cases, evidence of injury will need to be confirmed with other techniques, such as diagnostic anesthesia.

It is easy enough to infiltrate local anesthetic around the "injury" and ascertain whether this alters the horse's movement/behavior, although there can be difficulties in reproducing that behavior consistently enough to allow this. Bear in mind that the ultrasonographic appearance of most SSpL injuries changes little with time and false positives can be a problem. This also makes follow-up of genuine lesions difficult. SSpL abnormalities are common in areas of significant impingement of the dorsal spinous processes.

An assessment of the health of the DSPs is also possible during examination of the SSpL, in relation to their dorsal bony contour (well-spaced or close, smooth or roughened, presence of osteophytes, etc.). However, as only the very superficial

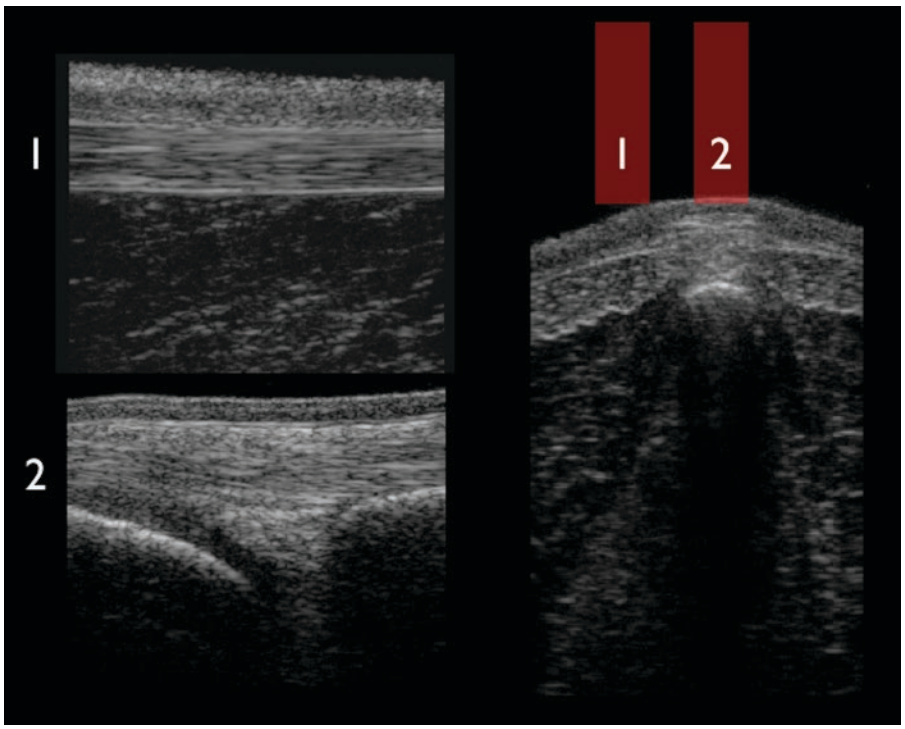


Figure 9.1 Care should be taken when imaging the supraspinous ligament (SSpL) that the transducer is midline (position 2). The aponeurosis of the longissimus muscles will appear as a striated, fibrous structure mimicking the ligament if the transducer is positioned to the left or right (position 1).

Vet-ebooks.com

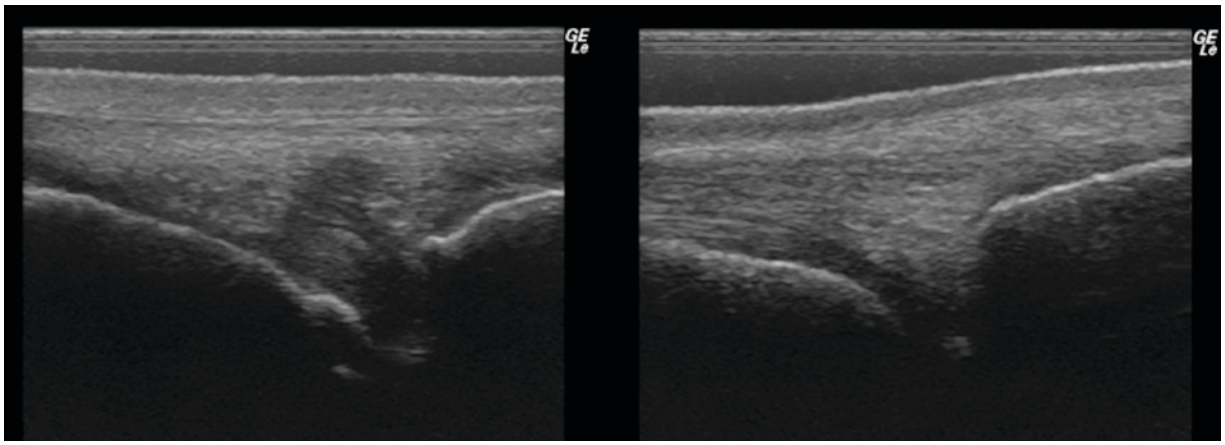


Figure 9.2 Longitudinal images of the supraspinous ligament (SSpL) and associated dorsal spinous processes (DSPs). Note the disruption to the longitudinal fiber pattern of the ligament, the close apposition of the DSPs, and the new bone production on the image to the left. Comparison with the adjacent interspinous region (to the right) can be helpful.

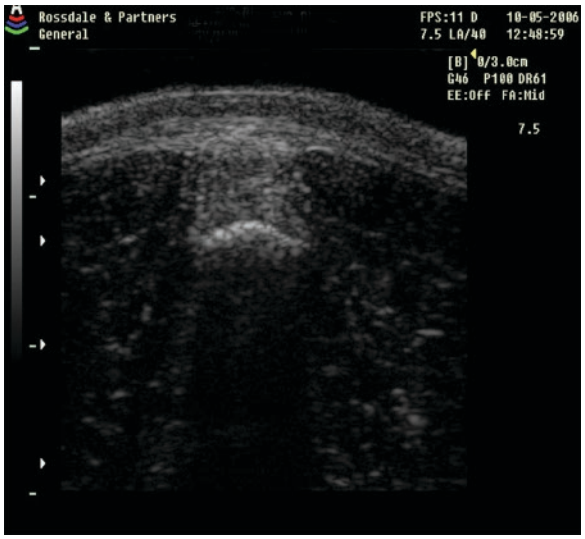


Figure 9.3 Transverse scans of a normal supraspinous ligament (SSpL) as an adjunct to longitudinal scans to ascertain the significance of changes seen on longitudinal images.

part of these structures can be visualized, the technique is only supplementary to radiography and scintigraphy.

It is practical to begin by performing a rapid, general appraisal of the ligament, running from cranial to caudal in the longitudinal plane. After this, move back to the cranial extent of the prepared area and scan longitudinally, identifying and recording areas of interest. If pathology is suspected, transverse scans (Figure 9.3) are used to try to ascertain the significance of changes. Suspicious areas should be marked, most easily by a short clip in the coat, to allow subsequent diagnostic anesthesia.



Figure 9.4 Postmortem specimen of the caudal thoracic intervertebral articulations (IVAs) viewed dorsally. Note their proximity to the dorsal spinous processes.

The Caudal Thoracic and Lumbar Facet Joints

The anatomy of the thoracic and lumbar joints differs makes imaging of the more cranial thoracic joints more difficult due to their proximity to the dorsal spinous processes (Figure 9.4). Fortunately, most pathology occurs in the last thoracic and cranial lumbar joints, which are easily imaged in horses without excessive subcutaneous fat or thick skin. The technique is compromised severely in patients with these last factors and in some horses it is impossible to obtain diagnostic images.

The technique aims to identify the articulation of the cranial articular process of one vertebra as it interdigitates with the caudal (and medial) process of the vertebra ahead of it (Figures 9.5 and 9.6). The first image to acquire is with the probe (a lower frequency curvilinear, ideally) at right angles to and just to the side of midline (Figure 9.7). By counting the ribs and following them up, the operator can get an idea of the vertebrae being imaged. Moving the

Vet-ebooks.com



Figure 9.5 Postmortem specimen of the lumbar intervertebral articulations (IVAs) viewed dorsolaterally. Note that they are more easily discernible than the thoracic IVAs.

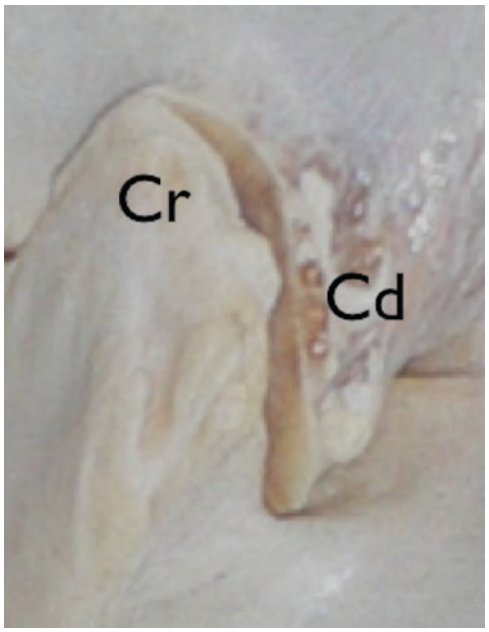


Figure 9.6 Postmortem specimen of the lumbar intervertebral articulations (IVAs) with their finger-like cranial and caudal projections interlocking.

probe backward (and, therefore, with the haircoat) the joints will appear and disappear from the field of view as the transducer heads caudally. Normal joints appear as the corner of a box, close to the junction of dorsal and transverse spinous processes. In thin-skinned horses and with high-quality equipment, it is common to be able to identify the individual cranial and caudal processes of each joint as well as the joint space. Disease of the intervertebral articulations (IVAs) results, regardless of the inciting cause being a stress fracture or osteoarthritis, in enlargement of the joint and the loss of this definition, with new bone production, which may progress to joint ankylosis (Figure 9.8). The ultrasound appearance is as if someone has stuck a ball onto the corner of the box, which takes on a rounded shape. It is important to compare adjacent joints on the same side of the horse to establish the validity of changes and also to compare the left and right sides.

Longitudinal images, obtained by placing the transducer parallel to and just to the side of midline, can enable adjacent joints to be imaged in the same field of view (Figure 9.9). It should be remembered that it is not uncommon for pathology to affect more than one joint, either on the same side or opposite sides of the horse, although it is very rare for this pathology to be symmetric, so even horses affected in several locations will have noticeable discrepancies in joint size and shape. Note also that low-grade disease affecting several joints is common in racehorses and an abnormal ultrasound appearance does not necessarily indicate that the joint is a current concern; scintigraphy should be considered to evaluate the significance of lesions further. Ultrasound-guided injection of affected joints can be useful. Once the affected joints have been identified, a curvilinear transducer is placed at right angles to the midline and the joint localized. Two techniques are available but with similar results – the aim is to guide the 3.5-inch 18-gauge spinal needle through the epaxial musculature and deposit the medication into, or close to, the joint. Whether the probe is positioned close to midline and the needle is directed from lateral or vice versa, the aim is to inject into multifidus close to the joint. A skin bleb of local anesthetic again reduces the discomfort to the patient. The author would typically use 5 mg of triamcinolone acetonide diluted in 1.5 ml of sterile saline, per joint. In many cases, there is evidence of disease at multiple sites and even if only one joint seems to be affected, consideration should be given to treating the contralateral or neighboring joints, as it is likely that these will have been under abnormal loading. The author prefers to place the needle very close to midline and direct it vertically downward, being guided by the ultrasound transducer positioned a little further toward him. The joints are very close to the base of the dorsal spinous processes and it sometimes surprises people how close to the midline the needle needs to be. If the site of insertion is correct, the needle should advance onto or into the joint, ideally inside the fascia of

Vet-ebooks.com

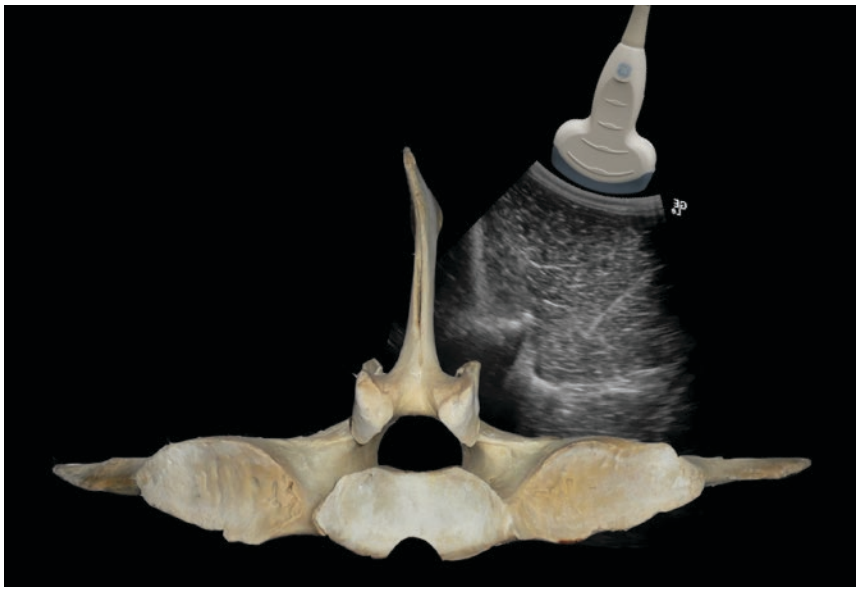


Figure 9.7 A frontal plane ultrasound image superimposed on an anatomical specimen showing the technique to image the caudal thoracic and lumbar IVAs.

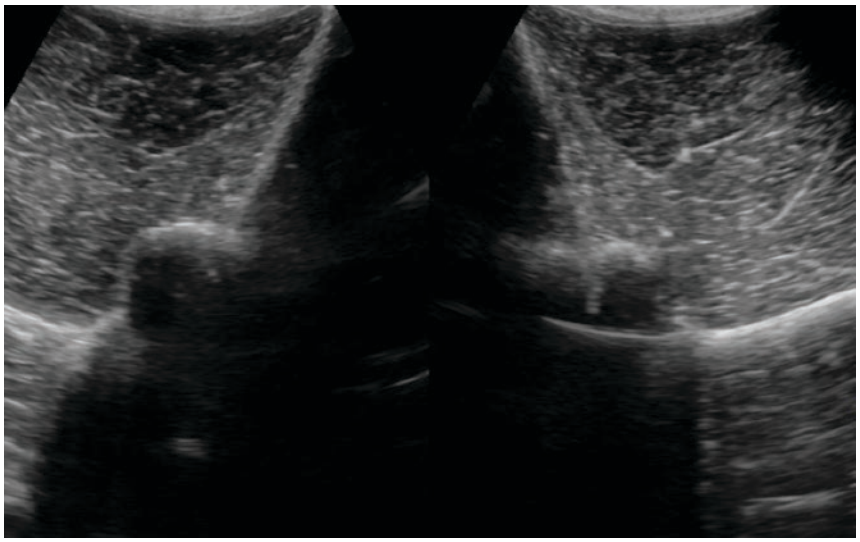


Figure 9.8 Osteoarthritis (OA) can be identified as enlargement and rounding of the IVA. The diseased joint is on the left of this image and is compared to the normal contralateral joint on the right.

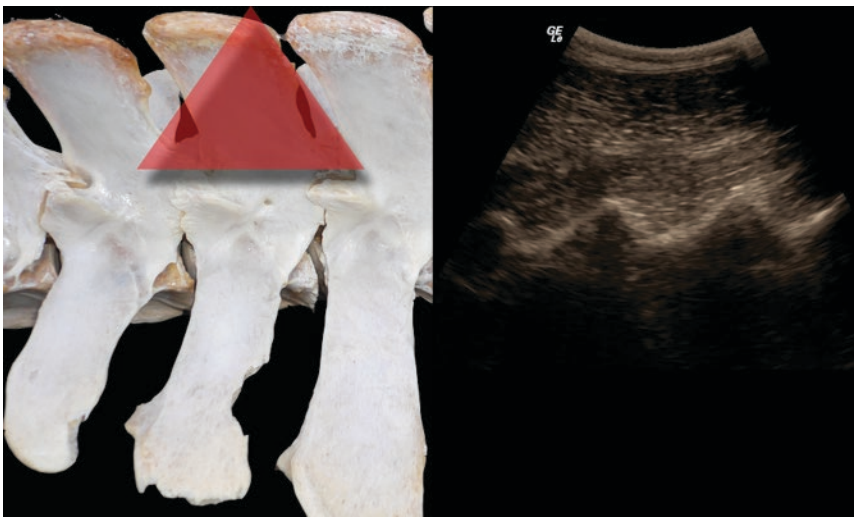


Figure 9.9 A sagittal plane ultrasound image superimposed on an anatomical specimen showing the technique to image the caudal thoracic and lumbar IVAs.

Vet-ebooks.com

multifidus. The transducer will need to be tilted toward the operator to allow room for the needle to be maneuvered and for the needle to be visualized.

The Epaxial Musculature

Views of the epaxial musculature of the thoracic and lumbar regions are easy to obtain at the same time as those of the SSpL. The longissimus and mulitfidus are particularly satisfying to image and, although clinical disease is rare, they are important during ultrasound-guided injection of the facet joints. Muscle atrophy can be appreciated and documented. Atrophy due to denervation injury is rare but an important differential diagnosis when cases present with muscle asymmetry. The characteristic marked increase in echogenicity throughout the affected muscle due to retention of connective tissue over muscle fibers, along with being able to rule out structural damage to the associated bony structures, may encourage an earlier return to exercise and the use of physiotherapy when prolonged rest is contraindicated.

Neck

Soft Tissues

The ligamentum nuchae can be imaged at its attachment on the occipital bone, most readily in the longitudinal plane, and appears as other ligamentous structures, with a strong fiber pattern which stands out from the less echogenic muscle tissue surrounding it. Mineralization of the ligament close to its cranial attachment (Figure 9.10) is a reasonably common finding and of uncertain significance in most horses.

In some cases, trauma to the occipital region can result in new bone formation and damage to the tendon of insertion of the semispinalis capitis (Figure 9.11). While undoubtedly painful and restricting in the acute and subacute phases, the cases seen in the author's clinic have returned to full function in the long term. In chronic cases, it can be useful to try to desensitize the region using local anesthetic in order to assess the significance of changes (Figure 9.12).

The muscles of the neck are a common site for post injection abscesses (Figure 9.13). Muscle soreness may precede ultrasonographic abnormalities, but if an abscess forms it produces the typical ultrasound appearance with a relatively uniform fluid-filled structure surrounded by a usually clearly defined boundary or capsule within the muscle tissue. The echogenicity of the abscess will be similar in whichever plane the transducer is positioned, unlike the muscle around it, helping to delineate its borders; it is usually somewhere between fluid and soft tissue in its appearance (Figure 9.14). The ultrasonographic appearance of a longstanding abscess is shown in Figure 9.15.

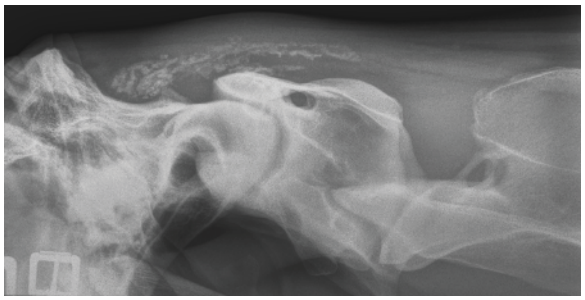


Figure 9.10 Lateral radiograph of the cranial cervical region showing dystrophic mineralisation within the soft tissues.

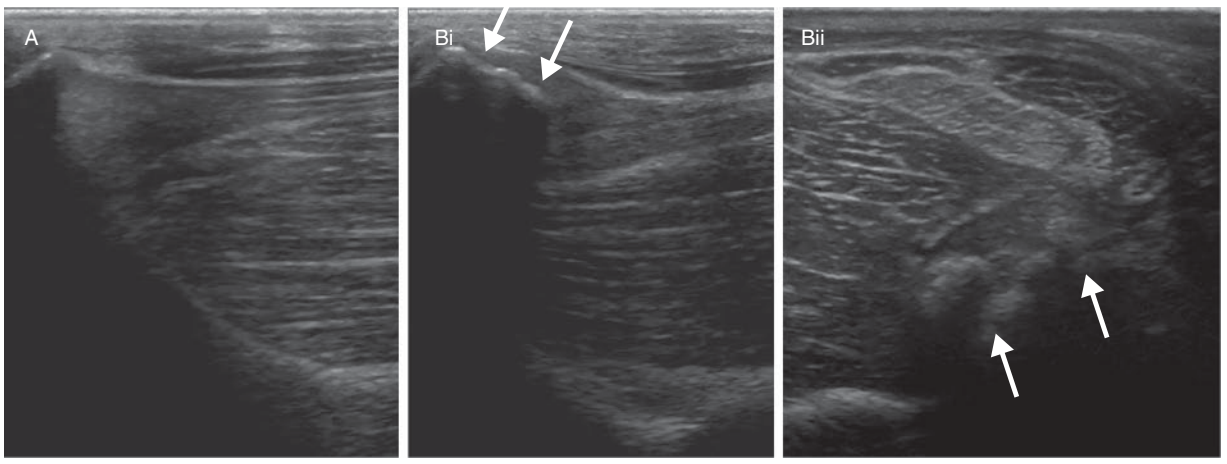


Figure 9.11 (A) Longitudinal image of the soft tissue attachments onto the squamous part of the occipital crest – normal side (rostral to the left). Note the smooth, concave bone surface and the longitudinal fibers of the semispinalis capitis tendon. (B) Abnormal side in longitudinal (left) and transverse (right) planes. Note irregular new bone formation in the attachment of the semispinalis capitis tendon (arrows).

Vet-ebooks.com

In some cases, swelling and infection may result from foreign body penetration. Ultrasonography can be invaluable in assessing the presence and nature of such objects (Figure 9.16)

Bones and Joints

The atlanto-occiptal (AO) joint is an occasional site of synovial sepsis secondary to osteomyeltis (most commonly, in the UK, caused by *Rhodococcus equi*



Figure 9.12 Local anesthetic is injected around an area of soft tissue damage so that the significance of the ultrasonographic changes could be assessed. This horse displayed consistent signs of head shaking which were not alleviated by this procedure.



Figure 9.13 Photograph showing the typical position and appearance of a post injection neck abscess.

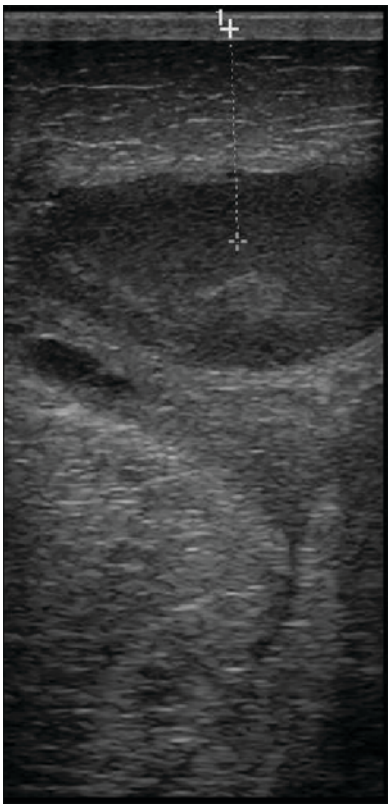


Figure 9.14 Typical ultrasonographic appearance of such an abscess, The callipers are used to aid the surgical approach for drainage (*source*: courtesy of Rob Pilsworth MRCVS).

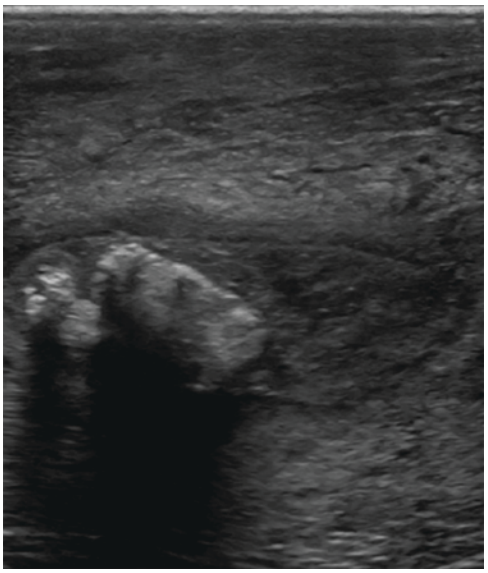


Figure 9.15 Ultrasonograph of a longstanding neck abscess. There is dystrophic mineralization of the soft tissues, which casts an acoustic shadow. More aggressive debridement was necessary in this case because of the extensive fibrosis and mineralized tissue.

Vet-ebooks.com

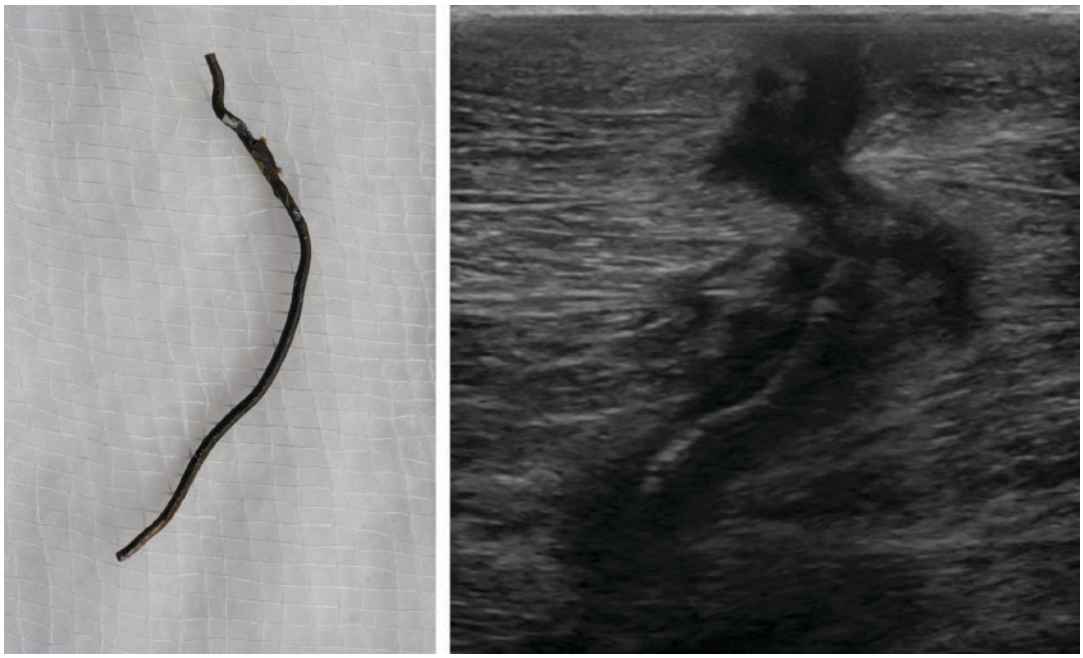


Figure 9.16 A wire embedded in the neck muscle caused a chronic, intermittently draining wound in this horse. The small skin lesion belied the size of the object buried within.

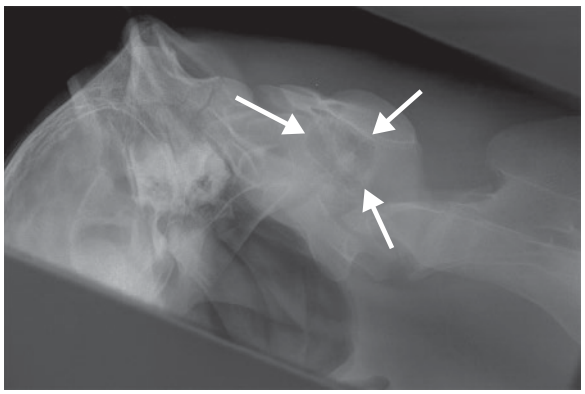


Figure 9.17 Lateral radiograph of the cranial cervical region of a Thoroughbred foal with bone lysis caused by osteomyelitis affecting the first cervical vertebra (arrows).



Figure 9.18 Photograph demonstrating the position of the transducer to obtain a longitudinal image of the atlanto-occiptal (AO) joint.

infection – Figure 9.17). The left and right joints have separate joint capsules, but are said to communicate occasionally, particularly in older horses. Longitudinal and transverse images of the joint can be obtained by placing the transducer to each side of midline (Figure 9.18).

The easiest landmark to identify on the scans beginning in the longitudinal plane is the smooth convex surface of the occipital bone with its thin layer of hypoechogenic cartilage. The joint space can be identified beneath a thin joint capsule that bridges the space to the atlas (Figures 9.19 and 9.20). In cases with synovial sepsis, the joint will be distended and the normally anechogenic fluid will often contain echogenic material, typical of an infected joint, or thickening of the joint capsule (Figure 9.21).

In two cases seen by the author, the infection was resolved with systemic antimicrobials and repeated to and fro lavage of the joint under sedation using ultrasound guidance, followed by injection of antimicrobials into the joint space.

Assessment of the AO region can also be used to facilitate cerebrospinal fluid (CSF) collection and, in neonates, it has been used to estimate CSF pressure in dysmature or premature foals (Figure 9.22).

Ultrasonography is now used commonly for the assessment of the caudal cervical IVAs and, in

Vet-ebooks.com

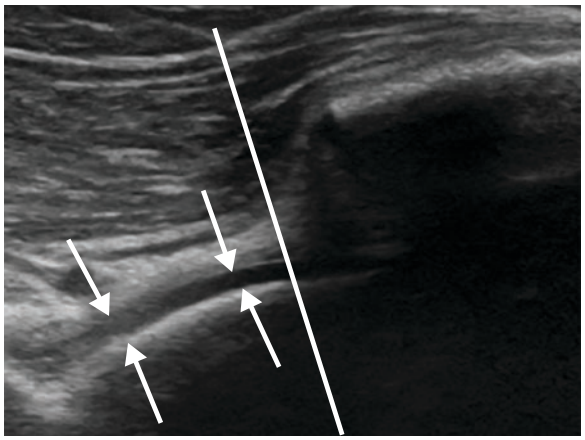


Figure 9.19 Longitudinal image of a normal AO joint. The cartilage overlying the occipital condyles can be seen as thick anechogenic lines (blue arrows). The cranial aspect of the atlas is the linear echogenic surface to the top right. Rostral is to the left.

particular, to facilitate ultrasound-guided injection of the C5/6 and C6/7 joints. Occasionally, trauma will result in fractures involving the joints, the secondary effects of which can be assessed (Figure 9.25). Caudal cervical osteoarthritis (OA) has been described as a cause of fore limb lameness and is recogniszd increasingly as a factor in poor performance cases. Although radiography is still the standard imaging modality for assessment of these joints, ultrasonography can assist radiological interpretation and is invaluable for treating this region. Either linear or microconvex transducers can be used, although the smaller footprint of the latter makes ultrasound-guided injection easier (Figures 9.23 and 9.25).

For ultrasound-guided injection, the horse should be sedated reasonably heavily and made to stand squarely, preferably in stocks. It can be very useful to use a head rest, so that the head and neck remain in the same position throughout the procedure. Two techniques are described, varying in

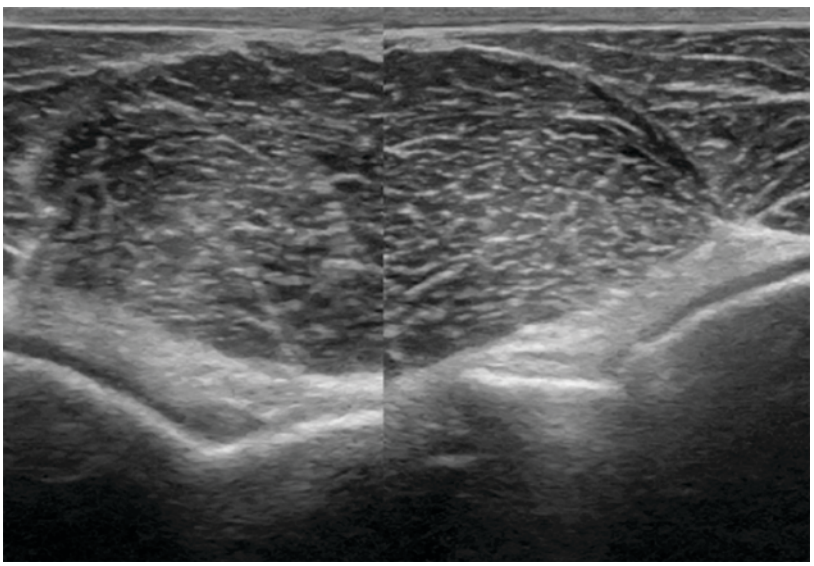


Figure 9.20 Composite transverse image of a normal AO joint. The red bar on Figure 9.19 indicates the position of this image on the longitudinal scan.

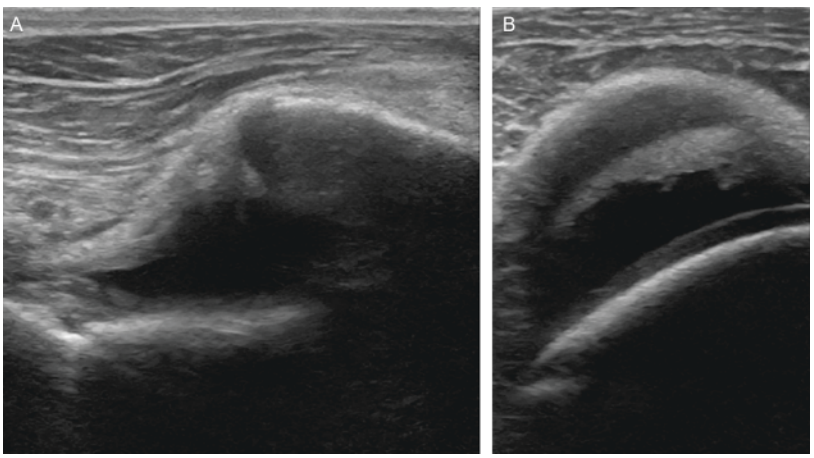


Figure 9.21 Ultrasonograph of the AO joint of the foal shown in Figure 9.17. (A) Longitudinal image. There is distension of the joint and thickening of the synovial lining and joint capsule. The cartilage cannot be seen clearly in this image; this is due to off-incidence artifact and not cartilage loss (compare with (B). (B) Transverse image, once more showing joint distension and synovial hypertrophy. The cartilage is clearly delineated to the right of the picture, but less clear to the left side. Again, this is an artifact and not due to cartilage disease.

Vet-ebooks.com

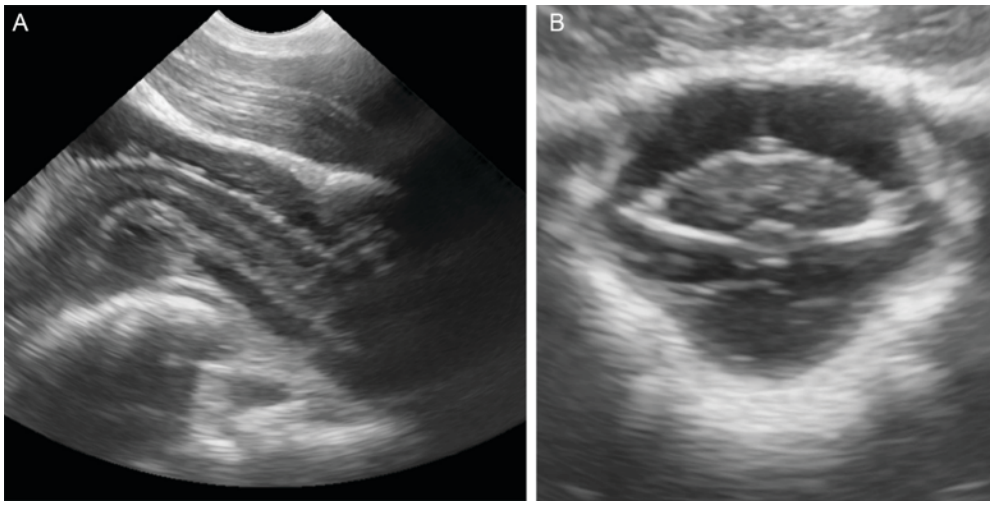


Figure 9.22 Longitudinal (left) and transverse (right) images of the AO region in a neonatal foal illustrating the normal position of the spinal cord within the vertebral canal.



Figure 9.23 In this image, the normal architecture of the intervertebral articulation (IVA) has been severely disrupted due to prolific new bone formation secondary to a fracture of the articular process.

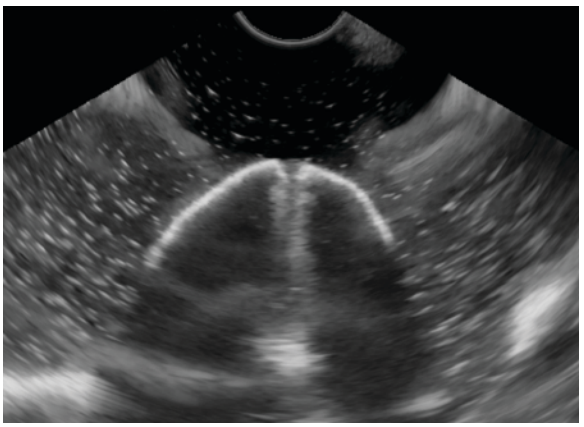


Figure 9.24 Photograph demonstrating the position of a micro-convex transducer to obtain an image of the C5/6 caudal cervical intervertebral articulation.



Figure 9.25 This image was acquired with a micro-convex transducer scanning a specimen in a water bath. Note the regular, clearly demarcated edges of the articular processes forming the borders of an easily recognisable joint space.

Vet-ebooks.com

their ultrasonographic approach to the joints. In one, the transducer is positioned along the long axis of the neck, but the author prefers to image perpendicular to this.

The joints to be treated are imaged before clipping the hair, using liberal application of surgical spirit. The C5/6, C6/7, and C7/T1 joints appear similar and are most easily assessed with a microconvex transducer, although it is possible to proceed with a high-frequency linear probe. In most horses, the musculature of the scapula/shoulder prevents imaging further back than C6/7 but in some patients the C7/T1 articulation can be seen. This should be borne in mind; it is often assumed that the most caudal joint imaged is always C6/7 but this may not be the case. If in doubt, a marker placed on the skin during radiographic assessment can be useful. The transverse processes of the caudal cervical vertebrae are palpated and the transducer placed above these, just in front of the shoulder musculature, oriented vertically to produce a transverse image of the joints. Once the joints have been identified, the hair can be clipped so that the site of injection and contact area for the transducer can be prepared. Once clipped and after a short scrub, a small bleb of local anesthetic is placed at the site of needle placement. The site for insertion of the needle is above (dorsal to) the contact point for the transducer and is estimated by imagining the course of the needle into the joint. However, the main rule is to start high as the angle of the needle direction should be steep to facilitate entry into the joint space which is angled sharply from laterodorsal to medioventral (Figure 9.26).

After placing the bleb, the site is prepared thoroughly. Usually, as it is most common to inject C5/6 and C6/7 on both sides of the neck, both joints on the left side can be prepared first so that they can be scrubbed together and then injected in one sterile procedure and then proceed to the right side.

The author injects 5 mg of triamcinolone acetonide into each joint, drawn up into 1.5 ml sterile saline. Some clinicians prefer to use methylprednisolone but withdrawal times must be taken into consideration in competition horses. A separate 18-gauge 3.5-inch spinal needle is used for each joint. The transducer is covered with a large sterile glove or a sterile probe sleeve, which is held open by the operator while a colleague fills the bottom with sterile ultrasound couplant gel, before the transducer is dropped into the glove or sleeve. A microconvex probe easily fits down one of the fingers of the glove. Sterile couplant gel is applied to the gloved end of the probe and the joint to be injected is visualized; surgical spirit between the skin and probe can also be used. For right-handed clinicians, the probe can be held in the left hand and the needle placed with the right; for the left side it is easier to face toward the rear of the horse (and toward the front of the horse for the right-sided joints). The transducer is positioned so that the joint space is seen at the side of the image, allowing more space to visualize the needle approaching the joint. The needle is pushed through the skin bleb and advanced toward the joint. As mentioned previously, the angle of approach should be steep, mimicking the angle of the joint, to maximize the chance of successful entry (Figure 9.27).

The most important thing to remember during any ultrasound-guided technique is to be *guided by the ultrasound*. Take time to ensure that the needle follows the path of the ultrasound beam – failures are often attributable to the path of the needle diverging from the ultrasound. In some cases, the needle advances easily through the joint capsule and a distinct change in resistance indicates successful centesis. In other cases, the needle encounters bone. If the

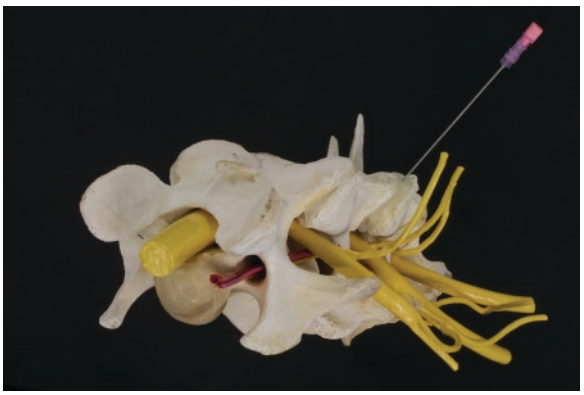


Figure 9.26 Photograph showing the correct orientation for placement of a spinal needle into the left C6/7 IVA. Note the steep angle of approach that follows the angle of the joint, maximizing the chances of successful centesis.

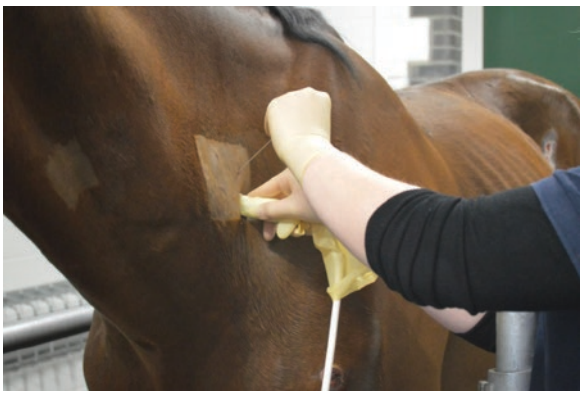


Figure 9.27 Photograph showing correct starting positions for the spinal needle and transducer prior to ultrasound-guided injection of the left C6/7 IVA.

Vet-ebooks.com

ultrasound image indicates that the tip of the needle is close to the joint, it is usually possible to "walk" the needle into the joint. Once into the joint space, avoid advancing the needle too far as it is, in theory, possible to enter the vertebral canal. Removal of the stilette occasionally prompts spontaneous flow of synovial fluid but more commonly aspiration with a syringe is necessary to confirm correct placement (Figure 9.28). Synovial fluid should be aspirated in all cases but, as with other joints, there are occasions when the needle is correctly placed but fluid cannot be obtained. Repeated placements of the needle (without coming back out through the skin – if this is necessary a new needle should be used) should be kept to a minimum, and if the clinician is confident about the position, the joint can be injected without obtaining fluid. Of course, it gets easier with practice. The transducer can be removed while the injection is performed, to allow the hub of the needle to be held with one hand and the syringe with the other during the injection. If the injection is visualized with ultrasound, injection of fluid creates a stream of bubbles which appear as moving hyperechogenic areas. The procedure is repeated for the next joint on the same side before moving equipment to the other side of the horse and starting again.

The horse is treated with a single dose of intravenous non-steroidal anti-inflammatory (usually phenylbutazone or firocoxib). The author usually advises three weeks of restricted turnout following treatment before any further exercise or physiotherapy. In many cases it is useful to suggest that the horse is fed from a height for this three-week period, attaching hay nets to the fencing or similar. This is based on the observation that most affected horses display difficulty/discomfort when reaching to the floor; several cases displayed acute episodes of either severe pain or neurological signs after grazing. It seems logical therefore to limit this (admittedly very normal activity!) for a short time after treatment.

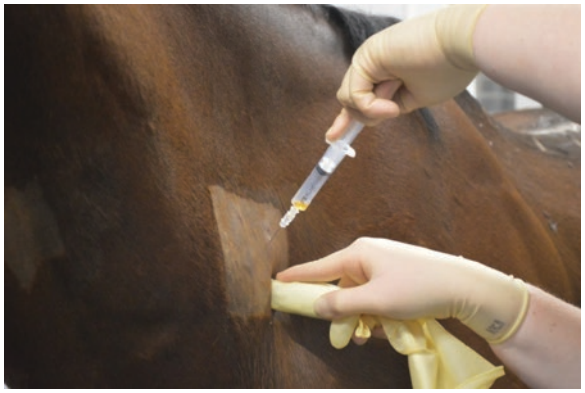


Figure 9.28 Photograph showing ultrasound-guided placement of a spinal needle into the left C6/7 IVA and successful aspiration of joint fluid, prior to medication.

Recommended Reading

Berg, L.C., Nielsen, J.V., Thoefner, M.B. et al. (2003). Ultrasonography of the equine cervical region: A descriptive study in eight horses. *Equine Veterinary Journal* 35(7): 647–655.

Bucca, S., Fogarty, U., and Farelly, B.T. (2008). Ultrasound examination of the atlanto-occipital space. In: *Color Atlas of Diseases and Disorders of the Foal* (ed. S.B. McAuliffe and N.M. Slovis). Philadelphia, PA: Saunders Elsevier.

Cousty, M., Firidolfi, C., Geffroy O. et al. (2011). Comparison of medial and lateral ultrasound-guided approaches for periarticular injection of the thoracolumbar intervertebral facet joints in horses. *Veterinary Surgery* 40(4): 494–499.

Denoix, J.M. (1999). Spinal biomechanics and functional anatomy. *Veterinary Clinics of North America: Equine Practice* 15(1): 27–60.

Fuglbjerg, V., Nielsen, J.V., Thomsen, P.D. et al. (2010). Accuracy of ultrasound-guided injections of thoracolumbar articular process joints in horses: A cadaveric study. *Equine Veterinary Journal* 42(1): 18–22.

Girodoux, M., Dyson, S., and Murray, R. (2009). Osteoarthritis of the thoracolumbar synovial intervertebral articulations: Clinical and radiographic features in 77 horses with poor performance and back pain. *Equine Veterinary Journal* 41: 130–138.

Nielsen, J.V., Berg, L.C., and Thoefner, M.B. et al. (2003). Accuracy of ultrasound-guided intra-articular injection of cervical facet joints in horses: A cadaveric study. *Equine Veterinary Journal* 35: 657–661.

Reef, V.B., Whittier, M., and Allam, L.G. (2004). Joint ultrasonography. *Clinical Techniques in Equine Practice* 3: 256–267.

Ricardi, G. and Dyson, S. (1993). Forelimb lameness associated with radiographic abnormalities of the cervical vertebrae. *Equine Veterinary Journal* 25: 422–426.

Sgorbini, M., Marmorini, P., Rota, A. et al. (2011). Ultrasound measurements of the dorsal subarachnoid space depth in healthy trotter foals during the first week of life. *Journal of Equine Veterinary Science* 31: 41–43.

Sisson, S. and Grossman, J.D. (1948). *The Anatomy of the Domestic Animals*. Philadelphia, PA: W.B. Saunders.

Vet-ebooks.com

10

Ultrasonography of the Head

Debra Archer

University of Liverpool, Wirral, UK

Introduction

Ultrasonographic assessment of the head has most frequently been utilized to image the ocular and periocular structures (see Chapter 25). Imaging modalities such as radiography, endoscopy, and, increasingly, computed tomography are more commonly utilized to image other structures of the head. This is largely due to the fact that a number of anatomical areas of interest, such as the nasal passages, paranasal sinuses, and cranium, are encased within bone, precluding ultrasonographic assessment of these structures. In addition, soft tissue structures, such as the guttural pouch, are air-filled in the normal horse, which limits ultrasonographic assessment of them. Bony structures such as the rami of the mandible may impede access when attempting to image soft tissue structures located in the caudal and more ventral regions of the head. However, ultrasonography has been shown to be a useful imaging modality in assessment of the temporomandibular joint and as an adjunctive technique for assessing the larynx and adjacent structures. Superficially located and other accessible soft tissue structures, such as salivary glands, masseter muscle, and tongue, can also be assessed ultrasonographically, as can the surface of the thin bones of the skull. Therefore, whilst its applications may be relatively limited in imaging of the non-ocular structures of the head, ultrasonography can provide valuable adjunctive information when assessing a variety of structures. Ultrasound guided procedures are likely to become more frequently utilized in the equine head as part of therapeutic interventions and assisting placement of certain nerve blocks.

Sedation may not be required in all horses but may improve image acquisition, particularly where the larynx is being assessed, to avoid movement artifact and improve patient compliance.

Temporomandibular Joint

Normal Anatomy and Scanning Technique

Scanning the temporomandibular joint requires a 7.5–10 MHz linear or convex transducer and a standoff may be required in thin horses with little periarticular fat. The standard views are caudolateral, lateral, and rostrolateral. Structures that can be visualized include all or part of the temporal bone, including the retro-articular process (on the caudolateral view), the mandibular fossa (on the lateral view), and the articular tubercle (on the rostrolateral view). Additionally, the condylar process of the mandible and the articular disc, cartilage, and fluid, as well as the joint capsule can be seen, along with the parotid salivary gland, parotidoauricularis muscle, and the transverse facial vein (on the rostrolateral view).

For the caudolateral view, place the transducer (with or without a standoff) over the dorsal aspect of the vertical ramus of the mandible centered over the temporomandibular joint (TMJ) in a transverse position (Figure 10.1). The long axis of the transducer should be positioned in a rostroventral to dorsocaudal direction so that it is oriented parallel to the frontal and nasal bones. The condylar process of the mandible and retro-articular process of the temporal bone can be visualized as thin hyperechoic lines (Figure 10.2). Sandwiched between these two bones

Atlas of Equine Ultrasonography, Second Edition. Edited by Jessica A. Kidd, Kristina G. Lu and Michele L. Frazer.
© 2022 John Wiley & Sons Ltd. Published 2022 by John Wiley & Sons Ltd.
Companion Website: www.wiley.com/go/kidd/atlas

Vet-ebooks.com

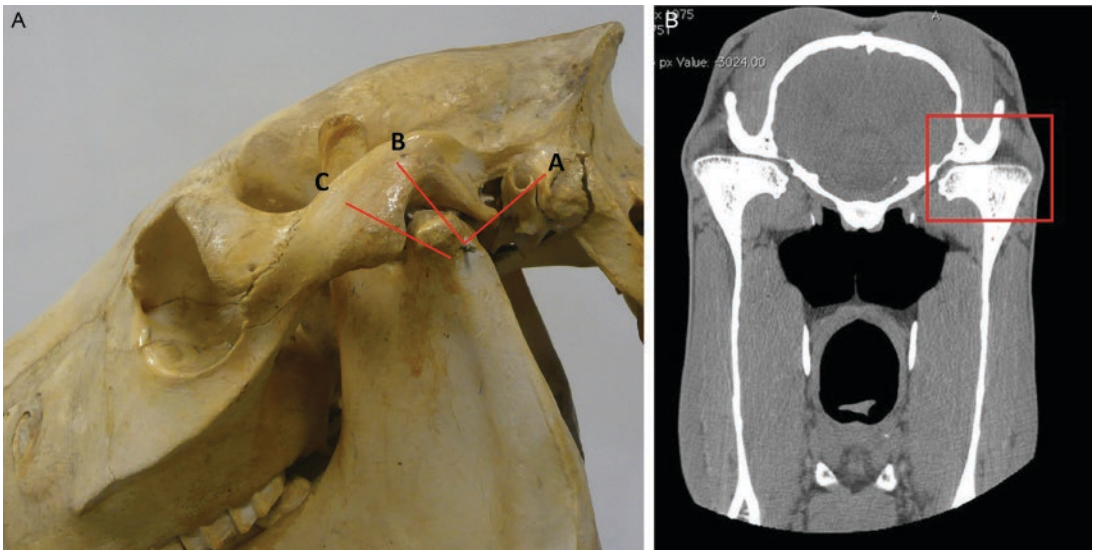


Figure 10.1 (A) Image of a cadaver skull of a horse demonstrating the position of the transducer over the temporomandibular joint in order to obtain caudolateral (1), lateral (2), and craniolateral (3) images. (B) Computed tomography cross-sectional image of a horse's head. The red box denotes the temporomandibular joint region; ultrasonographic assessment is limited to the lateral (abaxial) portions of the joint.

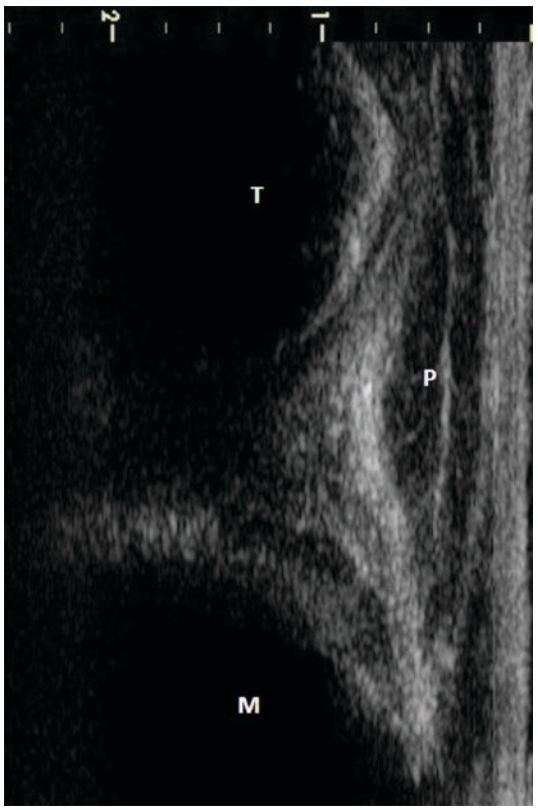


Figure 10.2 Caudolateral ultrasound image of the temporomandibular joint in a normal adult horse obtained using a linear transducer operating at 10 MHz. The retroarticular process of the temporal bone (T), mandibular condyle (M), and overlying parotid salivary gland (P) can be visualized. The intra-articular disc is triangular in shape and is sandwiched between these structures.

is the fibrocartilaginous intra-articular disc, which has a homogeneous, moderate echogenicity, similar to that of the menisci in the stifle joint (i.e., midway between muscle and fascial echogenicity). The base of this triangular-shaped structure is abaxial and approximately 2 cm wide in the adult horse; the disc then narrows axially. The disc also narrows toward the rostral aspect of the joint. Articular cartilage can be visualized as a hypoechoic layer between the bone and the intra-articular disc; this may be up to 3 mm thick in foals and is often barely visible in adult horses. It is uncommon to visualize any articular fluid. The parotid salivary gland lies superficial to these structures and the more hyperechoic TMJ capsule fibers can be seen to merge with this structure. The parotidoauricularis muscle can also be imaged in this view.

For the lateral view, rotate the probe by 90 degrees so that it is now in a rostro-dorsal to caudo-ventral orientation (Figure 10.1). The same structures can be visualized, with the mandibular fossa of the temporal bone now being visualized dorsally and the intra-articular disc again having a triangular shape (Figure 10.3). The parotidoauricularis muscle can sometimes be imaged in this view.

For the rostrolateral view, the whole probe should be moved rostrally by 1–2 cm and the dorsal tip rotated a further 30 degrees in a rostral direction (Figure 10.1). The articular tubercle of the temporal bone is visible dorsally and the mandibular condyle ventrally. The intra-articular disc now appears as a

Vet-ebooks.com

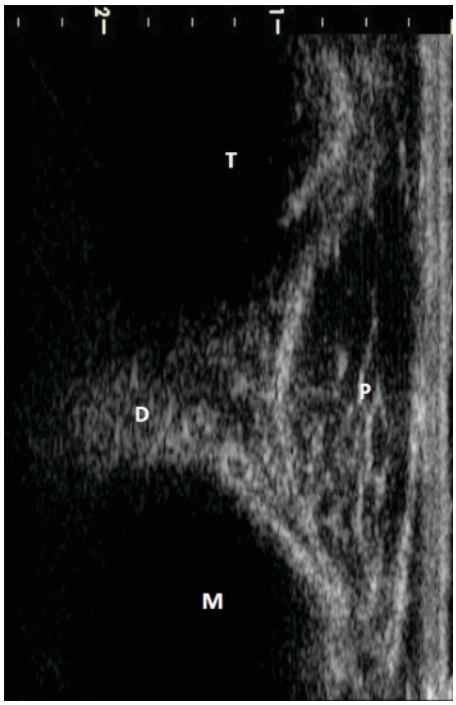


Figure 10.3 Lateral ultrasound image of the temporomandibular joint in a normal adult horse. The superficial bone and thin layer of cartilage of the mandibular fossa of the temporal bone (T) and mandibular condyle (M) can be visualized together with the triangular-shaped intra-articular disc (D) and the more superficially positioned parotid salivary gland (P).

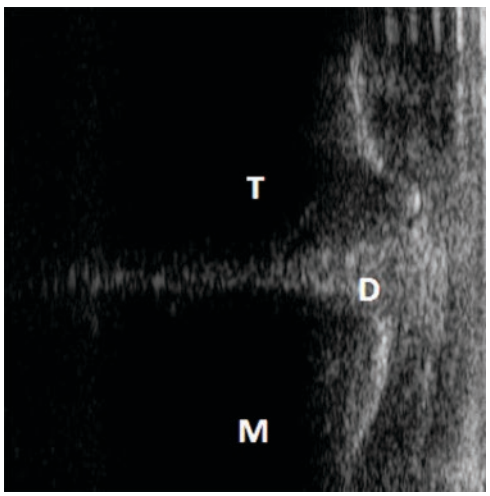


Figure 10.4 Rostral ultrasound image of the temporomandibular joint in a normal adult horse. The intra-articular disc (D) is more flattened in appearance and is positioned between the articular tubercle of the temporal bone (T) and the mandibular condyle (M).

thin wedge sandwiched between these two structures, and there is little in the way of soft tissue structures overlying this aspect of the joint (Figure 10.4). The transverse facial vein can often be visualized ventrally in this view.

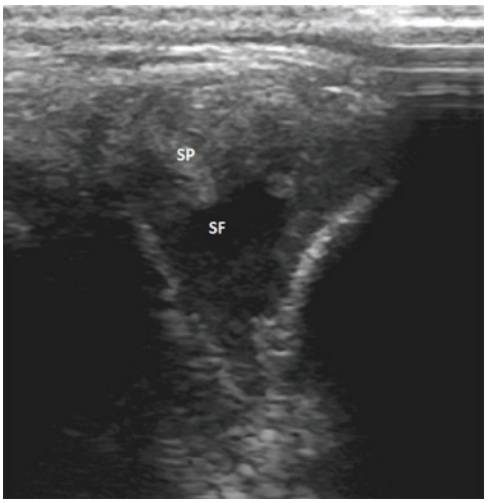


Figure 10.5 Lateral ultrasound image of an abnormal temporomandibular joint with dorsal to the right and ventral to the left of the image. There is increased synovial fluid (SF) within the joint and evidence of synovial membrane proliferation (SP). (*Source:* Image courtesy of Katie Garrett).

Ultrasonographic Abnormalities

Any disruption to the normal, smooth periarticular outline of the mandibular condyle or temporal bone or disruption to the substance of the intra-articular disc, for example tears or focal hypoechogenicity, is considered to be highly indicative of pathology within the TMJ (Figure 10.5).

Larynx

Normal Anatomy and Scanning Technique

Ultrasonography of the larynx requires an 8.5–12.5 MHz linear array or convex transducer. The standard views are rostrovental, midventral, caudoventral, and caudolateral. Structures that can be visualized include parts of the basihyoid bone including the lingual process, portions of the ceratohyoid and thyrohyoid bones, the base of the tongue, the insertion of the thyrohyoid muscles, the ventral and abaxial aspects of the thyroid and cricoid cartilages, portions of the cricoarytenoideus lateralis, cricoarytenoideus dorsalis and vocalis muscles, the vocal cords, and the abaxial aspects of the arytenoid cartilages.

To scan the larynx, the horse's head should be held in a slightly extended position and the transducer initially positioned over the ventral aspect of the larynx. For the rostrovental view, the transducer should be

Vet-ebooks.com



Figure 10.6 Positioning of the transducer in order to obtain the ventral transverse view of the larynx. This is facilitated by positioning the patient's head in a slightly extended position in order to position the larynx more caudally in relation to the mandible.

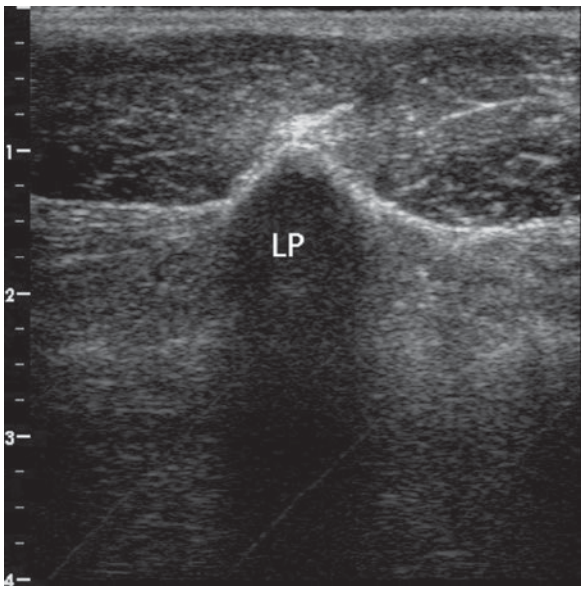


Figure 10.7 Transverse ventral ultrasound image imaged at the rostroventral window (just rostral to the base of the basihyoid bone) of the larynx in a normal adult horse using a linear transducer operating at 10 MHz. The surface of the lingual process (LP) of the basihyoid bone is identified as a semicircular hyperechoic line.

placed in a transverse position immediately rostral to the base of the basihyoid bone between the rami of the mandible (Figure 10.6). The lingual process of the basihyoid bone can be identified (Figure 10.7). In some horses, narrow width of the intermandibular space may prevent this view from being obtained if a linear transducer is used. The lingual process can be

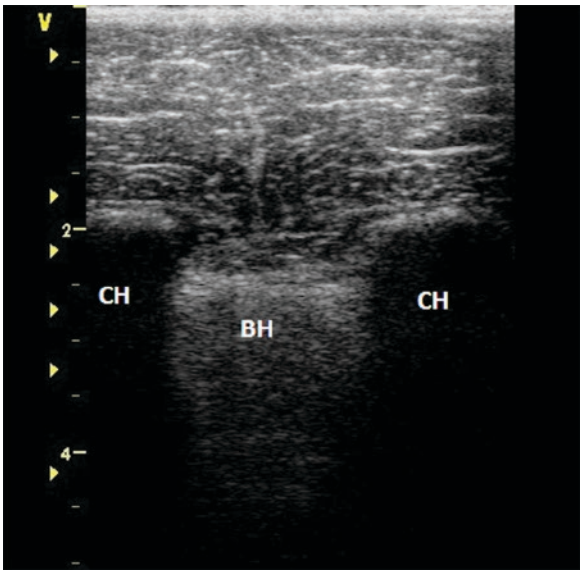


Figure 10.8 Transverse ventral ultrasound image imaged at the rostroventral window of the larynx in a normal adult horse with the transducer angled more rostrally. The base of the basihyoid bone (BH) appears as a linear hyperechoic line, and the ventral surface of the paired ceratohyoid bones (CH) can be seen as smaller linear hyperechoic structures that can be followed as they course in a dorsal direction.

followed caudally to the body of the basihyoid bone and, by rotating the transducer in a more longitudinal orientation, the ceratohyoid bones may be visualized as two, flat hyperechoic structures that course in a dorsal direction (Figure 10.8). The base of the tongue can be visualized but may require use of a lower-frequency transducer (2–5 MHz) to assess its full depth. The same structures can be visualized on the ventral midline (median) and just off the midline (paramedian) in a longitudinal view.

To obtain the midventral view, keep the transducer oriented longitudinally on the ventral midline, and by moving caudally the transducer should be positioned over the space between the basihyoid bone and thyroid cartilage. The caudal part of the basihyoid bone and rostral tip of the thyroid cartilage can be visualized at this location (Figure 10.9). Moving the transducer off midline (paramedian) allows the insertion of the thyrohyoid muscles onto the abaxial aspect of the thyroid cartilage to be visualized (Figure 10.10), and the thyrohyoid bones can be seen to course in a dorsocaudal direction.

To obtain the caudoventral view, move the transducer back into a transverse position on the ventral midline and move further caudally so that it overlies the cricothyroid notch. The vocal folds can be visualized as paired, hyperechoic, circular/triangular structures (Figure 10.11). Air within the lumen of the rima glottidis casts an acoustic shadow between these structures. By

Vet-ebooks.com

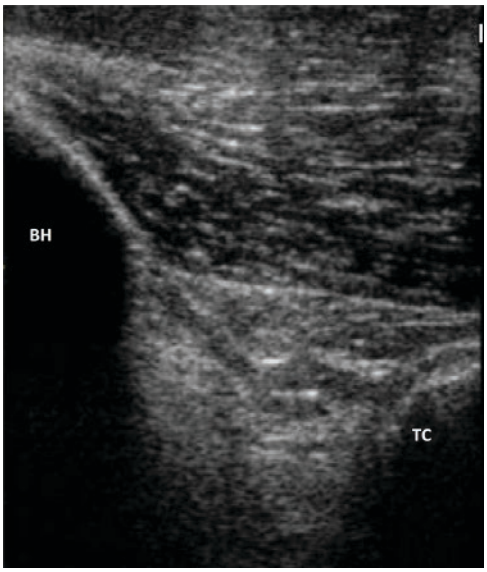


Figure 10.9 Longitudinal ultrasound image of the ventral midline of the larynx at the mid-ventral window. The caudal aspect of the basihyoid bone (BH) and cranial aspect of the thyroid cartilage (TC) can be visualized. Cranial is to the left of this image.

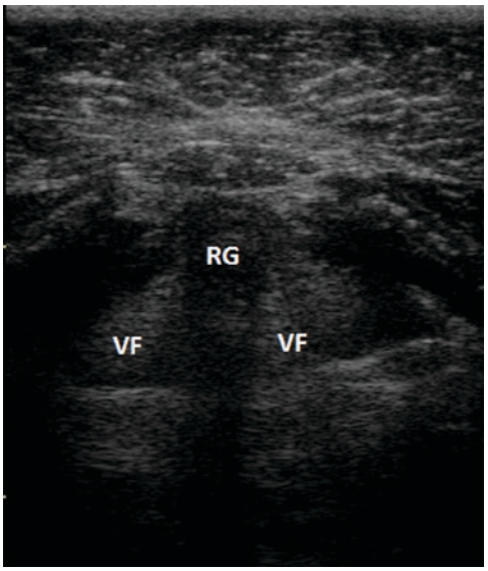


Figure 10.11 Transverse ultrasound image of the ventral aspect of the larynx at the cricothyroid notch (caudoventral window). Ventral is to the top of this image. Left and right vocal folds (VF) can be visualized in cross-section, with the rima glottidis (RG) lying between the two structures.

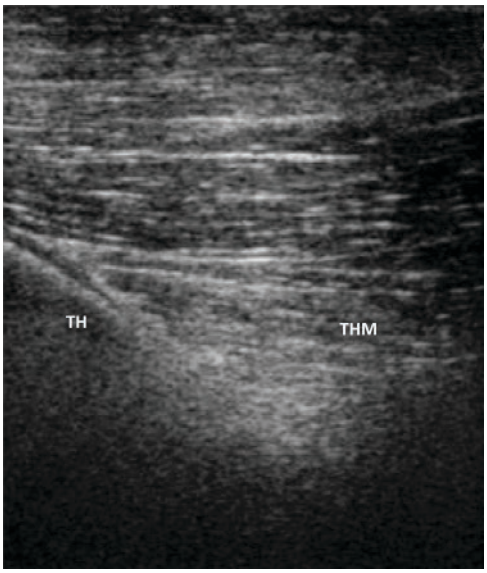


Figure 10.10 Longitudinal ultrasound image of the ventrolateral larynx; the insertion of the thyrohyoid muscle (THM) onto the abaxial aspect of the thyrohyoid bone (TH) can be visualized.



Figure 10.12 Positioning of the transducer in order to obtain the lateral transverse view of the larynx. This is facilitated by positioning the patient's head in a slightly extended position in order to position the larynx more caudally in relation to the mandible.

temporarily occluding the horse's nostrils, the patient can be made to take deeper respirations, enabling the vocal cords to be assessed dynamically.

The caudolateral view can be more technically challenging to obtain. Keeping the horse's head slightly extended and flexing the neck laterally away from the side being imaged can assist imaging of this region. Rotating the transducer so that it is in a longitudinal position (Figure 10.12) and moving dorsolaterally over the abaxial aspect of the larynx, the abaxial portions of the thyroid, cricoid, and arytenoid cartilages can be imaged (Figure 10.13). The cricoarytenoideus lateralis and vocalis muscles can be seen as roughly ovoid structures that lie deep to the thyroid and cricoid cartilages but superficial to the arytenoid cartilage. Additionally, the cricothyroid

Vet-ebooks.com

articulation can be assessed. Rotating the transducer into a transverse plane (Figure 10.14), enables the attachments of the cricoarytenoideus lateralis and vocalis muscles onto the bell-shaped contour of the arytenoid cartilage to be visualized. By moving the transducer more dorsally and angling the transducer slightly ventrally, the muscular process of the arytenoid cartilage, cricoarytenoid articulation, and lateral portion of the cricoarytenoideus dorsalis muscle can be imaged in some individuals.

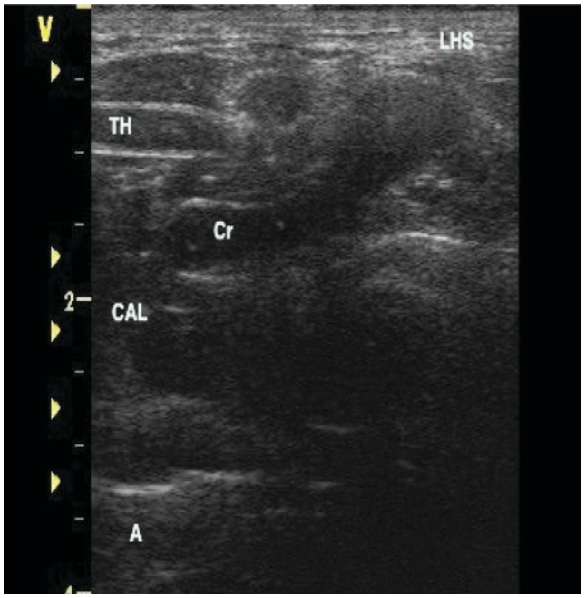


Figure 10.13 Longitudinal ultrasound image of the left lateral larynx centered over the abaxial aspects of the thyroid and cricoid cartilages. Cranial lies to the left and caudal to the right of this image. The caudodorsal abaxial portion of the thyroid cartilage (TH) and rostrodorsal abaxial portion of the cricoid cartilage (Cr) can be visualized, together with the cricoarytenoideus lateralis muscle (CAL) and ipsilateral arytenoid cartilage (A). (*Source:* Image courtesy of Neil Townsend).



Figure 10.14 Positioning of the transducer in order to obtain the dorsal longitudinal view of the larynx. This is facilitated by positioning the patient's head in a slightly extended position in order to position the larynx more caudally in relation to the mandible.

Ultrasonographic Abnormalities

Ultrasonographic examination of the larynx can provide important complementary or adjunctive information in a number of pathological conditions, including arytenoid chondritis (Figure 10.15), recurrent laryngeal neuropathy, congenital abnormalities such as fourth branchial arch defects (Figure 10.16), basihyoid bone malformation or cyst-like malformations of the laryngeal/tracheal cartilages, infection of the perilaryngeal soft tissue structures, or osteomyelitis of the basihyoid bone, and as a potential predictor of the likelihood of dorsal displacement of the soft palate (DDSP).

Tongue

Normal Anatomy and Scanning Technique

The rostral and mid portions of the tongue can be imaged by placing a linear 5–7.5 MHz transducer directly onto its dorsal surface after placing a Haussman gag and using an intra-oral approach, or by exteriorizing the rostral portion of the tongue. The mouth should be flushed with water to remove ingesta from the oral cavity and in order to reduce movement artifact; this is most easily performed following sedation of the horse. The tongue can be imaged in longitudinal and cross-sectional views (Figures 10.17 and 10.18). The more caudal portions, base of the tongue, and sublingual



Figure 10.15 Transverse ultrasound image of the lateral aspect of the larynx in a horse with arytenoid chondritis. Dorsal lies to the left and ventral to the right of this image. The arytenoid cartilage (A) lies in the center of this image and is enlarged, has an irregular contour, and has increased echogenicity within its substance. (*Source:* Image courtesy of Katie Garrett).

Vet-ebooks.com

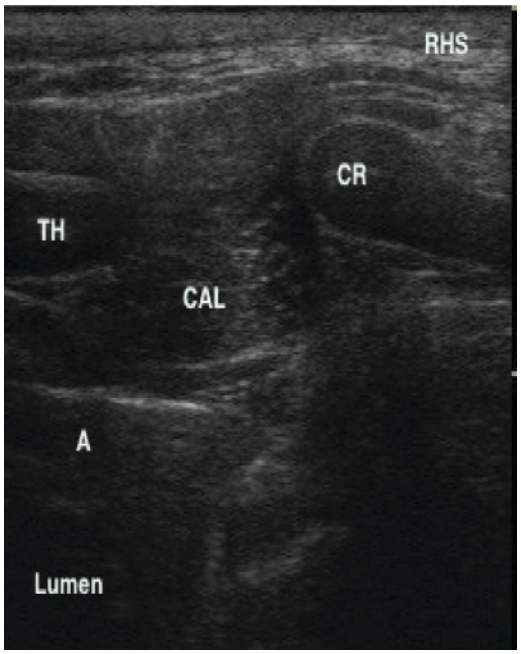


Figure 10.16 Longitudinal ultrasound image of the right lateral larynx in a horse with a fourth branchial arch deformity. The transducer is centered over the abaxial aspects of the thyroid (TH) and cricoid (CR) cartilages. The right cricothyroid articulation is absent and there is an abnormally wide space between the two cartilages in which the right cricoarytenoideus lateralis (CAL) muscle is visualized (in contrast to Figure 10.13). The ipsilateral arytenoid cartilage (A) lies abaxial to these structures. (*Source:* Image courtesy of Neil Townsend).

musculature can be examined using a submandibular approach, placing the transducer between the mandibular rami. Transducer frequencies of 5–10 MHz are required, depending on the size of the horse and depth required. The horse's head may be positioned in a neutral or slightly extended position and the tongue should be assessed in longitudinal and transverse planes (Figure 10.19). The transverse view may be impeded in smaller horses where a linear transducer is being used if the mandibular rami are positioned relatively closely together, thereby preventing physical contact of the probe with the soft tissues in this region.

The body of the tongue has a homogeneous, relatively hypoechoic appearance, and in transverse views, vascular structures can be imaged within its substance as circular hypoechoic structures. In a longitudinal view, the muscle fibers have a more hyperechoic, slightly wave-like appearance. The genioglossus muscles can also be visualized as parallel structures with a similar echogenicity, that lie superficial to the base of the tongue.

Ultrasonographic Abnormalities

Ultrasonographic assessment of the tongue may be helpful in cases of suspected foreign body penetration (usually metallic or wood in nature) or abscess formation within the tongue and adjacent structures.



Figure 10.17 Transverse ultrasound image of the rostral portion of the tongue with a linear transducer operating at 7.5 MHz placed directly onto the dorsal aspect of the tongue. The tongue has a relatively homogeneous echogenic appearance and vascular structures appear as circular hypoechoic structures within its substance and on the ventral aspect of the tongue.

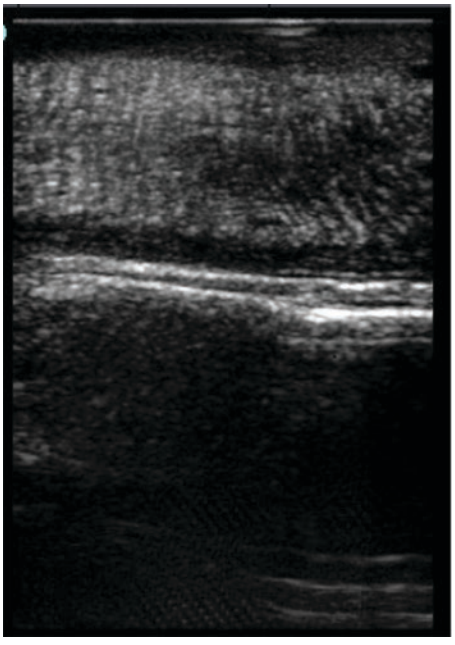


Figure 10.18 Longitudinal ultrasound image of the rostral portion of the tongue with a linear transducer operating at 7.5 MHz placed directly onto the dorsal aspect of the tongue. The muscle fibers have a slightly more echogenic, wave-like appearance.

Intra-operatively, ultrasonography may assist localization and removal of foreign bodies (particularly those that are radiolucent) within the tongue and adjacent soft tissue structures.

Vet-ebooks.com

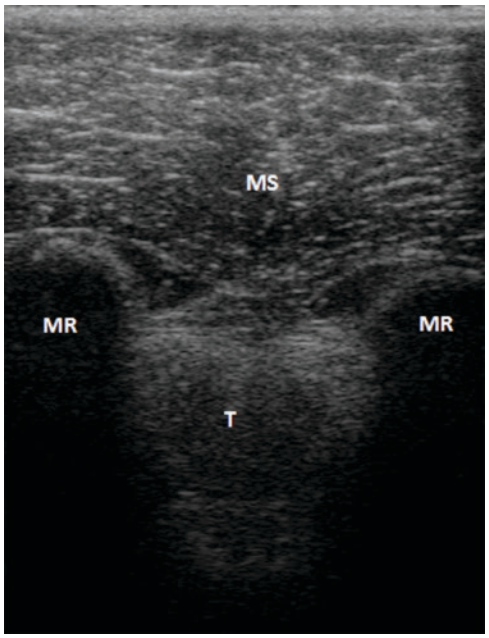


Figure 10.19 Transverse ultrasound image of the base of the tongue (T) and associated musculature (MS) obtained using a linear probe operating at 5 MHz positioned on the midline of the ventral aspect of the head between the rami of the mandible (MR) (submandibular view).

Salivary Glands

Normal Anatomy and Scanning Technique

The parotid gland and its duct can be imaged using a 6–10 MHz transducer set at a depth of around 4–8 cm. With the transducer in a longitudinally oriented plane over the abaxial aspect of the cranial cervical region just caudal to the vertical ramus of the mandible and cranial to the wing of the atlas, the substance (parenchyma) of the gland has a relatively hypoechoic appearance and lobules can be seen enclosed within more hyperechoic fascial tissue (Figure 10.20). The mandibular salivary glands can be imaged axial to the parotid salivary gland and abaxial to the ipsilateral guttural pouch. Axial to the parotid and mandibular salivary glands lie the ipsilateral guttural pouch and retropharyngeal lymph nodes. The parotid salivary duct can be imaged as it courses across the ventral aspect of the mandible, and in a rostro-dorsal direction across the lateral aspect of the mandible alongside the facial nerve and vein. Unless pathologic distension is present, this structure can be difficult to visualize. The sublingual salivary glands lie superficial to the base and midbody of the tongue and can be imaged via a submandibular approach (see section on the Tongue). Both are smaller than the parotid gland and are more difficult to visualize in the normal horse.

Ultrasonographic Abnormalities

Ultrasonography can assist diagnosis and assessment of obstructive sialolithiasis, foreign bodies, abscess formation, neoplastic infiltration, and generalized inflammation of the gland.

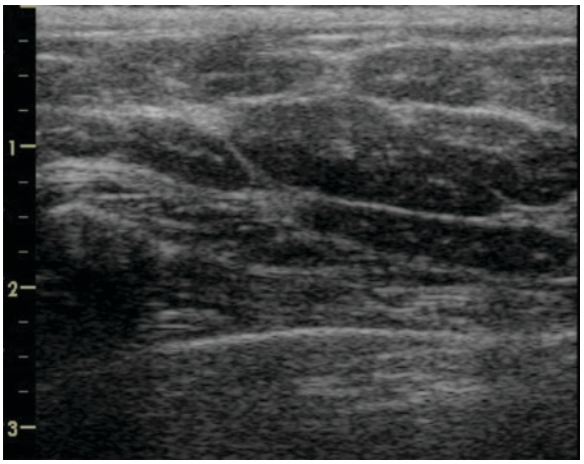


Figure 10.20 Transverse ultrasound image of the parotid salivary duct with a linear transducer operating at 10 MHz positioned vertically over the caudal aspect of the ventral ramus of the mandible. The substance of the gland is relatively hypoechoic and the lobules are enclosed within hyperechoic fascial tissues.

Assessment of Other Structures of the Head

The outline of the skull bones and normal foraminae can be visualized as a thin hyperechoic line. The normal vascular structures that run on the superficial aspect of the head, e.g., transverse facial vein and artery, are consistent in appearance with other vascular structures. Lymph nodes are visualized as ovoid, small structures with a homogeneous soft tissue echogenicity with a discrete more hyperechoic capsule. Ultrasonographic evaluation of pathological swellings of the head, particularly those of soft tissue density, can be particularly helpful. This may assist identification of abscesses, hematomas, dentigerous cysts, or soft tissue swellings, such as nasal atheromas or intra-oral masses. Ultrasonographic evaluation of swellings associated with draining tracts due to the presence of a foreign body or formation of a bony sequestrum (Figures 10.21 and 10.22) can provide useful diagnostic information. Ultrasonography can also assist diagnosis and management of fractures to the thin bones of the skull, which may be difficult to visualize radiographically (Figures 10.23 and 10.24), and can provide adjunctive information in the assessment of mandibular fractures (Figures 10.25 and 10.26) and masses (Figures 10.27 and 10.28).

Vet-ebooks.com



Figure 10.21 Dorsoventral radiograph obtained in a horse with a facial swelling associated with a draining tract where a portion of sequestered bone is evident (arrow).

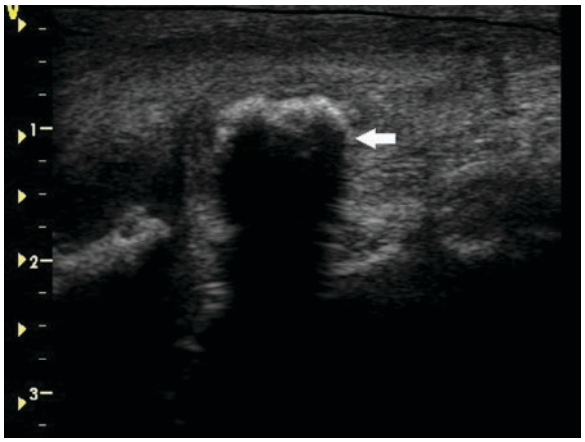


Figure 10.22 Ultrasound image of the same horse as in Figure 10.21. Discontinuity of the hyperechoic outline of the maxillary bone is evident on an ultrasound image of the site, consistent with a bone sequestrum (arrow). Ultrasonographic assessment assisted in more accurately localizing the site and assessing the depth and size of the sequestrum prior to surgical removal.

Ultrasound Guided Procedures

Ultrasound guided procedures are common in human medicine and are being increasingly adapted for use in the equine head. Use of a sterile probe cover enables ultrasound to be easily utilized whilst maintaining a sterile field. In addition to assisting identification of normal and abnormal anatomical structures, ultrasound may be utilized to identify specific nerves in the head for regional anesthesia or therapy (e.g., PENS; percutaneous electrical nerve stimulation). Visualization of the nerve and important adjacent structures prior to and during placement of the probe or needle is a key advantage over "blind" techniques. Ultrasound guided placement of PENS probes as therapy for trigeminal-mediated headshaking is important to avoid penetration of the infraorbital nerve during therapy, which would likely elicit an extreme reaction from the patient.

Ultrasound guided nerve blocks have been shown in people to reduce rates of complications, time taken

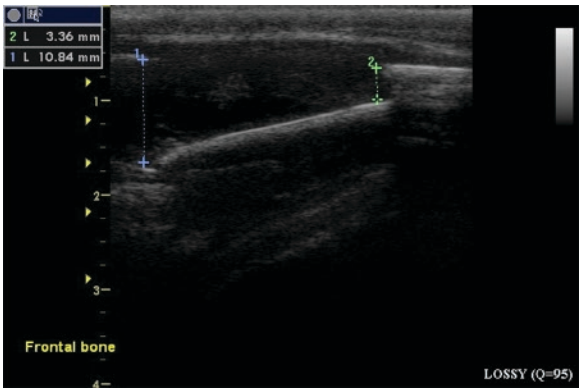


Figure 10.23 Ultrasound image of the frontal bone in a horse that sustained an open, depressed fracture of the skull. This enabled the size and shape of the fragment, together with the depth of depression into the paranasal sinuses to be accurately evaluated prior to surgical management (Figure 10.24).



Figure 10.24 Surgical management of the depressed fracture of the skull of the horse in Figure 10.23.

Vet-ebooks.com

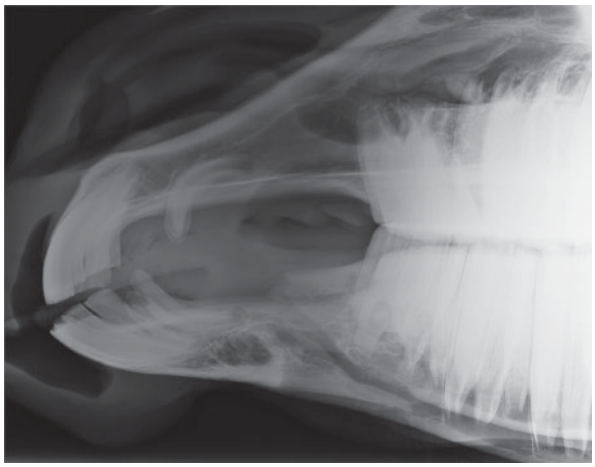


Figure 10.25 Latero-lateral radiograph of a horse that had sustained an open, oblique fracture of the horizontal ramus of the mandible.

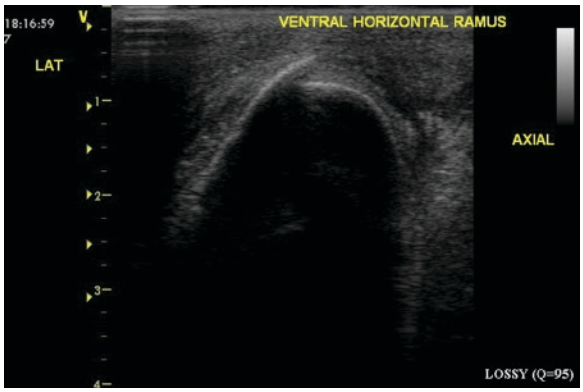


Figure 10.26 Ultrasonographic assessment of the mandible of the horse in Figure 10.25 demonstrates the discontinuity in the hyperechoic surface of the mandible consistent with a fracture.

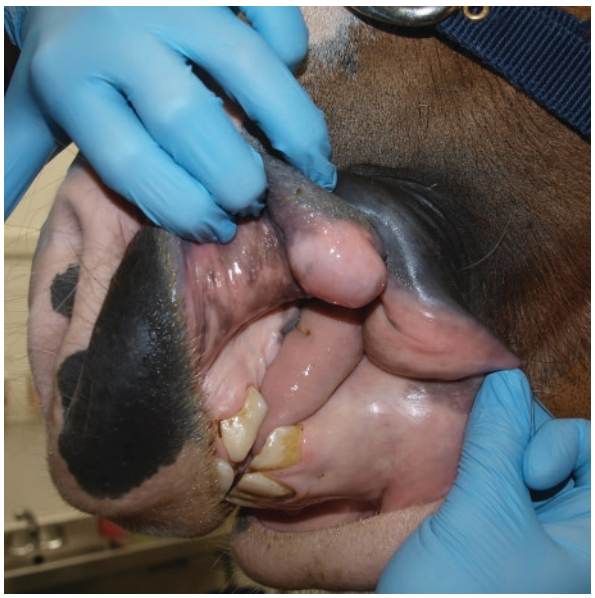


Figure 10.27 Assessment of a spherical mass in the oral cavity of a horse originating at the mucocutaneous junction of the upper lip.

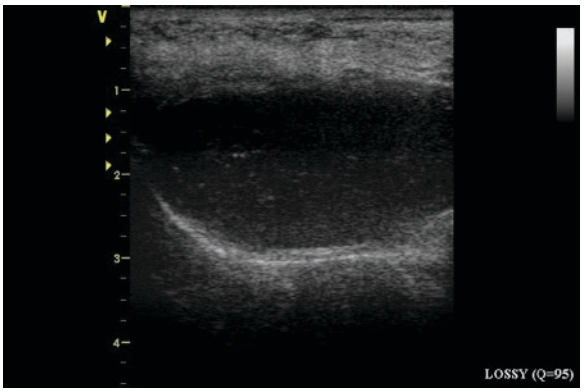


Figure 10.28 Transcutaneous ultrasound image centered over the mass in Figure 10.27, demonstrating a relatively hypoechoic appearance to the contents of the mass with some areas of slightly increased echogenicity consistent with mucoid contents (cyst). Ultrasonographic assessment enabled the presence of a foreign body to be ruled out.

to place nerve blocks, and the incidence of local anesthetic systemic toxicity. In addition, they result in better quality and duration of nerve blocks and quicker onset of local anesthesia. New techniques have been developed for use in the equine head and are an area of current, ongoing work. Ultrasound guided techniques have been described for placement of maxillary, retrobulbar, and internal auricular nerve blocks. A good working knowledge of the anatomy of the local structures is essential. Important adjacent structures such as large blood vessels can be identified with or without color flow Doppler. The nerves themselves are visualized in the transverse plane as single or multiple, round or ovoid hypoechoic areas (nerve fascicles) surrounded by relatively hyperechoic tissue (connective tissues between neuronal structures). In the longitudinal plane, the nerve appears as a hyperechoic band with multiple discontinuous hypoechoic stripes separated by hyperechoic lines. These techniques have been detailed in cadaver studies with a few limited case studies but with ongoing refinements, these techniques are likely to become increasingly utilized based on the results of efficacy and safety studies. Further details of the techniques including the anatomic landmarks are in the recommended readings.

Recommended Reading

Chalmers, H.J., Cheetham, J., Yaeger, A.E. et al. (2006). Ultrasonography of the equine larynx. *Veterinary Radiology & Ultrasound*, 47: 476–481.

Chalmers, H.J., Yaeger, A.E., and Ducharme, N.D. (2009). Ultrasonographic assessment of laryngohyoid position as a predictor of dorsal displacement of the soft palate in horses. *Veterinary Radiology & Ultrasound*, 50: 91–96.

Vet-ebooks.com

Garrett, K.S., Woodie, J.B., Cook, J.L. et al. (2010). Imaging diagnosis: Nasal septal and laryngeal cyst-like malformations in a Thoroughbred weanling colt diagnosed using ultrasonography and magnetic resonance imaging. *Veterinary Radiology & Ultrasound*, 51: 504–507.

Garrett, K.S., Woodie, J.B., and Embertson, R.M. (2011). Association of treadmill upper airway endoscopic evaluation with results of ultrasonography and resting upper airway endoscopic evaluation. *Equine Veterinary Journal*, 43: 365–371.

Hermans, H., Veraa, S., Wolschrijn, C.F. et al. (2019). Local anaesthetic techniques for the equine head, towards guided techniques and new applications. *Equine Veterinary Education*, 31: 432–440.

O'Neill, H.D., Garcia-Pereira, F.L., and Mohankumar, P.S. (2014). Ultrasound-guided injection of the maxillary nerve in the horse. *Equine Veterinary Journal*, 46: 180–184.

Reef, V.B. (1998). Ultrasonographic evaluation of small parts. In: *Equine Diagnostic Ultrasound* (ed. W.B. Saunders), 480–547. Philadelphiap PA: W.B.Saunders.

Roberts, V.L.H., Patel, N.K., and Tremaine, W.H. (2016). Neuromodulation using percutaneous electrical nerve stimulation for the management of trigeminal-mediated headshaking: A safe procedure resulting in medium-term remission in five of seven horses. *Equine Veterinary Journal*, 48: 201–204.

Rodriguez, M.J., Soler, M., Latorre, R. et al. (2007). Ultrasonographic anatomy of the temporomandibular joint in healthy pure-bred Spanish horses. *Veterinary Radiology & Ultrasound*, 48: 149–154.

Solano, M. and Pennick, D. (1996). Ultrasonography of the canine, feline and equine tongue: Normal findings and case history reports. *Veterinary Radiology & Ultrasound*, 37: 206–213.

Stauffer, S., Cordner, B., Dixon, J. et al. (2017). Maxillary nerve blocks in horses: An experimental comparison of surface landmark and ultrasound-guided techniques. *Veterinary Anaesthesia and Analgesia*, 44: 951–958.

Weller, R., Taylor, S., Maierl, J. et al. (1999). Ultrasonographic anatomy of the equine temporomandibular joint. *Equine Veterinary Journal*, 31: 529–532.

Vet-ebooks.com

Vet-ebooks.com

Section 2

Reproduction

Vet-ebooks.com

Vet-ebooks.com

Section 2a

Ultrasonography of the Stallion Reproductive Tract

Vet-ebooks.com

Vet-ebooks.com

11

Ultrasonography of the Internal Reproductive Tract

Malgorzata A. Pozor

College of Veterinary Medicine, University of Florida, Gainesville, FL, USA

The internal reproductive tract in a normal stallion consists of the pelvic urethra, the two vasa deferentia with their glandular portions (ampullae), the paired vesicular glands (seminal vesicles), the bilobed prostate, and the paired bulbourethral glands (Figure 11.1).

Normal Anatomy

The vasa deferentia run from the epididymal tails, through the inguinal canals, and turn backward toward the pelvic cavity, where their diameter increases to form the glandular portions of the vasa deferentia, called ampullae. The ampullae run over the dorsal surface of the urinary bladder, and dive under the isthmus of the prostate, where they come very close together, often holding the uterus masculinus between them [1]. The vasa deferentia narrow down again, and continue their course within the urethral wall, beyond the prostatic isthmus, to join the excretory ducts of the vesicular glands, and to form the short ejaculatory ducts [2]. The ejaculatory ducts open on the colliculus seminalis, a summit of the urethral mucosa, as the ejaculatory orifices. In approximately 15% of individuals, the vasa deferentia do not fuse with the excretory ducts of the vesicular glands, and open separately [1].

A rudimentary remnant of the uterus masculinus and the urogenital sinus, called utriculus masculinus, is often present within the colliculus seminalis and has its opening in the middle of this structure, between the ejaculatory orifices [3,4]. If the utriculus masculinus has a blind ending, it has a tendency to form cysts, which can enlarge with age, and may affect the ejaculatory process [5].

The vesicular glands have a shape of pyriform sacs, which lie on both sides of the bladder, and are partially enclosed in the urogenital fold. Each gland consists of the fundus, the body, and the neck or the excretory duct, which runs under the prostate before it unites with the ipsilateral vas deferens [6]. The mucous membrane of the vesicular glands has a columnar epithelium and forms a network of numerous folds [1].

The prostate gland lies on the neck of the bladder and the beginning of the urethra, and has two lobes, connected by the isthmus. The lobes have prismatic shapes, while the isthmus is a thin transverse band lying on the junction of the bladder neck and the urethra. The prostatic isthmus covers terminal parts of the ampullae, the necks of the vesicular glands, and the distal portion of the uterus masculinus. The prostate is completely enclosed in the musculo-glandular capsule, and has numerous spheroid or ovoid lobules separated by trabeculae [1]. The secretion is collected in central spaces of the lobules, called tubular diverticula, and is excreted via prostatic ducts to the urethra on both sides of the colliculus seminalis [1].

Just behind the prostate the lumen of the pelvic urethra dilates, and it then narrows again at the level of the ischial arch, between the bulbourethral glands. The caudal part of the prostate and the pelvic urethra are covered by the urethralis muscle, which consists of dorsal and ventral layers of transverse fibers, forming an elliptical sphincter around the urethra [1].

The bulbourethral glands are ovoid in shape, and are located on the both sides of the pelvic urethra [1]. These glands have a similar structure to the prostate and have numerous excretory ducts. The excretory ducts open to the urethra in two parallel rows of small

Atlas of Equine Ultrasonography, Second Edition. Edited by Jessica A. Kidd, Kristina G. Lu and Michele L. Frazer.
© 2022 John Wiley & Sons Ltd. Published 2022 by John Wiley & Sons Ltd.
Companion Website: www.wiley.com/go/kidd/atlas

Vet-ebooks.com

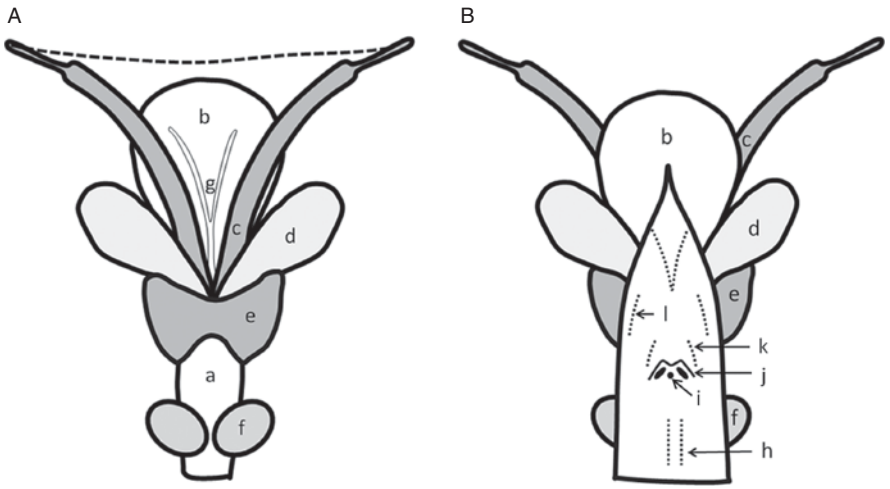


Figure 11.1 Diagram of the internal genitalia in a stallion: (A) dorsal view; (B) ventral view (urethra cut open). a: urethra; b: urinary bladder; c: ampulla of vas deferens; d: vesicular gland; e: prostate gland; f: bulbourethral gland; g: uterus masculinus; h: openings of bulbourethral ducts; i: opening to utriculus masculinus; j: colliculus seminalis; k: openings of prostatic ducts; l: openings of urethral glands.

papillae, just behind the prostatic ducts. Each bulbourethral gland is covered by the bulboglandularis muscle, which forms a capsule around the gland [6].

The blood supply to the stallion's internal genitalia is derived mainly from the prostatic artery, which gives off the numerous branches to all accessory sex glands and the terminal portion of the vasa deferentia [7].

Palpation *Per Rectum*

Transrectal ultrasonography (TRUS) is the method of choice for evaluating the internal genitalia in stallions [8], but palpation *per rectum* is always done first. The pelvic urethra is most prominent and easy to find. It lies directly on the midline, and is detectable just before it curves around the ischial arch as a firm tube. Since the entire length of the pelvic urethra in a mature stallion is only 10–13 cm (4–5 inches) [1], the examiner does not need to introduce his/her hand deeper than up to the wrist in order to detect this structure. Palpation of the prostate gland *per rectum* is unrewarding in the horse [9]: the capsule is thick and its surface is flat, making detection of this gland difficult.

The next structures of interest are the ampullae of the vasa deferentia. Both ampullae are palpable on the neck of the bladder, just before they dive under the isthmus of the prostate. They are rigid small tubes, often lying very close together, and are easily palpable using fingertips. If the urinary bladder is large, the ampullae are more spread apart, and are found on the lateral aspects of the bladder.

Narrow parts of the vasa deferentia are often too small to palpate. However, the internal vaginal rings should be located during palpation *per rectum*. In order to find one of these rings, the examiner's hand moves over the pelvic brim, turns laterally and sweeps the caudoventral aspect of the body wall on each side. The vaginal ring can be recognized as an elliptical slit, easily accommodating one to two fingertips. Palpation of the vas deferens or testicular vessels passing through the ring is difficult, but detection of a retained testis or herniating intestines is possible.

Palpation of the vesicular glands is often challenging in the stallion. They are detectable only when filled with secretion as fluctuant sacs lateral to the ampullae, or more cranially, occasionally hanging over the pelvic brim. The bulbourethral glands are not palpable, due to the thick muscular capsules that completely cover these glands.

Ultrasonography of the Normal Internal Reproductive Tract

Transrectal ultrasound evaluation (TRUS) of the internal genitalia is performed immediately after palpation *per rectum*. A linear transducer with a high frequency (7.5–10 MHz), and high resolution is needed to detect the fine structure of the internal genitalia. Small, micro-convex, transverse transducers are also very useful in evaluating the area of the colliculus seminalis. The easiest structure to detect is the pelvic urethra with its urethralis muscle (Figures 11.1 and 11.2). The dorsal and ventral layers of this muscle appear as thick hypoechoic lines, when the linear transducer is positioned on the midline, parallel to the long axis of the animal. The urethra itself is an echogenic tube, but contains a few structures with varied echogenicity. The colliculus seminalis can be visualized in the most caudal aspect of the pelvic urethra (Figures 11.2A, 11.2B, 11.2C, 11.3,

Vet-ebooks.com

and 11.4 (focus on 11.4 J)). It appears as a roundish, echogenic, or hypoechoic protrusion from the dorsal wall of the urethra, often with an anechoic outline due to the small accumulation of urine, prostatic secretion, or semen in this area. Single or multiple anechoic cysts of the colliculus seminalis may be also found (Figure 11.3). Most often, these cysts have an oval or tear shape, but can also be spindle shaped or rectangular. Occasionally, echogenic or hyperechoic contents may be observed within a cyst.

After localizing the colliculus seminalis, the examiner moves the transducer cranially, making an attempt to trace the ejaculatory ducts, the most terminal and narrow parts of the vasa deferentia, and the excretory ducts of the vesicular glands (Figure 11.4 (focus on 11.4G, 11.4H, 11.4I, and 11.5). All these ducts travel through the urethral wall, and can be seen as hyperechoic lines running parallel to each other. The vasa deferentia gradually thicken, and look like tips of sharpened pencils in a transition to the ampullae, which initially run under the isthmus of the prostate, and continue their path on the laterodorsal aspect of the urinary bladder (Figure 11.5, focus on 11.5B and 11.5C, and 11.6). Each ampulla of the vas

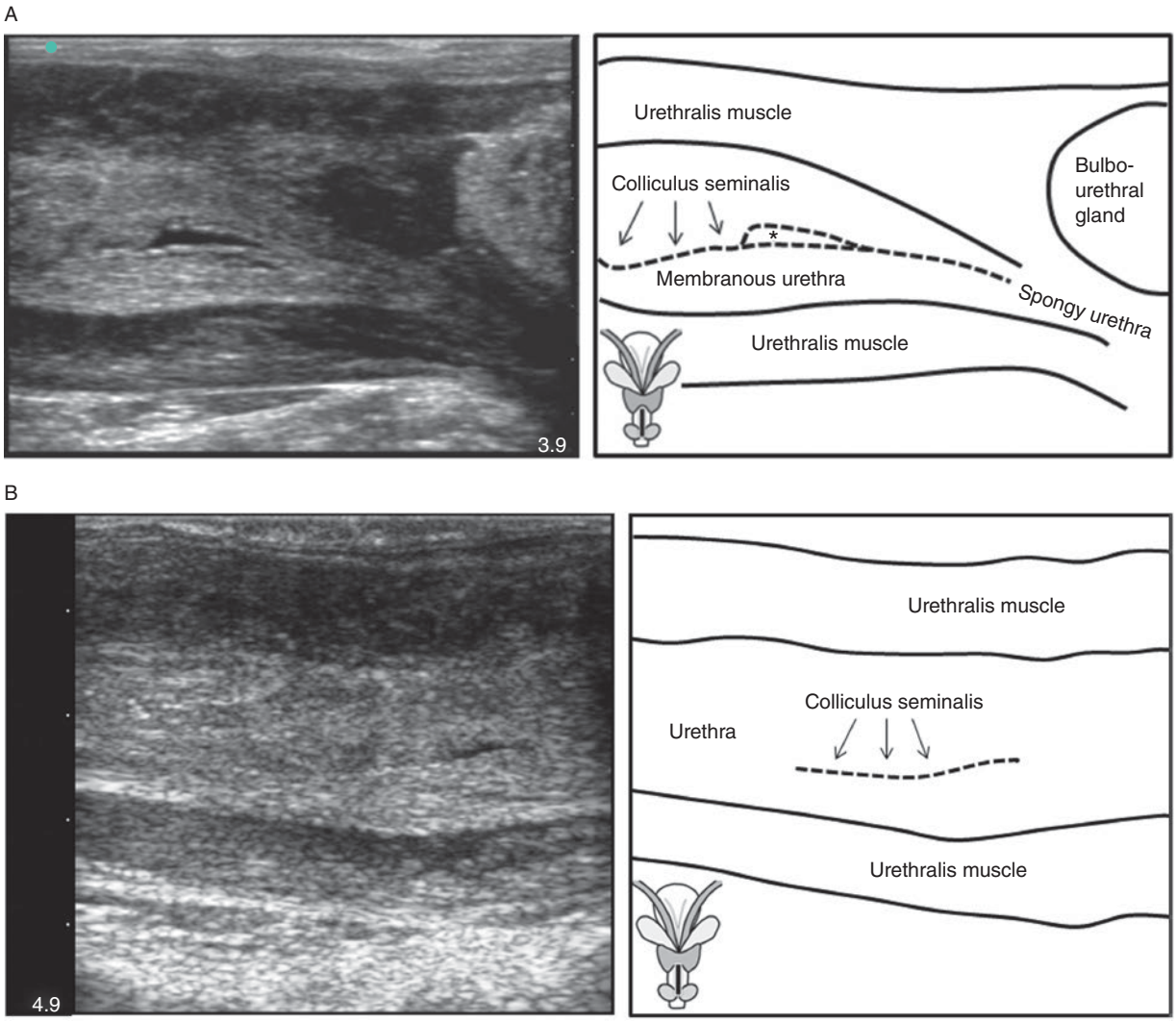
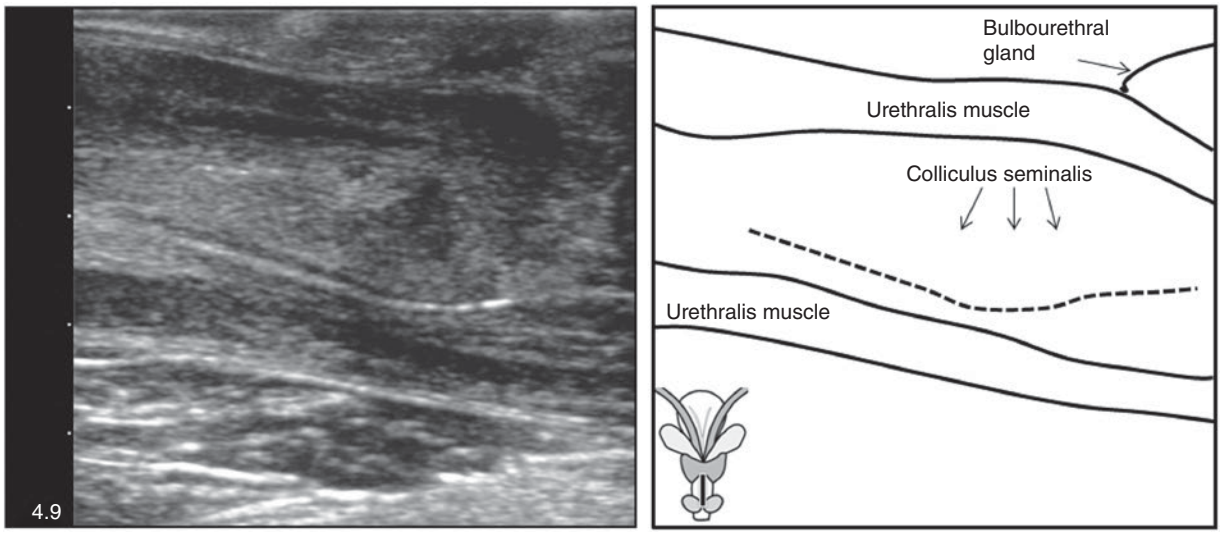


Figure 11.2 Pelvic urethra. (A) Ultrasound image of the distal part of the pelvic urethra (membranous urethra), and the proximal part of the spongy urethra. A small amount of anechoic semen, prostatic secretion, or urine is present in the urethral lumen, just behind the colliculus seminalis (*). (B) Ultrasound image of the membranous part of the pelvic urethra in a stallion. Urethralis muscle appears as two hypoechoic, thick lines, parallel to each other. Urethra is uniformly echogenic. This area often serves as a landmark during transrectal ultrasound examination of the internal genitalia of a stallion. (C) Ultrasound image of the membranous part of the pelvic urethra in a stallion. Colliculus seminalis is less echogenic than the urethra, and has a hyperechoic contour. (D) Ultrasound image of the membranous part of the pelvic urethra in an aged stallion. Terminal portions of the vasa deferentia (a) and the excretory ducts of the vesicular glands (b) contain hyperechoic concretions.

Vet-ebooks.com

C



D

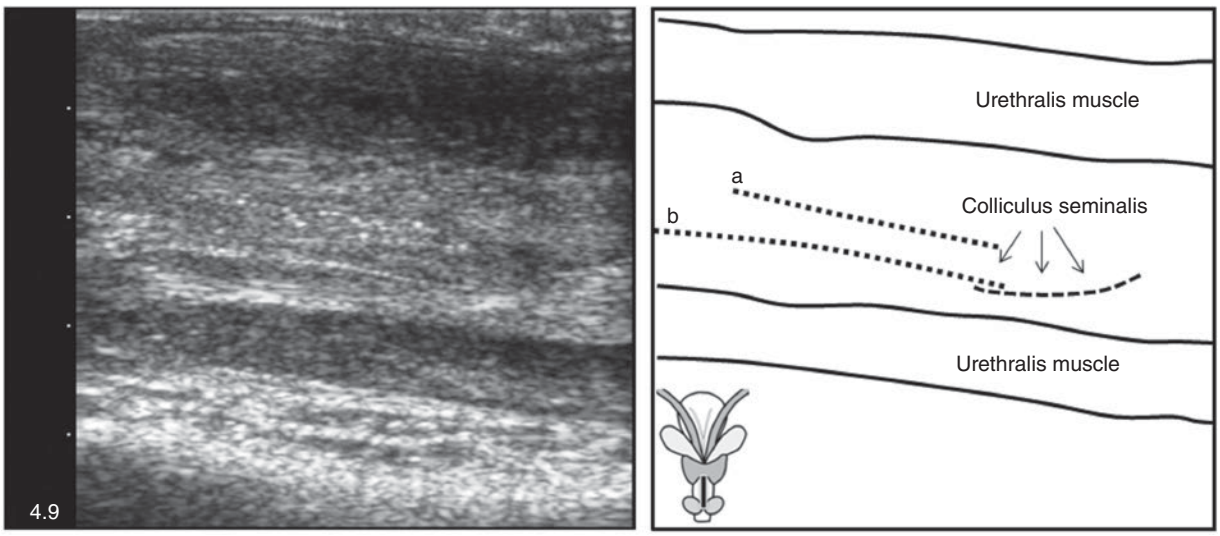


Figure 11.2 (Continued)

Vet-ebooks.com

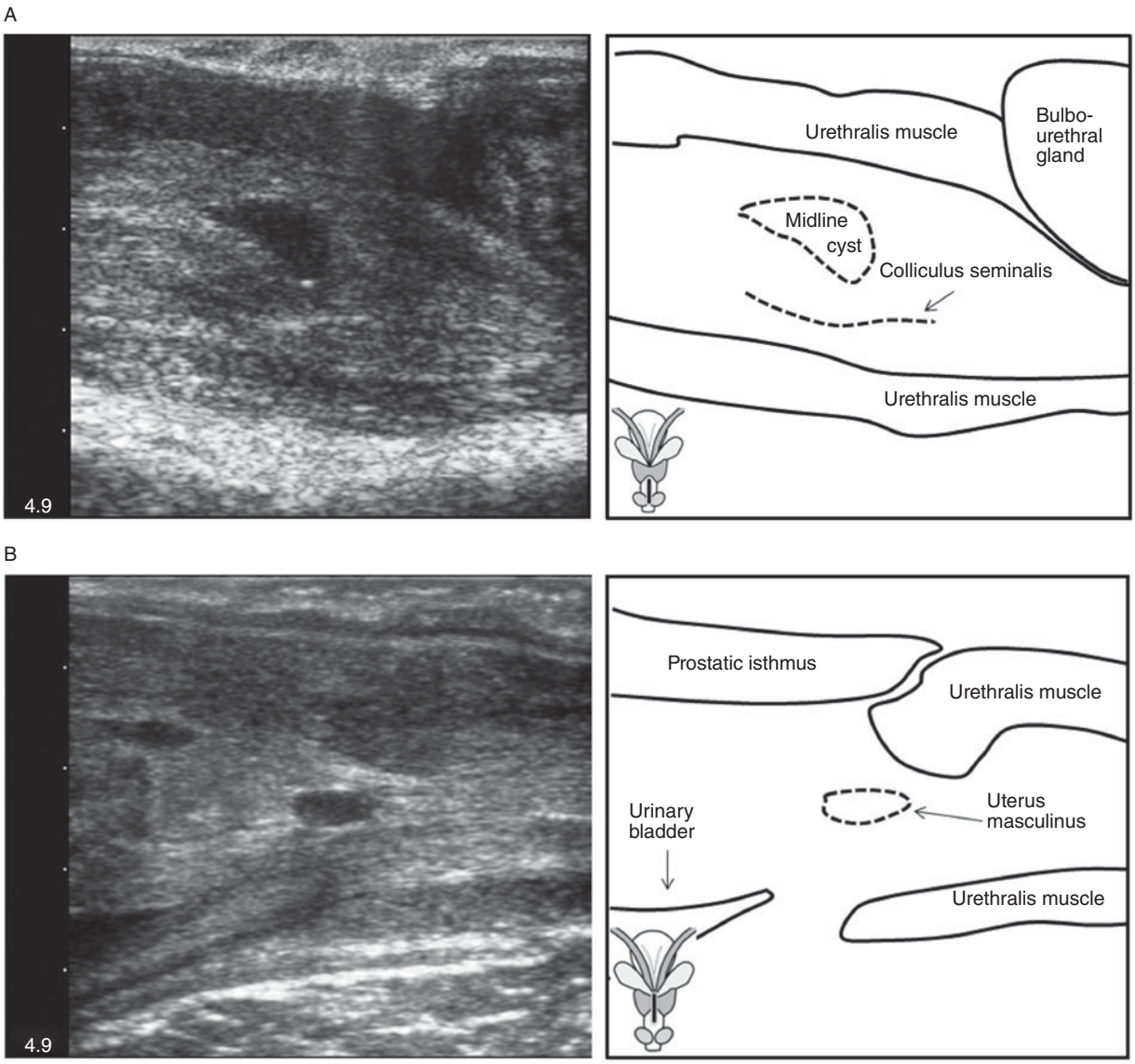
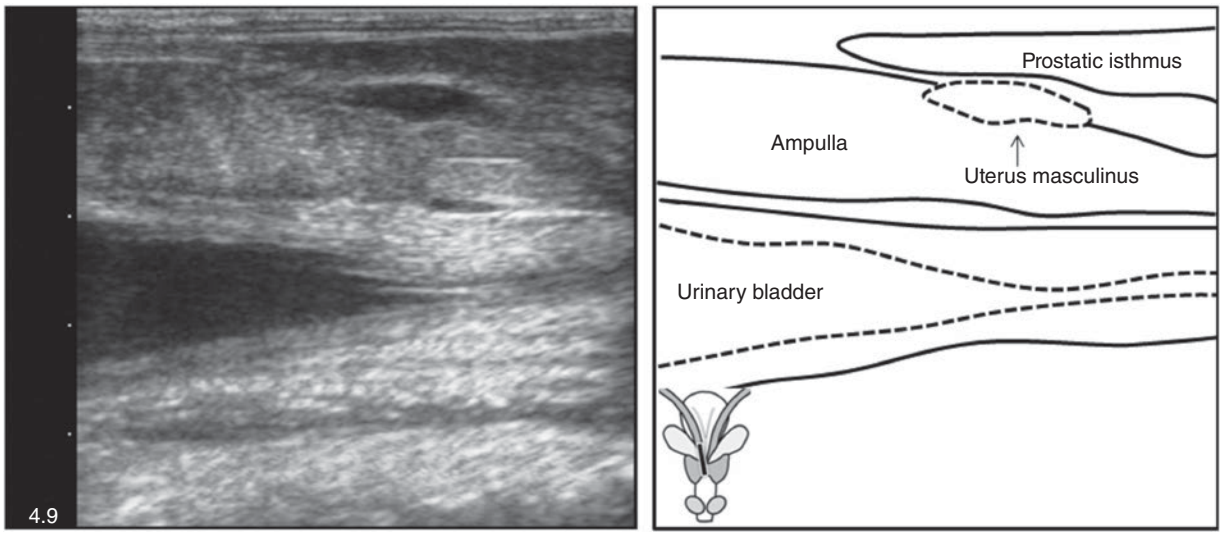


Figure 11.3 (A) Ultrasound image of a midline cyst of the colliculus seminalis in a stallion with ejaculatory problems. The cyst is anechoic and has a tear shape. (B) Ultrasound image of a small cyst of the uterus masculinus, which was found between the terminal parts of the ampullae of the vasa deferentia. This was an incidental finding; the stallion did not have any problems with ejaculation. (C) Ultrasound image of a spindle-shaped cyst of the uterus masculinus, which was found in the urogenital fold of a stallion. This stallion was experiencing ejaculatory problems. (D) Ultrasound image of a cyst near the terminal part of the ampulla of the vas deferens. A hyperechoic plug is present in the ampullary lumen.

Vet-ebooks.com

C



D

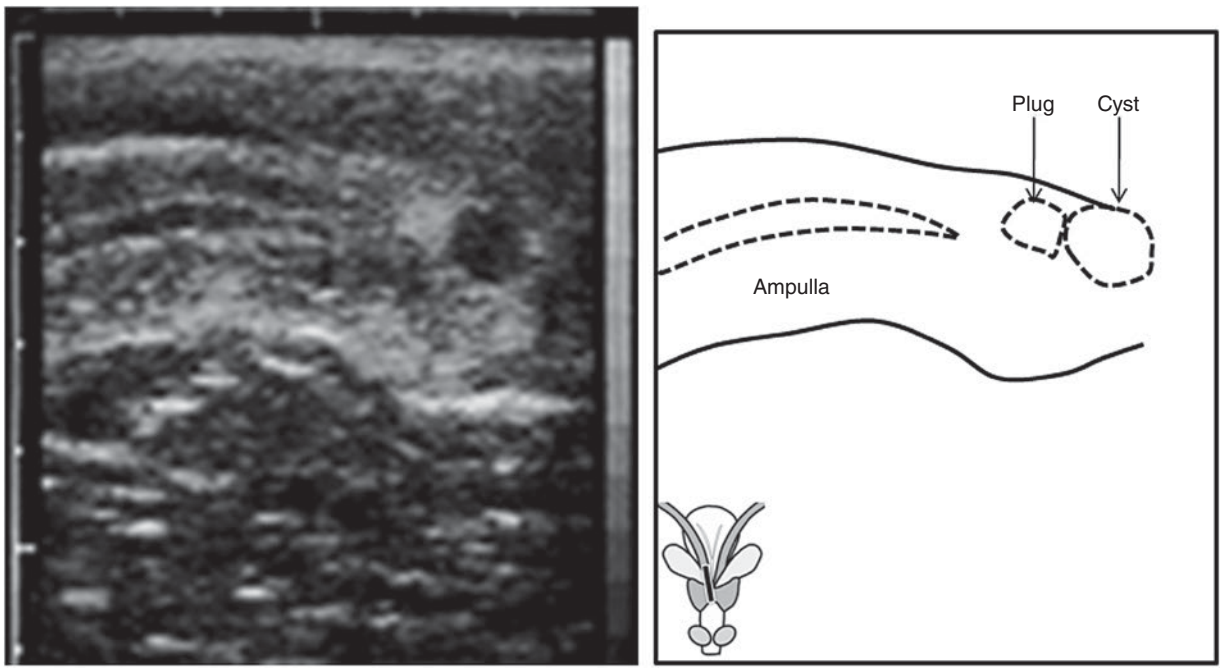
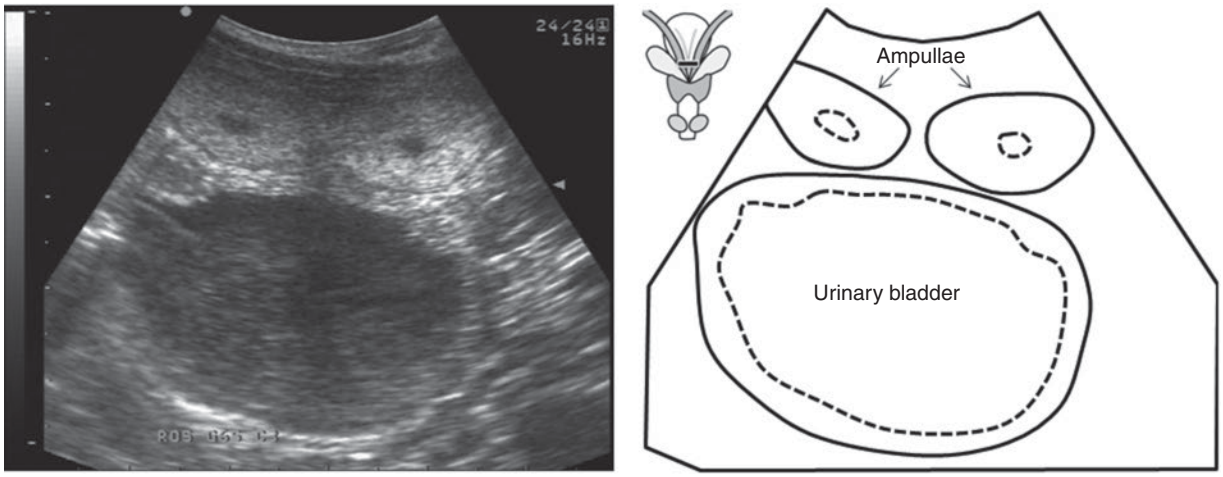


Figure 11.3 (Continued)

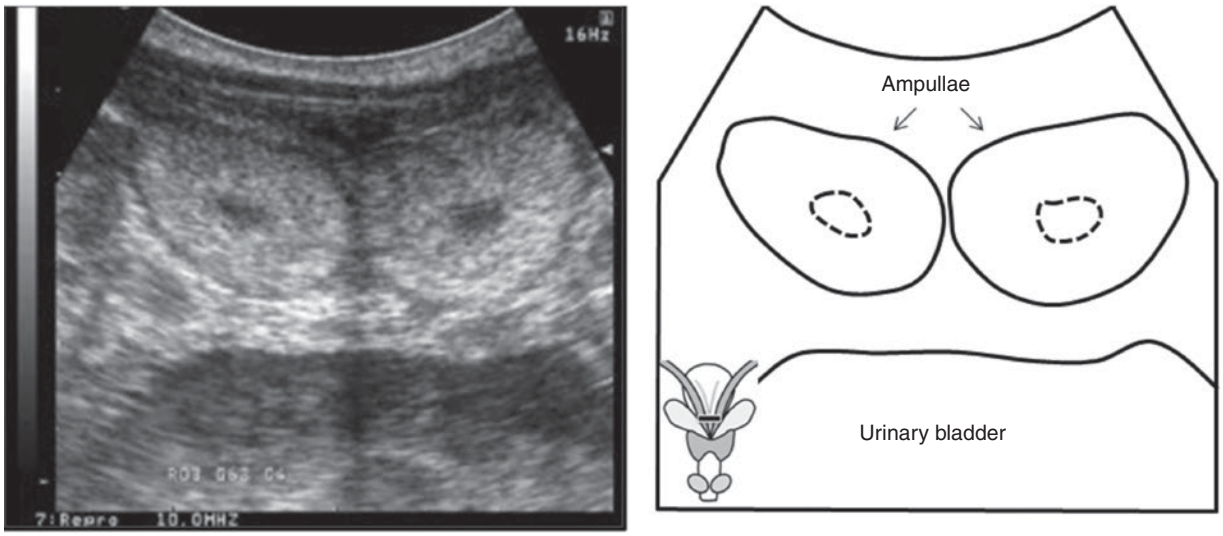
Figure 11.4 (A) Ultrasound image of the cross-sections of the ampullae of the vasa deferentia and the urinary bladder. (B) Ultrasound image of the cross-sections of the ampullae of vasa deferentia and the urinary bladder – close view. (C) Ultrasound image of the cross-sections of the ampullae of the vasa deferentia, the vesicular glands, and the urinary bladder. (D) Ultrasound image of the cross-sections of the ampullae of the vasa deferentia, and the prostatic isthmus in a sexually aroused stallion. (E) Ultrasound image of the cross-sections of the ampullae of the vasa deferentia, the excretory ducts of the vesicular glands, and the prostate. (F) Ultrasound image of the cross-sections of the ampullae of the vasa deferentia, the excretory ducts of the vesicular glands, and the prostate in a sexually aroused stallion. (G) Ultrasound image of the cross-sections of the very terminal portions of the ampullae of the vasa deferentia, the excretory ducts of the vesicular glands, and the prostatic ducts. (H) Ultrasound image of the cross-sections of the terminal portions of the vasa deferentia, excretory ducts of the vesicular glands, and the cyst of the uterus masculinus in a normal stallion. (I) Ultrasound image of the cross-sections of the terminal portions of the vasa deferentia, excretory ducts of the vesicular glands, and the utriculus masculinus in a normal stallion. (J) Ultrasound image of the cross-sections of the colliculus seminalis in a normal stallion.

Vet-ebooks.com

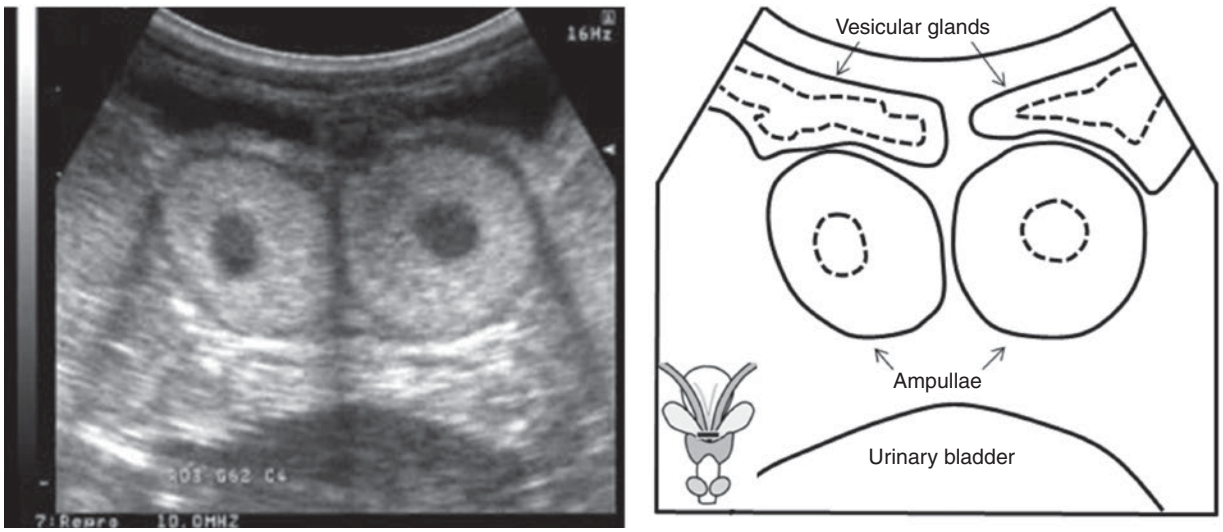
A



B

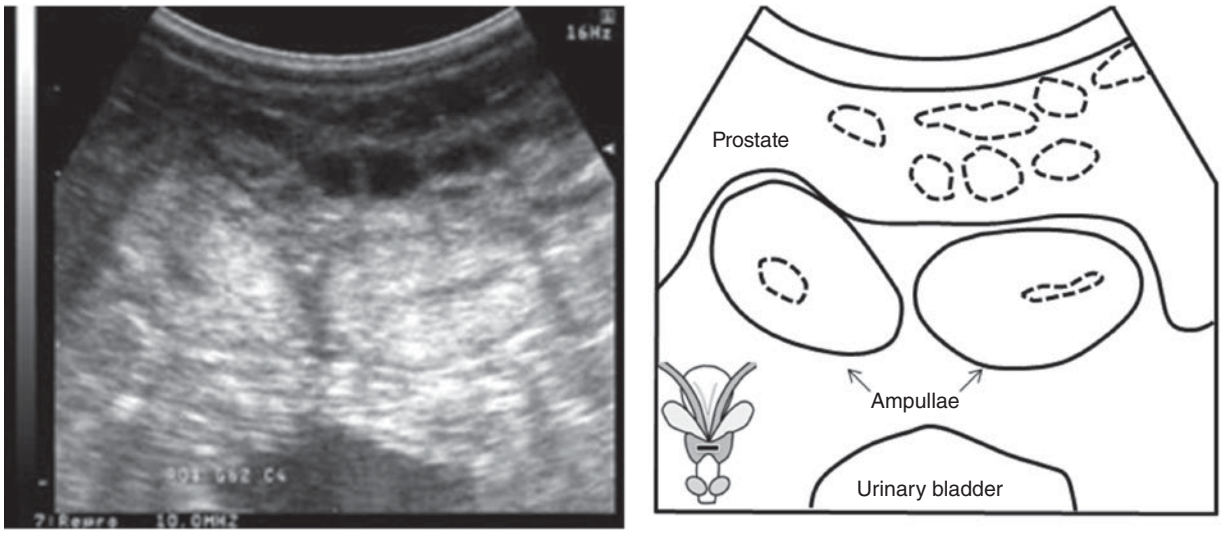


C

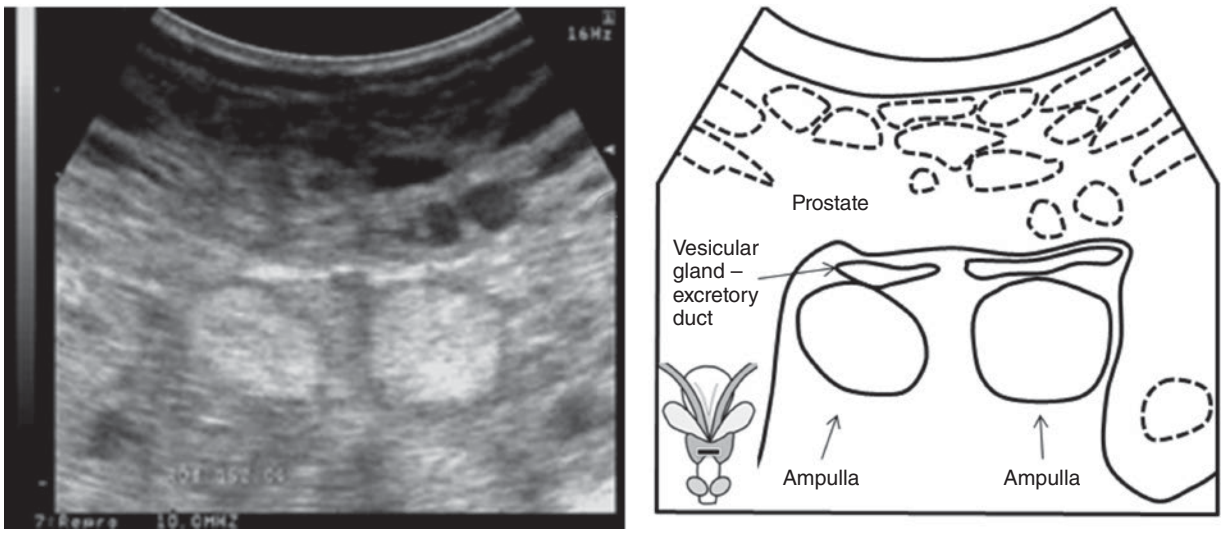


Vet-ebooks.com

D



E



F

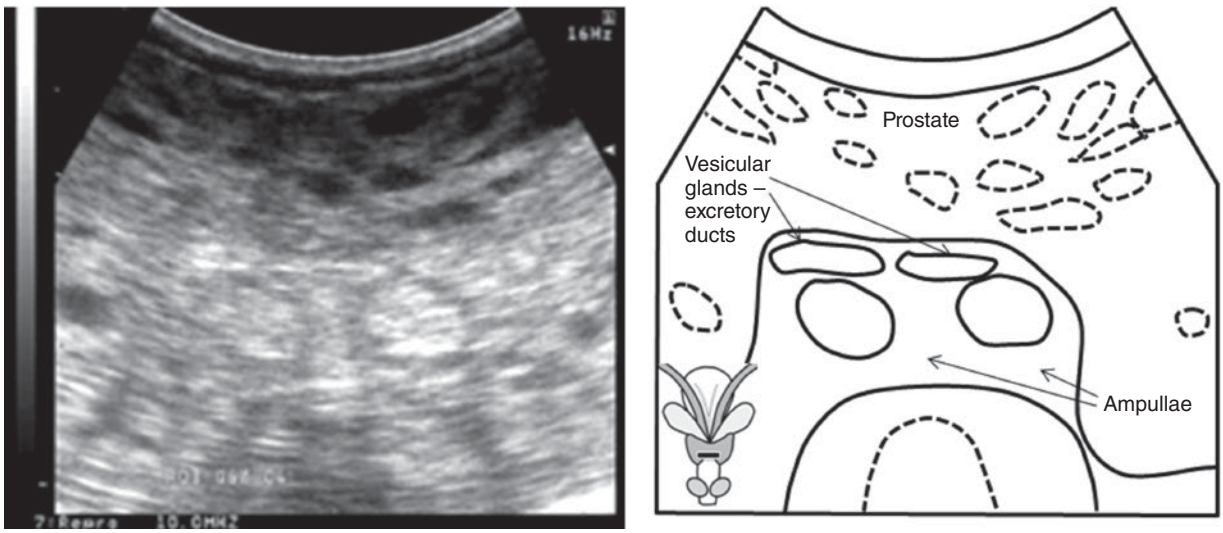
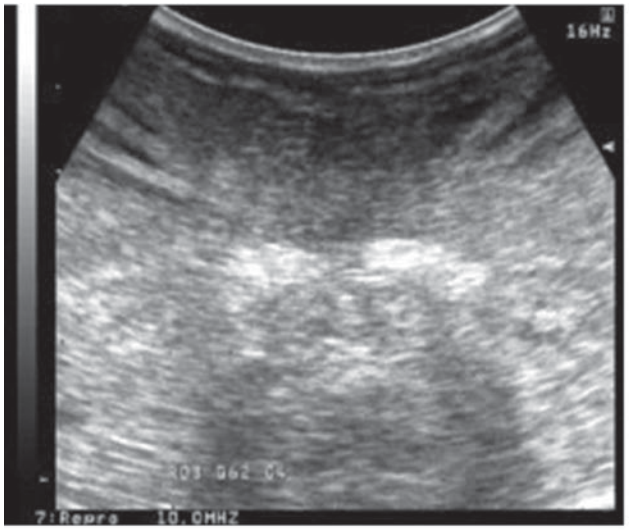
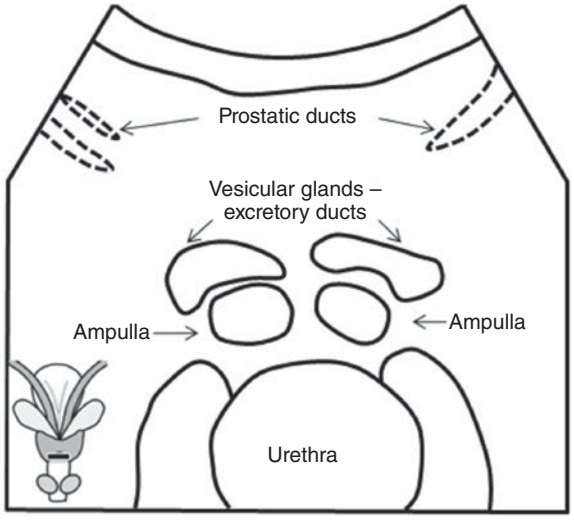


Figure 11.4 (Continued)

Vet-ebooks.com

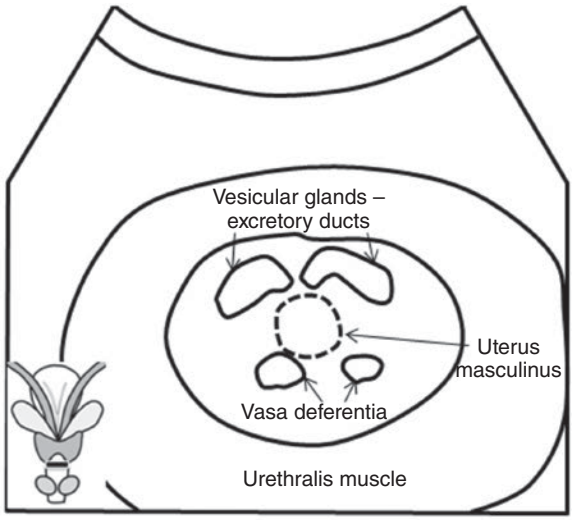
G





H





I



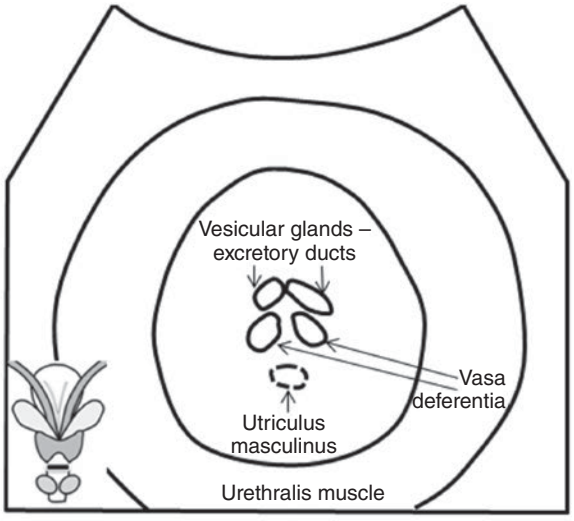


Figure 11.4 (Continued)

Vet-ebooks.com

J

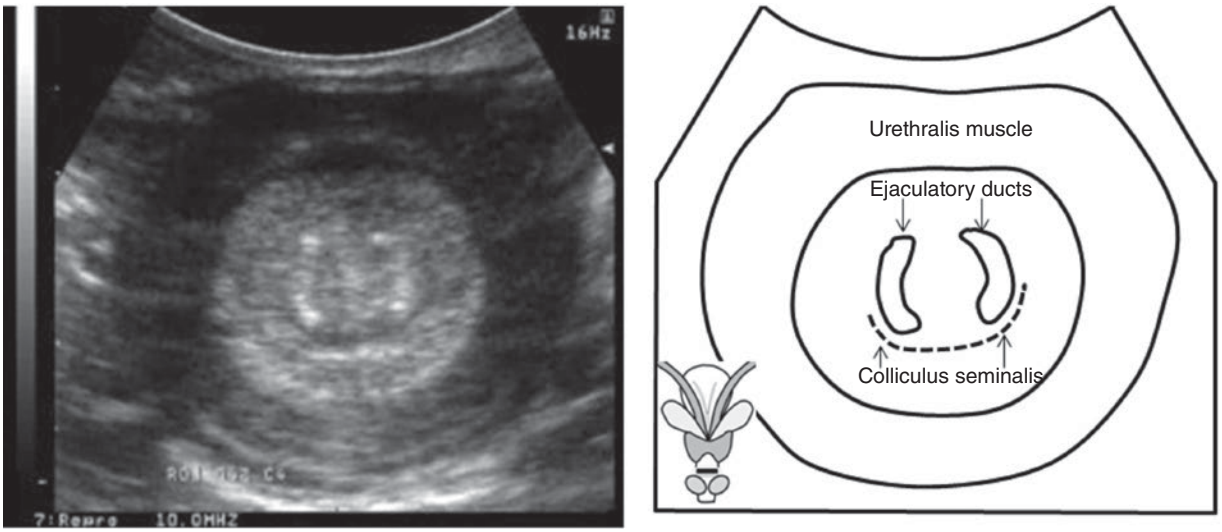


Figure 11.4 (Continued)

deferens appears as a thick, echogenic tube, which is separated from the surrounding structures by the hyperechoic layer of connective tissue. This tube often has a small, anechoic lumen (Figures 11.6A, 11.6B, and 11.6C) unless abnormally distended in a case of distal occlusion (Figures 11.7 and 11.8). Secretion of numerous tubulo-alveolar glands, which are present in the mucous membrane of the ampulla, can be visualized as hypoechoic spaces within the ampullary wall. Occasionally, hyperechoic, inspissated sperm appear in the lumen and in the glandular alveoli. Each ampulla can be traced individually, using the linear transducer, until it loses its glandular component and becomes a thin-walled vas deferens again (Figures 11.6D). Tracing the narrow part of the vas deferens is difficult, and requires good quality equipment and an experienced operator. The skill of tracing the vasa deferentia in a stallion can be helpful in localizing a cryptorchid testis (Figure 11.9).

The ultrasound appearance of the vesicular glands is variable, and depends on the amount of secretion. Most often, the fundus of each gland can be found either cranially to the bladder and laterally to the ipsilateral ampulla, or on the level of the bladder, dorsal to the ipsilateral ampulla. The normal vesicular gland has a thin, echogenic wall, and hypoechoic or echolucent content in the lumen (Figures 11.10A and 11.10B). However, if the secretion of the vesicular gland is very viscous and thick, it may have a highly echogenic or hyperechoic appearance (Figures 11.10D and 11.10E). This is often observed in stallions that have been exposed to mares for a prolonged period of time, and have not had an opportunity to ejaculate. Variations in ultrasonographic appearance of the vesicular glands in normal stallions make differentiation from abnormal glands difficult (Figures 11.11, 11.12, and 11.13).The shape of the most distal pole of the vesicular gland is usually roundish, like a fluid-filled sac, but it can be also triangular if the gland is compressed between the intestines and the bladder. The body of the gland can be traced caudally until it dives under the prostatic isthmus and becomes the excretory duct. The excretory ducts often have a hyperechoic appearance and penetrate through the urethral wall under a small angle. Occasionally, there is a small amount of anechoic or echogenic secretion in the body, or in the excretory ducts of the vesicular glands. Identifying empty vesicular glands may be difficult. In such cases, it may be easier to detect this gland tracing it from the midline of the urethra rather than trying to find it blindly (Figures 11.4 (focus on 11.4C, 11.4E, 11.4F, 11.4G, 11.4H, and 11.4I), 11.6 (focus on 11.6B and 11.6C), 11.10, 11.11, 11.12, 11.13, and 11.14).

The lobes of the prostate gland are easily visualized using ultrasonography. They are found on the both sides of the neck of the urethra, with the linear transducer held parallel to the long axis of the animal. The ultrasound appearance of the prostate is often described as "Swiss-cheese like," due to the multiple acini filled with anechoic secretion. The sizes of the acini vary, depending on the level of sexual stimulation of a stallion. Stallions exposed to mares prior to examination have large amounts of prostatic secretion stored in the acini and the tubular diverticula, which are easy to visualize. Stallions not exposed to mares may have only a few, small, anechoic spaces in their prostates. The rest of the prostatic lobe is uniformly echogenic with a hyperechoic capsule. The isthmus of the prostate is quite thin, but it may also contain spaces filled with secretion. The isthmus can

Vet-ebooks.com

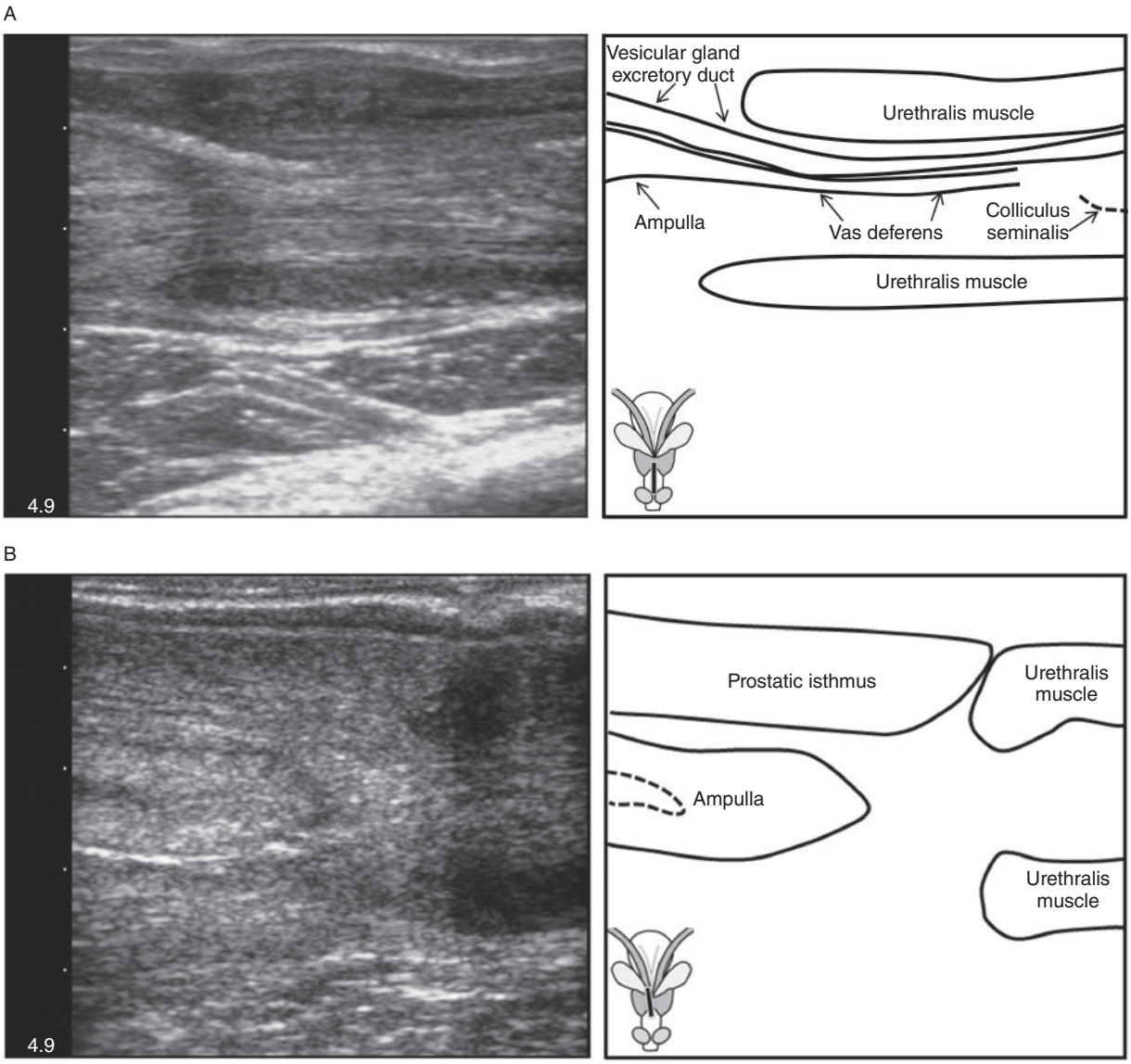
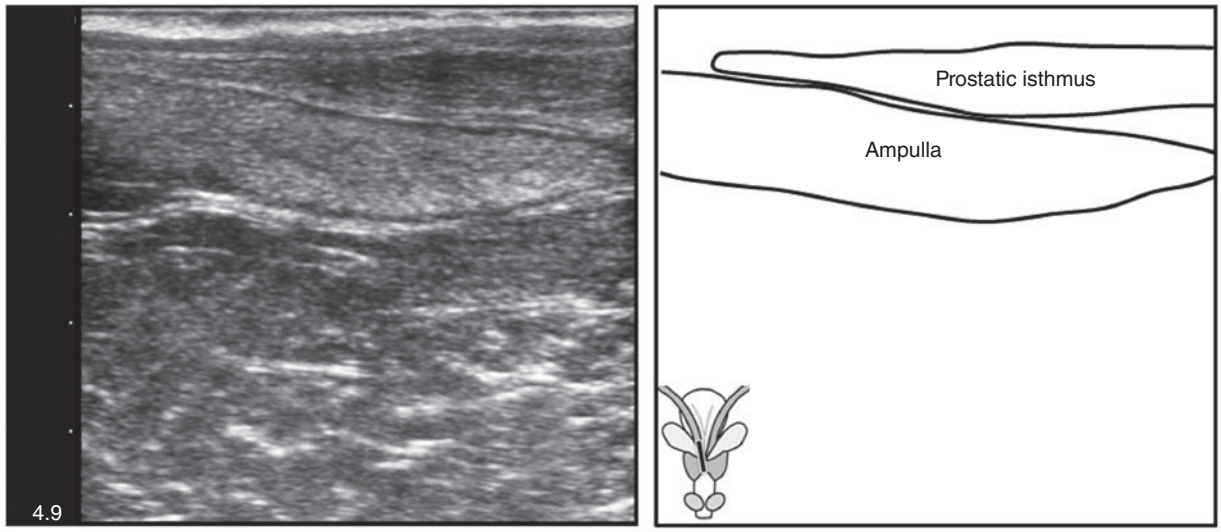


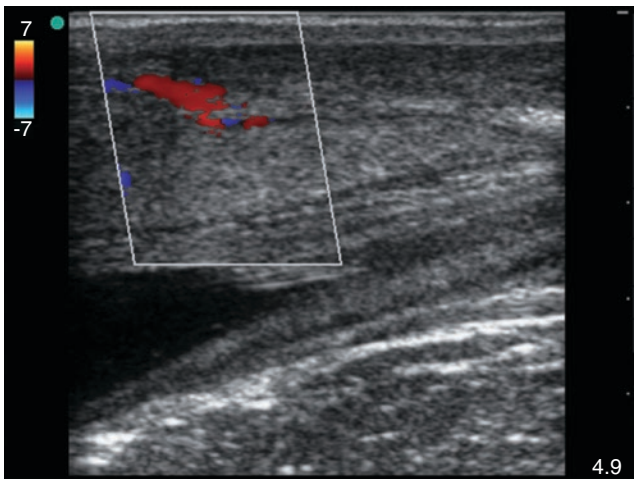
Figure 11.5 (A) Ultrasound image of the terminal portion of the vas deferens and the excretory duct of the vesicular gland. The vas deferens narrows down significantly before joining the excretory duct of the vesicular gland to form the ejaculatory duct. (B) Ultrasound image of the distal part of the prostatic part of the pelvic urethra. The ampulla of the vas deferens appears as an uniformly echogenic tube with a hypoechoic lumen. (C) Ultrasound image of the proximal part of the ampulla of the vas deferens. The ampulla is "diving" under the prostatic isthmus. (D) Color Doppler ultrasound image of the vas deferens branch of the prostatic artery. (E) Ultrasound image of the prostatic isthmus in a sexually aroused stallion. The prostatic acini are filled with anechoic secretion.

Vet-ebooks.com

C



D



E

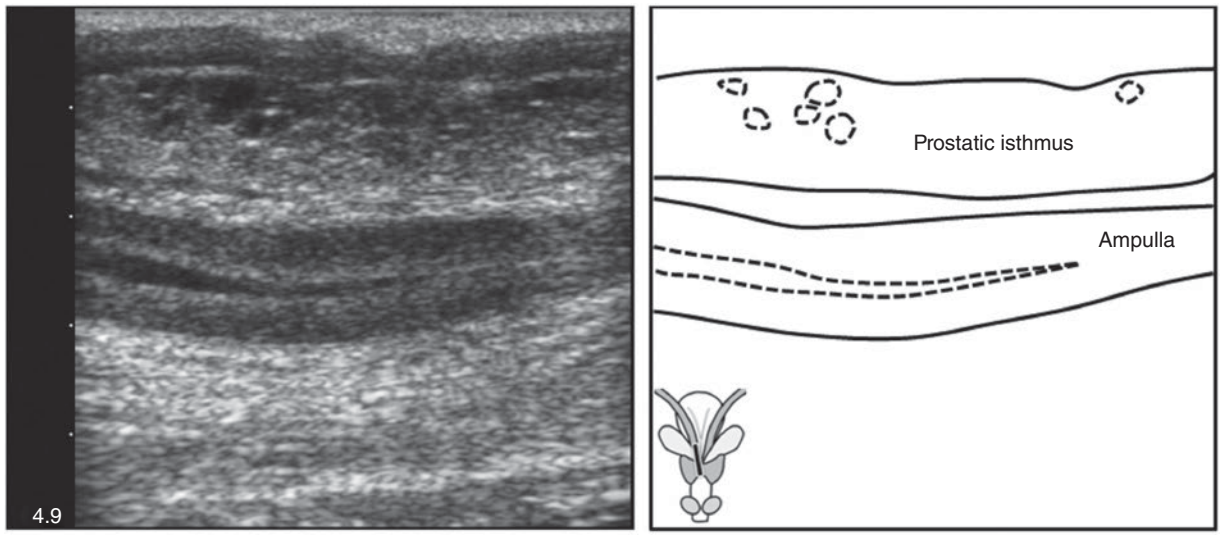


Figure 11.5 (Continued)

Vet-ebooks.com

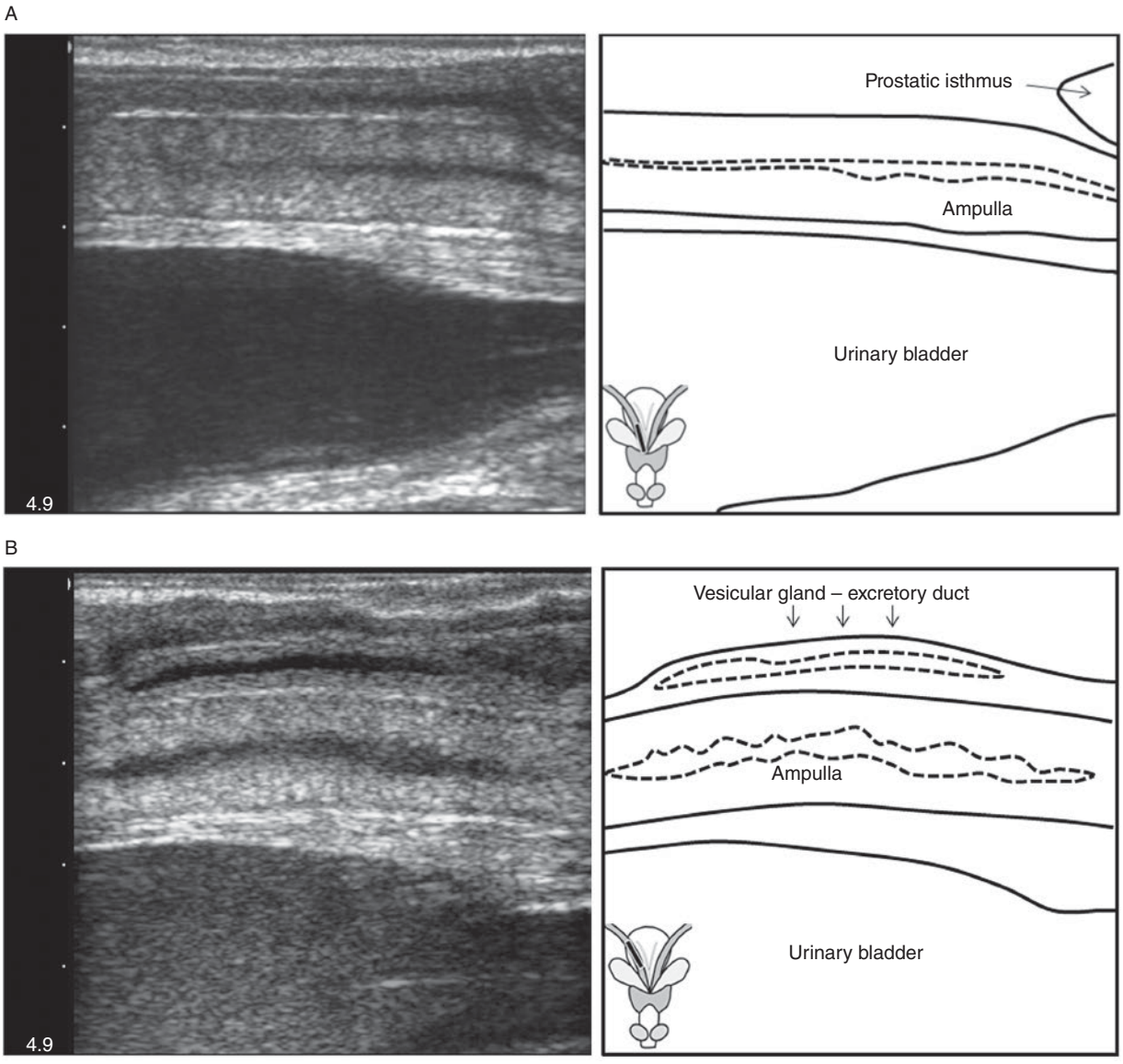
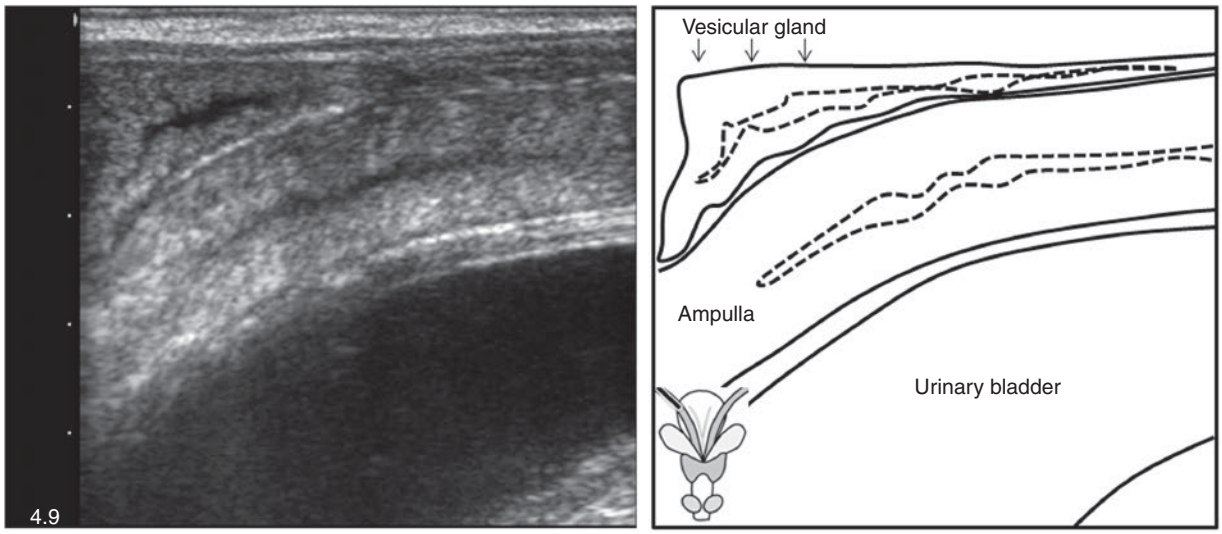


Figure 11.6 (A) Ultrasound image of the ampulla of the vas deferens – longitudinal section. The course of the entire ampulla is followed until it narrows down before entering the vaginal ring. (B) Ultrasound image of the ampulla of the vas deferens, as well as the excretory duct of the ipsilateral vesicular gland. (C) Ultrasound image of the distal part of the ampulla, which bends ventrally toward the ipsilateral vaginal ring. The fundus of the vesicular gland is lying on the top of the ampulla. (D) Ultrasound image of the narrow part of the vas deferens and its glandular part – the ampulla.

Vet-ebooks.com

C



D

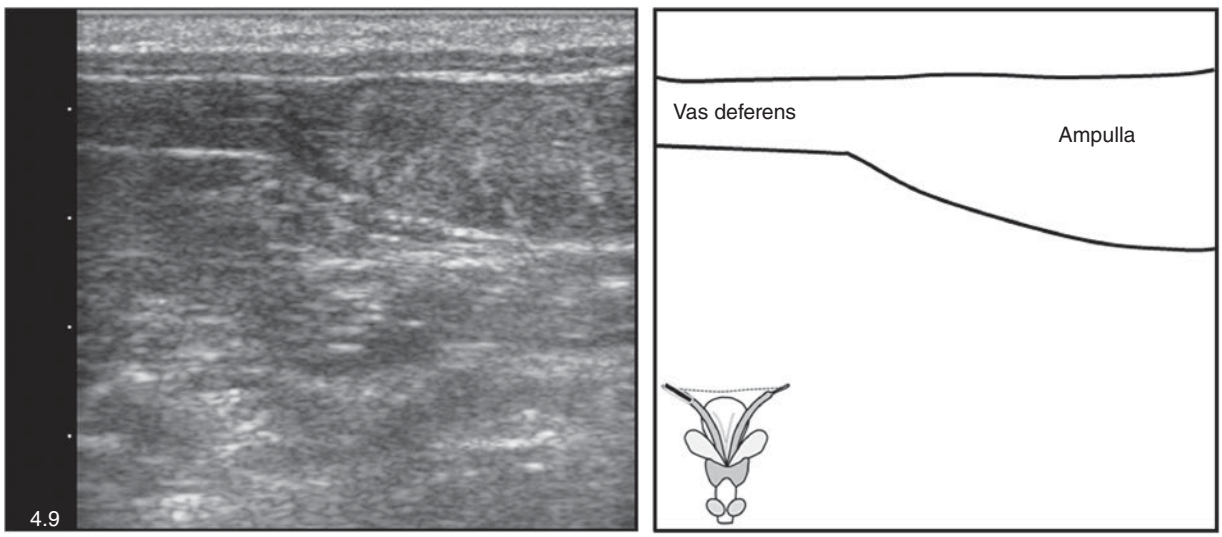


Figure 11.6 (Continued)

Vet-ebooks.com

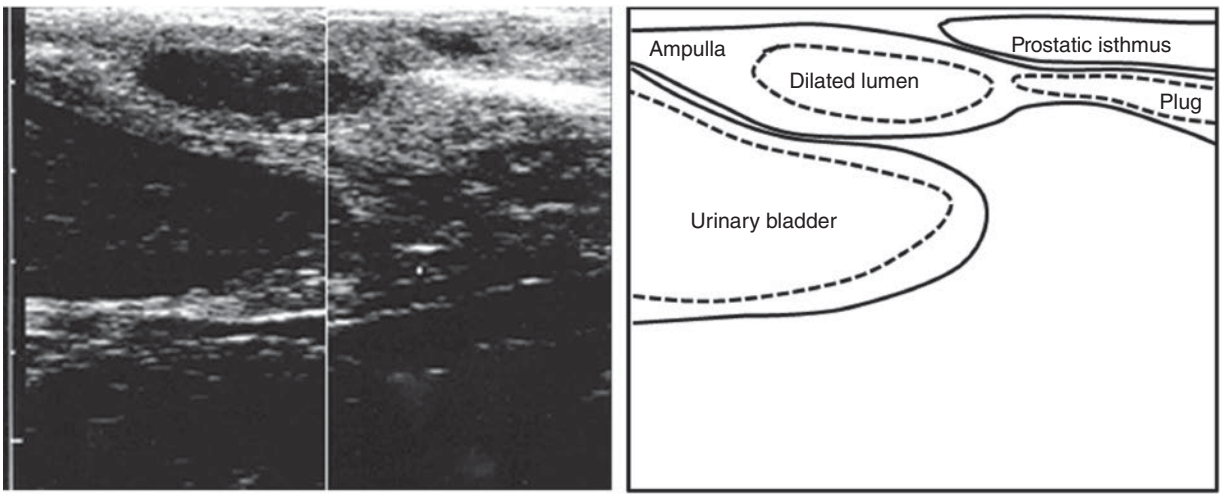


Figure 11.7 Ultrasound image of the occluded ampulla of the vas deferens. The ampullar lumen is significantly dilated. A long hyperechoic plug is present in the lumen of the vas deferens, just distal to the ampulla.

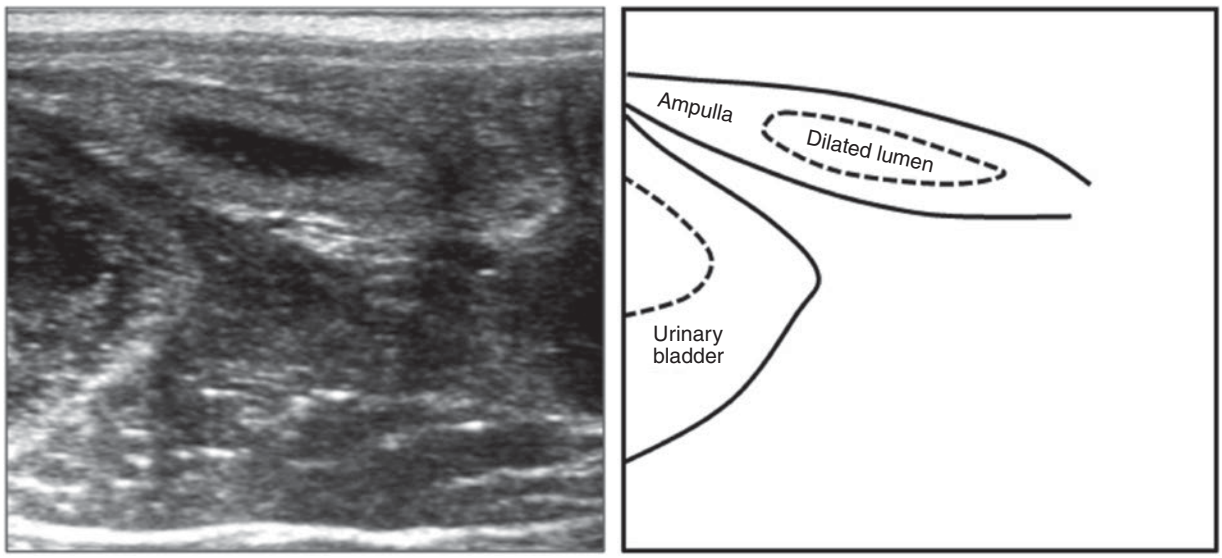


Figure 11.8 Ultrasound image of the dilated ampulla of the vas deferens.

be visualized dorsally to the distal portions of the ampullae (Figures 11.4 (focus on 11.4D, 11.4E, 11.4F, and 11.4G), 11.5 (focus on 11.5B, 11.5C, and 11.5D), 11.15, 11.16, and 11.17).

The bulbourethral glands are usually examined at the end of the ultrasound examination of the internal genitalia of a stallion. They are found on both sides of the most caudal portion of the pelvic urethra, at the level of the ischial arch where the urethra narrows. With the hand of the examiner partially out of the rectum, a transducer is moved slightly laterally and angled slightly caudolaterally to image the longitudinal section of the bulbourethral gland. The muscular capsule is hypoechoic and gives a nice outline of this ovoid gland. The appearance of the parenchyma of this gland is similar to that of the prostate lobe. The number and size of anechoic spaces with glandular secretions visualized during the examination depends on the sexual stimulation of the stallion (Figures 11.18, 11.19, 11.20, and 11.21).

The internal genitalia of the stallion can be also evaluated using small, micro-convex transducers, which are available as either "I" or "T" shaped finger-grip probes. These transducers are particularly helpful in visualizing cross-sections of the urethra, colliculus seminalis, ejaculatory ducts, vasa deferentia with ampullae, as well as the excretory ducts of the

Vet-ebooks.com

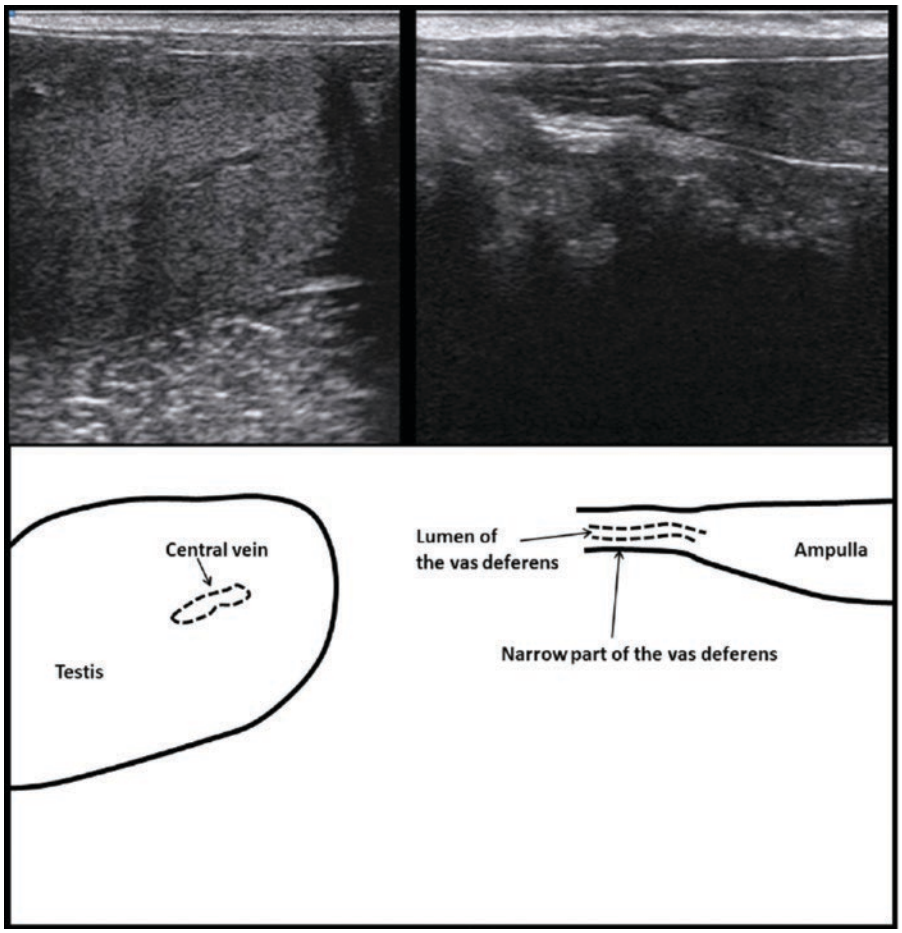


Figure 11.9 Ultrasound image of the abdominal testis of a cryptorchid. Typical features of testis are present: uniform echogenicity, hyperechoic capsule, anechoic central vein.

vesicular glands and the prostatic isthmus. Cysts of the colliculus masculinus and their effects on the ejaculatory ducts can be accurately identified using these transducers (Figure 11.4).

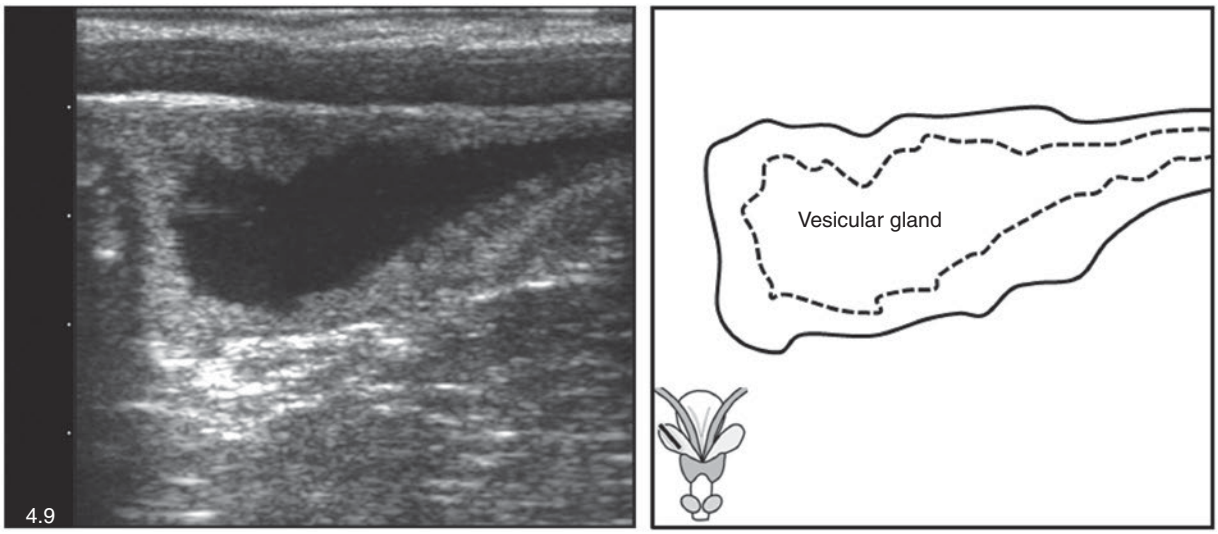
Blood vessels can be visualized using color Doppler ultrasonography. Prostatic arteries and their branches are located on the lateral and dorsal aspects of the accessory sex glands [7].

Pathologies of the Internal Genitalia

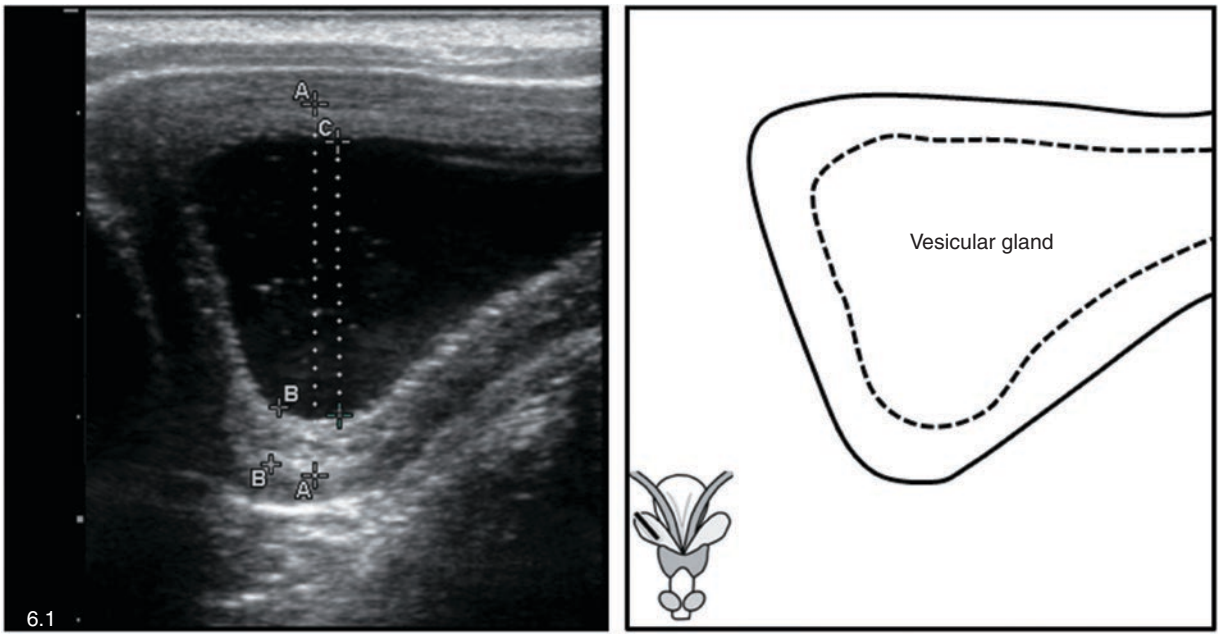
The most common pathological condition affecting the internal genitalia of stallions is ampullary occlusion. This problem occurs periodically in some individuals after prolonged periods of time of sexual abstinence and lack of ejaculation. The inspissated sperm accumulates in the terminal portions of the vasa deferentia causing partial or complete occlusion [10,11]. The back flow of semen causes significant distention of the ampullary lumen (Figure 11.7). Large cysts of the uterus masculinus in the area of the prostatic isthmus, or cysts of the utriculus masculinus in the colliculus seminalis, may compress the vasa deferentia or ejaculatory ducts and affect the ejaculatory process, and in the most severe cases, cause anejaculation (Figures 11.22, 11.23, and 11.24). Furthermore, this may contribute to the accumulation of sperm and bacteria, which form firm concretions causing occlusion. These occlusions may also form spontaneously, without any cystic structure spresent. This condition is commonly called "plugged ampullae," even thought the "plug" is usually located in the narrow portion of the vas deferens, close to the ejaculatory duct (Figure 11.7). The clinical signs of this condition are oligospermia, azoospermia, a low percentage of morphologically normal sperm, a high percentage of tail-less sperm heads, and a palpable enlargement of the distal ampullae. Ultrasound evaluation reveals the distended lumen of the ampullae, with either hypoechoic or echogenic contents. Hyperechoic concretions are also often found in the terminal, narrow parts of the vas deferens of the affected stallions (Figure 11.3 (focus on 11.3D), 11.7,

Vet-ebooks.com

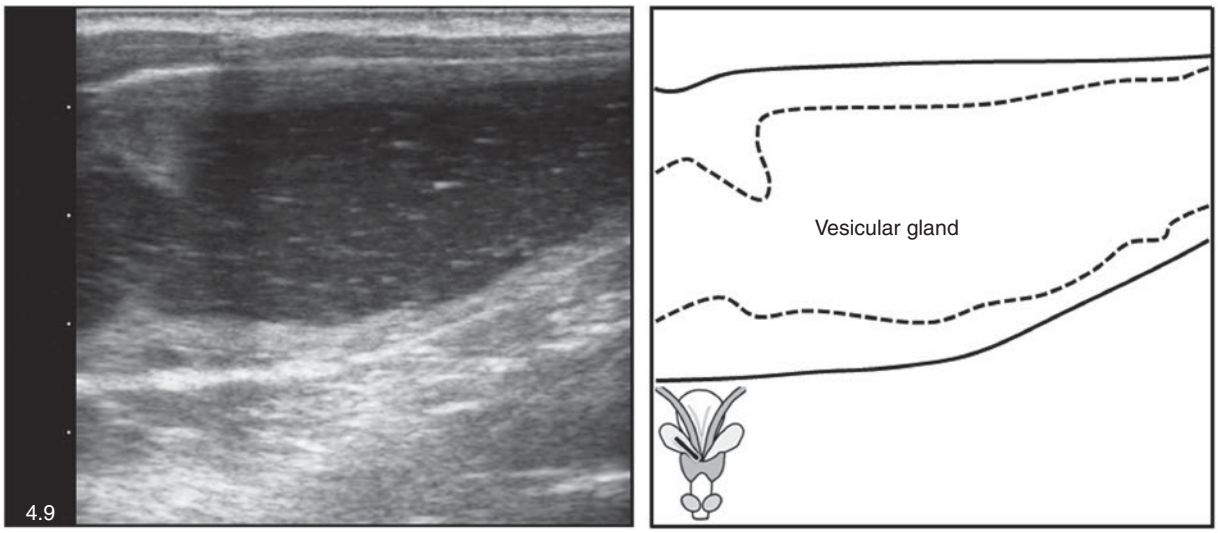
A



B



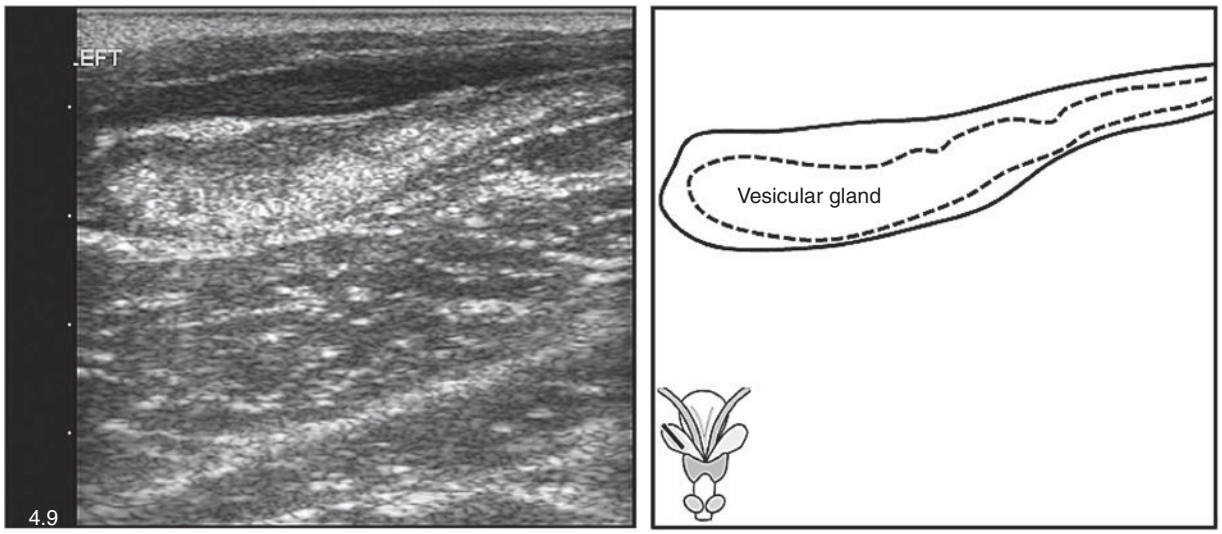
C



Vet-ebooks.com

Figure 11.10 (A) Ultrasound image of the fundus of the vesicular gland. The gland contains anechoic secretion. (B) Ultrasound image of the fundus of the vesicular gland. Measurements of the total diameter of the gland, thickness of the glandular wall, as well as diameter of the glandular lumen, are taken using the ultrasonographic caliper. (C) Ultrasound image of the vesicular gland in a stallion. The gland contains mildly echogenic secretion with hyperechoic concretions. This stallion was exposed to mares but did not have a chance to ejaculate for a prolonged period of time, which led to the formation of the viscous secretion. (D) Ultrasound image of the fundus of the vesicular gland. The gland contains hyperchoic secretion due to a high viscosity of the glandular secretion. (E) Ultrasound image of the vesicular gland in a teaser stallion.

D



E

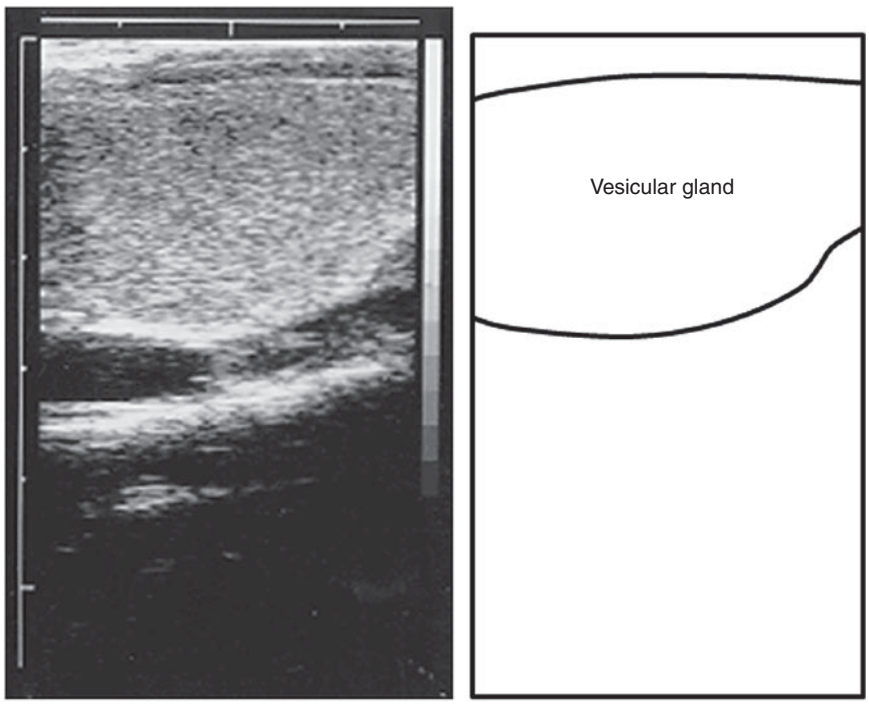


Figure 11.10 (Continued)

Vet-ebooks.com

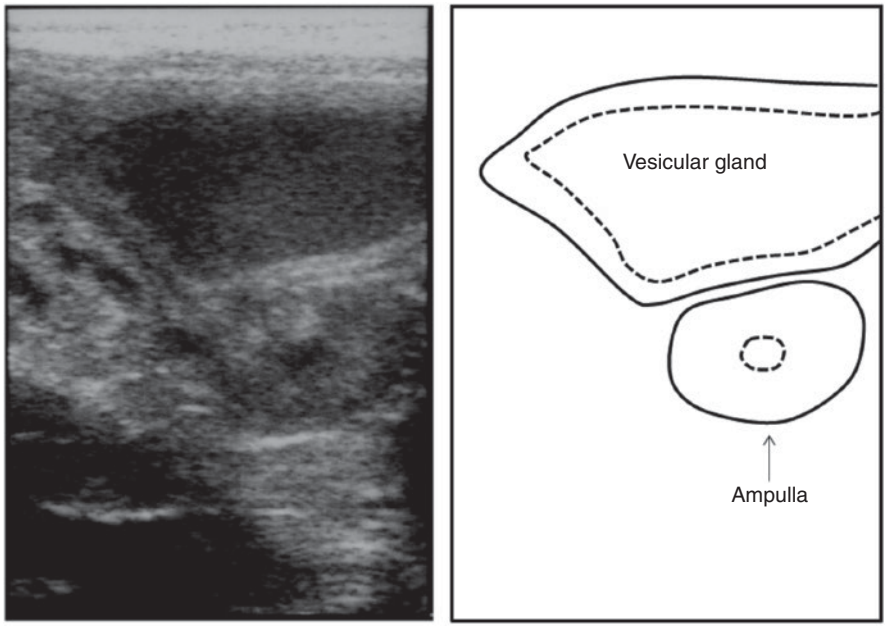


Figure 11.11 Ultrasound image of the vesicular gland and ampulla of the vas deferens (cross-section) in a stallion with seminal vesiculitis.

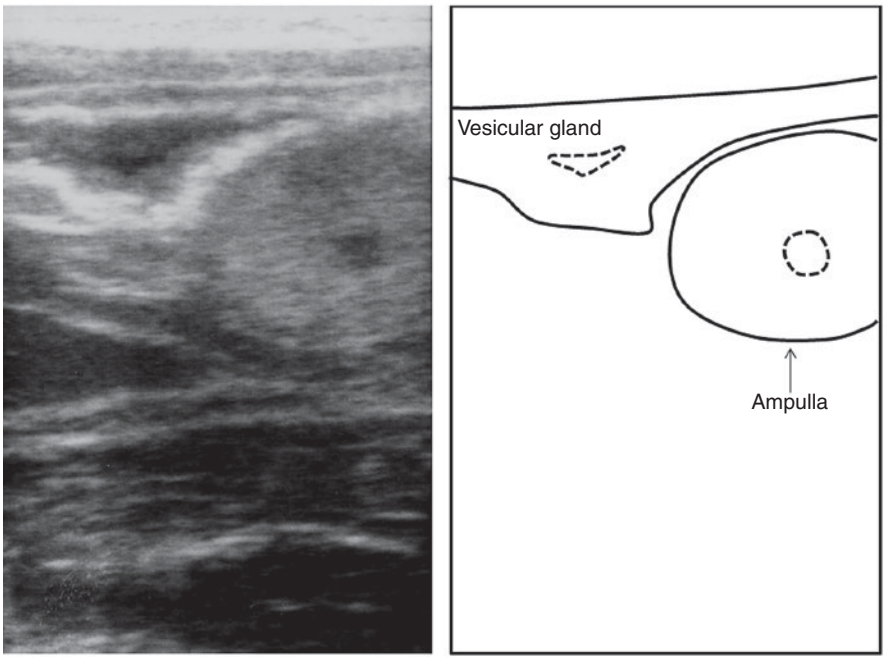


Figure 11.12 Ultrasound image of the vesicular gland and ampulla of the vas deferens (cross-section) in a stallion with seminal vesiculitis. The wall of the vesicular gland was thickened and had abnormally increased echogenicity.

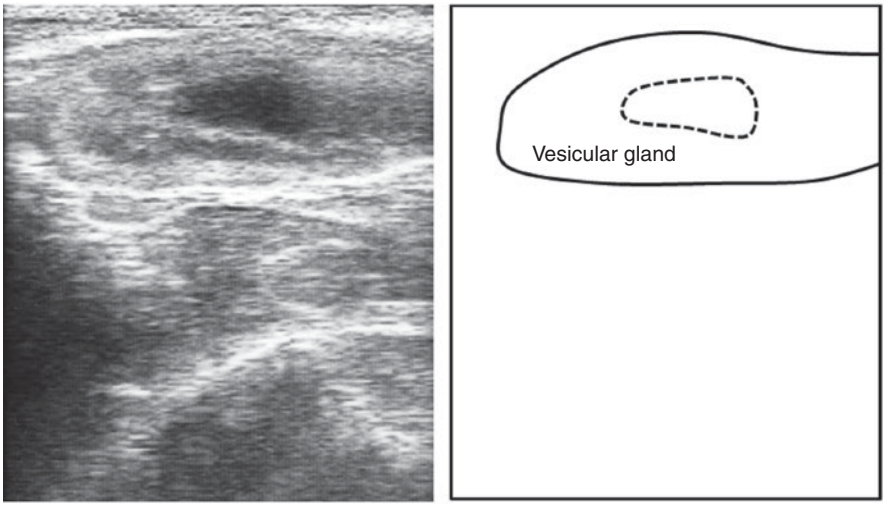


Figure 11.13 Ultrasound image of the vesicular gland in a stallion with seminal vesiculitis. The wall of the vesicular gland was significantly thickened.

Vet-ebooks.com

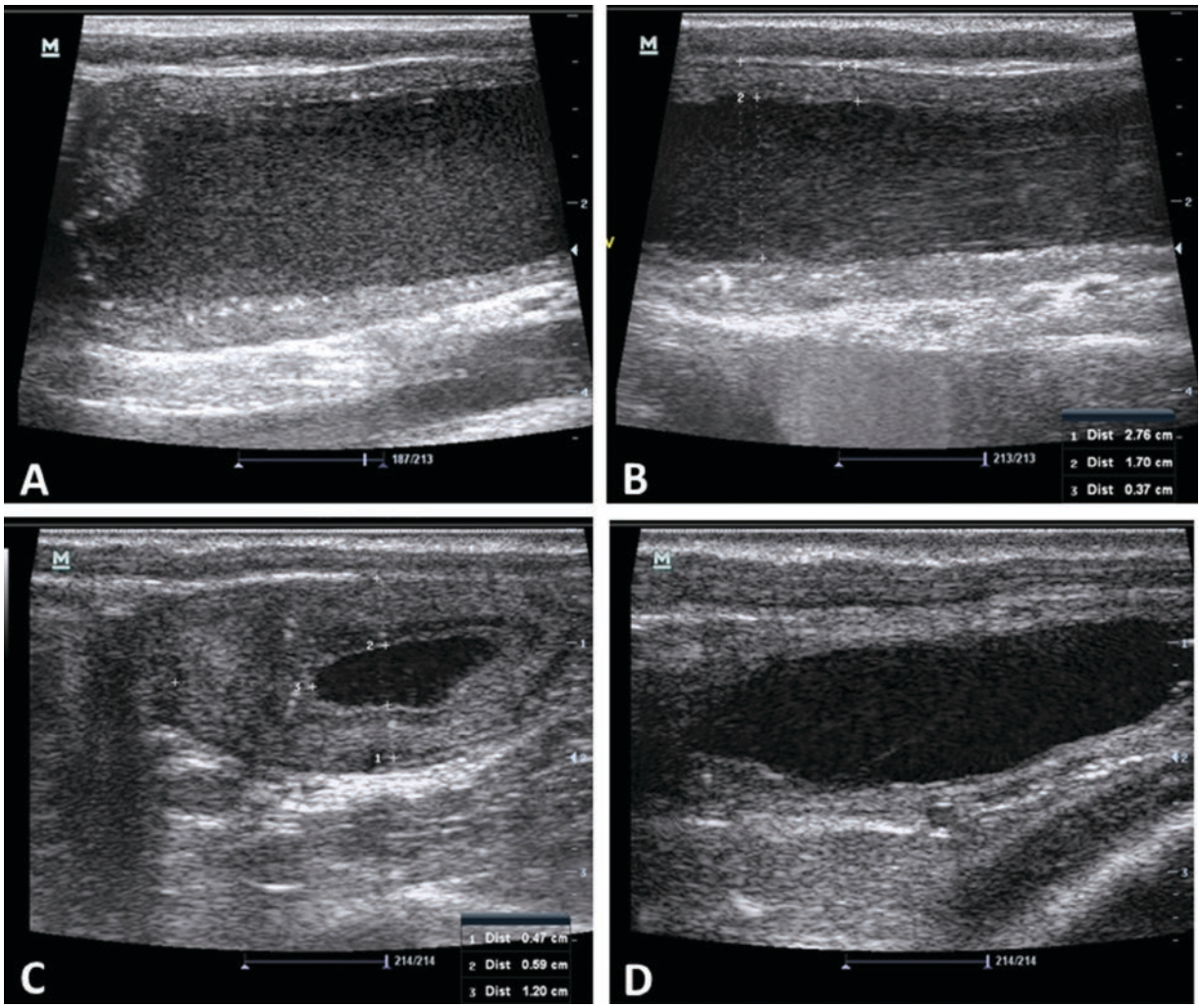


Figure 11.14 Ultrasound images of the vesicular gland in a stallion with seminal vesiculitis: the glands are enlarged, palpable per rectum, slightly sensitive during palpation, have moderately echogenic content, and thickened wall with hyperechoic specks (A and B); the luminal content is flushed out using transurethral endoscopic catheterization (C) and antibiotics are infused locally for 3–5 consecutive days (D).

and 11.8). All stallions with typical symptoms of ampullary occlusion have to be carefully examined for presence of the cystic uterus masculinus and the cystic utriculus masculinus prior to any treatment. Stallions accumulating sperm due to sexual abstinence respond well to manual massage of the ampullae, and/or administration of oxytocin (20 I.U., IV) 5–10 minutes before ejaculation. Large numbers of immotile spermatozoa are usually expelled. Small concretions of inspissated sperm can also be found in the first ejaculate. Multiple collections of semen are recommended in order to remove sperm stored in the excretory system. The quality of semen usually improves significantly after several semen collections. In contrast to so-called "sperm accumulators," stallions with ampullary occlusion due to the physical compression of the vas deferens do not respond to manual massage of the ampullae *per rectum*. Furthermore, low frequency of ejaculations is recommended for these individuals, since a high pressure of semen in the ampullae seems to be necessary to force its contents through the compressed ducts into the urethra, and to trigger the ejaculatory process [5]. Administration of oxytocin prior to semen collection seems to also be helpful in these cases. Ultrasound evaluation performed after successful ejaculation confirms that the diameter and contents of the ampullary lumen are appreciably decreased.

Seminal vesiculitis is a less common pathologic condition in stallions (Figures 11.11, 11.12, 11.13, and 11.14). Usually, it is due to bacterial infection, but the exact pathogenesis of this condition is not yet

Vet-ebooks.com

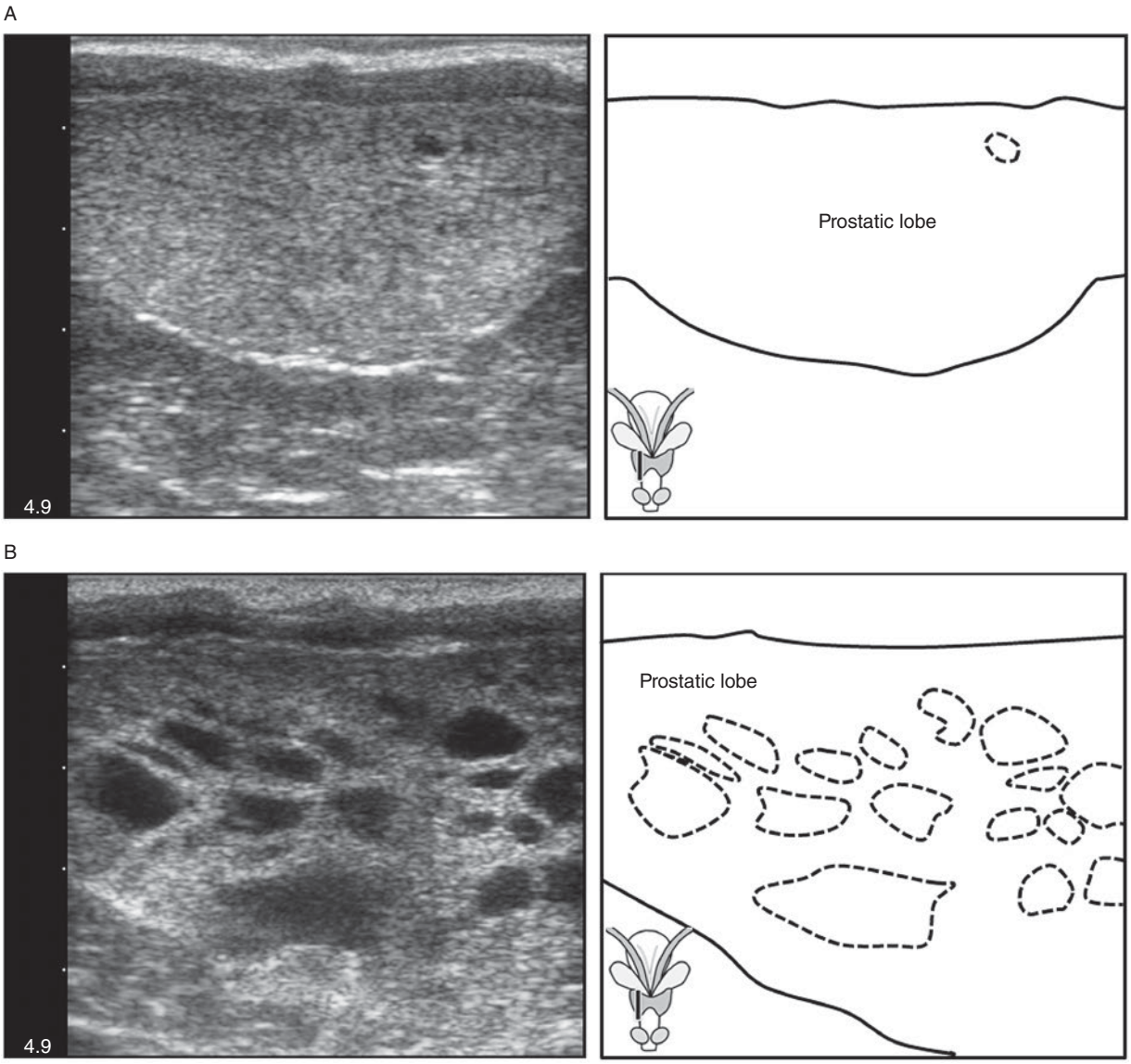
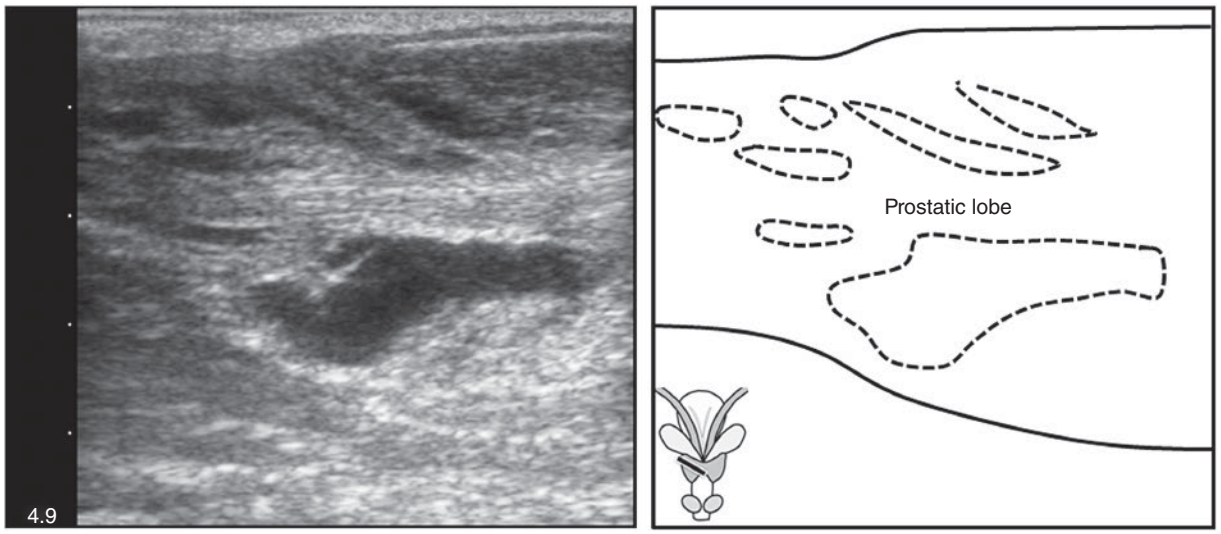


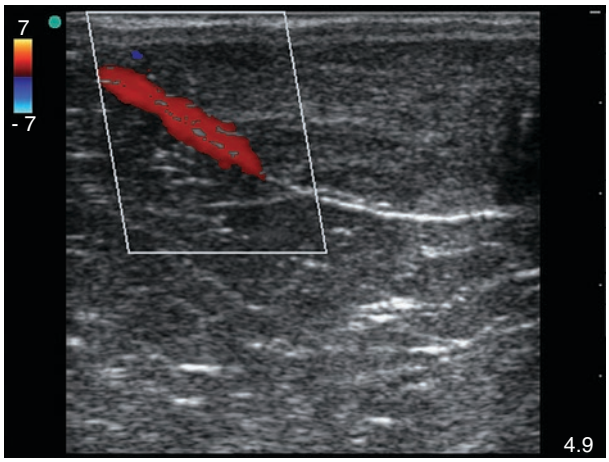
Figure 11.15 (A) Ultrasound image of the prostatic lobe of a stallion at sexual rest. (B) Ultrasound image of the prostatic lobe of a sexually aroused stallion. The prostatic acini are filled with anechoic secretion. (C) Ultrasound image of the prostatic lobe of a sexually aroused stallion – oblique section. The prostatic ducts are dilated by anechoic secretion. (D) Color Doppler ultrasound image of the prostatic vein. (E) Color Doppler ultrasound image of the prostatic vein and artery.

Vet-ebooks.com

C



D



E

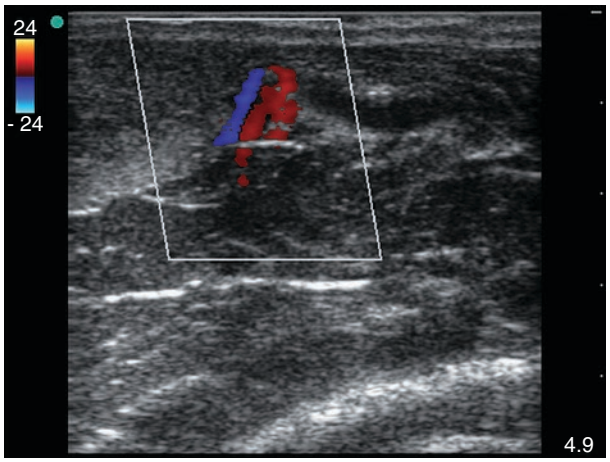


Figure 11.15 (Continued)

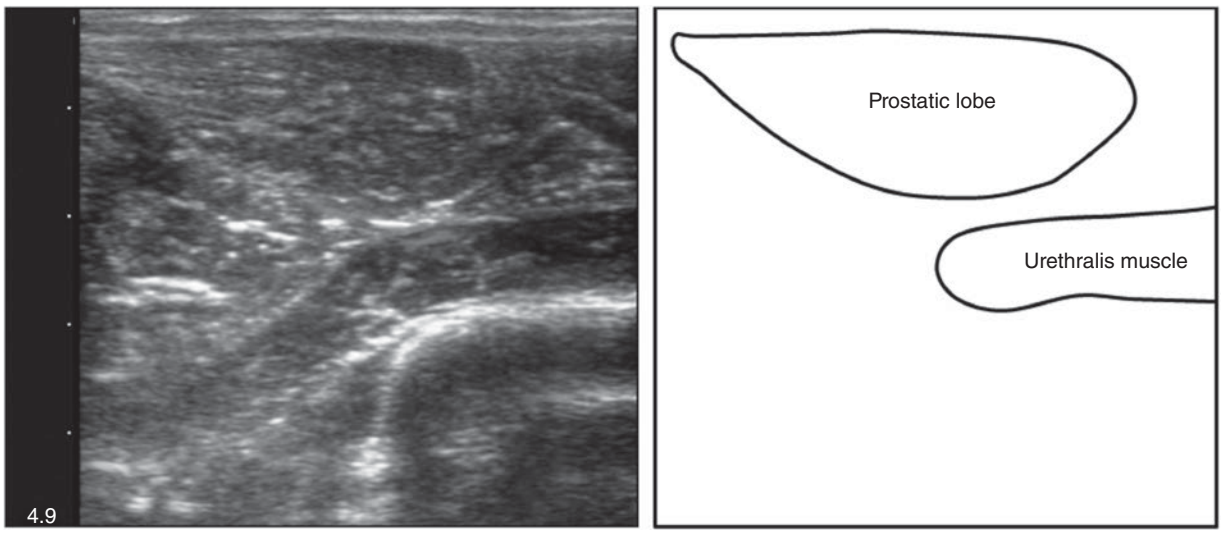


Figure 11.16 Ultrasound image of the prostatic lobe in a gelding. All accessory sex glands are significantly smaller in long-term geldings than in intact stallions [9].

Vet-ebooks.com

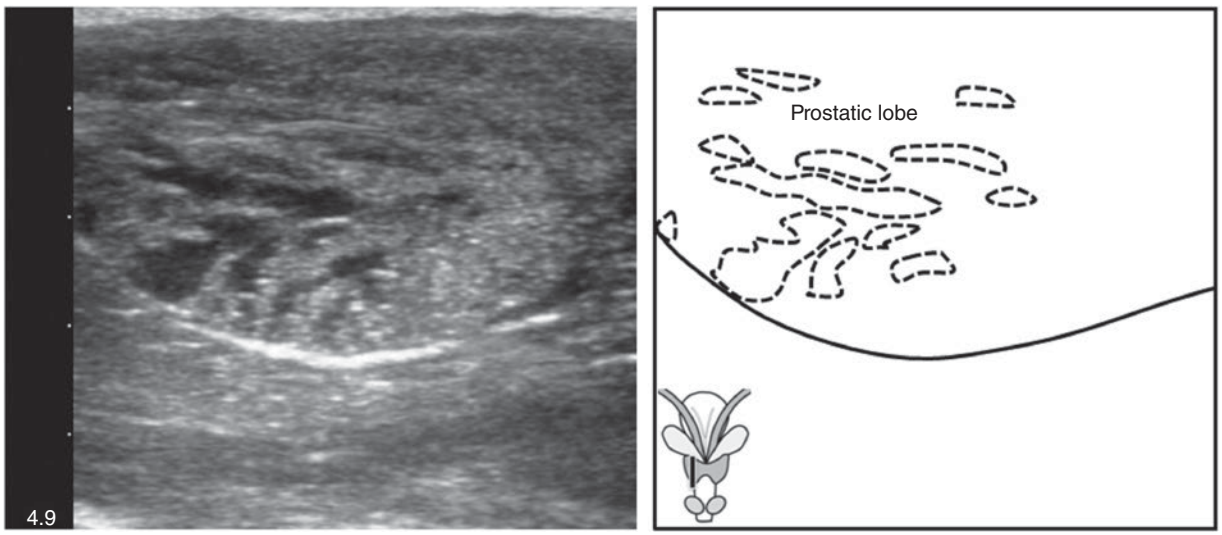


Figure 11.17 Ultrasound image of the prostatic lobe of the sexually aroused unilateral abdominal cryptorchid. This prostate has a size comparable with a prostate of an intact stallion, and contains a moderate amount of prostatic secretion.

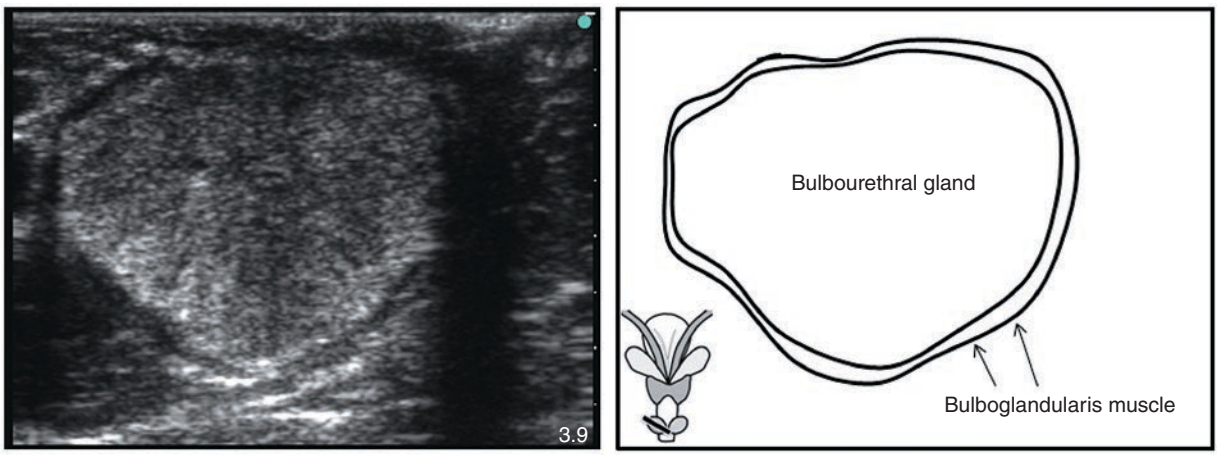


Figure 11.18 Ultrasound image of the bulbourethral gland in a sexually rested stallion. The gland is surrounded by the hypoechoic bulboglandularis muscle.

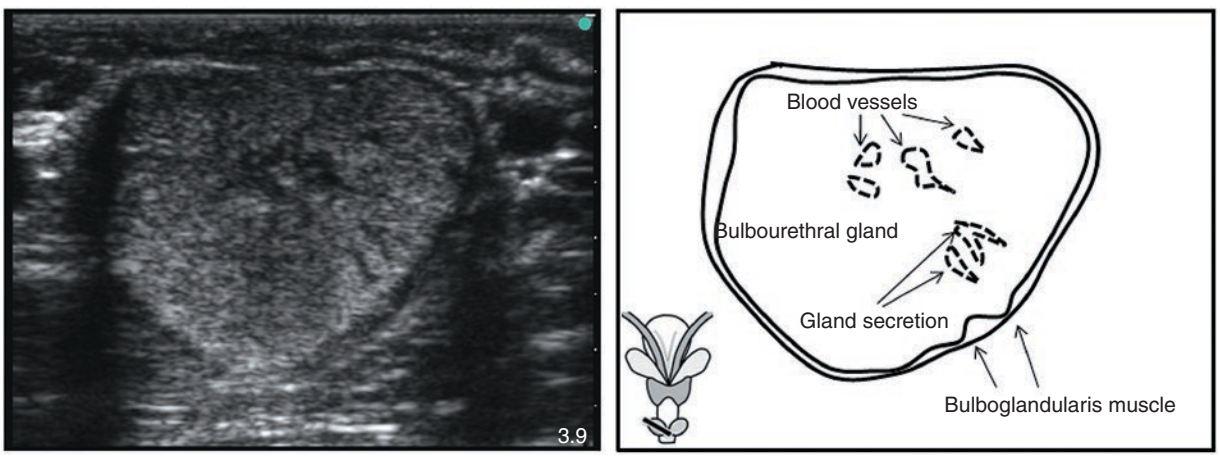


Figure 11.19 Ultrasound image of the bulbourethral gland. Blood vessels appear as hypoechoic spaces in the center of the gland.

Vet-ebooks.com

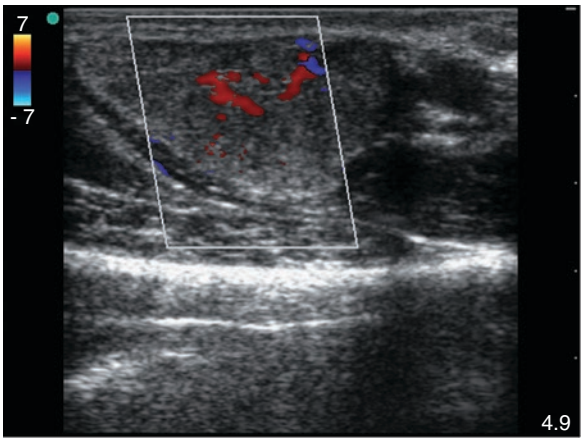


Figure 11.20 Color Doppler ultrasound image of the bulbourethral gland. Blood vessels appear as red and blue lines in the center of the gland.

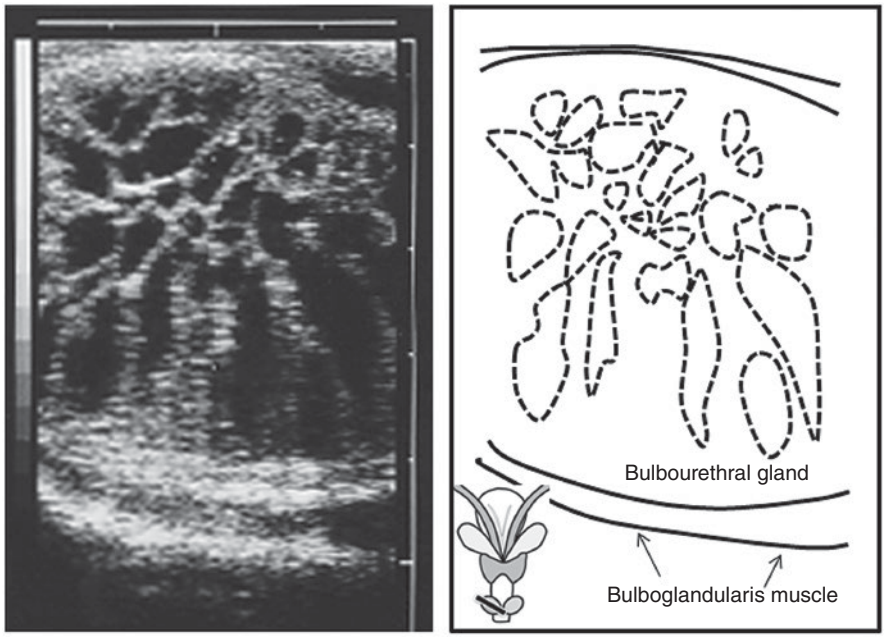


Figure 11.21 Ultrasound image of the bulbourethral gland in a teaser stallion after a long exposure to mares. The sacs and tubules are dilated with anechoic secretion.

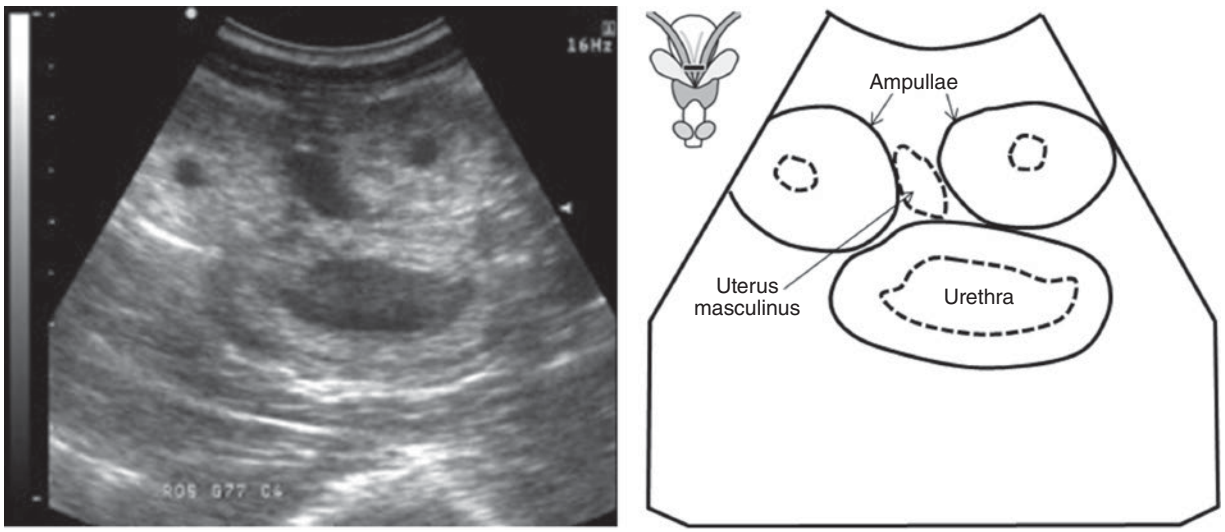


Figure 11.22 Ultrasound image of the cross-sections of the ampullae of the vasa deferentia and the urinary bladder. A large cyst of the uterus masculinus is also present between the ampullae. This stallion was experiencing ejaculatory problems.

Vet-ebooks.com

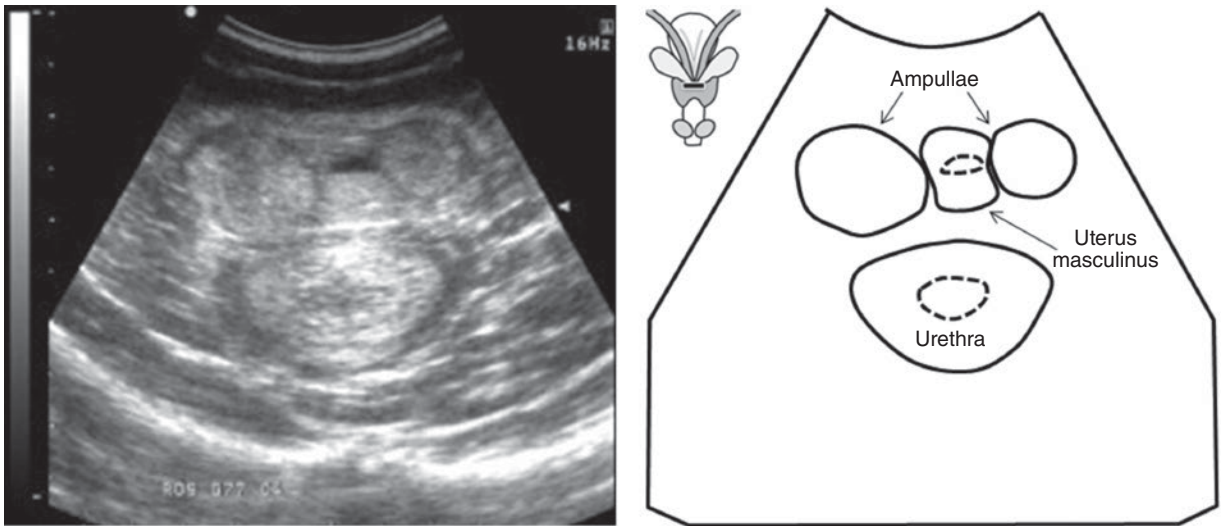


Figure 11.23 Ultrasound image of the cross-sections of the ampullae of the vasa deferentia and the urinary bladder in a stallion with ejaculatory problems. The multicystic uterus masculinus has anechoic, watery content, as well as echogenic, highly viscous content.

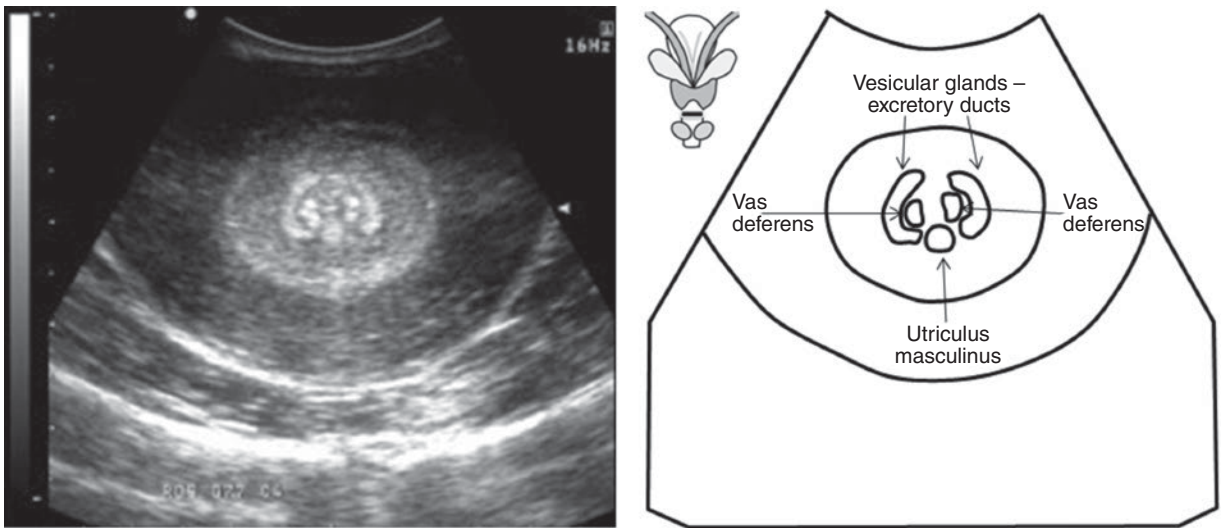


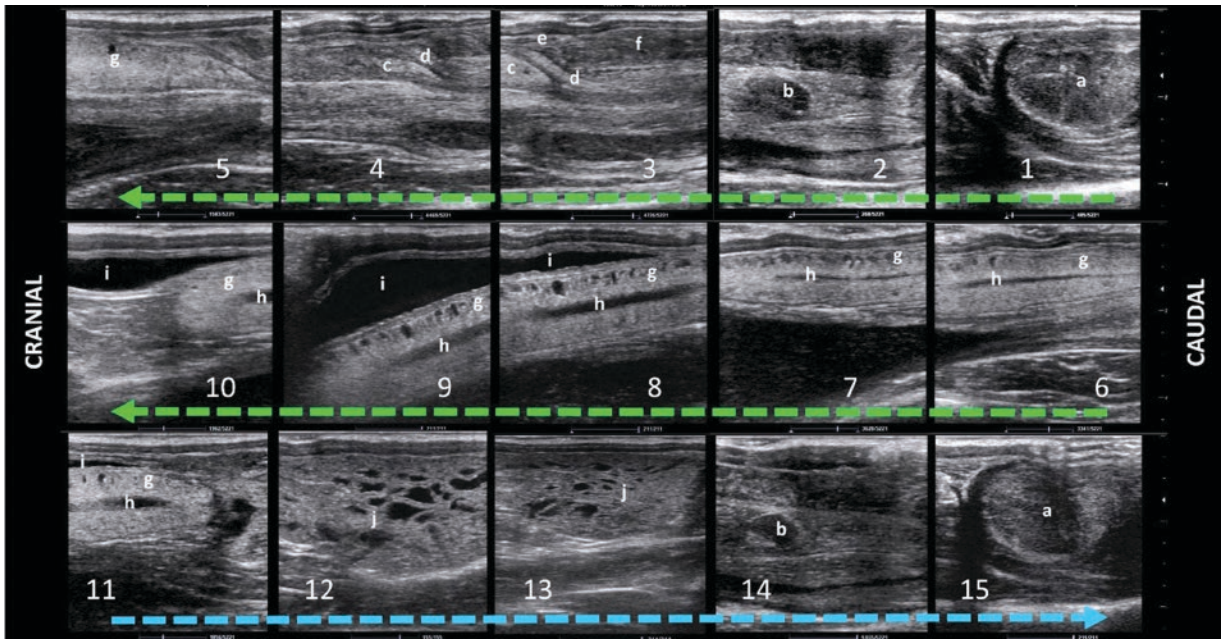
Figure 11.24 Ultrasound image of the cross-sections of the colliculus seminalis in a stallion with ejaculatory problems. The terminal portions of the vasa deferentia contain numerous hyperechoic concretions.

well known. Perhaps a reflux of urine and semen during ejaculation can contribute to this infection, or an ascending or descending infection coming from other sites of the reproductive tract. Clinical signs include a presence of inflammatory cells and/or blood in the ejaculate, positive bacterial culture from semen, and/or enlarged or painful vesicular glands [12]. Typically, as seen in the ultrasound evaluation, inflamed vesicular glands have thickened walls and cloudy luminal contents (Figures 11.11, 11.12, 11.13, and 11.14) [13]. However, echogenic luminal contents within seminal vesicles are not always indicative of seminal vesiculitis, as this appearance may also be seen in normal stallions [14]. Therefore, presumptive diagnosis is made from semen evaluation rather than based on the ultrasound examination alone. Seminal vesiculitis can be treated using antibiotics delivered directly into the lumen of the vesicular glands using a flexible endoscope. However, there are reports of a limited success with treatment of seminal vesiculitis using systemic antibiotics, such as enrofloxacin.

A Powerpoint file showing the recommended order of scanning for the stallion internal reproductive tract is available on the companion website: www.wiley.com/go/kidd/equine-ultrasonography.

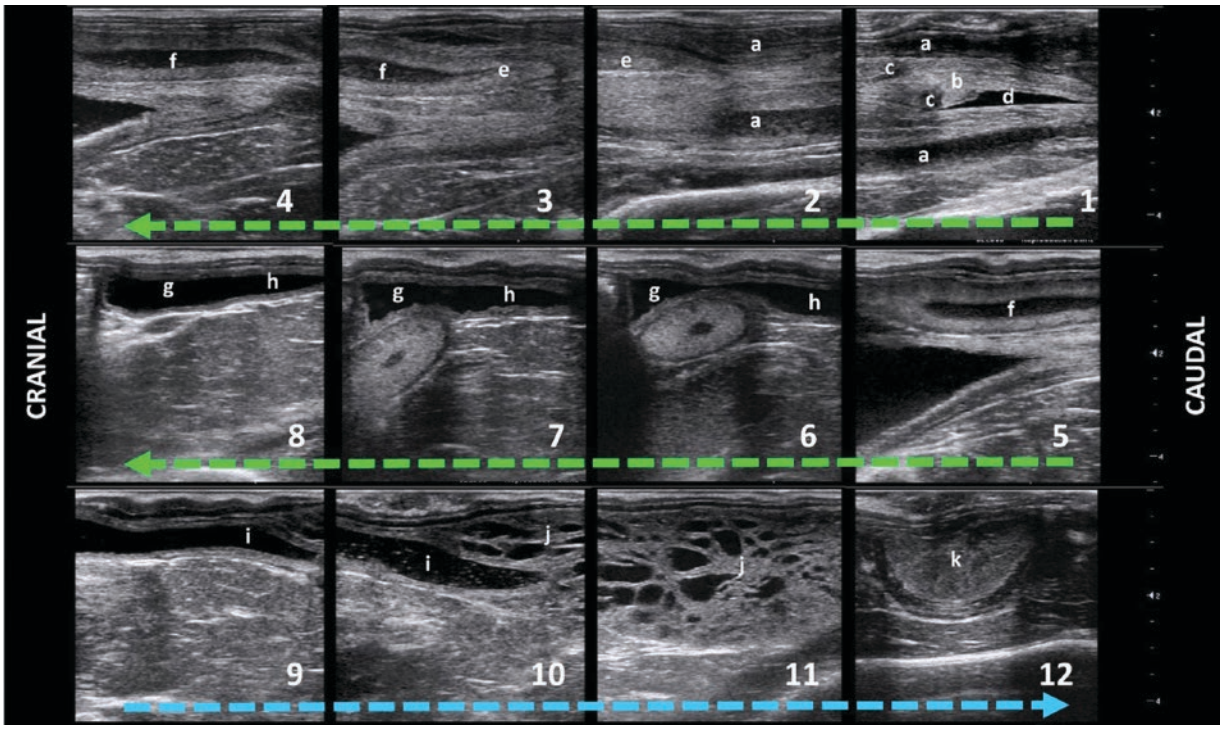
Vet-ebooks.com

CASE EXAMPLES



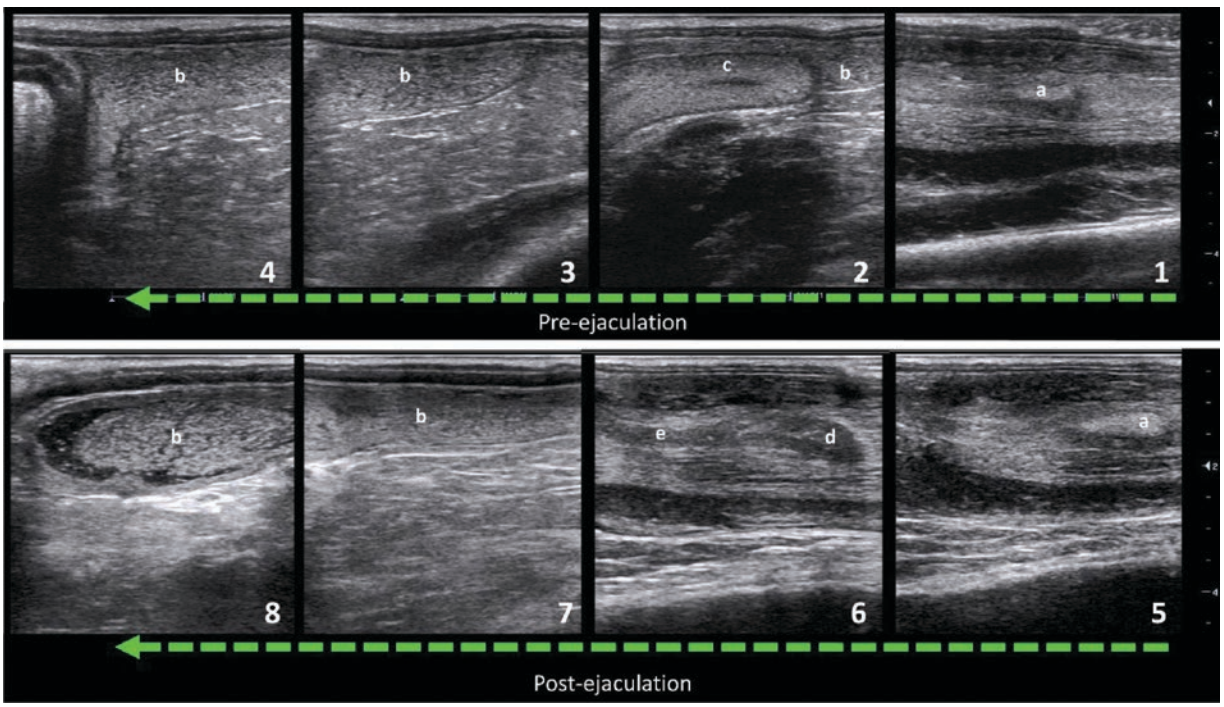
Normal Stallion. A series of the sequential ultrasound images of the accessory sex glands and the pelvic urethra of a normal stallion. The exam starts from the bulbourethral glands (image 1: a), and moves in a cranial direction, visualizing the pelvic urethra and the colliculus seminalis with a small midline cyst (image 2: b), terminal parts of the ampullae of the vasa differentia (image 3: c), the excurrent ducts of the vesicular glands (image 3: d), which are "diving" under the prostatic isthmus (image 3: e), and the urethralis muscle (image 3: f). Each ampulla is followed cranially (image 5: g), and its thick, glandular image, as well as its lumen is apparent (images 6, 7, 8, 9: g and h, respectively). The vesicular gland is seen on the top of the ampulla (images 7 and 8: i), while the contralateral gland, which is smaller, is visualized laterally to the ampulla (Image 10: i). The exam now moves in a caudal direction, following the ampullae and the vesicular glands (image 11: g, h, l). The prostatic lobes are visualized on both sides of the pelvic urethra (images 12 and 13: j). The exam is concluded by another visualization of the urethra, colliculus seminalis, and the bulbourethral glands (images 14 and 15). **Video clip is available.**

Vet-ebooks.com



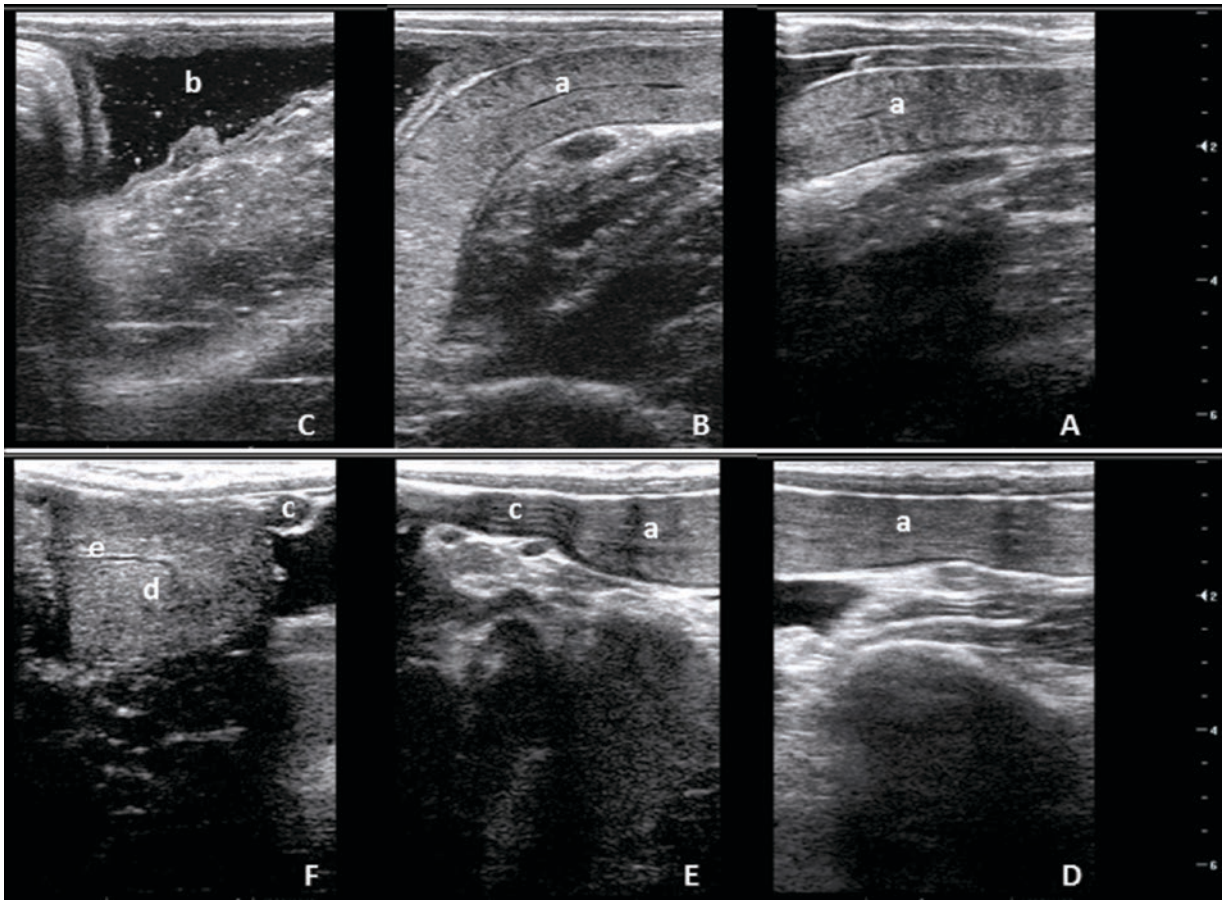
Occluded ampullae. A series of the sequential ultrasound images of the accessory sex glands and the pelvic urethra of a stallion with ejaculatory difficulties due to occluded ampullae. This exam was performed after three unsuccessful attempts to collect semen. The exam starts from the pelvic urethra with the urethralis muscle, and the colliculus seminalis, which has a small midline cyst (image 1: a, b, c, respectively). A small amount of secretions of the urethral glands and the prostate is also seen in the urethral lumen (image 1: d). Next structures to be seen, cranially to the colliculus seminalis, are the terminal parts of the ampullae of the vasa deferentia, and the ampullar lumens that are visibly dilated (images 3, 4, 5: e and f, respectively). Each ampulla is followed in the cranial-lateral direction to visualize the vesicular glands, with their nonechoic content (Images 6, 7, 8: g, h). The exam continues in a caudal direction, starting from the fundus, through the body, and the excretory duct of each vesicular gland (images 8, 9, 10; g, h, i, respectively). The excretory ducts of the vesicular glands are dilated due to an ejaculation. The prostate is visualized next (images 10, 11: j). The last structures that are examined are bulbourethral glands (image 12: k).

Vet-ebooks.com



Enlarged vesicular glands. A series of the sequential ultrasound images of the accessory sex glands and the pelvic urethra of a stallion with a history of ejaculatory difficulties and overproduction of viscous and thick secretions by the vesicular glands. The images 1–4 were taken prior to an attempt to collect semen; the images 5–8 were taken after one successful collection of semen. The initial exam showed hyperechoic content in an area of colliculus seminalis, likely thick gel in the excretory ducts of the vesicular glands/ejaculatory ducts (image 1: a), large vesicular glands with non-uniformly echogenic lumen – thick gel (images 2–4: b), and ampullae with normal lumen (image 2: c). Transrectal massage of the vesicular glands and the ampullae was performed shortly before an attempt to collect semen; 20 IU of oxytocin was also administered IV immediately before semen collection. The follow-up examination, performed after ejaculation, showed hyperechoic content in an area of the colliculus seminalis (image 5: a), a midline cyst of the colliculus seminalis (image 6: d), a longitudinal hypoechoic structure between the terminal portions of the vasa deferentia, most likely – uterus masculinus (image 6: e), and non-uniformly echogenic content of the vesicular glands (images 7 and 8: b). Semen evaluation did not reveal any signs of seminal vesiculitis: no inflammatory cells in semen, negative bacterial cultures taken from the urethra post-ejaculation, and from semen. **Video clip is available.**

Vet-ebooks.com



Cryptorchid. A series of sequential ultrasound images demonstrating tracing vasa deferentia, starting at their glandular portions – the ampullae. The ampulla bends ventrally toward the vaginal ring and the normally descended, scrotal testis (images A-C, from right to left); the vesical gland is easily found laterally to the ampulla (b). In a case of an abdominal cryptorchid stallion (images D-F, from right to left), the ampulla runs cranially, and the narrow part of the vas deferens (c) can be followed directly to the retained testis (d). The central vein of the testis is also visualized (e). **Video clip is available.**

References

1 Sisson, S. (1910). *A Textbook of Veterinary Anatomy*. Philadelphia PA: W.B. Saunders.

2 McFadyean, J. (1884). *The Anatomy of the Horse. A Dissection Guide*. Edinburgh and London: W. & A.K. Johnson.

3 Swoboda, A. (1929). Beitrag zur Kenntnis des Utriculus Masculinus der Haustiere. *Zeitschrift für Anatomie und Entwicklungsgeschichte* 89: 494–512.

4 Guyon, L. (1939). Recherches sur Litricule Prostatique chez le Cheval Entier ou Castre. *Comptes Rendus des Séances de la Société de Biologie et de ses Filiales* 131: 1167–1169.

5 Pozor, M., Macpherson, M.L. et al. (2011). Midline cysts of colliculus seminalis causing ejaculatory problems in stallions. *Journal of Equine Veterinary Science* 31: 722–731.

6 Little, V.L. and Holyoak, G.R. (1992). Reproductive anatomy and physiology of the stallion. *Veterinary Clinics of North America: Equine Practice* 8: 1–29.

7 Ginther, O.J. (2007). *Ultrasonic Imaging and Animal Reproduction: Color-Doppler Ultrasonography. Book 4*. Cross Plains WI: Equiservices.

8 Little, T.V. and Woods, G.L. (1987). Ultrasonography of accessory sex glands in the stallion. *Journala of Reproduction and Fertility* 35(Suppl): 87–94.

9 Nickel, R., Schummer, A., and Seiferle, E. (1979). *The Viscera of the Domestic Mammals*. Hamburg: Springer-Verlag.

10 Love, C.C., Riera, F.L., Oristaglio, R.M. et al. (1992). Sperm occluded (plugged) ampullae in the stallion. *Proceedings of the Society for Theriogenology* 117–125.

11 Klewitz, J., Probst, J., Baackmann, C. et al. (2012). Obstruktion der Samenleiterampullen ["plugged ampullae"] als Ursache einer Azoospermie bei einem Hengst. *Pferdeheilkunde* 28: 14–17.

12 Varner, D.D., Blanchard, T.L., Brinsko, S.P. et al. (2000). Techniques for evaluating selected reproductive disorders of stallions. *Animal Reproduction Science* 60–61: 493–509.

13 Malmlgren, L. (1992) Ultrasonography: A new diagnostic tool in stallions with genital tract infection? *Acta Veterinaria Scandinavica* 88(Suppl): 91–94.

14 Pozor, M. and McDonnell, S.M. (2002). Ultrasonographic measurements of accessory sex glands, ampullae, and urethra of normal stallions of various size types. *Theriogenology* 58: 1425–1433.

Vet-ebooks.com

12

Ultrasonography of the Penis

Malgorzata A. Pozor

College of Veterinary Medicine, University of Florida, Gainesville, FL, USA

Anatomy

The stallion penis consists of three parts: the root, the body or the shaft, and the glans. The root has two crura, which are attached to the tubera ischii via the ischiocavernous muscles on each side. Suspensory ligaments deliver further support and stabilization to this attachment [1]. The crura fuse below the ischial arch and form the laterally compressed corpus cavernosum. The urethra is surrounded by the corpus spongiosum, which starts at the bulb of the penis and continues all the way to the urethral process. The urethra lies in the urethral groove, on the ventral side of the penile body [1]. The bulbospongiosus muscle runs along the ventral aspect of the penis and encloses the corpus spongiosum of the urethra (Figure 12.1). The corpus cavernosum is enclosed by a thick fibrous sheet termed the tunica albuginea (Figure 12.1), the elastic properties of which allow limited expansion of the penis during erection [2]. Further anteriorly, the corpus cavernosum divides into three processes – one central process and two lateral processes. The central process is the longest and runs all the way into the glans penis. The glans penis is the most distal part of the penis and has two distinct parts – neck and corona glandis. The erectile body of the glans is called the corpus spongiosum glandis (Figure 12.2). The corpus spongiosum glandis has a dorsal process, which covers the dorsal and lateral sides of the corpus cavernosum penis for approximately 10–15 cm (4–6 inches) [3]. The glans can expand significantly during erection due to a profound elasticity of the surrounding tissues. The most distal part of the glans penis has a deep depression, the fossa glandis, which hosts the terminal portion of the urethra, the urethral process. Furthermore, the fossa glandis has a bilocular diverticulum, called the urethral sinus [3]. Smegma may accumulate in the urethral sinus and form thick "beans", which are often manually removed prior to semen collection (Figure 12.2).

The main source of blood supply to the stallion penis is the internal pudendal artery, as well as the obturator artery [4]. The internal pudendal artery gives off the artery of the bulb, the deep artery of the penis, and the dorsal artery of the penis. The obturator artery gives off the middle artery of the penis, which anastomoses with the dorsal artery of the penis and with the cranial artery of the penis [5]. The latter comes from the external pudendal artery.

Ultrasound Evaluation of the Stallion Penis

Ultrasound evaluation of the stallion penis is not performed routinely. However, this technique is helpful in detecting penile pathologies, mostly associated with paraphimosis, priapism, and penile trauma. Prior to the ultrasound examination of the penis in a normal stallion, sedatives are given to induce the penis to drop from the preputial cavity. Phenothiazine derivatives should be avoided as they can cause paraphimosis. High-frequency (7.5–10 MHz) linear or micro-convex transducers are recommended. Prior to the examination, the

Atlas of Equine Ultrasonography, Second Edition. Edited by Jessica A. Kidd, Kristina G. Lu and Michele L. Frazer.
© 2022 John Wiley & Sons Ltd. Published 2022 by John Wiley & Sons Ltd.
Companion Website: www.wiley.com/go/kidd/atlas

Vet-ebooks.com

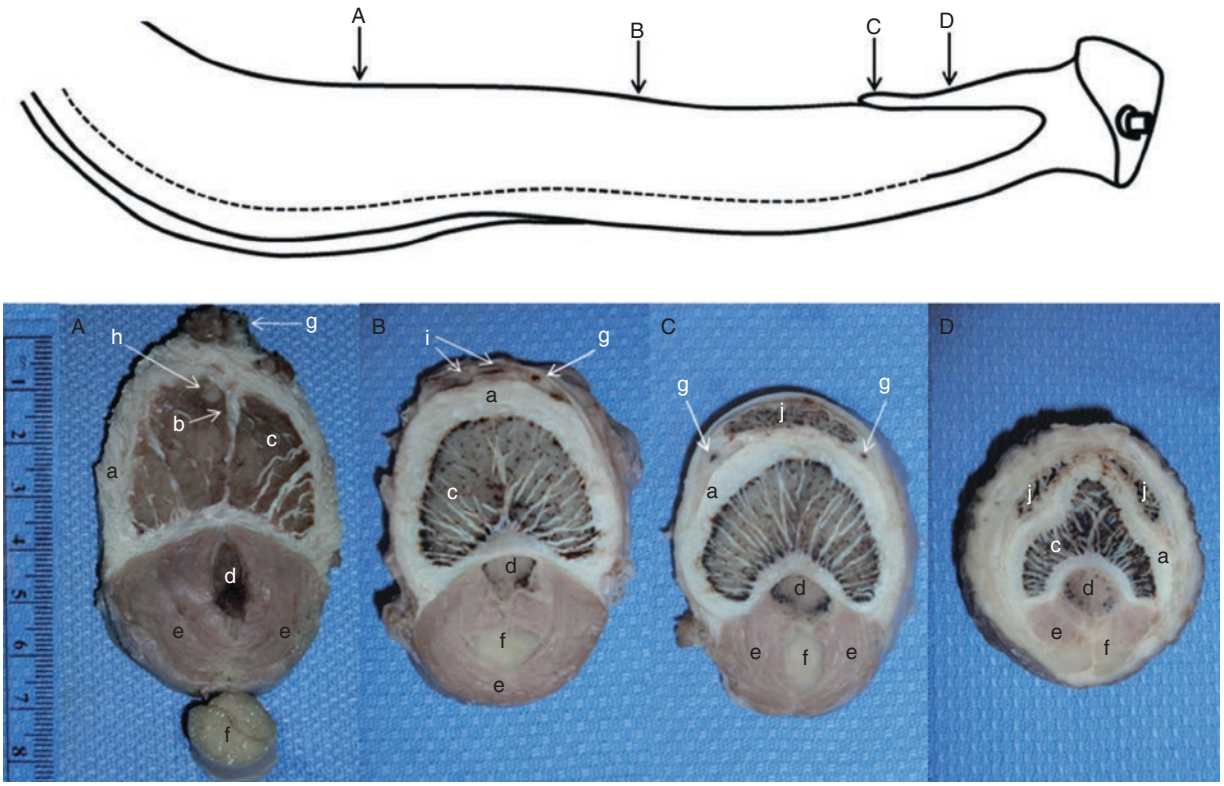


Figure 12.1 Diagram of stallion penis and cross-sections through a specimen: A – proximal part of the penile body; B – middle part of the penile body; C – free part of the penile body; D – distal part of the penile body. a: tunica albuginea; b: incomplete septum; c: corpus cavernosum; d: corpus spongiosum and urethra; e: bulbospongiosus muscle; f: retractor penis muscle; g: dorsal artery; h: deep artery; i: dorsal vein; j: corpus spongiosum glandis – dorsal process.

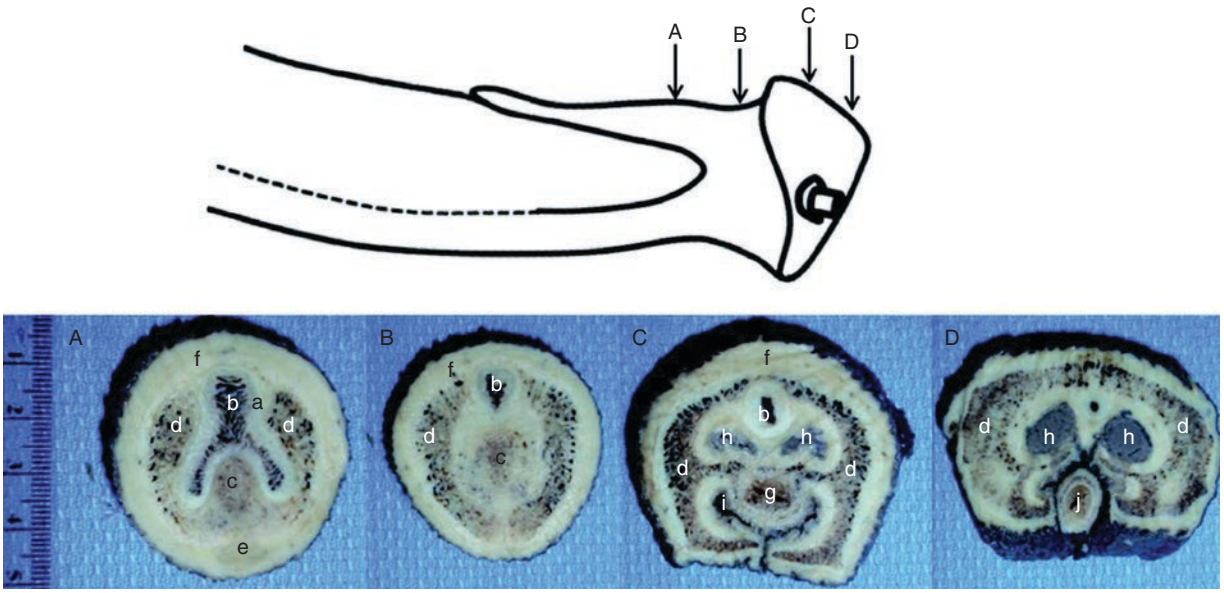


Figure 12.2 Diagram of a distal part of stallion penis and cross-sections through a specimen: (A) distal penis; (B) collum glandis; (C) corona glandis; (D) distal part of the glans penis. a: tunica albuginea; b: corpus cavernosum; c: corpus spongiosum and urethra; d: corpus spongiosum glandis; e: retractor penis muscle; f: connective tissue and penile fascias; g: urethra; h: diverticula of urethral sinus; i: fossa glandis; j: urethral process.

Vet-ebooks.com

penis should be washed with warm water in order to remove smegma, which could interfere with penetration of the ultrasound waves. A copious amount of warm ultrasound gel is then applied to the penis. Once the examination is completed, the remaining gel is washed off with warm water and a cotton towel.

The ultrasound architecture of the corpora cavernosa, the corpus spongiosum of the urethra, and the corpus spongiosum of the glans are visualized on the longitudinal and cross-sections of the organ (Figures 12.3, 12.4, 12.5, 12.6, 12.7, 12.8, 12.9, 12.10, 12.11, 12.12, 12.13, 12.14). The integrity of all these structures is carefully assessed. Color and power Doppler ultra-sonography may be helpful in visualizing the vascu-larization of the penis (Figures 12.3, 12.6, 12.7). Ultrasound evaluation of the erect penis is difficult in stallions. Some stallions may tolerate ultrasound evaluation after they have been exposed to estrous mare urine, which usually causes them to develop a penile erection. However, the operator has to be very cautious in order to avoid injury.

Spectral Doppler ultrasound assessment of the penile blood flow is often performed in men with erectile dysfunction after pharmacological induction of erection [6]. Prostaglandin E1 is injected into the corpora cavernosa in a "stepwise" fashion and any changes in the diameter of the cavernosal arteries, as well as in the peak systolic velocity (PSV) in these blood vessels are determined. Similar tests may be introduced to veterinary medicine.

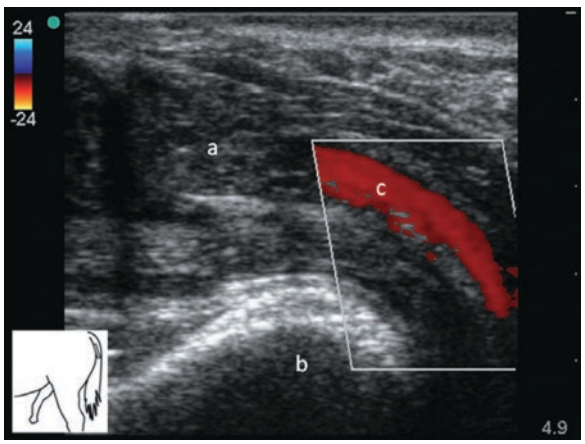


Figure 12.3 Color Doppler ultrasound image of the dorsal artery of the penis at the level of the ischial arch. a: penile bulb; b: ischial arch; c: dorsal artery of the penis.

Penile Pathologies

The most common penile pathology in a stallion is paraphimosis (inability to retract the penis back into the prepuce). Paraphimosis affects normal blood and lymphatic circulation in the penis leading to gravitational edema, especially in the preputial ring (Figures 12.15, 12.16, 12.17). The corpus spongiosum of the glans is thickened and contains dilated vessels and trabeculae (Figure 12.18). Blood flow is slow and blood clots are often formed in the corpus cavernosum, which can be visualized using ultrasonography (Figure 12.19). Priapism (persistent erection) occurs rarely in

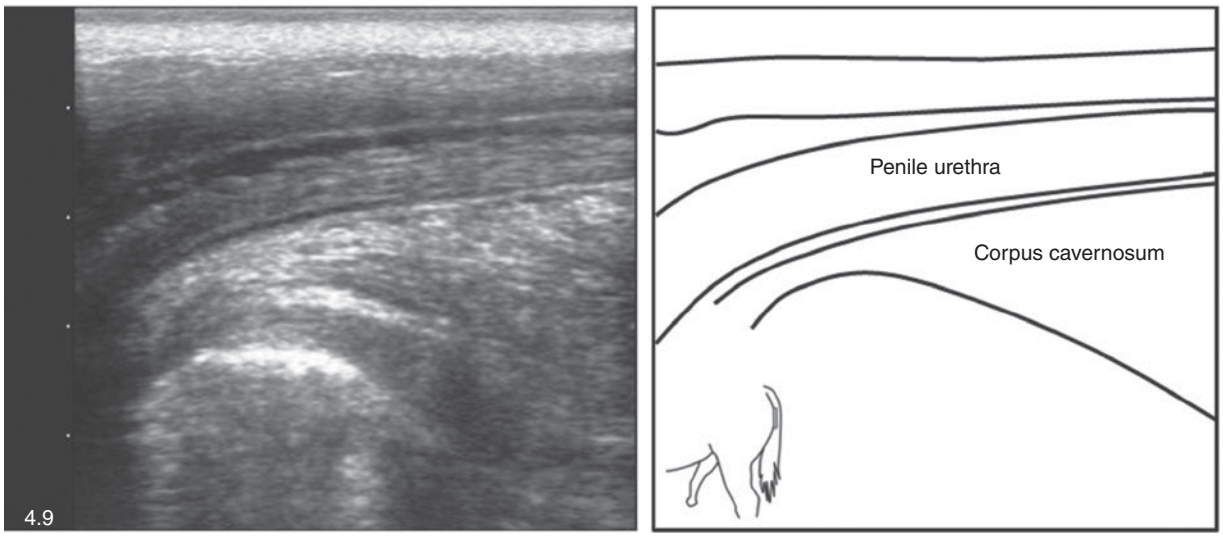


Figure 12.4 Ultrasound image of the penile urethra at the level of the ischial arch – longitudinal section.

Vet-ebooks.com

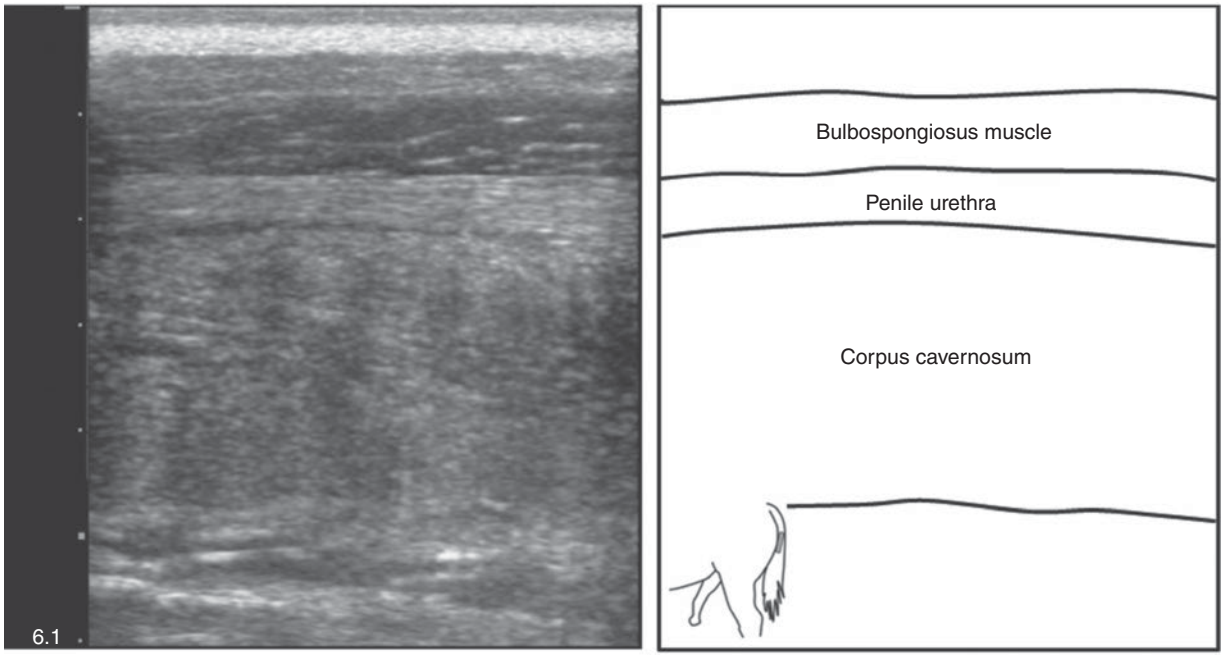


Figure 12.5 Ultrasound image of the proximal part of the penile body – longitudinal section.

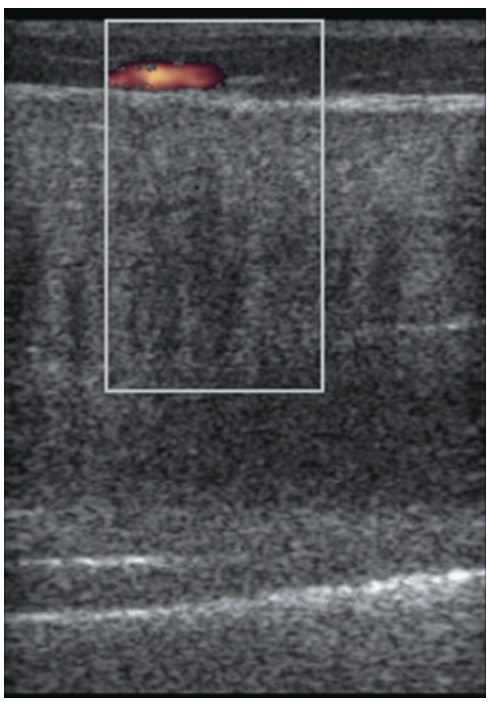


Figure 12.6 Power Doppler ultrasound image of the erect penis – longitudinal section. The dorsal artery of the penis is visualized on the dorsal surface of the penis (orange color).

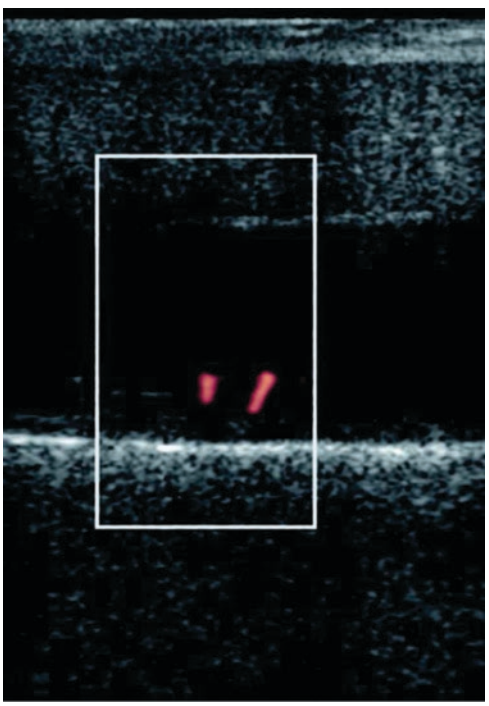


Figure 12.7 Power Doppler ultrasound image of the erect penis – longitudinal section. The helicine arteries appear as short, straight lines. These vessels assume a coiled disposition again when the penis becomes flaccid.

Vet-ebooks.com

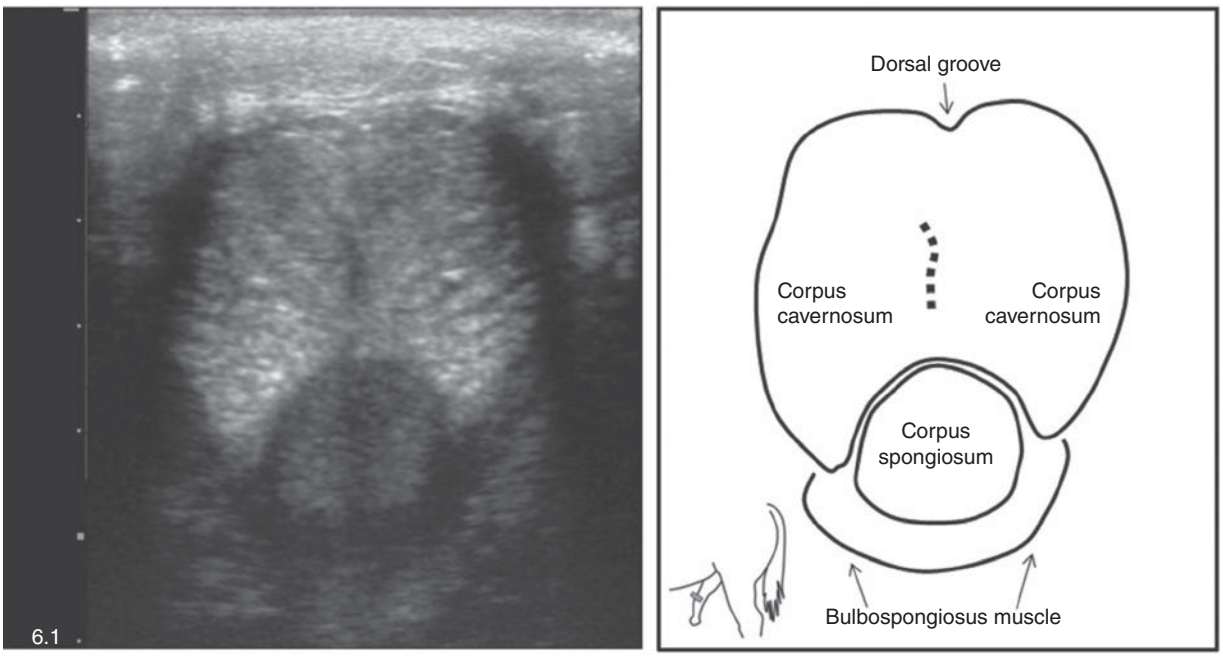


Figure 12.8 Ultrasound image of the free part of the penile body – cross-section. Trabeculae of the corpus cavernosum appear as hypoechoic spots. The incomplete septum (septum pectiniforme) and the dorsal groove are visible.

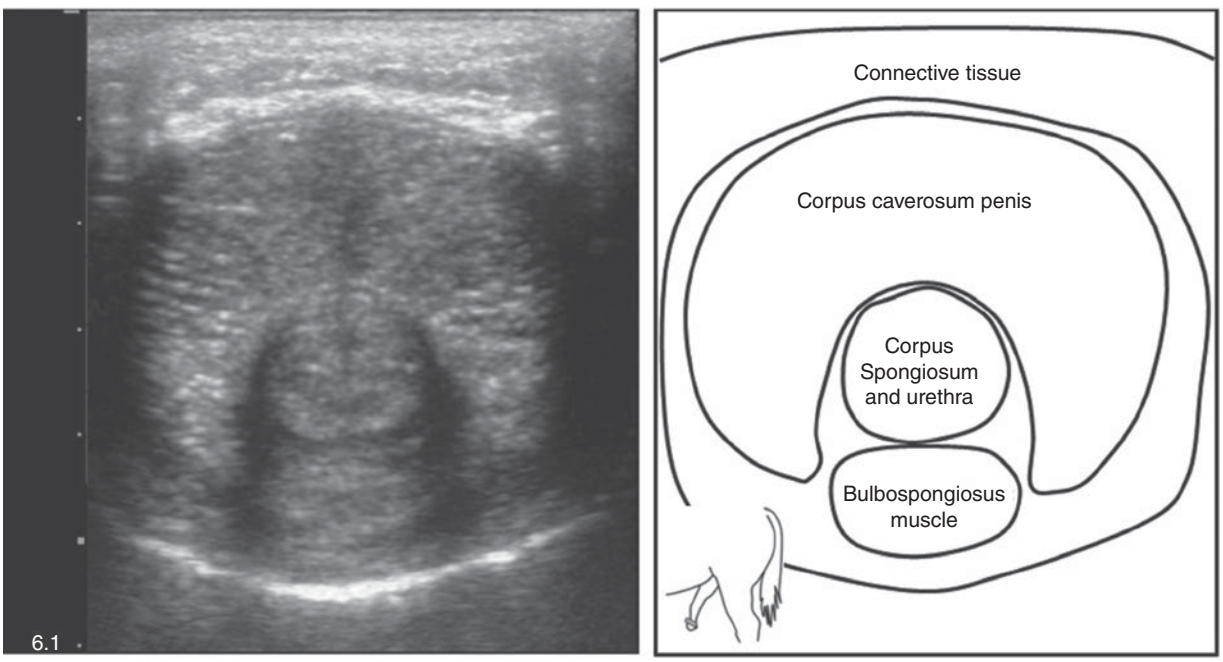


Figure 12.9 Ultrasound image of the free part of the penile body. The cross-section of the more distal part of the penile body becomes round.

Vet-ebooks.com

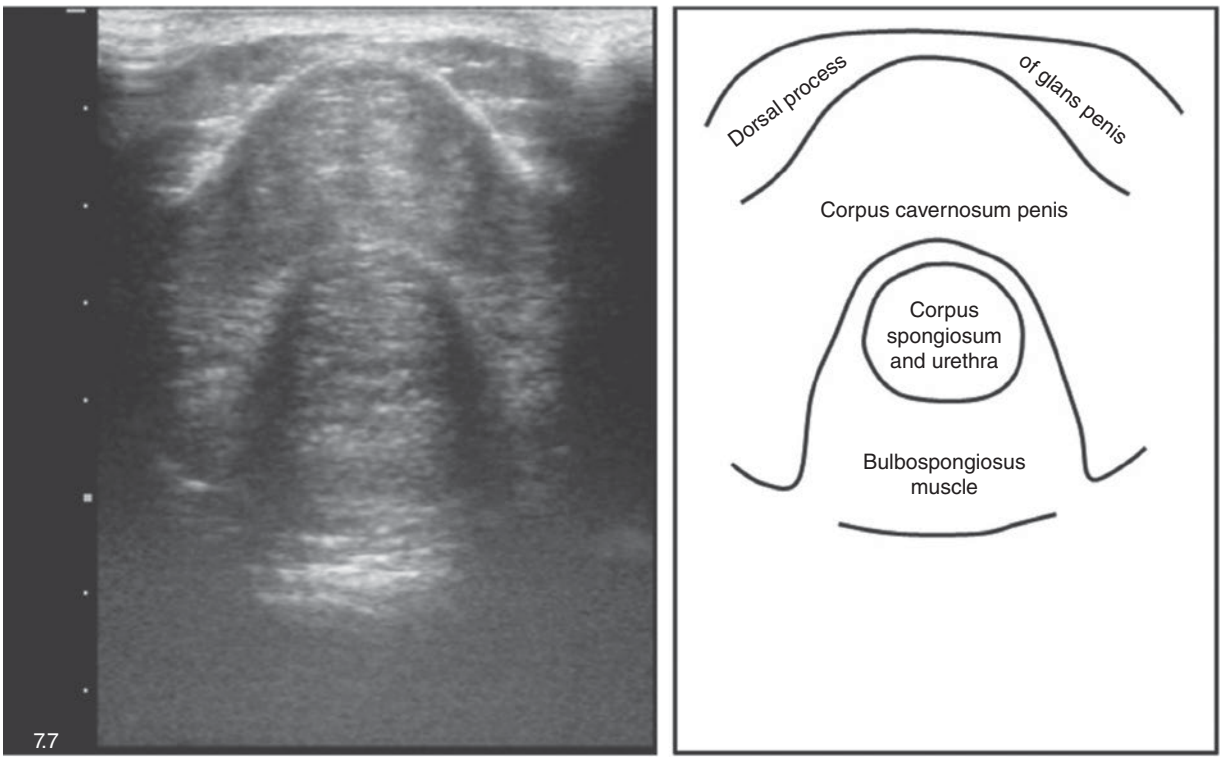


Figure 12.10 Ultrasound image of the penile body. The dorsal process of glans penis covers the dorsal aspect of the corpus cavernosum.

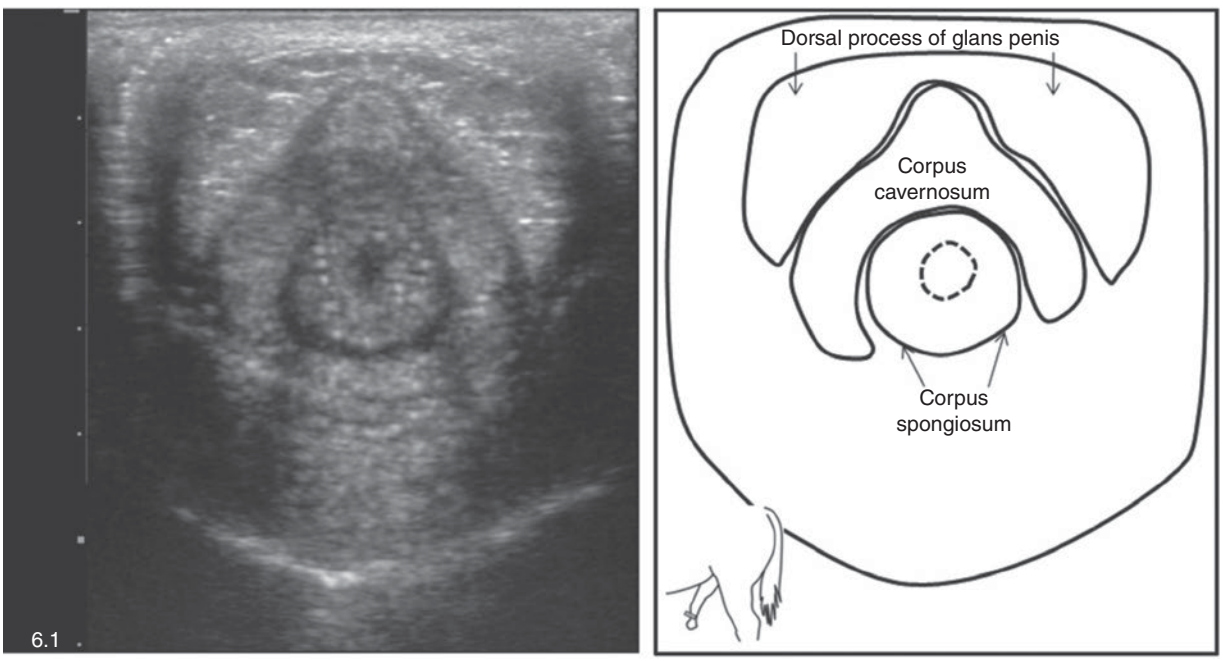


Figure 12.11 Ultrasound image of the more distal part of the penile body – cross-section. Distal process of glans penis becomes larger, while the corpus cavernosum becomes smaller.

Vet-ebooks.com

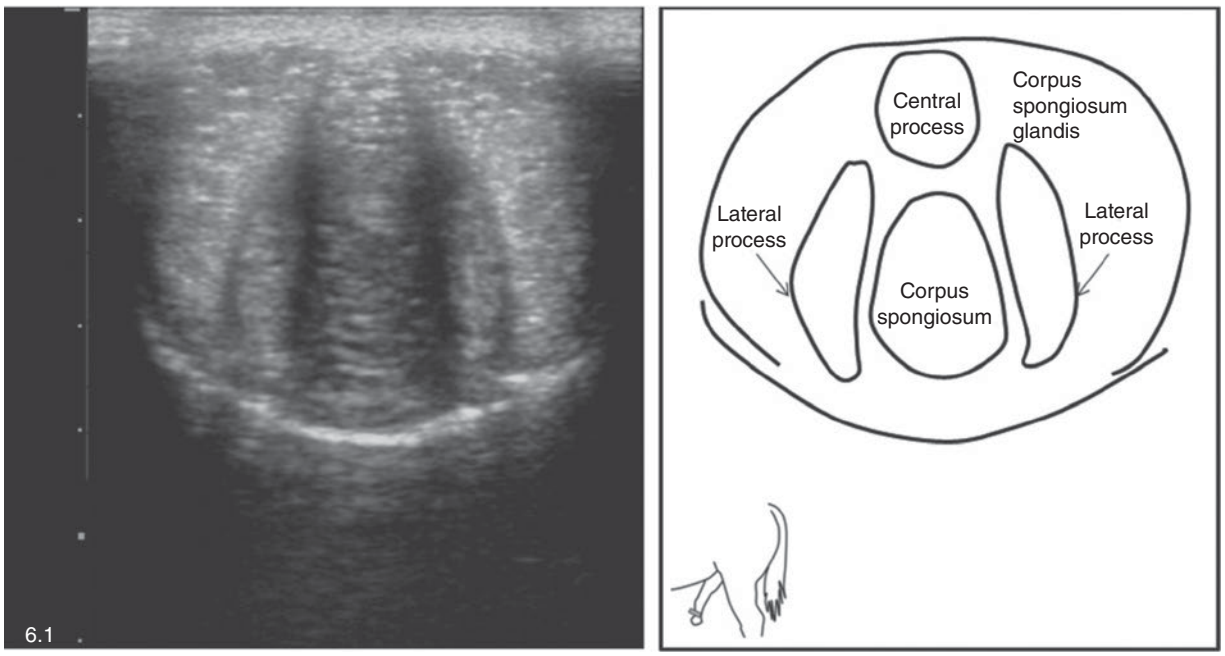


Figure 12.12 Ultrasound image of the distal part of the penile body – cross-section. Corpus cavernosum divides into three processes: long central, and two blunt, short lateral processes.

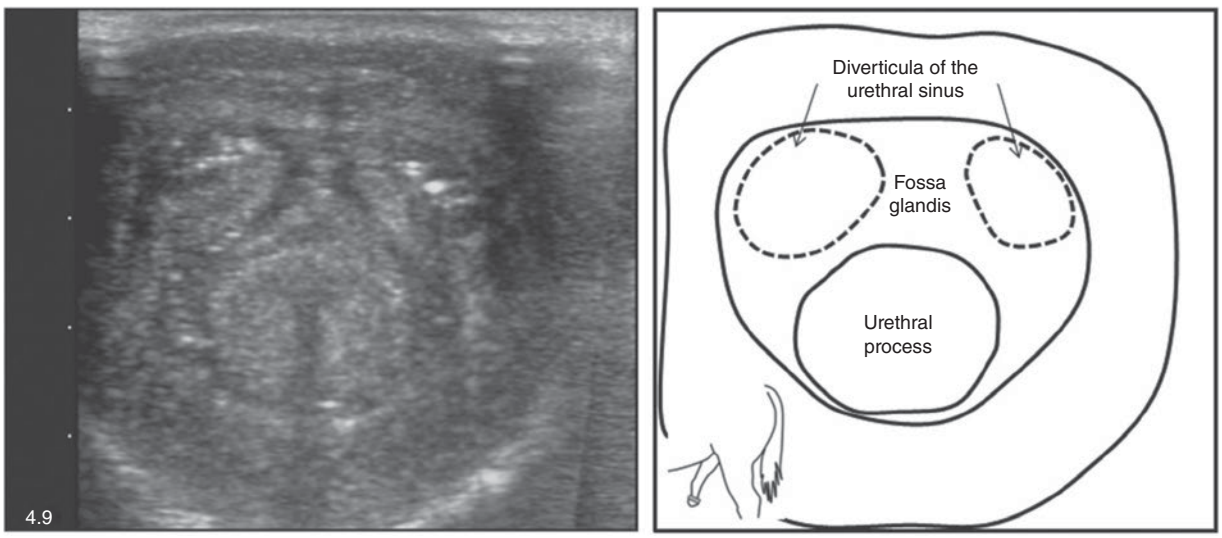


Figure 12.13 Ultrasound image of the glands penis. Hyperechoic smegma is accumulated in the urethral sinus.

Vet-ebooks.com

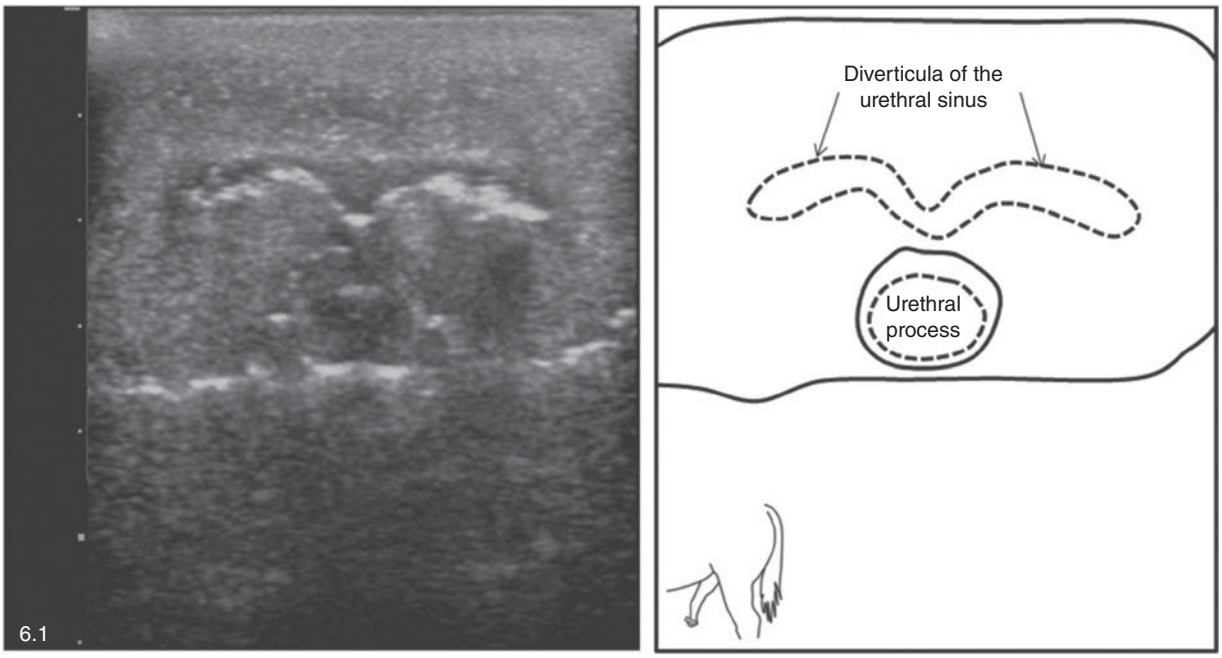


Figure 12.14 Ultrasound image of the urethral process and the urethral sinus with accumulated smegma.

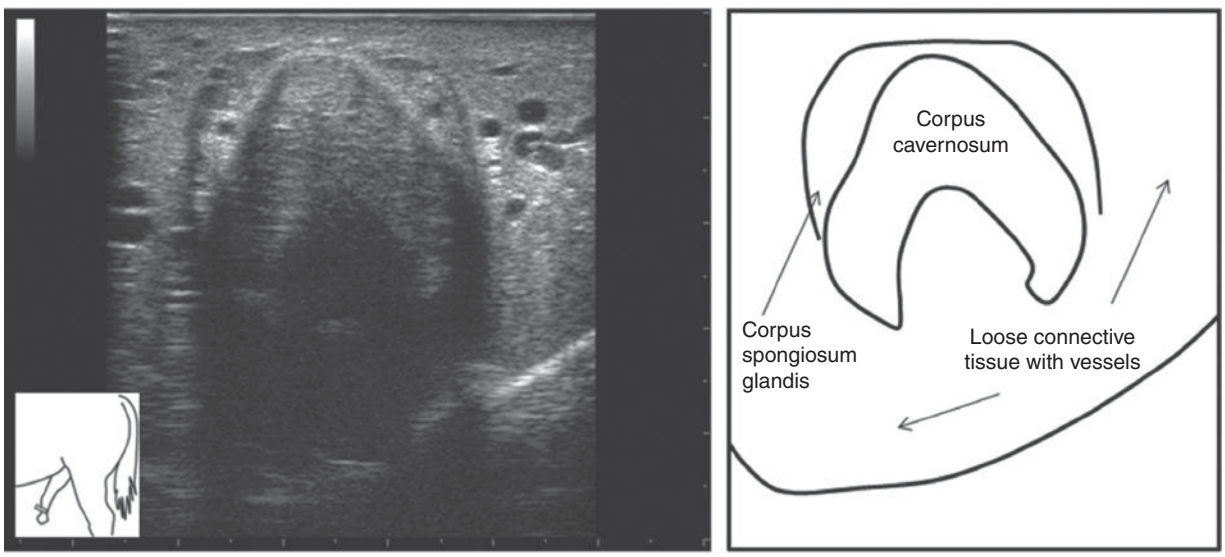


Figure 12.15 Ultrasound image of the distal part of the penile body in a stallion with chronic paraphimosis. Massive edema of the prepuce and the corona glandis are present. Vessels are engorged.

Vet-ebooks.com

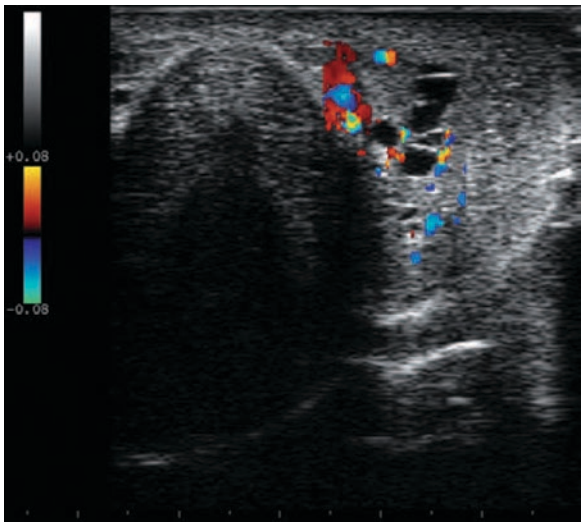


Figure 12.16 Color Doppler ultrasound image of the distal part of the penile body in a stallion with chronic paraphimosis. The preputial vessels are dilated.

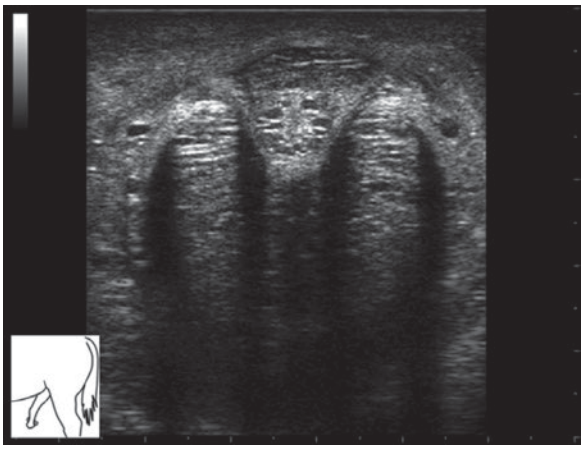


Figure 12.18 Ultrasound image of the distal part of the penile body in a stallion with chronic paraphimosis (ventral aspect). Trabeculae in the corpus spongiosum and the corpus cavernosum are engorged.

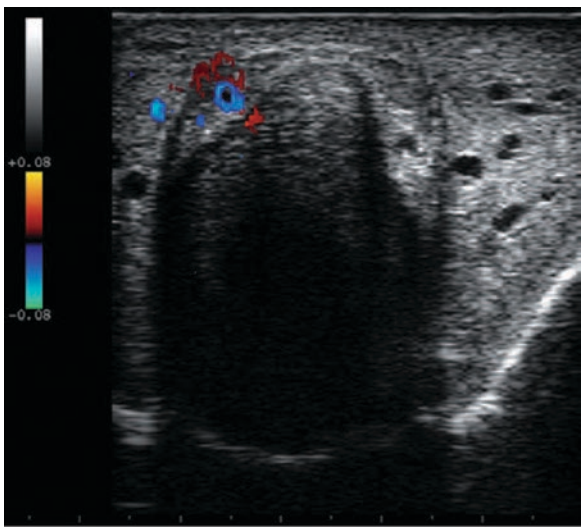


Figure 12.17 Color Doppler ultrasound image of the distal part of the penile body in a stallion with chronic paraphimosis. The vessels in the corpus spongiosum glandis are visualized and color coded.

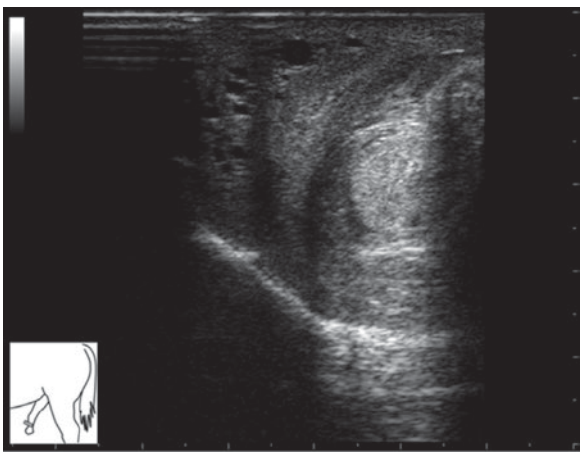


Figure 12.19 Ultrasound image of the distal part of the penile body in a stallion with chronic paraphimosis. Hyperechoic blood clot is present in the lateral process of the corpus cavernosum.

stallions, but can be devastating to the reproductive career.

Hyperechoic contents in the trabeculae of the corpus cavernosum and the corpus spongiosum of the glans suggest blood clotting (Figures 12.20, 12.21), which needs to be immediately addressed by an aggressive flushing with heparinized saline. Ultrasonography is also helpful in assessing the degree of damage caused by penile trauma (Figure 12.22). The integrity of the tunica albuginea is essential for penile function, and it therefore needs to be carefully examined. Rupture of the tunica albuginea has to be repaired surgically, while penile hematomas or mild contusions can be managed medically, supplemented with physiotherapy.

Vet-ebooks.com

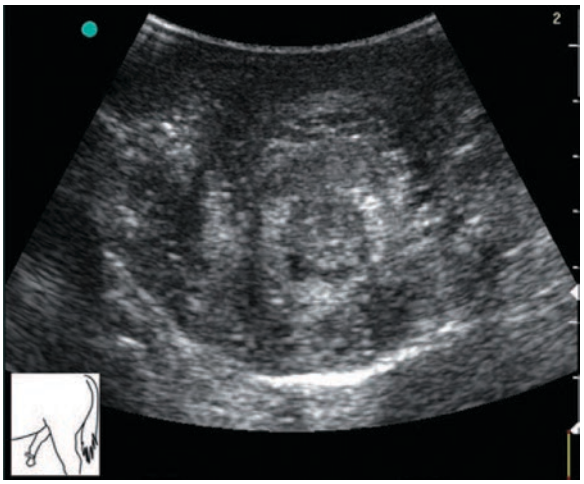


Figure 12.20 Ultrasound image of the distal part of the penile body in a stallion with priapism. Hyperechoic contents of the trabeculae of the corpus cavernosum and the corpus spongiosum suggest blood clotting. This was later confirmed during surgery.

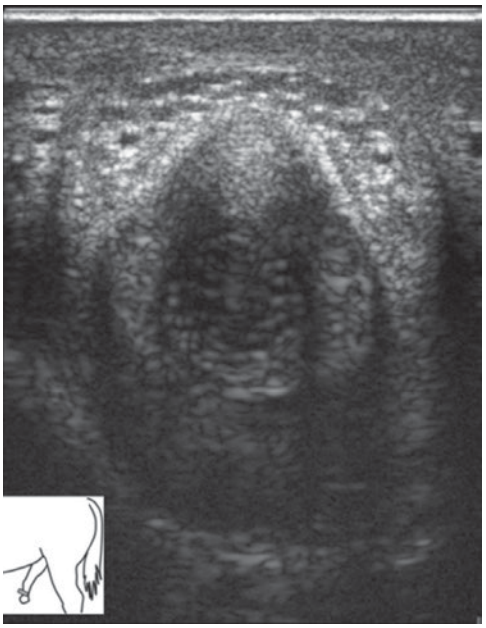


Figure 12.21 Ultrasound image of the distal part of the penile body in the stallion with priapism.

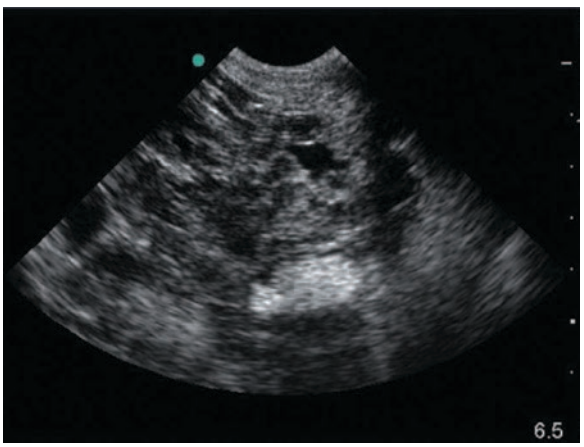


Figure 12.22 Ultrasound image of organizing hematoma of the penis in a stallion, due to a breeding accident.

References

1 Sisson, S. (1910) *A Textbook of Veterinary Anatomy*. W.B. Saunders, Philadelphia.

2 Nickel, R., Schummer, A., & Seiferle, E. (1979) *The Viscera of the Domestic Mammals*. Springer-Verlag, Hamburg.

3 Little, V.L. & Holyoak, G.R. (1992) Reproductive anatomy and physiology of the stallion. *Veterinary Clinics of North America: Equine Practice* 8: 1–29.

4 Budras, K., Sack, W.O., & Röck, S. (2009) *Anatomy of the Horse*, 5th edn. Schlütersche Verlagsgesellschaft mbH & Co. KG., Hannover.

5 Nickel, R., Schummer, A., & Seiferle, E. (1981) *The Anatomy of the Domestic Animals*, Volume 3. Verlag Paul Parey, Berlin, Hamburg.

6 Wilkins, C.J., Sriprasad, S., & Sidhu, P.S. (2003) Colour Doppler ultrasound of the penis. *Clinical Radiology* 58: 514–523.

Vet-ebooks.com

13

Ultrasonography of the Testes

Charles Love

Texas A&M University College of Veterinary Medicine, College Station, TX, USA

Ultrasonographic evaluation of the scrotal contents in the stallion includes the spermatic cord (the spermatic artery, ductus deferens, and spermatic venous network (pampiniform plexus), cremaster muscle, nerves, lymphatics), the epididymis (head, body and tail), the testis, vaginal cavity, and scrotum (skin, dermis). The clinician should be able to identify position, location, and the normal echoic pattern of these structures. The examination of the scrotal contents, in addition to determining normalcy, should also include measurement of the length, width, and height of each testis. These measures are then used to calculate testis volume and determine the efficiency of sperm production.

Stallion Position and Location

The clinician is required to perform the examination in the vicinity of the flank area of the stallion. For obvious reasons this is a risky position for the clinician. If semen collection is performed in conjunction with the evaluation, stallions tend to be more tractable following semen collection. Regardless, it is recommended to sedate the stallion to facilitate a thorough and complete evaluation. The ultrasound evaluation of the scrotal contents should be considered a stand-alone primary procedure and therefore sufficient time and patience should be allotted to allow for a thorough examination of the scrotal contents as well as an accurate measurement of the testes dimensions. An inadequate examination can result in erroneous testis measurements leading to an incorrect clinical interpretation.

The stallion can be evaluated from the left flank, either confined in a stock or free-standing in the stall following sedation.

Probe Type

The location of the scrotum is in a relatively restricted area between the hind legs of the stallion, which can limit manipulation and probe placement. The linear array probe commonly used for *per rectum* examination is satisfactory, but its size (i.e. length) can limit examination of discrete structures such as the epididymis. Sector probes can also be used, particularly the "finger" type probe, that is small (surface area ~2.5 cm) and allows easier access to specific areas of interest. The T-type linear probe allows ease of handling and placement in the scrotal area. See Figure 13.1.

Examination

Ultrasound evaluation should be preceded by a thorough manual evaluation of the scrotum and its contents to detect any specific areas that require scrutiny. Ultrasound gel or a similar lubricant can be applied to the probe. Since the scrotum in the stallion has very little hair there is no need to clip the scrotum. However, since sweat glands are present, artifactual changes due to lather and bubble formation require gel removal and gel reapplication to maximize image resolution.

Testis Measures

Measurement of the testis dimensions (width, height, and length) can be performed first.

Atlas of Equine Ultrasonography, Second Edition. Edited by Jessica A. Kidd, Kristina G. Lu and Michele L. Frazer.
© 2022 John Wiley & Sons Ltd. Published 2022 by John Wiley & Sons Ltd.
Companion Website: www.wiley.com/go/kidd/atlas

Vet-ebooks.com

Height

The height is measured by placing the probe ventrally and directing the beam dorsally so that the central vein is approximately two thirds of the distance from the surface and the spermatic artery can be visualized dor- sally. There is no need grasp or manipulate the testis for this measure (Figures 13.2, 13.3).

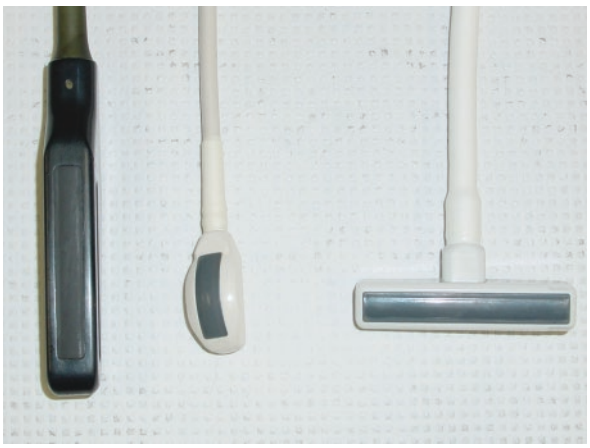


Figure 13.1 Ultrasound probes used for scrotal content evaluation. Left: standard linear array; middle: "finger" sector scanner; right: T-type linear array.

Length

The length is usually measured from the caudal aspect of the scrotum in the vicinity of the tail of the epididymis, directing the beam cranially. The ultrasound probe should be rotated slightly in a horizontal direction so that the maximum length is visualized. The maximum distance can be determined by visualizing the hyperechoic cranial edge of the tunica albuginea of the testis. Similar to the height measurement, the length should be measured *in situ* (Figure 13.4).

Width

The left testis is measured by placing the probe on the left lateral surface of the scrotum and directing the beam horizontally and medially (Figure 13.5). At the same time the right testis should be pushed dorsally so that the shape of measured testis is not distorted. For the measurement of the right testis, the left testis is pushed dorsally to allow measurement. Grabbing of the scrotal neck, similar to the technique used to measure ruminant testes, should be avoided for several reasons. First, it is easier to perform the examination using only one hand to manipulate the probe on the testis, while the testis hangs freely. Even if the testis is in

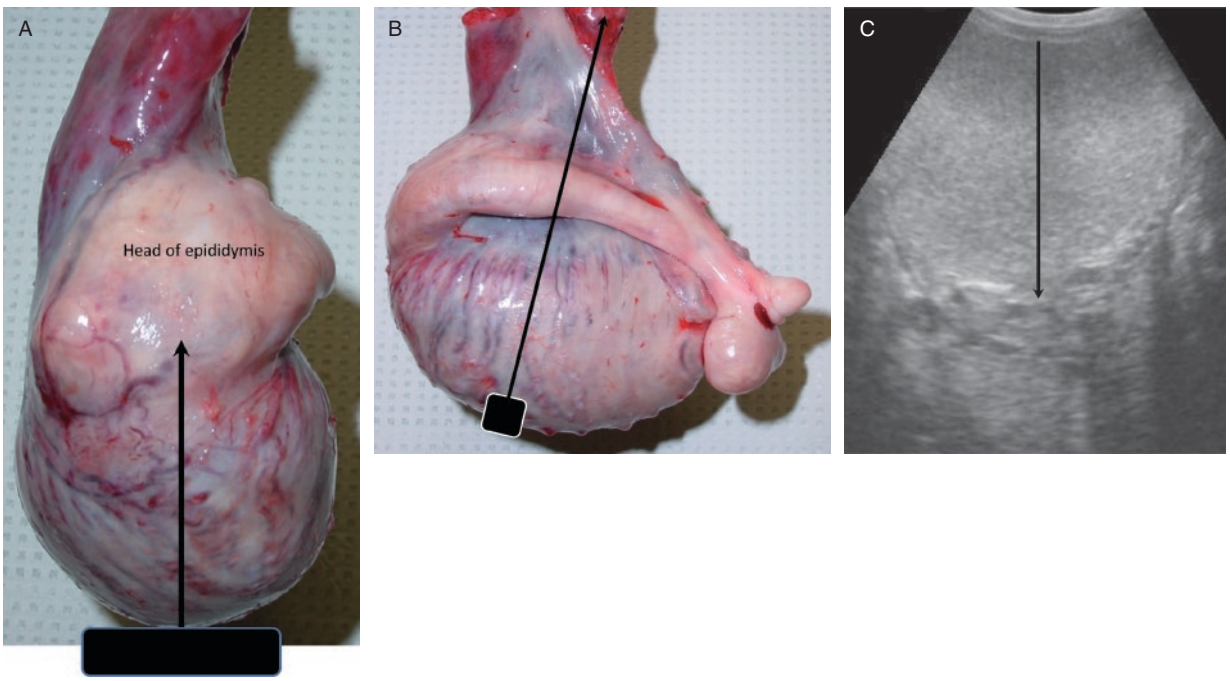


Figure 13.2 (A) Cranial–caudal view of the left testis. (B) Lateral view of the left testis. The height of the testis is measured by placing the ultrasound probe ventrally with the beam directed dorsally. (C) The line denotes the orientation of the arrow in B. Notice the hyperechoic line at the tip of the arrow identifying the tunica albuginea on the dorsal surface of the testis. Below the arrow (dorsal) is the caudal edge of the spermatic cord.

Vet-ebooks.com

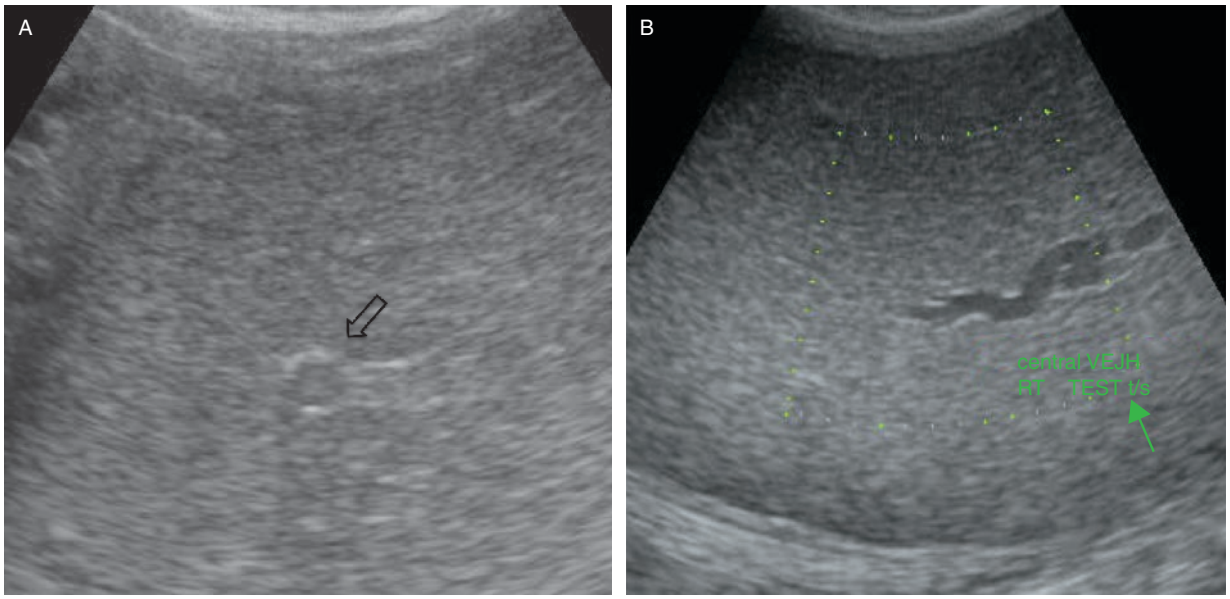


Figure 13.3 (A) Central vein in cross-section and (B) longitudinally.

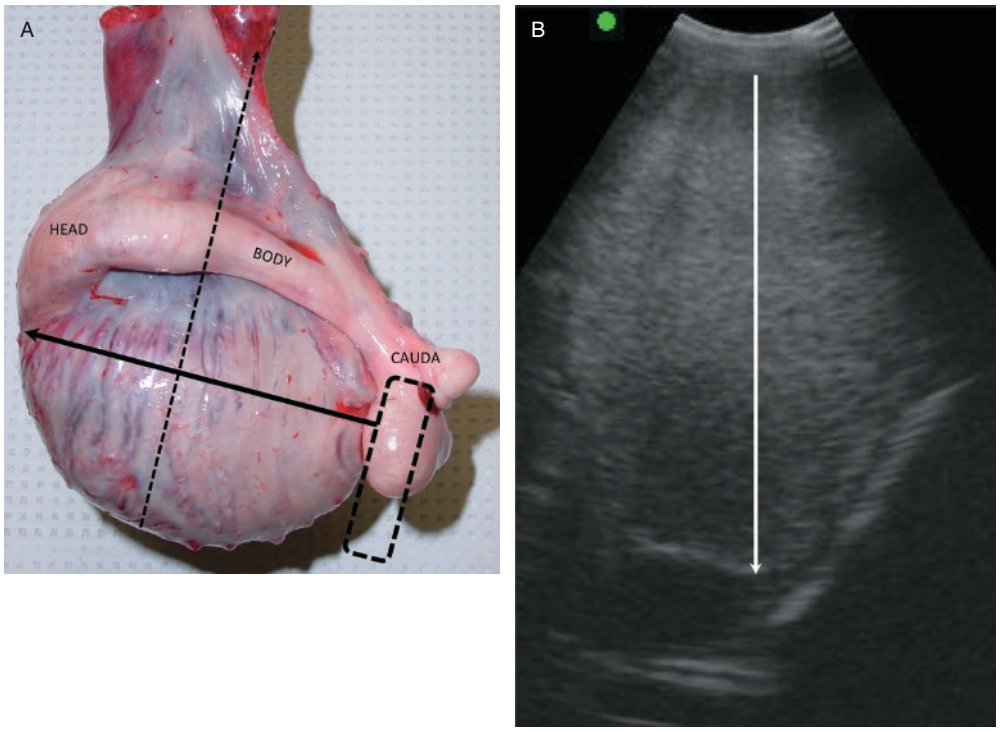


Figure 13.4 (A) Lateral view of the left testis. The solid black line shows the length measure that should extend from the cranial to the caudal edge of the testis, making sure to not include the cauda epididymis. The ultrasound probe is located caudally on the scrotum. Notice the long axis of the testis is not located horizontally, but rather is angled in a dorsocranial direction. (B) Ultrasound picture of the long axis of the testis. The white line corresponds to the black line in A. Notice the hyperechoic line at the tip of the arrow denoting the cranial edge of the testis.

Vet-ebooks.com

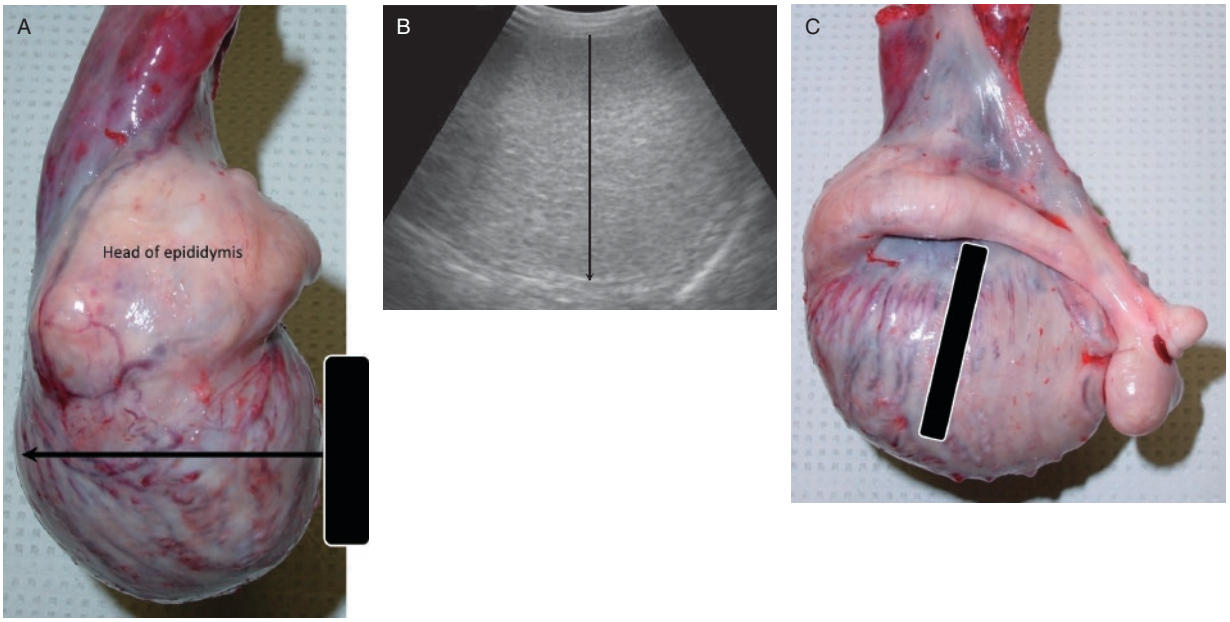


Figure 13.5 (A) Cranial–caudal view of the left testis. The width of the testis is measured by placing the ultrasound probe laterally at the widest point of the testis with the beam directed medially. (B) Line denotes the orientation of the beam in A. Notice the hyperechoic line at the end of the arrow identifying the tunica albuginea on the medial side of the testis. (C) The location of the probe on the lateral surface of the testis at the widest point of the testis.

an inguinal position, the testis can be accurately measured without the need to manually draw the testis into the scrotum. Second, it tends to cause strong contraction of the cremaster muscle, which may elicit a similarly strong response from the stallion (i.e. kick).

Qualitative Evaluation of the Scrotal Contents

The echotexture of the scrotal contents can be evaluated following testes measurement. A routine should be followed to ensure a thorough evaluation is completed. The routine followed by the author starts at the neck of the scrotum and visualizes the spermatic cord above the testis.

Spermatic Cord

The primary structure visualized is the tortuous spermatic artery as it winds to the testis (Figure 13.6). Pathology of the spermatic cord includes spermatic cord torsion, which commonly occurs 1–3 cm dorsal to the testis (Figures 13.7, 13.8, 13.9). Varicocele (Figure 13.10), dilation of the pampiniform plexus, while uncommon, may also be detected here. In addition, generalized edema resulting from inflammation, such as orchitis or epididymitis, may present as hyperechoic inconsistencies in the spermatic cord (Figure 13.11).

Testis

Following the examination of the spermatic cord the ultrasound probe is passed laterally on the testis to examine the parenchyma, which should be homogeneous in echotexture, devoid of hyper- or hypoechoic foci, commonly associated with neoplasia (Figures 13.12, 13.13) or benign structures (Figure 13.14). In cross-section the testis shape may be round to oblong.

Epididymis

The epididymis includes head, body, and tail regions that are located craniolaterally, dorsolaterally and caudally respectively, on the horizontally oriented testis. The epididymal tail (Figure 13.15) should be evaluated for location and size. Spermatic cord rotation of 180° occurs where the epididymal tail is located dorsocranially. In addition, the size and ultrasonographic appearance of the tail can vary from small, in the case of hypoplasia, to prominent, when the tail is distended with sperm or due to inflammation. A tail distended by sperm only, may be common in stallions at sexual rest or in cases of sperm accumulation when sperm accumulates from the ampulla all the way back to the ductus deferens and epididymis (Figures 13.16, 13.17).

Vaginal Cavity

The vaginal cavity is a potential space that communicates with the peritoneal cavity through the inguinal

Vet-ebooks.com

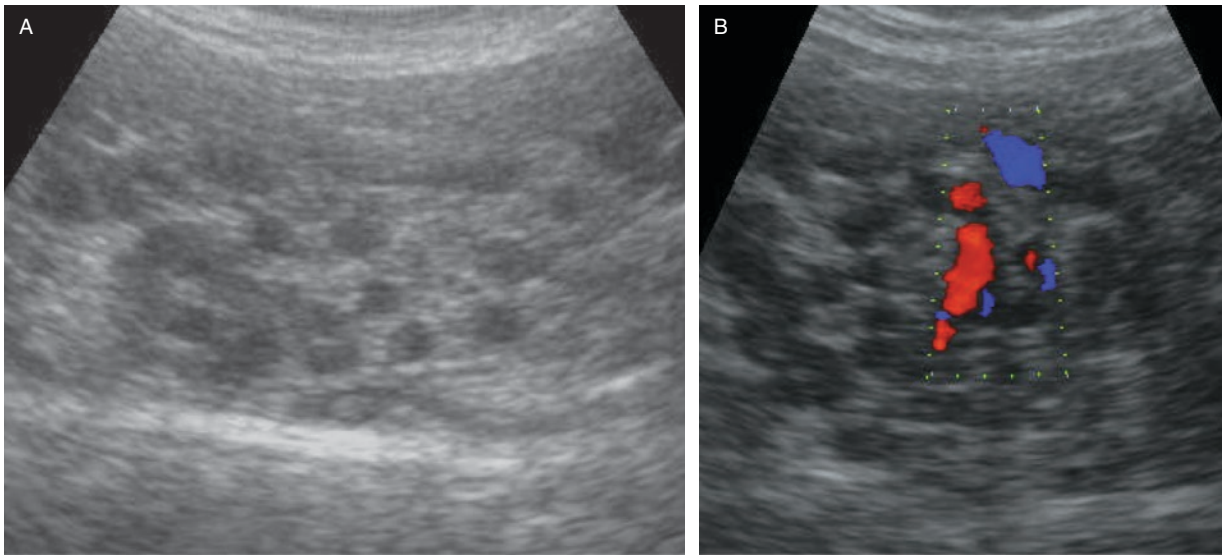


Figure 13.6 (A) Cross-section of the spermatic cord showing the spermatic artery and (B) confirming blood flow with Doppler ultrasound.

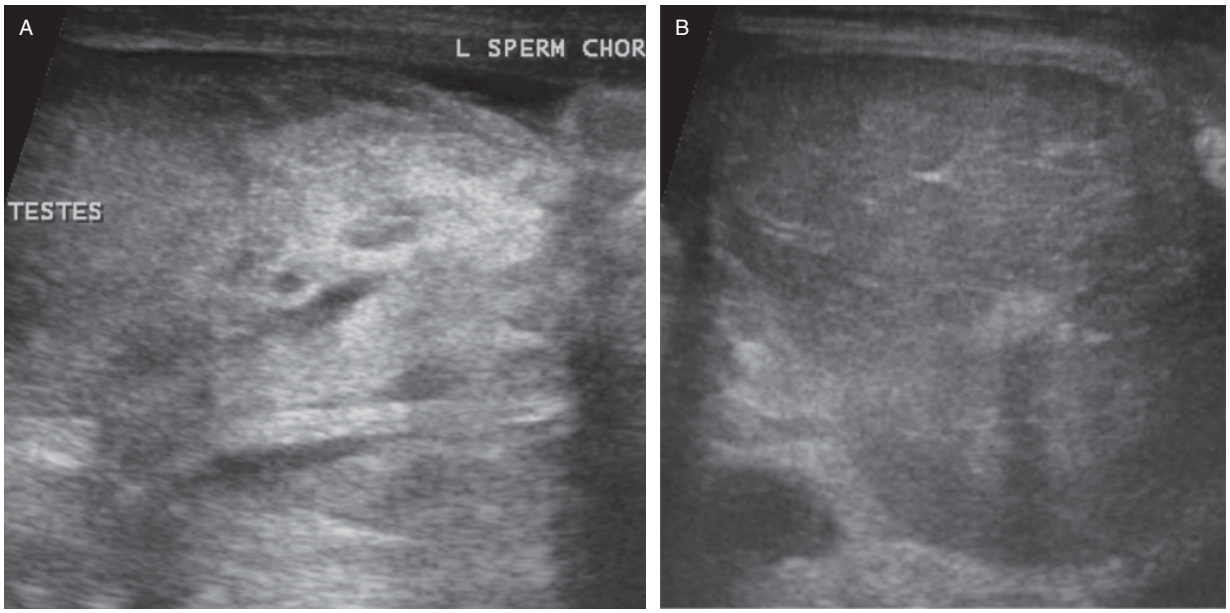


Figure 13.7 Spermatic cord torsion. (A) Spermatic cord dorsal to the testis in a case of spermatic cord torsion. Notice loss of the "Swiss cheese" appearance of the spermatic artery and the increase in the hyperechoic appearance of the cord due to loss of circulation, blood stagnation, and edema. (B) Testis associated with the cord lesion. Notice the hyperechoic areas, probably a result of venous congestion.

canal and therefore, peritoneal contents such as fluid and intestines have the potential to pass through the canal and occupy the vaginal cavity. In addition, circulatory (artery, vein, lymphatic) compromise to the spermatic cord can result in free fluid accumulation (hydrocele). This fluid tends to accumulate around the epididymal tail (Figure 13.18).

Measurement and Interpretation of Testes Volume

Measurement of testes size is an important part of the stallion breeding soundness evaluation since testes size is associated with sperm production. The number of sperm produced by the stallion may impact fertility

Vet-ebooks.com

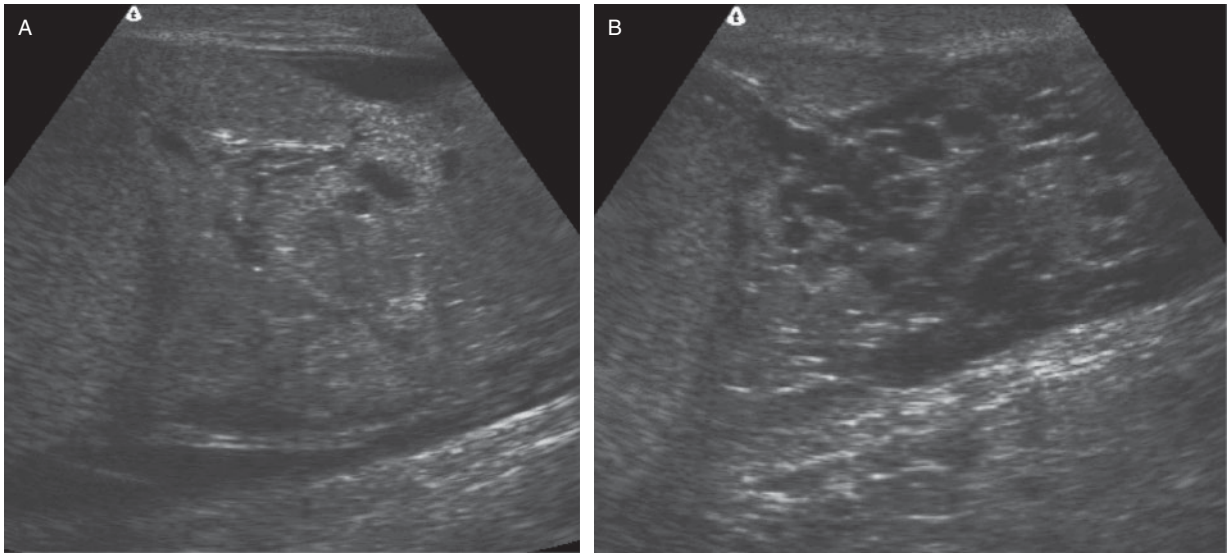


Figure 13.8 (A) Ultrasonographic appearance of a spermatic cord following torsion of the spermatic cord compared to (B) normal contralateral spermatic cord. Notice the lack of circulation in A compared to the hypoechoic areas of circulation in the normal cord.

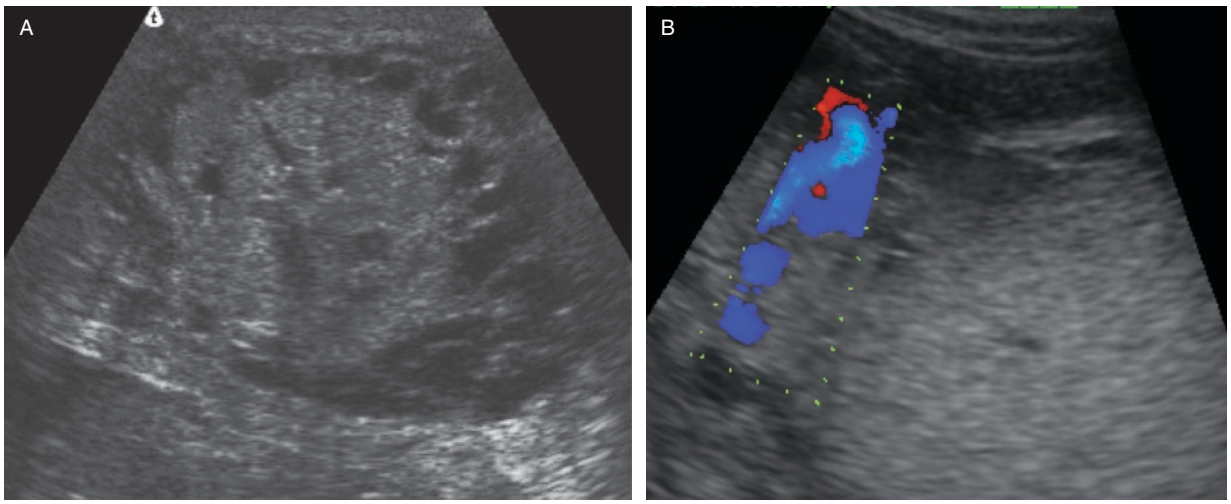


Figure 13.9 (A) Affected spermatic cord in Figure 13.8 1 day later, after the torsion has self-corrected. (B) The spermatic artery is patent (Doppler flow), but there is residual edema in the center of the cord.

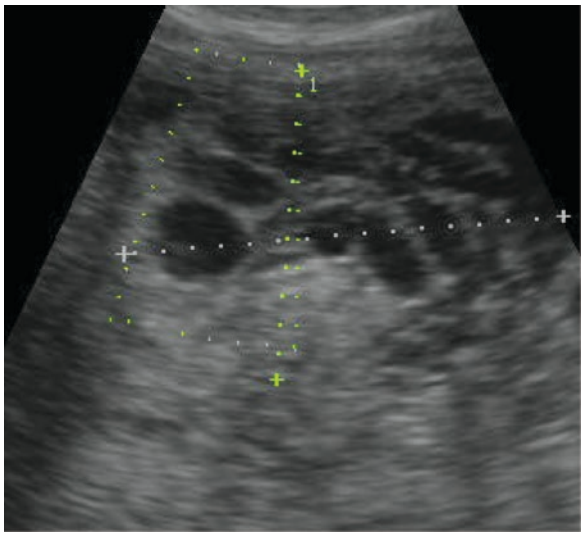


Figure 13.10 Distended venous supply (varicocele) dorsal to the testis.

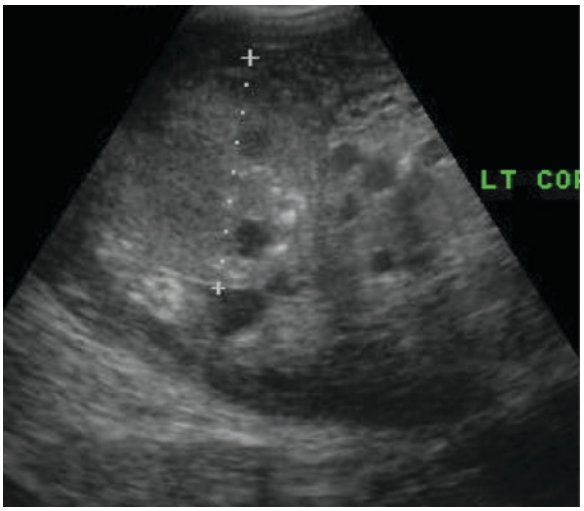


Figure 13.11 Generalized edema resulting from inflammation such as orchitis or epididymitis may present as hyperechoic inconsistencies in the spermatic cord.

Vet-ebooks.com

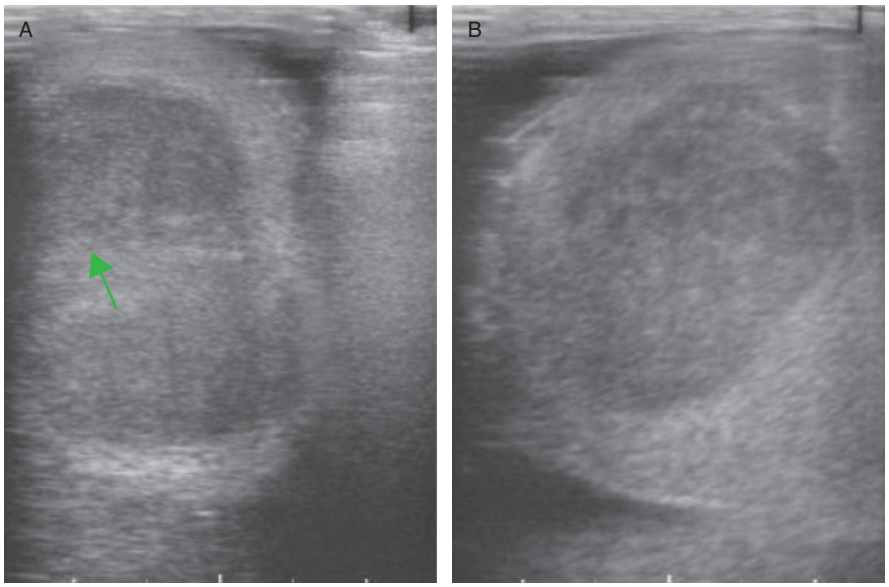


Figure 13.12 (A,B) Heterogeneous mass within the testis parenchyma that was diagnosed as a Sertoli cell tumor.

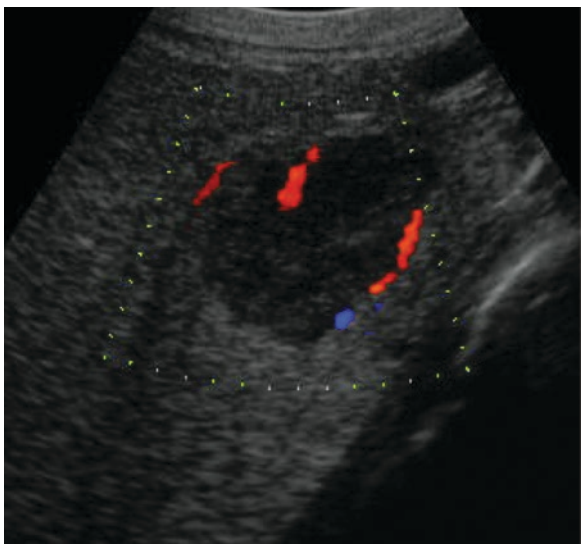


Figure 13.13 Heterogeneous mass within the testis parenchyma that was diagnosed as a seminoma. Notice the prominent vascular channels at the periphery and within the body of the mass.

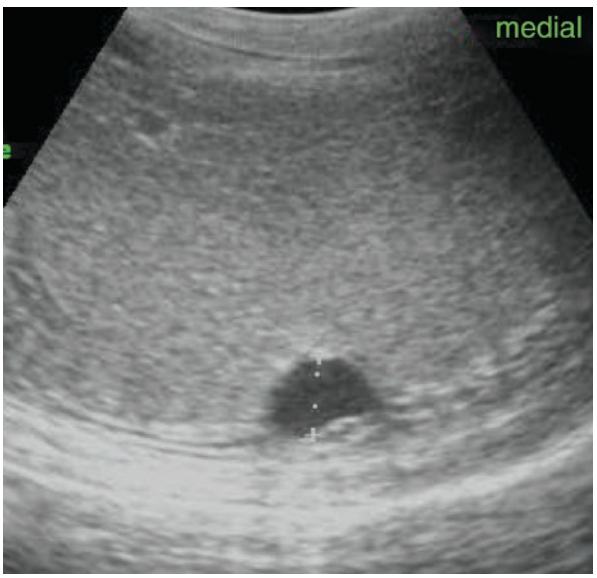


Figure 13.14 Discrete hypoechoic lesion beneath the tunica albuginea of the testis. These lesions tend to be benign, but should be monitored for growth and vascularity.

and, thus, the number of mares that a stallion can breed. Historically, testes size was determined using the linear measure, total scrotal width, in which calipers were used to measure the combined width of the testes, the mediastinum testes, and the scrotum. This technique, however, does not determine the three-dimensional shape (i.e. volume) of each testis. While the relationship of length, width, and height tends to be proportional, there are instances where they are not, and the determination of each dimension will more accurately determine volume.

Subsequently, ultrasonography has been introduced as a technique to measure and evaluate the testes. This technique has the advantage of being specific and accurate since the clinician can visualize the testis parenchyma and identify landmarks that assure measurement of the length, width, and height.

Measurements (length, width, and height) from each testis are performed as described in the preceding section. The measures from each testis are then inserted in a formula that approximates the volume of an ellipsoid [1]:

Vet-ebooks.com

Testis volume in cm^3

$$= \frac{4\pi}{3}\left(\frac{length\ in\ cm}{2}\right)\left(\frac{width\ in\ cm}{2}\right)\left(\frac{length\ in\ cm}{2}\right)$$

= 0.5238(length in cm)(width in cm)(height in cm)

The volumes from each testis are combined to give the total testicular volume (TTV).

The TTV is then inserted into the regression formula to calculate the expected daily sperm output (DSo). Formulae are based on the author's previous two publications in which semen was collected once daily for 7 consecutive days from reproductively normal stallions [2,3]. The total sperm number (in billions) was averaged from days 5–7 and this was considered to be daily sperm output. The TTV was then calculated after measuring the length, width, and height of each testis. The following regression formulae were created from that data:

Predicted DSO (billions) = 0.024 (TTV) – 1.26 [2]
= 0.024 (TTV) – 0.76 [3]

These formulae differ because there were more stallions included in the second study than the first. The only mathematical difference between the two formulae is the constant (i.e. 0.76 vs. 1.26). When calculating the expected DSo the author uses both formulae to give an expected range.

Example:

	Left testis	Right testis
Length (cm)	8.1	8.3
Width (cm)	4.2	5.0
Height (cm)	5.2	5.6
Volume (cm^3)	93	122
Total testes volume	215 cm^3	

The TTV of this stallion is 215 cm3. This value would then be inserted in the two formulae to give a range of expected DSo from 3.9–4.4 billion sperm.

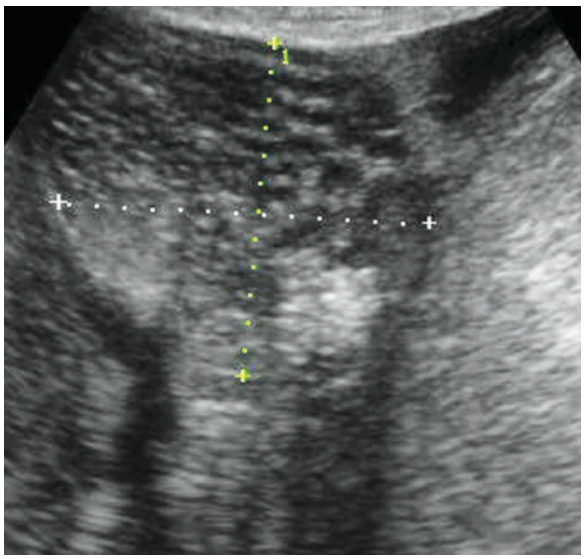


Figure 13.15 Epididymal tail. Notice the prominent lumen in cross-section.

Interpretation

The intent of measuring the TTV is as follows:

1) Determine the *absolute* volume measure. The average total testes volume for the population of stallions measured in the two studies was approximately 250 cm3. Based on this TTV the *average*

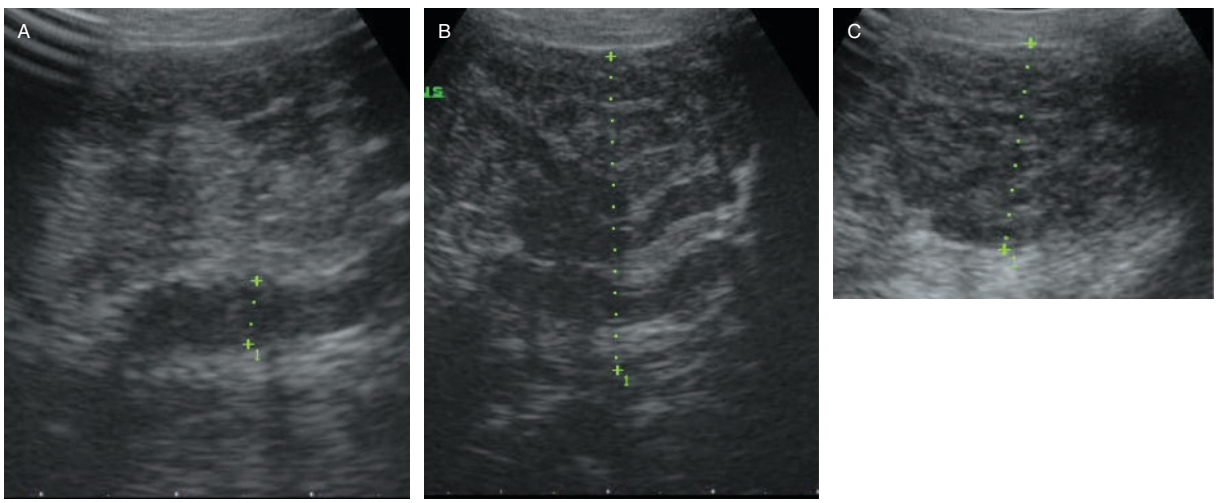


Figure 16 (A) Dilated (~0.5 cm) ductus deferens associated with (B) distended (~3.0 cm) cauda epididymal tail. (C) Contralateral epididymal tail that measures 1.7 cm.

Vet-ebooks.com

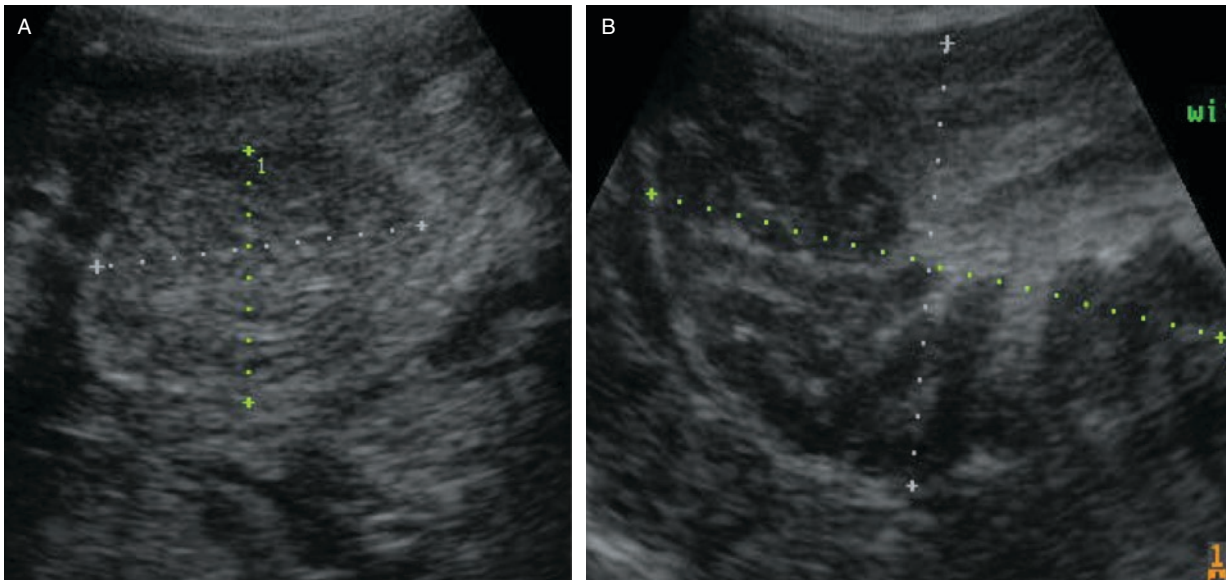


Figure 13.17 Comparison of the size and distension level of the (A) left (1.6 ×2.1 cm) and (B) right epididymal tails (2.5 × 4.0 cm) from the same stallion. Lack of a prominent lumen (A) may result from recent ejaculation or indicate reduced sperm production from that testis. A prominent lumen is usually due to sperm. It may be associated with plugged ampullae (accumulation) or may occur in a stallion at sexual rest.

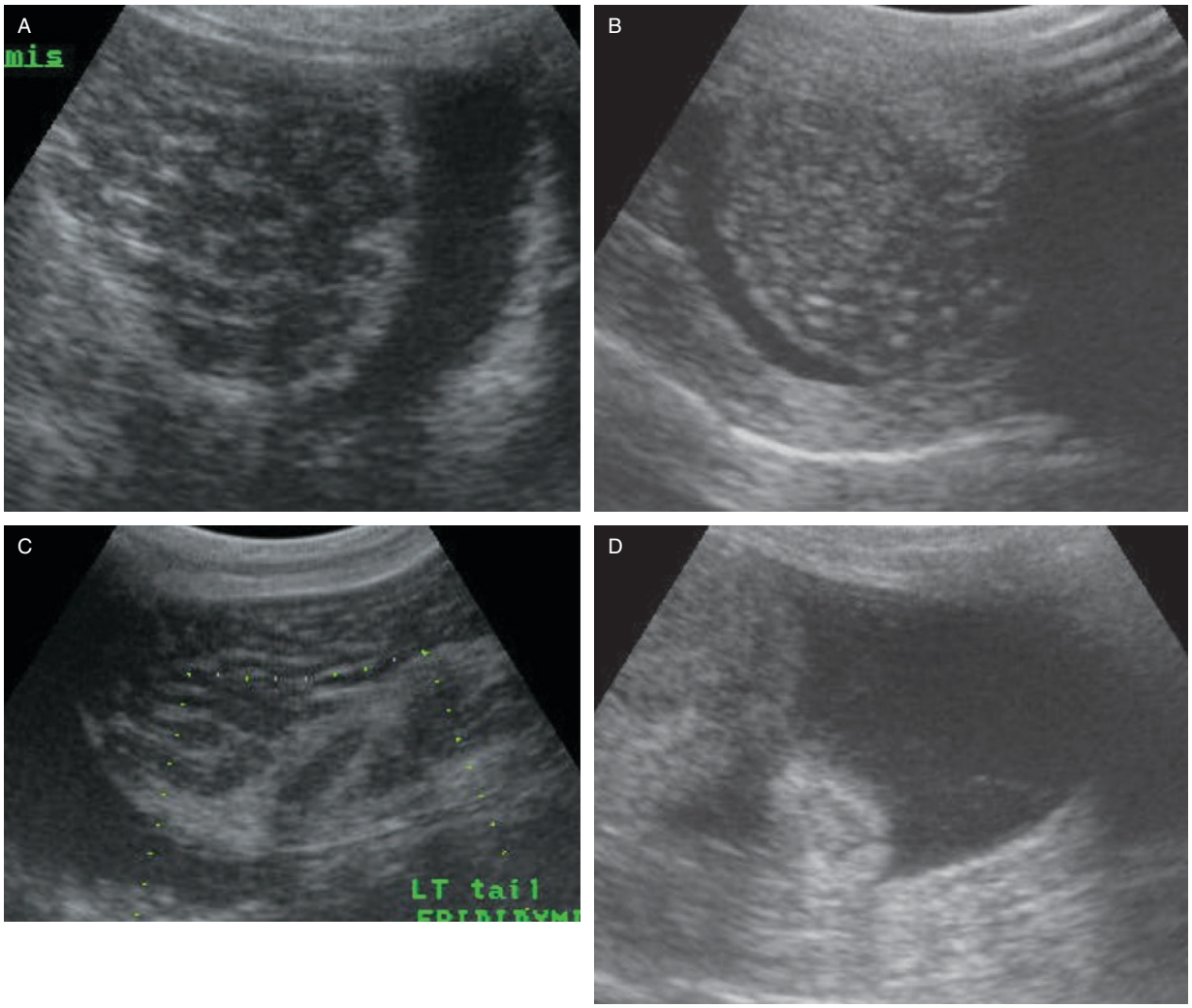


Figure 13.18 (A,B,C,D) Fluid (hydrocele) in the vaginal cavity around the epididymal tail.

Vet-ebooks.com

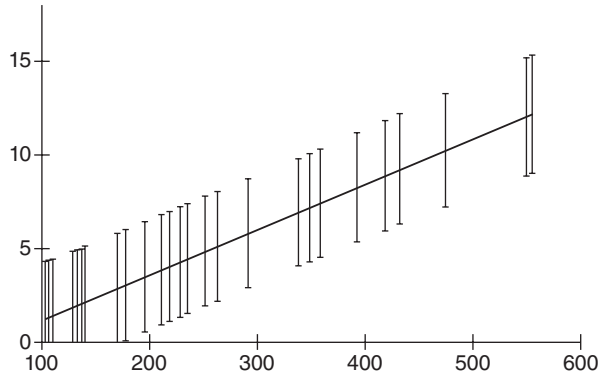


Figure 13.19 The relationship between total testes volume (TTV, cm^3) on the x-axis and predicted daily sperm output (billions) on the y-axis. Regression coefficient (y = 0.024 (TTV) – 1.26). Error bars represent ±2 standard deviations. (*Source*: Love et al, 1991 [2]. Reproduced with permission of Bioscientifica).

stallion should produce approximately 4.7–5.2 billion sperm when at DSo. This translates to a spermatogenic efficiency of approximately 18 million sperm/cm3 testis parenchyma/day. The absolute value becomes particularly important when measuring sexually immature stallions retired to stud following performance careers. The clinician is often asked to render an opinion on a stallion's testes size in relation to his potential as a breeding stallion. Recognizing that a 2–4-year-old stallion has a TTV similar to the average sexually mature stallion is useful when rendering an opinion. The clinician must also recognize that TTV alone does not "qualify" a stallion as fertile, but a "normal" testes size does reduce the risk of "subfertility."

2) Compare the *expected* DSo value to the *actual* number of sperm collected from the stallion (Figure 13.19). Ideally the clinician would like to collect a stallion once daily for 5–7 days to determine DSo. Oftentimes this is impractical due to time and mon- etary constraints and a lesser collection frequency is more practical. Stich *et al*. reported that testes volume will affect the number of days required to reach DSo with a smaller TTV (148–245 ml; ml = cm3) reaching DSo sooner (day 5) than medium (253–274 ml; day 6) or large testes (292–466 ml; day 6–7) [4]. In lieu of collecting from a stallion for 5–7 days, collecting two ejaculates 1 hour apart and using the second ejaculate as an approximation of DSo, is a useful compromise. In most cases, the clinician is not interested in whether the stallion is producing *too much* sperm, but rather whether he is producing *too little* when compared to the expected DSo value.

References

1 oberg, E.V. (1984) *Machinery's Handbook: A Reference for the Mechanical Engineer*, 22nd edn. Industrial Press, New york, 54.

2 Love, C.C., Garcia, M.C., Riera, F.R., & Kenney, R.M. (1991) Evaluation of measures taken by ultrasonography and caliper to estimate testicular volume and predict daily sperm output in the stallion. *Journal of Reproduction and Fertility* 44: 99–105.

3 Love, C.C., Garcia, M.C., Riera, F.R., & Kenney, R.M. (1990) Use of testicular volume to predict daily sperm output in the stallion. *Proceedings of the American Association of Equine Practitioners* 36: 15–21.

4 Stich, K., Brinsko, S., Thompson, J., et al. (2002) Stabilization of extragonadal sperm reserves in stallions: application for determination of daily sperm output. *Theriogenology* 58: 397–400.

Vet-ebooks.com

Vet-ebooks.com

Section 2b

Ultrasonography of the Mare Reproductive Tract

Vet-ebooks.com

Vet-ebooks.com

14

Use of Ultrasonography in the Evaluation of the Non-Pregnant Mare

Walter Zent

Hagyard Equine Medical Institute, Lexington, KY, USA

In preparation for the ultrasonographic evaluation of the non-pregnant mare, a manual transrectal examination of the reproductive tract should be performed. This palpation allows the examiner to arrange the mare's reproductive tract so as to make the ultrasonographic examination easier. The tract should be arranged so that it is free of any intestine and the ovaries should be positioned so that they are not behind the broad ligament. The operator should be able to follow the tract from one ovary to the other without any obstruction. This will allow the examination to be done without the interference of abdominal structures that can make the examination difficult and in some instances cause confusion in interpretation. More importantly, this examination allows the operator to become aware of possible abnormalities that will need closer visualization when the ultrasonographic examination is being performed.

In order to properly perform an ultrasonographic examination of the reproductive tract, it is very important that the mare be properly restrained. The amount of restraint that is required will differ greatly depending on the temperament of the mare and the quality of the available help. Older mares that have been examined multiple times often need very little restraint, while younger, more fractious individuals may need considerable restraint. It is very important that the animal is handled so that the safety of the animal, help, and veterinarian is maintained. Remember that the veterinarian is often the only professional involved and therefore the person responsible for the proper execution of the procedure. If stocks are not available, the mare is frequently positioned with the hindquarters in a stall door, in order to prevent too much lateral movement and give some protection to the operator and equipment. If the mare is not accustomed to being palpated, some form of minor sedation can be helpful. The author would rather not use ace-promazine for sedation as it will cause a profound loss of uterine tone and thus make examination difficult. Xylazine (0.5–1.1 mg/kg) will cause much less uterine relaxation and will provide ample sedation in most instances. Detomidine (0.02–0.04 mg/kg IV) is also a good choice. If the mare resists transrectal examination by persistent straining or if the operator must do extensive manipulation of the reproductive tract, a small dose of N-butylscopolammonium bromide (Buscopan, 20–40 mg IV) can be given to relax the rectum and make examination easier on the operator and the patient.

When ultrasonography is being performed, it is important for the operator to hold the probe in a manner that will allow the head of the probe to have full contact with the ovaries and uterus. The author believes that this can best be done by grasping the probe in a way that the index finger is placed along the dorsal surface of the probe, with the thumb on one side and the remaining fingers on the other, being careful not to cover the crystals on the bottom. The middle finger can be used as a guide to move the probe along the anterior edge of the uterus so that the probe will be easily centered over the uterus while the examination of the horns is being performed (Figure 14.1).

The examination should always be done in the same manner so that all of the structures are examined thoroughly and the operator will be able to cover the entire tract. The author palpates left handed so it is easiest for him to start at the right ovary, and then examine the right horn, left horn, left ovary, body, and cervix, ending with the vagina. It is very important that the operator makes sure that the entire uterus is examined. If the probe is held correctly, the horns of the uterus will appear

Atlas of Equine Ultrasonography, Second Edition. Edited by Jessica A. Kidd, Kristina G. Lu and Michele L. Frazer.
© 2022 John Wiley & Sons Ltd. Published 2022 by John Wiley & Sons Ltd.
Companion Website: www.wiley.com/go/kidd/atlas

Vet-ebooks.com

as a cross-section of a piece of sausage on the screen and can easily be followed from one ovary to the other (Figures 14.2A and 14.2B). The body of the uterus will be seen longitudinally (Figures 14.3A and 14.3B). When scanning the body of the uterus, sometimes the body is wider than the width of the probe and parts of the lateral areas can be missed. In order to make sure that the operator has covered the entire uterus, the probe is moved from left to right. This is particularly important when mares are being examined for very early pregnancies.

The ultrasound examination of the non-pregnant mare's reproductive tract can be done as a single examination, for reasons such as breeding soundness examination or purchase, or as one of a series of examinations, such as when the mare is being examined over several days for mating. Whatever the reason, it is important to remember that the ultrasonographic examination is only one part of the evaluation of the mare's reproductive tract and must be

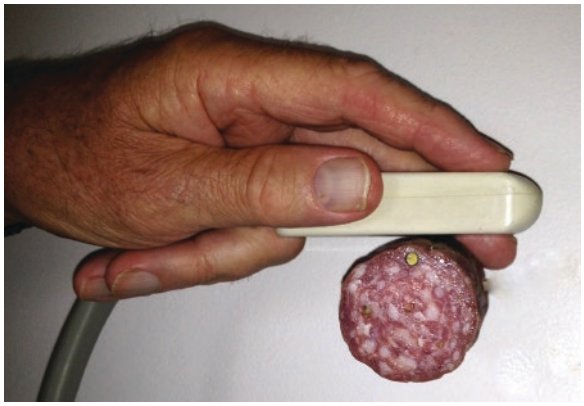


Figure 14.1 Proper method of gripping probe for good visualization of the uterus.

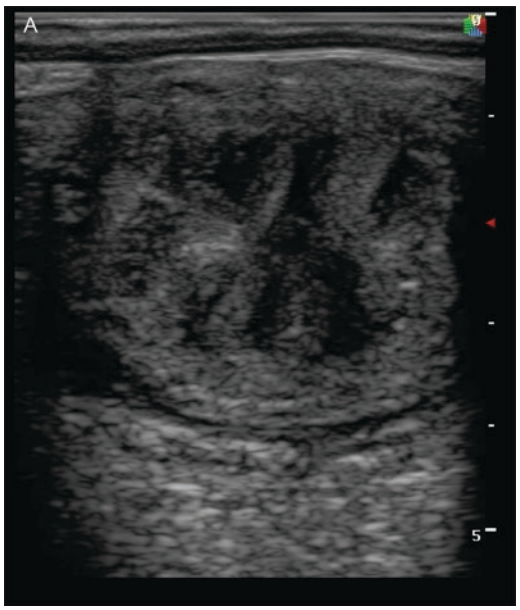


Figure 14.2A Cross-section of uterine horn.



Figure 14.2B Cross-section of uterine horn with estrous edema.

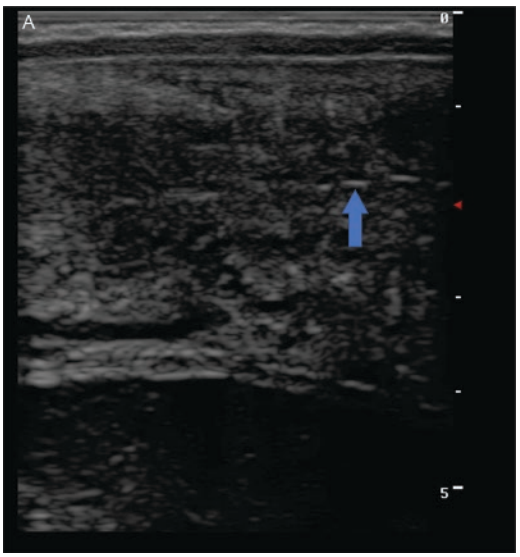


Figure 14.3A Longitudinal section of uterine body during diestrus; there is no edema and no fluid in the lumen of the uterus. The lumen is often visualized by a hyperechoic horizontal line (arrow).

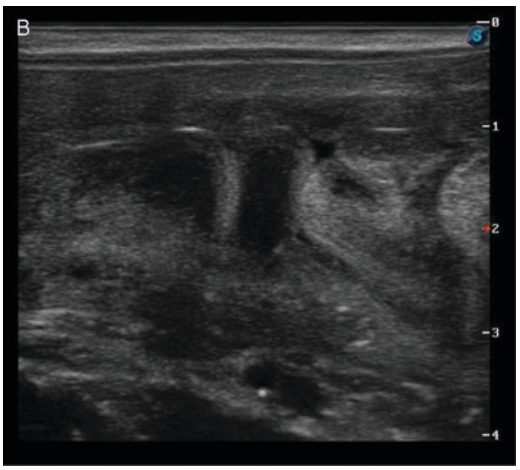


Figure 14.3B Longitudinal section of uterine body during estrus with edema and normal trace of anechoic intrauterine fluid.

Vet-ebooks.com

coupled with the history, the mare's mental condition (in behavioral estrus or not), a speculum examination to evaluate the condition of the vagina and cervix, and palpation of her reproductive tract. Only when all of this information is put together can a proper interpretation of the examination be made. The normal mare should go together like a puzzle and if she does not, then, in the author's view, she has deviated from normal.

It is important to be aware of the mare's position in her reproductive cycle, so that you know what you are expecting the normal mare's reproductive tract to look like. During the period of anestrus that mares pass through during the winter, most mares, on palpation, will have no follicular development, their uterus will be relaxed, and the cervix toneless. She will be non-responsive to the teaser and on speculum examination the vagina and cervix will be pale and dry. The cervix will have very little tone. The ultrasound examination will find ovaries that are very small and may have small, less than 10 mm follicles present on them and a uterus with no edema (Figure 14.4) and no fluid in the lumen.

The mare that is entering and passing through the transitional period will have a reproductive tract that shows many different degrees of development. This can be the most difficult period for a veterinarian to

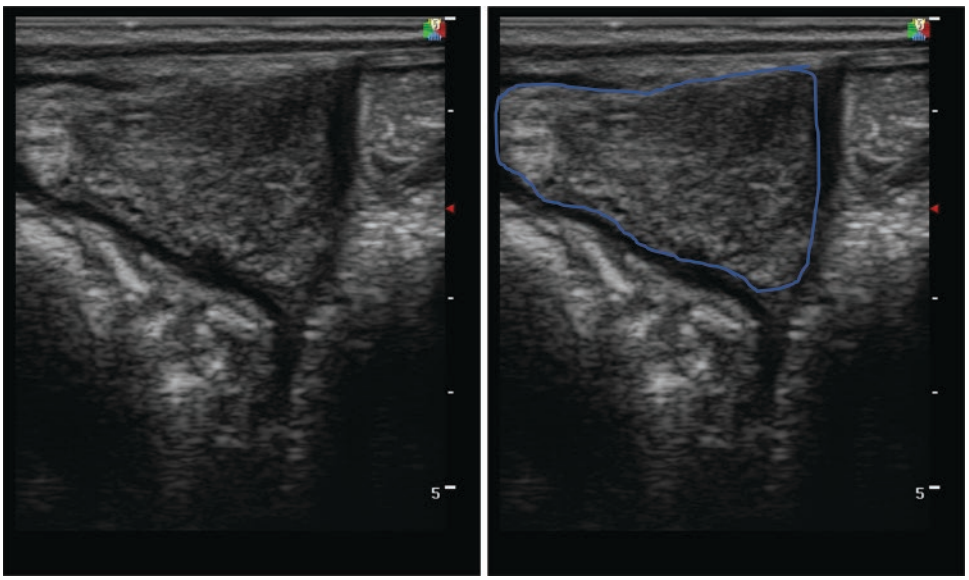


Figure 14.4 Cross-section of uterine body during transition from anestrus to cyclicity. There is no edema in the uterine wall or fluid in the lumen of the uterus.

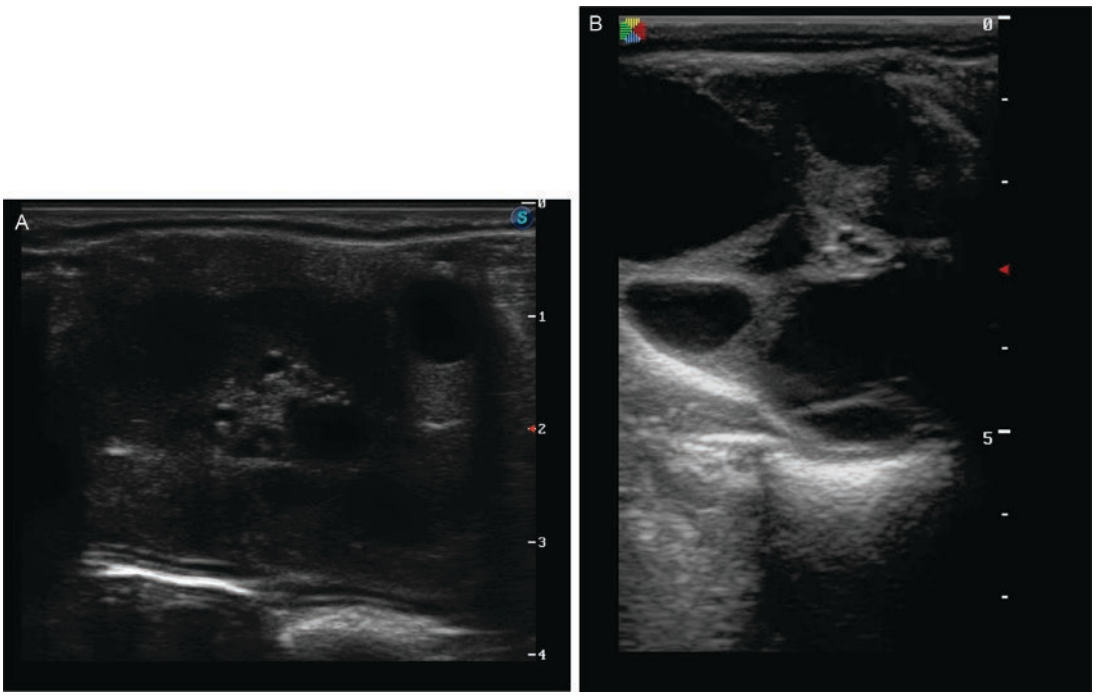


Figure 14.5 (A) Ovary during early transitional phase with a very small follicle present. (B) Ovary during transitional phase with several small follicles (cluster).

Vet-ebooks.com



Figure 14.6 Cervix during early estrus with some edema; cervix is beginning to relax.

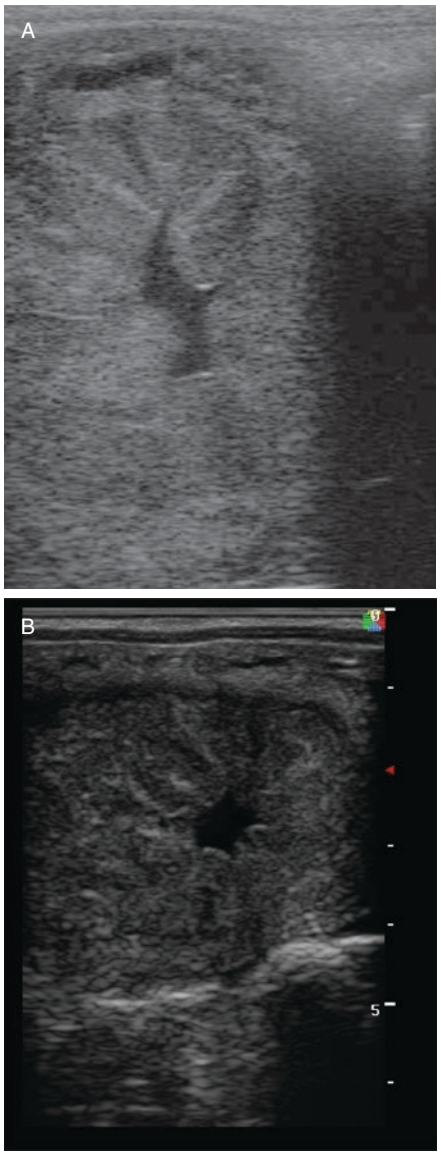


Figure 14.7 (A and B) Cross-section of uterus with edema and normal fluid that is often present during early estrus.

interpret. The ovaries may have no follicles or clusters of small follicles (Figure 14.5) and the mare may be showing strong estrous behavior or no estrous behavior at all. Often the most confusing times for owner and veterinarian are when the mare is showing strong estrus and has no follicles, which may be a normal finding during transition. The uterus usually has very little tone and no edema or fluid, and the cervix will be pale and relaxed. Ginther has described in great detail the changes that occur during this period of a mare's reproductive life [1].

As the mare moves into the cycling period, the first signs of estrus will be the beginning of uterine edema, follicular development, and the development of cervical edema, relaxation, and pinker color (Figure 14.6). As estrus progresses, uterine edema will increase and a small amount of fluid may normally be present in the mare's uterus (Figure 14.7), follicular activity will become greater with the development of a dominant follicle (Figures 14.8A, 14.8B, and 14.8C), and behavioral signs of estrus will increase. The approach of ovulation will be signaled by the reduction of uterine edema (Figure 14.9), further relaxation of the cervix (Figures 14.10A and 14.10B and vulva, and stronger behavioral signs of estrus. The follicle will lose its spherical shape and begin to migrate toward the ovulation fossa (Figure 14.11).

When ovulation occurs, the mare will begin to be less receptive to the teaser, the follicle will collapse and a corpus hemorrhagicum (Figure 14.12) will begin to form. The uterine edema will resolve and there should be no fluid in the mare's uterus. The mare's cervix will appear paler and begin to close (Figure 14.13). A much more detailed description of follicular growth and development can be found in [2].

As the mare enters diestrus, she will become nonreceptive to the stallion, the vulva will be less relaxed, and the cervix (Figures 14.14A, 14.14B, and 14.14C) will be closed, pale, and dry. The uterus will have some tone on palpation. The ovaries may or may not have palpable follicles and a corpus luteum will usually be palpable at the site of ovulation. Ultrasound examination of the uterus and ovaries should find a significant reduction in edema, no fluid in the lumen of the uterus (Figure 14.15), and the ovaries may or may not have significant follicular development but should have a visible corpus luteum (Figure 14.16) present at the site of ovulation.

It is important to remember that mares can be very much individuals and not always progress through their estrous cycle in a prescribed path. The examining veterinarians must use their clinical skills to properly interpret the mare's position in her estrous cycle, so that she can be properly managed.

Vet-ebooks.com

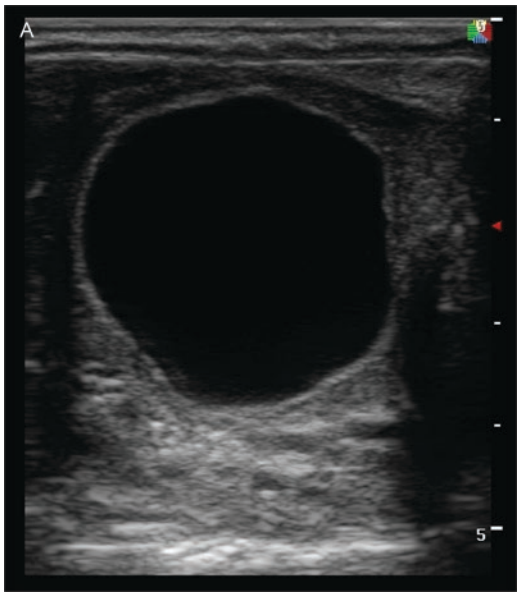


Figure 14.8A Dominant follicle developing during the middle of the estrus period.

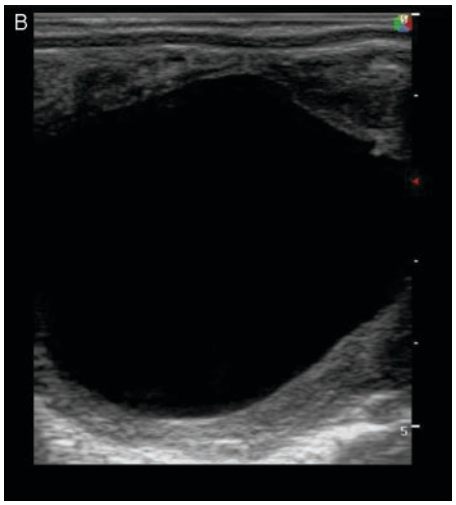


Figure 14.8B-C (B) Dominant follicle and (C) corresponding estrous edema.



Figure 14.9 Uterus with reduced estrous edema as ovulation approaches.

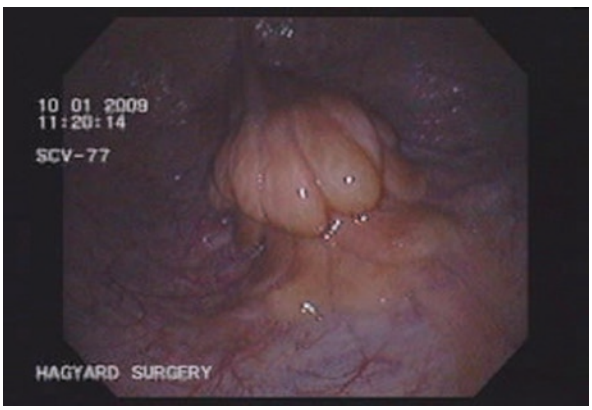


Figure 14.10A Cervix is relaxed and edematous as ovulation approaches.

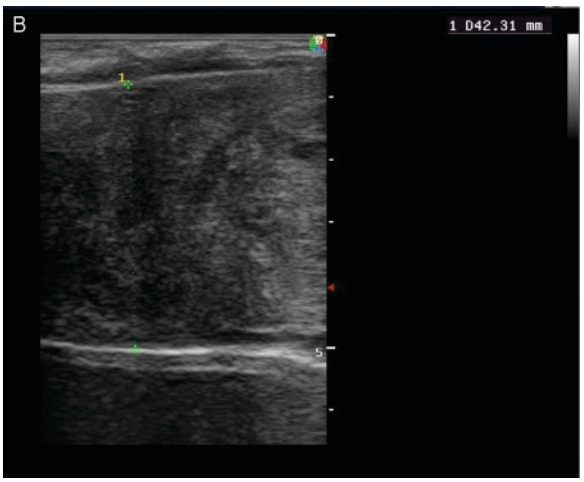


Figure 14.10B Longitudinal view (caudal to left) of a relaxed cervix. Details of cervical architecture can be difficult to appreciate during estrus.

Vet-ebooks.com

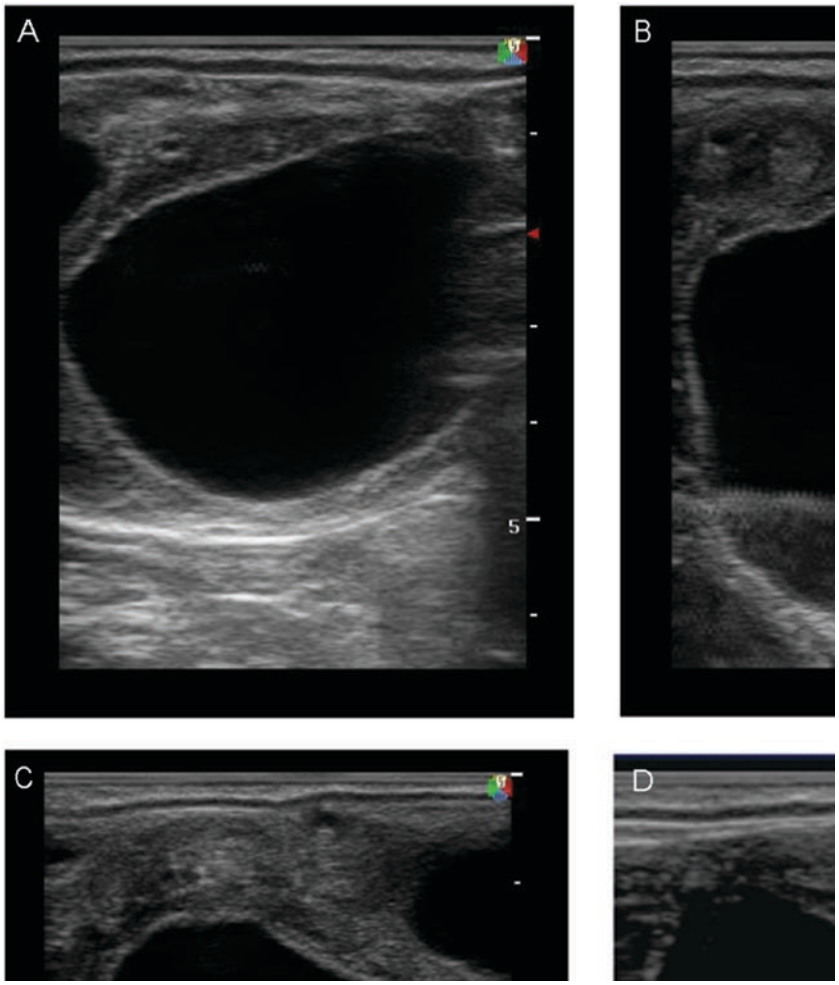


Figure 14.11A-D Preovulatory follicle has thickening of the follicular wall and loses its spherical shape.

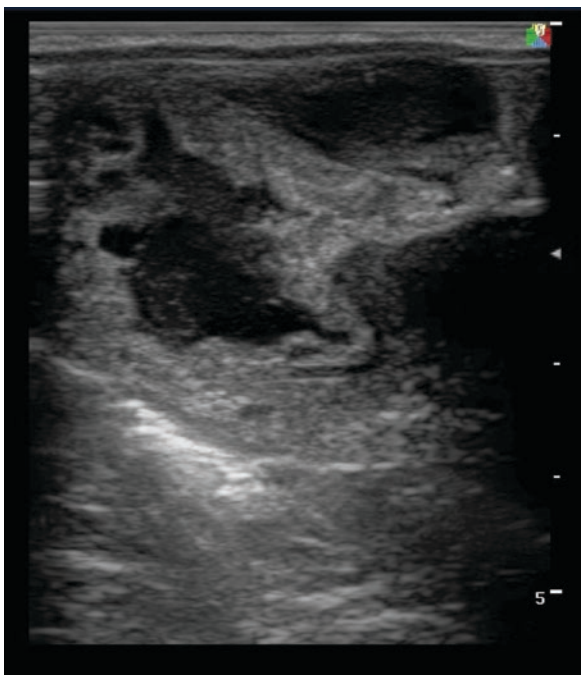


Figure 14.12 Corpus hemorrhagicum and secondary follicle.

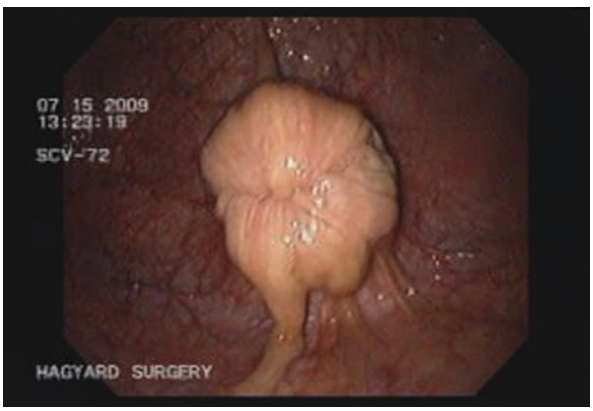


Figure 14.13 Cervix after ovulation.

Vet-ebooks.com



Figure 14.14A The cervix during diestrus is pale and closed.

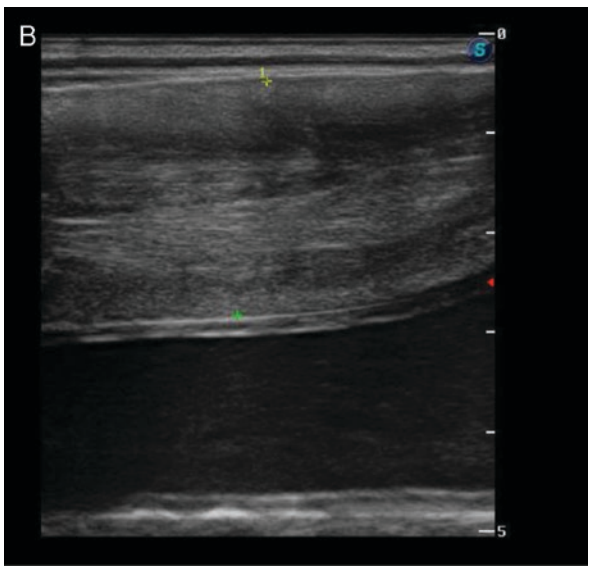


Figure 14.14B Longitudinal view of a normal diestrus cervix (caudal to left).

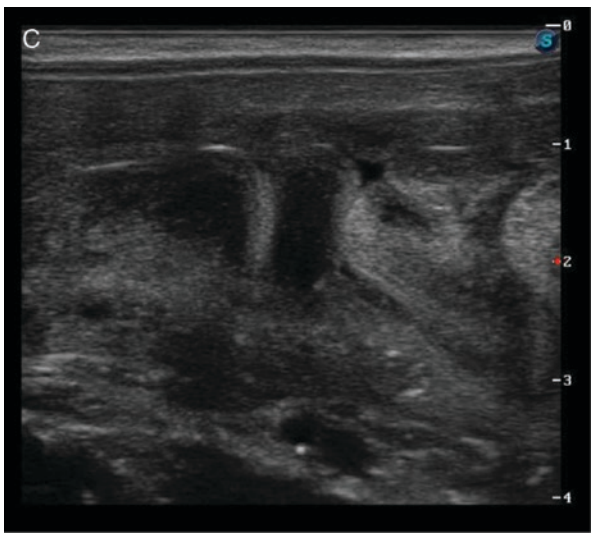


Figure 14.14C Longitudinal view of an abnormal cervix (caudal to left) for comparison. A ventral defect is present.

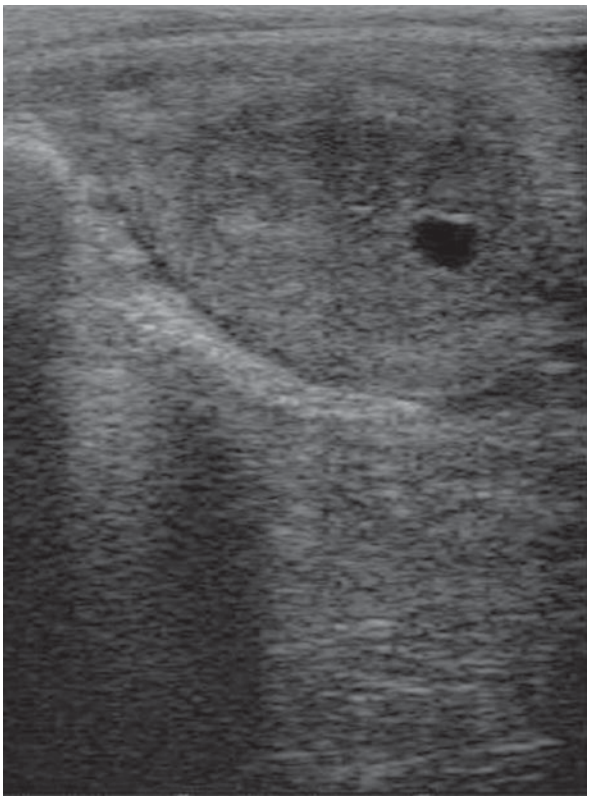


Figure 14.15 Diestrus uterus has lost its edema.

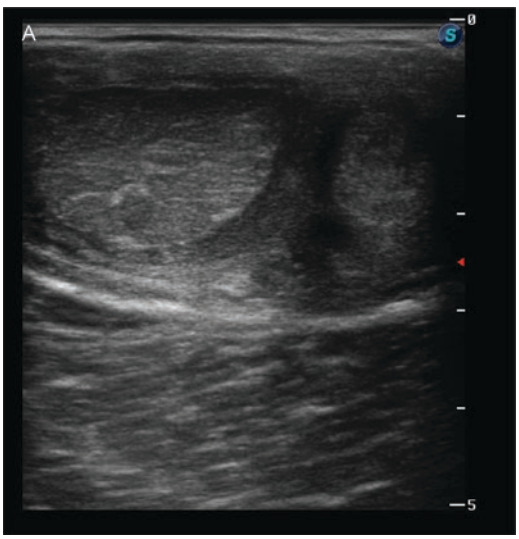


Figure 14.16A Ovary with a visible corpus luteum.

Vet-ebooks.com

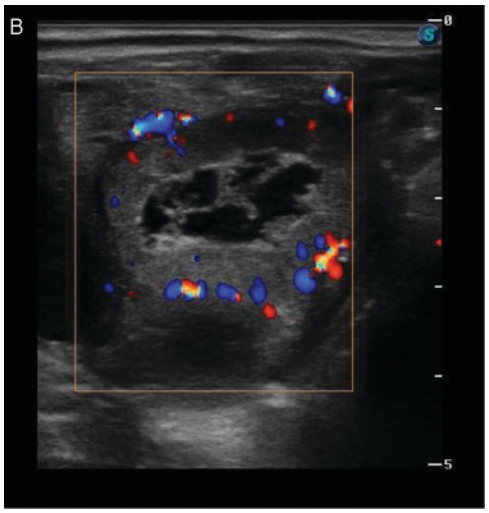


Figure 14.16B Corpus luteum with color doppler blood flow suggesting functionality [3].

References

1 Ginther, O.J. (1992). *Reproductive Biology of the Mare: Basic and Applied Aspects*, 2nd edn, 135–172. Cross Plains WI: Equiservices.

2 Gastal, E.L. (2011). Ovulation: Part 2. Ultrasonographic morphology of the preovulatory follicle. In: *Equine Reproduction*, 2nd edn (ed. A.O. McKinnon, E.L. Squires, W.E. Vaala et al.), 2032–2054. Oxford UK: Wiley Blackwell.

3 Ginther, O.J., Gastal, E.L., Gastal, M.O. et al. (2007), Luteal blood flow and progesterone production in mares. *Animal Reproduction Science* 99: 213–220.

Vet-ebooks.com

15

Use of Ultrasonography for Evaluation of Mare Reproductive Abnormalities

Ryan A. Ferris[1] *and Kristina G. Lu*[2]

[1] *Summit Equine, Gervais, OR, USA*
[2] *Hagyard Equine Medical Institute, Lexington, KY, USA*

Introduction

Ultrasound examination is a commonly utilized diagnostic tool used by veterinarians to evaluate the mare's reproductive tract, while significant advances in ultrasound technology now provide better-quality images and machines with battery power. The crux of the examination is the person performing the examination, no matter the capabilities of the ultrasound machine. In the author's experience, the ability to palpate the reproductive tract with good accuracy allows for an accurate and detailed ultrasound examination. The ultrasound machine will not replace good palpation skills.

While performing the examination, the probe is held in the hand below the middle finger and palm. This allows your other fingers to hold the ovary or trace the uterus as you scan the mare. A clinical tip in performing ultrasound examinations is to hold the probe in a 45–60-degree downward angle almost imaging the uterus from the front to the back, as opposed to holding the probe in a horizontal fashion. By holding the probe in this downward fashion, it is in the author's opinion that this enhances imaging of the uterine bifurcation, resulting in a more thorough ultrasound examination.

For consistency, every ultrasound examination is performed in the same manner. This can be adjusted but should include the following steps. Start the examination with the left ovary imaging from pole to pole (off the ovary all the way through the ovary and off the ovary) followed by measurement of any significant follicles (>30 mm). Scan down the left uterine horn up the right uterine horn to the right ovary. When imaging the uterine horns, the probe should be held perpendicular to the uterus keeping it circular in appearance. The right ovary is imaged similar to the left. Come back down the right uterine horn to the uterine body. The uterine body is imaged in longitudinal fashion by sweeping the hand/probe to the left and right as you move caudally. Continue the examination through the cervix and cranial vaginal vault. Careful assessment of the cervix and vaginal vault via ultrasound can detect abnormalities such as cervical tears and fluid (urine) in the vaginal vault.

Many ultrasound machines used in the equine reproductive field have a 5 MHz probe. However, with advancements in technology, many of the machines available today have 7–15 MHz probes that allow for greater detail of ovarian and uterine structures. Commonly, the authors of this chapter utilize ultrasound machines with a 7.5–10 MHz range. A common depth for routine scanning is 6–8 cm, depending on the length of the rectal probe. If the probe is relatively short, the depth may have to be increased (8 cm) to completely fit a dominant (40–45+ mm) follicle fully on the image. Setting up your ultrasound machine is key for consistent examinations and the image quality can be adjusted to fit your needs by altering gain, dynamic range, and other settings on your machine. Once you have identified the settings you prefer, these can often be saved as presets for future examinations.

Imaging the equine reproductive tract is unique in that it can vary greatly depending on the stage of the cycle, time of year (day length), age, parity, nutrition, and pathology. In many of these circumstances, one examination may not be enough to make a diagnosis and serial examinations may be required. Additionally, other diagnostics may be required to confirm the suspected pathology seen on ultrasound.

Atlas of Equine Ultrasonography, Second Edition. Edited by Jessica A. Kidd, Kristina G. Lu and Michele L. Frazer.
© 2022 John Wiley & Sons Ltd. Published 2022 by John Wiley & Sons Ltd.
Companion Website: www.wiley.com/go/kidd/atlas

Vet-ebooks.com

The goal of this chapter is to provide guidance in diagnosing common reproductive abnormalities. Comments will be brief regarding pathophysiology and treatments.

Ovaries

Anovulatory Follicles

Approximately 5–10% of follicles in a cycle will end with an anovulatory follicle. There are no signs to predict this event from occurring with normal follicular growth rates and normal rise of uterine edema. Mares that develop an anovulatory follicle during the season are at a higher risk of developing an anovulatory follicle in subsequent cycles. It is suspected that mares with metabolic disease (pars pituitary intermedia dysfunction and/or insulin resistance) are at an increased risk for developing anovulatory follicles [1]. Appropriate screening for metabolic disease should be considered in mares with anovulatory follicles (Figure 15.1). It should be noted that anovulatory follicles are relatively common during the spring and fall transition periods, and are considered normal events during these times of year.

These structures will often luteinize and eventually secrete progesterone. Thereafter, the majority will respond to prostaglandins but the time period from formation to response to prostaglandins is prolonged from a normal ovulation and will be 7–10 days from noting the debris in the follicular lumen, as noted in Figures 15.2A and 15.3. Following administration of

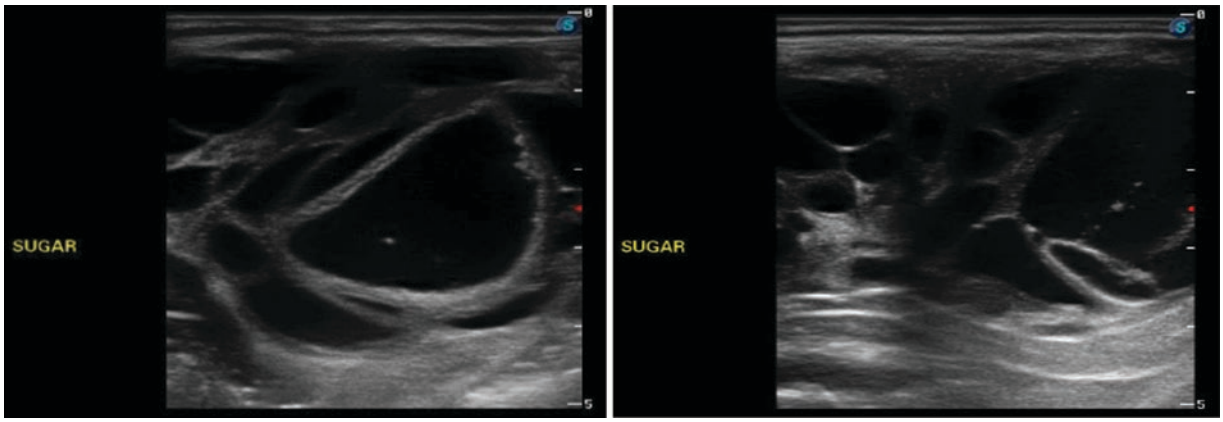


Figure 15.1 Images from mare presenting for failure to develop a dominant follicle and ovulate. Mare was diagnosed with insulin resistance and treated with metformin. Normal follicular development, ovulation, and pregnancy was established after treatment.

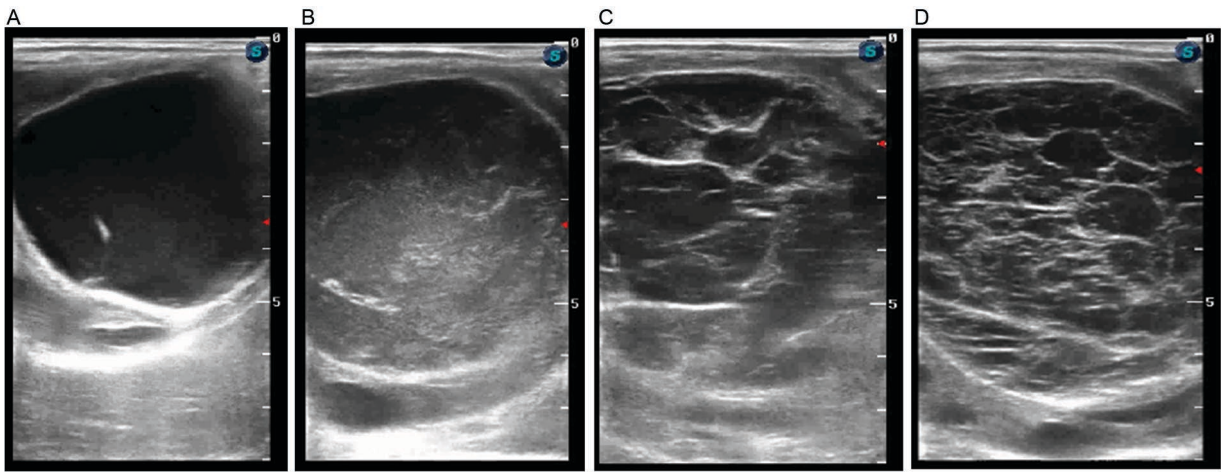


Figure 15.2 Development of an anovulatory follicle that failed to respond to an ovulation induction agent. The top figure is often first observed with an excessively thickened follicular wall and echogenic material free floating in the follicle. The hemorrhage in the follicle continues until a hematoma and eventual luteinization of the structure occurs. (A) 48 hours after GnRH agonist administration. Note flecks and debris in follicular fluid. (B) 72 hours after GnRH agonist administration. Note free blood in the follicular lumen. (C) 120 hours after GnRH agonist administration. The structure had fibrin strands and appears similar to a blood clot. (D) 144 hours after GnRH agonist administration. The structure has stabilized and formed a large mass on the ovary. The mare's progesterone value was 2.3 ng/mL.

Vet-ebooks.com

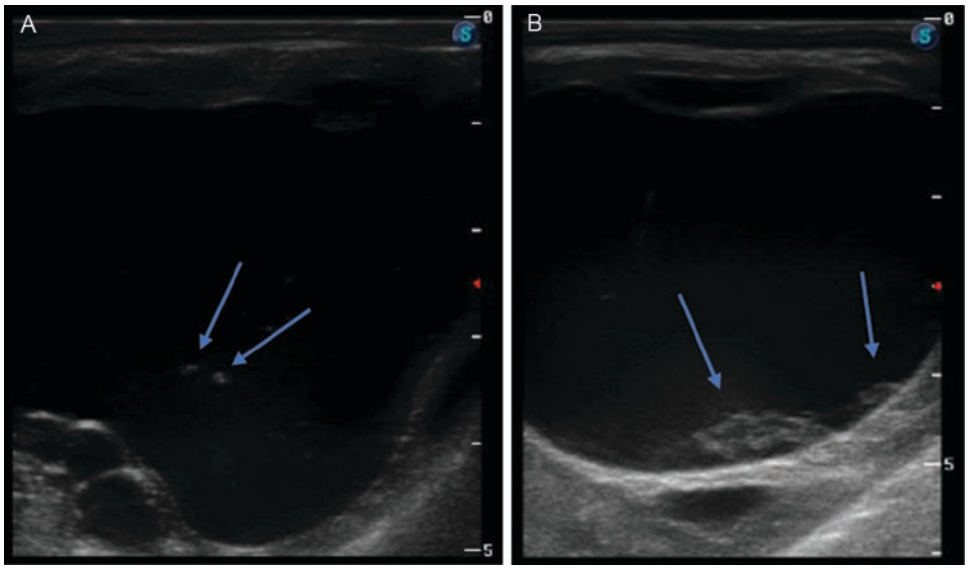


Figure 15.3 Anovulatory follicle 4 days apart. Hyperechoic material within the follicle is an indicator of the follicle being anovulatory.

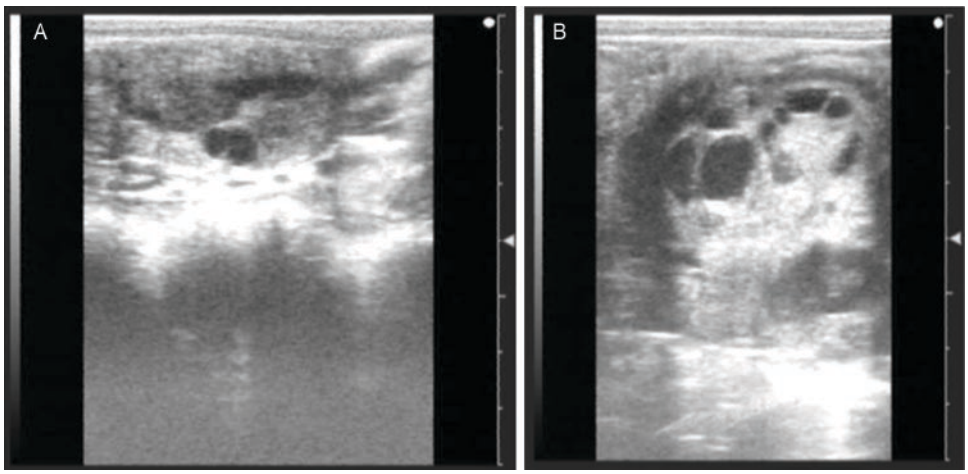


Figure 15.4 Image of a mare with a granulosa cell tumor. (A) Left ovary that is small and inactive due to production of inhibin by the tumor. (B) The ovary with the granulosa cell tumor where little normal ovarian tissue could be recognized.

prostaglandins, these structures will shrink in size and no longer be hormonally active. However, the remnants of these structures can be seen with ultrasound for several weeks to months following development of an anovulatory follicle.

Unfortunately, often by the time it is recognized that an anovulatory follicle has developed, the expense of breeding (live cover or artificial insemination) has already occurred. As the mare never ovulates, the oocyte is not released and is unable to be fertilized.

Granulosa Cell Tumor

A granulosa cell tumor (GCT) is the most common tumor of the ovary. The classical presentation is that of an enlarged ovary with the contralateral ovary being small and inactive (Figure 15.4). The contralateral ovary is inactive due to inhibin production by the GCT down regulating FSH release. Mare behavior is ambiguous with anestrus, nymphomania, or stallion-like behavior noted. During early development of a GCT, an abnormal area on the ovary may be noted but the mare may continue to cycle on the contralateral ovary and can become pregnant [2]

If presented with a mare with abnormal behavior and an abnormal area on the ovary, additional diagnostics to confirm or rule out a GCT are warranted. Currently, it is recommended that blood be submitted for inhibin, testosterone, progesterone, and Anti-Müllerian Hormone (AMH) to confirm suspicion of a

Vet-ebooks.com

GCT. Both authors have noted abnormal structures on the ovary that have taken 2–3 years to mature to the point of being able to be confirmed on a blood panel for a GCT. Careful evaluation of the ovary should be performed in these early detected tumors in which the contralateral ovary is still active to ensure that the abnormal ovary is removed. Surgical removal of the ovary will result in a drop in inhibin and resumption of cyclicality in 4–12 months. The broad range on return to cyclicity depends on when the ovary was removed in reference to the physiological breeding season.

Parovarian Cysts

Parovarian (or periovarian) cysts are remnants of embryonic development and cystic accessory structures. These structures do not appear to interfere with oocyte capture by the infundibulum or oocyte/early embryo migration within the oviduct. The greatest consequence of these structures is that they can appear to be within the ovarian parenchyma with cursory ultrasound examination. Occasionally these structures can be similar in appearance to a dominant follicle (Figure 15.5). This may result in mismanagement of the mare due to the inadvertent diagnosis of a large dominant follicle, not a parovarian cyst.

These structures are often easily identified with manual palpation of the ovary and oviduct region. If the tip of the uterine hold is held in the hand as you move toward the ovary, you will often feel the parovarian cyst followed by the ovary. A suggestion is to carefully palpate the ovaries and uterus of every mare at least for the first examination of the season to note any parovarian cysts that could cause diagnostic issues in the future.

Epithelial Inclusion Cysts

Epithelial inclusion cysts arise from the surface epithelium that lines the ovulation fossa and is taken up into the ovarian cortex during ovulation (Figure 15.6). These cystic structures are common in older mares. The effects on fertility are unknown but it is speculated that a large cyst or numerous cysts can obstruct the ovulation fossa, preventing release of the oocyte during ovulation.

Ovarian Hematoma

Ovarian hematomas can be similar in appearance to an anovulatory follicle (Figure 15.7). The distinction is that with an ovarian hematoma the mare ovulates normally, resulting in release of the oocyte. During formation of the corpus hemorrhagicum there is continued bleeding into the follicular space, resulting in formation of a large hematoma. These structures can be very large. Ovarian hematomas are not common and unless a distinct ovulation was recorded, the clinician should suspect a large fluid blood-filled follicle to most likely be an anovulatory follicle as opposed to an ovarian hematoma. Effects on pregnancy rates are not well described in the literature; however, these structures form post ovulation, so the oocyte is released and there is a chance of pregnancy.

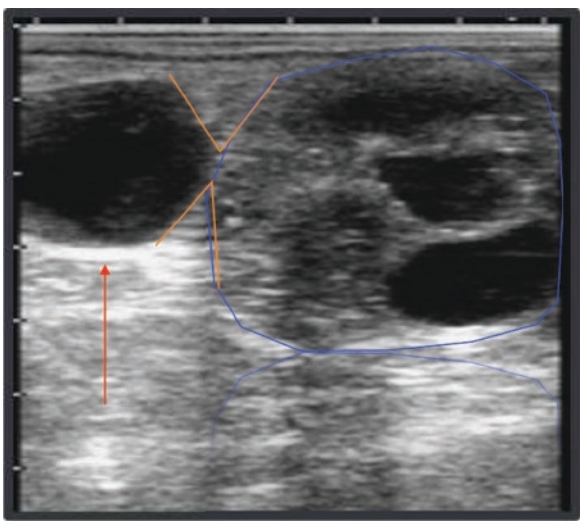


Figure 15.5 Image of ovary with adjacent parovarian cyst with ovary circled in blue, cyst highlighted by red arrow, and areas of tissue delineating ovary and cyst in orange.

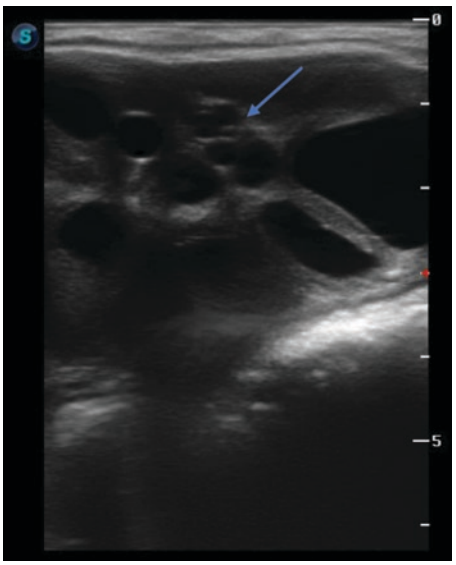


Figure 15.6 Image of epithelial inclusion cysts, indicated by blue arrow.

Vet-ebooks.com

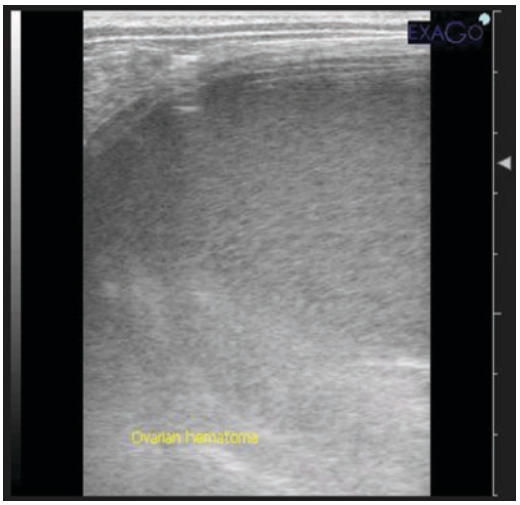


Figure 15.7 Image of a large ovarian hematoma. Mare was confirmed to have ovulated was checked 24 hours after ovulation of the primary follicle to evaluate if a large secondary follicle had ovulated and the large ovarian hematoma was observed. This structure remained on the ovary for over 4 months, when the mare was evaluated at the start of the next breeding season no evidence of the ovarian hematoma could be appreciated on the ovary.

Other Tumors

Other tumor types (teratoma, cystadenoma, or dysgerminoma) form on the ovary but they are rare in occurrence and many reproduction-focused clinicians will spend their career without ever seeing one of these cases.

Uterus

The uterus is as dynamic a structure as the ovary in its appearance during the normal estrous cycle. Additionally, there can be complicating factors such as the older multiparous mare with a deep dependent uterus that can be difficult to image. Careful examination (as described in the Introduction) of the uterus will allow one to be successful in detecting subtle abnormalities of the uterus.

For record-keeping systems, it is helpful for the clinician to use a scoring system for endometrial edema and free fluid. The endometrial edema is often scored on a system of 0–3 or 0–4 type scale; with a score of 0 indicating no edema (anestrus or diestrus) and a score of 3–4 indicating maximal edema. In my practice I expect most mares in estrus to have a grade 1 or 2 edema score. Mares with a grade 3 edema score often have "pathological" edema, indicating excessive inflammation occurring in the uterus.

A simple scoring system for uterine fluid can be used to score both the volume and echogenicity of the fluid. The following scoring system is used in my clinical practice: 0 – no intrauterine fluid; trace – < 1 cm of fluid in a focal spot (i.e., base of one uterine horn); small – < 1 cm of fluid in multiple locations; moderate – 1–3 cm of fluid in multiple locations; and large – > 3 cm of fluid in multiple locations. An echogenicity score is assigned from 1–4, with 4 being hypoechoic fluid and 1 being severely hyperechoic fluid.

No matter the scoring system used, consistency is key to being useful. As clinicians, we are trying to use decrease/increase in intrauterine fluid and echogenicity of the fluid to evaluate the success or failure of our treatments, and scoring systems can allow rapid assessment.

Intrauterine Fluid

Intrauterine fluid can be detected in a normal mare during estrus in scant quantities that should be hypoechoic. It is often thought that this fluid is mucus associated with estrus. If significant volume and/or hyperechogenic fluid (Figure 15.8) is detected, additional diagnostics should be considered such as endometrial culture and cytology, low volume lavage for culture and cytology, or an endometrial biopsy to characterize the fluid as normal, inflammatory, or infectious. During diestrus, the mare's uterus should always be free of fluid. If free intrauterine fluid is present in the uterus during diestrus, this is abnormal, and a diagnostic workup should be performed.

Following breeding, it is common in mares to accumulate inflammatory fluid within the uterus 24 hours after artificial insemination or live cover. This is often referred to as post mating or breeding induced endometritis (PMIE or PBIE) (Figure 15.9). The fluid volume is extremely variable between mares and also the extent of the inflammation. The echogenicity of the fluid can also vary from hypoechoic to highly echogenic in character. Common treatments performed are ecbolics, uterine lavage (Figure 15.10), and anti-inflammatories such as dexamethasone.

Endometrial Cysts

Endometrial cysts are dilations of the lymphatics or endometrial glands due to development of fibrosis obstructing lymphatic or glandular outflow (Figure 15.11). Endometrial glands are relatively small in size (< 1 mm) and are not likely to be detected on ultrasound examination. Lymphatic cysts can be quite large, up to 15 cm, but the majority are < 3 cm in size [3]. The cysts can be uni- to multilocular, with either a wide base like a blister or be pedunculated on a small narrow stalk.

The major consequence of endometrial cysts is that they can interfere with ultrasonographic detection of pregnancy (Figures 15.12, 15.13, 15.14, 15.15, and 15.16). It is crucial as part of the reproductive record to be able to list the presence of endometrial cysts, as

Vet-ebooks.com

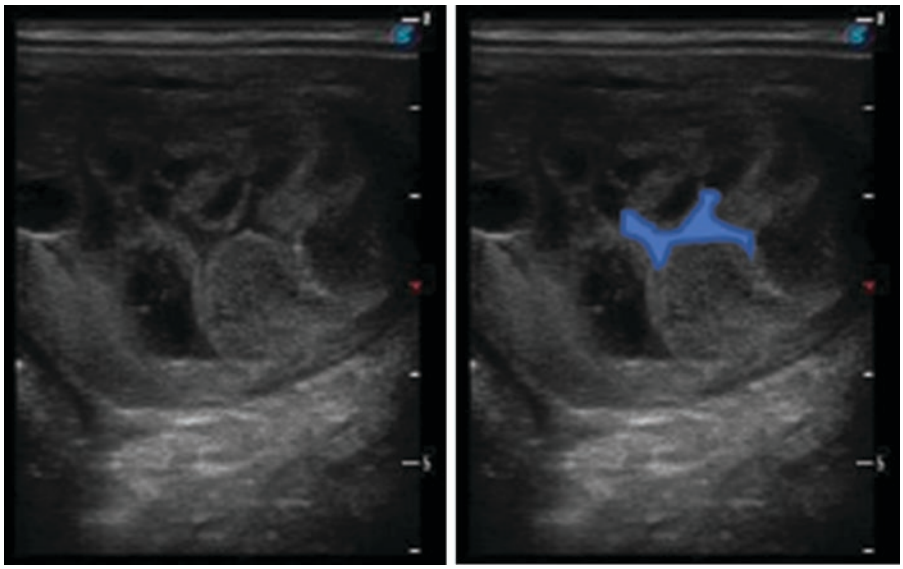


Figure 15.8 Ultrasound images show excessive endometrial edema with a trace amount of hyper echoic fluid. Uterine lumen is highlighted in blue.

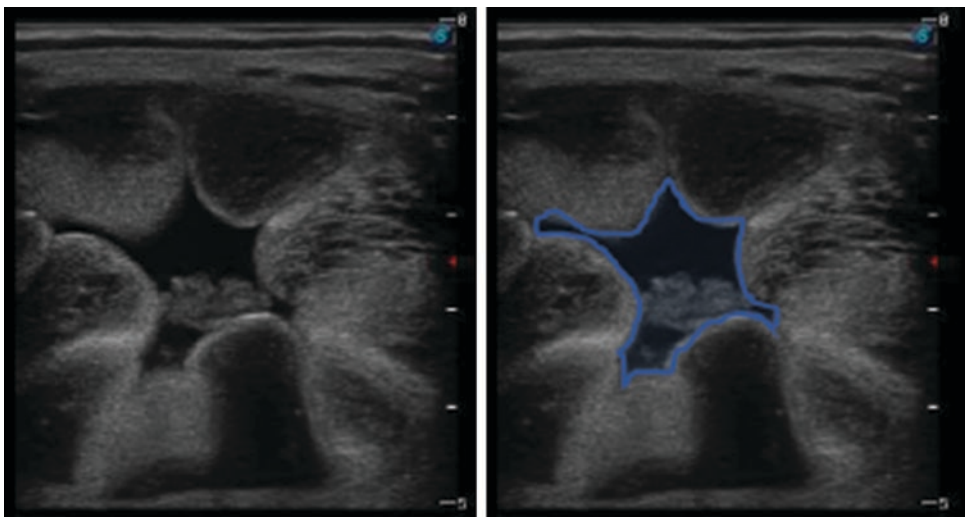


Figure 15.9 Ultrasound image of mare with excessive edema and small volume of intralumenal fluid with hyper echoic particles. This is a mare 24 hours after breeding with mating induced endometritis. Uterine lumen is outlined in blue to allow visualization of intralumenal debris.



Figure 15.10 Image of a mare being lavaged due to post breeding fluid. Ultrasound of the uterus can be performed at the end of the lavage to confirm all fluid has been removed from the uterus. Note the inflated balloon of the catheter on the left side of the image with fluid still present in the caudal uterine body to be recovered.

Vet-ebooks.com

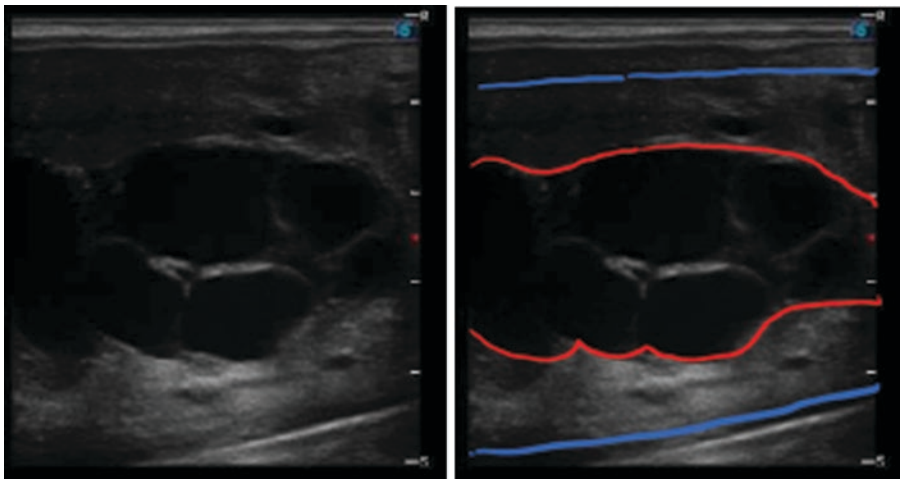


Figure 15.11 This image demonstrates a large cystic complex in the uterine body. The uterine lumen is outlined in blue, with an endometrial cystic complex outlined in orange.

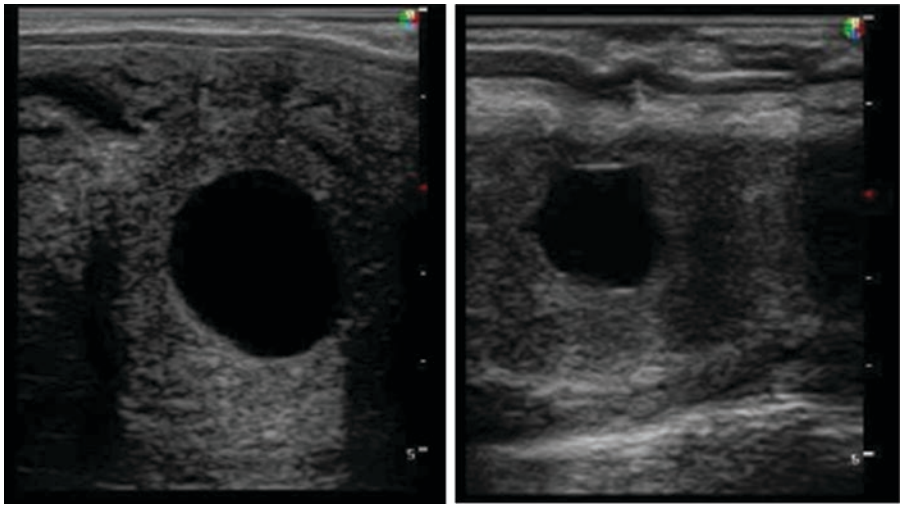


Figure 15.12 Endometrial cysts can have a similar ultrasonographic appearance to an embryonic vesicle. Image on left: round cyst of similar appearance of an ~14-day embryonic vesicle. There is an impression of a thickened wall of a cyst compared to a vesicle. Definitive differentiation: the presence of the cyst was known from evaluation prior to breeding, and the cyst was noted to be stationary in position and growth during pregnancy evaluations. Image on right: hyperechoic ultrasonographic artifacts at the dorsal and ventral positions on the cyst can give the appearance of a ~13-day embryonic vesicle.

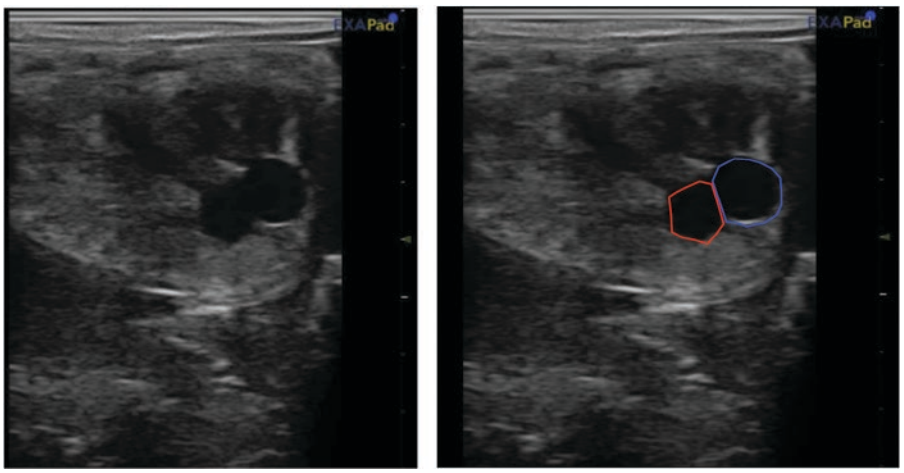


Figure 15.13 Left: 13-day pregnancy adjacent to a known endometrial cyst. Right: Cyst outlined in red, embryonic vesicle outlined in blue.

Vet-ebooks.com

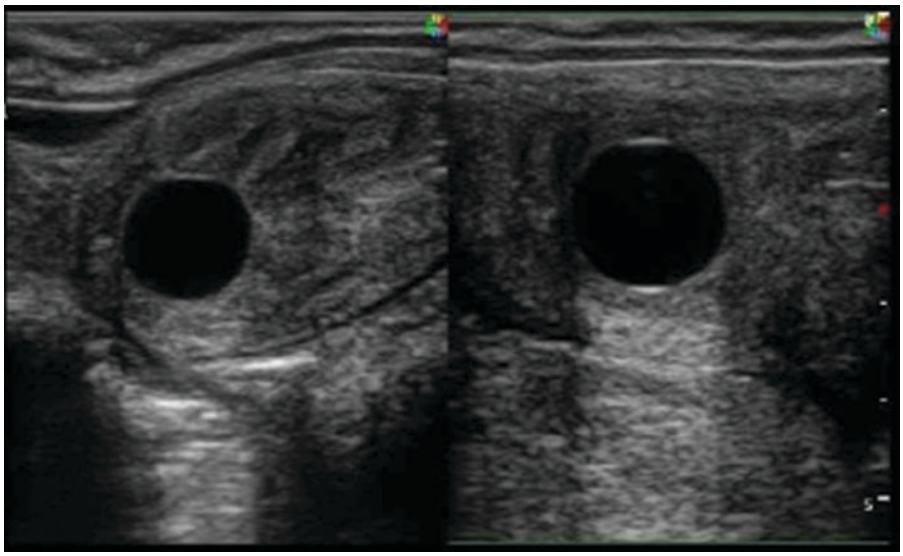


Figure 15.14 Image of embryonic vesicle (14-days gestation of left, 16-days gestation on right) as a comparison to the ultrasonographic appearance of endometrial cysts.

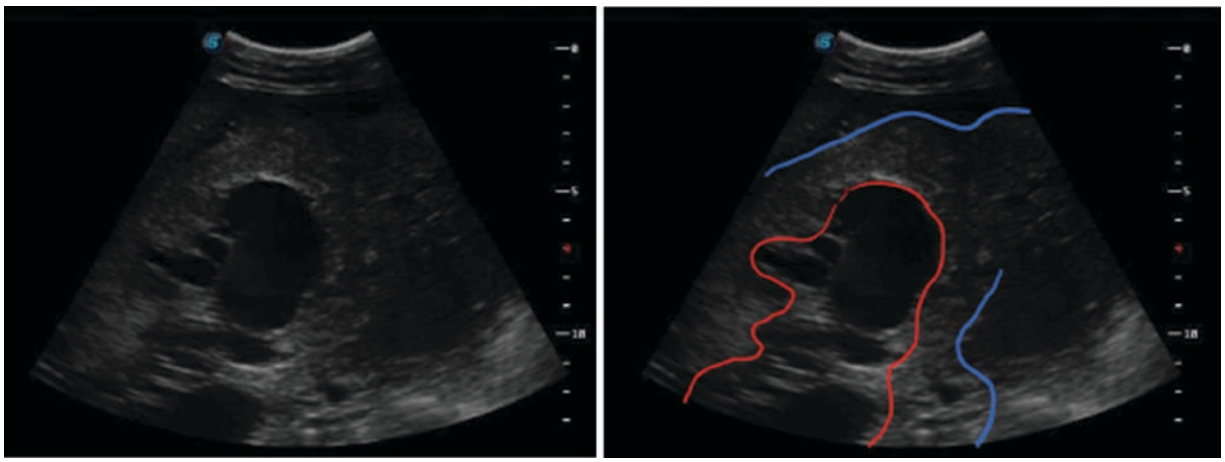


Figure 15.15 Endometrial cysts can be identified with transabdominal ultrasonography in a dependent uterus, for example post foaling. Blue outlines the uterus; orange outlines a cystic complex.

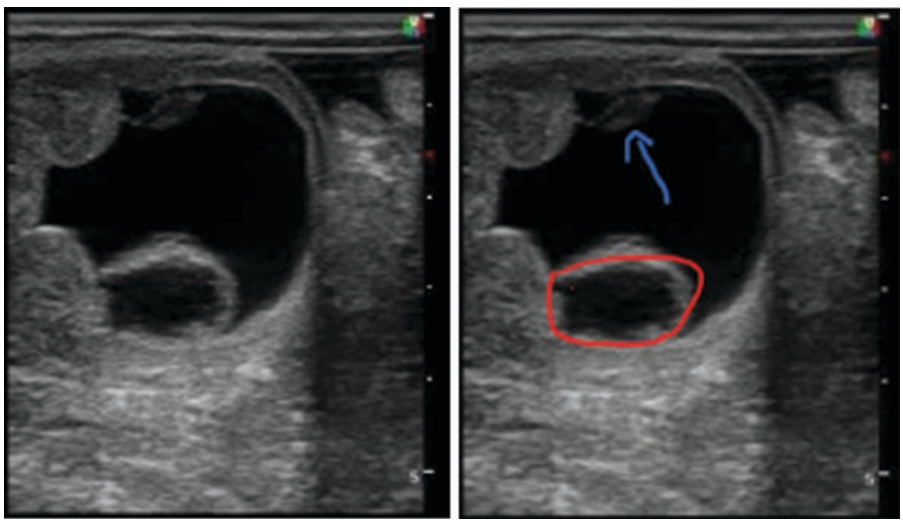


Figure 15.16 Endometrial cyst (orange) adjacent to a ~25-day gestation embryonic vesicle. The embryo proper (blue arrow) originated from a position against endometrium rather than against the endometrial cyst which may have increased odds of survival.

Vet-ebooks.com

some of these structures are indistinguishable from a pregnancy. If one has not examined the mare prior to the pregnancy examination, distinguishing signs include endometrial cysts do not move and do not grow significantly over a period of days; early pregnancies move throughout the uterus until day 16 when they fix in place and grow several millimeters a day during early development. If unsure that a structure is an endometrial cyst or a pregnancy, one can recheck the mare in 1–2 days; a pregnancy will be bigger and often in a different location.

Cysts can interfere with maintenance of pregnancy by: i) preventing embryonic vesicle movement throughout the uterus and thus interfering with signals for maintenance of the pregnancy; and ii) interfering with nourishment of an embryonic vesicle. This is especially evident if the embryo fixes next to an endometrial cyst.

Air In the Uterus

Air can easily be detected in the lumen of the uterus due to the bright hyperechoic artifacts (Figure 15.17). Air indicates poor perineal conformation resulting in aspiration of air into the vaginal vault and uterus or indicates something has penetrated the vulva of the mare recently (a vaginal procedure such as collection of an endometrial culture or the mare has been bred (artificial insemination or live cover)).

Mucus/Biofilm

It has been recognized in mares with sub-fertility that a hyperechoic line can be appreciated where the endometrial folds come into contact (Figures 15.18, 15.19, and 15.20). It has been suspected that this may be an indication of excessive mucus or potentially a biofilm. Confirming this with endometrial biopsy has been problematic due to the inability to biopsy the exact same location with the abnormal appearance imaged on ultrasound. If the hyperechoic areas are seen on ultrasound, it is suggested that a diagnostic workup be performed to identify potential causes of inflammation and infection.

Endometrial Cups

Endometrial cups are fetal in origin and form around 35–40 days of pregnancy. These specialized cells migrate from the embryo and invade into the endometrium. The role of endometrial cup cells are to secrete pregnant mare serum gonadotrophin (PMSG), resulting in formation of secondary corpora lutea to help maintain pregnancy. These cells are hormonally active until approximately 150 days gestation, when the maternal immune system destroys the endometrial cup cells. This hormonal activity remains present despite pregnancy loss [4]. Uncommonly, endometrial cups persist beyond the normal time frame, resulting in erratic cyclicity until the endometrial cup cells are destroyed [5]. Persistent endometrial cups can be visualized via ultrasound typically at the base of one uterine horn (Figures 15.20, 15.21, and 15.22).

Uterine Artery Rupture

It is well recognized that peripartum uterine artery rupture can occur. While these events are readily recognized in mares with significant hemorrhage, in many instances the hemorrhage is sub-clinical. The first time the hemorrhage is noted is at the first reproductive examination after foaling. These abnormal structures can range from a large hematoma covering a uterine horn to identification of dilated uterine arteries (Figure 15.23).

Marble

Intrauterine marbles have been used for estrus suppression [6]. Intrauterine marbles can evade routine detection by presumably having an appearance similar to the pelvis or gastrointestinal gas (Figure 15.24). Thorough transrectal palpation prior to ultrasonography may aid in detection of an intrauterine marble.

Fetal Bones (Figure 15.25)

Leiomyoma (Figure 15.26)

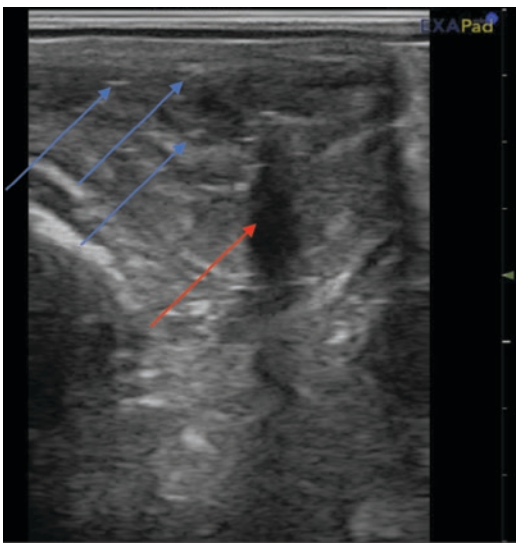


Figure 15.17 Image of the uterus with air in the lumen. Note the echogenic spots (blue arrows) and area where the air is blocking the ultrasound waves from penetrating the tissue (red arrow).

Vet-ebooks.com

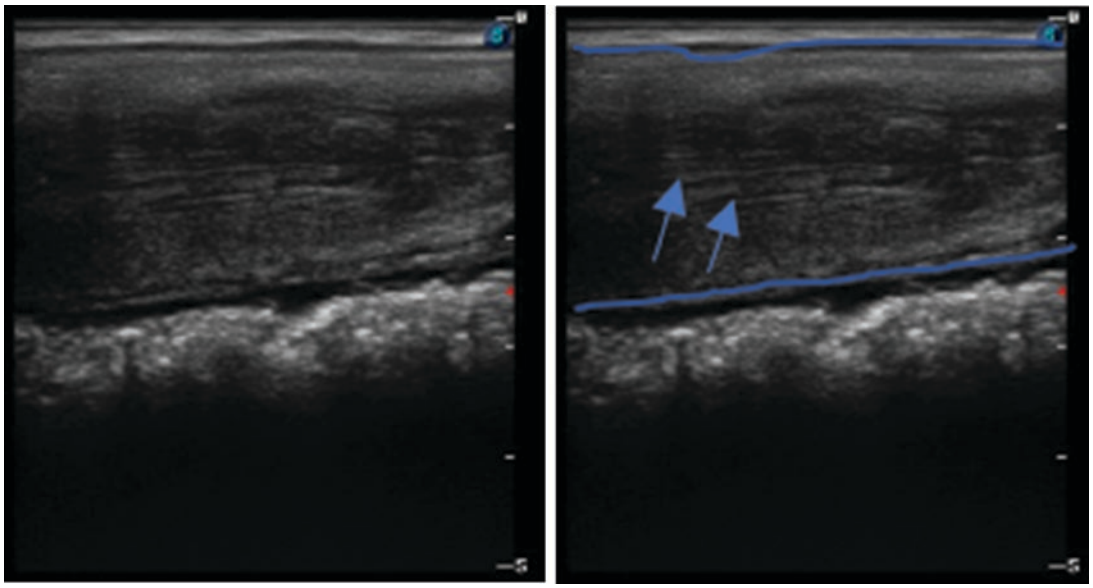


Figure 15.18 Linear hyperechoic lines (arrows) within the uterine body (outlined) in this mare were associated with endometrial mucus as diagnosed on biopsy and *Streptococcus equi zooepidemicus* endometritis on culture.

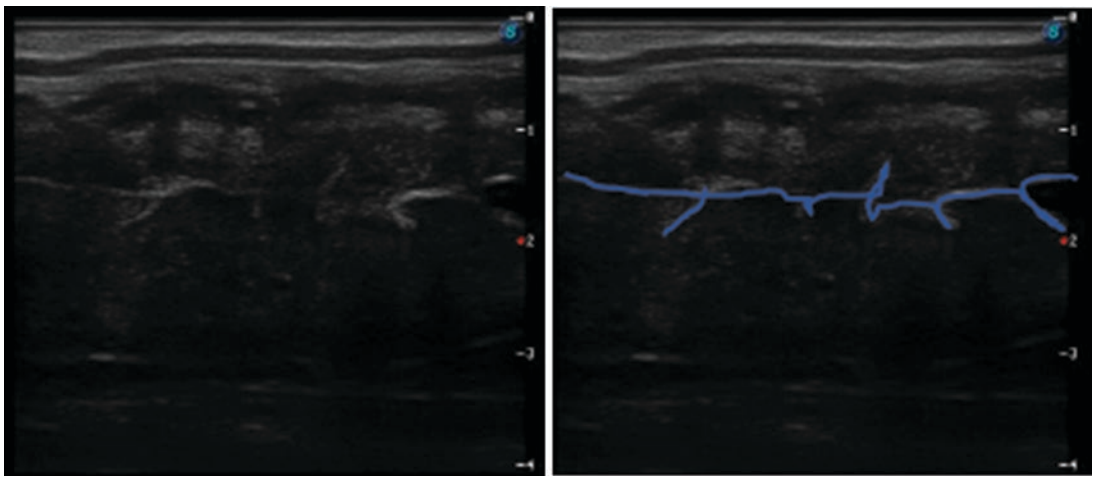


Figure 15.19 Intrauterine mucus associated with bacterial endometritis. Mucus delineated with blue line.

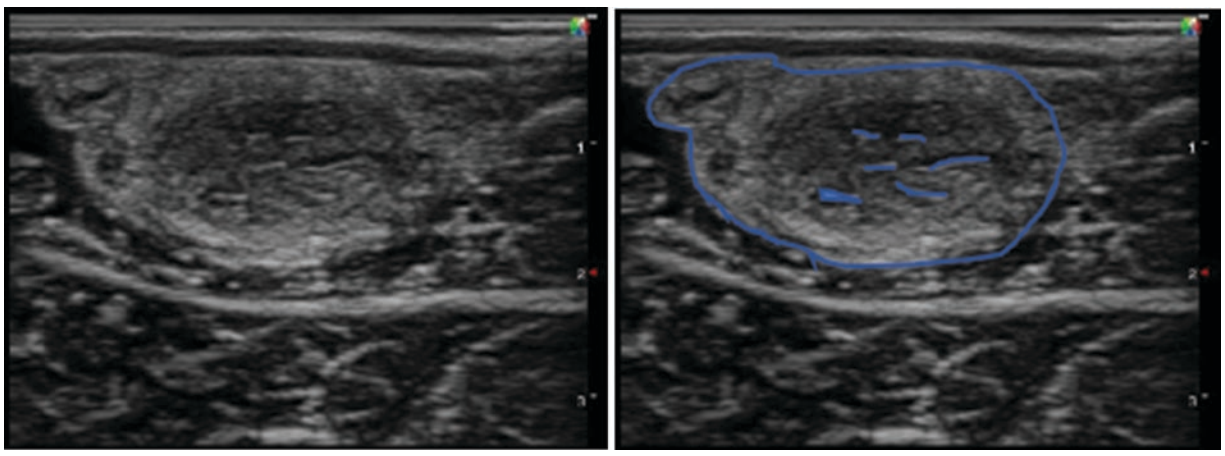


Figure 15.20 Endometrial mucus suggestive of endometritis. Uterus outlined in blue, mucus indicated by blue lines.

Vet-ebooks.com

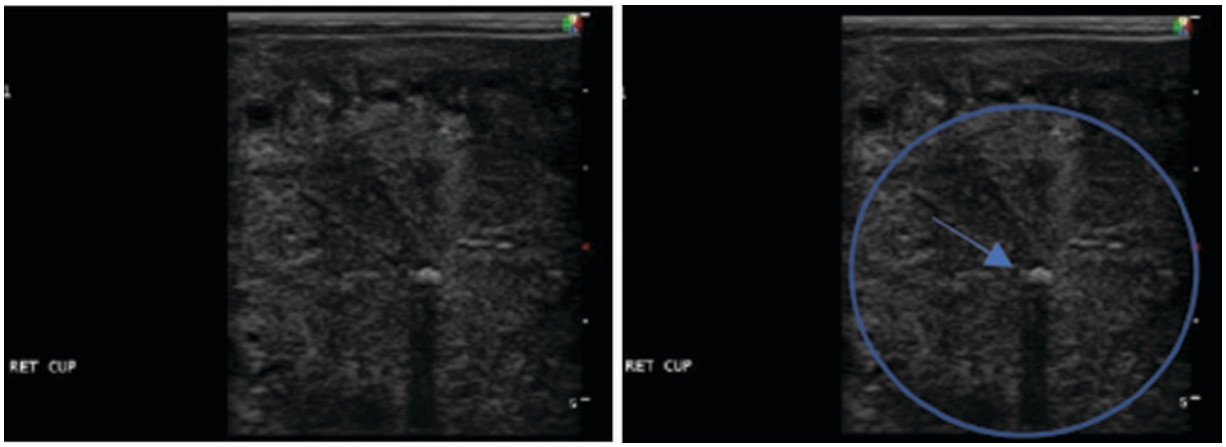


Figure 15.21 Uterine horn in cross-section (circle) and a calcified endometrial cup (arrow).

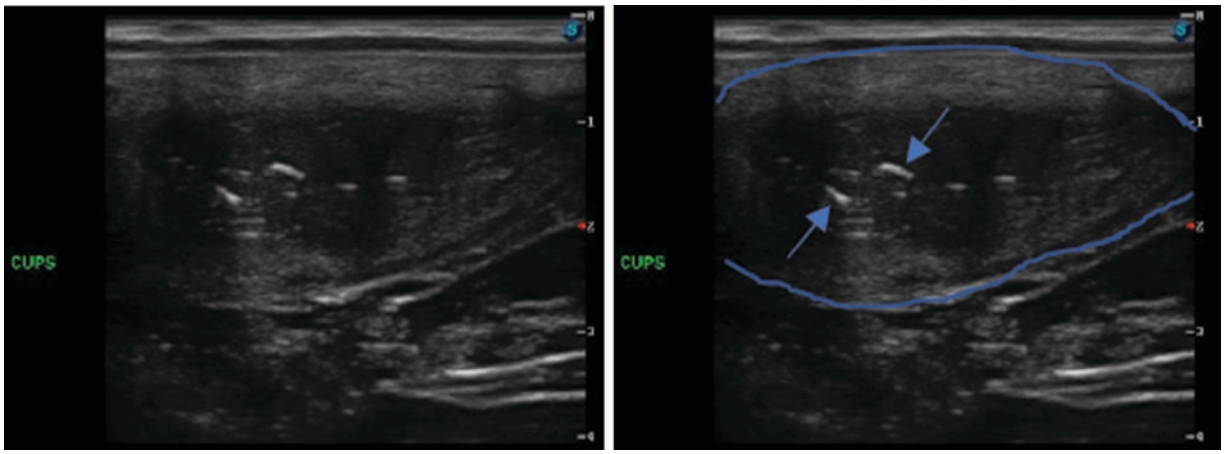
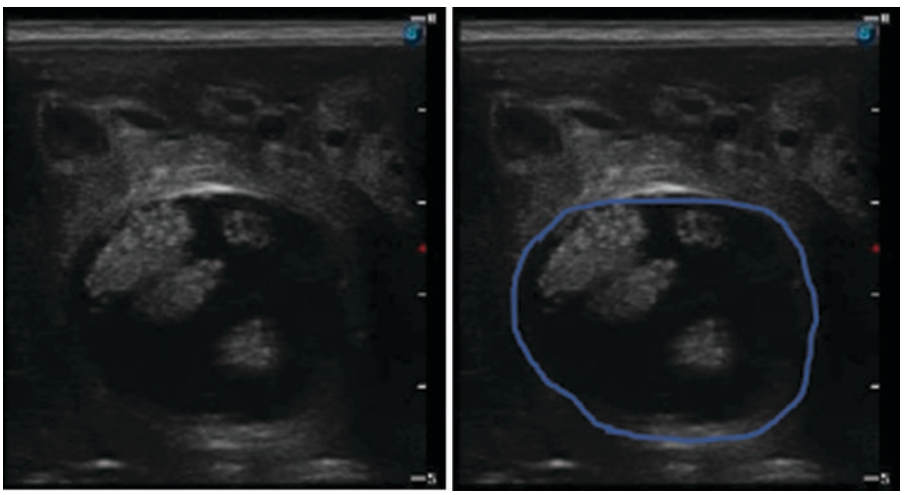


Figure 15.22 Image of retained endometrial cups as highlighted by the blue arrow.

Figure 15.23 Image of a dilated middle uterine artery (outlined in blue) containing evidence of blood clots. It was suspected this occurred at the previous foaling. Due to the mare foaling late in the season the mare was not examined until the next breeding season.



Vet-ebooks.com

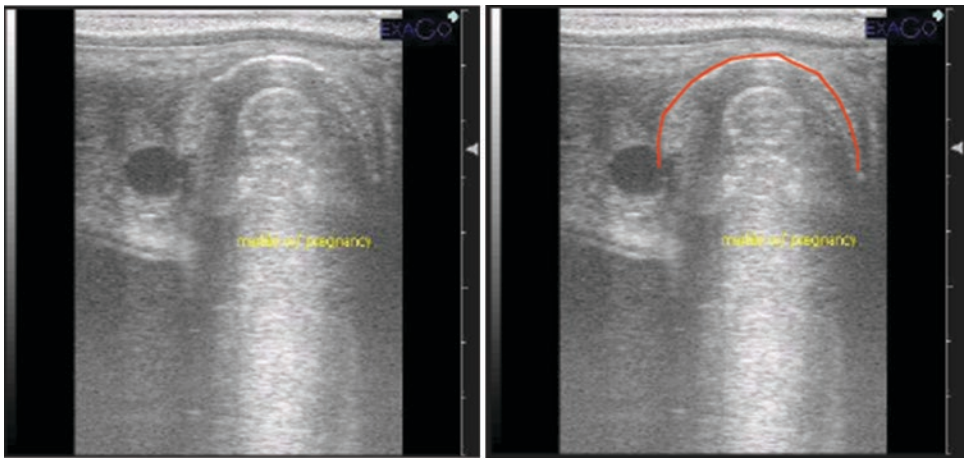


Figure 15.24 Left Image of a mare presenting for a 14-day pregnancy exam after being bred in hand. A marble was noted sitting adjacent to the 14-day pregnancy. Right Image has the marble highlighted in red.

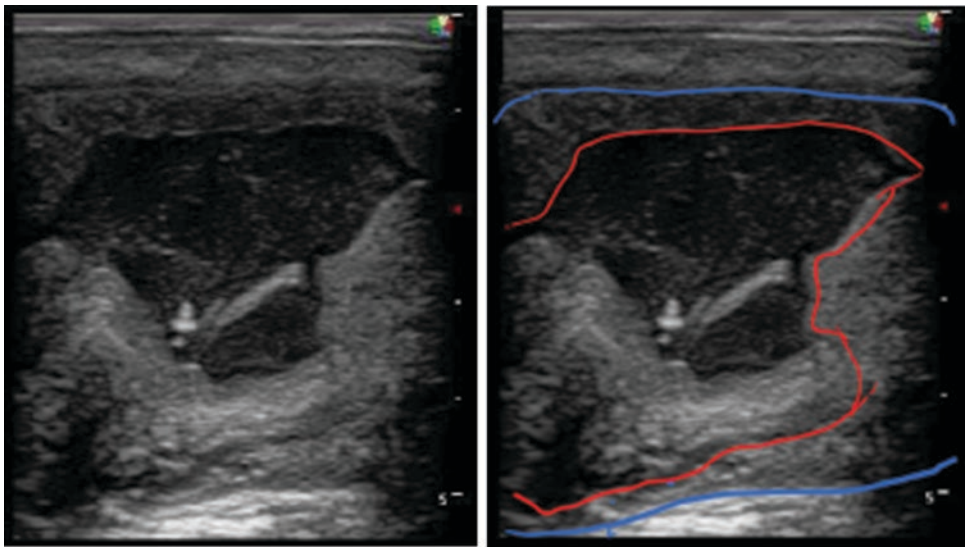


Figure 15.25 Images of purulent material and fetal bones with uterus outlined in blue and intrauterine material outlined in red. Mare presented for mid-gestational pregnancy evaluation. The previous pregnancy evaluation was at 60 days gestation. Altrenogest had been administered daily in an attempt to aid in pregnancy maintenance. Progestagen administration prevented cervical dilation upon fetal death. Case management included discontinuing altrenogest, prostaglandin F-2alpha to ensure absence of luteal tissue, gentle manual cervical dilation, and uterine lavage to facilitate removal of the fetal skeleton.

Cervix

The cervix can be successfully visualized with ultrasonography by continuing to follow the caudal uterine body. Increased tissue echogenicity can be detected indicating the change from uterus to cervix. The cervix is evaluated in longitudinal fashion with the probe held parallel to the cervix. The cervix can be evaluated in both estrus and diestrus. While cervical abnormalities are not common, ultrasound examination of the cervix can be rewarding in some problem mares.

Failure to Relax in Estrus

In mares with cervical injury (Figure 15.28) or older maiden mares, it is common for the cervix to not relax during estrus (Figure 15.27). While the size or failure to relax in estrus is not apparent on ultrasound, often these mares will accumulate fluid in the caudal uterine body in estrus and after breeding.

Vagina

Often during a reproductive examination, the ovaries and uterus are the focus of the examination with little attention focused on the cervix and vaginal vault. As the probe is removed from the mare, continuing the ultrasound evaluation will allow the practitioner to identify subtle changes in the vaginal vault.

Vet-ebooks.com

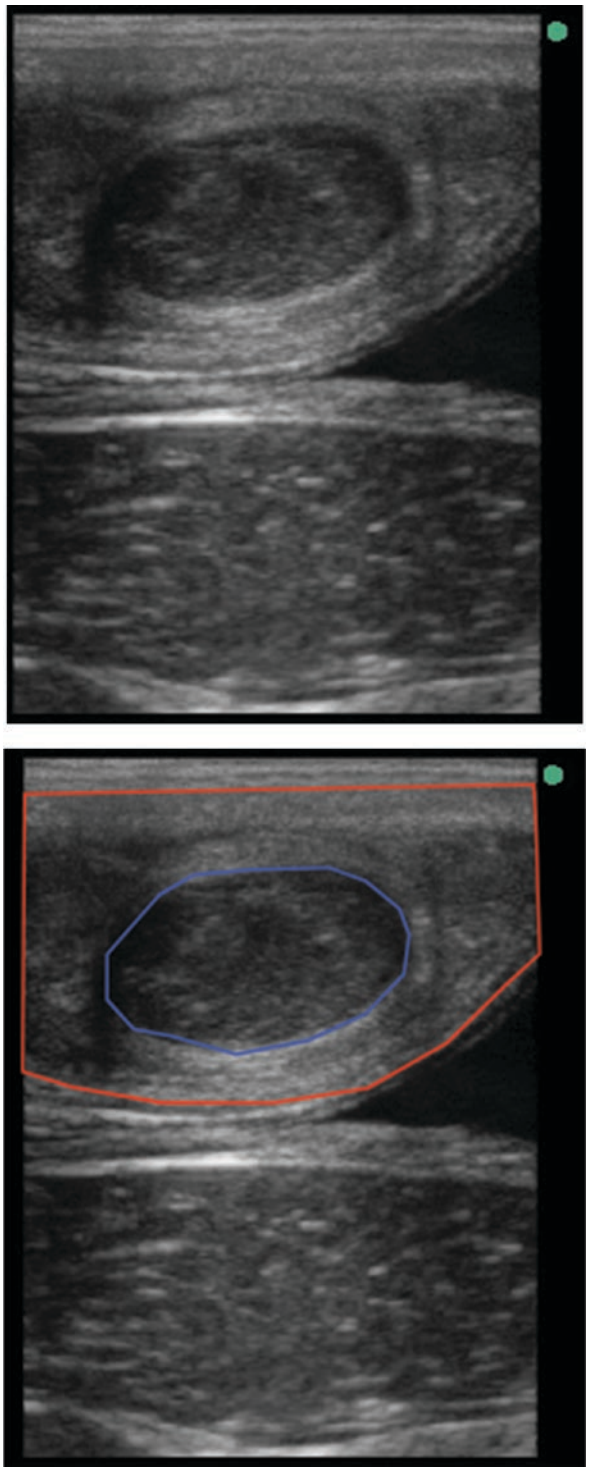


Figure 15.26 Left: the uterus at the start of the breeding season with abnormal echogenic mass present. Hysteroscopy with guided biopsy confirmed diagnosis of a leiomyoma. Right: the uterus is circled in red and the leiomyoma in blue. Leiomyomas are slow growing tumors that resemble smooth muscle. If the tumor is active or aggressive in nature, a leiomyosarcoma is likely. Uterine tumors are rare in occurrence.

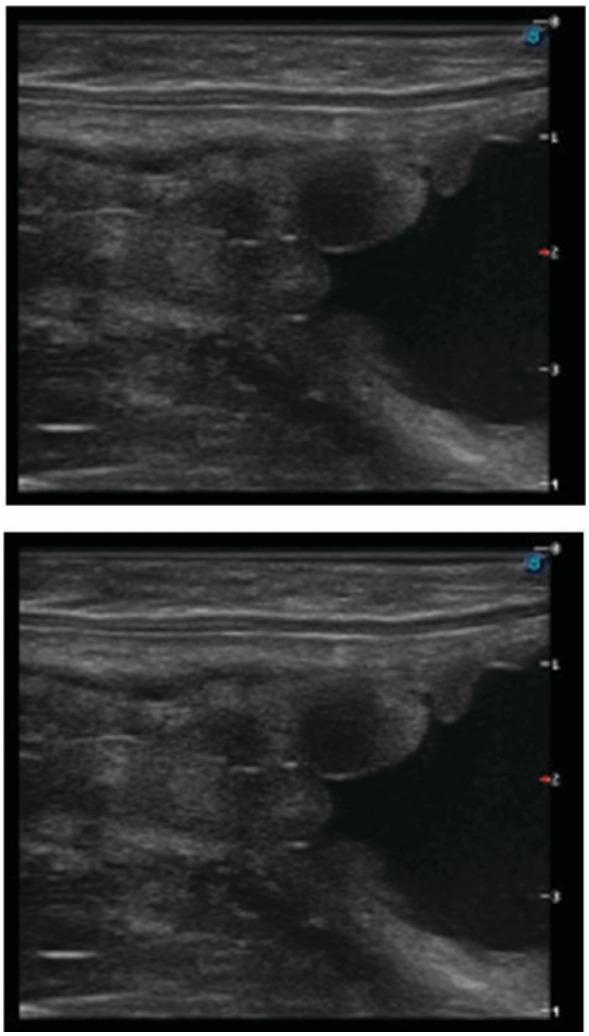


Figure 15.27 Image of anechoic intrauterine fluid adjacent to the cervix. This image is from a mare in estrus. Endometrial culture and cytology revealed no microbial growth and no inflammation. The pattern of the fluid immediately cranial to the cervix suggests failure of proper cervical relaxation during estrus. Blue lines outline cervix and uterus. Orange delineates the cervical lumen.

Urovagina

During peak estrus, fluid may be noted in the cranial vaginal vault or in the uterus (Figure 15.30). If this fluid has appearance similar to urine as seen in the bladder, additional diagnostics are warranted (Figure 15.29). A diagnosis of urovagina can be confirmed with speculum examination to evaluate color, odor, and to facilitate collection of fluid for creatinine concentration or cytological evidence of urine crystals. Note many mares will accumulate urine in the vaginal vault or uterus during peak estrus. Urine may not be appreciated on ultrasound or speculum exams during early or late estrus, or in diestrus.

Bladder (Figure 15.31)

Vet-ebooks.com

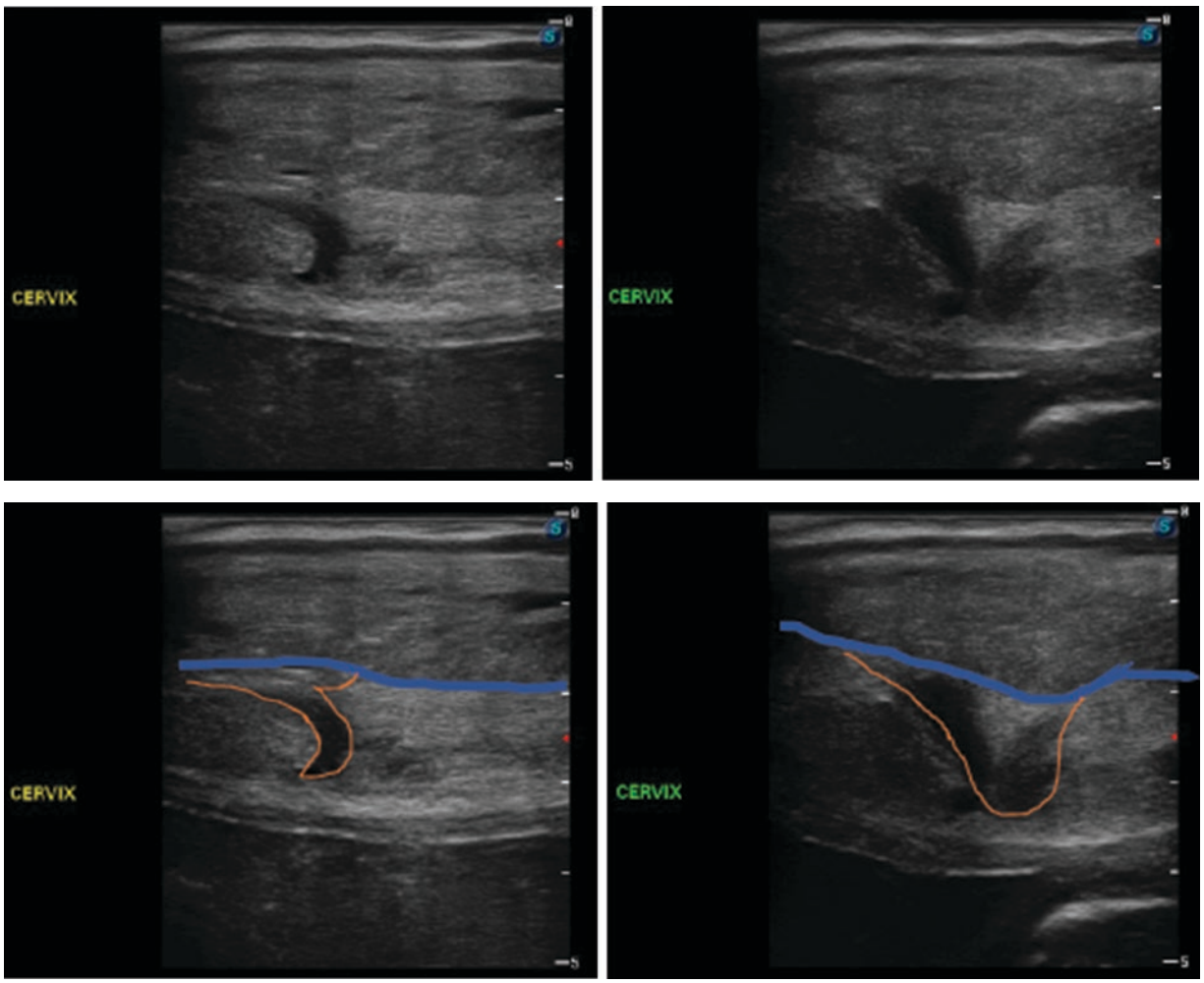


Figure 15.28 Defect in the ventral cervix. The cervix is viewed longitudinally with a linear transducer held parallel to the cervix. The right images are sagittal. Ultrasonographic impression of a cervical defect should be confirmed with a digital cervical examination while the cervix is closed during diestrus. Focal mid cervix body defects may act as a nidus for ascending infection. Blue delineates normal cervical lumen. Orange outlines the cervical defect.

Vet-ebooks.com

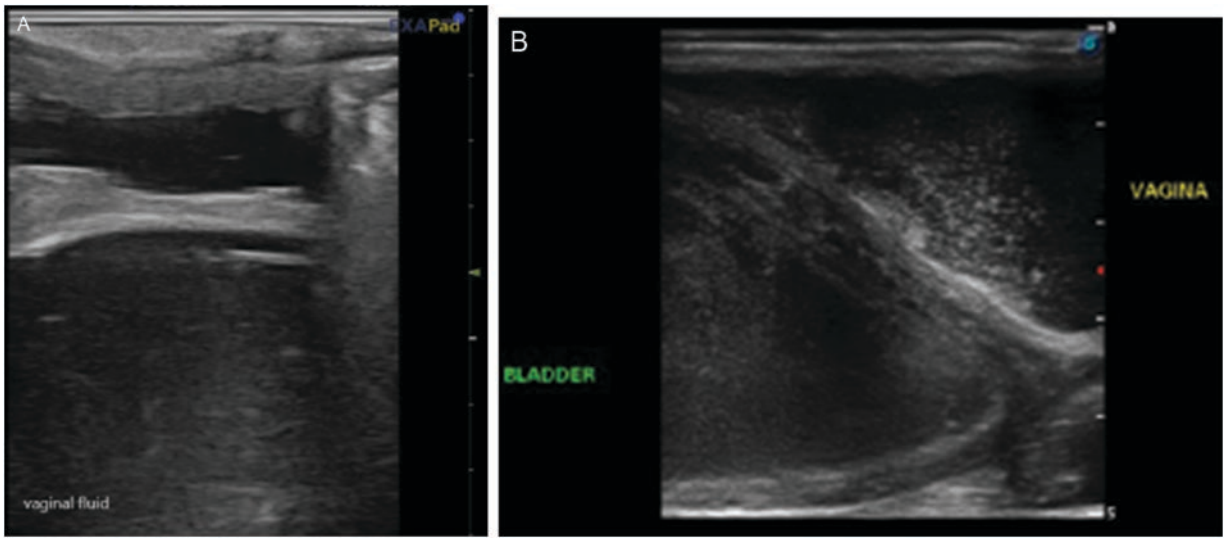
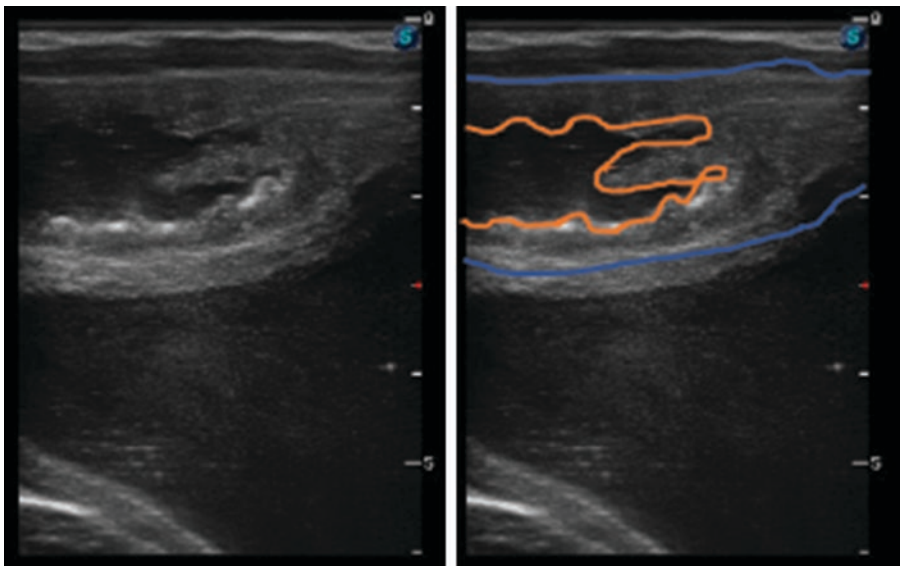


Figure 15.29 (A) Image of mare with free fluid in the vaginal vault. Speculum examination revealed fluid consistent with urine accumulation. (B) Image including bladder and vagina distended with urine.

Figure 15.30 Vaginal fluid secondary to endometritis. Vagina and cervix outlined in blue sitting above the bladder. Vaginal lumen and fluid outlined in orange.



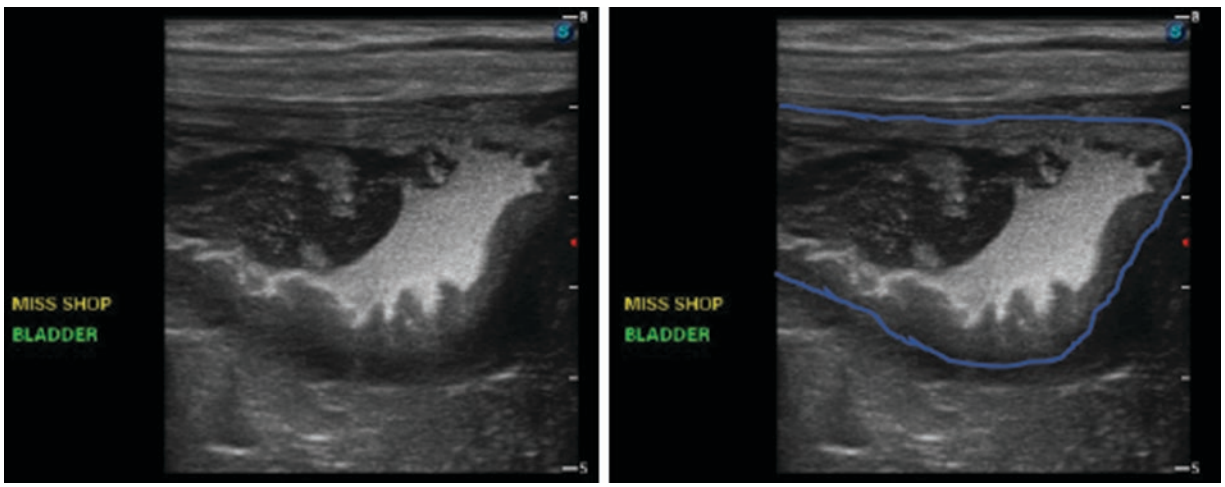


Figure 15.31 Transrectal image of the bladder in a mare diagnosed with Streptococcus equi zooepidemicus cystitis. The cystitis presumably contaminated the vestibule and thus the vagina and uterus during breeding and reproductive procedures leading to recurrent endometritis. [same mare as Figure 15.18]. Resolution of cystitis ended recurrent bacterial endometritis.

Vet-ebooks.com

References

1 McCue, P. and Squires, E. (2002). Persistent anovulatory follicles in the mare. *Theriogenology* 58: 541–542.

2 McCue, P.M., Roser, J.F., Munro, C.J. et al. (2006). Granulosa cell tumors of the equine ovary. *Veterinary Clinics of North America-Equine Practice* 22(3): 799–817. http://doi.org/10.1016/j.cveq.2006.08.008

3 Kenney, R.M. (1978). Cyclic and pathologic changes of the mare endometrium as detected by biopsy, with a note on early embryonic death. *Journal of the American Veterinary Medical Association* 172(3): 241–262.

4 Antczak, D.F., de Mestre, A.M., Wilsher, S. et al. (2013). The equine endometrial cup reaction: A fetomaternal signal of significance. *Annual Review of Animal Biosciences* 1(1): 419–442. http://doi.org/10.1146/annurev-animal-031412-103703

5 Crabtree, J.R., Chang, Y., and De Mestre, A.M. (2012). Clinical presentation, treatment and possible causes of persistent endometrial cups illustrated by two cases. *Equine Veterinary Education* 24(50): 251–259

6 Nie, G.J., Johnson, K.E., Braden, T.D. et al. (2003). Use of an intra-uterine glass ball protocol to extend luteal function in mares. *Journal of Equine Veterinary Science* 23(6): 266–273. http://doi.org/10.1053/jevs.2003.75

Vet-ebooks.com

16

Transrectal Ultrasonography of Early Equine Gestation – the First 60 Days

Chelsie A. Burden

Goulburn Valley Equine Hospital, Victoria, Australia

Introduction

Early examination of the mare's reproductive tract for the purpose of pregnancy detection, evaluation of the uterine environment, and development of the pregnancy during the first 60 days of gestation is best accomplished via transrectal palpation and ultrasonography. Effective and efficient breeding management of the mare is facilitated by an accurate detection of pregnancy. Furthermore, prompt detection of mares who fail to become pregnant on a given breeding cycle, or whose pregnancies fail to develop properly during early gestation, present the opportunity for follow-up diagnostics and rebreeding attempts within the confines of a limited breeding season. Early detection of multiple or twin pregnancies provides the opportunity for effective reduction prior to endometrial cup formation. For the purposes of this discussion, gestational age will be measured as days from ovulation, where the date of ovulation is identified as day 0 (zero).

Transrectal Technique

Transrectal palpation and/or ultrasonography of the reproductive tract of the mare is a standard part of any reproductive practitioner's examination. The practitioner is essential to successful transrectal examination on multiple levels. Palpation skills are necessary to locate structures of interest such as the uterus and ovaries and differentiate these organs from the intestinal tract [1]. Appropriate restraint of the mare is indicated for the safety of both the mare and clinician. The risk of damage to the rectal mucosa and the possibility of creating a fatal rectal tear during the course of any transrectal examination should be foremost in the examiner's mind; movement and manipulation within the rectum should be gentle and vigilant to reduce such risk. Methods of restraint may include physical or chemical restraint. A mare might be placed in stocks or be twitched to reduce movement during examination, and foals should be positioned or confined to the front or side of the mare to reduce the anxiety of the mare [2]. A maiden mare or fractious mare may require sedation and/or muscle relaxants to reduce the risk of injury during transrectal examination. An alpha-2-adrenergic agonist, e.g., detomidine (0.01–0.08 mg/kg IV) and butorphanol (0.03–0.08 mg/kg IV) is a useful combination along with a smooth muscle relaxant such as N-butylscopolammonium bromide (0.3 mg/kg IV; Buscopan®) or propantheline bromide (0.014–0.07 mg/kg IV; Propan-B, 2.5–3 ml/500 kg mare) [3]. The ample use of lubricant facilitates the safe removal of fecal material from the mare's rectum and the safe movement of the examiners hand and arm against the rectal mucosa, as well as providing effective contact between the ultrasound probe and rectal mucosa. A lubricant should be of the proper consistency and free of air bubbles to establish adequate contact and achieve the best image during ultrasonography. Furthermore, during pregnancy diagnosis and evaluation, it is important that practitioners be gentle but systematic in their manipulation in order to thoroughly ultrasound the mare's reproductive tract without damage to the developing embryonic vesicle [2].

Atlas of Equine Ultrasonography, Second Edition. Edited by Jessica A. Kidd, Kristina G. Lu and Michele L. Frazer.
© 2022 John Wiley & Sons Ltd. Published 2022 by John Wiley & Sons Ltd.
Companion Website: www.wiley.com/go/kidd/atlas

Vet-ebooks.com

Once all fecal material has been safely evacuated, the practitioner first performs a gentle palpation of the mare's internal reproductive tract to include ovaries, uterus, and cervix. The transrectal palpation allows orientation of the reproductive organs prior to ultrasonography along with evaluation of uterine and cervical tone. Visualizing an accurate mental picture of the reproductive anatomy will help accurately facilitate the interpretation of what is imaged with ultrasonography.

The cervix, in early pregnancy (10–30 days), can be palpated on the floor of the pelvis as a longitudinal, rigid, toned structure such as in diestrus. The ovaries should be palpated for completeness of examination; however, the corpus luteum is not palpable in the mare and adds little knowledge to pregnancy diagnosis. Uterine tone in the normal pregnant mare will be consistent with diestrus with a prominent tubular anatomy. The swelling of the uterus, indicating presence of a conceptus, is not palpable until 28 to 30 days gestation (slightly earlier in the maiden mare) at the base of the fixated horn. The swelling at this stage of gestation is a 3-4 cm in diameter ventral bulge [4]. With the development of pronounced uterine tone in the pregnant mare, the uterine horns may become kinked, especially at the base, sometimes turning back along the uterine body. Palpation can help identify this when it is present, and allows for gentle manual repositioning to facilitate a complete examination. By 60 days gestation, the conceptus swelling fills the pregnant horn and measures roughly 12 cm in diameter [4]. In the author's experience, mares palpated under chemical restraint will often have less palpable tone to the reproductive tract due to smooth muscle relaxant effects of the sedative. Once palpation is completed, the ultrasound probe can be introduced into the mare's rectum.

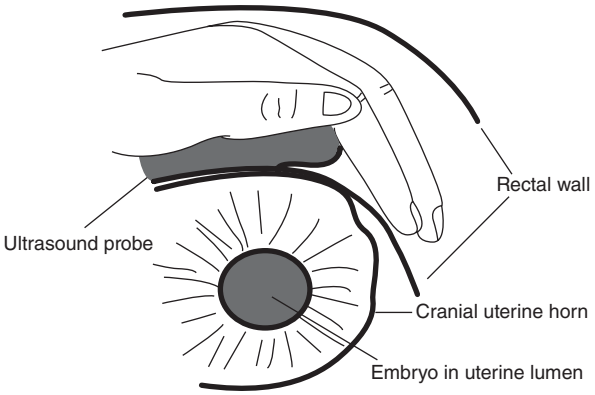


Figure 16.1 Probe cupped within the examiner's hand allowing palpation of the internal reproduction tract while controlling the probe at all times. The tips of the practitioner's fingers are free to gauge the rectal wall and "hook" the cranial aspect of the uterus facilitating complete imaging of the entire uterine lumen.

Imaging Technique

In most instances, it is standard practice to use a 5–10 MHz linear probe to perform transrectal reproductive ultrasonography in real time (B mode) [1,2]. All figures provided in this chapter were captured using a SonoSite M-Turbo® ultrasound system. Care should be taken to choose a probe that has smooth sides and rounded edges to protect the rectal wall during the course of the exam. The ample use of lubricant will help produce good contact between the probe surface and rectal wall with minimal pressure. The goal is a clear image without distorting the shape of, or possible damage to, the structures being examined (Figure 16.1). Scanning technique, instrument adjustment, and an understanding of the anatomic structures examined will provide the best image for interpretation [1]. It is helpful to position the ultrasound scanner close to the operator and at eye level to reduce body strain and facilitate viewing and adjustment of the image quality. Again, the mare must be properly restrained for safety and interpretation; excessive movement will interfere with image quality and could lead to misinterpretation of an image or inability to image the entire reproductive tract [1,2].

While well described in previous chapters, liquids (follicular fluid, yolk-sac fluid) do not reflect sound waves and produce a non-echogenic or anechoic, black image. In contrast, dense tissues (fetal bone) or an air interface reflect most of the sound beam producing a hyperechoic, white image. In addition to tissue density, the organization of the tissue results in characteristic patterns allowing identification of internal organs including the uterus and cervix. These patterns will vary depending on the reproductive status (estrus, diestrus, pregnancy) [4]. The early spherical equine embryo is mobile within the mare's uterus for the first 16 days of gestation allowing maternal recognition of pregnancy to occur. Fixation occurs at the base of a uterine horn around gestational day 17 [4]. Detection of an equine pregnancy prior to fixation requires the practitioner to thoroughly scan the entire uterine lumen for presence of embryonic vesicle(s).

The uterine body is imaged from cervix to apex in a longitudinal plane and each horn in a cross-section [4] (Figure 16.2). As the tip of each horn is visualized to its conclusion, each ovary should then be imaged noting the presence or absence and number of corpora lutea (CLs) present (Figure 16.3). The practitioner should develop a routine whereby they systematically and completely scan the uterus (Figure 16.4a). When imaging the cross-section of the horns it is important to center the round,

Vet-ebooks.com

cross-sectional image on the ultrasound screen noting the direction of orientation of the probe and the image. This helps the practitioner stay on the uterus and avoid skipping over a section of the uterine horn (Figure 16.4b). This is especially true at the bifurcation as the dependent weight of pregnancy can position the uterus ventrally at the base of the gravid horn making visualization difficult in early gestation. When scanning longitudinally along the uterine body, gently rotating the probe along the long-axis so that the image of the uterine body appears as thick as possible dorsal to ventral, helps image the lumen of the body completely. Lastly, carefully scanning the cervix and vagina and noting the bladder as the probe is withdrawn from the rectum completes the examination and will highlight the presence of urovagina or pneumovagina.

Early Embryonic Imaging

The normal equine pregnancy develops in a predictable sequence in regards to size and development of visible structures through the embryonic stage (< 40 days) and throughout the fetal period [4]. There is no significant difference in the size of the conceptus between pony mares and horses in the first 40 days of pregnancy development; however, fixation occurs earlier at day 15 in the pony mare than the horse at days 16

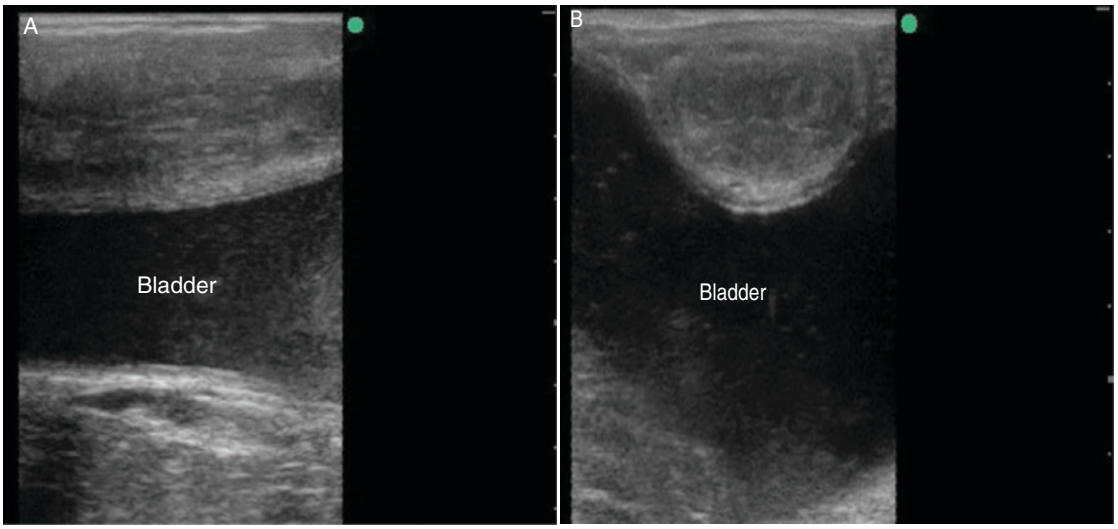


Figure 16.2 (A) Longitudinal view of the uterine body sitting dorsal to the bladder. (B) Cross-section of the uterine horn sitting dorsal to the distended bladder.

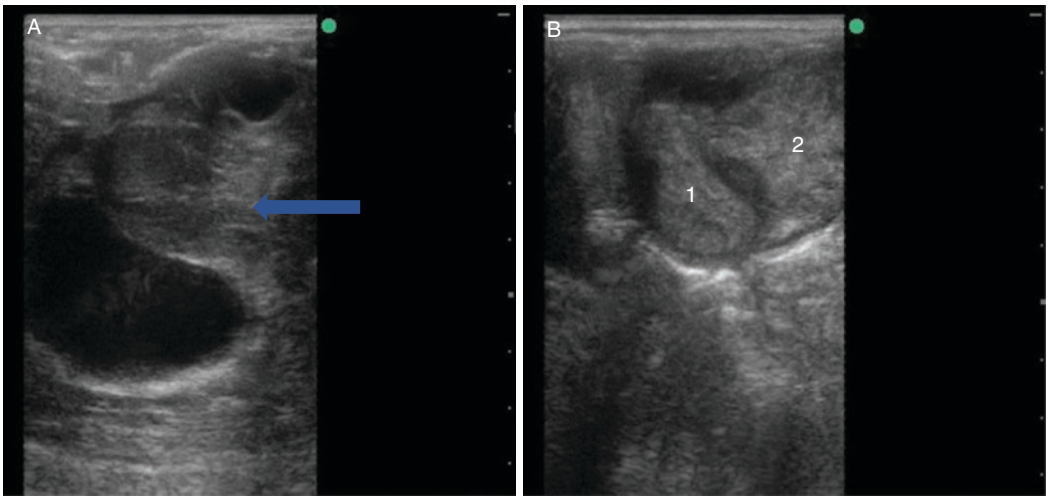


Figure 16.3 (A) A single corpus luteum (arrow) appears as a homogenous structure next to an anechoic, fluid-filled follicle on the ovary. (B) An early pregnancy ultrasonography examination with two distinct corpa lutea on one ovary alerting the practitioner to the possibility of twin pregnancy as he/she completes the examination of the uterine horns and body.

Vet-ebooks.com

to 17 [5,6]. While being gentle and non-disruptive to the developing pregnancy, it is good technique to carefully scan through the entire embryonic vesicle and piece together a three-dimensional image in the mind's eye of what is presented on the screen (Figure 16.5). Ideally, the practitioner will already have performed transrectal ultrasonography on the mare and made note of any abnormalities such as uterine cysts that are of similar size to a developing embryonic vesicle (Figure 16.6).

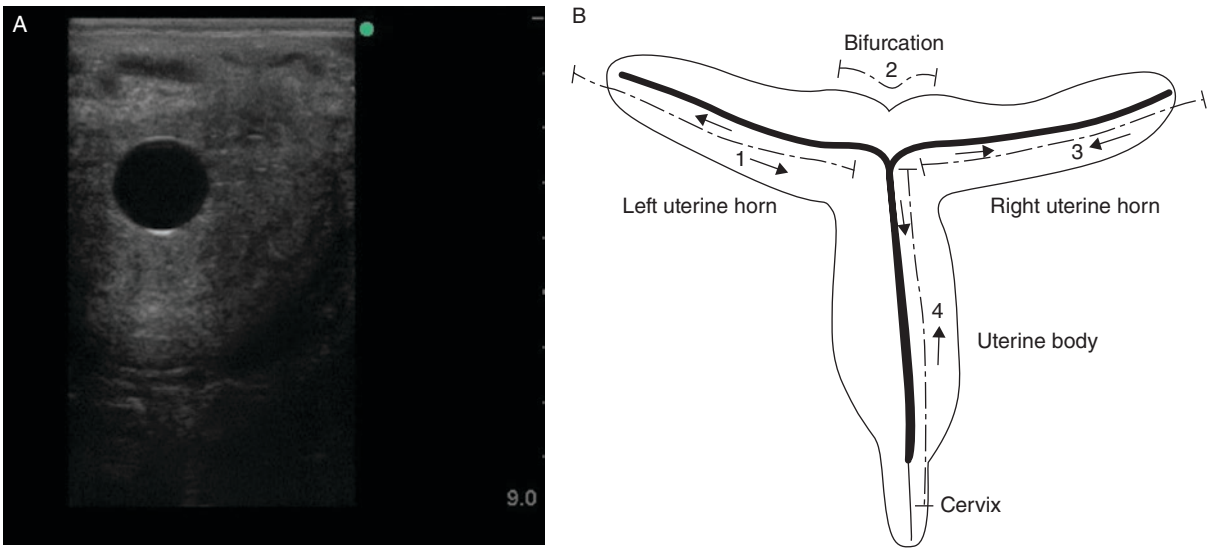


Figure 16.4 (A) Cross-sectional ultrasonography of cranial aspect of the uterine horn. A 15-mm vesicle is present at the tip of the uterine horn. A technique for completely evaluating the uterus is important as the early pregnancy is motile and can be imaged throughout the entire uterine lumen from days 10 to 16 post-ovulation. (B) A technique for completely evaluating the entire uterus is described. As the bifurcation of the uterus is an easily palpable point of orientation: 1) ultrasonography begins at the base of one horned out to its tip, back down to the horn base; 2) thoroughly through the bifurcation from the base of one horn to the other; 3) from the base of the opposing horn out to the horn tip and back down again to the base of the horn and bifurcation; and 4) from the bifurcation and apex of the uterine body moving caudally through the uterine body back to the cervix. Longitudinal ultrasonography of the uterine body should be done slowly and methodically to visualize the entire lumen of the uterine body.

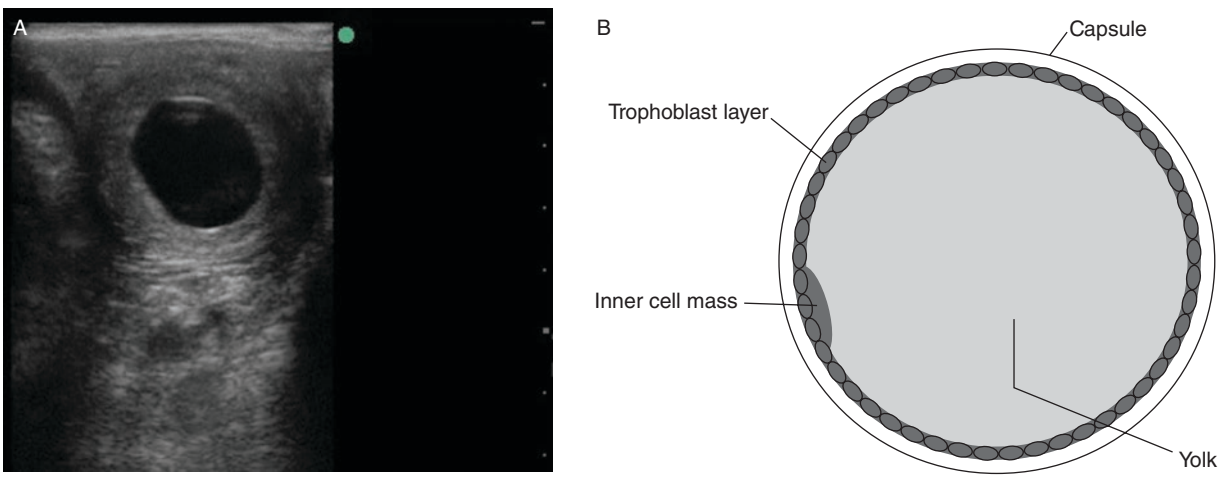


Figure 16.5 (A) Ultrasonography of the uterine horn containing the developing embryonic vesicle. The yolk sac is anechoic surrounded by the gray soft tissue density of the uterine wall. The spherical vesicle is positioned centrally within the uterine lumen; the toned uterine lumen "expands" immediately around the embryo accommodating its size while remaining in visual apposition immediately in front of and behind the embryo(s). While the early developing embryo is visualized as a simple growing anechoic sphere on ultrasonography, cellular differentiation is rapidly occurring. (B) During embryonic development (day 12) the embryonic vesicle is composed of a spherical layer of trophoblast cells (ectoderm) and endoderm. The capsule protects the embryo and helps the developing vesicle maintain a spherical shape around its yolk sac. By day 14, as seen in Figure 16.5A, a mesodermal layer is added with a specialized embryonic disc region expanded against the glycoprotein capsule [5].

Vet-ebooks.com

Days 9 to 16

Although the developing embryo enters into the uterus between days 5 and 6 post-ovulation [4], it is not possible to identify a developing embryonic vesicle via ultrasonography until days 9 or 10 post-ovulation when sufficient yolk sac fluid has developed. By day 12, the vesicle reaches ~ 8 mm in size, growing 1.5 mm/day [4] (Figure 16.7). The stage of early diagnosis is dependent on practitioner skill and the quality of image and machinery available. Some practitioners may choose to delay early pregnancy detection until day 14 when the conceptus is 14 to 18 mm in diameter and growing at a faster rate (3.5 mm/day) (Figure 16.8a). There is often a characteristic specular reflection, visible as lines of bright echogenicity dorsally and ventrally when visualizing an embryonic vesicle (Figure 16.8b). This is an artifact formed from the spherical shape and can help differentiate the pregnancy from slightly irregular uterine cysts [2,4] (Figure 16.9). The image of the pregnant mare uterus at this stage will be consistent with a normal, non-pregnant diestrus mare. Uterine and cervical tone should be palpably increased and no endometrial edema or free uterine fluid visible. One or more ovulatory CLs should be identifiable on one or both ovaries and the follicle sizes will vary. [Video 1 shows ultrasonography of the non-pregnant mare in diestrus. Small follicles are visualized on the left ovary, a corpus luteum on the right ovary, and a normal uterus with no endometrial edema or pathology seen.]

Days 17 to 20

By day 16 to day 17, the embryonic vesicle is fixed at the base of either uterine horn and measures

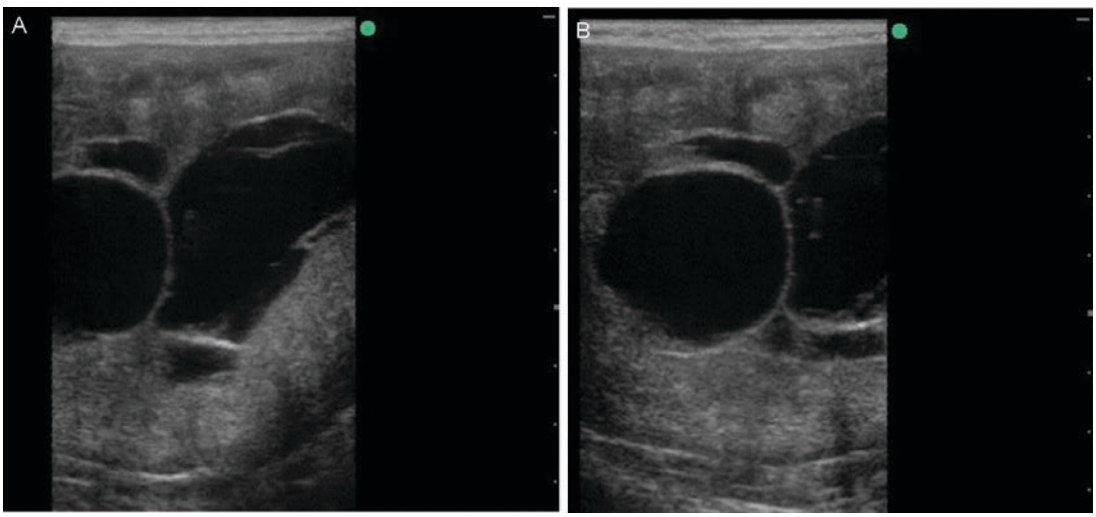


Figure 16.6 (A) A large cluster of uterine cysts visible at the uterine bifurcation. (B) A 23-mm embryonic vesicle is located adjacent to the cluster of cysts. The embryonic vesicle imaged is spherical and of appropriate size for the stage of gestation. If the practitioner is familiar with the mare or has previously mapped the cysts, this is enough to confirm the mare is pregnant. If in doubt, a repeat ultrasonography examination in 1 to 3 days to confirm growth or change in location of the developing vesicle is warranted.

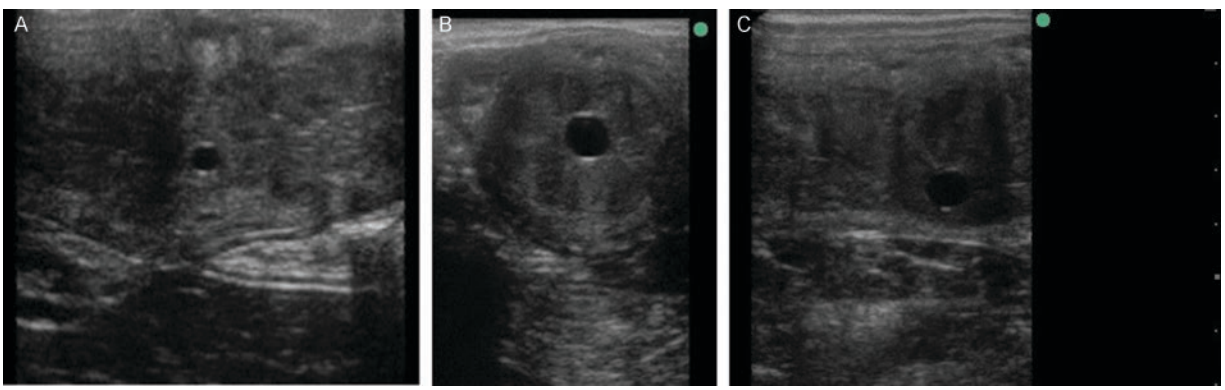


Figure 16.7 (A) 5.5-mm 11-day embryonic vesicle in the uterine body. (B) 8-mm 12-day embryonic vesicle in the uterine horn. (C) 8-mm 12-day embryonic vesicle visualized in the uterine body. Markers to the right of the image are in 1-cm increments.

Vet-ebooks.com

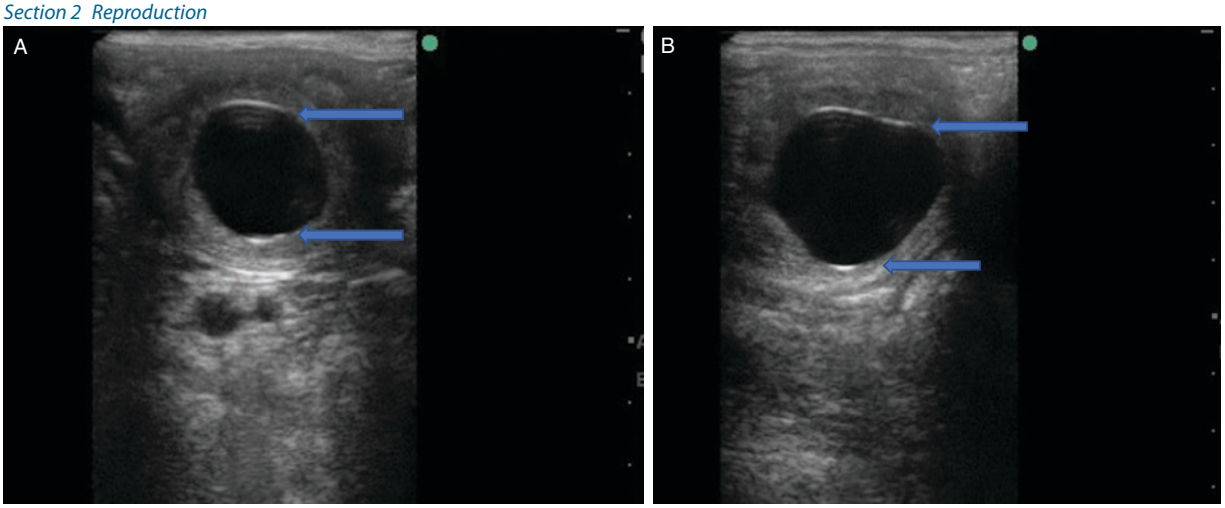


Figure 16.8 (A) 14-day embryonic vesicle in the uterine horn. The uterine wall remains toned and in visual apposition surrounding the embryo. The characteristic specular reflection is seen dorsally and ventrally on the circumference of the embryo (arrows). (B) 15-day embryonic vesicle in the uterine horn. The toned uterine lumen accommodates the moving embryonic vesicle. As the vesicle remains spherical in shape, specular reflections are still visible (arrows), although the image appears irregular due to pressure exerted dorsally on the uterus during ultrasonography.

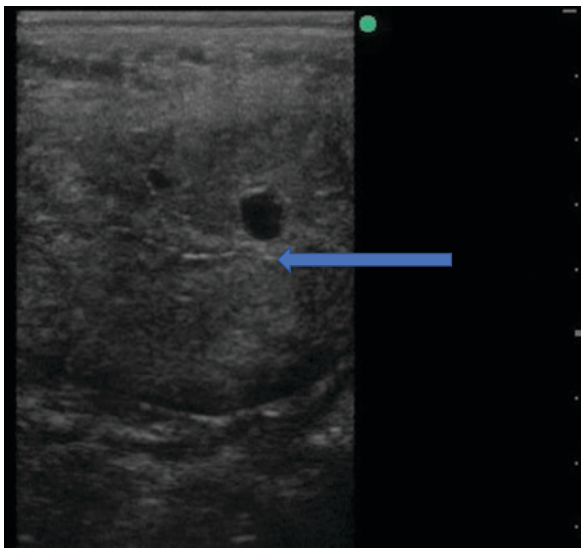


Figure 16.9 Two small uterine cysts visualized during an early ultrasonography examination. While both cysts are anechoic, the slight irregular shape and location off-center of the uterine lumen (white line at the arrow) confirm a cystic structure. [Video 4 – ultrasonography of a mare with a corpus luteum on each ovary, a single 14-day vesicle, and multiple small endometrial cysts].

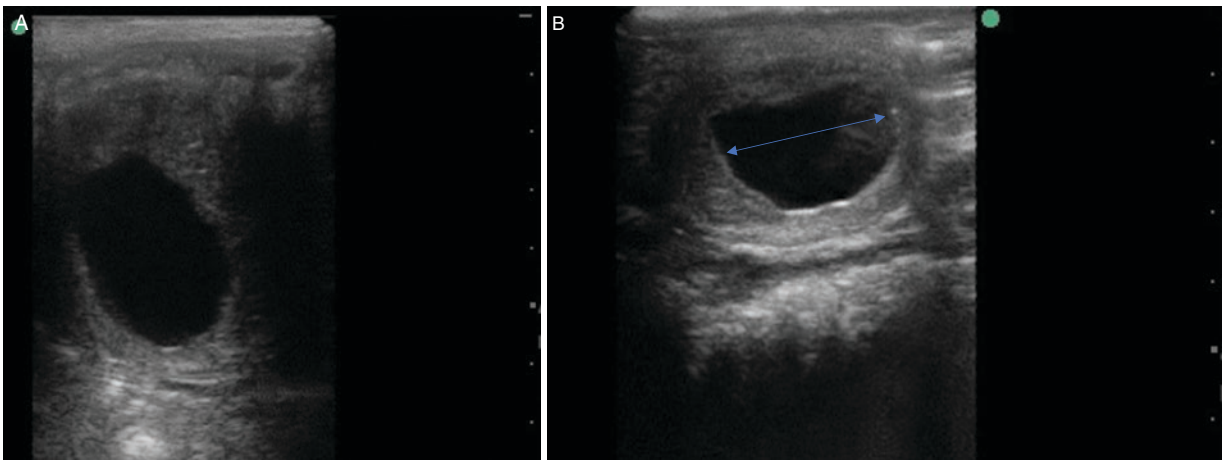


Figure 16.10 (A and B) 17-day vesicle. The fluid-filled embryo takes on an irregular contour after losing its capsule. It also begins to expand longitudinally to form an ovoid shape. The vesicle continues to grow but at a decreased rate. The practitioner can appreciate this growth by measuring the vesicle distally along the horn from the base (B).

Vet-ebooks.com

approximately 25 mm in size with a slightly ovoid shape (Figure 16.10). Between approximately day 18 and day 20, the embryo loses its spherical structure allowing the trophoblast cells, that form the chorionic surface of the placenta, to conform to the irregular surface of the surrounding endometrium (Figure 16.11). Normal embryonic vesicles become orientated allowing the embryonic disc to position adjacent the ventral surface of the uterine lumen [4]. The presence of a slight edema pattern surrounding the vesicle is normal in the author's experience; the corpus luteum should still be visible with distinctive uterine tone palpable (Figure 16.12). A widespread edema pattern may be an indicator of early embryonic loss [4,6] (Figure 16.13).

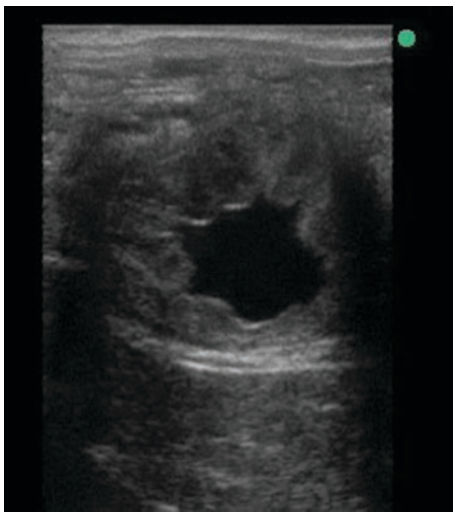


Figure 16.11 A 18-day embryonic vesicle. At this time, it is easy to visualize the irregular shape of the vesicle as it comes into apposition with the irregular contour of the endometrium.

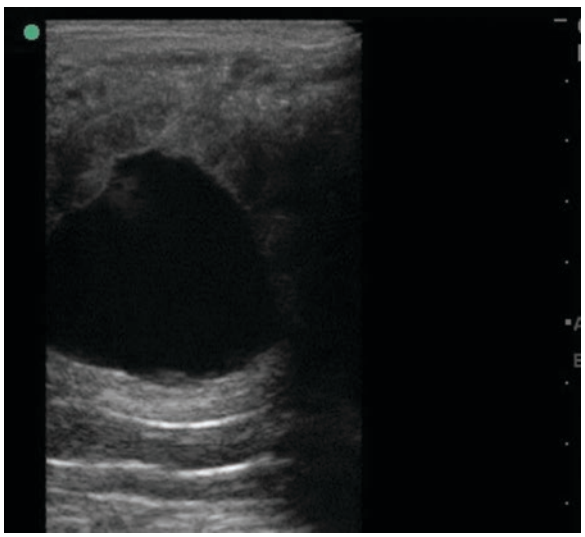


Figure 16.12 20-day embryonic vesicle. Practitioners may note mild endometrial edema directly surrounding the developing pregnancy. In the author's experience, this is considered a normal variation and is more pronounced when using higher-quality ultrasonography.

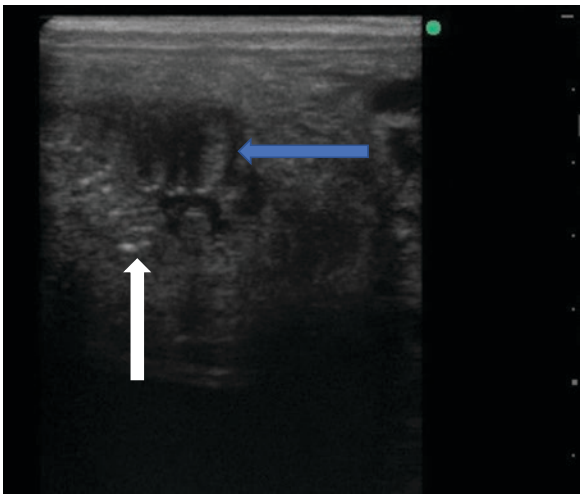


Figure 16.13 Presence of intrauterine fluid, air, or excessive endometrial edema surrounding the pregnancy or throughout the uterus in the pregnant mare is not a normal variation but indicative of uterine pathology that could result in embryonic loss if not appropriately treated. A resorbing pregnancy is seen above with increased uterine edema (blue arrow) and hyperechoic flecks of intrauterine air (white arrow) visualized. [Video 5 shows a 14-day vesicle floating in a small amount of intrauterine fluid.] [Video 6 shows a 14-day vesicle floating in cloudy intrauterine fluid with excessive uterine edema.] [Video 7 – early embryonic death with resorption of the vesicle].

Days 21 to 28

On or about days 21 to 23, the developing allantoic cavity first becomes visible as it emerges from the hindgut of the embryo proper [4] (Figure 16.14). Over the course of the next eight days, the allantoic cavity enlarges and moves the embryo proper progressively dorsally through the embryonic vesicle (Figure 16.15). Also, during this period, the embryo proper has increased in size and a detectable heartbeat has developed. These features make this gestational age a common landmark for monitoring the development and viability of the pregnancy. Color-Doppler flow imaging can be utilized to confirm the presence of a heartbeat from this stage forward, while the heartbeat becomes more pronounced and more readily detectable as the embryo proper increases in size [2] (Figure 16.16).

Days 30 to 40

From day 30 to day 35, the embryo proper continues its dorsal migration through the embryonic

Vet-ebooks.com

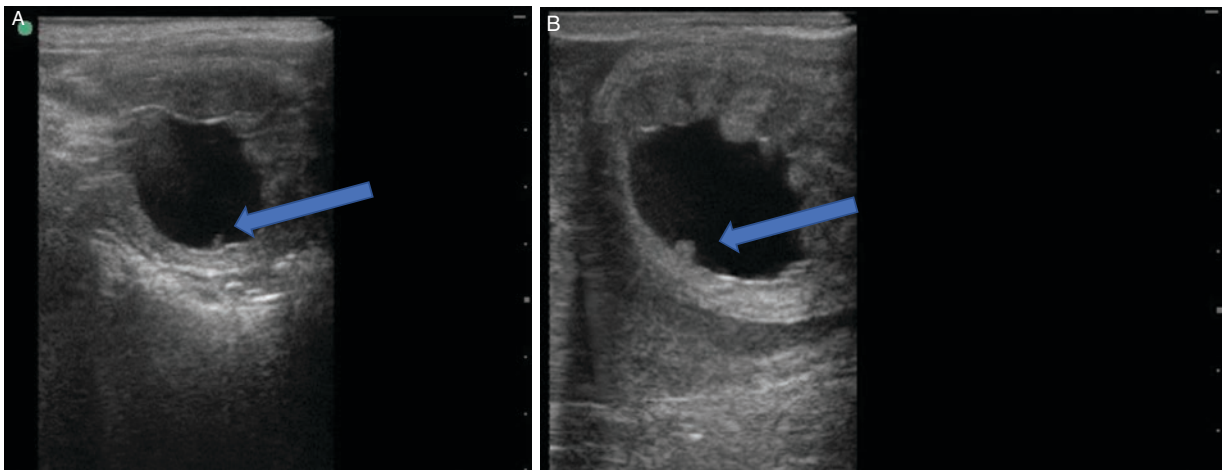


Figure 16.14 (A) 20–21-day embryo. The embryo proper first becomes visible as a small, ventral, echogenic projection (arrow) into the fluid-filled embryonic vesicle. (B) The embryo proper can be visualized as early as days 19 to 20 with experience but is reliably seen by the practitioner at day 21 (arrow).

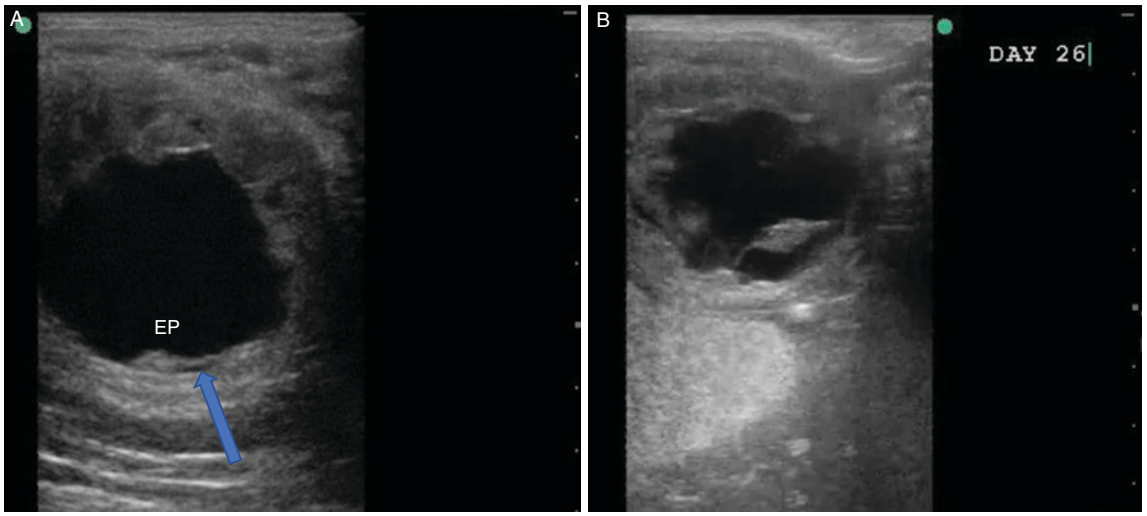


Figure 16.15 (A) The allantoic cavity (arrow) is first visualized ventral to the embryo proper (EP) in the normally positioned pregnancy, day 23. The allantoic fluid is anechoic and differentiated from the yolk sac only by the developing allantoic membrane. (B) As the allantoic cavity enlarges and the yolk sac decreases in size, the embryo proper moves dorsally within the vesicle.

vesicle until it is almost resting against the dorsal wall, with a small yolk sac still visible dorsally (Figure 16.17). True implantation of the embryo does not begin to occur until later in equine gestation, days 32 to 38 [4]. Beginning on about day 35, trophoblast cells migrate from the chorionic girdle region of the embryonic vesicle to invade the endometrium and form the endometrial cups. Once the endometrial cups form, they will remain functional through a variable lifespan (days 35–120 +) whether or not the developing embryo/fetus remains viable [4]. Production of the hormone, equine chorionic gonadotropin (eCG), by the formed endometrial cups stimulates the development of secondary CLs on both ovaries (Figure 16.18). The endometrial cups themselves are not normally discernible within the endometrium on routine ultrasonography. Mineralized structures in non-pregnant mares with retained endometrial cups may be visible at the base of a previously pregnant horn in rare instances of endometrial cup retention.

Early Fetal Imaging: Days 40 to 60

By day 40 the fetus is dorsal within the allantoic cavity with the majority of the yolk sac absorbed and circumferentially enclosed by the allantoic membranes (Figure 16.19). Between days 45 and 50 the umbilical cord lengthens and the fetus begins a ventral descent

Vet-ebooks.com

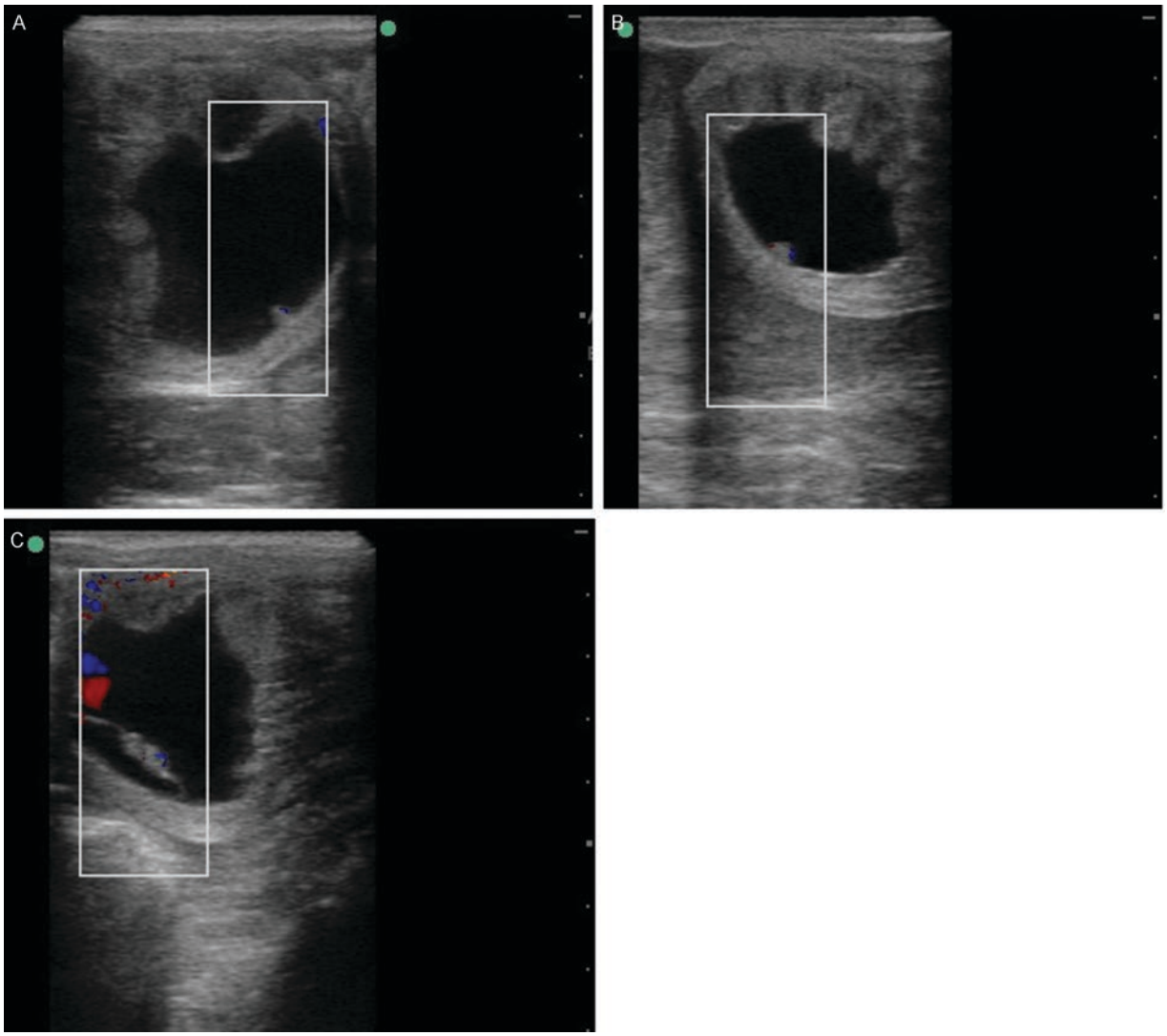


Figure 16.16 (A and B) Color-doppler flow ultrasonography confirming a viable heartbeat in a 21-day and 22-day embryo proper. (C) A 25-day embryo proper with readily detectable heartbeat using color-doppler flow imaging.

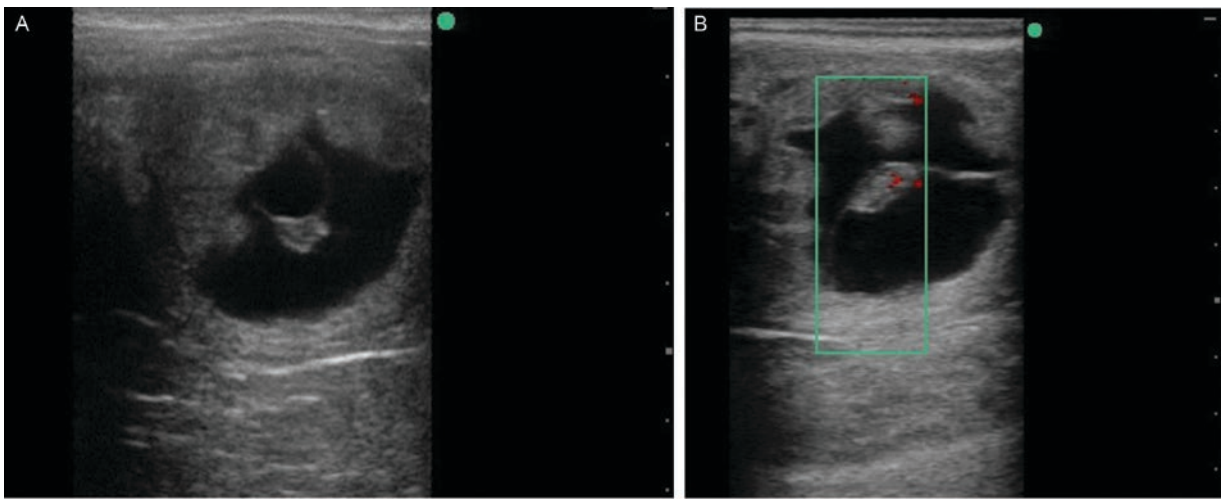


Figure 16.17 (A) 29-day developing embryo. (B) 32-day developing embryonic vesicle with heartbeat. It should be noted that this pregnancy was abnormal with the embryo proper positioned dorsally on early ultrasonography. It remained viable throughout all subsequent examinations; a live healthy foal was born at term.

Vet-ebooks.com

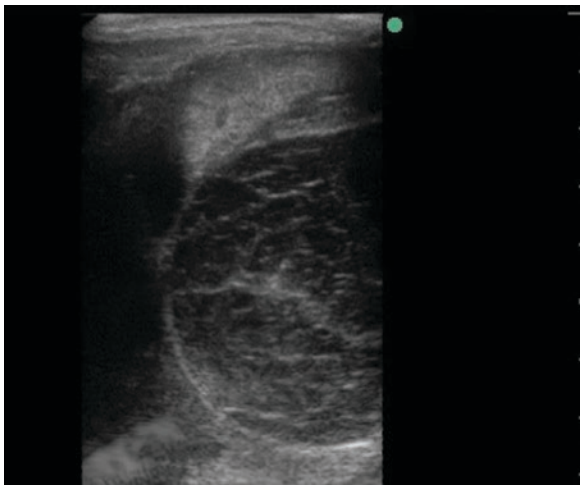


Figure 16.18 Accessory corpora lutea on the ovary. Production of equine chorionic gonadotropin (eCG) (pregnant mare serum gonadotropin (PMSG)) by the endometrial cups stimulated the development of secondary/accessory CLs on both ovaries. In the image above, the primary CL is noted dorsal to the accessory CL, which is similar to a hemorrhagic follicle in appearance. [Video 8 – multiple accessory CLs on each ovary in the pregnant mare.].

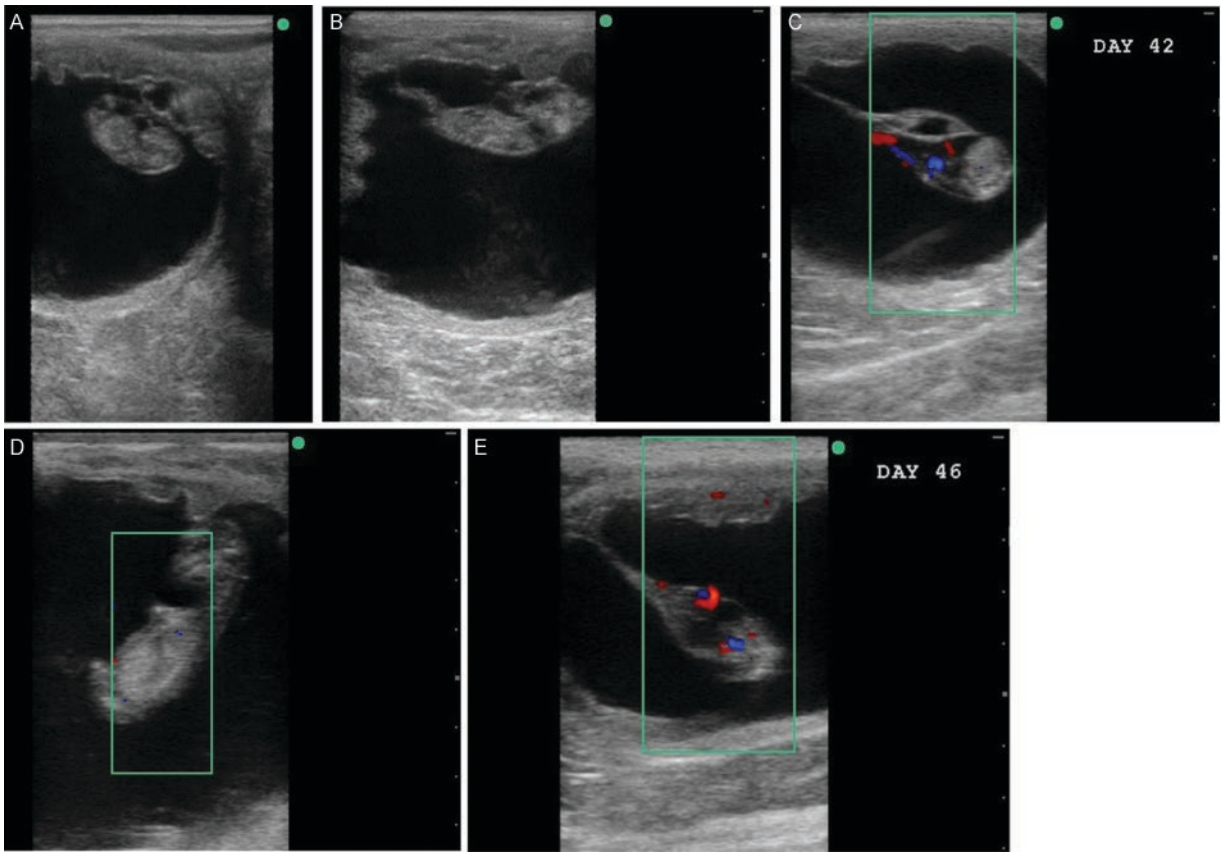


Figure 16.19 (A) Day 40 fetus located dorsally within the allantoic cavity. The umbilical cord is beginning to form as the allantoic membrane encloses around the remaining yolk sac. (B) 42-day fetus. (C) Cross-sectional view of a 42-day fetus. Fetal heartbeat along with umbilical blood flow (arrow) is highlighted by color-doppler ultrasonography and is helpful when the thoracic cavity cannot be easily imaged. (D) 45-day fetus. (E) 46-day fetus. The majority of the fluid seen is allantoic fluid (AL) and extends beyond the base of the uterine horn and into the cranial body of the uterus.

Vet-ebooks.com

through the allantoic cavity, suspended by the umbilical cord (Figure 16.20). The envelopment of the yolk sac by the allantochorion placenta is almost complete. The yolk sac may be visible as a small anechoic structure within the umbilical cord [4] (Figure 16.21). By day 60 of gestation the fetus has come to rest once again against the ventral surface of uterine horn, with multiple features of the developing fetus easily discernible [4] (Figures 16.22 and 16.24). Spontaneous fetal movement, in addition to an identifiable heartbeat, confirms fetal viability at the time of examination (Figure 16.23) [Video 2]. The chorioallantoic membranes continue to expand and become readily apparent from the gravid horn and into the bifurcation of the uterus by 60 days gestation. Fetal movements likewise develop on a characteristic time line and have been previously described as the development of a head nod by day 40, whole body motion by day 45, limb motion after day 45, body raises by day 50, and fetal mobility by day 55. As the fetus ages the frequency and duration of spontaneous fetal movement also increases [7]. Understanding the normal timeline of embryonic, fetal, and placental development makes it possible to evaluate appropriate development relative to a known ovulation date, or to estimate gestational age of a pregnancy when an ovulation date is unknown. In the majority of successful pregnancies, the

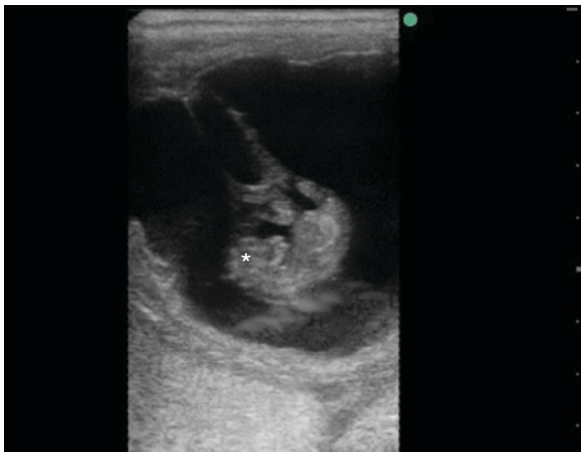


Figure 16.20 Day 48 fetus descending into the allantoic cavity following elongation of the umbilical cord. A fetal head (*) is easily discernible from the body and developing hind limb in the image above.

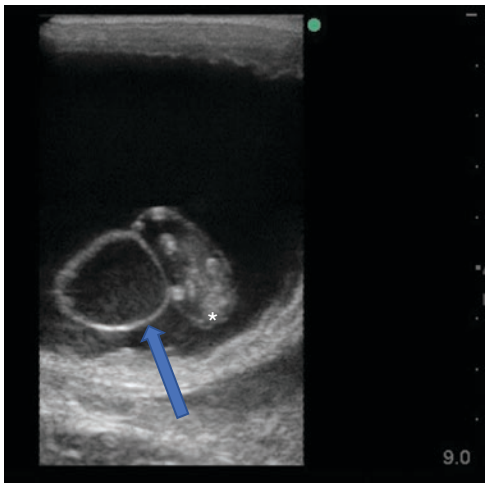


Figure 16.21 Day 50 fetus. An umbilical dilation (yolk sac remnant) (arrow) is noted adjacent to the fetus. The fetus is positioned to visualize the ventral abdomen with the head tucking into the chest (*) and all four limbs exposed.

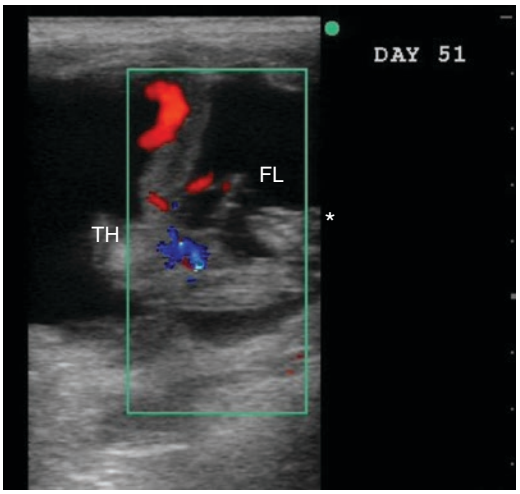


Figure 16.22 Day 51 fetus descending ventrally in the allantoic space. The fetal head, eye (*) are distinct along with the neck, an outstretched front limb (FL), and tailhead (TH). Color-doppler ultrasonography highlights the thorax and viable heartbeat along with blood flow through the umbilical structures.

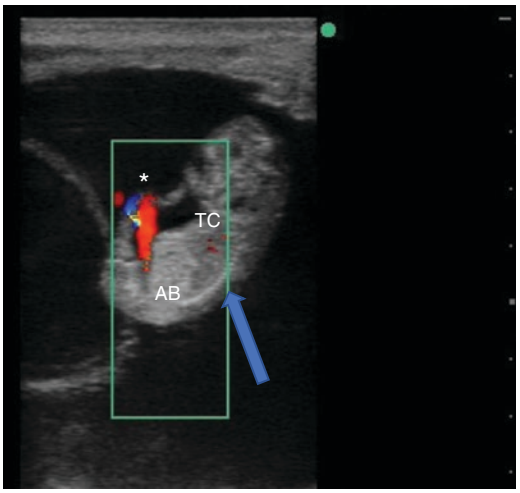


Figure 16.23 Fetal viability confirmed using color-flow ultrasonography. The fetus is laying dorsoventrally with spinal bones providing an easy orientation point (arrow). The thoracic cavity (TC) and abdomen (AB) are easily differentiated. Blood flow is highlight through both the heart and umbilical vasculature (*).

Vet-ebooks.com

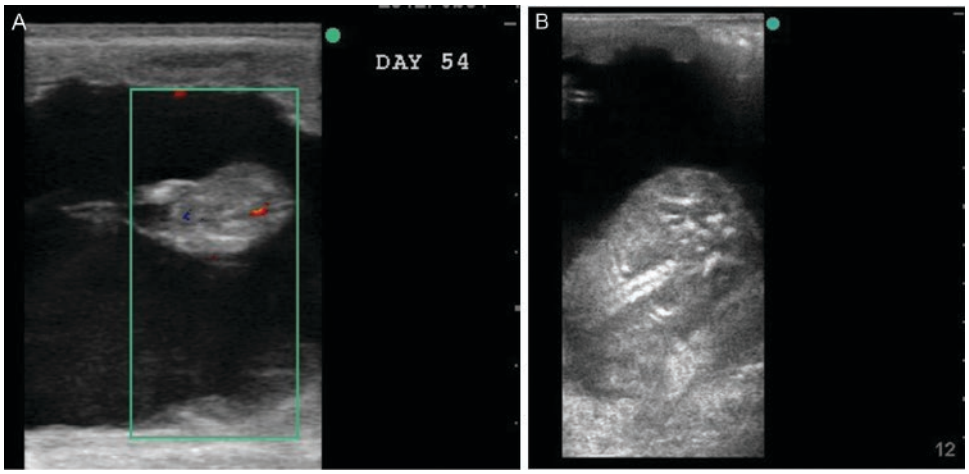


Figure 16.24 (A) Cross-sectional image of the transversely positioned fetus. Both hind limbs are visualized along with blood flow through the fetal aorta. (B) 60-day fetus laying ventrally on the base of the uterine horn within the allantoic space. The hyperechoic fetal spine, rib, and pelvic bones are easily visualized.

landmarks of development are reliable, constant, and a key feature when interpreting the ultrasonography images produced by the examination.

Pregnancy Failure

Most practitioners elect to perform multiple pregnancy exams of the normal pregnant mare during the first 60 days of gestation. At each examination, the uterus is thoroughly imaged and an assessment of pregnancy development recorded. The schedule, based on client and practitioner preference, is set up enabling early identification and management of twin pregnancy along with detection of any abnormalities. The ability to identify anomalies early allows management or the initiation of an appropriate therapy in the attempt to maintain pregnancy. Early pregnancy examination is generally performed on day 14 to 15 post-ovulation for initial pregnancy diagnosis. In the instance of embryo transfer, the recipient mare may be initially examined at day 12 (5 days post transfer) to ensure the presence of an adequate corpus luteum, uterine tone, and lack of edema to support pregnancy maintenance. If any aberrations (no vesicle seen, smaller than expected vesicle, potential for multiple pregnancies) are noted during the early pregnancy scan, mares should be re-examined at intervals of 1 to 3 days to monitor growth or demise of the developing vesicle or to confirm a negative pregnancy status (Figure 16.25). Normal early pregnant mares would be scheduled forward for ultrasonography at days 25 to 28 post-ovulation to confirm presence of a fetal heartbeat. Ultrasonography at days 33 to 35 post-ovulation is important as failure of normal development or noted loss of pregnancy allows termination and re-breeding prior to endometrial cup formation (Figure 16.26). The final examination is performed between day 45 and 60 post-ovulation. Presence of secondary corpora lutea can be monitored along with fetal wellbeing; furthermore, many stud farms required certification of pregnancy at 45 days gestation. Periodic examinations beyond day 45 help to identify mares that fail to maintain a viable pregnancy despite endometrial cup formation, and may offer insight into reasons for pregnancy failure at these later dates. More frequent ultrasonography examinations may be useful

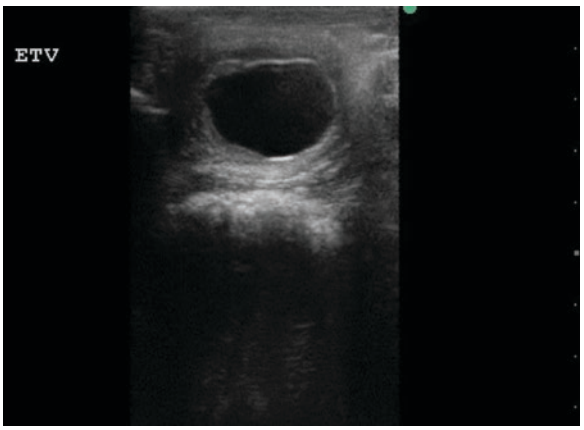


Figure 16.25 24-day non-viable, empty trophoblastic vesicle (ETV). The trophoblast layer of the developing embryo is present, and the yolk sac remains allowing the look of a normally developing vesicle that will halt in development with lack of an embryo proper seen at any stage. Resorption of the pregnancy may occur in some instances. However, in the author's experience, prostaglandin is utilized following repeat ultrasonography in 1 to 3 days to confirm ETV and not a viable embryonic vesicle that is delayed in development.

Vet-ebooks.com

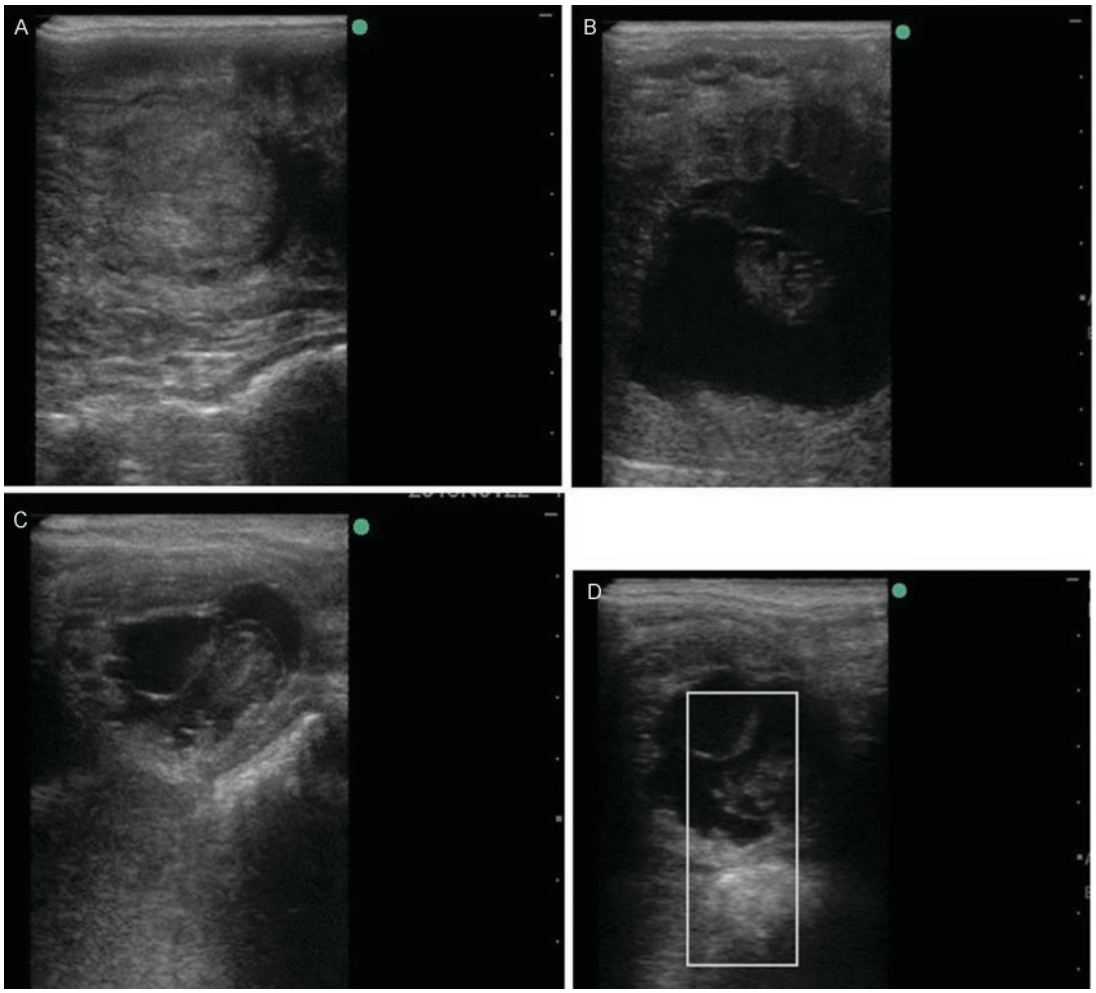


Figure 16.26 Non-viable pregnancies seen between 33 to 39 days gestation. (A) 33-day resorbing vesicle with fetal component remaining in a mass-like structure in the cranial body of the uterus. (B) 38-day pregnancy with no detectable heartbeat. (C) Same pregnancy on repeat ultrasonography day 40; allantoic fluid resorption is noted. (D) 39-day pregnancy with no detectable heartbeat confirmed using color-doppler flow ultrasonography. [Video 9 – non-viable pregnancy. No detectable heartbeat; cloudy allantoic fluid noted ventral to fetus.].

to the practitioner when managing mares that are being supplemented with altrenogest, exogenous progesterone. or other treatments necessary for pregnancy maintenance.

Pregnancy loss prior to day 40 has been reported to occur in 10–15% of equine pregnancies overall [8]. Incidence of abnormal embryonic development characterized by presence of an embryonic vesicle without an embryo proper (empty trophoblastic vesicle) is reported at less than 5% of overall pregnancies in one study but was significantly higher for mares with abnormal conceptuses noted during early pregnancy examination [9]. Another study reported incidence of 10–15% in the young mare and 20–30% in the aged mare [10]. Embryos that "fix" in locations other than the base of a uterine horn (i.e., uterine body) may also represent an increased risk of loss. Not every pregnancy between days 0 and 60 that varies in its development from the expected progression is doomed to fail, and it is sometimes important to watch and be patient. Many pregnancies that start out small for gestational age or behind in the expected development will "catch up" in their development and go on to successfully produce normal, viable foals at term. An embryo that has a heartbeat but with an otherwise small allantoic vesicle size often survives, the pregnancy is normally maintained and results in birth of a healthy foal. On the contrary, the earlier a failure can be discovered, the better chance of terminating early and reducing the time lost in establishing a new viable pregnancy [10].

Ultrasound findings indicative of possible impending embryonic loss include an embryo that is small

Vet-ebooks.com

for its gestational age, an embryo that fails to increase in size or progress in development, failure of an embryonic vesicle to develop a visible embryo proper, embryo in improper alignment relative to the ventral surface of the vesicle, failure of an embryo to develop a heartbeat at the expected time, or loss of a previously detected heartbeat [4,9,11] (Figure 16.27). Examinations that fail to identify an embryo at days 14 and 15 can be followed by examinations even as late as day 18 that reveal a mare that has failed to return to estrus and now has an identifiable embryo. Likewise, it is therefore sensible in many instances to perform serial examinations over the course of several days to be sure that an embryo is truly absent prior to administering prostaglandin. The lack of identification of an embryo proper as early as day 20 post-ovulation and onward is associated with a high embryo loss rate [10].

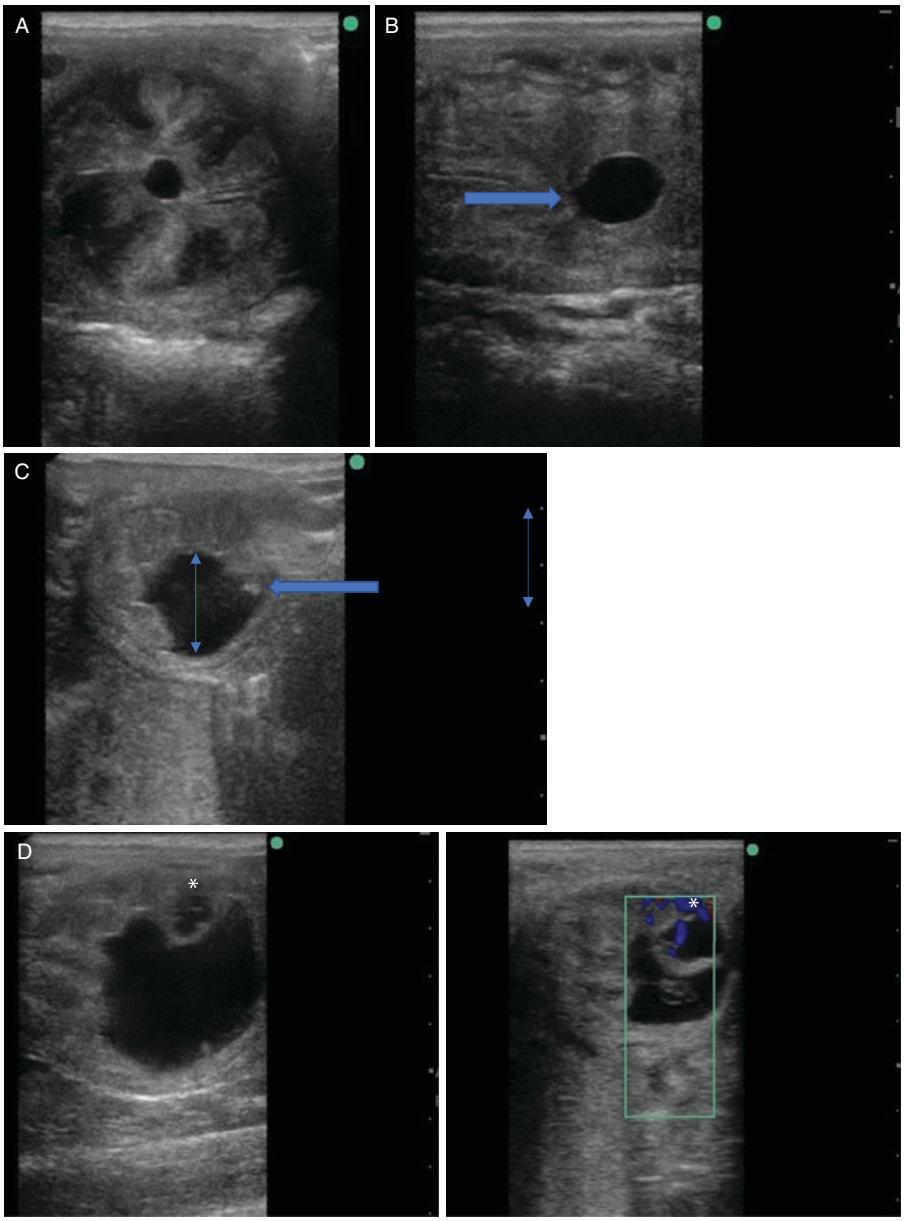


Figure 16.27 (A) Excessive, widespread uterine edema surrounding a day 13 embryonic vesicle. The finding of abnormal endometrial edema may represent inflammation and/or failure of luteal function. Pregnancy loss and return to estrus are imminent if left untreated. (B) 14-day embryonic vesicle within a small amount of fluid (arrow). (C) 21-day embryonic vesicle measuring only 12 mm. An embryo proper can be visualized (arrow) but is located along the dorsal aspect of the vesicle. Markers to the right of the image are in 1-cm increments. (D) The left image shows a 21-day embryonic vesicle, endometrial cyst (*) seen dorsally, adjacent to the vesicle. The right image depicts the non-viable pregnancy at 35 days with resorbing allantoic space and no detectable heartbeat seen.

Vet-ebooks.com

Distinguishing Endometrial Cysts from Developing Embryos

The presence of endometrial cysts in a mare's uterus can complicate accurate pregnancy detection [12]. While glandular endometrial cysts are typically microscopic, lymphatic cysts can range in size from 10 mm to several centimeters in diameter [13]. Like the early equine embryo, endometrial cysts appear as fluid-filled structures within the lumen of the endometrium. In general, cysts do not appear as perfectly round structures and are usually "off center" relative to the uterine lumen, extending partially if not fully into the wall of the endometrium on the ultrasound image (Figure 16.28). Likewise, cysts do not usually appear to increase in diameter over the course of several days, although sometimes cysts do prove to be somewhat dynamic and increase in size on ultrasonography relative to estrus and diestrus. Importantly, cysts do not move like an early embryonic vesicle. Mapping or documenting the location of endometrial cysts can help the practitioner distinguish an early positive pregnancy.

Many times, however, a practitioner is presented with a mare for pregnancy examination that he or she did not manage through the breeding or may not have accurate breeding dates. If the presented mare also has unfamiliar and/or undocumented

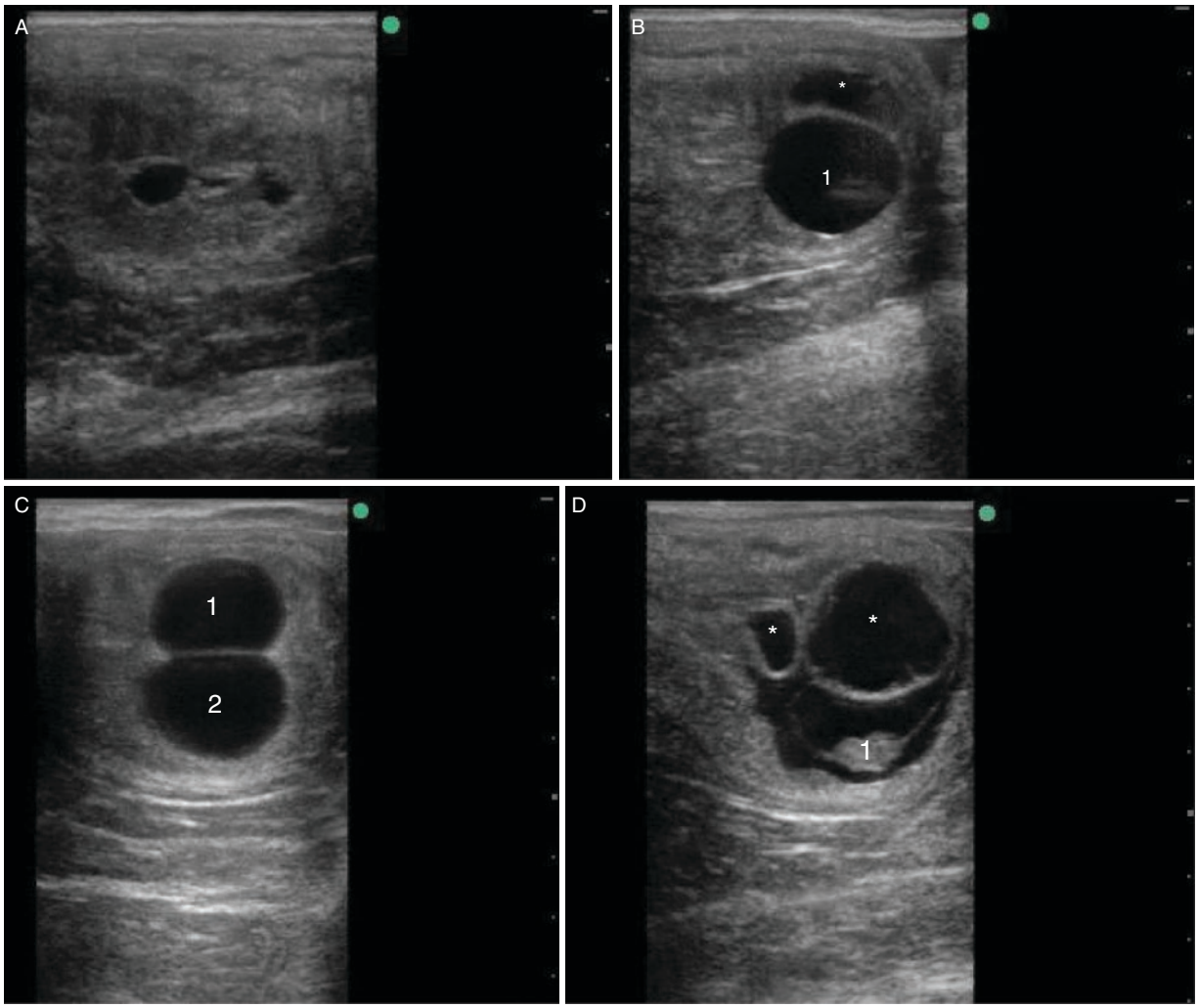


Figure 16.28 (A) Two small cysts located central within the lumen of the uterine body. While the smaller cyst to the right is notably irregular, the more spherical structure to the left could be mistaken for an embryonic vesicle. Mapping cysts is useful when a mare has an endometrial cyst that resembles an early embryo that can be confused as a twin pregnancy. (B) 14-day embryonic vesicle and cyst (*). (C) 14-day twin embryonic vesicles. In some mares, the presence of numerous or multiloculated cystic structures, even when known and thoroughly documented, may make it impossible to be sure of the presence of an embryo until a heartbeat can be definitively detected (D). This is especially problematic when multiple CLs are noted on ultrasonography or when asynchronous ovulations are probable. [Video 10 – asynchronous twin embryos with multiple endometrial cysts.].

Vet-ebooks.com

endometrial cysts, this can make accurate diagnosis of an early embryo or the presence of multiple embryos challenging [Video 3 shows a 15-day vesicle, single CL amid multiple endometrial cysts]. In such instances, it may become necessary and prudent to follow the mare over the course of multiple examinations.

Conclusion

As in all effective reproductive management, accurate and thorough record-keeping will greatly aid the practitioner in identifying and interpreting the images that appear on the ultrasound screen during the course of pregnancy examinations during the first 60 days of gestation. Thorough and gentle examination techniques provide for efficient examinations that can be accomplished in a minimal amount of time with little discomfort to the mare and little risk to the developing pregnancy.

Acknowledgments

This chapter is an expansion of the original chapter produced by Christine Schweizer in the first edition.

The author would like to further thank Dr Angus O. McKinnon for contributing images to this chapter.

Video Links

1) https://youtu.be/EZMTaPXdvX4
2) https://youtu.be/Tt5zGmxPvTQ
3) https://youtu.be/vlRIjgdaZe8
4) https://youtu.be/IDuq-85GiE0
5) https://youtu.be/BtDBMyvySgE
6) https://youtu.be/MRfMZSxvnEk
7) https://youtu.be/2qFOgwiREvw
8) https://youtu.be/x1MHq0OzjKI
9) https://youtu.be/UftSHUP1Spg
10) https://youtu.be/V476RbKvDrQ

References

1 Pierson, R.A., Kastelic, J.P., and Ginther, O.J. (1988). Basic principles and techniques for transrectal ultrasonography in cattle and horses. *Theriogenology* 29(1): 1–20.

2 Pycock, J.F. (2011). Ultrasonography. In: *Equine Reproduction*, 2nd edn (ed. A.O. McKinnon, E.L. Squires, W.E. Vaala, et al.), 1914–1921. Oxford: Wiley Blackwell.

3 Kannegieter, N. and Collins, C. (2010). Keeping liability risks low for equine practitioners: Rectal tears. *Australian Veterinary Journal* 88(12): N10–11.

4 Pycock, J.F. (2007). Pregnancy diagnosis in the mare. In: *Current Therapy in Equine Reproduction* (ed. J.C. Samper, J.F. Pycock, and A.O. McKinnon), 335–342. St Louis: Saunders Elsevier.

5 Bergfelt, D.R. and Ginther, O.J. (1996). Ovarian, uterine and embryo dynamics in horses versus ponies. *Journal of Equine Veterinary Science* 16(2): 66–72.

6 Bergfelt, D.R. and Adams, G.P. (2011). Pregnancy. In: *Equine Reproduction*, 2nd edn (ed. A.O. McKinnon, E.L. Squires, W.E. Vaala, et al.), 2065–2079. Oxford: Wiley Blackwell.

7 Ginther, O.J. (1998). Equine pregnancy: Physical interactions between the uterus and conceptus. *Proceedings of the 44th Annual Convention for the American Association of Equine Practitioners* 44: 73–104.

8 Allen, W.R. (2001). Luteal deficiency and embryo mortality in the mare. *Reproduction in Domestic Animals* 36(3–4): 121–131.

9 Vanderwall, D.K., Squires, E.L., Brinsko, S.P. et al. (2000). Diagnosis and management of abnormal embryonic development characterized by formation of an embryonic vesicle without an embryo in mares. *Journal of the American Veterinary Medical Association* 217(1): 58–63.

10 Newcombe, J.R. and Cuervo-Arango, J. (2012). The relationship between the positive identification of the embryo proper in equine pregnancies aged 18–28 days and its future viability: A field study. *Journal of Equine Veterinary Science* 32: 257–261.

11 Vanderwall, D.K. (2011). Early embryonic loss. In: *Equine Reproduction*, 2nd edn (ed. A.O. McKinnon, E.L. Squires, W.E. Vaala, et al.), 2118–2122. Oxford UK: Wiley Blackwell.

12 Ball, B.A. (2011). Embryonic loss. In: *Equine Reproduction*, 2nd edn (ed. A.O. Mckinnon, E.L. Squires, W.E. Vaala, et al.), 2325–2338. Oxford UK: Wiley Blackwell.

13 Stanton, M.E. (2011). Uterine cysts. In: *Equine Reproduction*, 2nd edn (ed. A.O. McKinnon, E.L. Squires, W.E. Vaala, et al.), 2665–2668. Oxford UK: Wiley Blackwell.

Vet-ebooks.com

17

Use of Early Gestation Ultrasonography in Twin Management

Richard Holder

Hagyard Equine Medical Institute, Lexington, KY, USA

The development of twin-management techniques with the use of ultrasound has saved millions of dollars for horse owners and turned the incidence of abortions due to twinning from commonplace to a rare occurrence.

Avoidance of twinning can be attempted in several different ways. Careful examination of the ovaries to detect multiple follicles to try to breed between the ovulations, or not breeding at all with the presence of multiple follicles, lessens the incidence of twinning. Avoiding use of ovulation induction products (e.g., deslorelin, hCG), which may encourage multiple follicles to ovulate, would reduce the incidence of twinning. However, the presence of multiple follicles and multiple ovulations increase the chance of mares becoming pregnant; consequently, in the author's opinion, it is better to increase the chance of becoming pregnant and deal with the occurrence of twins should they occur, rather than have a non-pregnant mare.

When twins do occur, there are many useful questions that should be considered when deciding to manually reduce a twin vesicle during early gestation (~14–16 days of gestation):

- Are there definitely multiple vesicles or is it a cyst and a singleton?
- Is the vesicle that I am leaving definitely a pregnancy?
- Will the vesicle move? (cysts are reluctant to move)
- Has the vesicle grown from the day before? (cysts rarely change size – pregnancies increase in size rapidly, ~ 3 mm per day, at this stage)
- Is the vesicle large enough to be easily pinched or is it so small it may be difficult to express?
- If I have difficulty, cannot express the twin and have to try again later, will I know which vesicle I manipulated?
- Should I let the vesicles grow a day? What day of pregnancy is it?
- Should I come back in a few hours or try to separate the unilateral twins now?
- Is there a good chance the twin will reduce on its own? Approximately 75% unilateral twins at 17 days reduce on their own. There is a greater chance twins will reduce on their own if they are of different sizes (personal experience)
- Is there a large size discrepancy between the vesicles? Is the size discrepancy related to ovulation dates?

All of these questions should be answered before manually reducing a twin.

Examination for pregnancy at the proper stage of gestation is mandatory to detect twins and have the opportunity to successfully express the selected twin vesicle. Some practitioners like to check 15–16 days from breeding to be sure they are still in the mobility phase. Some like to check 14–15 days from ovulation. It is sometimes difficult to tell exactly when ovulation occurs and accuracy of ovulation date is dependent upon when the mare is checked post breeding. If the mare is examined 2 days after breeding for ovulation then ovulation could have occurred anytime from when she was last checked before breeding to 2 days after breeding. This could be a 3-day span. Personal preference dictates when the examinations are done, but it is important not to wait longer than 16 days from conception. After that time, if the twins are unilateral, they could be very difficult to separate. The

Atlas of Equine Ultrasonography, Second Edition. Edited by Jessica A. Kidd, Kristina G. Lu and Michele L. Frazer.
© 2022 John Wiley & Sons Ltd. Published 2022 by John Wiley & Sons Ltd.
Companion Website: www.wiley.com/go/kidd/atlas

Vet-ebooks.com

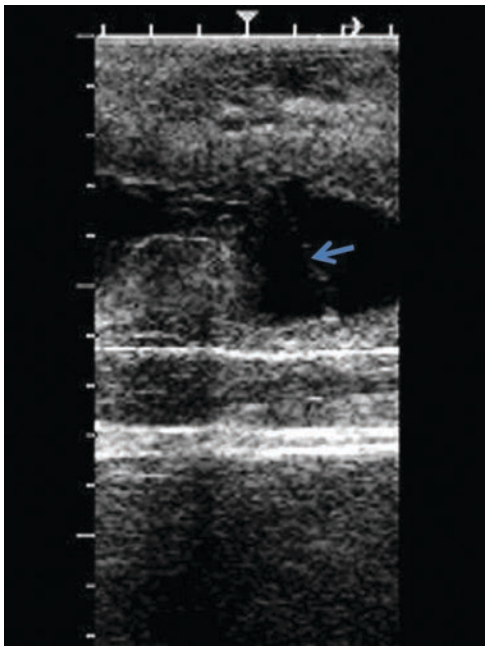


Figure 17.1 Twin vesicles. Careful evaluation may be necessary to observe the line of demarcation (arrow) between closely apposed twins.

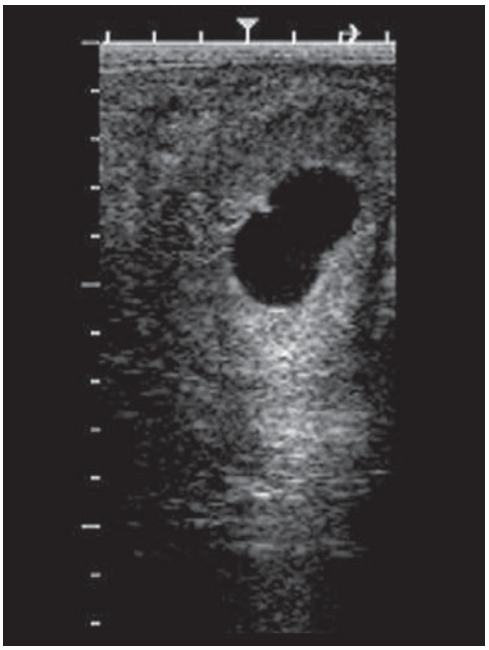


Figure 17.2 Twin vesicles. When twins are in close apposition and less than 16 days of gestation, re-evaluation at a later time (a few hours) may reveal them to have separated.

author uses 15–16 days from breeding because the pregnancy cannot be any older than 15 or 16 days.

At 14–15 days from conception the vesicles are in their mobility phase and can be found anywhere in the uterus. A thorough examination of the mare's uterus is mandatory, regardless of the number of ovulations thought to have occurred. It is important to examine the most distal tip of each horn and near the cervix. If the examination occurs after 16 days from conception and the twins are unilateral, it is often difficult to separate the vesicles due to increased tone of the uterus resulting from the progesterone influence from the corpus luteum and fragility of the vesicles. Thus, the examination is best done during the mobility phase, before 17–18 days post conception.

During the mobility phase the twins can be separated, even if they are unilateral and in close proximity. Sometimes two yolk sac membranes will come together forming a very faint line indicating twins (Figure 17.1). This can be difficult to see. If the twins are touching closely it is sometimes best to leave and return in 4–5 hours (Figure 17.2). If they are in the mobility phase they frequently will separate on their own when given time to move (Figure 17.3). If they continue to be in close proximity or re-examination is not possible, 10 mg IV of acepromazine maleate (Vedco, Inc., Saint Joseph, MO, USA) relaxes the uterus. Allow about 5 minutes after acepromazine administration before attempting to separate

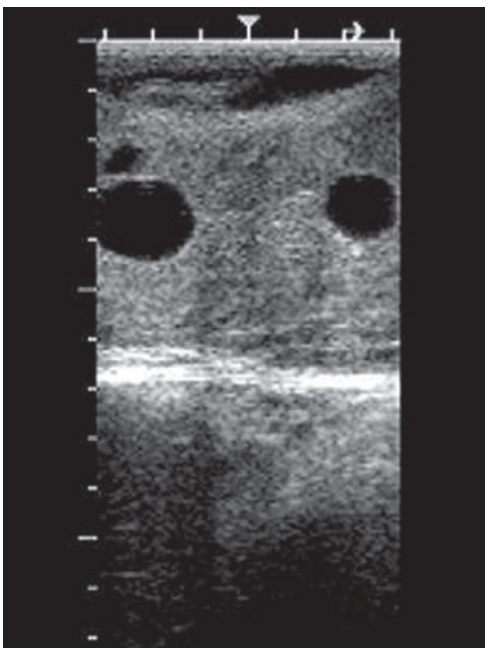


Figure 17.3 Separated twin vesicles in the uterine body. The size difference may be due to different gestational ages or to compromised growth of the smaller vesicle due to an infirmity.

unilateral twins transrectally. The twins can then be separated manually much more easily with less risk of unintentionally injuring either vesicle. The trick is to only injure the vesicle you are trying to rupture and not both. A twin vesicle is more easily expressed in a

Vet-ebooks.com

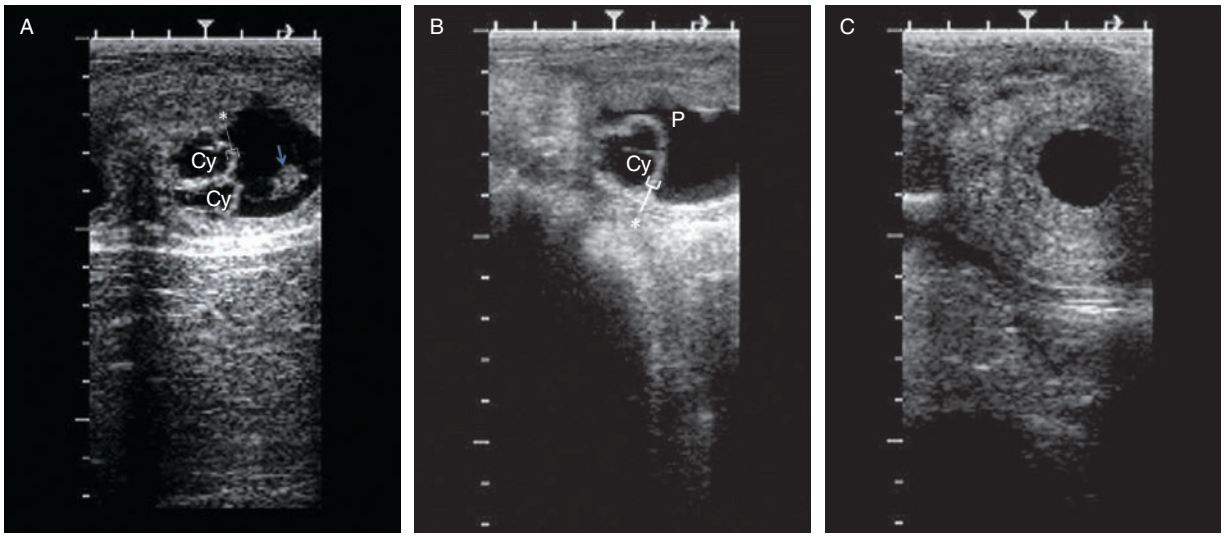


Figure 17.4 (A) 29-day pregnancy adjacent to two cysts (Cy). Identifying a heartbeat within the embryo (blue arrow) differentiates pregnancy from cysts. Note the hyperechoic, thick walls of these cysts. (B) Endometrial cyst (Cy) with hyperechoic wall (*) protruding into a pregnancy (P). (C) Endometrial cyst that appears similar to a pregnancy.

maiden mare than in a post-foaling mare with a larger uterus because the wall of the maiden mare's uterus is thinner.

If the mare is straining or resisting your examination, it is important to use a rectal spasmolytic such as N-butylscopolammonium bromide (Buscopan Injectable Solution, 60 mg IV, Boehringer Ingelheim Vetmedica, Saint Joseph, MO, USA) or propantheline (30 mg IV), to allow ease in handling the uterus. It is difficult to use delicate manipulation when the mare is straining against you. Sometimes gentle nudging of both vesicles will slightly separate them enough to allow placement of the ultrasound transducer between them to gently spread them apart. Slow and gentle pushing of the transducer into the area between the vesicles causes the vesicles to separate. For good results it is best to manipulate the uterus and vesicles as little as possible. With proper technique the percentage of normal single pregnancies at 60 days from twins that have been pinched at ~ 15 days is equal to a group of mares pregnant with a single pregnancy at ~ 15 days (personal experience).

If there are cysts present in the uterus, it is critical to be certain that the vesicle being left is a true pregnancy. A cyst can often be identified by having a visible wall that can be readily seen (Figures 17.4A and 17.4B). Cysts usually have an irregular shape and thickened wall, while the vesicle of a 15-day pregnancy should be spherical or slightly oval in shape with a wall that is difficult to visualize (Figures 17.5 and 17.6). Occasionally cysts appear just like a pregnancy (Figure 17.4C). Pregnancies at 18 + days can be slightly irregular in shape (Figure 17.7). A cyst cannot move much in comparison to a vesicle that can move from one end of the uterus to the other before 17 days. A cyst does not grow in size when examined the next day, while a pregnancy grows very noticeably at the 14–15-day stage. The size of the vesicle should be the proper size for the number of days of the pregnancy.

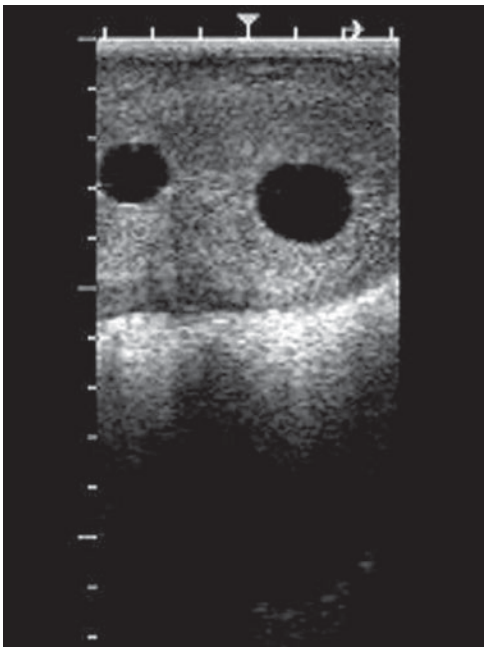


Figure 17.5 Twin vesicles of different diameters, either from ovulations that occurred on different days or due to growth rate differences.

When encountering two vesicles of different sizes it is a good idea to try to reduce the smaller twin if possible (Figure 17.5). Sometimes a vesicle is smaller than expected because it is from a later ovulation, but it is possible that it is smaller because it is

Vet-ebooks.com

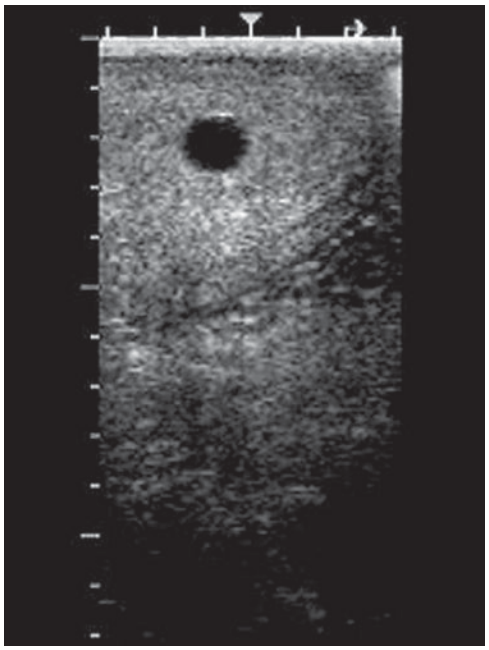


Figure 17.6 Unexpectedly small vesicle for a 15-day gestational pregnancy evaluation (markers beside image are 10 mm apart).



Figure 17.7 21-day pregnancy. After 17–18 days of gestation, vesicles can have an irregular shape that can make distinguishing them from an endometrial cyst difficult. Embryo proper indicated with arrow.

defective for some reason. If a vesicle is smaller than 15 mm, it is frequently evasive and difficult to express (Figure 17.6). It is preferable to let a vesicle grow 1 day to become larger than 15 mm to facilitate expressing it and to avoid extensive manipulation of the uterus. Letting the vesicle grow 1 day is another good way to differentiate a cyst from a pregnancy; the pregnancy should increase noticeably in size daily while the cyst will remain the same size. Monitoring the vesicles with measurements and saved ultrasonographic images is useful to determine size changes.

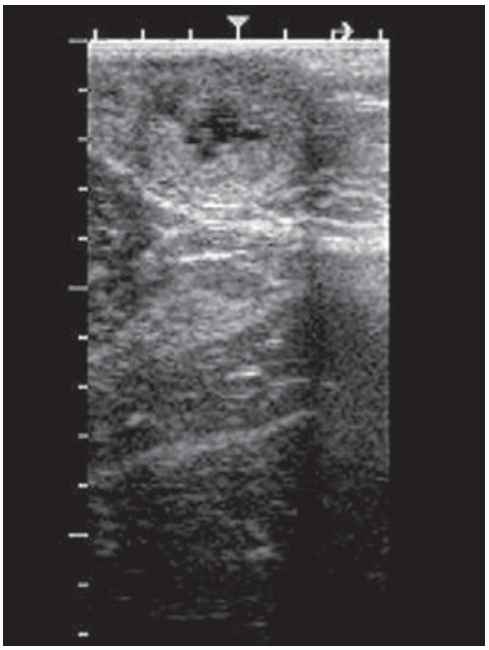


Figure 17.8 Vesicle after pinch.

When a vesicle is reduced it can be pinched between the thumb and forefingers or it can be expressed by pressure between the transducer and the pelvis. There should be a very slight fremitus (vibration) felt as the vesicle ruptures and a small amount of free fluid is visible in the uterus at the spot of the rupture (Figure 17.8). Frequently, the fluid from the ruptured vesicle migrates toward, and can be seen around, the pregnancy that is still present (Figure 17.9). If a twin is near the cervix, it can be expressed by forming a cup with four fingertips around the vesicle and dragging the hand posteriorly, toward the cervix, pressing down on the floor of the pelvis until the vesicle ruptures. The ability to express a vesicle is difficult at first, but becomes much easier with experience. If you are expressing a twin in the horns of the uterus while one twin is in the body or near the cervix, be careful that the forearm does not put pressure on and accidentally rupture a twin near the cervix. If the twin is in the horn of the uterus it usually can be pushed to the tip of the horn where it can be easily trapped and expressed.

After the vesicle is reduced, in the author's opinion, it is worthwhile to treat the mare with flunixin meglumine (1.1 mg/kg IV) once daily for 3 days. This has

Vet-ebooks.com

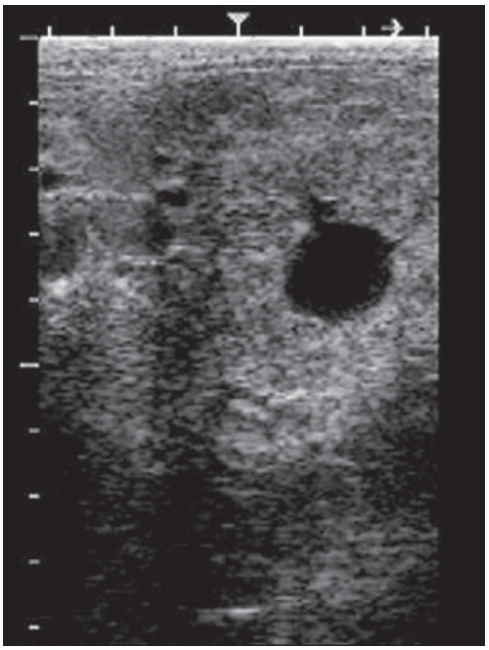


Figure 17.9 Trace anechoic fluid from pinched vesicle surrounding remaining vesicle.

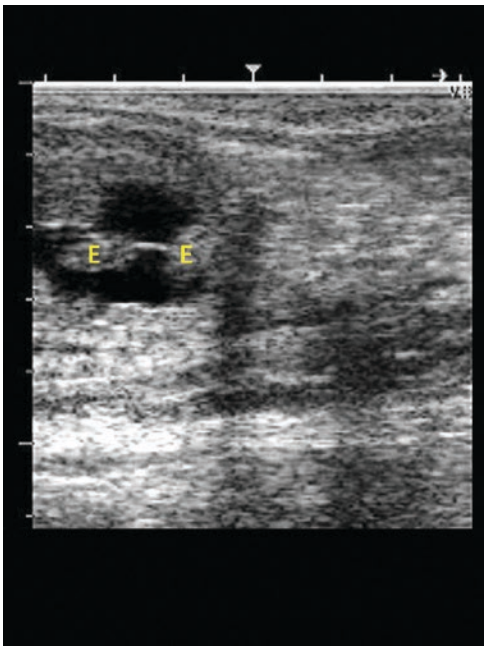


Figure 17.10 28-day adjacent twins. E: embryo.

an anti-prostaglandin effect in case there is a prostaglandin release from the manipulation of the uterus or in response to fluid from the pinched vesicle. It is important to remember to minimize manipulation of the remaining vesicle whenever possible. Some clinicians recommend altrenogest (0.044 mg/kg PO SID) in case there is compromise of the corpus luteal tissue supporting the pregnancy.

Occasionally, more than two pregnancies are present (Figure 17.11). The procedure is the same as for twin reduction; however, some clinicians like to reduce one vesicle and come back the next day to reduce one more. This prevents a large amount of fluid from the rupture of two vesicles being released into the uterus at one time.

It is possible when examining a mare during the mobility phase at 15 days post ovulation that the mare could have a 14–15-day pregnancy and a 9–10-day pregnancy. Missing the 9–10-day pregnancy would be easy to do because of its small size. A transrectal scan 4–5 days later at 19–20 days from breeding should alleviate that problem, because the 9–10-day pregnancy would have grown and be easy to see at that time.

The next exam should be at 28–30 days of gestation, again looking for twins that could have been missed. If twins are found at this stage and are bilateral they can be expressed with about a 50–60% success rate (personal experience). If the twins found at this examination are unilateral, it is very difficult to express one without injuring the other (Figure 17.10). In this case, it is best to follow the twins until about 33–34 days of gestation to see if they reduce to a singleton on their own. Finding two viable heartbeats is the best indicator of twins persisting. At ~ 35 days, the endometrial cups are forming, which may prevent the mare from returning to estrus if pregnancy loss were to occur. The endometrial cups produce pregnant mare serum gonadotropin (PMSG; equine chorionic gonadotrophin), causing secondary corpora lutea development for maintenance of the pregnancy. Prior to endometrial cup formation, and taking into consideration if there is time to rebreed in the breeding season, the mare can be given prostaglandin to return to estrus and rebreed. Most mares do well becoming pregnant again from these subsequent breedings. If it is too late in the breeding season to rebreed the mare, it is best to see if the twin reduces on its own. The author has had poor results from manually expressing twins past 40 days, or trans-vaginal twin aspiration and transabdominal twin injection.

If twins are found after fixation there are several procedures that can be attempted past 40 days from conception. One technique involves traumatizing usually the smaller of the two fetuses, through manipulation and percussion using manual compression or the ultrasound probe. A success rate approaching 50% may be attained [1]. Multiple attempts may be necessary to complete reduction and it is often difficult to assure manipulation of the same fetus at each attempt.

Another technique is transabdominal injection of KCl into the heart of the fetus, using the assistance

Vet-ebooks.com

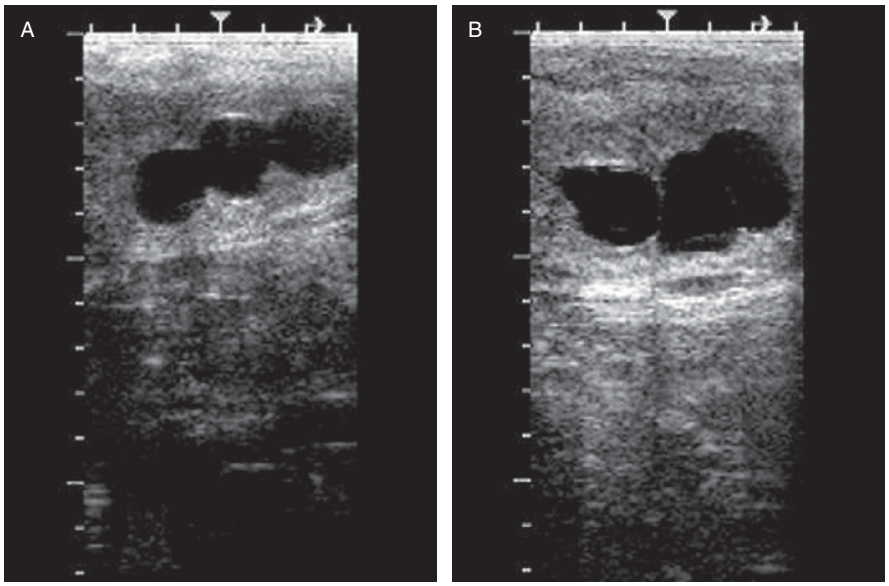


Figure 17.11 (A and B) Triplets.

of an ultrasound biopsy guide connected to the transducer [2]. This may result in a success rate near 40% [3]. Injections of 10–20 cc of procaine penicillin G into the thorax or abdomen of the fetus resulted in a 50–60% success rate [1]. The optimal time for this procedure is 115–130 days of gestation. No difference in survival rate were seen when NSAIDs, antibiotics, and altrenogest are used post procedure [1].

If twins persist beyond 60 days, the author recommends a procedure associated with a approximate 50–60% success rate [4]: manual cranio-cervical dislocation of the fetal head to terminate one fetus in an attempt to preserve the other. This can be performed transrectally after 60–70 days up to about 110 days of gestation. This involves grasping the head of the fetus and breaking down the tissue at the base of the posterior skull to sever it from the spinal cord. This does not immediately result in death of the twin but it will usually die in a few weeks. The untouched twin will be born normally about 50–60% of the time, while 40–50% of mares will abort both fetuses. This technique can be very difficult to perform transrectally, consequently a sterile surgical procedure was developed via a sterile surgical flank incision and grasping the head of the fetus through the uterine wall and dislocating it. The head is dislocated by manual manipulation at the base of the fetal skull with the thumb. The uterine wall stays intact. An advantage of this procedure is that a fetal sex determination can be performed and when there is a filly and a colt, the owner can select which sex to keep. A fetal sex determination is performed with transrectal ultrasonography during the surgery by another practitioner (Video 54), and the proper fetus is identified for elimination to the surgeon going in through the flank.

Video 54 Ultrasound of 58-day twins with views to allow fetal sexing

http://bit.ly/1fB0AJi

(This will take you directly to the video on Wiley Blackwell's companion website.)

It is important to remember that manual expression of one vesicle pre-fixation (> 17 days) results in a live foal rate equal to that of a single normal pregnancy present at 16 days. The ability to express a vesicle is difficult at first but becomes much easier with experience.

Recommended Reading

Ginther, O.J. (1992). *Reproductive Biology of the Mare: Basic and Applied Aspects*, 2nd edn. Cross Plains WI: Equiservices.

Sheerin, P.C. (2010). Manual reduction of twins in the mare: Effect of operator, mare age, and treatment. *Proceedings of the American Association of Equine Practitioners* 56: 322.

Vet-ebooks.com

References

1 McKinnon, A.O. and Rantanen, N.W. (1998). *Twins in Equine Diagnostic Ultrasonography* (ed. N.W. Rantanen and A.O. McKinnon), 141–156. Baltimore MD: Williams & Wilkins.

2 Ball, B.A. (2000). How to do a transabdominal reduction of twin pregnancies in a mare. IVIS Document number. A0202–0400. www.IVIS.org

3 Rantanen, N.W. (1990). Ultrasound guided fetal cardiac puncture for twin reduction in mares. *Proceedings of Annual Meeting of Society of Theriogenology*, 169–170.

4 Wolfsdorf, K.E., Rodgerson, D., and Holder, R. (2005). How to manually reduce twins between 60 and 120 days gestation using cranio-cervical dislocation. *Proceedings of the American Association of Equine Practitioners* 51: 284–287.

Vet-ebooks.com

18

Use of Ultrasonography in Equine Fetal Sex Determination between 55 and 200 days of Gestation

Richard Holder

Hagyard Equine Medical Institute, Lexington, KY, USA

Fetal sex determination between 55 days and 200 days of gestation is a worthwhile service to provide for clients. The procedure is difficult to learn and will require approximately 300–400 attempts at diagnosis to become accurate and confident of your diagnosis. Once it is learned it will rapidly become easier and quicker with each subsequent examination.

Stages of Gestation

There are primarily three different stages of gestation during which the determinations can be made: i) between 55 and 90 days gestation; ii) between 90 and 150 days gestation; and iii) beyond 150 days gestation.

Fetal Development at Different Stages

55–60 days. The fetus is very accessible but it is small. The genital tubercle is difficult to see, and the tubercle may or may not have fully migrated.

60–70 days. This is the *ideal time* for the examination. The fetus is readily accessible, the genital tubercle is distinct and fully migrated.

70–80 days. The fetus is slightly more difficult to reach and the tubercle is slightly less distinct.

80–90 days. It is more difficult to access the fetus, the tubercle is less distinct, the genitalia development is just beginning. Maiden mares often can be done at this time.

90–110 days. The fetus is usually accessible and the genitalia are gradually becoming more evident.

110–120 days. This is the *ideal time* for examination at the mid-gestation stage. The fetus is very accessible and the genitalia are very well developed.

120–140 days. The genitalia are well developed, but the posterior of the fetus may be difficult to access.

140–150 days. The fetal genitalia is prominent but the posterior may be difficult to access.

150 + days. The fetus is large with an anterior presentation and the posterior is usually out of reach transrectally. The transabdominal approach is best after 150 days of gestation.

Fetal Sexing 55–90 days of Gestation

This stage involves finding the genital tubercle, a small, ~ 2 mm, hyperechoic bilobed structure, resembling an equal sign. It is the precursor to the penis in the male and the clitoris in the female. The genital tubercle must be identified and located in relation to other fetal anatomic structures. The tubercle can be seen as early as 52 or 53 days of gestation located between the hind legs on the ventral midline. As the fetus ages, the tubercle appears to migrate toward the umbilical cord in the male and toward the tail in the female. Around day 55 from conception the tubercle has usually migrated enough to make a determination. At this time the fetus is easily accessible by transrectal palpation and an accurate determination (99% + accuracy) can be made a very high percentage (~98%) of the time with one examination. This examination of the fetus takes 10 seconds to 2–3 minutes, depending on the experience of the examiner. The fetus is easily accessible until around 75 days of gestation. At this

Atlas of Equine Ultrasonography, Second Edition. Edited by Jessica A. Kidd, Kristina G. Lu and Michele L. Frazer.
© 2022 John Wiley & Sons Ltd. Published 2022 by John Wiley & Sons Ltd.
Companion Website: www.wiley.com/go/kidd/atlas

Vet-ebooks.com

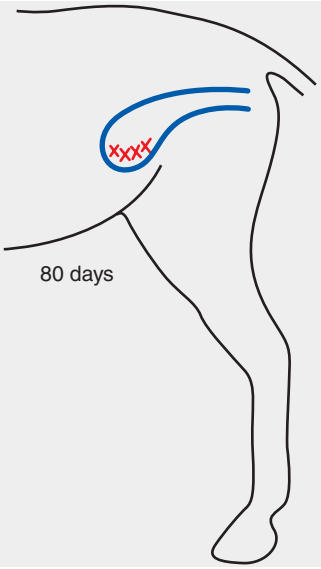


Figure 18.1 Schematic of the uterus and fetal location within the abdomen at 80 days of gestation.

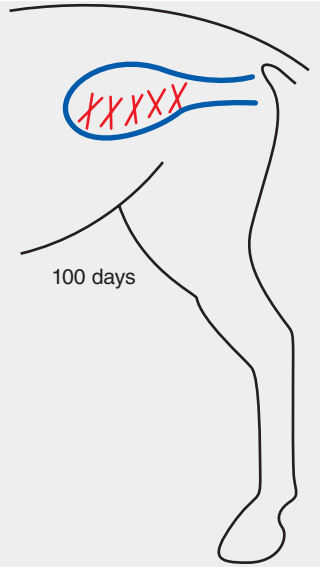


Figure 18.2 Schematic of the uterus and fetal location within the abdomen at 100 days of gestation.

time, in some mares, the fetus can be difficult to access. Usually, it can be done until about day 80.

At about 80 days of gestation, the fluid of the pregnancy pulls the uterus over the rim of the pelvis. The fetus is small and falls to the most ventral part of the uterus in the allantoic fluid. However, after ~90 days, the uterus does not continue to move more ventrally into the abdomen. It actually elevates in the abdominal cavity as it becomes larger and the fetus is usually visible again at about 90–95 days of gestation. As the fetus grows it elevates in the abdominal cavity, extends back near the pelvic cavity, and is readily visible after around 100 days. At this time the external genitalia are used to make a sex determination (Figures 18.1 and 18.2).

Fetal Sexing 90–150 days of Gestation

At 90 days the fetus comes back into view, as the uterus seems to elevate dorsally in the abdominal cavity and is easily accessible. The genital tubercle is less prominent now but the external genitalia (penis, prepuce, glans penis, and the gonads in the male, and the mammary gland, teats, clitoris, and the gonads in the female) are just beginning to be evident. Determinations are somewhat more subjective at this stage because of the need to evaluate the tissue densities between prepuce and muscle or mammary gland and muscle. Other fetal tissues frequently obscure the genitalia. The optimum time for determination at this stage is between 110 and 125 days. It is usually not as clear as the genital tubercle evaluations, and it may take anywhere from 30 seconds to 5–10 minutes. A sex determination can be made 90% of the time at this stage, with 98 +% accuracy, with one examination.

Fetal Sexing after 150 days of Gestation

If the posterior part of the fetus cannot be accessed transrectally, it is worthwhile to attempt transabdominal ultrasonography using a 2.5–3.5 MHz sector scanner. With the proper equipment good visualization of the posterior area of the fetus can frequently be achieved. The transducer should be placed on the midline of the mare's abdomen slightly anterior to the udder and moved anteriorly until the fetus is located. Locate the heart of the fetus for orientation and locate the umbilical entrance to the abdomen. Follow the ventral midline of the fetus posteriorly from the umbilical entrance to the abdomen until the base of the tail is reached. In the male, the prepuce and hyperechoic area of the glans penis will be seen just posterior to the abdominal entrance of the umbilical cord. The mammary gland and teats of a female fetus will also be seen in this area. Moving posteriorly it is also possible to see a clitoris on the fetal ventral midline (perineum) before the base of the tail is reached.

The external genitalia on a transabdominal scan appear the same as the 100 + day transrectal views but they are not quite as clear. When attempting transabdominal fetal sexing, the fetal heart, umbilical entrance into the abdomen, and the fetal ventral midline between the hind legs are the most useful markers. Adjusting the ultrasound to a deep penetration

Vet-ebooks.com

reduces the visual size of the fetus and allows for better visualization of a larger area of the fetus. This is helpful in relating the location of certain structures to other fetal anatomic structures. The genitalia can be seen on the fetal ventral midline, between the umbilical entrance to the abdomen and the base of the tail. These include the prepuce, glans penis, penis, and gonads in a colt and the mammary gland, teats, clitoris, and gonads in a filly. These structures are difficult to visualize but can be differentiated with adequate practice.

Ultrasonographic Planes

- Plane I (primarily useful for colts) (Figure 18.3)
- Plane II female (ideal view for filly diagnosis) (Figure 18.4)
- Plane II male (similar to female view but slightly more anterior for colts) (Figure 18.5)
- Plane III (primarily useful for colt diagnosis) (Figure 18.6, focus on Figure 18.6A)

Take Home Hints

1) If the image is not clear, push down gently on the uterus with the probe to bring the fetus closer to the probe. This changes the focal point for various areas of the fetus and creates movement of the allantoic fluid, causing the fetus to change position slightly.
2) If the view of fetus is not productive, turn the transducer 90 degrees to the left. If the view is still not productive, turn the transducer 180 degrees to the right. Somewhere in this 180-degree span is the proper scanning plane for viewing the tubercle.
3) If the mare is straining, do not hesitate to use propantheline (30 mg IV) or butylscopolamine bromide (Buscopan, Boehringer Ingelheim GmbH) (40 mg IV) to lessen straining. This enables one to move the probe to various positions to get different angles of view of the fetus.
4) Darkened ambient light frequently makes the detail of the genital tubercle easier to recognize.
5) It may be necessary to extend the transducer in front of the hand to reach older fetuses. This is difficult to do without a stiff transducer cord.
6) Evacuate fecal material as far anteriorly as possible.
7) In a 55–90 day determination, view a cross-section of the fetal abdominal cavity to identify ribs. This will give a dorsoventral orientation. The ribs will be on the dorsal aspect. (the dorsoventral orientation is very critical in differentiating the hyperechoic tailhead and tibias). Proceed posteriorly until you have moved off the fetus. The bright spot on the dorsal area of the posterior fetus as you move back on the fetus will be the tailhead. The two bright spots on the ventral area of the posterior fetus will be the tibias.

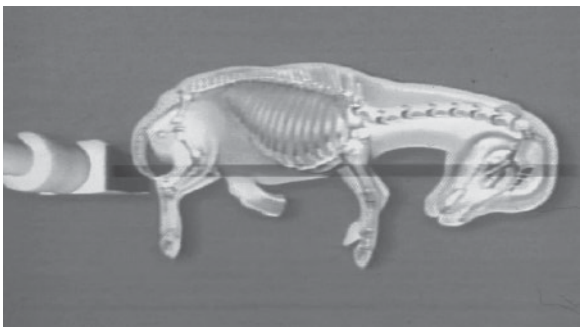


Figure 18.3 Plane I, primarily useful for colt diagnosis.

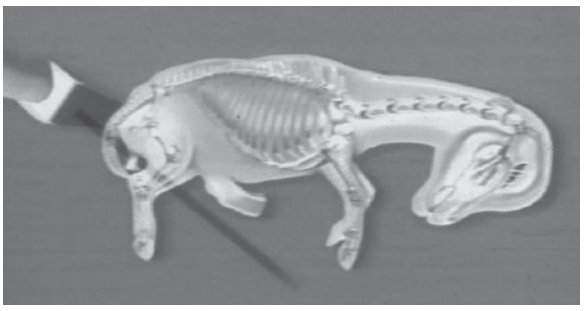


Figure 18.4 Plane II female. Ideal view for filly diagnosis.

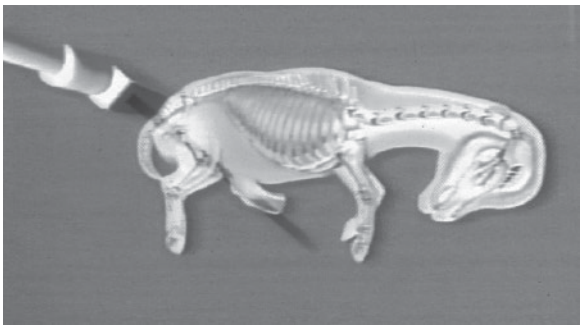


Figure 18.5 Plane II male. Ideal view for colt diagnosis.

Procedure at 55–90 days

Place proper restraint on the mare and evacuate feces thoroughly. If the mare is straining, a smooth muscle relaxant may need to be given (propantheline 30 mg or Buscopan 30–40 mg IV). First, determine the anterior–posterior positioning of the fetus. Find the skull (good anterior marker), the heart (good ventral

Vet-ebooks.com

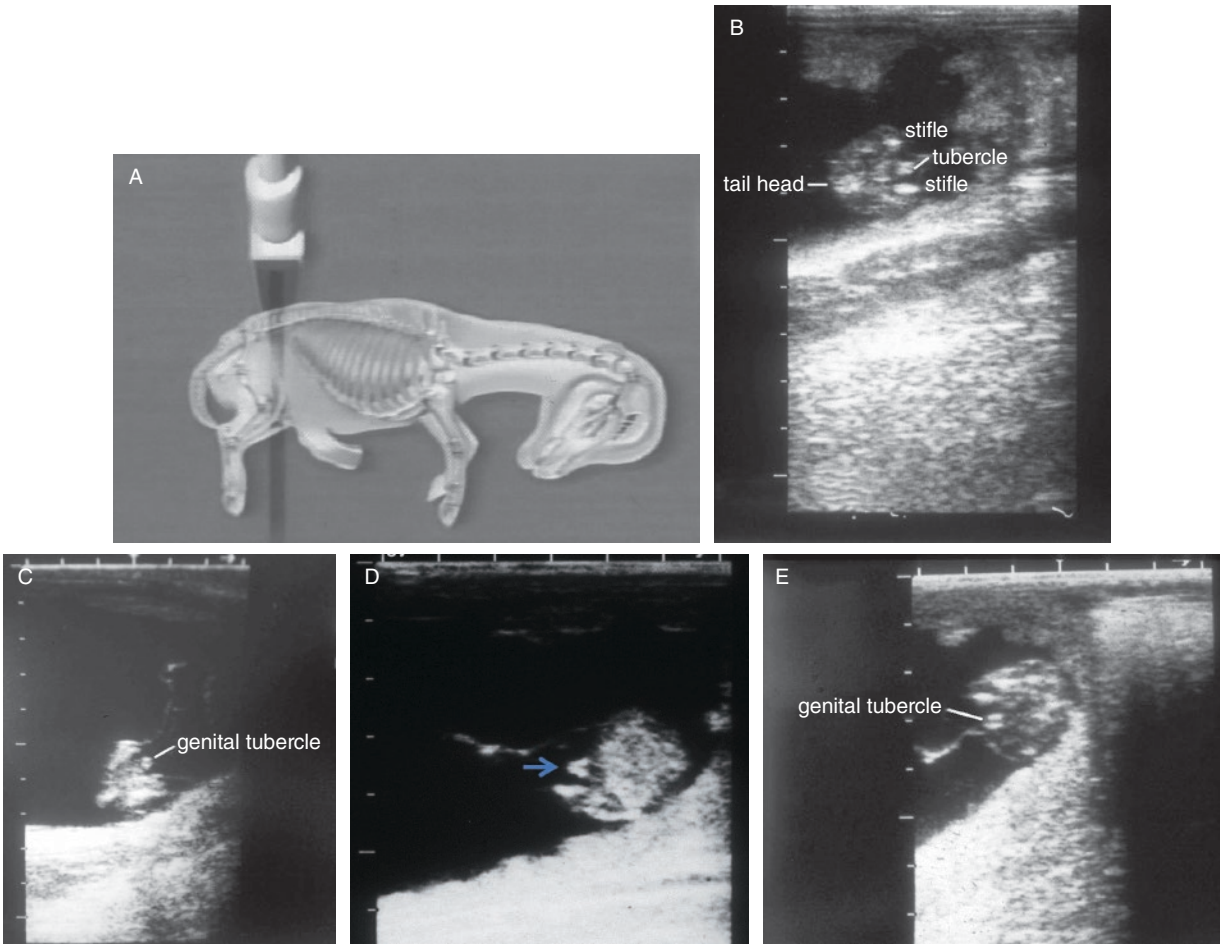


Figure 18.6 (A) Plane III, primarily useful for colt diagnosis. (B) Colt. (C) Colt. (D) Colt, with a prominent hyperechoic bilobed genital tubercle (arrow). (E) Colt.

marker), and the umbilical entrance to the abdomen (good ventral marker), which appears as a 3–4-mm dark hole on the posterior abdominal midline (Figure 18.7, focus on 18.7B). The ribs coming off the vertebrae (Figures 18.8 and 18.9) and the tail are good dorsal and posterior markers, respectively (Figures 18.10, 18.11, and 18.12 (focus on 18.12A), and 18.13 (focus on 18.13A)). Using these markers for orientation, scan the area to see if an obvious genital tubercle is present.

Next, try to get a transverse view of the abdomen where the plane of the ultrasound beam transects the fetus perpendicular to the axis of the fetal spine (plane III) (Figures 18.6, 18.8, 18.9, and 18.14). It is necessary to look for markers (ribs) that identify dorsal and ventral orientation of the fetus. The spinal column exhibits as a hyperechoic equal sign and is a good dorsal marker (this looks slightly like a genital tubercle but is on the dorsal side rather than the ventral side) (Figure 18.9). Ribs coming off of the vertebrae are often the most useful dorsal marker (Figures 18.8 and 18.9). The umbilical cord entering the abdominal cavity is a very good ventral marker (Figure 18.15). These markers give an idea of where you should be looking for the genital tubercle.

The genital tubercle for the male will be on the ventral midline just posterior to the umbilical entrance into the abdominal cavity (Figures 18.7A, 18.7B, and 18.7C). The genital tubercle for the female will be on the fetal ventral midline just under the tail head (Figure 18.12). If you have a transverse ultrasound plane (perpendicular to the axis of the spine), continue with this plane until you leave the posterior part of the fetus. After there is no fetus in view, keeping this same plane, ease back toward the fetus. The first hyperechoic area that you see on the dorsal side will be the tailhead. The next hyperechoic areas will be the genital tubercle just under the tail (in a female) and two hyperechoic areas (tibias), with no muscle mass around them, about 1–2 cm from the tail, depending on the age of the fetus (Figures 18.12 and 18.13A). There now should be three or four hyperechoic areas in view. If it is a colt, there will be three hyperechoic areas forming a tailhead–tibia triangle

Vet-ebooks.com

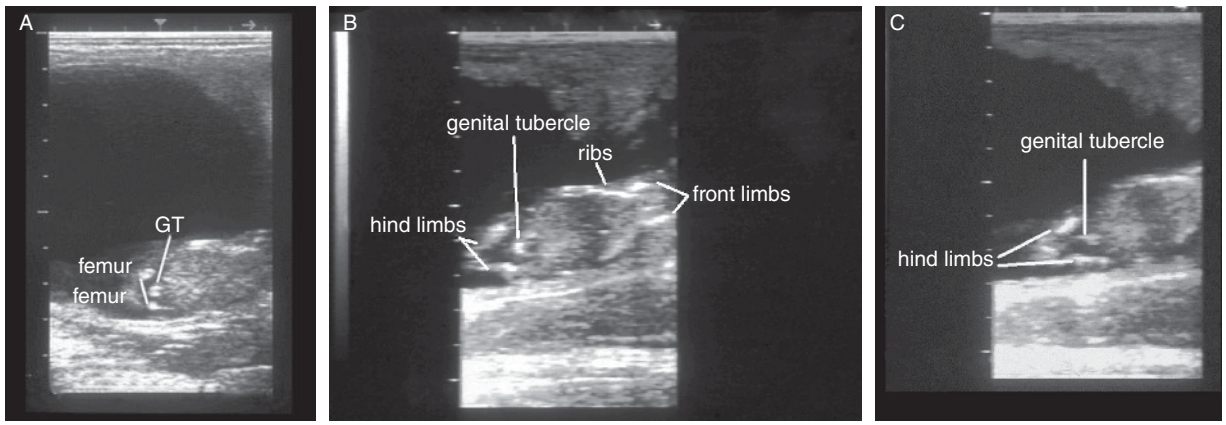


Figure 18.7 (A) Colt, viewed in plane I. GT: genital tubercle. (B) Colt, viewed in plane I; note the anechoic umbilical entrance to the abdominal cavity just cranial to the genital tubercle. (C) Colt, viewed in Plane I.

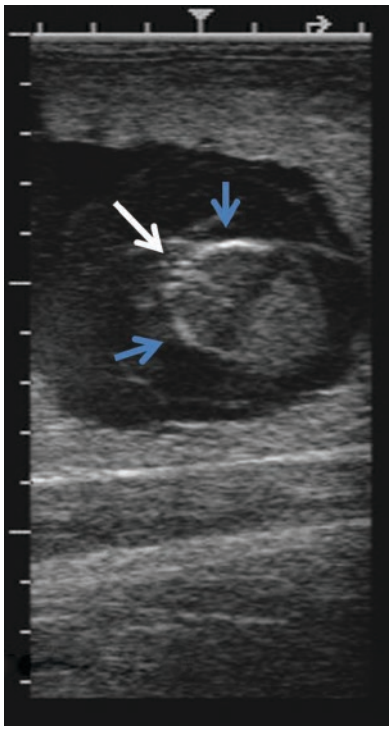


Figure 18.8 Axial transverse plane of fetus with hyperechoic ribs (blue arrows) and vertebrae (white arrow). Ribs are an easily viewed dorsal reference.

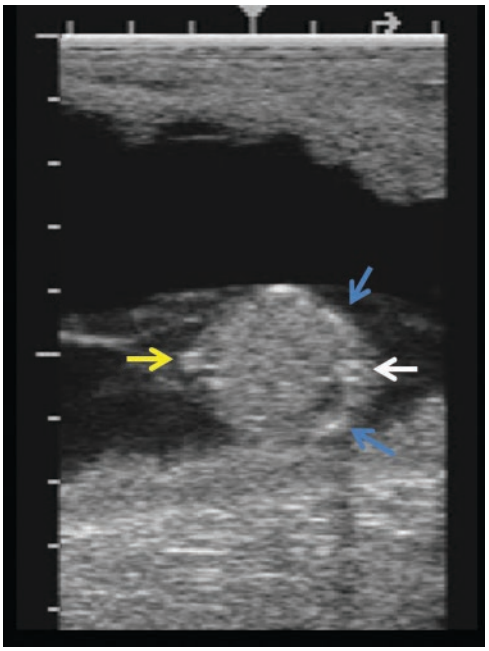


Figure 18.9 Colt, 65 days of gestation, viewed with Plane III technique. Ribs (blue arrows) and vertebrae (white arrow) provide dorsal reference. Genital tubercle indicated with yellow arrow.

with no hyperechoic area within this triangle (Figure 18.11). If it is a filly, a bilobed hyperechoic equal sign will appear within the tailhead–tibia triangle slightly closer to the tailhead (Figures 18.12 and 18.13A). This view is a requirement for identifying a filly. A colt tubercle can be visualized from many different angles including a frontal plane (plane I, Figures 18.7A and 18.7B) that exhibits the front legs, ventral abdomen, and hind legs. The tubercle will appear on the ventral midline slightly anterior to a line drawn between the stifles and slightly posterior to the umbilical entrance into the abdominal cavity (Figures 18.7A, 18.7B, and 18.7C).

If there is a negative filly view (nothing within the triangle) then advance the plane of the scan anteriorly on the fetus. The male tubercle will appear just at the ventral edge of the abdominal wall as a hyperechoic bilobed equal sign (Figure 18.6D). By moving the ultrasound plane toward plane I you will see the umbilical entrance to the abdominal cavity (appears as a small black hole, Figure 18.7B). If you move the transducer to plane II you will see a tubercle between the hind legs (Figures 18.6B, 18.6C, and 18.6E). The tubercle should be anterior to a line drawn

Vet-ebooks.com

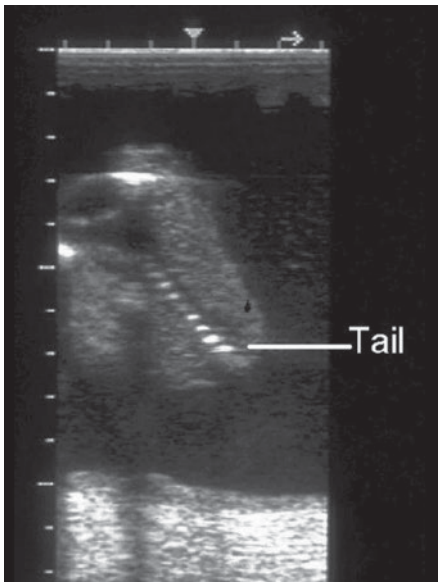


Figure 18.10 Posterior fetus viewing the tail. Line points to the most dorsal aspect of tail.

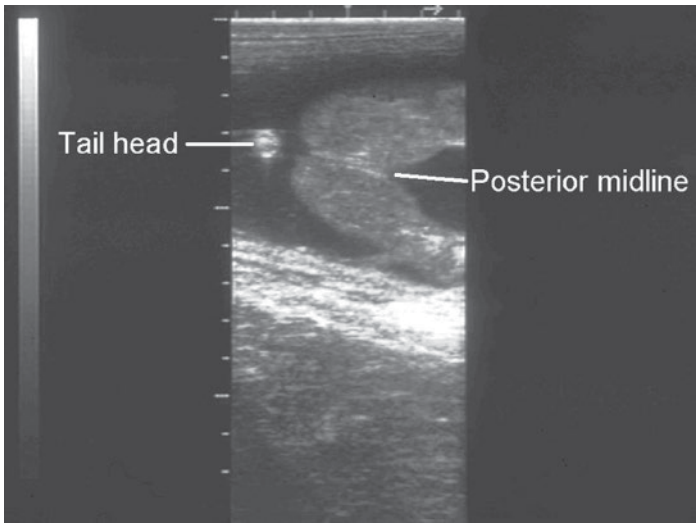


Figure 18.11 Posterior fetus, 113 days of gestation. Tailhead is dorsal reference. Posterior midline discernable with absence of clitoris suggesting a colt.

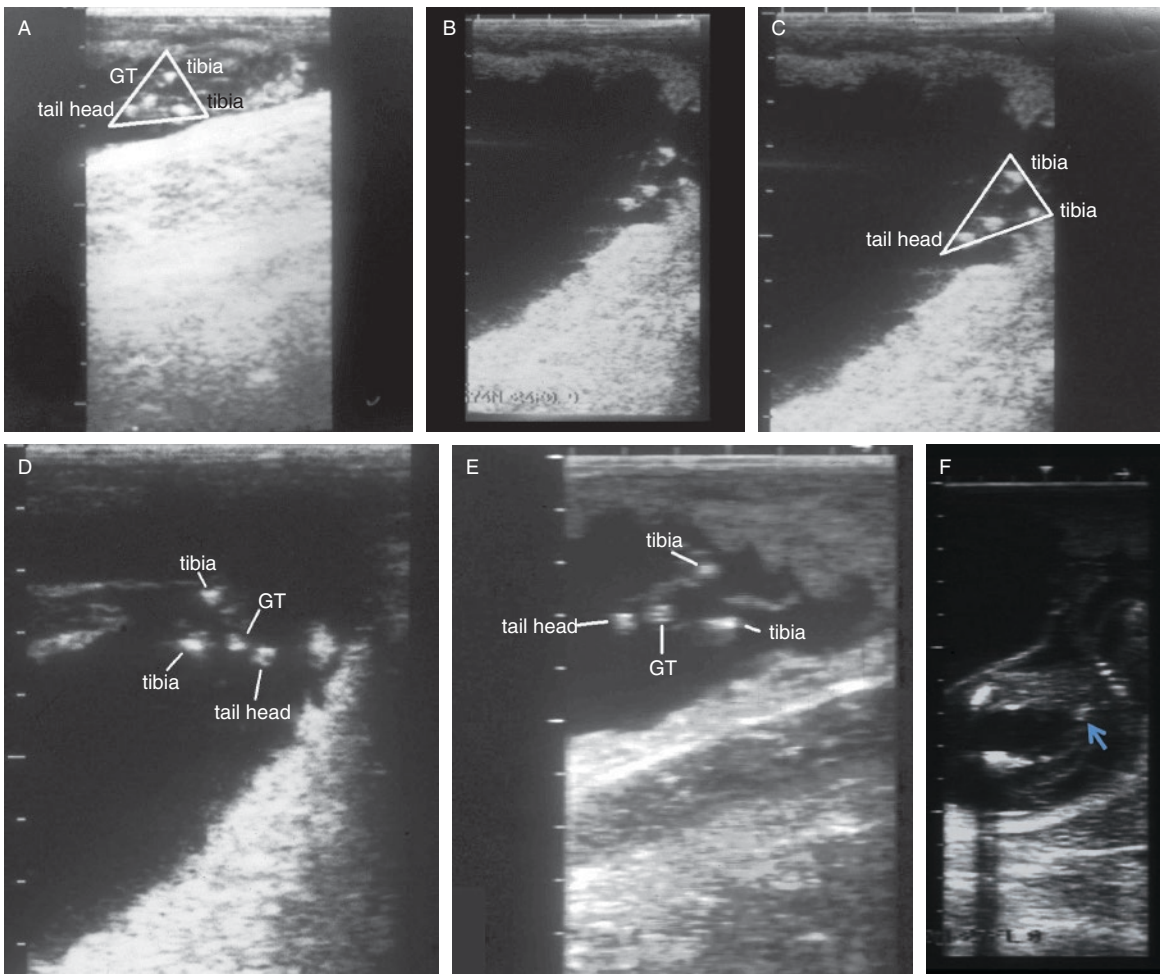


Figure 18.12 (A) Filly, 63 days of gestation. Tailhead provides dorsal reference. GT: genital tubercle in the middle of triangle created by tailhead and tibias. (B) Filly. (C) Filly. (D) Filly; GT: genital tubercle. (E) Filly. (F) Filly, 78 days of gestation. Tailhead and tail to right, tibias to the left, with clitoris (arrow) within the triangle formed by the tailhead and tibias.

Vet-ebooks.com

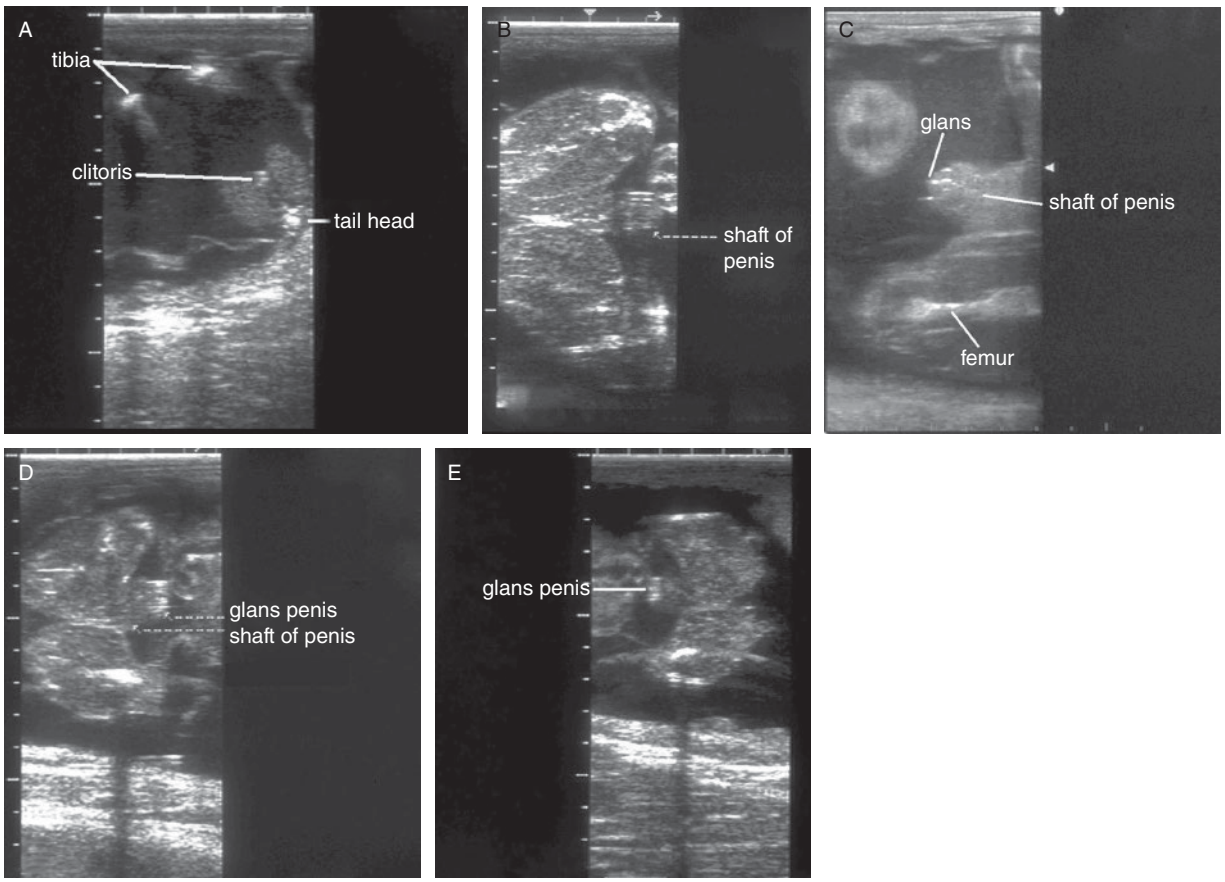


Figure 18.13 (A) Filly. Tailhead provides dorsal reference. (B) Colt. (C) Colt. (D) Colt. (E) Colt.

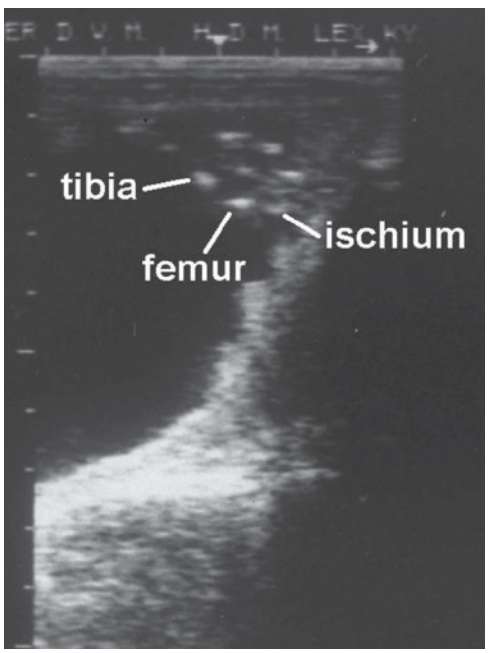


Figure 18.14 Pelvic bones, visualized while orienting for plane II or plane III views.

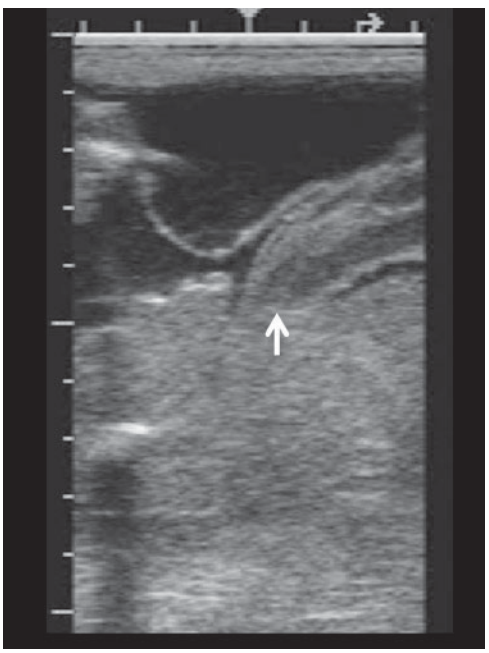


Figure 18.15 Colt, 115 days of gestation. Oblique sagittal view of penis caudal (left) to umbilical cord insertion (indicated with arrow). The umbilical cord attachment to the fetus is a good ventral reference.

Vet-ebooks.com

between the stifles to make sure it is a colt. Remember that at 52–53 days the tubercle is between the hind limbs in both male and female. We have to wait at least until 55 days of gestation to determine which direction the tubercle appears to be moving. If the tubercle is anterior to a line drawn between the stifles it will be a colt. If the tubercle is posterior to a line between the stifles it will be a filly. If it is difficult to decide, wait 3 or 4 days and look again.

Procedure 90–150 days

This procedure involves finding the external genitalia of the fetus. After 90 days the fetus begins to come back into transrectal view with the ultrasound. It is best to scan the entire fetus to get oriented anteriorly, posteriorly, dorsally, and ventrally. It is good to get a cross-sectional view of the posterior abdomen (Figure 18.16, focus on 18.16F) and keeping that plane move off the fetus posteriorly. As one comes back on to the fetus it is possible to get the same tailhead–tibia triangle with the clitoris showing up just under the tailhead within the triangle (Figures 18.12F and 18.13A). If the structure on the midline is too close to the tail it could be the anus (Figure 18.17). If nothing is under the tailhead, notice the prominent ventral midline (appears as a white line) (Figure 18.12). In a filly, following the prominent ventral midline posteriorly to the tailhead will lead to the clitoris (small round hyperechoic mass (Figures 18.12F, 18.13A, 18.18, and 18.19)), that may appear as two hyperechoic dots lying on each side of the ventral midline (Figure 18.20). Following the ventral midline anteriorly from the tailhead leads to the mammary gland (Figure 18.21). The mammary gland consists of three distinct parts: the bright small hyperechoic teats, on each lateral side of the gland (Figures 18.21A, 18.21B, and 18.21C), and two dense halves of the mammary gland separated by a hypoechoic line between the two halves (Figure 18.21). Preputial tissue is not as dense as a mammary gland and does not have a hypoechoic line separating the halves, and obviously has no hyperechoic teats.

In a male, following the ventral midline posteriorly using plane II, nothing is encountered before

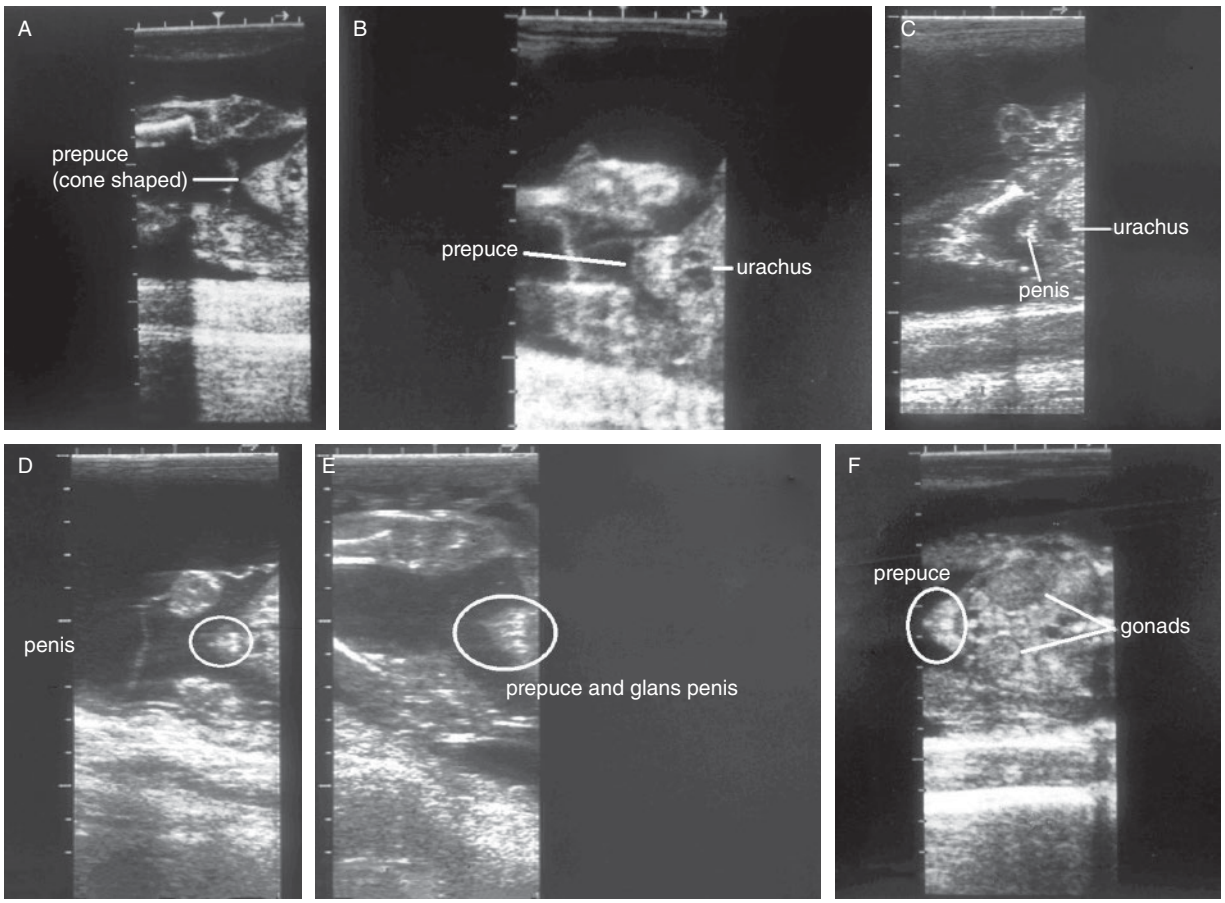


Figure 18.16 (A) Colt. (B) Colt. (C) Colt, 94 days gestation. (D) Colt, 95 days of gestation. (E) Colt, 117 days of gestation. (F) Colt, with prepuce and gonads in view.

Vet-ebooks.com

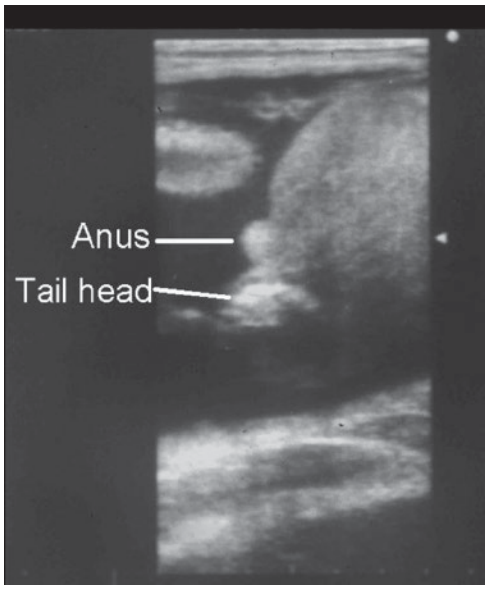


Figure 18.17 122 day fetus with tailhead and anus in view.

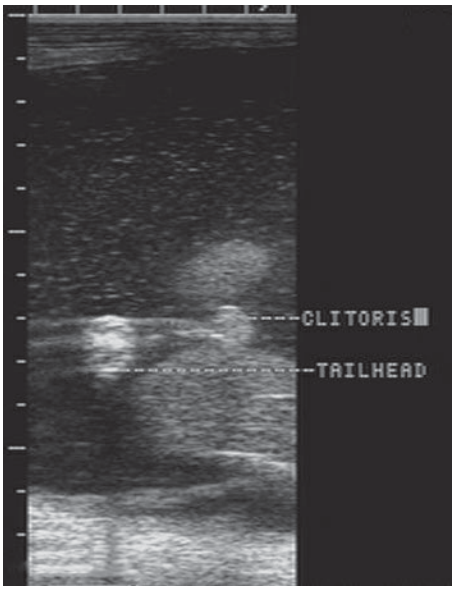


Figure 18.19 Filly, 110 days of gestation.

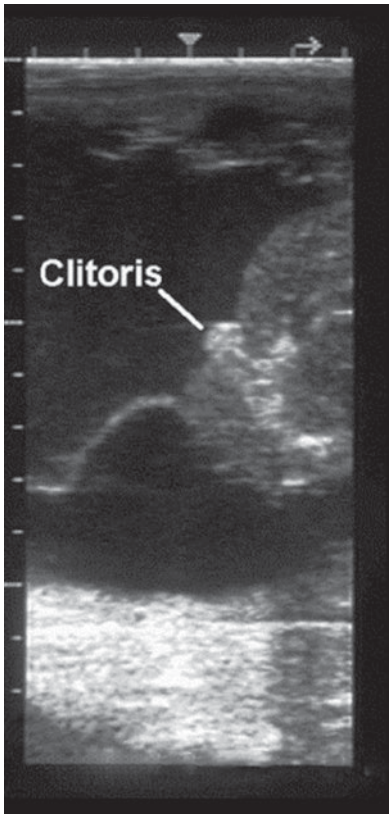


Figure 18.18 Filly.

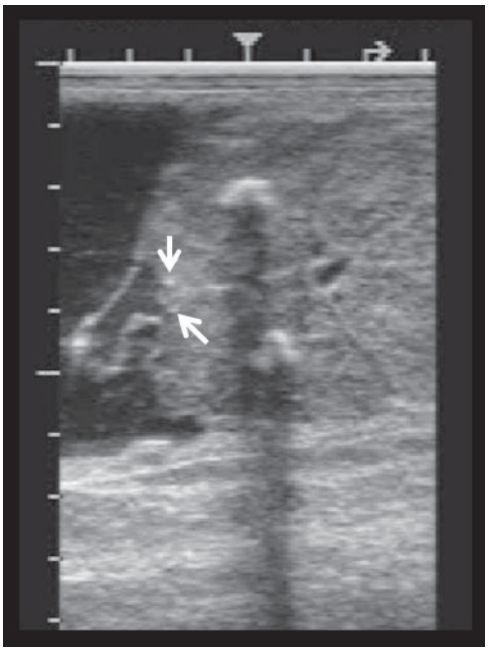


Figure 18.20 Filly, 105 days of gestation. Clitoris indicated by arrows.

reaching the tailhead (Figure 18.11). Following the ventral midline anteriorly from the tailhead will lead to the prepuce (a cone-shaped structure that comes to a point (Figures 18.16A and 18.16B)). The penis can often readily be seen as a shaft-like structure with a bright hyperechoic mass on the end (Figures 18.13B, 18.13C, 18.13D, and 18.13E). This bright hyperechoic tip is the glans penis. Figure 18.22 is a sagittal view through the flank of a shaft of a penis with a hyperechoic tip. Using a plane III view (a cross-section of the posterior abdomen) the prepuce will be seen as a cone-shaped structure off the ventral abdomen. Frequently the hyperechoic mass of the glans penis will be seen within the prepuce (Figure 18.16). It is

Vet-ebooks.com

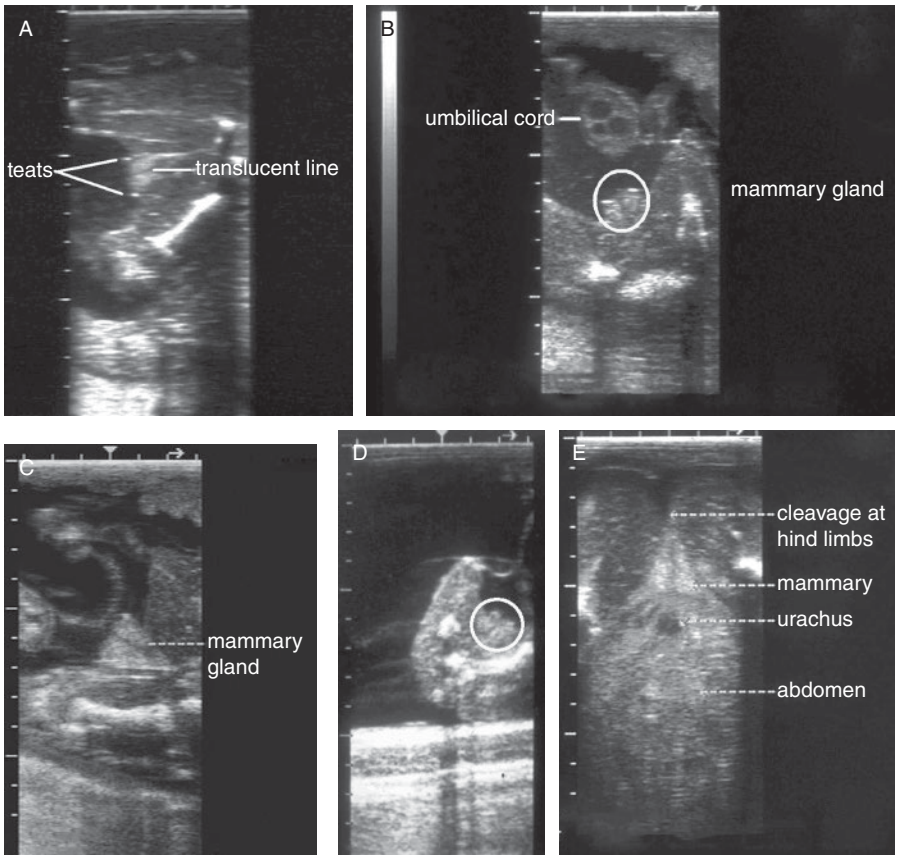


Figure 18.21 (A) Filly, 124 days of gestation. (B) Filly, mammary gland within white circle. (C) Filly, 129 days of gestation. (D) Filly, mammary gland within white circle. (E) Filly, 134 days gestation, Plane I view.

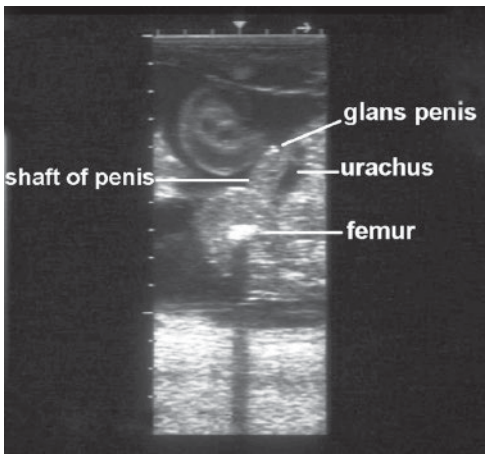


Figure 18.22 Sagittal view of colt, 109 days of gestation.

possible to get a plane III view of the glans penis without any of the prepuce in view (the glans penis frequently protrudes out the front of the prepuce). This will appear as a hyperechoic mass off the ventral abdominal wall just posterior to the umbilical entrance into the abdominal cavity (Figure 18.16C). The main marker to be utilized is the prominent ventral midline (Figure 18.11).

If the external genitalia is difficult to differentiate, an examination of the gonads using color Doppler may be helpful. The gonads can readily be seen but in the authors opinion should be used to support a diagnosis and not to make a diagnosis. The male gonads usually appear very homogeneous (Figure 18.23), whereas the female gonads have a central dense area surrounded by a more translucent cortical ring. Color Doppler will exhibit a central vein and a localized peripheral pampiniform plexus mass of color in the male. The female will exhibit a peripheral ring of color in the cortical area of the gonad (Figure 18.24). This requires an ultrasound machine with adequate sonographic technology and a practitioner with adequate experience. These can be difficult determinations and in the author's opinion are not reliable for a diagnosis by themselves.

Procedure for Transabdominal Scan Post 150+ Days

Mares usually do not object to transabdominal ultrasonography. At times the transabdominal examination can be a lengthy procedure. Do not hesitate to sedate the mare if she becomes uneasy. Alcohol is applied

Vet-ebooks.com

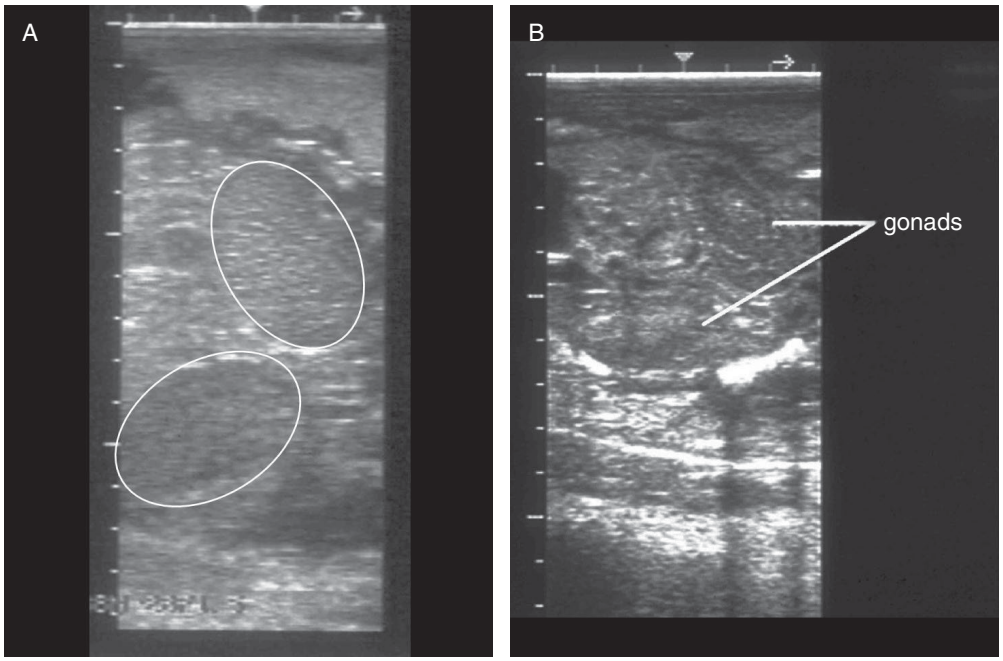


Figure 18.23 (A) Colt, 130 days of gestation. Gonads (circled) have homogeneous appearance. (B) Filly, 119 days of gestation. Female gonads have a central dense area surrounded by a more translucent cortical ring.

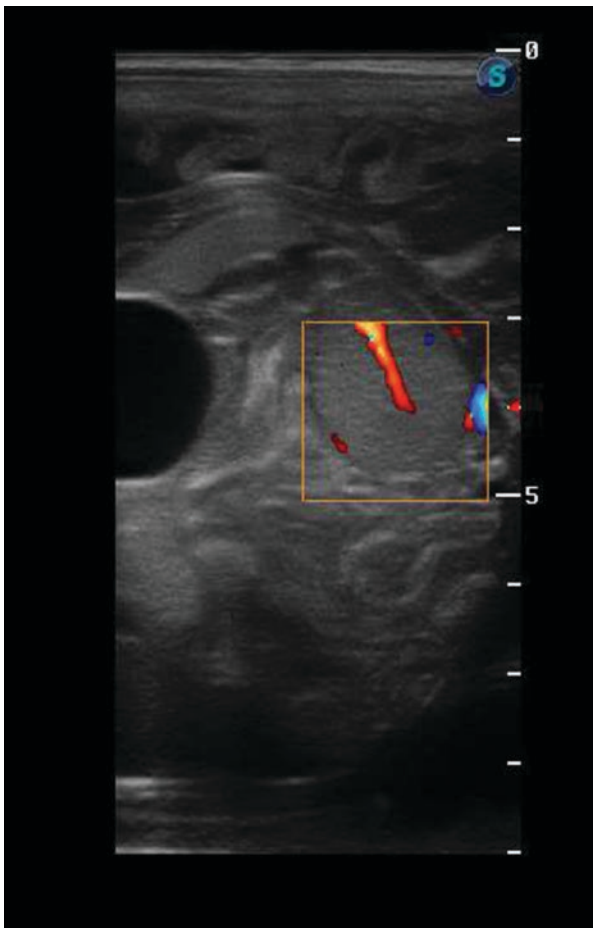


Figure 18.24 (A) Colt, homogenous texture with central vein.

liberally over the ventral midline of the mare's abdomen. Lubricant can be used to enhance coupling. It is good to have a stool to sit on during the examination.

Scan the entire mare abdominal ventral midline until the fetus is located. When the fetus is located, locate the beating heart then proceed posteriorly on the fetus. Locate the umbilical entrance to the abdominal wall (Figure 18.15). The transducer must be manipulated in many different directions to expose recognizable anatomic structures. Moving very slowly, look for a hyperechoic mass (glans) just posterior the umbilicus. If nothing is seen, slowly proceed posteriorly until the area of the posterior abdominal midline between the hind legs is evident. A prepuce, glans, and penis in the male (Figure 18.13D) or the triangular mammary gland and teats in the female will be on this midline (Figure 18.21A). If nothing is definitely identifiable proceed along the fetal ventral midline between the hind legs to the tailhead. The clitoris can be seen on the midline in a female before the tailhead is reached. At this stage of gestation the external genitalia are large and can be seen but it is often difficult to distinguish between a mammary gland and a prepuce. The prepuce will have varying degrees of a hyperechoic glans and penis (Figures 18.13B, 18.13C, 18.13D, and 18.13E), whereas a triangular mammary gland will have no definite hyperechoic area except for two small hyperechoic teats (Figure 18.21A). The triangular mammary gland will be more dense and echoic than the surrounding tissue. Frequently, the two

Vet-ebooks.com

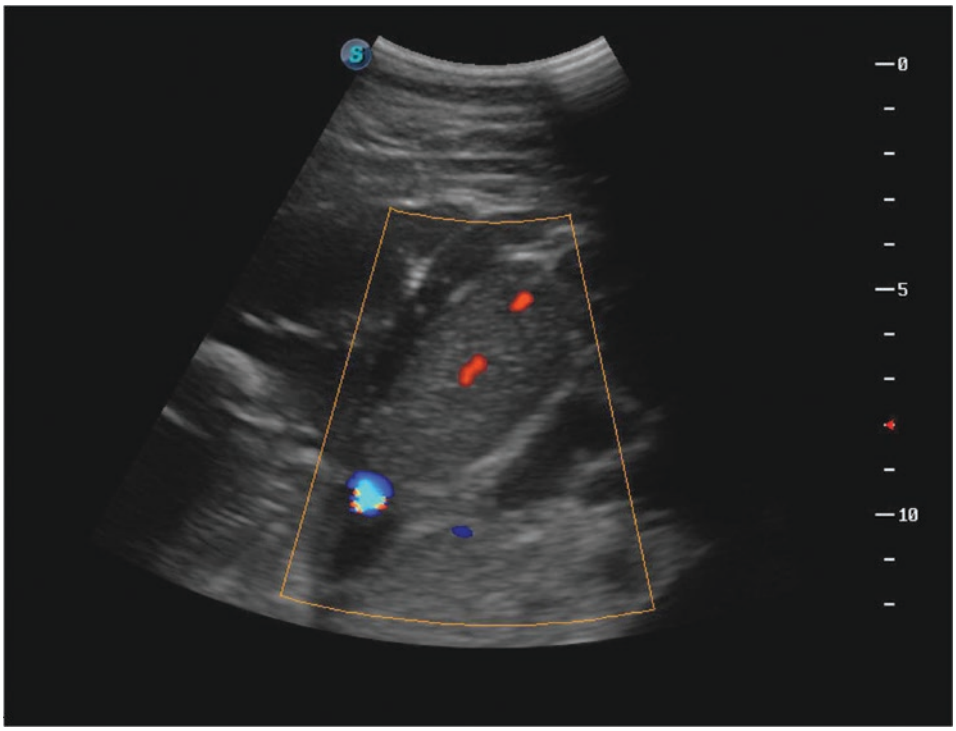


Figure 18.24 (B) Colt, homogeneous texture with central vein and pampiniform plexus.

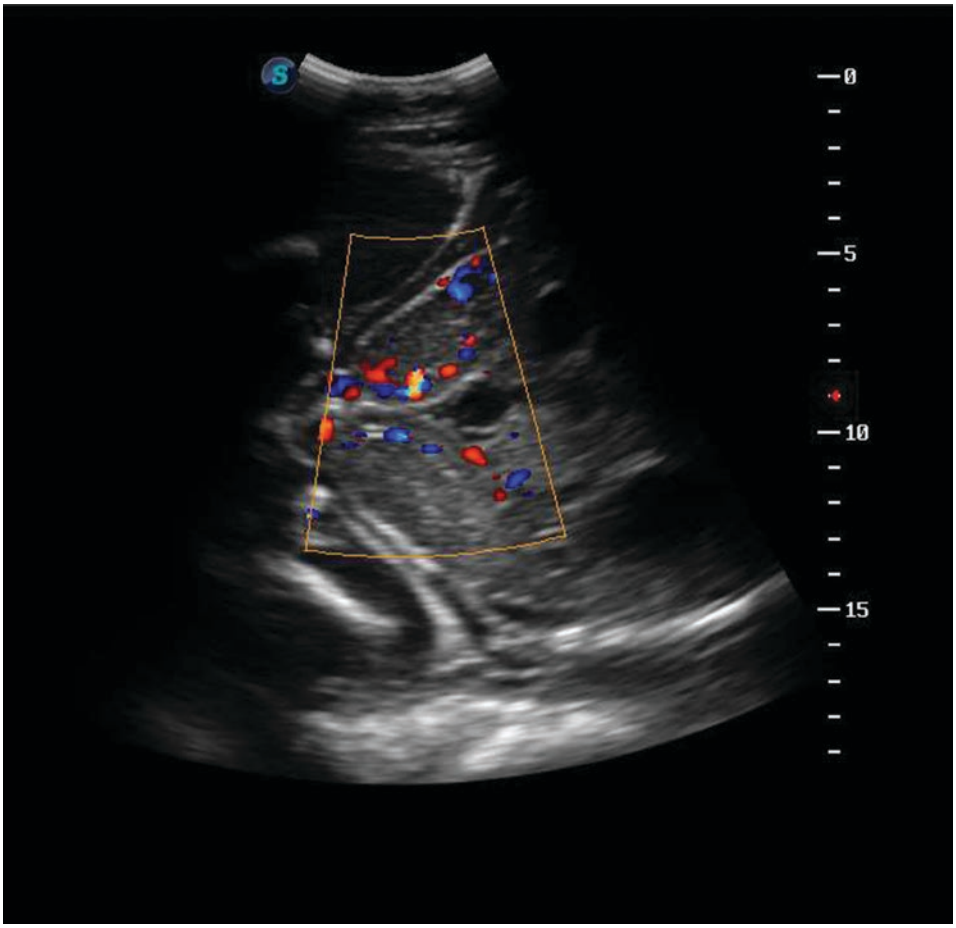


Figure 18.24 (C) Filly, with the junction between cortex and medulla highlighted with Color Doppler.

Vet-ebooks.com

halves of the mammary gland are divided by a translucent line (Figures 18.21A, 18.21B, 18.21C, 18.21D, and 18.21E). These scans are difficult at first and may take considerable time. Trying different sides of the mare sometimes gives better exposure if the posterior fetus is not on the midline. This also allows switching and resting of the arms handling the transducer.

Post 150 days, is not the preferred time to do fetal sexing. However, clients sometimes decide at a later date that it needs to be done. Days 60–70 is still the optimum time to do the sexing: it is quicker and easier for the mare and the practitioner and cheaper for the client!

CAUTION!!

Do not issue a certificate indicating the sex with a plan to reexamine the mare at a later date to verify your diagnosis. If the farm receives a certificate, they may not feel it is necessary to verify the diagnosis and a mistake could be made. Issue certificates only when you are 100% certain of your diagnosis and no subsequent examinations are needed.

Recommended Reading

Ginther, O.J. (1985). *Ultrasonic Imaging and Animal Reproduction: Horses*. Cross Plains, WI: Equiservices.

Ginther, O.J., Curran, S., and Ginther, M. (1995). *Fetal Gender Determination in Cattle and Horses (Video)*. Cross Plains, WI: Equiservices. (Instructional video available from Equiservices, 4343 Garfoot Road, Cross Plains WI, 53528 (telephone 608-798-4910)).

Holder, R.D. (1997). *A Guide to Equine Fetal Sexing 55–150 Days*. (Instructional video available from Hagyard Equine Medical Institute, 4250 Iron Works Pike, Lexington, KY, 40505 (telephone 859-255-8741)).

Holder, R.D. (2001). Sex determination in the mare between 55–150 days gestation. *Proceedings of the 46th Annual Convention of the American Association of Equine Practitioners* 46: 321–324.

Holder, R.D. (2003). Determination of fetal gender. In: *Current Therapy in Equine Medicine*, 5th edn (ed. N.E. Robinson), Chapter 52, 288–294. Philadelphia, PA: Saunders.

Holder, R.D. (2007). Fetal sex determination. In: *Current Therapy in Equine Reproduction* (ed. J.C. Samper, J. Pycock, and A.O. McKinnon), Chapter 53, 343–356. St Louis, MO: Saunders Elsevier.

Holder, R.D. (2011). *Equine Reproduction*, 2nd edn (ed. A.O. McKinnon, E.L. Squires, W.E. Vaala, et al.), Chapter 218, 2080–2093. Oxford, UK: Wiley Blackwell.

Vet-ebooks.com

19

Use of Ultrasonography in Fetal Development and Monitoring

Stefania Bucca

Equine Veterinary Medical Center, Doha, Qatar

Introduction

During the last three decades, the equine breeding industry has enjoyed major advancements in reproductive efficiency, due to improvements in stallion and mare management, in addition to veterinary research and intervention. Most innovations have resulted in the development of assisted reproductive technologies, aimed at improving gamete harvesting and handling, embryonic development, and ultimately conception rates. In spite of much emphasis being placed on early embryonic life, pregnancy monitoring in the mare remains a neglected area of reproductive surveillance and, once passed 60 days pregnancy, gestational profiling of the mare is generally disregarded, unless emergency circumstances require it. Additionally, the literature offers limited information on the pathophysiology of adverse gestational conditions. Resultingly, the interpretation of unfavorable pregnancy outcomes often remains, at best, speculative.

Ultrasound technology represents the most reliable, non-invasive tool for pregnancy evaluation in the mare and a complete sonographic profile of the feto-placental unit provides a very informative basis for the assessment of fetal well-being. Fetal well-being and optimal development are suggestive of a highly functional placenta, efficient feto-maternal exchange pathways, and a sound genetic component. But in the presence a low viability fetus (i.e., stunted growth, decreased levels of activity, sustained cardiac rhythm, and frequency abnormalities), it may be challenging to identify the initial source of fetal compromise, as the three compartments (fetal, placental, and maternal) are intricately connected by a network of vascular, biochemical, and hormonal signals. Maternal medical conditions and underlying endocrine disorders may further complicate the interpretation of findings.

The need for additional diagnostic tools, elucidating some of the mechanisms compromising fetal well-being, has resulted in the application of Doppler technology to a number of feto-maternal vascular structures. A similar trend has been applied for decades to the human pregnancy, where screening for feto-maternal Doppler velocimetry parameters is carried out at set intervals throughout gestation.

Pregnancy Database

Mares at risk of a complicated pregnancy and/or delivery should have a minimum data base established, through the collection of historical, biophysical, and biochemical parameters. Medical and reproductive histories of the mare aid in determining current and recurrent gestational threats, in order to formulate a monitoring plan for that pregnancy. Evaluation of feto-placental compromise, as well as the response to treatment, commonly requires sequential examinations of the pregnant mare and assessment of several factors, including biophysical and biochemical traits. Biophysical parameters are generally obtained by means of ultrasonography and fetal electrocardiography, while hormonal profiling, mammary secretions, and

Atlas of Equine Ultrasonography, Second Edition. Edited by Jessica A. Kidd, Kristina G. Lu and Michele L. Frazer.
© 2022 John Wiley & Sons Ltd. Published 2022 by John Wiley & Sons Ltd.
Companion Website: www.wiley.com/go/kidd/atlas

Vet-ebooks.com

fetal fluid analysis represent the biochemical parameters more frequently evaluated.

Real-time ultrasonography (US) provides a non-invasive means to assess feto-placental parameters throughout gestation. Different circumstances require US evaluation of the pregnancy in equine practice:

- Elective feto-placental evaluation of pregnant mares with histories of previous complicated gestations, in order to identify early signs of derangement in fetal growth, development, and responsiveness [1–9].
- Routine scanning of term mares, carried out on some breeding farms, to assess fetal presentation, aiming at implementing strategies for a safe delivery, when abnormalities are detected [7,10].
- Emergency feto-placental evaluation, performed when gestational complications or maternal disease are present and fetal distress/compromise may be anticipated [11–15]. Under these circumstances, clinicians are often requested to assess fetal viability and formulate a prognosis on pregnancy outcome, on the basis of findings.
- Twin reduction by intracardiac/intra-thoracic injection (procaine penicillin), carried out at around 4 months gestation, via ultrasound guided transabdominal puncture with a spinal needle [16]. Viability of each individual fetus should be assessed prior to reduction, in order to select the least viable co-twin to undergo procedure.
- Twin reduction by cranio-cervical dislocation of one fetus is performed between 60 and 120 days and requires assessment of fetal viability both prior to and after procedure [17].
- Fetal sexing can be carried out up to 8 to 9 months of gestation, until fetal hind limbs become engaged into the pregnant horn, preventing adequate visualization. Equine fetal gender can be determined transrectally up to 4 months gestation and then by transabdominal scanning [18–21].
- Some fetal congenital abnormalities may be identified during the course of routine late gestational scans

Imaging of the Equine Pregnancy

Ultrasound assessment of the feto-placental unit aims at ensuring the following conditions:

1) Adequate growth and development
2) Appropriate levels of activity and responsive patterns
3) Adequate environment

Equipment

Full investigation of feto-placental well-being requires a combination of transrectal and transabdominal techniques [15]. The quality of image obtained by transabdominal ultrasonography prior to day 100 of gestation is usually of little diagnostic value.

Linear array transducers are most commonly used for transrectal ultrasonography, due to the wide popularity among clinicians in the reproductive field, ease of transducer orientation within the narrow equine pelvis, and image interpretation.

Dedicated 5 to 8 MHz transducers or multi-frequency (6–10 MHz) probes provide adequate transrectal imaging. High frequencies (7.5–10 MHz) are required when detailed structural studies are carried out, as for cervical assessment and measurement of the combined thickness of the utero-placental unit (CTUP).

Sector and convex technologies best suit transabdominal ultrasonography. Linear technology may be employed by this route, but linear transducers are less likely to obtain good contact to the mare's abdominal wall. Transducer frequencies ranging from 2–6 MHz are required to image the fetus up to term and 5–8 MHz to obtain detailed studies of the utero-placental unit.

Patient Preparation and Technique: Transrectal Approach

Transrectal ultrasonography should always be performed at any stage of gestation to evaluate the caudal aspect of the gravid uterus. Mares are best examined restrained in stocks to ensure safety of equipment and operator. Chemical restraint should be avoided as it tends to displace the uterus forward, away from the operator's hand. The rectal ampulla is evacuated and the uterus palpated as far forward as it can be reached, to evaluate its content, distension, and cervical tightness and length. Gentle ballotment of the uterine body will reveal the presence of fetal parts, depending on stage of gestation, fetal presentation, and proximity of the fetus to the operator's hand. The US transducer is then placed into the rectum as far as the operator's arm can reach and, as it is withdrawn, palpation findings are confirmed and further investigated.

Parameters to be assessed by transrectal examination include: cervix, combined thickness of the utero-placental unit (CTUP) at the cervical pole, amnion, fetal fluids and fetal eye, bi-parietal diameter, and fetal peripheral pulses (carotid pulse) when the fetus is in anterior presentation.

Vet-ebooks.com

Patient Preparation and Technique: Transabdominal Approach

Transabdominal evaluation of the equine pregnancy can be successfully carried out from day 100 gestation to term. In the summer months, the fine coat of some breeds will make clipping and shaving quite facultative and liberal application of alcohol and US gel allows sufficient contact for adequate US imaging. In breeds with coarser coats and in colder months, clipping will become necessary, sometimes followed by close shaving or application of hair-removing creams. The area to be prepared for scanning should be brushed and washed first to remove mud and manure soiling the hair. Alcohol may be irritating on clipped skin and mineral or vegetable oils may be a better coupling medium, when frequent scanning or prolonged periods of fetal monitoring can be anticipated. The transducer should be adequately protected, particularly if mineral oil is used. In mid to late gestation, clipping should extend from the mammary gland to the xiphoid area of the sternum ventrally and should follow two curved lateral lines outspreading to each mid abdomen, while reaching from stifle to sternum. More conservative clipping may be carried out up to mid gestation, particularly with young, primiparous mares. The boundaries of the gravid uterus within the mare's abdomen vary depending on gestational age, parity, and uterine dynamics. Mares should be adequately restrained in stocks, in quiet and relaxed surroundings. Stocks with "split" lateral doors serve best for this purpose, as the bottom half door will protect the operator from the mare's lower limbs. Excessive maternal anxiety may have fetal implications in terms of heart rate accelerations.

Sedation of mares subjected to US examination for fetal well-being assessment should be avoided, as administration of sedatives, though well tolerated by the gravid mare [22], will depress fetal activity, cardiac frequency [23], and reactivity. The US unit should be placed at operator's eye level, in dim light, and close enough to maintain easy access to the keyboard. The cranio-caudal orientation of the US probe should be determined. US gel is applied over the transducer's head and scanning will commence over the midline, from the mammary gland to the xiphoid process of the sternum, until fetal parts and fluids are encountered. Parasagittal scans are then performed to delineate the boundaries of the pregnancy within the mare's abdomen. Transverse scans will further localize the fetus and identify the ribcage and the cardiac area; the probe head is then oriented parallel to the fetal spinal cord. Fetal presentation and position are determined. Once fetal orientation has been identified, US investigations of anatomical structure and physiological events may commence.

Adequate Growth and Development

Intrauterine growth restriction (IUGR) has been defined as a deviation from (or a reduction in) expected fetal growth and is caused by multiple adverse conditions, inhibiting fetal growth potential [24]. Foals affected by IUGR represent a high risk group because of cumulative adverse effects on intrauterine survival, delivery, and post-natal adaptation, that could affect them later in life [25,26]. The presence of multiple fetuses implies a variable degree of IUGR. Several parameters can be measured to estimate fetal size in order to identify growth trends and developmental patterns. Orbital diameters/eye volume, aortic diameter, biparietal diameter and, to a lesser extent, fetal chest and femur length have all been reported as useful indicators of fetal growth. Due to their size, the latter two parameters cannot be consistently measured in full, particularly in late gestation. The aortic diameter correlates to fetal size more efficiently than other fetal structures and reference values for different gestational ages are available in the literature [26].

Orbital Diameters/Eye Volume

The fetal eye is best assessed by transrectal ultrasonography, when the fetus is in anterior presentation. Greater detail can be obtained by this route. Several studies have demonstrated a linear correlation between orbital measurements/eye measurements/eye volume and gestational age [15,26,27]. Only in late gestation, fetal eye measurements seem to plateau [9], indicating restricted growth until foaling.

No correlation though could be established between fetal eye measurements and weight of the neonate at birth. Asymmetrical IUGR may occur in mid to advanced gestation, with the fetus experiencing relatively normal head growth, resulting from preferential circulation to vital organs (brain and heart), but its body weight and somatic organs may be seriously reduced in size. Fetal eye measurements should be taken from still sonograms of the entire orbital area, when the lens is visualized (Figure 19.1). Two perpendicular diameters are measured and their sum recorded. Several measurements are taken and the average recorded for future reference.

Vet-ebooks.com

Eye volume is calculated as follows: eye width × eye width × eye depth [9].

Aortic Diameter

Fetal aorta can be imaged per rectum only up to mid gestation. The aortic diameter should be assessed on a longitudinal scan, close to the base of the heart, just past the aortic arch (Figure 19.2), dorsal to the trachea and its bifurcation (Figure 19.3), in close proximity to the spinal cord, within the left hemithorax (Figure 19.4). Measurements should be taken during systole and a "cine recall system" proves extremely useful in obtaining the appropriate cardiac timing, particularly when FHR frequencies are elevated. Although the two vessels both traverse the fetal chest in a cranio-caudal direction, the aorta should be distinguished from the vena cava by its echodense walls, marked pulsatile activity, and the more dorsal course within the thorax, close to the spinal cord. As many as five measurements should be obtained during the course of one examination and the average calculated.

Biparietal Diameter

The fetal head is identified by transrectal or transabdominal ultrasonography and the image is frozen when the maximal cross-sectional area of the skull is obtained [28], just above the temporo-mandibular joints (Figures 19.5, 19.6, and 19.7).

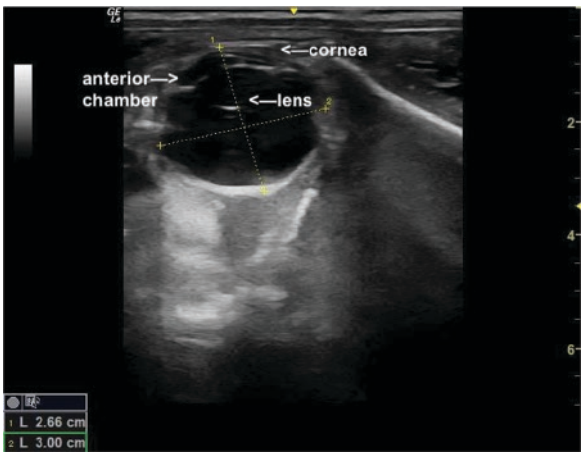


Figure 19.1 Transrectal linear sonogram of a fetal eye, 211 days gestation. Measurements of the orbital diameters were taken from a still image, when the lens was visualized.

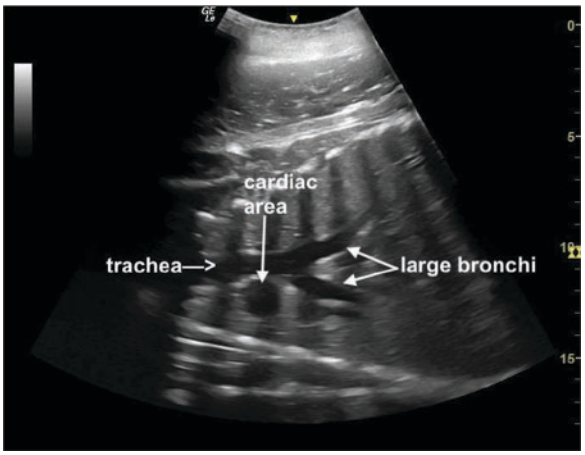


Figure 19.3 Transabdominal convex sonogram of a 227-days-old fetus, showing the cranial chest ventral to the aorta, where the trachea bifurcates into the major bronchi.

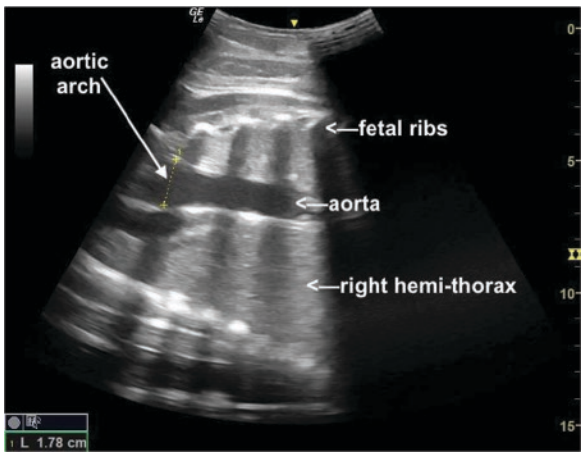


Figure 19.2 Transabdominal convex sonogram of a 234-days-old fetus, showing the cranial chest and aorta. Measurements of the aortic diameter were taken as the aorta emerges from the cardiac area, past the aortic arch.

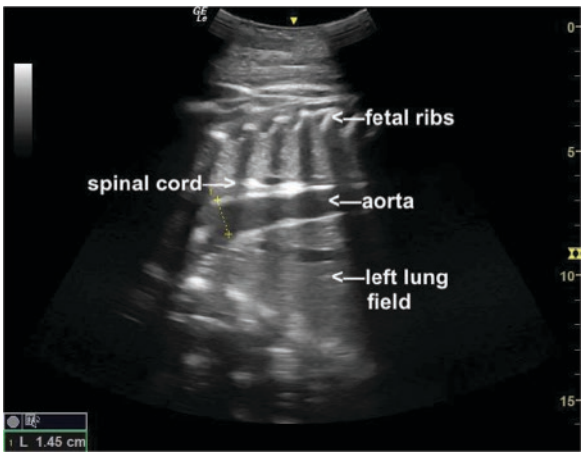


Figure 19.4 Transabdominal convex sonogram of a 215-days-old fetus, showing the cranial chest, with a longitudinal view of the aorta within the left hemithorax, in close proximity to the spinal cord.

Vet-ebooks.com

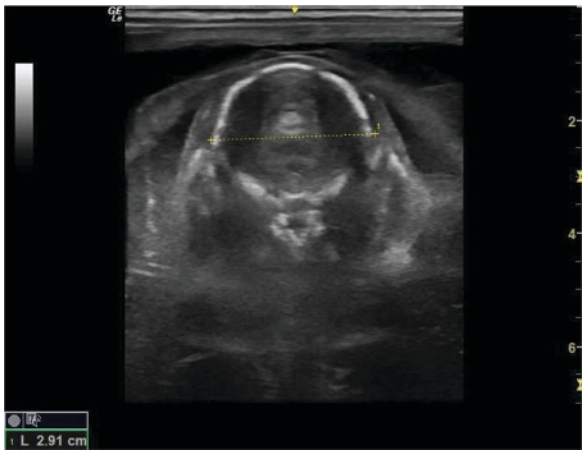


Figure 19.5 Transrectal linear sonogram of a fetal skull, 121 days gestation. The bi-parietal diameter is measured at its widest point, between the two temporo-mandibular joints.

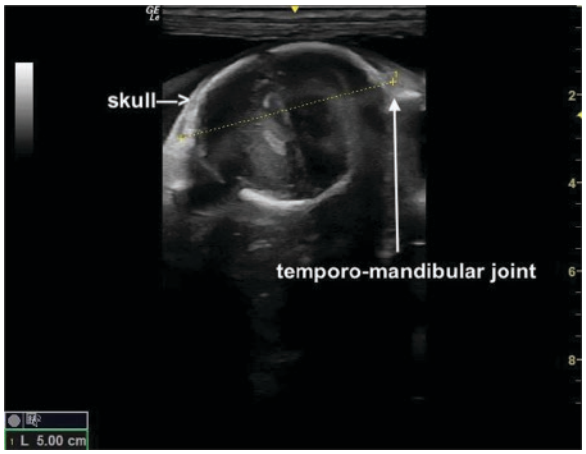


Figure 19.6 Transrectal linear sonogram of a fetal skull, 212 days gestation. The bi-parietal diameter is measured at its widest point, between the two temporo-mandibular joints.

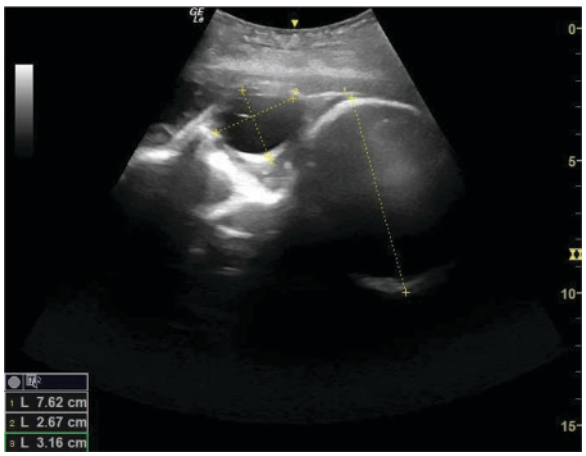


Figure 19.7 Transabdominal convex sonogram of a 244-days-old fetus showing the head, where the eye and the skull can be identified.

Appropriate Levels of Activity and Responsive Patterns

Fetal activity is required to promote antenatal body strength and motion, to assure successful postnatal adaptation, and represents one of the most sensitive indicators of fetal viability, in association with fetal heart rate (FHR), FHR reactivity, and fetal tone. FHR accelerations and decelerations depend on a functional central nervous system (CNS) and occur in response to environmental alterations and fetal activity.

Fetal Heart Rate (FHR) and FHR Reactivity

FHR and FHR reactivity represent the most sensitive indicators of fetal well-being. FHR reactivity indicates changes in cardiac frequency, occurring in response to different stimuli. FHR declines as gestation progresses and increases during activity in the healthy, responsive fetus.

Recordings of FHR are obtained by M-mode echocardiography. The fetal cardiac area is identified within the thorax (Figure 19.8) and multiple assessments of FHR and rhythm are made by placing the M-mode cursor over cardiac structures displaying the most dynamic range of excursion (Figure 19.9). This will help to obtain high-quality tracings, where heart rate can be easily calculated and rhythm objectively evaluated. FHR is automatically calculated by the cardiac calculation package, in-built in the US unit.

Several FHR tracings are recorded, both at rest and after activity throughout the course of the examination. Recordings during fetal activity may be quite

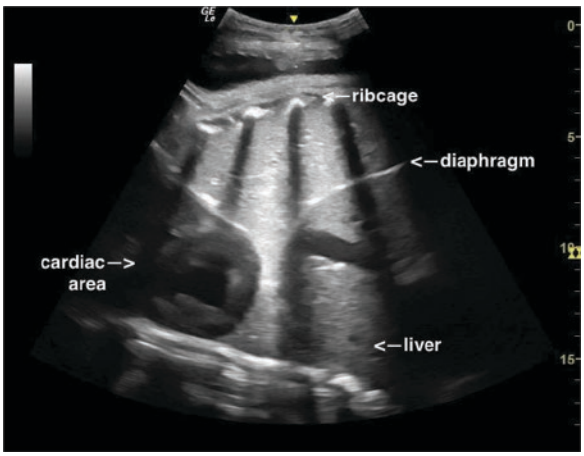


Figure 19.8 Transabdominal convex sonogram of a 268-days-old fetus, showing the chest, the cranial abdomen, and the diaphragm.

Vet-ebooks.com

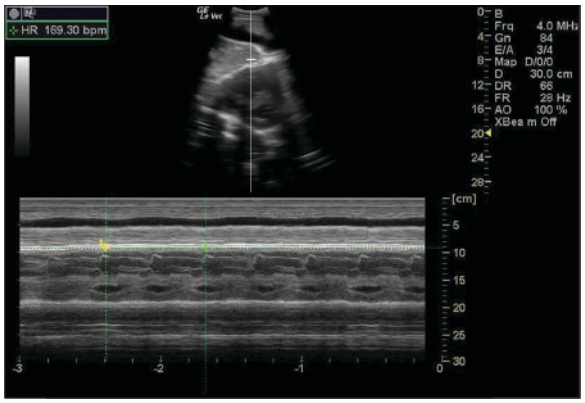


Figure 19.9 Transabdominal convex sonogram, showing an M-mode tracing of cardiac activity, taken from a 279-days-old fetus with tachycardia, while its dam was being treated for acute colic.

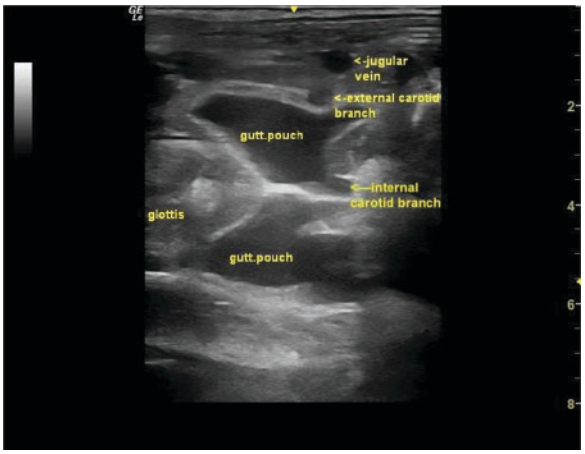


Figure 19.10 Transrectal linear sonogram of the throat area of a 224-days-old fetus. The external and internal carotid branches are identified over the upper guttural pouch.

challenging to obtain, as the fetus tends to move in and out of the angle of incidence of the M-mode cursor. FHR accelerations of 25 to 40 beats per minute (bpm) for approximately 30 seconds are usually recorded during activity. Movements without FHR accelerations may be observed and accelerations in the absence of stimuli are occasionally detected (5% incidence). Sustained tachycardia [23] or a large range of FHRs may indicate fetal distress, but could be brought on by painful maternal conditions or systemic disease. Sustained bradycardia [23,29,30], inappropriate FHR for gestational age, or lack of heart rate reactivity suggests CNS depression, probably attributable to hypoxia and may indicate impending fetal demise.

Asystole may be detected by transabdominal ultrasound in association with lack of activity. Fetal cardiac rhythm is usually regular, and cardiac arrhythmias [29] are commonly associated with a negative outcome.

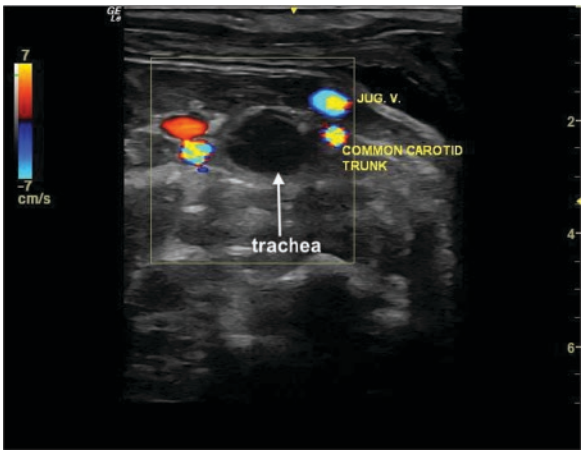


Figure 19.11 Transrectal, linear, color Doppler sonogram of the cross-sectional upper neck of a 230-days-old fetus, showing the position of the jugular veins and the carotid arteries (common carotid trunk), in relation to the trachea.

Peripheral Pulses

The external carotid can be evaluated transrectally in the fetus in anterior presentation, when the head and upper neck are visualized. A distinct pulsatile activity may be observed as the external carotid artery courses over the lateral compartment of the ipsilateral guttural pouch. The dark background offered by the guttural pouches, filled with fetal fluids, provides an ideal contrast to the hyperechoic wall of the artery (Figure 19.10). The common carotid trunk can be identified by B-mode and color Doppler ultrasonography in close proximity to the fetal trachea and the jugular vein, in longitudinal and cross-sectional views of the neck (Figures 19.11, 19.12, 19.13, and 19.14). M-Mode or Doppler technology may be used to obtain pulse/spectral tracings and calculate frequency. A direct correlation of peripheral pulses and fetal heart rate has been demonstrated [31]. Assessment of peripheral pulses provides an easy and effective instrument for transrectal field evaluation of fetal well-being in late gestation, when anterior presentation prevails. The fetal thyroid can be identified on each side of the upper trachea, medial to the carotid artery (Figure 19.14).

Fetal Activity

Fetal activity and tone reflect CNS function and development, with decreased activity and declining muscular strength resulting from depressed CNS function. Activity is required to ensure satisfactory muscular development and skeletal joint function, to

Vet-ebooks.com

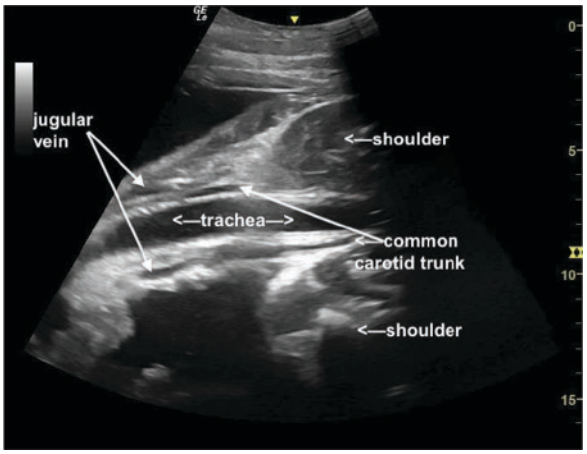


Figure 19.12 Transabdominal convex sonogram of a 234-days-old fetus, with a longitudinal view of the neck, displaying the position of jugular veins and carotid arteries in relation to the trachea.

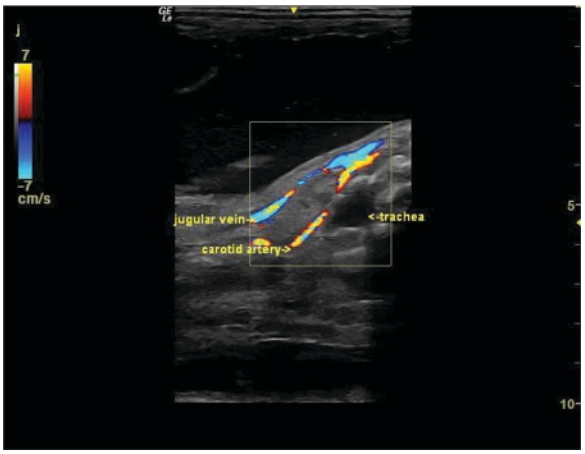


Figure 19.13 Transrectal, linear, color Doppler, longitudinal sonogram of the neck of a 183-days-old fetus, showing the position of the jugular vein and the carotid artery (common carotid trunk), in relation to the trachea.

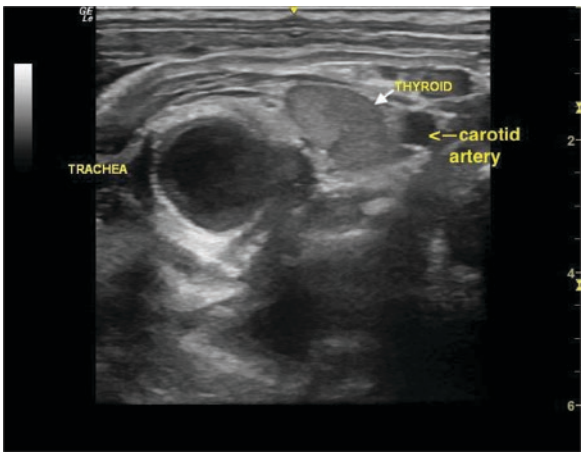


Figure 19.14 Transrectal linear sonogram of the throat area of a 236-days-old fetus, with cross-sectional views of the trachea, thyroid, and carotid artery.

guarantee successful postnatal adaptation. Dormant (inactive) phases are observed at all stages of pregnancy, but are more common and prolonged in late gestation, when they can last up to 60 minutes or longer on occasion. Therefore, caution should be used in the interpretation of fetal activity, and reassessments are advisable. Lack of fetal movements has been associated with a negative outcome; however, sudden bouts of excessive activity followed by abrupt cessation have also been recorded in fetuses that subsequently died [14]. The healthy equine fetus is usually very active, displaying a whole array of major and fine-tuned movements during episodes of activity. Major fetal movements include rotation along short and long axis and horizontal or vertical whole body shifting within the uterus; sometimes a combination of few of the above may be observed during a single episode of fetal activity. The number of major fetal movements per hour tends to decrease as gestation advances, although a sudden increase in fetal activity is consistently observed 24–48 hrs prior to foaling [8]. A large range of fine-tuned movements may be observed during fetal monitoring sessions, including flexion and extension of limbs, neck and head, nostril flaring, blinking, "suckling activity" (Figure 19.15), tail wagging, etc. Rhythmical breathing movements may be observed in all fetuses in advanced gestation (from 7 months gestation), when the diaphragm and the ribcage are visualized (Figure 19.8). Nevertheless, fetal breathing is intermittent in nature and cannot be consistently evaluated. Fetal breathing implies the synchronous movement of chest wall and diaphragm. Excessive convexity of the diaphragm associated with a disproportionate chest excursion is sometimes observed in distressed fetuses.

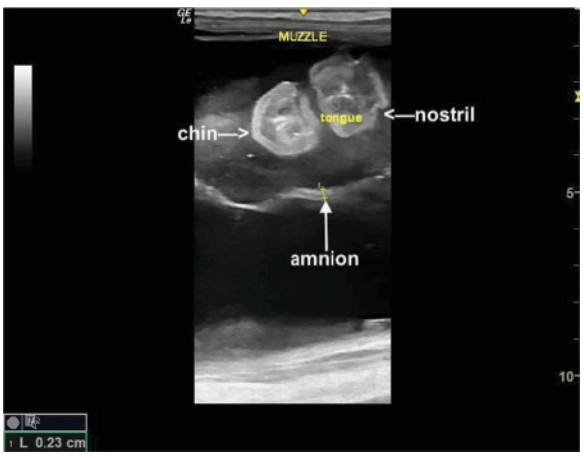


Figure 19.15 Transrectal linear sonogram of the muzzle of a 190-days-old fetus, where nostrils, tongue, and chin can be identified. Minor episodes of activity, such as nostril flaring and suckling motion, are commonly observed from mid gestation to term in this area.

Vet-ebooks.com

Adequate Environment

Evaluation of fetal environment includes assessment of fetal orientation, volume and quality of fetal fluids, combined thickness and contiguity of the utero-placental unit, cervical size and echotexture, and should confirm the presence of a single fetus.

Fetal Orientation: Presentation

Abnormal presentation may cause dystocia and early detection may prevent a serious perinatal crisis, by implementation of specific delivery strategies. A study conducted on 150 light breed horse pregnancies demonstrated that up to 8 months gestation the probability of finding the fetus in anterior presentation were about 50%, in posterior presentation 25%, and in transverse presentation 25% [8]. Under normal circumstances, fetal mobility gradually decreases as gestation advances and, after 9 months gestation, rotation along the short-axis allowing changes in presentation is restricted by fetal body size and the encasing of the fetal hind limbs within the gravid uterine horn [5]. Anterior presentation is easily diagnosed by transrectal ultrasonography, when fetal head structures are identified, in particular, eye, skull, and guttural pouches. The neck of the fetus is frequently flexed, with the head resting on its ribcage (Figure 19.16). Under those circumstances, when transrectal imaging of the head is not possible, identification of the tracheal rings will help confirming anterior presentation (Figure 19.17). Transverse and posterior presentations in advanced gestation may be diagnostically challenging on transrectal examination alone, as only hooves are often visualized on US. Sometimes, segments of the umbilical cord are noticed in the caudal body of the uterus, suggesting the unlikelihood of an anterior presentation, or an abnormally long cord. Multiparous mares carrying a fetus in transverse presentation close to term frequently demonstrate an abnormally shaped abdomen, overstretched crossways. Presentation should be confirmed by a transabdominal scan, whenever a clear interpretation of transrectal findings is not possible. This is often the case in mares with a flaccid pendulous abdomen and mares that sustained ruptures of the abdominal wall or of the pre-pubic tendon in previous pregnancies.

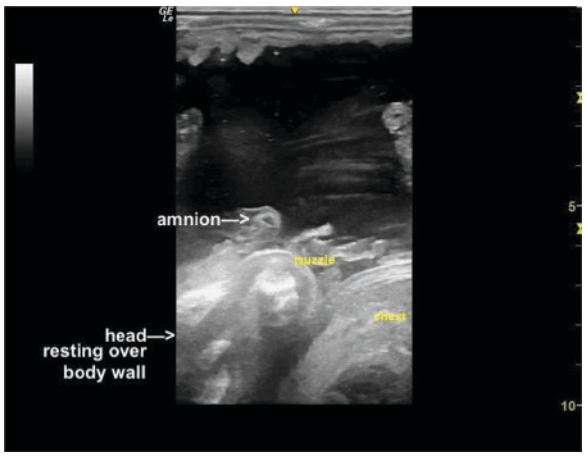


Figure 19.16 Transrectal linear sonogram of a 152-days-old fetus, resting its head against its chest.

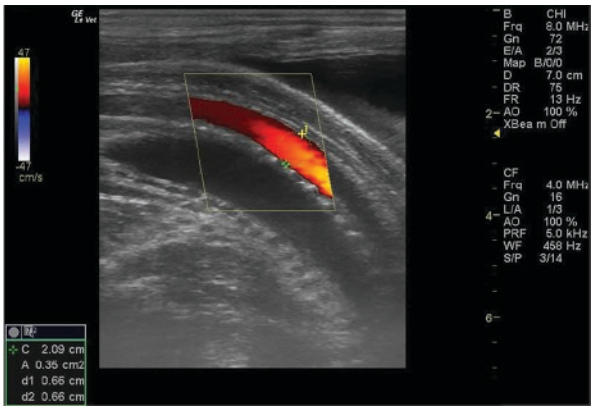


Figure 19.17 Transrectal, linear, color Doppler longitudinal sonogram of the neck of a 243-days-old fetus, showing strong color signal over the common carotid trunk, adjacent to the trachea. The fetal head is not visible as the neck is flexed downward.

Volume and Quality of Fetal Fluids

The equine pregnancy includes an allantoic and an amniotic compartment. Distribution of allantoic fluid is directly related to fetal dynamics and uterine tone, with no preferential area of maximal fluid depth detectable. Amniotic fluid tends to collect more frequently around the cranio-ventral half of the fetus, while the amniotic membrane is usually found in close proximity to the fetal upper body (Figure 19.18). Pathological increase of fetal fluids has been reported to occur in each compartment (hydramnion and hydroallantois) [32–35], placing the fetus at risk of severe compromise. Amniotic integrity should be carefully evaluated in the presence of hydropic conditions, as excessive amniotic fluid may result in amniotic tearing and mixing of fetal fluids from the two communicating compartments (Figures 19.19 and 19.20). Minimal and maximal allantoic and amniotic fluid depth measurements are reported in the literature [7,8] but, as a rule, fetal fluid depths in excess of 22 cm, recorded over several areas of the mare's ventral

Vet-ebooks.com

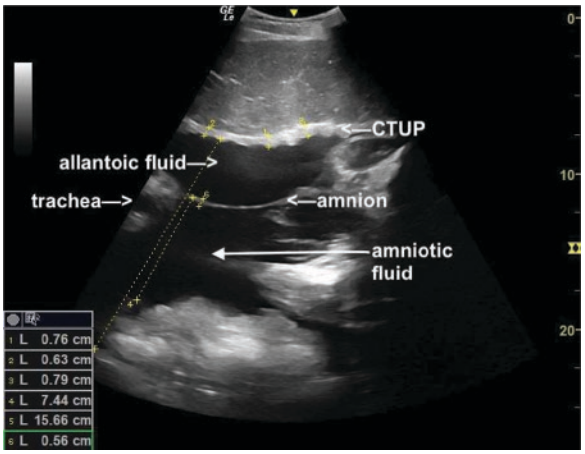


Figure 19.18 Transabdominal convex scan at 268 days gestation, showing a pocket of amniotic fluid, collecting ventral to the fetal neck. Allantoic fluid surrounds the amniotic pouch.

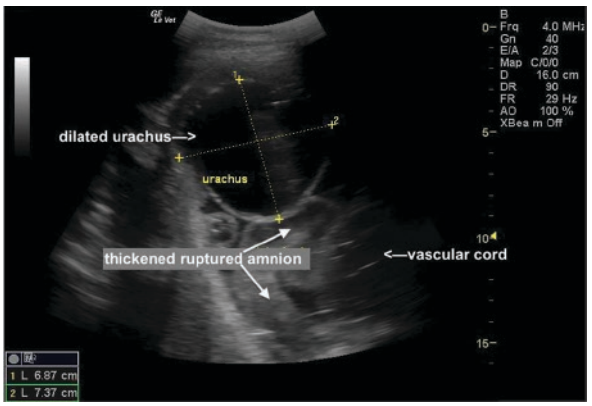


Figure 19.19 Transabdominal convex scan of a mare with hydrops of fetal membranes, at 286 days gestation. A large urachal pouch is impinging over a thickened, ruptured amnion, encasing part of the umbilical cord.

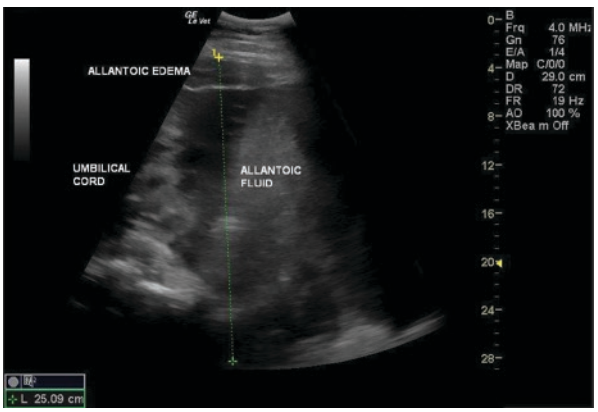


Figure 19.20 Transabdominal convex sonogram at 277 days gestation, showing excessive fetal fluid accumulation, over 25 cm in depth.

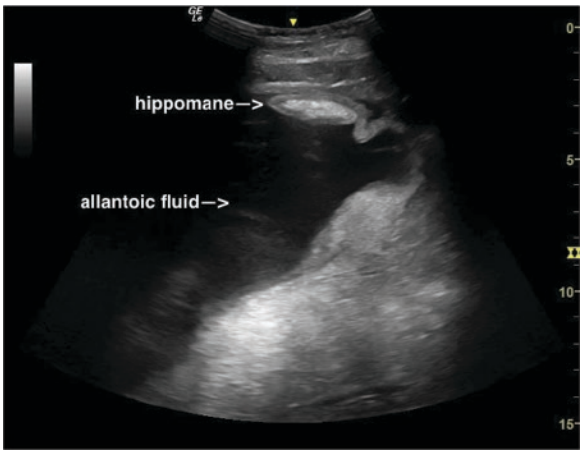


Figure 19.21 Transabdominal convex sonogram in late gestation, showing the hippomane within the allantoic compartment.

abdomen, should be considered excessive and monitored (Figure 19.21). Transrectal findings usually confirm the suspicion of a hydropic condition by identifying marked enlargement of the uterine body, preventing palpation of fetal body parts. Free floating particles (vernix) are commonly observed swirling within fetal fluids and become more visible during episodes of fetal activity, particularly in the amniotic sac. The hippomane is defined as an allantoic calculus and can often be visualized floating within the allantoic fluid, with its typical oval shape and onion like, concentrical structure (Figure 19.21). Sudden release of meconium (fetal diarrhea) in the amniotic compartment may sometimes be observed in highly distressed fetuses just prior to birth, stillbirth, or abortion. Accumulation of a thick layer of sediment in the most ventral areas of the allantois is sometimes observed in association with hydroallantois and when fetal activity is profoundly depressed. Markedly reduced volumes of allantoic fluid (oligohydroallantois) [36] may be observed in mares with severe systemic illness, where the repercussions of maternal malaise result in a decreased fetal urine output. The condition is associate with a poor fetal outcome [36]. Objective assessment of fetal fluid depth requires extensive scanning of the mare's abdomen and is best carried out during phases of fetal quiescence.

Assessment of the Equine Gravid Cervix

A high degree of correlation between cervical size, sonographic appearance, and rectal palpation findings was demonstrated by a 2011 study, conducted on light horse breed mares, carrying uncomplicated

Vet-ebooks.com

pregnancies [37]. The study provided reference parameters on cervical size and echotexture and identified the time when cervical remodeling physiologically takes place, leading to relaxation (Figures 19.22, 19.23, and 19.24). Comparably to the pregnant human cervix, cervical remodeling in the mare is a slow and gradual process, initiating as early as nine months of gestation and taking several weeks to achieve completion. Prior to nine months, the gravid equine cervix shows minimal variation in vertical diameters and echotexture and any substantial deviation should be interpreted as a potential sign of premature cervical relaxation and adequately monitored. Premature cervical relaxation represents a critical predisposing factor in the pathogenesis of ascending placentitis and the associated changes in cervical US parameters precede increases in the combined thickness of the utero-placental unit. Early identification of cervical remodeling at an inappropriate time (prior to nine months gestation), allows for the implementation of strategic measures aimed at preventing the development of ascending placentitis and possibly avoid a gestational crisis [38]. Ultrasonographic cervical assessment should also seek for the presence and extent of non-homogenous echotexture areas involving muscularis, mucosa or lumen, or a combination of them, suggesting previous cervical damage. Segmental, fluid filled, luminal dilations of the pregnant cervix may compromise its competence and potentially lead to ascending placentitis (Figure 19.25). Additional signs of premature cervical ripening include: a) cervical funneling, whereby the allantochorion penetrates the cervical lumen through a dilated cranial cervical

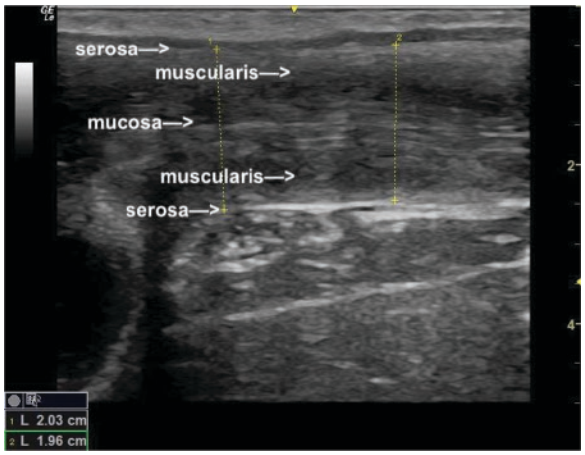


Figure 19.22 Transrectal linear sonogram of the cranial cervix at 250 days gestation, with compact inner striation (mucosa) and homogenous outer layers (muscularis), within the normal range of vertical diameters.

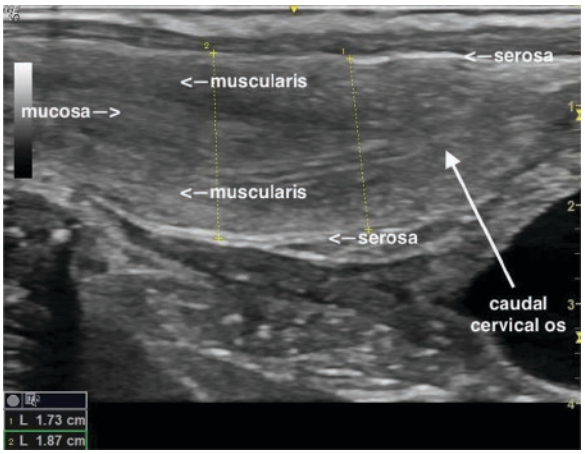


Figure 19.24 Transrectal linear sonogram of the caudal cervical segment, at 250 days gestation, showing compact inner striation (mucosa) and homogenous muscularis layer, within the normal range of vertical diameters.

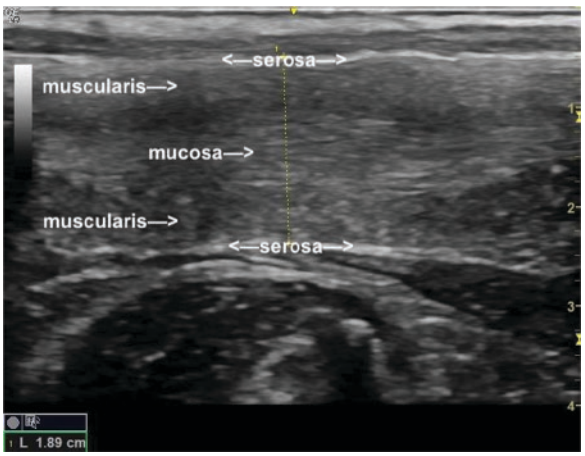


Figure 19.23 Transrectal linear sonogram of the middle cervical segment at 250 days gestation, showing compact mucosa, homogenous muscularis, and hyperechoic serosa.

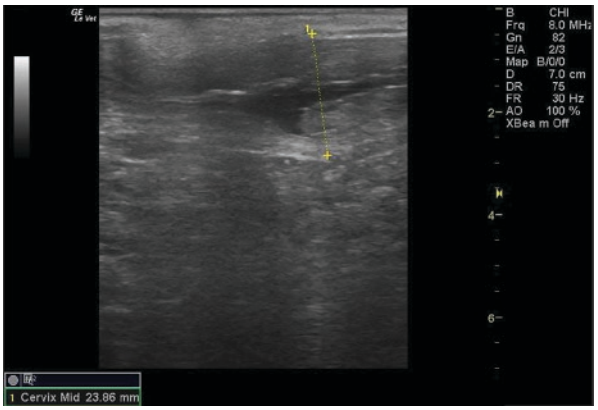


Figure 19.25 Transrectal linear sonogram of the cranial cervix at 232 days gestation, showing disrupted cervical tubularity and a fluid filled, mid-body, segmental dilation. The mare aborted approximately 4 weeks later, with evidence of ascending placentitis.

Vet-ebooks.com

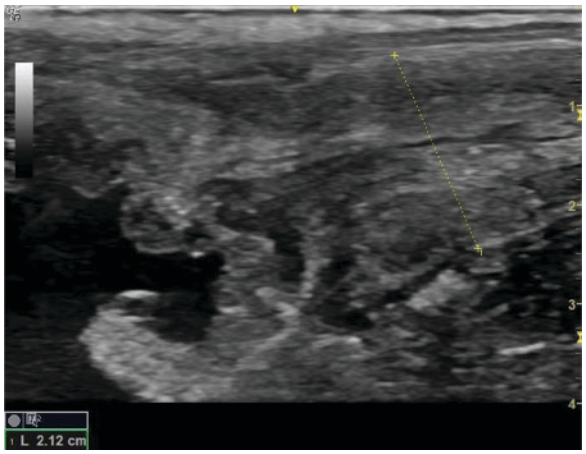


Figure 19.26 Transrectal linear sonogram of the cervix at 227 days gestation, showing cranial cervical funneling and associated allanto-chorial bulging into the lumen.

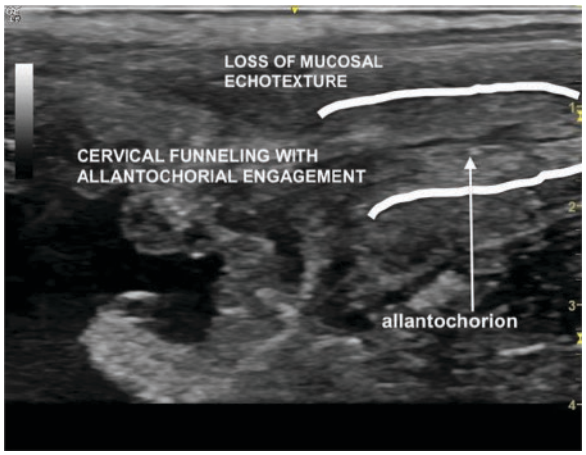


Figure 19.27 Same as Figure 19.26, with highlighted allanto-chorial outline, as it protrudes into the cranial cervix.

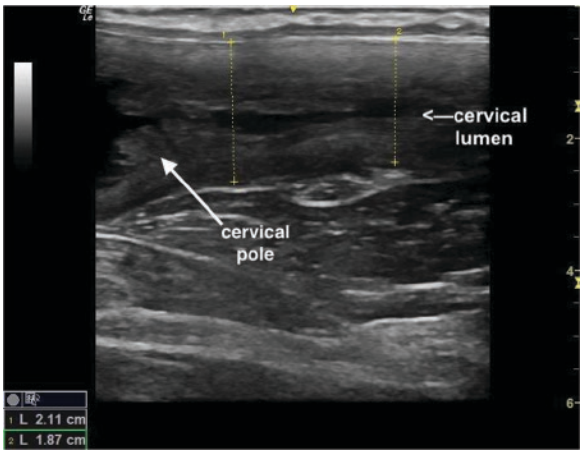


Figure 19.28 Transrectal linear sonogram of the cervix at 244 days gestation, showing loss of allanto-chorial integrity and fetal fluid accumulation within the cervical lumen. The mare aborted approximately 36 hours later.

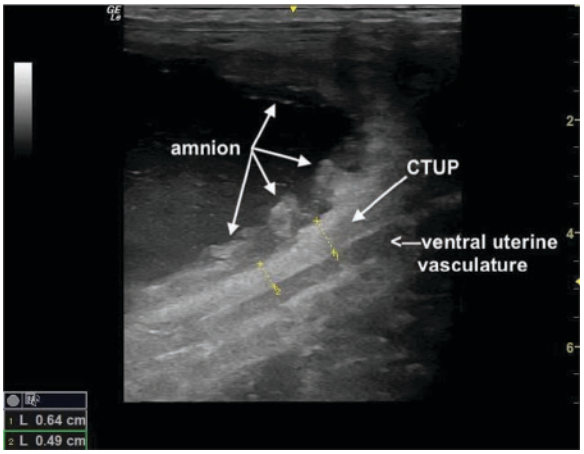


Figure 19.29 Transrectal linear sonogram of the caudal gravid uterus at 250 days gestation, showing measurement of the combined thickness of the utero-placental unit, using the ventral uterine vasculature as landmark; the amnion features in close contact to the allantois.

os (Figures 19.26 and 19.27); and b) the presence of a discrete anechoic line throughout the lumen, indicating rupture of the allantochorion, with escaping allantoic fluid (Figure 19.28).

Combined Thickness and Continuity of the Utero-placental Unit (CTUP)

The need for adequate uteroplacental contact is highlighted by the difficulty mares have at maintaining dizygotic twin gestations. However, small areas of separation of the allantochorion from the uterus are commonly observed in normal pregnancies without any apparent ill effect on the health of the fetus. An average combined thickness of the uteroplacental unit of 1.26 ± 0.33 cm had been initially reported in mares with normal term pregnancies, in light breeds, but wider measurement ranges feature in more recent publications [8,12,39–42]. Measurements should be taken from the caudal aspect of the ventral uterine body, as it merges into the cranial cervical os, avoiding areas of compression of the uteroplacental thickness by the fetus. The uterine ventral vasculature represents a useful landmark to define the lower boundary (Figure 19.29). Several CTUP assessments should be made on each scanning session according to fetal dynamics, as forward displacement of the fetus into the mare's abdomen may create a vacuum effect and transiently increase the CTUP at the cervical pole of several

Vet-ebooks.com

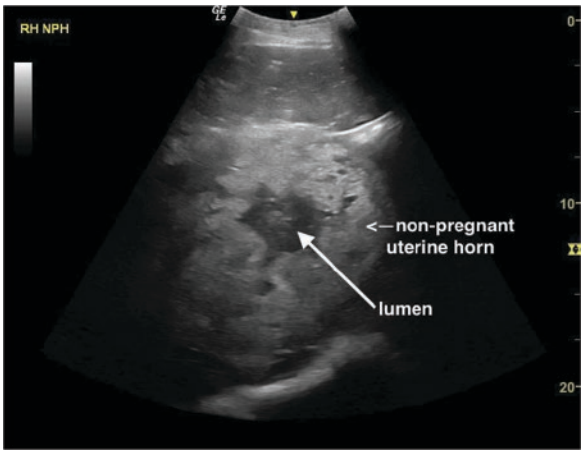


Figure 19.30 Transabdominal convex sonogram at 284 days gestation showing a cross-sectional view of the non-pregnant uterine horn.

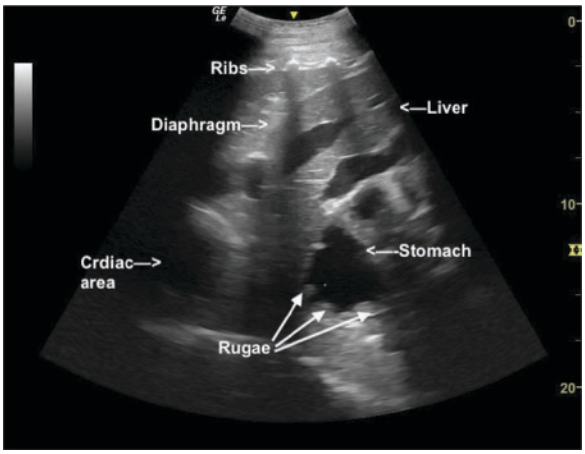


Figure 19.31 Transabdominal convex sonogram of a term fetus, showing cranial abdominal organs, in close proximity to the diaphragm. The stomach displays prominent mucosal rugae. The mare foaled approximately 40 hours later.

millimeters. This is particularly true in aged mares, where the allantochorion may also appear convoluted.

The thickness of the uteroplacental unit is affected by numerous factors, which may reduce the efficiency of placental function. Such conditions include placentitis/degenerative changes of fetal membranes, placental edema, and premature placental separation. Large and/or progressively enlarging areas of placental separation may lead to inefficient exchanges, adversely affecting fetal growth and well-being and often resulting in red bag delivery at parturition.

Abnormally thin uteroplacental units have also been associated with intrauterine growth restriction and poor fetal outcome. Since only the parts of the uterus and placenta in proximity to the ventral abdominal wall can be thoroughly examined (by transabdominal ultrasonography), focal areas of placental abnormality may be missed. The non-pregnant horn has a folded, thickened appearance and, although normal, could be mistakenly interpreted as utero-placental thickening (Figure 19.30). The lumen of the non-pregnant horn is relatively small but may suddenly enlarge to accommodate higher volumes of fetal fluids in response to uterine dynamics and fetal shifting; a marked decrease in CTUP of the non-pregnant horn can be observed under these circumstances.

Other Fetal Organs

Great anatomical detail may be obtained by serial US examination of the equine developing fetus. Spleen and liver can be visualized in the cranial abdomen, adjacent to the diaphragm (Figures 19.31 and 19.32).

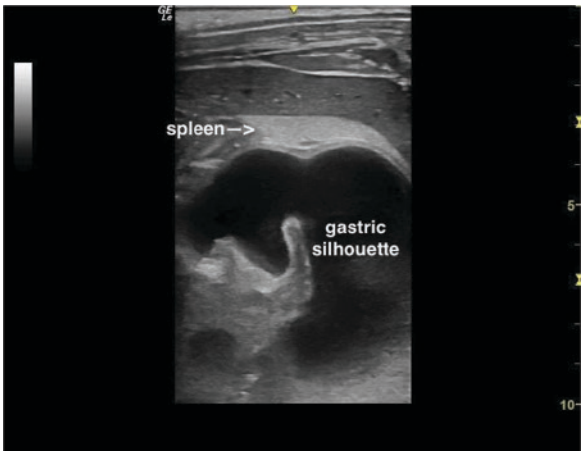


Figure 19.32 Transrectal linear sonogram of the cranial abdomen of a 158-days-old fetus in transverse presentation, featuring stomach and spleen.

The two organs can be easily distinguished by the higher echogenic appearance of the spleen and its close proximity to the gastric outline (Figure 19.32). The stomach is a landmark for fetal orientation and its anechoic, bean-shaped silhouette facilitates fetal orientation in a cranio-caudal fashion, due to its location within the left cranial abdomen and identifies fetal position: left lateral recumbency, with the stomach in close proximity to the transducer's footprint (Figure 19.33) and right lateral recumbency, with the stomach visualized on the opposite half of the abdomen (Figure 19.34). Fetal rotation along its longitudinal axis is confirmed by the sudden change of proximity of the gastric silhouette to the US transducer. Gastric volume increases as gestation advances, to reach a plateau by term. Abnormal gastric filling has been observed in association with hydramnion

Vet-ebooks.com

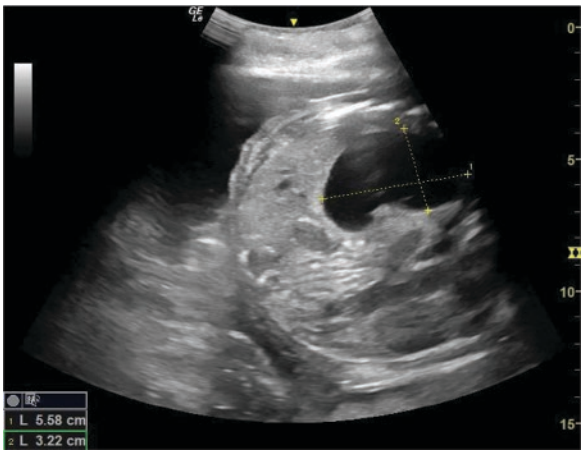


Figure 19.33 Transabdominal sonogram of a 214-days-old fetus, in left lateral recumbency, with the stomach in close proximity to the transducer footprint.

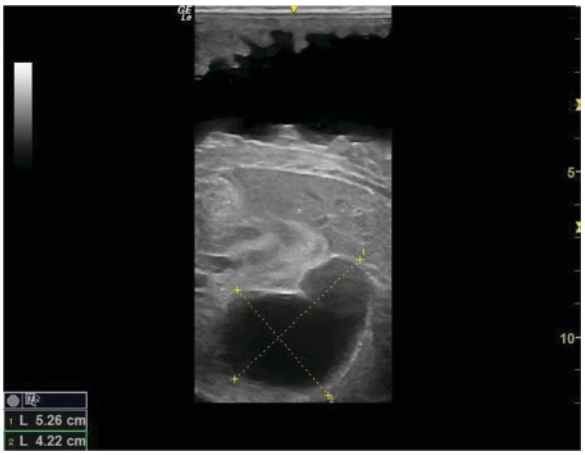


Figure 19.34 Transabdominal sonogram of a 218-days-old fetus, in right lateral recumbency, with the stomach on the opposite abdominal side of the transducer footprint.

(Figure 19.35) and has been partly attributed to a disrupted swallowing pattern [43], often associated with abnormalities of the head [33]. An interesting recent study from Agnew et al. [58], described the sonographic characteristics of the fetal GI tract and identified, in normal gestations, changes that occur with progressing fetal maturity, as an indication of fetal readiness for birth. The assessment included presence of stomach rugae (Figure 19.31), bowel segment definition, bowel segment dilation, intestinal content, and peristalsis. The study concluded that stomach rugae, peristalsis, and intestinal content represent the most predictive parameters indicating fetal maturation and days prepartum. Loops of small and large intestine may be identified within the fetal abdomen (Figures 19.36 and 19.37) and their content assessed as gestation progresses. The fetal gonads occupy the caudo-ventral abdomen (Figures 19.37 and 19.38),

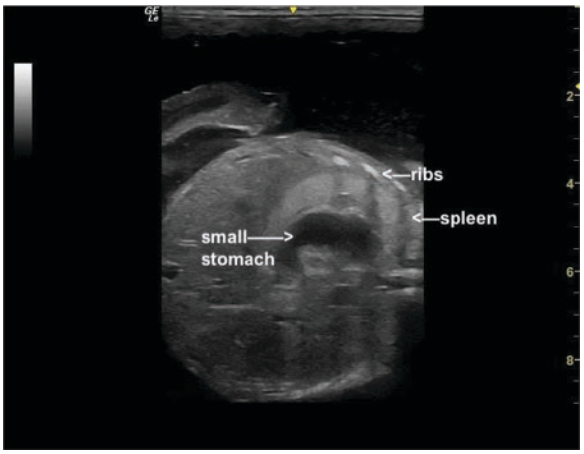


Figure 19.35 Transrectal linear sonogram of a 110-days-old fetus, with a notably small size stomach and reduced fluid content. The mare aborted 2 weeks later out in the field, but the fetus was not found.

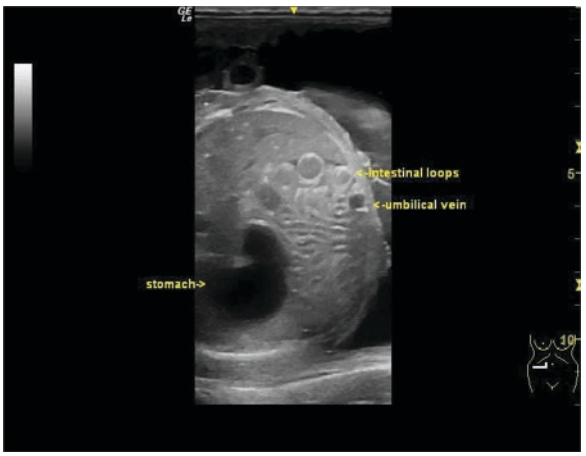


Figure 19.36 Transrectal linear sonogram of a 158-days-old fetus, showing a cross-sectional view of the cranial abdomen, featuring liver, gastric silhouette, and multiple intestinal loops.

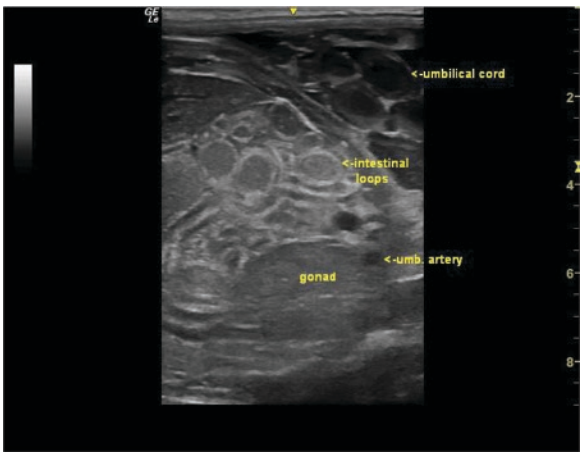


Figure 19.37 A close-up view of the caudal abdomen of a 180-days-old fetus, featuring a detailed map of intestinal loops, the gonad, and the fetal root of the umbilical cord.

Vet-ebooks.com

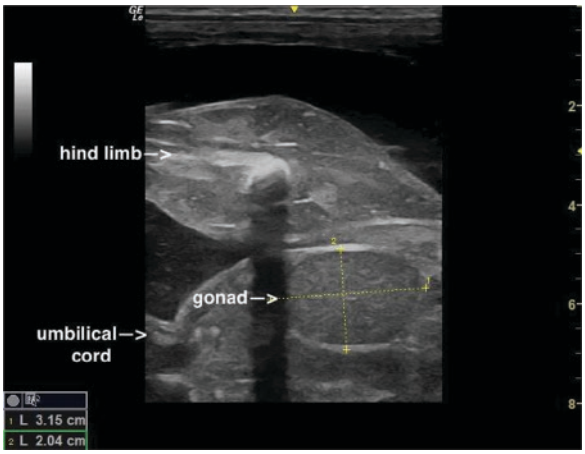


Figure 19.38 Transrectal linear sonogram of the caudal abdomen of a 127-days-old fetus in transverse presentation, featuring gonad and umbilicus.

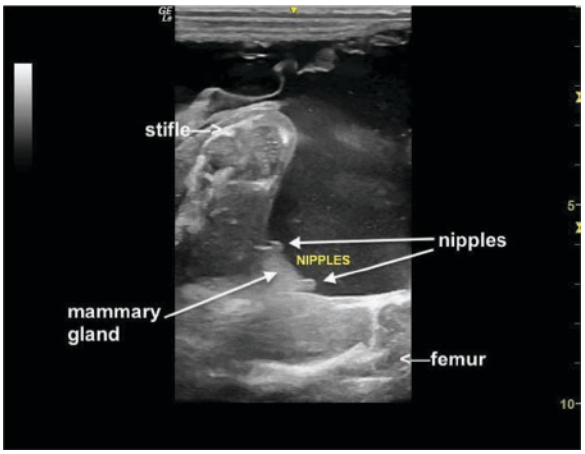


Figure 19.41 Transrectal linear sonogram of a 135-days-old filly fetus. Cross-sectional view showing mammary gland and nipples.

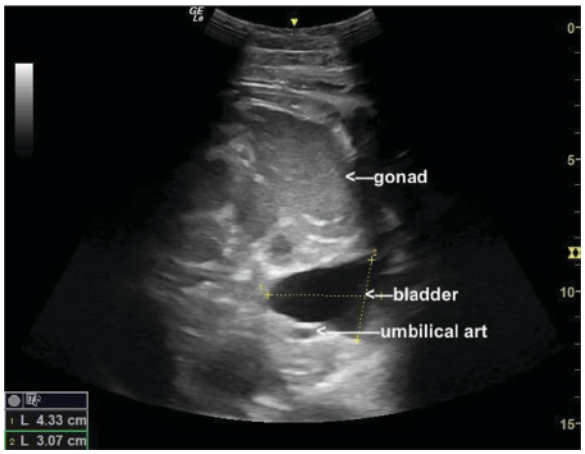


Figure 19.39 Transabdominal convex sonogram of the caudal abdomen of a 224-days-old fetus, showing the caudal pole of the gonad adjacent to the bladder.

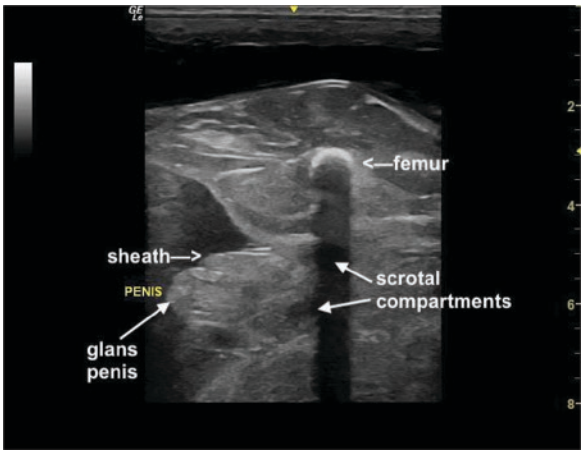


Figure 19.42 Transrectal linear sonogram of a 141-days-old male fetus, displaying a cross-sectional view of the penis encased within the sheath. The outline of the scrotal compartments is visible, closer to the abdominal contour.

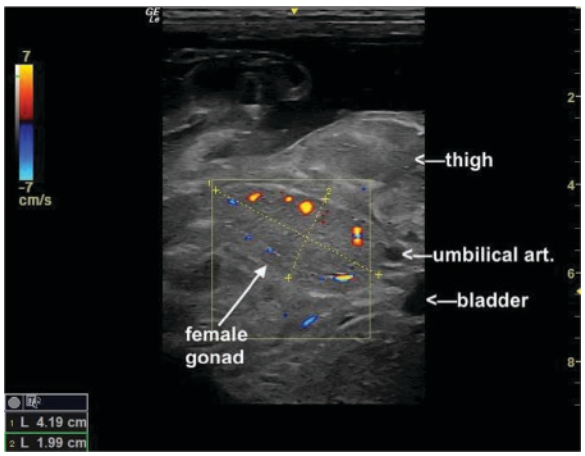


Figure 19.40 Transrectal linear sonogram of a 124-days-old filly fetus. Color Doppler of the female gonad in a frontal view, showing different vascular patterns between cortex and medulla.

adjacent to the bladder (Figure 19.39) and the structural distinction between male and female represent a mainstay in fetal gender determination in mid to advanced gestation [21] (Figure 19.40). Primary fetal sex organs can also be identified in advanced gestation (Figures 19.41, 19.42, and 19.43) and fetal sexing can be carried out by transabdominal sonography up to 240–260 days gestation [21].

Umbilical Cord (UC)

The UC can be easily imaged by US in mid to advanced gestation (Figures 19.44 and 19.45), but rarely in its entirety. Its attachment to the dorsal wall of the gravid uterus makes transabdominal US visualization of the placental root rather difficult in mid to

Vet-ebooks.com

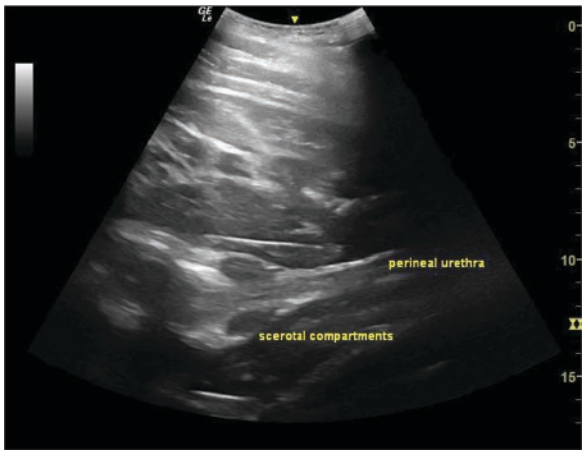


Figure 19.43 Transabdominal convex sonogram of the caudal abdomen of a 244-days-old fetus, showing the scrotal compartments and the perineal urethra.

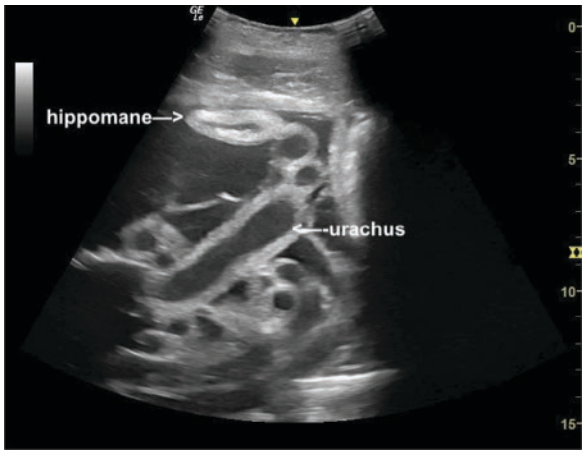


Figure 19.44 Transabdominal convex sonogram at 224 days gestation, showing umbilical cord and hippomane; the urachus appears mildly enlarged.

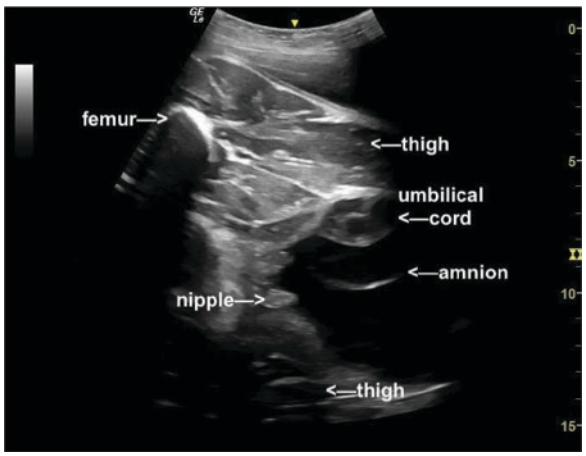


Figure 19.45 Transabdominal convex sonogram of the hindquarters of a 245-days-old female fetus, showing the umbilical cord in close contact with the inner thigh.

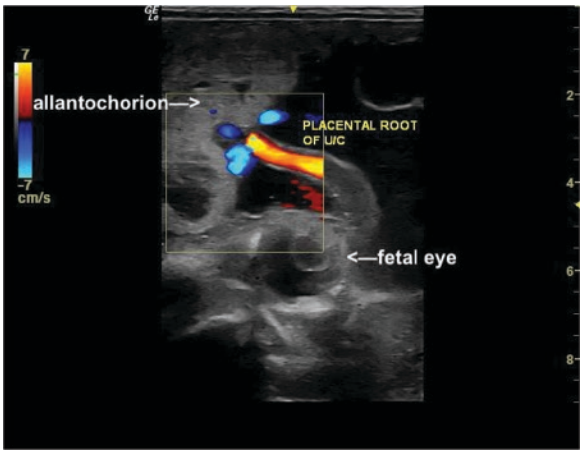


Figure 19.46 Transrectal linear, color Doppler sonogram at 120 days gestation, showing the fetal head close to the placental root of the umbilical cord.

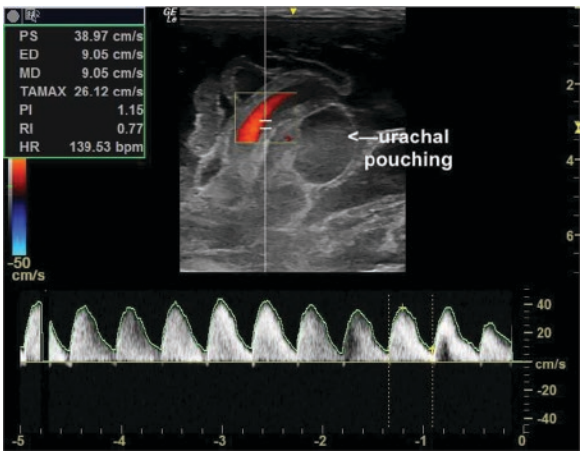


Figure 19.47 Transrectal linear, color Doppler sonogram of the umbilical cord at 180 days gestation, displaying a discrete area of urachal pouching. An increased resistive index (RI) for gestational age, is suggestive of cord blood flow alteration.

advanced gestation, due to the depth of the mare's abdomen and the presence of large loops of intestine with gas content. Transrectal imaging of the placental root of the umbilical cord can be accomplished in early to mid gestation (Figure 19.46).

Mild, intermittent episodes of compression, entanglement with fetal parts, or excessive UC torsion may result in urachal engorgement and pouching (Figures 19.47, 19.48, 19.49, and 19.50), due to the thin, pliable structure of the urachal wall (Figure 19.51). As the condition aggravates and/or becomes more persistent, multiple urachal diverticula will develop, with progressive bladder distension (Figure 19.52) and perivascular sacculation of the cord. Significant

Vet-ebooks.com

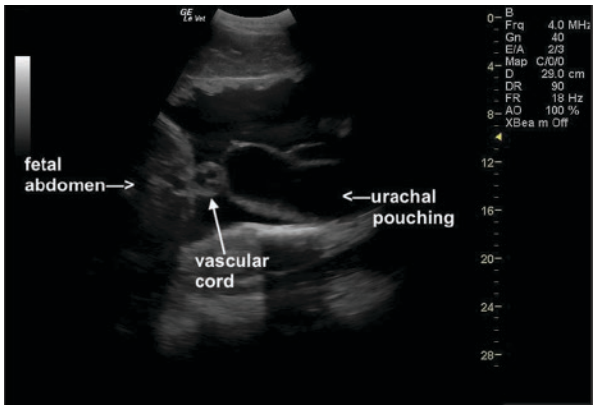


Figure 19.48 Transabdominal convex sonogram of the umbilical cord at 234 days gestation, displaying a discrete area of urachal enlargement (pouching).

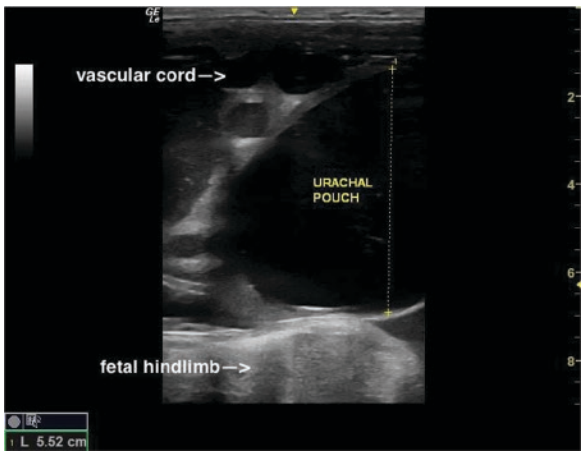


Figure 19.49 Transrectal linear sonogram of the umbilical cord at 234 days gestation (same fetus as in Figure 19.48), displaying marked urachal dilation, close to the fetal umbilicus.

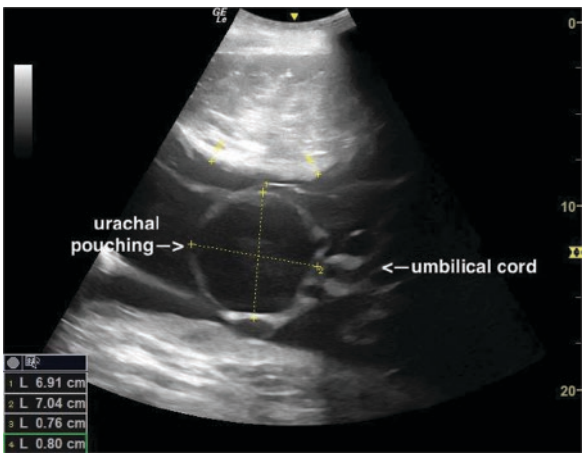


Figure 19.50 Transabdominal convex sonogram of the umbilical cord at 234 days gestation, displaying a distended urachus. The urachal wall is relatively hypoechoic and intimately connected to the vascular structures of the umbilical cord. These features differentiate urachal dilations from segmental, ossified remnants of the yolk sac, presenting with a hyperechoic wall (segmental ossification (see Figure 19.53).



Figure 19.51 Umbilical cord specimen from an aborted fetus (Figures 19.48, 19.49, and 19.50), with strangulating cord compromise. The urachal pouch at the umbilical cord root had been dissected to show its inner cavity.

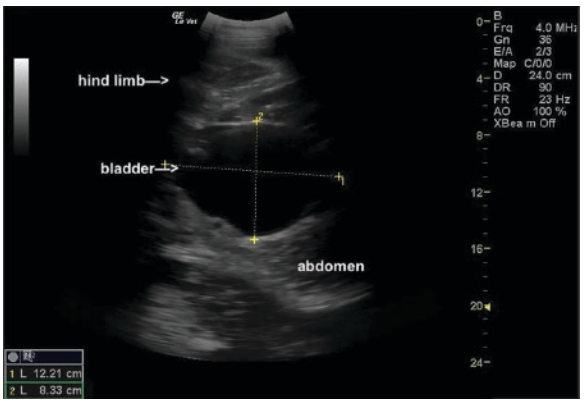


Figure 19.52 Transabdominal convex sonogram of the caudal abdomen of a 275-days-old fetus, with obstructive cord disease, resulting in chronic bladder enlargement.

obstructive/strangulating disease of the UC will result in vascular compromise and bladder enlargement and the increased intra-abdominal pressure may lead to abnormal accumulation of peritoneal fluid (ascites). Segmentally ossified remnants of the vitelline sac [44] may occasionally cause abortion by cord strangulation, when looping tightly around UC vascular structures (Figures 19.53 and 19.54).

Umbilical obstruction due to cord torsion is widely recognized as one of the major causes of abortion, stillbirth, and neonatal loss and in the UK the

Vet-ebooks.com

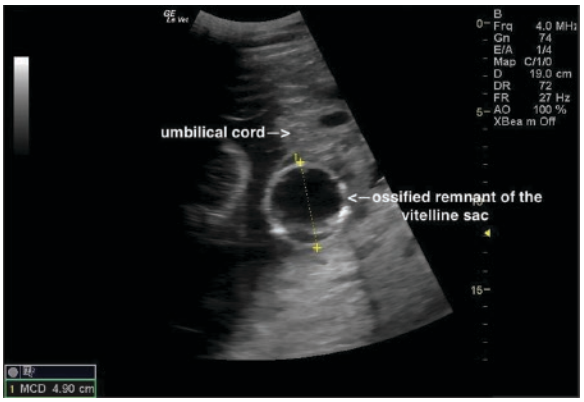


Figure 19.53 Transabdominal convex sonogram of the umbilical cord of a fetus 217-days-old, presenting with segmental ossification of the remnant of the yolk sac.



Figure 19.54 Wrapping of a pedunculated ossified remnant of the yolk sac around the umbilical cord, as a cause of abortion in a 245 days gestation, Arabian mare.

condition has been reported to be responsible for 38.8% of all equine abortions. UC torsion may separately involve each cord segment, or affect both amniotic and allantoic compartments simultaneously. Excessive UC length or shortness are risk factors for significant placental pathology and fetal death, but the factors governing cord length are unknown. It seems rather simplistic to consider cord length as the sole factor responsible for pathological UC torsion, as post-partum cord length evaluation frequently reports healthy neonates associated with cords well in excess of 100 cm. In addition, aborted fetuses in late gestation often present with cord lengths within normal range (36–83 cm Whitwell), measured after de-torsion of the affected segment (author personal observations). Fetal distress tends to associate with frenzied hyperactivity, as commonly observed with fetal infection, acute hypoxia, maternal disease (i.e., uterine torsion), and painful conditions and finally placental pathology (i.e., placental thrombosis, hydropic conditions). Excessive activity may lead to frequent changes in presentation, resulting in progressively constrictive cord torsion. In normal size and development fetuses, abortion caused by acute and severe cord torsion tends to occur prior to 9 months gestation, as beyond this time, fetal size and engagement of hind limbs into the pregnant horn will prevent further rotation along the short-axis. Later in gestation and up to term, severe UC obstruction is more commonly associated with cord entanglement by fetal parts or compression against maternal pelvic bones. Intrauterine growth restricted fetuses, due to their small size, may continue changing presentation until term and therefore continue aggravating cord torsion if they fail to encase their hindquarters into the pregnant horn, as it generally occurs in the presence of hydropic conditions. In view of the above considerations, it can be hypothesized that severe cord torsion is a fetal response pattern, common to a variety of stressful conditions.

Doppler Velocimetry Parameters of the Equine Pregnancy

Doppler ultrasonography represents an additional tool to characterize pregnancy blood flow [45] throughout gestation, providing an insight on maternal (uterine arteries) [46–49], fetal (umbilical and carotid arteries) [50–52], and potentially placental circulation (intraplacental circulation) in the mare. The latter vascular compartment though, has yet to be thoroughly investigated due to its vastness and complexity.

Doppler technology has become an important clinical instrument for assessing placental performance in healthy and high-risk human pregnancies, where Doppler scans of maternal uterine arteries (UA), fetal umbilical circulation, and other fetal vessels (i.e., middle cerebral artery, ascending/descending aorta, renal arteries) are routinely performed at set times during gestation [45,53–55]. These parameters provide a critical, qualitative assessment of fetal health and placental vascular perfusion by identifying changes in Doppler indices. Placental dysfunction, in actual fact, impairs the development of the placental

Vet-ebooks.com

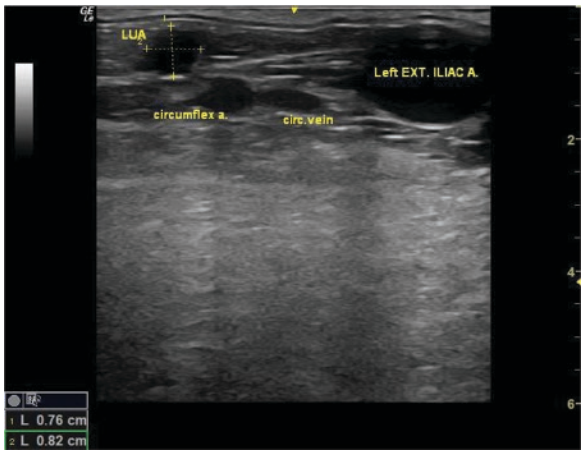


Figure 19.55 Transrectal linear sonogram of the left uterine artery (LUA), at 185 days. Measurements and Doppler vessel interrogation are carried out as the artery emerges from the ventral wall of the external iliac artery and in proximity of the circumflexa ilium profunda artery and vein.

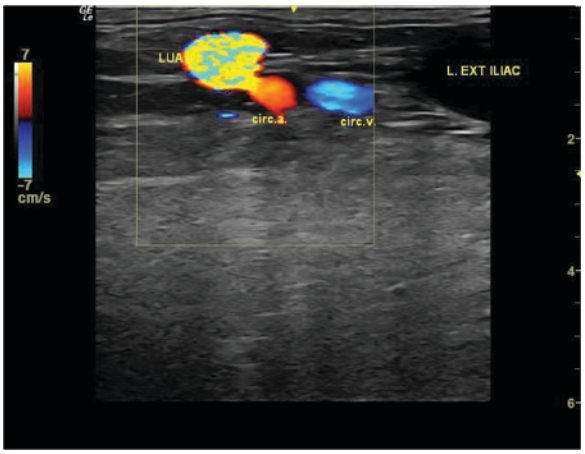


Figure 19.56 Color Doppler sonogram of Figure 19.55.

vascular bed and alters Doppler indices by increasing vascular resistance. The applications of Doppler technology to the equine pregnancy are still limited, due to initial difficulties in accessing some of the relevant vascular structures. Advanced ultrasound technology, available on portable units, with user-friendly color and pulsed-wave Doppler applications, has recently generated a renewed interest in the assessment of reproductive and gestational blood flow in the mare.

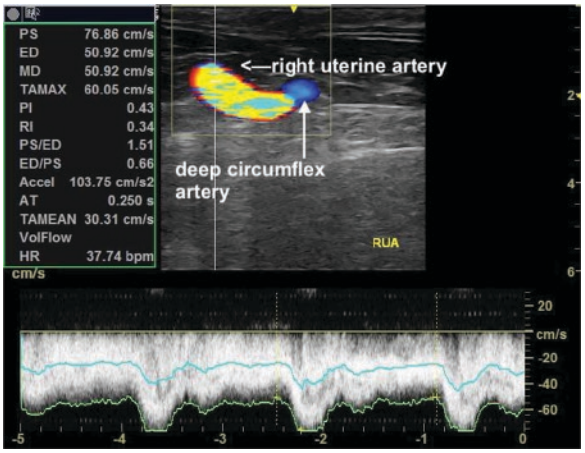


Figure 19.57 Transrectal linear sonogram of a Doppler spectral waveform of the right uterine artery (RUA), at 196 days gestation.

Assessment of Maternal Circulation

The maternal vascular compartment is assessed through Doppler interrogation of the uterine arteries (UA). Recording of abnormal UA Doppler indices may suggest alterations in placental perfusion.

In the mare, the uterine arteries are visualized per rectum throughout gestation, employing linear or micro-convex ultrasound transducers, with frequencies ranging between 5 and 10 MHz. In order to obtain consistent readings of vascular parameters, Doppler evaluation of each uterine artery is carried out about 2 to 5 cm from its origin from the external iliac artery, in close proximity to the *circumflexa ilium profunda* artery (Figures 19.55, 19.56, and 19.57).

Doppler studies by Bollwein et al. [46], Ousey et al. [47], Bailey et al. [48], and more recently Klewitz et al. [49], have analyzed blood flow to the pregnant uterus of the mare throughout gestation. Most of the above studies dealt with a small number of mares, but Klewitz et al. included 51 pregnant mares and reported on naturally occurring pregnancy abnormalities in this group.

The results of all the above studies uniformly indicate a progressive decrease in peripheral blood flow resistance and an increase in uterine blood flow, the latter being particularly evident during the last trimester of pregnancy. Ultimately, in normal pregnancies, haemodynamic changes of the uterine arteries progress from a high resistance/low flow pattern during the first half of gestation to a low resistance/high flow system in the second half, when placental development reaches completion and fetal demands are high. The above changes take place in response to fetal growth and development of the placental microcirculation. Ousey [47] reported that aged mares demonstrate a trend for reduced uterine blood flow, particularly in the last trimester of pregnancy, together with reduced placental microvillus surface

Vet-ebooks.com

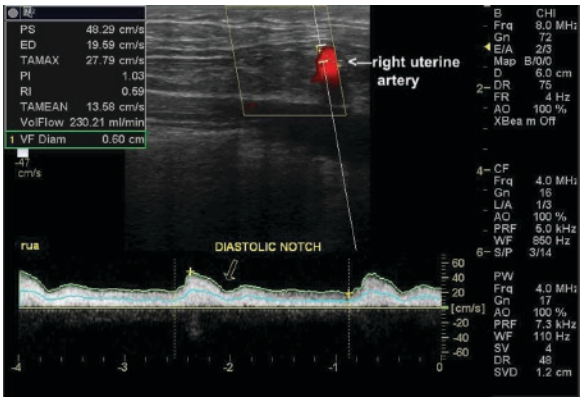


Figure 19.58 Transrectal linear sonogram of a Doppler spectral waveform of the right uterine artery (RUA) at 118 days gestation, with diastolic notch.

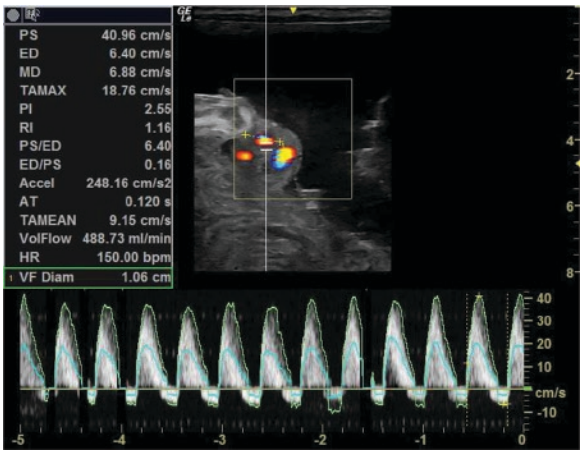


Figure 19.59 Doppler spectral waveform of the umbilical artery of a 115-days-old fetus, displaying a negative end diastolic flow.

densities and lighter foals at term. It was therefore suggested that reduced uterine blood supply may be an important contributory factor for pregnancy loss in aged mares.

A negative diastolic flow, or diastolic notch (Figure 19.58), has been described by Klewitz et al. [49], as a common feature on the spectral graph of early gestational mares, up to 150 days, while a prolonged display of the notch is a sign of lower uterine perfusion and associated with disorders of the human pregnancy. Eight mares in Klewitz et al.'s study were associated with gestational abnormalities, but calculation of Doppler indices of the uterine arteries proved a disappointing indicator of a dysfunctional utero-placental unit, with four mares showing increased blood flow in advanced gestation prior to abortion, while four more mares with placentitis demonstrated increased pulsatility index (PI) only during the first half of pregnancy. Conclusions drawn from the Klewitz et al. and Bailey et al.'s studies suggest that interpretation of uterine arteries' vascular dynamics alone will not provide sufficient evidence to assess pregnancy viability. Doppler indices ratios between different vascular compartments may offer more sensitive values to assess pregnancy viability.

Assessment of Fetal Circulation

Evaluation of the fetal vascular compartment in the equine pregnancy mostly relies on Doppler interrogation of the fetal intracranial and umbilico-placental circulations, with alteration of the latter reflecting more specifically placental pathology. Doppler velocimetry indices of the carotid artery are the subject of current investigation, aiming at establishing fetal intracranial hemodynamic patterns, throughout gestation.

Umbilical Circulation

Doppler studies of umbilical cord flow in equids were carried out by McGladdery et al. [50], Bollwein et al. [46], and more recently Panzani et al. [51], on small numbers of equid pregnancies and finally McGladdery et al. in 2016 [52], in 10 Thoroughbred mares. Bollwein et al.'s study included four pregnant mares, where umbilical flow was evaluated transrectally at the placental root of the umbilical cord. This study reported a gradual decrease in the umbilical arterial resistive index (RI), followed by a rise during the last weeks of pregnancy, in net contrast with the other two studies. McGladdery et al. (six pony mares) and Panzani et al. (six jennies) employed transabdominal ultrasonography to evaluate umbilical cord blood flow and both authors reported a steady decrease in RI and PI from mid gestation to term. In the 2016 study, McGladdery et al. evaluated umbilical flow monthly in 10 pregnant Thoroughbred mares by transrectal and transabdominal pulsed wave Doppler ultrasonography, from 65 days until parturition. Absent end diastolic flow was observed in gestations < 120 days (Figure 19.59). Results indicate a gradual decline in resistance index from 120 to 227 days, but visualization of the cord vessels was inconsistent after 250 days. Calculation of umbilical artery Doppler indices provides an objective assessment of feto-placental circulation (Figures 19.60 and 19.61). Climbing values in umbilical artery RI, during the second half of gestation, are suggestive of significant blood flow reduction and should be monitored and investigated for additional signs of cord compromise (Figure 19.62).

Vet-ebooks.com

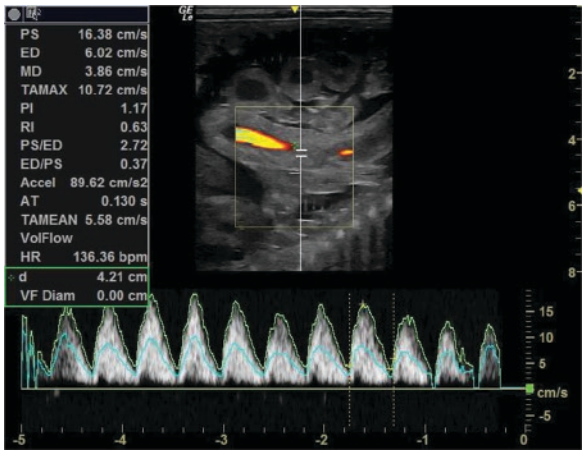


Figure 19.60 Doppler spectral waveform of the umbilical artery at 132 days gestation.

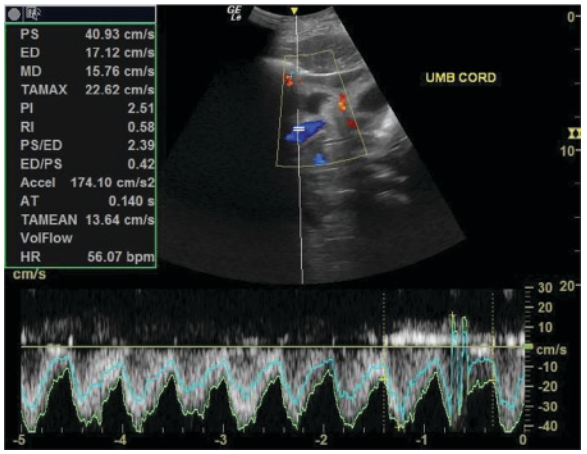


Figure 19.61 Doppler spectral waveform of the umbilical artery at 168 days gestation, showing declining RI values.

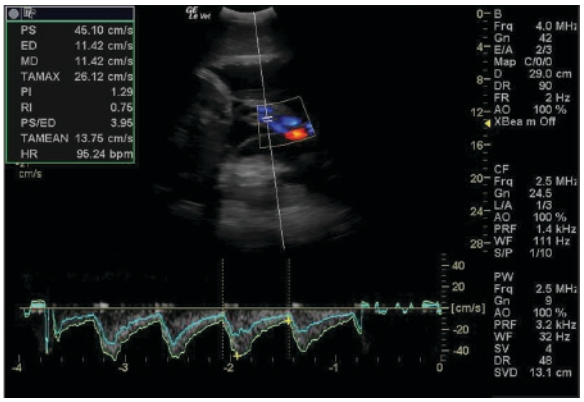


Figure 19.62 Doppler spectral waveform of the umbilical artery of a 234-days-old fetus with cord compromise, showing elevated RI. Fetal demise occurred about 48 hours later.

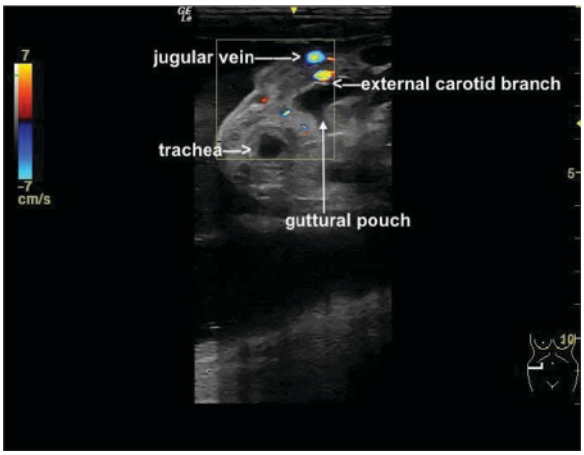


Figure 19.63 Transrectal linear color Doppler of a 200-days-old fetus, outlining the external carotid branch course over the lateral compartment of the guttural pouch.

Intracranial Circulation

The Middle Cerebral Artery (MCA), a branch of the internal carotid artery, has emerged as the vessel of choice in the Doppler assessment of human fetal intracranial circulation [56]. MCA Doppler indices provide information on blood volume redistribution, for example, in the presence of IUGR or fetal anemia. Alterations in MCA blood flow indices are carefully monitored in human patients carrying pregnancies with a high risk of an unfavorable outcome, as they are more sensitive indicators than other fetal parameters (i.e., late cardiac decelerations), particularly when both maternal uterine and fetal MCA waveforms are altered at the same time. In the equine fetus, the MCA cannot be visualized by ultrasound, due to substantial anatomical differences with the human fetus. The carotid artery, though, can be accessed both by transrectal (with the fetus in anterior presentation) [10] and transabdominal ultrasonography at three different sites: i) the common carotid trunk, along the fetal trachea, within the jugular groove (Figures 19.10, 19.11, 19.12, 19.13, 19.14, and 19.17); ii) the external carotid branch, running over the lateral compartment of the ipsilateral guttural pouch (Figure 19.63); and iii) the internal carotid branch (Figure 19.10). A high carotid RI characterizes intracranial circulation in the healthy fetus throughout gestation [57] (Figure 19.64).

Placental insufficiency, which leads to a reduction in nutritive supplies and fetal oxygen partial pressure, is one of the most important factors responsible for IUGR and fetal hypoxia. Inadequate placental perfusion leads gradually to fetal hypoxia and blood redistribution favoring the fetal brain, adrenal gland, and heart, with decreased blood flow to other parts of the body. Blood flow redistribution ultimately causes Intrauterine Growth Restriction, resulting in smaller, stunted growth neonates. IUGR can lead to long-term metabolic consequences, such as an

Vet-ebooks.com

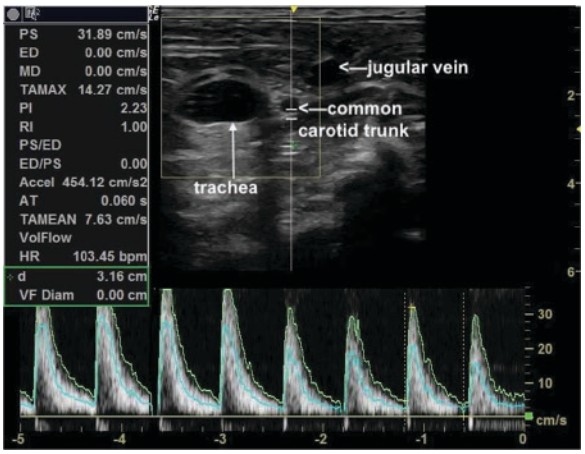


Figure 19.64 Doppler spectral waveform of the carotid artery at 224 days gestation, showing a physiologically elevated RI.

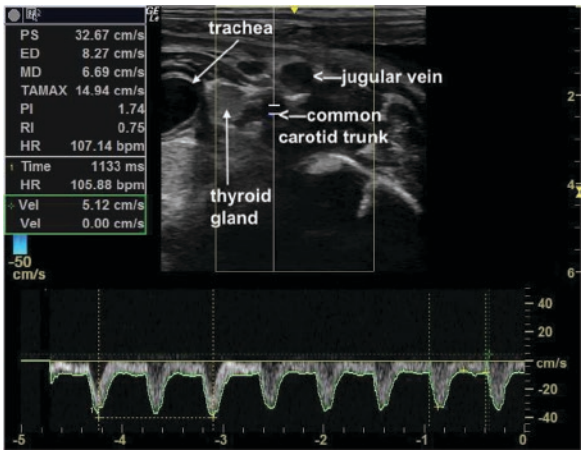


Figure 19.65 Doppler spectral waveform of the carotid artery at 234 days gestation, showing marked reduction in RI.

increased propensity for some of the most common diseases of adult life, whereas fetal hypoxia is the leading cause of perinatal morbidity and mortality [59]. Fetal hypoxia activates a range of biophysical, cardiovascular, endocrine, and metabolic responses. Fetal cardiovascular responses to hypoxia include modification of fetal heart rate, increase in arterial blood pressure, and redistribution of cardiac output toward vital organs: these are probably the most important adaptive reactions responsible of maintaining fetal homeostasis. The redistribution of blood flow toward the fetal brain is known as the "brain sparing effect," as increased blood supply to the fetal brain is one of the compensatory mechanisms in cases of decreased placental blood flow. Doppler assessment of the fetal cerebral and umbilico-placental circulations can detect fetal blood flow redistribution during hypoxia and quantify the degree of this redistribution. Under brain sparing effect conditions, a significant drop in carotid RI can be detected on Doppler ultrasonography (unpublished data) (Figure 19.65). Although the brain-sparing effect attempts to compensate for the reduced oxygen delivery to the fetal brain, it has become clear that this phenomenon cannot always prevent the development of brain lesions and the most important sequelae of fetal hypoxia is the development of perinatal brain damage, resulting in a spectrum of neurological disabilities.

Equine Biophysical Profile Score (BPS)

Fetal biophysical profile score refers to the assessment of a number of biophysical variables by means of ultrasonography, to identify fetal compromise. In human medicine, BPS is a standard tool in antenatal fetal evaluation, generally utilized after 28 weeks of gestation. The test combines fetal heart rate monitoring and fetal ultrasound to evaluate heart rate, breathing, activity, muscle tone, and amniotic fluid depth.

An equine BPS was originally developed by Brandemuhel and Pipers [2] adapted from the human model, for use in late gestational mares, that was revisited by a later publication by Reef et al. [12]. Due to substantial anatomical and functional differences between human and equine pregnancies, the initial five parameters score was later revised and integrated with additional US variables to include FHR, aortic diameter, level of activity, utero-placental thickness and contact, and minimal/maximal allantoic fluid depth. Each parameter is graded from 0 to 2 points, where an abnormal score gets 0 while a normal score gets 2 and then added up to yield a number from 0 to 12. A score of 8 or less ensures a negative fetal outcome, but a maximal score does not guarantee an uncomplicated delivery, because unforeseen periparturient events may happen.

Biophysical profile score calculations are recommended for mares at increased risk of gestational complications or pregnancy loss, but their prognostic value remains limited. In view of the increasing knowledge and understanding of fetal physiology and the application of more advanced imaging technologies, Doppler included, additional parameters should be integrated into this 6-parameter scoring system to make it a more predictive instrument for fetal outcome.

References

1 Pipers, F.S. and Adams Brendemuehl, C.S. (1984). Techniques and application of transabdominal

Vet-ebooks.com

ultrasonography in the pregnant mare. *Journal of the American Veterinary Medical Association* 185: 766–771.
2 Adams Brendemuehl, C.S. and Pipers, F.S. (1987). Antepartum evaluation of the equine foetus. *Journal of Reproduction and Fertility* 35(Suppl): 565–573.
3 Jeffcott, L.B. and Whitwell, K.E. (1973). Twinning as a cause of foetal and neonatal loss in the thoroughbred mare. *Journal of Comparative Pathology* 83: 91–105.
4 Renaudin, C.D., Gillis, C.L., Tarantal, A.F. et al. (1998). Ultrasonographic evaluation of equine fetal growth from 100 days gestation to parturition. In: *Proceedings of the 7th International Symposium on Equine Reproduction* 171–172.
5 Ginther, O.J. (1998). Equine pregnancy: Physical interactions between the uterus and conceptus. In: *Proceedings of the 44rd Annual Convention of the American Association of Equine Practitioners* 73–103.
6 Adams Brendemuehl, C.S. (1990). Fetal assessment. In: *Equine Clinical Neonatology* (ed. A.M. Koterba, W.H. Drummond, and P.C. Kosch), 16–33. Philadelphia and London: Lea & Febiger.
7 Reef, V.B., Vaala, W.E., Worth, L.T. et al. (1995). Ultrasonographic evaluation of the foetus and intrauterine environment in healthy mares during late gestation. *Veterinary Radiology & Ultrasound: The Official Journal of the American College of Veterinary Radiology and the International Veterinary Radiology Association* 36: 533–541.
8 Bucca, S., Fogarty, U., Collins, A. et al. (2005). Assessment of feto-placental well-being in the mare from mid-gestation to term: Transrectal and trans-abdominal ultrasonographic features. *Theriogenology* 64: 542–557.
9 Turner, R.M., McDonnell, S.M., Feit, E.M. et al. (2006). Real-time ultrasound measure of the fetal eye (vitreous body) for prediction of parturition date in small ponies. *Theriogenology* 66(2): 331–337.
10 Bucca, S., Carli, A., and Fogarty, U. (2001). How to assess fetal viability by transrectal ultrasound evaluation of fetal peripheral pulses. In: *Proceedings of the 53rd Annual Convention of the American Association of Equine Practitioners* 321–324.
11 Ginther, O.J. and Griffin, P.G. (1993). Equine fetal kinetics; presentation and location. *Theriogenology* 40: 1–11.
12 Reef, V.B., Vaala, W.E., Worth, L.T. et al. (1996). Ultrasonographic assessment of fetal well-being during late gestation: Development of a biophysical profile. *Equine Veterinary Journal* 28: 200–208.
13 Bucca, S. (2006). Diagnosis of the compromised equine pregnancy. *Veterinary Clinics of North America* 22: 749–761.
14 Reimer, J.M. (1997). Use of transcutaneous ultrasonography in complicated latter-middle to late gestation on pregnancies in the mare: 122 cases. In: *Proceedings of the 43rd Annual Convention of the American Association of Equine Practitioners* 259–261.
15 Bucca, S. (2011). Ultrasonographic monitoring of the fetus. In: *Equine Reproduction*, 2nd edn (ed. A.O. McKinnon, E.L. Squires, W.E. Vaala, et al.), 39–54. New York: Blackwell Publishing.
16 Rantanen, N.W. and Kincaid, B. (1988). Ultrasound guided fetal cardiac puncture: A method of twin reduction in the mare. In: *Proceedings of the 34th Annual Convention of the American Association of Equine Practitioners* 173–179.
17 Wolfsdorf, K.E., Rodgerson, D., and Holder, R. (2005). How to manually reduce twins between 60 and 120 days gestation using cranio-cervical dislocation. In: *Proceedings of the 51st Annual Convention of the American Association of Equine Practitioners* 284–287
18 Curran, S. and Ginther, O.J. (1993). Ultrasonic fetal gender diagnosis during months 5 to 11 in mares. *Theriogenology* 40: 1127–1135.
19 Holder, R.D. (2001). Fetal sex determination in the mare between 55 and 150 days gestation. In: *Proceedings of the 47th Annual Convention of the American Association of Equine Practitioners* 321–324
20 Bucca, S. (2005). Fetal gender determination from mid to advanced gestation by ultrasound. *Theriogenology* 64: 558–563.
21 Bucca, S. (2011). Fetal gender determination from mid gestation to term. In: *Equine Reproduction*, 2nd edn (ed. A.O. McKinnon, E.L. Squires, W.E. Vaala, et al.), 2094–2098. New York: Blackwell Publishing.
22 McGladdery, A.J., Cottrill, C.M., and Rossdale, P.D. (1990). Abstract. Effects upon the foetus of sedative drugs administered to the mare. In: *Proceedings of the Second International Conference on Veterinary Perinatology* (ed. P.D. Rossdale), 14. Cambridge UK: International Society of Veterinary Perinatology.
23 Smith, L.J. and Schott, H. (1990). Abstract. Xylazine induced foetal bradycardia. In: *Proceedings of the Second International Conference on Veterinary Perinatology* (ed. P.D. Rossdale), 36. Cambridge UK: International Society of Veterinary Perinatology.
24 Kliegman, R. and Das, U.G. eds. (2002). Intrauterine growth retardation in fanaroff. In: *Neonatal and Perinatal Medicine Diseases of the Fetus and Infant*, 228–262. St Louis MO: Mosby.
25 Rossdale, P.D. (2004). The maladjusted foal: Influences of intrauterine growth retardation and birth trauma. In: *Proceedings of the 50th Annual Convention of the American Association of Equine Practitioners* 75–126.
26 Reef, V.B., Vaala, W.E., Worth, L.T. et al. (1996). Ultrasonographic assessment of fetal well-being during late gestation: Development of a biophysical profile. *Equine Veterinary Journal* 28: 200–208.
27 McKinnon, A.O., Voss, J.L., Squires, E.L. et al. (1993). Diagnostic ultrasonography. In: *Equine Reproduction*

Vet-ebooks.com

(ed. A.O. McKinnon and J.L. Voss), 266–302. Philadelphia and London: Lea & Febiger.
28 Pantaleon, L.G., Bain, F.T., Zent, W. et al. (2003). Equine fetal growth and development. *Compendium of Veterinary Education* 25(6): 470–476.
29 Yamamoto, K., Yasuda, J., and Too, K. (1992). Arrhythmias in the newborn thoroughbred foals. *Equine Veterinary Journal* 24: 169–173.
30 Colles, C.M., Parkes, R.D., and May, C.J. (1978). Foetal electrocardiography in the mare. *Equine Veterinary Journal* 10: 32–37.
31 Bucca, S., Carli, A., and Fogarty, U. (2007). How to assess fetal viability by transrectal ultrasound evaluation of fetal peripheral pulses. In: *Proceedings of the 53rd Annual Convention of the American Association of Equine Practitioners* 321–324
32 Allen, W.E. (1986). Two cases of abnormal equine pregnancy associated with excess foetal fluid. *Equine Veterinary Journal* 18: 220–222.
33 Sertich, P.L., Reef, V.B., Oristaglio-Turner, R.M. et al. (1994). *Hydrops amnii* in a mare. *Journal of the American Veterinary Medical Association* 204: 1481–1482.
34 Oppen, T.V. and Bartmann, C.P. (2001). Two cases of hydroallantois in the mare. *Pferdeheilkunde* 17(6): 593–596.
35 Christensen, B.W., Troeddson, M.H.T., Murchie, T.A. et al. (2006). Management of hydrops amnion in a mare resulting in birth of a live foal. *Journal of the American Veterinary Medical Association* 228(8): 1228–1233.
36 Vaala, W.E. and Sertich, P.L. (1984). Management strategies for mares at risk for periparturient complications. *Veterinary Clinics of North America: Equine Practice* 10: 237–265.
37 Bucca, S. (2011). Fogarty ultrasonographic cervical parameters throughout gestation in the mare. *AAEP Proceedings* 57: 235–241.
38 Bucca, S. (2013). How to manage cervical incompetence by application of a cervical cerclage suture in the pregnant mare. *AAEP Proceedings* 59: 28–33.
39 Colon, J.L. (2008). Trans-rectal ultrasonographic appearance of abnormal combined utero-placental thickness in late-term gestation and its incidence during outline survey in a population of Thoroughbred mares. In *Proceedings of: 54th Annual American Association of Equine Practitioners Convention* 279–285
40 Renaudin, C.D., Troedsson, M.H.T., Gillis, C.L. et al. (1997). Ultrasonographic evaluation of the equine placenta by transrectal and transabdominal approach in the normal pregnant mare. *Theriogenology* 47: 559–573.
41 Troedsson, M.H.T., Renaudin, C.D., Zent, W.W. et al. (1997). Transrectal ultrasonography of the placenta in normal mares and mares with pending abortion: A field study. In: *Proceedings of the 43rd Annual Convention of the American Association of Equine Practitio*ners 256–258.
42 Sheerin, P.C., Morris, S., Kellerman, A. et al. (2003). Diagnostic efficiency of transrectal ultrasonography and plasma progestins profiles in identifying mares at risk of premature delivery. In: *Proceeding of the Focus on Equine Reproduction Meeting* 22–23.
43 Wintour, A.M., Barnes, A., Brown, A.J. et al. (1977). The role of deglutition in the production of hydramnios. *Theriogenology* 8: 160.
44 Cassar, T.I.Y., Fallon, L.H., Martinez, E.H. et al. (2006). Segmental ossification of involuted yolk sacs in equine umbilical cords. *Animal Reproduction Science* 94: 439–442.
45 Abramowicz, J.S. and Sheiner, E. (2008). Ultrasound of the placenta: A systematic approach. Part II: Functional assessment (Doppler). *Placenta* 29: 291–299.
46 Bollwein, H., Weber, F., Woschee, I. et al. (2004). Transrectal Doppler sonography of uterine and umbilical blood flow during pregnancy in mares. *Theriogenology* 61: 499–509.
47 Ousey, J.C., Kollig, M., Newton, R. et al. (2012). Uterine haemodynamics in young and aged pregnant mares measured using Doppler ultrasonography. *Equine Veterinary Journal* 44(Suppl 41): 15–21.
48 Bailey, C.S., Heitzman, J.M., Buchanan, C.N. et al. (2012). B-mode and Doppler ultrasonography in pony mares with experimentally induced ascending placentitis. *Equine Veterinary Journal. Supplement* 44(Suppl 43): 88–94.
49 Klewitz, J., Struebing, C., Rohn, K. et al. (2015). Effects of age, parity and pregnancy abnormalities on foal birth weight and uterine blood flow in the mare. *Theriogenology* 83: 721–729.
50 McGladdery, A.L., Ousey, J., and Rossdale, P.D. (1992). Serial Doppler ultrasound studies of the umbilical artery during equine pregnancy. In: *Proceedings of the 3rd International Conference on Veterinary Perinatology*, Davis, 37–38.
51 Panzani, D., Farhi, M., Bucca, S. et al. (2014). Trans-rectal and trans-abdominal Doppler sonography of the umbilical arterial blood flow during normal and pathological pregnancies in jennies. In: *Proceedings of the 11th ISER*, Hamilton NZ, 209–210.
52 McGladdery, A.L. and Ousey, J. (2016). Vascular impedance of the umbilical cord artery during equine pregnancy. *Equine Veterinary Journal* 48: 1–30.
53 Gramellini, D., Folli, M.C., Raboni, S. et al. (1992). Cerebral-umbilical Doppler ratio as predictor of

Vet-ebooks.com

adverse perinatal outcome. *Obstetrics and Gynecology* 79: 416–420.

54 Bamfo, J.E.A.K. and Odibo, A.O. (2011). Diagnosis and management of fetal growth restriction. *Journal of Pregnancy* 2011: 1–15. Article ID 640715, 15 pages. doi:10.1155/2011/640715.

55 Oros, D., Figueras, F., Cruz-Martinez, R. et al. (2011). Longitudinal changes in uterine, umbilical and fetal cerebral Doppler indices in late-onset small-for-gestational age fetuses. *Ultrasound in Obstetrics & Gynecology: The Official Journal of the International Society of Ultrasound in Obstetrics and Gynecology* 37: 191–195.

56 Theera Tongsong, M.D., Chanane Wanapirak, M.D., Supatra Sirichotiyakul, M.D. et al. (2007). Middle cerebral artery peak systolic velocity of healthy fetuses in the first half of pregnancy. *Journal of Ultrasound in Medicine: Official Journal of the American Institute of Ultrasound in Medicine* 26: 1013–1017.

57 Bucca, S., Sousa De Oliveira, I.R., Cunanan, J.C. et al. (2020). Doppler indices of the equine fetal carotid artery throughout gestation. *Theriogenology* 156: 196–204.

58 Agnew, M.E., Slack, J.A., Stefanovski, D. et al. (2018). Sonographic appearance of the late gestation equine fetal intestine. *Journal of Equine Veterinary Science* 66: 235.

59 Rossdale, P. and Ousey, J. (2010). Fetal programming for athletic performance in the horse: Potential effects of IUGR. *EVJ* 14: 98–112.

Vet-ebooks.com

Section 3

Internal Medicine

Vet-ebooks.com

Vet-ebooks.com

20

Thoracic Ultrasonography, Non Cardiac

Peter R. Morresey

Rood and Riddle Equine Hospital, Lexington, KY, USA

Thoracic Ultrasonography

Ultrasonography allows rapid, stall-side diagnosis of respiratory system disease, largely replacing the need for radiography. With ultrasonography, the pleural surfaces, pleural space, and surface of the lung can be evaluated; however, deeper pulmonary structures are not able to be visualized. In some cases of thoracic disease, pathology of the pleural space and lung may be sufficiently subtle to be unable to be detected by auscultation, radiography, or percussion, yet changes may be readily detected by ultrasonography. Severity of pulmonary consolidation is better assessed with ultrasonography than other diagnostic modalities, and consolidation can be readily identified in horses with pleural effusion. The musculature of the thoracic wall, bony and cartilaginous continuity of the ribs, and the integrity of the diaphragm can also be evaluated.

Ultrasonographic Technique

Regardless of the direction chosen, examination should be systematic and complete, allowing the operator to develop a technique that is highly repeatable between examinations. The entire thorax can be examined in a dorsal to ventral direction from the third to seventeenth intercostal space (ICS). While clipping this area provides the best image, removal of hair is best reserved for discrete areas of pathology, if at all necessary, to maintain acceptable cosmesis. Acoustic gel can be used to provide coupling; however. adequate contact can be achieved by thoroughly wetting the hair with isopropyl alcohol before slicking down the hair to remove trapped air.

The probe in placed centrally in the ICS aligned with the ribs to maximize the acoustic window. Beginning at the most dorsal aspect of the visualized lung, the probe is traversed down the ICS past the level of the diaphragm to ensure the entire lung field and pleural space are imaged. The probe is generally placed perpendicular to the thoracic wall; however, the areas shielded by the ribs can be assessed during horizontal oscillations applied to the probe to sweep the ultrasound beam along this plane. Assessment of the cranial thorax (cranial to the third ICS) presents some difficulty as the triceps musculature covers this area. The probe may be applied to the triceps muscle with depth adjusted to allow pleural and pulmonary evaluation. Alternatively, the probe can be placed under the right triceps musculature with this limb protracted cranially, and the probe angled appropriately to image the cranial mediastinum.

Normal Anatomy

Heart

Within the cranial thorax, the heart lies deep to the triceps musculature [1]. The cardiac notch of the lung allows visualization of the heart, extending from the third rib to the fourth ICS on the right side, and the third to sixth ribs on the left side [1]. Assessment of the heart by echocardiography is detailed in Chapter 21: Cardiology: Introduction.

Atlas of Equine Ultrasonography, Second Edition. Edited by Jessica A. Kidd, Kristina G. Lu and Michele L. Frazer.
© 2022 John Wiley & Sons Ltd. Published 2022 by John Wiley & Sons Ltd.
Companion Website: www.wiley.com/go/kidd/atlas

Vet-ebooks.com

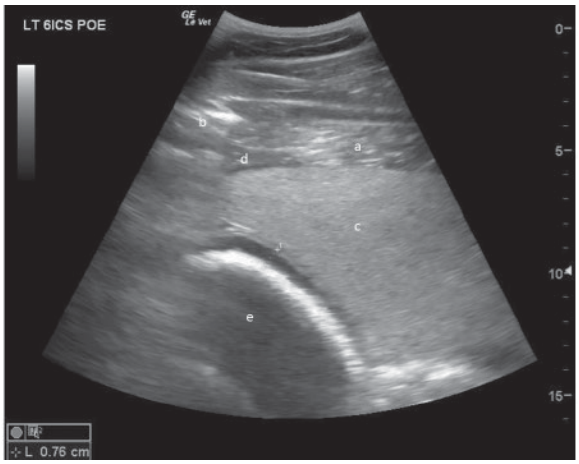


Figure 20.1 Normal diaphragm. The diaphragm (a) separates the thoracic and abdominal cavities. It inserts on the thoracic wall at approximately the eighth to ninth costal cartilage and curves caudodorsally to the eighteenth rib. It then reflects craniomedially and ends at the seventeenth ICS. Lung tip (b), spleen (c), liver (d), and the curved surface of the stomach (e). This sonogram was obtained from the left sixth ICS with a curvilinear probe operating at 4.0 MHz at a depth of 16 cm.

Diaphragm

The diaphragm extends cranially to contact the heart, with the most ventral aspect reflecting caudally. Visual separation between the lung fields and the abdominal viscera is demarcated by the hyperechoic diaphragmatic musculature which reflects on to the thoracic wall (Figure 20.1). If diaphragmatic musculature is absent, contact is occurring between the viscera and the lungs resulting from discontinuity of the diaphragm. Pleural and peritoneal fluid may be noted on either side of the diaphragm, sharply delineating it free from direct contact with viscera.

Left Hemithorax

Caudal to the heart, the left liver lobe can be visualized deep to the diaphragm. Traversing caudally, the spleen will come into view, adjacent and medial to the left lobe of the liver. The stomach may be noted in cross-section deep to this interface alongside the splenic vein. The spleen is visible between the seventh and seventeenth ICS [2].

Right Hemithorax

Ventral and caudal to the heart, the diaphragm and right lobe of the liver can be visualized extending from the ninth to sixteenth ICS, with the large colon medial to the liver or in apposition with the diaphragm [2]. Dorsally, as on the left side, the lung fields are easily visualized moving across the screen in time

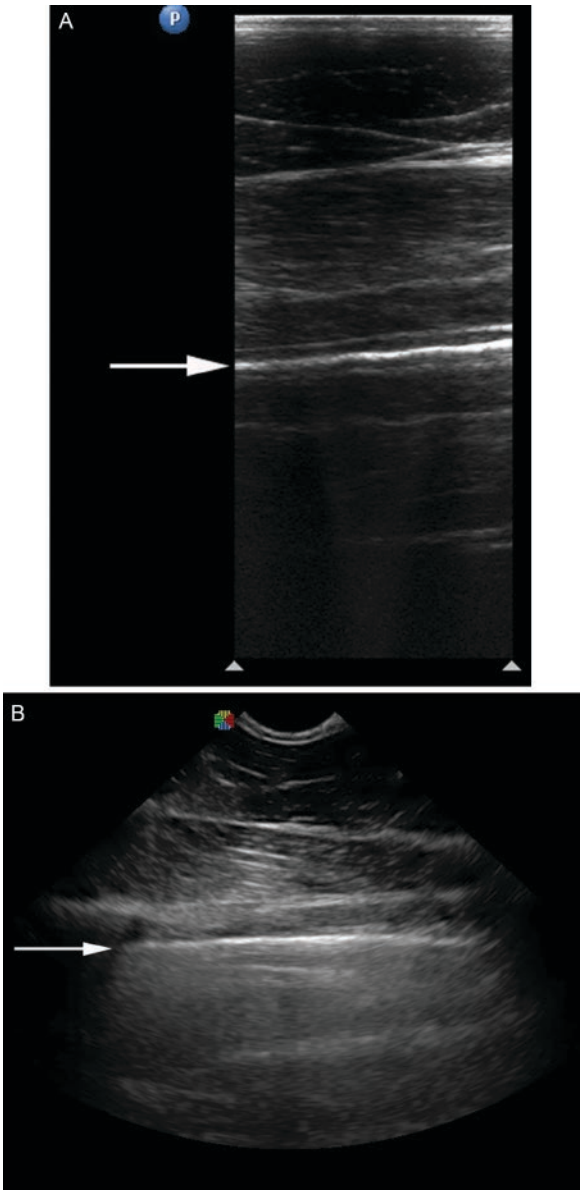


Figure 20.2 Normal lung. Ultrasound is used to image the superficial areas of lung contacting the thoracic body wall. This lung field is triangular in shape and extends caudally to the 16th ICS. In these images, the hyperechoic line (arrow) is the pleural surface of normal lung. (a) This sonogram was obtained from the left, 8th ICS using a linear probe operating at 5.0 MHz at a depth of 8 cm. (b) This sonogram was obtained from the left, 8th ICS using a micro-convex probe operating at 6.6 MHz at a depth of 6 cm.

with inspiration and expiration during breathing. Mid-thorax, deep to the diaphragm, the liver and right dorsal colon may be seen in close apposition. Caudally, between ICS sixteen and seventeen, the cranial aspect of the right kidney is visible [2].

The apposition of the parietal and visceral pleura may be noted as a hyperechoic interface (Figure 20.2). Motion of the pulmonary parenchyma can be seen

Vet-ebooks.com

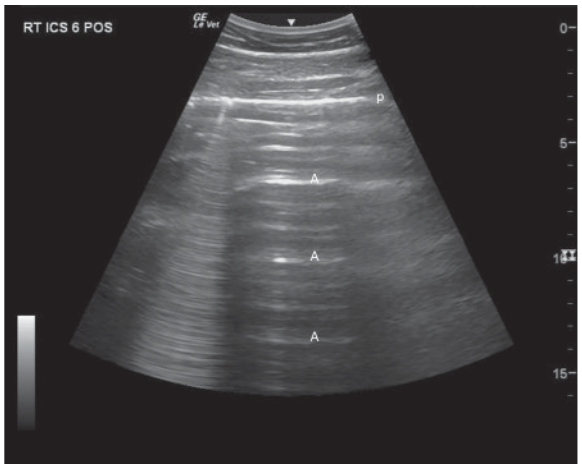


Figure 20.3 Normal lung. The pleural interface appears as a hyperechoic line (p). Multiple parallel hyperechoic lines are evenly spaced through the pulmonary parenchyma, known as A lines (A). This sonogram was obtained from the right sixth ICS using a curvilinear probe operating at 4 MHz at a depth of 15 cm.

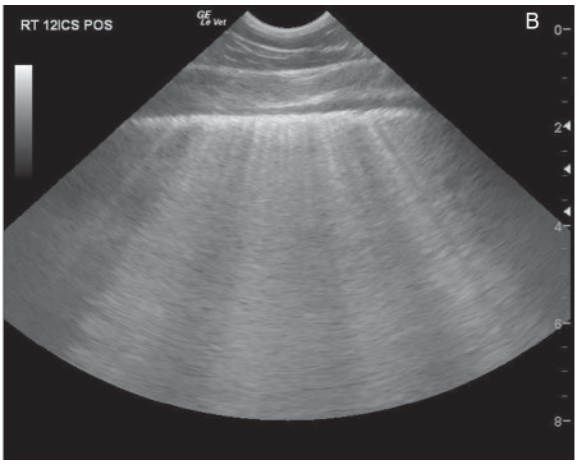


Figure 20.4B Abnormal lung, widespread inflammation. Similar changes are present to Figure 20.6a; however, B lines are more densely located indicating more severe pulmonary inflammatory changes are present. This sonogram was obtained from the right twelfth ICS using a curvilinear probe operating at 8 MHz at a depth of 8 cm.

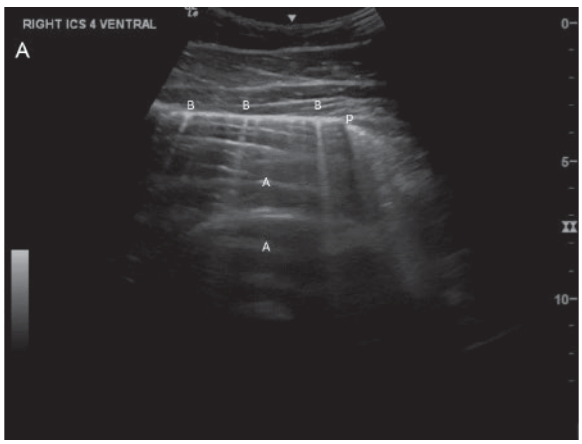


Figure 20.4A Abnormal lung, inflammation. Multiple radiating hyperechoic lines ("comet-tail artifact") radiate from the pleural surface (p) parallel to the main ultrasound beam into the pulmonary parenchyma perpendicular to the A lines (A). These are known as B lines (B) and represent areas of non-aerated lung surface. They may be few and discrete (a and b), multiple (c), or coalesce with more severe inflammation such as interstitial pneumonia resulting in shadowing of widespread areas of the pulmonary parenchyma (d). This sonogram was obtained from the right fourth ICS using a curvilinear probe operating at 4 MHz at a depth of 13 cm.

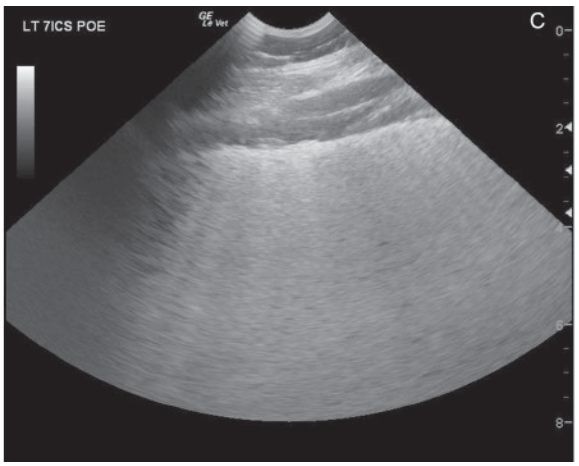


Figure 20.4C Interstitial pneumonia. Severe inflammatory changes involving the pulmonary surface and parenchyma lead to coalescing of B lines resulting in widespread shadowing of deeper structures. This sonogram was obtained from the left seventh ICS using a curvilinear probe operating at 8 MHz at a depth of 8 cm.

synchronously with thoracic excursions during respiration.

An anechoic space from a small amount of fluid (up to 3.5 cm reported) [1] is present in the majority of horses over the right cranioventral lung field. This may also be present in a lesser amount on the left side in these horses. This fluid creates separation of the parietal and visceral pleura. This is not an indicator of a disease state, rather this is thought necessary for lubrication of the pleural surfaces allowing unimpeded movement between the parietal and visceral pleura.

Pulmonary Appearance

Normal aerated lung surface appears as a smooth hyperechoic interface at the pleura of the thoracic wall sliding perpendicularly to the long-axis of the ultrasound beam. Parallel, hyperechoic lines beneath the pleural line and at even spaces of the distance between the ultrasound probe and the visceral-parietal

Vet-ebooks.com

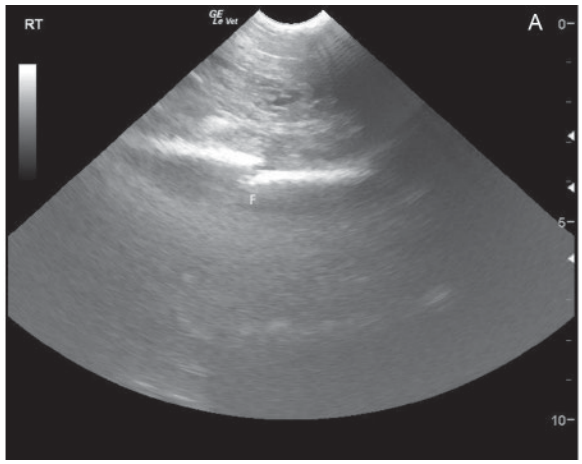


Figure 20.5A Fractured rib. Neonatal rib fracture with minimal displacement of distal segment making diagnosis by palpation potentially difficult (F). This sonogram was obtained from the right thorax using a micro-convex probe operating at 6.0 MHz at a depth of 10 cm.

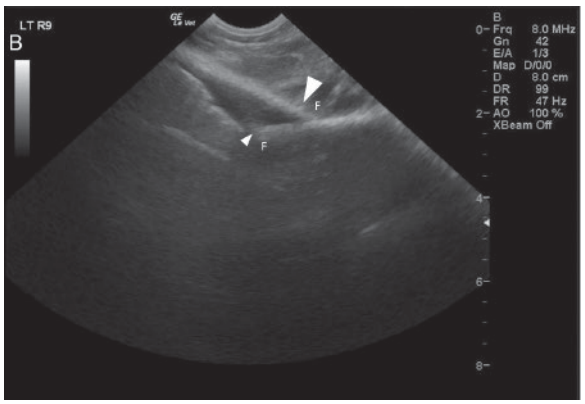


Figure 20.5b Fractured rib. Neonatal rib fracture with overriding fracture ends (F). An acute fractured rib in a neonatal foal; the proximal (arrowhead) overrides the distal fragments (small arrowhead) which is directed medially. Pleural hemorrhage and thoracic wall hemorrhage result. This sonogram was taken from the left thorax, ninth rib using a micro-convex probe operating at 8.0 MHz at a depth of 8 cm.

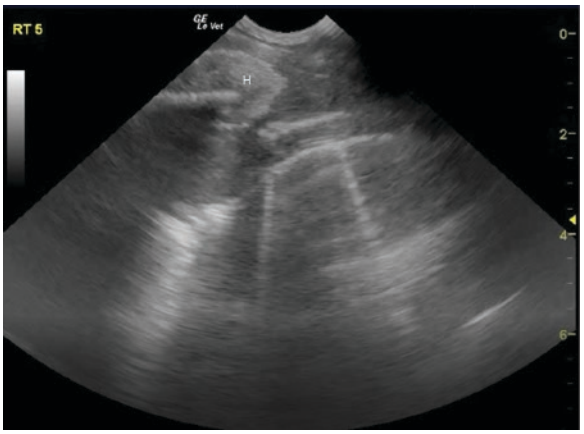


Figure 20.6 Fractured rib with associated hematoma. This image shows a fractured rib end with an organizing hematoma (H), the initial stage of fracture stabilization allowing subsequent callus formation. This sonogram of the right fifth rib was obtained with a probe operating at 8.0 MHz at a depth of 8 cm.

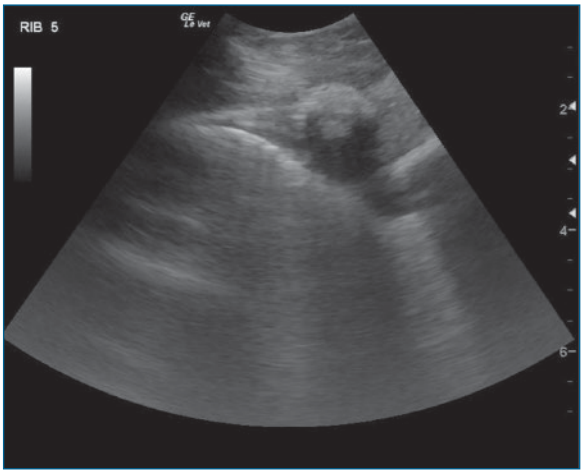


Figure 20.7 Fractured rib with mural hematoma and callus formation. This image shows a fractured rib with an organizing hematoma and the initial stage of fracture stabilization (callus formation). This sonogram of the right fifth rib was obtained with a probe operating at 8.0 MHz at a depth of 8 cm.

pleural interface, may appear within the pulmonary parenchyma (Figure 20.3). These are known as A-lines and result from multiple acoustic reflections between the pleura and the probe. Loss of aeration is represented by B-lines, traveling perpendicular to A-lines, which radiate from the pleural surface into the pulmonary parenchyma (Figure 20.4). These are colloquially known as the comet-tail artifact. They range from solitary, multiple discrete, to coalescing, which indicate a more widespread loss of aeration and shadow deeper pulmonary structures.

Pathology of the Thoracic Wall

Rib fractures are more readily detected by ultrasonography than radiography in neonatal foals [3]. Changes in continuity of the hyperechoic border of the ribs, overriding of fracture ends, as well as the size and location of rib fragments, are visualized (Figure 20.5). Disruption of the costochondral junctions may also be noted, with often no indicative clinical signs [4]. Associated subcutaneous and intramural hematomas

Vet-ebooks.com

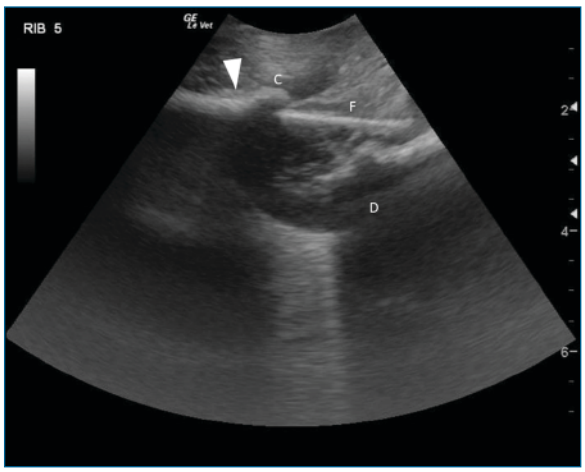


Figure 20.8 Fractured rib with distal fragment and lung trauma. The proximal rib (arrowhead) contains a callus (C) connecting to a fragment (F) and is overriding the distal portion (D). The adjacent lung displays increased echodensity consistent with pulmonary contusion. This sonogram was taken from the left thorax, fifth rib using a micro-convex probe operating at 8.0 MHz at a depth of 8 cm.

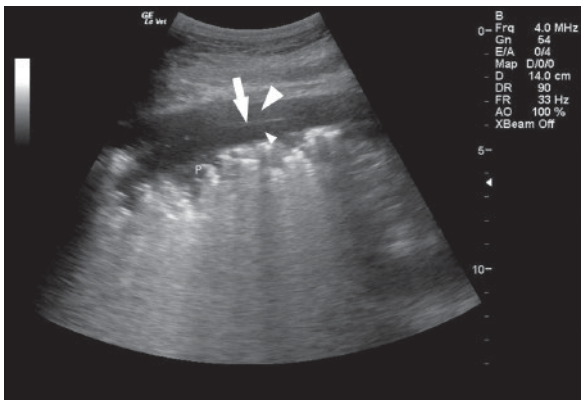


Figure 20.9 Pleuritis. Thickened parietal pleura (arrowhead) is separated from thickened visceral pleura (small arrowhead) by a hyperechoic line (arrow). The pulmonary margin is irregularly echodense compatible with cellular infiltration and inflammation (P). This sonogram was obtained from the right ninth ICS using a curvilinear probe operating at 4.0 MHz at a depth of 14 cm.

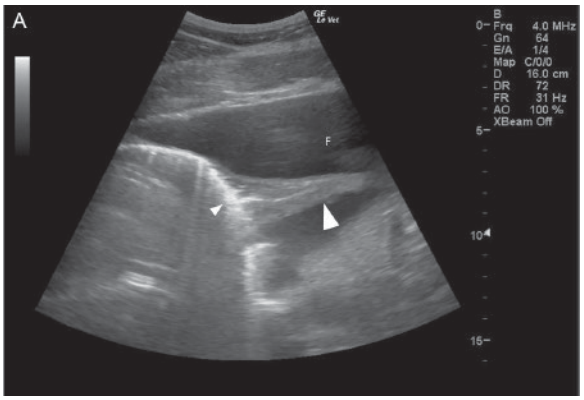


Figure 20.10A Pleural effusion. Pleuropneumonia. This image shows pleural effusion (F) surrounding atelectic (collapsed) lung (arrowhead). The margin between aerated and non-aerated lung is hyperechoic (small arrowhead). This sonogram was obtained with a curvilinear probe operating at 4.0 MHz at a depth of 13 cm.

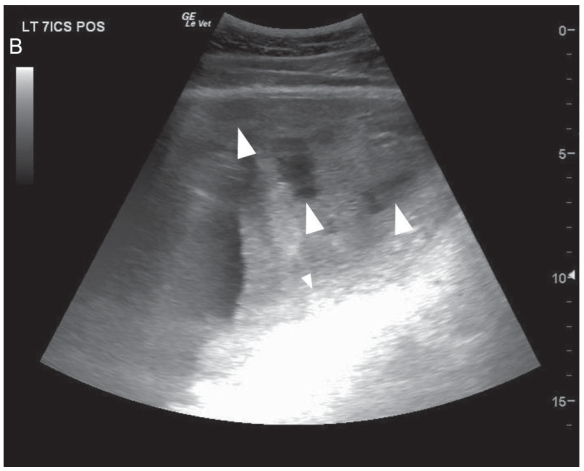


Figure 20.10B Fibrinous pleuritis. Fibrin has coalesced in the pleural space and pocketing of fluid is present (arrowheads). Enhanced transmission of the ultrasound beam through the fluid and fibrin has caused an enhancement of the reflection at the tissue interface (small arrowhead). This sonogram was obtained from the left seventh ICS with a curvilinear probe operating at 4.0 MHz at a depth of 15 cm.

can also be detected and their extent assessed (Figure 20.6, 20.7). Pulmonary damage can also be assessed (Figure 20.8).

Pathology of the Pleural Space

Pleuritis

Uniformly aerated lung adjacent to the parietal pleura creates a hyperechoic gas echo and is responsible for the smooth appearance of healthy lung sliding past the thoracic wall during breathing. With pleuritis, comet tail artifacts result from discrete small amounts of fluid in the pleural space or cellular infiltrate into the pulmonary periphery (Figure 20.9). This leads to transmission of the ultrasound beam and then reflection at an air interface, resulting in the classic hyperechoic shadowing appearance. This hyperechoic shadow is a non-specific indicator of pulmonary pathology and may result from inflammatory conditions, pulmonary edema, metastatic infiltrative conditions, granulomatous diseases, fibrosis, and acute

Vet-ebooks.com

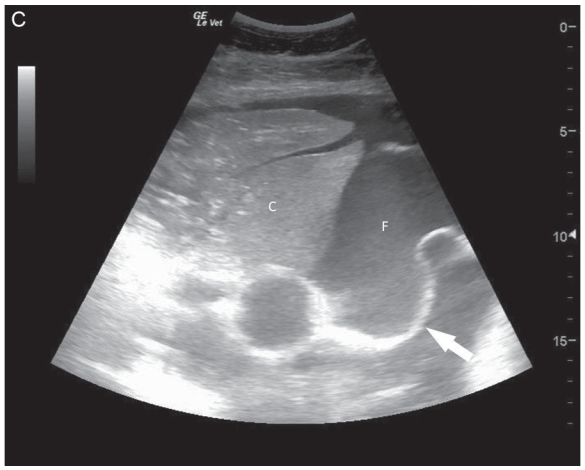


Figure 20.10C Pleuropneumonia. This image shows the pericardial diaphragmatic ligament (arrow) surrounded by pleural fluid (F). This structure is not visualized in the normal thorax but is visible in pleural fluid and distinct from the appearance of fibrin. Consolidated lung is also visible (C). This image was obtained from the left seventh ICS using a curvilinear probe operating at 4.0 MHz at a depth of 17 cm.

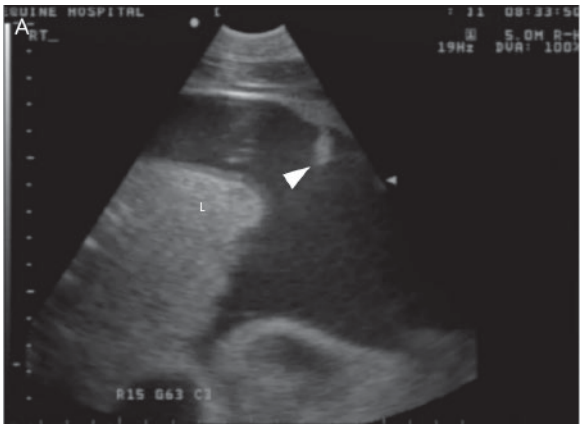


Figure 20.12A Acute hemothorax. Recent hemorrhage within the pleural cavity swirls with respiratory movements. Some fibrin (arrowhead) has deposited on the thoracic pleura. Lung is atelectic (L). This sonogram was obtained from the right sixth ICS with a curvilinear probe operating at 4.0 MHz at a depth of 14 cm.

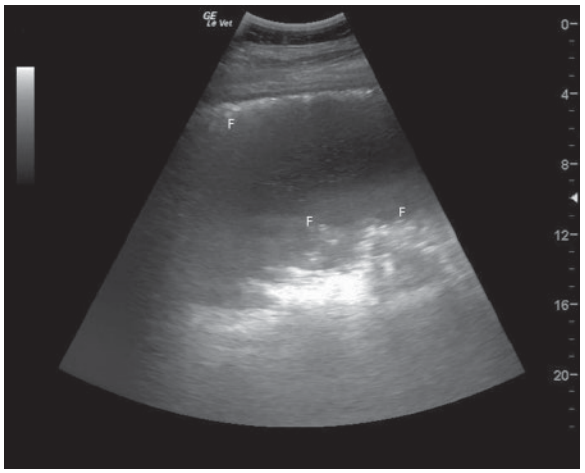


Figure 20.11 Pleural space gas. In this image of pleural effusion, hyperechoic foci are present within the pleural fluid (F) indicating the presence of gas. This image was obtained from the left seventh ICS with a curvilinear probe operating at 4.0 MHz at a depth of 22 cm.

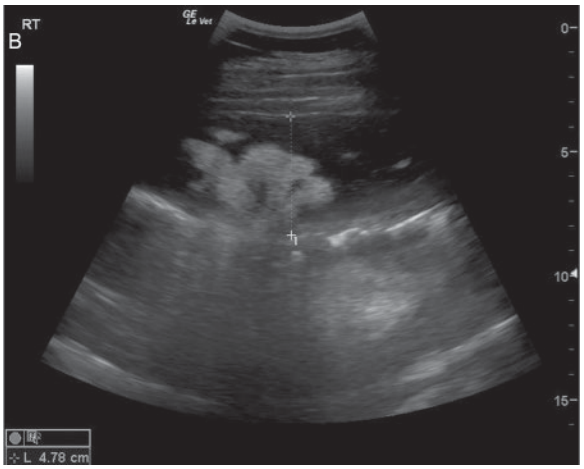


Figure 20.12B Hemothorax, organizing. Clotting has occurred with echodense masses (arrowhead) present within relatively hypoechogenic fluid. This sonogram was taken from the right seventh ICS using a curvilinear probe operating at 4.0 MHz at a depth of 16 cm.

infectious causes of disease [5,6]. Resolved areas of pleural or pulmonary inflammation also retain this appearance.

Pleural Effusions

Pleural effusions are typically a transudate or modified transudate and are, therefore, anechoic in appearance (Figure 20.10). Most cases result from bacterial pneumonia, with a minority resulting from neoplasia [7]. Thoracic lymphadenopathy may also be present with neoplastic effusions [8]. As cell count and protein content increase, ultrasonographic character progresses from hypoechogenic to echogenic. Fibrin strands appear filamentous and echogenic in relation to the fluid around them. They may coalesce to form fluid pockets in a web-like structure joining the lungs, parietal pleura, and diaphragm, or consolidate to a relatively echogenic mass. The accumulation of fibrin is associated with increased mortality [9]. The pericardial diaphragmatic ligament, when highlighted floating in increased pleural fluid, should not be confused with pathological fibrin

Vet-ebooks.com

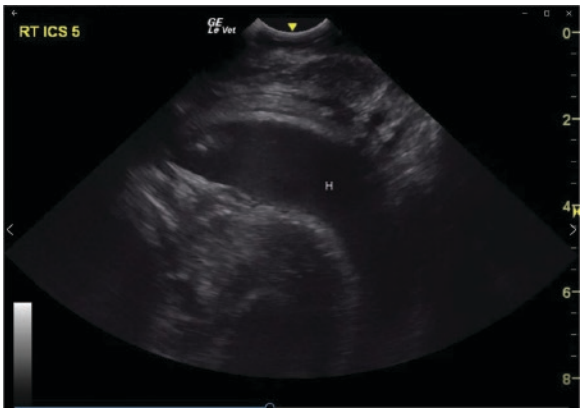


Figure 20.13 Hemopericardium. Hemorrhage within the pericardial sac (H) is secondary to a myocardial laceration, caused by rib fracture in the case. The myocaridium (M, arrowhead) and pericardium (P, small arrowhead) are widely separated in this image obtained from the right fifth ICS using a curvilinear probe operating at 4.0 MHz at a depth of 8 cm.

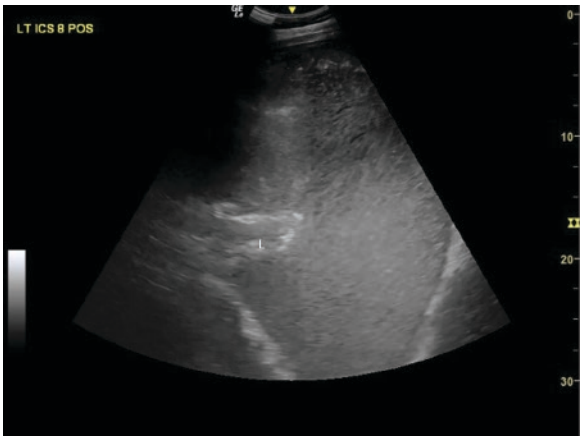


Figure 20.14 Pyothorax. A large quantity of turbid fluid is present in this case of pyothorax in a horse, having progressed from bacterial pleuropneumonia. Fluid appears to swirl with ventilation. Atelectic lung is present (L). This sonogram was obtained from the left eighth ICS with a curvilinear probe operating at 4.0 MHz at a depth of 30 cm.

deposition. The pericardial diaphragmatic ligament is visualized as an undulating uniform solitary hyperechoic strand, in contrast to fibrin which is more filamentous and composed of multiple strands which often form multiple fluid pockets of a honeycomb appearance. The fluid pockets can be a precursor to pleural abscess formation.

Small, hyperechogenic foci within the pleural fluid suggests the presence of gas indicating anaerobic infection or bronchopleural fistula formation. Gas echoes within pleural fluid (Figure 20.11) are a reliable indicator of anaerobic infection [10].

Hemothorax

Hemothorax images as a large, relatively anechoic effusion in the pleural space (Figure 20.12). With respiratory movements, swirling is noted which is likely the result of erythrocyte rouleaux formation. Swirling of the blood may also indicate continued blood loss to the thoracic cavity. Clot formation may be visualized as a heterogenous comparatively hyperechoic mass within anechoic fluid. Hemorrhage may also be present in the pericardial sac as a result of myocardial trauma (Figure 20.13). This allows visualization of the pericardium due to separation from the myocardium and fluid on both sides.

Pyothorax

Pyothorax appears as a large quantity of turbid fluid within the pleural space swirling in time with ventilatory movements, which may solidify over time to form a heterogenous hyperechoic mass. Pocketing with trabecular fibrin may be present, and formation may be considered a progression of pleuritis (Figure 20.14).

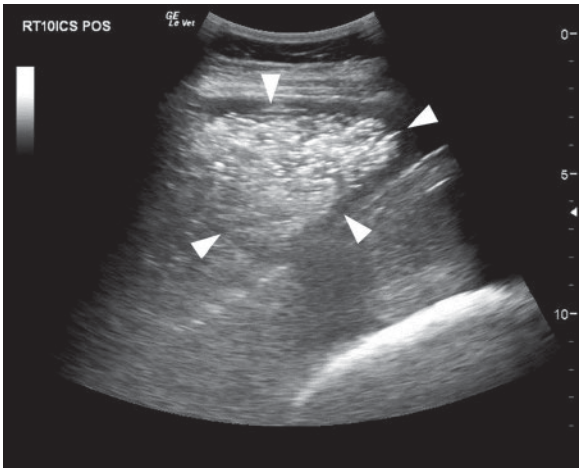


Figure 20.15 Pleural abscess. A pleural abscess (delineated by arrowheads) appears as an encapsulated heterogeneous mass at the diaphragmatic reflection in an adult horse. This sonogram was obtained from the right tenth ICS using a curvilinear probe operating at 4.0 MHz at a depth of 14 cm.

Pleural Abscess

Abscesses may form on the pleural surface (Figure 20.15) and image as hypo- or hyperechoic, encapsulated structures.

Vet-ebooks.com

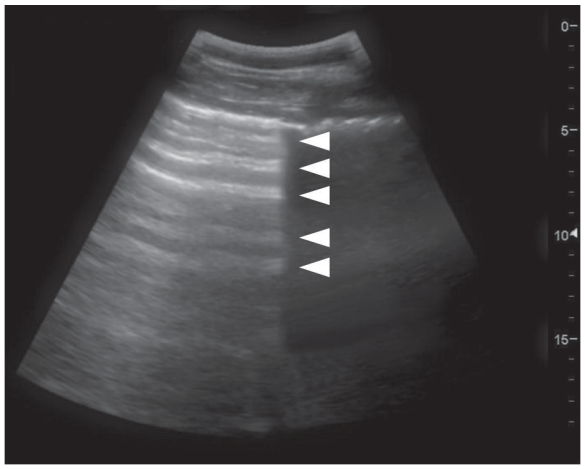


Figure 20.16 Pneumothorax. Air in the pleural cavity separates the lung parenchyma from the thoracic wall. Reverberating, hyperechoic lines (arrowheads) shadow more medial structures. This finding is confirmatory of pneumothorax. This sonogram was obtained from the left fifteenth ICS using a curvilinear probe operating at 4.0 MHz at a depth of 19 cm.

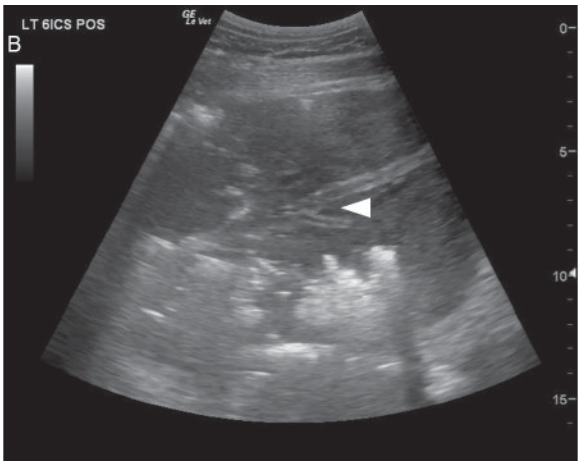


Figure 20.17B Pulmonary consolidation. A branching airway (arrowhead) is clearly delineated within an area of consolidated lung. This sonogram was obtained from the left sixth ICS using a curvilinear probe operating at 4.0 MHz at a depth of 16 cm.

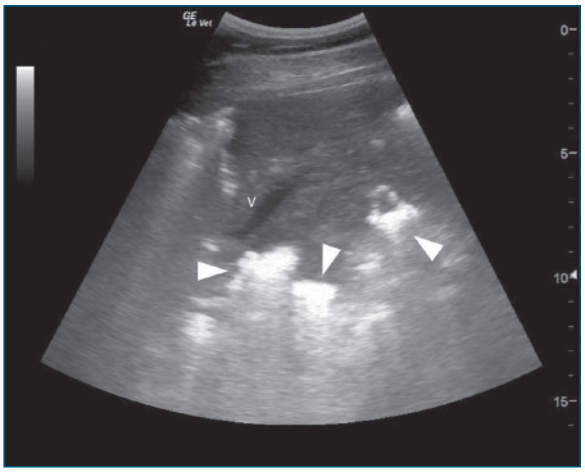


Figure 20.17A Pulmonary consolidation. Enhanced transmission of ultrasound is possible through more echodense pulmonary parenchyma. Blood vessels (V) and airways are apparent. Hyperechoic areas with shadowing indicate areas of gas/air trapping (arrowheads). This sonogram was obtained from the left ninth ICS using a curvilinear probe operating at 4.0 MHz at a depth of 16 cm.

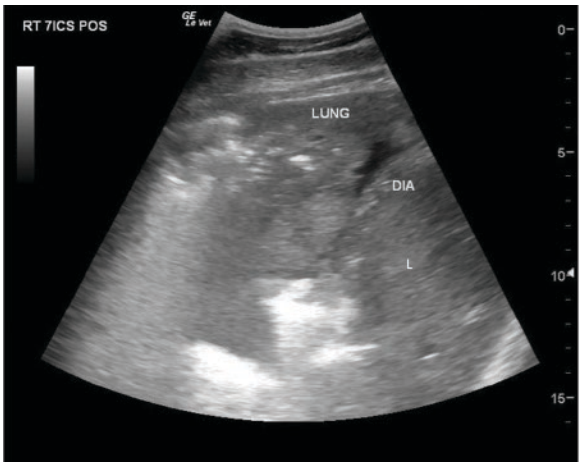


Figure 20.17C Pulmonary consolidation. Consolidated lung (LUNG) is present with air-trapping. The diaphragm is visible (DIA) applied to the liver (L). This sonogram was obtained from the right seventh ICS with a curvilinear probe operating at 4.0 MHz at a depth of 16 cm.

Pneumothorax

Pneumothorax, or the presence of gas within the pleural space, results in loss of the normal pulmonary architecture. A hyperechoic reverberating line is present in place of the parietal pleural reflection (Figure 20.16). Scanning the ICS from dorsal to ventral will ascertain the interface between air accumulation and normal lung parenchyma movement. Lung sliding with ventilation movements will be absent where visceral and parietal pleura are separated by gas. A recent study has demonstrated ultrasonography to be more sensitive than radiography for the detection of small volume pneumothorax [11]. As pneumothorax may be the sole pathology and located dorsally, examination of the entire thoracic cavity from dorsal to ventral is important to detect this condition.

Vet-ebooks.com

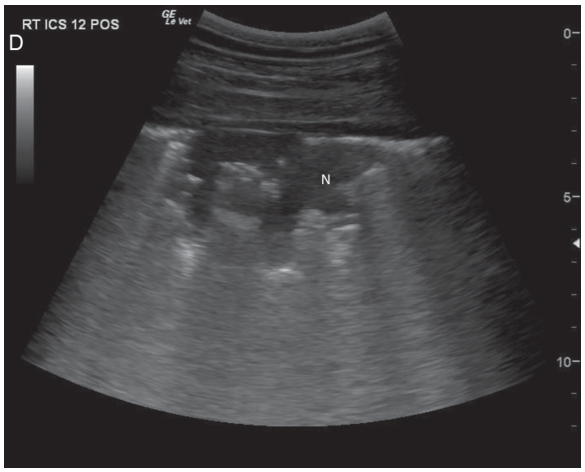


Figure 20.17D Equine multinodular pulmonary fibrosis. Multiple coalescing relatively hypoechogenic structures are present on the lung surface (N); however, normally aerated lung more medially has obscured deeper lesions. At necropsy, the lung was uniformly populated with granulomatous foci. Equine herpesvirus 5 infection was confirmed. This sonogram was obtained from the right twelfth ICS with a curvilinear probe operating at 4.0 MHz at a depth of 12 cm.

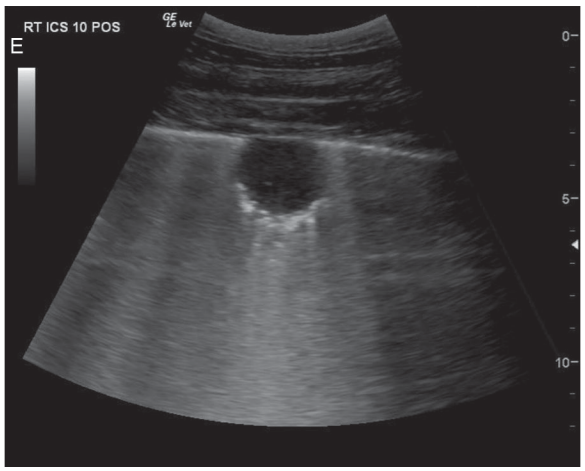


Figure 20.17E Equine multinodular pulmonary fibrosis. Discrete well demarcated hypoechoic lesion on the pulmonary surface. Same horse as Figure 20.19d. This sonogram was obtained from the right tenth ICS with a curvilinear probe operating at 4.0 MHz at a depth of 12 cm.

Pneumopericardium

Air within the pericardium has been reported secondary to trauma and iatrogenically [12]. It appears as a hyperechoic line forming an acoustic shadow along the dorsal and cranial border of the heart. Motion of the acoustic shadowing is in time with the heartbeat.

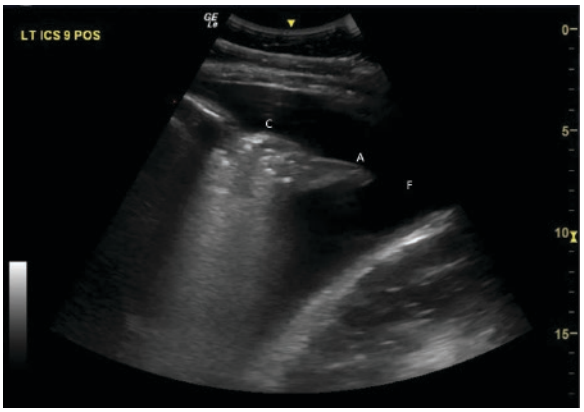


Figure 20.18 Pulmonary atelectasis. Non-aerated atelectic lung (A) is collapsed and adjacent to consolidated lung (C) with air trapping. Fluid surrounds and delineates the abnormal lung. This sonogram was obtained from the left ninth ICS with a curvilinear probe operating at 4.0 MHz at a depth of 18 cm.

Pulmonary Pathology

Pulmonary Consolidation

The most common cause of pulmonary consolidation is pneumonia. Consolidated lung appears as hypoechoic areas within the lung (Figure 20.17). Consolidated areas may be of varying shape, ranging from irregular to spherical. The overall shape of the lung is preserved. Accumulation of fluid and cellular infiltration alters the echogenicity of the lung as these areas area are poorly aerated and hence not acoustically reflective. The pulmonary vascular and bronchial trees may still be evident; however, if tissue degeneration ensues these structures will be lost, and the area becomes more hypoechoic. Diffuse small hypoechoic areas throughout the lung fields may be indicative of a multifocal disease process such as neoplasia or granulomatous lung disease. Air trapping within consolidated lung will appear as multiple discrete hyperechoic foci that shadow deeper structures.

Pulmonary Atelectasis

Pulmonary atelectasis is collapse or compression of lung parenchyma secondary to another disease process and appears relatively hypoechoic. It may result from airway obstruction, pleural effusion, or pneumothorax. When associated with pleural effusion, the cranioventral lung tip is affected. The tip is bathed within pleural fluid and is sometimes highly motile (Figure 20.18). Pneumothorax leads to compression of the more dorsal aspect of the lung resulting in a hypoechoic region of lung at the junction of normal parenchyma and the reverberation artifact resulting from pleural space air (Figure 20.16).

Vet-ebooks.com

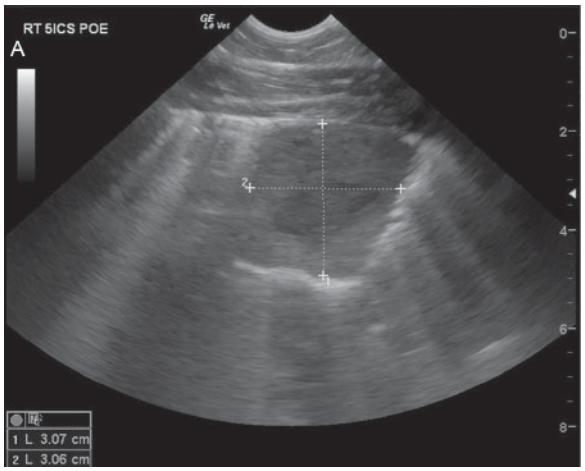


Figure 20.19A Pulmonary abscess, foal. An abscess of heterogenous echodensity is delineated within the pulmonary parenchyma by a hyperechoic margin. This results from reflection of ultrasound waves at the abscess:aerated lung interface. This sonogram was obtained from the right fifth ICS with a microconvex probe operating at 8 MHz at a depth of 8 cm.

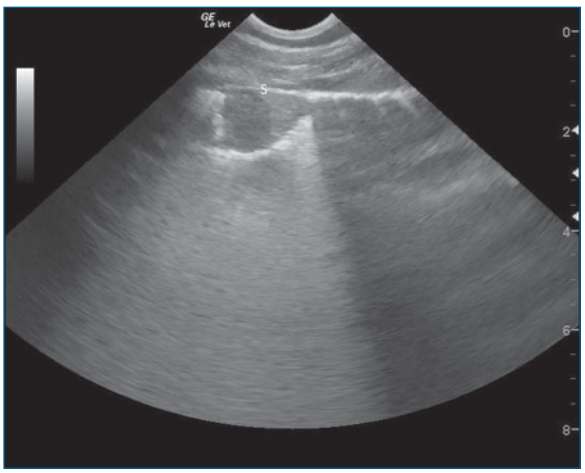


Figure 20.19B Pulmonary abscess, foal. The more fluid content of this abscess (compared to Figure 20.21a) enhances transmission of the ultrasound beam and results in a more pronounced reflection at the fluid–tissue interface. A more hyperechoic interface results, with increased shadowing of more medial structures. Abscess content has also visibly separated vertically under gravity (S). This sonogram was obtained from the right fifth ICS with a microconvex probe operating at 8 MHz at a depth of 8 cm.

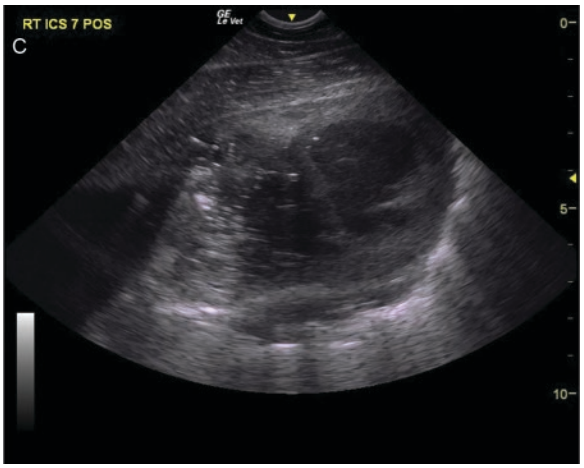


Figure 20.19C Pulmonary abscess, weanling. A large heterogenous abscess with irregular margins. This sonogram was obtained from the right seventh ICS with a microconvex probe operating at 10 MHz at a depth of 10 cm.

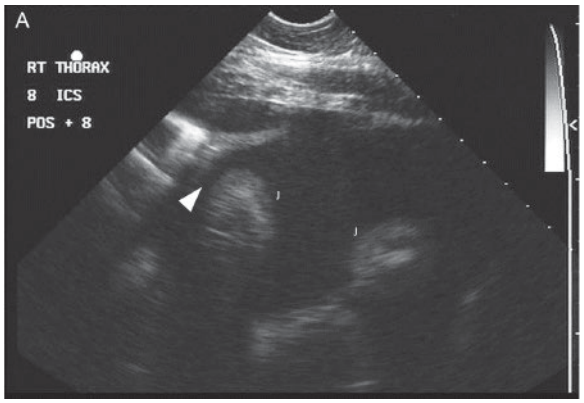


Figure 20.20A Diaphragmatic hernia, intestinal entrapment. This image shows herniation of small intestine into the pleural cavity. Increased pleural fluid is present. The loops of jejunum (J) are thick-walled and in direct apposition with the lung parenchyma (arrowhead). Diaphragm is not visible between the intestine and lung. This sonogram was obtained from the right eighth ICS with a curvilinear probe operating at 3.5 MHz at a depth of 12 cm.

Pulmonary Abscessation

Pulmonary abscesses that contact the surface of the lung or those abscesses that result from pleural space disease can be imaged with ultrasonography (Figure 20.19). They may also be seen within consolidated lung but cannot be imaged if aerated lung that is not compressed is present between the abscess and the ultrasound transducer. They may appear as a heterogenous hypoechoic region with hyperechoic blurred margins of irregular width, an irregular or round shape, and a lack of pleural separation. Gas may also be present leading to a mixture of hyperechoic and hypoechoic reflections and shadowing within the cavitation. There is a significant association between the presence of hyperechoic gas echoes and the presence of anaerobic infection [10].

Vet-ebooks.com

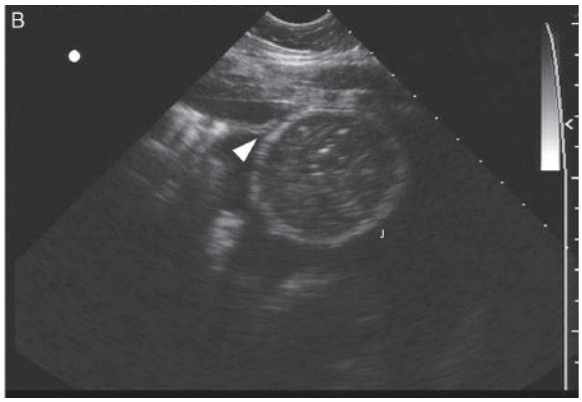


Figure 20.20B Diaphragmatic hernia, intestinal entrapment. This image shows herniation of small intestine into the pleural cavity with subsequent entrapment. Increased pleural fluid is present. The loops of jejunum (J) are thin-walled, distended, amotile, and in direct apposition with the lung parenchyma (arrowhead). Diaphragm is not visible between the intestine and lung. This sonogram was obtained from the right seventh ICS with a curvilinear probe operating at 3.5 MHz at a depth of 12 cm.

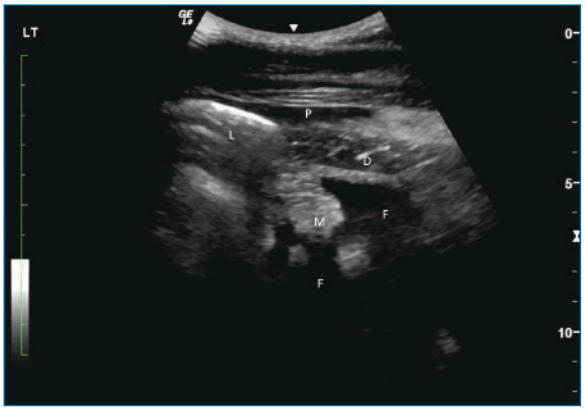


Figure 20.21 Mesothelioma, pleural, and peritoneal fluid. The diaphragm (D) is delineated on each side by pleural (P) and peritoneal (F) fluid. Lung is present (L). Tumor masses (M) are adherent to the diaphragm on the peritoneal side. This sonogram was obtained from the left twelfth ICS with a curvilinear probe operating at 4 MHz at a depth of 12 cm.

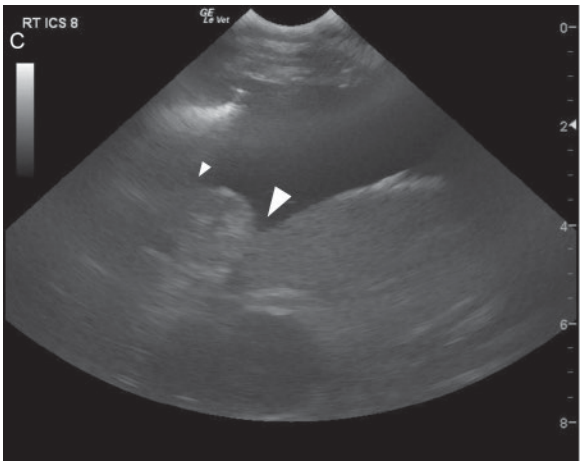


Figure 20.20C Diaphragmatic disruption. Increased pleural fluid is present. Direct apposition of intestine to both liver (arrowhead) and lung (small intestine) parenchyma without a diaphragm present is diagnostic. This sonogram was obtained from the right eighth ICS with a curvilinear probe operating at 4 MHz at a depth of 8 cm.

Interstitial Pneumonia

Diffuse inflammation of the lung parenchyma can result in interstitial pneumonia (Figure 20.4C). Interstitial pneumonia has a characteristic appearance, with diffuse shadowing-out or a "ground glass" appearance. Interstitial pneumonia is the result of fulminant inflammation from a variety of causes which include bacteria, viral or fungal infection, environmental factors, and acute lung injury (ALI).

Increased Pulmonary Volume

Increased pulmonary volume may occur with severe equine asthma. As seen with ultrasound, lungs fields in affected horses may extend more caudally than normal and have a distorted dorsal border suggesting expansion of the lung field from pulmonary hyperinflation or emphysema [13]. Variation in the caudal extent of the lung fields is noted between horses; however, the seventeenth ICS consistently does not contain lung in the normal horse [13].

Diaphragmatic Disruption

Herniation of abdominal content into the thoracic cavity (Figure 20.20) may be suspected where curved, hyperechoic interfaces attenuate the ultrasound beam and cause reverberation cranial and dorsal to the diaphragmatic line [14]. Peristaltic waves may also be noted when intestine has herniated into the thoracic cavity. Anechoic fluid may be noted ventrally in the thorax consistent with concurrent pleural effusion. Architecture of the cranially displaced viscera may be abnormal due to strangulation or infarction. The muscular borders of the diaphragmatic tear may appear thickened and irregular as they retract through loss of tension (Figure 20.20C). Herniation through the central tendon may be difficult to detect as the defect is not visible and viscera may not be sufficiently adjacent to the thoracic wall to allow imaging by ultrasonography.

Vet-ebooks.com

Neoplastic disease, including lymphosarcoma or hemangiosarcoma, may manifest as nodular lesions in the diaphragm (Figure 20.21).

Limitations of Thoracic Ultrasonography

With respect to intrapulmonary disease, radiography remains a superior diagnostic modality. Ultrasound is unable to penetrate air-filled lung raising the specter of significant pathology being shielded from view by normally aerated lung parenchyma. In these cases, when used in conjunction with ultrasonography, radiography allows the most thorough imaging of the thoracic content to be achieved.

Summary

Thoracic ultrasonography allows rapid assessment of pleural and pulmonary health. However, ultrasonography should not be considered a substitute for a thorough physical examination of the patient and careful thoracic auscultation. Rather, the information it provides the clinician with is complementary and confirmatory in nature, adding weight to clinical suspicions already raised from the horse's history and physical examination.

Reference List

1 Rantanen, N.W. (1986). Diseases of the thorax. *Veterinary Clinical of North American Equine Practice* 2(1): 49–66.

2 Rantanen, N. (1981). Ultrasound appearance of normal lung borders and adjacent viscera in the horse. *Veterinary Radiology* 22(5): 217–219.

3 Jean, D., Picandet, V., Macieira, S. et al. (2007). Detection of rib trauma in newborn foals in an equine critical care unit: A comparison of ultrasonography, radiography and physical examination. *Equine Veterinary Journal* 39(2): 158–163.

4 Jean, D., Laverty, S., Halley, J. et al. (1999). Thoracic trauma in newborn foals. *Equine Veterinary Journal* 31(2): 149–152.

5 Gross, D.K., Morley, P.S., Hinchcliff, K.W. et al. (2004). Pulmonary ultrasonographic abnormalities associated with naturally occurring equine influenza virus infection in standardbred racehorses. *Journal of Veterinary Internal Medicine* 18(5): 718–727.

6 Marr, C.M. (1993). Thoracic ultrasonography. *Equine Veterinary Education* 5(1): 41–46.

7 Johns, I., Marr, C., Durham, A. et al. (2017). Causes of pleural effusions in horses resident in the UK. *Equine Veterinary Education* 29(3): 144–148.

8 Janvier, V., Evrard, L., Cerri, S. et al. (2016). Ultrasonographic findings in 13 horses with lymphoma. *Veterinary Radiol Ultrasound* 57(1): 65–74.

9 Tomlinson, J.E., Reef, V.B., Boston, R.C. et al. (2015). The association of fibrinous pleural effusion with survival and complications in horses with pleuropneumonia (2002–2012): 74 cases. *Journal of Veterinary Internal Medicine* 29(5): 1410–1417.

10 Reimer, J.M., Reef, V.B., and Spencer, P.A. (1989). Ultrasonography as a diagnostic aid in horses with anaerobic bacterial pleuropneumonia and/or pulmonary abscessation: 27 cases (1984–1986). *Journal of Am erican Veterinary Medical Association* 194(2): 278–282.

11 Partlow, J., David, F., Hunt, L.M. et al. (2017). Comparison of thoracic ultrasonography and radiography for the detection of induced small volume pneumothorax in the horse. *Veterinary Radiol Ultrasound* 58(3): 354–360.

12 Durando, M.M., Zarucco, L., Schaer, T.P. et al. (2006). Pneumopericardium in a horse secondary to sternal bone marrow aspiration. *Equine Veterinary Education* 18(2): 75–79.

13 Bakos, Z., Voros, K., Kellokoski, H. et al. (2003). Comparison of the caudal lung borders determined by percussion and ultrasonography in horses with recurrent airway obstruction. *Acta Veterinary Hungarica* 51(3): 249–258.

14 Hartzband, L.E. Kerr, D.V., and Morris, E.A. (1990). Ultasonographic diagnosis of diaphragmmatic rupture in a horse. *Veterinary Radiology* 31(1): 42–44.

Vet-ebooks.com

21

Ultrasonography of the Heart

Katharyn J. Mitchell[1] *and Colin C. Schwarzwald*[2]

[1] *College of Veterinary Medicine, Cornell University, Ithaca, USA*
[2] *Clinic of Equine Internal Medicine, University of Zurich, Zurich, Switzerland*

Over the last four decades, echocardiography has become a standard diagnostic tool in equine cardiology. Development of M-mode, two-dimensional (2-D) real-time echocardiography, and introduction of various Doppler modalities, including continuous-wave (CW) Doppler, pulsed-wave (PW) Doppler, and color flow Doppler, provided the basis for comprehensive evaluation of internal cardiac structures, chamber dimensions, blood flow characteristics, and mechanical function of the equine heart [1–3]. Newer echocardiographic modalities, including tissue Doppler imaging (TDI) and 2-D speckle tracking (2DST) have become valuable advanced tools for assessment of subtle changes to cardiac function in horses [4–11]. The practical application of three-dimensional real-time echocardiography is currently being explored. This modality potentially will provide the clinician with additional information about the valvular structures, better understanding of complex congenital malformations, and theoretically, a more accurate assessment of cardiac chamber size, particularly the right ventricle (RV), which is currently difficult to accurately evaluate due to it complex geometric shape.

Nonetheless, accurate and reliable assessment of chamber dimensions and mechanical function of the heart remains challenging and is limited by a variety of technical, anatomical, and physiological issues that must be considered when performing echocardiographic examinations [3,12,13]. Knowledge of the technical principles of ultrasonography, strict adherence to a routine protocol in order to obtain high-quality standard sonographic images, and comprehensive understanding of normal cardiac anatomy and abnormal findings in horses with heart disease, are prerequisites to the successful use of echocardiography. Also, despite the availability of quantitative echocardiographic methods, subjective assessment of recordings remains a cornerstone of echocardiography and must not be neglected. Finally, independent of the methods used, the information obtained during echocardiography should be critically assessed in the light of medical history and clinical findings.

Technical Considerations

The ultrasonographic equipment should include a phased-array sector transducer working at frequencies between 1.5 and 3.5 MHz. Tissue harmonic imaging often improves the image quality, particularly in the far field and in large horses, by providing a higher signal-to-noise ratio, better contrast, and higher spatial resolution. Frame rates of at least 15 Hz (15 images/second) are required for real-time 2-D imaging of the moving structures of the heart, but frame rates of 25 Hz or higher are preferable. Newer applications such as anatomical M-mode [14] or 2-D speckle tracking [6–8] demand a frame rate between 40 and 90 Hz to achieve sufficient temporal resolution. Color TDI requires frame rates of > 120 Hz [5,9]. The depth of penetration should reach at least 25 to 30 cm to scan the heart of an adult horse. Simultaneous recording of a surface ECG is required and allows exact timing of flow events, wall motion, and echocardiographic measurements. Modern echocardiography systems offer digital raw data storage of still frames and cine loop recordings. This is extremely useful, since it reduces the contact time with the patient and allows post processing and off-line analysis of the stored data. Capturing various measurements at the correct timing within cardiac

Atlas of Equine Ultrasonography, Second Edition. Edited by Jessica A. Kidd, Kristina G. Lu and Michele L. Frazer.
© 2022 John Wiley & Sons Ltd. Published 2022 by John Wiley & Sons Ltd.
Companion Website: www.wiley.com/go/kidd/atlas

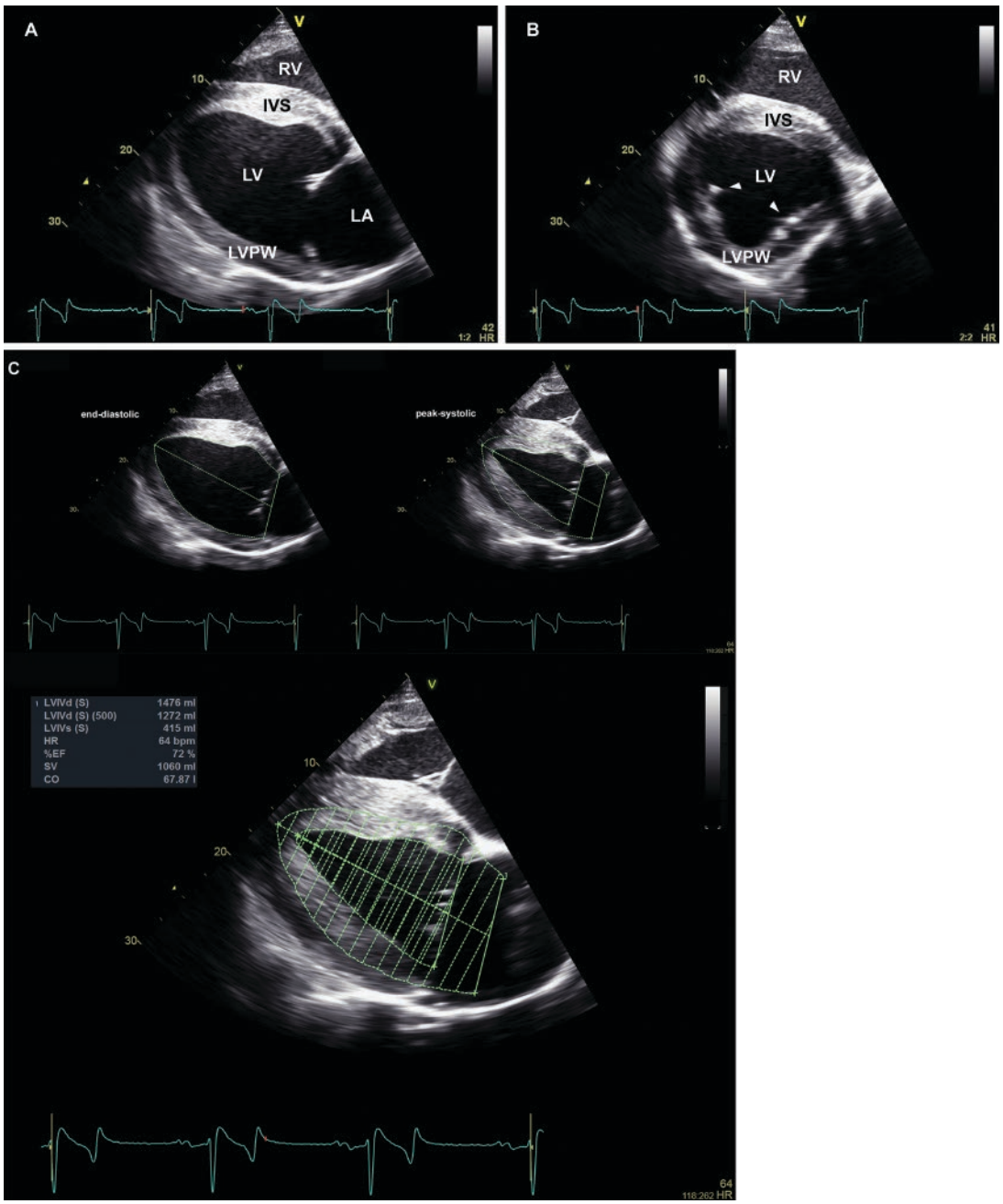
Vet-ebooks.com

cycle is critical and therefore, cine loop recordings provide the observer with opportunities to capture several measurements throughout the cardiac cycle (particularly useful for measurements of area or volume).

Ultrasonographic Anatomy of the Normal Equine Heart

The echocardiographic examination should take place in a location where the horse can be safely restrained. If possible, the patient should not be sedated prior to the examination, since cardiac dimensions, indices of cardiac function, and color Doppler signals of regurgitant flow or shunt flow might be altered because of drug effects on preload, afterload, contractility, heart rate, and rhythm [15–19]. However, some horses do not tolerate the echocardiographic procedure and require sedation to allow safe examination with sufficient quality and at normal heart rates. Clipping of the hair coat may be required to improve image quality, particularly in horses with thicker coats.

A systematic approach using standardized image planes is important for comparison of studies over time and for comparison of studies obtained by different examiners (Figures 21.1, 21.2, 21.3, 21.4, and



Vet-ebooks.com

Figure 21.1 Standard echocardiographic views for assessment of left ventricular size and function. (A) Right-parasternal long-axis 4-chamber view centered on the left ventricle (LV). The transducer is positioned in the right 4th intercostal space at a level slightly above the olecranon, angled caudally, and rotated clockwise to the 1-o'clock position. Slight changes in transducer placement may be necessary to optimize the image plane. This view is best suited to assess the structures, dimensions, and mechanical function of the LV. Since this image is centered on the LV, the left atrium (LA) may not be imaged in its entirety throughout the cardiac cycle. Assessment of the right heart is limited due to its anatomical position, its complex geometry, and its visualization in the narrow near field of the imaging sector. (B) Right-parasternal short-axis view of the LV at the level of the chordae tendineae (arrowheads). This view is obtained by rotating the transducer 90 degrees clockwise from a 4-chamber view. It is commonly used for measurement of the diameter and the area, respectively, of the LV and evaluation of LV systolic function. (C) Same image plane as in (A), showing tracings (green dotted lines) of the LV internal area and longitudinal axis at end-diastole (top left) and peak-systole (top right). The bottom image shows the end-diastolic area tracing superimposed to the peak-systolic area tracing (green dotted lines). Applying a geometric model such as the modified (single-plane) Simpson's model of discs allows calculation of the estimated LV volume at end-diastole (LVIVd) and peak-systole (LVIVs), ejection fraction [%EF = (LVIVd – LVIVs)/LVIVd × 100], stroke volume [SV = LVIVd – LVIVs], and cardiac output [CO = SV × HR]. HR, heart rate; LVIVd (S) (500), LVIVd estimated by Simpson's model and allometrically scaled to a body weight of 500 kg. (D) Right-parasternal short-axis view (top) and corresponding M-mode recording (bottom) of the LV at the chordal level. The motion of the interventricular septum (IVS) and the left-ventricular free wall (LVFW) are displayed over time. Care must be taken that the LV is bisected by the cursor line into two symmetrical parts throughout the cardiac cycle. The right ventricle (RV) and the right-ventricular free wall (RVFW) are displayed in the near field. A small amount of spontaneous echo contrast is commonly seen in the ventricular lumen (arrowheads). Measurement of LV wall thickness and internal dimensions, evaluation of septal motion, and calculation of LV fractional shortening (%FS) allow assessment of LV size and systolic function. The blue dotted lines indicate measurement of the IVS, the left-ventricular internal diameter (LVID), and the LVFW at end-diastole (defined as the onset of the electrocardiographic QRS complex) and at peak systole (defined as the time at which the LV internal lumen is narrowest). These measurements allow calculation of the LV fractional shortening [%FS = (LVIDd – LVIDs)/LVIDd × 100], mean wall thickness at end-diastole [MWTd = (IVSd + LVFWd)/2], and relative wall thickness at end-diastole [RWTd = (IVSd + LVFWd)/LVIDd]. LVIDd(500), left-ventricular internal diameter allometrically scaled to a body weight of 500 kg; LA Diam (max)/LVIDd, ratio of maximum LA diameter to LVIDd; d: measurements at end-diastole; s: measurements at peak systole. (E) Anatomical M-mode (AMM) image of the LV (bottom), reconstructed from a digitally stored 2-D cineloop recording obtained from a right-parasternal short-axis view at the chordal level (top). Notice that the AMM cursor (green line) can be freely positioned on the 2-D image, independent of the sector apex, to bisect the IVS, the LV cavity, and the left-ventricular posterior wall (LVPW; also called left ventricular free wall, LVFW) into two equal parts throughout the cardiac cycle. A small amount of spontaneous echo contrast is commonly seen in the ventricular lumen (arrowheads). (*Source*: C and D: with permission from Schwarzwald, C.C. (2019) Equine echocardiography. Veterinary Clinics: Equine Practice 35(1): 43–64).

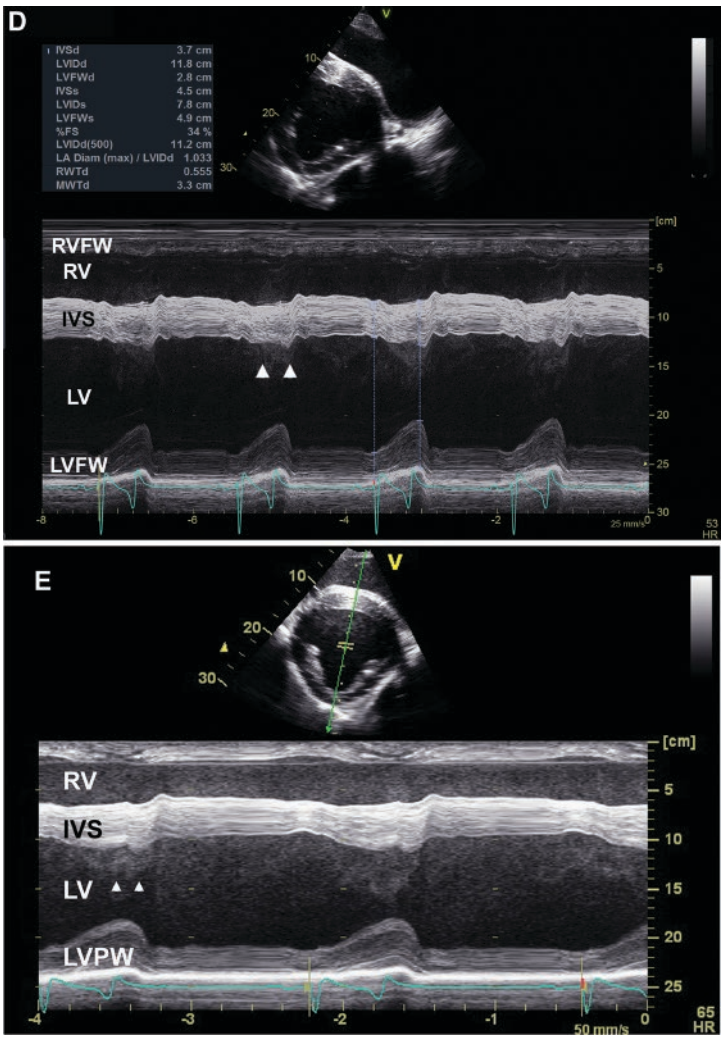


Figure 21.1 (Continued)

Vet-ebooks.com

Figure 21.3 Standard echocardiographic views for assessment of the great vessels. (A) Right-parasternal long-axis view of the left ventricular outflow tract (LVOT). Starting from a 4-chamber view (Figure 21.1A), the transducer is angled more cranially, tilted dorsally, and rotated to the 2-o'clock position to obtain this view. It is best suited to assess the structures, dimensions, and function of the aortic valve, the sinus of valsalva, and the ascending aorta (Ao) and the pulmonary artery (PA). The diameter of the PA should be smaller than the diameter of the aorta. Chordae tendineae are seen in the left ventricular (LV) cavity (arrowheads). (B) Right-parasternal long-axis view of the right ventricular outflow tract (RVOT). Starting from an LVOT view (A), the transducer is angled more cranially to obtain this view; occasionally the transducer will have to be moved one intercostal space cranially. The right atrium (RA), the tricuspid valve, the right ventricle (RV), the RVOT, the pulmonic valve, the pulmonary artery (PA), and a cross-section through the right coronary artery (arrow) can be visualized. (C) Left-parasternal long-axis view of the LVOT. The transducer is positioned in the 5th or 4th intercostal space at a level slightly above the olecranon and angled slightly cranially. (D) Left-parasternal long-axis view of the RVOT. Starting from the LVOT view (C), the transducer is moved one intercostal space cranially to obtain this image. LA: left atrium; LV: left ventricle.

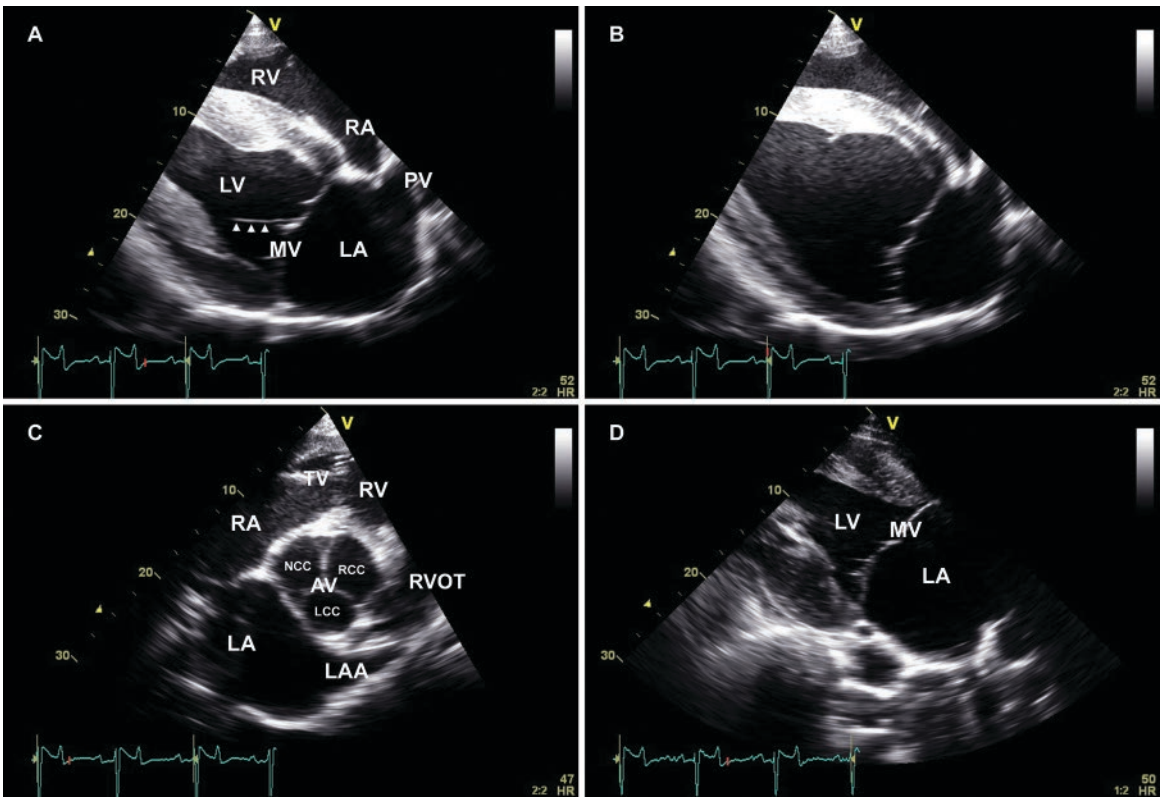


Figure 21.2 Standard echocardiographic views for assessment of left atrial size and function. (A) and (B) Right-parasternal 4-chamber view centered on the left atrium (LA), to image the LA in its entirety throughout the cardiac cycle. At an imaging depth of 30 cm, this view is best suited to assess the mitral valve (MV) apparatus, LA dimensions, and LA mechanical function. Only in rare cases (e.g., giant draft breeds, horses with severe cardiomegaly), can the LA not be displayed in its entirety from this window. (A) Image recorded at the end of ventricular systole, one frame prior to opening of the MV, when the LA is at its maximum dimensions. Chordae tendineae are seen in the left ventricular (LV) cavity (arrowheads). (B) Image recorded at the end of diastole, immediately after closure of the MV, when the LA is at its minimum dimensions. Note the obvious change in LA dimensions within a single cardiac cycle (i.e., between (A) and (B)), indicating that timing of measurements of LA dimensions is critical. Generally, LA dimensions should be assessed at the end of ventricular systole (A). (C) Right-parasternal short-axis view at the level of the aortic valve. This view is obtained by rotating the transducer 90 degrees clockwise from a right-parasternal left-ventricular outflow tract view (Figure 21.3A). In this view, the aortic valve (AV) with its three cusps is visible in the center of the image. The surrounding structures include right atrium (RA), tricuspid valve, right ventricle (RV), right-ventricular outflow tract (RVOT), LA, and left atrial appendage (LAA). The apparent triangular separation (at the 12-o'clock position) evident between the non coronary cusp (NCC) and the right coronary cusp (RCC) is a normal finding and does not represent an anomaly. In this view, the end-systolic size of the LA and LAA can be measured and compared to the aortic area. (D) Left-parasternal long-axis view of the LA, MV, and LV. The transducer is positioned in the 5th intercostal space slightly above the olecranon, oriented perpendicular to the chest wall and angled dorsally. This view has traditionally been used for assessment of LA dimensions. However, as opposed to the right-parasternal views (A) and (B), this view often does not allow imaging of the LA in its entirety due to interference with the ventral lung border. Nonetheless, imaging LA and MV from a left thoracic window provides additional information and should complement the right-parasternal views. LCC: left coronary cusp of the aortic valve; PV: pulmonary vein; TV: tricuspid valve.

Vet-ebooks.com

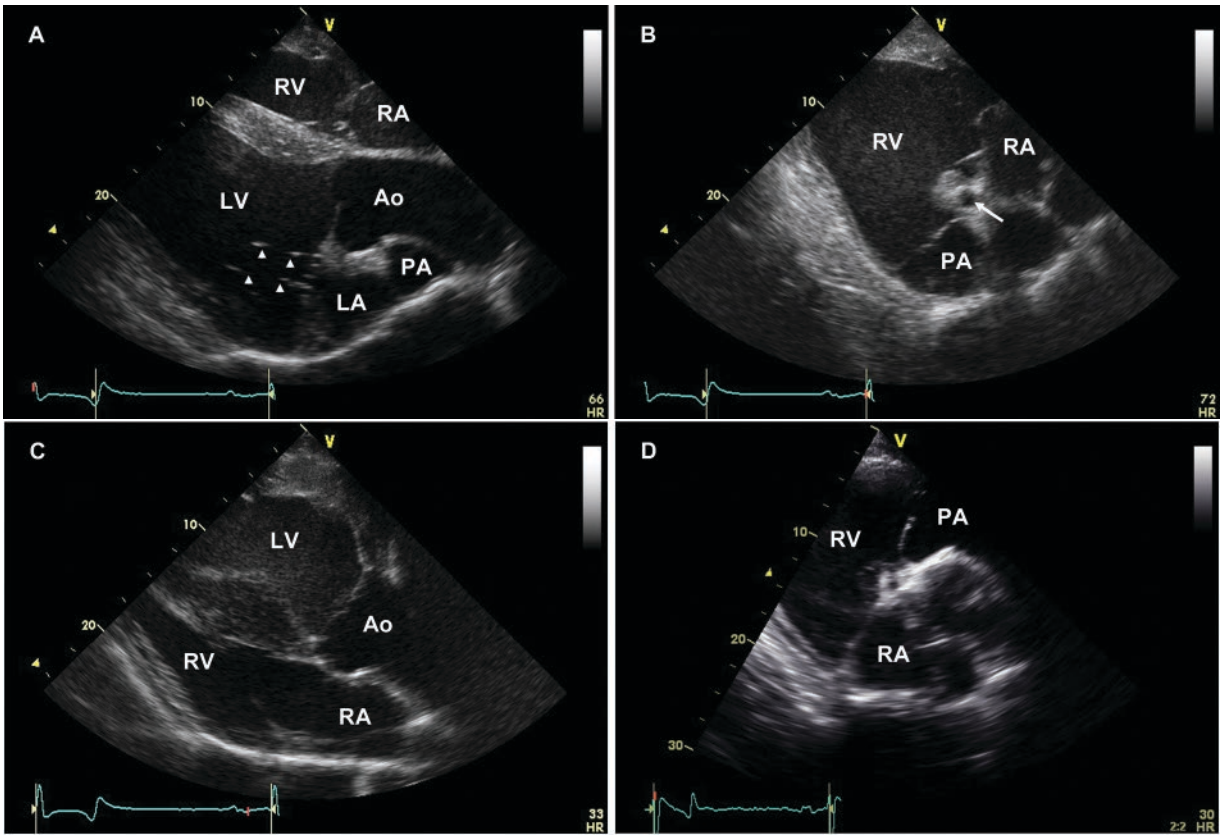


Figure 21.4 Mitral and aortic valve motion. (A) M-mode recording of mitral valve motion obtained from a right-parasternal short-axis view at the level of the mitral valve. The M-mode cursor (dotted line) is placed across the MV leaflets. The motion of the septal mitral leaflet and the time of mitral valve closure (MVC) and opening (MVO) can be identified on the M-mode tracing. The E wave (E) represents early-diastolic opening of the mitral valve during passive inflow of blood from the left atrium into the ventricle. The A wave (A) represents late-diastolic opening of the mitral valve during atrial contraction. The E point-to-septal separation (EPSS) can be increased with aortic regurgitation (regurgitant jet impinging on the valve), LV dilation with left ventricular failure (reduced transmitral flow), or mitral stenosis/tethering (rare defects or acquired from endocarditis). (B) M-mode recording of aortic valve motion obtained from a right-parasternal short-axis view of the aorta. The M-mode cursor (dotted line) is placed across the aortic valve leaflets. Motion of the left-coronary cusp and the time of aortic valve opening (AVO) and aortic valve closure (AVC) can be identified. This view has traditionally been used for assessment of aortic size and left atrial dimensions, but has largely been replaced by 2-D methods (Figures 21.2 and 21.3). Ao: aorta; LAA: left atrial appendage; RV right ventricle; TV: tricupsid valve.

Vet-ebooks.com

21.5). By convention, the structures nearest to the transducer are displayed at the top of the screen. The dorsal (in the long-axis views) and cranial (in the short-axis views) structures of the heart are displayed to the right side of the screen.

Indications and Clinical Use of Echocardiography in Horses

Echocardiography can be used to identify cardiac disorders, assess hemodynamic and structural consequences of disease, and monitor response to treatment and progression of disease (Figures 21.6–21.28). Echocardiography is indicated in horses with heart murmurs to differentiate physiological flow murmurs from pathological murmurs and assess their clinical relevance; to detect underlying cardiac disease in horses with cardiac dysrhythmias; to diagnose or rule out cardiac disease in horses with exercise intolerance, poor performance, collapse, or episodic weakness; to screen for endocarditis or pericarditis in horses with fever of unknown origin; to diagnose or rule out pericardial disease in horses with muffled heart sounds; to diagnose the cause of persistent tachycardia (e.g., because of severe myocardial disease); to detect pulmonary hypertension in horses with severe respiratory disease; to diagnose suspected congenital cardiac defects; and to determine the cause of heart failure and monitor

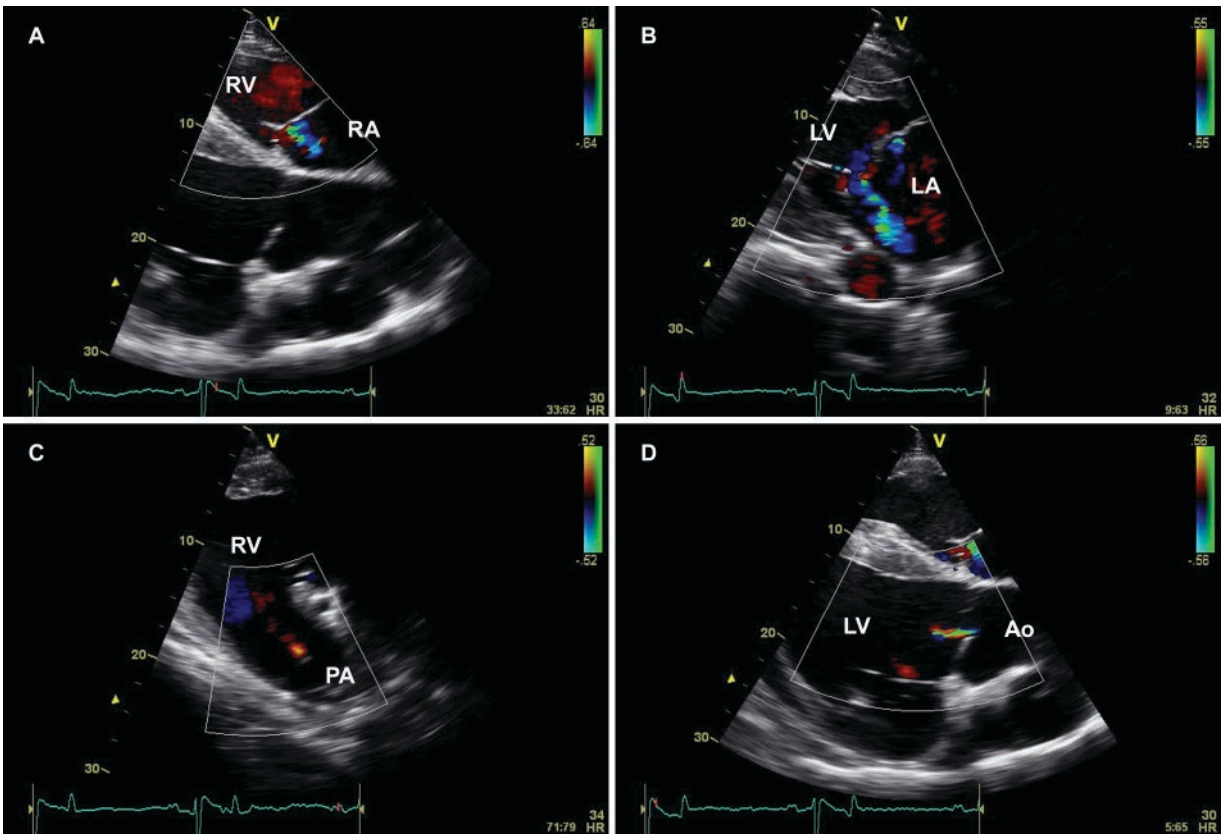


Figure 21.5 Color Doppler findings in apparently healthy horses. Color Doppler recordings obtained from an 8-year-old healthy Hanoverian Warmblood gelding in athletic condition (eventing). Blood flow toward the transducer is coded in red to yellow and flow away from the transducer is coded in shades of blue to cyan. Flow that is turbulent according to the system algorithm is colored in green. Traces of valvular regurgitation are frequently found on echocardiograms of healthy horses with normal exercise capacity, often even in absence of an audible murmur. Many of these small regurgitant jets are evident only in distinct imaging planes and most are not considered clinically relevant. (A) Right-parasternal left ventricular outflow tract view. The region of interest (ROI) is positioned over the tricuspid valve. Trivial tricuspid regurgitation is evident in the right atrium (RA) during systole, color-coded in blue, cyan, and green. (B) Left-parasternal long-axis view with the ROI positioned over the mitral valve. Mild mitral regurgitation is evident in the left atrium (LA) during systole. Two distinct regurgitant jets (color-coded in blue, cyan, and green) are seen: a small jet originating from the parietal leaflet and a larger jet stemming from the septal leaflet. (C) Right-parasternal right ventricular outflow tract (RVOT) view. The ROI is positioned over the pulmonic valve. Trivial, low-velocity pulmonic insufficiency (color-coded in red) is evident in the RVOT during diastole. (D) Right-parasternal left ventricular outflow tract view. The ROI is positioned over the aortic valve. A trace of aortic insufficiency (color-coded in green) can be seen in the left ventricle (LV) at end-diastole, immediately before opening of the aortic valve. Ao: aorta; PA: pulmonary artery; RV: right ventricle.

Vet-ebooks.com

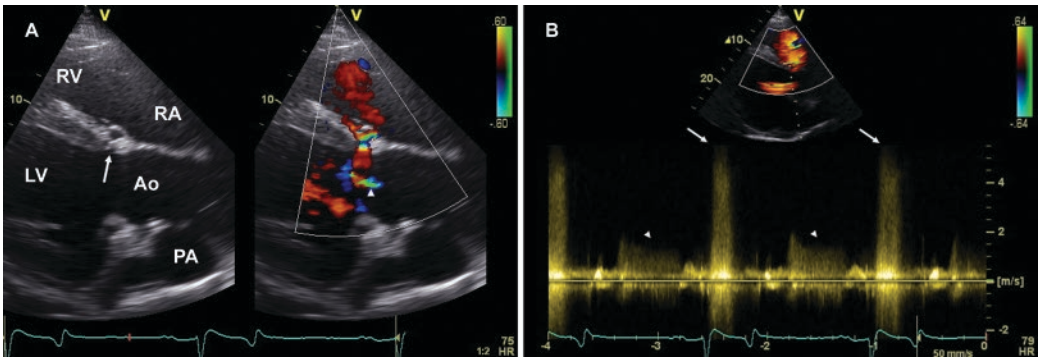


Figure 21.6 Restrictive ventricular septal defect. (A) Right-parasternal long-axis view of the left ventricular outflow tract obtained from a 3-year-old Friesian filly with a restrictive paramembranous ventricular septal defect. The small defect (arrow) can easily be missed on the grayscale image (left). Color flow mapping facilitates identification of the defect and clearly shows transseptal blood flow (right). Notice the classic color aliasing pattern in which flow changes from dark red, to yellow, to blue, and finally to a green turbulent encoding. A small aortic regurgitant jet is seen as well (arrowhead). The size of the pulmonary artery (PA) relative to the aorta (Ao) appears normal and does not suggest significant pulmonary hypertension. (B) Long-axis echocardiogram and corresponding continuous-wave Doppler recording indicating left-to-right shunt flow through the ventricular septal defect. The peak systolic velocity (arrows) is 5.25 m/s, corresponding to a high (normal) left-to-right pressure gradient of 110 mmHg (modified Bernoulli equation: $dp = 4 \times v_{max}^2$). The diastolic flow component (arrowheads) corresponds to aortic regurgitant flow or diastolic shunt flow. LV: left ventricle; RA: right atrium; RV: right ventricle.

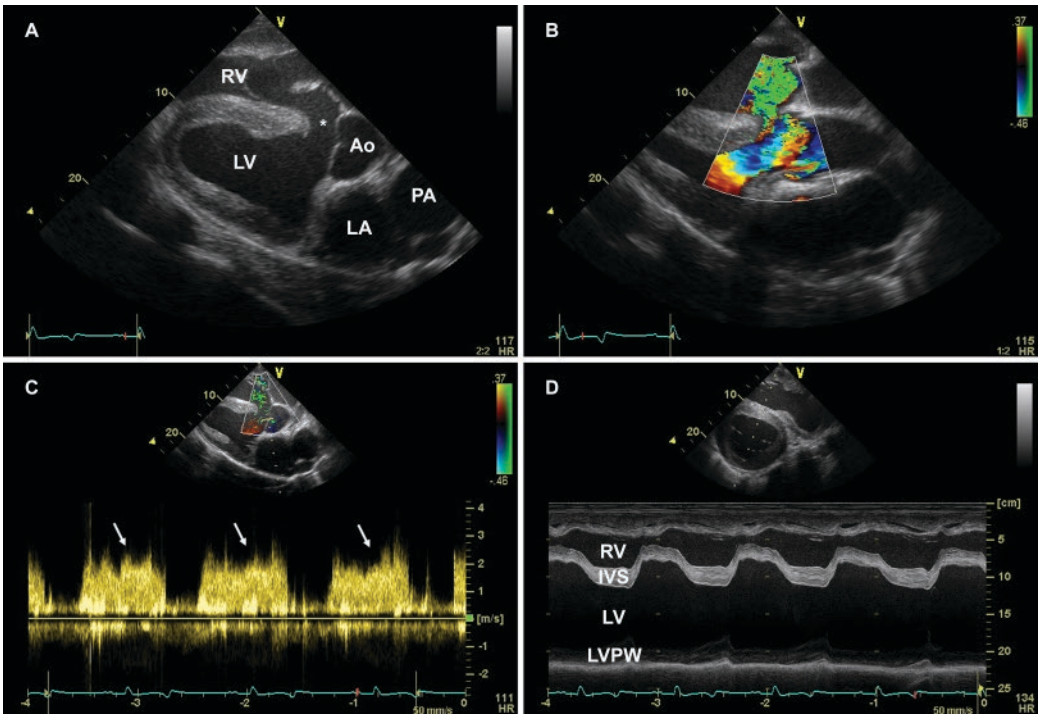


Figure 21.7 Non-restrictive ventricular septal defect. (A) Right-parasternal long-axis view obtained from a 1-year old Paint filly with a non-restrictive paramembranous ventricular septal defect. Obvious malalignment occurs from the aortic root to the ventricular septum, characterized by over-riding or straddling of the root over the defect. The large defect, with an estimated size of 3.6 cm, is evident immediately below the aortic valve (asterisk). The pulmonary artery (PA) appears enlarged compared to the aorta (Ao), indicating increased transpulmonary flow due to left-to-right shunting or pulmonary hypertension. (B) Color Doppler echocardiogram in a right-parasternal long-axis view indicates systolic flow through the defect. Notice the region of proximal flow convergence in the left ventricular outflow tract, characterized by acceleration of blood flow leading to aliasing (sudden color change from yellow to blue), and the turbulent flow in the right ventricle, color-coded in green. (C) Long-axis echocardiogram and corresponding continuous-wave Doppler recording indicating left-to-right shunt flow through the ventricular septal defect (arrows). The peak systolic velocity is 2.6 m/s, corresponding to a (very low) left-to-right pressure gradient of 27 mmHg. Flow is detected during systole and from mid-diastole to end-diastole. The lack of significant flow during early diastole is either due to translational motion of the heart, causing the defect to move out of the cursor line, transient equilibration of early-diastolic ventricular pressures, or cyclical obstruction or diversion of flow by the prolapsing tricuspid valve. (D) Short-axis echocardiogram and corresponding M-mode recording of the left ventricle (LV). The large end-diastolic LV diameter and the hyperkinetic motion of the interventricular septum (IVS) indicate left ventricular volume overload. The fractional shortening of the left ventricle is 39%, indicating that the systolic function of the left ventricle is preserved. The relative wall thickness is 0.29 (normal 0.4–0.6), indicating the ventricular walls are thinner than expected for the diameter of the ventricle. LA: left atrium; LVPW: left ventricular posterior wall; RV: right ventricle.

Vet-ebooks.com

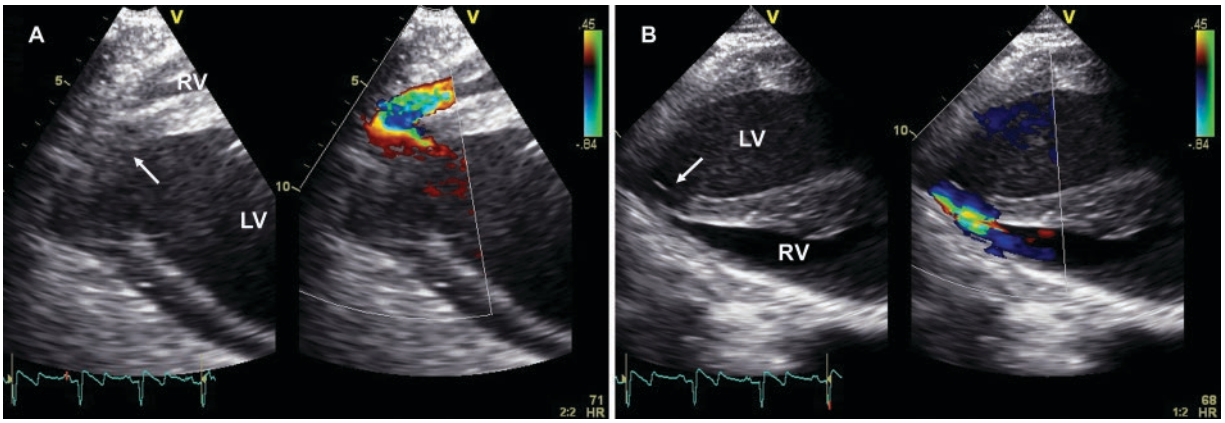


Figure 21.8 Apical muscular ventricular septal defect. Right (A) and left (B) parasternal long-axis view of the left (LV) and right ventricle (RV) in a 4-month-old Thoroughbred colt presented with a right-sided grade 3/6 holosystolic apical murmur that had been detected as an incidental finding. The image plane is focused on the apical part of the interventricular septum. In B-mode (A and B: left), a hypoechoic area in the septum (arrows) suggests the presence of a muscular ventricular septal defect. Color Doppler imaging (A and B: right) allowed to confirm the presence of a defect. Notice the region of proximal flow convergence in the LV (A), characterized by acceleration of blood flow leading to aliasing (sudden color change from yellow to blue). Turbulent flow in the RV is color-coded in green. Post-mortem examination one year after the initial examination (for reasons other than the cardiac malformation) revealed severe chronic endocardial fibrosis and complete closure of the ventricular septal defect.

progression and response to treatment in horses with signs of congestive heart failure.

Assessment of Chamber Dimensions

One of the main goals of echocardiography is detection of cardiac chamber under filling or dilation and grading of the enlargement, if present, as mild, moderate, or severe. Left atrial (LA) and left ventricular (LV) dimensions can be quantified using linear measurements, area measurements, or volumetric estimates that are based on two-dimensional echocardiography (2DE) and M-mode echocardiography (Figures 21.1 and 21.2) [3,7,13,14,20,21].

The relationship between LV chamber diameter and wall thickness can be evaluated using relative wall thickness (RWT), which is calculated as [IVSd + LVFWd]/LVIDd where IVSd is interventricular septal thickness in diastole, LVFWd is the LV free wall thickness in diastole (also termed LV posterior wall, LVPW), and LVIDd is the LV internal diameter in diastole when measured in short-axis. The RWT can indicate physiological remodeling or eccentric hypertrophy (e.g., as seen in athletic horses following training), pathological concentric hypertrophy (Figure 21.23), or dilation (Figures 21.7 and 21.17) [10,22,23]. Care is required when evaluating the cardiac dimensions of horses with systemic illness, as decreased preload resulting from hypovolemia or dehydration can lead to under-filling of the LV (the so-called raisin heart) with the RWT becoming falsely increased (pseudohypertrophy).

In horses, assessment of LA size has traditionally been limited to subjective evaluation and measurement of the LA diameter from a left-parasternal long-axis view (Figure 21.2D). However, with contemporary echocardiographic systems, right-parasternal long-axis and short-axis views (Figures 21.2A, 21.2B, and 21.2C) are preferred, since they allow visualization of the LA in its entirety and provide sufficient anatomical landmarks for consistent and reliable measurement of LA dimensions [19].

Objective quantification of the right atrial (RA) and RV dimensions is difficult because the geometrical shape of the right heart is complex and the internal dimensions of the RA and RV cavity largely depend on transducer placement and imaging plane [24]. Subjective assessment of the right heart chambers in multiple image planes is, therefore, important.

Assessment of Systolic Left Ventricular Function

The echocardiographic detection of early myocardial failure and deterioration of systolic function has important prognostic implications. Most of the indices used in clinical practice serve to evaluate global systolic LV function. Echocardiographic indices of systolic ventricular function generally do not only reflect contractility, but are, to a variable extent, influenced by preload, afterload, heart rate, and rhythm [3,12]. The 2-D ejection phase indices are based on measurements of LV dimensions. Left ventricular ejection fraction (EF% = SV/LVEDV × 100, where SV is stroke volume and LVEDV is LV end-diastolic volume), is based on geometrical estimates of LV volumes and has traditionally been the standard index of LV systolic function (Figure 21.1C). The LV fractional shortening (FS% = [LVIDd-LVIDs]/LVIDd × 100,

Vet-ebooks.com

where LVIDd and LVIDs are the LV internal short-axis diameters at end-diastole and at peak systole, respectively), is an approximation of the EF% and is the most commonly used index of LV systolic function in horses. In fact, LV fractional shortening is often the only index used in routine echocardiography, because it can be easily calculated from M-mode recordings (Figures 21.1D and 21.1E) [3,12,13,25].

Newer echocardiographic methods, including TDI and 2D speckle tracking (Figure 21.24), allow quantitative assessment of myocardial wall motion velocity, strain (i.e., myocardial deformation), and strain rate (i.e., myocardial deformation rate) and provide additional options for assessment of regional and global ventricular function [4–8,26].

Studies have investigated the use of TDI to detect systolic myocardial dysfunction in horses with various cardiovascular diseases [10,11,27,28]. The methodologies used were slightly different between research groups (color vs. pulsed-wave TDI), which makes direct comparison of the results difficult, but there was evidence of altered systolic velocities and timing intervals, particularly in horses with primary myocardial disease but also horses with AR and MR. Less data is available for 2DST, although one study demonstrated decreased LV strain in horses with severe myocardial dysfunction after lasalocid intoxication [28], while a case report demonstrated decreased LV strain with nutritional myodegeneration [27].

To date, the evidence suggests that TDI and 2DST offer a small advantage over the conventional methods, particularly for assessment of subclinical systolic ventricular function in horses, although the clinical relevance of these findings is currently unclear.

Assessment of Diastolic Left Ventricular Function

Diastolic ventricular dysfunction may play a role in pericardial and myocardial disease in horses. However, the clinical relevance of diastolic dysfunction in other types of cardiac disease is not yet clear. Doppler-derived transmitral flow velocities and tissue Doppler analyses of mitral annular or myocardial velocities are commonly used in humans and small animals for assessment of diastolic LV function and filling pressures [3,12]. Transmitral flow velocity profiles can be recorded by PW Doppler, but optimal alignment with blood flow and consistent placement of the sample volume relative to the mitral valve is very difficult in adult horses. Therefore, transmitral flow velocity measurements in horses are relatively unreliable and may not be suitable to detect minor changes in diastolic LV function [20,21,29]. Conversely, TDI indices of LV wall motion are easier to obtain than transmitral flow velocity measurements and can be helpful for assessment of LV diastolic function in horses (Figure 21.24) [5,9]. Decreased early diastolic LV velocities have been observed using TDI in horses with myocardial disease, AR, and following prolonged exercise in endurance horses [10,11,27,30].

Assessment of Left Atrial Function

The last 15 years have seen a rise in the popularity of assessment of LA function (i.e., reservoir, conduit, and booster pump phases of the cardiac cycle) during routine echocardiography and an increase in the literature supporting the clinical relevance of LA dysfunction. Normal LA booster pump function is absent in horses with atrial fibrillation (AF), while all three phases may be altered in horses suffering from MR, AR, or other cardiac disease. Persistent LA contractile dysfunction can be detected in horses after conversion from AF to sinus rhythm, likely attributed to AF-induced atrial remodeling [21,31,32]. LA size and LA mechanical function can easily be assessed in horses by use of 2DE variables, including LA area and LA fractional area changes (Figure 21.2) [19,20]. Additionally, TDI of the LV myocardium has shown increased late diastolic velocities (resulting from an increased atrial contribution to ventricular filling) in horses with AR, myocardial disease, and following prolonged exercise in endurance athletes [10,11,27,30].

Hemodynamic Assessment

The hemodynamic load placed on the heart by cardiac disorders can be estimated by combining echocardiographic information on chamber size and wall thickness, myocardial motion, LV systolic and diastolic function, and intracardiac blood flow. Doppler studies can be used to assess intracardiac pressures and pressure gradients. Normal pressure gradients drive blood flow through heart, valves, and large vessels at speeds ranging from 0.25 to 1.5 meters per second (m/s). Abnormally high velocities can be found in many cardiac conditions, including ventricular septal defects and valvular regurgitations, in which pressure gradients drive blood across a restrictive orifice resulting in flow acceleration (Figures 21.6, 21.7, 21.10, 21.13, 21.15, 21.17, 21.18, 21.19, and 21.28). The pressure gradients are either reflections of normal intracardiac pressures or consequences of pathologically increased pressures. Pressure gradients can be estimated from flow velocities measured using Doppler echocardiography, by employing the simplified Bernoulli equation ($dp = 4 \times V_{max}$ [2]; where dp is the pressure gradient in mmHg and V_{max} is the peak velocity in m/s). The main indications to measure pressure gradients in

Vet-ebooks.com

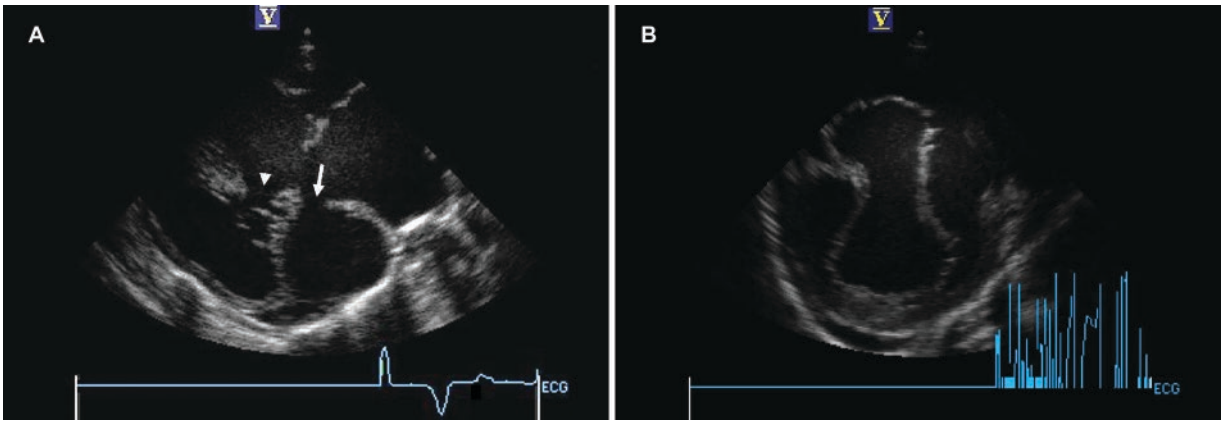


Figure 21.9 Endocardial cushion defect. (A) Right-parasternal 4-chamber view obtained from a 4-month-old Morgan colt with a complete endocardial cushion defect. The primum atrial septal defect is evident in the ventral atrial septum (arrow) and an inlet ventricular septal defect component (arrowhead) is observed below the common atrioventricular valve. (B) Right-parasternal short-axis view at the level of the common atrioventricular valve. The ECG electrodes were displaced resulting in the artifact to the lower right.

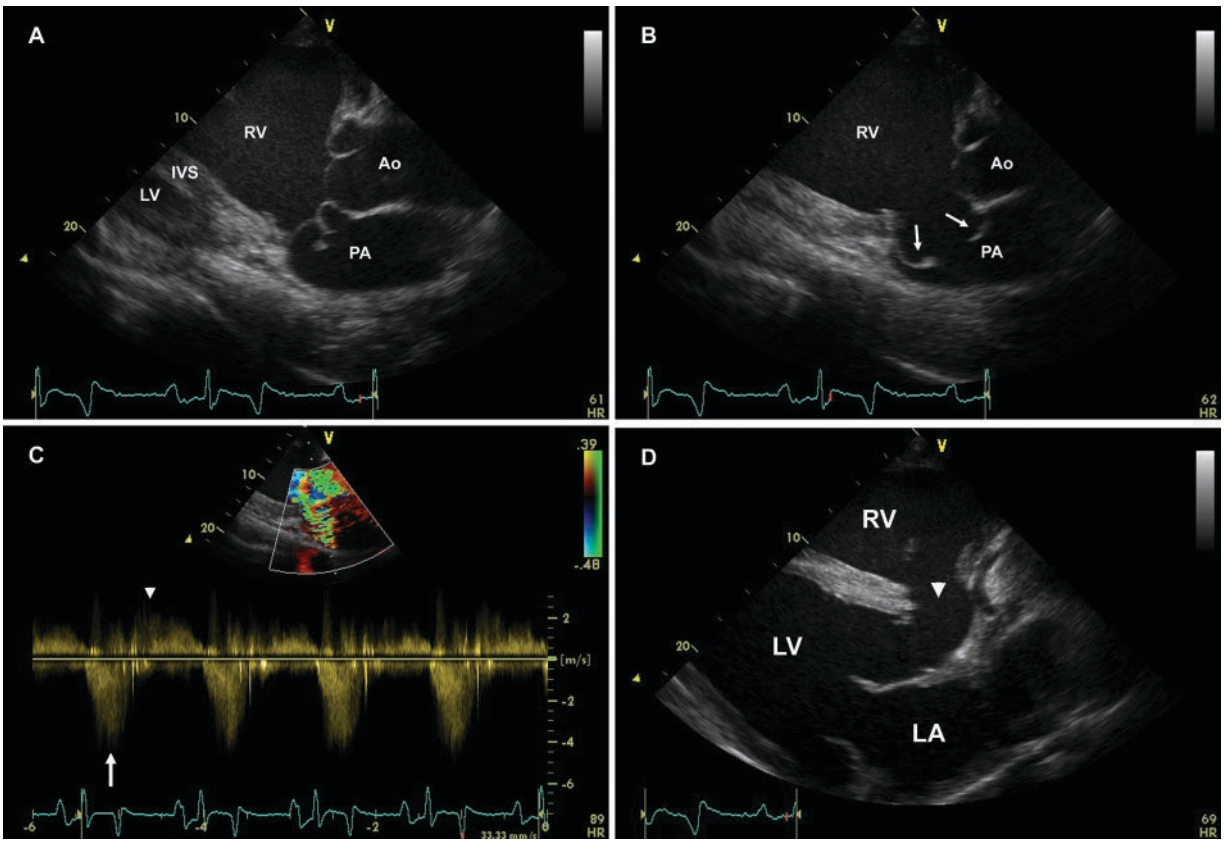


Figure 21.10 Double outlet right ventricle and endocardial cushion defect. (A) Off-angled right-parasternal long-axis view obtained from a 2-year-old Quarter horse colt with complex congenital heart disease including double outlet right ventricle, large atrioventricular septal defect, malformed atrioventricular valves, and valvular pulmonic and aortic stenoses. Both great vessels originate from the right ventricle (RV) and can be displayed side-by-side, typical of double outlet and/or transposed great vessels. (B) Pulmonary and aortic valvular stenosis related to valvular dysplasia, thickening, and fusion of the leaflets. Doming of the pulmonic valves is visible during systole (arrows). (C) Continuous-wave Doppler recording of pulmonic outflow (arrow) and pulmonic regurgitation (arrowhead). The peak systolic outflow velocity is 4.2 m/s (corresponding to a pressure gradient of 71 mmHg), indicating pulmonary valvular stenosis of moderate severity. (D) Right-parasternal 4-chamber view. The left ventricle (LV) communicates with the RV across a large atrioventricular septal defect (arrowhead). Ao: aorta; IVS: interventricular septum; LA: left atrium; PA: pulmonary artery.

Vet-ebooks.com

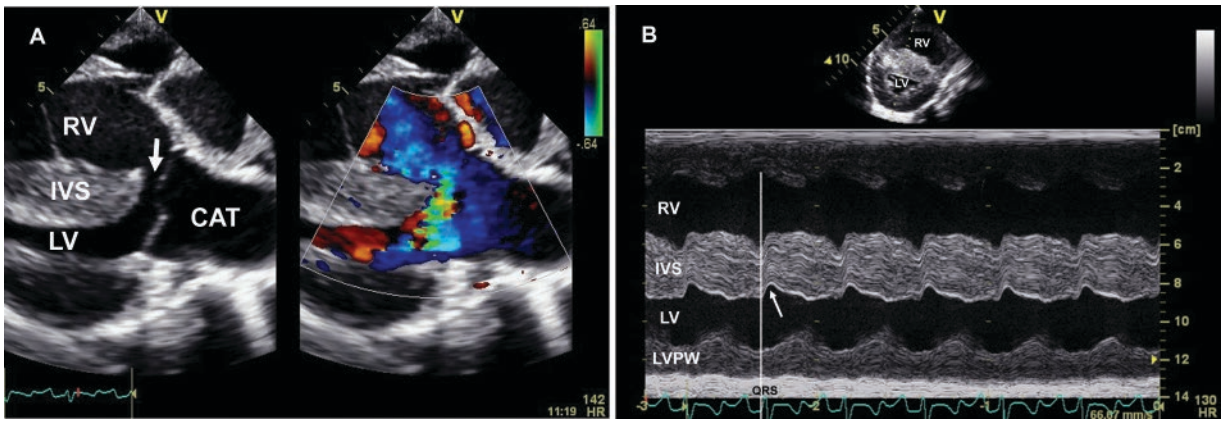


Figure 21.11 Common arterial trunk. (A) B-mode (left) and color Doppler (right) echocardiogram in a right-parasternal long-axis view obtained from a 15-day-old Friesian filly with a common arterial trunk (CAT). Only one great vessel is evident overriding a ventricular septal defect (arrow) and communicating with both ventricles. (B) M-mode echocardiogram in a right-parasternal short-axis view. The right ventricle (RV) is dilated and hypertrophied, indicating volume and pressure overload. The left ventricle (LV) appears small and its wall is hypertrophied. Notice the flat motion of the interventricular septum (IVS) with early-systolic paradoxical motion (arrow). The vertical line indicates the beginning of systole (i.e., the onset of the QRS complex). The LV fractional shortening is low at 26%. LVPW: left ventricular posterior wall.

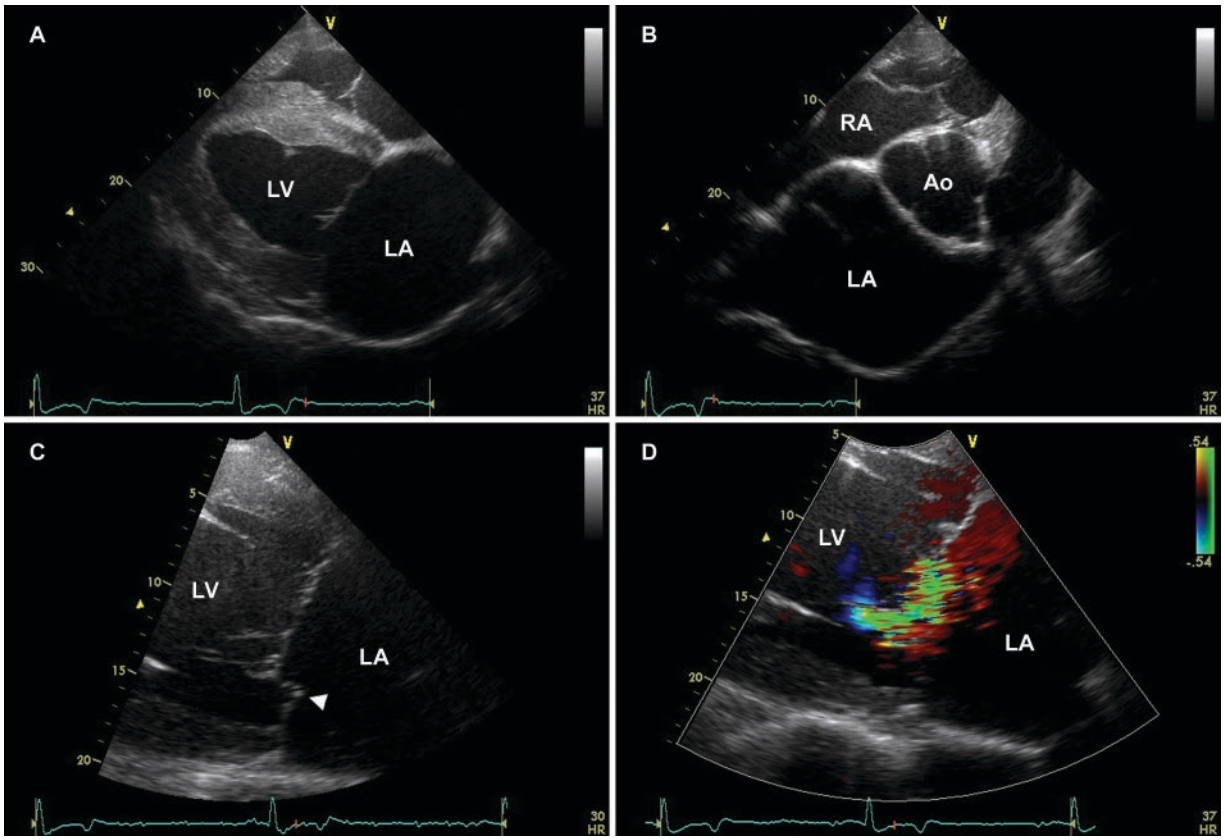


Figure 21.12 Mitral regurgitation. (A) Right-parasternal 4-chamber view obtained from a horse with mitral regurgitation. The left atrium (LA) appears markedly enlarged and has a rounded appearance, indicating severe volume overload. (B) Right-parasternal short-axis view at the level of the aorta (Ao) and the left atrium (LA). The LA appears markedly enlarged. (C) Left-parasternal long-axis view. The septal (anterior) mitral valve leaflet is prolapsing into the LA during systole (arrowhead). (D) Color Doppler imaging in the same imaging plane as shown in (C) indicates turbulent blood flow within the LA (color-coded in green) during systole, consistent with mitral regurgitation. (E) Left-parasternal long-axis view in an imaging plane that is only slightly different from the one shown in (C). Nodular thickening of the parietal (posterior) mitral valve leaflet is now visible (arrowheads). (F) Color Doppler imaging in the same plane as shown in (E) indicates turbulent blood flow within the LA (color-coded in green) during systole.

Vet-ebooks.com

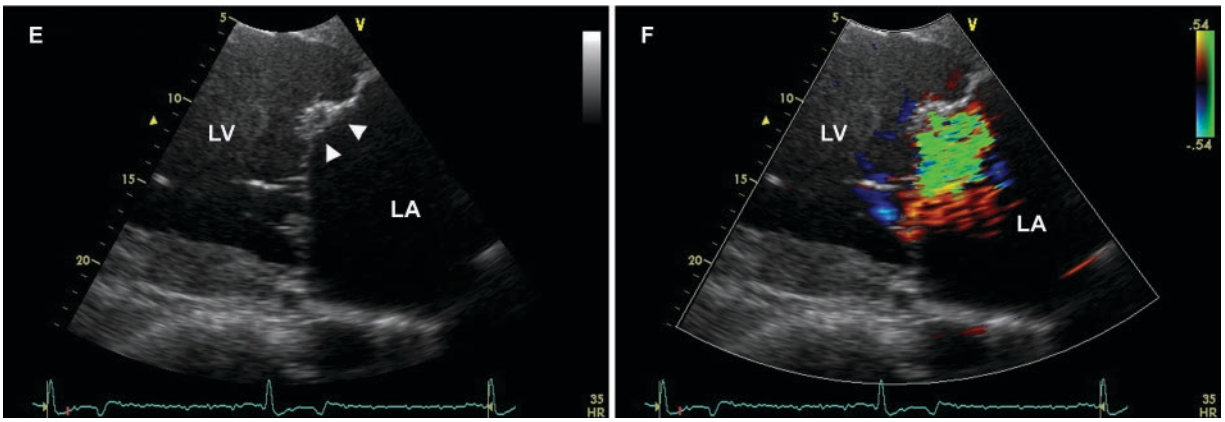
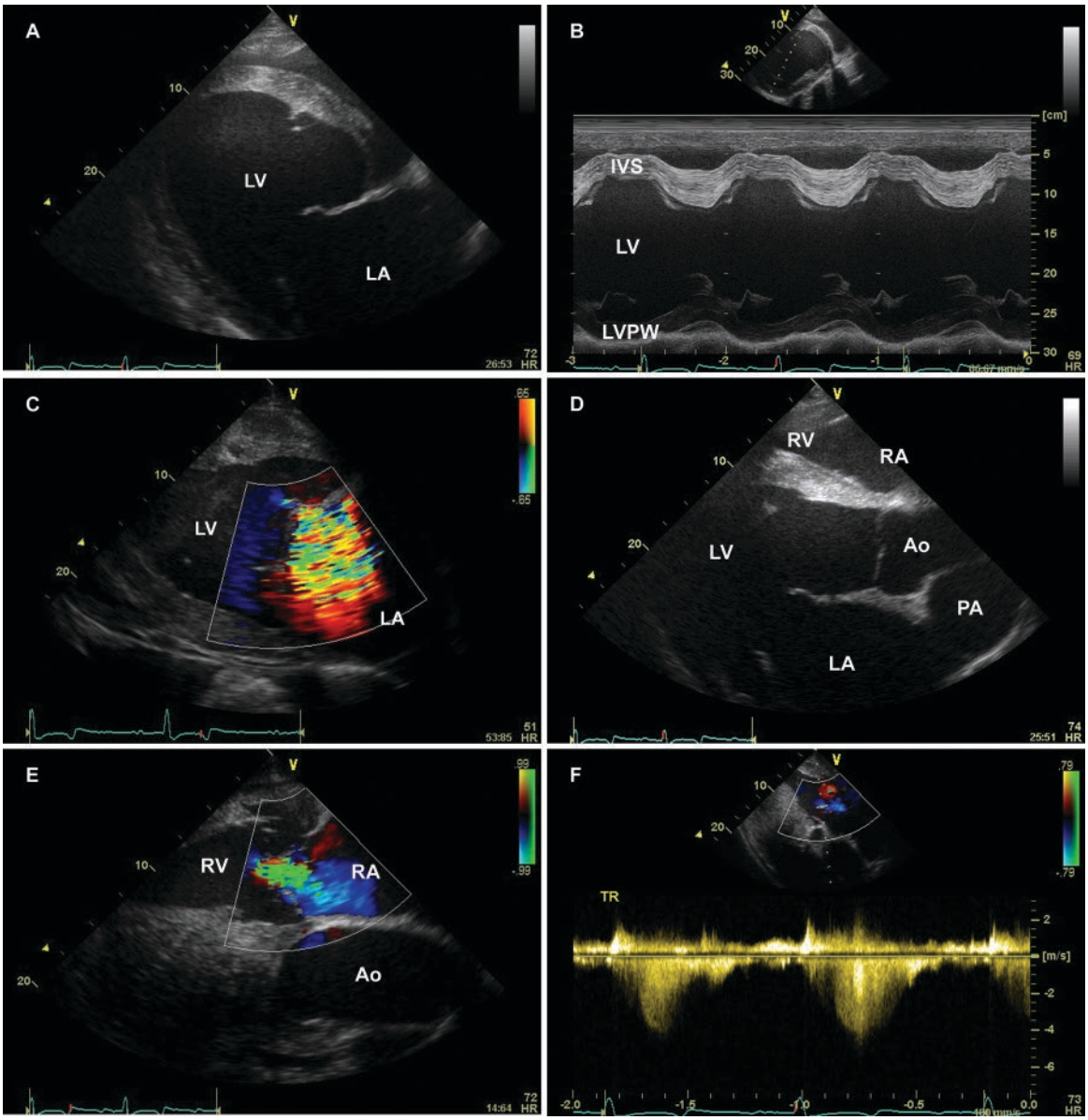


Figure 21.12 (continued) Notice the slightly different appearance of the area of turbulent flow compared to (D). Quantification of regurgitation by assessing the area of regurgitant flow within the receiving chamber (i.e., the LA) is problematic, because the Doppler-derived flow signal is largely influenced by imaging plane and direction of flow, gain settings, orifice size and shape, driving pressure, and receiving chamber characteristics. LV: left ventricle; RA: right atrium.



Vet-ebooks.com

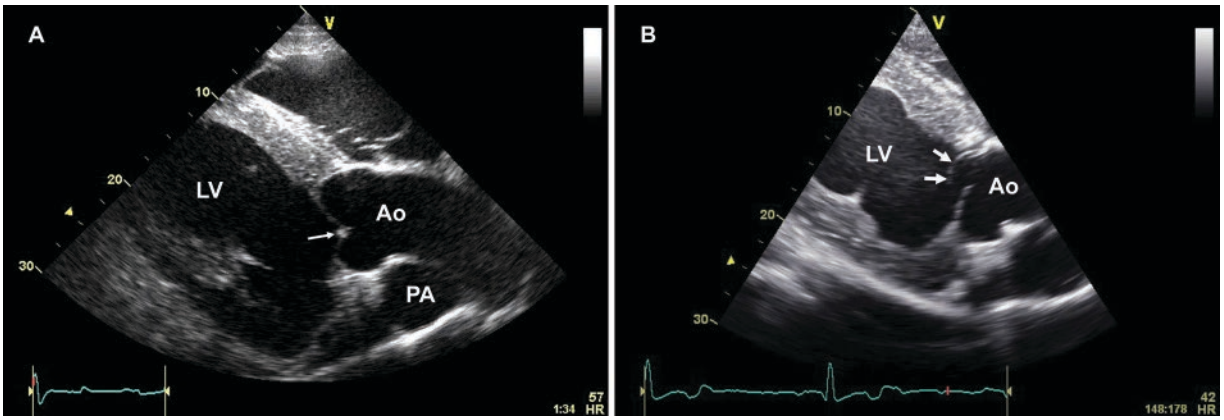


Figure 21.14 Aortic valve lesions. (A) Right-parasternal long-axis view obtained from a 15-year-old Thoroughbred gelding with aortic regurgitation. Nodular thickening of the aortic valve cusps is evident (arrow). (B) Right-parasternal long-axis view obtained from a 12-year-old Arabian gelding with aortic regurgitation. Aortic valve prolapse is evident (arrows). Ao: aorta; LV: left ventricle: PA: pulmonary artery.

horses are to support the diagnosis of pulmonary hypertension by interrogation of regurgitant flow at the tricuspid valve and/or the pulmonic valve (Figures 21.10, 21.13, 21.17, 21.18, and 21.19) and in the assessment of ventricular septal defects by interrogation of shunt flow (Figures 21.6 and 21.7). Parallel alignment with blood flow is crucial because excessive angle of interrogation (i.e., > 20 degrees) will lead to an underestimation of flow velocities and pressure gradients.

Assessment of Valvular Regurgitation

The Doppler technology of current echocardiographic systems is very sensitive to detect valvular regurgitation and care must be taken not to over interpret the echo findings, particularly in otherwise healthy animals without abnormal clinical findings and in the absence of heart murmurs (Figure 21.5). Assessment of valvular regurgitation should be achieved using an integrated qualitative and quantitative approach, combining clinical examination (including auscultation of a typical murmur), and echocardiographic findings. Measurement of cardiac chamber dimensions provides information on the hemodynamic relevance of chronic valvular regurgitation. Abnormal timing and direction of transvalvular flow, as well as flow turbulence, can be detected by 2-D color Doppler, color M-mode, and spectral Doppler echocardiography. The regurgitant signal in the "receiving chamber" can be interrogated in multiple imaging planes to identify origin, extent, timing, and duration of the regurgitation [33]. However, color Doppler echocardiography describes blood flow direction and velocity, but not absolute volumetric flow. The Doppler-derived regurgitant signal is largely

Figure 21.13 Mitral regurgitation and left-sided congestive heart failure. Echocardiogram obtained from a 3-year-old female Standardbred with mitral regurgitation and left-sided congestive heart failure. (A) Right-parasternal long-axis 4-chamber view. The left atrium (LA) and the left ventricle (LV) are severely dilated. The right heart appears small. (B) M-mode echocardiogram of the LV in a right-parasternal short-axis view demonstrating LV enlargement and hyperdynamic motion of the interventricular septum (IVS). The LV fractional shortening was 39%. (C) Color Doppler echocardiogram in a left-parasternal long-axis view focused on the mitral valve. A large area of turbulent blood flow (color-coded in yellow and green) is visible during systole in the LA, consistent with mitral regurgitation. (D) Echocardiogram in a right-parasternal long-axis view. The LA and the LV are severely dilated. The pulmonary artery (PA) appears enlarged compared to the aorta (Ao), strongly suggesting pulmonary hypertension secondary to severe mitral regurgitation. (E) Color Doppler echocardiogram in a right-parasternal long-axis view focused on the tricuspid valve. An area of turbulent blood flow (color-coded in green) is visible during systole in the right atrium (RA), consistent with tricuspid regurgitation. (F) Continuous-wave Doppler recording of the tricuspid regurgitant jet in a tilted right-parasternal long-axis view. A high-velocity flow pattern is visible during systole. The peak velocity is 4.5 m/s, corresponding to a maximum systolic pressure gradient across the tricuspid valve of 81 mmHg (modified Bernoulli equation: $dp = 4 \times v_{max}^2$). Therefore, the estimated systolic pulmonary artery pressures (assuming a right atrial pressure of 5 mmHg) would be 86 mmHg, indicating pulmonary hypertension secondary to severe mitral regurgitation. Notice that malalignment of the Doppler beam with blood flow may lead to underestimation of peak velocities and pressure gradients. LVPW: left ventricular posterior wall; RV: right ventricle.

Vet-ebooks.com

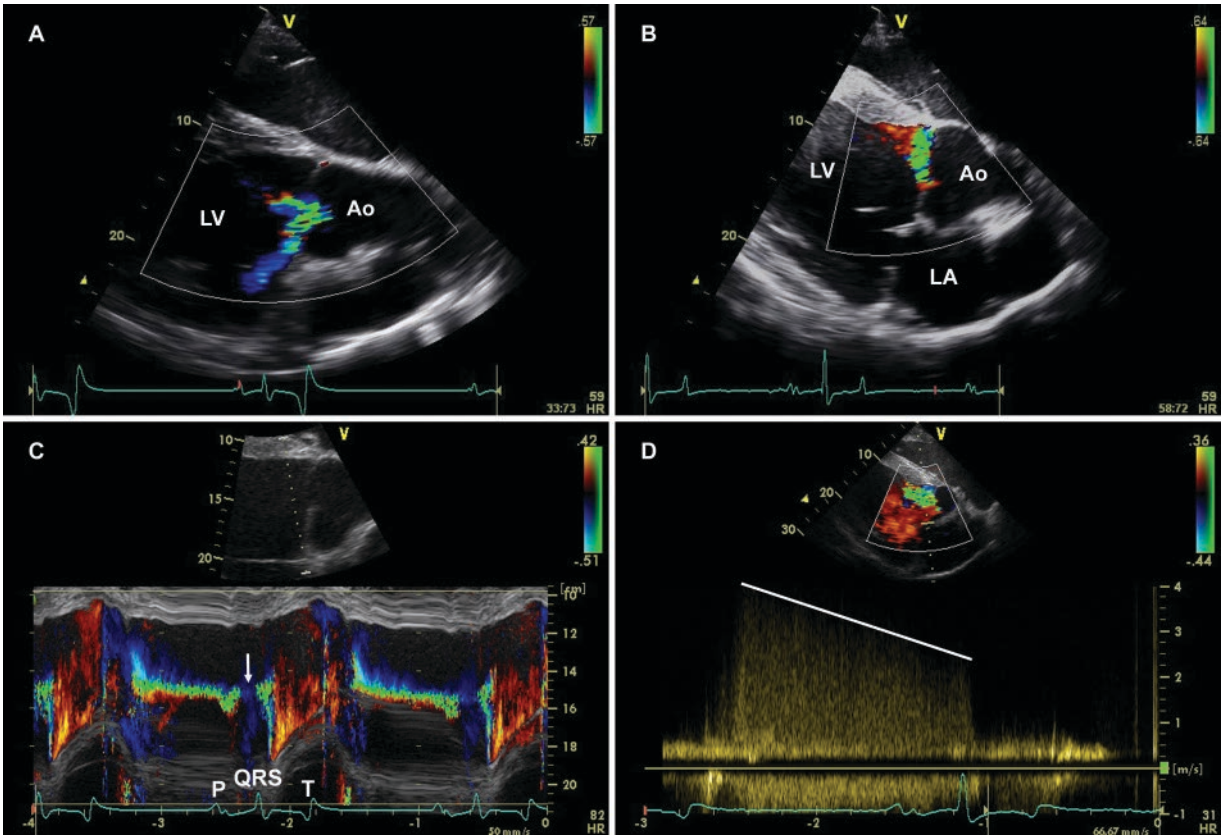


Figure 21.15 Aortic regurgitation. (A) Color Doppler echocardiogram in a right-parasternal long-axis view obtained from a 13-year-old Warmblood mare with aortic regurgitation. The diastolic regurgitant jet is visible as a small area of turbulent flow (color-coded in green) at the coaptation points of the valve leaflets. The image has the appearance of two jets: a central jet and an eccentric jet directed toward the mitral valve. Based on receiving chamber analysis, the severity of the regurgitation would be graded as mild. (B) Color Doppler echocardiogram in a right-parasternal long-axis view obtained from a 15-year-old Warmblood mare with aortic regurgitation. The diastolic regurgitant jet is visible as an area of turbulent flow (color-coded in green) that appears to be directed toward the interventricular septum. Based on receiving chamber analysis, the severity of the regurgitation would be graded as mild. (C) Color M-mode echocardiogram in a right-parasternal long-axis view obtained from a horse with aortic regurgitation. The cursor line is placed immediately below the aortic valve (top). An ECG is recorded simultaneously for timing. This imaging mode is particularly useful for timing of flow events and identifying brief regurgitant signals or normal valve closure noise. In this case, an aortic regurgitant jet is visible as a turbulent flow pattern (color-coded in green), starting at the beginning of diastole (i.e., after the T wave) and ending at the onset of systole (i.e., immediately after the QRS complex). Notice the absence of turbulent flow during the PQ-interval (arrow). This can be explained by a change in left ventricular pressure occurring after atrial contraction or a reorientation of the regurgitant jet relative to the cursor owing to translational movement of the heart. (D) Continuous-wave Doppler recording of a diastolic aortic regurgitant jet from a right-parasternal long-axis view. The absolute velocities are not accurate in this recording because of lack of adequate alignment with blood flow. However, this recording can be used for timing of flow events (an ECG is recorded simultaneously for timing). Furthermore, the change in jet velocity (which can be expressed as "pressure half-time") reflects the rate of decline in pressure gradient between the aorta and the left ventricle and may be useful to assess the severity of regurgitation as long as ventricular relaxation is normal. A relatively flat or gradual slope of the velocity envelope (white line) indicates mild (AR), a steep slope indicates severe AR. (A), (B), and (D) It is important to notice that for a comprehensive assessment and staging of AR severity, in addition to assessing the size of the AR jet, one should also take into account left-ventricular size, shape and systolic function. Ao: aorta; LA: left atrium; LV: left ventricle; PA: pulmonary artery.

Vet-ebooks.com

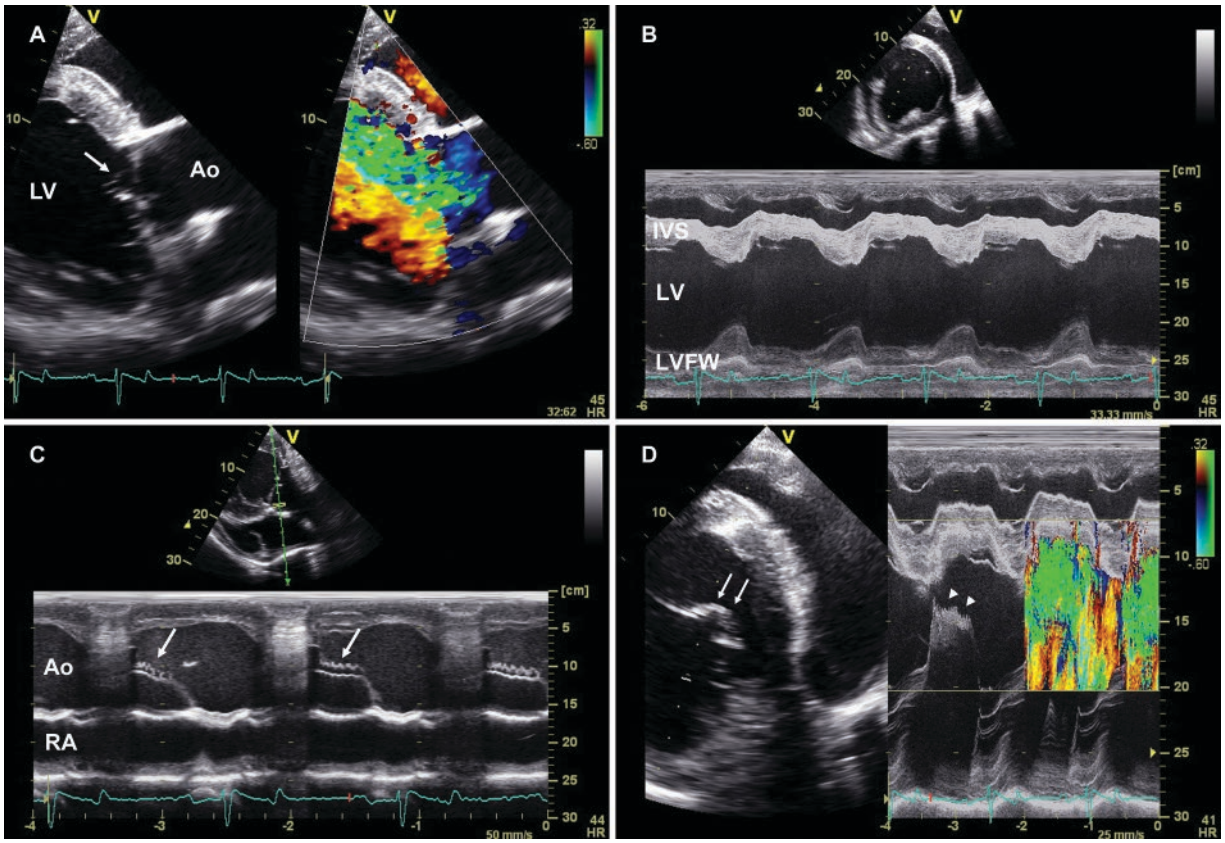


Figure 21.16 Aortic regurgitation. Echocardiogram of a 21-year-old Hanoverian Warmblood gelding with severe aortic regurgitation and left ventricular volume overload. (A) B-mode (left) and color Doppler (right) echocardiogram of the left ventricular outflow tract in a right-parasternal long-axis view. The aortic valve cusps are irregularly thickened and aortic valve prolapse is evident during diastole (arrow). A large regurgitant jet is visible in the left ventricular outflow tract during diastole (green). (B) M-mode echocardiogram of the left ventricle (LV) in a right-parasternal short-axis view demonstrating LV enlargement and hyperdynamic motion of the interventricular septum (IVS). The LV fractional shortening was 46%. (C) M-mode echocardiogram of the aortic valve in a left-parasternal long-axis view. Notice the high-frequency vibrations of the aortic cusp during diastole (arrows) caused by the regurgitant blood flow. (D) Two-dimensional (left), M-mode (middle), and color M-mode (right) echocardiogram of the mitral valve in a right-parasternal short-axis view. Notice the prolapse (arrows) and the high-frequency vibrations (arrowheads) of the septal leaflet of the mitral valve, caused by rapid, turbulent regurgitant flow in the left ventricular outflow tract during diastole (color-coded in green). Ao: aorta; LVFW: left ventricular free wall; RA: right atrium.

Vet-ebooks.com

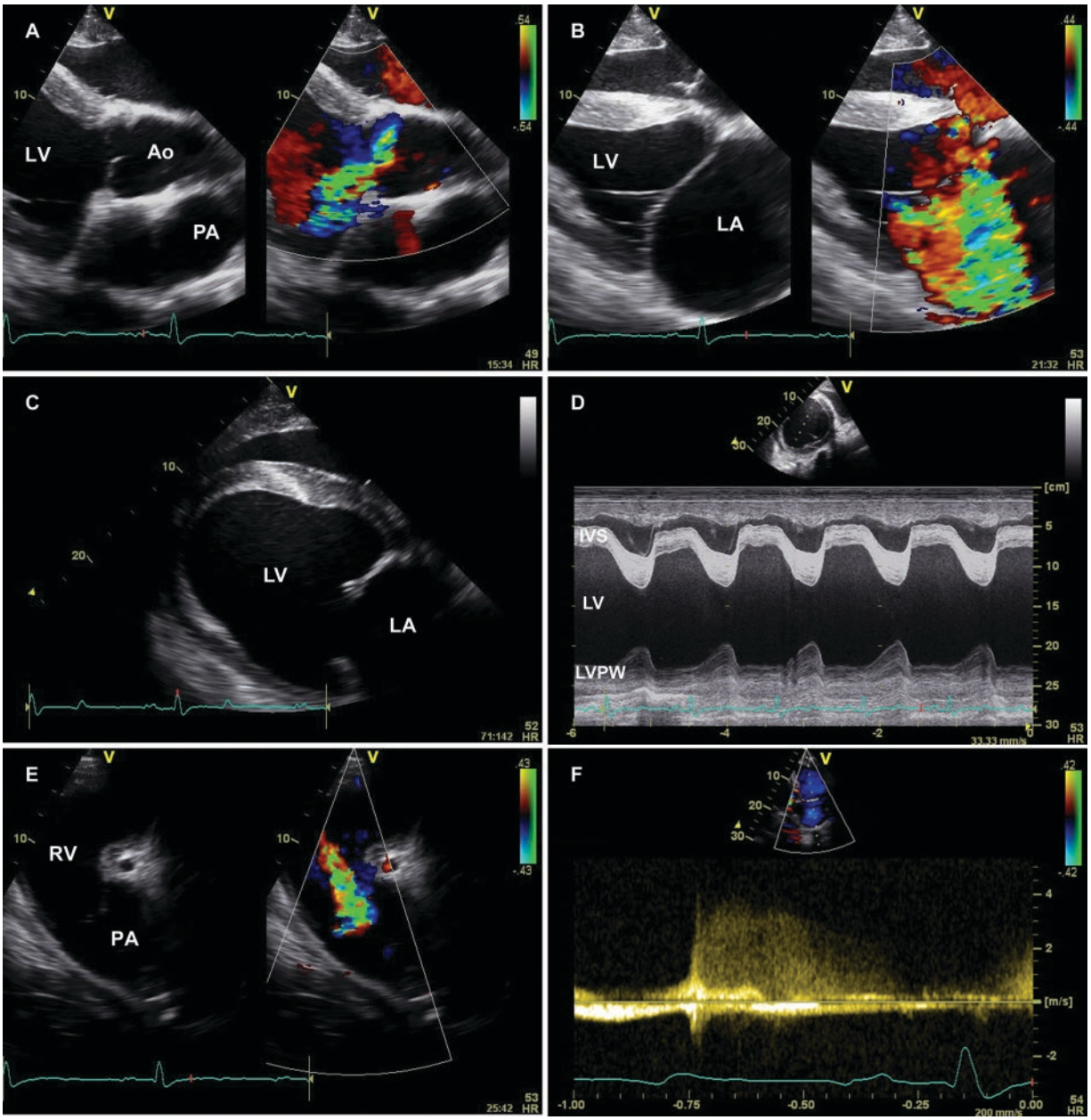


Figure 21.17 Aortic regurgitation, mitral regurgitation, and pulmonary hypertension. Echocardiogram of a 7-year-old Westphalian Warmblood mare with severe aortic and mitral regurgitation. (A) Right-parasternal view of the left-ventricular outflow tract. A B-mode image (left) and a color flow Doppler image (right) are displayed side by side. The aortic cusps are slightly thickened. An eccentric aortic regurgitant jet (color-coded in green) is seen during diastole, directed toward the septal mitral valve leaflet. Notice the prominent appearance of the pulmonary artery (PA) compared to the aortic root (Ao), suggesting increased pulmonary artery pressures. (B) Right-parasternal 4-chamber view, focused on the left atrium (LA) and the mitral valve. A B-mode image (left) and a color flow Doppler image (right) are displayed side by side. A large mitral regurgitant jet (color-coded in green) is seen in the LA during systole. The LA appears rounded and severely enlarged. (C) Right-parasternal 4-chamber view, focused on the left ventricle (LV). The LV is enlarged and has a rounded appearance, indicating LV volume overload. (D) Short-axis echocardiogram and corresponding M-mode recording of the LV. The large end-diastolic LV diameter and the hyperkinetic motion of the interventricular septum (IVS) indicate severe LV volume overload. The fractional shortening of the left ventricle is 53%, indicating preserved LV systolic function in the presence of an increase in preload (due to volume overload) and a decrease in afterload (due to mitral regurgitation). The relative wall thickness is 0.26 (normal 0.4–0.6), indicating the ventricular walls are thinner than expected for the diameter of the ventricle. (E) Right-parasternal view of the right-ventricular outflow tract. A B-mode image (left) and a color flow Doppler image (right) are displayed side by side. Color flow mapping shows a pulmonic regurgitant jet during diastole (color-coded in green). (F) Spectral Doppler recording of the pulmonic regurgitant jet. The maximum diastolic velocity of the regurgitant jet is 3.7 m/s, corresponding to a pressure gradient of 55 mmHg (modified Bernoulli equation: $dp = 4 \times v_{max}^2$). Therefore, the estimated mean pulmonary artery pressure (assuming a right ventricular diastolic pressure of 5 mmHg) would be 60 mmHg, indicating pulmonary hypertension. LVPW: left ventricular posterior wall; RV: right ventricle.

Vet-ebooks.com

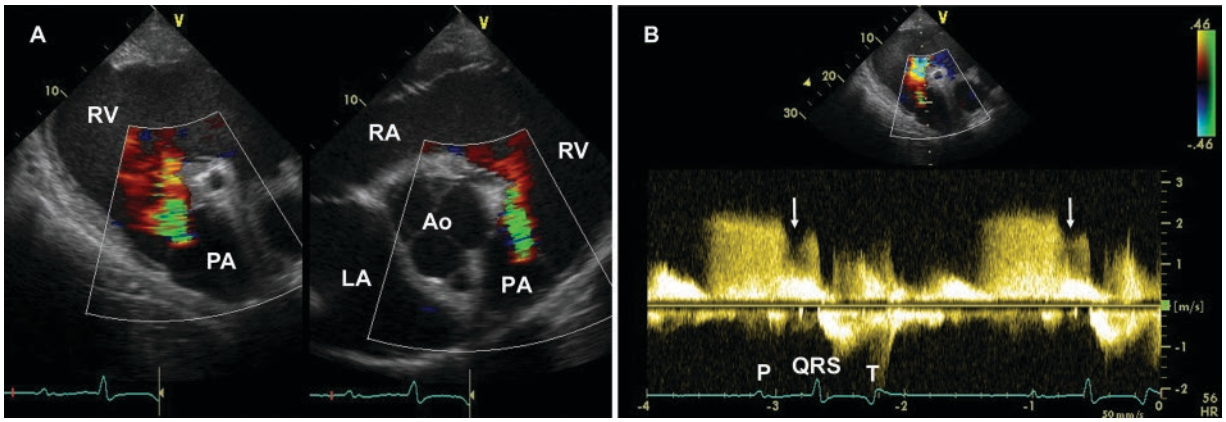


Figure 21.18 Pulmonic insufficiency. (B) Right-parasternal long-axis view of the right ventricular outflow tract (left) and right-parasternal short-axis view at the level of the aortic and pulmonic valve (right). Color Doppler imaging shows diastolic turbulent blood flow within the right-ventricular outflow tract (color-coded in green), consistent with pulmonic insufficiency. Pulmonic insufficiency rarely is clinically relevant, but it can be used to estimate mean and diastolic pulmonary artery pressures by spectral Doppler. (B) Continuous-wave Doppler recording of a pulmonic regurgitation jet in a right-parasternal long-axis view of the right ventricular outflow tract, showing mid- to end-diastolic regurgitant flow. The maximum velocity is approximately 2.35 m/s, corresponding to a transvalvular pressure gradient of 22 mmHg (modified Bernoulli equation: $dp = 4 \times v_{max}^2$). The end-diastolic velocity is approximately 1.75 m/s, corresponding to a transvalvular pressure gradient of 12 mmHg. Therefore, the estimated mean and diastolic pulmonary artery pressures (assuming a right ventricular diastolic pressure of 5 mmHg) would be 27 and 17 mmHg, which is within normal limits for horses. Notice the sudden decrease in jet velocity during the PQ-interval (arrows), which can be explained by a temporary reduction of regurgitant flow caused by a sudden rise in right ventricular pressure occurring after atrial contraction or by transient reorientation of the regurgitant jet relative to the cursor line. Ao: aorta; LA: left atrium: PA: pulmonary artery; RA: right atrium; RV: right ventricle.

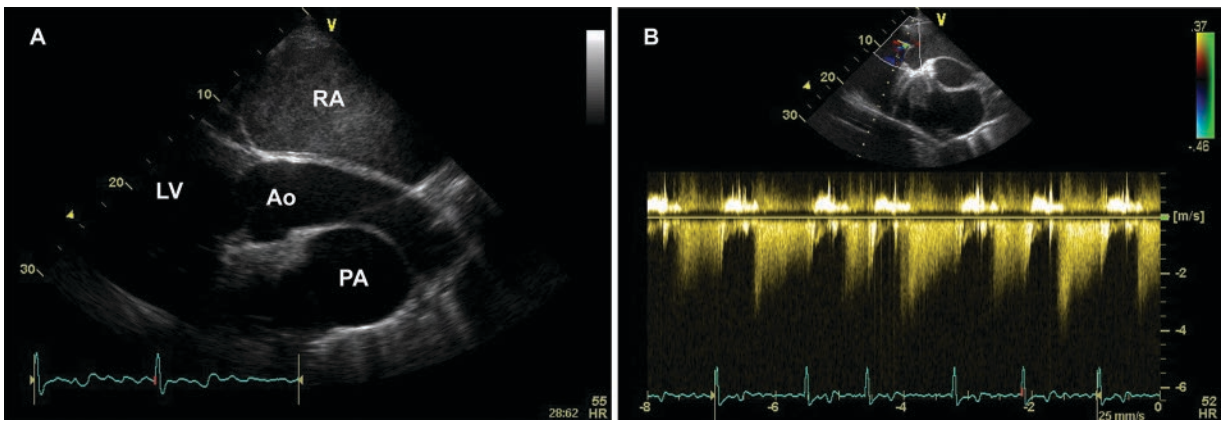


Figure 21.19 Pulmonic insufficiency and pulmonary hypertension (A) Right-parasternal view of the left ventricular outflow tract obtained from an 11-year-old Paint gelding with severe mitral regurgitation, atrial fibrillation, and left-sided congestive heart failure. Enlargement of the right atrium (RA) and severe pulmonary artery (PA) dilation is evident, consistent with pulmonary hypertension. Notice also the marked spontaneous echo contrast (SEC) in the right atrium. Although some degree of SEC is considered normal in horses, this amount of SEC is unusual. The exact cause of SEC is unknown, but it may be associated with low flow states, systemic inflammation, or abnormal coagulation. (B) Continuous-wave Doppler recording of pulmonic insufficiency in a left-parasternal long-axis view of the right ventricular outflow tract, showing diastolic regurgitant flow. The varying peak velocities can be explained by differences in cycle lengths (due to atrial fibrillation), motion of the heart (and the regurgitant jet) relative to the cursor line, and possibly respiratory variations. The highest maximum early-diastolic velocity in this spectral Doppler recording was 4 m/s, corresponding to a trans-valvular pressure gradient of 64 mmHg (modified Bernoulli equation: $dp = 4 \times v_{max}^2$). Assuming a right ventricular diastolic pressure of 5 mmHg, the estimated mean pulmonary artery pressure (MPAP) would be at least 69 mmHg, indicating marked pulmonary hypertension. Ao: aorta; LV: left ventricle.

Vet-ebooks.com

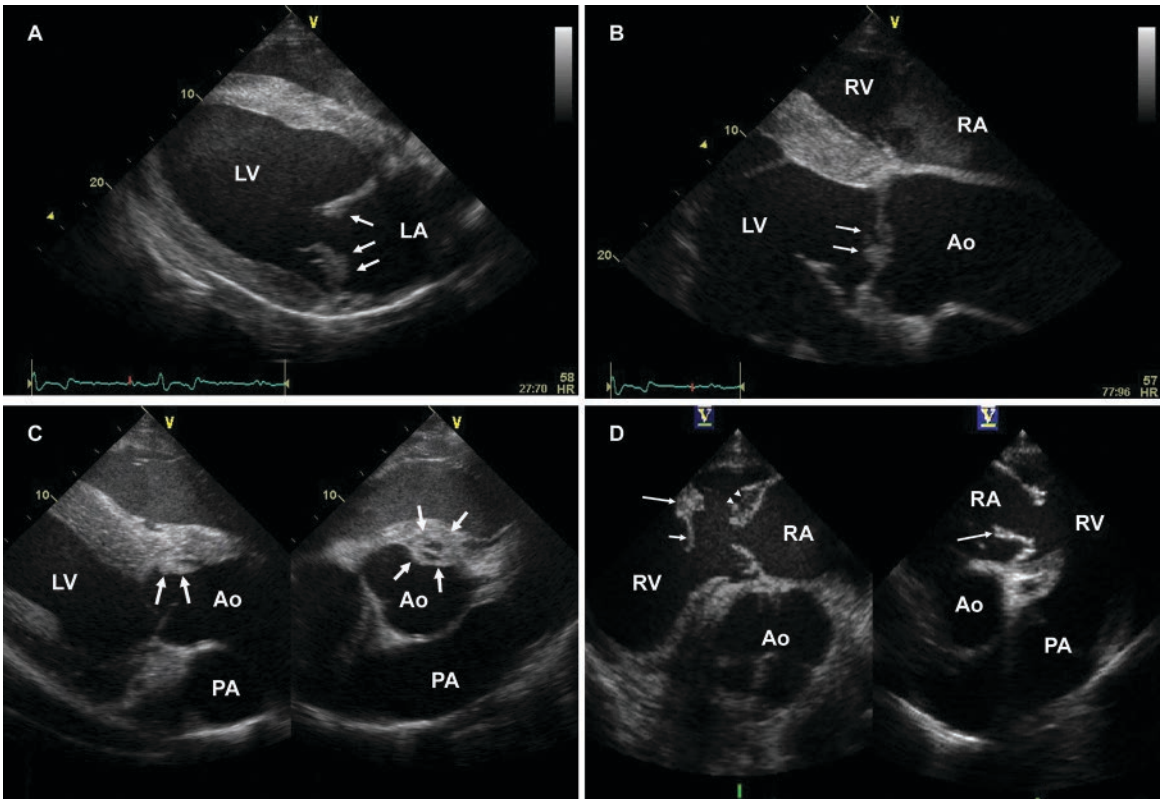


Figure 21.20 Infective endocarditis. (A) Echocardiogram in a right-parasternal 4-chamber view. The mitral valve leaflets appear thickened. Echogenic masses are evident, attached to the atrial surface of the mitral valve leaflets (arrows). Focal lesions of endocarditis typically face the valvular surface facing into the direction of blood flow. (B) Right-parasternal view of the left ventricular outflow tract obtained from a 10-year-old Quarter horse gelding with bacterial endocarditis. The cusps of the aortic valve appear thickened. Echogenic masses are attached to the free edges of the cusps (arrows). (C) Right-parasternal view of the aortic valve in long-axis (left) and short-axis (right) obtained from a 3-year-old female horse with bacterial endocarditis and aortic root abscess resulting in marked thickening of the aortic wall and periaortic tissues. A vegetative lesion is seen within the sinus of Valsalva (arrows). In short-axis view, the lesion appears as an echogenic, demarcated, loculated mass that is located between the non-coronary and the right-coronary cusp, possibly involving the atrial septum. (D) Echocardiogram obtained from a 6-year-old Quarter horse mare with severe pleuropneumonia, endocarditis, and tricuspid chordal rupture. In a right-parasternal long-axis view (left), the rupture chord (short arrow) is visible within the right ventricle (RV). Vegetations are visible at the papillary muscle (long arrow) and at the tricuspid valve leaflet (arrowheads). In short-axis view (right), a flail leaflet (arrow) is visible within the right atrium (RA) during systole. The prominent appearance of the pulmonary artery (PA) compared to the aorta (Ao) is suggestive of pulmonary hypertension. LA: left atrium; LV: left ventricle.

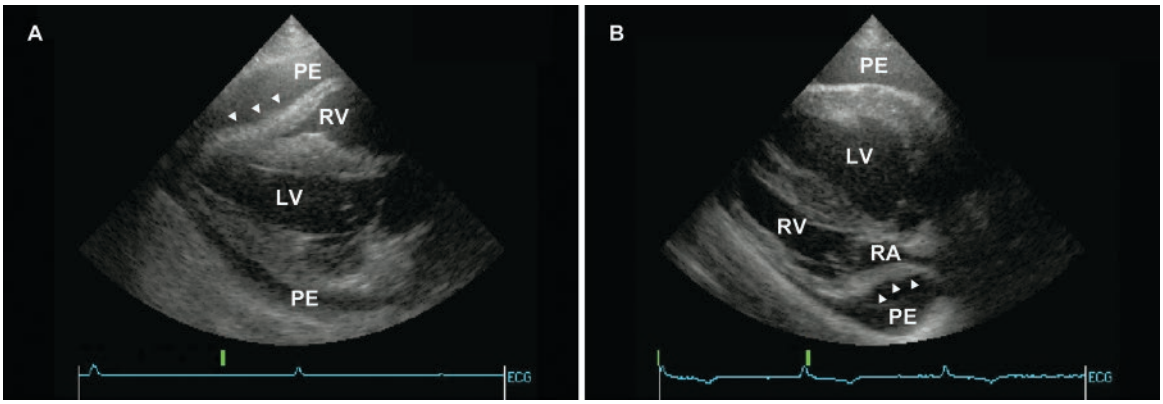


Figure 21.21 Pericardial effusion and cardiac tamponade. (A) Right-parasternal long-axis recording obtained from a horse with pericardial effusion and cardiac tamponade. The heart is surrounded by the anechoic effusion (PE). Right ventricular (RV) collapse is evident (arrowheads). (B) Left-parasternal long-axis recording. Right atrial (RA) collapse becomes obvious in this view (arrowheads), indicating hemodynamically relevant effusion and cardiac tamponade. LV: left ventricle. (*Source*: Courtesy of Dr John D Bonagura).

Vet-ebooks.com

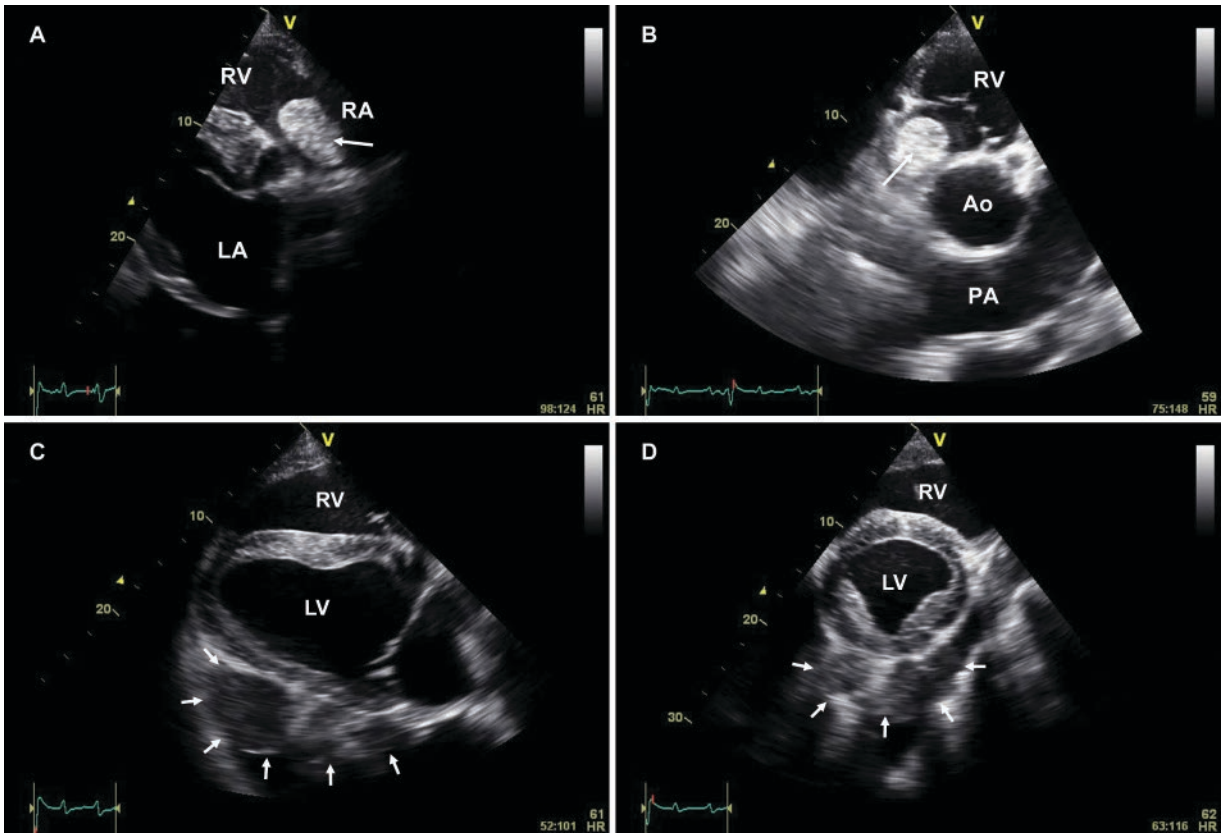


Figure 21.22 Mass lesions in right atrium and pericardium (A and B). Echocardiogram in a right-parasternal long-axis (A) and short-axis (B) view recorded from a 23-year-old, 380-kg Pony gelding with metastasizing adenocarcinoma. A hyperechoic, well demarcated mass (arrow) is visible within the right atrium (RA). In necropsy, this mass was confirmed to be a thrombus containing neoplastic cells, extending from the caudal vena cava to the right atrium. (C) and (D) Righ-parasternal long-axis (C) and short-axis (D) view of the same horse. Multiple hypoechogenic pericardial masses are visible (arrows). Ao: aorta; LA: left atrium; LV: left ventricle; PA: pulmonary artery; RV: right ventricle.

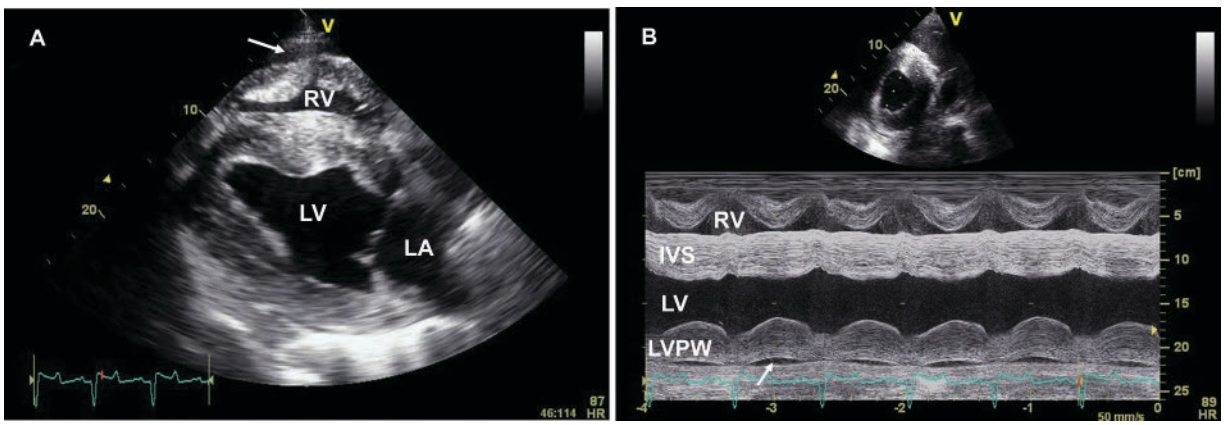
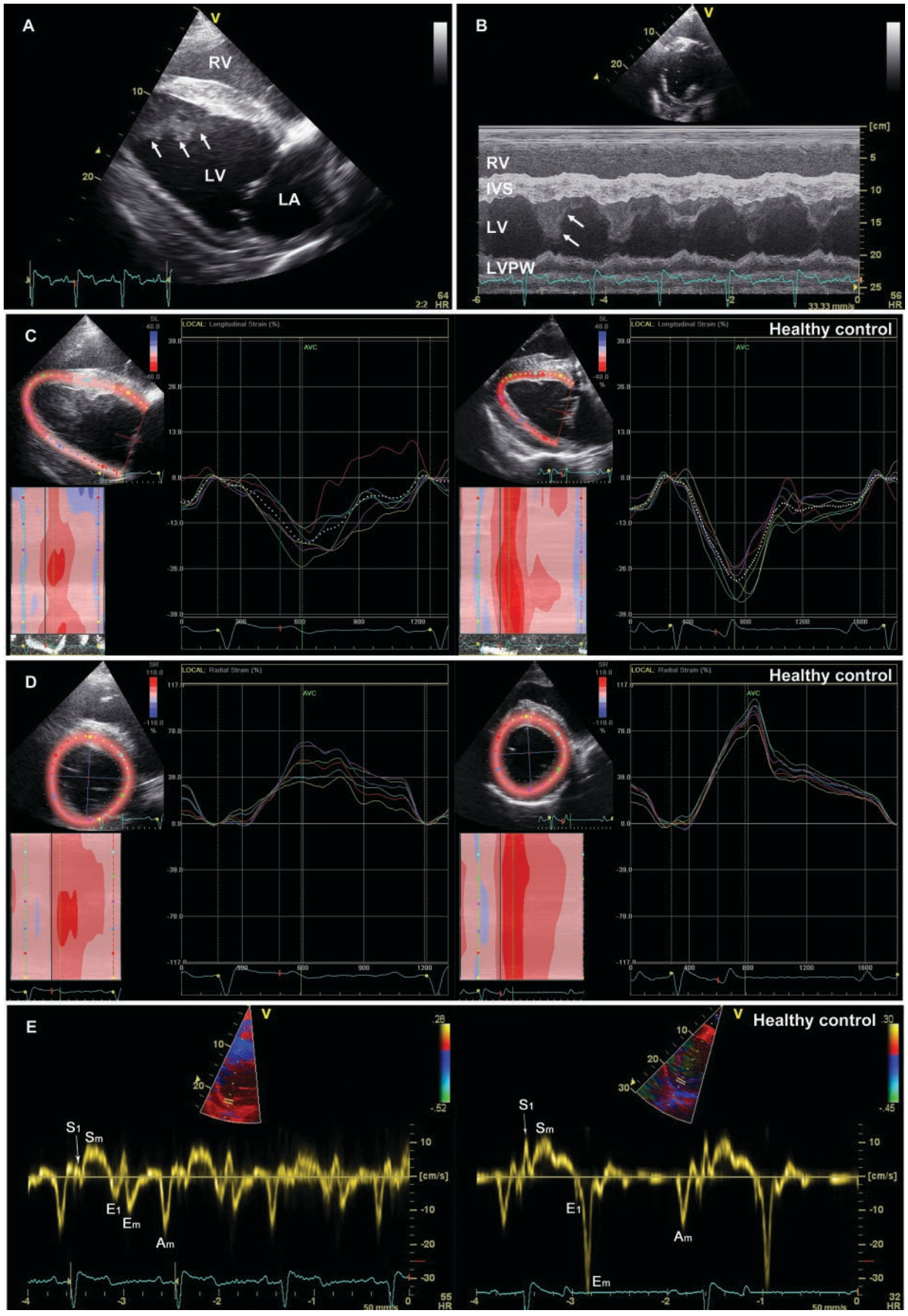


Figure 21.23 Myocarditis (A) Right-parasternal 4-chamber view obtained from a 32-year-old Icelandic Horse gelding with myocarditis of undetermined etiology. The right ventricular (RV) free wall, the interventricular septum, and the left ventricular (LV) peripheral wall are thickened and show heterogeneous echogenicity. Notice the mild pericardial effusion (arrow). (B) Short-axis echocardiogram and corresponding M-mode recording of the LV. The interventricular septum (IVS) and the left ventricular posterior wall (LVPW) are thickened, whereas the internal dimensions of the LV appear small. The relative wall thickness is 1.03 (normal 0.4–0.6) indicating the myocardium is thickened relative to the LV diameter. The motion of the IVS seems flat. The fractional shortening of the left ventricle is 34%. Mild pericardial effusion is evident (arrow). LA: left atrium.

Vet-ebooks.com



Vet-ebooks.com

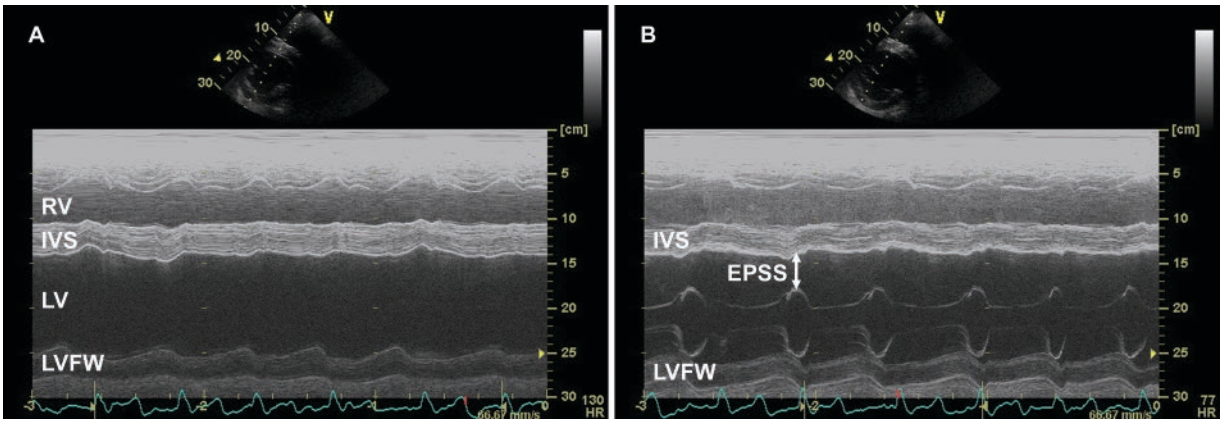


Figure 21.25 Dilated cardiomyopathy. Echocardiogram of a 14-year-old Appaloosa mare presented with congestive heart failure. The findings were compatible with a diagnosis of dilated cardiomyopathy. (A) M-mode echocardiogram in a right-parasternal short-axis view at the level of the chordae tendineae. Notice the hypokinetic motion of the interventricular septum (IVS) and the left ventricular free wall (LVFW), indicating severely depressed left ventricular (LV) systolic function. The LV fractional shortening was 11% (normal 30–45%). (B) M-mode echocardiogram in a right-parasternal short-axis view at the level of the mitral valve. The increased E-point-to-septal separation (EPSS) is consistent with LV dilation and LV failure (resulting in reduced transmitral flow). Other causes for an increased EPSS such as aortic regurgitation (regurgitant jet impinging on the valve) and mitral stenosis (rare) were ruled out in this case. RV: right ventricle.

Figure 21.24 Nutritional myocardial damage. Echocardiographic examination in a 22-year-old Arabian mare suffering from nutritional masseter myopathy with concurrent myocardial damage (cardiac troponin I concentration 11.6 ng/mL; normal < 0.06 ng/mL). This case study demonstrates the clinical use of advanced echocardiographic indices for the assessment of systolic and diastolic LV function in horses with myocardial disease. (A) B-mode recording of the left ventricle in right-parasternal long-axis 4-chamber view. Left atrial (LA), left ventricular (LV), and right ventricular (RV) dimensions appear normal. There is marked spontaneous echo contrast in the LV (arrows). This can be found in healthy horses, but may become more distinct with low output states, bradycardia, and possibly systemic inflammation. (B) M-mode recording of the LV in a right-parasternal short-axis view. Notice the flat motion of the interventricular septum (IVS) and the LV posterior wall (LVPW), suggesting poor LV systolic function (LV fractional shortening 22%; normal 30–45%). Marked spontaneous echo contrast is evident (arrows). (C) Two-dimensional speckle tracking (2DST) analyses of a LV long-axis recording. Trace screens of the 2DST software are shown, displaying the following information. Top left, 2-D image with the segmented ROI and parametric color coding at the time of aortic valve closure. Bottom left, M-mode with parametric color coding. Right, trace display for longitudinal segmental strain (i.e., relative myocardial deformation). The horizontal axis represents the time in ms, the vertical axis represents radial strain in %. The colors of the trace correspond to the colors of the segmented ROI. An ECG is superimposed for timing. The start and the end of the cycle (R waves) are marked on the ECG with yellow dots. Time of aortic valve closure (AVC) is indicated by a green vertical line, dividing the cycle in its systolic and diastolic component. The dotted line indicates the instantaneous average over all segments at the respective time of the cardiac cycle (global strain). Note that peak longitudinal strain in this case (left) is reduced compared to the healthy control (right), indicating depressed LV systolic function. (D) 2DST analyses of a LV short-axis recording. Trace screens of the 2DST software are shown, displaying radial segmental strain (for further explanations see (C)). Note that peak radial strain (left) in this case is reduced compared to the healthy control (right), indicating depressed LV systolic function. (E) Pulsed-wave tissue Doppler (PW TDI) analysis of the LV free wall recorded at the level of the chordae tendineae in a right-parasternal short-axis view. The horizontal scales of the spectral tracings indicate the time in sec, the vertical scales indicate the velocity in cm/sec. The E_m/A_m inversion (left) indicates diastolic dysfunction and impaired ventricular relaxation. Notice the normal E_m/A_m ratio in the healthy control (right) for comparison. S_1: peak radial wall motion velocity during isovolumic contraction; S_m: peak radial wall motion velocity during ejection; E_1: peak radial wall motion velocity during isovolumic relaxation; E_m: peak radial wall motion velocity during early diastole; A_m: peak radial wall motion velocity during late diastole.

Vet-ebooks.com

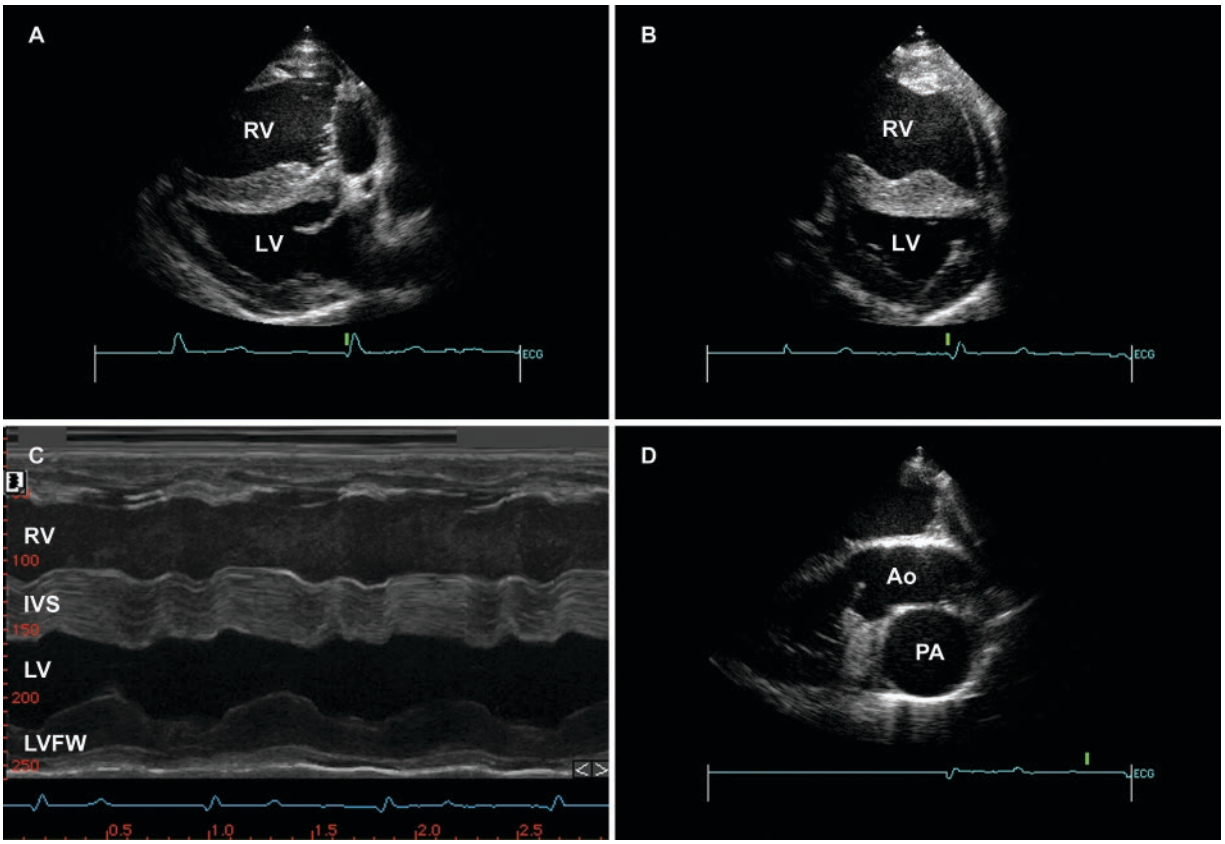


Figure 21.26 Cor pulmonale. Echocardiogram of a 16-year-old American Paint horse gelding with cor pulmonale secondary to severe granulomatous pneumonia. (A) and (B) Right-parasternal long-axis 4-chamber view (A) and right-parasternal short-axis view (B) at end-diastole. Right ventricular (RV) enlargement with bulging of the interventricular septum into the left ventricle (LV) is evident, suggesting chronic RV pressure overload. (C) M-mode echocardiography of the LV in a right-parasternal short-axis view shows enlargement of the RV, small LV, and flattened motion of the interventricular septum (IVS). (D) Right-parasternal long-axis view across the ascending aorta (Ao) and the pulmonary artery (PA). The diameter of the pulmonary artery, seen in short-axis, is larger than the aortic diameter, consistent with pulmonary hypertension. This was confirmed by transvenous cardiac catheterization, revealing end-expiratory pulmonary artery pressures of 82/42 mmHg (systolic/diastolic). LVFWL: left ventricular free wall.

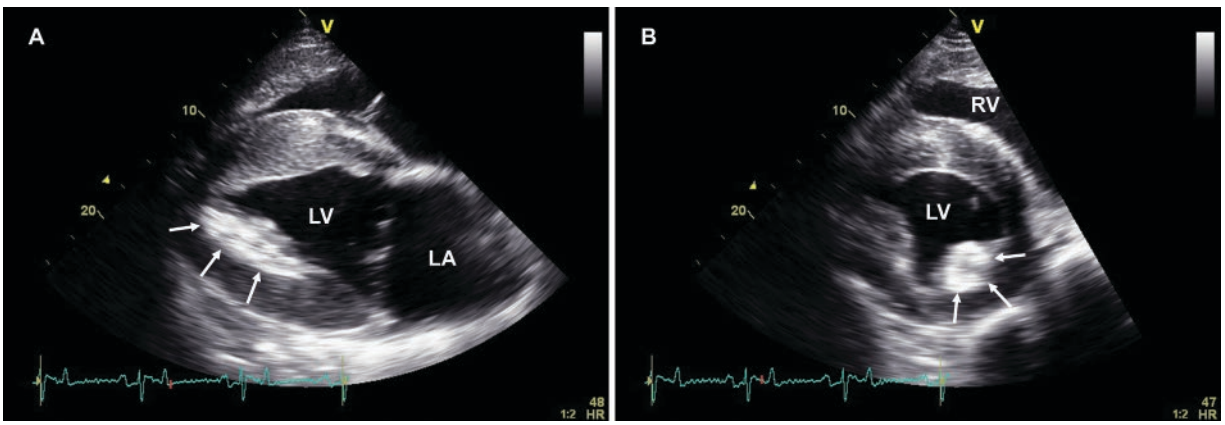


Figure 21.27 Papillary muscle ischemia. Echocardiogram of a 15-year-old Swiss Warmblood gelding with acute transient mitral regurgitation that occurred after physical exhaustion two days prior to the examination. Blood cardiac troponin I concentration was 2.15 ng/mL (normal < 0.06 ng/mL) on the day of the echocardiographic examination, indicating acute myocardial damage. (A) and (B) Right-parasternal long-axis 4-chamber view (A) and right-parasternal short-axis view at the level of the papillary muscles (B). Notice the distinct hyperechoic area in the region of the parietal papillary muscle of the mitral valve. Differential diagnoses for hyperechoic myocardium include ischemia, infarction, myocarditis, infiltration, amyloidosis, and fibrosis. Based on the history of physical exhaustion and the transient nature of the mitral regurgitation, acute focal ischemia was considered most likely. Blood cTnI concentrations returned to normal within 5 days.

Vet-ebooks.com

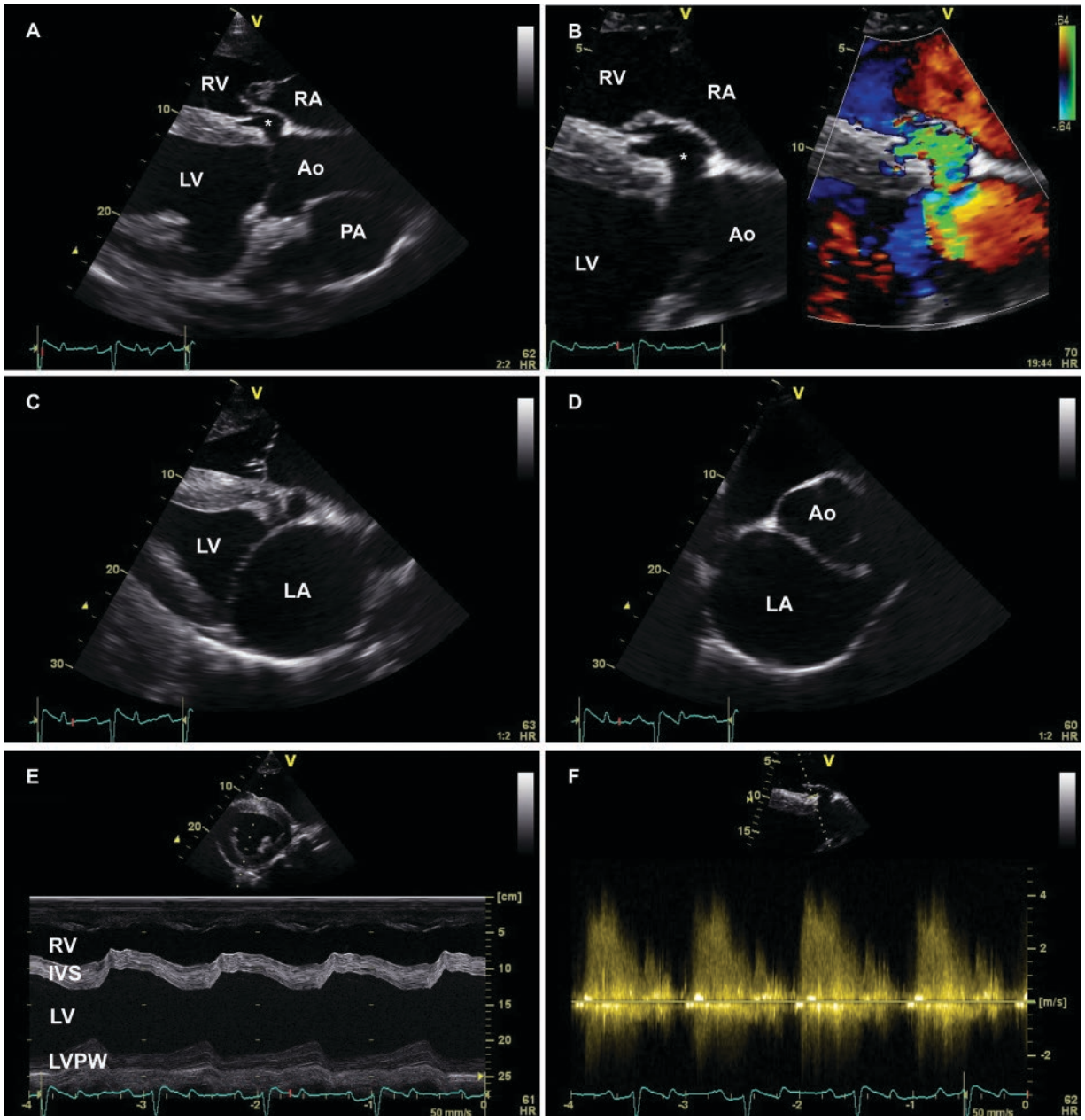


Figure 21.28 Aortic root rupture. (A) Right-parasternal long-axis view of the left ventricular outflow tract obtained from a 21-year-old Paso Fino gelding with a ruptured aortic root. The defect (asterisk) connects the aortic root (Ao) with the right ventricle (RV). The pulmonary artery (PA) appears enlarged relative to the aortic root, indicating increased transpulmonary flow due to left-to-right shunting or pulmonary hypertension. (B) B-mode (left) and color Doppler (right) recording zoomed in on the defect. The defect is located very close to the membranous part of the ventricular septum. However, close inspection of the B-mode recording reveals that the defect is located on the arterial side of the aortic valve, indicating that this defect is an aortic root rupture rather than a ventricular septal defect. Color flow mapping shows left-to-right flow through the defect. Notice the area of proximal flow convergence and concurrent aliasing (sudden color shift from yellow to cyan), visible within the aortic sinus during diastole. (C) and (D) Right-parasternal 4-chamber view (C) and right-parasternal short-axis view of aorta (Ao) and left atrium (LA). The LA is enlarged and has a rounded appearance, indicating left-sided volume overload resulting from left-to-right shunting of blood through the defect. (E) Short-axis echocardiogram and corresponding M-mode recording of the left ventricle (LV). The large end-diastolic LV diameter and the hyperkinetic motion of the interventricular septum (IVS) indicate left ventricular volume overload due to left-to-right shunt. The systolic function of the LV appears adequate, with a fractional shortening of 35%. (F) Continuous-wave Doppler (CWD) recording indicating continuous left-to-right shunt flow through the defect, with a predominantly diastolic flow component. The peak velocity is approximately 4.0 m/s, corresponding to a (mid-to-end-diastolic) pressure gradient between Ao and RV of 64 mmHg (modified Bernoulli equation: $dp = 4 \times v_{max}^2$). LVPW: left ventricular posterior wall; RA: right atrium.

Vet-ebooks.com

influenced by gain settings, direction of flow, orifice size and shape, driving pressure, and characteristics of the receiving chamber. Quantification of regurgitation by assessing signal strength of the spectral Doppler regurgitant signal or measuring the area of regurgitation within the receiving chamber is therefore neither very accurate nor reliable. Integration of subjective assessment of the receiving chamber size, objective measurements, and evaluation of the size of the regurgitant flow together into a severity scoring system can aid the observer in the assessment of clinical relevance of the regurgitation [23,34].

References

1 Reef, V.B. (1998). Cardiovascular ultrasonography. In: *Equine Diagnostic Ultrasound*, 1st edn (ed. V.B. Reef), 215–272. Philadelphia PA: W.B. Saunders.

2 Schwarzwald, C.C. (2018). Disorders of the cardiovascular system. In: *Equine Internal Medicine*, 4th edn (ed. S.M. Reed, W.M. Bayly, and D.C. Sellon), 387–541. St Louis MO: Saunders Elsevier.

3 Boon, J.A. (2011). *Veterinary Echocardiography*. Oxford UK: Wiley-Blackwell.

4 Sepulveda, M.F., Perkins, J.D., Bowen I.M, et al. (2005). Demonstration of regional differences in equine ventricular myocardial velocity in normal 2-year-old Thoroughbreds with Doppler tissue imaging. *Equine Veterinary Journal* 37(3): 222–226.

5 Schwarzwald, C.C., Bonagura, J.D., and Schober, K.E. (2009). Methods and reliability of tissue Doppler imaging for assessment of left ventricular radial wall motion in horses. *Journal of Veterinary Internal Medicine* 23(3): 643–652.

6 Schwarzwald, C.C., Schober, K.E., Berli, A.S.J. et al. (2009). Left ventricular radial and circumferential wall motion analysis in horses using strain, strain rate, and displacement by 2D speckle tracking. *Journal of Veterinary Internal Medicine* 23(4): 890–900.

7 Schefer, K.D., Bitschnau, C., Weishaupt, M.A..et al. (2010). Quantitative analysis of stress echocardiograms in healthy horses with 2-dimensional (2D) echocardiography, anatomical M-mode, tissue Doppler imaging, and 2D speckle tracking. *Journal of Veterinary Internal Medicine* 24(4): 918–931.

8 Decloedt, A., Verheyen, T., Sys, S. et al. (2011). Quantification of left ventricular longitudinal strain, strain rate, velocity, and displacement in healthy horses by 2-dimensional speckle tracking. *Journal of Veterinary Internal Medicine* 25(2): 330–338.

9 Decloedt, A., Verheyen, T., Sys, S. et al. (2013). Evaluation of tissue Doppler imaging for regional quantification of radial left ventricular wall motion in healthy horses. *American Journal of Veterinary Research* 74(1): 53–61.

10 Koenig, T.R., Mitchell, K.J., and Schwarzwald, C.C. (2017). Echocardiographic assessment of left ventricular function in healthy horses and in horses with heart disease using pulsed-wave tissue doppler imaging. *Journal of Veterinary Internal Medicine* 31(2): 556–567.

11 Ven, S., Decloedt, A., De Clercq, D. et al. (2018). Detection of subclinical left ventricular dysfunction by tissue Doppler imaging in horses with aortic regurgitation. *Equine Veterinary Journal* 50(5): 587–593.

12 Otto, C.M. (2004). *Textbook of Clinical Echocardiography*. Philadelphia PA: Elsevier Saunders.

13 Lang, R.M., Bierig, M., Devereux, R.B. et al. (2006). Recommendations for chamber quantification. *European Journal of Echocardiograph: The Journal of the Working Group on Echocardiography of the European Society of Cardiology* 7(2): 79–108.

14 Grenacher, P.A. and Schwarzwald, C.C. (2010). Assessment of left ventricular size and function in horses using anatomical M-mode echocardiography. *Journal of Veterinary Cardiology: The Official Journal of the European Society of Veterinary Cardiology* 12(2): 111–121.

15 Patteson, M.W., Gibbs, C., Wotton, P.R. et al. (1995). Effects of sedation with detomidine hydrochloride on echocardiographic measurements of cardiac dimensions and indices of cardiac function in horses. *Equine Veterinary Journal. Supplement* 19: 33–37.

16 Gehlen, H., Kroker, K., Deegen, E. et al. (2004). Influence of detomidine on cardiac function and hemodynamic in horses with and without heart murmur. *Schweizer Archiv Fur Tierheilkunde* 146(3): 119–126.

17 Buhl, R., Ersboll, A.K., Larsen, N.H. et al. (2007). The effects of detomidine, romifidine or acepromazine on echocardiographic measurements and cardiac function in normal horses. *Veterinary Anaesthesia and Analgesia* 34(1): 1–8.

18 Menzies-Gow, N.J. (2008). Effects of sedation with acepromazine on echocardiographic measurements in eight healthy thoroughbred horses. *The Veterinary Record* 163(1): 21–25.

19. Huesler, I.M., Mitchell, K.J., and Schwarzwald, C.C. (2016). Echocardiographic assessment of left atrial size and function in warmblood horses: reference intervals, allometric scaling, and agreement of different echocardiographic variables. *Journal of Veterinary Internal Medicine* 30(4): 1241–1252.

20 Schwarzwald, C.C., Schober, K.E., and Bonagura, J.D. (2007). Methods and reliability of echocardiographic assessment of left atrial size and mechanical function in horses. *American Journal of Veterinary Research* 68(7): 735–747.

21 Schwarzwald, C.C., Schober, K.E., and Bonagura, J.D. (2007a). Echocardiographic evidence of left atrial

Vet-ebooks.com

mechanical dysfunction after conversion of atrial fibrillation to sinus rhythm in 5 horses. *Journal of Veterinary Internal Medicine* 21(4): 820–827.

22 Navas de Solis, C., Slack, J. et al. (2013). Hypertensive cardiomyopathy in horses: 5 cases (1995–2011). *Journal of the American Veterinary Medical Association* 243(1): 126–130.

23 Boegli, J., Schwarzwald, C.C., and Mitchell, K.J. (2019). Diagnostic value of non-invasive pulse pressure measurements in warmblood horses with aortic regurgitation. *Journal of Veterinary Internal Medicine* 33(3): 1446–1455.

24 Decloedt, A., De Clercq, D., Ven Sofie, S. et al. (2017). Echocardiographic measurements of right heart size and function in healthy horses. *Equine Veterinary Journal* 49(1): 58–64.

25 Giguere, S., Bucki, E., Adin, D.B. et al. (2005). Cardiac output measurement by partial carbon dioxide rebreathing, 2-dimensional echocardiography, and lithium-dilution method in anesthetized neonatal foals. *Journal of Veterinary Internal Medicine/ American College of Veterinary Internal Medicine* 19(5): 737–743.

26 Stoylen, A. *Strain rate imaging: Cardiac deformation imaging by ultrasound/echocardiography – Tissue Doppler and Speckle tracking*. http://folk.ntnu.no/stoylen/strainrate (accessed 06 April 2022).

27 Schefer, K.D., Hagen, R., Ringer, S.K. et al. (2011). Laboratory, electrocardiographic, and echocardiographic detection of myocardial damage and dysfunction in an Arabian mare with nutritional masseter myodegeneration. *Journal of Veterinary Internal Medicine* 25(5): 1171–1180.

28 Decloedt, A., Verheyen, T., Sys, S. et al. (2012). Tissue Doppler imaging and 2-dimensional speckle tracking of left ventricular function in horses exposed to lasalocid. *Journal of Veterinary Internal Medicine* 26(5): 1209–1216.

29 Blissitt, K.J. and Bonagura, J.D. (1995). Pulsed wave Doppler echocardiography in normal horses. *Equine Veterinary Journal. Supplement* 19: 38–46.

30. Flethoj, M., Schwarzwald, C.C., Haugaard, M.M. et al. (2016). Left ventricular function after prolonged exercise in equine endurance athletes. *Journal of Veterinary Internal Medicine* 30(4): 1260–1269.

31 De Clercq, D., van Loon, G., Tavernier, R. et al. (2008). Atrial and ventricular electrical and contractile remodeling and reverse remodeling owing to short-term pacing-induced atrial fibrillation in horses. *Journal of Veterinary Internal Medicine* 22(6): 1353–1359.

32 Decloedt, A., Schwarzwald, C.C., De Clercq, D. et al. (2015). Risk factors for recurrence of atrial fibrillation in horses after cardioversion to sinus rhythm. *Journal of Veterinary Internal Medicine* 29(3): 946–953.

33 Young, L.E., Rogers, K., and Wood, J.L. (2008). Heart murmurs and valvular regurgitation in thoroughbred racehorses: Epidemiology and associations with athletic performance. *Journal of Veterinary Internal Medicine* 22(2): 418–426.

34 Ven, S., Decloedt, A., Van Der Vekens, N. et al. (2016). Assessing aortic regurgitation severity from 2D, M-mode and pulsed wave Doppler echocardiographic measurements in horses. *Veterinary Journal (London 1997)* 210: 34–38.

Vet-ebooks.com

22

Ultrasonography of the Liver, Spleen, Kidneys, Bladder, and Peritoneal Cavity

Nathan Slovis

McGee Medical and Critical Care Center, Hagyard Equine Medical Institute, Lexington, KY, USA

Liver

The liver (Figures 22.1, 22.2, 22.3, 22.4, 22.5, 22.6, 22.7, 22.8, 22.9, and 22.10) is the largest of the abdominal organs, occupying most of the right quadrant and extending across the midline. The liver can be located in the right cranioventral and midabdomen between the 7th and 14th intercostal spaces (ICS) and dorsally in the 14th ICS. It can also be located on the left side cranioventrally between the 6th and 9th ICS. On the right side, the right dorsal colon (RDC) is deep to the liver and the duodenum is located between the RDC and liver in the mid portion of the abdomen. On the left side, the liver will be in contact with the stomach and the spleen. Because the liver lies superficially in the young animal, a 5 to 7 MHz transducer is optimal, while a 3.5 or even a 2.0 MHz will be necessary in the older, adult horse. Hepatic vessels and bile ducts can be seen diffusely, with the portal vein and caudal *vena cava* being the largest vessels observed on the right side. The liver is characterized as homogeneously hypoechoic and uniform throughout compared to the spleen.

Spleen

The spleen (Figures 22.11, 22.12, 22.13, 22.14, 22.15, and 22.16) is imaged between the 7th ICS and the paralumbar fossa (PLF) on the left side and in the 9th ventral ICS on the right side in contact with the liver. The splenic vein is located on the medial aspect of the spleen, caudal and dorsal to the stomach, in the 11th to 12th mid-ICS. The spleen interfaces caudally with the left kidney and is homogenously echogenic, with few vessels seen. The splenic hilar vessels are usually easily seen, while the intrasplenic vessels typically requires Doppler for identification

Kidneys

The left and right kidneys (Figures 22.17, 22.18, 22.19, 22.20, 22.21, 22.22, 22.23, 22.24, 22.25, 22.26, and 22.27) differ in ultrasonographic appearance and location. The right kidney is located ventral to the transverse spinous processes between the 14th and 16th ICS from 2 cm dorsal to the tuber coxae (TC) to 12 cm ventral. The right kidney has a more oval anatomical shape in the longitudinal view than the left kidney. The left kidney can be visualized from the 15th ICS to the caudal border of the left PLF and from 2 cm dorsal to 15 cm ventral to the dorsal margin of the TC. From the dorsal plane, the left kidney has a more heart-triangular shape than the right kidney. The renal cortex is hypoechoic compared to the surrounding tissues. However, when compared to the adjacent medulla, it is considered echodense with a slightly mottled appearance. The adjacent medulla is less echogenic than the renal cortex. The renal cortex usually measures ≤ 1 cm in thickness. In the cranial and caudal extremities of each kidney, acoustic anisotropy will be observed between the renal cortex and medulla, resulting in the cortex and medulla in these areas appearing more echogenic than in the center of the kidney. The left kidney is generally considered larger than the right kidney, with the length measuring up to 16 cm and the width measuring

Atlas of Equine Ultrasonography, Second Edition. Edited by Jessica A. Kidd, Kristina G. Lu and Michele L. Frazer.
© 2022 John Wiley & Sons Ltd. Published 2022 by John Wiley & Sons Ltd.
Companion Website: www.wiley.com/go/kidd/atlas

Vet-ebooks.com

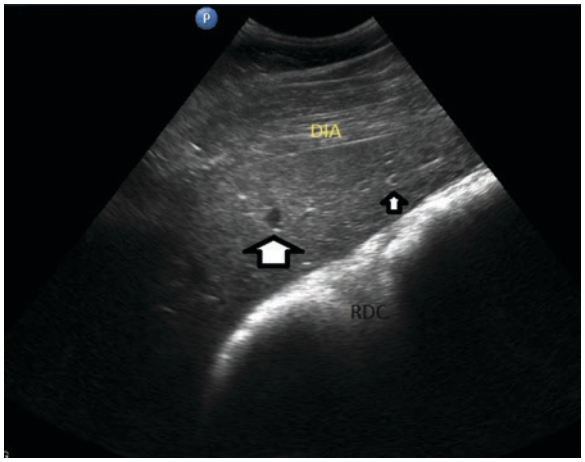


Figure 22.1 Normal liver. This imaeftge shows normal liver in a 12-year-old Thoroughbred mare. The hepatic veins (small arrow) image as small, tubular, or circular structures with a thin wall. The portal veins (large arrow) usually have a thicker and more echogenic wall than the hepatic veins. The right dorsal colon (RDC) is medial to the right lobe of the liver. The diagram (Dia) is superficial to and "covers" the liver. The sonogram was obtained from the right 10th ICS using a curvilinear probe operating at 5.0 MHz at a displayed depth of 18 cm. The left side of this image is dorsal and the right side is ventral.

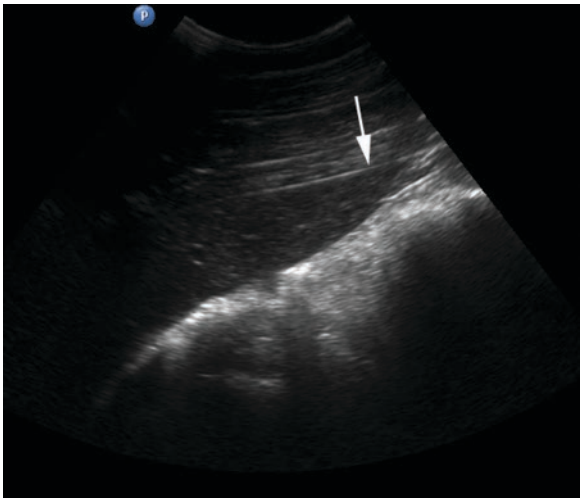


Figure 22.2 Normal liver. In this image from the mare in Figure 22.1, the liver has normal, tapered edges (arrow). Rounded edges are abnormal and may occur in cases of hepatitis or hepatic lipidosis. The sonogram was obtained from the right 10th ICS, 5–7 cm ventral to the image of Figure 22.1, using a curvilinear probe operating at 5.0 MHz at a displayed depth of 18 cm. The left side of this image is dorsal and the right side is ventral.

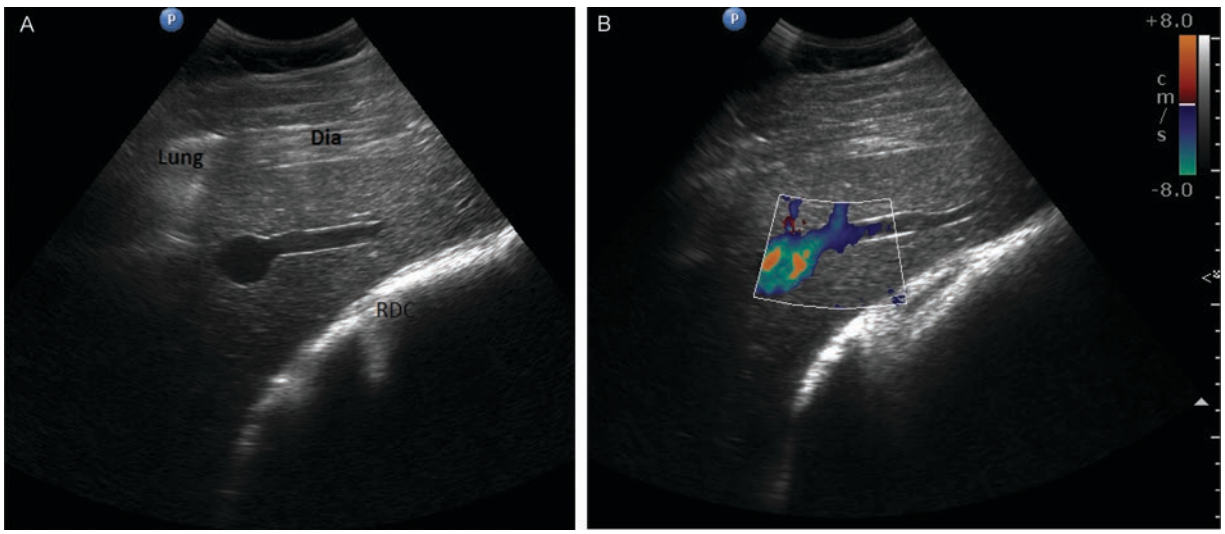


Figure 22.3 Normal liver. (**A**) In this image from the mare in Figure 22.1, the portal veins are prominent with a thick, echogenic wall. This is a normal anatomical finding of the liver. The ventral tip of the lung can be visualized "covering" the liver on the left side of this image. The diagram (Dia) is superficial to the liver. Right dorsal colon (RDC) is visible. The sonogram was obtained from the right 8th ICS using a curvilinear probe operating at 5.0 MHz at a depth of 18 cm. The left side of this image is dorsal and the right side is ventral. (**B**) Color flow Doppler confirms that the linear structure is the portal vein and not a dilated bile duct.

Vet-ebooks.com

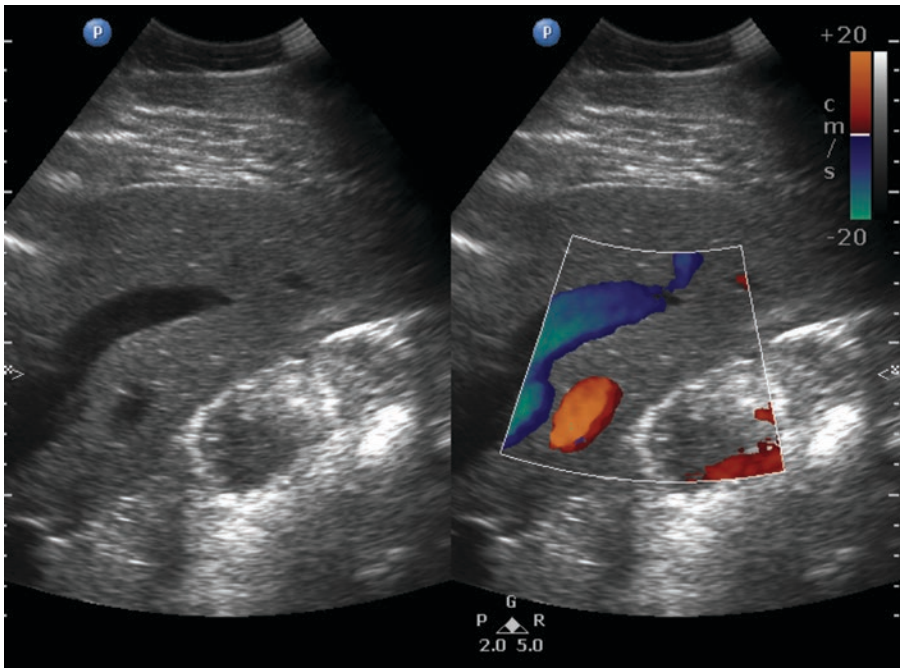


Figure 22.4 Normal portal vein. This image shows the portal vein in a normal, 3-year-old racehorse. The color Doppler was used to confirm that the liner structure was the portal vein and not a dilated bile duct. With color, Doppler, direction, and velocity of blood flow can be evaluated. Although color may vary with machine, typically, red indicates flow toward the transducer, while blue indicates flow away from the tranducer. Brighter hues indicate faster velocity of blood flow, while duller colors indicate slower velocity of blood flow. Turbulent blood flow produces a mixture of colors. This sonogram was obtained from the right abdomen using a curvilinear probe operating at 3.5 MHz at a depth of 18 cm.

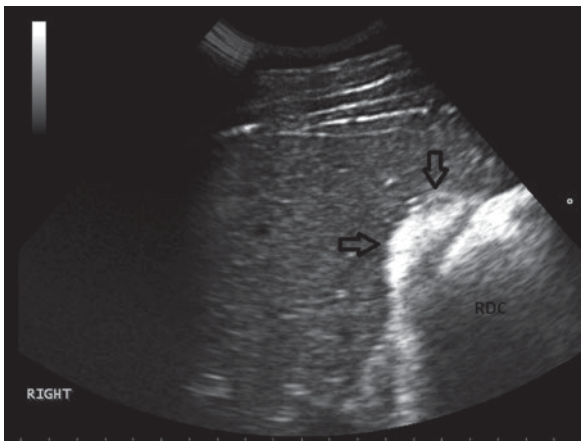


Figure 22.5 Normal liver and duodenum. This image shows the duodenum (arrows) located medial to the right lobe of the liver in a 12-year-old Thoroughbred gelding. The right dorsal colon (RDC) is medial to the duodenum. The duodenum is easily recognized because of its oval and flattened appearance with a hyperechoic center. During peristalsis, the duodenum will appear to have an oval to round shape. Note the normal homogeneously hypoechoic sonographic appearance of the liver. The sonogram was obtained from the right 14th ICS using a curvilinear probe operating at 3.5 MHz at a displayed depth of 15 cm. The left side of this image is dorsal and the right side is ventral.

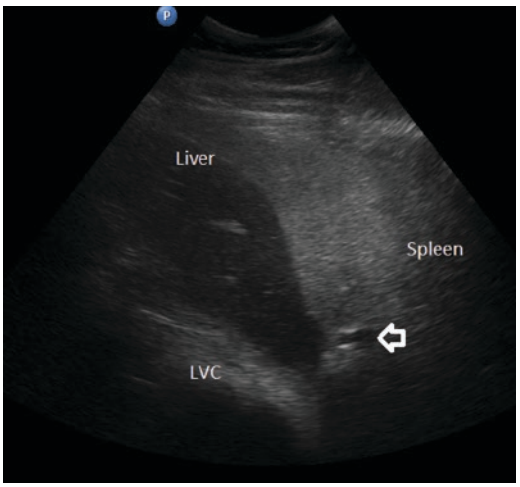


Figure 22.6 Cranioventral abdomen. This image shows the left, cranioventral abdomen obtained from a 12-year-old pregnant Thoroughbred mare. In the normal horse, the spleen is more echogenic and more homogenous than the liver which is located medial to the spleen. If the liver is the same echogenicity as the spleen, cholangiohepatitis or hepatitis should be suspected. The hyperechoic, curvilinear structure adjacent to the liver is the left ventral colon (LVC). The splenic vein (small arrow) is visualized in the spleen. The sonogram was obtained from the left, cranioventral abdomen using a curvilinear probe operating at 5.0 MHz at a displayed depth of 17 cm. The left side of this image is dorsal and the right side is ventral.

Vet-ebooks.com

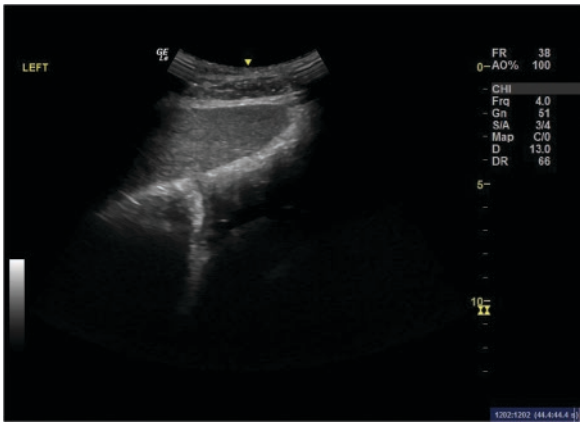


Figure 22.7 Hepatitis. Note the round edges which is different from the tapered edges noted in the normal liver. The image is obtained using a curvilinear probe operating at 4.0 MHz at a displayed depth of 13 cm.

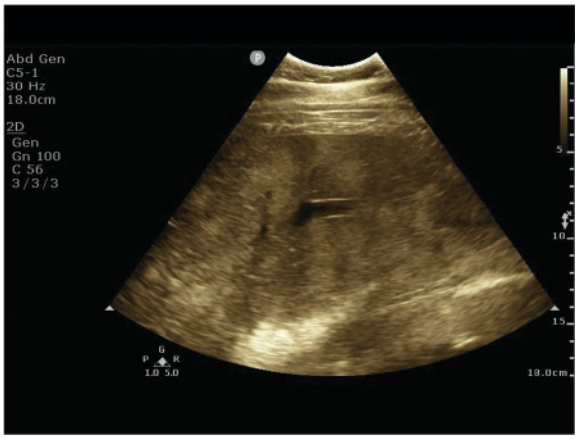


Figure 22.8 Acute hepatitis. This image is from an 8-year-old pregnant mare presenting with pyrexia, SDH, and bile acids above the reference range, but GGT within the reference range. The liver is markedly enlarged with multifocal areas of increased echogenicity. The sonogram was obtained from the left cranioventral using a curvilinear probe operating at 5.0 MHz at a displayed depth of 18 cm. The left side of the image is dorsal and the right side is ventral.

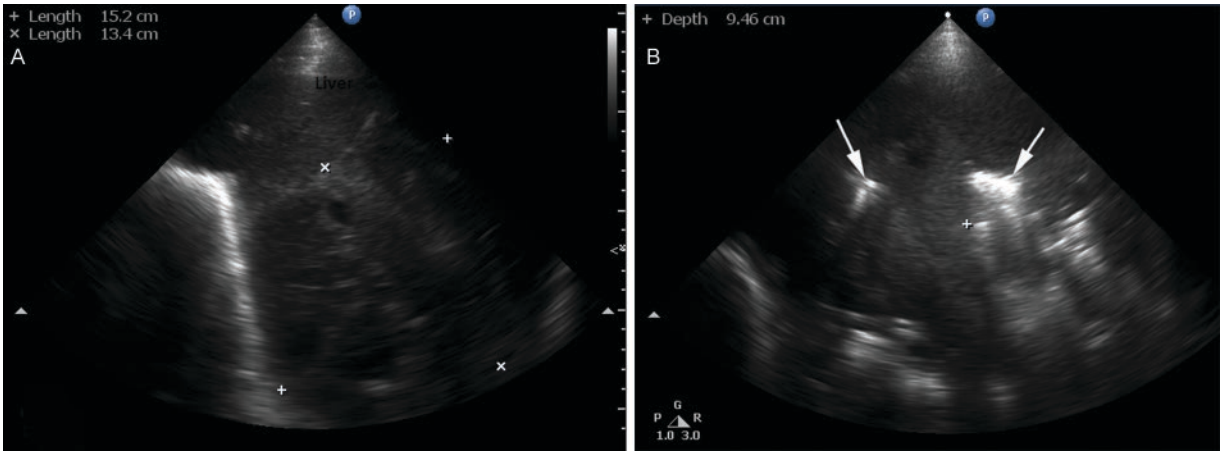


Figure 22.9 Amyloidosis. These images are liver from a 5-year-old Tennessee Walking Horse stallion. The stallion had a history of hyperglobulinemia, anorexia, and intermittent pyrexia for three weeks prior to examination. The animal had been treated with sulfadiazine/trimethoprim (30 mg/kg PO q 12 hours) for three weeks with minimal improvement. (**A**) A large mass was imaged adjacent to the liver. In this image, ascertaining if the mass is located medial to the liver or in the liver is difficult. The owners declined a biopsy at the time of the initial examination and the horse was, therefore, discharged with Chloramphenicol (50 mg/kg PO q 8 hours) and Metronidazole (15 mg/kg PO q 8 hours). The sonogram was obtained from the right 9th ICS using a curvilinear probe operating at 3.0 MHz at a displayed depth of 21 cm. The left side of this image is dorsal and the right side is ventral. (**B**) The horse was examined again 19 days later for pyrexia and continued anorexia. The sonogram revealed large, hyperechoic structures (arrows) within the liver's parenchyma. Based on histopathology of a biopsy sample, the hyperechoic structures were identified as amyloid deposits and the horse was diagnosed with amyloidosis. The owners opted to euthanize the horse. If the amyloid deposits had been more calcified, an acoustic shadow would have been noted from the near surface of the amyloid deposits. The sonogram was obtained from the right 11th ICS using a curvilinear probe operating at 3.0 MHz at a displayed depth of 19 cm. The left side of this image is dorsal and the right side is ventral.

Vet-ebooks.com

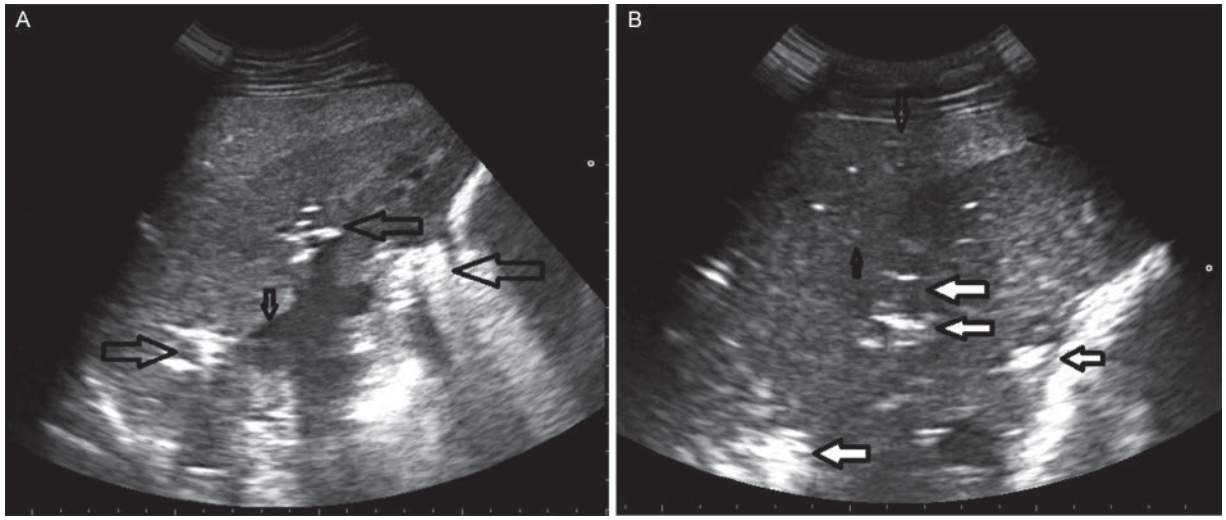


Figure 22.10 Bile duct stricture. This image shows the liver from a 3-month-old Thoroughbred colt diagnosed with a gastric outflow obstruction (stricture) affecting the proximal duodenum. The stricture also incorporated the common bile duct opening. The bile duct stricture resulted in cholestasis and severe suppurative cholangiohepatitis. (A) Note the enlarged bile duct (small arrow) and the abscesses (large arrows) within the liver's parenchyma. An acoustic shadow is present medial to the abscess. The foal had a gastrojejunostomy performed and was placed post-operatively on potassium penicillin (22,000 IU/kg IV q 6 hours), metronidazole (15 mg/kg PO q 8 hours), and gentamicin (6 mg/kg IV SID) for 10 days and then changed to chloramphenicol (50 mg/kg PO q 6 hours) along with the metronidazole. The sonogram was obtained from the right 11th ICS using a curvilinear probe operating at 3.5 MHz at a displayed depth of 17 cm. The left side of this image is dorsal and the right side is ventral. (B) The foal was examined 20 days after discharge from the clinic. His clinical condition had improved and he had been afebrile since treatment. The sonogram of the right lobe of the liver in the 12th ICS shows a diffuse area of increased echogenecity in the parenchyma of the superficial right lobe representing an area of hepatic cirrhosis. The suppurative hepatitis was responding to the prescribed treatment program based on the horse's improved improved blood parameters (white blood cell count, SDH, bile acids, and fibrinogen values in reference range) along with the decreased size of hepatic abscessation (white arrows) from the previous examination. However, the GGT remained above the reference range secondary to chronic scarring and fibrosis in the liver. The sonogram was obtained from the right 12th ICS using a curvilinear probe operating at 3.5 MHz at a depth of 13 cm. The left side of this image is dorsal and the right side is ventral.

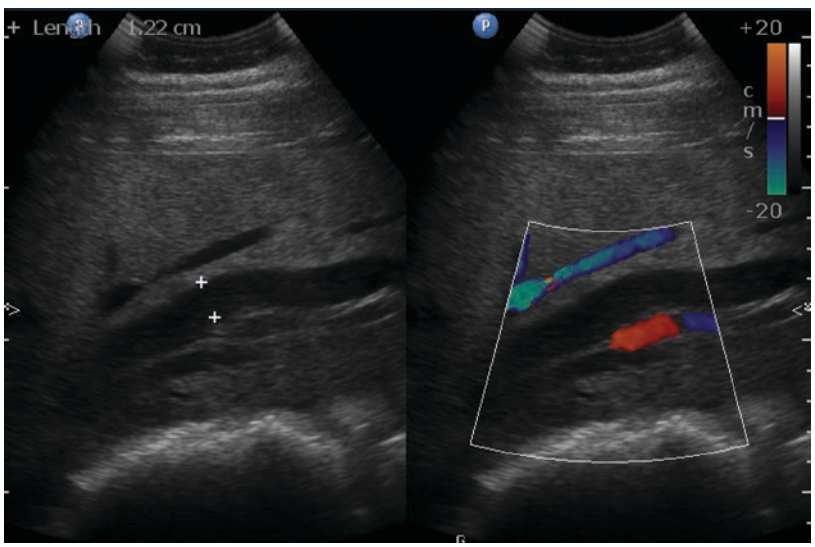


Figure 22.11 Cholangiohepatitis. This image is liver from a mare diagnosed with *Bacteroides fragilis* cholangiohepatitis. On initial examination, the mare had GGT, SDH, and bile acid values above the reference range. Endoscopy of her duodenum revealed a patent bile duct. The mare was treated with potassium penicillin (22,000 IU/kg IV q 6 hours) and metronidazole (15 mg/kg PO q 8 hours) for two weeks and then changed to Sulfadiazine/Trimethoprim (30 mg/kg PO q 12 hours) with metronidazole for another four weeks. The mare also received natural vitamin E (10,000 IU PO q 24 hours) and S-Adenosyl-l-methionine (20 mg/kg PO q 24 hours). Note the distended bile duct and portal veins indicating portal hypertension. Differentiating a distended hepatic vessel from a bile duct without color flow Doppler may not be possible. The sonogram also shows diffuse, increased echogenicity within the liver. Histopathology of a biospy sample of the distended bile duct indicated fibrosis around the portal triad. Seven weeks after diagnosis of cholangiohepatitis, the liver values were within the reference range and the bile duct could not be identified ultrasonographically. The diffuse, increased echogenicity was unchanged from initial examination, but the mare had gained weight and delivered a live foal. The sonogram was obtained from the right 12th ICS using a curvilinear probe operating at 3.5 MHz at a displayed depth of 17 cm. The left side of this image is dorsal and the right side is ventral. [Image 002a and Image 002B. Video 2].

Vet-ebooks.com

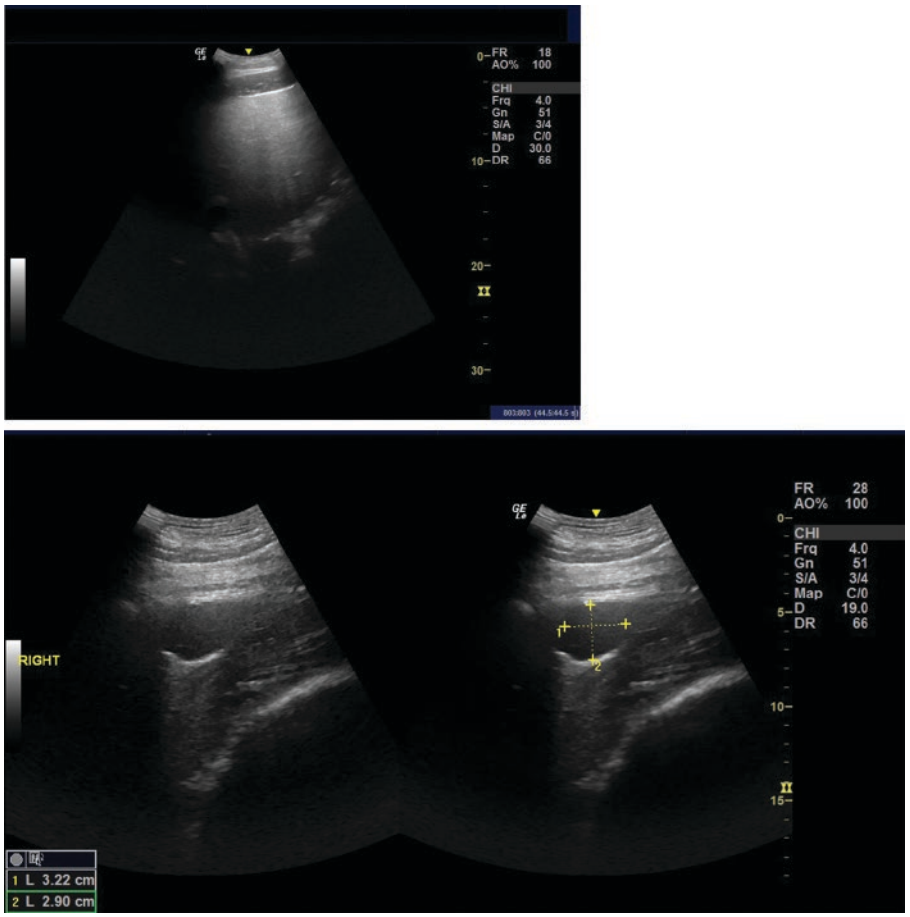
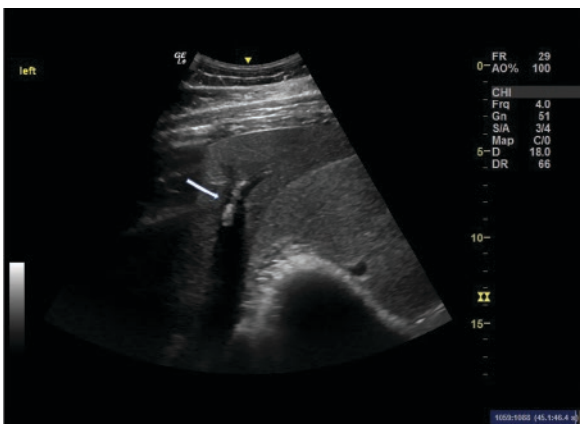


Figure 22.12 Cholangiohepatitis and bile duct distention. This image shows a liver from a 13-year-old Draft cross used for fox hunting. Eight months previously, he had been diagnosed with cholangiohepatitis with cholelithiasis. He had previously been treated with minocycline (4 mg/kg PO BID) and pentoxifylline (6 grams PO TID), as well as 100 ml DMSO in 1L NaCL IV (3 doses per month for 8 weeks). (A) The bile duct (cursors) is severely dilated. It is noted in the right ICS 7 adjacent to the diaphragm and measures 3.2 by 2.9 cm (had previously measured 5.0 cm in diameter). Sonogram obtained from the right ICS 7 using a curvilinear probe operating at 4.0 MHz at a displayed depth of 19 cm. Left side of the image is dorsal and the right side is ventral. (B) Diffusely hyperechoic liver with focal hyperechoic foci characteristic of small cholelithes (arrows). Sonogram obtained from the 12th ICS using a curvilinear probe operating at 4.0 MHz at a displayed depth of 30 cm. Left side of the image is dorsal and the right side is ventral.

Figure 22.13 Cholelithiasis and fibrosing cholangiohepatitis. This image is from a 4-year-old Quarter Horse barrel racing gelding that presented for depression and GGT levels above the reference range. The spleen is located medial to the liver and is more echogenic and more homogenous than the liver. The liver has a distended bile duct with a cholelith (arrow). Note the variably hyperechoic appearance of the hepatic parenchyma. Biopsy findings are portal tract expansion with dense collagenous tissue, bile duct hyperplasia, and chronic neutrophilic inflammation. Portal tracts are frequently bridged by fibrous tissue. Crystalline material is in the sinusoids, indicative of continued bile stone formation. The sonogram was obtained from the left cranioventral using a curvilinear probe operating at 4.0 MHz at a displayed depth of 17 cm. The left side of the image is dorsal and the right side is ventral.



Vet-ebooks.com

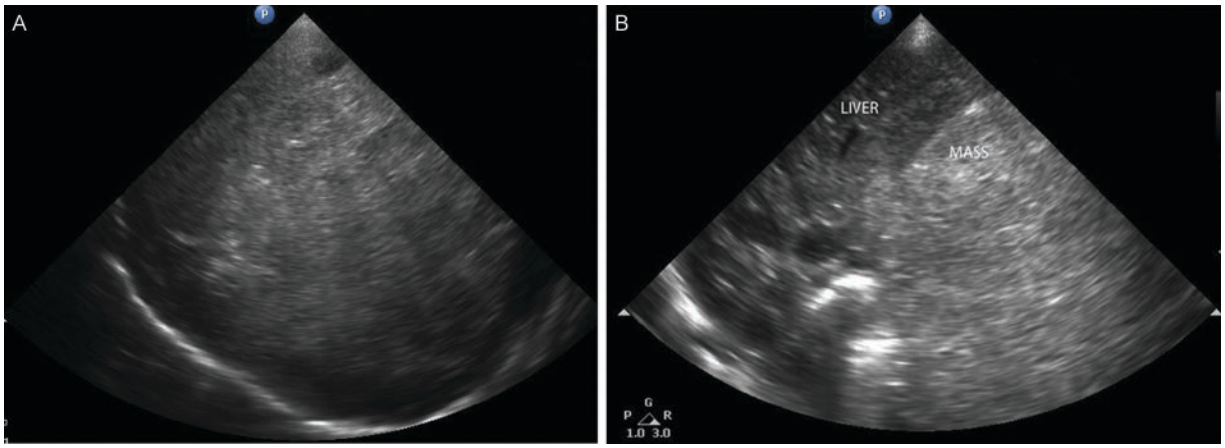


Figure 22.14 Hepatoblastoma. This image shows liver from a 2-week-old, premature foal. The foal was referred to the clinic at two hours of age for weakness and a pendulous abdomen. Palpation of the abdomen revealed a firm mass in the abdomen. (**A**) The sonogram revealed a large, 12 cm by 12 cm, heterogenous, hyperechoic mass within the liver. The mass was a hepatoblastoma involving only the quadrate lobe of the liver. This image was obtained from ventral abdomen using a microconvex probe operating at 5.0 MHz at a depth of 18 cm. (**B**) Normal liver has a more homogenous, hypoechoic architecture compared to the hyperechoic hepatoblastoma (mass) identified in the quadrate lobe. This image was obtained from ventral abdomen, right of midline, with a microconvex probe operating at 5.0 MHz at a depth of 12 cm.

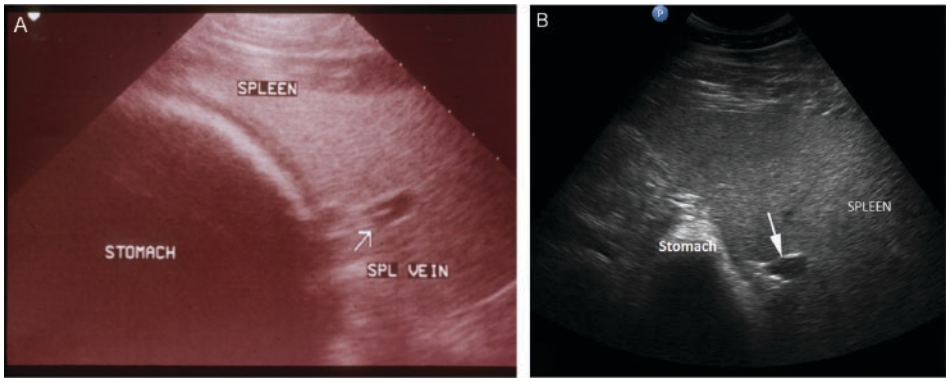


Figure 22.15 Stomach spleen relationship. (**A** and **B**) These images show stomach and spleen from a 3-year-old Thoroughbred filly. The stomach can be easily recognized by its hyperechoic, curvilinear appearance and its location next to the splenic vein (arrow). The spleen is homogenous and echogenic. The sonogram was obtained at the left 9th ICS using a curvilinear probe operating at 3.5 MHz at a displayed depth of (**A**) 12 cm and (**B**) 17 cm. The left side of this image is dorsal and the right side is ventral.

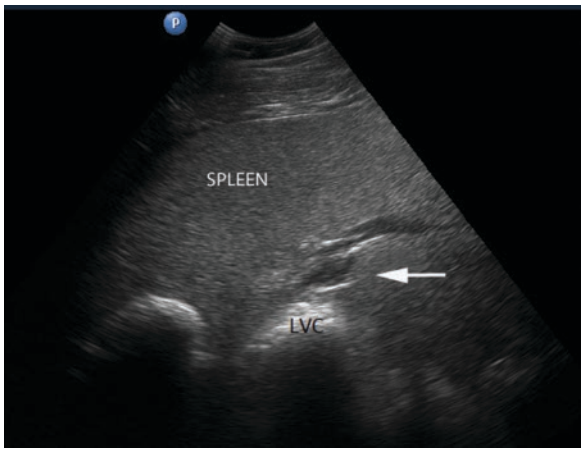


Figure 22.16 Normal spleen. This image shows normal spleen from a 10-year-old pregnant Thoroughbred mare. The spleen is homogenous and echogenic. Note how the splenic vein (arrow) is easily visualized along the medial aspect of the spleen. Medial to the spleen is the left ventral colon (LVC). This sonogram was obtained from the left 12th ICS using a curvilinear probe operating at 5 MHz at a displayed depth of 25 cm. The left side of the image is dorsal and the right side is ventral.

Vet-ebooks.com

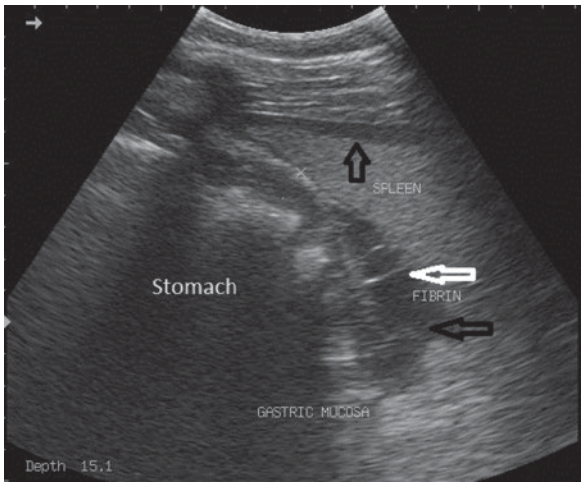


Figure 22.17 Adhesions between spleen and stomach. This image is from a 6-month-old Thoroughbred colt with acute colic signs. The colt, on arrival, had sinus tachycardia (heart rate of 90 beats per minute), injected mucus membranes, and a prolonged capillary refill time. The colt was diagnosed with a perforated gastric ulcer and peritonitis. Fibrin adhesions (white arrow) are seen between the spleen and the stomach. Free fluid (black arrows) is visualized in the abdominal cavity. The normal homogenous echogenicity of the spleen is maintained. The sonogram was obtained from the left 9th ICS using a curvilinear probe operating at 2.0 MHz at a depth of 15 cm. The left side of this image is dorsal and the right side is ventral.

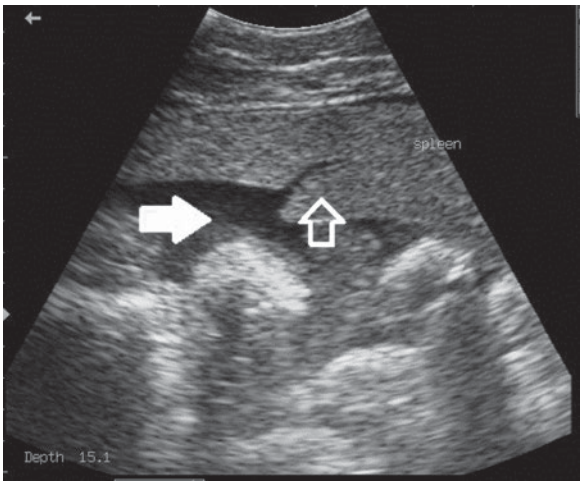


Figure 22.19 Splenic tear. This image is from a Thoroughbred colt. The colt was traumatized on the track when it collided with another horse. The colt presented in hemorrhagic shock and was given 7 liters of whole blood and the hemostatic agent aminocaproic acid (20 mg/kg diluted in liter saline, IV, q 6 hours). The spleen had a tear (hollow arrow) that resulted in hemoabdomen (solid arrow). Note how contracted or thin the spleen is secondary to the large blood loss. The sonogram was obtained just ventral to the paralumbar fossa using a curvilinear probe operating at 2.0 MHz at a displayed depth of 15 cm. The left side of this image is dorsal and the right side is ventral.

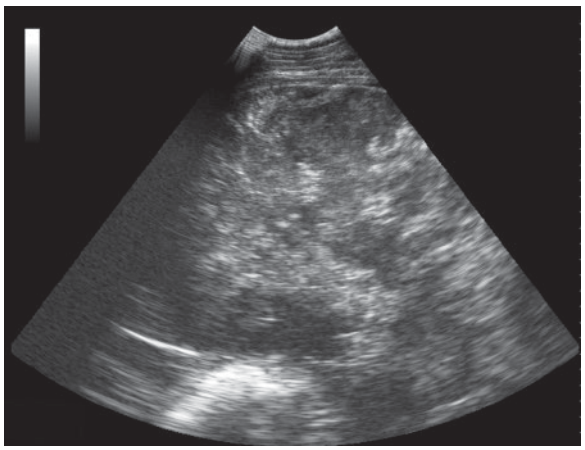


Figure 22.18 Lymphosarcoma. This image is from a yearling Thoroughbred filly with weight loss and intermittent signs of colic. In this image, the spleen has a heterogenous echogenicity and is swollen with a "round" appearance. The spleen extended across midline 8–10 cm. A biopsy was performed and lymphosarcoma was diagnosed based on histopathology. The sonogram was obtained from the left 14th ICS using a curvilinear probe operating at 3.5 MHz at a depth of 27 cm. The left side of this image is dorsal and the right side is ventral.

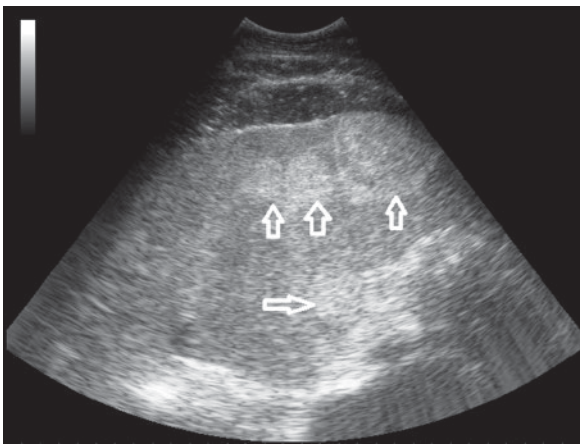


Figure 22.20 Hemangiosarcoma. This image is from a Thoroughbred stallion with weight loss, intermittent colic, and anemia (hematocrit 15, reference range 34–49%). On arrival, the stallion's mucus membrane color was pale pink with a prolonged capillary refill time. The spleen had a heterogenous echogenicity with well demarcated masses (white arrows). A biopsy was taken of the spleen and histopathology confirmed hemangiosarcoma. This sonogram was obtained from the left abdomen, caudal to the last rib, with a curvilinear probe operating at 3.5 MHz at a depth of 25 cm.

Vet-ebooks.com

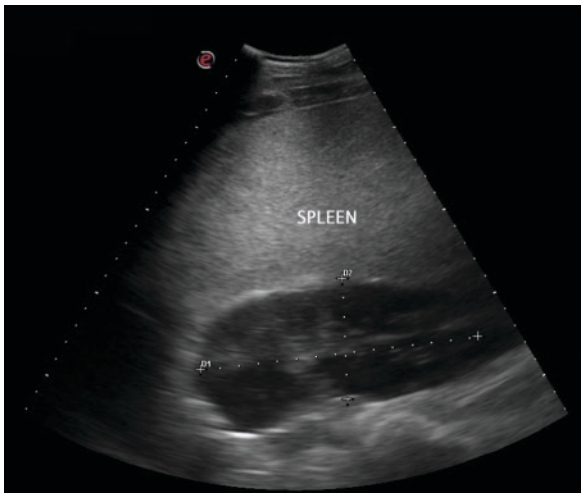


Figure 22.21 Normal left kidney. This image is of the left kidney obtained from 3-year-old Thoroughbred filly. The kidney has a hypoechoic architecture compared to the spleen. Normally, the renal pelvis is echogenic secondary to intrapelvic fat and fibrous tissue. Visualizing the cortex and medulla with adequate detail may be difficult because of the left kidney's depth in the abdomen. Transrectal examination of the left kidney will provide a more detailed view of the organ. The left kidney in an adult horse usually measures 15–16 cm by 10 cm. This sonogram was obtained from the left, lateral abdomen, caudal to the last rib, with a curvilinear probe operating at 3.5 MHz at a depth of 22 cm.

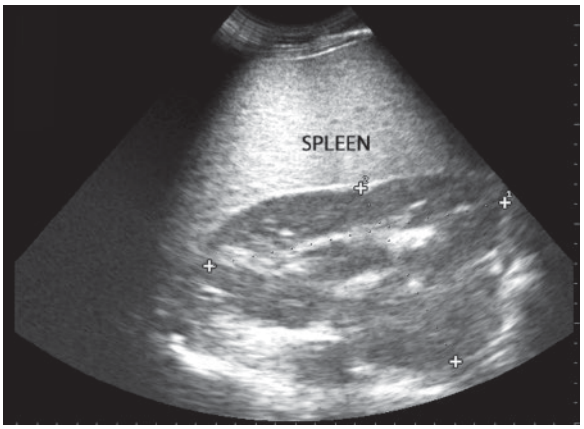


Figure 22.23 Normal left kidney. This image is of a normal left kidney in an 8-month-old Thoroughbred colt. Note the heart or triangular shape to the kidney. This view can be difficult at times to obtain in the adult horse due to the left kidney's depth and location. The sonogram was obtained from the left 17th ICS using a curvilinear probe operating at 3.5 MHz at a depth of 21 cm. The left side of this image is dorsal and the right side is ventral.

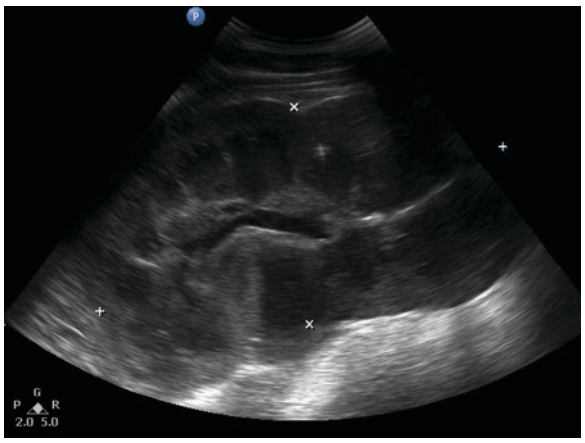


Figure 22.22 Normal right kidney. This image is of the right kidney obtained from a yearling Thoroughbred filly. The kidney was visualized at the 16th ICS, just ventral to the tuber coxae. The ureter can be noted adjacent to the renal pelvis. The diameter of the ureter is considered normal. Note the normal heterogenous echogenicity between the cortex and the medulla. This is a normal size and sonographic appearance for the right kidney. The sonogram was obtained from the right 16th ICS with a curvilinear probe operating at 5.0 MHz at a depth of 15 cm. The left side of this image is dorsal and the right side is ventral.

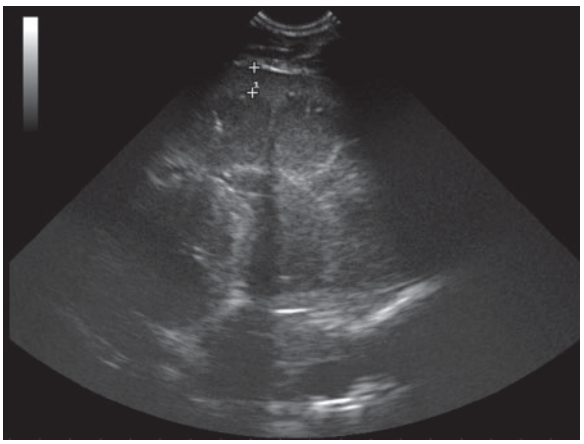


Figure 22.24 Normal right kidney. This image is of the right kidney in a yearling Thoroughbred colt. The cortex (cursors) of this horse's kidney is of normal thickness (< 1 cm). Note the normal hyperechogenic appearance of the cortex compared to the hypoechoic echogenicity of the medulla. This sonogram was obtained from the right lateral abdomen, caudal to the last rib with a curvilinear probe operating at 3.5 MHz at a depth of 14 cm.

Vet-ebooks.com

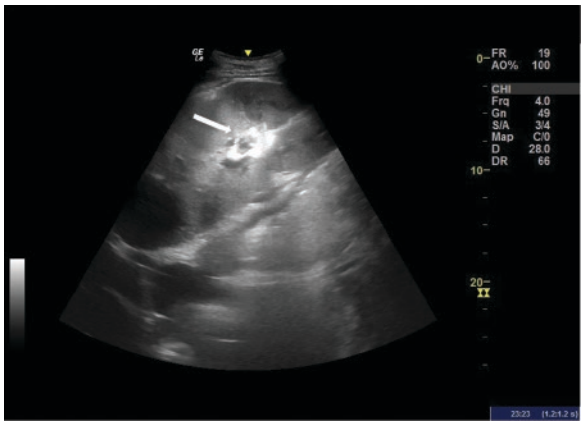


Figure 22.25 Nephritis. This image is from a mare that presented in endotoxemic shock secondary to a uterine tear; 48 hours after admission, the mare was azotemic with hematuria. *Klebsiella pneumoniae* and *E. coli* were isolated from the urine. This image of the right kidney is characteristic of a severe nephritis with no visible distinction between the cortex and medulla. This mare also has a renal cyst (arrow). This sonogram was obtained from the right lateral abdomen, caudal to the last rib with a curvilinear probe operating at 4.0 MHz at a depth of 28 cm. The left side of this image is dorsal and the right side is ventral.

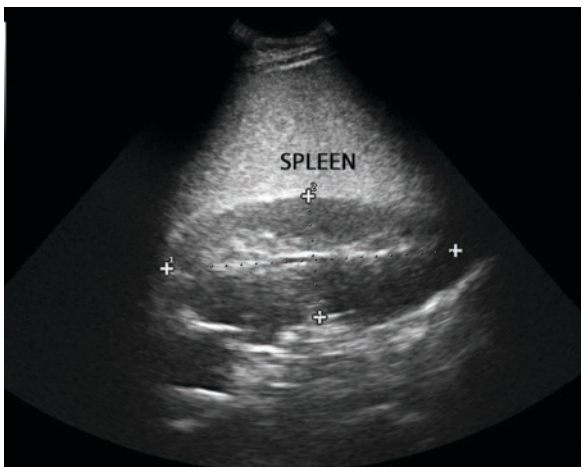


Figure 22.26 **Ne**phritis. This image is from a post partum, 19-year-old, Thoroughbred mare with nephritis. The mare had urinary incontinence immediately after foaling and, three weeks later, had intermittent episodes of fever. This image shows an enlarged left kidney with similar echogenecity between the cortex and medulla. Therefore, visible delineation is not seen between cortex and medulla. Ascending *E. coli* nephritis was diagnosed based on urine culture and sonographic appearance of the kidney. The mare was treated with sulfadiazine/trimethoprim (30 mg/kg PO q 12 hours) for two weeks and she recovered from her nephritis. Typically, horses with nephritis have a sonogram appearance of homogenous echogenecity of the entire kidney with subsequent loss of distinction between the cortex and the medulla. The sonogram was obtained at the paralumbar fossa using a curvilinear probe operating at 3.0 MHz at a depth of 24 cm. The left side of this image is dorsal and the right side is ventral.

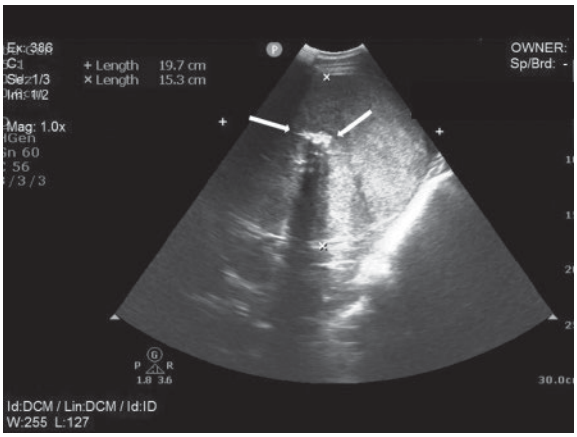


Figure 22.27 Nephritis and nephrolith. This image is from a pregnant Thoroughbred mare that presented with vague colic signs. This image shows a hyperchoic structure (arrows) that casts an acoustic shadow within the renal pelvis. The kidney is enlarged, measuring 19.7 by 15.3 cm. The image shows similar echogenicity between the cortex and medulla which is characteristic of nephritis. The cause of the colic was unknown and may have been associated with the nephritis. *Streptococcus zooepidemicus* was isolated from urine collected by an endoscopic microbiology aspiration catheter that was placed in the right ureter. The sonograph was obtained at the right paralumbar fossa using a curvilinear probe operating at 3.0 MHz at a depth of 30 cm. The left side of the image is dorsal and the right side is ventral.

10–11 cm in an adult horse. The right kidney usually measures 15 cm in width and 10–11 cm in length in the adult horse.

Bladder

Bladder (Figures 22.28, 22.29, 22.30, 22.31, 22.32, 22.33, 22.34, 22.35, 22.36, and 22.37) can be evaluated transrectally and sometimes transabdominally by scanning the caudal, ventral abdomen in the adult horse. The bladder in the neonate is easily visualized with transabdominal ultrasound. Bladder volume and wall thickness varies with degree of fill.

Uroperitoneum secondary to perforation of the urinary bladder is a common abnormality in the neonate. In the adult horse it is a less common medical diagnosis. Ultrasound imaging of uroperitoneum demonstrates variable volumes of hypoechoic to echogenic peritoneal effusion with free floating intestinal organs. The bladder walls may be collapsed and folded. Perforations in other areas of the urinary tract other than the bladder may occur. These include rupture of the urachus, ureter, or kidney. Confirmation of uroperitoneum requires analysis of an abdominocentesis sample.

Vet-ebooks.com

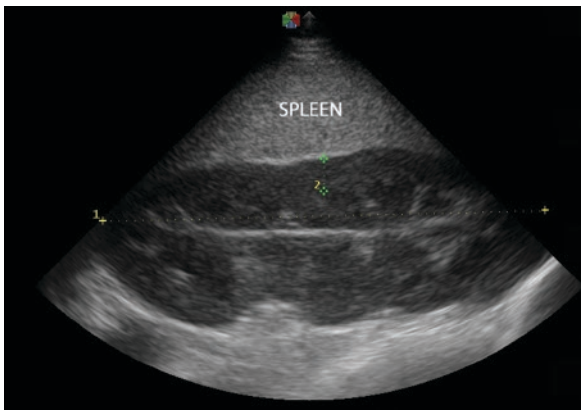


Figure 22.28 Leptosporosis. This image is the left kidney in a 3-month-old Thoroughbred colt with pyrexia and azotemia. The colt was diagnosed with leptospirosis based on positive PCR for leptosporosis in a urine sample. The kidney is markedly enlarged (18.7 cm by 13.7 cm) for a 3-month-old foal. The cortical thickness was abnormal at 1.36 cm (normal thickness is < 1 cm). The kidney still maintains the normal heterogenous echogenicity between the cortex and the medulla. The foal was treated with doxycycline (10 mg/kg PO q 12 hours for 14 days) and recovered. The sonogram was obtained at the paralumbar fossa using a curvilinear probe operating at 3.0 MHz at a depth of 16.5 cm. The left side of this image is dorsal and the right side is ventral.

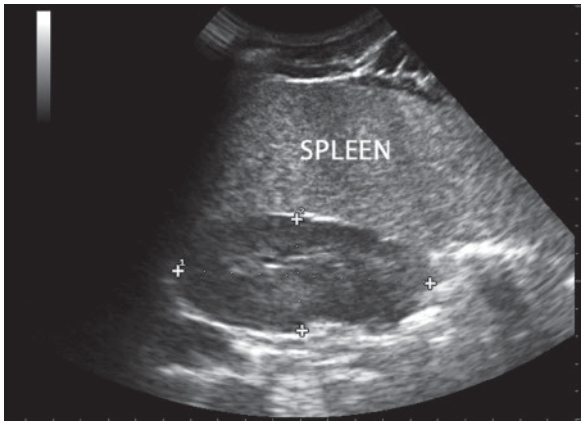


Figure 22.29 Renal dysplasia. This image is of the left kidney from a 4-month-old Thoroughbred filly with lethargy and azotemia. This filly had been treated on the farm with intravenous fluids because of azotemia, but the azotemia did not resolve. The left kidney had abnormal sonographic architecture. Note the small size of the kidney along with the homogenous echogenicity of the kidney. The cortex and the medulla cannot be distinquished from each other and assessing the corticomedullary junction is difficult. The renal pelvis could not be adequately visualized. This filly was diagnosed with bilateral renal dysplasia and was humanely euthanized. The sonogram was obtained ventral to the paralumbar fossa with a curvilinear probe operating at 3.5 MHz at a displayed depth of 15 cm. The left side of this image is dorsal and the right side is ventral.

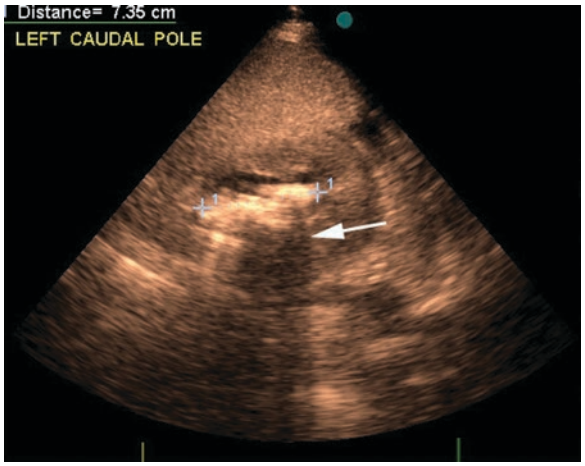


Figure 22.30 Nephrolith. This image is of the left kidney in a 10-year-old Thoroughbred mare with a history of intermittent fevers. In this image, the hyperechoic structure casting the acoustic shadow is most likely a nephrolith. The fevers were related to colitis and the nephrolith in the kidney was an incidental finding. Unlike humans, horses can often pass kidney stones with little evidence of pain. The sonogram was obtained ventral to the left paralumbar fossa using a curvilinear probe operating at 2.5 MHz at a depth of 28 cm. The left side of this image is dorsal and the right side is ventral.

Vet-ebooks.com

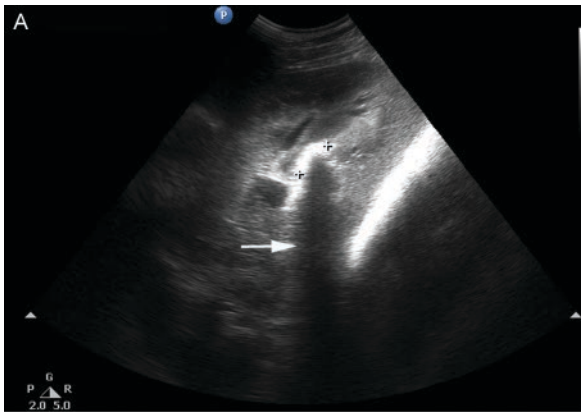


Figure 22.31 Nephrolith. This image is of the right kidney in a 12-year-old, pregnant, Thoroughbred mare with cystitis and nephrolith. (**A**) This image shows a hyperechoic structure (cursors) that cast an acoustic shadow (arrow) within the renal pelvis. **(B)** Ureteroscopy revealed a nephrolith and calcium carbonate sediment within the renal pelvis. The mare was treated with 1 oz oral of ammonia chloride divided between 3 feedings and potassium penicillin (20,000 IU IV q 6 hours) for severe *Streptococcus zooepidemicus* cystitis and nephritis. The sonogram was obtained from the right 16th ICS using a curvilinear probe operating at 5.0 MHz at a depth of 21 cm. The left side of this image is dorsal and the right side is ventral.

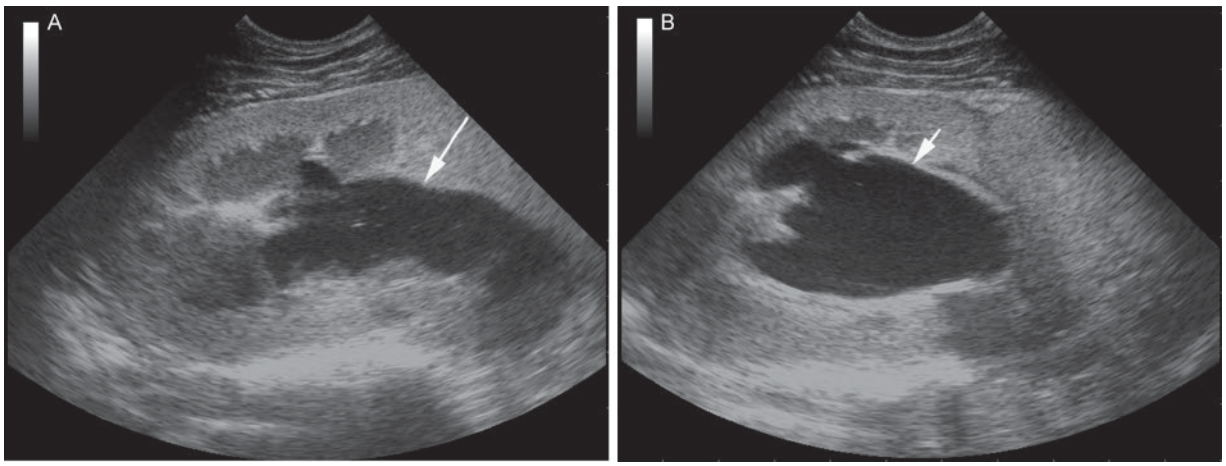
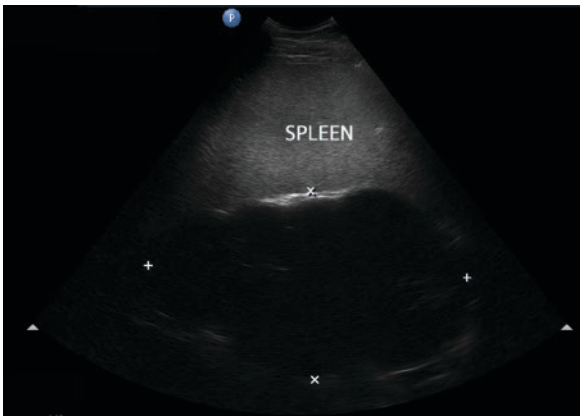


Figure 22.32 Hydroureteronephrosis. (**A** and **B**) These images are of the right kidney in an aged Thoroughbred mare with hydroureteronephrosis. Endoscopy was used to diagnose stricture of the right ureteral opening at the trigome of the bladder. Only a small amount of urine was observed exiting the strictured ureter into the bladder. This image shows a distended renal pelvis and proximal ureter (arrow) prior to opening the strictured ureter with a splint. The sonogram was characteristic of a hydroureteronephrosis. The sonogram was obtained from the right 16th ICS with a curvilinear probe operating at 7.5 MHz at a displayed depth of 8 cm. The left side of this image is dorsal and the right side is ventral.

Figure 22.33 Hydronephrosis. This image is the left kidney in an aged, pregnant, Thoroughbred mare with hydronephrosis. The mare was diagnosed with hydronephrosis secondary to a proximal ureteral stone. The sonogram was obtained from the left paralumbar fossa using a curvilinear probe operating at 5.0 MHz at a depth of 30 cm. The left side of this image is dorsal and the right side is ventral.



Vet-ebooks.com

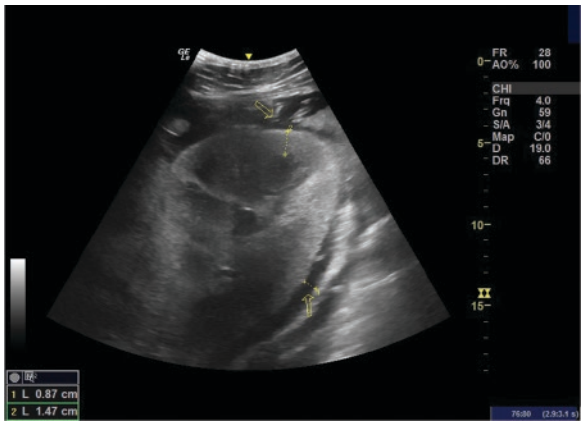


Figure 22.34 Perirenal edema and nephritis. This image is the right kidney from an 8-year-old Thoroughbred mare with *E. coli* nephritis and acute renal failure. This image demonstrates perirenal edema (arrows). The renal cortex is more echogenic than normal and thickened measuring 1.47 cm (normal cortex thickness in an adult horse should be < 1 cm). The sonogram was obtained in the right paralumbar fossa with a curvilinear probe operating at 4.0 MHz at a displayed depth of 19 cm. The left side of the image is dorsal and the right side is ventral.

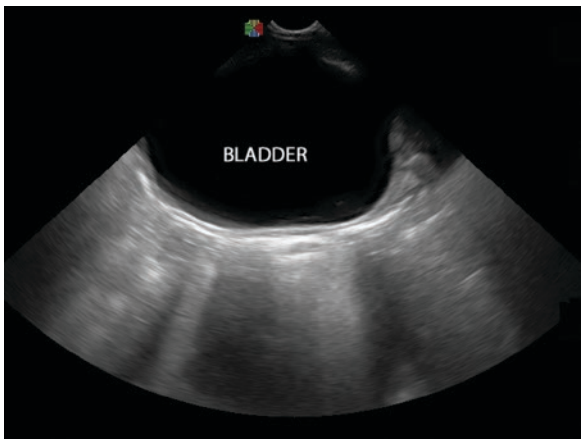


Figure 22.35 Normal bladder in foal. This image shows a normal bladder in a neonatal foal. When bladder diameter exceeds 8–9 cm and the walls of the bladder become thin and turgid, the foal may be at risk of rupturing the bladder and catheterization may be warranted. This image was obtained from the caudal aspect of ventral midline with a microconvex probe operating at 5.0 MHz at a depth of 12 cm.

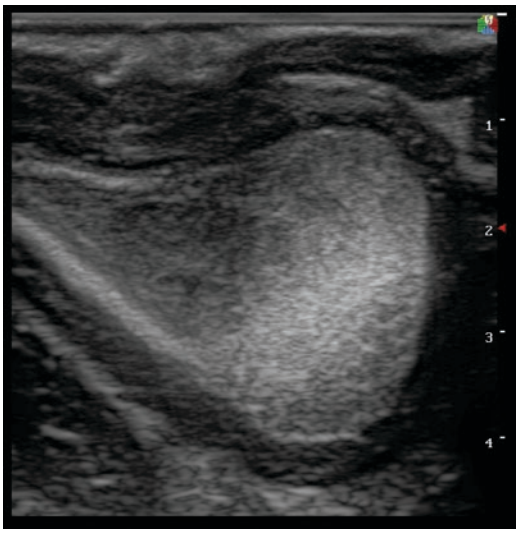


Figure 22.36 Normal bladder in adult. This image shows a normal bladder in an adult horse. Note the different echogenicities within the bladder caused by swirling urine. This sonogram was obtained transrectally with a linear probe operating at 7.5 MHz at a depth of 5 cm.



Figure 22.37 Normal bladder in adult. This image is a normal bladder with a small volume of urine in an adult horse. Wall thickness is designated by cursors. As the bladder fills with increasing volumes of urine, the bladder walls will stretch and become thin compared to the bladder wall in this image. This sonogram was obtained transrectally with a linear probe operating at 7.5 MHz at a depth of 5 cm.

Vet-ebooks.com

Peritoneal Cavity

Ultrasound is a non-invasive diagnostic tool that can be utilized to evaluate fluid in the peritoneal cavity (Figures 22.38, 22.39, 22.40, 22.41, 22.42, 22.43, 22.44, 22.45, 22.46, 22.47, 22.48, 22.49, and 22.50). Normal peritoneal fluid is anechoic and becomes more echogenic with increasing levels of cellularity. Peritonitis is a diffuse inflammatory process in the abdomen, usually of infectious etiology. Ultrasound helps to quantify the extent of the peritonitis and to characterize the peritoneal fluid. Fibrinous peritonitis can be described as septated because of the loculated appearance of the fluid. The abdomen and associated gastrointestinal and abdominal viscera should be assessed with ultrasound for a cause of peritonitis including abdominal abscess, tumor, or necrotic bowel.

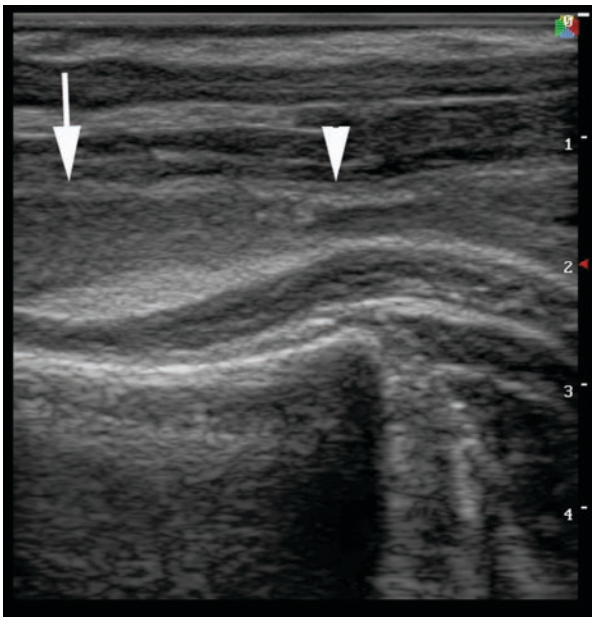


Figure 22.39 Dilated urethra. This image shows the urethra (arrowhead) in an adult horse. Note the area of urethral dilation (arrow). This sonogram was obtained transrectally with a linear probe operating at 7.5 Mhz at a depth of 5 cm.

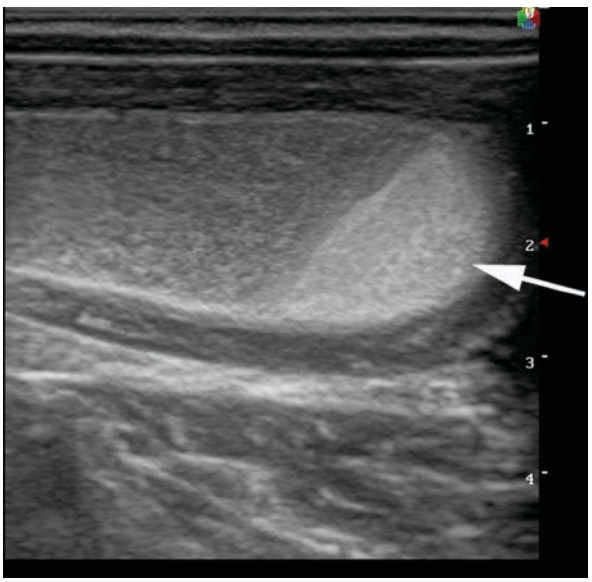


Figure 22.38 Normal bladder with sediment. In this normal bladder, hyperechoic sediment (arrow) is visualized in the bladder. Although some sediment is normal, it can lead to the formation of urinary calculi. This sonogram was obtained transrectally with a linear probe operating at 7.5 Mhz at a depth of 5 cm.

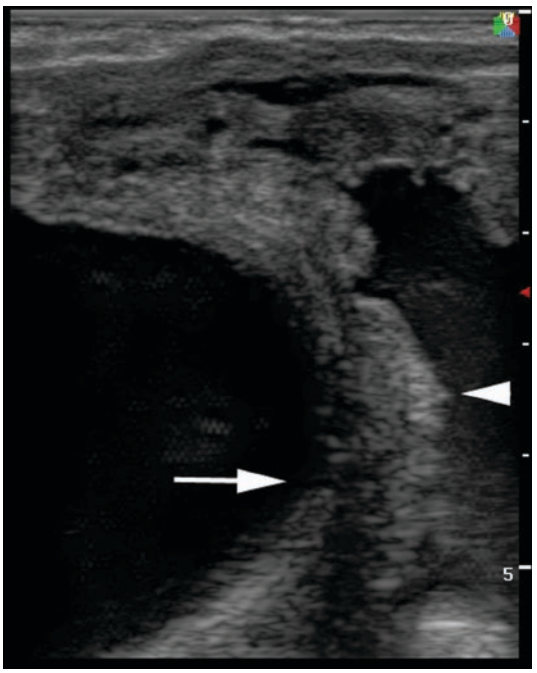


Figure 22.40 Bladder wall defect. This image shows a defect (arrow) in the wall of the bladder. A hyperechoic structure (arrowhead) has formed at the defect and is likely a hematoma. This sonogram was obtained transrectally with a linear probe operating at 7.5 Mhz at a depth of 5 cm.

Vet-ebooks.com



Figure 22.41 Uroperitoneum. This image shows urine (F) in the abdomen of a neonate from ruptured bladder. Note the hypoechoic fluid around the intestine. Uroperitoneum is confirmed by demonstrating a peritoneal fluid creatinine level twice that of the peripheral blood. Although commonly considered a neonatal complication, ruptured bladder can also occur in adults, particularly periparturient mares. This sonogram was obtained from the ventral abdomen with a microconvex probe operating at 5.0 Mhz at a depth of 11 cm.

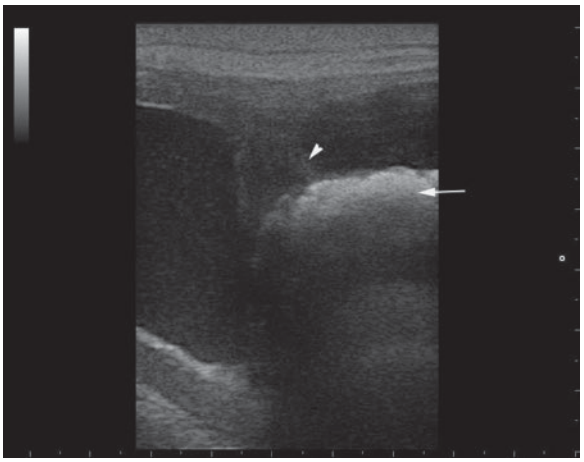


Figure 22.42 Urinary calculi. This image shows a urolith in the bladder of a 20-year-old Arabian stallion presenting for urinary incontinence of one month duration. The urolith is delineated by an echogenic surface (arrow) and acoustic shadow ventral to the stone surface. A bladder mucosal adhesion (arrowhead) to the surface of the urolith has occurred. This sonogram was obtained transrectally with a linear probe operating at 5.0 MHz at a depth of 7 cm. (*Source*: This image was obtained courtesy of Dr Fairfield Bain, University of Queensland Veterinary Medical Centre, Queensland, Australia).

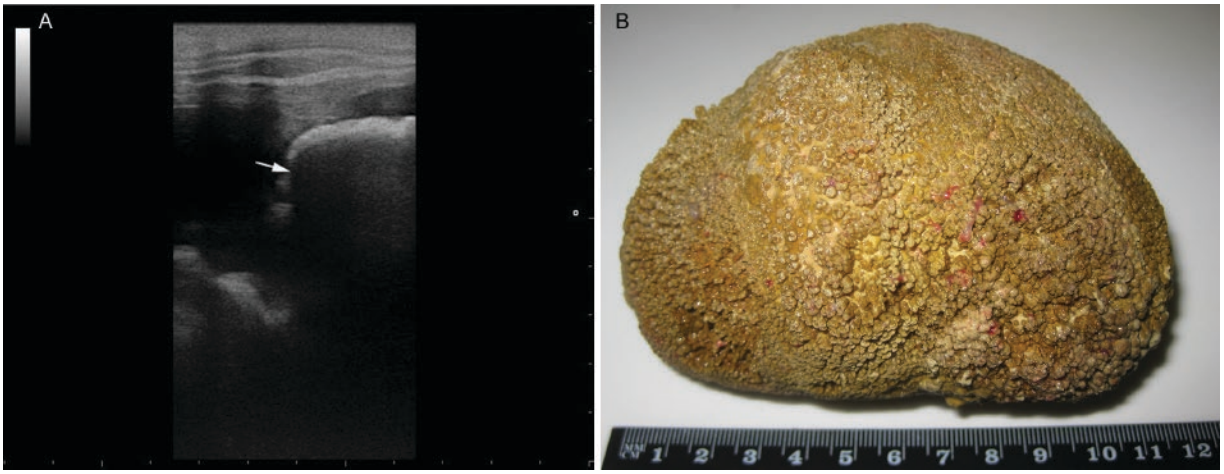


Figure 22.43 Urinary calculi. (**A**) This image shows another view of the urolith from the horse in Figure 22.36. This sonogram was obtained transrectally with a linear probe operating at 5.0 MHz at a depth of 7 cm. **(B)** This picture shows the urolith after surgical removal. (*Source*: These images are courtesy of Dr Fairfield Bain, University of Queensland Veterinary Medical Centre, Queensland, Australia).

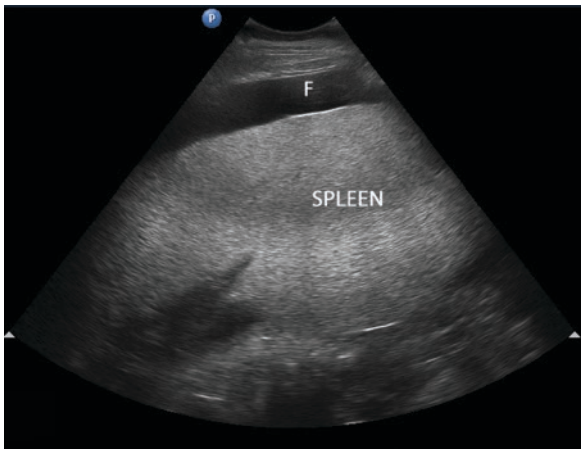


Figure 22.44 Figure 22.45 Bacterial peritonitis. This image shows peritonitis in a Thoroughbred mare. The free fluid in the abdomen has caused the spleen to move medial, away from the body wall. Bacterial peritonitis was confirmed by cytological analysis of an abdominocentesis sample. This sonogram was obtained from the left 14th ICS with a curvilinear probe operating at 5.0 MHz at a depth of 23 cm. The left side of the image is dorsal and the right side is ventral.

Vet-ebooks.com

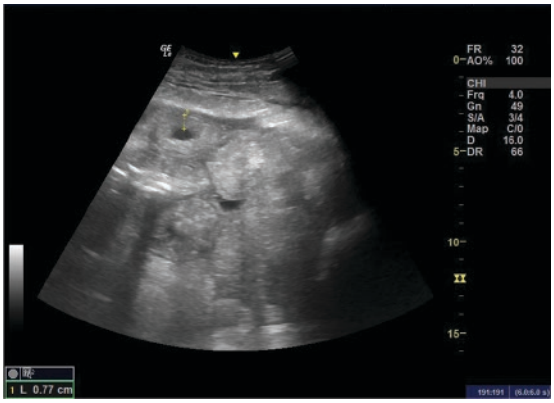


Figure 22.45 Bacterial peritonitis. This image is from a gelding diagnosed with *Actinobacillus equii* peritonitis. The walls of the jejunum (cursors) are thickened. This sonogram was obtained in the caudal abdomen adjacent to inguinal region with a curvilinear probe operating at 4.0 MHz at a depth of 16 cm.

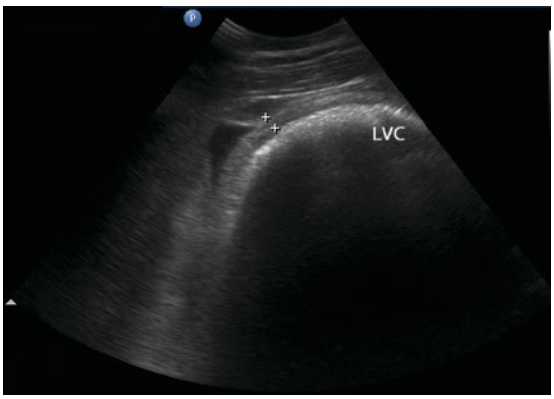


Figure 22.46 Intestinal wall in peritonitis case. This image is from the horse with bacterial peritonitis in Figure 22.38. The wall (cursors) of the left ventral colon (LVC) is thickened secondary to the intraabdominal inflammatory response. This sonogram was obtained from the left, ventral abdomen with a curvilinear probe operating at 5.0 MHz at a depth of 15 cm.

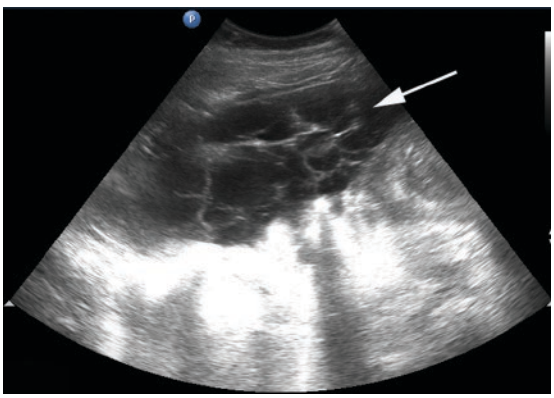


Figure 22.47 Fibrinous peritonitis. This image is from a 10-year-old Thoroughbred mare three days after she had a difficult foaling. The mare was pyrexic (102.5 F) and colicky. The mare was diagnosed with fibrinous peritonitis based on her ultrasound findings and after analysis of an abdominocentesis sample. Note the loculated appearance of the fibrin (arrow) characteristic of fibrinous peritonitis. The sonogram was obtained from the right, ventral abdomen with a curvilinear probe operating at 5.0 MHz at a depth of 16 cm.

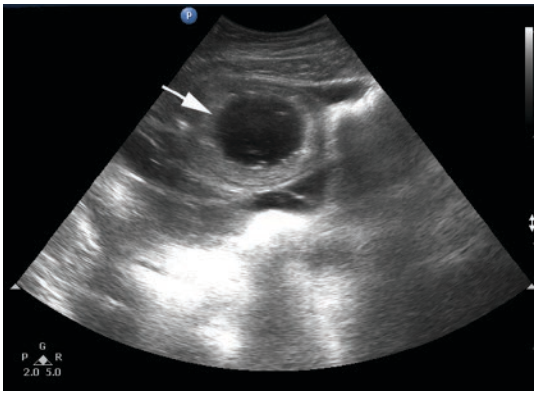


Figure 22.48 Thickened jejunum in peritonitis case. This image shows a loop of jejunum (arrow) with markedly thickened walls in a mare diagnosed with bacterial peritonitis. Note the hypoechoic areas of free peritoneal fluid adjacent to the loop of intestine. Small intestine with thickened walls is commonly diagnosed in cases of severe bacterial peritonitis. Normal wall thickness of small intestine is ≤ 3 mm. This sonogram was obtained from the right, ventral abdomen with a curvilinear probe operating at 5.0 MHz at a depth of 16 cm.

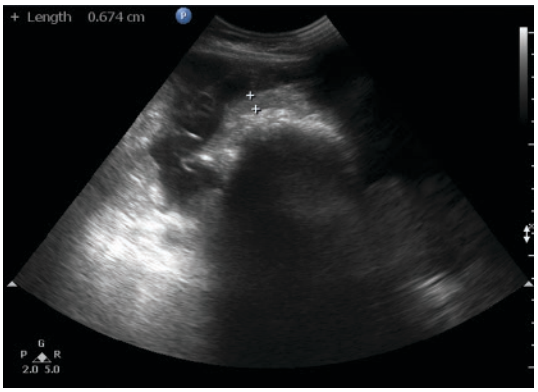


Figure 22.49 Thickened colon in fibrinous peritonitis case. This image is from a Warmblood colt presenting for fevers (102.3 °F) and inappetance. The sonogram revealed fibrinous peritonitis with a marked thickened wall (cursors) of the left ventral colon. *Actinobaccilus* spp. was isolated from the abdominal fluid. The sonogram was obtained from the left, ventral abdomen with a curvilinear probe operating at 5.0 MHz at a depth of 15 cm.

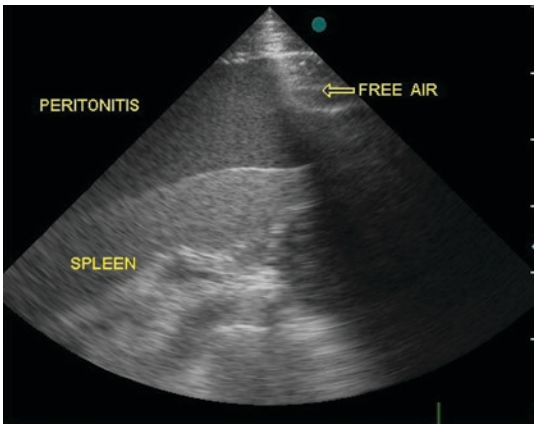


Figure 22.50 Gastric rupture. This image is from a horse diagnosed with gastric rupture. Hyperechoic abdominal fluid and pneumoperitoneum (arrow) are present. This sonogram was obtained from the left 13th ICS with a curvilinear probe operating at 3.5 MHz at a depth of 30 cm.

Vet-ebooks.com

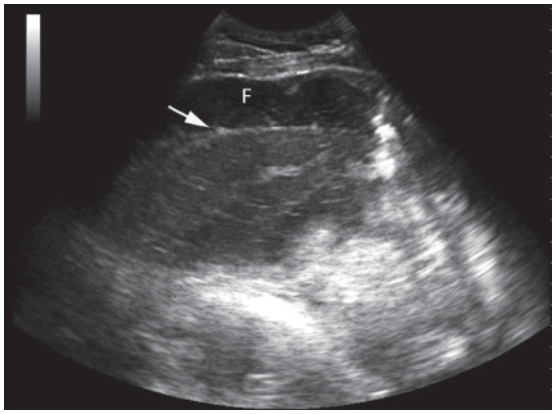


Figure 22.51 Peritoneal fibrin tags. This image is from a 3-month-old Thoroughbred filly presenting for ptylasim and fevers. Fibrin tags (arrow) are on the liver surface and excessive hyperechoic fluid (F) is in the abdomen. The sonogram was obtained from the right 10th ICS with a curvilinear probe operating at 3.5 MHz at a depth of 19 cm.

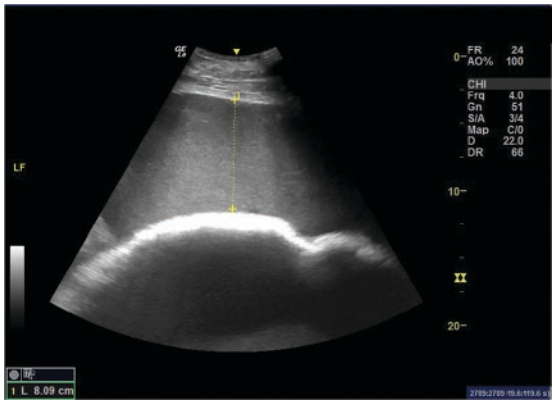


Figure 22.52 Bacterial peritonitis. This image shows peritonitis in a filly that was recovering from severe colitis. The free fluid (cursors) is hyperechoic. Bacterial peritonitis was confirmed by cytological analysis of peritoneal fluid obtained from abdominocentesis. The filly was euthanized and necropsy findings were perforated cecal ulcer. This sonogram was obtained from the ventral abdomen with a curvilinear probe operating at 4.0 MHz at a depth of 22 cm.

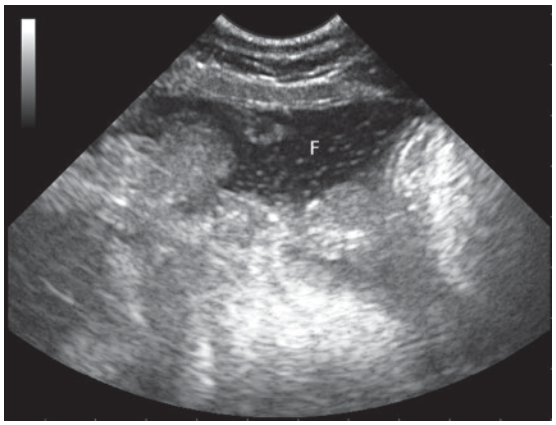


Figure 22.53 Exudative peritonitis. This image shows hyperechoic free fluid (F) in the abdomen. The white blood cell count of the fluid was 84,000 cells/µl. Note the hyperechoic foci in the fluid. This sonogram was obtained from the ventral abdomen with a curvilinear probe operating at 5.0 MHz at a depth of 8 cm.

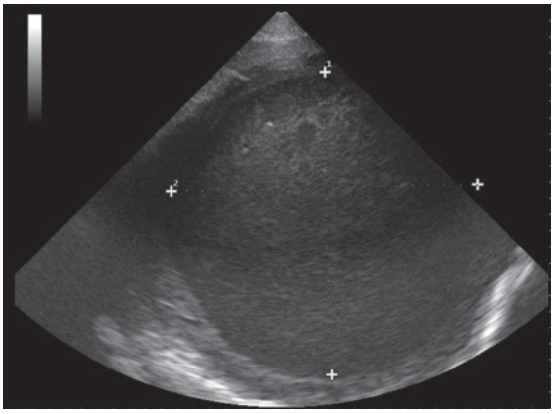


Figure 22.54 Internal abscess. This image is from the filly in Figure 22.45. A large, internal abscess (cursors) is visible in the messentery of the large colon. *Rhodococcus equi* infection was confirmed at necropsy. This sonogram was obtained from the left ventral abdomen with a curvilinear probe operating at 3.5 MHz at a depth of 25 cm.

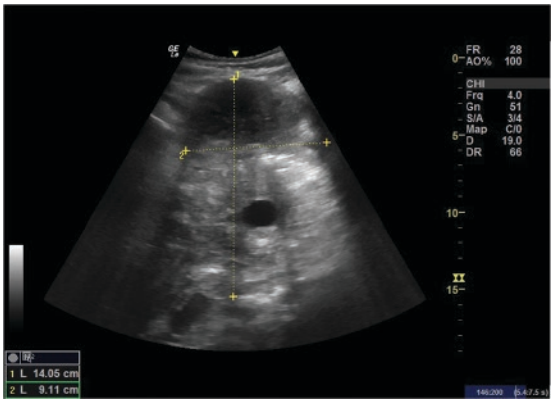


Figure 22.55 Internal abscess. This image is from a 3-month-old Thoroughbred filly with a large internal abscess (cursors) associated with the colonic mesentery. The filly had *Rhodococcus equi* isolated from a transtracheal wash sample. The filly had been treated for 3 months with Clarithromycin (7.5 mg/kg PO BID) and Rifampin (5 mg/kg IV BID). The sonogram was obtained from the left ventral abdomen with a curvilinear probe operating at 4.0 MHz at a depth of 19 cm.

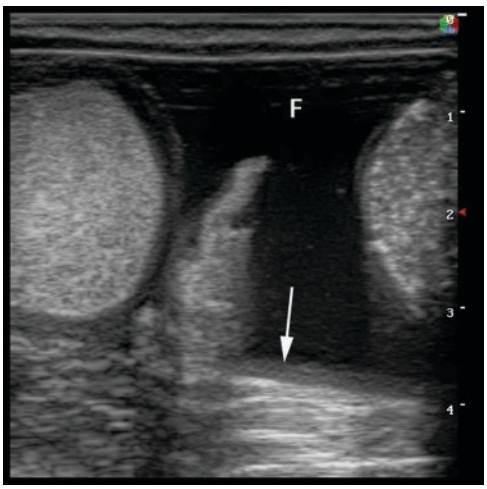


Figure 22.56 Transrectal view of peritonitis. This image shows free fluid (F) in the abdomen of an aged gelding. Note the fibrin tags on the peritoneal surface (arrow). This image was obtained transrectally with a linear probe operating at 5.0 MHz at a depth of 5 cm.

Vet-ebooks.com

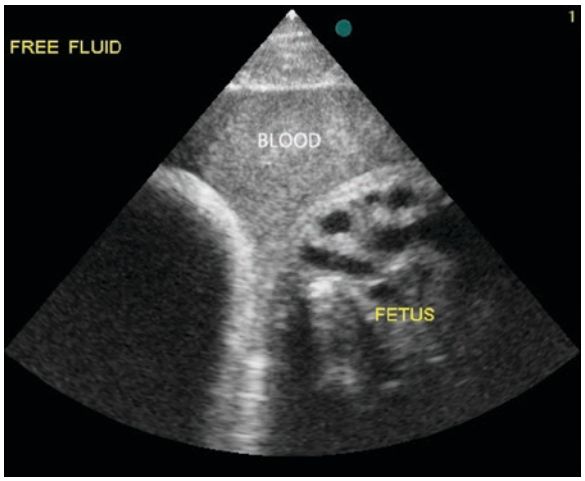


Figure 22.57 Hemoperitoneum. This image is from a mare at 10 months gestation exhibiting clinical signs of colic. She was diagnosed with periparturient hemorrhage based on ultrasound findings and analysis of an abdominocentesis sample. Hyperechoic, swirling free fluid (blood) is visualized in the abdomen adjacent to the fetus and colon. This sonogram was obtained from the ventral abdomen with a curvilinear probe operating at 22 cm.

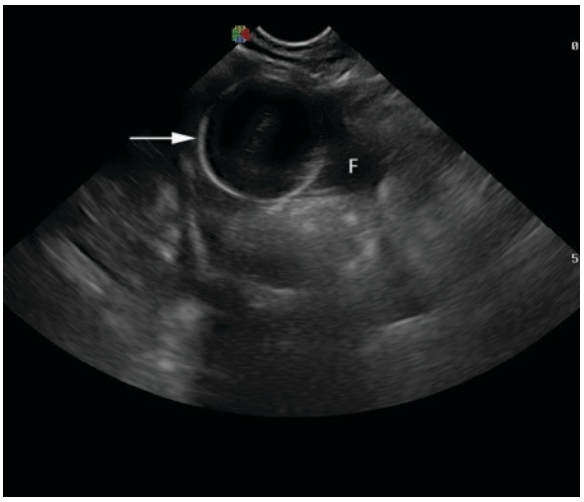


Figure 22.59 Abdominal drain. This image is from a neonatal foal with peritonitis. The thin walled, circular structure (arrow) is the inflated cuff of an abdominal drain. Note the free peritoneal fluid (F) adjacent to the cuff. This sonogram was obtained from the ventral abdomen with a microconvex prove operating at 5.0 MHz at a depth of 8 cm.

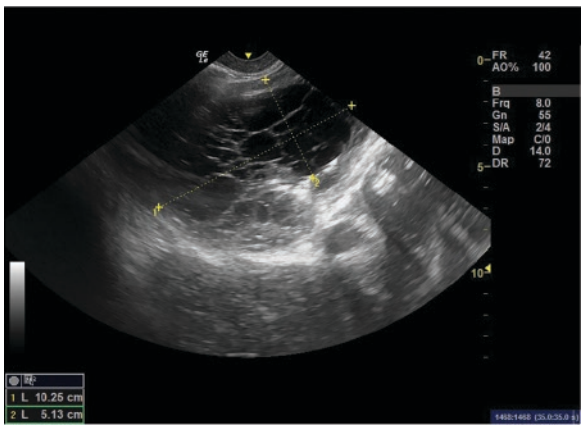


Figure 22.58 Internal abscess. The image is from a mare that had a cranial vaginal tear communicating with the peritoneal cavity after a fetotomy. This image shows an infected hematoma just cranial to the cervix and dorsal aspect of her uterus in the peritoneal cavity. The vaginal tear was sutured and the mare had an abdominal drain placed. The mare presented 3 weeks later with fevers. Examination per rectum revealed a soft tissue mass in the caudal abdomen. The mare was treated with 6 weeks of chloramphenicol (50 mg/kg PO TID) and recovered. This sonogram was obtained transrectally with a microconvex probe operating at 8.0 MHz at a depth of 14 cm.

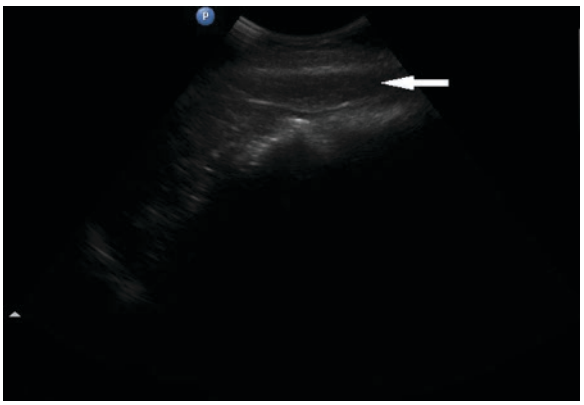


Figure 22.60 Intraabdominal fat. This image shows intraabdominal body fat in a gelding. The hyperechoic layer (arrow) is fat and should not be confused with free peritoneal fluid. This image was obtained from the ventral abdomen with a curvilinear probe operating at 3.5 MHz at a depth of 15 cm.

Vet-ebooks.com

Recommended Reading

Arnold, C.E. and Chaffin, M.K. (2010). Abdominal abscesses in adult horses: 61 cases (1993–2008). *Journal of the American Veterinary Medical Association* 241(12): 1659–1665.

Budras, K. and Sack, W.O.(2003). *Anatomy of the Horse: An Illustrated Text*, 4th edn. Hanover: Schlutersche GmbH and Co.

Draper, A.C., Bowen, I.M., and Hallowell, G.D. (2012). Reference ranges and reliability of transabdominal ultrasonographic renal dimensions in thoroughbred horses. *Veterinary Radiology and Ultrasound* 53(3): 336–341.

Feuss, S.M. and Chaffin, M.K. (2011). Sonographic characteristics of intraabdominal abscessation and lymphadenopathy attributable to *Rhodococcus equi* infections in foals. *Veterniary Radiology and Ultrasound* 52(4): 462–465.

Ness, S.L. and Bain, F.T. (2012). Ultrasonographic visualization of colonic mesenteric vasculature as an indicator of large colon right dorsal displacement or 180° volvulus (or both) in horses. *Canadian Veterinary Journal* 53(4): 378–382.

Vet-ebooks.com

23

Ultrasonography of the Gastrointestinal Tract

*Rana Bozorgmanesh**

**The author acknowledges the prior contribution of Fairfield T. Bain*
Hagyard Equine Medical Institute, Lexington, KY, USA

Ultrasonography can be performed to evaluate a significant portion of the gastrointestinal tract from the caudal pharynx and esophagus in the neck, to the stomach, and large and small intestines within the abdominal cavity. Depending on location and depth, probes of multiple frequencies may be utilized to image the specific structure of interest. Higher frequency (7.5 mHz or greater) probes can be used to image superficial structures, such as the esophagus, or to obtain the highest detail of intestinal surfaces (if reasonably superficial). Evaluation of the abdominal cavity as it pertains to the gastrointestinal tract includes evaluation of the stomach, small intestine, and large intestine. Typically, the author performs the trans-abdominal ultrasound examination in a cranial-to-caudal fashion on each side. However, in situations such as a violently painful colic case or a colicky horse with a high heart rate, the most pertinent structures are often evaluated first, such as the stomach to identify severe distention and immediate need for nasogastric intubation. The more systematic examination starts cranially at the third intercostal space, just caudal to the elbow, and progresses caudally scanning dorsal to ventral in each intercostal space from the diaphragm margin ventrad. Cranially on the left side, the liver is visible adjacent to the spleen. Moving caudally, the stomach is visualized adjacent to the spleen. The stomach is evaluated for contents and size. The normal stomach in the adult horse usually extends over four to five intercostal spaces. Normal small intestine has minimal visible structure. It may be visible with variable motility just ventromedial to the spleen on the left side. The colon is visible ventromedial to the spleen on the left side. On the right side, the large colon is visible in the cranial abdomen. Progressing caudally, the liver is visible ventral to the margin of the lung fields over most of the mid-abdomen. Horses in their mid-teens and older may have atrophy of the liver and it may not be readily visualized with ultrasound. The duodenum is visible ventromedial to the liver from the twelfth intercostal space to just ventral to the right kidney. The right dorsal colon is ventromedial. Ventral-medial to the duodenum is the right dorsal colon. The cecum will be visible in the right paralumbar fossa and extends ventrally along the costal arch and can be distinguished by its lateral vasculature.

On occasion, trans-rectal ultrasonographic examination may be useful in further characterizing abdominal masses, rectal masses, or intestinal surfaces.

The gastrointestinal anatomy within the abdominal cavity can be dynamic, especially in colic cases where abnormal intestinal motility and distention can be involved. As such, the author emphasizes the importance of serial ultrasonographic evaluations over time to determine if changes have occurred such as position of the colon or amount of gastric or small intestinal distension.

Esophagus

The esophagus (Figure 23.1) can be imaged from just caudal to the pharynx in the upper neck on the left side along most of its course to the distal neck. It is located just dorsal to the trachea and ventral to the

Atlas of Equine Ultrasonography, Second Edition. Edited by Jessica A. Kidd, Kristina G. Lu and Michele L. Frazer.
© 2022 John Wiley & Sons Ltd. Published 2022 by John Wiley & Sons Ltd.
Companion Website: www.wiley.com/go/kidd/atlas

Vet-ebooks.com

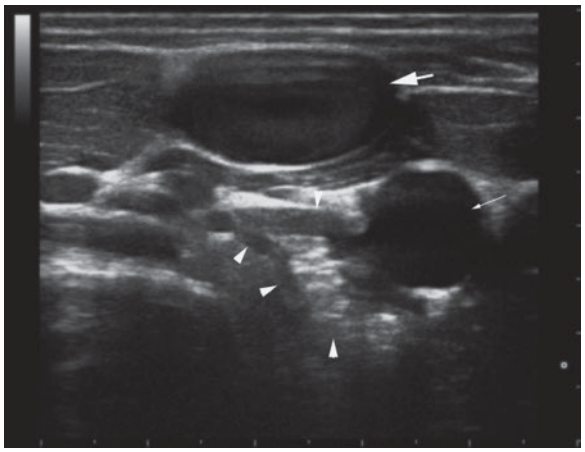


Figure 23.1 Normal esophagus. The normal esophagus is demonstrated by the arrowheads. The trachea is in the bottom left corner of the image. The jugular vein is noted by the large arrow and the carotid artery by the small arrow. This sonogram was obtained from the jugular groove, middle third of the neck, using a linear probe operating at 12 MHz at a depth of 5 cm.

jugular vein and carotid artery. The muscularis appears hypoechoic, whereas the lumen appears echogenic.

Stomach

The normal stomach (Figures 23.2 and 23.3) is imaged adjacent to the spleen on the left side of the abdomen.

Gastric impaction should be considered in animals with a prolonged clinical history of inappetence, mild colic signs, and sonographic evidence of solid gastric luminal content visible over more than five intercostal spaces. These cases can also present with more acute colic signs and when passage of a nasogastric tube is attempted, resistance is met at the cardia or just beyond. Gastric distention (Figures 23.4, 23.5, 23.6, and 23.7) from solid ingesta, fluid, or gas is a concern when the stomach extends beyond approximately five rib spaces.

Small Intestine

The duodenum (Figures 23.8 and 23.9) can be imaged along its course on the right side. It is first seen cranially as it appears between the left liver lobe and the right dorsal colon, and then progresses caudal to a point ventral to the right kidney.

Duodenal distension (Figure 23.10) can occur with distal small intestinal obstruction, post-operative ileus, or duodenal stricture and obstruction, as well

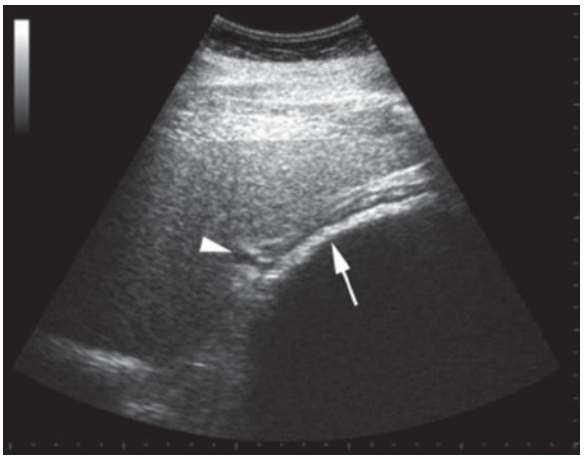


Figure 23.2 Spleen–stomach relationship. This image demonstrates the normal appearance of the stomach adjacent to the spleen. The normal, feed containing stomach should appear as an echogenic curved line (arrow) against the medial surface of the spleen. The splenic portal vein (arrowhead) is seen along the medial aspect of the spleen. This sonogram was obtained from the left 10th ICS with a curvilinear probe operating at 3.5 MHz at a depth of 18 cm.

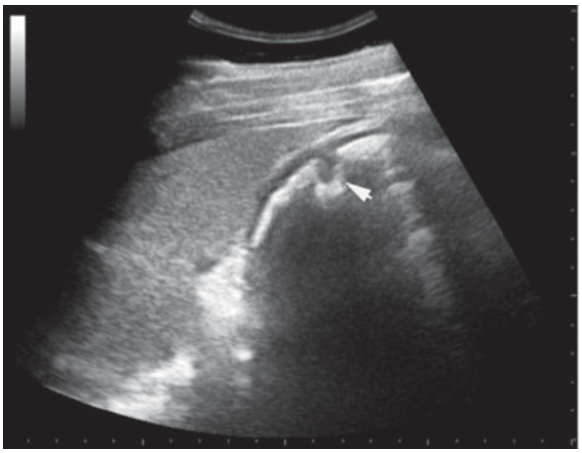


Figure 23.3 Gastric fold. This image shows the normal appearance of stomach adjacent to the spleen in a horse fasted for gastroscopy. A gastric fold (arrowhead) is visible on the surface of the stomach. This sonogram was obtained from the left 11th ICS using a curvilinear probe operating at 3.5 MHz at a depth of 18 cm.

as varying degrees of thickening and distension with enteritis or proximal enteritis syndrome.

Duodenitis (Figure 23.11) and duodenal stricture (Figure 23.12) can produce gastric outflow obstruction in foals. The thickened segment of duodenum can often be imaged along its course on the right side of the abdomen. Ultrasound can be useful in making the initial diagnosis (which is typically then confirmed gastroscopically), as well as monitoring medical therapy and aid in evaluation of post-operative patients that had gastrojejunostomy to relieve the gastric outflow obstruction.

Vet-ebooks.com

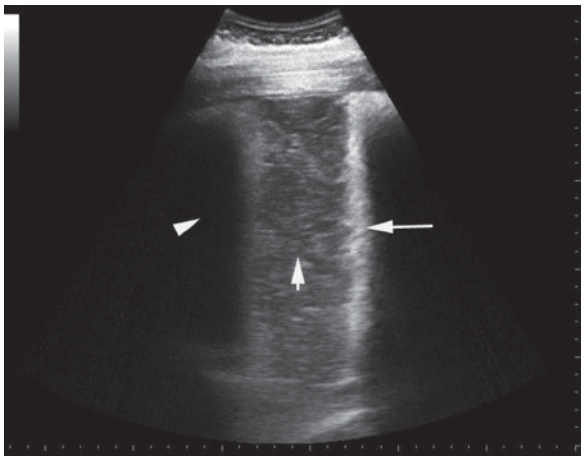


Figure 23.4 Gastric distention. This image demonstrates a fluid filled, distended stomach (short arrow) in an adult horse. Solid material ventrally (arrowhead) creates an acoustic shadow. A gas-fluid interface (long arrow) is present dorsally. This sonogram was obtained from the left 14th ICS with a curvilinear probe operating at 3.5 MHz at a depth of 23 cm.

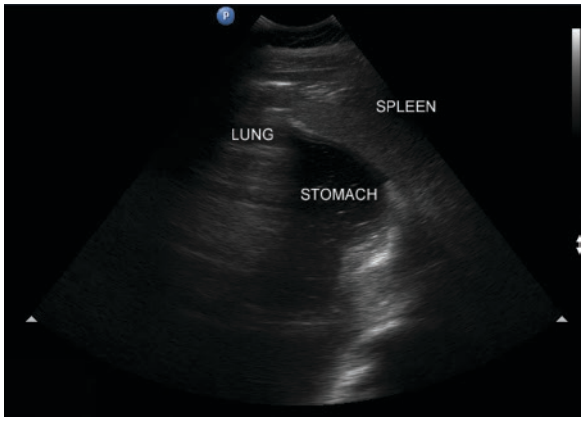


Figure 23.5 Gastric distention. Fluid content is visualized in the stomach. The cranial aspect of the stomach is obscurred by the caudodorsal tip of the lung. This sonogram was obtained from the left 14th ICS using a curvilinear probe operating a depth of 20 cm.

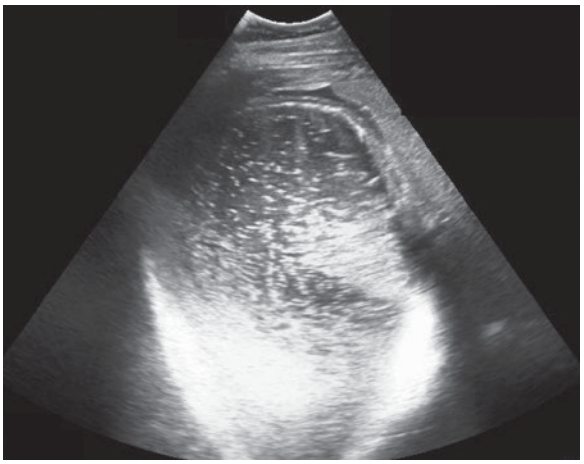


Figure 23.6 Gastric distension. Fluid content is visualized in the stomach. The caudal aspect of the stomach is adjacent to the cranial edge of the spleen. This sonogram was obtained from the left 14th ICS using a curvilinear probe operating a depth of 28 cm.

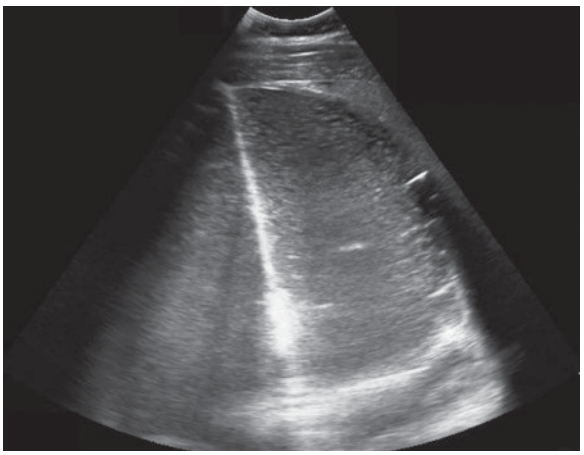


Figure 23.7 Gastric distension with stomach tube in place. Fluid content is visualized in the stomach. An acoustic shadow from the indwelling stomach tube is present at the caudal margin of the stomach. This sonogram was obtained from the left 14th ICS using a curvilinear probe operating a depth of 28 cm.

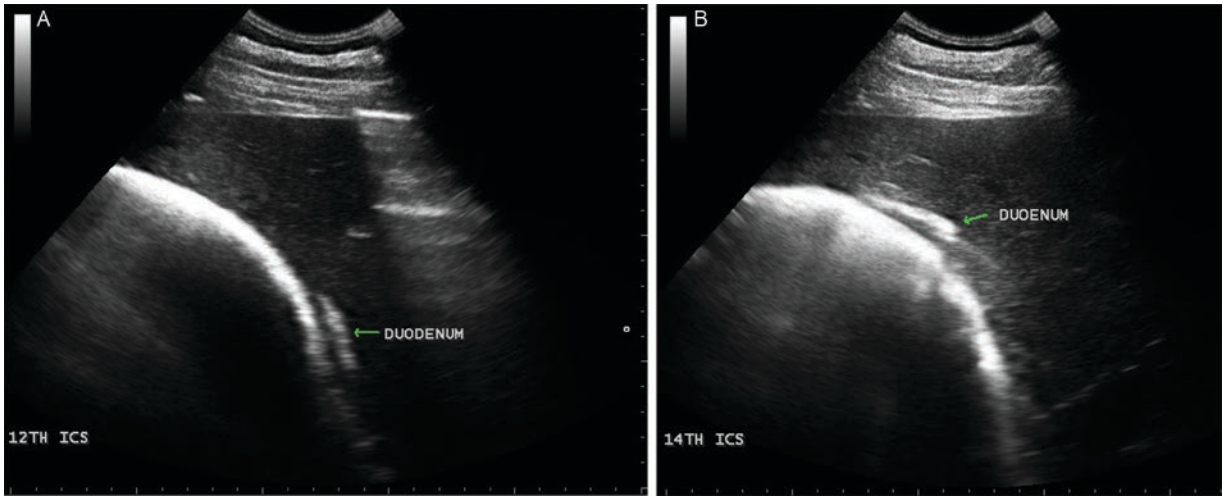


Figure 23.8 Normal duodenum, 12th and 14th ICS. (A) and (B) These images show normal duodenum. The cranial aspect of the duodenum is visible between the left liver lobe and the right dorsal colon. The echogenic material is luminal content within the duodenum. These sonograms were obtained from the right ((A) 12th and (B) 14th ICS using a curvilinear probe operating at 6.6 MHz at a depth of 18cm.

Vet-ebooks.com

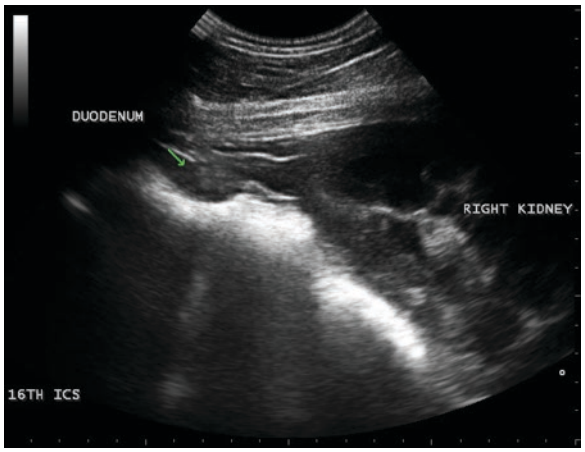


Figure 23.9 Normal duodenum, 16th ICS. This image shows normal duodenum ventral to the right kidney and ventromedial to the right dorsal colon. This sonogram was obtained from the right 16th ICS with a curvilinear probe operating at 6.6 MHz at a depth of 15 cm.

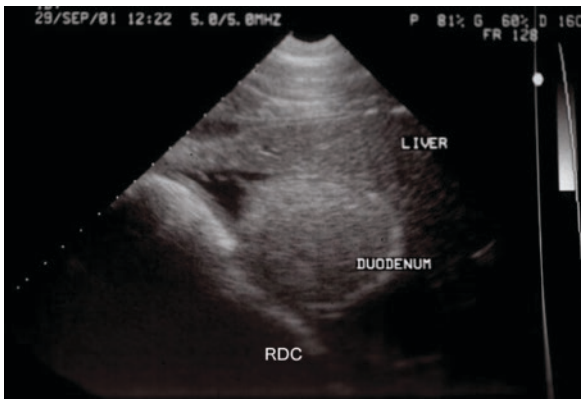


Figure 23.10 Duodenal distension associated with post operative ileus. The duodenum is imaged between the liver and right dorsal colon (RDC) secondary to post-operative ileus. A small pocket of hypoechoic, free peritoneal fluid is seen adjacent to the duodenum. This sonogram was obtained from the right 14th ICS with a curvilinear probe operating at 5.0 MHz at a depth of 15 cm.

Normal jejunum (Figure 23.13) usually has a non-descript appearance on ultrasound. It is usually visible just ventral and medial to the spleen in the caudal left abdomen around the level of the costal arch.

Small intestinal distention (Figures 23.14, 23.15, 23.16, 23.17, 23.18, 23.19, 23.20, 23.21, 23.22, 23.23, 23.24, 23.25, and 23.26) can indicate strangulating or non-strangulating obstruction, enteritis, or altered motility such as occurs with post-operative ileus. Clinical history, severity of clinical signs, and occasionally other diagnostic aids such as abdominocentesis are required to differentiate between these types of lesions prior to confirmation by exploratory surgery.

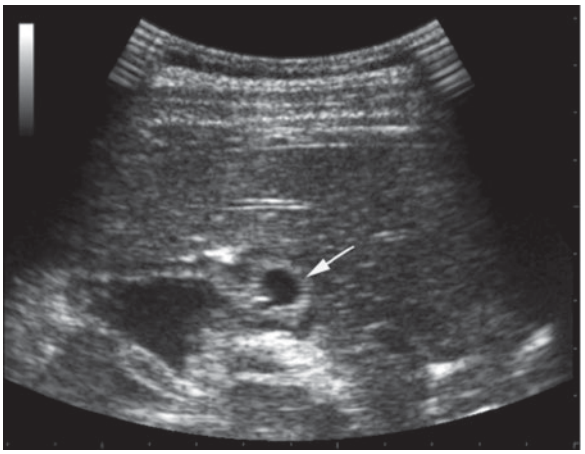


Figure 23.11 Duodenitis. This image demonstrates thick-walled duodenum (arrow) with echogenic luminal material in a 3-year-old Quarter Horse mare that presented with colic and gastric reflux. *Salmonella* spp. was isolated from the gastric fluid suggesting it may have been an etiology for the duodenitis. Normal duodenal wall thickness in an adult horse is ≤ 3 mm This sonogram was obtained from the right 12th ICS with a curvilinear probe operating at 5.0 MHz at a depth of 8cm.

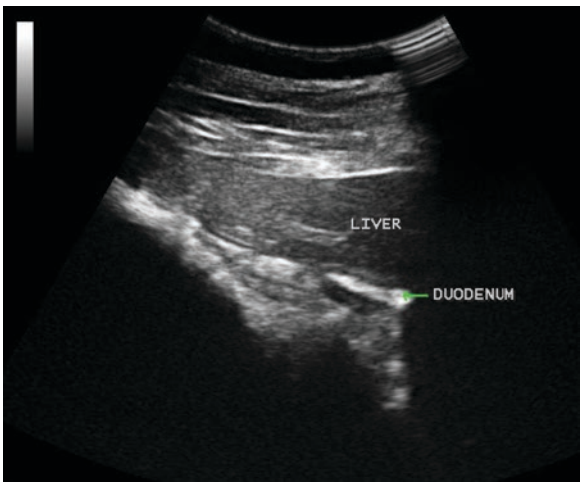


Figure 23.12 Duodenal stricture. This image demonstrates duodenal thickening and stricture producing clinical signs consistent with gastric outflow obstruction in a 6-month-old Hanovarian filly. Duodenal stricture is more common in foals than adult horses and may be secondary to ulceration of the duodenum and pyloric region. Ulceration can be multifactorial in cause, but may be associated with previous rotavirus infection. This sonogram was obtained from the right 14th ICS with a curvilinear probe operating at 6.6 MHz at a depth of 12 cm.

The observation of markedly distended, poorly motile segments of small intestine with ventral sedimentation of particulate material (Figures 23.15, 23.16, 23.17, 23.18, 23.19, 23.20, and 23.21) is most often suggestive of a strangulating lesion of the small intestine such as small intestinal volvulus, entrapment in a mesenteric rent, or epiploic foramen entrapment. However, this pattern of ultrasonographic change in the small

Vet-ebooks.com

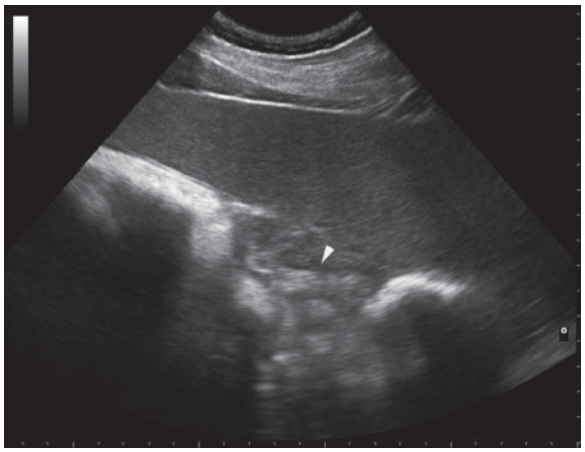


Figure 23.13 Normal small intestine. Normal small intestine (arrowhead) is located just medial to the spleen in the caudal left abdomen. It has a non-descript appearance. Wall thickness should not exceed 3 mm. This sonogram was obtained from the caudal left abdomen with a curvilinear probe operating at 6.6 MHz at a depth of 15 cm.

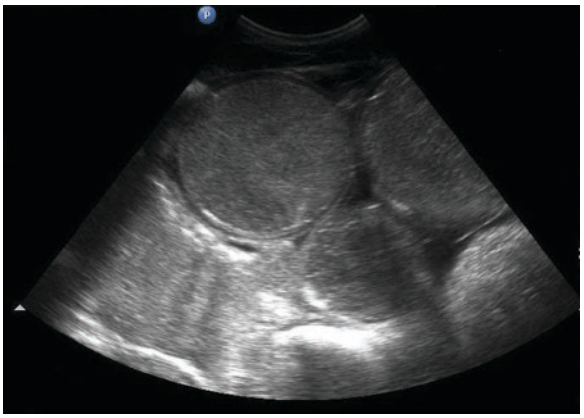


Figure 23.15 Small intestinal volvulus in a yearling. Multiple, fluid-distended, non-motile segments of small intestine are visualized in a yearling presenting for severe abdominal pain of several hours duration. Eight feet of non-viable small intestine were resected at surgery. This image was obtained from the ventral abdomen with a curvilinear probe operating at 3.5 Mhz at a depth of 15 cm.

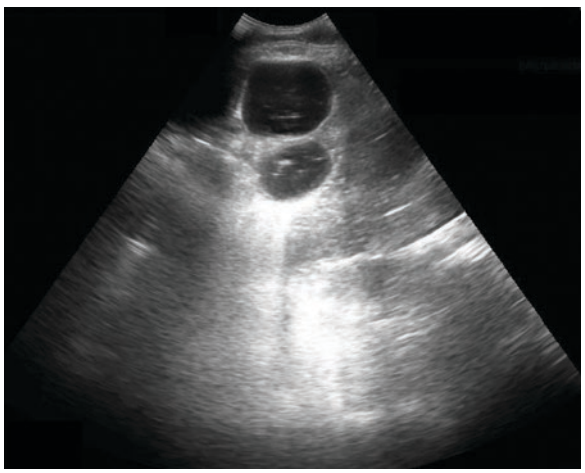


Figure 23.14 Post-operative ileus in a post-foaling mare with peritonitis following repair of a uterine tear. There are multiple dilated, non-motile loops of small intestine. The mare refluxed for several days until motility eventually normalized. This sonogram was obtained from the ventral abdomen using a curvilinear probe operating a depth of 29 cm.

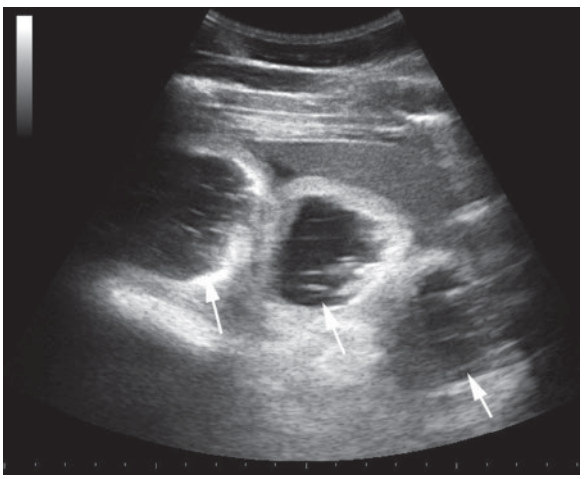


Figure 23.16 Mesenteric defect. Fluid-distended, poorly motile, thick walled small intestine (arrows) in the left ventral abdomen is imaged in a yearling colt with acute severe colic. The walls of the small intestine measured greater than the normal 3 mm. Serosanginous peritoneal fluid was observed on abdominocentesis. Multiple segments of thick-walled, red and purple small intestine associated with a mesenteric defect were found at surgery. This sonogram was obtained from the left abdomen with a curvilinear probe operating at 3.5 MHz at a depth of 15 cm.

Vet-ebooks.com

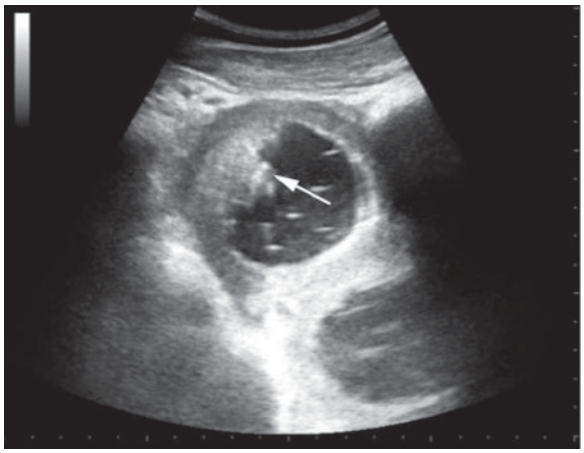


Figure 23.17 Small intestinal strangulation. This image from the patient in Figure 23.15 shows small intestinal distention from a messenteric defect. Particulate matter (arrow) has settled to the ventral-most aspect of the small intestine. This ventral sedementation indicates the chronicity of the small intestinal damage. Small intestinal strangulation was confirmed at surgery. This sonogram was obtained from the left abdomen with a curvilinear probe operating at 3.5 MHz at a depth of 15 cm.

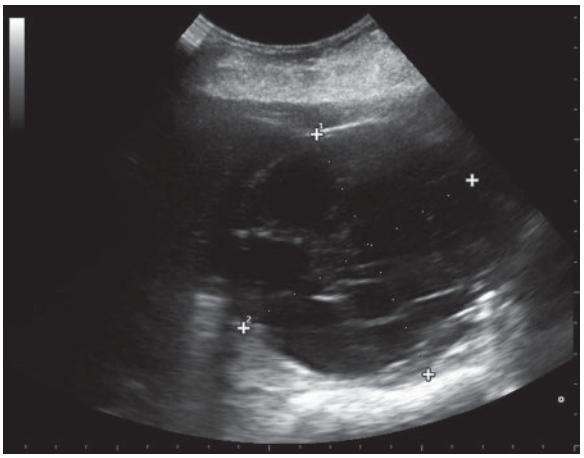


Figure 23.19 Lipoma. This 14 cm, discrete, hypoechoic mass (cursors) was located in the mid-ventral abdomen. Associated sonographic imaging showed dilated, poorly motile small intestine. Postmortem examination confirmed this mass to be a lipoma strangulating a segment of small intestine. Imaging the lipoma in cases of small intestinal strangulation is rare. The finding of fluid distended, non-motile and/or thickened small intestine (see Figures 23.19 and 23.20) in an aged animal is the most consistent ultrasound finding with strangulating lipomas. This sonogram was obtained from the ventral abdomen with a curvilinear probe operating at 6.6 MHz at a depth of 14 cm.



Figure 23.18 Small intestinal volvulus with ventral sedimentation. This image demonstrates fluid distended small intestine with ventral sedimentation of particulate material associated with small intestinal volvulus. Particulate matter has settled ventrally by gravity due to ileus and chronicity of the lesion. Ventral is to the left in this image. This image was obtained from the left abdomen with a curvilinear probe operating at 3.5 MHz at a depth of 15 cm.

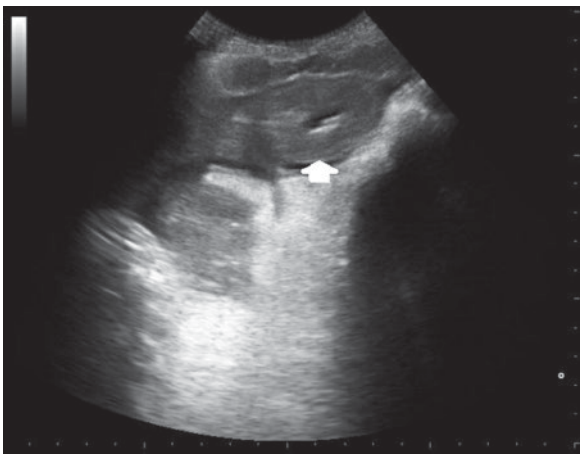


Figure 23.20 Strangulating lipoma. This image demonstrates a thickened segment of small intestine (arrow) consistent with vascular compromise from strangulating lipoma (see Figure 23.18). This sonogram was obtained from ventral abdomen with a curvilinear probe operating at 5.0 MHz at a depth of 15 cm.

Vet-ebooks.com

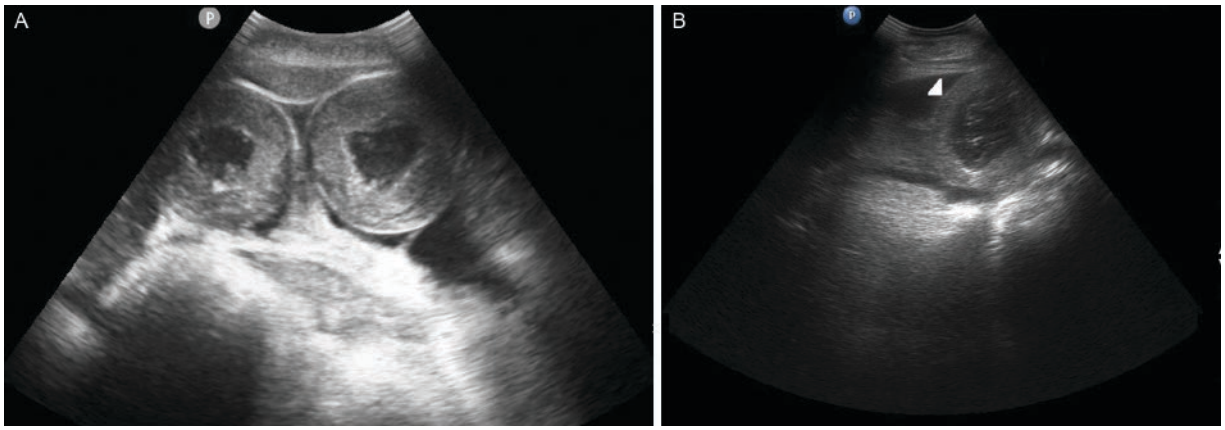


Figure 23.21 Lipoma with strangulated small intestine. (A) and (B) These images demonstrate strangulated, non-viable small intestine secondary to strangulation around the stalk of a lipoma. Note the thickened and echogenic intestinal walls (arrowheads) consistent with vascular engorgement and stasis and the indistinct serosal surfaces. These images were obtained from ventral abdomen, left of midline with a curvilinear probe operating at (A) 5.0 MHz at a depth of 12 cm and (B) 3.5 MHz at a depth of 20 cm.

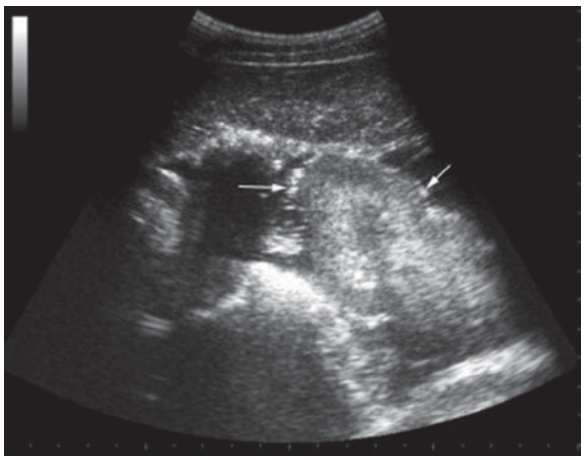


Figure 23.22 Peritonitis with fecal contamination. This image demonstrates peritonitis associated with gastric rupture following small intestinal strangulation around the stalk of a lipoma. Numerous echogenic gas bubbles (arrows) are seen adherent to the intestinal serosa and parietal peritoneal surface. Note the thickened, indistinct intestinal wall of the compromised small intestine. This sonogram was obtained from the ventral abdomen with a curvilinear probe operating at 3.5 Mhz at a depth of 15 cm.

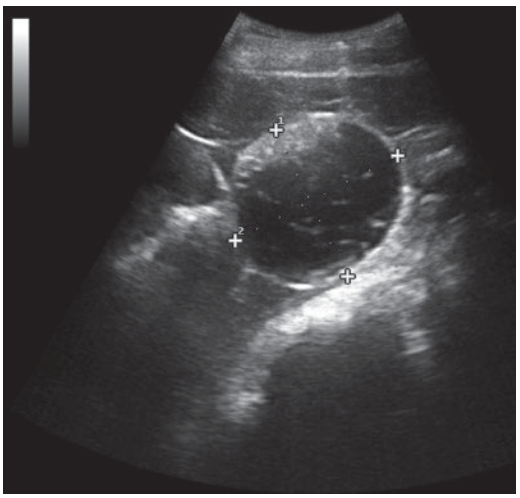


Figure 23.23 Non-strangulating entrapment of small intestine. This image demonstrates marked fluid distension of small intestine (cursors) with poor motility and ventral sedimentation of particulate material in the left ventral abdomen of an adult Quarter Horse. Non-strangulating entrapment of the small intestine associated with large colon impaction was confirmed at surgery. This sonogram was obtained from the left inguinal region with a curvilinear probe operating at 2.5 MHz at a depth of 19 cm.

intestine can also be observed with non-strangulating, obstructive lesions such as ileal impactions (Figure 23.24) and non-strangulating entrapment of the small intestine (Figure 23.23).

Ultrasound imaging can be useful in identifying enteritis (Figures 23.25, 23.26, and 23.27) as confirmation of clinical signs (colic, fever) and supportive laboratory data (leucopenia, with or without hypoproteinemia). In both foals and adult horses, ultrasound may help identify enteritis by imaging thickened, variably echogenic and variably motile walls of the small intestine that often have some luminal fluid present. Small intestinal loops may or may no be distended.

Lawsonia intracellularis infection in weanling to yearling aged animals typically causes thick-walled, edematous small intestine consistent with proliferative enteritis (Figures 23.28 and 23.29). Edematous thickening of the large intestine may also be present as a result of marked hypoalbuminemia (Figure 23.29).

Jejunojejunal intussusception (Figure 23.30) images as multiple layers of intestine creating a "bull's eye" appearance.

Vet-ebooks.com

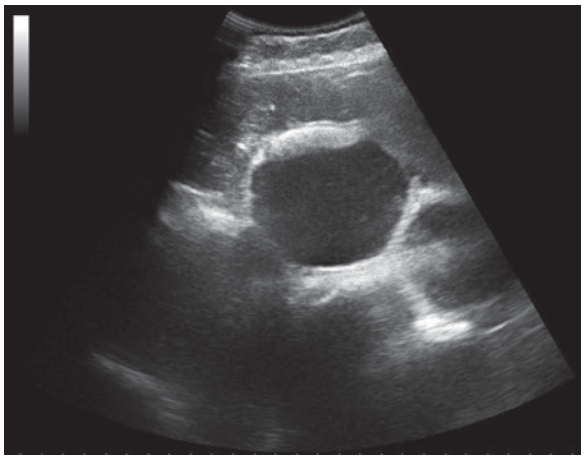


Figure 23.24 Ileal impaction. This image demonstrates poorly motile, fluid-distended small intestine with a small amount of ventral sedimentation of particulate material in the caudal-ventral right abdomen. Ileal impaction was confirmed at surgery. This image was obtained from the ventral abdomen, right of midline, with a curvilinear probe operating at 3.5 MHz at a depth of 21 cm.

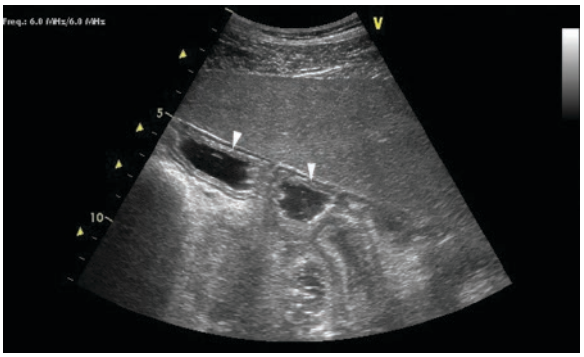


Figure 23.25 Enteritis in an adult horse. This image demonstrates thickened small intestine (arrowheads) associated with enteritis in an adult horse. Multiple echogenic foci within the small intestinal wall are consistent with inflammation. This sonogram was obtained from the left abdomen with a curvilinear probe operating at 6.0 MHz at a depth of 15 cm.

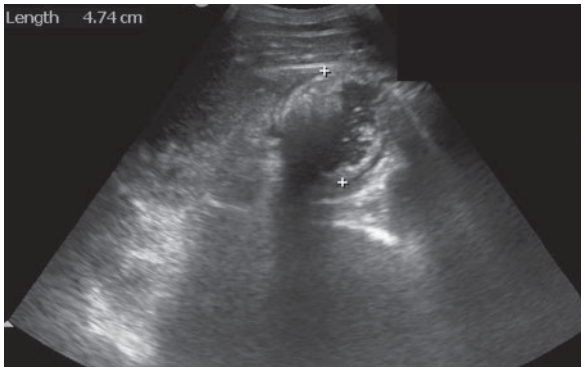


Figure 23.26 Anterior enteritis. This image demonstrates a loop of distended small intestine with slightly thickened wall in a horse diagnosed with anterior enteritis based on characteristic clinicopathologic findings, as well as fevers and persistent reflux over several days. This sonogram was obtained from the ventral abdomen using a curvilinear probe operating at 3.5 MHz at a depth of 17 cm.

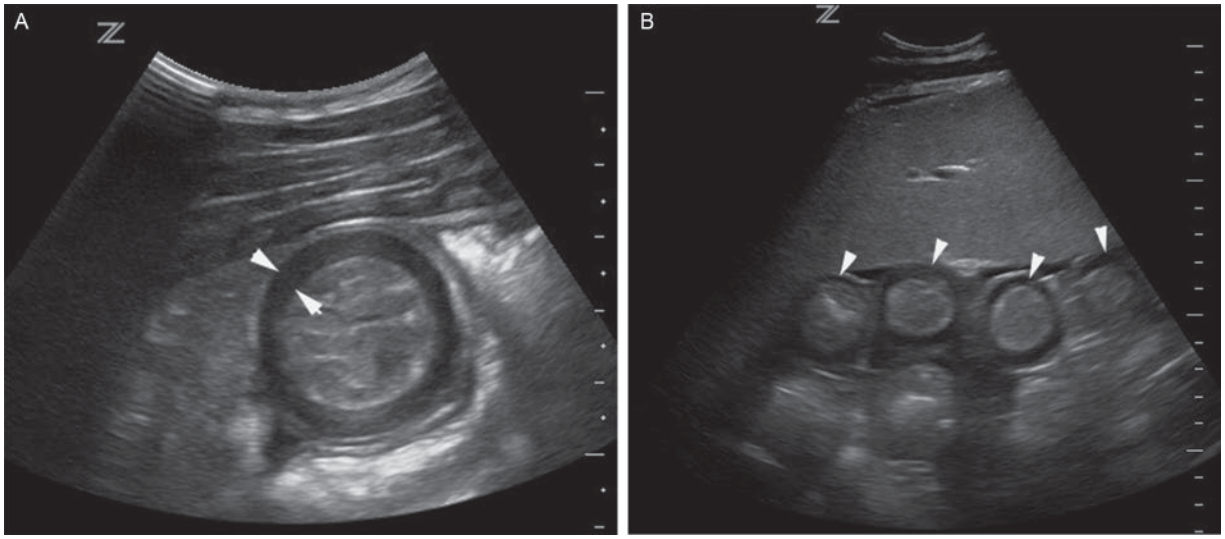


Figure 23.27 Small intestinal muscular hypertrophy. (A) This image demonstrates small intestinal muscular hypertrophy in a 7-year-old Thoroughbred stallion with clinical signs of recurrent colic secondary to non-strangulating obstruction of the small intestine. The arrows indicate the thickened, hypoechoic tunica muscularis layer of the small intestinal wall. (B) This image is another view of the same segment of small intestine showing a thick, hypoechoic layer representing hypertrophy of the tunica muscularis of the small intestine. These sonograms were obtained from left abdomen with a curvilinear probe operating at 3.5 MHz at a depth of 17 cm. (*Source*: Images courtesy of Dr Sally Ness, Cornell University.)

Vet-ebooks.com

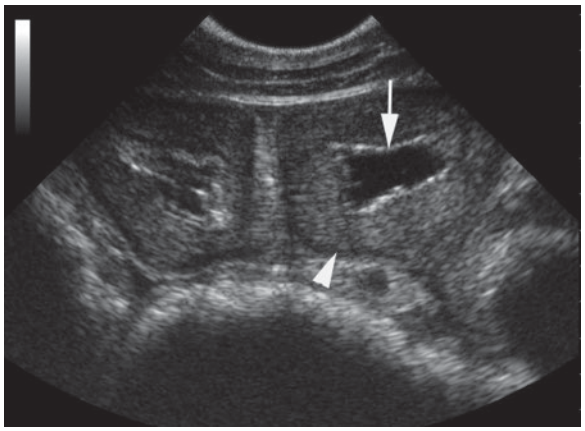


Figure 23.28 *Lawsonia intracellularis* infection. This image demonstrates marked thickening of the small intestinal wall in an 8-month-old Hanovarian colt with peripheral edema, hypoproteinemia, and hypoalbuminemia. The small intestinal changes (thickening of walls) were from proliferative enteropathy secondary to *L. intracellularis* infection. The arrowhead indicates the serosa and the arrow indicates the mucosal surface of the small intestinal wall. This sonogram was obtained from the ventral abdomen with a microconvex probe operating at 8.0 Mhz at a depth of 12 cm.

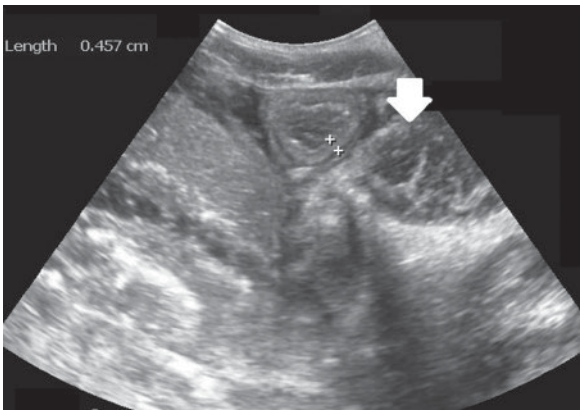


Figure 23.29 *Lawsonia intracellularis* infection with hypoproteinemia-associated colon wall edema. This image demonstrates thickening of the small intestinal wall in a 7-month-old Thoroughbred colt with *L. intracellularis* infection. The arrow indicates severe hypoproteinemia associated edema of the colon wall (adjacent to a thickened loop of small intestine). This sonogram was obtained from the ventral abdomen using a curvilinear probe operating a depth of 13 cm.

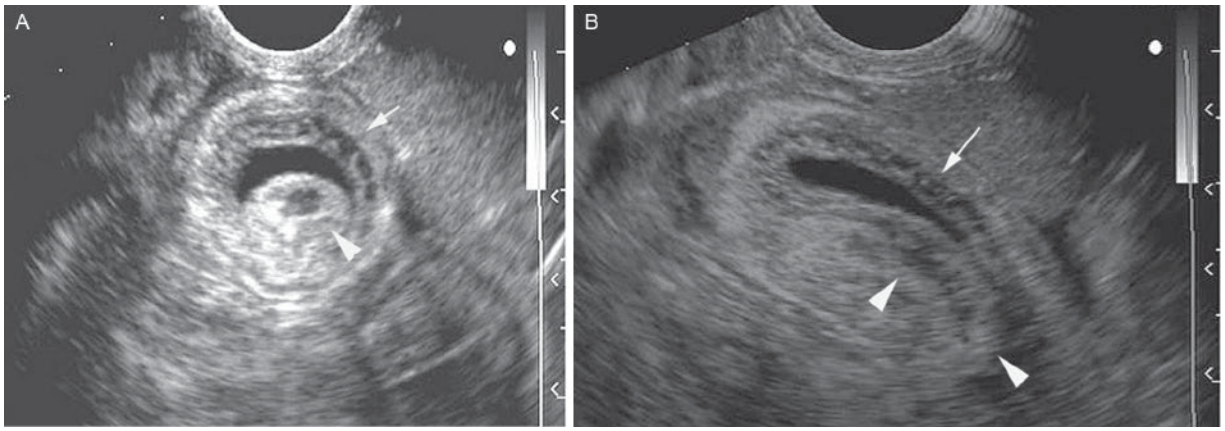


Figure 23.30 Jejunojejunal intussusception. These images demonstrate (A) cross-sectional and (B) longitudinal views of a jujunojejunal intussusception. A loop of jejunum telescoped into another loop of jejunum to create the classic "bull's eye" appearance. Note the layers consisting of the outer intussuscepien (arrows) and inner intussusceptum (arrowheads) portions. The lesion can be transient and serial ultrasonographic examination may be needed to identify the lesion. These sonograms were obtained from the ventral abdomen with a microconvex probe operating at 5.0 MHz at a depth of 6 cm.

Large Intestine

The large colon and cecum normally occupy much of the ventral aspect of the abdominal cavity and are identified ultrasonographically by their location and surface appearance. The right dorsal colon (Figure 23.31) is usually identified by its position just ventral and medial to the right liver lobe. The ventral colon (Figure 23.32) is ventral-most in the abdomen and can sometimes be identified by the sacculations along its surface.

Gas produces a series of horizontal parallel reverberations on ultrasound (Figure 23.33). Gas-distended colon will produce this appearance and can be found with displacements and other obstruction of the large intestine such as impaction or enterolith.

Nephrosplenic entrapment (Figures 23.34 and 23.35) can be demonstrated ultrasonographically by the presence of colon within the nephrosplenic space as seen through the upper left abdominal wall and paralumbar fossa. The colon should obscure visualization of the left kidney and will occasionally displace

Vet-ebooks.com

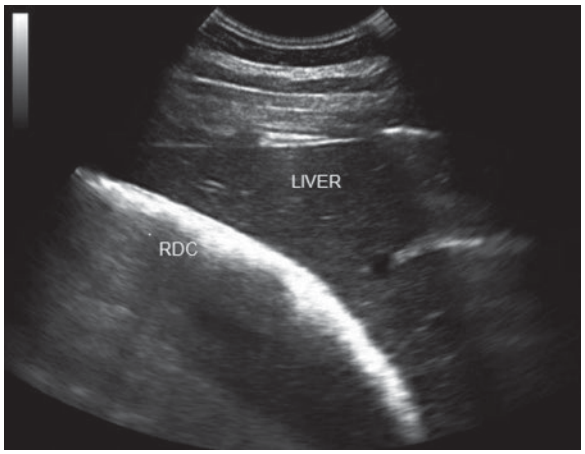


Figure 23.31 Normal right dorsal colon. The curved, echogenic surface of the luminal material of the right dorsal colon (RDC) is imaged from the right side and is located ventral and medial to the right liver lobe. Ventral is to the left in this image. This sonogram was obtained from the right ventral abdomen with a curvilinear probe operating at 6.6 MHz at a depth of 15 cm.

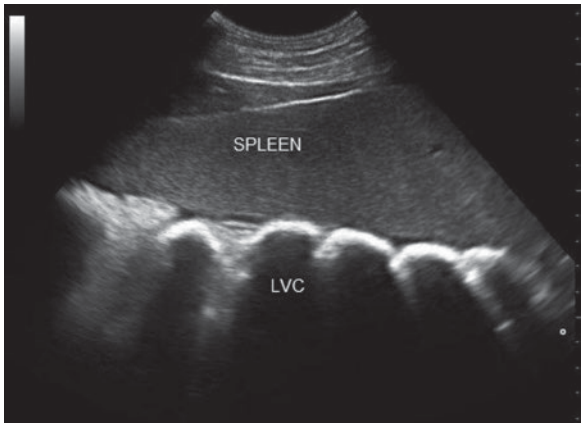


Figure 23.32 Normal left ventral colon. The multiple, short, curved echogenic structures represent the sacculations of the left ventral colon (LVC) as seen on the left side just ventral and medial to the ventral aspect of the spleen. This sonogram was obtained from the left ventral abdomen with a curvilinear probe operating at 6.6 Mhz at a depth of 17 cm.

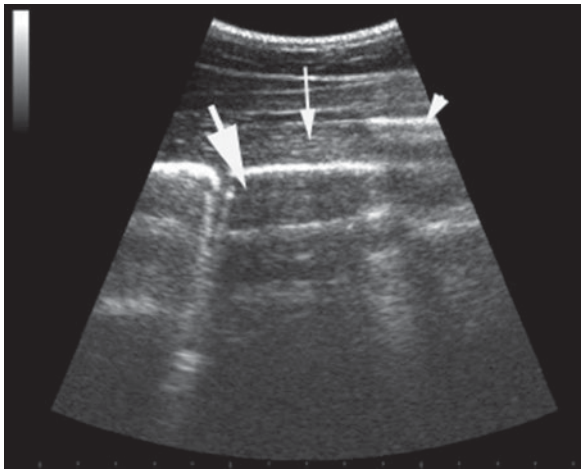


Figure 23.33 Colonic tympany. Colonic tympany images as horizontal reverberations from the colon wall. Causes for gas distended colon include large intestinal displacement, impactions, or enteroliths. Gas-distended colon (thick arrow), the diaphragm (thin arrow), and the air-filled lung (arrowhead) are visible. This sonogram was obtained from left ventral abdomen with a curvilinear probe operating at 5.0 MHz at a depth of 12 cm.



Figure 23.34 Nephrosplenic entrapment. Nephrosplenic entrapment, or left dorsal displacement of the colon, images as colon in the nephrosplenic space. The colon obscures the ultrasound view of the left kidney and may force the spleen medial off the body wall. Pockets of free peritoneal fluid may be present around the spleen and colon. This sonogram was obtained from the left, lateral abdomen with a curvilinear probe operating at 3.5 MHz at a depth of 18 cm.

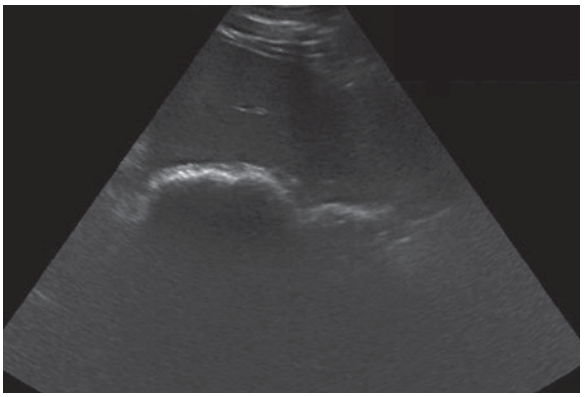


Figure 23.35 Nephrosplenic entrapment. This image demonstrates the presence of colon in the nephrosplenic space, seen adjacent to the spleen and obscuring the view of the left kidney. This sonogram was obtained from the left lateral abdomen using a curvilinear probe operating at a depth of 28 cm.

Vet-ebooks.com

the spleen away from the body wall. There may also be the presence of a small quantity of anechoic fluid around the colon.

Right dorsal displacement of the colon (Figures 23.36 and 23.37) can be implied by finding the medial colonic vasculature against the body wall on the right side of the abdomen. Typically with a right dorsal displacement the vessel is > 1 cm in diameter and is usually identified over several intercostal spaces, near the ventral aspect of the ribs, although with time, medical treatment, and mobility of the colon, the location of the vessels can change.

Right dorsal colitis (Figures 23.38 and 23.39) is a unique, focal, ulcerative change in the right dorsal colon associated with a history of excessive or prolonged administration of non-steroidal anti-inflammatory medications. Ultrasound imaging can demonstrate edema and thickening of the right dorsal colon along its

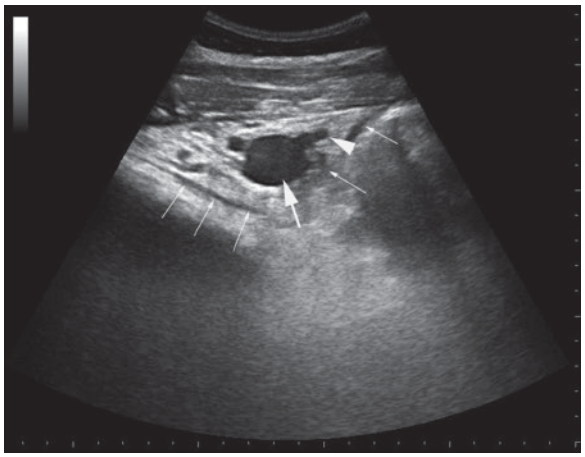


Figure 23.36 Right dorsal displacement of the colon. Right dorsal displacement of the colon may result in engorgement of the colonic vessels. Distended colonic vein (arrow) and artery (arrowhead) and medial mesocolon (long thin arrows) are imaged adjacent to the right body wall just ventral to the 12th intercostal space. This sonogram was obtained from the right ventral abdomen with a curvilinear probe operating at 3.5 MHz at a depth of 17 cm.

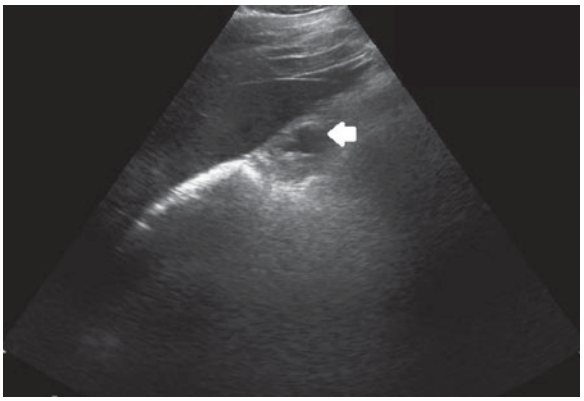


Figure 23.37 Right dorsal displacement of the colon. This image demonstrates a distended mesenteric vessel (arrow) due to a right dorsal displacement of the large colon. This sonogram was obtained from the right ventral abdomen with a curvilinear probe at a depth of 28 cm.

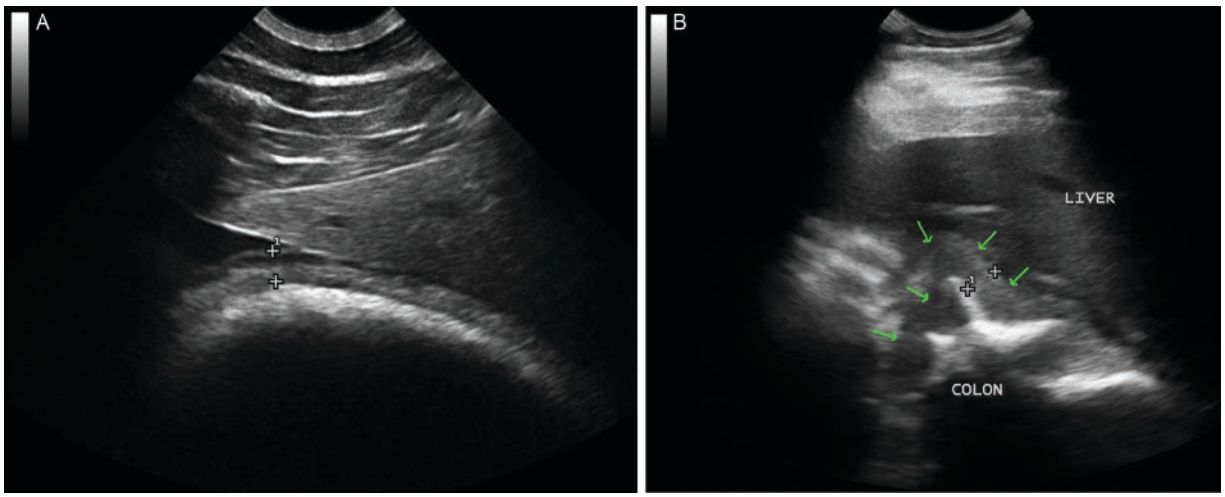


Figure 23.38 Right dorsal colitis. (A) This image demonstrates right dorsal colitis secondary to administration of non steroidal anti-inflammatory drugs (NSAIDs). Note the thickened wall of the right dorsal colon. This case was from a 2-year-old colt with history of NSAID use following throat surgery. The colt was febrile, hypoproteinemic, and hypoalbuminemic. This sonogram was obtained from the right abdomen with a curvilinear probe operating at 6.6 Mhz at a depth of 21 cm. (B) This image is one month after initial presentation. The colon wall is thickened and echogenic (cursors). A thin, hypoechoic layer below the serosa is suggestive of edema. This is compatible with mucosal fibrosis of a healing mucosal ulceration of the right dorsal colon. This sonogram was obtained from the right abdomen with a curvilinear probe operating at 6.6 Mhz at a depth of 21 cm.

Vet-ebooks.com

course on the right side of the abdomen. Cases may be mildly colicky and are also often hypoproteinemic and may also be leucopenic in some instances. Serial evaluation may be useful in following the clinical course and response to medical management.

Colitis cases (Figures 23.40, 23.41, 23.42, 23.43, 23.44, and 23.45) may display signs of colic as well as demonstrating colon wall edema. These cases are usually differentiated clinically from other causes of colic by the lesser degree of pain and presence of fever, diarrhea, and leucopenia. In some instances, the patient will present prior to the onset of diarrhea, and ultrasound examination will be useful in providing information to support the diagnosis of colitis by demonstration of a thick, edematous colon wall and/or increased fluid in the lumen.

Torsion or volvulus of the colon (Figures 23.46, 23.47, 23.48, and 23.49) most often is diagnosed in a postpartum mare with acute onset of severe abdominal pain with abdominal distension and palpation of a gas-distended large intestine on rectal examination. Ultrasound examination typically demonstrates diffuse colon wall

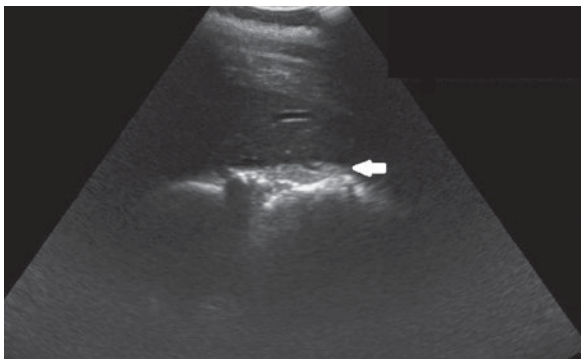


Figure 23.39 Right dorsal colitis. This image demonstrates focal right dorsal colon wall edema in a Standardbred filly with a history of prolonged NSAID use and recent colic episodes. Clinicopathologic abnormalities included leucopenia and hypoproteinemia. This sonogram was obtained from the right abdomen with a curvilinear probe at a depth of 21 cm.

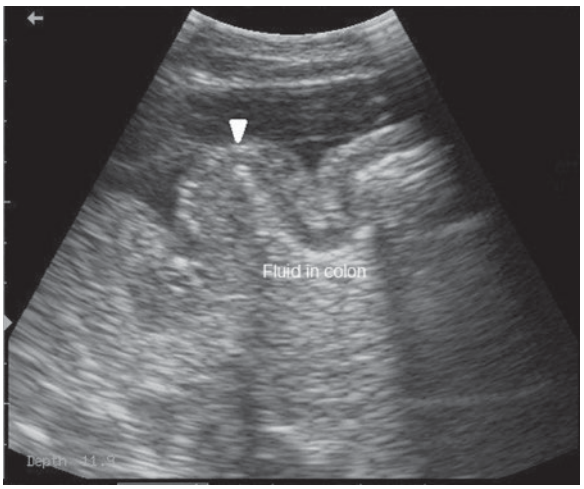


Figure 23.41 Colitis from Salmonellosis. This image demonstrates thickened and edematous colon in a horse diagnosed with Salmonellosis. Note the visible fluid content in the lumen of the colon. This image was obtained from the left ventral abdomen with a curvilinear probe operating at 2.0 MHz at a depth of 12 cm. (*Source*: Image courtesy of Dr Nathan Slovis, Hagyard Equine Medical Institute, Lexington, Kentucky.)



Figure 23.40 Colonic fluid. This image demonstrates increased fluid content in the lumen of the large colon. This image was obtained from the ventral abdomen with a curvilinear probe operating at 2.0 MHz at a depth of 20 cm. (*Source*: Image courtesy of Dr Nathan Slovis, Hagyard Equine Medical Institute, Lexington, Kentucky.)

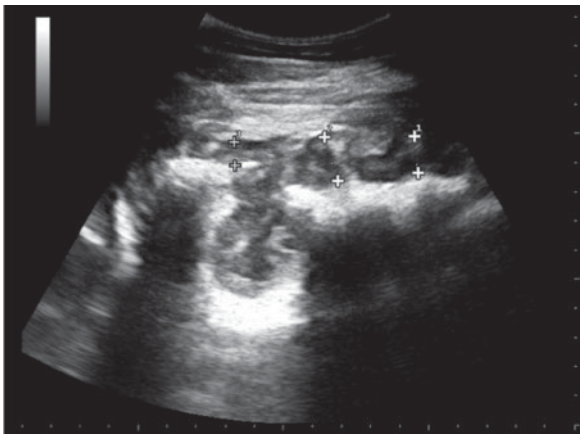


Figure 23.42 Colitis in adult. This image demonstrates a thickened and edematous colon wall from a horse with colitis. The corrugated appearance is sometimes seen with inflammatory processes. This image was obtained from the left abdomen with a curvilinear probe operating at 3.5 MHz at a depth of 14 cm.

Vet-ebooks.com

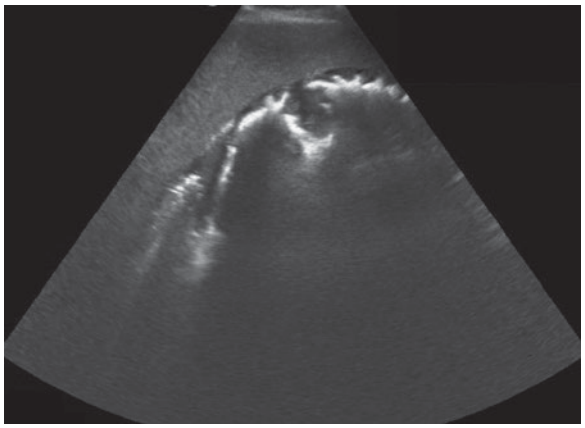


Figure 23.43 Colitis in an adult. This image demonstrates mild colon wall edema in a horse with colitis. This image was obtained from the left abdomen with a curvilinear probe operating 3.5 MHz at a depth of 30 cm.

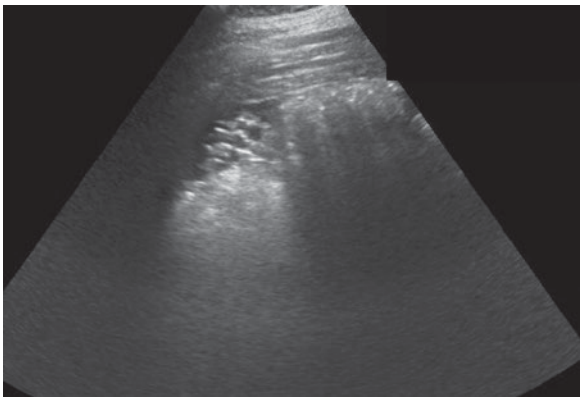


Figure 23.45 Potomac Horse Fever colitis. This image demonstrates colon wall edema in a 10-year-old Thoroughbred mare that presented with diarrhea, high fevers, and leucopenia. Fecal PCR testing yielded a positive result for Potomac Horse Fever. This image was obtained from the right craniolateral abdomen with a curvilinear probe operating at 3.5 MHz at a depth of 23 cm.

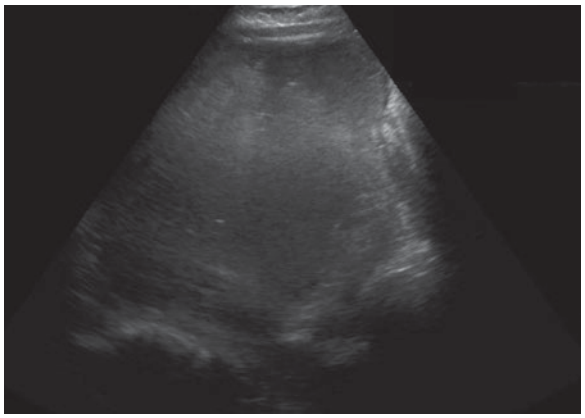


Figure 23.44 Colitis in an adult. This image demonstrates increased fluid content in the lumen of the large colon in a horse with colitis. This image was obtained from the right ventral abdomen with a curvilinear probe operating at 3.5 MHz at a depth of 30 cm.

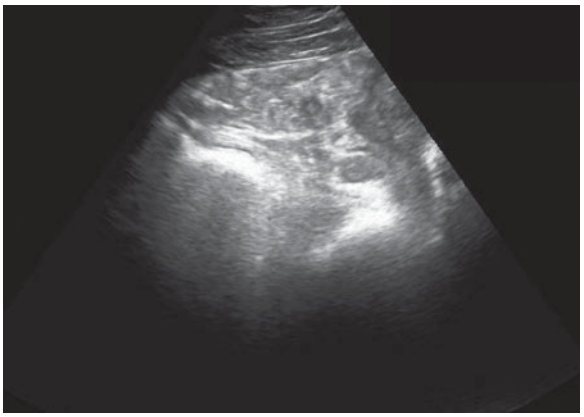
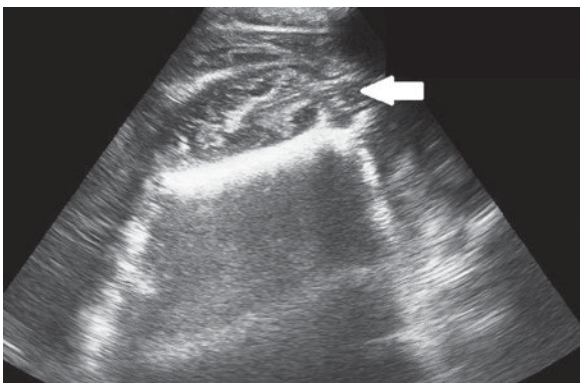


Figure 23.46 Colon torsion. This image is from a 12-year-old mare that presented 1-month post-foaling for severe colic. The characteristic marked colon wall edema along with the severe colic signs prompted immediate referral for exploratory laparotomy where a colon torsion was confirmed and corrected. This image was obtained from the right abdomen with a curvilinear probe operating at 3.5 MHz at a depth of 30 cm.

Figure 23.47 Colon torsion. Colon torsion usually results in vascular compromise to the colon visible as wall edema. The colon wall is severely edematous (arrow). This sonogram was obtained from the right abdomen with a curvilinear probe operating at 3.5 MHz at a depth of 20 cm.



Vet-ebooks.com

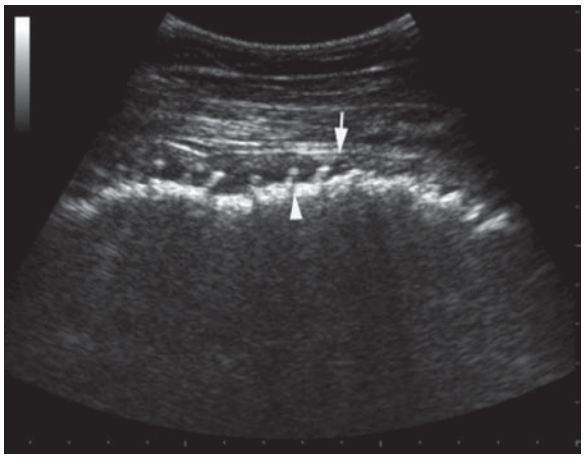


Figure 23.48 Colon torsion. This image is from a mare with a colon torsion prior to surgical correction. The colon wall (arrow) is thickened and edematous. Luminal content (arrowhead) is visualized adjacent to the colon wall. This sonogram was obtained from the ventral abdomen with a curvilinear probe operating at 3.5 MHz at a depth of 11 cm.

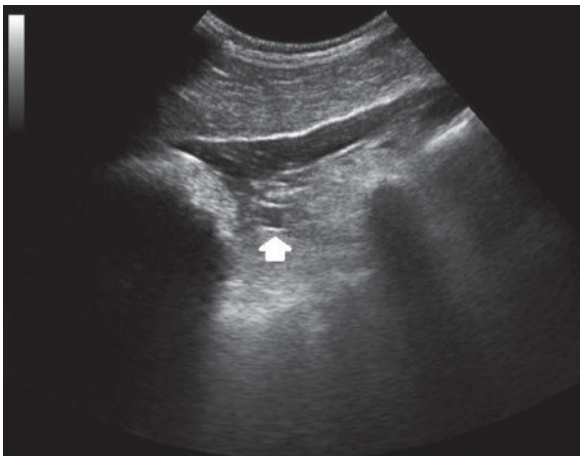


Figure 23.50 Lateral cecal vessels. A lateral vessel of the cecum (arrow) is visible just caudal to the costal arch on the right side of the abdomen. This sonogram was obtained from the right abdomen with a curvilinear probe operating at 6.6 MHz at a depth of 14 cm.

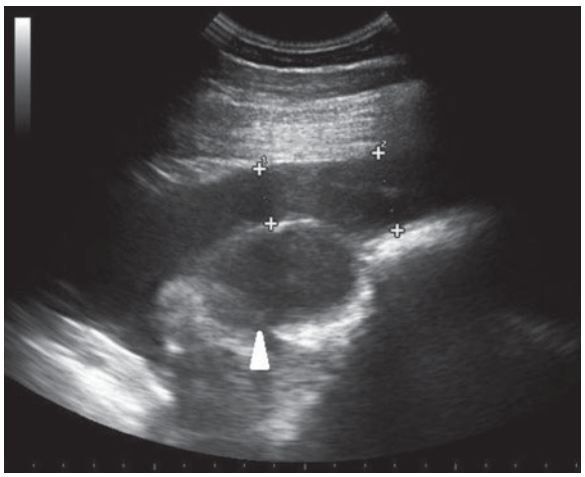


Figure 23.49 Reperfusion injury after correction colon torsion. This image is from a 12-year-old Thoroughbred mare 12 hours after surgical correction of a colon torsion. The right dorsal colon is imaged through the 10th intercostal space. Thickening of the colon wall from edema (cursors) is suggestive of significant reperfusion injury. A focally, extensive, hypoechoic area (arrowhead) within the submucosa is suggestive of a submucosal hematoma. Hematoma formation within the colon wall may indicate a coagulopathy associated with large and small vessel injury secondary to the colon torsion. The mare's clinical status deteriorated and she was euthanized 6 hours after this ultrasound examination. This sonogram was obtained from the ventral abdomen with a curvilinear probe operating at 6.6 MHz at a depth of 15 cm.

edema, and can provide information as to wall thickness and potential for vascular compromise.

The cecum (Figure 23.50) can be imaged from its base in the upper right paralumbar fossa, along the costal arch, down to its apex near the ventral abdomen. The lateral vessels of the cecum can usually be seen on ultrasound.

Cecal impaction (Figure 23.51) is most often diagnosed by rectal palpation of a firm mass within the cecal base. Ultrasound can determine the extent of cecal distension and character of the cecal wall.

Cecocolic intussusception (Figure 23.52) can be observed on ultrasound where the trilayer appearance of thickened, edematous, intussuscepted cecal wall is seen within the lumen of the right ventral colon. The trilayer is composed of the outer most mucosa with the central echogenic layer of muscularis and innermost layer of serosa. The intussusception can be demonstrated more easily when it is surrounded by liquid luminal content within the right ventral colon. Cecal inversion (Figure 23.53) also appears as a trilayer appearance consisting of cecal wall and the inverted cecal apex.

Ultrasound changes seen with typhlitis (Figure 23.54) include thickening and edema of the cecal base wall.

Vet-ebooks.com

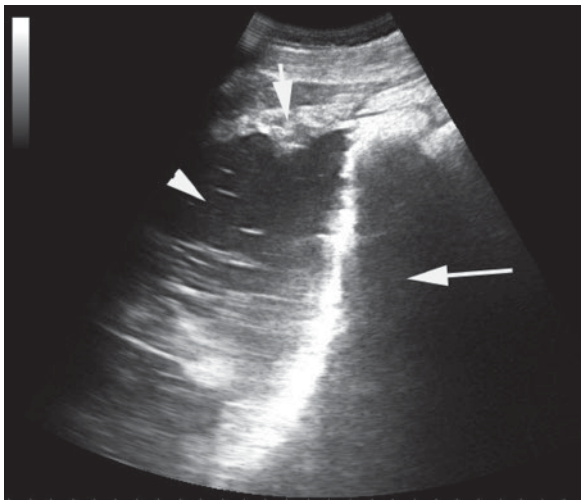


Figure 23.51 Cecal impaction. Cecal impaction is usually diagnosed by rectal palpation, but may be visible ultrasonographically. The solid, intraluminal mass (long arrow) in the cecal base is visible adjacent to the fluid-filled cecal lumen (arrowhead) ventrally. The lateral cecal wall (short arrow) is visible. This sonogram was obtained from the right, lateral abdomen with a curvilinear probe operating at 2.5 MHz at a depth of 23 cm.

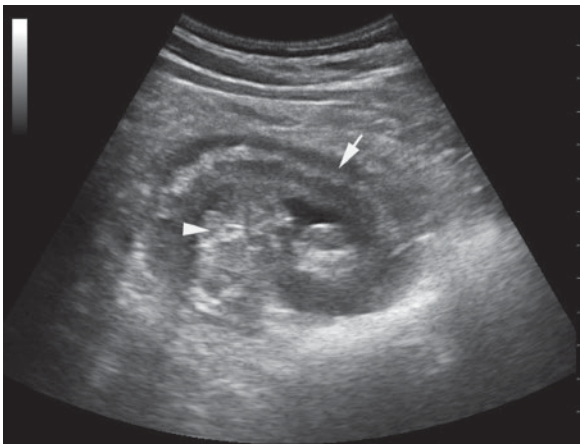


Figure 23.53 Cecal inversion. Cecal inversion images as edematous trilayer appearance of cecal wall (arrow) with inverted cecal apex (arrowhead). This lesion was present in the midventral abdomen of a weanling Quarter Horse foal with clinical signs of intermittent colic over 2 days. Cecal inversion was confirmed at surgery. This image was obtained from ventral abdomen with a curvilinear probe operating at 6.6 MHz at a depth of 13 cm.

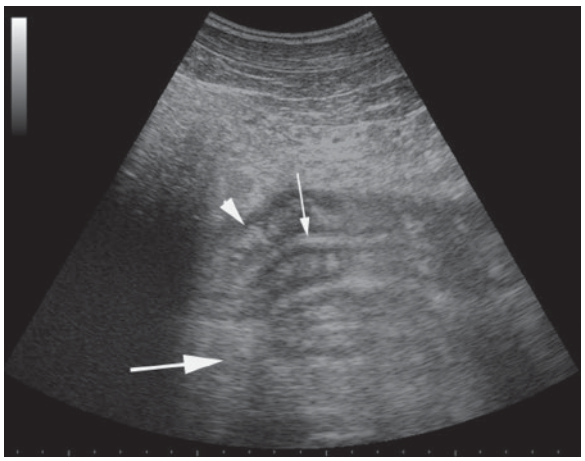


Figure 23.52 Cecocolic intussusception. The cecum is intussuscepted into the lumen of the right ventral colon (long thick arrow). The cecal mucosal surface (arrowhead) and serosal surface (long thin arrow) are visible. Cranial is to the left in this image. This sonogram was obtained from right ventral abdomen with a curvilinear probe operating at 5.0 MHz at a depth of 17 cm.

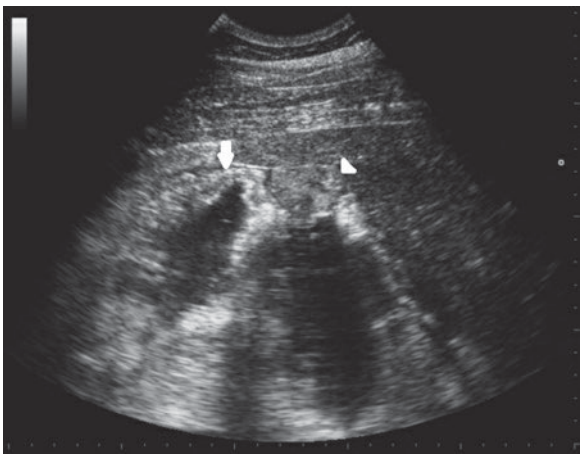


Figure 23.54 Typhlitis. The thickened wall of the cecal base (arrow) is consistent with typhlitis. The duodeum (arrowhead) is visible dorsally. This sonogram was obtained from the right lateral abdomen with a curvilinear probe operating at 6.6 MHz at a depth of 19 cm.

Vet-ebooks.com



Figure 23.55 Perirectal abscess. This image shows two abscesses (arrowheads) in the dorsal wall of the rectum. This sonogram was obtained transrectally with a linear probe operating at 5.0 MHz at a depth of 8 cm. (*Source*: Image courtesy of Dr Nathan Slovis, Hagyard Equine Medical Center, Lexington, Kentucky.)

Rectum

Transrectal ultrasound may be used to image abnormalities including abscesses (Figure 23.55) in the rectum wall.

Recommended Reading

Bithell, S., Habershon-Butcher, J.L., Bowen, I.M. et al. (2010). Repeatability and reproducibility of transabdominal ultrasonographic intestinal wall thickness measurements in Thoroughbred horses. *Veterinary Radiology and Ultrasound* 51(6): 647–651.

Busoni, V., De Busscher, V., Lopez, D. et al. (2011). Evaluation of a protocol for fast localised abdominal sonography of horses (FLASH) admitted for colic. *Veterinary Journal* 188(1): 77–82. doi: 10.1016/j.tvjl.2010.02.017. Epub 2010 Mar 26.

Epstein, K., Short, D., Parente, E. et al. (2008a). Gastrointestinal ultrasonography in normal adult ponies. *Veterinary Radiology and Ultrasound* 49(3): 282–286.

Epstein, K., Short, D., Parente, E. et al. (2008b). Serial gastrointestinal ultrasonography following exploratory celiotomy in normal adult ponies. *Veterinary Radiology and Ultrasound* 49(6): 584–588.

Gomaa, N., Uhlig, A., and Schusser, G.F. (2011). Effect of Buscopan compositum on the motility of the duodenum, cecum and left ventral colon in healthy conscious horses. *Berl Munch Tierarztl Wochenschr* 124(3–4): 168–174.

Hendrickson, E.H., Malone, E.D., and Sage, A.M. (2007). Identification of normal parameters for ultrasonographic examination of the equine large colon and cecum. *Canadian Veterinary Journal* 48(3): 289–291.

Kihurani, D.O., Carstens, A., Saulez, M.N. et al. (2009). Transcutaneous ultrasonographic evaluation of the air-filled equine stomach and duodenum following gastroscopy. *Veterinary Radiology and Ultrasound* 50(4): 429–435.

Lores, M., Stryhn, H., McDuffee, L. et al. (2007). Transcutaneous ultrasonographic evaluation of gastric distension with fluid in horses. *American Journal of Veterinary Research* 68(2): 153–157.

Mitchell, C.F., Malone, E.D., Sage, A.M. et al. (2005). Evaluation of gastrointestinal activity patterns in healthy horses using B mode and Doppler ultrasonography. *Canadian Veterinary Journal* 46(2): 134–140.

Norman, T., Chaffin, K., and Schmitz, D. (2010). Effects of fasting and intraluminal contrast enhancement on ultrasonographic appearance of the equine small intestine. *Veterinary Radiology and Ultrasound* 51(6): 642–646.

Vet-ebooks.com

24

Equine Ocular Ultrasonography

Rodolfo Gialletti

University of Perugia, Perugia, Italy

Introduction

Equine ocular ultrasonography (EOUS) provides a complete image of globe structures, regardless of opacities in the ocular media and eyelid swelling [1,2]. A feasible and easy to perform procedure that is safe and practical, EOUS can be performed in the standing horse, as sedation or local nerve block is required only in some cases [1,3].

EOUS should always be included in an ophthalmologic examination, especially when, in conditions such as corneal disease, uveitis, cataracts, or trauma, ocular opacities preclude adequate evaluation of posterior structures using ophthalmoscopy and slit-lamp biomicroscopy [1].

In human and veterinary medicine, ultrasonography (US) is crucial for investigating ocular opacities in conditions such as corneal disease, uveitis, cataracts, or trauma [4] and essential when screening candidates for cataract surgery and for diagnosing posterior segment diseases [1,5,6].

Additionally, US in veterinary medicine is a very useful diagnostic tool for many other ophthalmic conditions such as enophthalmos, buphthalmos, or exophthalmos, ocular protrusion, and suspected disparity in eyeball sizes [7,8].

In human beings, ocular US is remarkably important in emergency cases of acute vision loss and acute posterior ocular disease [4,9].

The Bedside Ocular Ultrasound is used by trained general physicians to diagnose retinal detachment with a high degree of accuracy; moreover, its features such as speed, non-invasiveness, and cost-effectiveness make it an ideal tool for busy emergency medicine clinicians [6].

US visualizes intraocular structures in case of loss of transparency and accurately distinguishes between diseases that need immediate ophthalmologic intervention (e.g., retinal detachment, vitreal hemhorrhage, etc.) and those that require only outpatient-type follow-up treatment [5,10].

Although clinical examination is the gold standard for diagnosing eye abnormalities, in case of ocular media loss of transparency, US becomes essential for diagnosis. Ocular surface and anterior segment pathologies, i.e., involving the eyelids, cornea, anterior chamber, lens, vitreous, and retina are recognized and diagnosed better by clinical examination but, in cases of ocular media loss of transparency (i.e., diffuse corneal edema or cataract), US examination is more reliable, thus becoming crucial for diagnosis [11].

Equine Ocular Ultrasonography Technique

The equine ocular ultrasonography technique diagnostic technique is easy to perform, non-invasive, pain-free, and usually well-tolerated. Although EOUS is usually conducted on the standing horse, the sonographer's safety is ensured by sedating it, usually by administering α-2 agonists like xylazine hydrochloride(0.3–0.4 mg/kg IV) or detomidine hydrochloride (0.04–0.08 mg/kg IV) with or without butorphanol (0.01–0.02 mg/kg IV) in cases of trauma or severe pain[8]. Sometimes local anesthesia may suffice (oxybuprocaine hydrochloride 0.4% on the cornea) or a supra-orbital, auriculo-palpebral nerve

Atlas of Equine Ultrasonography, Second Edition. Edited by Jessica A. Kidd, Kristina G. Lu and Michele L. Frazer.
© 2022 John Wiley & Sons Ltd. Published 2022 by John Wiley & Sons Ltd.
Companion Website: www.wiley.com/go/kidd/atlas

Vet-ebooks.com

block [12,13]. Even though eyelid hair does not usually need to be shaved, the supra-orbital area may need to be if images are required of the retro-bulbar space [14]. Corneal damage is a counter-indication to this approach [8].

A US scan of the eye and the orbital area can be performed by positioning the transducer on the eyelid (transpalpebral) or directly on the cornea (transcorneal).

Although transcorneal ultrasound provides best-quality images, it is not always well tolerated. Therefore, corneal anesthesia by instilling tetracaine solution 0.5% or proparacaine solution 0.5% into the eye is recommended.

An auriculo-palpebral nerve block can also facilitate the scan, particularly in cases with severe blepharospasm or ocular pain. A standoff pad must be used to assess the cornea and anterior chamber when using this technique.

Trans-palpebral ultrasound is easier to perform, and is usually well tolerated by the horse, but does, however, create more artifacts because of the eyelid-cornea interface [12,15]. A sterile ultrasound coupling gel is recommended for use with either technique. It should be applied directly to the cornea or the eyelid, to facilitate transducer contact with the eye. When the gel is applied directly to the cornea, the eye should be thoroughly washed after the scan [12], so as to prevent potential gel-related irritation. EOUS is not indicated or should only be performed with care when corneal perforation is imminent.

The retrobulbar space is scanned by positioning the US transducer on the eyelid or eye for in-depth eyeball visualization or by placing it over the supraorbital fossa to visualize features behind the eye. In some horses with masses in the retrobulbar space, scanning through the supraorbital fossa yields better images, which can be used to perform ultrasound-guided aspiration or biopsies of the retrobulbar masses [12,15].

The type of transducer or probe and the frequency are selected according to the features to be scanned. Frequency is inversely proportional to depth. Very deep tissue penetration is not usually required in EOUS, but high resolution images need to be obtained [16]. In clinical practice, the 10 MHZ frequency is usually selected as it penetrates about 3–4 cm of the anterior chamber. Lower frequencies (5–7.5 MHz) which penetrate to a depth of 6–10 cm are suitable for visualizing the posterior chamber and the retrobulbar space [8,16,17]. Probes with greater frequencies are not used on horses. Convex or linear probes may be used as long as they are equipped with a small head [16,18]. To achieve optimal images, gains should be adjusted in accordance with the anatomical area to be scanned. Lowest gains should be used to visualize lesions and the highest for the vitreous and posterior chamber [12].

Color Doppler is used to assess eye and orbital vascularization and to determine whether the intra-ocular mass and retro-bulbar space are vascularized or not [17].

Whatever technique is selected, the approach must always be systematic. The eyeball should be fully scanned by placing the probe horizontally and moving it in a dorsal-ventral direction with a marker at 3 o'clock for the right eye and at 9 o'clock for the left (transverse scanning plane) and then placing the probe vertically for movement in the medial-lateral direction with a marker at 12 o'clock (sagittal scanning plane). Conventionally, markers are on the right of images [13]. Oblique scanning planes are used for in-depth exploration in particular cases [19]. Remember that exerting undue pressure while scanning will deform the eyeball. Both eyes ahould be scanned so as to compare whatever measurements are taken and to assess any sub-clinical abnormalities in the apparently healthy eye [8].

When patient and equipment are ready for the scan, the eye should be methodically scanned in real time, usually moving from one anatomical landmark to the next in this order: cornea, anterior chamber, iris and ciliary body, crystalline lens, vitreous, retina, choroid, sclera, and extra-ocular areas [13].

US scans may be performed in (Figure 24.1) A-mode or, more commonly in clinical practice, in B-mode.

EOUS in A-Mode

Although EOUS in A-mode is rarely used, it provides precise measurements and is useful for biometric US studies [18].

Images obtained with EOUS in A-mode show four vertical peaks, with the height of each representing echo intensity. The horizontal axis shows the distance between the anatomic feature and the probe [17]. Peak morphology produces typical images of the tissues the ultrasound passes through and the morphology changes in the presence of pathogens.

Converting the space between two peaks into distance provides measurements of the anterior-posterior eyeball axis, the depth of the two chambers, and the axial crystalline thickness [16].

EOUS in B-Mode

The B-mode two-dimension (2-D) modality is the simplest, fastest, and most used technique, as it provides 2-D images in real time. As in all US images of body parts, the ocular US distinguishes images as anechoic, hypoechoic, and hyperechoic [17].

Vet-ebooks.com

Overall, a healthy eye appears as an oval image with four clear hyperechoic structures. Moving from the anterior to the posterior they are the cornea, iris, posterior crystalline capsule, and the retina/choroid/sclera complex, which physiologically cannot be detected separately on US images. These structures border the eye chambers and the crystalline nucleus which are hypoechoic. The anterior and vitreous chambers are visualized but the posterior chamber is usually invisible [15,17]. Other, less echoic structures include the iris, the corpora nigra, the optic nerve, peri-orbital fat, and extrinsic eye muscles.

In a trans-eyelid scan, the eyelids appear as a hyperechoic layer adhering to the probe.

Measurement taken during a US scan can be compared with reference values and the healthy eye values.The eyeball should have a diameter of 39.4 ± 2.3 mm, and a slightly larger vertical diameter (42.5 ± 3.6 mm) [19,20].

Cornea

Both the trans-eyelid and trans-corneal approaches visualize the cornea, though with the latter, pad use is recommended. The cornea appears as a fine, regular curvilinear hyperechoic line (corneal epithelium), an anechoic area (corneal stroma), and an unbroken, 2.33 ± 0.39 mm thick, hyperechoic line which should not vary in the entire cornea (corneal endothelium) [12,19,20].

The most common corneal abnormalities are:

- Corneal Edema
- Corneal Infiltrates
- Stromal Abcesses
- Corneal Ulcers

Anterior and Posterior Chambers

The anterior chamber is bordered by the cornea, iris, ciliary body, and the anterior surface of the crystalline lens. The posterior chamber, lying between the iris and the anterior lens surface, appears as a fine anechoic line which is often hard to visualize in the horse. The complex measures about 4.22 ± 1.29 mm [12,19,20]. Since it contains acqueous humor, it appears uniformly anechoic in physiological conditions, providing a good contrast for identifying and examining other ocular structures. Echoes in these chambers must be considered as abnormal as they indicate increased cellularity in the acqueous humor. During the scan, no undue pressure should be applied to the probe so as to avoid deforming the chamber. Pathological findings in the chambers include:

- Blood (*ifema*)
- Fibrin
- Pus (*ipopion*)
- Synechiae, adhesions between the cornea and the iris or crystalline lens, which are usually linked to chronic inflammation
- Changes in depth (whether more or less) due to lens dislocation or subluxation, uveitis, and/or glaucoma or trauma – related anterior chamber collapse so that the cornea overlies the crystalline lens
- Foreign bodies
- Intra-ocular mass in the anterior chamber [11].

Iris and Ciliary Bodies

In a standard EOUS scan, the iris and ciliary bodies appear as a single irregular hyperechoic structure extending from the periphery to the center, posterior to the anterior chamber and lateral to the crystalline lens. The *corpora nigra* are visualized as irregular hyperechoic structures on the anterior edge of the iris that protrude into the anterior chamber. Cysts, appearing as spheres with an anechoic content, may occasionally be detected on the iris and/or the ciliary bodies (Figure 24.32). Other common findings are a rounded iris, due to previous inflammation and/or post-uveitis glaucoma [8], crystalline lens dislocation or subluxation, and neoplasias (adenoma, adenocarcinoma, melanoma). Iris thickness is 2.5 ± 0.66 mm; ciliary body thickness is 3.99 ± 1.13 [19].

Crystalline

The crystalline or lens includes an anechoic nucleus and anterior and posterior surfaces that appear on a US scan as two hyperechoic curvilinear bands, one convex and the other concave. Often both bands are not visible on one scan. As the crystalline lens is roundish in shape, only areas perpendicular to the suspensory ligaments can be visualized [1], so the probe needs to be rotated during the scan for its complete visualization. Lens dimensions: antero-posterior 11.93 ± 1,10 mm; diameter about 20 mm [12,19,20]. The most common EOUS findings are:

- Variations in dimensions (due to cataract, lens resorption, trauma-related rupture)
- Changes in position (dislocation or subluxation)
- Changes in echoic status (cataract)
- Lens rupture [11].

Vet-ebooks.com

The Vitreous Chamber

The vitreous chamber is bordered anteriorly by the posterior surfaces of the iris/ciliary bodies and the crystalline lens and posteriorly by the retina/choroid/sclera complex. Containing vitreous humor, it measures approximately 17.37 ± 1.98 mm [12,19,20].

Its most common pathologies are:

- Variation in dimensions (posterior crystalline lens dislocation)
- Extraneous material (blood due to trauma, fibrin due to infection or inflammation, vitreous degradation, asteroid hyalosis, lipid and calcium-containing spheres that are visualized as echoic granules)
- Retina detachment
- Mass or neoplasia
- Change in echoic status (e.g., due to uveitis)
- Posterior vitreous detachment

Increasing the gains is often needed to achieve better images of the vitreous chamber and visualize abnormalities like, for example, vitreous membranes, which are fibrous layers that develop after inflammation and clot formation [17].

Retina/Choroid/Sclera

In healthy eyes the retina, choroid, and sclera cannot be distinguished separately on a US scan. Altogether, they form the posterior eye segment, appearing as a hyperechoic circular concave line that borders the vitreous. Retina detachment is the most common abnormality in this segment. Choroid detachment may be found but is extremely hard to visualize.

Choroid melanoma may protrude into the vitreous.

Retrobulbar Area

Since visualization of this region requires tissue penetration to a depth of 6–8 cm, lower frequency probes are used [8]. Clearly visible on US images are the optic nerve, extraocular muscles, retrobulbar fat, and the optic disc.

The optic nerve appears as hyperechoic triangle posterior to the optic disc. The extraocular muscles, which surround the eyeball and the optic nerve, are slightly less echoic than the optic nerve. Fat appears as heterogeneous echogenicity. At further depth, bone is visualized as a smooth hyperechoic surface with a typical bone US pattern.

The most common abnormalities in this site, and the reason why it is usually scanned, are retrobulbar mass or abscess, and bone trauma to the eye cavity.

Principal Diseases of the Equine Eye and Appurtenances. US Scanning

Keratitis

Keratitis is an inflammation of the cornea. It may be dry, or eosinophilic and ulcerative. It is caused by bacteria, viruses, fungi, trauma, or other external agents. Corneal layers are hard to distinguish separately on a standard EOUS scan with the usual frequency.

Stromal Abscess and Corneal Infiltrates

Corneal abscesses are often due to ulcers or small corneal lesions that do not heal, become infected with foreign bodies or bacteria, and persist in the stroma. Abscesses may also be secondary to uveitis. In cases of stromal abscesses or corneal infiltrates, US images show a thickened, widely hypoechoic cornea. Use of a high frequency probe (over 10 mHz) aids imaging (Figures 24.3, 24.4, 24.8, 24.9).

Corneal Ulcer

This lesion to one or more corneal layers is caused by environmental agents (foreign bodies, etc.), lack of lacrimal film (dry eye, kerato-conjunctivitis, etc.), or continual contact with eyelashes and eyelid hair (entropion).

An EOUS scan is not indicated in cases of corneal ulcer. Although it may be helpful if severe eyelid edema prevents direct eye examination, it should be performed with great care so as not to cause any further injury. A pad should be used. Images show a thickened, irregular, pitted corneal surface (Figure 24.6).

Corneal Edema

Corneal edema, a symptom of many eye diseases, develops due to injury to the endothelium or, in some cases, the epithelium. Even though uveitis is its main cause, corneal edema may be consequent to trauma, glaucoma, surgery, keratitis, and aging. In EOUS images, the cornea appears thickened, with hypoechoic central and stromal layers. The endothelium, its deepest layer, appears as a broken line with alternating hyperechoic and anechoic areas (Figures 24.2, 24.5).

Anterior Chamber Synechiae

Synechiae in the anterior or posterior chambers are usually secondary to eye diseases like chronic uveitis and corneal perforation or abscess. They appear as hyperechoic lines stretching from the cornea to the iris or crystalline lens. The iris adheres to the cornea

Vet-ebooks.com

if the synechiae are in the anterior chamber and to the crystalline lens if they are in the posterior. EOUS can investigate any eventual abnormalities underlying the synechiae [12].

Blood, Pus, Fibrin Accumulates in the Anterior and/or Posterior Chamber

Blood (*ifema*), pus (*ipopion*), and fibrin accumulation in these chambers are secondary to trauma or bacterial infection. Early stage accumulates are hard to visualize on EOUS because they are made up of cells that are not yet organized and are too small in themselves to reflect an echo. At later stages, organized structures are detected. Blood, fibrin, and pus tend to be mobile but settle ventrally due to gravity. When accumulates are immobile, they are hard to differentiate from organized hematoma, granuloma, or neoplasia (Figures 24.7, 24.11, 24.12).

Uveitis

Uveitis, the most common cause of equine blindness, is an inflammation of the iris and/or the ciliary body due to systemic disease or directly to other eye disease. It may be acute or chronic (ERU = Equine Recurrent Uveitis). Clinical features include anterior chamber distension and some or all of the following signs that are detected by US:

- Eyelid or corneal edema
- Conjunctival hyperemia
- Acqueous humor opacity due to the presence of inflammatory cells, fibrin, and blood (ifema)
- Miosis
- Darker, opaque, and swollen iris
- Anterior or posterior synechiae
- Crystalline opacity and cataract
- Crystalline sub-luxation or dislocation
- Vitreous apacity or degradation opacità
- Fundus oculi abnormalities [16] (Figure 24.13)

Iris Cysts

Cysts in the iris, which are occasionally detected in an EOUS scan, appear as spheres with hyperechoic walls and an anechoic center. They form in the iris epithelium but may detach from it and float in the acquaeous humor, develop in the iris stroma or in the *corpora nigra*. They are usually asymptomatic [8].

Ciliary Body Cysts

Cysts in the ciliary body are easily visualized in an EOUS scan. They may appear as single entities or in clusters on the vitreous side. They are a common feature in some breeds like the Rocky Mountain Horse in which they are found as congenital ophthalmic abnormalities [8].

Iris Prolapse

Iris prolapse is usually caused by trauma or corneal disease. It is often associated with fibrin, blood (ifema), and/or pus (ipopion) deposits in the anterior chamber. The standard eye examination cannot be performed because of the accumulates in the anterior chamber, inflammation, and miosis. The correct EOUS technique is the transpalpebral approach, conducted with the lightest possible pressure so as to not worsen iris prolapse [12] (Figure 24.10).

Glaucoma

Glaucoma is characterized by increased intra-ocular pressure. Although it may be primary, it is frequently secondary in the horse to uveitis, trauma, intra-ocular growths, blood (ifema), chronic intra-ocular inflammation, anterior lens dislocation, and any other agent that causes an imbalance in acqueous humor production and elimination. The first signs of glaucoma are corneal edema, pupil dilation, and lens dislocation. Although glaucoma is usually diagnosed by measuring intra-ocular pressure by means of a tonometer, the EOUS is useful for assessing glaucoma-related conditions in the entire eye, for establishing its etiology and the differential diagnosis with exophthalmos due to a retrobulbar mass (Figure 24.28).

In glaucoma, the anterior chamber volume is increased. Sometimes the iris is rounded as visualized by iris thickening and swelling toward the cornea. If only one eye is affected by glaucoma, intra-ocular pressure should be measured in the other for comparative purposes. If both eyes are affected, measurements should be compared with referenced standards [12].

Small Eyeball

A reduced eyeball size may be congenital or secondary to trauma or chronic uveitis which lead to atrophy. Congenital small eyeball appears on the EOUS as a small sized normal eye, while secondary atrophy images depict a smaller, deformed eyeball [12] (Figures 24.29, 24.30).

Aphakia

Aphakia indicates lack of the crystalline lens. A congenital abnormality, it is often associated with microphthalmia [16].

Vet-ebooks.com

Microphakia

Microphakia, a congenital eye malformation, is due to an abnormally small crystalline lens. It is usually associated with lens cataract [16].

Cataract

Cataract refers to any form of crystalline lens opacity, whether localized or widespread. It is classified as congenital if present at the horse's birth, juvenile if it develops within 24 months of birth, and then adult or senile. The causes may be idiopathic, hereditary, or congenital. Otherwise, the cataract may be secondary to uveitis, trauma, or systemic disease. Impairments to sight are related to cataract site and extension. In cases of cataract, EOUS is helpful when corneal edema or other opacities prevent a standard eye examination. The EOUS distinguishes early stage changes in cataract formation from mature cataracts which appear as thickening, with sometimes irregular and more or less greater echogenicity at the lens edges, according to cataract extension and severity [13]. The crystalline lens nucleus usually fills with echoic material and may appear as widened or deformed. In some cases, lens diameter is larger or smaller than normal [12,16]. The EOUS classifies cataract stage and position. Stage is assessed by measuring lens size and echoic status. Scotty et al. found that lens echogenicity closely correlated with cataract grade [1]. Cataract is also graded according to whether it involves the entire lens, or only the cortex or nucleus (Figure 24.14).

Before cataract surgery, the EOUS should examine the posterior eye segment to check for abnormalities like retina detachment or vitreous degradation that are often associated with cataract. Increasing the gains will make them more visible [12] (Figure 24.15).

Post-operatively, EOUS is indicated for visualizing any complications.

Crystalline Lens Dislocation or Sub-luxation

Crystalline lens dislocation is caused by rupture of the zonular strands that physiologically hold the lens in position. Rupture often follows trauma but may be caused by chronic uveitis or glaucoma [12] (Figures 24.17, 24.21). Dislocation is often associated with anterior segment opacity in which case the EOUS is a precious tool [13]. Dislocation is posterior when the lens moves back into the vitreous or anterior if it falls forward into the anterior chamber, where it often generates secondary glaucoma. The EOUS identifies the lens echoic status in its abnormal position and the symptoms consequent to its dislocation [8]. A dislocated lens is clearly visible on EOUS [13], as are echoic areas or lesions due to coagulated blood or hemorrhage in both chambers [12] (Figures 24.18, 24.19, 24.20).

Lens Rupture

Lens rupture is usually secondary to uveitis or trauma. EOUS visualizes breakage in the echoic lens line. Lens rupture usually causes hemorrhage in the eyeball or crystalline and echoic material from the collapsed lens is visible in the anterior chamber or the vitreous [12] (Figures 24.22, 24.23).

Vitreous Opacity

A standard eye examination may not be able to explore vitreous opacity in depth and an EOUS is crucial for diagnosis. Vitreous opacity may derive from diverse causes, e.g., vitreous trauma leading to bleeding, vitreous degradation or detachment, inflammation, asteroid hyalosis, and ophthalmitis . Echodensities vary in the EOUS with the diverse causes of opacity, but there is always an increase in local or widespread echogenicity in the usually anechoic vitreous chamber [12] (Figure 24.27).

Puntiform, focal, and hyperechoic lesions often indicate hemorrhage, fibrin, white blood cells, and asteroid hyalosis. When lesions are more widespread, they show serious celular infiltrates.

Hemorrhage apears as multiple hyperechoic areas with communicating chambers in the vitreous due to coagulated blood. Sometimes secondary signs like retina detachment or cataract, which often develop during episodes of bleeding, are visible on the EOUS. Hemorrhage may be hard to distinguish from other infiltrating pathologies without using Doppler in some cases. The EOUS visualizes, however, echoic patterns of vortexes and focal coagulations that disappear at the next scan [13].

Vitreous degeneration, which is often detected in elderly horses, may lead to secondary inflammation and consequently to cataract formation. Although vitreous degeneration may not be clinically evident, the EOUS shows increased vitreous opacity with widespread areas of varying echoic status throughout the chamber, due to diverse degrees of liquefaction. Gains should be increased when scanning the vitreous chamber. Vitreous inflammation, which is often associated with recurrent uveitis, appears as areas of varying echoic status with free hyperechoic material corresponding to fibrin or pus in the chamber.

Asteroid hyalosis, as observed in some cases, is not usually of clinical importance. Usually

Vet-ebooks.com

constituted of calcium phosphate crystals, it appears as free, highly reflective, and hyperechoic on the EOUS [16].

Retina Detachment

Although retina detachment may be congenital, it is more often acquired, deriving from several causes. The most common are exudative chorioretinitis and recurrent uveitis, vitreous membrane traction, glaucoma, cataract, neoplasias, infection, trauma [8,12], and as a complication of phacoemulsification surgery. Detachment may be complete or partial. Even though the EOUS is a useful diagnostic tool for assessing it, the retina cannot be distinguished from the choroid or the sclera on ultrasound images as all three delineate the vitreous chamber (see above). Complete retina detachment appears as a "V" shaped image, the so-called "seagull's wings" with the wings indicating the retina [13] as it still adheres to the optic disc [8]. Partial retina detachment appears as a hyperechoic convex line which should not be confused with other hyperechoic findings in the vitreous chamber like pseudomembrane or fibrin filaments [13]. In chronic or very old partial retina detachment, the convex line appears even more hyperechoic because of dystrophic calcifications in the inter retina-choroid space. Acute detachment is often associated with hemorrhage in the vitreous chamber [12] (Figures 24.24; 24.25; 24.26).

Assessing the area below the detached retina is crucial. If it is anechoic, it indicates a fluid-like ooze which might be reabsorbed. Echoic material suggests hemorrhage, neoplastic infiltrates, or inflammatory cells may be present [16].

Intra-Ocular Mass

EOUS provides very good information on mass presence, type, size, extension, and organ involvement. Masses may originate from inflammatory processes, infections, cysts, neoplasms, or foreign bodies. Intra-ocular masses in the horse are most often found in the anterior segment of the eye, particularly in the iris and ciliary bodies [16]. Consequently, the echoic profile of intra-ocular masses varies greatly. Abscesses, for example, can range from a hypoechoic to anechoic status and are sometimes associated with local inflammation which makes them hard to define. Foreign bodies yield diverse echoic patterns that create acoustic windows and are often surrounded by anechoic fluid. Although intra-ocular tumors are rare in horses, they can involve the cornea, iris, ciliary bodies, and optic nerve. The most common intra-ocular tumor is melanoma, particularly in the iris (Figure 24.31). On EOUS, melamoma display the typical soft tissue echoic pattern which is easily distinguished from intra-ocular cysts with their thin hyperechoic wall and anechoic center [12].

Retrobulbar Diseases

EOUS of the retrobulbar area is indicated for cases of exophthalmos and trauma [16]. EOUS is also usually indicated for other pathologies such as hematoma, cysts, neoplasms, cellulitis, and hemorrhage [8,12]. EOUS visualizes the mass and provides very good information on its site, size, features, and organ involvement [18]. A trans-scleral scanning plane should be used to visualize this area well and avoid the crystalline lens. Since the echoic patterns of retrobulbar masses and extra-orbital muscles may be similar, the healthy eye should also be scanned. The EOUS also detects fractures as breakages in hyperechoic bone surface [8]. Images of well-defined masses usually show hematoma, abscesses, and tumors while more diffuse images are indicative of hemorrhage, cellulitis, and aggressive neoplasms. Mass vascularization can be assessed with the Doppler [13].

Retrobulbar abscesses appear as well-defined areas with a capsule containing echoic fluid which is sometimes stratified. Images are very similar to a retrobulbar hematoma with internal hyperechoic areas indicating clot formation within the hematoma or foreign body calcification [18]. The most common retrobulbar neoplasms in the horse are optic nerve medullo-epitelioma, hemangioma, fibroma, microglioma, granulocyte, sarcoma, lipoma, adenocarcinoma, lymphosarcoma, multilobar osteoma, and melanoma [12]. Ultrasound images of neoplasms vary greatly in accordance with the type of tumor. Some tumors may even erode orbital bone [18] (Figure 24.35).

Retrobulbar cellulite, which is often detected in horses, appears as a hyperechoic infiltration spreading through the tissues [12]. EOUS of the retrobulbar area is also useful for sample-taking and echo-guided biopsies of lesions *in situ* [16].

Eyelid Edema

Eyelid edema occurs frequently in horses and is generally secondary to eye disease or trauma. Eyelids may also be the site of sarcoid neoplasms, abscesses, foreign bodies, and Habronema cysts. EOUS diagnoses the type of lesion and differentiates between infiltrating and diffuse lesions [12] (Figures 24.33; 24.34).

Vet-ebooks.com

Artifacts

A good knowledge of anatomy and ultrasound principles is required when assessing EOUS images, so as not to confuse artifacts with real images [13].

A US artifact is defined as false or distorted information due to echoes that are abnormal for site or intensity. They are usually generated through ultrasound–tissue interactions and may lead to errors in diagnosis if they are not recognized as artifacts. Poor technique, e.g., not using enough gel, etc., is the main cause of artifacts during an ultrasound scan. Here are the three main artifacts that may arise with this technique:

1) *Reverberation*: Artifacts are generated when the ultrasound beam originating in the probe has a perpendicular encounter with a highly echoic anatomic structure like, for example, the crystalline lens. The beam bounces back to the probe to ping-pong back and forth over and over again. Images show a series of echoic bands that decrease in intensity at equal distances from each other.
2) *Absorption*: Artifacts occur mainly with signal attenuation due to its absorption by viscous friction which counteracts ultrasound oscillation. Highly echoic substances like gas or air, which may be found between eyelid and cornea in a transpalpedral scan, or strongly attenuating substances like bone or foreign bodies, muffle or completely reflect the ultrasound signal. The consequent lack of posterior echoes thus creates a posterior acoustic shadow.
3) *Baum's Bump* artifacts, which are observed in a B-mode scan, create the illusion of an uprising Fundus oculi. They develop when the ultrasounds are refracted quickly from the center of the lens toward its periphery [16].

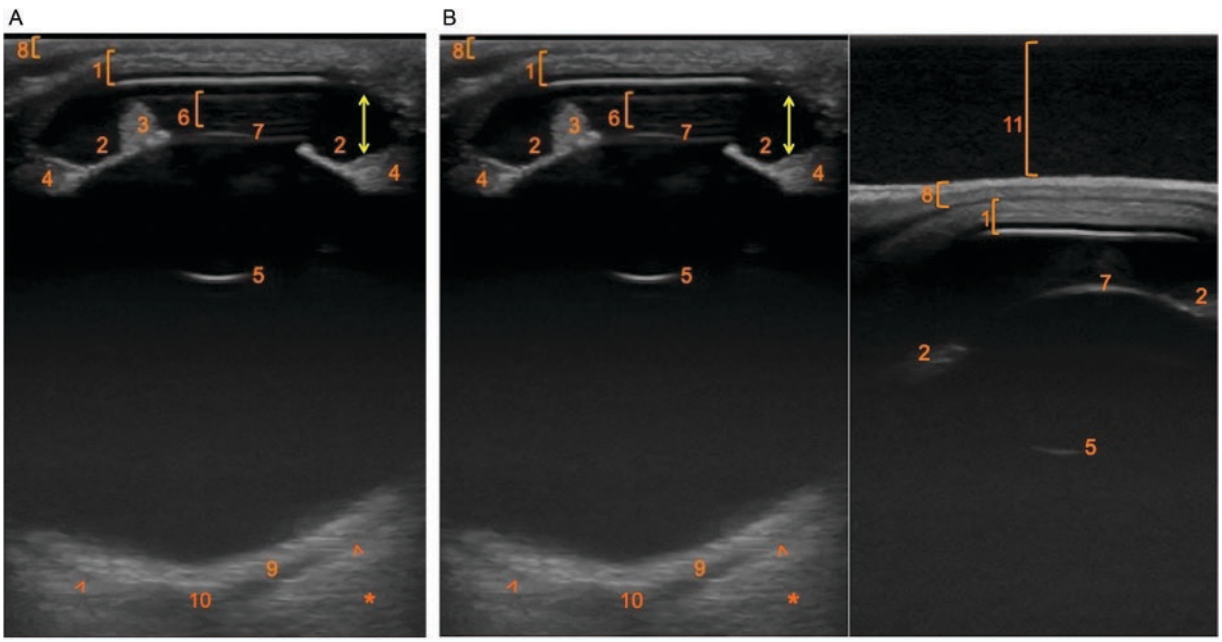


Figure 24.1 Normal eye. (A) This image is a transpalpebral longitudinal scan of a normal eye. The cornea (1) appears uniformly echogenic. The anterior chamber (yellow arrow) appears uniformly anechoic. The iris leaflets (2) appear as echoic linear bands continuous with the ciliary body (4) immediately posterior. The corpora nigra (3) are highly variable in structure and sonographic appearance, but are often seen protruding into the anterior chamber on longitudinal images. Between the iris/ciliary body and the posterior wall of the eye, the only echogenic structures are the portion of the anterior (7) and posterior lens capsule (5) that fall within the primary ultrasound beam. The vitreous is uniformly anechoic. The retina, choroid, and sclera (9) appear in combination as a hyperechoic band defining the posterior aspect of the globe. Reverberation artifacts (6), reduplication, or multiple-signal echoes are commonly seen. These most commonly occur due to lack of ultrasound gel resulting in air becoming trapped between the hairs. 1: Cornea; 2: Iris; 3: Corpora nigra; 4: Ciliary body; 5: Posterior lens capsule; 6: Reverberation artifacts in the anterior chamber; 7: Anterior lens capsule; 8: Eyelid; 9: Retina/choroid; 10: Optic nerve; extraocular muscles (arrowheads); retrobulbar fat (asterick). (B) This image is ultrasound examination of a normal eye with a standoff pad. Ultrasound transducer placement for transpalpebral examination of the equine eye in the horizontal plane with the use of an ultrasound standoff pad (11). The use of the standoff device allows us to make a better evaluation of the most superficial structures such as the eyelids, cornea, and anterior chamber, as can be compared from the previous pictures without a standoff pad. 1: Cornea; 2: Iris; 5: Posterior lens capsule; 7: Anterior lens capsule; 8: Eyelid.

Vet-ebooks.com

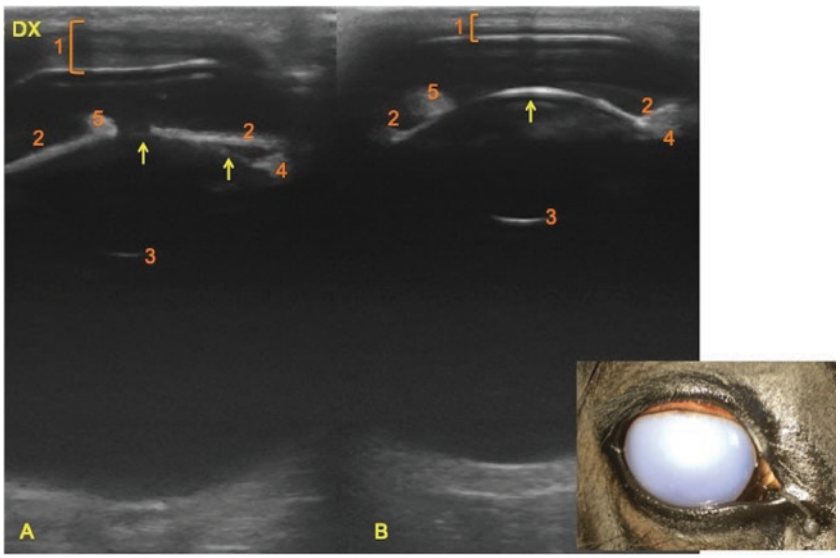


Figure 24.2 Corneal edema. This image is ultrasound scans of both eyes of the same horse. (A) The right eye has corneal edema and (B) the left eye has normal anatomical structures. Corneal edema is visualized in the ultrasound image as well as the picture. The ultrasound shows the increased corneal thickness (A), also in relation to the healthy eye (B). The edema does not allow visualilzation of the rear portions of the eye, but with ultrasound, we can evaluate all the anatomical structures of the eye as well as the structures of the posterior district. Miosis is also observed in the diseased eye (A) compared to the healthy eye (B). 1: Cornea; 2: Iris; 3: Posterior lens capsule; 4: Ciliary body; 5: Corpora nigra; 6: Anterior lens capsule (yellow arrows).

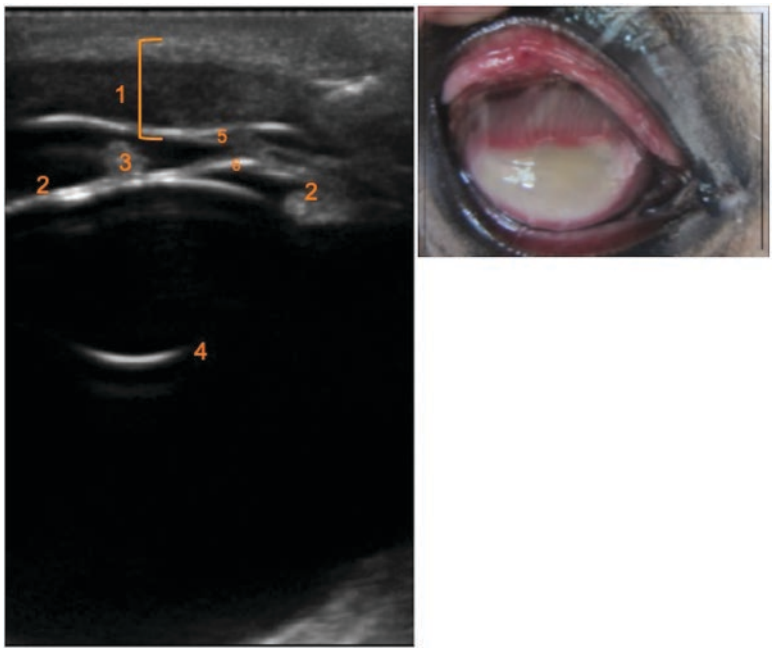


Figure 24.3 Keratitis and stromal abscess. This image is from an 8-year-old quarter horse with keratitis and a stromal abscess. The ultrasound examination allows us to evaluate the structures beyond the cornea which is very thickened and hinders any visual evaluation. The chronicity of the lesion is perceived with the formation of adhesions between iris and cornea (5) and between iris and lens (6) with the pupillary block in miosis. These are important indications for choosing therapy and assessing prognosis. 1: Cornea; 2: Iris; 3: Corpora nigra; 4: Posterior lens capsule; 5: Irido-cornea adhesion; 6: Irido-anterior lens capsule adhesion.

Vet-ebooks.com

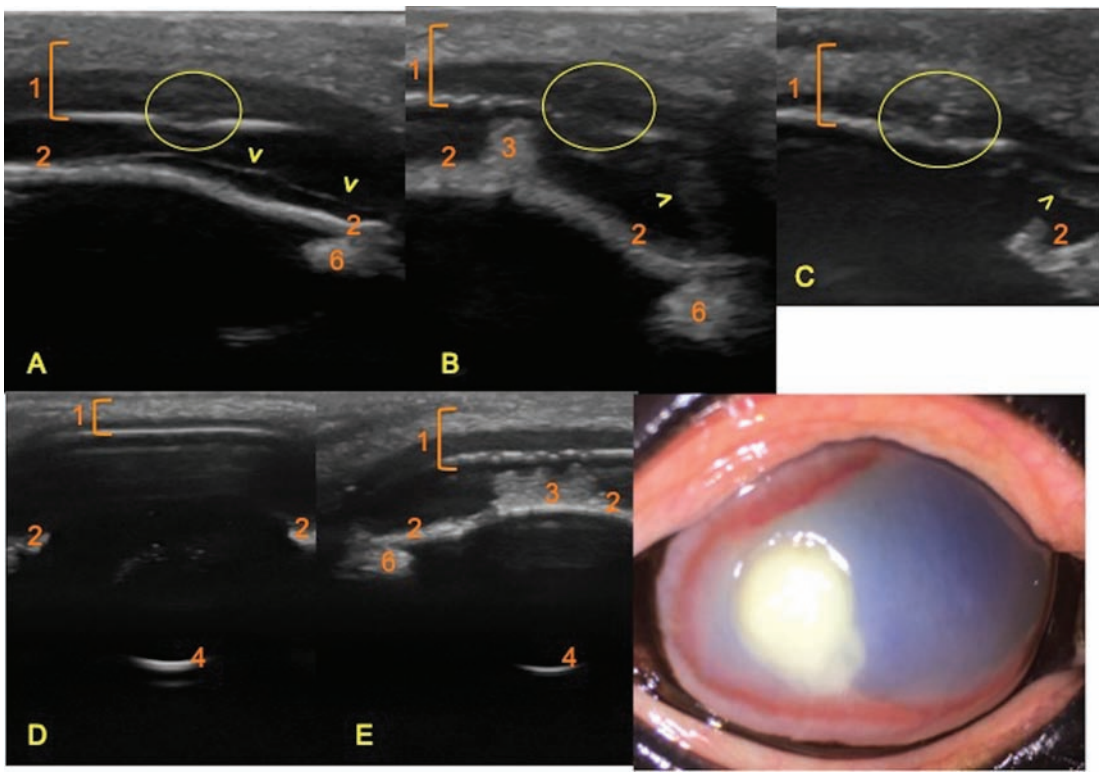


Figure 24.4 Stromal abscess and anterior uvetitis. These images are from a 3-year-old Thoroughbred with a stromal abscess and anterior uveitis. (A, B, and C) The stromal abscess is visible within the yellow circles and exhibits the typical appearance of non-uniform hypoechoic thickening with hyperechoic areas. (D and E) The normal eye (D) and diseased eye (E) are shown together for comparison. The thickening of the cornea (1) is evident in (E). We have the ultrasound of the diseased eye with the ultrasound comparison between the eye with an abscess (E) and the healthy eye (D). This condition is typically accompanied by significant anterior uveitis, which is evidenced here by miosis (A, B, and E) and fibrin within the anterior chamber (yellow arrowheads). In the first three ultrasounds, the effect of cycloplegic therapy with miosis in A) and B) and mydriasis in C) can be evaluated. 1: Cornea; 2: Iris; 3: Corpora nigra; 4: Posterior lens capsule; 5: Fibrin in the anterior chamber; 6:= Ciliary body.

Vet-ebooks.com

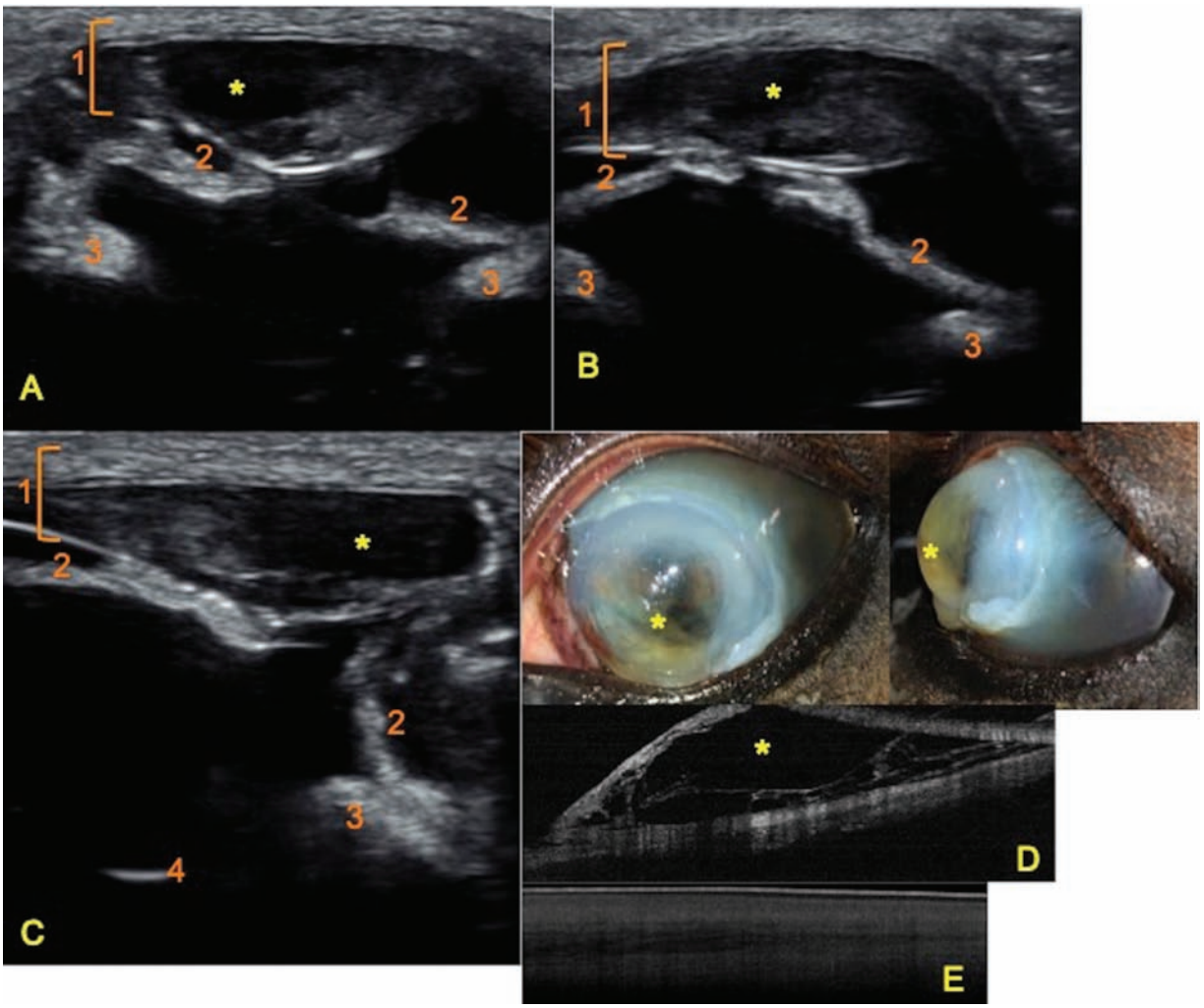


Figure 24.5 Melting ulcer. These images are from a 4-year-old Thoroughbred with an extensive corneal injury and subsequent melting ulcer with prominent cellular infiltrate caused by Staphylococcus spp. Images A, B, and C are the ultrasounds with particular reference to the anterior district, while D and E are images made with Optical Coherence Tomography (OCT) in two different portions of the cornea. Image (E) is OCT where the corneal edema begins and image (D) is where the cornea takes on a bubble-like appearance (yellow asterisk). The cornea is thickened (1) and has large anechoic areas with a bubble-like appearance (yellow asterisk). Volume of the anterior chamber is reduced with pupillary miosis and the iris is in close contact with the cornea. 1: Cornea; 2: Iris; 3: Ciliary body; 4: Lens.

Vet-ebooks.com

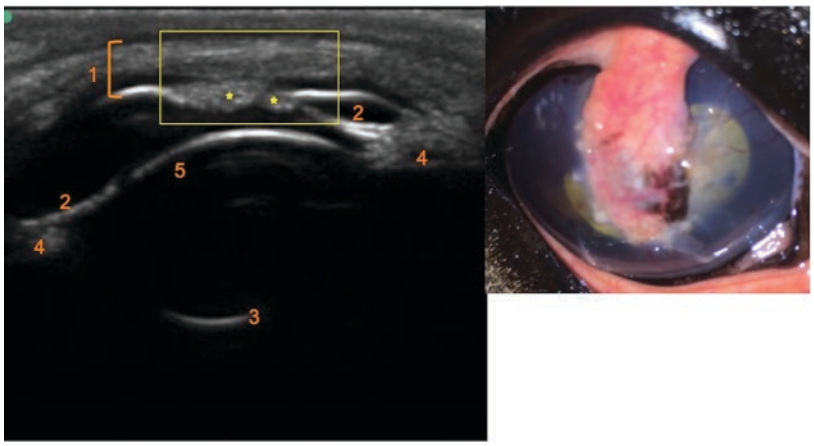


Figure 24.6 Descemetocele. This image is of an eye with severe corneal ulcer and descemetocele and treated with a conjunctival graft. Discontinuity of the corneal endothelium with iris prolapse and adhesion between the iris and cornea (yellow asterisks) is seen within the yellow rectangle. The anterior chamber is still present and the prognosis for vision is good. 1: Cornea; 2: Iris; 3: Posterior lens capsule; 4: Ciliary body; 5: Anterior lens capsule.

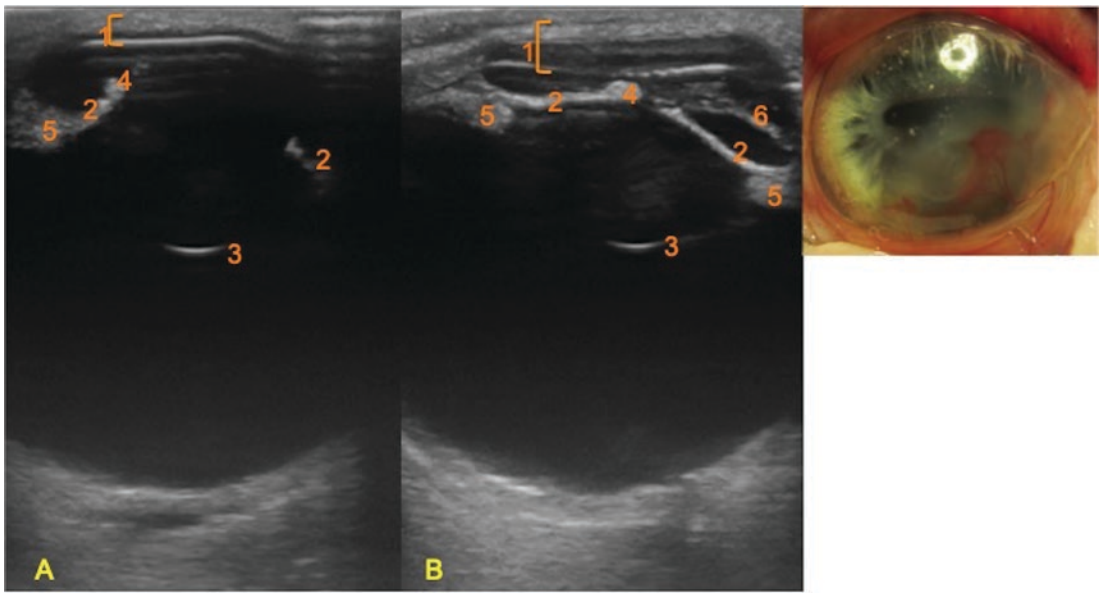


Figure 24.7 Stromal abscess and anterior uveitis. This image is from a 5-year-old Appaloosa horse with a corneal lesion, likely stromal abscess, and anterior uveitis. This is an ultrasound comparison of the normal right eye (A) and the pathological left eye (B). The increased echogenicity within the cornea is the result of a corneal stromal abscess and corresponding edema. This condition is typically accompanied by significant anterior uveitis, which is evidenced here by miosis. Note the thickened cornea (1) and the location of the corpora nigrum (4) and the dependent iris leaflet nearer to the central axis of the eye than usual, and fibrin (6) within the anterior chamber. 1: Cornea; 2: Iris; 3: Posterior lens capsule; 4: Corpora nigra; 5: iliary body; 6: Fibrin in the anterior chamber.

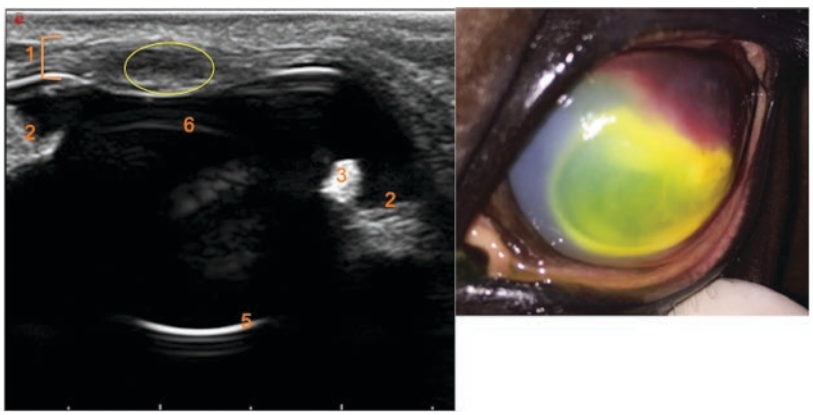


Figure 24.8 Corneal stromal abscess. This image is from a yearling English Thoroughbred with a corneal stromal abscess. The sonogram reveals anechoic to hypoechoic material (yellow circle) forming the corneal stromal abscess. Corneal edema and vascularization made direct visualization of the abscess difficult. From the ultrasound, it is possible to evaluate the condition of the pupil. The pupil is mydriatic due to treatment with cycloplegic drugs. 1: Cornea; 2: Iris; 3: Corpora nigra; 4: Posterior lens capsule; 5: Anterior lens capsule.

Vet-ebooks.com

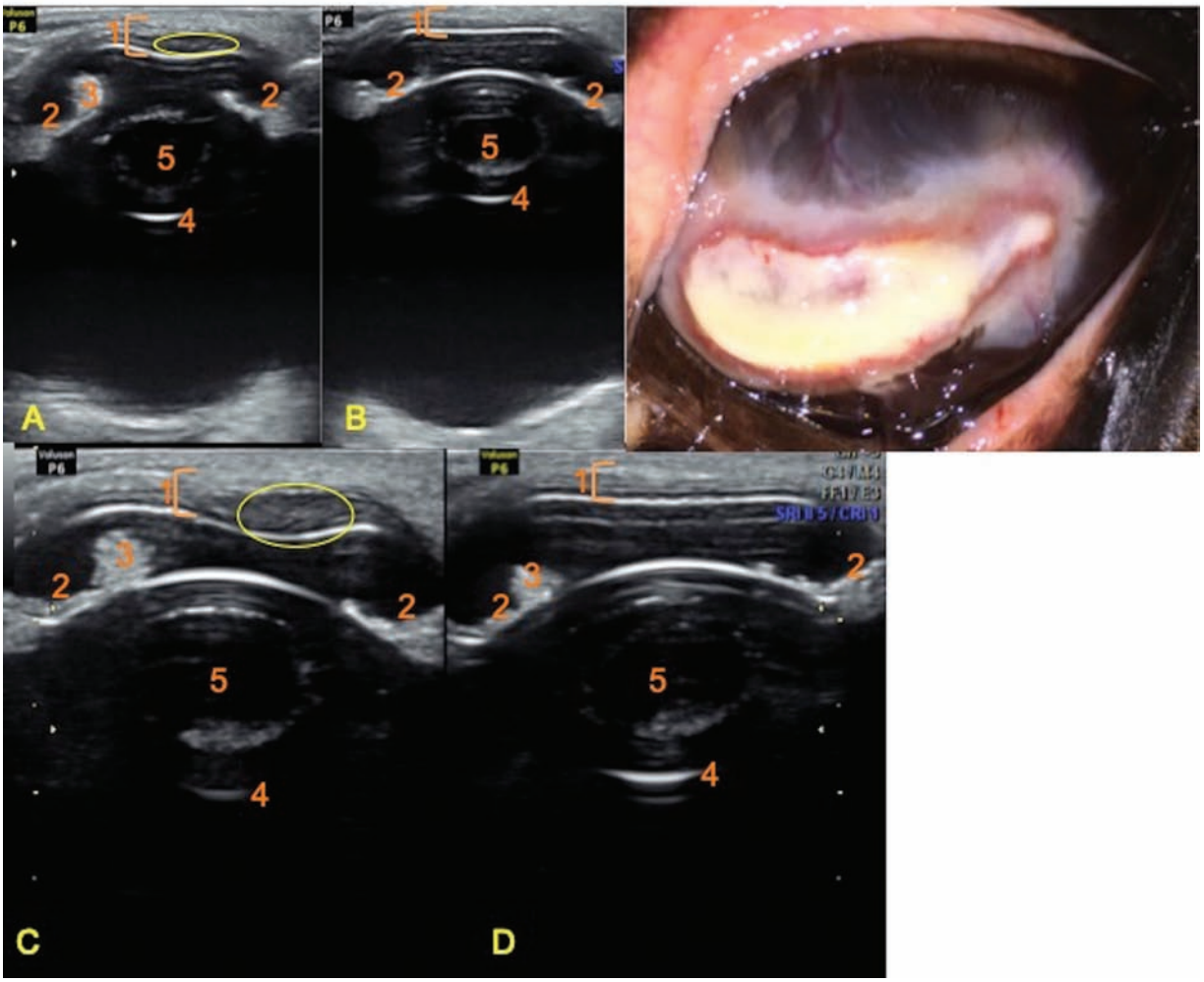


Figure 24.9 Stromal corneal lesion. This image is from a 23-year-old Maremmano with an extensive stromal corneal lesion. The lesion is a fungal plaque with yellow cellular infiltrate beneath the plaque and red vascularization at the edge of the plaque. The images show side-by-side comparison of the pathological left eye (A and C) and normal right eye (B and D). In A) and B), we performed ultrasound trans-eyelid over the entire eyeball to assess any reduction or alteration of the globe into the vitreous cavity. In C) and D), the scan is more superficial to better evaluate the anterior districts. Senile immature cortical cataract (5) are seen in both eyes. Note the corneal thickening with hypoechogenicity of the stroma. 1: Cornea; 2: Iris; 3: Corpora nigra; 4: Posterior lens capsule; 5: Lens.

Vet-ebooks.com

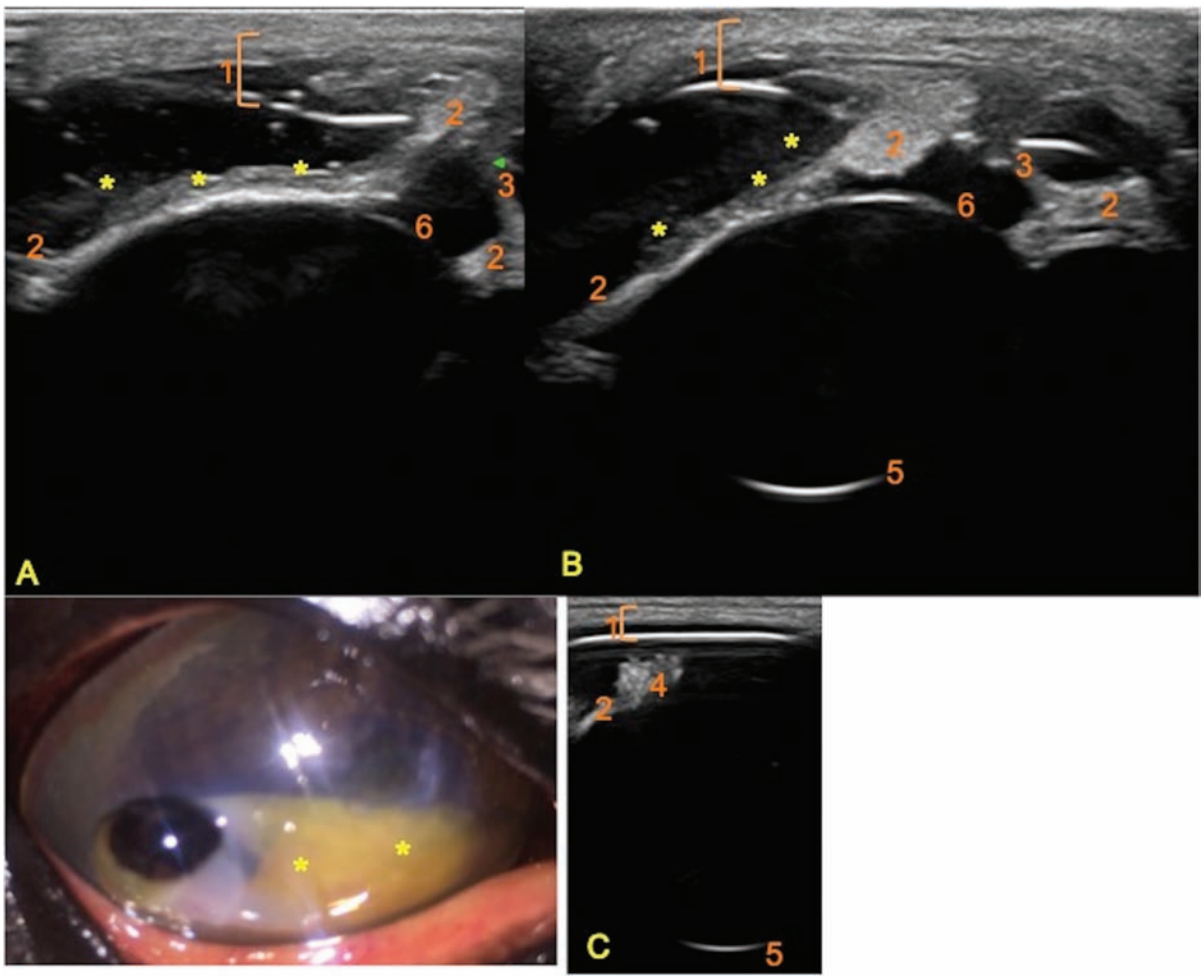


Figure 24.10 Perforated corenal ulcer and iris prolapse. This image is from an 11-year-old horse with a perforated corneal ulcer and iris prolapse. The images show ultrasound comparison between the eyes of the same horse, one with corneal perforation (A and B) and the other normal (C). An increase in corneal thickness with a corneal discontinuity (1) can be noted. The penetration of the iris into the cornea with adhesions between iris and cornea is evident (2,3). Hyperechoic filaments into the anterior chamber (yellow asterisks) are deposits of fibrin (anterior synechiae). 1: Cornea; 2: Iris; 3: Adhesion/fibrin between the iris and cornea; 4: Corpora nigra; 5: Posterior lens capsule; 6: Anterior lens capsule.

Vet-ebooks.com

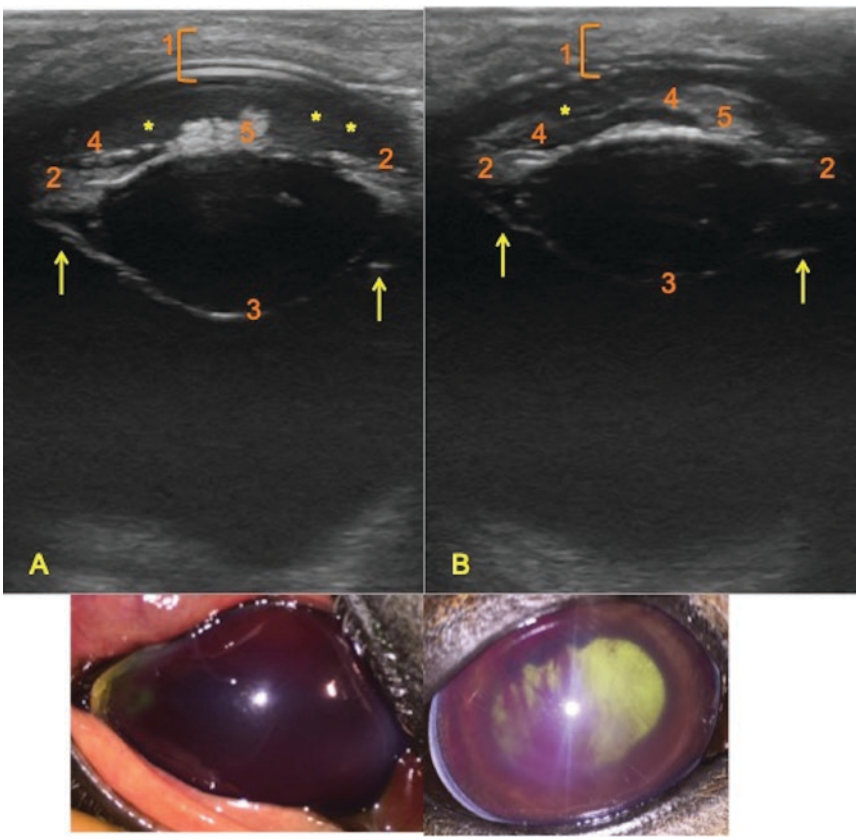


Figure 24.11 Hyphema. This image is the left eye of a 7-year-old polo horse who suffered blunt trauma. Fibrin and hyphema are seen in the anterior chamber. The images are immediately following the blunt trauma (A) and after 6 days of therapy (B). The anterior chamber is filled with hypoechoic material which is consistent with hyphema (yellow asterisks), and thin hyperechoic material represents fibrin (4). The thin hyperechoic lines in the vitreal chamber (yellow arrows) represent the presence of inflammatory vitreal debris. Note the changes detected by ultrasonography after 6 days of treatment. The amount of free blood (yellow asterisks) in the anterior chamber is reduced and fibrin (4) is increased. The corpora nigra (5) changes from pupillary miosis to that of mydriasis. 1: Cornea; 2: Iris; 3: Posterior lens capsule; 4: Fibrin in the anterior chamber; 5: Corpora nigra.

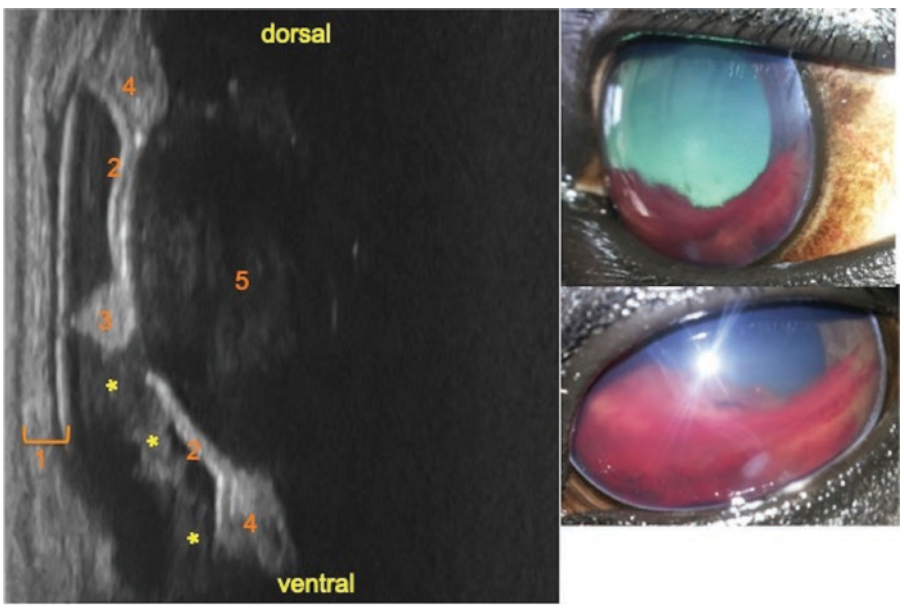


Figure 24.12 Hyphema. This image is from a 7-year-old Friesian horse with hyphema in an anterior chamber following recent ocular trauma. The image is transpalpebral sonogram in horizontal or transverse scan orientation. In this scan, the coagulated blood is in the ventral part of the eye due to gravity (yellow asterisks). 1: Cornea; 2: Iris; 3: Corpora nigra; 4: Ciliary body; 5: Lens.

Vet-ebooks.com

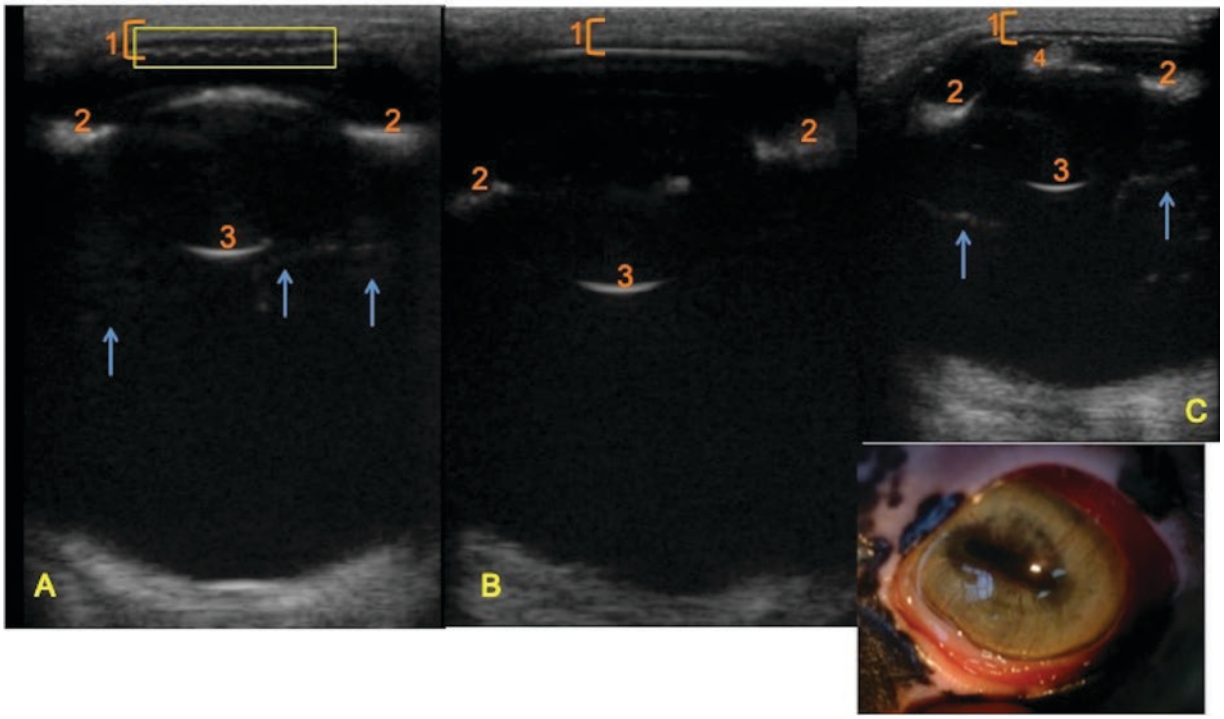


Figure 24.13 Anterior uveitis. This image is from an 8-year-old paint mare with unilateral anterior uveitis. These images are a comparison of a normal eye (B) and an eye with uveitis (A and C). Hypoechoic material is within the posterior chambers (blue arrows) in the horse with uveitis. The hypoechoic material within the posterior chamber is inflammatory debris, probably fibrin or vitreous degeneration, that is typical in anterior uveitis. The lens is normal in position and shows no signs of cataracts. The cornea is irregular as evidenced in the yellow rectangle. These are typical signs of keratitis and anterior uveitis. 1: Cornea; 2: Iris; 3: Posterior lens capsule; 4: Corpora nigra.

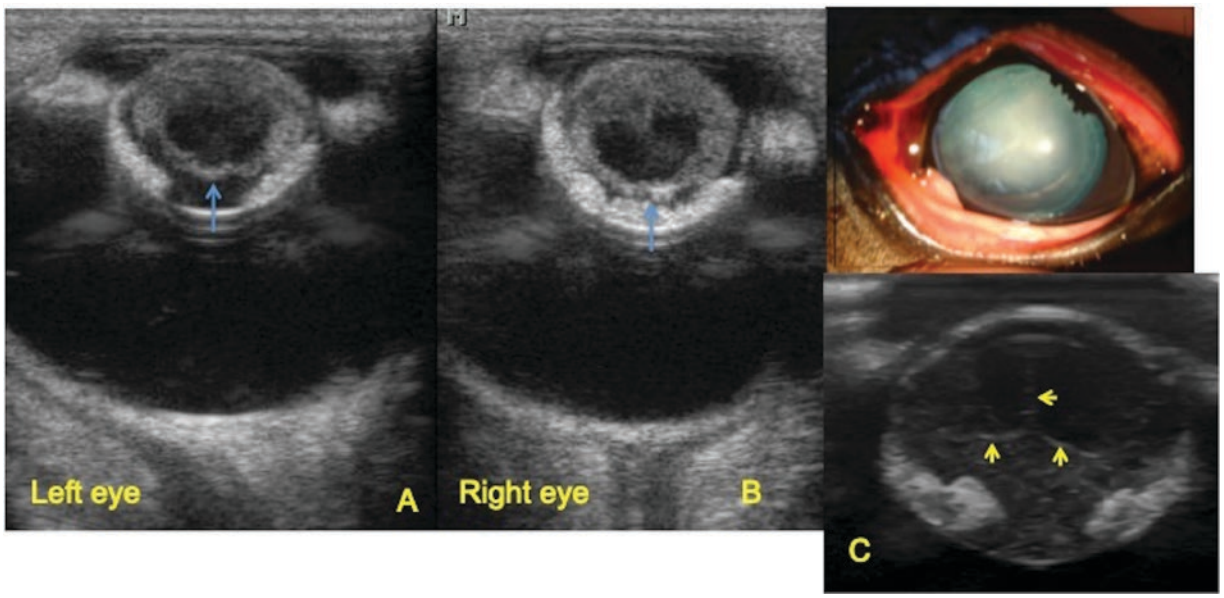


Figure 24.14 Congenital cataracts. (A and B) These images are from a 3-month-old foal with bilateral congenital immature cataracts. The blue arrows indicate cortical sclerosis of the lens. A hyperechoic thickening in the region of the lens cortex is a cataract. In a normal eye, only the anterior and posterior lens capsule should generate hyperechoic margins. (C) This image is from a 2-month-old foal. Lens sclerosis is less than images A and B. The suture lines of the lens to Ypsilon (yellow arrows) are visible. Both foals have alterations except for the lens which is the ideal condition for phacoemulsification surgery.

Vet-ebooks.com

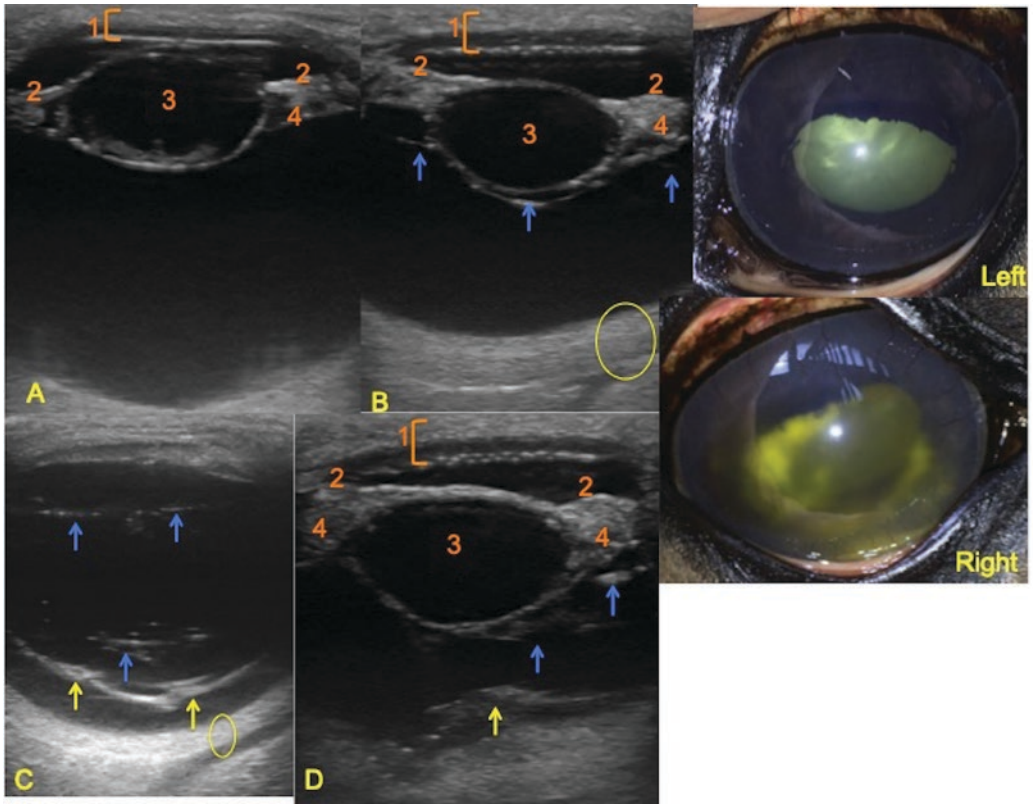


Figure 24.15 Cataracts and uveitis. These images are from a 5-month-old foal with bilateral cataracts and uveitis. Images from the left (A and C) and right (B and D) eye are shown for comparison. The right eyeball (B) is smaller than the left eyeball. (A) An apparent opacity of the lens related to hyperechoic anterior and posterior lens capsule is visible around the hypoechoic center of the lens, indicatings signs of immature bilateral cataracts. The ciliary bodies (4) appear thickened. In the vitreous humor, are vitreal opacities (yellow arrows): mobile, linear, or point-like hyperechoic areas not continuous with the fundus. The yellow circle shows the hyperechoic choroid/retina and is very thickened, especially in the right eye. (B) Hypoechoic material is present within the posterior chamber and is probably fibrin and vitreal degeneration (blue arrows). Although these cataracts are in a young foal, they are not simple congenital cataracts, but associated with uveitis; therefore, phacoemulsification surgery has a very poor prognosis for resolution. 1: Cornea; 2: Iris; 3: Posterior lens capsule.

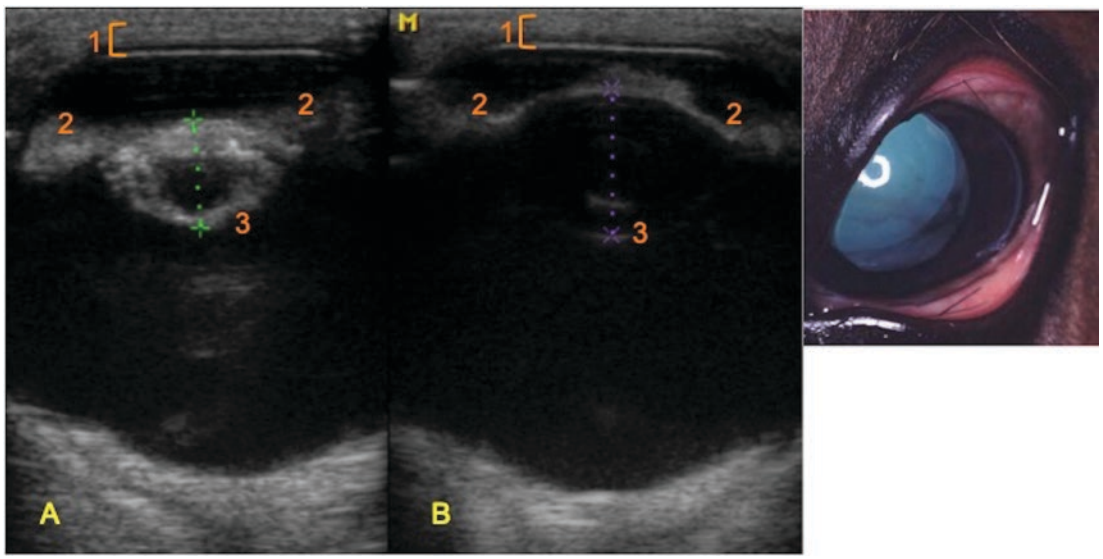


Figure 24.16 Microphakia. This image is from a 3-year-old Standardbred horse with a microphakia. An ultrasound comparison of the two eyes of the same horse shows a cataract in left eye (A) and a normal right eye (B). The left eye (A) has increased echogenicity of the lenticular fibers representing a cataract. In comparison with the right eye (B), note this is not a simple cataract in the right eye (B), but a reduction in the volume of the lens indicating microphakia or ventral lens coloboma with cataracts. The ultrasound examination is very important to differentiate this lesion from lens luxation. 1: Cornea; 2: Iris; 3: Posterior lens capsule.

Vet-ebooks.com

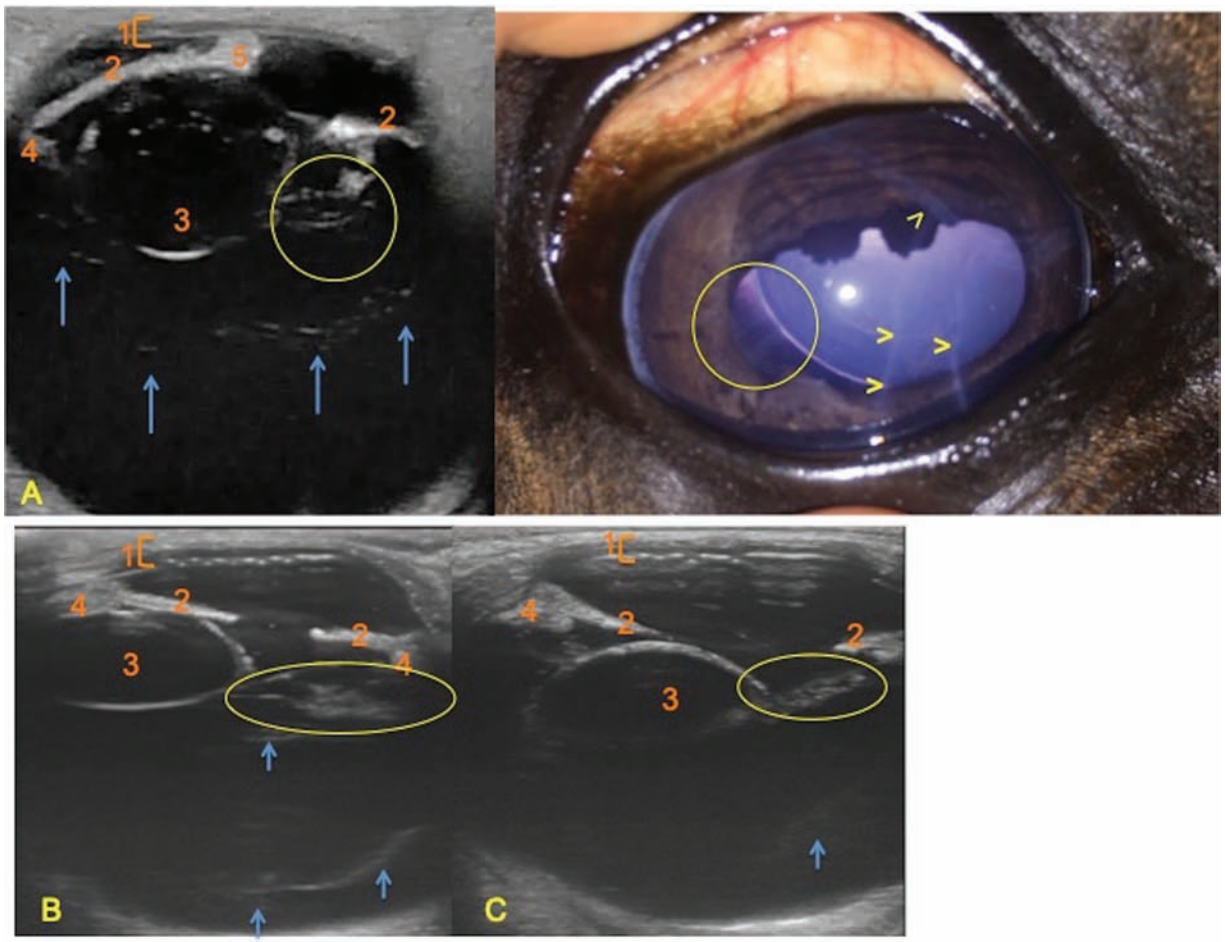


Figure 24.17 Medial lens subluxation. This image is from a 15-year-old horse with medial lens subluxation. Note the lack of zonular attachments along the lateral border (yellow circles) of the lens. Posterior lens subluxation, mild corneal edema, and keratitis with irregular cornea are present. Hyperechoic structure (blue arrow) represent vitreal debris, likely fibrin, and vitreal degeneration. The lens has thickening hyperechoic signs of immature cataracts. This horse was diagnosed with secondary glaucoma associated with lens instability, confirmed by the presence of multiple Haab's striae, evident in the photo of the eye (yellow head arrows). 1: Cornea; 2: Iris; 3: Lens; 4: Ciliary body; 5: Corpora nigra.

Vet-ebooks.com

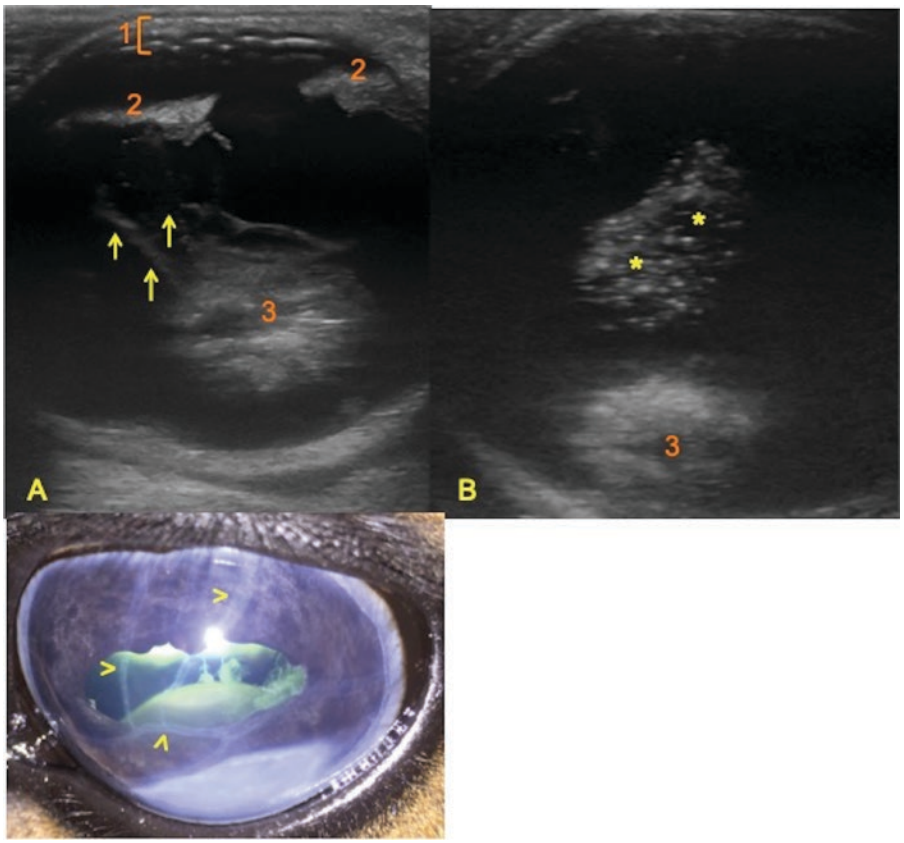


Figure 24.18 Posterior lens luxation. This image is from a 13-years-old Hannover horse with posterior lens luxation. The hyperechoic cataractous lens (3) has torn from its zonular attachments (yellow arrows) and is displaced into the posterior segment. The iris leaflets are prominent, anterior to the displaced lens. The asterisks indicate the presence of inflammatory debris in the vitreous appearing as hyperechoic material in the posterior segment. This lesion is vitreal degeneration secondary to chronic uveitis (ERU). Chronic uveitis with instability of the lens creating changes in intra-ocular pressure is suggested by the presence of Haab's striae (yellow arrowheads). 1: Cornea; 2: Iris; 3: Lens.

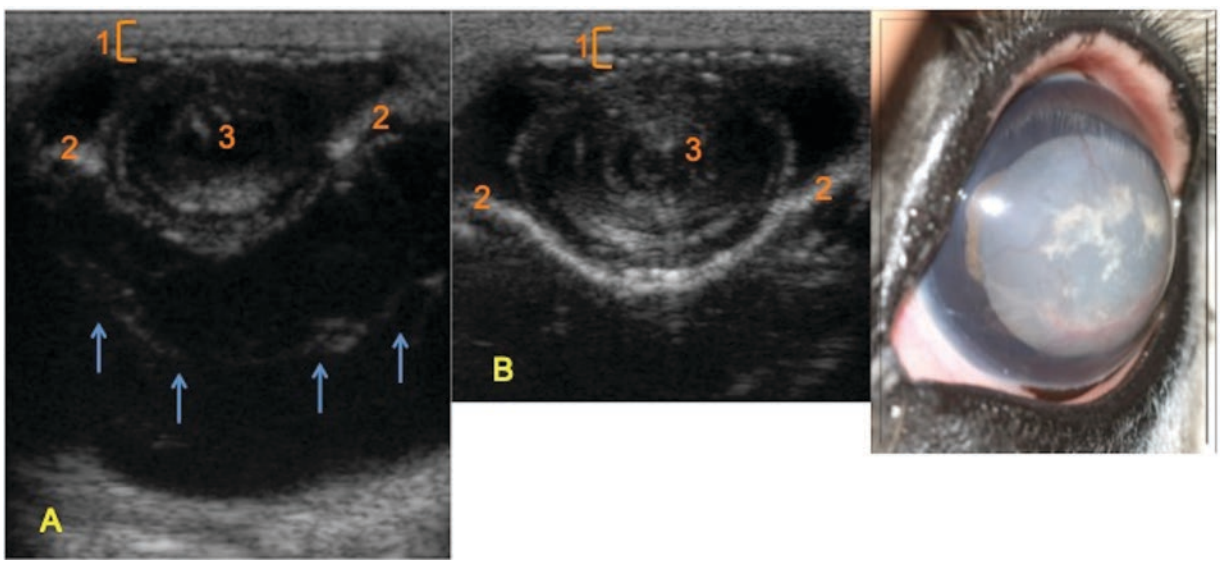


Figure 24.19 Anterior lens luxation. This image is from a 9-year-old Lipizzaner Horse with lens luxation into the anterior chamber. Keratitis is present from corneal irregularity (A and B), due to contact of the lens to the corneal endothelium. The lens has a mature cataract highlighted by the hyperechogenicity of the lenticular fibers involving nuclear and cortical. Vitreal debris (blue arrows) is fibrin and vitreal degeneration. 1: Cornea; 2: Iris; 3: Lens.

Vet-ebooks.com

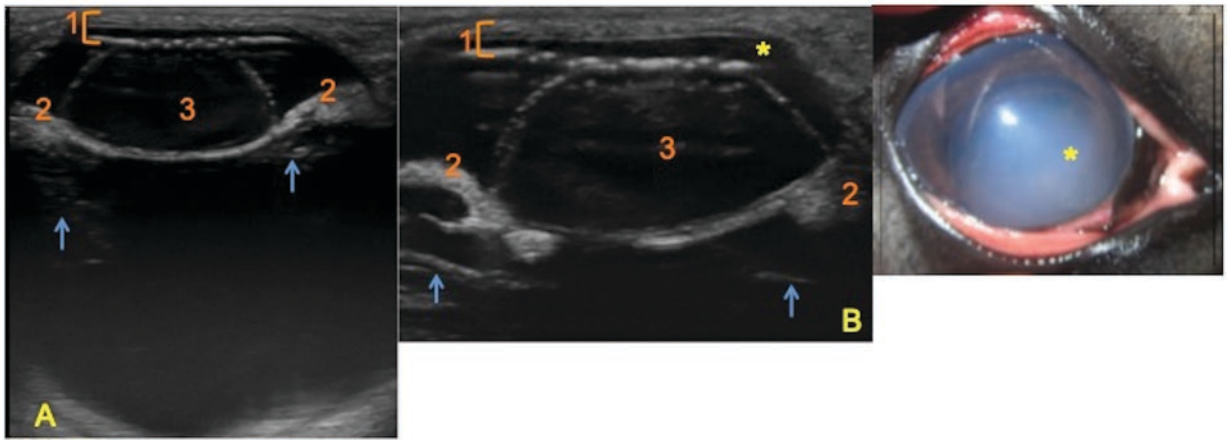


Figure 24.20 Anterior lens luxation. This image is from an 18-year-old Arabian stallion with anterior lens luxation. Note the position of the lens within the anterior chamber in front of the iris. The hyperechoic strands behind the iris (blue arrows) represent vitreal debris, likely fibrin, and vitreal degeneration. There is slight corneal edema (yellow asterisk) characterized by corneal discontinuity. The hyperechoic line which delimits the lens shows a slight opacity of the anterior and posterior capsule. There are no cataract changes in nuclear and cortical. 1: Cornea; 2: Iris; 3: Lens.

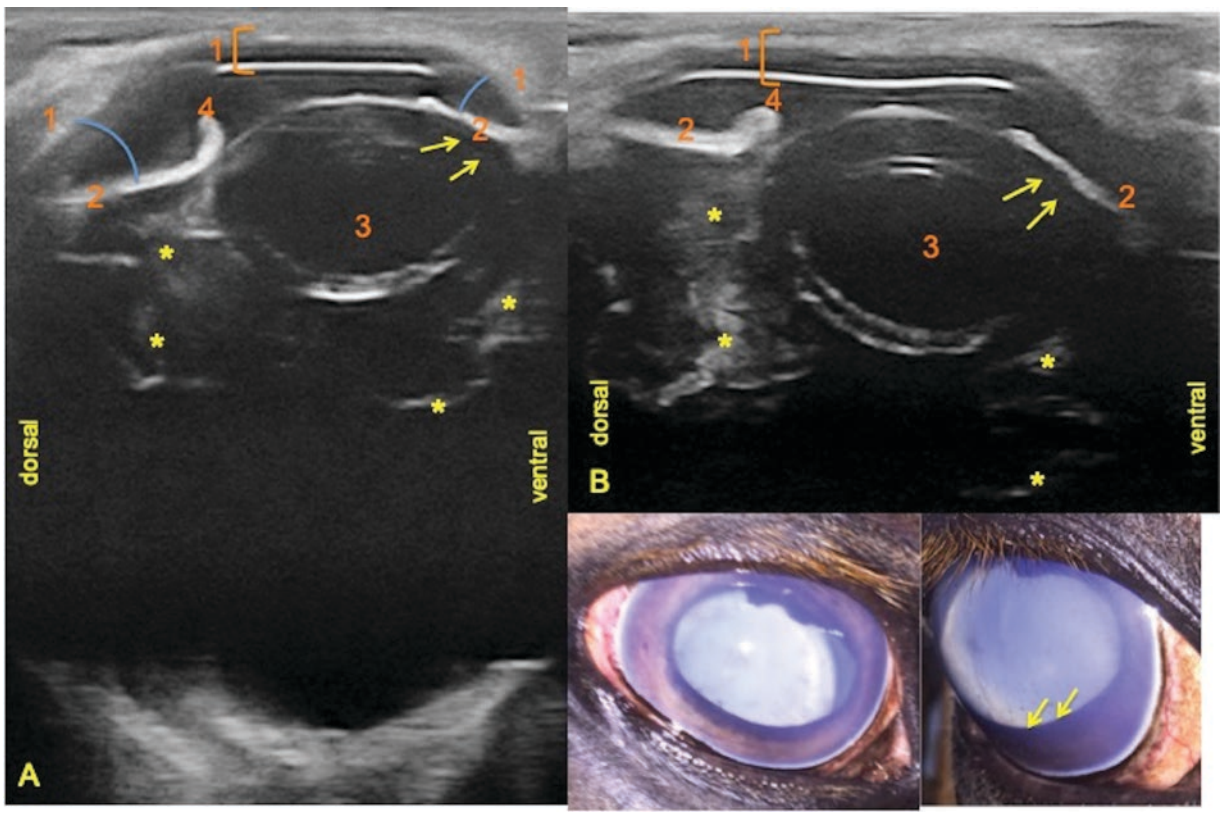


Figure 24.21 ERU and glaucoma, This image is from a 12-year-old show jumping horse with acute corneal edema. This horse has superior subluxation from trauma or associated with chronic equine recurrent uveitis (ERU) and secondary glaucoma. Although the cornea is diffusely edematous, the edge of the lens is readily identified during direct retro-illumination, but with ultrasound examination, many other things are visible. Through transpalpebral ultrasound examination with the probe in the horizontal or transverse scan orientation, ventral displacement of the lens, following the direction of the yellow arrows in (A) and (B) is evident. The lens displacement ventrally causes a closure of the angular aqueous plexus due to the lens being pushed onto the iris. This condition reduces the drift of the aqueous humor due to glaucoma. A large space exists between the cornea and iris dorsally, while this space is reduced ventrally (yellow arrows). Vitreal opacities (yellow asterisks) in the vitreous humor are mobile, linear, or point-like hyperechoic areas not continuous with the fundus. The central part of the lens shows some areas characterized by increased echogenicity. The anterior and posterior lens cortices have cataractous changes. A cortical cataract (3) is visualized. 1: Cornea; 2: Iris; 3: lens; 4: Corpora nigra.

Vet-ebooks.com

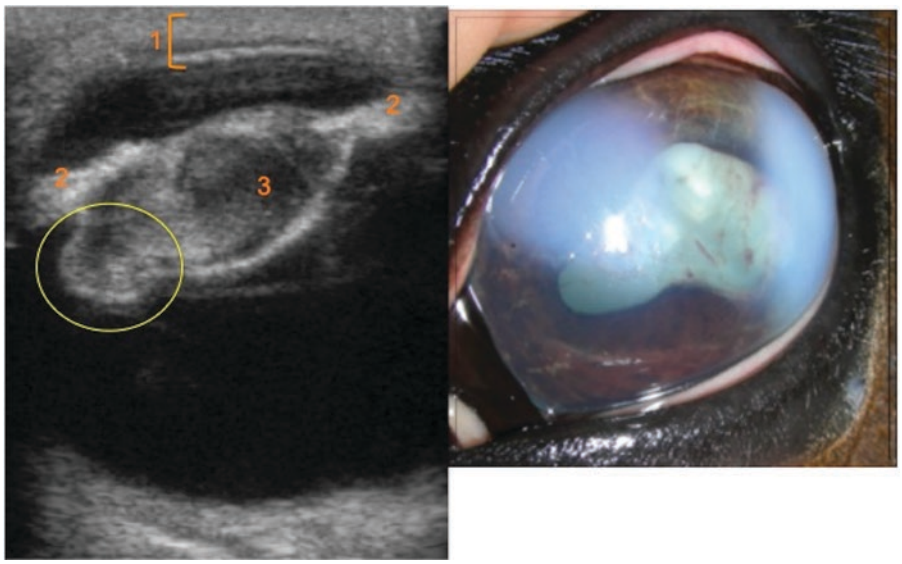


Figure 24.22 Rupture lens capsule. This image is from a 13-year-old mare showing rupture of the lens capsule. From the image, the lens cortex can be seen protruding into the anterior chamber ventrally. (A) A uveitic cataractous lens with rupture of the posterior capsule (yellow circle is present. The rupture was characterized ultrasonographically by a discontinuity of the lens capsule with echogenic material in the surrounding aqueous humor or vitreous, resulting in exposure of intra-lenticular antigen and phacoclastic uveitis. 1: Cornea; 2: Iris; 3: Lens.

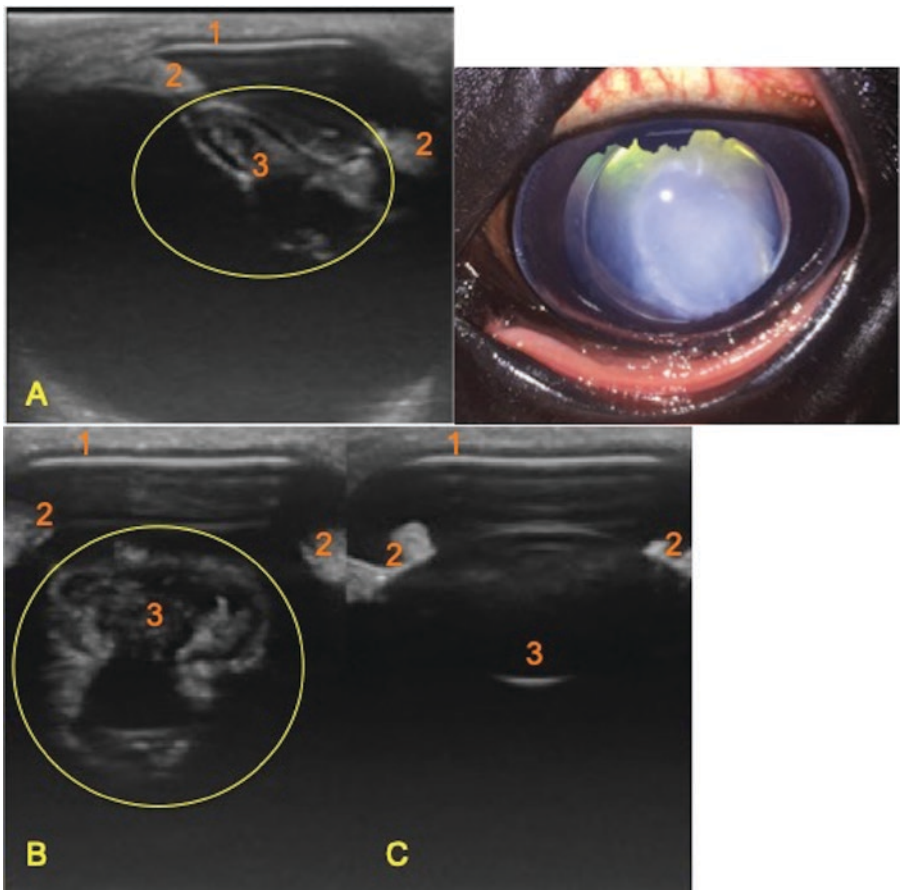


Figure 24.23 Posterior lens capsule rupture. These images are from a yearling with posterior lens capsule rupture in the left eye. Images are shown with the probe oriented in the horizontal or transverse direction (A) and longitudinal or sagittal scan direction (B). (C) is comparison with the contralateral right eye which is normal. A cataract was noted in the lens and the integrity of the posterior lens capsule was compromised, consistent with a capsular rupture, resulting in the echogenic lens material dispersed in the vitreous. 1: Cornea; 2: Iris; 3: Lens.

Vet-ebooks.com

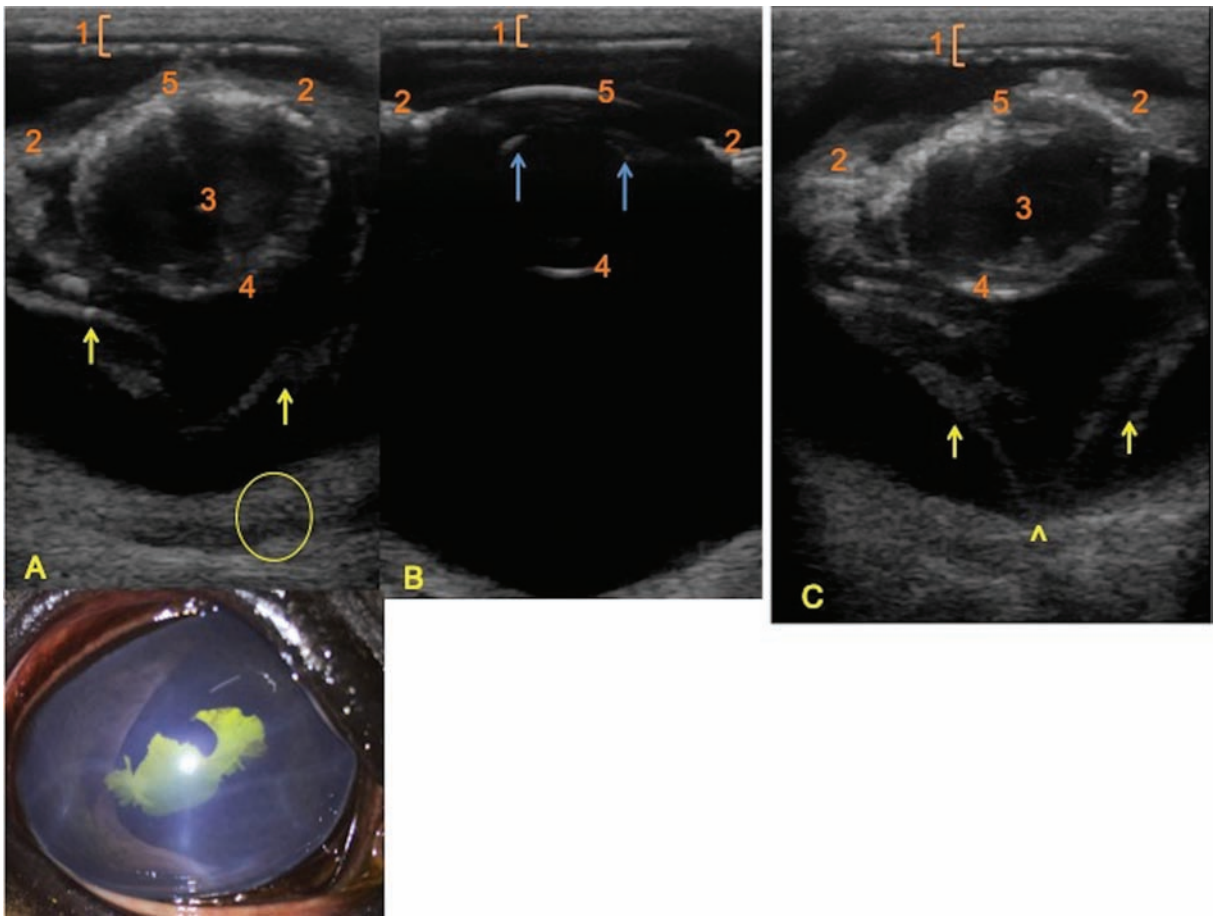


Figure 24.24 Equine recurrent uveitis and retinal detachment. These images are from a 10-year-old Quarter Horse with equine recurrent uveitis (ERU) and retinal detachment. The right eye (A) and left eye (B) are shown in a horizontal scan and the right eye (C) is shown in a transverse scan. The right eyeball is visibly smaller than the left eyeball (Phthisis bulbs). Adhesions are seen between the iris and the anterior lens capsule. Mild corneal edema is characterized by the discontinuity of the cornea in (A) and (C). Diffuse, immature, anterior, and posterior cortical cataracts are seen in (A) and (C). A slight cortical opacity of the lens (blue arrow) is seen in the healthy eye (B). In the vitreous chamber, hyperechogenic curvilinear structures (yellow arrows) indicate retinal detachment. Retinal detachment appears as the classic "seagull sign" with the wings representing the retina. Note that the retina remains attached at the level of the optic nerve head (yellow arrowhead). The region of the choroid-sclera (yellow circle) appears very thickened, consistent with posterior uveitis. 1: Cornea; 2: Iris; 3: Lens; 4: Posterior lens capsule; 5: Anterior lens capsule.

Vet-ebooks.com

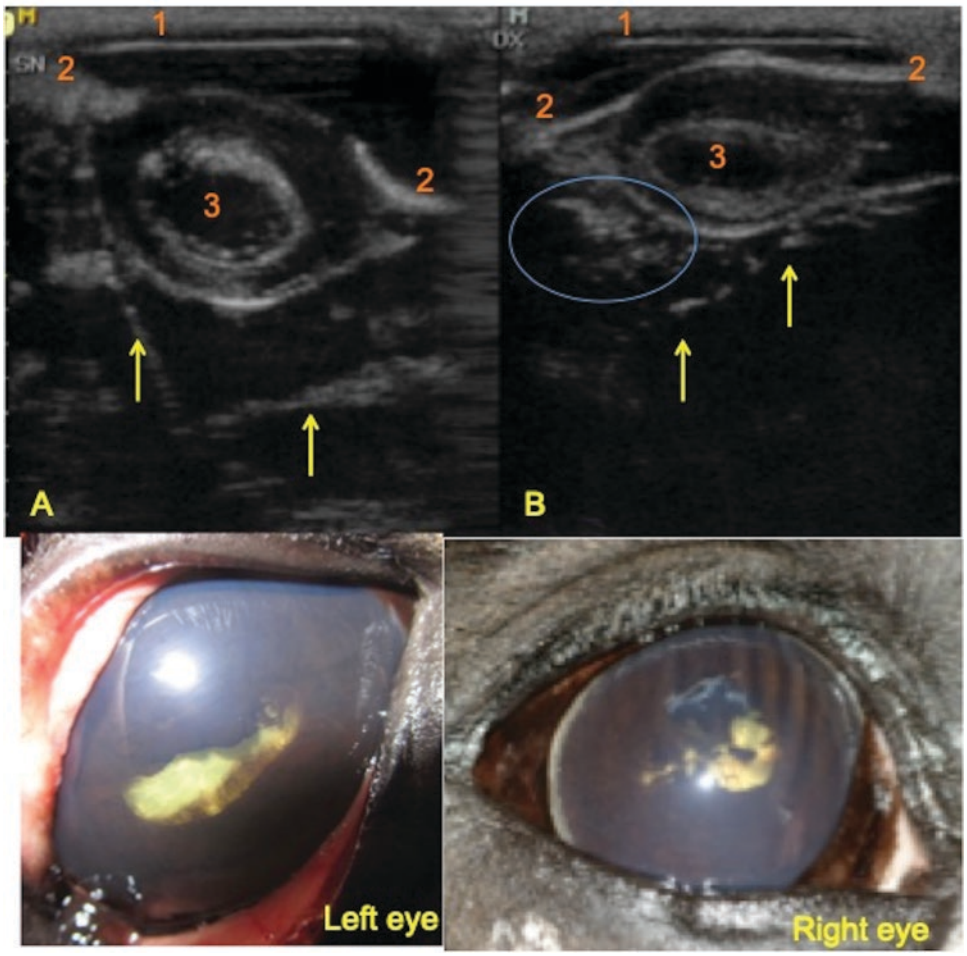


Figure 24.25 Bilateral cataract with retinal detachment. These images are from a 17-year-old appaloosa with blindness due to episodes of equine recurrent uveitis (ERU). The horse has bilateral cataract with retinal detachment. Ultrasound of the left eye (A) and of the right eye (B) are shown. The increased echogenicity of the lenticular fibers represents cataracts. The thin, hyperechoic lines in the vitreal chamber (yellow arrows) represent a complete retinal detachment. Inflammatory debris is in posterior chambers (blue circles). 1: Cornea; 2: Iris; 3: Lens.

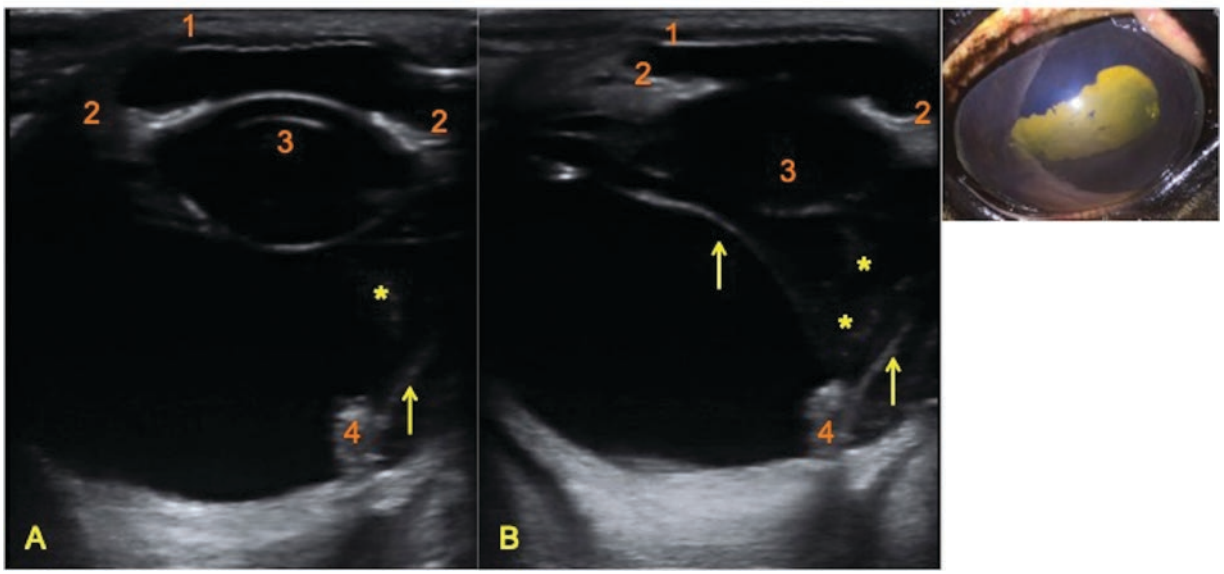


Figure 24.26 Retinal detachment. These images are from a 5-year-old female trotter with partial retinal detachment. In the vitreous humor, vitreal opacities are mobile, and linear or point-like hyperechoic areas not continuous with the fundus (yellow asterisks). Hyperechoic globosity that continues with a thin line, prolapsed into the vitreous is a partial retinal detachment. 1: Cornea; 2: Iris; 3: Lens; 4: Retinal.

Vet-ebooks.com

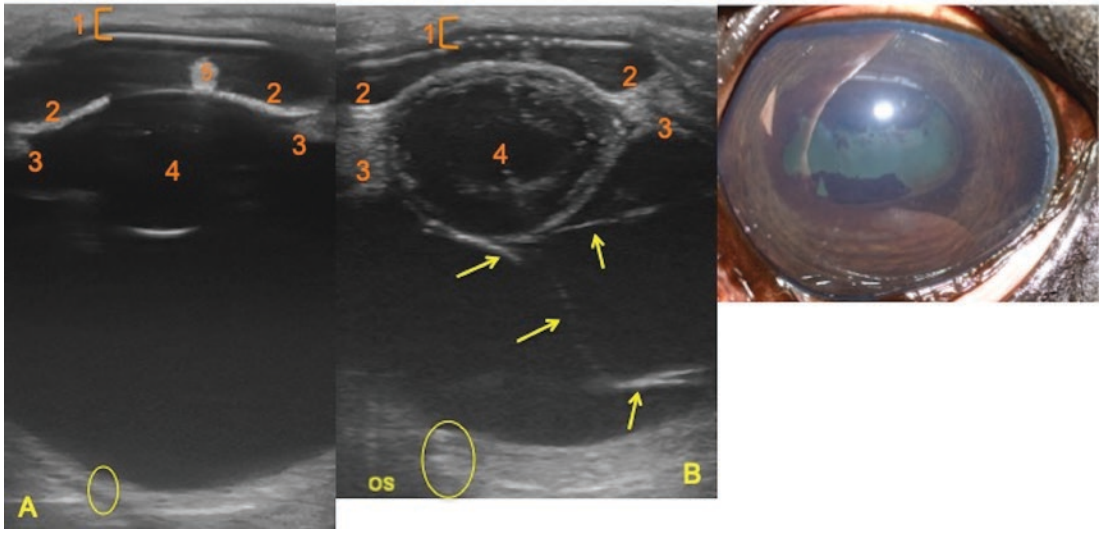


Figure 24.27 Equine recurrent uveitis. These images are from a 23-year-old Arabian horse with equine recurrent uveitis (ERU) cataract and adhesions of the anterior capsule of lens and iris. Ultrasound comparison between the normal right eye (A) and left eye (B) with uveitis demonstrates the reduction of volume of the left eyeball with respect to the right one. The lens of the left eye (B) shows a modification of size and shape associated with an irregularity of the crystalloid surface. Also seen is an increase in the echogenicity of the lens, an immature cataract. This is an immature capsular cataract with lens capsular-iris adhesions. Chronic uveitis with corpora nigra atrophy is evident in the ultrasound comparison between images (A) and (B). Hypertrophy of ciliary bodies in the eye with uveitis (B) compared to a normal eye (A) is seen. In the posterior segment, vitreal opacities (yellow circle) are seen as mobile, linear, or point-like hyperechoic areas not continuous with the fundus. Remarkable chorion-retinal thickening typical of ERU (yellow circle) is seen. 1: Cornea; 2: Iris; 3: Ciliary body; 4: lens; 5: Corpora nigra.

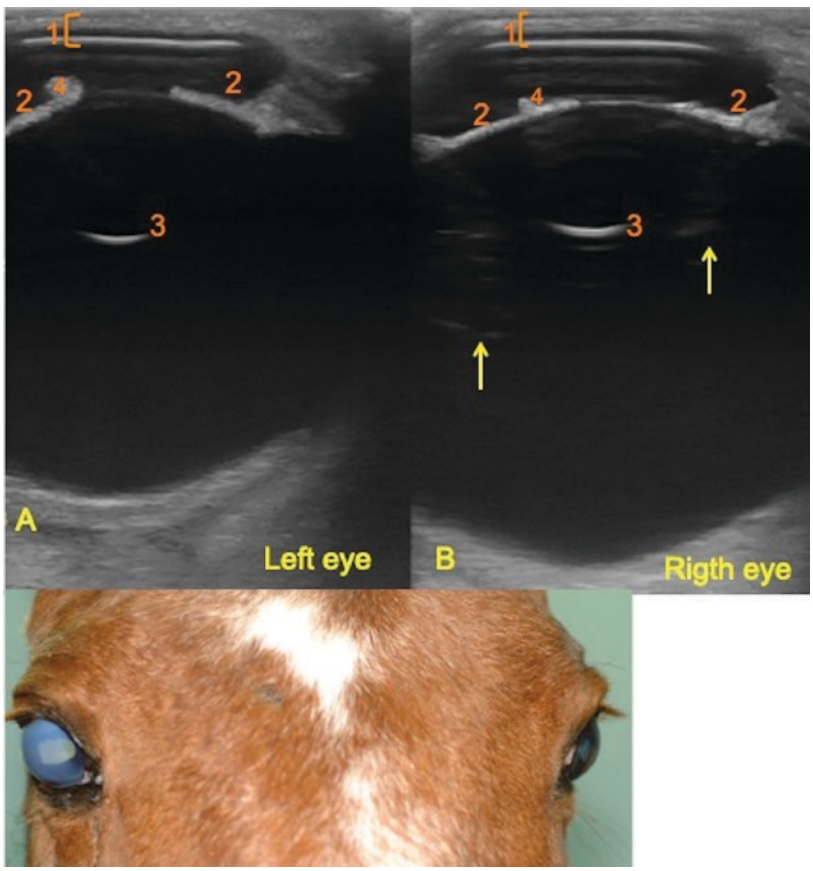


Figure 24.28 Glaucoma. These images are from a 7-year-old gelding with acute corneal edema. This horse had chronic glaucoma with diffuse corneal edema and mydriasis. Ultrasound comparison between normal eye (A) and pathological eye (B) demonstrates the increased size of the right eyeball (B). Vitreous debris (yellow arrows) is present. Equine glaucoma most commonly occurs secondary to a predisposing cause, typically chronic intraocular inflammation as seen with equine recurrent uveitis (ERU). 1: Cornea; 2: Iris; 3: Posterior lens capsule; 4: Corpora nigra.

Vet-ebooks.com

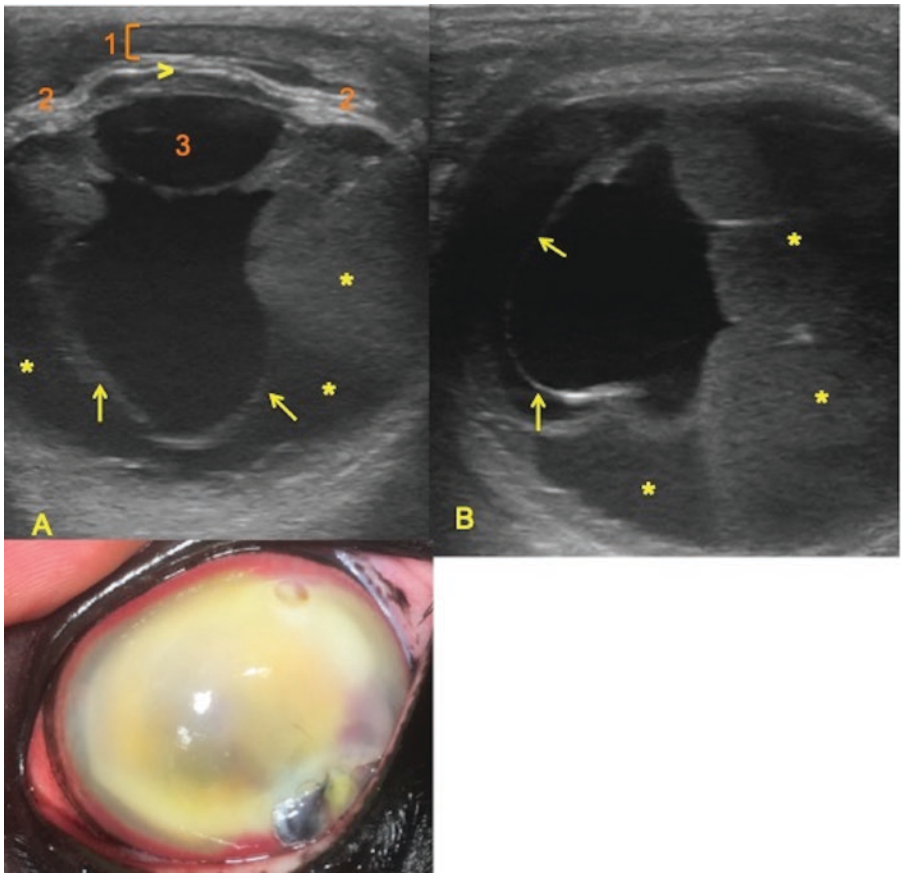


Figure 24.29 Blunt Trauma. These images are transpalpebral sonograms obtained from a 6-year-old Standardbred with recent severe ocular blunt trauma. The blunt trauma caused extensive intraocular injury, including retinal detachment (yellow arrows), the classic "seagull sign," choroidal rupture with intraocular hemorrhage (yellow asterisks). Uveal tissue (yellow arrowhead) is thickened. 1: Cornea; 2: Iris; 3: Lens.

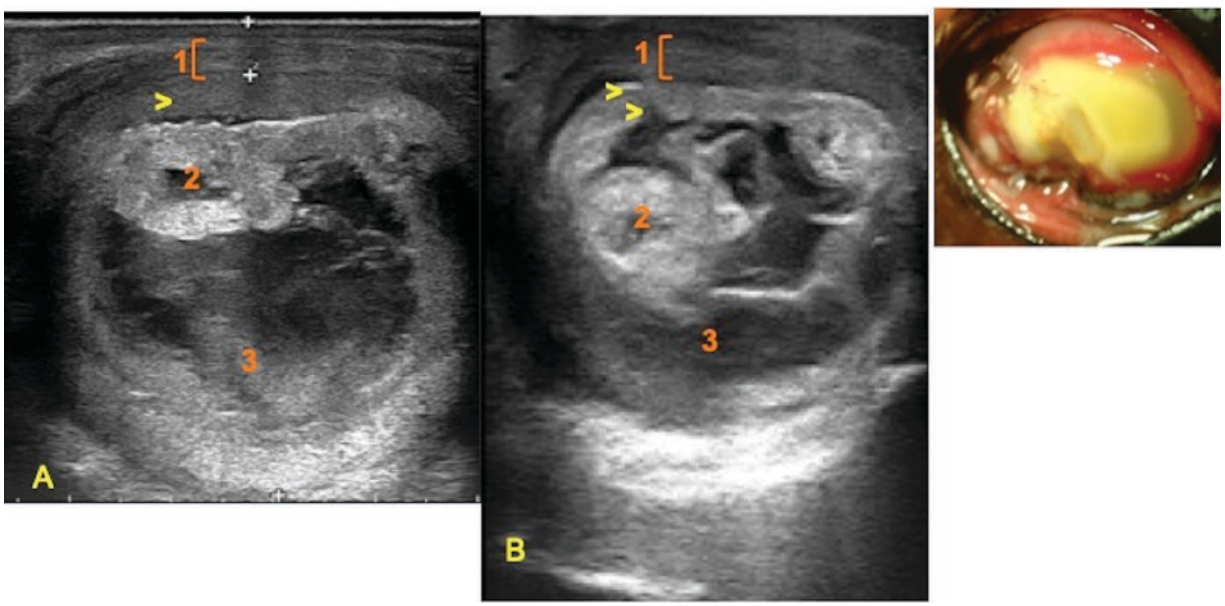


Figure 24.30 Endophthalmitis following penetratig wound to globe. These images are a transpalpebral sonogram picture of the right eye from a 2-year-old Maremmano horse with endophthalmitis following a penetrating wound to the globe. Transverse (A) and Longitudinal (B) images of the eye are shown. Note the profound thickening of uveal tissue (arrowheads). The cornea is thickened with lens modification. A heterogeneous mass can be visualized in the vitreous chamber. This mass has a layer of anechoic fluid and an area with more echoic content. Hypoechoic material in the vitreous chamber adjacent to the mass is most consistent with fibrin. The mass in the vitreous chamber was consistent with a chronic abscess.The marked and diffuse echogenicity represent severe cellular infiltration of the vitreous. 1: Cornea; 2: Lens; 3: Vitreous chamber.

Vet-ebooks.com

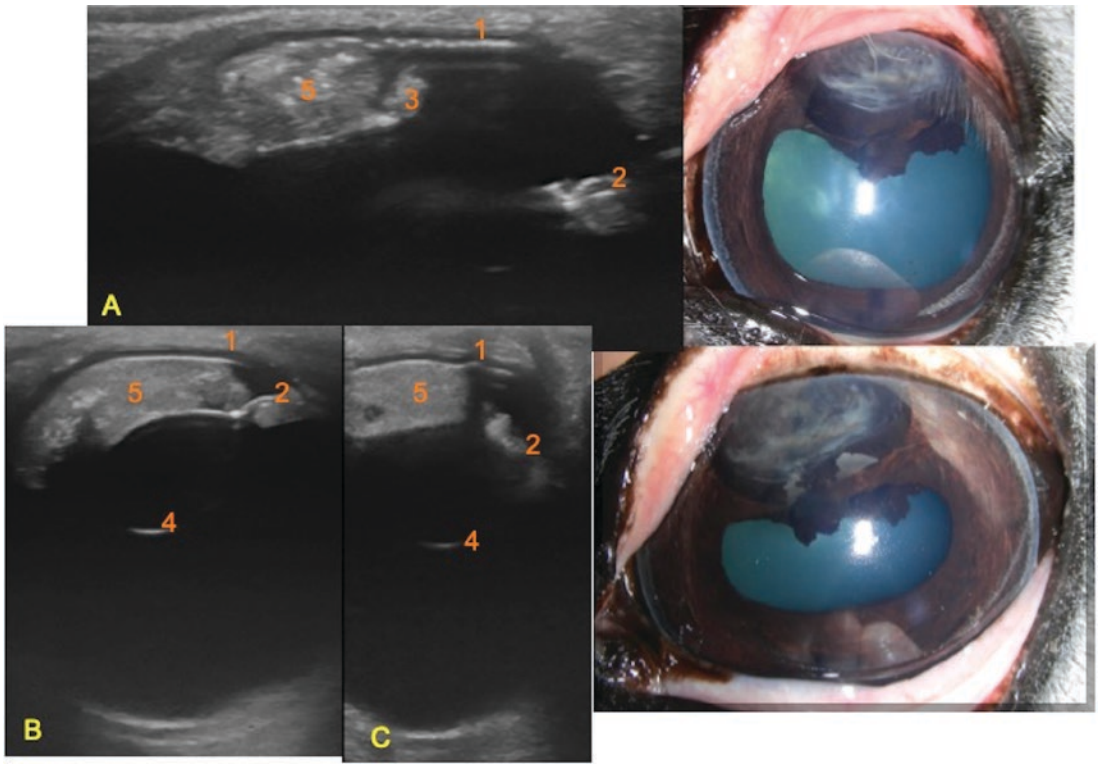


Figure 24.31 Melanoma. These images are from a gray, 19-year-old gelding with iris melanoma. A mass lesion is associated with the anterior surface of the iris and is protruding into the anterior chamber and is in contact with the posterior surface of the cornea. The lesions were contiguous in other sections and were diagnosed as melanoma from histopathology. The ultrasound aspect of melanoma is a well-defined hyperechoic compact mass (5). 1: Cornea; 2: Iris; 3: Corpora nigra; 4: lens; 5: Melanoma.

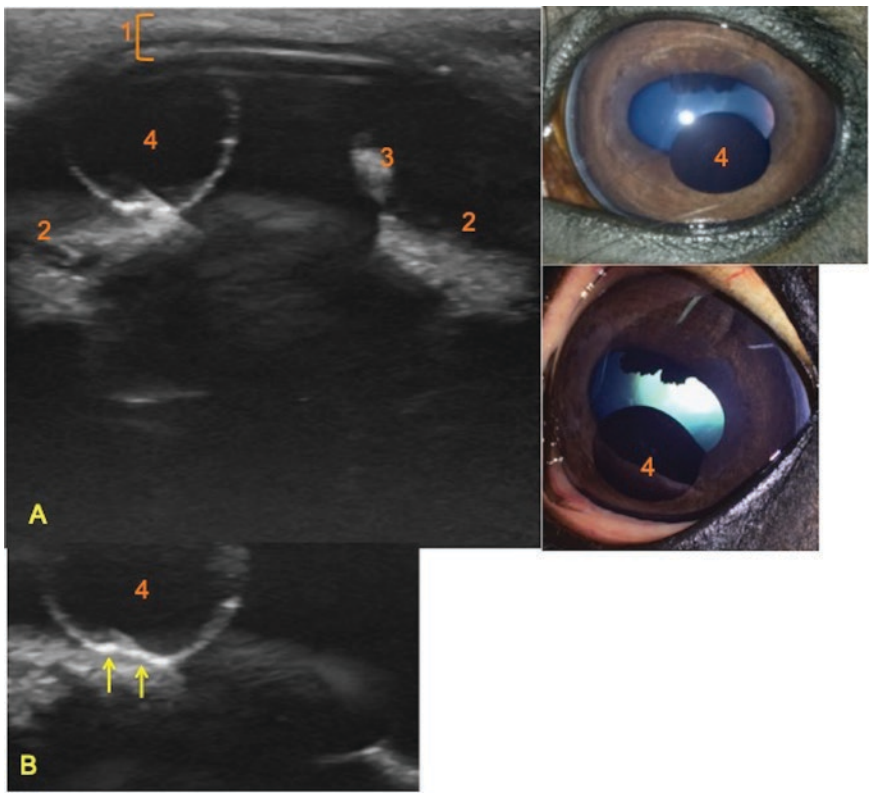


Figure 24.32 Iris Cyst. These images are from a 7-year-old horse with an iris cyst along the ventral pupillary margin. The iris cyst appears ultrasonographically as a circular neoformation with a hyperechogenic border and anechoic content. The liquid content determines a rear reinforcement artifact (yellow arrows). Ultrasonography helps us in the differential diagnosis with the masses present in the anterior chamber (f. melanoma). 1: Cornea; 2: Iris; 3: Corpora nigra; 4: Iris cyst.

Vet-ebooks.com

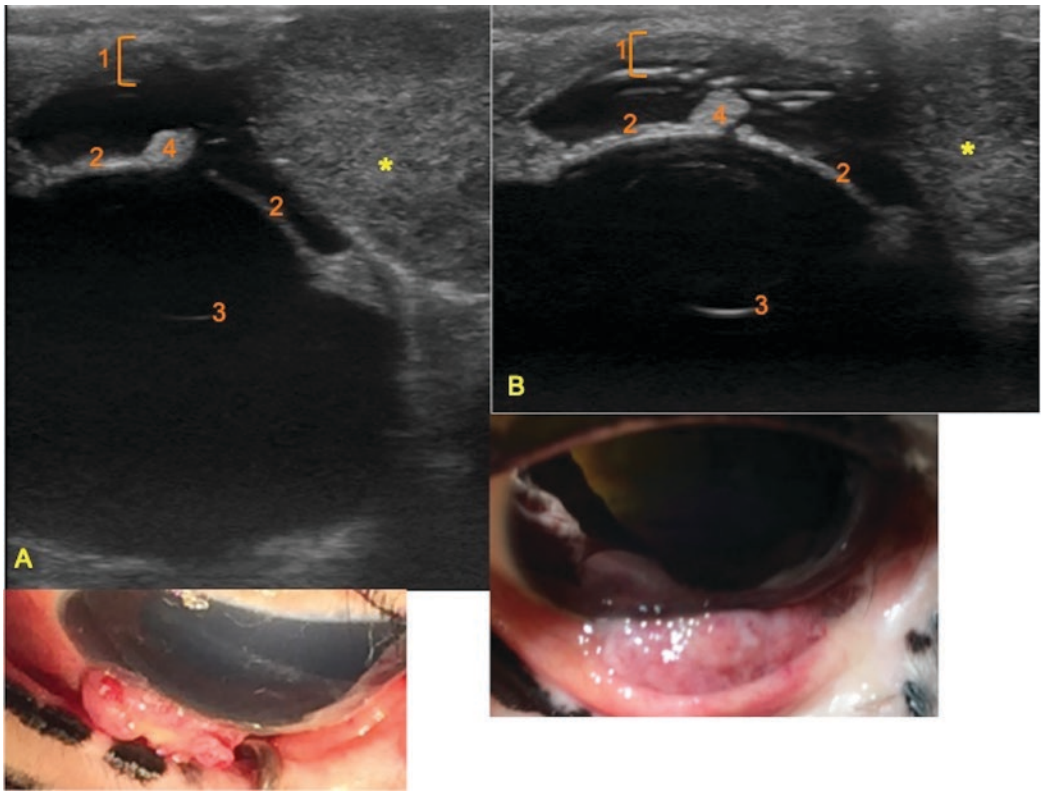


Figure 24.33 Squamous cell carcinoma. These images are from a 10-year-old paint mare presenting for squamous cell carcinoma (SCC) on the lower palpebral conjunctiva, the scleral ventral conjunctiva, and the corneal epithelium. Ultrasound examination shows that the mass (yellow asterisks) which affects the ventral part of the eye is also in continuity with the cornea and results in a considerable thickening of the cornea. 1: Cornea; 2: Iris; 3: Posterior lens capsule; 4: Corpora nigra.

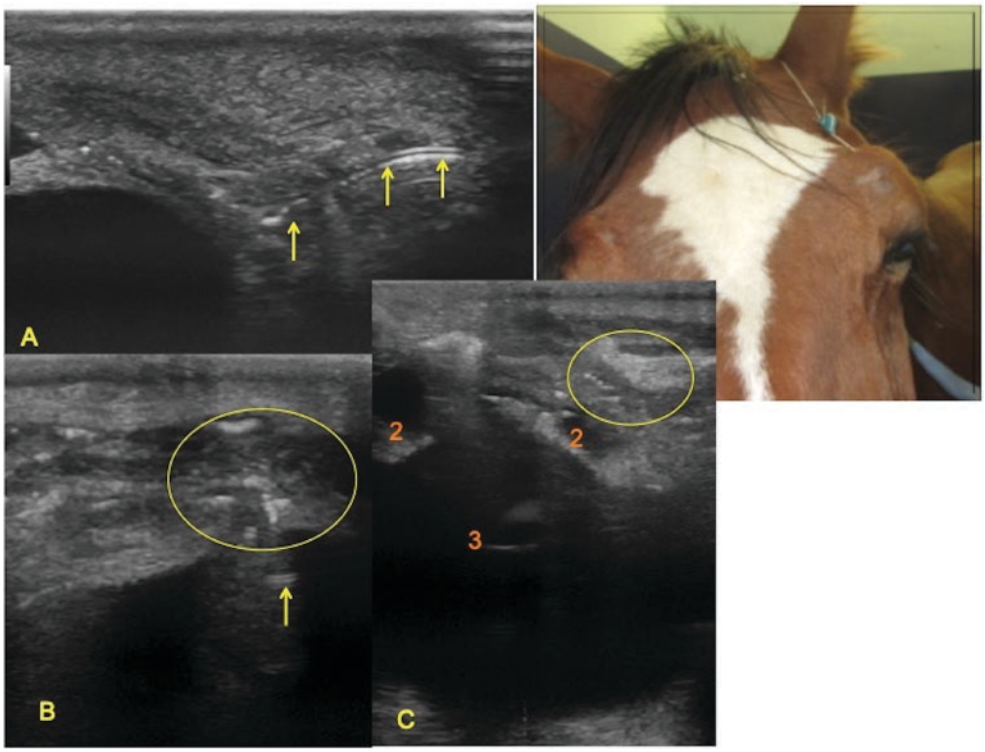


Figure 24.34 Upper eyelid swelling. This image is from a 7-year-old Hannover horse with upper eyelid swelling. A corneal ulcer was treated with local therapy administered through a sub-palpebral eye lavage catheter. The horse presented with acute swelling of the upper eyelid. The ultrasound examination confirmed the increase in the volume of the eyelid. Presence of a diffusely anechoic area to alternating hyperechoic thickening (yellow circle) and the presence of the sub-palpebral eye lavage catheter (yellow arrows) are evident. 1: Cornea; 2: Iris; 3: lens.

Vet-ebooks.com

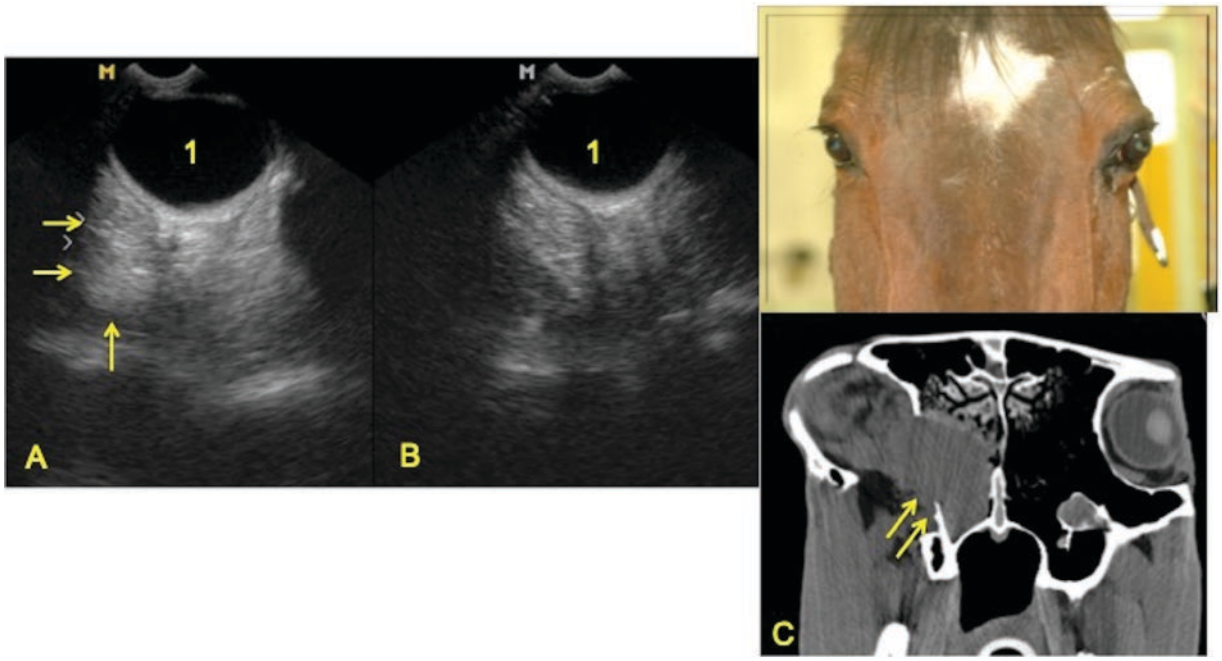


Figure 24.35 Exophthalmos. This image is from a 28-year-old horse with unilateral exophthalmos of the left eye. The image shows ultrasound comparison of the left eye (A) and right eye (B). A hyperechoic mass lesion (yellow arrows) is present posterior to the globe (1). The presence of the mass was then confirmed by the TC (C). Histopathology of a biopsy sample confirmed a diagnosis of squamous cell carcinoma (SCC).

References

1 Scotty, N.C., Cutler, T.J., Brooks, D.E. et al. (2004). Diagnostic ultrasonography of equine lens and posterior segment abnormalities. *Veterinary Ophthalmology* 7(2): 127–139.

2 Marchegiani, A., Fruganti, A., Cerquetella, M. et al. (2017). Penetrating palpebral grass awn in a dog. Unusual case of a penetrating grass awn in an eyelid. *Journal of Ultrasound* 20: 81–84.

3 Laus, F., Paggi, E., Marchegiani, A. et al. (2014). Short communication ultrasonographic biometry of the eyes of healthy adult donkeys. *The Veterinary Record* 174: 326–328.

4 Schott, M., Pierog, J., and Williams, S. (2013). Ultrasound in emergency medicine. *The Journal of Emergency Medicine* 44(6): 1136–1139.

5 Blaivas, M., Theodoro, D., and Sierzenski, P.R. (2002). Clinical practice a study of bedside ocular ultrasonography in the emergency department. *Academic Emergency Medicine: Official Journal of the Society for Academic Emergency Medicine* 9: 791–799.

6 Vrablik, M.E., Snead, G.R., Minnigan, H.J. et al. (2015). The diagnostic accuracy of bedside ocular ultrasonography for the diagnosis of retinal detachment: A systematic review and meta-analysis. *Annals of Emergency Medicine* 65: 199–203.

7 Reef, V.B. (1998). Ultrasonografic evaluation of small parts. In: *Equine Dignostic Ultrasound* (ed. V.B. Reef). 480–547, W.B. Saunders.

8 Whitcomb, M.B. (2002). How to diagnose ocular abnormalities with ultrasound. In: *Proceedings of the AAEP 2002*, 272–275.

9 Woo, M.Y., Hecht, N., Hurley, B. et al. (2016). Test characteristics of point-of-care ultrasonography for the diagnosis of acute posterior ocular pathology. *Can J Ophthalmol Can D'ophtalmologie* 51 (5): 336–341.

10 Shinar, Z., Chan, L., and Orlinsky, M. (2011). Use of ocular ultrasound for the evaluation of retinal detachment. *The Journal of Emergency Medicine* 40(1): 53–57.

11 Gialletti, R., Marchegiani, A., Valeriani, T. et al. (2018). A survey of ocular ultrasound abnormalities in horse: 145 cases. *Journal of Ultrasound* 21: 53–59.

12 Seco Diaz, O. (2005). Ultrasound of the equine eye and adnexa and clinical applications. *Clinncal Techniques in Equine Practice* 3(3): 317–325.

13 Scotty, N.C. (2005) Ocular ultrasonography in horses. *Clinncal Techniques in Equine Practice* 4(1): 106–113.

14 Reef, V.B. (2006) *How to Do an Ultrasound Examination of the Eye*. XII SIVE Congress, Bologna.

15 Rantanen, N. and Ewing, R. (1981). Principles of ultrasound application in animals. *Veterinary Radiology* 22: 196–203.

Vet-ebooks.com

16 Gilger, B. (2017). *Equine Ophthalmology*, 3rd edn. Chichester, UK: Wiley.
17 Plummer, C. and Reese, D. (2014). *Ultrasonography of the eye and orbit. In: Atlas of Equine Ultrasonography* (ed. J. Kidd, K. Lu, and M. Frazer), 445–453. Chichester, UK: Wiley.
18 Ramirez, S. and Tucker, R. (2004). Ophthalmic imaging. *Veterinary Clinical North America: Equine Practice* 20(2): 441–457.
19 Hallowell, G.D. and Bowen, I.M. (2007). Practical ultrasonography of the equine eye. *Equine Veterinary Education* 19(11): 600–605.
20 Valentini, S., Tamburro, R., Spadari, A. et al. (2010), Ultrasonographic evaluation of equine ocular diseases: A retrospective study of 38 eyes. *Journal of Equine Veterinary Science* 30(3): 150–154.

Vet-ebooks.com

25

Ultrasonography of the Soft Structures of the Neck

Massimo Magri

Clinic Veterinaria Spirano, Spirano (BG), Italy

Preparation and Scanning Technique

Optimal equipment for ultrasonography of structures of the neck should include a high frequency, 10–12 MHz linear probe and a 6.6 MHz microconvex probe. These two probes allow visualization with maximal definition of both superficial and deep structures. However, many structures of the neck can be visualized using only a 5–7.5 MHz linear probe typically used for equine obstetrics. Best images are obtained by clipping the hair with a surgical clipper blade and applying coupling gel; however, alcohol will also serve as an adequate contact medium. Ideally, place an examination glove or similar over the probe because continued exposure to coupling gel, particularly alcohol, can cause degradation of the probe and potentially affect image quality and life span of the probe (Figure 25.1). Orientation of the probe must be kept constant over time to obtain comparable images. When scanning in the longitudinal axis (Figure 25.2A), orient the probe so that distal structures are on the left side of the screen and proximal structures are on the right (Figure 25.2B). When scanning in the cross (short) axis (Figure 25.2C), orient the probe so that ventral structures are on the left side of the screen and dorsal structures are on the right (Figure 25.2D).

Structures visualized when scanning the neck include major blood vessels (jugular veins and carotid arteries), parotid salivary glands, maxillary salivary glands, guttural pouches, thyroid glands, lymph nodes, esophagus, trachea, and muscle. All structures are bilateral, except for the esophagus, trachea, sternohyoid muscle, and sternothyroid muscle, so suspicious images can be compared to the opposite side assuming a lesion or abnormality is unilateral.

For practical reasons we have divided the neck in three scanning regions: upper cervical region, jugular groove, and lateral region.

Upper Cervical Region

In this region, it is possible to visualize the following structures (Figure 25.3):

- Parotid salivary glands
- Guttural pouches
- Mandibular salivary glands
- Carotid artery and its bifurcations
- Lymph nodes
- Thyroid gland
- Unidentified masses

The main ultrasound landmarks of this region are (Figure 25.4):

- Wing of the atlas
- Caudal border of the mandible
- Stylohyoid angle (Figures 25.5 and 25.15)
- Internal carotid artery and occipital artery bifurcation from common carotid artery (Figures 25.26 and 25.28)
- Jugular bifurcation

Parotid Salivary Glands

The parotid salivary gland (Figures 25.6, 25.7, 25.8, 25.9, and 25.10) is a well-demarcated, bilateral,

Atlas of Equine Ultrasonography, Second Edition. Edited by Jessica A. Kidd, Kristina G. Lu and Michele L. Frazer.
© 2022 John Wiley & Sons Ltd. Published 2022 by John Wiley & Sons Ltd.
Companion Website: www.wiley.com/go/kidd/atlas

Vet-ebooks.com



Figure 25.1 Probe protection. Protect the probe from coupling gel or alcohol with an examination glove or similar covering.

multilobulated structure located in the upper cervical region, below the ear, immediately underneath the skin and parotidoauricular muscle. The gland extends from the vertical ramus of the mandible and wing of the atlas cranially to the linguofacial vein distally. Medially, it is adjacent to the guttural pouches and retropharyngeal lymph nodes. The gland has a hyperechoic capsule and septa and a hypoechoic to anechoic parenchyma. It is approximately 2 cm thick and 20 cm long. The salivary duct (Stensen's duct) is normally not visible with ultrasonography. Abnormalities of the parotid salivary gland are rare, but obstruction of the duct may cause dilation of the salivary duct. In addition, neoplasia, particularly melanomas (Figures 25.08, 25.09, 25.10) may infiltrate this gland. Localized enlargement of unknown origin

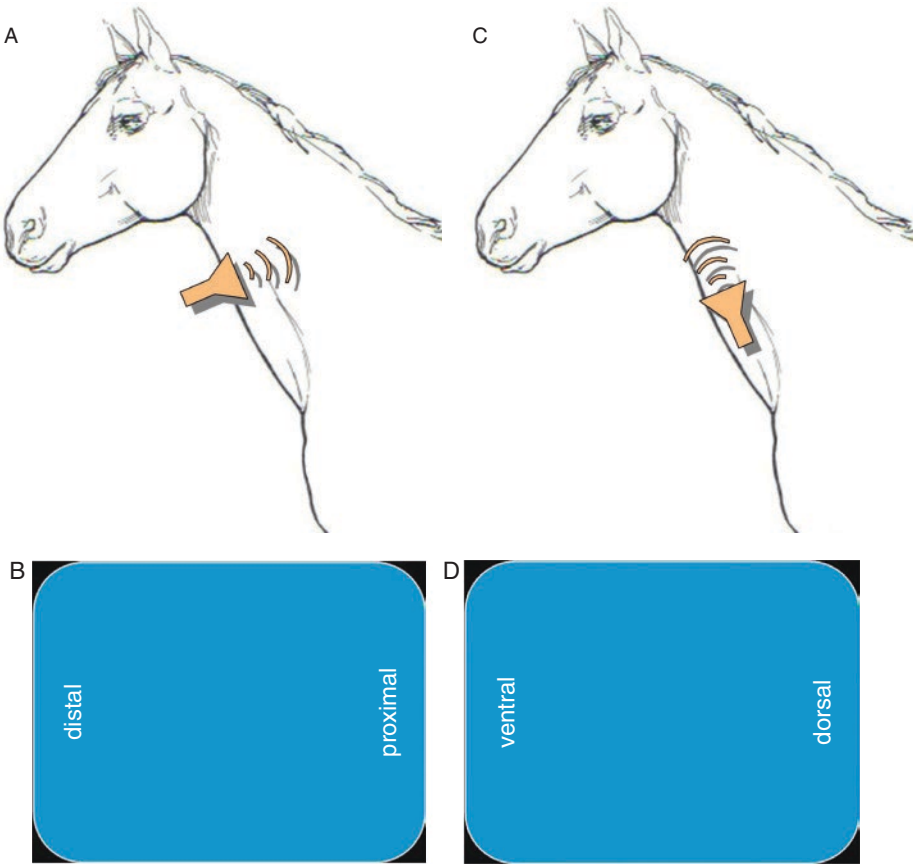


Figure 25.2 Probe orientation. (A) This image shows orientation of probe for obtaining longitudinal view. (B) Position the probe so the distal aspect of the neck is on the left side of the screen and the proximal aspect is on the right. (C) This image shows orientation of probe for cross-sectional view. (D) Position the probe so the ventral aspect of the neck is on the left side of the screen and the dorsal is on the right.

Vet-ebooks.com

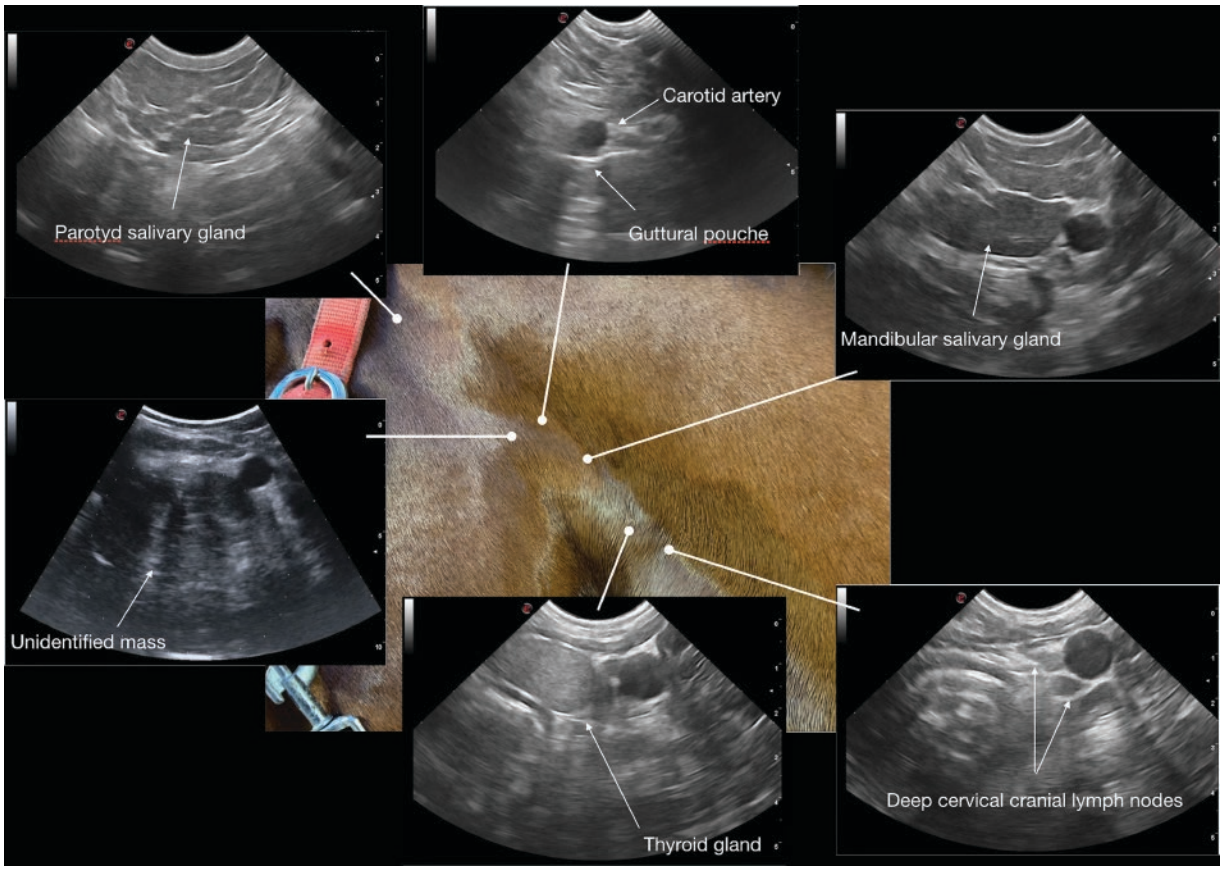


Figure 25.3 The main ultrasound sites and associated structures in the upper cervical region. This picture illustrates scan sites for images of the parotid gland, guttural pouches, carotid artery, mandibular salivary gland, lymph nodes, and thyroid gland.

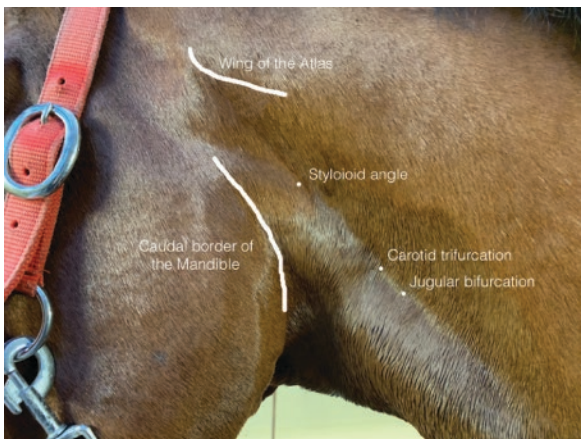


Figure 25.4 This picture illustrates the main ultrasound landmarks of the upper cervical region.

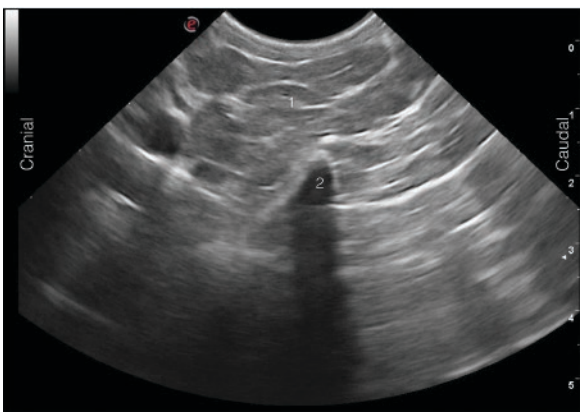


Figure 25.5 Sonogram of the left upper cervical region, cross-sectional view, obtained from a normal adult horse at the level of the temporo-mandibular joint. The parotid salivary gland (1) is visible below the skin and the parotidoauricular muscle, the angle of the stylohyoid bone (2) is clearly visible, casting a strong acoustic shadow. This sonogram was obtained with a wide-bandwidth 4–9 MHz micro-convex linear array transducer, operating at 6.0 MHz, at a display depth of 5 cm.

Vet-ebooks.com



Figure 25.6 Diagram of the localization of parotid salivary gland.

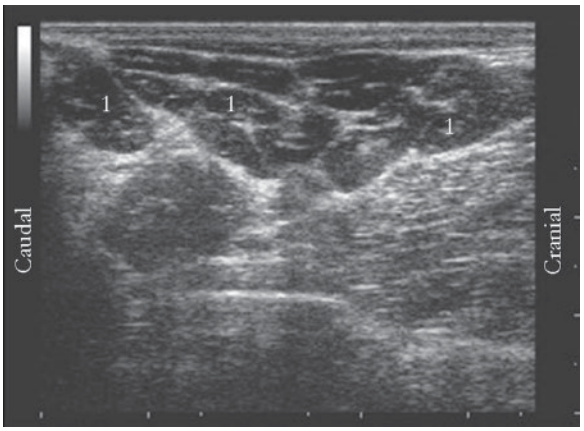


Figure 25.7 Parotid salivary gland. This image is a cross-sectional view of the left parotid salivary gland obtained from a normal adult horse. Hypoechoic, multilobulated, structures of the glandular parenchyma (1) are surrounded by hyperechoic capsule and septa. This sonogram was obtained with a wide-bandwidth 10.0 MHz linear array transducer, operating at 12.0 MHz, at a display depth of 5 cm.



Figure 25.8 Parotid salivary gland. This picture is of a 9-year-old Criollo gelding with a marked atrophy of the right parotid salivary gland (1) and a prominent ectatic duct (2).

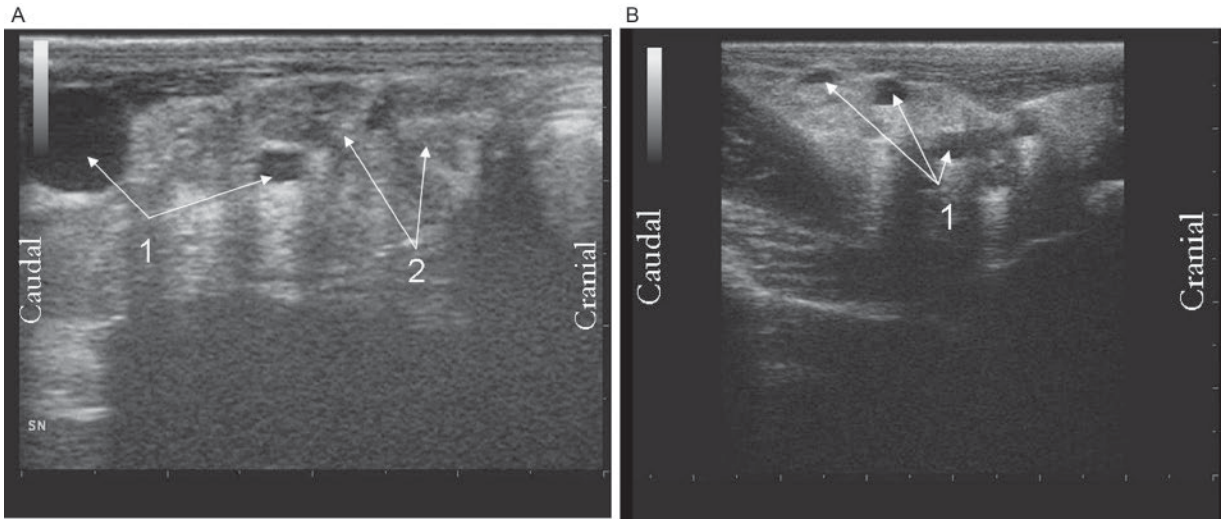


Figure 25.9 Parotid salivary gland. (A and B) These sonograms are of the right proximal cervical region obtained from the case in Figure 26.9. The glandular parenchyma (2) is visible only in a very small area. The remaining area of the parotid region is characterized by the presence of the ectatic duct (1) and fibrous tissue that is not homogeneous. A marked acoustic enhancement artifact is present in the far wall of the dilated ducts, confirming that these structures are fluid filled. These sonograms were obtained with a wide-bandwidth 10.0 MHz linear array transducer, operating at 12.0 MHz, at a display depth of 5 cm.

Vet-ebooks.com

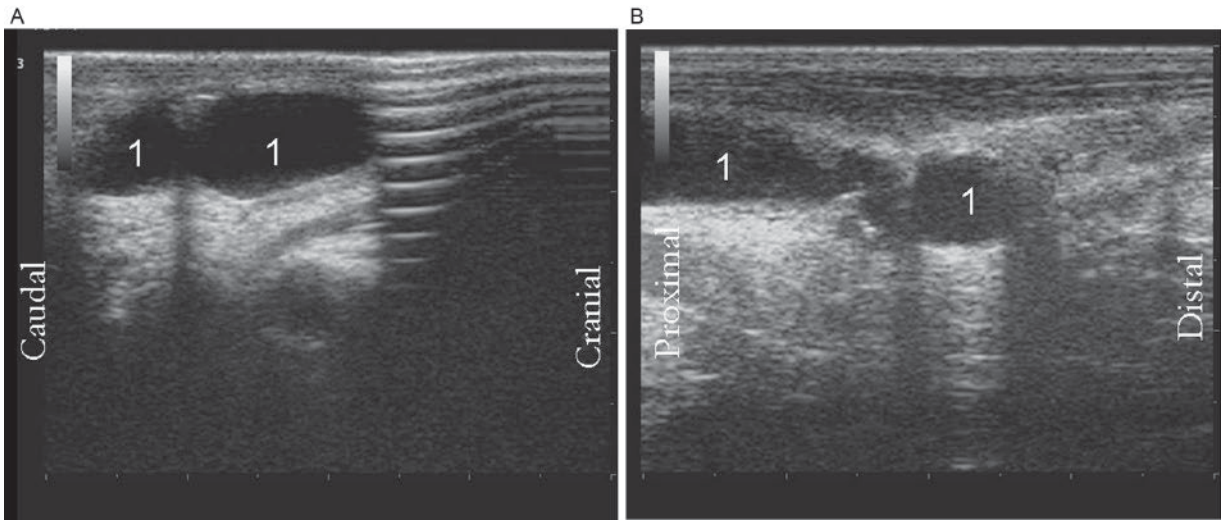


Figure 25.10 Parotid salivary gland. These images are (A) cross-sectional and (B) longitudinal views of the right mandibular edge obtained from the case in Figure 26.9. The parotid salivary duct (1) is distended and anechoic. The duct has a tortuous course and a thickened wall. These sonograms were obtained with a wide-bandwidth 10.0 MHz linear array transducer, operating at 12.0 MHz, at a display depth of 5 cm.



Figure 25.11 This picture is of a 20-year-old grey horse diagnosed with melanoma. The swelling in the proximal cervical region was irregular, firm, nodular, and not painful.

can be detected as an incidental finding (Figures 25.13 and 25.14).

Guttural Pouches

The guttural pouches (Figure 25.15) are ventral diverticula of the Eustachian tube and extend from the nasopharynx to the middle ear. They contain air and have a capacity of 300–500 ml in adults.

Due to the pouches' air content, only the walls of the medial and lateral compartments are detectable in the normal horse. However, when an abnormal fluid collection is present, it is visible.

The walls of the lateral and medial pouch compartments are readily located. The lateral compartment wall can be seen superiorly, at the level of the tempo-mandibular joint, just below the parotid salivary gland (Figure 25.16). The medial compartment wall can be seen inferior to the common carotid artery, just before the trifurcation (Figures 25.17 and 25.18). A mirror artifact, consequent to the air, can occur and should not be confused with an abnormality.

Guttural pouch tympany (Figure 25.19) occurs in young animals, usually less than 1 year of age, when the salpingopharyngeal fold, the flap of tissue covering the pharyngeal opening, fails to let air escape the guttural pouch. With the flap functioning as a one-way valve, the pouch fills with air. Some cases are mild, while others progress to respiratory distress from occlusion of the pharyngeal area from the distended guttural pouch [1] (Figure 25.20).

Guttural pouches may contain exudate or chondroids (inspissated pus) with guttural pouch empyema (Figures 25.21, 25.22, 25.23, and 25.24). Empyema may occur secondary to any respiratory disease, but infection with *Streptococcus equi* is a common finding. The pouches may contain blood if trauma occurs to any structure associated with the guttural pouch. A common finding in guttural pouch trauma and hemorrhage is fracture of the stylohyoid bone or a lesion at the insertion of the longus capitis and rectus capitis muscles. Another cause of blood in the pouch is guttural pouch mycosis. A fungal plaque forms in the pouch and causes erosion of a blood vessel, usually the internal carotid artery, resulting in hemorrhage into the guttural pouch.

Vet-ebooks.com

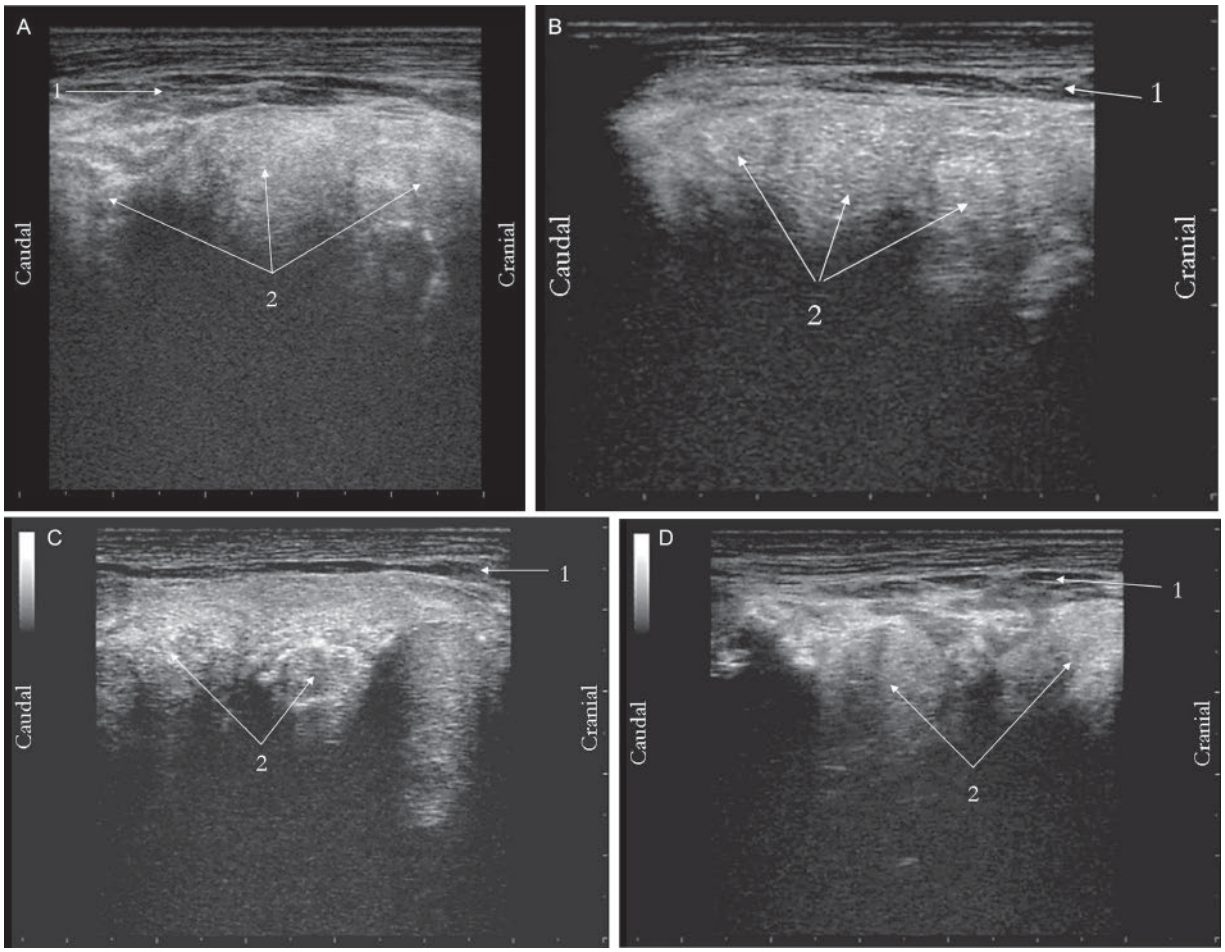


Figure 25.12 Melanoma. This series of sonograms (A), (B), (C), and (D) is of the right proximal cervical region obtained from the case in Figure 26.11. The glandular parenchyma (1) is reduced to a thin layer; beneath it various hyperechoic masses (2) characterized by a variable echogenicity are present. These sonograms were obtained with a wide-bandwidth 10.0 MHz linear array transducer, operating at 12.0 MHz, at a display depth of 5 cm.

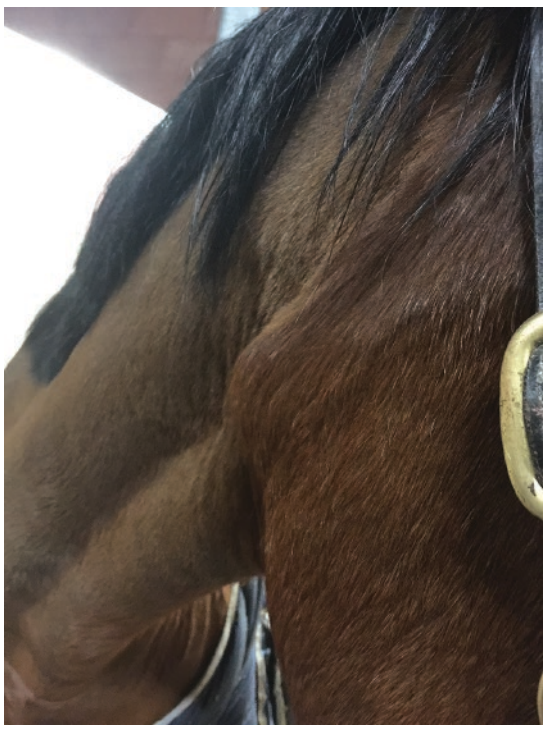


Figure 25.13 This picture is of a 14-year-old mare that presented with an upper cervical swelling that was, unilateral, firm, nodular, and not painful.

Vet-ebooks.com

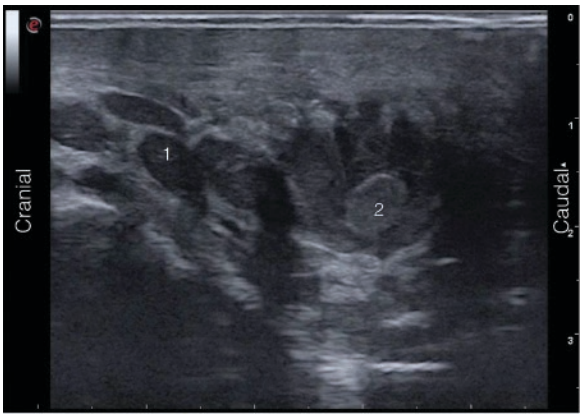


Figure 25.14 This sonogram is of the left upper cervical region obtained from the case in Figure 25.13. The glandular parenchyma (1) is normal, except for the presence of a small mass with homogeneous echogenic appearance (2), surrounded by an area of altered glandular parenchyma with dishomogeneous hypoechogenic apperance. These sonograms were obtained with a wide-bandwidth 10.0 MHz linear array transducer, operating at 10.0 MHz, at a display depth of 3.5 cm.



Figure 25.15 Diagram of the localization of guttural pouch and the stylohyoid angle.

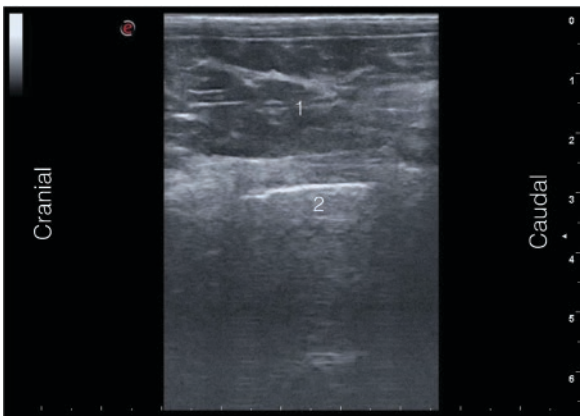


Figure 25.16 Wall of the lateral compartment of the guttural pouch. This image is a longitudinal view of the left parotid salivary gland (1) and the wall of the lateral compartment of the guttural pouch (2), obtained from a normal adult horse. The hyperechogenic line of the wall of the lateral compartment of the guttural pouch has a reverberation artifact due to the air content of the normal guttural pouch. This sonogram was obtained with a wide-bandwidth 3.0–13.0 MHz linear array transducer, operating at 5.0 MHz, at a display depth of 6.5 cm.

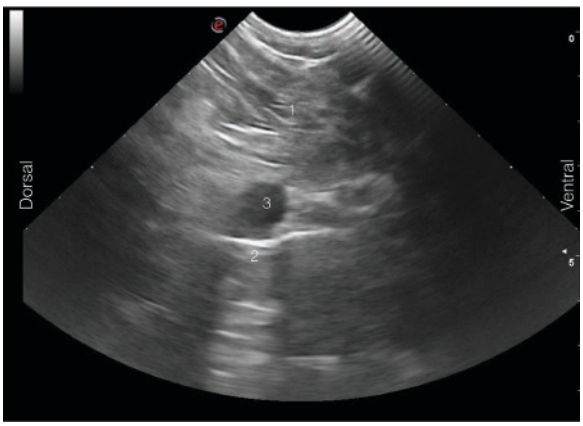


Figure 25.17 Wall of the medial compartment of the guttural pouch. This image is a cross-sectional view of the wall of the medial compartment of the guttural pouch (2), just beneath the common carotid artery, a few centimeters caudal to the carotid bifurcation, obtained from a normal adult horse. The hyperechogenic line of the wall of the medial compartment of the guttural pouch has a reverberation artifact due to the air content of the normal guttural pouch. This sonogram was obtained with a wide-bandwidth 4–9 MHz micro-convex linear array transducer, operating at 6.0 MHz, at a display depth of 8 cm.

Vet-ebooks.com

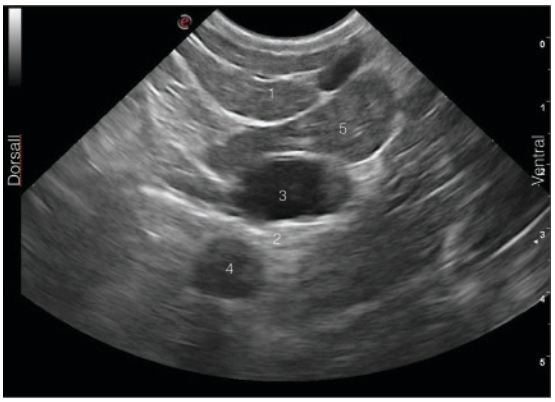


Figure 25.18 Wall of the medial compartment of the guttural pouch. This image is a cross-sectional view of the wall of the medial compartment of the guttural pouch (2), just beneath the common carotid artery (3), a few centimeters caudal to the carotid bifurcation, obtained from a normal adult horse. The hyperechogenic line of the wall of the medial compartment of the guttural pouch can sometimes produce a mirror artifact (4) that reproduce the carotid common artery image distal to the wall of the medial compartment of the guttural pouch. The parotid salivary gland (1) and the mandibular salivary gland (5) are also visible. This sonogram was obtained with a wide-bandwidth 4–9 MHz micro-convex linear array transducer, operating at 6.0 MHz, at a display depth of 5 cm.



Figure 25.19 Guttural pouch tympany. This picture is of a 3-month-old Arab Thoroughbred filly with guttural pouch tympany. The foal had marked distension of the throatlatch region, was in respiratory distress, and required an emergency tracheostomy. The percussion exam revealed a tympanic sound in the upper part of the enlargement and a dull sound in the lower part.

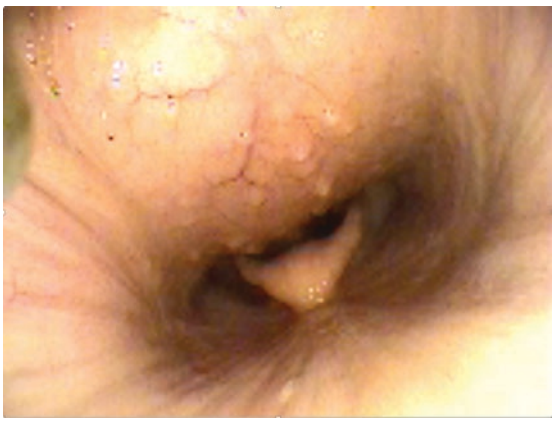


Figure 25.20 Guttural pouch tympany. Endoscopic examination of a clinical case of guttural pouch tympany. The upper part of the laryngeal area is markedly compressed by the air content of both the guttural pouches, considerably decreasing the airway passage.

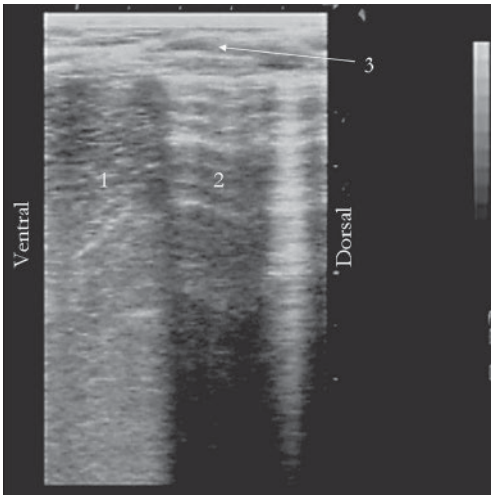


Figure 25.21 Guttural pouch tympany. This image is a longitudinal view of the right parotid and laryngeal region. A well-defined distinction between the upper (2) and the lower (1) portion of the right guttural pouch is evident. The upper portion is filled with air (2) that casts a typical reverberation artifact. The lower portion is filled with mucus (1) that has a mildly echogenic, non-homogeneous appearance. This sonogram was obtained with a wide-bandwidth 5.0 MHz linear array, transrectal transducer, operating at 5.0 MHz, at a display depth of 4 cm.

Vet-ebooks.com

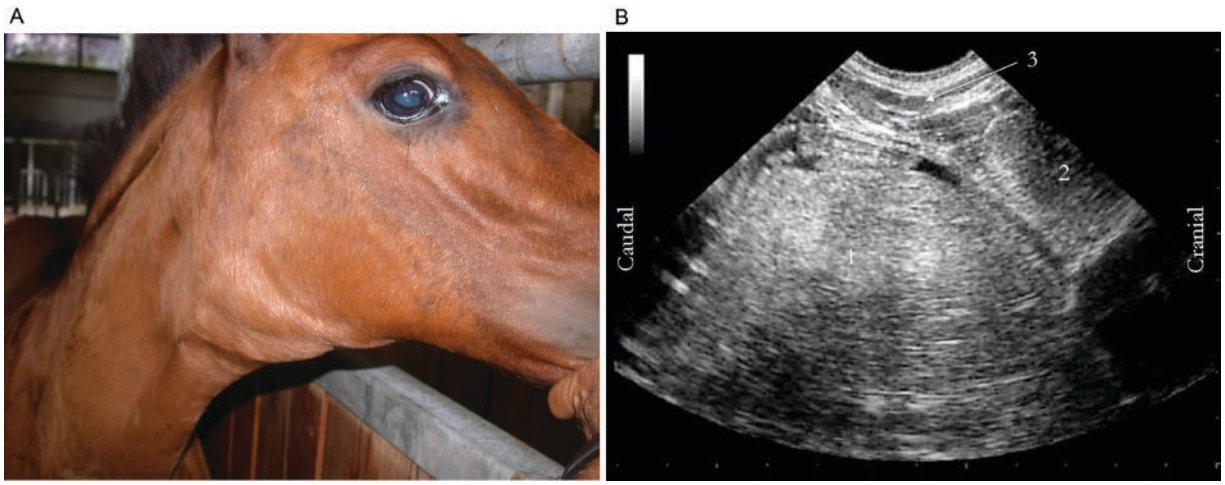


Figure 25.22 Guttural pouch empyema. (A) This picture is of a 5-month-old Spanish colt with guttural pouch empyema with an abscess inside the pouch. The foal had marked distension of the throatlatch region and clinical signs of respiratory distress. The mass was firm, not painful, and not adhered to the skin. (B) This image is a cross-sectional view of the right, lateral, laryngeal region. A well demarcated hyperechoic mass (1) is visible deep to the parotid salivary gland (3) and in contact with an enlarged, but architecturally normal, lymph node (2). This mass is inside the guttural pouch which has a visible wall and peripheral layer of hypoechogenic material. This sonogram was obtained with a wide-bandwidth 6.6 MHz micro-convex linear array transducer, operating at 6.6 MHz, at a display depth of 9 cm.

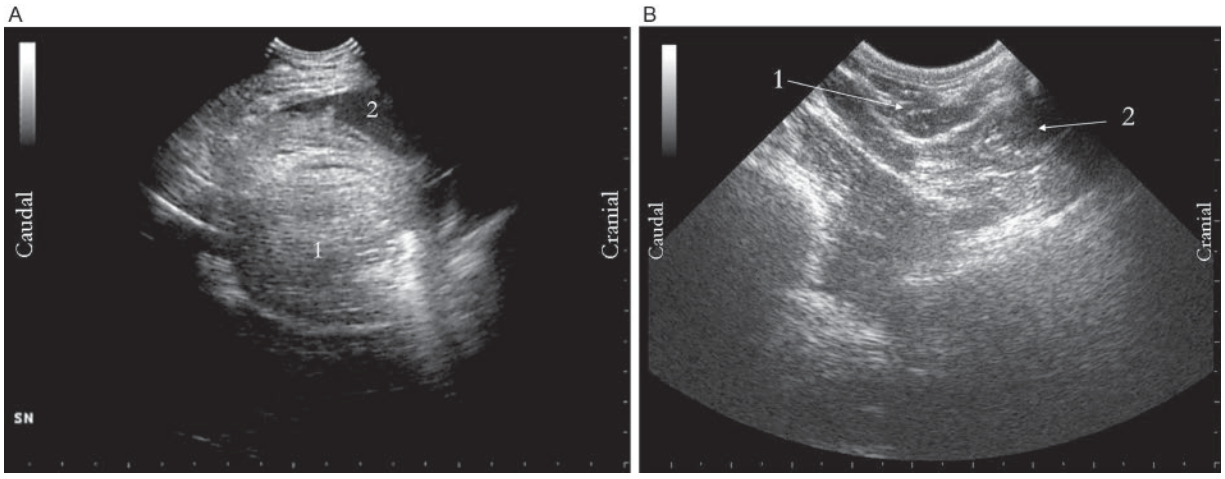


Figure 25.23 Guttural pouch empyema. (A) This image is a cross-sectional view of the right lateral laryngeal region obtained from the case in Figure 26.22 after insertion of a Foley catheter and copious lavages of the guttural pouch with a diluted acetylcysteine solution. The echogenic mass (1) is still clearly visible and well defined, but the outer layers are slowly dissolving in the lavage fluid (2). This sonogram was obtained with a wide-bandwidth 6.6 MHz micro-convex linear array transducer, operating at 6.6 MHz, at a display depth of 7 cm. (B) This image is a cross-sectional view of the right lateral laryngeal region obtained from the case in Figure 26.22 after clinical resolution of guttural pouch empyema. The echogenic mass has completely disappeared and the normal structures of the region, the parotid salivary gland (1) and the lymph node (2), are visible. This sonogram was obtained with a wide-bandwidth 6.6 MHz micro-convex linear array transducer, operating at 6.6 MHz, at a display depth of 14 cm.

Mandibular Salivary Glands

The mandibular salivary gland (Figure 25.25) is medial to the parotid salivary gland and lateral to the carotid artery and the guttural pouches; its echogenicity is similar to the parotid salivary gland from which it is divided by an echogenic septum (Figure 25.26).

Carotid Artery

The carotid artery (Figures 25.27 and 25.28) is an important landmark, particularly at the point where it divides into the external carotid artery, internal carotid artery, and occipital artery. The wall is thicker than that of the jugular vein and the vessel is not compressible.

Vet-ebooks.com

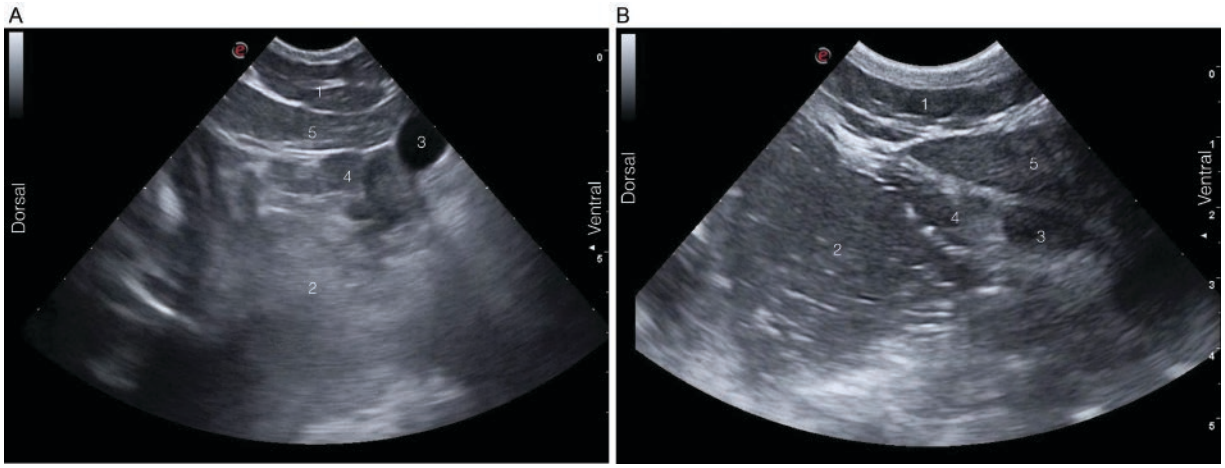


Figure 25.24 (A) (right) and (B) (left): Guttural pouch empyema. These pictures are of an 8-year-old KWPM mare with guttural pouch empyema. The mare had a bilateral purulent discharge from the nostrils. Ultrasound exam has revealed a bilateral empyema of the medial compartment of the guttural pouches (2), with enlarged retropharyngeal lymph nodes (4). Common carotid artery (3), mandibular salivary gland (5), and parotid salivary gland (1) are also visible. This sonogram was obtained with a wide-bandwidth 4–9 MHz micro-convex linear array transducer, operating at 6.0 MHz, at a display depth of 5 cm.



Figure 25.25 Diagram of the localization of the mandibular salivary gland.

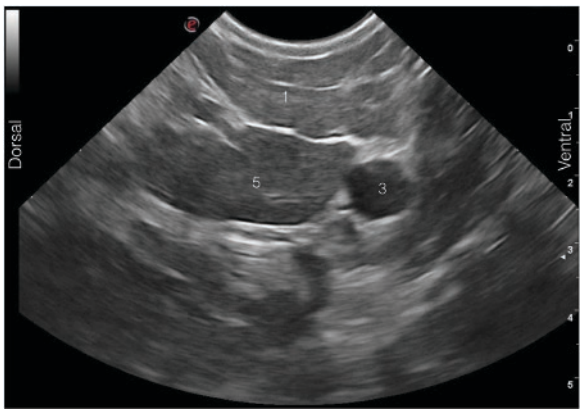


Figure 25.26 Mandibular salivary gland. This image is a cross-sectional view of the left mandibular salivary gland obtained from a normal adult horse. Hypoechoic, multilobulated structures of the glandular parenchyma (5) are surrounded by a hyperechoic capsule; the echogenicity is similar to the parotid salivary gland (1). The common carotid artery (3) is visible. This sonogram was obtained with a wide-bandwidth 4–9 MHz micro-convex linear array transducer, operating at 6.0 MHz, at a display depth of 5 cm.

Vet-ebooks.com



Figure 25.27 Diagram of the localization of the bifurcation of the common carotid artery (1) into the external carotid artery (2), internal carotid artery (3), and occipital artery (4).

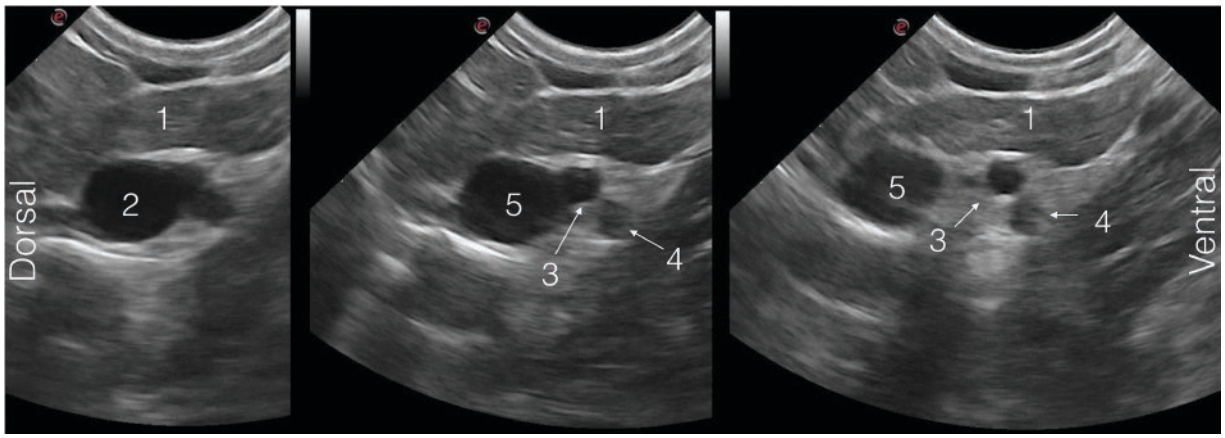


Figure 25.28 Sonogram of the left upper cervical region, cross-sectional view, obtained from a normal adult horse at the level of the bifurcation of external carotid artery (5), internal carotid artery (3), and the occipital artery (4) from the common carotid artery (2). The parotid salivary gland (1) is visible. This sonogram was obtained with a wide-bandwidth 4–9 MHz micro-convex linear array transducer, operating at 6.0 MHz, at a display depth of 5 cm.

Lymph Nodes

Lymph nodes (Figures 25.29 and 25.30) are well-demarcated structures with a hyperechoic capsule and a hypoechoic, homogeneous parenchyma. Major lymph nodes of the neck include the parotid lymph node, located under the cranial aspect of the parotid salivary gland, the medial retropharyngeal lymph nodes (Figure 25.31), located on the dorsolateral aspect of the pharynx near the bifurcation of the common carotid artery, the lateral retropharyngeal lymph nodes (Figure 25.32), located along the lateral side of the guttural pouch ventral to the mandibular salivary gland, and, lastly, the deep cervical cranial lymph nodes (Figures 25.33, 25.34, and 25.35), located immediately rostral to the ramification of the external jugular vein. Lymph nodes may enlarge secondary to lymphadenitis or infection (Figures 25.36, 25.37, 25.38, 25.39, 25.40, and 25.41). When abscesses form in lymph nodes, the parenchyma loses its homogeneous appearance and typically appears hypoechoic to anechoic. Necrotic material and cellular debris may appear as hyperechoic areas in the abscessed lymph node. Draining tracts may be visualized ultrasonographically, coursing from the abscessed lymph node to other internal structures or to the exterior. Neoplastic infiltrates to lymph nodes image as areas of increased echogenicity or complete loss of normal lymph node architecture.

Thyroid Gland

The thyroid gland (Figures 25.42 and 25.43) is bilateral with a narrow isthmus connecting the two lobes. It is located in the upper cervical region, caudal to the larynx, at the level of the second to fourth tracheal rings. It is approximately 2 cm thick, 2 cm wide,

Vet-ebooks.com

Figure 25.29 Diagram of the localization of the bifurcation of the common carotid artery (5) and the jugular vein (4) used as landmarks to localize the deep cervical lymph nodes (3), the medial retropharyngeal lymph nodes (1), and the lateral retropharyngeal lymph nodes (2).

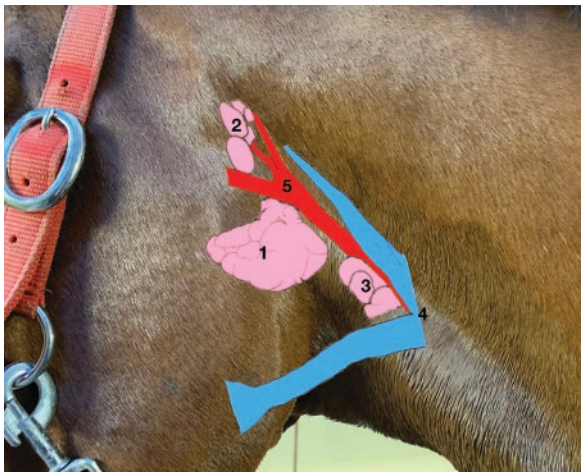


Figure 25.30 Normal lymph node. This image is a cross-sectional view of the left lateral laryngeal region of a normal adult horse. A lymph node (1) is visible with its characteristic hypoechoic, homogeneous appearance. It is near the thyroid gland (2) and lateral to the trachea (3). This sonogram was obtained with a wide-bandwidth 6.6 MHz micro-convex linear array transducer, operating at 6.6 MHz, at a display depth of 6 cm.

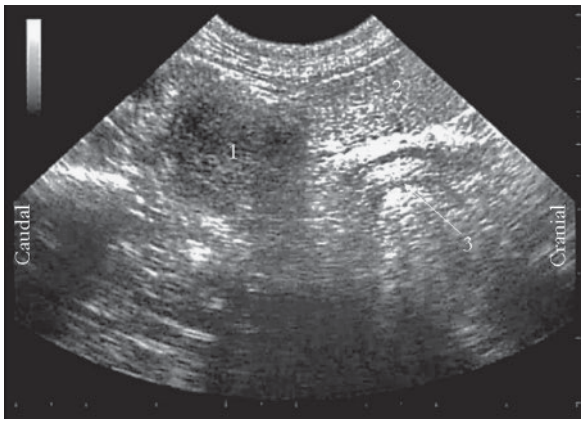


Figure 25.31 Normal lymph node. This image is a cross-sectional view of the left lateral laryngeal region of a normal adult horse. Two medial retropharyngeal lymph nodes (4) are visible with their characteristic hypoechoic, homogeneous appearance. They are near the common carotid artery (3) and wall of the medial compartment of the guttural pouch (2), underneath the parotid salivary gland (1). This sonogram was obtained with a wide-bandwidth 4–9 MHz micro-convex linear array transducer, operating at 6.0 MHz, at a display depth of 8 cm.

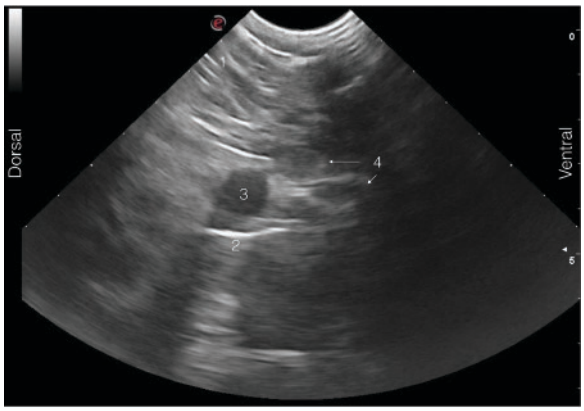
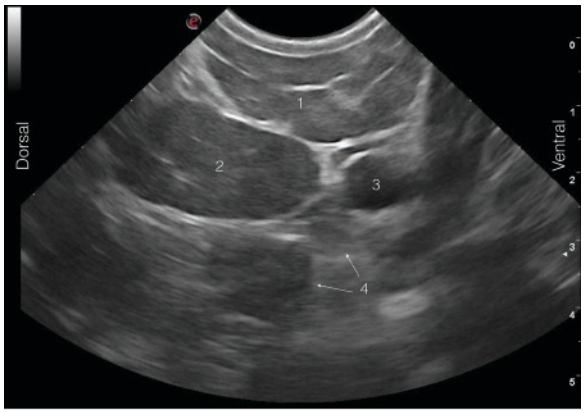


Figure 25.32 Normal lymph node. This image is a cross-sectional view of the left lateral laryngeal region of a normal adult horse. Two lateral retropharyngeal lymph nodes (4) are visible with their characteristic hypoechoic, homogeneous appearance. They are near the common carotid artery (3) and the mandibular salivary gland (2), underneath the parotid salivary gland (1). This sonogram was obtained with a wide-bandwidth 4–9 MHz micro-convex linear array transducer, operating at 6.0 MHz, at a display depth of 5 cm.



Vet-ebooks.com

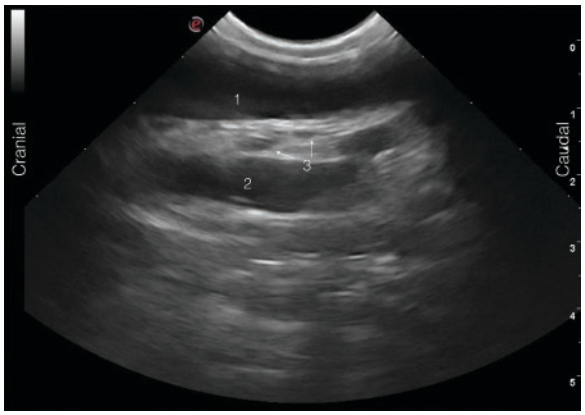


Figure 25.33 Normal lymph node. This image is a longitudinal view of the left lateral laryngeal region of a normal adult horse. The deep cervical cranial lymph nodes (3) are visible with their characteristic hypoechoic, homogeneous appearance. They are between the bifurcation of the maxillary vein (1) and the linguofacial vein (2). This sonogram was obtained with a wide-bandwidth 4–9 MHz micro-convex linear array transducer, operating at 6.0 MHz, at a display depth of 5 cm.

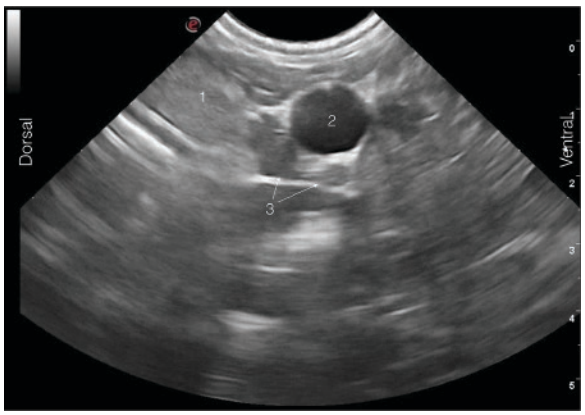


Figure 25.34 Normal lymph node. This image is a cross-sectional view of the left lateral laryngeal region of a normal adult horse. The deep cervical cranial lymph nodes (3) are visible with their characteristic hypoechoic, homogeneous appearance. They are between the common carotid artery (2) and the thyroid gland (1). This sonogram was obtained with a wide-bandwidth 4–9 MHz micro-convex linear array transducer, operating at 6.0 MHz, at a display depth of 5 cm.

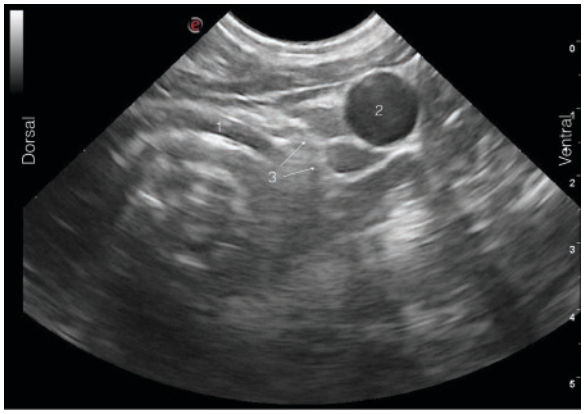


Figure 25.35 Normal lymph node. This image is a cross-sectional view of the left lateral laryngeal region of a normal adult horse. The deep cervical cranial lymph nodes (3) are visible with their characteristic hypoechoic, homogeneous appearance. They are between the trachea (1) and the common carotid artery (2). This sonogram was obtained with a wide-bandwidth 4–9 MHz micro-convex linear array transducer, operating at 6.0 MHz, at a display depth of 5 cm.

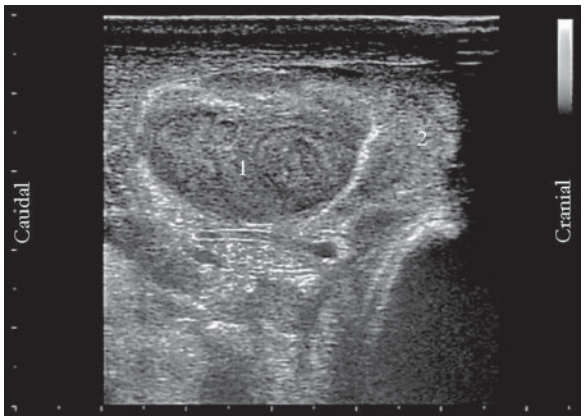


Figure 25.36 Laryngeal lymph node abscess. This image is a cross-sectional view of the right lateral laryngeal region of a 6-month-old filly. An abscess (1) is visible where the deep cervical lymph nodes are normally located, near the thyroid gland (2). The abscess has a well-defined, hyperechoic capsule with hypoechoic contents and a swirling appearance. This sonogram was obtained with a wide-bandwidth 10.0 MHz linear array transducer, operating at 12.0 MHz, at a display depth of 5 cm.

Vet-ebooks.com



Figure 25.37 Retropharyngeal lymph node abscess. This image is a cross-sectional view of the right retropharyngeal region of a weanling. An abscess is visible where a lymph node is normally located in the retropharyngeal area. The horse was diagnosed with *Streptococcus equi* (strangles) based on culture results of a fine-needle aspirate from the abscess. This sonogram was obtained with a micro-convex transducer, operating at 6.6 MHz, at a display depth of 8 cm. (*Source*: Image courtesy of Dr Michael Beyer, Equine Health Care PSC, Versailles, Kentucky).

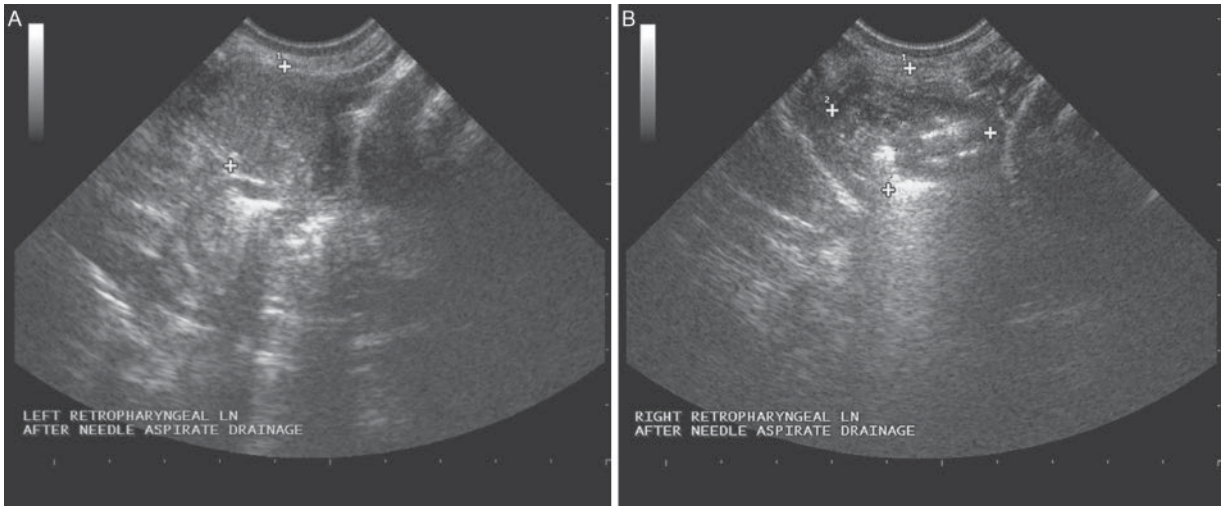


Figure 25.38 Retropharyngeal lymph node abscess after aspirate. These images are cross-sectional views of the retropharyngeal region of the weanling in Figure 26.24. These images show the left (A) and right (B) retropharyngeal lymph nodes after a fine-needle aspirate and drainage of exudate. These sonograms were obtained with a micro-convex transducer, operating at 6.6 MHz, at a display depth of 8 cm. (*Source*: Images courtesy of Dr Michael Beyer, Equine Health Care PSC, Versailles, Kentucky).

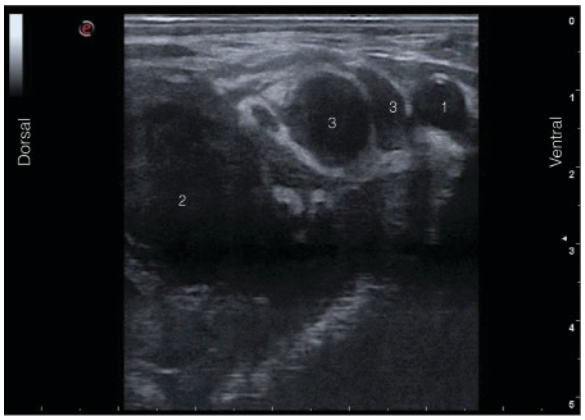


Figure 25.39 Retropharyngeal lymph node abscess. This image is a cross-sectional view of the left lateral laryngeal region of an adult horse with guttural pouches empyema. Two distinct abscesses (3) are visible where the retropharyngeal lymph nodes are usually located between the common carotid artery (1) and the medial compartment of the guttural pouches, filled with fluid (2). This sonogram was obtained with a wide-bandwidth 10.0 MHz linear array transducer, operating at 12.0 MHz, at a display depth of 5 cm.

Vet-ebooks.com



Figure 25.40 Retropharyngeal lymph nodes. This image is a cross-sectional view of the right lateral laryngeal region of an adult horse with guttural pouches empyema. The retropharyngeal lymph nodes (3) are enlarged and visible between the common carotid artery (4), the mandibular salivary gland (2), and the medial compartment of the guttural pouches, filled with fluid (5). The parotid salivary gland (1) is visible under the skin. This sonogram was obtained with a wide-bandwidth 4–9 MHz micro-convex linear array transducer, operating at 6.0 MHz, at a display depth of 9 cm.

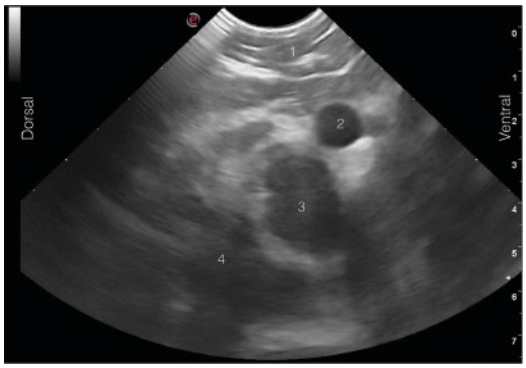


Figure 25.41 Retropharyngeal lymph node abscess. This image is a cross-sectional view of the left lateral laryngeal region of an adult horse with guttural pouches empyema. An abscess (3) is visible where the retropharyngeal lymph nodes are usually located between the common carotid artery (2) and the medial compartment of the guttural pouches, filled with fluid (4). A well-defined capsule is present around the abscess. The parotid salivary gland is visible under the skin (1). This sonogram was obtained with a wide-bandwidth 4–9 MHz micro-convex linear array transducer, operating at 6.0 MHz, at a display depth of 7 cm.



Figure 25.42 Diagram of the localization of the thyroid gland.

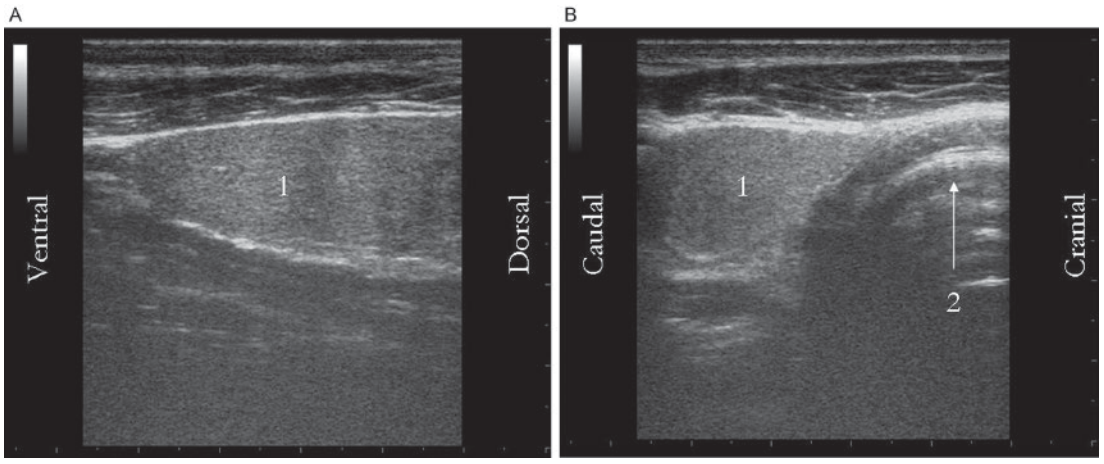


Figure 25.43 Thyroid gland. These images are (A) longitudinal and (B) cross-sectional views of the left thyroid gland obtained from a normal adult horse. The glandular parenchyma (1) has a homogeneous echogenic appearance with a well-defined capsule. It is approximately 2 cm thick and 5 cm long. It has a round elongated aspect and a thinner part adjacent to the trachea (2). This sonogram was obtained with a wide-bandwidth 10.0 MHz linear array transducer, operating at 12.0 MHz, at a display depth of 5 cm.

Vet-ebooks.com

and 5 cm long. Ultrasonographically, it appears as an oval, homogeneous, echogenic structure. Although abnormalities are rare, enlargement can occur with hyperthyroidism, hypothyroidism, euthyroidism, abscesses, hematomas, tumors (Figures 25.44, 25.45, and 25.46), cyst (Figure 25.47), or as an incidental finding (Figures 25.48 and 25.49).

Unidentified Masses

Unidentified masses in the upper cervical region may present as dysphagia. Externally the horse may appear normal (Figure 25.50), but an endoscopic exam (Figure 25.51) can reveal a larynx that is compressed dorsally and unilaterally. In this case, ultrasound exam of the upper cervical region confirmed a mass medial to the common carotid artery, along with an enlarged lymph node, probably neoplastic (Figures 25.52, 25.53, and 25.54). Ultrasound guided biopsy of the mass identified the mass as a carcinoma. CT scan of the region showed the true extent of the mass (Figures 25.55).

Jugular Groove

In this region, it is possible to visualize the following structures (Figure 25.56):

- Jugular vein
- Carotid artery
- Trachea
- Esophagus

Jugular Vein

The jugular vein (Figures 25.57, 25.58, 25.59, 25.60, 25.61, 25.62, 25.63, and 25.64) is visible in the jugular

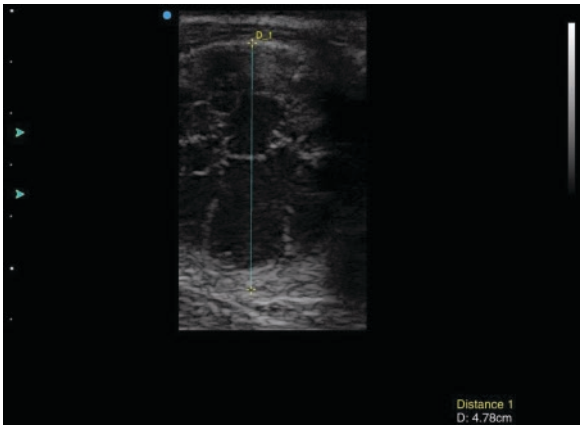


Figure 25.44 Thyroid gland. Left lobe of the thyroid gland, enlarged, with a spongy gelatinous heterogeneous appearance. This sonogram was obtained with a 5.0 MHz bandwidth linear array transducer, at a display depth of 6 cm. (*Source*: Images courtesy of Dr Jessica Kidd, Stanford-in-the-Vale, England).

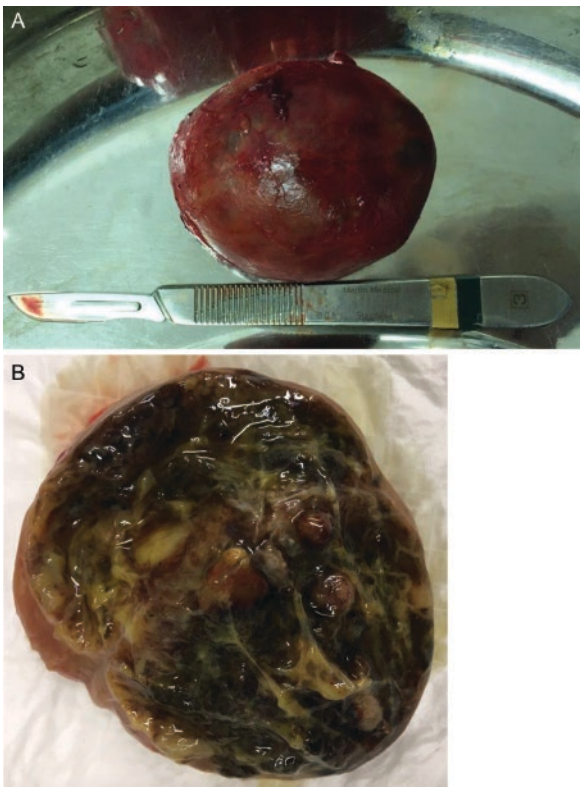


Figure 25.45 Thyroid gland. Anatomic specimen of the left thyroid lobe (A) surgically removed from the case in Figure 26.44. On cut section (B) there are many pockets of brown hemorrhagic fluid. A histological diagnosis of benign adenoma functionally active with no evidence of atrophy was reported. (*Source*: Images courtesy of Dr Jessica Kidd, Stanford-in-the-Vale, England).

Vet-ebooks.com



Figure 25.46 Thyroid gland. Left lobe of the thyroid gland (1), enlarged, with an homogeneous appearance and a large pocket of fluid. A histological diagnosis of benign adenoma was reported. This sonogram was obtained with a 4.0 MHz bandwidth linear array transducer, at a display depth of 11 cm. (*Source*: Images courtesy of Prof Rodolfo Gialletti Università degli Studi di Perugia, Perugia).

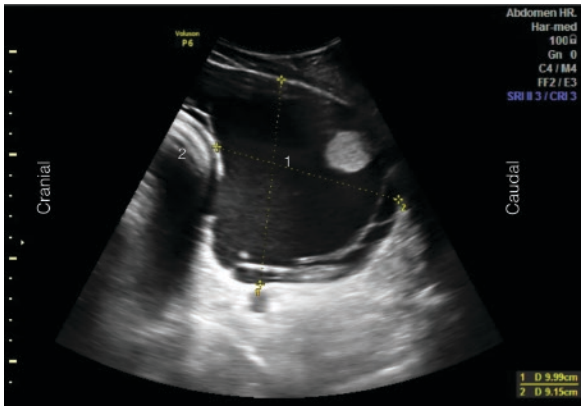


Figure 25.47 Thyroid gland. Left lobe of the thyroid gland, enlarged, with a large hypoechoic area surrounding a small portion of normal glandular tissue. This sonogram was obtained with a wide-bandwidth 2–10 MHz convex linear array transducer, operating at 2.0 MHz, at a display depth of 16 cm. (*Source*: Images courtesy of Prof Rodolfo Gialletti Università degli Studi di Perugia, Perugia).

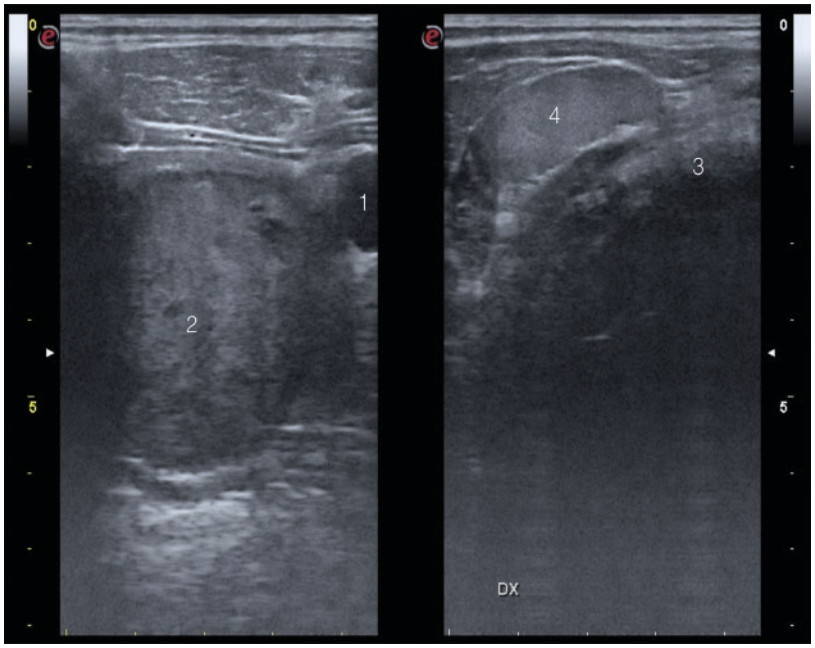


Figure 25.48 Thyroid gland. The left lobe of the thyroid gland (2) is enlarged, with a non-homogenous appearance, compared to the right lobe of the thyroid gland (4). Visible also are the common carotid artery (1) and the trachea (3). These sonograms were obtained with a wide-bandwidth 10.0 MHz linear array transducer, operating at 12.0 MHz, at a display depth of 8 cm.

Vet-ebooks.com

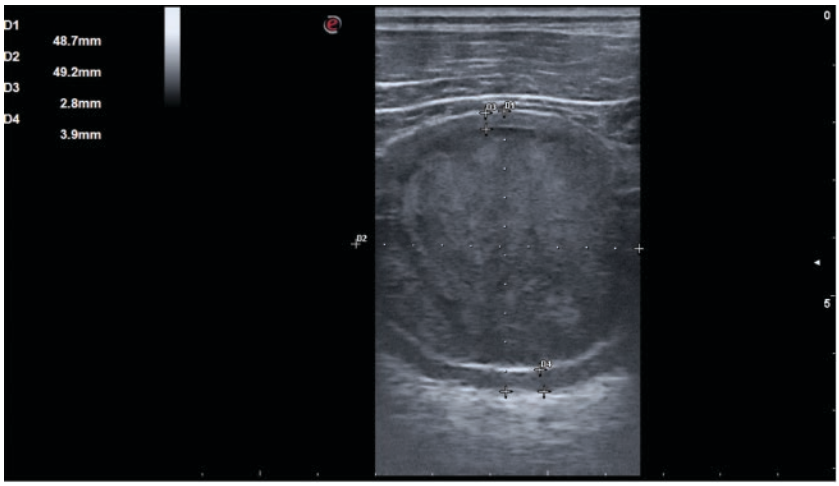


Figure 25.49 Thyroid gland. Image of the left lobe of the thyroid gland from the case in Figure 25.48; a well-defined capsule approximately 3 mm thick with a double wall and a hypoechogenic internal appearance inside is present, surrounding a non-homogeneous hypoechogenic parenchyma. This sonogram was obtained with a wide-bandwidth 10.0 MHz linear array transducer, operating at 12.0 MHz, at a display depth of 8 cm.



Figure 25.50 Unidentified mass. This picture is of a 22-year-old horse presenting with dysphagia. The upper cervical region was normal and not painful.

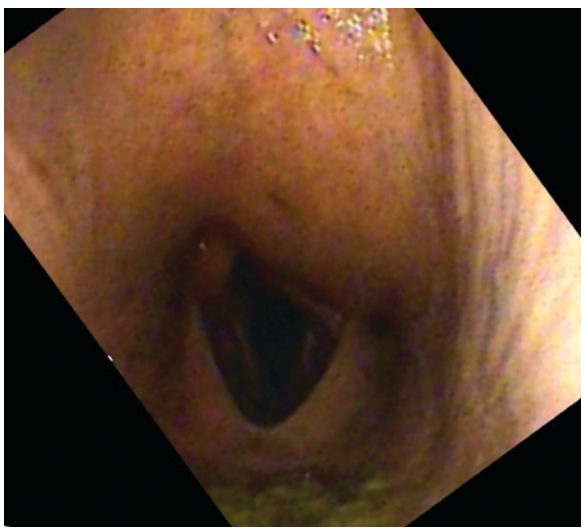


Figure 25.51 Unidentified mass. Endoscopic exam of the clinical case in Figure 26.49. The upper left part of the laryngeal area is markedly compressed by an unidentified mass, and dorsal displacement of the soft palate with considerable food material on the laryngeal floor is present.

Vet-ebooks.com



Figure 25.52 Unidentified mass. This image is a cross-sectional view of the left lateral laryngeal region of the case in Figure 26.49. An enlarged, non-homogeneous retropharyngeal lymph node (3) is visible, located between the common carotid artery (2) and an unidentified mass (4) where normally is visualized the medial compartment of the guttural pouch. The parotid salivary gland (1) is visible beneath the skin. This sonogram was obtained with a wide-bandwidth 4–9 MHz micro-convex linear array transducer, operating at 6.0 MHz, at a display depth of 8 cm.



Figure 25.53 Unidentified mass. This image is a cross-sectional view of the left lateral laryngeal region of the case in Figure 26.49. An enlarged, non-homogeneous retropharyngeal lymph node (2) with a thick hyperechogenic capsule is visible below the parotid salivary gland (1). This sonogram was obtained with a wide-bandwidth 4–9 MHz micro-convex linear array transducer, operating at 6.0 MHz, at a display depth of 8 cm.

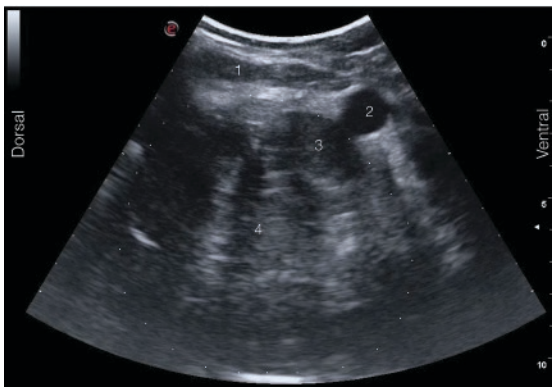


Figure 25.54 Unidentified mass. This image is a cross-sectional view of the left lateral laryngeal region of the case in Figure 26.48. An enlarged, hypoechogenic retropharyngeal lymph node (3) is visible, inside a large mass of varying echogenic appearance (small dots), between the parotid salivary gland (1) and the common carotid artery (2). This sonogram was obtained with a wide-bandwidth 4–9 MHz micro-convex linear array transducer, operating at 6.0 MHz, at a display depth of 10 cm.

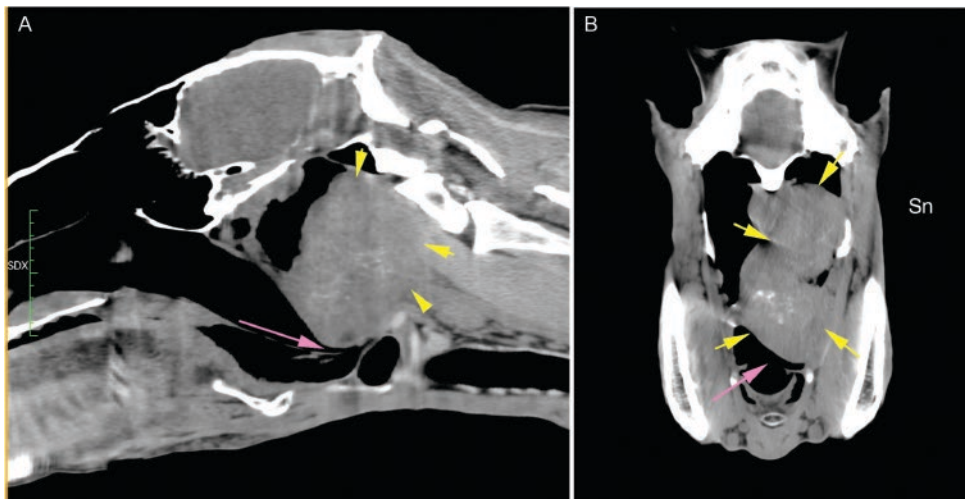


Figure 25.55 Unidentified mass. Longitudinal (A) and cross-section (B) CT scan of the upper cervical region of the case in Figure 26.48 showing the real dimensions of the mass.

Vet-ebooks.com

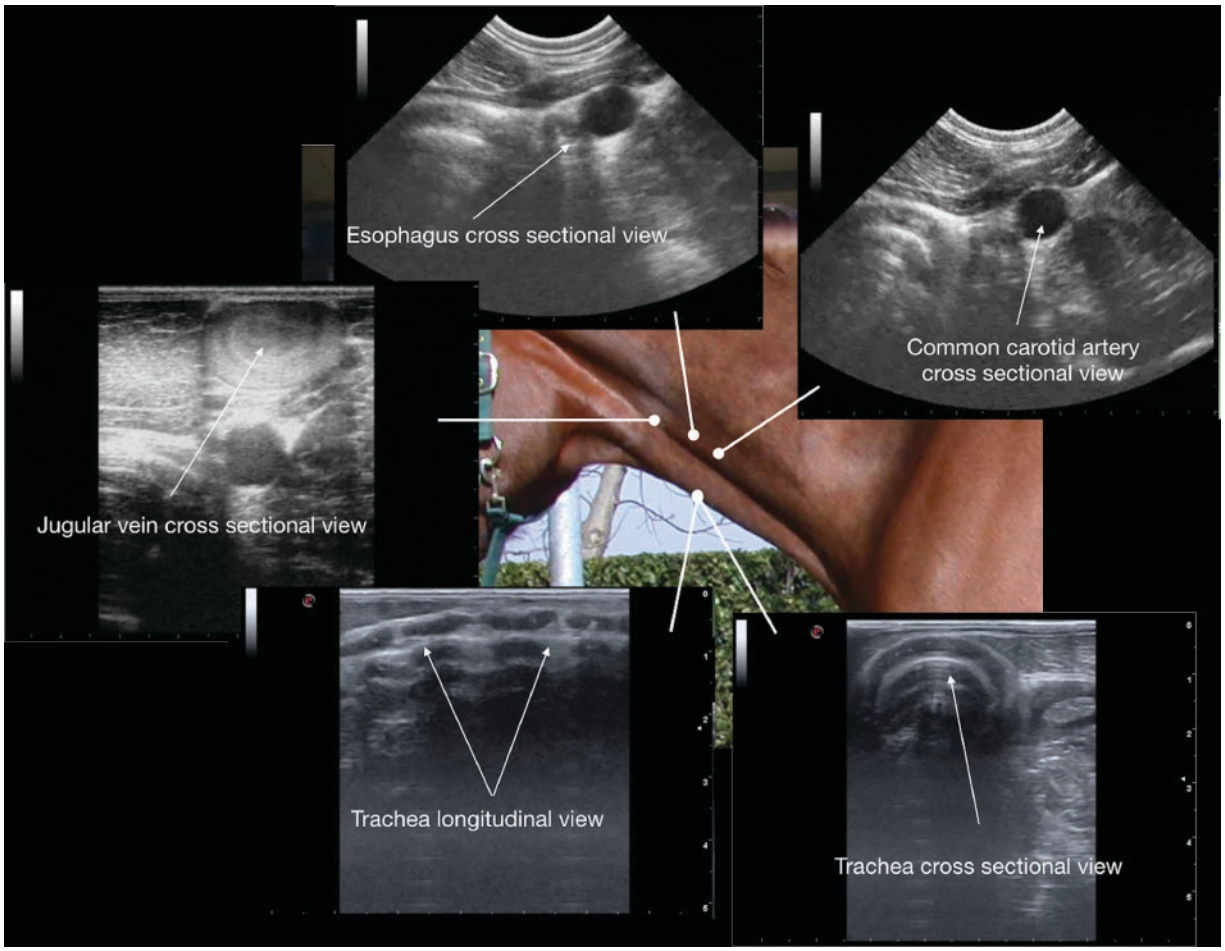


Figure 25.56 Main ultrasound structures in the jugular groove region. This picture illustrates images of the structures identifiable along the entire length of the jugular groove, jugular vein, esophagus, common carotid artery, and trachea.

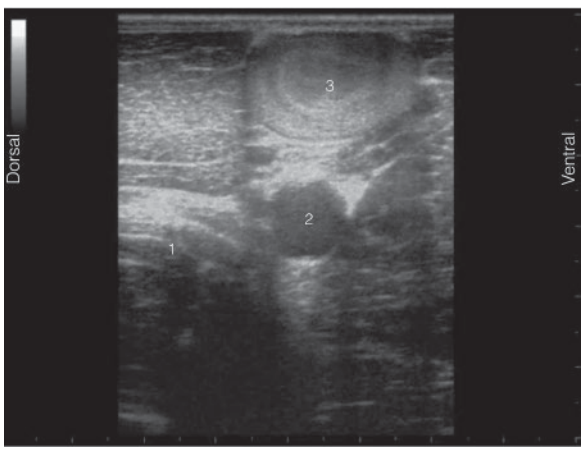


Figure 25.57 Jugular vein and carotid artery. This image is a cross-sectional view of the left jugular region obtained from a normal adult horse. The jugular vein (3) has been occluded in the distal cervical region. Therefore, the jugular vein remains distended when pressure is applied from the ultrasound probe. The blood inside the vein has a hyperechoic, swirling appearance. The carotid artery (2) is deeper than the jugular vein and the blood has a hypoechoic appearance. The trachea (1) is on the median axis. This sonogram was obtained with a wide-bandwidth 10.0 MHz linear array transducer, operating at 12.0 MHz, at a display depth of 5 cm.

Vet-ebooks.com

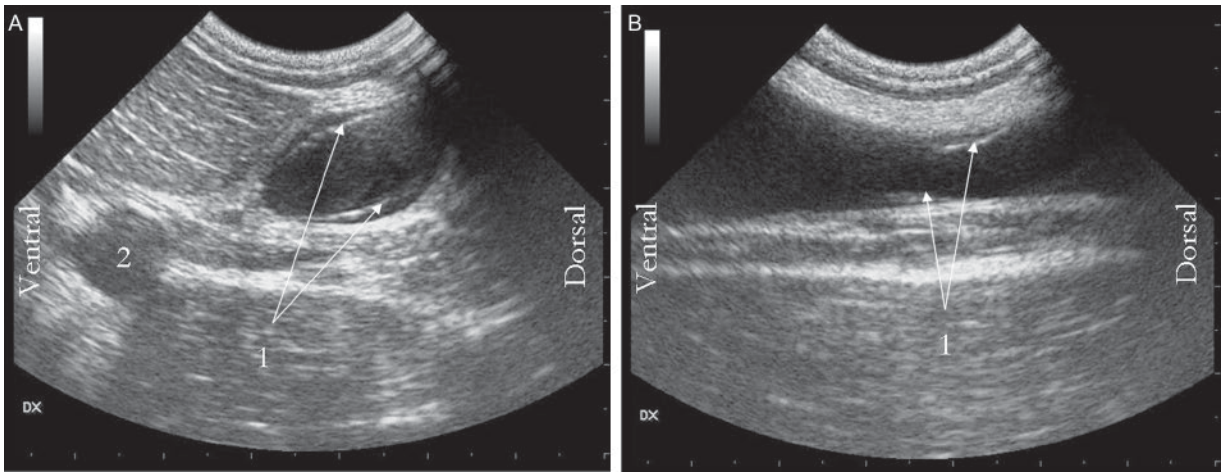


Figure 25.58 Jugular vein. These images are (A) cross-sectional and (B) longitudinal views of the left jugular region from a normal adult horse. Valves (1) are visualized adjacent to the vessel wall. The carotid artery (2) is deep to the jugular vein. This sonogram was obtained with a wide-bandwidth 6.6 MHz micro-convex linear array transducer, operating at 8.0 MHz, at a display depth of 5 cm.

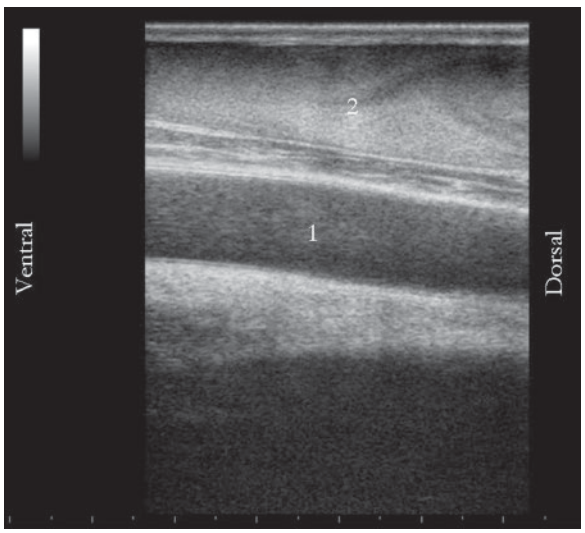


Figure 25.59 Jugular vein and carotid artery. This image is a longitudinal view of the left jugular groove obtained from a normal adult horse. The carotid artery (1) is deep to the jugular vein (2). The jugular vein has a thick wall, while the carotid artery has a thin wall. Blood in the carotid artery is hypoechoic, while blood in the jugular vein is hyperechoic and swirling. This sonogram was obtained with a wide-bandwidth 10.0 MHz linear array transducer, operating at 12.0 MHz, at a display depth of 5 cm.

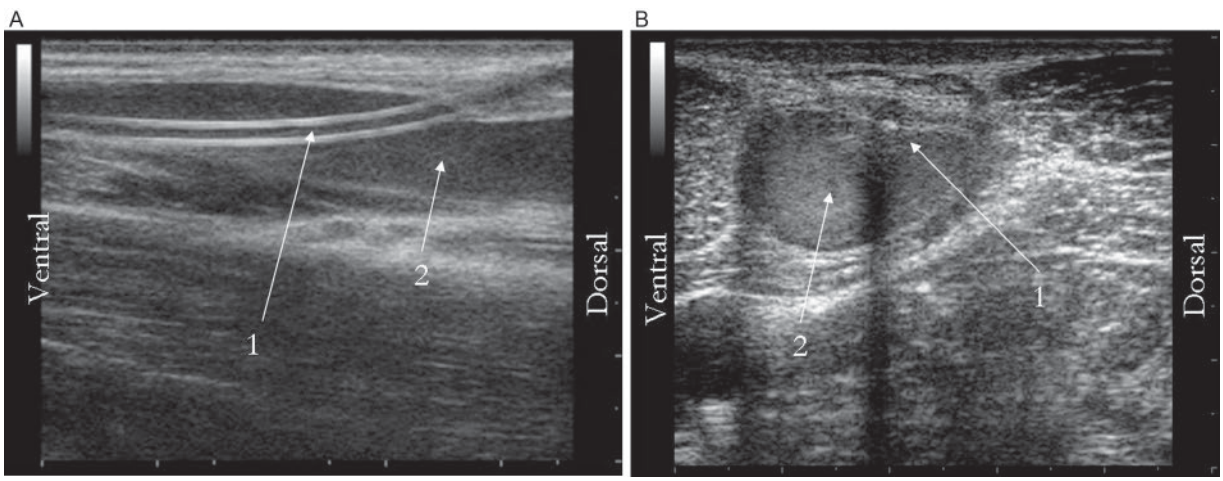


Figure 25.60 Jugular vein. These images are (A) longitudinal and (B) cross-sectional views of the left jugular region from an adult horse with an intravenous catheter. The intravenous catheter (1) is visualized in the lumen of the jugular vein (2). This sonogram was obtained with a wide-bandwidth 10.0 MHz linear array transducer, operating at 12.0 MHz, at a display depth of 5 cm.

Vet-ebooks.com

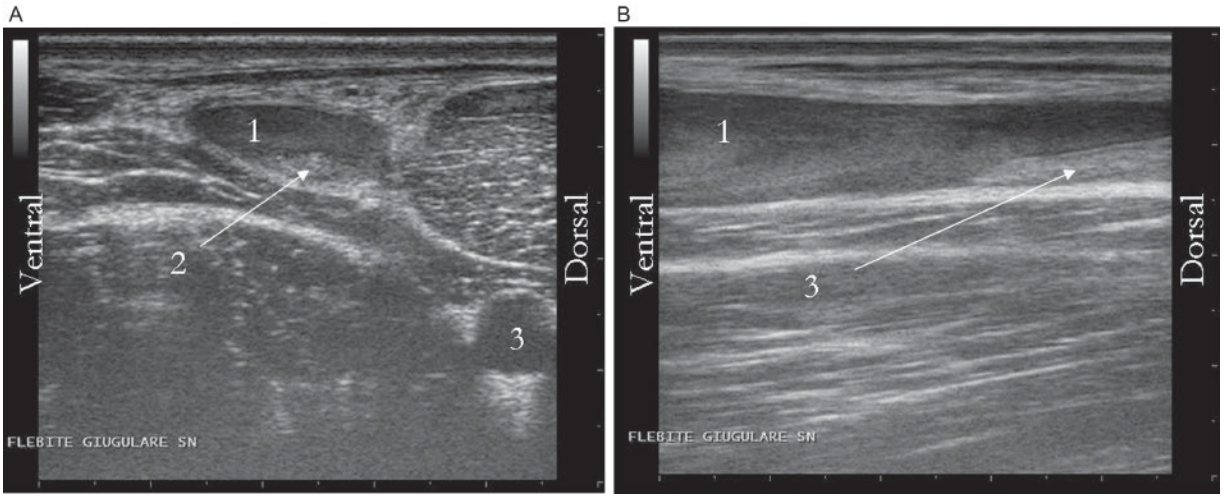


Figure 25.61 Jugular vein. These images are (A) cross-sectional and (B) longitudinal views of the left jugular vein from an adult horse with an intravenous catheter. A hyperechoic clot (2) with well-defined margins is visible inside the jugular vein (1). The carotid artery (3) is visualized deep to the jugular vein. These sonograms were obtained with a wide-bandwidth 10.0 MHz linear array transducer, operating at 12.0 MHz, at a display depth of 4 cm.



Figure 25.62 Jugular vein. This image is of a clinical case of right jugular phlebitis with a draining tract.

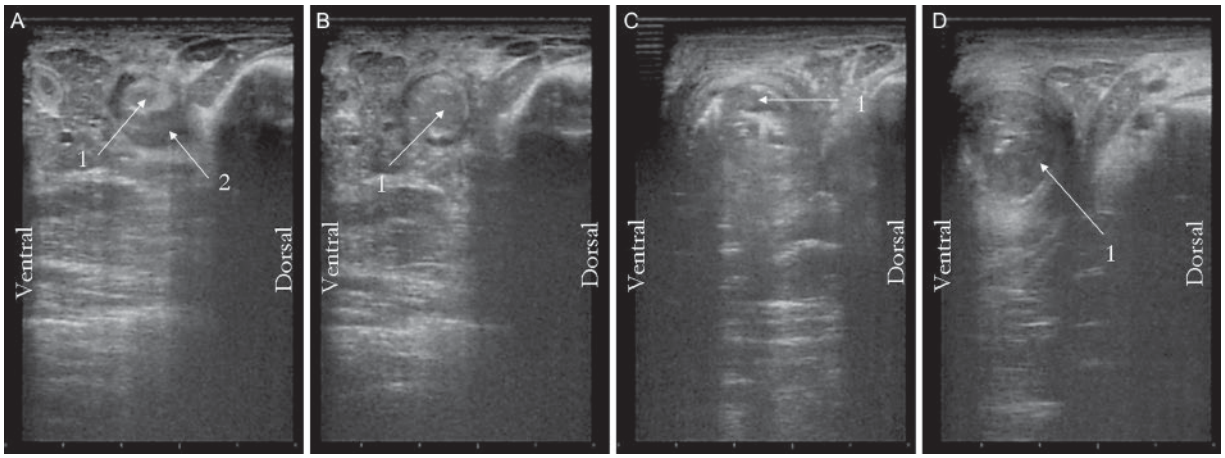


Figure 25.63 Jugular vein. These images are cross-sectional views from proximal (A) to distal (D) of the right jugular region obtained from the clinical case in Figure 26.9. A well-demarcated, hyperechoic clot (1) is visible inside the jugular vein (2). These sonograms were obtained with a wide-bandwidth 10.0 MHz linear array transducer, operating at 12.0 MHz, at a display depth of 5 cm.

Vet-ebooks.com

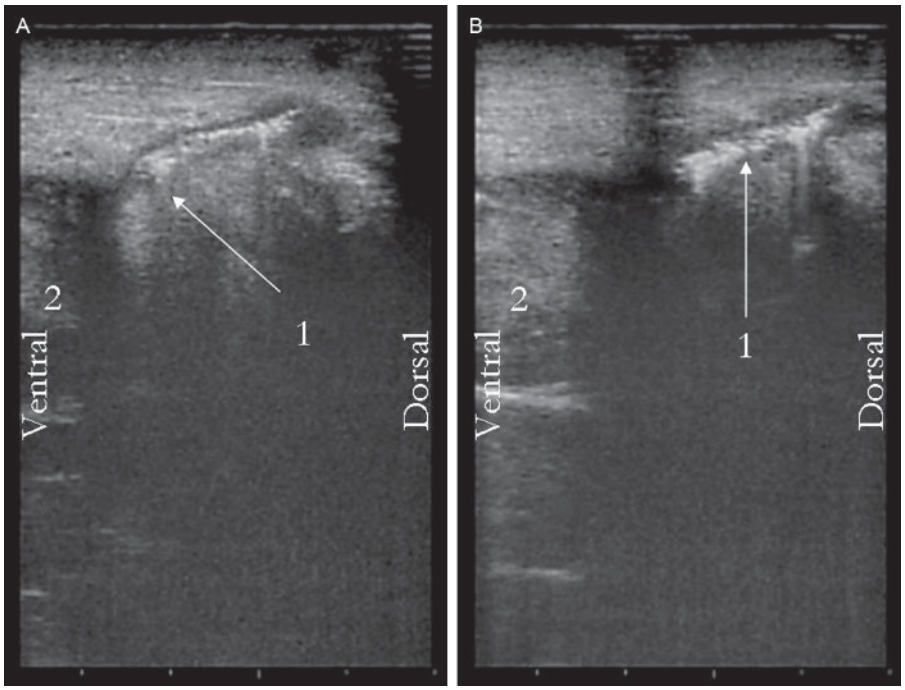


Figure 25.64 Jugular vein. These images are longitudinal views from proximal (A) to distal (B) of the right jugular region obtained from the clinical case in Figure 26.9. A draining tract (1) is visible coming from the jugular vein (2). These sonograms were obtained with a wide-bandwidth 10.0 MHz linear array transducer, operating at 12.0 MHz, at a display depth of 4 cm.

groove, from the mandibular branch to the thoracic inlet. Normally, it is thin walled and easily compressible with the ultrasound probe. The blood inside the jugular vein has a hyperechoic, swirling appearance when compared to blood in the adjacent carotid artery. The distal part of the vein should be compressed to dilate the proximal portion of the vessel being scanned to aid in correctly visualizing all the structures, including the valves of the vein. Valves are normal structures that can easily be confused with a small thrombus. Valves appear as thin structures adjacent to the walls of the vessel and move in synchrony with blood flow.

Ultrasound of the jugular vein can confirm correct placement of an intravenous catheter in the vessel lumen and may aid in detecting early signs of catheter-associated thrombus, as well as jugular vein thrombi not associated with intravenous catheter or vessel trauma. Thrombi appear as hyperechoic structures in the vessel lumen or attached to the vessel wall. Margins may be smooth and well demarcated or pedunculated in appearance. A correctly positioned intravenous catheter may exhibit on ultrasound a fibrin envelope or sleeve around the catheter before a thrombus forms [2]. Initially, blood flow is maintained, but the thrombus may increase in size to cause inflammation of the vessel (thrombophlebitis) and, potentially, complete occlusion of the vessel. Other changes associated with thrombophlebitis include perivasculitis of the surrounding soft tissue and thickening of the vessel wall [2]. Thrombophlebitis can eventually occlude the jugular vein completely, resulting in a fibrous cord, no blood flow, and no signs of inflammation (Figure 25.65).

Carotid Artery

The carotid artery (Figures 25.57 and 25.60) is visible in the jugular groove medial to the jugular vein and lateral to the trachea. The wall is thicker than that of the jugular vein and the vessel is not compressible. The blood is hypoechoic compared to blood in the jugular vein. In the proximal neck, the carotid artery is separated from the jugular vein by the omohyoid muscle, but in the middle and distal neck, the muscle thins and the carotid artery and jugular vein are in close proximity to each other.

Trachea

The trachea (Figure 25.66) is a tubular structure composed of tracheal rings, that image as hypoechoic areas, and tough membranes, that image as hyperechoic areas. The inner surface is hyperechoic because of mucus containing gas microbubbles. Tracheal mucus or fluid is identifiable by ultrasound in the distal neck where the trachea becomes more horizontal (Figures 25.67 and 26.68). Tracheal

Vet-ebooks.com

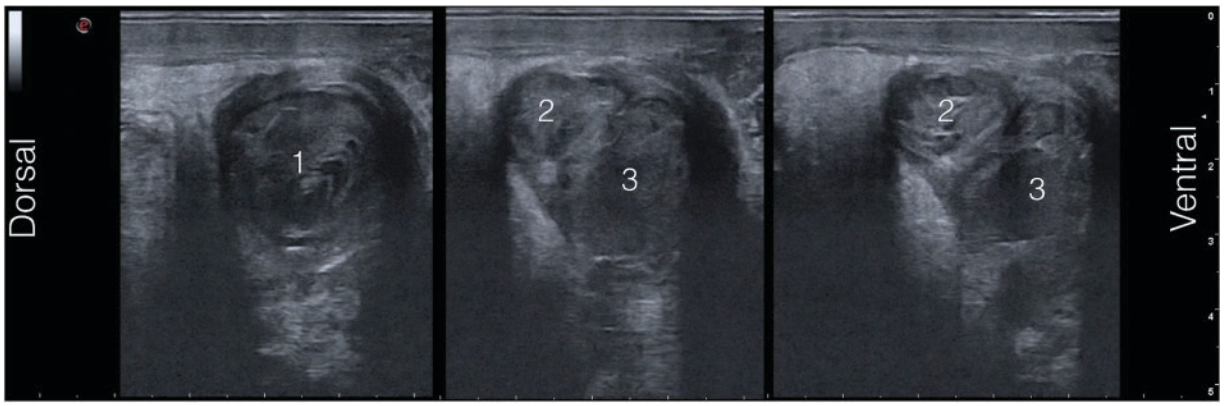


Figure 25.65 Jugular vein. These images are cross-sectional views of the left jugular vein (3) at the level of the jugular bifurcation into the maxillary vein (2) and the linguofacial vein (1) obtained from a clinical case of chronic jugular phlebitis. All the veins are almost completely occluded by fibrous tissue. These sonogram were obtained with a wide-bandwidth 3.0–13.0 MHz linear array transducer, operating at 5.0 MHz, at a display depth of 5 cm.

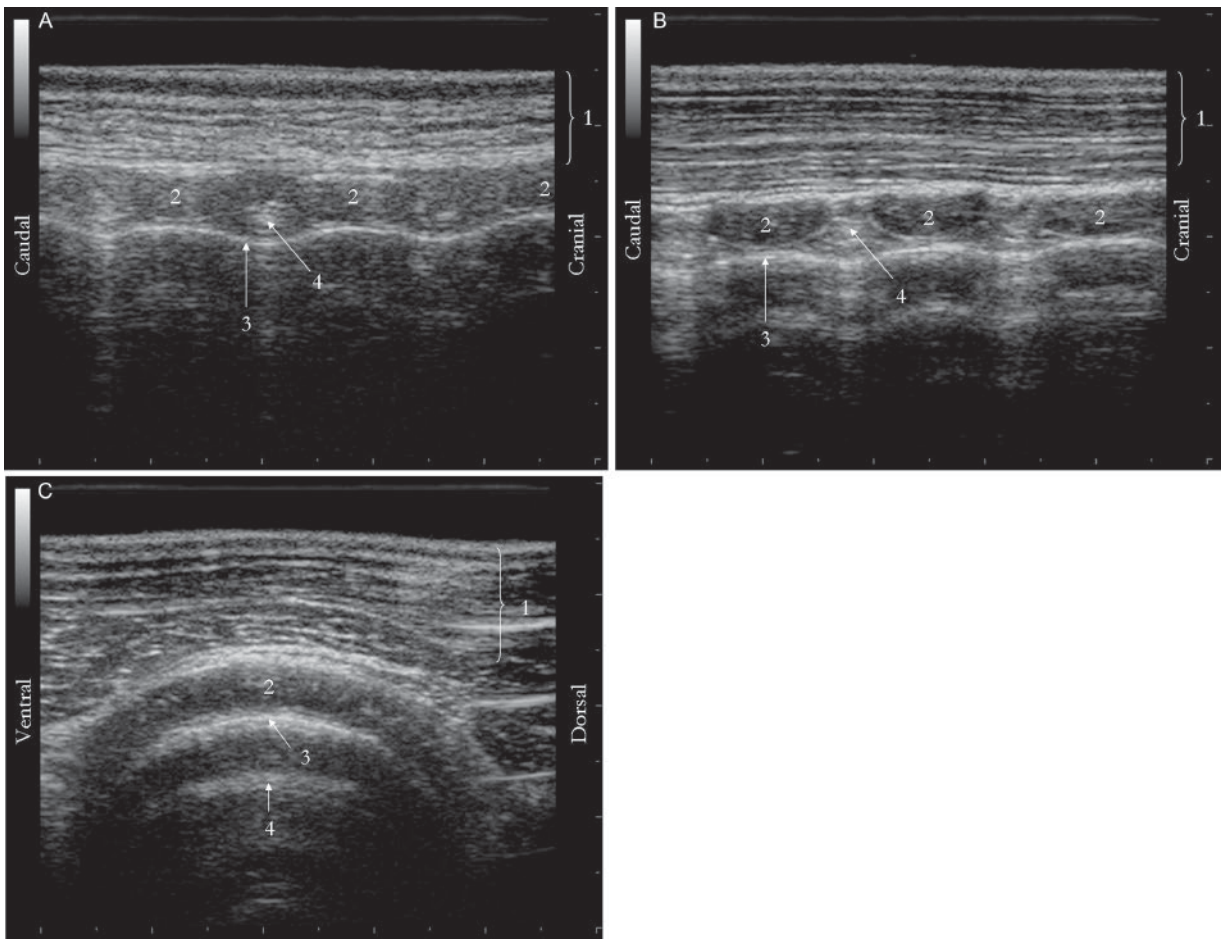


Figure 25.66 Normal trachea. These images are (A) longitudinal view of the proximal trachea, (B) longitudinal view of the middle trachea, and (C) cross-sectional view of the middle trachea in a normal adult horse. Cutis, subcutis, and muscles (1) are superficial to the trachea. Tracheal rings (2) are hyperechoic in the proximal part and hypoechoic in the middle and distal parts of the trachea. The mucosal surface of the trachea (3) is hyperechoic and casts a reverberation artifact due to the presence of air in the mucus. The membranes between the tracheal rings (4) are hyperechoic. These sonograms were obtained with a wide-bandwidth 10.0 MHz linear array transducer, operating at 12.0 MHz, at a display depth of 4 cm.

Vet-ebooks.com

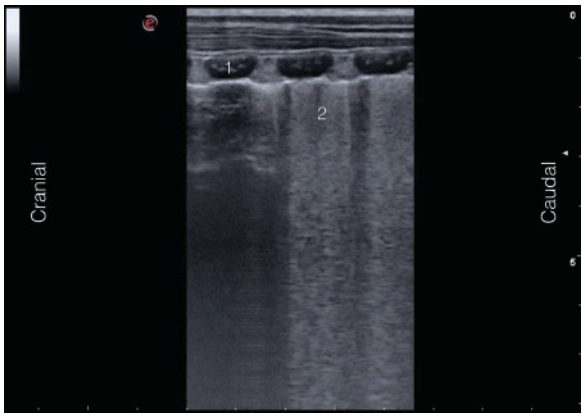


Figure 25.67 Trachea with fluid. This image is a longitudinal view of the distal trachea (1); the presence of fluid (2) inside the tracheal lumen is clearly visible. This sonogram was obtained with a wide-bandwidth 3.0–13.0 MHz linear array transducer, operating at 5.0 MHz, at a display depth of 8 cm.

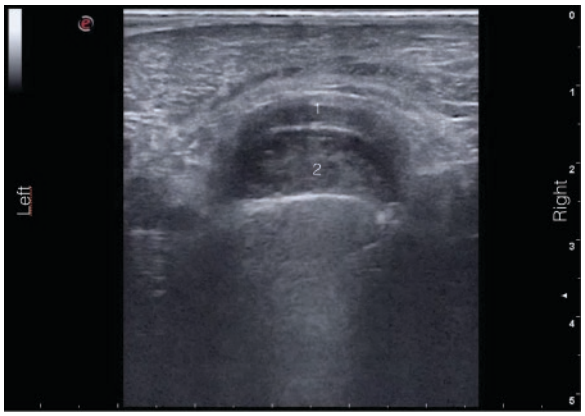


Figure 25.68 Trachea with fluid. This image is a cross-sectional view of the distal trachea (1); the presence of fluid (2) inside the tracheal lumen is clearly visible. This sonogram was obtained with a wide-bandwidth 3.0–13.0 MHz linear array transducer, operating at 5.0 MHz, at a display depth of 5 cm.

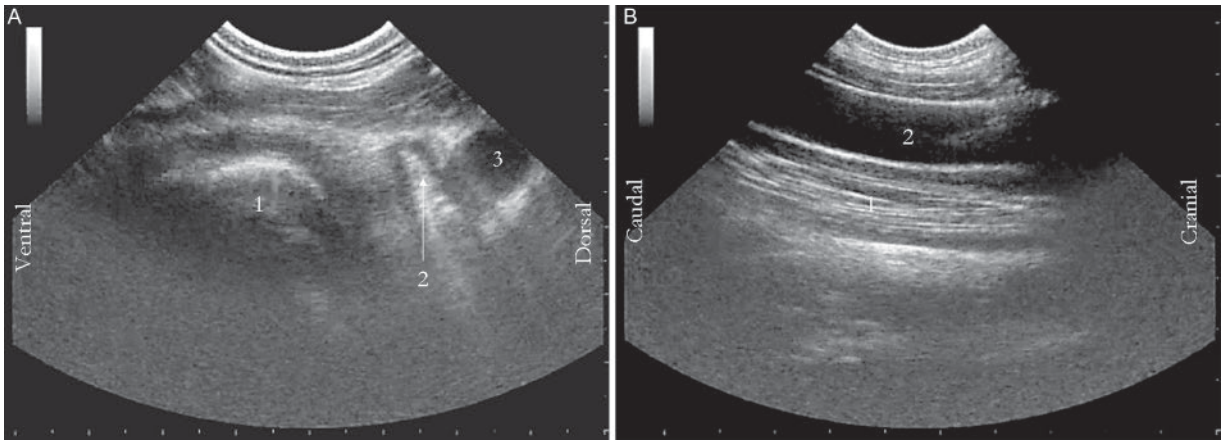


Figure 25.69 Normal esophagus. These images are (A) cross-sectional and (B) longitudinal views of the left jugular region from a normal adult horse. The esophagus (2) is visible between the carotid artery (3) and the trachea (1). The esophageal mucosal folds appear as alternating hyperechoic and hypoechoic lines. The esophageal wall has a hypoechoic appearance. These sonograms were obtained with a wide-bandwidth 6.6 MHz micro-convex linear array transducer, operating at 6.6 MHz, at a display depth of (A) 6 and (B) 8 cm.

rupture and subcutaneous emphysema may result from trauma. Peritracheal abscesses may result from trauma or as complications from transtracheal washings.

Esophagus

The esophagus (Figures 25.69, 25.70, and 25.71) is a tubular structure with a 3–4 mm thick wall formed by an outer, hypoechoic, muscular layer and an inner, hyperechoic, serosal layer. The lumen is irregular due to the mucosal folds covered by mucus containing gas. In the cranial third of the neck, the esophagus is located on the median line, deep to the trachea. In the middle and caudal thirds of the neck, it is usually located left of the trachea. However, some normal horses will have an esophagus located to the right of the trachea. The esophagus is normally collapsed except during swallowing.

Esophageal obstruction (Figures 25.72 and 25.73), commonly referred to as choke, is a leading cause of esophageal pathology. Feed material is the most common cause of obstruction and appears as an echogenic mass in the lumen of the esophagus. Initially, obstruction results in esophageal dilation, but prolonged or repeated episodes may lead to esophageal stricture, diverticulum, or rupture. External trauma, such as a kick, or use of a nasogastric tube may also result in esophageal pathology. Megaesophagus (Figures 25.74 and 25.75), or profound dilation of the esophagus, may occur from a congenital defect, obstruction, or other esophageal

Vet-ebooks.com

Figure 25.70 Normal esophagus with food bolus. This image is a longitudinal view of the left jugular region of a normal adult horse. The normal esophagus (1) with a food bolus (3) is visible deep to the carotid artery (2). This sonogram was obtained with a wide-bandwidth 6.6 MHz micro-convex linear array transducer, operating at 6.6 MHz, at a display depth of 8 cm.

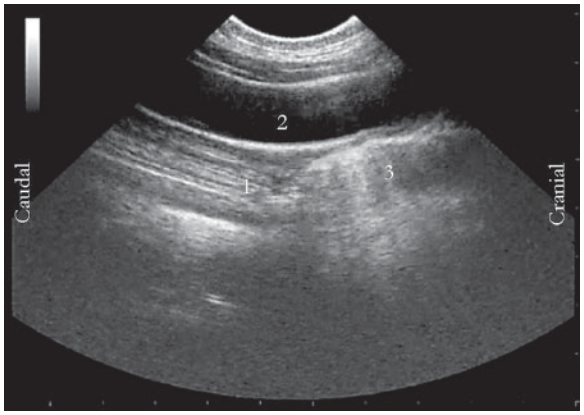


Figure 25.71 Esophagus with nasogastric tube. This image is a cross-sectional view of the left jugular region of a normal adult horse with a nasogastric tube in the esophagus. The esophagus (5) is visible between the carotid artery (3) and the trachea (1) near the scalenus muscle (4). The nasogastric tube (2) is well identified inside the esophageal lumen, confirming its correct positioning. This sonogram was obtained with a wide-bandwidth 6.6 MHz micro-convex linear array transducer, operating at 6.6 MHz, at a display depth of 6 cm.

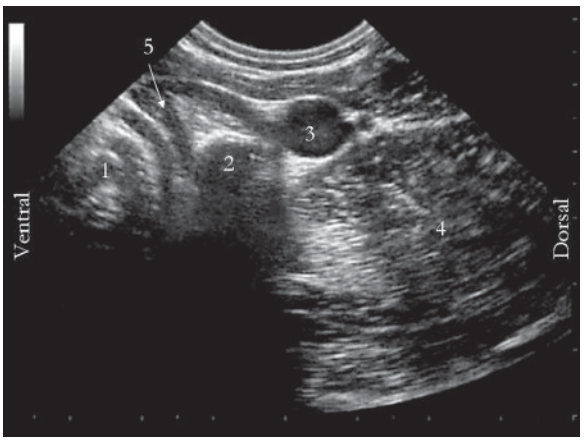


Figure 25.72 Esophageal choke. This image is a longitudinal view of the left distal jugular region of an adult Spanish horse with esophageal choke. The cranial part of the esophagus is filled with fluid (2), while the more caudal part has solid content (1). This sonogram was obtained with a wide-bandwidth 6.6 MHz micro-convex linear array transducer, operating at 6.6 MHz, at a display depth of 10 cm.

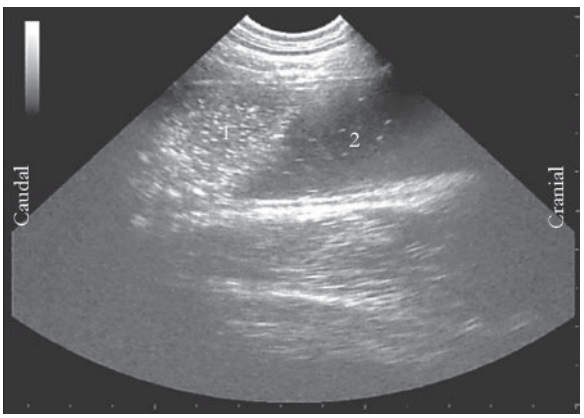
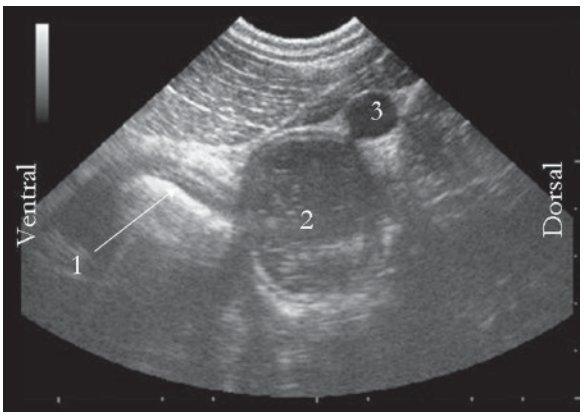


Figure 25.73 Esophageal choke. This image is a cross-sectional view of the left distal jugular region of an adult Spanish horse with esophageal choke. The fluid-filled esophagus (2) is visualized between the trachea (1) and carotid artery (3). This sonogram was obtained with a wide-bandwidth 6.6 MHz micro-convex linear array transducer, operating at 6.6 MHz, at a display depth of 8 cm.



Vet-ebooks.com

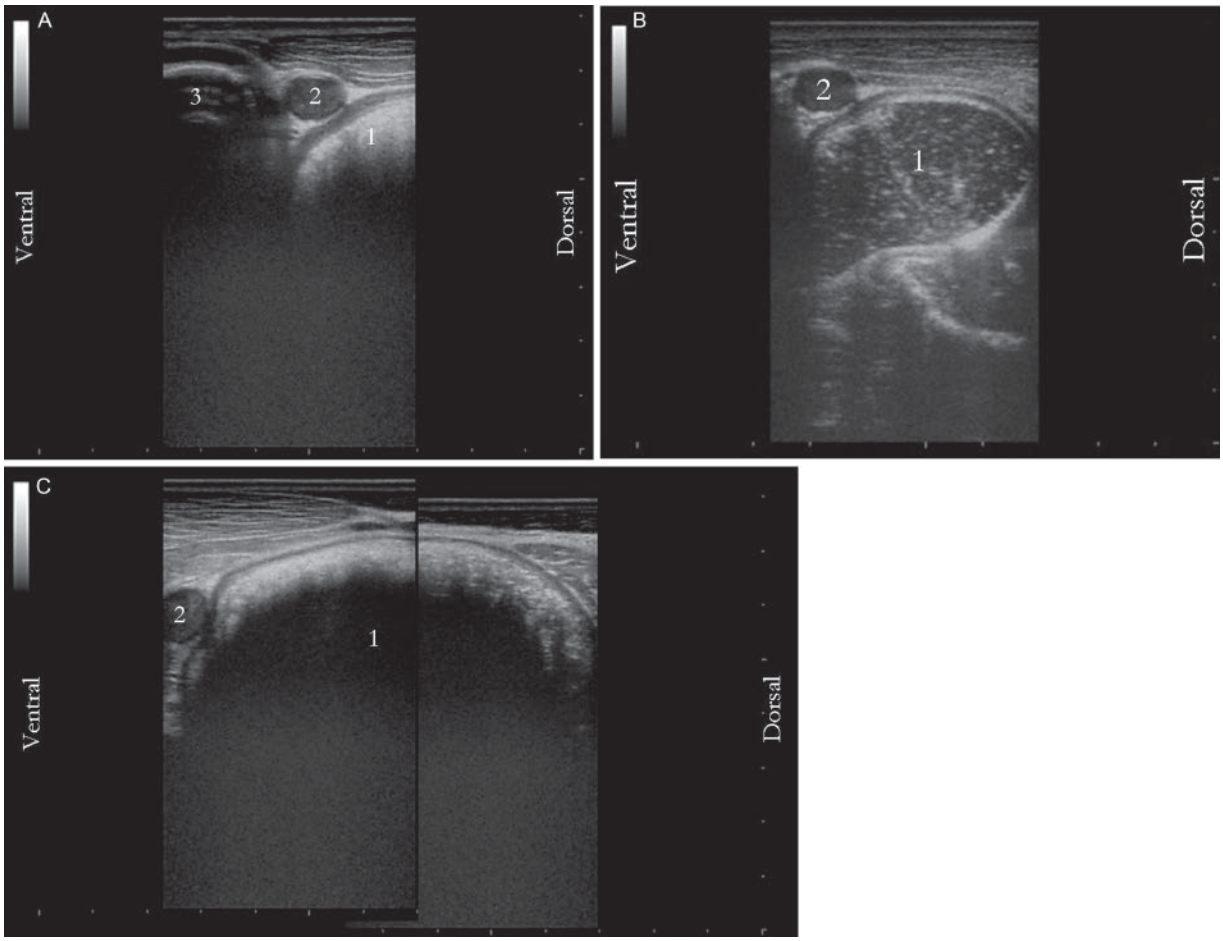


Figure 25.74 Megaesophagus. These images are cross-sectional views of the left distal jugular region of a 13-year-old Welsh pony with megaesophagus. (A) The esophagus (1) is distended and has a thickened wall with hyperechoic material in the lumen. The location between the carotid artery (2) and the trachea (3) is abnormal. (B) The esophagus (1) is filled with fluid and visualized near the carotid artery (2). (C) At the base of the neck, the esophagus (1) is dilated to almost 8 cm in diameter. Two image planes were required to visualize the extent of the megaesophagus. The carotid artery (2) is adjacent to the megaesophagus. These sonograms were obtained with a wide-bandwidth 10.0 MHz linear array transducer, operating at 12.0 MHz, at a display depth of 8 cm.

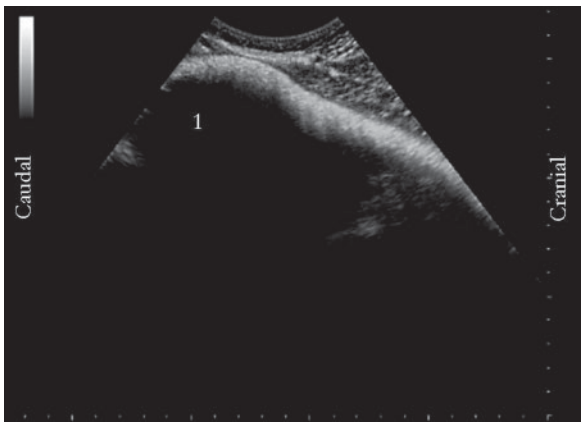


Figure 25.75 Megaesophagus. This image is a longitudinal view of the left distal jugular region of a 13-year-old Welsh pony with megaesophagus. In this part of the esophagus (1), a 2 cm layer of hyperechoic material is present. This sonogram was obtained with a wide-bandwidth 3.5 MHz covex linear array transducer, operating at 3.5 MHz, at a display depth of 15 cm.

Vet-ebooks.com

trauma. Esophageal fistulas (Figure 25.76) may develop secondary to trauma or as a result of passage of a nasogastric tube.

Lateral Region

In this region, it is possible to visualize the muscles of the neck

Muscles

Muscle (Figure 25.77) has hypoechoic fibers and hyperechoic fascia. The ultrasonographic appearance of each muscle varies depending on the quantity of connective tissue and fat present inside it. The omohyoid muscle forms the medial border of the jugular groove; it originates at the subscapular fascia and inserts on the basihyoid bone. The sternohyoid and sternothyroid muscles, often called the strap muscles, course along the ventral surface of the trachea. Both muscles originate at the sternum, but the sternohyoid inserts on the basihyoid bone, while the sternothyroid inserts on the thyroid cartilage of the larynx. The sternocephalic muscle forms the ventral border of the jugular groove and extends from the sternum to the head. The brachiocephalic muscle forms the dorsal border of the jugular groove; it originates on the head of the humerus and inserts at the poll. Other superficial muscles of the neck include the splenius, cervical rhomboid, and cervical ventral serratus [3].

Swellings in muscle should be scanned in order to assess their nature, depth, and topographic relationship to normal structures of the neck, particularly blood vessels. The ultrasound appearance of muscle swelling is highly variable depending on cause. Diffuse infection, abscesses (Figures 25.78 and 25.79), and neoplasia (Figure 25.80) are differentials for swelling in or adjacent to muscles of the neck.

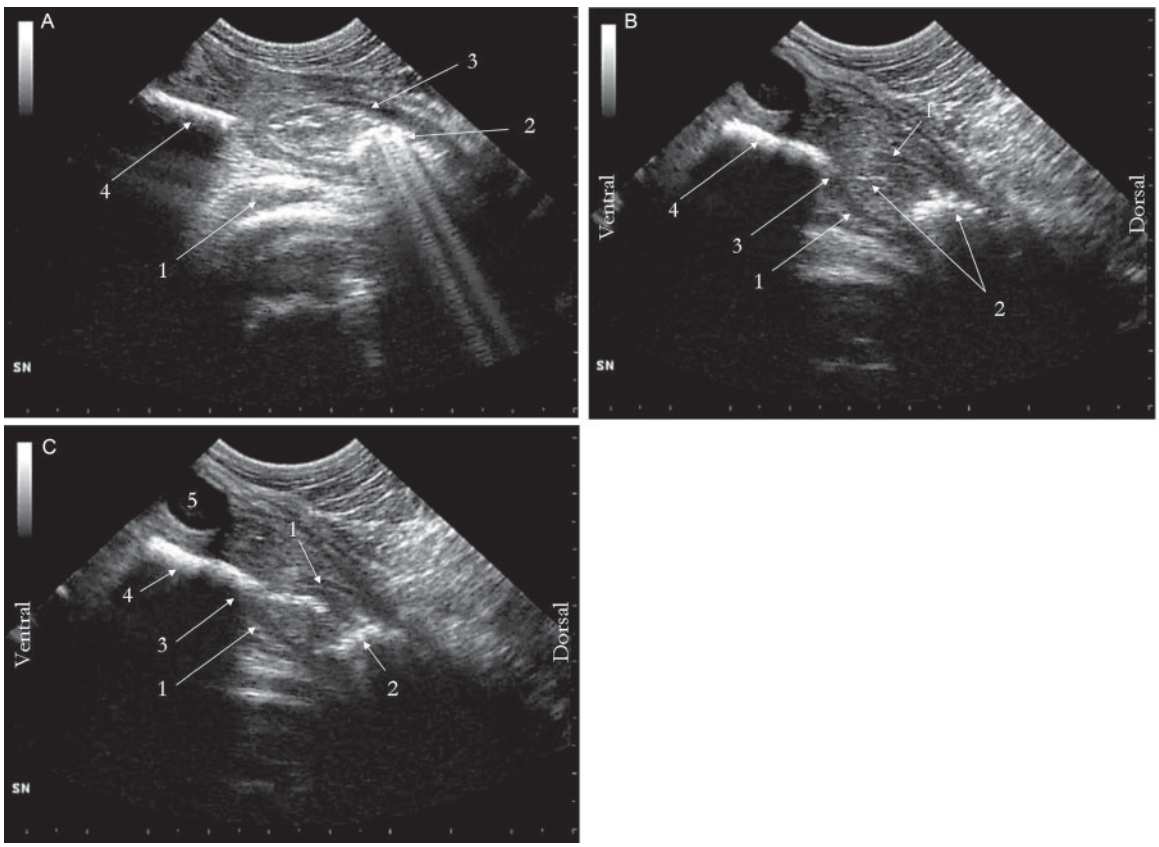


Figure 25.76 Esophageal fistula. These images are cross-sectional views of the left jugular region from (A) cranial to (C) caudal of a 9-year-old Standardbred mare with an esophageal fistula and diffuse cellulitis at the base of the neck. (A) The hypoechoic esophageal wall (3) surrounds hyperechoic material in the esophageal lumen. The trachea (1) is deep to the esophagus. Hyperechoic material (4) is present outside the esophageal lumen. An acoustic shadow artifact (2) is present. (B) The esophageal wall (1) is visible with hyperechoic material inside the esophageal lumen (2). Hyperechoic material is present outside the esophageal lumen (4) secondary to an esophageal fistula (3). The jugular vein (5) is visible. (C) Esophageal wall (1), hyperechoic material inside the esophageal lumen (2), point of rupture of the esophageal wall (3), and hyperechoic material crossing the esophageal wall (4). The jugular vein (5) is visible. These sonograms were obtained with a wide-bandwidth 6.6 MHz micro-convex linear array transducer, operating at 6.6 MHz, at a display depth of 7 cm.

Vet-ebooks.com

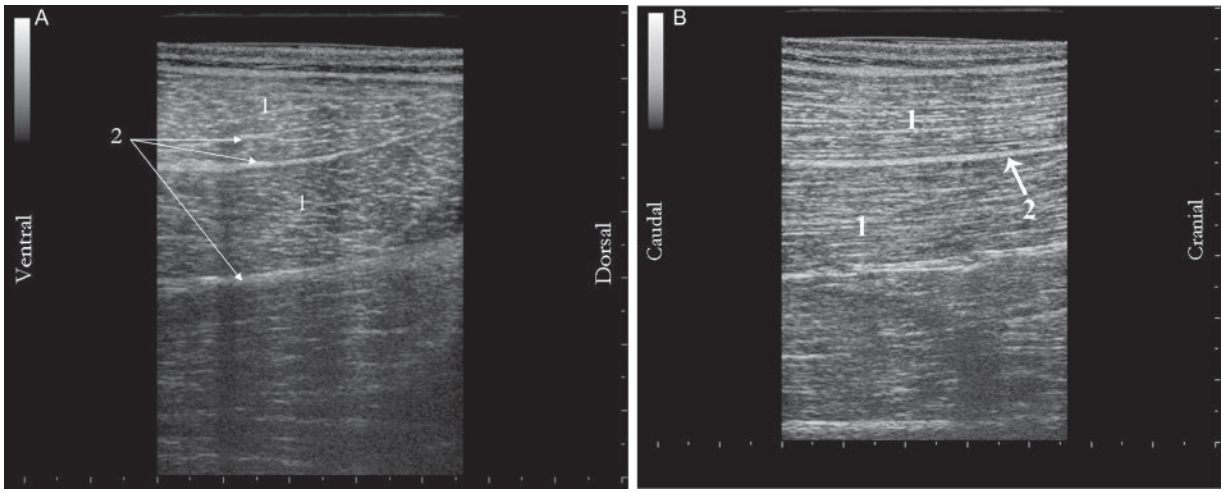


Figure 25.77 Neck muscles. These images are (A) cross-sectional and (B) longitudinal views of the lateral neck in a normal adult horse. The muscle fibers (1) have a hypoechoic, heterogeneous appearance, while the fascia (2) is hyperechoic. These sonograms were obtained with a wide-bandwidth 10.0 MHz linear array transducer, operating at 12.0 MHz, at a display depth of 7 cm.

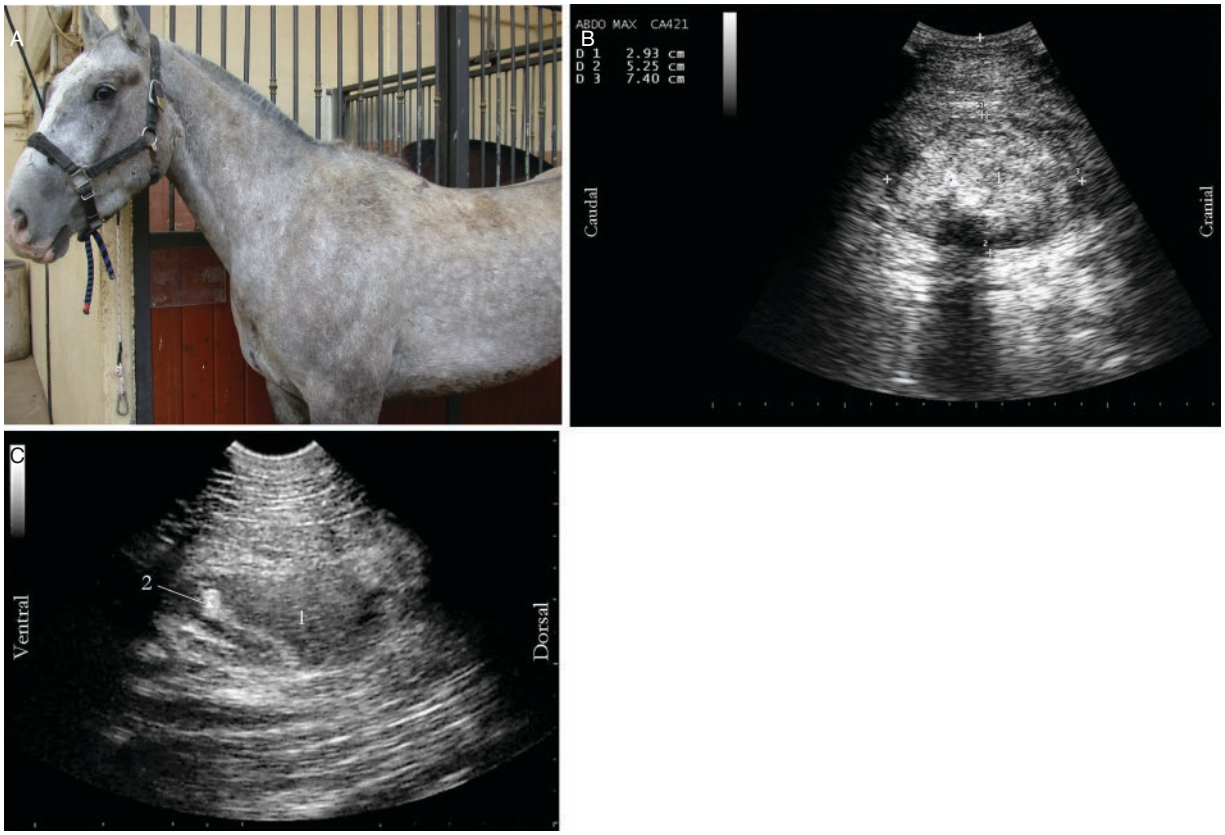


Figure 25.78 Neck abscess. (A) This picture is of a 13-year-old Criollo horse with a suspected abscess. A firm, painful mass and a fistula with mucopurulent exudate is present at the base of the neck to the left of the trachea. (B) This image is a longitudinal view of the base of the neck. A well-defined mass (1) is visible 2.52 cm deep. This mass has a homogeneous, hypoechoic structure with a thick and well-demarcated hyperechoic capsule. (C) This image is a cross-sectional view of the base of the neck. The same hypoechoic mass (1) is visible with a hyperechoic structure identified as a necrotic fragment (2). These sonograms were obtained with a wide-bandwidth 3.5 MHz convex linear array transducer, operating at 5.0 MHz, at a display depth of 12 cm.

Vet-ebooks.com

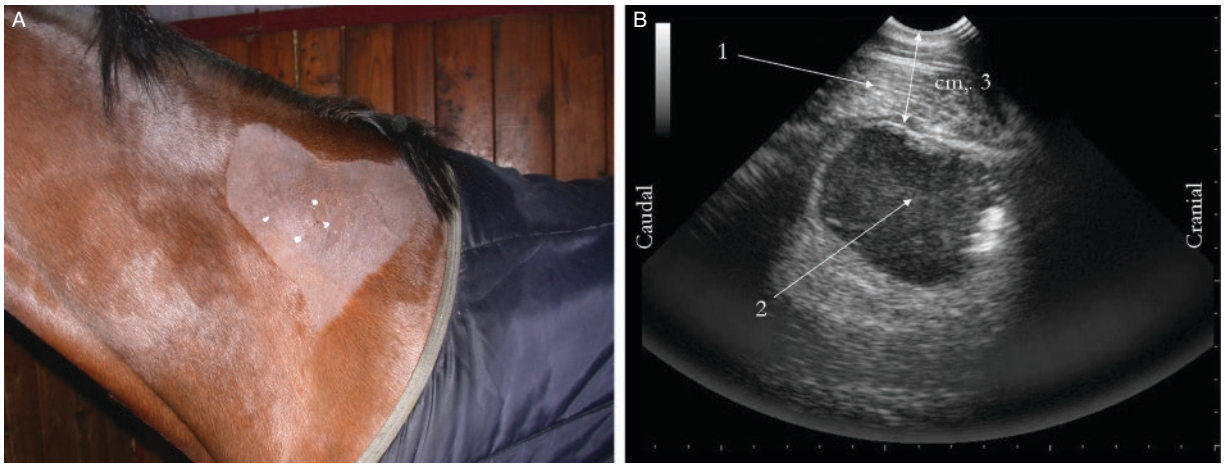


Figure 25.79 Neck abscess. (A) This picture is of a 9-year-old Hanover horse with a suspected abscess. A firm, painful mass is present on the lateral side of the neck. (B) This image is a longitudinal view of the lateral side of the neck. A hypoechoic mass (2) is visible, 3 cm deep, with a well-defined hyperechoic capsule. The superficial muscle layer (1) is visible. This sonogram was obtained with a wide-bandwidth 3.5 MHz convex linear array transducer, operating at 5.0 MHz, at a display depth of 13 cm.

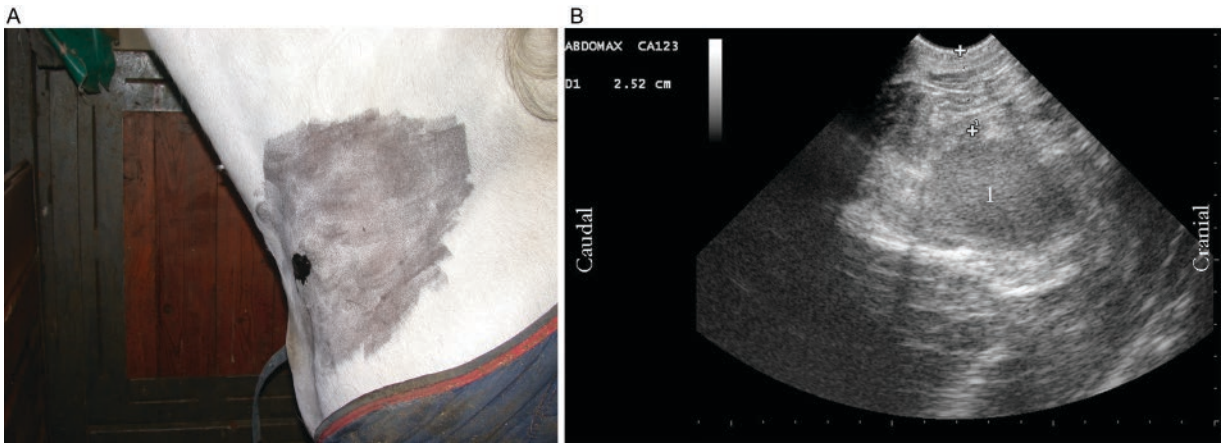


Figure 25.80 Melanoma. (A) This picture is of a 10-year-old Spanish horse with suspect melanoma. A firm, slightly painful mass and a fistula with black exudate are present at the base of the neck to the left of the trachea. (B) This image is a longitudinal view of the base of the neck. A well-defined mass (1) is visible 2.93 cm deep, measuring 5.25 cm by 7.40 cm. The mass does not have a homogeneous echogenic appearance. This sonogram was obtained with a wide-bandwidth 3.5 MHz convex linear array transducer, operating at 3.5 MHz, at a display depth of 15 cm.

Recommended Reading

Pasquini, P., Spurgeon, T., and Pasquini, S. (2003). General. In: *Anatomy of Domestic Animals*, 10th edn, 439–440. Pilot Point: Sudz.

Rathmanner, M. and Rijkenhuizen, A.B.M. (2012). Ultrasonography of the upper cervical region (EUCR) in the horse. *Pferdeheilkunde*, 28: 5.

References

1 Wheat, J.D. (1962). Tympanites of the guttural pouch of the horse. *Journal of the American Veterinary Medical Association* 140: 453–454.

2 Gardner, S.Y., Reef, M.B., and Spencer, P.A. (1991). Ultra-sonographic evaluation of 46 horses with jugular vein thrombophlebitis: 1985–1988. *Journal of the American Veterinary Medical Association* 199: 370–373.

3 Pasquini, P., Spurgeon, T., and Pasquini, S. (2003). Muscle. In: *Anatomy of Domestic Animals*, 10th edn, 210–211. Pilot Point: Sudz.

Vet-ebooks.com

26

Ultrasonography of Vascular Structures

Rana Bozorgmanesh

The author acknowledges the prior contribution of Fairfield T. Bain
Hagyard Equine Medical Institute, Lexington, KY, USA

Jugular Vein

The jugular vein is often evaluated ultrasonographically, particularly when thrombophlebitis is suspected in horses with or without intravenous catheters in place. Early signs of thrombophlebitis can be detected ultrasonographically prior to any obvious external indication, including thickening of the wall and/or clot formation. Ultrasound examination of more advanced cases might show partial or complete blockage of the vein and abscess formation. Perivascular injection of medications may cause a local reaction including a focal cellulitis or abscessation (Figures 26.1, 26.2, 26.3, 26.4, 26.5, 26.6, 26.7, 26.8, 26.9, 26.10, 26.11, and 26.12). The jugular vein can be imaged along the neck from its entry into the thoracic inlet distally throughout its course to the bifurcation into the internal and external jugular vein branches just caudal to the ramus of the mandible. To facilitate evaluation, the jugular vein should be distended by occlusion distally near the thoracic inlet, and then the probe can be used to trace the vein along its course. Thorough evaluation involves imaging in both longitudinal and transverse planes. The author likes to scan from distal to proximal along the vein with particular focus on the region of concern (e.g., site of intravenous catheter insertion or palpable thickening of the vein or perivenous tissues).

Distal Limb Vasculature

In addition to ultrasound of the jugular vein, imaging of the vascular system can include examination of distal limb vasculature (Figures 26.13 and 26.14). This is most often performed when a horse has persistent swelling in a limb or has a pattern of tortuous, distended cutaneous vessel.

Lateral Thoracic Vein

The lateral thoracic vein (Figure 26.15) can be imaged along the lateral aspect of the thorax just caudal to the point of the elbow. This vessel is most commonly imaged to assist in intravenous catheter placement when the jugular vein cannot be used for intravenous catheter access.

Iliac Arteries and Aorta

Transrectal ultrasound evaluation of the iliac arteries (Figure 26.16 and 26.17) is performed to diagnose possible thrombosis. Historically, thrombosis of these arteries has been associated with *Strongylus vulgaris* infection. However, other causes include trauma, foaling complications, or the presence of a hypercoagulable state from another disease process. Thrombosis of an iliac artery should be considered in

Atlas of Equine Ultrasonography, Second Edition. Edited by Jessica A. Kidd, Kristina G. Lu and Michele L. Frazer.
© 2022 John Wiley & Sons Ltd. Published 2022 by John Wiley & Sons Ltd.
Companion Website: www.wiley.com/go/kidd/atlas

Vet-ebooks.com

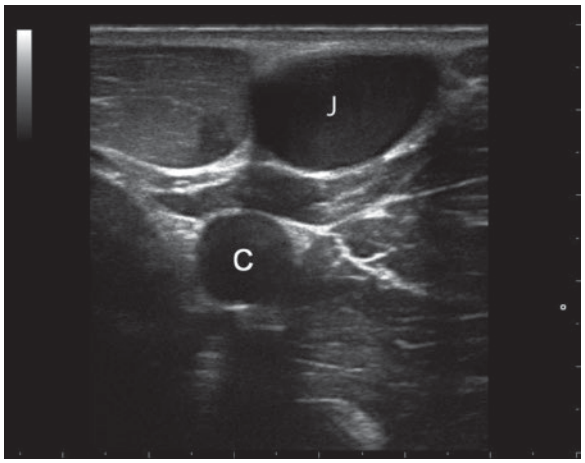


Figure 26.1 Normal jugular vein. The normal jugular vein and its relation to the underlying carotid artery and esophagus varies along its course in the neck. This image shows the close approximation of the jugular vein (J) and carotid artery (C) in the distal third of the neck. The jugular vein is distended with some increasing echogenicity of the blood from stasis. The walls of this normal vein are thin and crisply echogenic. The normal musculature of the neck can be seen surrounding the vein and artery. This sonogram was obtained from the jugular groove with a linear probe operating at 7.5 MHz at a depth of 5 cm.

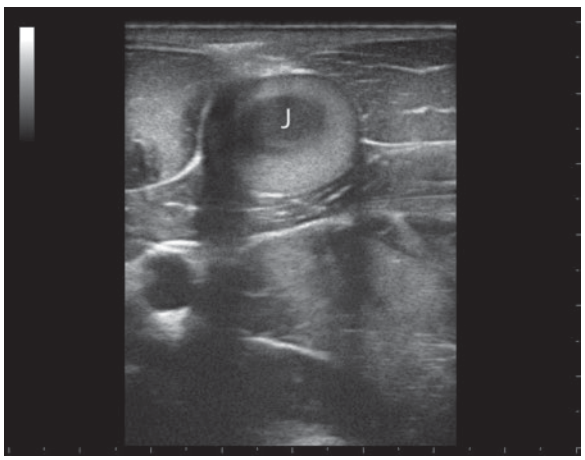


Figure 26.2 Occluded jugular vein. This image shows the jugular vein (J) occluded distally. Occlusion of the jugular vein will obstruct normal blood flow and swirling echogenicity of the normal blood will be observed during the first several seconds after occlusion. This sonogram was obtained from the jugular groove with a linear probe operating at 7.5 MHz at a depth of 5 cm.

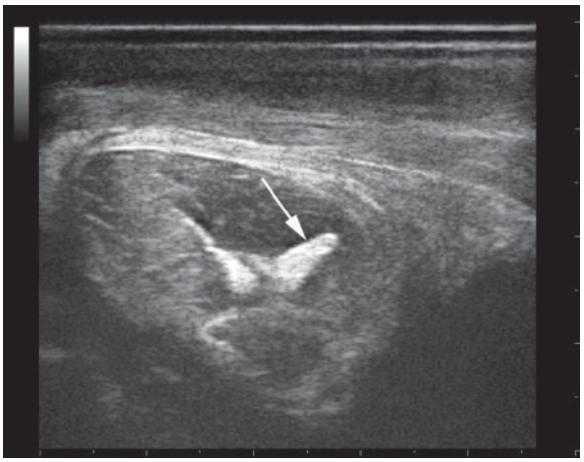


Figure 26.3 Myositis near jugular vein. The main indication for imaging the jugular vein is concern for possible thrombosis. Clinical evaluation of the vein would include palpation of the vein along its course, both before and after distal occlusion. Some patients may have significant perivenous swelling or swelling along the jugular groove of the neck, and ultrasound can be useful to differentiate perivenous inflammation from actual jugular thrombosis or thrombophlebitis. This sonogram shows a central region of echogenicity (arrow) within the cervical muscles consistent with inflammation from intramuscular injection from attempted venous injection in a fractious horse. In this patient, the swelling in the neck was from the focal myositis rather than the jugular vein. This sonogram was obtained from the jugular groove with a linear probe operating at 7.5 MHz at a depth of 4 cm.

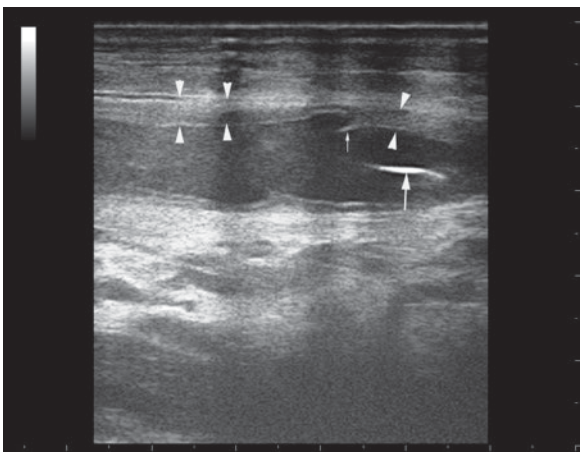


Figure 26.4 Intravenous catheter. Swelling, firmness, or thickening of the jugular vein associated with the presence of an intravenous catheter is one of the more common indications for ultrasound evaluation of the jugular vein. This patient with an intravenous catheter in place (arrow) has sonographic evidence of early phlebitis with thickening of the jugular vein wall (arrowheads). A venous valve (small arrow) is also seen in this image. This sonogram was obtained from the jugular groove with a linear probe operating at 7.5 MHz at a depth of 5 cm.

Vet-ebooks.com

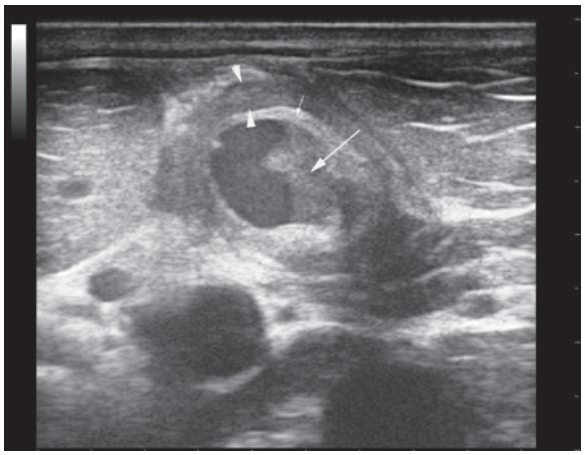


Figure 26.5 Jugular thrombosis. Jugular thrombosis often starts at the site of a traumatic venipuncture in an animal with a prothrombotic state or at the site of entry into the vein of an intravenous catheter. This image shows an asymmetric jugular venous thrombus (long arrow) in a transverse image of the jugular vein. The vein has thickening of the tunica media (arrowheads) and also thickening of the intimal layer (short arrow). These findings indicate jugular phlebitis with developing luminal thrombus formation. This sonogram was obtained from the jugular groove with a linear probe operating at 7.5 MHz at a depth of 4 cm.

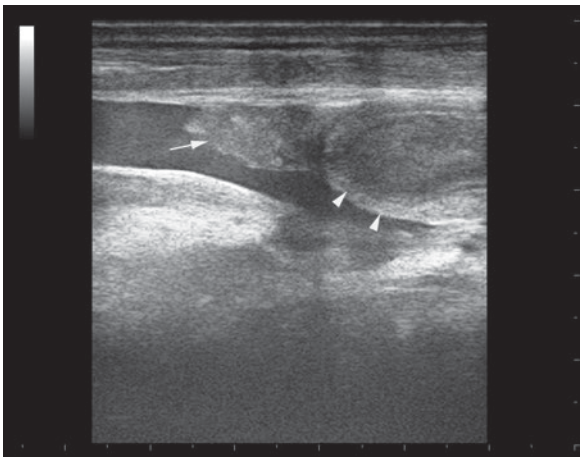


Figure 26.6 Intraluminal thrombus. This image is a longitudinal view of a jugular vein with an intraluminal thrombus. The smooth margins of the older component of the thrombus are seen (arrowheads) along with a more recent, actively proliferating clot (arrow) on the distal edge of the thrombus. The proximal aspect (cranial on the horse) of the vein is to the right. This sonogram was obtained from the jugular groove with a linear probe operating at 7.5 MHz at a depth of 5 cm.

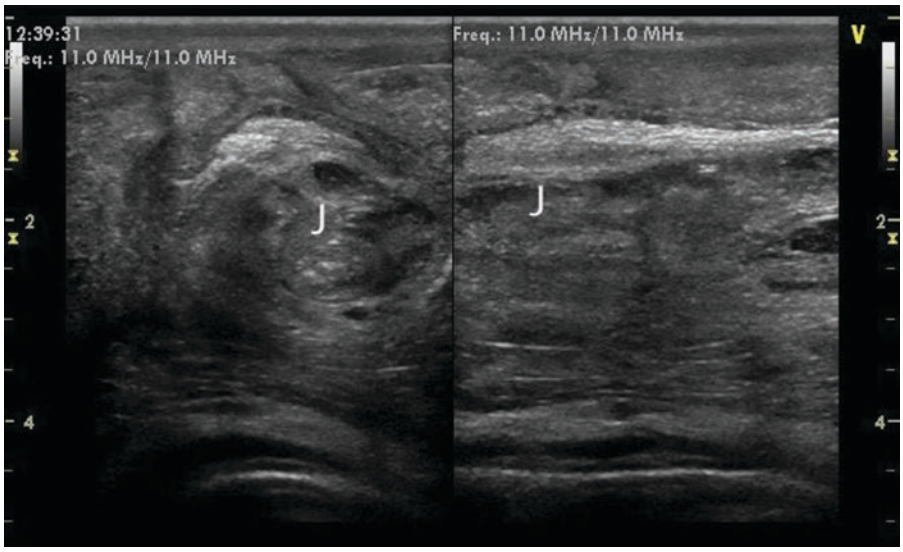


Figure 26.7 Thrombophlebitis of jugular vein. Jugular thrombophlebitis may progress from a partially occlusive thrombus to complete occlusion of the vein. Ultrasound imaging is helpful in differentiating the process of thrombosis from septic thrombophlebitis. This patient had complete occlusion of the jugular vein (J) with an irregular, laminar pattern of thrombosis. The vein has multiple, small echogenic foci that give some concern for possible sepsis. Transverse (left) and longitudinal (right) views are included. This sonogram was obtained from the jugular groove with a linear probe operating at 7.5 MHz at a depth of 5 cm.

Vet-ebooks.com

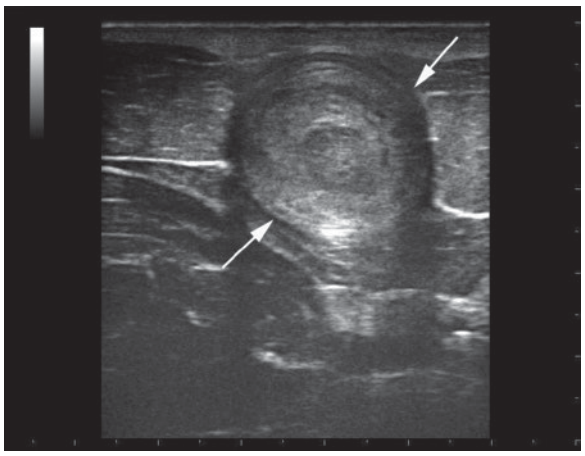


Figure 26.8 Chronic jugular vein thrombosis. This image is a transverse view of a chronic, organized jugular vein thrombosis (arrows indicate outer border of jugular vein) with complete occlusion of the lumen. The thrombus has a laminar pattern. This sonogram was obtained from the jugular groove with a linear probe operating at 7.5 MHz at a depth of 5 cm.

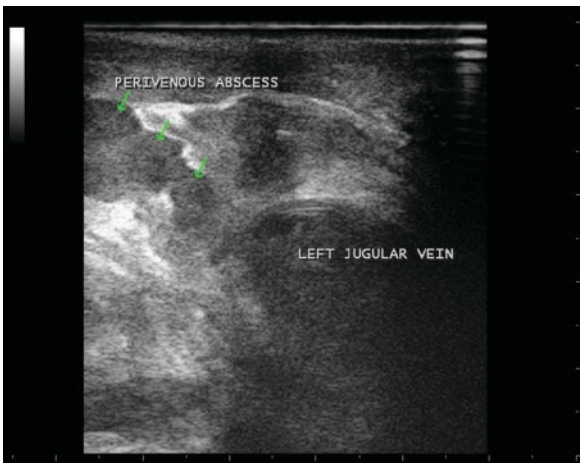


Figure 26.9 Thrombophlebitis from IV catheter. Some cases of jugular thrombophlebitis will occur as extensions from a perivenous, subcutaneous infection along the tract created by an intravenous catheter. This patient had a perivenous abscess present along the catheter tract in addition to thrombosis of the jugular vein. This sonogram was obtained from the jugular groove with a linear probe operating at 7.5 MHz at a depth of 5 cm.

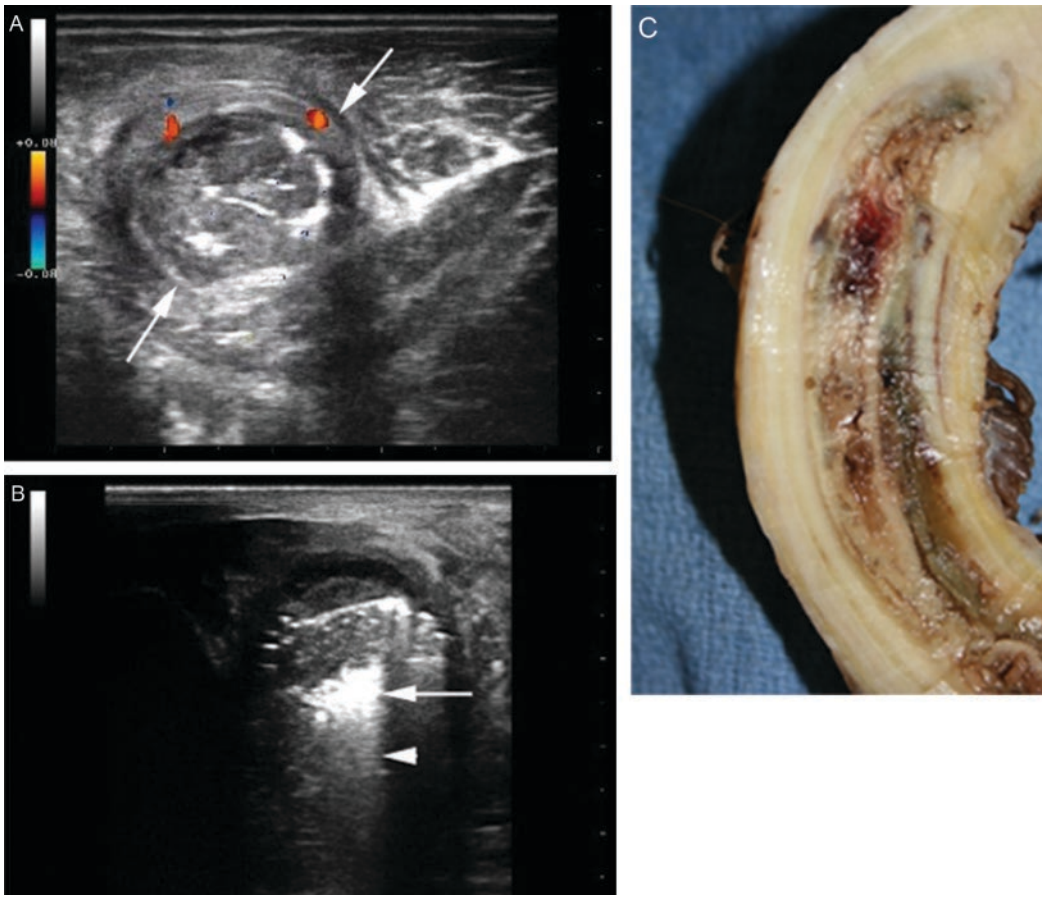


Figure 26.10 Jugular thrombophlebitis from anaerobic infection. This patient had a progressive, septic jugular thrombophlebitis with an anaerobic infection following a dental procedure involving an infected tooth root. The vein had rapid occlusion with a thrombus containing multiple echogenic foci and regions of obvious intraluminal gas. Postmortem evaluation revealed the mixed laminated pattern with regions of suppurative exudate. (A) This image shows septic jugular thrombophlebitis (arrows mark outer border of jugular vein) with echogenic regions consistent with suppurative exudate. Color flow Doppler indicates absence of luminal blood flow. (B) This image shows echogenic shadowing (arrowhead) consistent with suppurative exudate containing gas (arrow). This was associated with a septic anaerobic infection of the jugular thrombophlebitis. These sonograms were obtained from the jugular groove with a linear probe operating at 7.5 MHz at a depth of 4 cm. (C) This image is a postmortem longitudinal section of the septic anaerobic jugular thrombophlebitis demonstrating the mixed laminated appearance of the luminal thrombosis with intervening regions of suppurative exudate.

Vet-ebooks.com

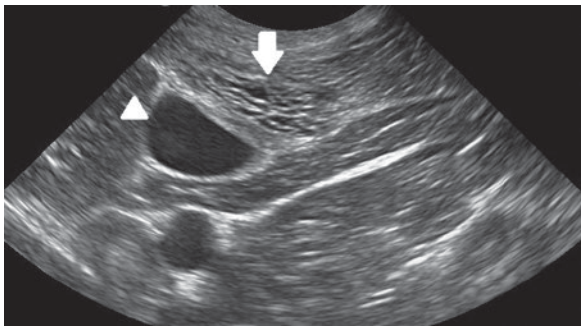


Figure 26.11 Perivascular cellulitis/edema. This patient developed an obvious firm perivascular swelling following inadvertent extravasation of a medication. There is notable perivascular edema/cellulitis adjacent to and compressing the jugular vein (arrow-head) as a result (arrow). The swelling resolved with topical therapy. This sonogram was obtained from the jugular groove with a microconvex probe operating at 5.0 MHz at a depth of 4 cm.

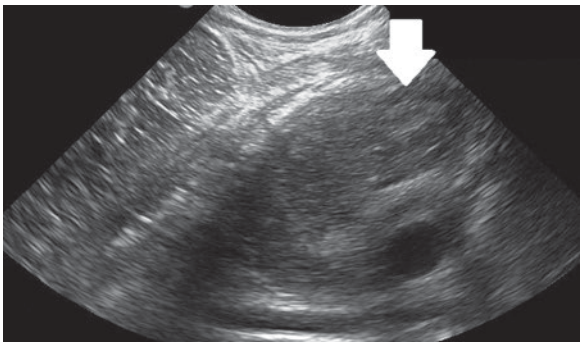


Figure 26.12 Perivascular abscess. This Standardbred gelding was presented to the clinic with neck swelling and pain. There was no history of intravenous catheter placement; however, multiple medications had been administered intravenously before his last race three weeks prior to presentation. A large perivascular abscess (arrow) was identified ultrasonographically and was lanced open under general anesthesia. This sonogram was obtained from the jugular groove with a microconvex probe operating at 5.0 MHz at a depth of 5 cm.

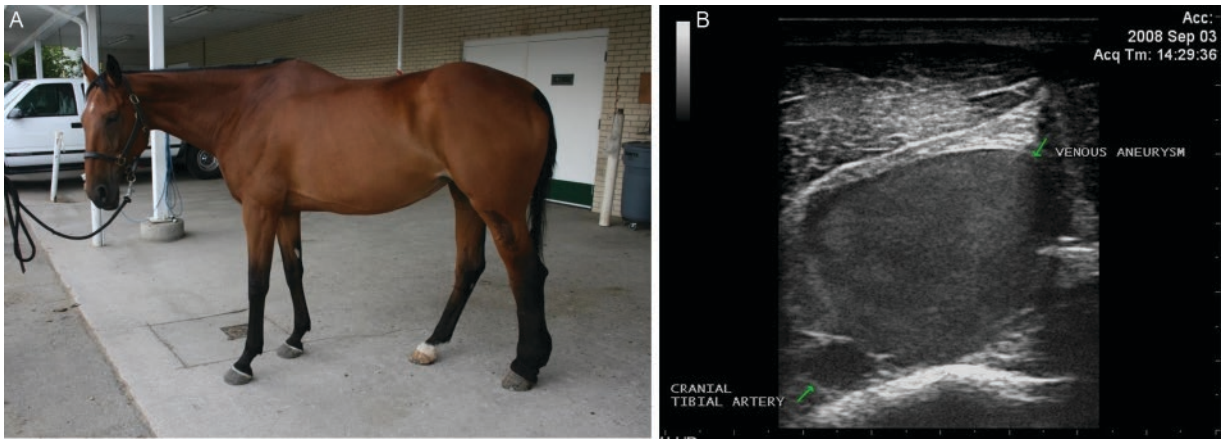


Figure 26.13 Arteriovenous fistula. (A) This image is of a horse with a three month history of rear limb swelling following trauma to the dorsum of the hock. The left rear leg had a pattern of distended veins in the skin on the gaskin along the proximal margin of the swelling. (B) Ultrasound image (transverse view) of the tortuous skin vessels in the hind limb shows a dilated region (aneurysm) within the vein adjacent to the underlying cranial tibial artery suggesting the presence of an arteriovenous fistula creating turbulent blood flow. This sonogram was obtained from the craniolateral aspect of the hind limb, near the hock, with a linear probe operating at 7.5 MHz at a depth of 6 cm.

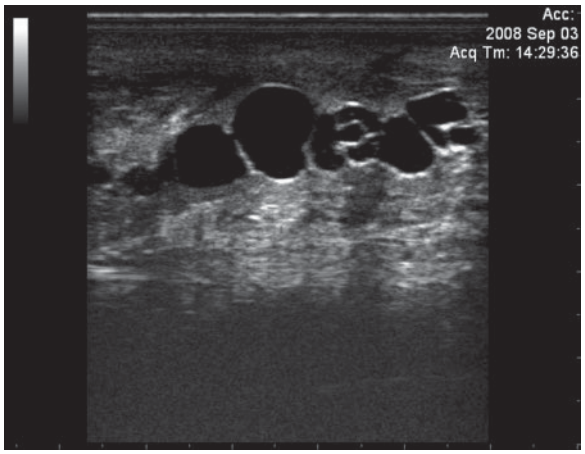


Figure 26.14 Chronic lymphangitis. This longitudinal ultrasound image of the swollen distal limb in Figure 26.11 shows multiple, tortuous, dilated lymphatic vessels (label) within the subcutaneous tissues consistent with lymphatic obstruction. This is a common finding with clinical cases of chronic lymphangitis. This sonogram was obtained from the craniolateral aspect of the hind limb, near the hock, with a linear probe operating at 7.5 MHz at a depth of 6 cm.

Vet-ebooks.com

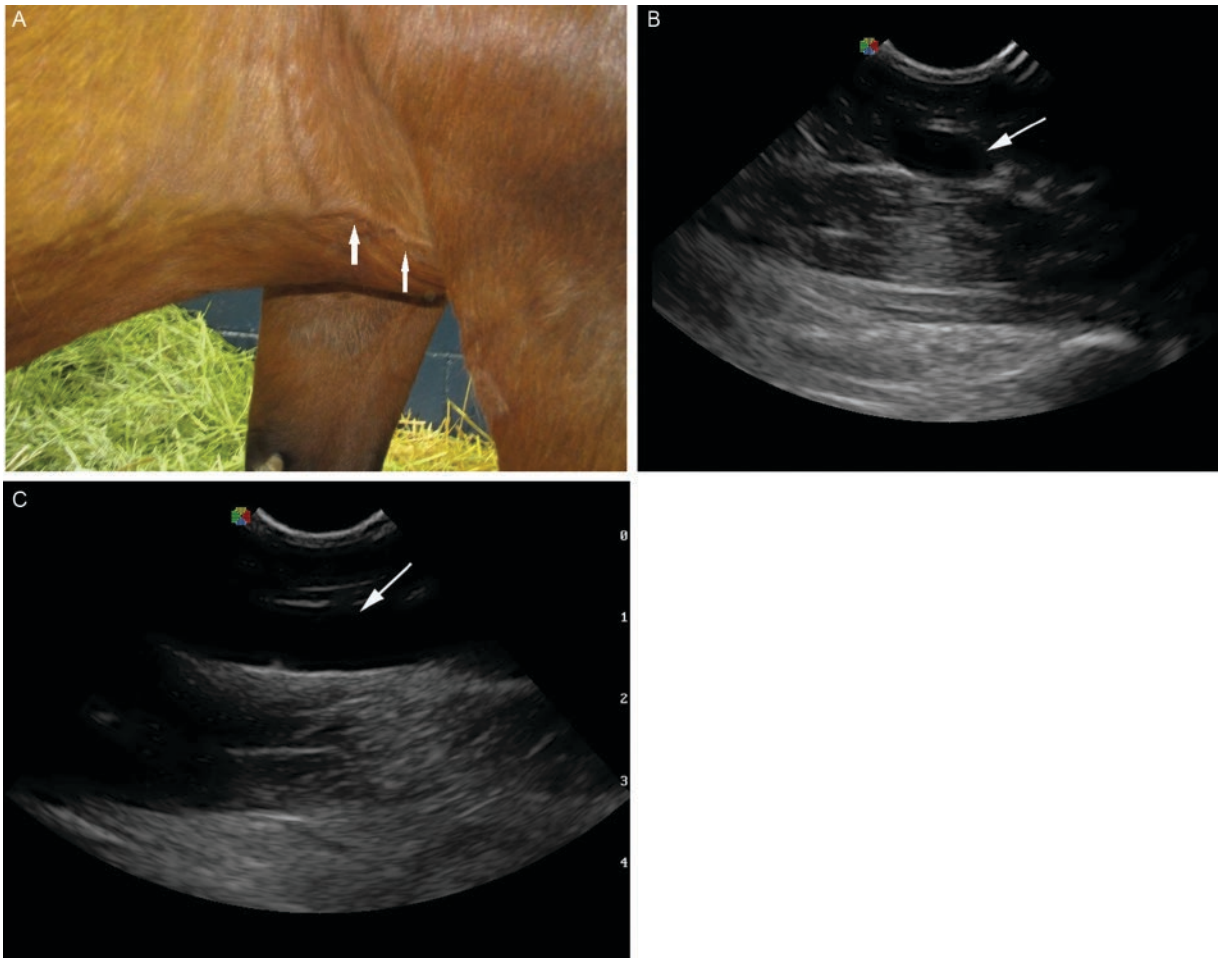


Figure 26.15 Lateral thoracic vein. (A) This image shows the location of the lateral thoracic artery (arrow) in a pregnant broodmare. This image shows (B) cross-sectional and (C) longitudinal views of the lateral thoracic vein. The vein courses superfically along the ventro-lateral aspect of the thoracic cavity caudal to the elbow. This vessel can be used for IV catheter placement when the jugular vein can not be used. This sonogram was obtained from the lateral chest wall, caudal to the 7th ICS, with a linear probe operating at 5.0 MHz at a depth of 5 cm.

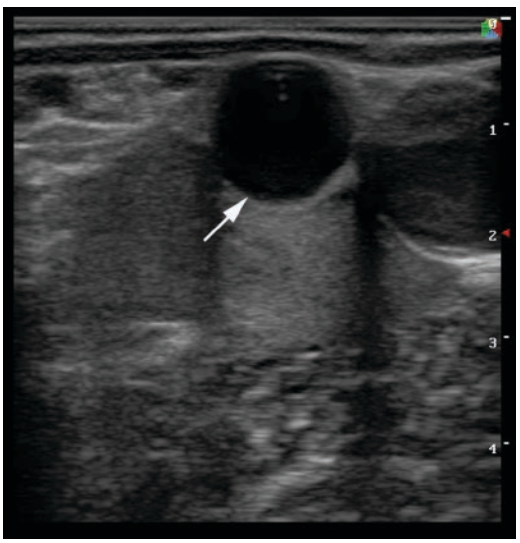


Figure 26.16 Iliac artery. This image shows a normal iliac artery (arrow) in a gelding. This sonogram was obtained transrectally using a linear probe operating at 5.0 MHz at a depth of 5 cm.

Vet-ebooks.com

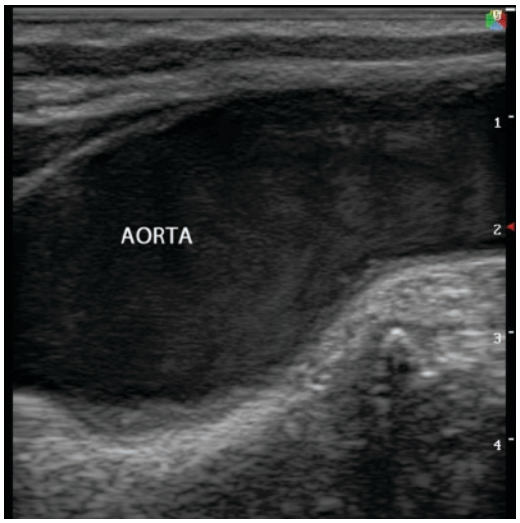


Figure 26.17 Plaque in iliac artery. This image shows a hyperechoic structure (arrowhead) in an iliac artery (arrow). This small plaque was an incidental finding in an aged gelding. Clinical signs from thrombosed iliac artery do not usually occur until the vessel lumen is almost completely occluded. Most thrombosed iliac arteries are chronic before they are diagnosed. This image was obtained transrectally using a linear probe operating at 5.0 MHz at a depth of 5 cm.

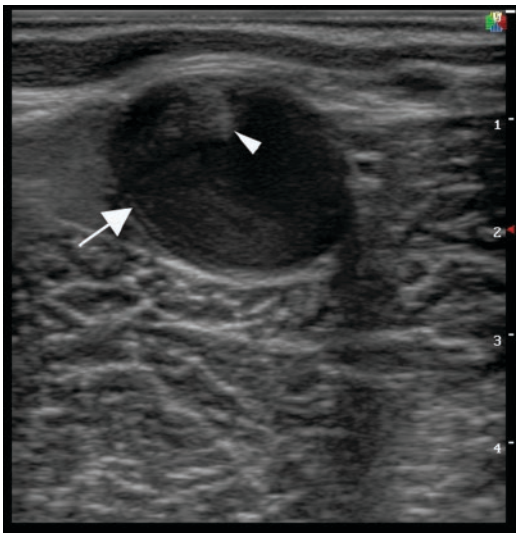


Figure 26.18 Aorta. This is an image of the aorta. This image was obtained transrectally using a linear probe operating at 5.0 MHz at a depth of 5 cm.

horses with undiagnosed or nebulous hind limb lameness or a distal hind limb that is cooler than the contralateral limb. The distal aorta (Figure 26.18) may also be imaged transrectally.

Recommended Reading

Duggan, V.E., Holbroo, T.C., Dechant, J.E. et al. (2004). Diagnosis of aorto-iliac thrombosis in a quarter horse foal using Doppler ultrasound and nuclear scintigraphy. *Journal of Veterinary Internal Medicine* 18(5): 753–756.

Geraghty, T.E. and Love, S. (2009). Assessment of subclinical venous catheter-related diseases in horses and associated risk factors. *Veterinary Record* 164(8): 227–231.

Hilton, H., Aleman, M., Textor, J. et al. (2008). Ultrasound-guided balloon thrombectomy for treatment of aorto-iliac-femoral thrombosis in a horse. *Journal of Veterinary Internal Medicine* 22(3): 679–683.

Vaughn, B. and Whitcomb, M.B. (2010). Imaging diagnosis-arterial and venous thromboses of the proximal limb in two Thoroughbred racehorses. *Veterinary Radiology Ultrasound* 5(3): 305–310.

Vet-ebooks.com

27

Umbilical Remnant Preparation and Scanning Technique

Massimo Magri

Clinica Veterinaria Spirano, Spirano (BG), Italy

Optimal equipment to scan the umbilical remnant in the foal is a high-frequency, 10–12 MHz linear probe, although a cursory examination can be performed with a transrectal, 5–7.5 MHz linear probe. Ideally, clip the hair with a #40 surgical clipper blade from the xiphoid caudal to the inguinal region and apply coupling gel. However, wetting the area with alcohol is often sufficient. The probe should be covered with an examination glove or similar to prevent damage to the probe from alcohol (Figure 27.1).

Although most foals tolerate this procedure without sedation, it may be required in some foals to minimize stress of the procedure. In the author's experience, the best way to perform this examination is to stand beside the foal, with an assistant restraining the foal at the shoulder, next to the mare. One hand holds the probe while the other stretches the skin. The umbilical remnant can also be scanned with the foal in lateral recumbency. The ultrasonographer is behind the foal's back with head and legs restrained by an assistant.

Orientation of the probe must be kept constant over time to obtain comparable images. In the longitudinal axis view, orientate the probe so the caudal abdomen is on the left side of the screen, and the proximal abdomen is on the right. In the transverse (short) axis view, orientate the probe so the right abdomen is on the left side of the screen and the left abdomen is on the right (Figure 27.2).

Structures imaged when scanning the umbilical area include the external umbilical remnant, umbilical arteries, urachus, and umbilical hernia if present. The umbilical remnant is located along the ventral midline of the abdomen (Figure 27.3), a few centimeters from the surface. To locate and recognize the different structures, the easiest way is to start with the cross-sectional view of the external umbilical remnant and move cranially to the xiphoid cartilage. Then, start at the external umbilical remnant again and move caudally to the pelvic rim. In the male, the presence of the penis makes scanning the most caudal part difficult. If an abnormal structure is suspected, a longitudinal scan should be performed. This scan plane is more difficult to visualize due to the tubular structure of the umbilical structures.

External Umbilical Remnant

The external umbilical remnant contains the umbilical vein, the two umbilical arteries, and the urachus (Figure 27.4). These structures normally atrophy within a few days after birth and detach from the skin.

Infection is the main pathology of the external umbilical remnant. Clinically, this pathology is characterized by a local swelling and a draining tract (Figure 27.5A). Sonographically, it is characterized by an enlarged external umbilical remnant filled with hypoechoic to echoic fluid (Figures 27.5B and 27.5C).

Umbilical Vein

The umbilical vein runs cranially from the umbilicus to the xiphoid cartilage, along the midline, very close to the skin surface (Figure 27.6A). When it reaches the xiphoid cartilage, it courses deep to reach the

Atlas of Equine Ultrasonography, Second Edition. Edited by Jessica A. Kidd, Kristina G. Lu and Michele L. Frazer.
© 2022 John Wiley & Sons Ltd. Published 2022 by John Wiley & Sons Ltd.
Companion Website: www.wiley.com/go/kidd/atlas

Vet-ebooks.com



Figure 27.1 Probe protection. Protect the probe from coupling gel or alcohol with an examination glove or similar covering.

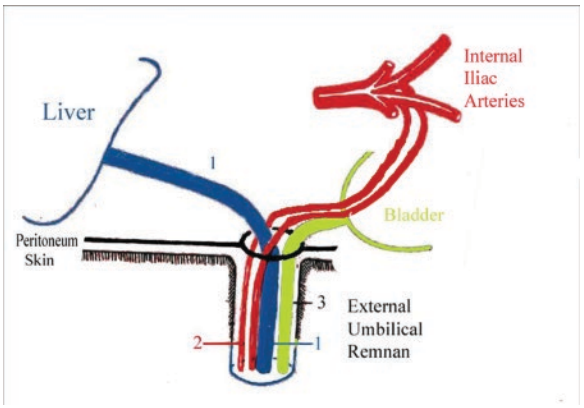


Figure 27.3 Umbilical remnants. This diagram illustrates the umbilical remnants including umbilical vein (1), umbilical arteries (2), and urachus (3).

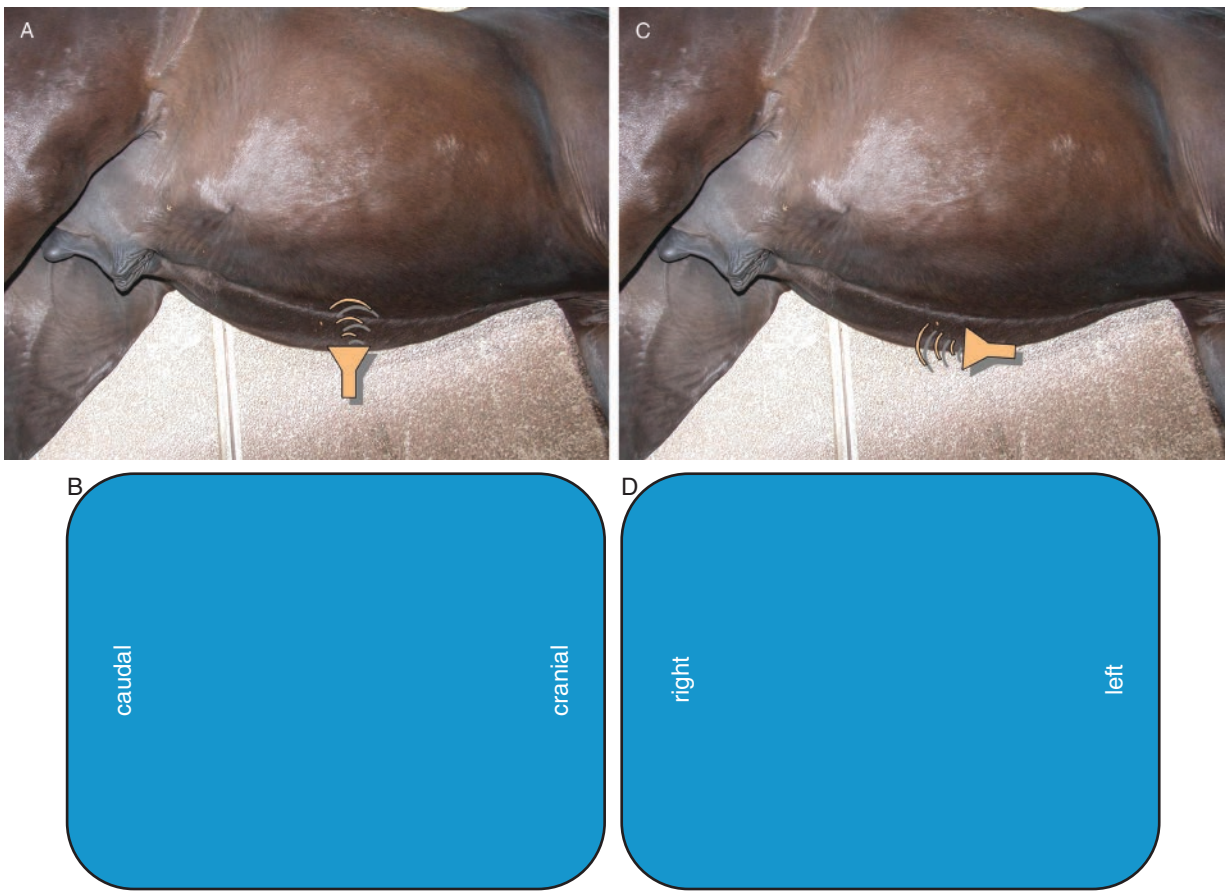


Figure 27.2 Probe orientation. (A) This image shows orientation of probe for obtaining the longitudinal view. (B) Position the probe so the caudal aspect of the umbilical structures are on the left side of the screen and the cranial aspect is on the right. (C) This image shows orientation of probe for the cross-sectional view. (D) Position the probe so the right aspect of the umbilical structures is on the left side of the screen and the left is on the right.

Vet-ebooks.com

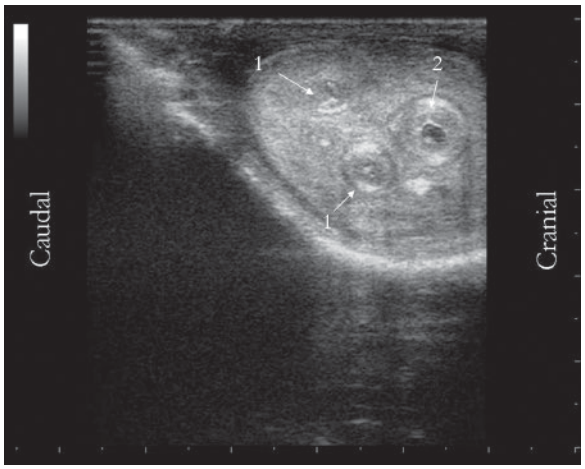


Figure 27.4 External umbilical remnant. This image is longitudinal view of external umbilical remnant obtained from a normal 3-day-old foal. The two umbilical arteries (1) and umbilical vein (2) are identified. The vein has a thicker wall than the arteries and has a hypoechoic center. The urachus is in the space between the two arteries, but it is not possible to distinguish it from the surrounding tissues. This sonogram was obtained with a wide-bandwidth 10.0 MHz linear array transducer, operating at 12 MHz, at a display depth of 5 cm.

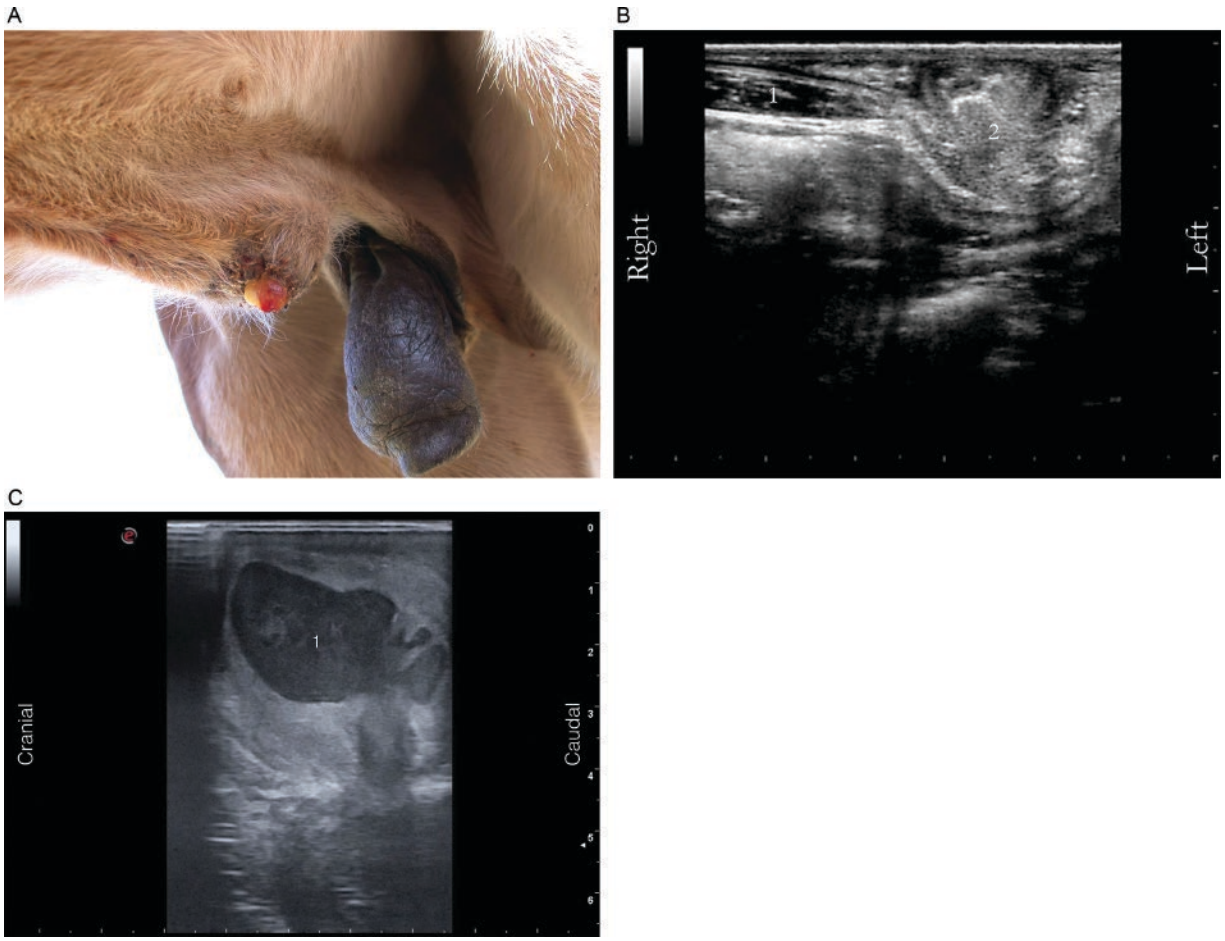


Figure 27.5 Infected external umbilical remnant. (A) This image of a foal shows an infected external umbilical remnant. (B) This image shows the cross-sectional view of the external umbilical remnant. Echogenic material (2) is present inside the external umbilical remnant outside the abdominal wall (1). The umbilical vein and arteries are not identifiable. This sonogram was obtained with a wide-bandwidth 10.0 MHz linear array transducer, operating at 12.0 MHz, at a display depth of 5 cm. (C) This image shows the longitudinal view of the external umbilical remnant. Echogenic material (1) is present inside the external umbilical remnant, surrounded by a thick capsule. This sonogram was obtained with a wide-bandwidth 10.0 MHz linear array transducer, operating at 12.0 MHz, at a display depth of 6,5 cm.

Vet-ebooks.com

liver (Figure 27.6B). In the fetus, the umbilical vein transports blood from the placenta to the fetal liver. The umbilical vein is connected to the abdominal wall by a reflection of the peritoneum (Figure 27.7). It atrophies after birth and becomes the round ligament of the liver, part of the falciform ligament. The umbilical vein is an oval or elliptical structure with a thin echogenic wall and a hypoechoic center. Its diameter is 10 mm (or less) near the umbilicus (Figure 27.8A), but diameter decreases moving cranially (Figure 27.8B). It is located directly over the linea alba and this is used as the landmark to identify the vein. The vein can move laterally only a few centimeters from this landmark due to the peritoneal reflection. However, this slight lateral movement may occur when the scan is performed in lateral recumbency.

Infection is the main pathology of the umbilical vein, although it is less common than infection of the umbilical arteries and the urachus. The infected umbilical vein is enlarged (more than 10 mm), with hypoechoic to echoic material within it and a thickened wall (Figures 27.9, 27.10, and 27.11). Some blood can be visible ultrasonographically for a few days after birth. It has a swirling appearance, typically described as smoke. The wall of the umbilical vein is not thickened (Figure 27.12).

Umbilical Arteries

The umbilical arteries (Figures 27.13, 27.14, and 27.15) run caudally from the umbilicus toward the bladder. The urachus is located between the two arteries. When the umbilical arteries reach the bladder, they move away from each other, running close to the lateral aspect of the bladder. In the fetus, the arteries transport blood from the internal iliac arteries to the placenta. They atrophy after birth and become the round ligaments of the bladder. The diameter of the two arteries and urachus near the umbilical stump should be 24 mm or less. They can be visualized ultrasonographically for almost the entire length of the bladder. Infection of the umbilical arteries and of the urachus is the most common pathology of the internal umbilical remnant. An infected umbilical artery becomes enlarged, with a thickened wall and hypoechogenic to echogenic material inside the lumen.

Urachus

The urachus (Figure 27.16) is located between the umbilical arteries. In the fetus, the urachus transports urine from the fetal bladder to the allantoic

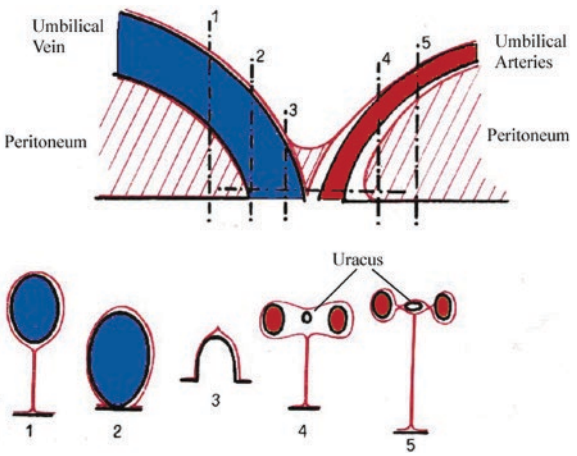


Figure 27.7 Umbilical remnants. The diagram of the umbilical remnants shows the relationship between the umbilical structures and the peritoneum.

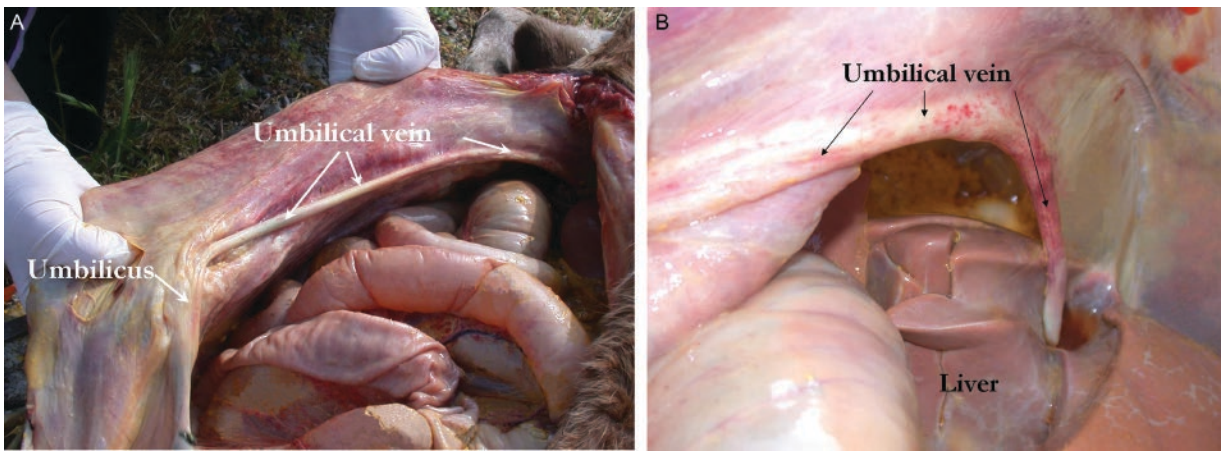


Figure 27.6 Umbilical structures. (A) This image of an anatomical specimen shows the umbilical structures from the umbilicus cranially. (B) This image of a post-mortem specimen shows the umbilical vein deepening to the liver.

Vet-ebooks.com

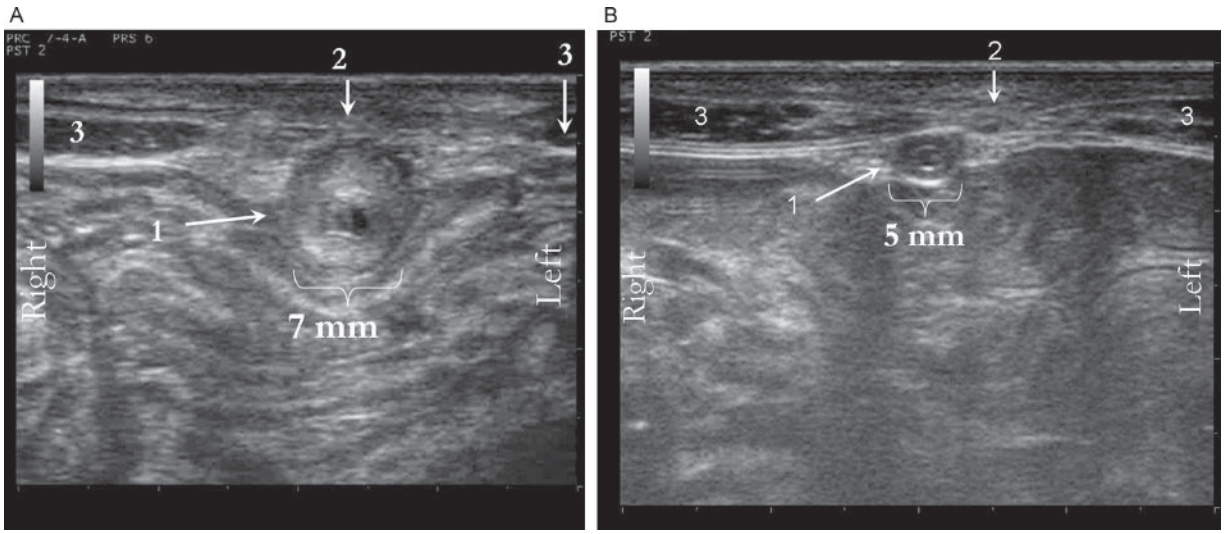


Figure 27.8 Umbilical vein. (A) This image is a cross-sectional view of the umbilical vein, near the umbilicus, in a normal 4-day-old foal in the standing position. The umbilical vein (1) is well defined, with a 2–3 mm echoic wall and a hypoechoic center. It is close to the linea alba (2), located between the abdominal wall muscles (3). The linea alba is used as a landmark to identify the umbilical vein. This sonogram was obtained with a wide-bandwidth 10.0 MHz linear array transducer, operating at 12.0 MHz, at a display depth of 3 cm. (B) This image is a cross-sectional view of the umbilical vein, near the xyphoid, in a normal 4-day-old foal in right lateral recumbency. The umbilical vein (1) is well defined with a 2 mm hypoechoic wall, an echoic inner and outer rim, and a hypoechoic center. The diameter is smaller at the xyphoid than at the umbilicus. It is located to the right side of the linea alba (2) due to the recumbent position. The abdominal wall muscles (3) are easily identified on both sides of the linea alba. This sonogram was obtained with a wide-bandwidth 10.0 MHz linear array transducer, operating at 12.0 MHz, at a display depth of 3 cm.

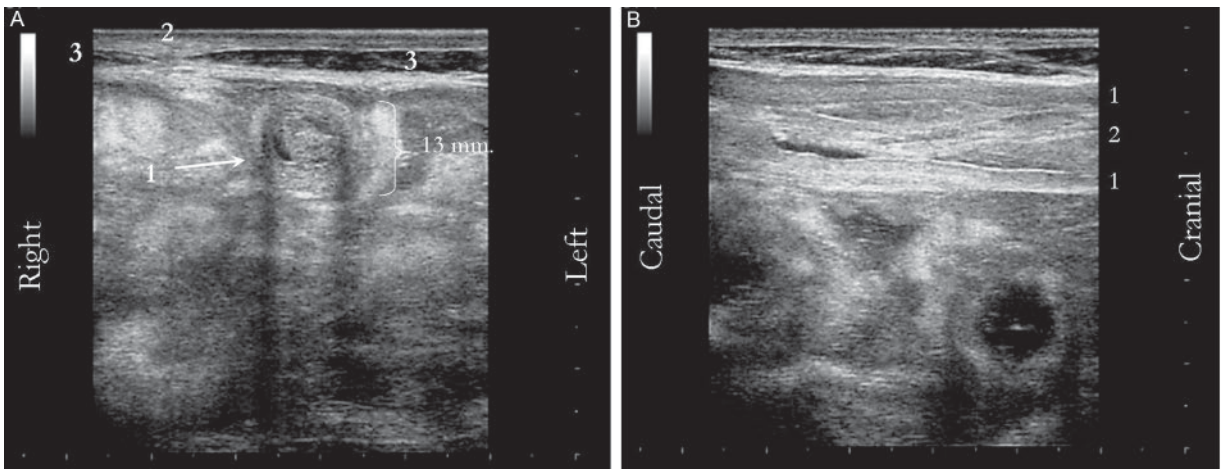


Figure 27.9 Umbilical pathology. These images are from a 7-day-old foal. (A) This image is a cross-sectional view of the umbilical vein with foal in left lateral recumbency. The umbilical vein (1) appears thickened, with an echoic wall and an echoic center and is surrounded by a thin layer of hypoechoic fluid. The diameter is larger than normal at 13 mm It is located to the left side of the linea alba (2) due to the recumbent position. The abdominal wall muscles (3) are easily identified at both sides of the linea alba. This sonogram was obtained with a wide-bandwidth 10.0 MHz linear array transducer, operating at 12.0 MHz, at a display depth of 5 cm. (B) This image is a longitudinal view of the umbilical vein with the foal in left lateral recumbency. The umbilical vein appears thickened with an echoic wall (1) and luminal content (2) of various echogenicities. This sonogram was obtained with a wide-bandwidth 10.0 MHz linear array transducer, operating at 12.0 MHz, at a display depth of 5 cm.

Vet-ebooks.com

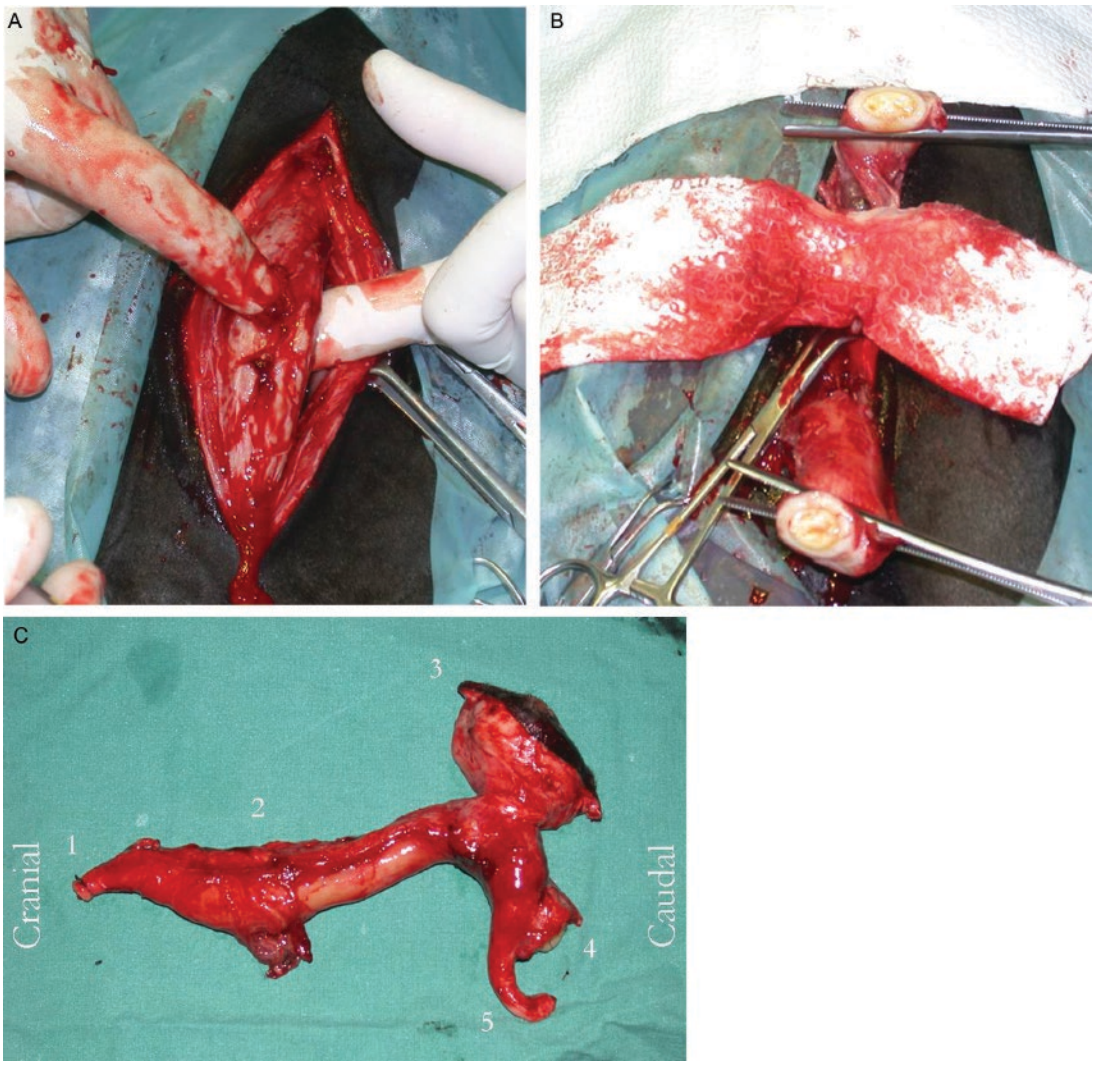


Figure 27.10 Intraoperative findings infected umbilicus. These images are from the case in Figure 27.9. (A) The umbilical vein is thickened. (B) Purulent material is present inside the thickened umbilical vein. (C) This image is an anatomical specimen identifying the normal umbilical vein (1), thickened and infected umbilical vein (2), umbilicus (3), urachus (4), and umbilical artery (5).

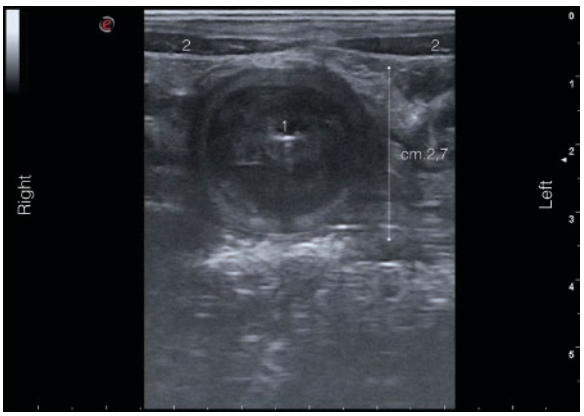


Figure 27.11 Umbilical vein. This image is of umbilical pathology in 8-day-old foal. (A) This image is a cross-sectional view of the umbilical vein with the foal in the standing position. The umbilical vein (1) appears thickened, with an echoic wall and an echoic center surrounded by not homogeneous material. The diameter is larger than normal at 2.7 cm.

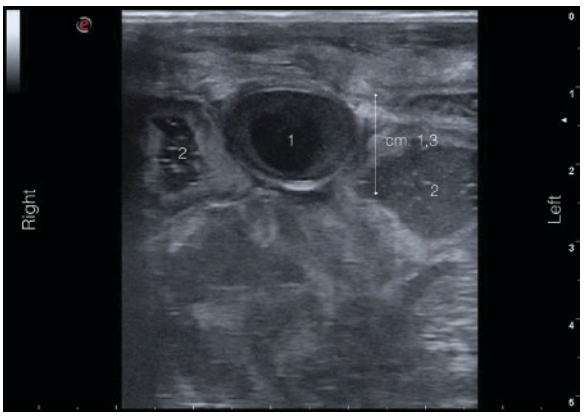


Figure 27.12 Umbilical vein. This image is a cross-sectional view of the umbilical vein, in a normal 3-day-old foal in the standing position. The umbilical vein (1) is well defined, with a 2–3 mm echoic wall and swirling content. This sonogram was obtained with a wide-bandwidth 3.0–12.0 MHz linear array transducer, operating at 12.0 MHz, at a display depth of 5 cm.

Vet-ebooks.com

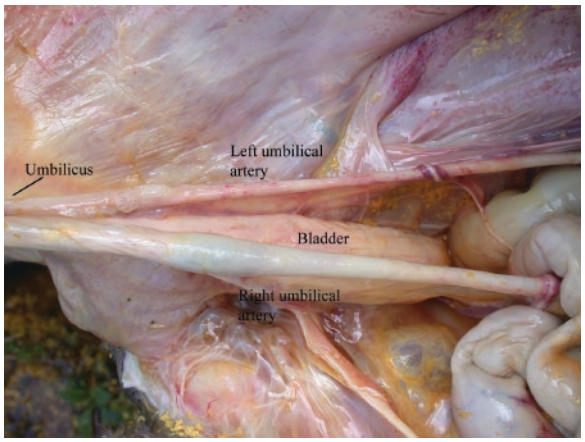


Figure 27.13 Umbilical structures. This image of an anatomical specimen shows the umbilical structures from the umbilicus caudally.

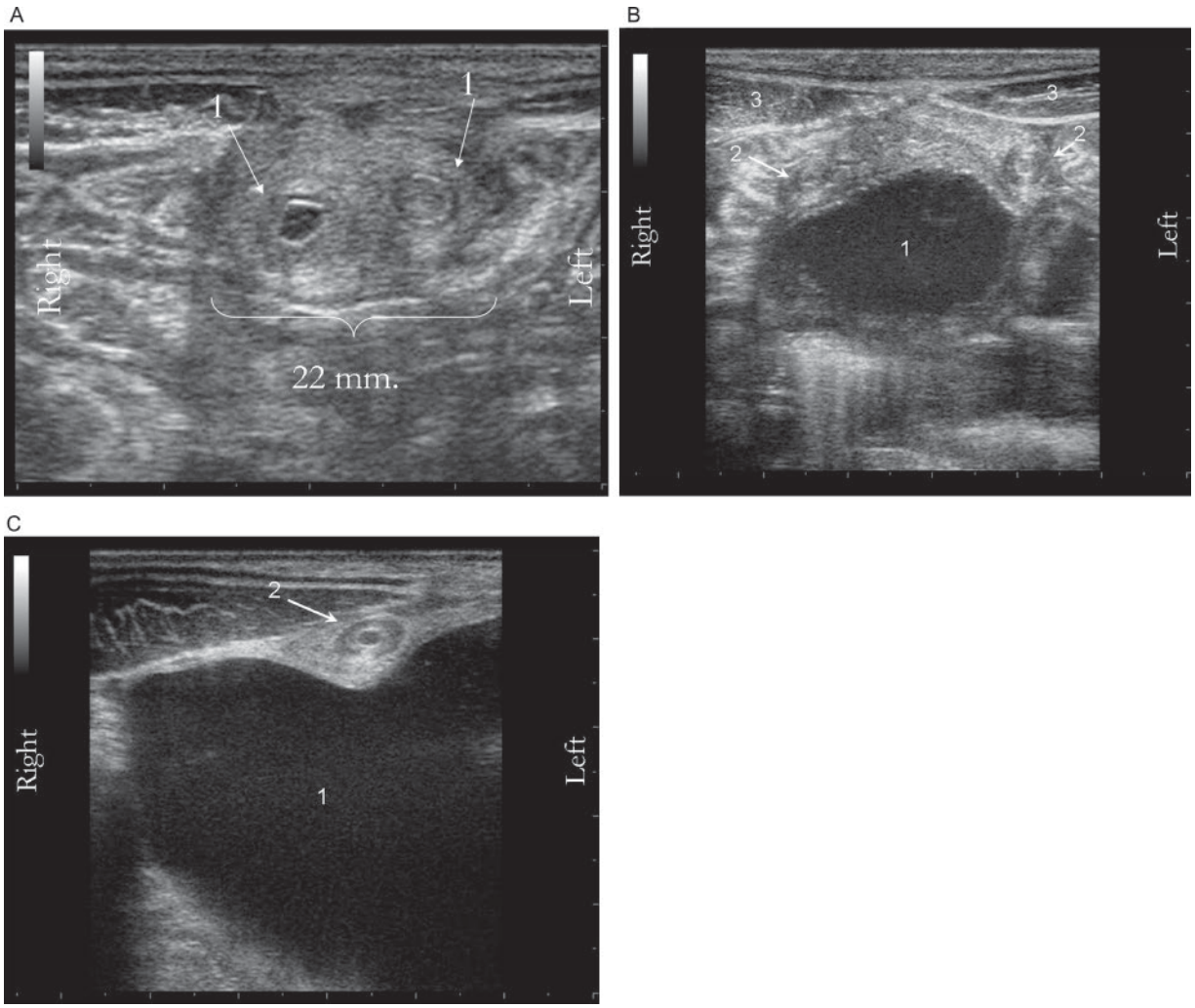


Figure 27.14 Umbilical arteries. These images are cross-sectional views of umbilical arteries in a normal 4-day-old foal in standing position. (A) Near the umbilicus, the umbilical arteries (1) have a 2–3 mm echoic wall and a hypoechoic (right artery) to echoic (left artery) center. The urachus is not identifiable in this sonogram. The total measure of the umbilical arteries–urachus complex is normally less than 25 mm. This sonogram was obtained with a wide-bandwidth 10.0 MHz linear array transducer, operating at 12.0 MHz, at a display depth of 3 cm. (B) At the level of the bladder (1), the umbilical arteries (2) normally have a diameter of less than 12 mm. Abdominal wall muscles (3) are seen on both sides of bladder. This sonogram was obtained with a wide-bandwidth 10.0 MHz linear array transducer, operating at 12.0 MHz, at a display depth of 5 cm. (C) The umbilical artery (2) is visible along the bladder (1). The diameter of the umbilical arteries does not change from the umbilicus to the bladder. This sonogram was obtained with a wide-bandwidth 10.0 MHz linear array transducer, operating at 12.0 MHz, at a display depth of 5 cm.

Vet-ebooks.com

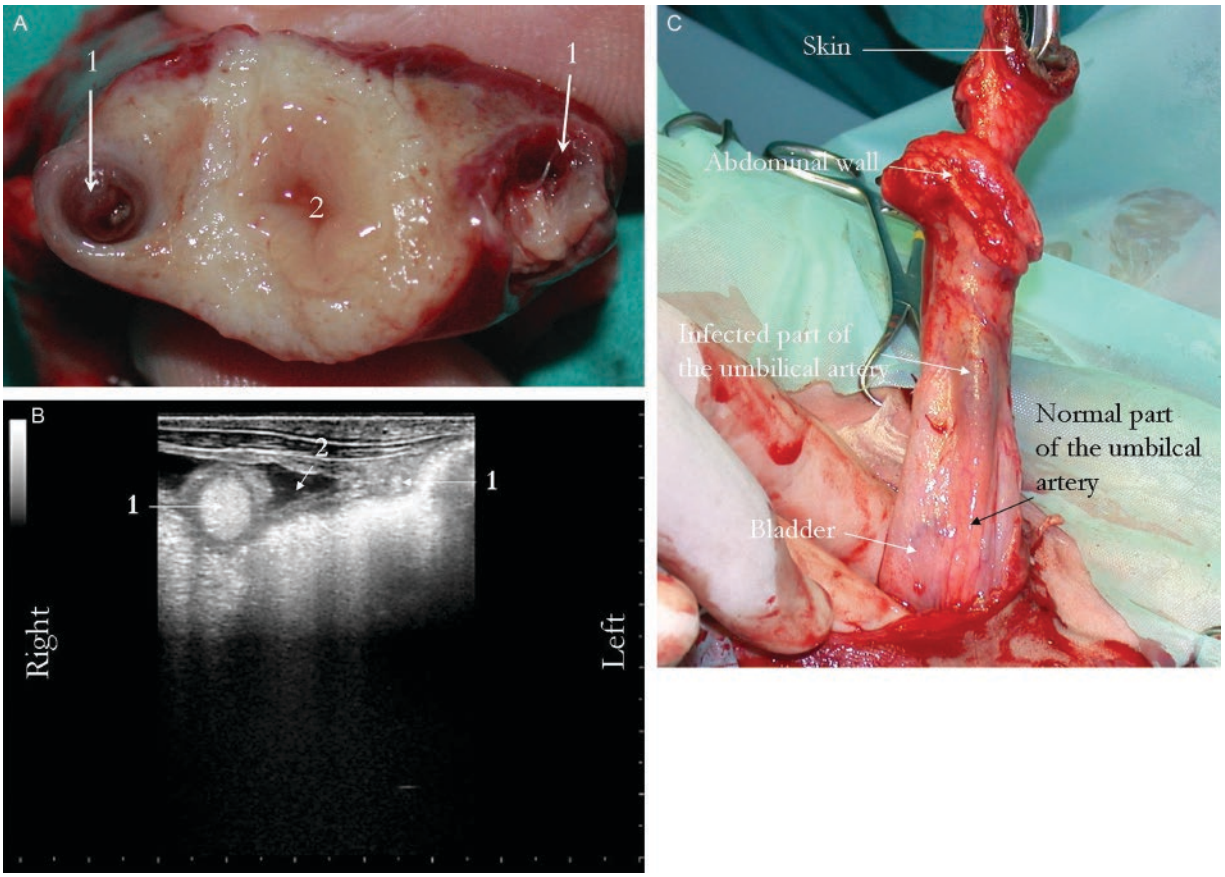


Figure 27.15 Umbilical arteries. (A) This image of an anatomical specimen shows the umbilical arteries (1) and the transition point between the urachus and the bladder (2). (B) This image is a cross-sectional view of the umbilical arteries (1), along the bladder (2), obtained from a 9-day-old foal with suspected umbilical pathology. The right umbilical artery is enlarged, with a hypoechoic wall and echogenic material inside. This sonogram was obtained with a wide-bandwidth 10.0 MHz linear array transducer, operating at 12.0 MHz, at a display depth of 5 cm. (C) This image is intraoperative findings of an infection of the left umbilical artery.

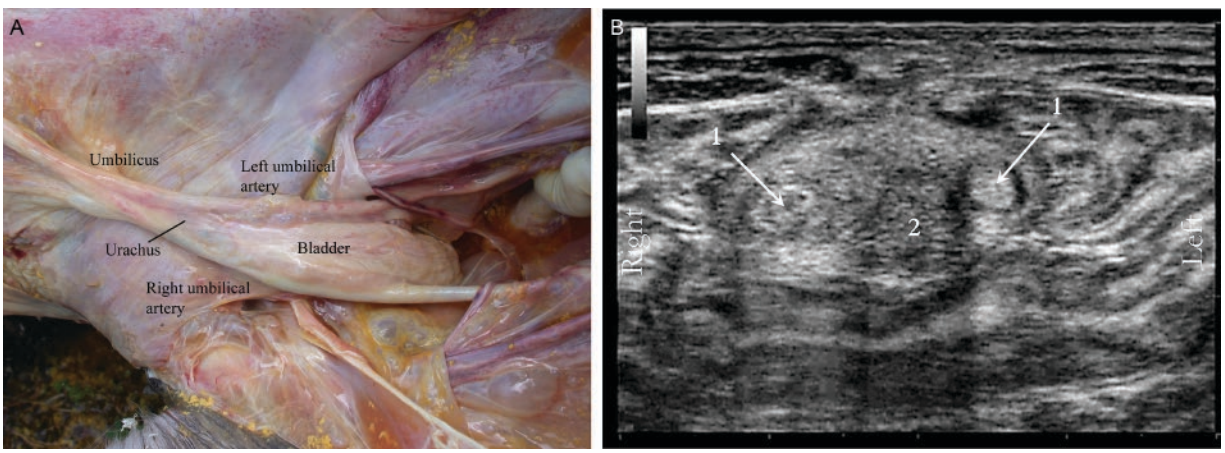


Figure 27.16 Umbilical structures. (A) This image of an anatomical specimen shows the umbilical structures from the umbilicus caudally. (B) This image is a cross-sectional view of internal umbilical remnant, caudal to the umbilicus, obtained from a normal 4-day-old foal in the standing position. The urachus (2) is a poorly defined structure between the umbilical arteries (1). This sonogram was obtained with a wide-bandwidth 10.0 MHz linear array transducer, operating at 12.0 MHz, at a display depth of 3 cm.

Vet-ebooks.com

cavity. It closes and atrophies along its entire length after birth and becomes the median ligament of the bladder. The urachus is only a potential space and normally does not contain fluid, so it is not a distinct structure ultrasonographically. Patent urachus is a frequent pathology of the neonate. The urachus may not atrophy correctly and, thus, maintains a degree of patency. Also, it may begin to atrophy but become patent after a few days as a consequence of other pathology. The urine normally drains continuously in small quantities, so identifying this structure ultrasonographically may not be possible. Therefore, a patent urachus may appear sonographically normal. When infected, the urachus enlarges causing an increase in diameter of the umbilical arteries–urachus complex. The infected urachus typically has a thin wall with hypoechoic to hyperechoic material in the lumen (Figure 27.17). Infection of the urachus can result in leakage of urine into the abdomen resulting in uroperitoneum. Urine may also leak from the urachus into the subcutaneous tissue of the body wall resulting in body wall edema.

Umbilical Hernia

The most frequent umbilical hernia (Figures 27.18, 27.19, and 27.20) in the foal is small (2–3 cm), manually reducible, and not painful. It usually contains peritoneal fluid, the umbilical remnant, and sometimes omentum or small intestine. Rarely, a part of

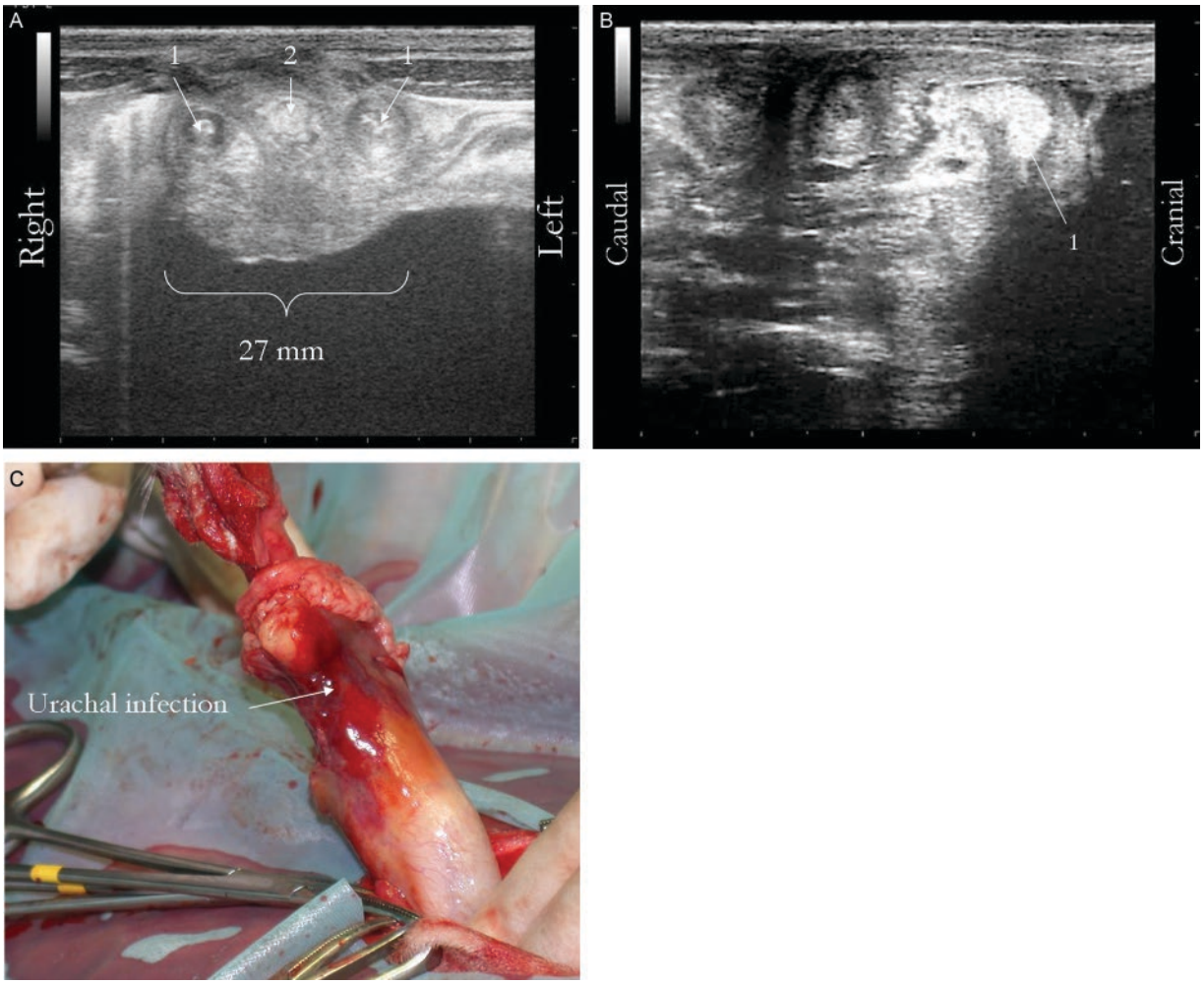


Figure 27.17 Internal umbilical remnant. (A) This image shows a cross-sectional view of the internal umbilical remnant, caudal to the umbilicus, obtained from a 7-day-old foal with suspected umbilical pathology. The infected urachus (2) is a well defined echoic structure between the umbilical arteries (1). The diameter of the umbilical arteries–urachus complex is 27 mm. (B) This image is a longitudinal view of the infected urachus from the same foal. The infected urachus (1) is a well defined, non-linear, echoic structure. These sonograms were obtained with a wide-bandwidth 10.0 MHz linear array transducer, operating at 12.0 MHz, at a display depth of 4 cm. (C) Intraoperative findings of an urachal infection.

Vet-ebooks.com

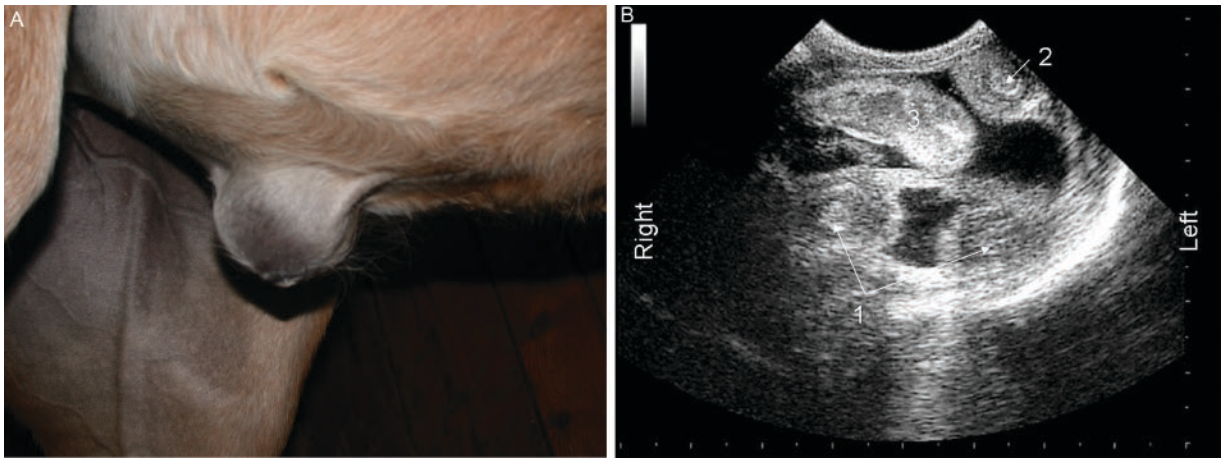


Figure 27.18 Umbilical hernia. (A) This image is an umbilical hernia in a foal. (B) This image shows a cross-sectional view of an umbilical hernia. Anechoic peritoneal fluid surrounds the umbilical arteries (1), umbilical vein (2), and a loop of small intestine (3). This sonogram was obtained with a wide-bandwidth 6.6 MHz micro-convex linear array transducer, operating at 8.0 MHz, at a display depth of 6 cm.

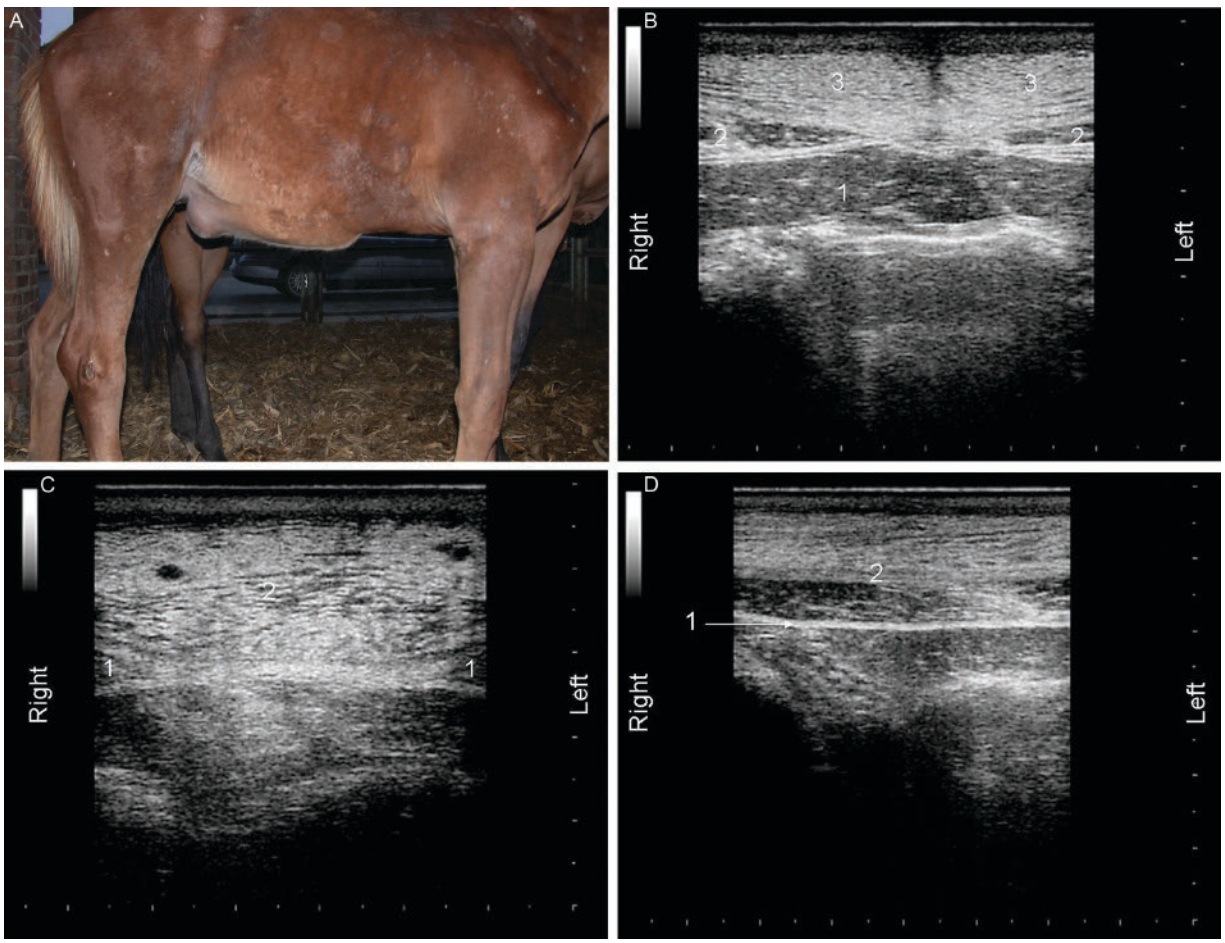


Figure 27.19 Complicated umbilical hernia. (A) This image is of a complicated umbilical hernia. (B, C) These images show a cross-sectional view of the abdominal wall. Subcutaneous edema (3) is visualized outside the abdominal muscular wall (2) and retroperitoneal fat (1) is visualized inside the abdomen. These sonograms were obtained with a wide-bandwidth 10.0 MHz linear array transducer, operating at 12.0 MHz, at a display depth of 5 cm. (D) This image is a longitudinal view of the abdominal wall near the umbilicus. A thick layer of subcutaneous edema (2) is outside the abdominal wall (1). This sonogram was obtained with a wide-bandwidth 10.0 MHz linear array transducer, operating at 12.0 MHz, at a display depth of 6 cm.

Vet-ebooks.com

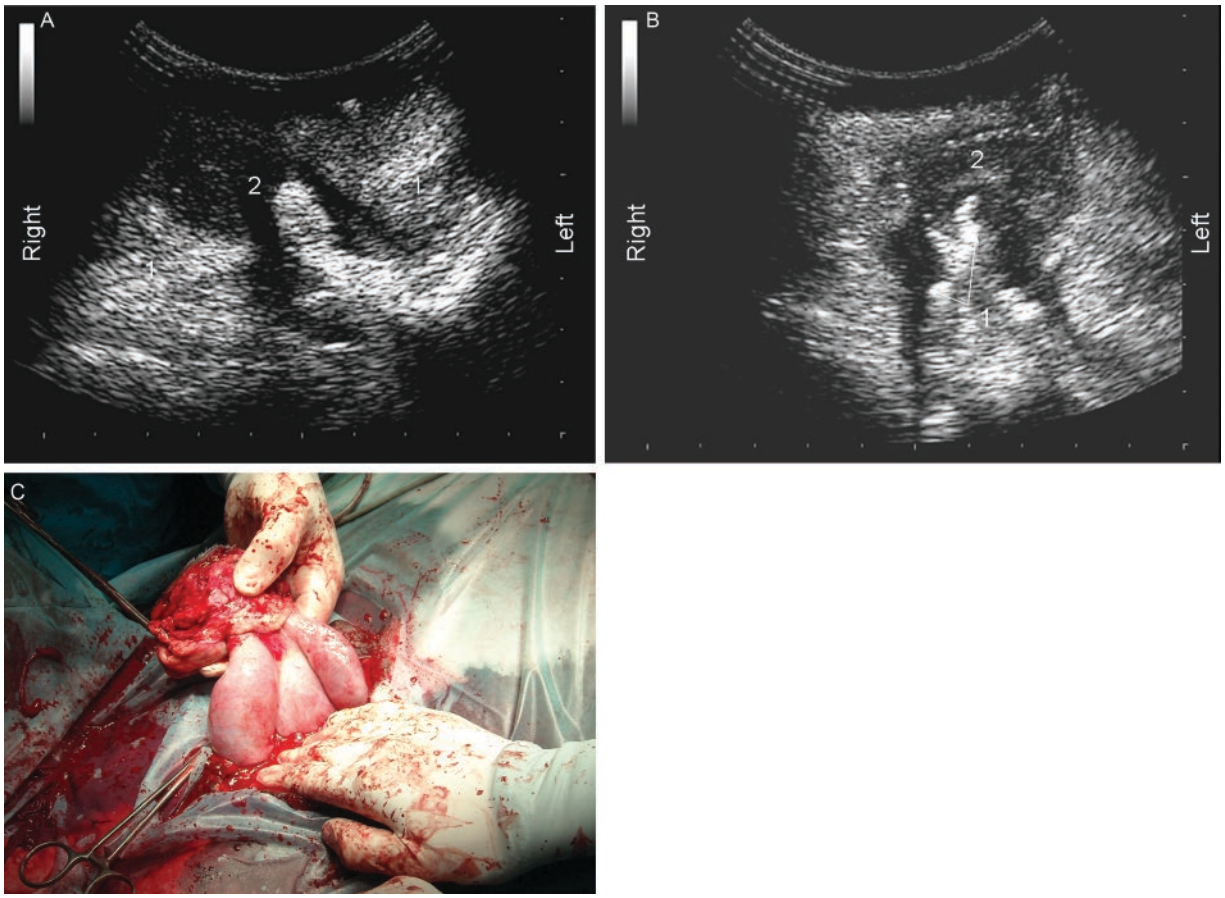


Figure 27.20 Umbilical hernia. (A) This image shows a cross-sectional view of the umbilical hernia from Figure 27.16. A structure with hypoechoic external layer (2) and an echoic internal layer is visualized in the abdominal wall defect (1). This sonogram was obtained with a wide-bandwidth 3.5 MHz convex linear array transducer, operating at 5.0 MHz, at a display depth of 8 cm. (B) Cross-sectional view of umbilical hernia. The structure (2) inside the hernia has a well defined echoic structure (1) that is suggestive of intestine in the hernia sac. This sonogram was obtained with a wide-bandwidth 3.5 MHz convex linear array transducer, operating at 5.0 MHz, at a display depth of 8 cm. (C) Intraoperative findings of the previous case. Part of the cecum is adhered to the hernia sac.

the large colon or cecum can be involved (Figure 27.18b). A complicated hernia has a varied clinical appearance, but it is usually characterized by swelling of the ventral part of the abdomen, is painful, and is not manually reducible. A draining tract can be present. A complete ultrasound examination is very important to evaluate the presence of infection and of intestinal portions.

Recommended Reading

Franklin, R.P. and Ferrell, E.A. (2002). How to perform umbilical sonograms in the neonate. In: *Proceedings of the 48th American Association of Equine Practitioners Annual Convention*.

Lavan, R.P., Crayer, T., and Madigan, J.E. (1977). Practical method of umbilical ultrasonographic examination of one-week-old foals: The procedure and the interpretation of age-correlated size ranges of umbilical structures. *Journal of Equine Veterinary Science* 17: 96.

Pokar, J. (2004). Diseases of umbilical structures and urinary bladder in foals: Ultrasound as a valuable aid for diagnosis and therapy. *Praktische Tierarzt* 85: 646–653.

Reef, V.B. (1998). Pediatric abdominal ultrasonography. In: *Equine Diagnostic Ultrasound* (ed. V.B. Reef), 364–403. Philadelphia PA: Saunders.

Reef, V.B. and Collatos, C.A. (1998). Ultrasonography of the umbilical structures in clinically normal foals. *American Journal of Veterinary Research* 49: 2143–2146.

Reimer, J.M. (1993). Ultrasonography of umbilical remnant infections in foals. In: *Proceedings of the 39th American Association of Equine Practitioners Annual Convention* 247.

Walston, R.N. (2006). Case 12–1 umbilical infection/patent urachus. In: *Equine Neonatal Medicine – A Case Based Approach*, 1st edn (ed. M.R. Paradis), 233–238. Philadelphia PA: Elsevier Saunders.

Vet-ebooks.com

28

Post Foaling Complications

Peter R. Morresey

Rood and Riddle Equine Hospital, Lexington, KY, USA

Introduction

Abdominal discomfort in the post foaling mare may result from normal uterine contractions or be indicative of visceral compromise. The uterus and associated structures may be affected or non-reproductive viscera may be involved. Fever, inappetence, and development of generalized sepsis may be the result of disruption of blood supply, contusion, laceration, necrosis, and perforation of either the intestinal and genital tracts. Transabdominal ultrasonography allows non-invasive assessment of peritoneal fluid quantity and quality, visceral disposition, and gives clues as to visceral integrity. Transrectal ultrasonography, when appropriate, improves identification and evaluation of structures distinguished by palpation *per rectum*.

Technique

A lower frequency transducer (3.5 MHz or similar) is preferred in larger horses as penetration of the ultrasound beam is enhanced. Smaller horses and foals can be adequately imaged with higher-frequency probes. Clipping of the abdomen with the use of ultrasound coupling gel may give the best image; but in practical settings, wetting with alcohol and slicking down hair in the direction of growth to expel air is sufficient. Clipping of a suitable acoustic window may be unavoidable in horses with matted or seasonally long hair coats. The probe is then held perpendicular to the abdominal wall and then systematically moved in a dorsal-ventral direction and, when along the midline, cranial-caudal. The more cranial aspects of the abdominal cavity are located within the thoracic rib cage and imaging of this area uses a similar technique to that detailed for thoracic ultrasonography.

Normal Anatomy

Examination of the left side of the horse reveals the liver applied medially to the diaphragm and ventrally to the lung fields variably between the seventh to ninth intercostal spaces (ICS) [1]. The liver is lateral to the spleen in this region, with the stomach visualized deep to this interface; however, the stomach may have variable contact with the body wall depending on degree of fill. The spleen is imaged over the majority of the left side of the abdominal cavity medial to the body wall from the paralumbar fossa to the eighth ICS, and further cranially medial to the liver as noted above. The spleen extends ventrally to the midline and may extend to the right ventral abdomen. Spleen size is variable. The left kidney lies medial to the spleen and is found from the sixteenth ICS through the paralumbar fossa. Gas filled viscera may obstruct complete visualization of the left kidney.

Examination of the right side of the abdominal cavity reveals liver variably from the sixth to the fifteenth ICS medially and lung and diaphragm ventrally [1]. The right kidney is located dorsally and superficially in the same region, adjacent to the caudal most aspects of the liver in the fourteenth to seventeenth ICS region.

The intestinal tract is imaged via the caudal and ventral abdomen. The small intestine is variable in

Atlas of Equine Ultrasonography, Second Edition. Edited by Jessica A. Kidd, Kristina G. Lu and Michele L. Frazer.
© 2022 John Wiley & Sons Ltd. Published 2022 by John Wiley & Sons Ltd.
Companion Website: www.wiley.com/go/kidd/atlas

Vet-ebooks.com

location and can be seen on the left, right, and often both sides of the abdomen. Ventral colon is applied to the ventral abdominal wall and identified by sacculations (haustra). The liver is not imaged from the ventral abdomen in the normal horse [1]. The right dorsal colon can be seen applied to the liver medially on the right side. The cecum is noted in the right paralumbar fossa traversing caudally and ventrally before the cecal tip trends cranially.

The bladder, when urine filled, is located on the ventral midline of the caudal abdomen. The nonpregnant uterus is not discernible in the absence of pathology. Varying stages of pregnancy and uterine pathology can be noted, depending on uterine size and disposition.

Common Variations

Portions of the intestinal tract (jejunum) may be noted lateral to the spleen on the left side, with some appearing dorsal and lateral to the dorsal most aspect of the spleen. In the absence of colonic content trapped in the nephrosplenic space, this does not appear to cause problems. Peritoneal fluid can often be imaged accumulated dorsal to the spleen.

Limitations of Transabdominal Ultrasonography

The limitations of transabdominal ultrasonography are a result of the size of the abdominal cavity relative to the penetrating ability of the ultrasound transducer which depends on the nominal frequency. Gas shadowing is commonplace and can obscure deeper structures from view. The anatomy of the horse provides a challenge as a considerable proportion of the abdominal cavity lies within the caudal rib cage.

Pathology of the Abdominal Boundaries

Ruptured Body Wall, Ruptured Rectus Abdominis, and Prepubic Tendon

Discontinuities of the abdominal wall are present, with alterations of the expected contour. Subcutaneous edema, pockets of fluid, hemorrhage, and muscle fiber disruption are visible with ultrasonography (Figure 28.1). Diagnosis of the specific tissue involved can be difficult [2]. Abdominal wall ruptures laterally tend to occur at the junction of the rectus abdominis and oblique muscles. Muscle layers tend to tear along their fiber direction. Rupture of the peritoneum allows intestine to directly appose the subcutaneous musculature or skin. Prepubic tendon rupture results in ventral abdominal wall deviation, elevation of the tailhead, regional edema, and pain cranial to the mammary gland [2]. Herniation of intestine through abdominal wall tears has the potential to result in incarcerated intestine [2]. Large tears may allow colon to herniate, while extensive amounts of jejunum can herniate through small tears.

Diaphragmatic Hernia

Diaphragmatic hernia is a rare parturient complication [3] and can also be found in athletic horses. Viscera reported to be involved in diaphragatic hernias include small intestine, large intestine, stomach,

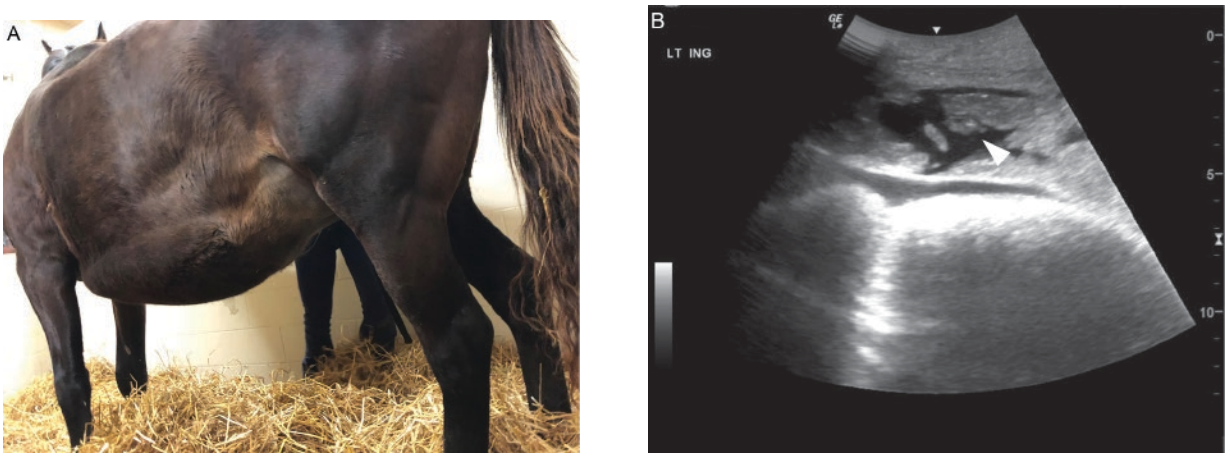


Figure 28.1 Body wall defect. (A) The inguinal region and ventral body wall of a post foaling mare is viewed from the caudal aspect. Bulging of the inguinal region is present, with edema extending cranially. (B) Left inguinal region of mare in picture (A). The peritoneum remains intact; however, disruption of muscles and hemorrhage is apparent (arrowhead). This sonogram was obtained in the left inguinal region using a curvilinear probe operating at 4 MHz at a depth of 12 cm.

Vet-ebooks.com

spleen, and liver [4,5]. The colon appears as a thick-walled, sacculated structure with fluid and gas content. The small intestine appears as multiple, tubular fluid-filled structures. If structures are no longer contained within the peritoneum (hernial sac), a diaphragmatic rupture has occurred. With ultrasonography, intrathoracic intestine may be visualized appearing cranial to the diaphragm and shadowing the lung due to gaseous content. Pleural fluid may be increased. Strangulation of intestine may result in visualization of thickened intestinal wall and increased peritoneal and pleural fluid (Figure 28.2). An intraluminal air-fluid interface may be present [6]. Prognosis is considered guarded. One review involving variable horse signalments found a survival rate in diagnosed cases of diaphragmatic hernia to be 23%. This increased to 46% survival rate following surgical correction [4].

Retroperitoneal Hemorrhage (Perirenal)

Perirenal hemorrhage may occur secondary to renal pathology, or from direct trauma to the kidney itself. Blunt force trauma sustained during prolonged dystocia may induce perirenal hemorrhage (Figure 28.3).

Pelvicitis

Transrectal ultrasonography may detect fluid or fibrin caudal to the peritoneal reflection (Figure 28.4). Caudal vaginal or rectal trauma during parturition may be sufficient to cause hemorrhage, tissue necrosis, sepsis, or perforation. This may not be reflected in grossly observable changes in the adjacent peritoneal cavity.

Pathology of the Peritoneal Cavity

Changes in the peritoneal fluid reflect the altered integrity of the viscera within the peritoneum. These include ultrasonographically detectable changes in peritoneal fluid amount, echogenicity, and sometimes disposition. Increase in value of two or more

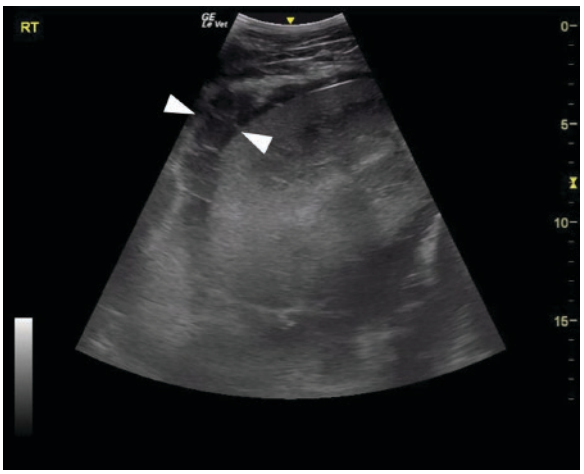


Figure 28.3 Perirenal hemorrhage. Perirenal hemorrhage (traumatic) is delineated between arrowheads. This sonogram was obtained in the right paralumbar fossa using a curvilinear probe operating at 4 MHz at a depth of 18 cm.

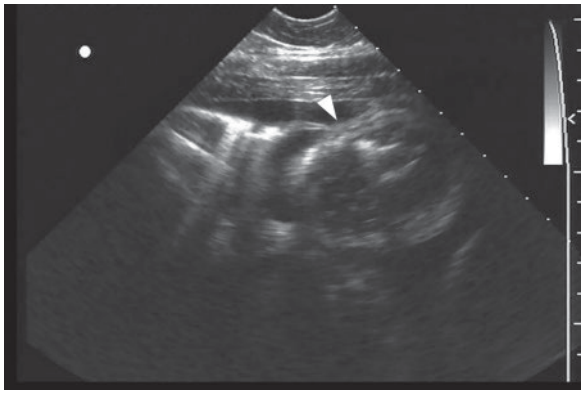


Figure 28.2 Diaphragmatic hernia. Small intestine is thick-walled and amotile (arrowhead) lying in apposition to the lung. This sonogram was obtained in the left 6th intercostal space using a mechanical sector probe operating at 3.5 MHz at a depth of 12 cm.

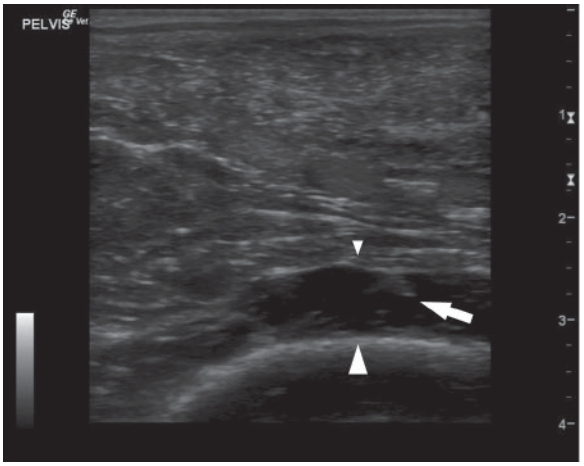


Figure 28.4 Pelvicitis. Fluid accumulation between the pelvis (large arrowhead) and ventral aspect of the urethra (small arrowhead) contains discrete, irregular hyperechoic strands (arrow) consistent with fibrinous inflammation. This sonogram was obtained transrectally using a linear probe operating at 6 MHz at a depth of 4 cm.

Vet-ebooks.com

fluid variables, including total protein, nucleated cell count, and percentage neutrophils, is considered significant [7].

Hemoperitoneum

Periparturient hemorrhage can develop in mares of any age or parity; however, it is more common in older mares [8–10]. While the genital tract is the most likely source in the periparturient mare, examination of the liver, spleen, and kidneys is prudent. Mesenteric disruption can also lead to hemoperitoneum.

Hemoperitoneum has a characteristic ultrasonographic appearance in the initial stages of hemmorhage. The fluid appears cellular and swirling (smoke-like) in response to diaphragmatic and visceral movements (Figure 28.5). Appearance will vary with rate of formation, volume of hemorrhage, and duration of bleed. With time, clot formation occurs ventrally, with relatively anechoic fluid remaining dorsally (Figure 28.6). Hemorrhage may be acute and overwhelming, intermittent and repeated, or chronic and persistent at low levels.

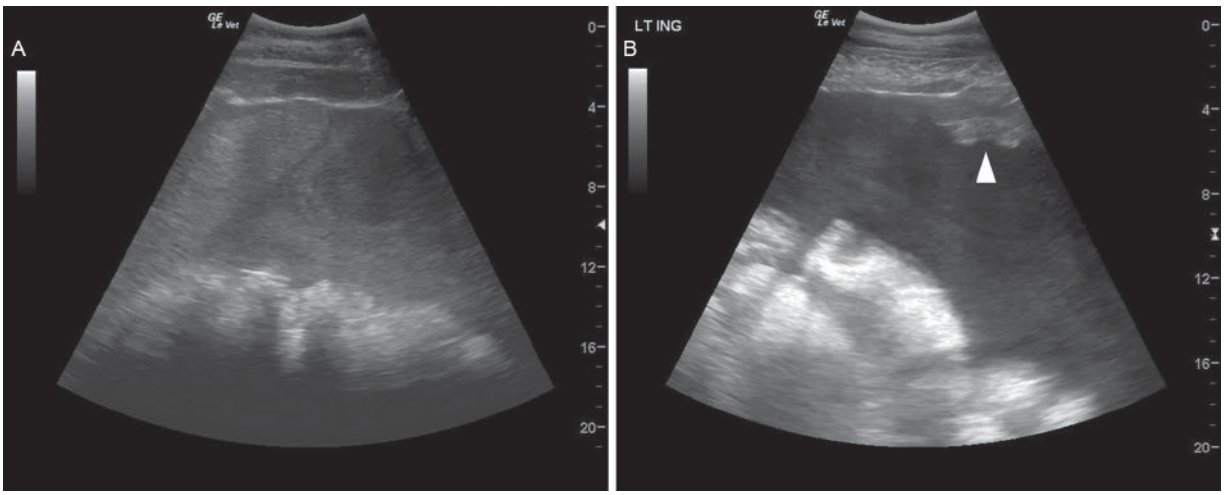


Figure 28.5 (A) Hemoperitoneum, acute. In the early stages of hemoperitoneum formation, blood appears with a swirling smoky echogenicity due to rouleaux formation and mixing due to both visceral and diaphragmatic movements. This sonogram was obtained from the ventral abdomen using a curvilinear probe operating at 4 MHz at a depth of 21 cm. (B) Hemoperitneum, subacute. The initial stages in the formation of a blood clot in the peritoneum is shown in this image. Clot formation on the peritoneum is apparent (arrowhead). Hemorrhage may be ongoing leading to a similar appearance to (A). This sonogram was obtained from the ventral abdomen using a curvilinear probe operating at 4 MHz at a depth of 21 cm.

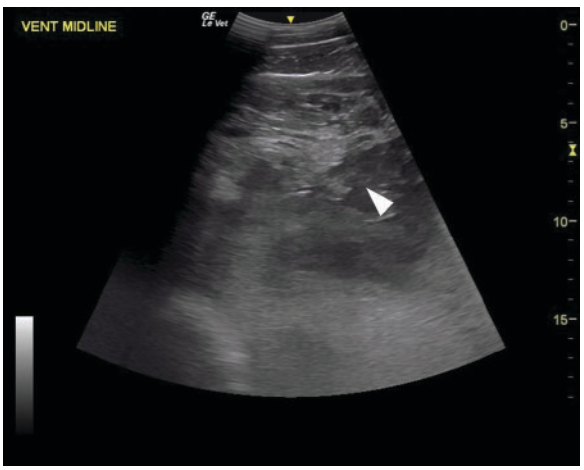


Figure 28.6 Hematoma formation during resolving hemoperitoneum. Extensive hematoma formation and reduction in peritoneal fluid volume is present in this sonogram from hemoperitoneum of 72 h duration. An organizing hematoma on the peritoneum is present (arrowhead). This sonogram was obtained from the ventral abdomen using a curvilinear probe operating at 4 MHz at a depth of 19 cm.

Peritonitis

Peritonitis (Figure 28.7) may result when intestinal bruising, strangulation, and ischemia progress to mural necrosis and rupture of the affected intestinal segment. The condition may progress over a number of days, with abdominal discomfort and fever preceding overt signs of sepsis. This results from progressive bacterial translocation across devitalized intestine or uterine wall. Spillage of gastrointestinal content precipitates a rapid onset of systemic deterioration. Peritonitis has also been reported secondary to bladder wall necrosis [11]. Peritoneal fluid appears echogenic, cellular to flocculent to turbid, and may in advanced cases contain fibrin strands free or attached

Vet-ebooks.com

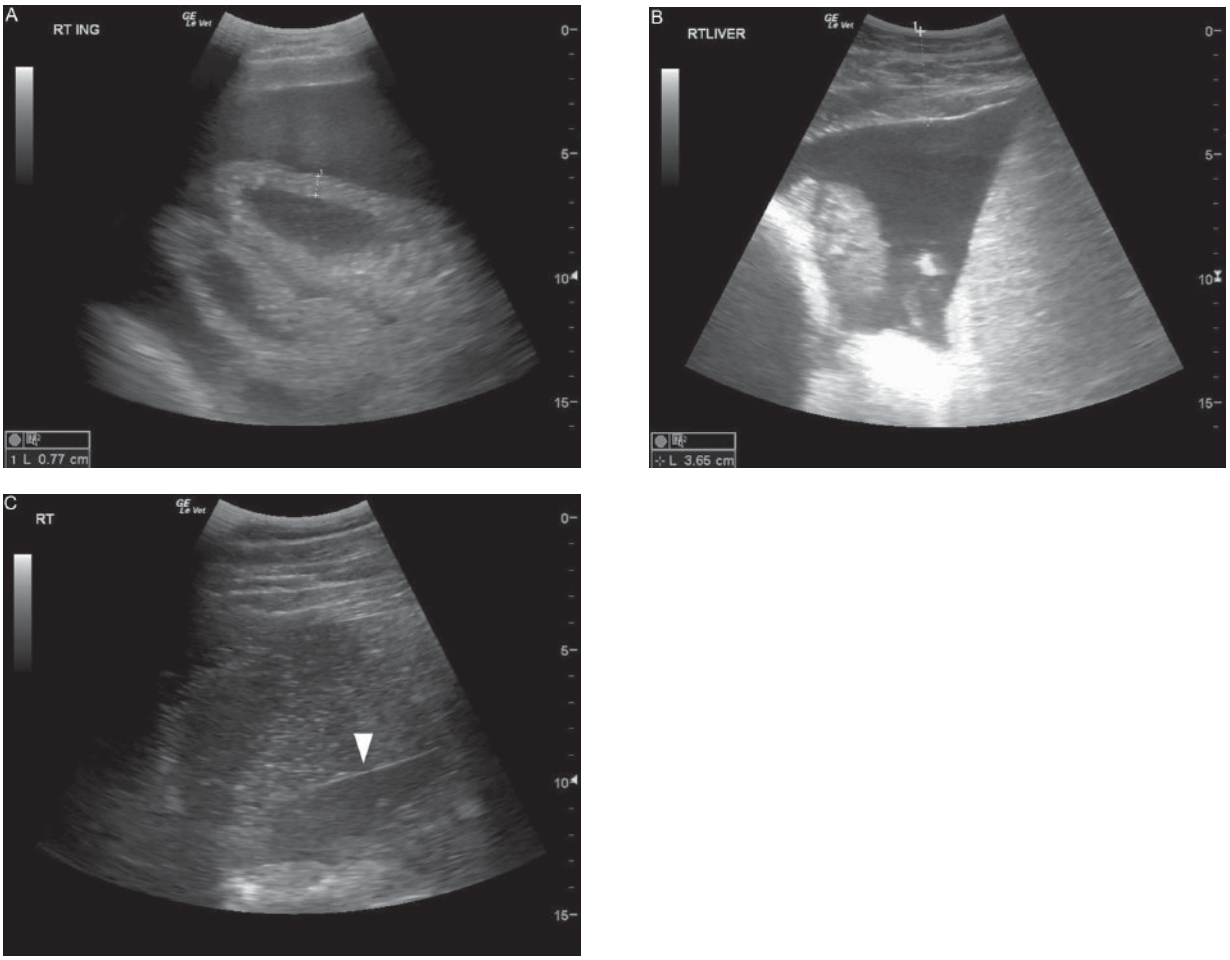


Figure 28.7 Peritonitis. (A) Flocculent peritoneal fluid is a hallmark finding in peritonitis. Intestinal wall thickness may be visibly increased. This sonogram was obtained from the right inguinal region using a curvilinear probe operating at 4 MHz at a depth of 16 cm. (B) Peritonitis. Markedly increased volume of peritoneal fluid may be noted, with entrapment by viscera in regions not usually present. This sonogram was obtained from the right cranioventral abdominal region using a curvilinear probe operating at 4 MHz at a depth of 16 cm. (C) Peritonitis, advanced. A large quantity of turbid peritoneal fluid in present in the right cranioventral abdominal region. The right liver lobe (arrowhead) is displaced from the body wall. This sonogram was obtained from the right cranioventral abdominal region using a curvilinear probe operating at 4 MHz at a depth of 15 cm.

to regional peritoneal (visceral and parietal) surfaces (Figure 28.8). Volume of peritoneal fluid may be highly variable: small in acute or dehydrated patients and large where spillage of intestinal or uterine content has occurred. Gas echoes or highly echogenic particles are consistent with a ruptured viscus. Mesenteric abscess formation may result in chronic cases (Figure 28.9).

Cystitis, Uroperitoneum, and Bladder Rupture

The urine-filled bladder may routinely be imaged in the inguinal region via the transabdominal or transrectal routes. The bladder content and wall dimensions give clues as to ongoing inflammatory and/or infectious processes (Figure 28.10). The bladder wall may become traumatized and devitalized by compression against the pelvic brim. This pressure may be sufficient to cause rupture (Figure 28.11) during parturition [12]. This is reported to be a rare occurrence [13]. Uroperitoneum may result [14], with a large volume of anechoic peritoneal fluid containing increased creatinine and echogenic calcium carbonate crystals [3]. The viscera may be outlined by anechoic fluid, and the bladder may be seen folded and collapsed upon itself [15]; however, the lesion is often not visualized.

Vet-ebooks.com

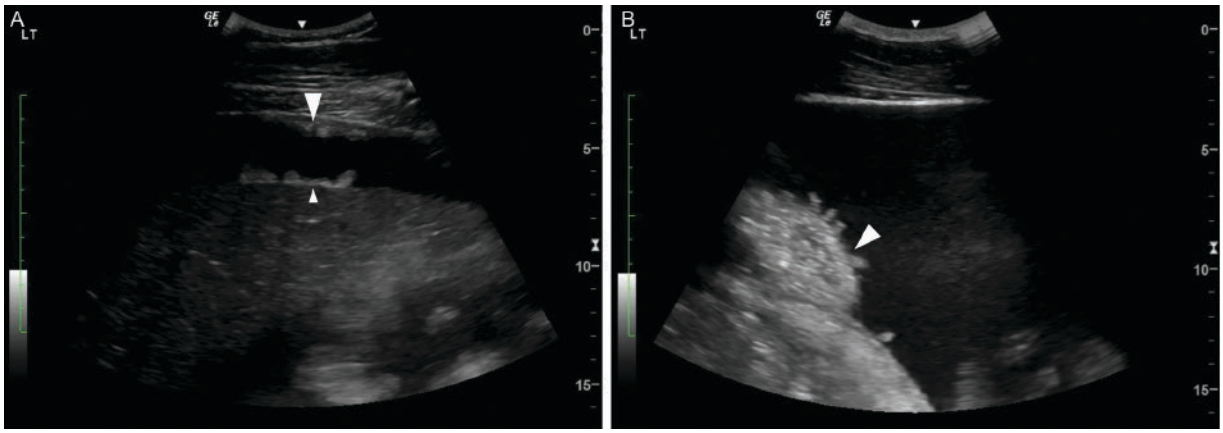


Figure 28.8 Peritonitis, fibrinous. (A) Fibrin deposition may be present in peritonitis, affecting both the visceral (large arrowhead) and parietal (small arrowhead, liver) peritoneal surfaces. This sonogram was obtained from the right cranioventral abdominal region using a curvilinear probe operating at 4 MHz at a depth of 16 cm. (B) Peritonitis, fibrinous. Fibrin deposition on the small intestine (arrowhead). A large quantity of turbid peritoneal fluid is present. This sonogram was obtained from the right cranioventral abdominal region using a curvilinear probe operating at 4 MHz at a depth of 16 cm.

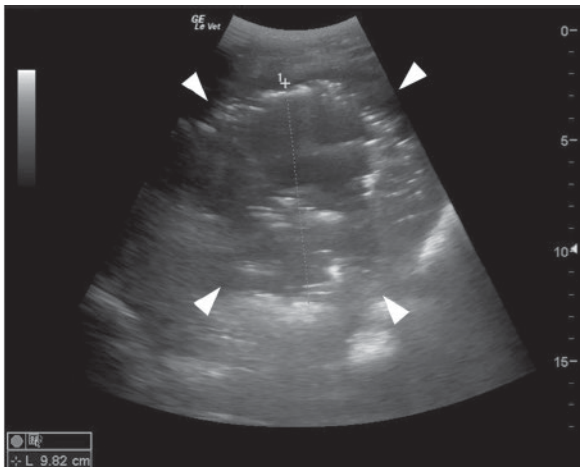


Figure 28.9 Mesenteric abscess. Irregularly shaped mass of varying echodensity delineated by arrowheads, developed secondary to peritonitis resulting from uterine rupture post partum. This sonogram was obtained from the right inguinal region using a curvilinear probe operating at 4 MHz at a depth of 18 cm.

Pathology of the Abdominal Viscera

Uterus and Associated Structures

Broad Ligament Hematoma

The arterial supply to the uterus is within the broad ligament. The majority consists of the uterine artery (from the external iliac artery), with a cranial branch supplying the proximal uterine horn and a caudal branch supplying the distal uterine horn and body. This is anastomosed cranially by a uterine branch of the ovarian artery, and caudally by a uterine branch of the vaginal artery [16]. Rupture has been reported before, during, and after parturition, though it occurs most commonly during parturition [10]. Rupture of these vessels leads to hematoma formation between the layers of the broad ligament (Figure 28.12). The hematoma initially appears uniformly hyperechoic. With time, a heterogenous appearance develops, with separation of the blood into anechoic fluid and areas of hyperechoic organizing hematoma (Figure 28.13). Rupture of the broad ligament hematoma in the acute to subacute phase will allow leakage of blood into the peritoneal cavity. If rapid hemostasis is not achieved, the rupture may precipitate profound life-threatening hypovolemia. Chronically, scar tissue or regional calcification may result. A consistently reported predilection for side of rupture has not been reported; however, most tears occur in the proximal uterine artery [10,17].

Mural Hematoma

Trauma to the uterine wall may cause hemorrhage within or between any or all of the endometrium, myometrium, and serosal layers. Initially appearing as a hyperechoic mass, this subsequently progresses to anechoic fluid adjacent to heterogenous organizing tissue (Figure 28.14). Over time, abscessation may develop or the hematoma may dissect into the uterine lumen or peritoneal cavity. A full-thickness uterine defect may result from pressure necrosis with potential for peritonitis or pneumoperitoneum. If contained and chronic, scar tissue may result.

Vet-ebooks.com

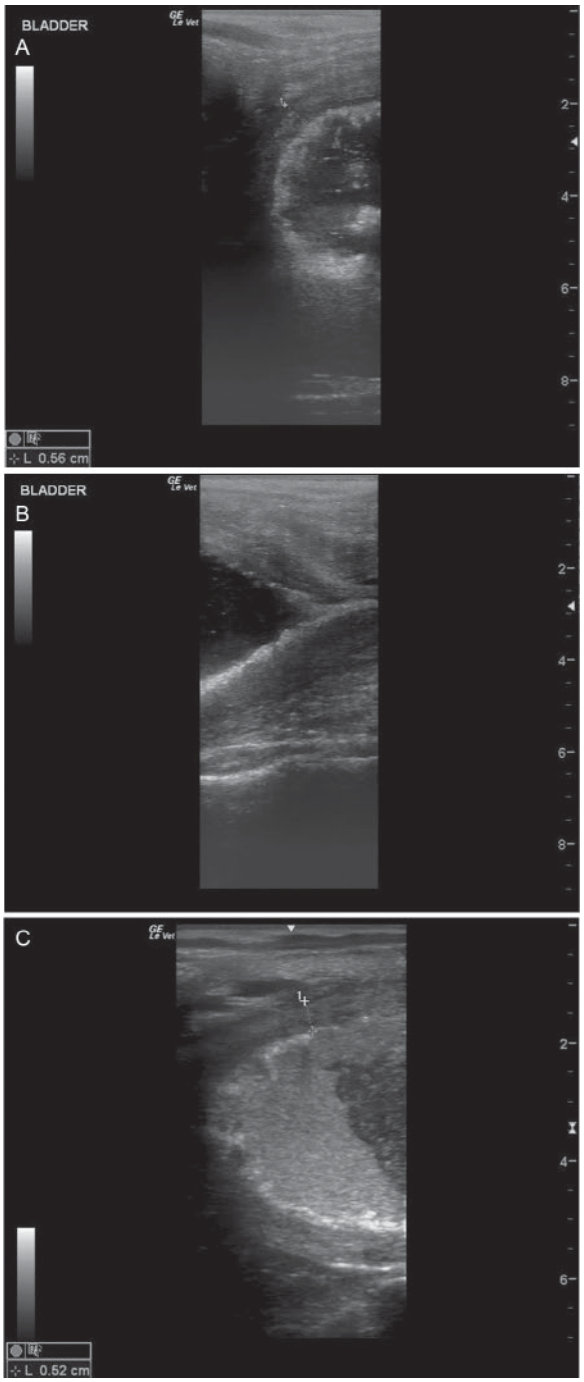


Figure 28.10 (A) Cystitis with urinary calculi. Transrectal ultrasonography of bladder with cystitis (as evidenced by thickened bladder wall) and multiple hyperechoic foci within the lumen. This sonogram was obtained transrectally using a linear probe operating at 10 MHz at a depth of 9 cm. (B) Cystitis with urinary calculi. Transrectal ultrasonography of bladder with cystitis. Multiple coalescing hyperechoic foci are adjacent to the bladder wall. This sonogram was obtained transrectally using a linear probe operating at 10 MHz at a depth of 9 cm. (C) Sabulous cystitis. Transrectal ultrasonography of bladder with sabulous cystitis. An accumulation of heterogenous granular material (arrowhead) in the ventral region of the bladder is delineated by a near straight line. This sonogram was obtained transrectally using a linear probe operating at 10 MHz at a depth of 8 cm.

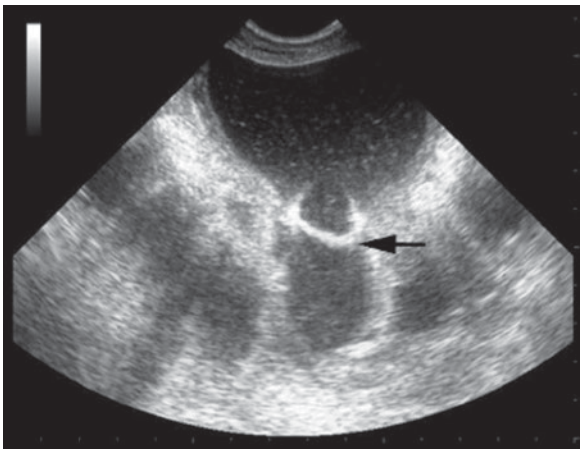


Figure 28.11 Ruptured bladder. This image shows a defect in the bladder (arrow). Ruptured bladder should be considered as a differential diagnosis for a mare with increased abdominal fluid either prior to or after foaling. This sonogram was obtained from the caudal aspect of ventral midline using a curvilinear probe operating at 3.5 MHz at a depth of 25 cm. (*Source*: Image courtesy of Dr Fairfield Bain, University of Queensland Veterinary Medical Centre, Queensland, Australia).

Intrauterine Fluid

The presence of a small amount of fluid within the uterine lumen is common in the initial post-partum period (Figure 28.15). However, uterine involution progresses rapidly and persistence of a high volume of fluid indicates failure of uterine clearance (Figure 28.16). Post-partum lochia is predominantly hypoechoic in nature. Intraluminal hemorrhage appears uniformly echogenic in nature consistent with the appearance of peritoneal hemorrhage (described above) (Figure 28.17). The source of the hemorrhage is not major vessels, but rather endometrial and/or mural vasculature. Septic fluid appears flocculent and heterogenous, with gas production appearing as a hyperechoic interface in necrotizing metritis (Figure 28.18).

Mural Laceration, Necrosis, and Perforation

The peritoneal cavity may display hemorrhage, peritonitis, or both concurrently, depending on the degree of loss of mural integrity and its duration of formation. Acute full thickness laceration of the uterine wall may appear initially as hemoperitoneum before progressing to septic peritonitis (Figure 28.19). Mural necrosis followed by perforation may initially present with signs of peritoneal inflammation before rupture occurs and fulminant bacterial peritonitis ensues. Expulsion of intraluminal uterine fluid will exacerbate peritonitis, especially if endometritis is present post partum. Sudden onset of colic signs post uterine lavage with concurrent appearance of a large volume of relatively anechoic peritoneal fluid (sourced from the lavage

Vet-ebooks.com

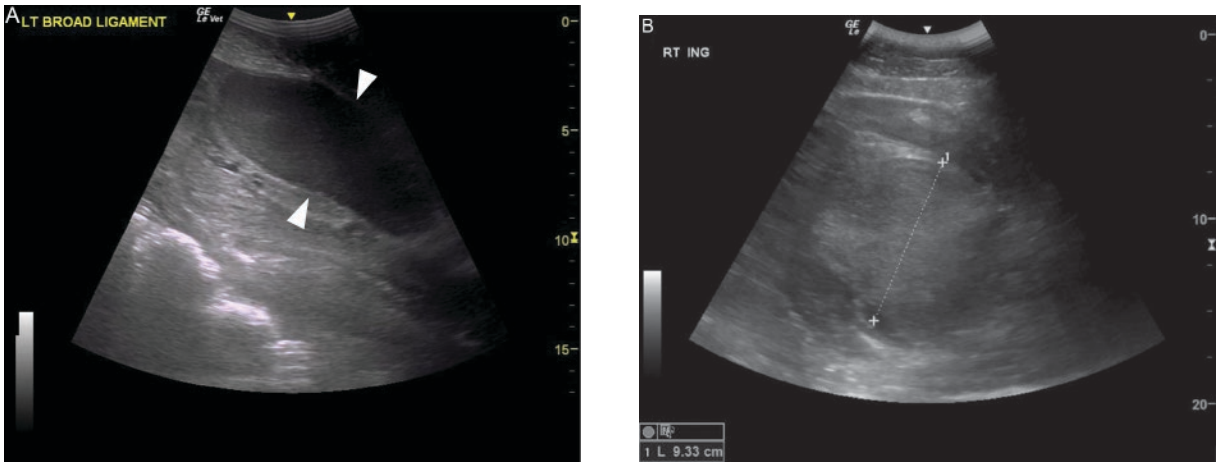


Figure 28.12 (A) Broad ligament hematoma, acute. Image obtained from left inguinal region. Blood accumulation within layers of the broad ligament delineated by arrowheads. This sonogram was obtained from the left inguinal region using a curvilinear probe operating at 4 MHz at a depth of 17 cm. (B) Broad ligament hematoma, subacute. Image obtained from right inguinal region. Blood accumulation within layers of the broad ligament delineated by caliper line. This sonogram was obtained from the right inguinal region using a curvilinear probe operating at 4 MHz at a depth of 20 cm.

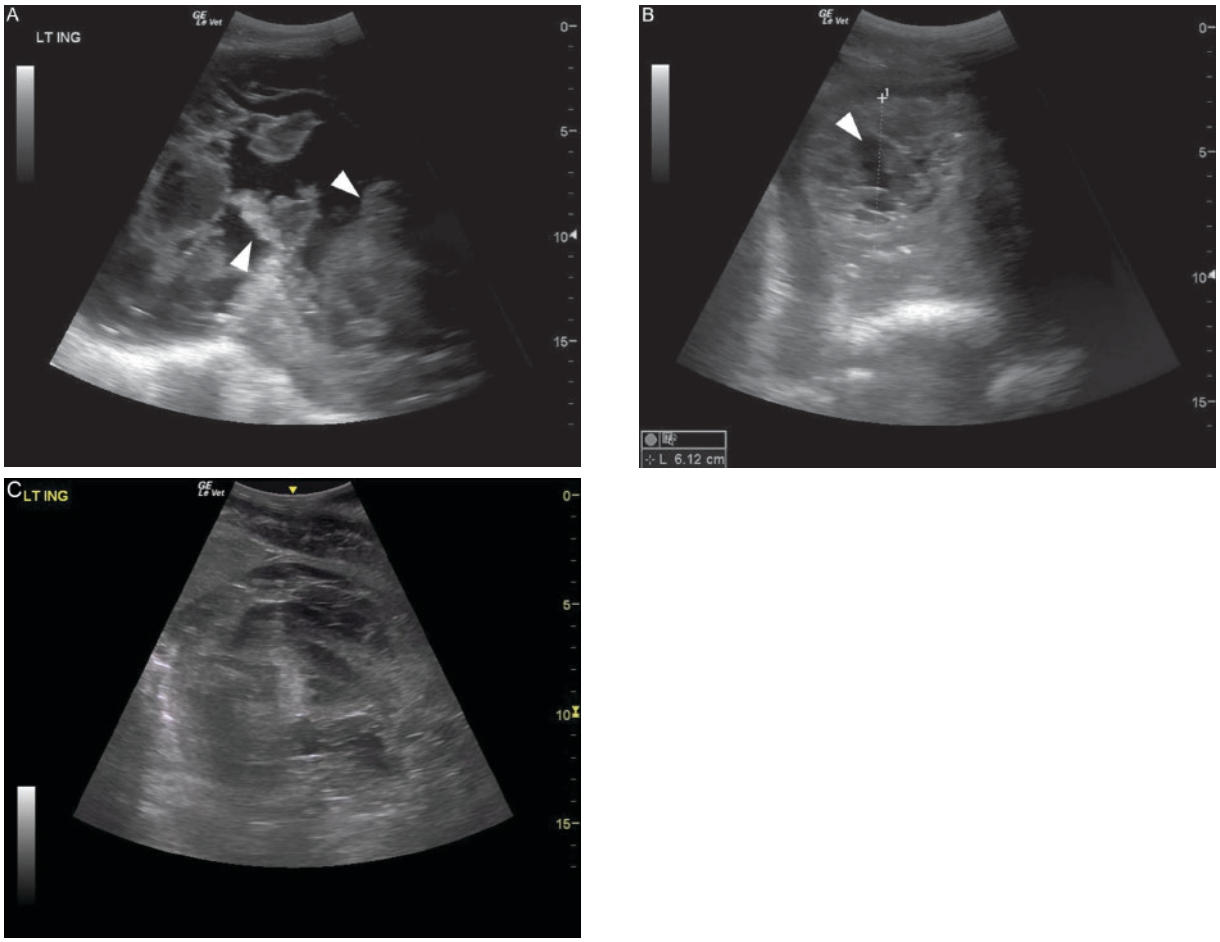


Figure 28.13 (A) Broad ligament hematoma, organizing. Image obtained from left inguinal region. Blood accumulation within layers of the broad ligament has begun to separate into serum and clot (arrowheads). This sonogram was obtained from the left inguinal region using a curvilinear probe operating at 4 MHz at a depth of 19 cm. (B) Broad ligament hematoma, organized. Image obtained from right inguinal region. Blood accumulation within layers of the broad ligament (delineated by calipers) has separated into serum (arrowhead) and clot. This sonogram was obtained from the left inguinal region using a curvilinear probe operating at 4 MHz at a depth of 16 cm. (C) Broad ligament hematoma, organized. Image obtained from left inguinal region. The hematoma contained within the broad ligament has organized and all serum has been withdrawn. The concentric layered appearance is typical. This sonogram was obtained from the left inguinal region using a curvilinear probe operating at 4 MHz at a depth of 17 cm.

Vet-ebooks.com

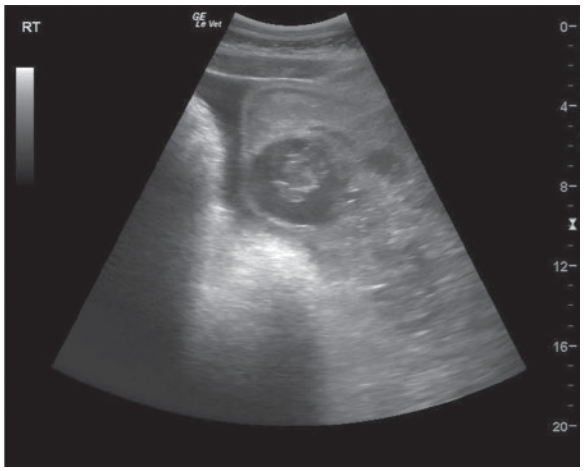


Figure 28.14 Mural hematoma, uterus. This hematoma within the uterine wall has become rounded and taken on the characteristics of an organizing blood clot. This sonogram was obtained from the right inguinal region using a curvilinear probe operating at 4 MHz at a depth of 20 cm.

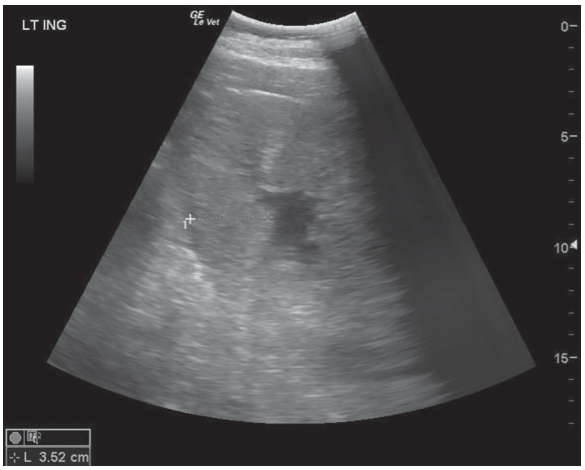
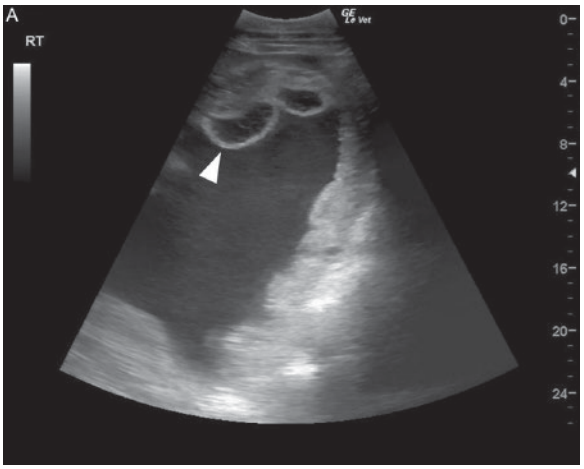


Figure 28.15 Involuting uterus. The uterus rapidly decreases in overall size and expels residual fluid while relocating into the inguinal region in the initial post-partum period. A small quantity may be evident as in this uterus three days following delivery of a live fetus. This sonogram was obtained from the left inguinal region using a curvilinear probe operating at 4 MHz at a depth of 18 cm.



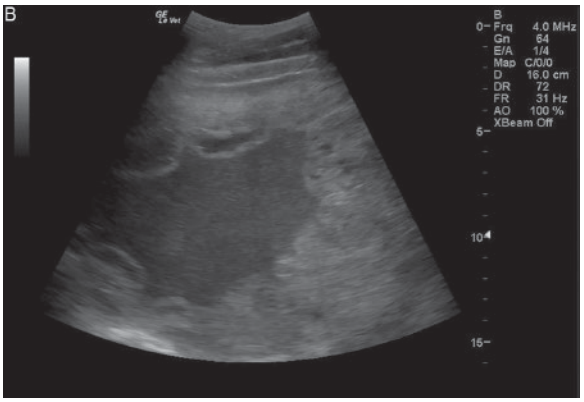


Figure 28.16 Septic intraluminal fluid. (A) A persistently enlarged uterus, visible in the cranial ventral abdomen, following parturition is highly suggestive of compromised uterine clearance. In the initial post-partum period, endometritis and metritis are possible differential diagnoses. Endometrial edema (arrowhead) is often visible of lesser echodensity than the turbid intraluminal fluid. This sonogram was obtained from the right cranial ventral abdominal region using a curvilinear probe operating at 4 MHz at a depth of 26 cm. (B) A persistently enlarged uterus, visible in the cranial ventral abdomen, with markedly turbid fluid compatible with endometritis. This sonogram was obtained from the right cranial ventral abdominal region using a curvilinear probe operating at 4 MHz at a depth of 16 cm.

fluid and uterine content) is highly suggestive of a pre-existing uterine perforation. Tears are more likely to be occur in the uterine body [18], and may be visible ultrasonographically.

Inverted Uterine Horn

Inverted uterine horn may occur following uncoordinated uterine contraction or uterine fatigue post foaling, or overzealous traction in cases of placental retention. The characteristic target sign appearance may be difficult to obtain with transabdominal ultrasonography (Figure 28.20).

Retained Placenta

Retained placenta should not be confused with the ultrasonographically prominent definition of the endometrium and myometrium resulting from edema in the wall of the post-partum uterus. The presence of an extra tissue layer with variable or discontinuous attachment to the endometrium is highly suggestive of placental retention (Figure 28.21). Gas echoes within intraluminal fluid may be present due to bacterial decomposition (Figure 28.22). Small fragments retained in the more proximal regions of the uterine horns may be difficult to image transabdominally.

Vet-ebooks.com

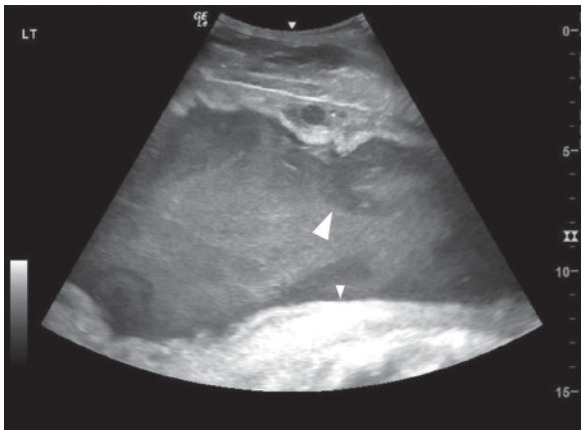


Figure 28.17 Intraluminal hemorrhage, uterus. Bleeding into the uterus may occur secondary to laceration of endometrial vessels. Blood may appear to swirl or be of varying echodensity similar to peritoneal blood (arrowhead). Enhanced echotransfer through fluid may cause hyperechogenicity of deeper structures (small arrowhead). This sonogram was obtained from the left inguinal region using a curvilinear probe operating at 4 MHz at a depth of 15 cm.

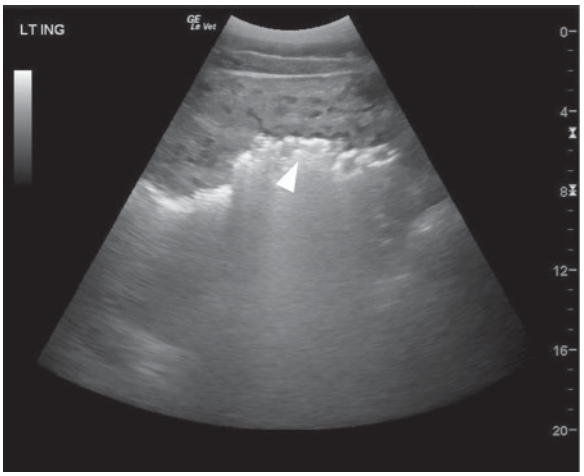
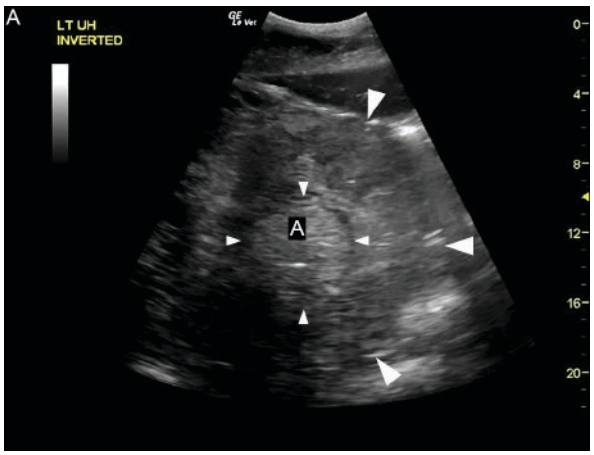


Figure 28.18 Pneumouterus, metritis. Gas production may occur with severe metritis, the result of tissue necrosis. A hyperechoic tissue interface (arrowhead) may be visible. This sonogram was obtained from the left inguinal region using a curvilinear probe operating at 4 MHz at a depth of 20 cm.



Figure 28.19 Uterine tear, peritonitis. Uterine tears can result in contamination of the peritoneal cavity with uterine content resulting in peritonitis. This sonogram was obtained from the ventral abdomen, left of midline, using a curvilinear probe operating at 3.5 MHz at a depth of 20 cm.



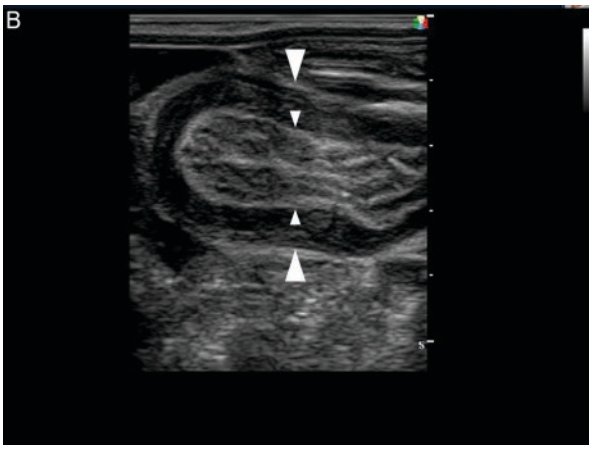


Figure 28.20a (A) Inverted uterine horn, transabdominal. Cross-section of post-partum uterine horn with wall indicated by arrowheads. The horn tip is inverted, and margins demarcated (small arrowheads) with minimal separation fluid visible. This sonogram was obtained from the left inguinal region using a curvilinear probe operating at 4 MHz at a depth of 22 cm. (B) Inverted uterine horn, transrectal. Cross-section of post-partum uterine horn with wall indicated by arrowheads. The horn tip is inverted, margins demarcated (small arrowheads). Note the multilayered appearance and edematous outer layer of the uterine wall. This sonogram was obtained transrectally using a linear probe operating at 7.5 MHz at a depth of 5 cm.

Vet-ebooks.com

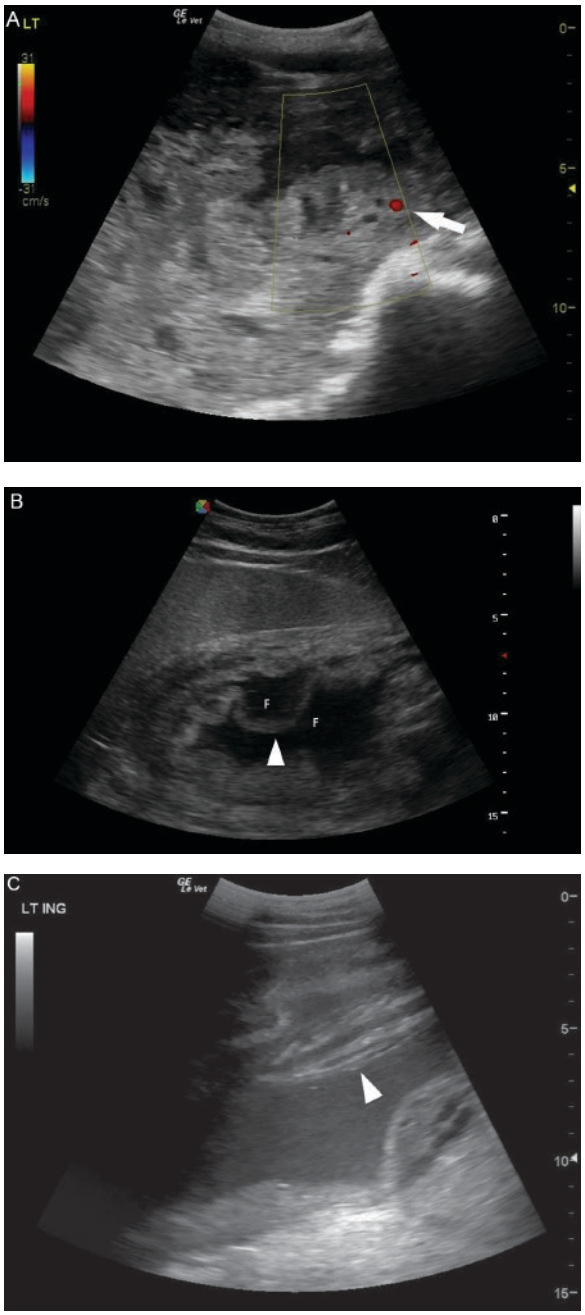


Figure 28.21 (A) Normal uterine edema in post-partum mare. Uterine edema is a normal finding in a post-partum mare. This image was taken 12 hours post foaling. Loose folding of the uterine wall and prominent endometrial edema is a common finding. Color Doppler identifies a vessel (arrow) in the uterine wall. This sonogram was obtained from the left inguinal region using a curvilinear probe operating at 4.0 MHz at a depth of 12 cm. (B) Retained placenta, transverse view. Note the irregular contour of the retained placental tissue relative to the uterine wall. Fluid (F) of identical echogenicity is present on both sides of the free placental membrane (arrowhead). This sonogram was obtained from the left inguinal area using a curvilinear probe operating at 4.0 MHz at a depth of 15 cm. (C) Retained placenta, longitudinal view. Note the layering of folded retained placental tissue (arrowhead) within intraluminal fluid. This sonogram was obtained from the left inguinal area using a curvilinear probe operating at 4.0 MHz at a depth of 15 cm.

When suspected, secondary indicators such as the presence of increased or turbid intraluminal fluid warrant investigation ultrasonographically *per rectum* or manually *per vaginum*.

Pneumometra

Accumulation of air in the uterus has been reported as cause of post-partum colic [19]. This appears as hyperechogenic particles within intraluminal fluid or as a hyperechoic gas interface adjacent to the uterine wall obscuring ventral structures (Figure 28.23). Poor perineal conformation or trauma results in failure of the perineal, vestibular, or cervical seals allowing aerophagia.

Vaginal Fluid

Fluid may accumulate in the vaginal vault (Figure 28.24) in the post-foaling mare from urine pooling, hemorrhage, trauma, or infection.

Gastrointestinal Tract

The only indication of intestinal compromise or rupture may be the onset of fulminant peritonitis and clinical signs of endotoxemia as the entirety of the intestinal tract cannot be imaged. No ultrasonographic findings are pathognomonic for any particular lesion; however, deviation from normal viscera location or size provides information complementary to other examinations and supports further investigation. Ultrasonography is superior to other methods to assess the presence or absence of intestinal motility.

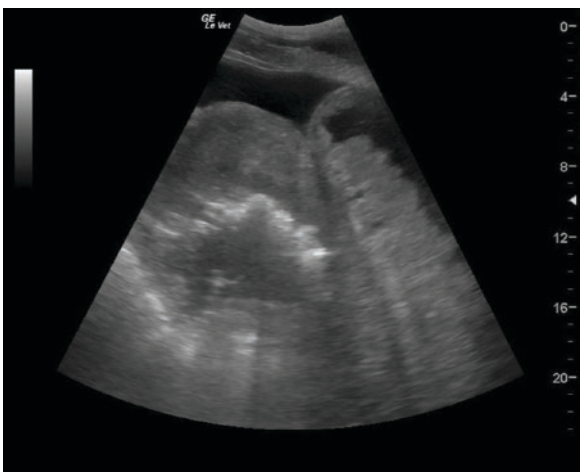


Figure 28.22 Retained placenta, gas decomposition. Placental tissue is firmly adhered to the uterine wall. The hyperechoic line (arrow) is gas production from septic decomposition of the placental tissue. This sonogram was obtained from the left inguinal area using a curvilinear probe operating at 4.0 MHz at a depth of 20 cm.

Vet-ebooks.com

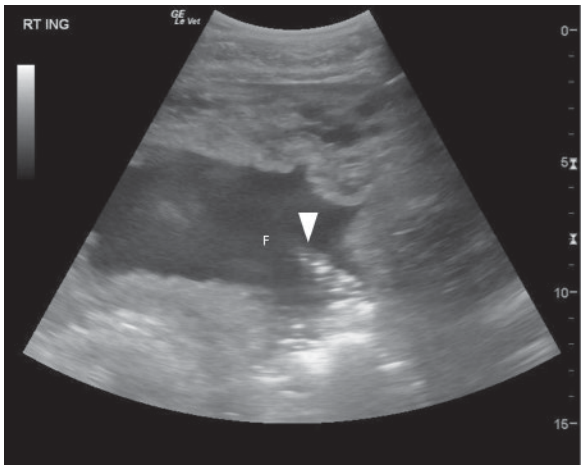


Figure 28.23 Aerophagia. Gas in intraluminal uterine fluid. This image shows hyperechoic foci (arrowhead) within the intraluminal fluid (F). These foci are gas pockets and suggest either aerophagia or uterine infection with a gas-producing organism. This sonogram was obtained from the right inguinal area using a curvilinear probe operating at 4.0 MHz at a depth of 12 cm.

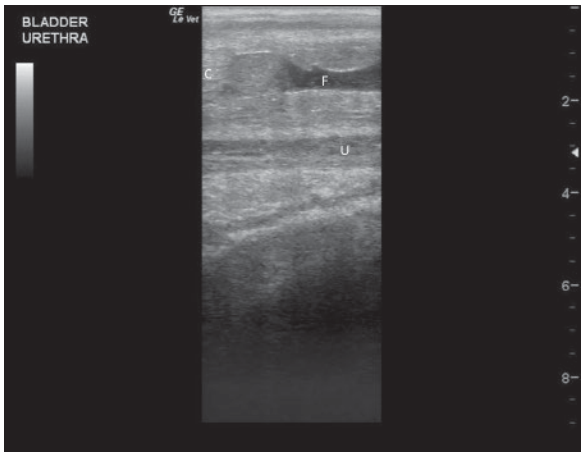


Figure 28.24 Vaginal fluid. Incompetence of the perineal seal due to poor vestibulovaginal conformation may allow fluid accumulation in the cranial vagina (F). The cervix (C) and urethra (U) are also visible. This sonogram was obtained transrectally using a linear probe operating at 6 MHz at a depth of 9 cm.

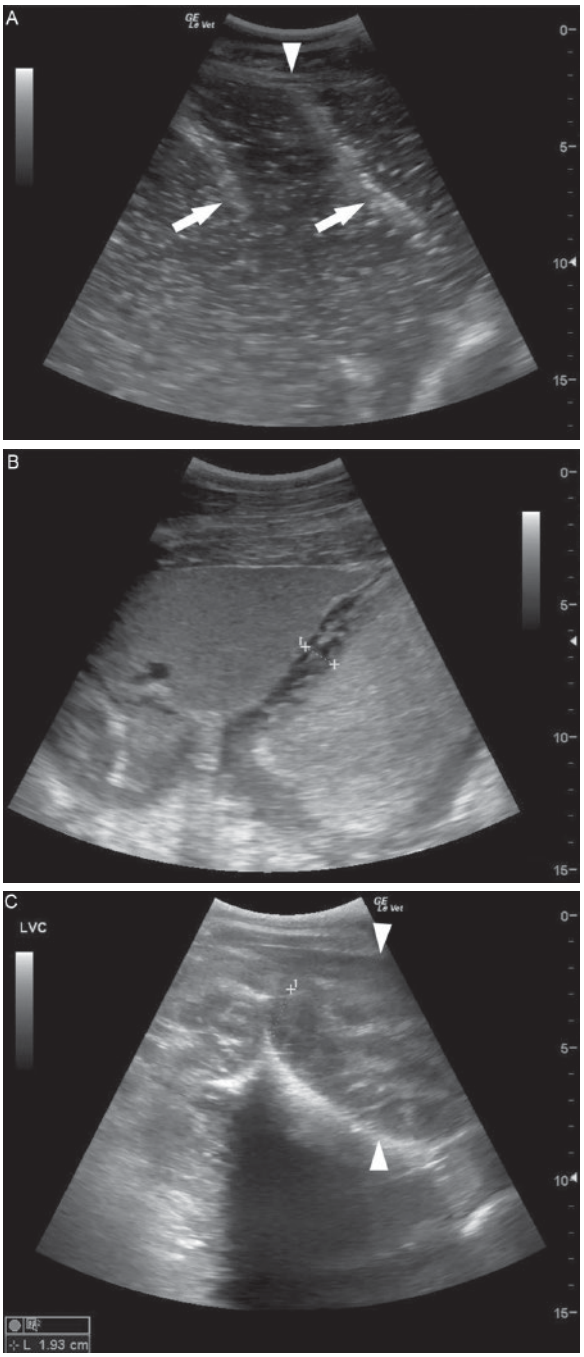


Figure 28.25 (A) Ventral colon, colitis. This image of the right ventral colon shows increased luminal fluid and prominent outlining of the haustra (arrows). Note the loss of sacculations along the colon wall (arrowhead). This sonogram was obtained from the right ventral abdomen with a curvilinear probe operating at 4.0 MHz at a depth of 15 cm. (B) Edema of colon wall. The left dorsal colon wall (caliper) is grossly thickened and edematous. Causes for edematous colon wall include colitis, peritonitis, and colon torsion. This sonogram was obtained from the left abdomen using a curvilinear probe operating at 4.0 MHz at a depth of 13 cm. (C) Typhlocolitis, thickened left ventral colon. This post-partum mare developed severe, necrotizing typhlocolitis. Note the thickened wall (arrowheads) of the left ventral colon. This sonogram was taken from the left ventral abdomen with a curvilinear probe operating at 4.0 MHz at a depth of 12 cm.

Large Colon

Increased wall thickness and loss of sacculations due to profound distension may be visible in the post-partum mare in colitis, peritonitis, or colon torsion (Figure 28.25). The large colon is at increased risk of torsion in the post-partum mare [20]. In one review, this was the most common diagnosis for referral emergency presentations of post-partum mares [9]. More chronic cases may have vague presenting clinical signs including inappetence and depression [21]. The presence of nonsacculated large colon in the left ventral portion of the abdomen

Vet-ebooks.com

is considered indicative of large colon volvulus [22]. With colonic displacement or torsion, the cecal and colonic mesenteric vessels are visible in the right paralumbar fossa coursing ventrally and becoming engorged and tortuous [23,24]. With colitis, luminal contents are increased and uniformly hyperechoic and thickened colon wall is present.

Small Colon

The small colon may suffer bruising from compression during foaling, or avascular necrosis from disruption of the mesenteric attachments. Segmental necrosis and entrapment may result from rents in the mesocolon [25]. Lesser trauma may result in impaction and colic. The small colon cannot be directly visualized transabdominally, but increased peritoneal fluid with inflammatory changes in conjunction with signs of endotoxemia may be the first indication of devitalization.

Cecum

The most likely site of post-partum rupture is the tip of the cecum [3]. In parturient mares, fetal hoof on tympanic cecal wall is thought to lead to pressure necrosis [26]. Signs consistent with peritonitis are usually the first indication of cecal compromise as mural compromise may be small and inaccessible to ultrasonographic evaluation.

Duodenum

Duodenitis-proximal jejunitis is associated with thickening of the wall to greater than 4 mm. With small intestinal ileus, the duodenum is often distended, becoming round without effective peristalsis (Figure 28.26). The luminal content becomes hypoechoic with small numbers of hyperechoic particles.

Jejunum

Ultrasonography has been reported 100% sensitive and 100% specific for small intestinal strangulation when distension, mural thickening, and loss of motility are noted [27]. Separation of content and development of hypoechoic fluid occurs in the obstructed segment (Figure 28.27). Strangulated small intestine is most commonly found in the ventral abdomen and lower flank regions. Involved regions can be differentiated from the remainder of the jejunum by their marked increase in wall thickness. Dilated small intestine with motility is associated with large colon lesions, and wall thickening with motility is present in peritonitis [27].

Stomach

Gastric stasis, distension (Figure 28.28), and rupture has also been reported secondary to other complications post partum including small intestinal ileus [28].

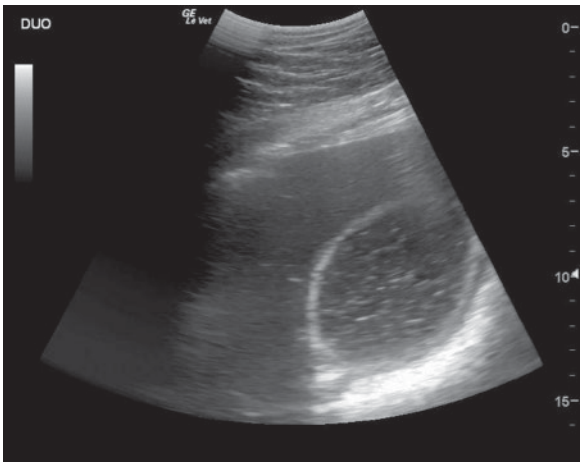


Figure 28.26 Duodenal dilation. The duodenum is markedly distended and amotile which can be indicative of gastric dilation or proximal small intestinal motility deficits. This sonogram was taken from the right dorsal abdomen with a curvilinear probe operating at 4.0 MHz at a depth of 15 cm.

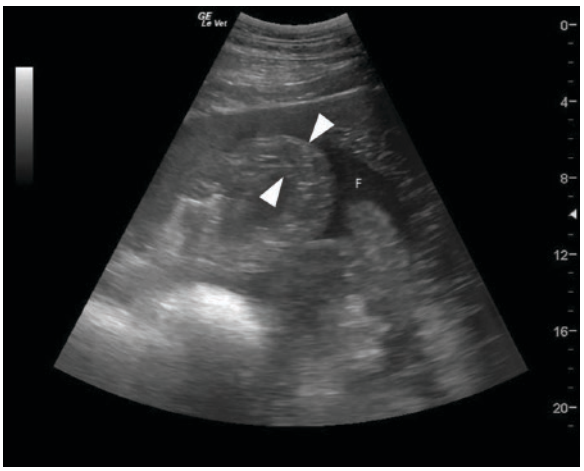


Figure 28.27 Thickened jejunal wall. This image shows an amotile loop of jejunum with thickened walls (arrowheads). Flocculent peritoneal fluid (F) indicates intestinal devitalization with ensuing peritonitis. This sonogram was taken from the right inguinal region using a curvilinear probe operating at 4.0 MHz at a depth of 18 cm.

In these cases, the characteristic shape and location of the stomach is changed. The stomach wall appears as a large, curvilinear fluid-gas interface in the left cranial abdomen (ICS 11-13), caudal to the liver and craniomedial to the spleen [29]. Dorsocaudal displacement of the stomach wall from this region is compatible with experimental gastric distension [29]. With stasis, the contact area of the stomach to the body wall is markedly increased, and travels dorsocaudally. Where rupture has occurred, the arc of the stomach wall becomes irregular from loss of appropriate tension and displaced from close application to the liver and spleen.

Vet-ebooks.com

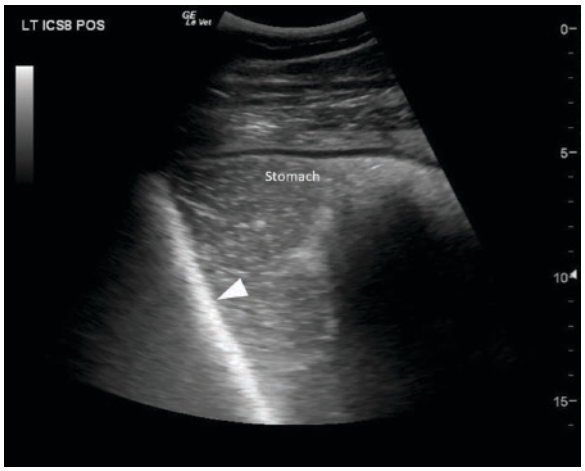


Figure 28.28 Dilated stomach. The stomach was dilated in this post-partum mare secondary to enteritis. The stomach has increased contact with the body wall. The hyperechoic line (arrowhead) is a prominent air–fluid interface in the stomach. This sonogram was taken from the left eighth ICS using a curvilinear probe operating at 4.0 MHz at a depth of 15 cm.

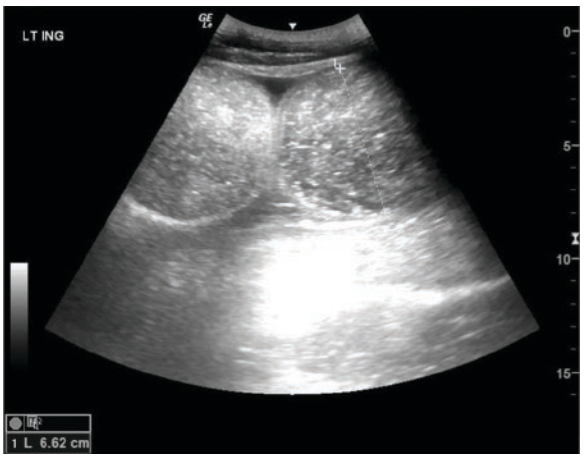


Figure 28.29 Entrapped small intestine. This image shows small intestine entrapped through a mesenteric rent. Wall thickness may increase with time; earlier indications include dilation, amotility, and stagnant content. This sonogram was taken from the left inguinal region using a curvilinear probe operating at 4.0 MHz at a depth of 16 cm.

Mesenteric Rent

Small colon or jejunum may become incarcerated through a tear in the mesentery [30]. Alternatively, disruption of the mesenteric blood supply may cause mural necrosis to ensue. This is especially important for the small colon due to its relatively short mesocolon which can tear with passage of the fetus [3,25]. Affected jejunum may be visualized with thickened wall, distension, and lack of motility (Figure 28.29). Small colon necrosis may not be directly visualized unless transrectally imaged; however, peritoneal fluid changes indicating increased cellularity and volume are indirect indicators of compromise.

Summary

Ultrasonography provides a rapid and non-invasive method of assessing the viscera and genital tract of the post foaling mare. Visualization of the entire abdominal content is not possible, but rather, in conjunction with consideration of the amount and characteristics of the peritoneal fluid, decisions regarding the health of the mare can be made.

Reference List

1 Reef, V.B., Whittier, M., and Allam, L.G. (2004). Sonographic evaluation of the adult abdomen. *Clinical Techniques in Equine Practice* 3(3): 294–307.
2 Hanson, R.R. and Todhunter, R.J. (1986). Herniation of the abdominal wall in pregnant mares. *Journal of the American Veterinary Medical Association* 189(7): 790–793.
3 Frazer, G.S. (2003). Post partum complications in the mare. Part 2: Fetal membrane retention and conditions of the gastrointestinal tract, bladder and vagina. *Equine Veterinary Education* 15(2): 91–100.
4 Romero, A.E. and Rodgerson, D.H. (2010). Diaphragmatic herniation in the horse: 31 cases from 2001–2006. *The Canadian Veterinary Journal. La Revue Veterinaire Canadienne* 51(11): 1247–1250.
5 Moll, H.D., Wallace, M.A., Sysel, A. et al. (1999). Large colon strangulation due to a diaphragmatic hernia in a mare: A case report. *Journal of Equine Veterinary Science* 19(1): 58–59.
6 Hartzband, L.E., Kerr, D.V., and Morris, E.A. (1990). Ultrasonographic diagnosis of diaphragmatic rupture in a horse. *Veterinary Radiology* 31(1): 42–44.
7 Frazer, G., Burba, D., Paccamonti, D. et al. (1997). The effects of parturition and peripartum complications on the peritoneal fluid composition of mares. *Theriogenology* 48(6): 919–931.
8 Arnold, C.E., Payne, M., Thompson, J.A. et al. (2008). Periparturient hemorrhage in mares: 73 cases (1998–2005). *Journal of the American Veterinary Medical Association* 232(9): 1345–1351.
9 Dolente, B.A., Sullivan, E.K., Boston, R. et al. (2005). Mares admitted to a referral hospital for postpartum emergencies: 163 cases (1992–2002). *Journal of Veterinary Emergency and Critical Care* 15(3): 193–200.

Vet-ebooks.com

10 Williams, N.M. and Bryant, U.K. (2012). Periparturient arterial rupture in mares: A postmortem study. *Journal of Equine Veterinary Science* 32(5): 281–284.

11 Snalune, K.L. and Mair, T.S. (2006). Peritonitis secondary to necrosis of the apex of the urinary bladder in a post parturient mare. *Equine Veterinary Education* 18(1): 20–26.

12 Nyrop, K., DeBowes, R., Cox, J. et al. (1984). Rupture of the urinary bladder in two postparturient mares. *The Compendium on Continuing Education for the Practicing Veterinarian* 6(9): S510–S513.

13 Higuchi, T., Nanao, Y., and Senba, H. (2002). Repair of urinary bladder rupture through a urethrotomy and urethral sphincterotomy in four postpartum mares. *Veterinary Surgery* 31(4): 344–348.

14 Jones, P.A., Sertich, P.S., and Johnston, J.K. (1996). Uroperitoneum associated with ruptured urinary bladder in a postpartum mare. *Australian Veterinary Journal* 74(5): 354–358.

15 Wong, D.M., Leger, L.C., Scarratt, W.K. et al. (2004). Uroperitoneum and pleural effusion in an American Paint filly. *Equine Veterinary Education* 16(6): 290–293.

16 Lofstedt, R. (1994)/ Haemorrhage associated with pregnancy and parturition. *Equine Veterinary Education* 6(3): 138–141.

17 Ueno, T., Nambo, Y., Tajima, Y. et al. (2010). Pathology of lethal peripartum broad ligament haematoma in 31 Thoroughbred mares. *Equine Veterinary Journal* 42(6): 529–533.

18 Javsicas, L.H., Giguère, S., Freeman, D.E. et al. (2010). Comparison of surgical and medical treatment of 49 postpartum mares with presumptive or confirmed uterine tears. *Veterinary Surgery* 39(2): 254–260.

19 Livesey, L.C., Carson, R.L., and Stanton, M.B. (2008). Postpartum colic in a mare caused by pneumouterus. *Veterinary Record* 162(19): 626–627.

20 Hance, S.R. and Embertson, R.M. (1992). Colopexy in broodmares: 44 cases (1986–1990). *Journal of the American Veterinary Medical Association* 201(5): 782–787.

21 Doyle, A.J., Freeman, D.E., Sauberli, D.S. et al. (2002). Clinical signs and treatment of chronic uterine torsion in two mares. *Journal of the American Veterinary Medical Association* 220(3): 349–353.

22 Abutarbush, S.M. (2006). Use of ultrasonography to diagnose large colon volvulus in horses. *Journal of the American Veterinary Medical Association* 228(3): 409–413.

23 Grenager, N.S. and Durham, M.G. (2011). Ultrasonographic evidence of colonic mesenteric vessels as an indicator of right dorsal displacement of the large colon in 13 horses. *Equine Veterinary Journal* 43: 153–155.

24 Ness, S.A.L., Bain, F.T., Zantingh, A.J. et al. (2012). Ultrasonographic visualization of colonic mesenteric vasculature as an indicator of large colon right dorsal displacement or 180-¦ volvulus (or both) in horses. *The Canadian Veterinary Journal* 53(4): 378.

25 Dart, A.J. Pascoe, J.R, and Snyder, J.R. (1991). Mesenteric tears of the descending (small) colon as a postpartum complication in two mares. *Journal of the American Veterinary Medical Association* 199(11): 1612–1615.

26 Platt, H. (1983). Caecal rupture in parturient mares. *Journal of Comparative Pathology* 93(2): 343–346.

27 Klohnen, A. Vachon, A.M., and Fischer, A.T. (1996). Use of diagnostic ultrasonography in horses with signs of acute abdominal pain. *Journal of the American Veterinary Medical Association* 209(9): 1597–1601.

28 Hillyer, M.H. Smith, M.R.W., and Milligan P.J.P. (2008). Gastric and small intestinal ileus as a cause of acute colic in the post parturient mare. *Equine Veterinary Journal* 40(4): 368–372.

29 Lores, M., Stryhn, H., McDuffee, L. et al. (2007). Transcutaneous ultrasonographic evaluation of gastric distension with fluid in horses. *American Journal of Veterinary Research* 68(2): 153–157.

30 Gayle, J.M., Blikslager, A.T., and Bowman, K.F. (2000). Mesenteric rents as a source of small intestinal strangulation in horses: 15 cases (1990–1997). *Journal of the American Veterinary Medical Association* 216(9): 1446–1449.

Vet-ebooks.com

29

Neonatology

J. Barry David

Hagyard Equine Medical Institute, Lexington, KY, USA

The ultrasound machine is one of the most useful pieces of equipment in the neonatal intensive care unit (NICU). The indications to use ultrasonography are numerous and the images in this chapter were generated while investigating the potential causes of fever, colic, tachycardia, tachypnea, anemia, hypoproteinemia, azotemia, and abnormal heart or lung sounds, in the NICU patient. Other uses for ultrasound in neonates include the diagnosis of ocular problems, arthropathies, tendon and ligament injuries, and the investigation of swelling in various locations.

The neonate's size and lack of body fat makes it easier to get quality ultrasound images as compared to an adult horse. In addition, due to their small size, one can use ultrasound probes with a higher frequency, which will also improve image quality. Generally, the use of a 5–10 mHz curvilinear probe, with alcohol as a contact medium, will produce excellent diagnostic images for most of the examinations on foals. An exception for this is echocardiography where sector probes remain the gold standard to obtain quality, diagnostic cardiac images. All considered, neonates are amenable to ultrasound, no matter what probe the practitioner has. A 5 mHz linear probe can produce quality diagnostic images during thoracic and abdominal examinations.

The medical/physical condition of the neonate will dictate the position of the patient during the examination. Ultrasonography of a standing foal provides the clinician with images of the internal organs that are in the most recognized orientation; but frequently the neonatal patient is recumbent. If a foal is recumbent, the image of the pulmonary tissue can change significantly. The down-side lung on a recumbent neonate typically has sonographic changes that may or may not be associated with pathology; the changes may be the result of perfusion/ventilation mismatch. Conversely, a recumbent neonate's upper lung appearing sonographically abnormal is significant. The orientation of the abdominal organs in a recumbent foal will change slightly compared to the standing foal, but minimal differences in the echogenic characteristics of the organs are seen between the standing and recumbent foal. The position of the heart during ultrasound examination of the recumbent neonate may preclude the sonographer from obtaining standard diagnostic views, as opposed to a standing foal. However, most of the time, an accurate diagnosis of the cause of a particular murmur can be made in a recumbent foal. When scanning the foal's heart, the hair over the cranioventral thorax, on and behind the triceps muscle, may need to be clipped, but many times the foal's haircoat is thin enough to scan without clipping. Generally, only alcohol is required as a contact medium, but ultrasound gel may facilitate obtaining quality cardiac images. While scanning the heart, the ultrasound probe should be placed between the cranial intercostal spaces, with the longitudinal plane oriented parallel to the rib surfaces. The neonate's intercostal spaces are narrow, which may make the acquisition of diagnostic images challenging.

Ideally, a recumbent foal will be maintained in a sternal position to aid in preventing the development of pneumonia of the dependent lung, but in

Atlas of Equine Ultrasonography, Second Edition. Edited by Jessica A. Kidd, Kristina G. Lu and Michele L. Frazer.
© 2022 John Wiley & Sons Ltd. Published 2022 by John Wiley & Sons Ltd.
Companion Website: www.wiley.com/go/kidd/atlas

Vet-ebooks.com

some cases (e.g., seizure activity, rib fracture), maintaining sternal recumbency is not possible. When the foal must remain in lateral recumbency during the examination, assess the sonographic appearance of the independent or upper lung. After the upper lung is scanned, the foal should be turned, and after a short period of time, the other lung can be scanned. Clipping a foal's chest for thoracic ultrasonography is generally not necessary and the use of alcohol, as a contact medium, is most practical. The clinician should perform a complete and thorough examination of each side of the foal's chest. The entire lung field should be investigated by placing the probe dorsally, in each intercostal space, with the longitudinal plane of the probe parallel to the rib surface, and slowly moving it ventrally until the diaphragm is visualized. The more cranial regions of the lung can be imaged directly through the triceps muscle. The scanning technique to search for rib fractures is identical to scanning lungs, except now the probe is placed directly on the rib surface. The diaphragm is an important structure to identify as it separates the pleural cavity from the peritoneal cavity. Being able to identify the diaphragm will allow the clinician to determine whether an abnormal accumulation of fluid is in the chest or abdomen. It will also be important to visualize the diaphragm to make a diagnosis of diaphragmatic hernia.

When scanning a neonate's abdomen, clipping the foal's hair is usually not necessary to obtain clear, diagnostic images. As with the thorax, alcohol is a practical, rapidly applied contact medium. When scanning the lateral aspects of the abdomen, the technique is the same as scanning the thorax; place the probe in the intercostal space, with the probe's longitudinal plane parallel to the rib surface and move slowly ventrally. Organs that will normally be visualized on the left lateral abdomen in the neonate include the liver, spleen, left kidney, stomach, and portions of the intestinal tract. Visualizing the stomach full of milk may be a normal finding if the foal has just nursed and is not demonstrating signs of colic. Organs visible on the right lateral side of the neonate's abdomen include the right dorsal colon, duodenum, liver, and right kidney. The bladder, ventral and dorsal colons, small colon, small intestine, internal umbilical structures, and often the kidneys can be visualized from the ventral abdomen. Although the orientation of the organs may be altered by recumbency, the differences between images obtained in the standing neonate, compared to a recumbent one, are generally not significant. The exception to this statement is if the foal has an accumulation of fluid in the abdomen. Abdominal fluid is easier to identify and quantify when the neonate is in the standing position. The following images provide some examples of neonatal ultrasonography.

Thoracic Cavity

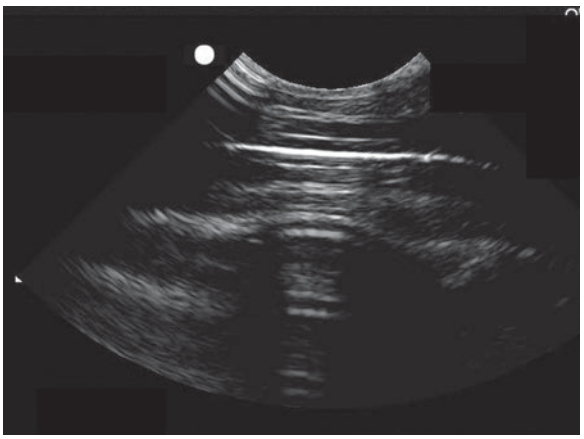


Figure 29.1 Normal lung surface. Healthy lung surface appears as a bright white line, as air reflects the sound waves, with recurrent parallel reverberation artifact lines below it. Diagnostic lung images are obtained by scanning dorsally to ventrally, down each intercostal space, on both sides of the chest. Pneumonia is one of the most prevalent problems in the recumbent neonate due to ventilation/perfusion mismatches. This image was obtained using a curvilinear probe operating at 6–10 MHz at a depth of 4 cm.

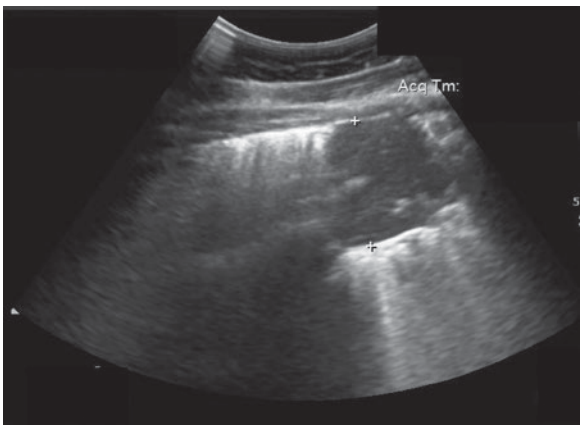


Figure 29.2 Bronchopneumonia. This image illustrates a region of lung that does not have the normal bright white line air interface. The pulmonary parenchyma is diseased and sound waves now can penetrate the consolidated lung tissue that is devoid of air. This patient required antibiotic therapy for treatment of pneumonia. This image was obtained from the left 6 ICS using a 6–10 curvilinear probe operating at a depth of 11 cm.

Vet-ebooks.com

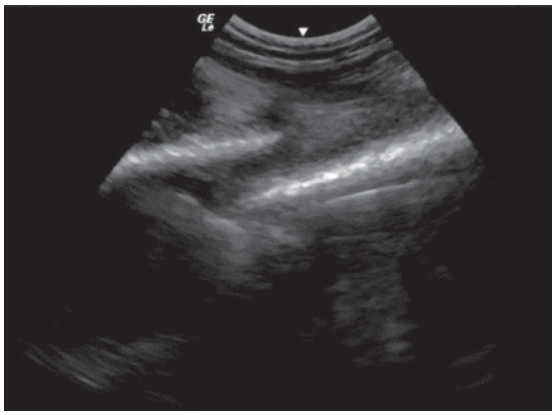


Figure 29.3 Rib fracture. This image was obtained by directing the ultrasound probe, dorsally to ventrally, in a longitudinal fashion, along the rib surface. The healthy rib surface reflects sound waves and creates a bright white line. When the boney surface is disrupted or fractured, ultrasound beams will penetrate the fracture site. It may be difficult to image the fracture until the fracture ends displace. Rib fractures can be managed conservatively but may require surgical intervention if the sharp end(s) of the fracture traumatize the lung surface, diaphragm, or the heart. This image was obtained from the left 6 rib using a 6–10 MHz microconvex probe operating at a depth of 4 cm.

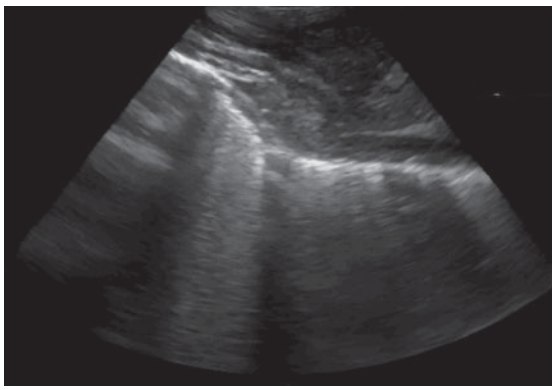


Figure 29.4 Hematoma from rib fracture. In this image, hematoma is caused by a rib fracture compressing the lung. Lung surface damage is apparent on the right side of the image with the loss of the bright white line on normal lung surfaces. In this case, the hematoma formed on the fractured ends of the ribs may protect the lung surface from further trauma from the sharp rib fracture end(s). This image was obtained with a curvilinear probe operating at 6–10 MHz probe at a depth of 6 cm.



Figure 29.5 Diaphragmatic hernia. Another complication of rib fracture is a diaphragmatic hernia. Particularly with caudal rib fractures, the sharp ends can lacerate the diaphragm and result in herniation of abdominal content into the pleural space. This image was obtained from the 12th intercostal space on the right side of the foal's abdomen. In this image, a loop of small intestine (+ markers) is just dorsal to the diaphragm and the liver (arrow) is just ventral to the diaphragm. Dorsal is the left side of the image, ventral is on the right. This image was obtained from the 12th intercostal space on the right side of the foal's abdomen using a 6–10 MHz curvilinear probe at a depth of 21 cm. [Refer to video 1].

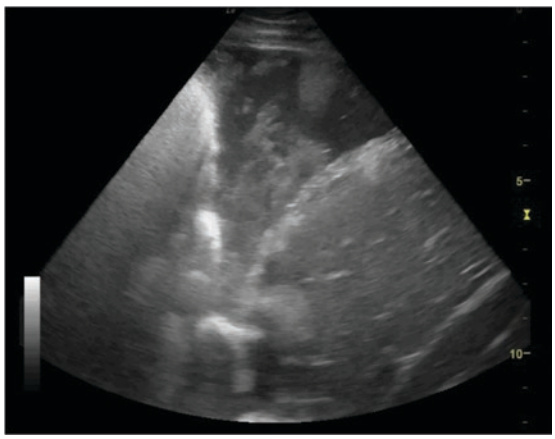


Figure 29.6 Hemothorax. Hemothorax is another potential complication of rib fracture if the fractured rib end lacerates the lung or pericardium. In this image, collapsed lung surface (arrow) appears as a bright white line. The diaphragm (arrowhead) is the thick curved line adjacent to the liver. Blood clots and strands of fibrin are present in the pleural space. The blood in the pleural space appears cellular in this image. This image was obtained using curvilinear probe operating at 6–10 MHz at a depth of 12 cm. [Refer to video 2].

Vet-ebooks.com

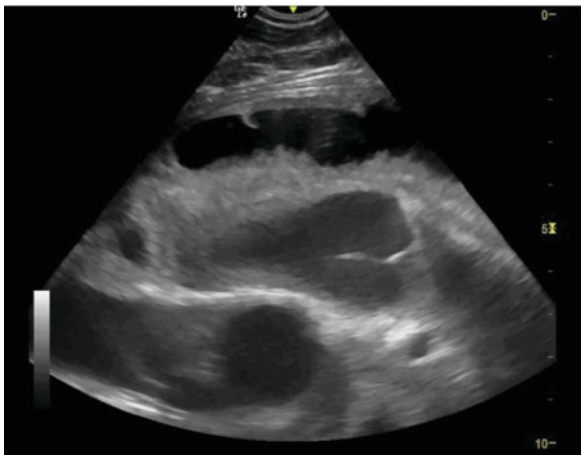


Figure 29.7 Hemopericardium. Hemopericardium is another complication of rib fracture. It occurs when a sharp end of the rib fracture has lacerated the pericardium and the pericardial space begins to contain blood. In this image, the hypoechoic area (asterisk) is blood within the pericardium. The right ventricle (RV) is visualized. The condition may stabilize, or if trauma and bleeding continue, cardiac tamponade may develop. This image was obtained using a curvilinear probe operating at 6–10 MHz at a depth of 10 cm.



Figure 29.8 Pentalogy of fallot. Congenital cardiac defects are generally difficult to identify clinically unless a severe murmur or arrhythmia is present. In this case, a grade 4/6 systolic murmur, bilaterally, was auscultated at presentation. In addition, the foal remained cyanotic in the face of nasal oxygen supplementation and IV fluid therapy. Cardiac ultrasonography identified a presumed Pentalogy of Fallot: ventricular septal defect, overriding aorta, pulmonary stenosis, right ventricular hypertrophy, and atrial septal defect. This image was obtained using a curvilinear probe operating at 6–10 MHz at a depth of 10 cm. [Refer to video 3].

Abdominal Cavity

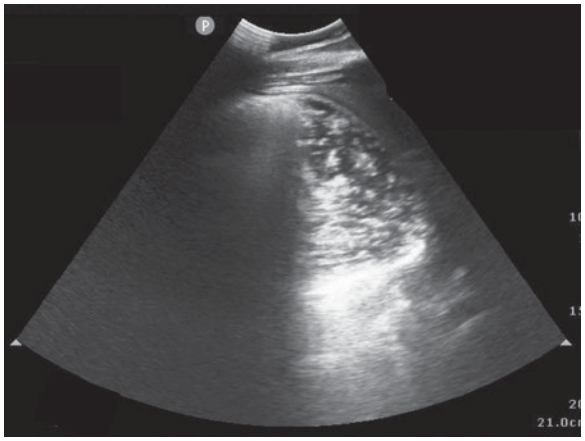


Figure 29.9 Enlarged Stomach. The cranial border of the spleen is visible just to the right of the distended stomach. Dorsal is left, ventral is on the right side of the image. The stomach is normally not easily visualized and generally does not extend past the 12-13th intercostal space. Stomach distention results from either physiologic or physical obstruction of gastric outflow. Gastric decompression is indicated in this patient. This image was obtained from the left side of the abdomen at the 14th ICS using a curvilinear probe operating at 6-10 MHz at a depth of 21 cm.

Vet-ebooks.com

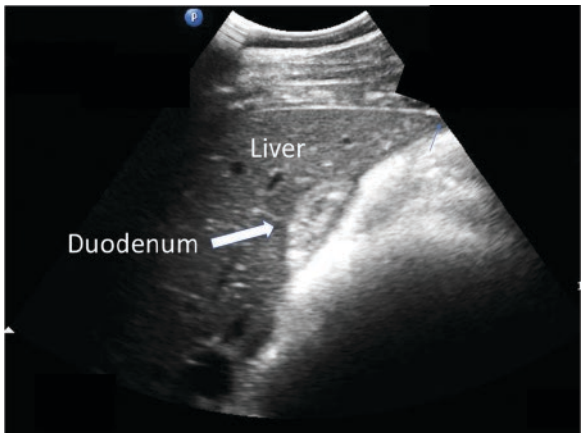


Figure 29.10 Duodenitis. The caudal border of the right lobe of the liver is visible to the left of the duodenum and the right dorsal colon is to the right of the duodenum. The walls of the duodenum appear thickened, and the organ remains mildly distended. The duodenum can be imaged from the right cranioventral abdomen and traced caudo-dorsally up to the cranial pole of the right kidney. The normal neonatal duodenum has thin (< 4 mm) walls and is consistently motile. This image was obtained from the right lateral abdomen with a 6–10 MHz curvilinear probe operating a depth of 15 cm.

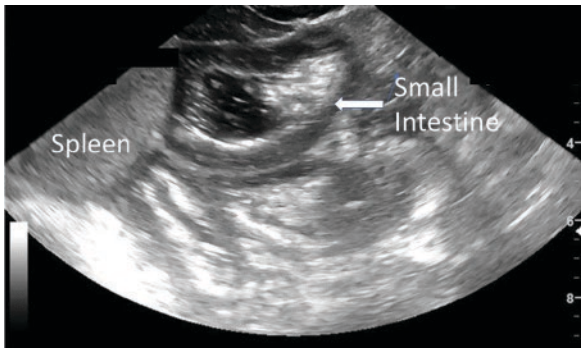


Figure 29.11 Enteritis. Several loops of distended small intestine are imaged in the left caudoventral abdomen. The caudal border of the spleen is visible to the left of the large loop of small intestine. These loops have edematous walls that are > 4 mm thick, moderately distended, and flaccid. Enteritis may lead to stomach distension, as seen in Figure 29.9. This image was obtained from the left ventral abdomen using a curvilinear probe operating at 6–10 MHz at a depth of 8 cm.

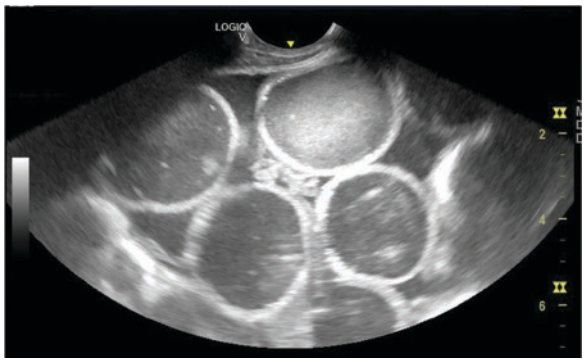


Figure 29.12 Small intestinal volvulus. Several loops of distended, circular small intestine are visible from the ventral abdomen. Differentiating small intestinal volvulus and enteritis can be difficult, though generally, the loops of the small intestine are less edematous and more distended with volvulus compared to cases of enteritis. A neonate with a volvulus typically shows signs of severe abdominal pain that does not respond to analgesics, and surgery is required to correct the problem. This image was obtained from the ventral abdomen using a 6–10 MHz curvilinear probe at a depth of 8 cm.



Figure 29.13 Small intestinal intussusception. A typical "bull's eye" or "doughnut" lesion suggestive of an intussusception is visualized in the top left corner of the image. This condition results when a portion of the small intestine "telescopes" into another portion. The intussuscipiens is the outer or receiving portion of the bowel and the intussusceptum is the inner or entering segment of the bowel. The cause for this problem is generally not known. A small intestinal intussusception in the neonate may resolve spontaneously, may resolve with heavy sedation, or it may require surgical correction with possible intestinal resection. This image was obtained from the left abdomen with a curvilinear probe operating at 6–10 MHz at a depth of 10 cm. [Refer to video 4].

Vet-ebooks.com

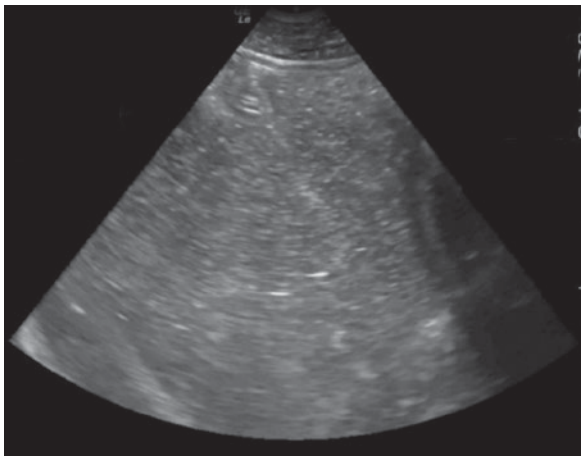


Figure 29.14 Colitis. A common problem in neonates, colitis frequently appears as a mass of hyperechoic fluid contained within a viscus. The cecum and both the dorsal and ventral colons may appear distended with swirling ingestia of a fluid nature. Fecal diagnostics are indicated in these cases and the use of prokinetics may be indicated. This image was obtained from the right abdomen using a curvilinear probe operating at 6–10 MHz at a depth of 10 cm. [Refer to video 5].

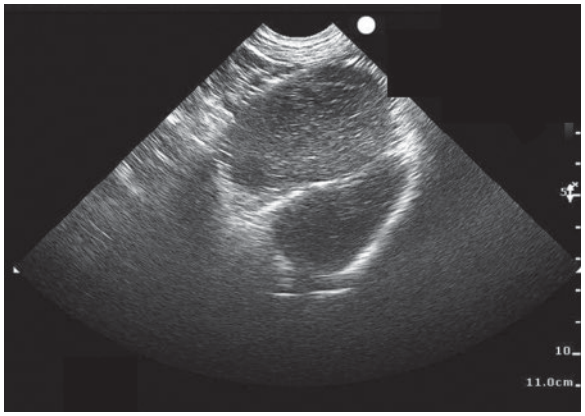


Figure 29.15 Meconium impaction. This image depicts both the dorsal and ventral colon full of meconium. Unlike a foal with diarrhea, the colon does not appear distended, and the fecal mass appears stationary. In some cases of a high meconium impaction, A gas distended colon may inhibit the sonographer's ability to identify the impacted section of bowel. This image was obtained from the right cranioventral abdomen using a curvilinear probe operating at 6–10 MHz at a depth of 11 cm.

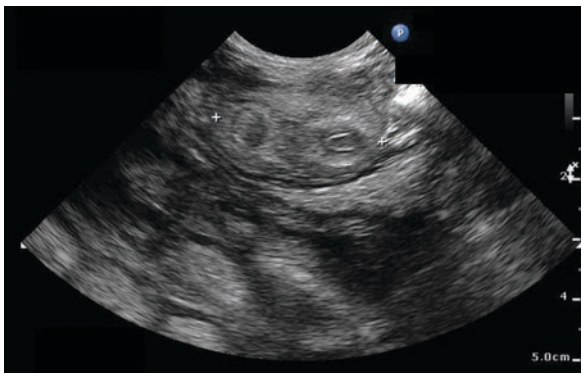


Figure 29.16 Urachus – omphalitis. The urachus is imaged from the ventral midline, moving caudally toward the bladder. The urachus is the extension of the allantois from the fetal bladder to the umbilical cord and is located between the two circular umbilical arteries, in the image above. The normal neonatal internal umbilical diameter is < 2 cm. Normal umbilical artery measurements are < 1 cm. Enlargement of the structures is indicative of infection. In cases of omphalitis, antibiotic therapy is indicated; and the structure's size should be monitored with serial sonograms. If the size of the internal structure(s) does not decrease with antibiotic therapy, surgical resection should be considered. This image was obtained from ventral midline using a 6–10 MHz curvilinear probe operating at a depth of 5 cm.

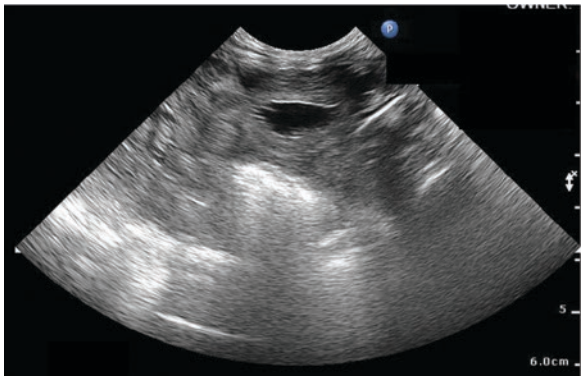


Figure 29.17 Umbilical vein-omphalophlebitis. The umbilical vein is imaged on the ventral midline and extends cranially from the umbilicus to the liver. The normal neonatal umbilical vein is < 1 cm in diameter. Enlargement of the structure is generally indicative of infection and should be addressed with antibiotic therapy and potentially surgical resection/marsupialization. This image was obtained from the ventral midline using a curvilinear probe operating at 6–10 MHz at a depth of 6 cm.

Vet-ebooks.com

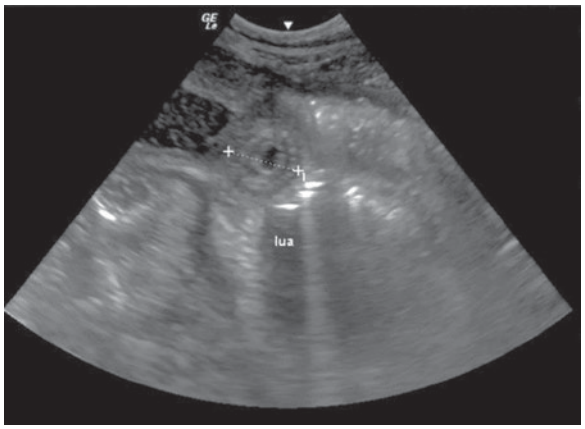


Figure 29.18 Umbilical artery–umbilical arteritis. The right and left umbilical arteries course from the umbilical stump caudally and dorsally to the right and left internal iliac arteries, passing closely on either side of the body of the bladder. The normal umbilical artery size is < 1 cm in diameter. Enlargement of one or both arteries is generally indicative of infection and should be addressed with antibiotic therapy and potentially surgical resection. This image was obtained from the ventral midline using a 6–10 MHz curvilinear probe operating at a depth of 5 cm.

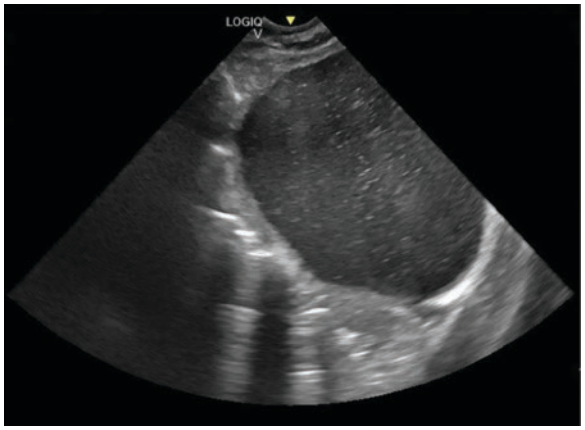


Figure 29.19 Normal bladder. This is an image of an intact, normal bladder in a Thoroughbred neonate. The echogenicity of the urine will vary; dilute urine is non-echogenic, while concentrated urine will often have echogenic flecks suspended throughout the bladder. The image was obtained with 6–10 mHz curvilinear probe placed on midline of the caudoventral abdomen at a depth of 10 cm.

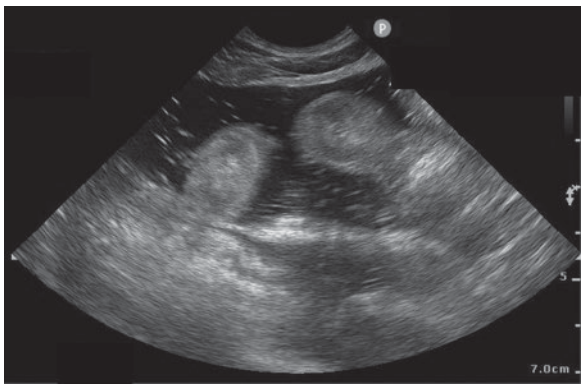


Figure 29.20 Uroperitoneum. Slightly echogenic free fluid is present in the ventral abdominal cavity and an intact bladder is not apparent. Two loops of thickened small intestine are floating in the fluid. The diagnosis of uroperitoneum is confirmed by obtaining a peritoneal fluid sample and comparing the creatinine concentration of the peritoneal fluid to the creatinine concentration of the serum. If the free peritoneal fluid is urine, the creatinine concentration of the peritoneal fluid will be at least two-fold higher than the creatinine concentration of the serum. Defect of a kidney, ureter, or the urachus, as well as the bladder, can result in uroperitoneum. Differential diagnoses for suspected cases of uroperitoneum should also include peritonitis, hemoperitoneum, and GI tract perforation. This image was obtained from ventral abdomen with a curvilinear probe operating at 6–10 MHz at a depth of 7 cm. [Refer to video 6].

Vet-ebooks.com

Index

Note: Page numbers followed by "*f*" denotes figure and "*t*" denotes table respectively.

a

abdominal cavity 576–579
abdominal fluid 574
abdominal viscera, pathology of 563–568
abnormal navicular bone flexor surface 40*f*
abscess 211, 213*f*, 214, 540
  aortic root 438*f*
  dorsal carpus 137*f*
  of heterogenous echodensity 418
  internal 462*f*, 463*f*
  laryngeal lymph node 522*f*
  mesenteric 562, 563*f*
  neck 538*f*, 539*f*
  perirectal 480*f*
  perivascular 544*f*
  pleural 415, 415*f*
  pulmonary 418, 418*f*
  retrobulbar 487
  retropharyngeal lymph node 523*f*, 524*f*
  stromal 484, 489*f*, 490*f*
  subsolar 35*f*
absorption 3
accessory carpal bone (ACB) 130, 131, 132*f*
accessory ligament of the deep digital flexor tendon (ALDDFT) 89, 90, 96
  desmitis 118, 120, 120*f*
  distal insertional desmopathy 121*f*
  fore limb 122*f*
  hind limb 120, 122
accessory ligament of the SDFT (AL-SDFT) 89, 132, 133*f*
  desmitis 140*f*
acepromazine, use in separating unilateral twins 364
acetabulum 235, 236, 236*f*, 237*f*
acoustic coupling gel (ACG) 30, 409
acoustic enhancement artifact 14–15, 14*f*
acoustic impedance 2–3, 2*t*
acoustic shadowing artifact 15, 15*f*
acute hepatitis 449*f*
acute synovitis 55, 56*f*
acute tendinitis, of biceps brachii tendon 162*f*, 164*f*
adenocarcinoma 439*f*
adhesion 76
  bladder mucosal 460*f*
  deep digital flexor tendon 31, 39, 73
  spleen and stomach 453*f*
adjacent medulla 446
adult:
  bladder in 458*f*
  colitis in 476*f*, 477*f*

Atlas of Equine Ultrasonography, Second Edition. Edited by Jessica A. Kidd, Kristina G. Lu and Michele L. Frazer.
© 2022 John Wiley & Sons Ltd. Published 2022 by John Wiley & Sons Ltd.
Companion Website: www.wiley.com/go/kidd/atlas

Vet-ebooks.com

horse, enteritis in 472*f*
aerophagia 569*f*
air, in uterus 339, 339*f*
air-soft–tissue interface 4
allantoic cavity 354*f*
amniotic fluid 390
A-mode, equine ocular ultrasonography 482
ampullae 271
occluded 297
per rectum 290
plugged 286
of vasa deferentia 276*f*–280*f*, 294*f*, 295*f*
of vas deferens 283*f*–284*f*
ampullar lumen 285*f*
amyloidosis 449*f*
anechoic fluid 419
annular ligament syndrome (ALS) 76–77
anovulatory follicles 332–333, 332*f*, 333*f*
antebrachiocarpal joint (ACJ) 128
anterior chambers 483
fibrin accumulation in 485
synechiae 484–485
anterior lens luxation 499*f*, 500*f*
Anti-Müllerian Hormone (AMH) 333
aorta 386, 546*f*
cranial chest and 386*f*
vascular structures 540, 546
aortic diameter:
fetus, 234 days gestation 384, 386*f*
aortic regurgitation 434*f*, 435*f*, 436*f*, 441*f*
aortic root
abscess 438*f*
rupture 443*f*
aortic valve closure (AVC) 441*f*
aortic valve lesions 433*f*
aphakia 485
arteriovenous fistula 544*f*
arthritis 55–57
arthroscopy 84
articular cartilage 256
articular long bone fractures 67
artifacts 11–17, 488
absorption technique 488
acoustic enhancement 14–15, 14*f*
acoustic shadowing 15, 15*f*
B-line 13, 14, 14*f*
comet-tail 12, 13, 14, 411*f*, 412, 413
definition 11
edge artifact, blood vessel 230
edge shadowing 15, 16*f*
eye, Baum's Bump 488
mirror-image 17
operator error 11–12
reverberation 12–14, 12*f*, 13*f*
reverberation technique 488, 488*f*
ring-down 12, 13, 14*f*
side-lobe 16–17, 17*f*
slice-thickness 15–16, 16*f*
artifactual sediment 16
asteroid hyalosis 486
asystole 388
atlanto-occiptal (AO) joint 249, 251*f*
assessment 250
composite transverse image 251*f*
longitudinal image 251*f*, 252*f*
synovial sepsis 250
attenuation 2
causes of 2
auriculo-palpebral nerve block 482
axial resolution 5, 6*f*

b

back
caudal thoracic and lumbar facet joints 245–248
epaxial musculature 248
indications 243
interspinous ligaments 243–245
supraspinous ligaments 243–245, 244*f*, 245*f*
ultrasound assessment 243
bacterial peritonitis 460*f*, 461*f*, 462*f*
bandage bows 103, 105, 105*f*
basihyoid bone, lingual process of 258
Bedside Ocular Ultrasound 481
biceps brachii tendon 149, 161–163
acute tendinitis 162*f*, 164*f*
distal insertion 155, 158*f*
enthesopathy 155
normal proximal 161*f*
origin 160*f*

Vet-ebooks.com

proximal 164*f*
bicipital bursa 155, 162, 163, 166
bicipital bursitis 161
chronic 165*f*, 166*f*
proximal humeral osteitis and 166*f*
septic 163
bicipital tendinitis 161, 163
bile duct stricture 450*f*, 451*f*
biophysical profile score (BPS) 403
bladder 455–458
adult 458*f*
with cystitis 564*f*
foal 458*f*
normal 579*f*
rupture 459*f*, 562–563, 564*f*
with sediment 459*f*
urinary calculi 460*f*
urine-filled 562
uroperitoneum 460*f*
wall defect 459*f*
"B-line" artifacts 13, 14, 14*f*
blood (ifema) 485
blunt force trauma 560
blunt trauma 505*f*
B-mode 3–4
equine ocular ultrasonography 482–483
bone cyst. *See* cyst-like lesions
bones 134–136, 143, 146
fragment 63*f*
neck 249–254
bone-soft–tissue interface 3, 4, 4*f*
bony injuries 122–126
bony structures
tarsus 181, 183
brachialis muscle 149
brachiocephalic muscle forms 537
brain sparing effect 403
broad ligament hematoma 563, 565*f*
bronchopneumonia 574*f*
broodmare, pregnant 545*f*
"bucket-handle" tear 217*f*, 218
bulbospongiosus muscle 300
bulbourethral glands 271, 272, 285
color Doppler ultrasound image 294*f*
in sexually rested stallion 293*f*
ultrasound image of 293*f*
bursae 143
buscopan (N-butylscopolammonium bromide) 323, 347, 365, 372

C

calcaneal bursa 180
calcaneal tendon 174
calcification 77
biceps brachii tendon 162
calcinosis circumscripta 226
capsular rupture 225
cardiology. *See also* echocardiography
normal equine heart, ultrasonographic anatomy of 422, 426
technical considerations 421–422
carotid artery 518
jugular groove 532
jugular vein and 529*f*–530*f*, 532
carpal canal (CC) 131, 132*f*, 133*f*, 143*f*
carpometacarpal joint (CMCJ) 128
carpus
anatomy and scanning technique 128–134
bones 143, 146
dorsal 128–129, 129*f*
joints and bone 134–136
joint surfaces 146
lateral 129–130, 130*f*, 131*f*
medial 130–131, 131*f*, 133*f*
palmar 131–134, 134*f*, 135*f*
superficial soft tissues 143
surgery 146
tendons and ligaments 143
ultrasonographic abnormalities 136–146
cartilage dissection 60
cataracts 486
congenital 496*f*
and uveitis 497*f*
caudal cervical vertebrae 253
caudal cruciate ligament (CaX) 198*f*, 200, 201*f*, 203
caudal horn tears 218, 219*f*
caudal thoracic joints 245–248
caudal vaginal 560

Vet-ebooks.com

cecal impaction 478, 479*f*
cecal inversion 478, 479*f*
cecocolic intussusception 478, 479*f*
cecum 465, 478, 559, 570, 578*f*
cellulitis
  focal 540
  perivascular 540*f*
central process 300
cephalic vein (CV) 132
cervix 325, 342
  abnormal 329*f*
  after ovulation 328*f*
  diestrus 329*f*
  during early estrus 326*f*
  in early pregnancy 348
  estrus, failure to relax in 342
  intrauterine fluid adjacent to 343*f*
  ovulation approaches 327*f*
  250 days gestation 392*f*
  244 days gestation 393*f*
  277 days gestation 393*f*
  232 days gestation 392*f*
  vagina and 345*f*
  ventral 344*f*
chip fracture
  distal craniomedial radius 145*f*
  multiple palmar 146*f*
chip fractures 61, 63
choke 534
cholangiohepatitis 450*f*, 451*f*
cholelithiasis 451*f*
chondromalacia patellae 210
chorioallantoic membranes 357
choroid 484
chronic acetabular fracture 238*f*
chronic collateral ligament desmitis 66
chronic hypertrophic synovitis 57, 58*f*, 59
chronic laminitis 37*f*
chronic lymphangitis 544*f*
chronic scapular fracture 159*f*
chronic synovitis 56, 203, 210
chronic tendinopathy 100–102, 101*f*
ciliary body cysts 485
"cine recall system" 386
circumflexa ilium profunda artery 400
clitoris, in female 370
cold effusion 55, 203
colitis 578*f*
  in adult 476*f*, 477*f*
  Potomac Horse Fever 477*f*
  right dorsal 475*f*, 476*f*
  from Salmonellosis 476*f*
collateral ligaments (CL):
  complete rupture 64
  desmitis 174
  desmitis and tears 215
  desmopathy 64
  diffuse 65*f*
  of distal interphalangeal joint 26, 28*f*
  of elbow joint 149–150
  hock 173–174
  injury in horse 65*f*
  medial 64, 65*f*
  structure 54*f*
collateral sesamoidean ligament. *See* "T" ligament
colliculus masculinus:
  cross-sections of 295*f*
  cysts of 286
  utriculus masculinus in 286
colliculus seminalis 272, 273
  midline cyst of 275*f*–276*f*
colon:
  gas-distended 473, 474*f*
  large 569
  left ventral 474, 474*f*
  lumen of 476*f*
  right dorsal 473, 474*f*
  right dorsal displacement of 475, 475*f*
  small 570
  torsion 477*f*, 478*f*
  torsion or volvulus of 476*f*
  ventral 559
  wall 475*f*
color Doppler 482
  in horses 426*f*, 433*f*
  portal vein 448*f*
color flow Doppler 19, 20*f*, 421, 429
  of luminal blood flow 543*f*
colt. *see* fetus

Vet-ebooks.com

combined thickness of the utero-placental unit (CTUP) 384, 393–394
comet-tail artifact 12, 13, 14, 411*f*, 412, 413
common arterial trunk (CAT) 431*f*
common carotid artery, bifurcation of 520*f*
common digital extensor (CDE) tendon 52, 60*f*
common digital extensor tendon (CDET) 90, 129, 138*f*, 142*f*
congenital cataracts 496*f*
console 5
continuous-wave (CW) Doppler 19–20, 19*f*, 421, 429, 430*f*, 433*f*, 437*f*
contralateral ovary 333, 334
contrast tenography 43
convex probes 7
core lesions 205
cornea 483
corneal anesthesia 482
corneal damage 482
corneal edema 484, 489*f*, 492*f*
corneal ulcer 484, 494*f*
corpa lutea 349*f*
corpora cavernosa 300, 302
corpora lutea (CLs) 348
corpora nigra 483, 485
cor pulmonale 442*f*
corpus cavernosum 302, 305*f*
  dorsal aspect 305*f*
  processes 306*f*
  trabeculae of 304*f*, 308*f*, 309*f*
corpus hemorrhagicum 328*f*, 334
corpus luteum 326, 329*f*, 330*f*, 348, 349*f*
corpus spongiosum 302
  glandis 300
  trabeculae in 308*f*, 309*f*
coxofemoral joint 236*f*
cranial cruciate ligament (CrX) 200, 201*f*, 205*f*, 222*f*
  complete rupture of 223*f*
“cranial drawer” 220
cranial meniscotibial ligaments (CMTL) 202, 215, 220*f*
  of medial meniscus 220*f*
  tears 218
cranial thorax 409
cranial tibial muscle 177
cranial tibial tendon 177
cranioventral abdomen 448*f*
crena marginis solearis 34*f*
cricoarytenoideus lateralis muscle (CAL) 259, 260*f*
cross-sectional area (CSA) 91, 93, 96
cruciate ligament (XL) injuries 220
cryptorchid 286*f*, 299
crystalline 483
crystalline lens 485, 486
  dislocation 486
crystalline material 451*f*
cunean bursa 180
cunean tendon (CT) 177, 182*f*
curvilinear transducers 7
cystitis 562
  bladder with 564*f*
  sabulous 564*f*
  with urinary calculi 564*f*
cyst-like lesions 59–61
cysts
  ciliary body 485
  endometrial 335, 337*f*, 338*f*, 339, 361–362
  epithelial inclusion 334, 334*f*
  iris 485, 506*f*
  lymphatic 335
  parovarian 334, 334*f*
  uterine 350

d

daily sperm output (DSo) 317, 318
deep digital flexor tendon (DDFT) 25, 29, 31, 37*f*, 38*f*, 39*f*, 69, 72, 73, 73*f*, 77*f*, 86, 89, 90
  accessory ligament of 123*f*
  chronic 78*f*
  cross-sectional areas 91
  lateral 175, 180
  lesions 35
  marginal tears detection 78*f*, 79*f*
  medial 175, 180, 183*f*
  mid-substance tendinopathy 77*f*
  over-strain midsubstance injuries 77
  septic carpal canal and 143*f*

Vet-ebooks.com

tears 79–80
tendinopathy/desmopathy 106
tendonitis of 177
transverse image of 182*f*
transverse transcuneal ultrasound of 33*f*
trauma 80
deep distal sesamoidean ligaments (DDSL) 67
depth 8
descemetocele 492*f*
desmitis 92, 106, 144*f*
accessory ligament of the DDFT 118–120, 120*f*
accessory ligament of the SDFT 140*f*
body of SL 113–117, 115*f*, 116*f*
collateral ligaments 174, 215
of long plantar ligament 108*f*, 175
of medial PL 205
proximal suspensory 107–113, 109*f*, 110*f*, 111*f*
suspensory ligament branches 117–118
detomidine 323
diagnostic ultrasonography 5
diaphragmatic hernia 559–560, 560*f*
diastolic left ventricular function 429
diestrus 348
cervix 329*f*
non-pregnant mare in 351
uterus 329*f*, 335
diffuse collateral ligament injury 65
diffuse tendinopathy 93, 94
digital annular ligaments 44, 47
digital extensor tendons 52
digital flexor tendinopathy
lateral 125*f*
digital flexor tendon sheath 68–73, 74*f*, 75*f*
deep digital flexor tendon abnormalities 77–80, 77*f*
infected, characteristics of 73*f*
manica flexoria 70, 71*f*, 72
normal ultrasonographic anatomy 69–73
palmar/plantar annular ligament syndrome 76–77
percutaneous trauma to 73*f*
primary tenosynovitis 73–76
proximal pouch 69, 70*f*
sepsis of 73
superficial digital flexor tendon abnormalities 80–82
digital sheath tenosynovitis 76
dissecting lesion 206
distal interphalangeal (DIP) joint 25, 86
abnormalities 29
collateral ligaments 26, 28*f*
normal ultrasonographic appearance 28*f*
osteoarthritis 30*f*
palmar/plantar pouch 26
ruptured collateral ligament 30*f*
ultrasound-guided injection 28*f*
distal interphalangeal joint (DIPJ) 31
distal limb vasculature 540
distal radial artery (DRA) 132
distal sesamoid bone (DSB) 29, 30, 31*f*
flexor surface and distal aspect 31
fractures 35
hyperechoic flexor cortical surface of 32*f*
proximal displacement 38*f*
severe fibrocartilage degeneration of 39*f*
distal sesamoidean impar ligament (DSBIL) fibers 31, 35, 38*f*
hypoechogenic appearance 38*f*
distal sesamoidean ligaments (DSLs) 41–42, 67
abnormalities 42–44
Doppler. *See also* Doppler imaging
carotid artery 403*f*
color 426*f*
color flow 19, 20*f*, 421
continuous-wave 19–20, 19*f*, 421, 429, 430*f*
echocardiography 429, 433
Middle Cerebral Artery 402
modes 18
power 20
pulsed-wave 18–19, 19*f*, 421, 429
right uterine artery 401*f*
scans of maternal uterine arteries 399
spectral 18, 18*f*
technology 383
umbilical artery 401*f*, 402*f*
velocimetry parameters 399–400
Doppler imaging 17–20

Vet-ebooks.com

color flow Doppler 19, 20*f*
continuous wave Doppler 19–20, 19*f*
negative frequency shift 17–18, 18*f*
positive frequency shift 17, 18*f*
power Doppler 20
pulsed wave Doppler 18–19, 19*f*
spectral Doppler 18, 18*f*
Doppler shift 18, 18*f*, 20
dorsal carpus 128–129, 129*f*
abscess 137*f*
normal neonate 136*f*
premature foal 136*f*
dorsal sacroiliac ligaments 231, 232, 234*f*, 235, 235*f*
central hypoechogenic regions with 235*f*
normal appearance of 234*f*, 235*f*
ventral parts of 235
dorsal spinous processes (DSPs) 244, 245*f*
duodenal distension 466, 467*f*
duodenal stricture 467*f*
duodenitis 466, 467*f*, 570, 577*f*
duodenum 448*f*, 466, 467*f*, 468*f*, 479*f*, 570
dystrophic mineralization, neck 249*f*

e

early pregnancy examination 358
echocardiogram 436*f*
echocardiography 426. *See also* cardiology
detection 428
Doppler 429, 433
endocardial cushion defect 430*f*
great vessels 424*f*
in horses. *See* horses, echocardiography in
left atrial size and function 424*f*, 428
left ventricular size and function 423*f*, 428
methods 429
mitral and aortic valve motion 425*f*
restrictive ventricular septal defect 427*f*
echogenicity 3–4, 99*f*
of intrauterine fluid 335
edge refraction. *See* edge shadowing artifact
edge shadowing artifact 15, 16*f*
elbow 148–149
abnormalities 148–155
biceps brachii muscle 155
biceps brachii tendon 155, 161–163
collateral ligaments of 149–150
craniomedial aspect of 158*f*
dorsal aspect of 149*f*
infraspinatus muscle 166–167
lateral collateral ligament of 149–150, 152*f*, 153*f*, 154*f*
medial collateral ligament 153*f*
osteoarthritis 149, 151*f*
preparation and scanning technique 148
scapulohumeral joint 167–172
septic arthritis of 150*f*
supraspinatus muscle and tendons 163–166
triceps brachii muscle 155
ulnaris lateralis muscle 150, 155, 156*f*, 157*f*
ultrasonographic anatomy 148–155
electronic transducers 6
embryo. *See also* pregnancy
day 18 353*f*, 360
day 15 352*f*, 360
day 14 352*f*, 360, 361*f*
day 17 352*f*
day 13 360*f*
day 32 355*f*
day 20 353*f*, 354*f*
day 25 355*f*
day 29 355*f*
day 21 354*f*, 355*f*, 360*f*
day 22 355*f*
distinguishing from endometrial cysts 361–362
pregnancy stage 349
embryo proper (EP) 354*f*, 355*f*
empty trophoblastic vesicle (ETV) 358*f*
endocardial cushion defect 430*f*
endocarditis 426
endometrial culture 335
endometrial cups 339, 341*f*, 354
endometrial cysts 335, 337*f*, 338*f*, 339, 361–362
major consequence of 335
pregnancy adjacent to 337*f*
ultrasonographic appearance of 337*f*, 338*f*
endometrial edema 335, 336*f*, 566*f*
abnormal 360*f*
endometrial glands 335

Vet-ebooks.com

endometritis 340*f*
endophthalmitis 505*f*
enteritis 577*f*
in adult horse 472*f*
anterior 472*f*
post-partum mare secondary to 571*f*
proliferative 471
small intestinal volvulus and 577*f*
enthesophytes 59, 64, 110, 118
enthesophytosis 44
envelope 18
epaxial musculature 248
epicondyles 149
epididymal tail 317*f*, 318*f*
epididymis 310, 312*f*
epididymitis 313, 315*f*
epithelial inclusion cysts 334, 334*f*
E-point-to-septal separation (EPSS) 441*f*
equine chorionic gonadotropin (eCG) 354, 356*f*
equine multinodular pulmonary fibrosis 417*f*
equine ocular ultrasonography (EOUS) 481
in A-mode 482
anterior and posterior chambers 483
anterior chamber synechiae 484–485
aphakia 485
blood 485
in B-mode 482–483
cataract 486
ciliary body cysts 485
cornea 483
corneal edema 484, 489*f*
corneal infiltrates 484
corneal ulcer 484
crystalline 483
crystalline lens dislocation/ sub-luxation 486
eyelid edema 487
fibrin accumulation 485
glaucoma 485, 504*f*
intra-ocular mass 487
iris and ciliary bodies 483
iris cysts 485
iris prolapse 485
keratitis 484, 489*f*
lens rupture 486
microphakia 486, 497*f*
pus *(ipopion)* 485
retina/choroid/sclera 484
retina detachment 487, 502*f*, 503*f*
retrobulbar area 484
retrobulbar diseases 487
small eyeball 485
stromal abscess 484, 489*f*, 490*f*
technique 481–483
uveitis 485
vitreous chamber 484
vitreous opacity 486–487
equine pregnancy
biophysical profile score 403
doppler velocimetry parameters of 399–400
imaging of 384
transabdominal evaluation of 385
equine recurrent uveitis (ERU) 502*f*, 503*f*, 504*f*
equine reproductive tract 331
equine shoulder 155
equipment, pelvis 229
erect penis, ultrasound evaluation of 302, 303*f*
esophagus 465–466
choke 535*f*
fistula 537*f*
with food bolus 535*f*
jugular groove 534, 537
with nasogastric tube 535*f*
normal 466*f*, 534*f*
estrous edema 324*f*, 327*f*
estrus, failure to relax in 342
excessive pressure 11
exophthalmos 508*f*
extensive hematoma 561*f*
extensor carpi radialis bursa (ECRB) 129
extensor carpi radialis tendons (ECRT) 129
extensor tendons 67, 90, 122
external carotid 388
external carotid artery 518
external genitalia 371, 379
after 150 days of Gestation 371
90-150 days 377

Vet-ebooks.com

post 150+ days 380
on transabdominal scan 371
external iliac artery 563
external jugular vein 540
external trauma 534
external umbilical remnant 547, 549*f*
exudative peritonitis 462*f*
eye
normal 488*f*
volume, fetal 385–386
eyelid edema 487

f

facies flexoria 31
fascicular pattern 86
feed material 534
female
clitoris in 370
genital tubercle for 373
femoropatellar joint 191–194
abscesses 211, 214
degenerative joint disease 208*f*
effusion 203–204
hematomas 211, 214
inflammatory changes in 207*f*
non-inflammatory effusion of 206
osteochondrosis 206, 209
patellar fractures 209–210
patellar ligament injuries 204–206, 207*f*
stifle 191–194, 191*f*
femorotibial joints 214–226
caudal aspect 202–203
collateral ligament desmitis and tears 215
cranial aspect of 199–202, 199*f*
cruciate ligament injuries 220
lateral 195, 198*f*
long digital extensor muscle 225
medial 194–195, 197*f*, 224*f*
medial aspect 216*f*
meniscal injuries 215, 218, 220
miscellaneous 225–226
osseous cyst-like lesions 220
osteoarthritis 220–221
peroneus tertius tendon 225
septic arthritis 221, 225
fetal activity 387, 388–389
hydroallantois and 391
fetal cardiac rhythm 388
fetal development and monitoring. *See also* equine pregnancy; fetus
activity 387, 388–389
adequate environment 390
adequate growth and development 385
aortic diameter 386, 386*f*
biophysical profile score 403
biparietal diameter 386, 387*f*
combined thickness of the utero-placental unit 393–394
equine gravid cervix, assessment of 391–393
equipment 384
eye volume 385–386
fetal circulation, assessment of 401
fetal heart rate 387–388
FHR reactivity 387–388
intracranial circulation 402–403
maternal circulation, assessment of 400–401
orbital diameters 385–386
other organs 394–396
peripheral pulses 388
pregnancy database 383–384
responsive patterns 387
transabdominal approach 385
transrectal approach 384
umbilical circulation 401
umbilical cord 396–399
fetal eye 385–386
measurements 385, 386*f*
fetal heart rate (FHR) 387–388
accelerations 388
fetal hypoxia 403
fetal movements 357
fetal orientation 390
fetal sex determination 368. *See also* fetus, colt; fetus, filly
55–90 days 370–371
90–150 days 371
plane I 372*f*
plane II female 372*f*
plane III 373*f*

Vet-ebooks.com

plane II male 372*f*
procedure at 55–90 days 372–377
procedure 90–150 days 377–379
stages of gestation 370–372
take home hints 372
transabdominal scan post 150+ days, procedure for 379–382
ultrasonographic planes 372
fetal sexing. *See* fetal sex determination
fetal size, aortic diameter 385
fetal well-being 383
assessment 385
and optimal development 383
sensitive indicators of 387
transrectal field evaluation 387
fetlock 86
acute synovitis 55, 56*f*
articular long bone fractures 67
bone fragment 63*f*
chronic hypertrophic synovitis 57, 58*f*
chronic synovitis 56
cyst-like lesions 59–61
deep digital flexor tendon abnormalities 77–80, 77*f*
digital flexor tendon sheath. *See* digital flexor tendon sheath
dorsal aspect of 52, 58*f*, 70*f*
dorso-medioproximal aspect of 64
four quadrants of 50*f*
hemarthrosis 56*f*
intersesamoidean ligament. *See* intersesamoidean ligament
normal anatomy 51–55
osteoarthritis 59
osteochondral fragments 61–64
osteochondrosis 59–61, 61*f*, 62*f*
palmar aspect 53
palmar/plantar annular ligament of 72, 72*f*
palmar/plantar P1 fragments 67
periarticular injuries 67
plantar aspect of 51
plantaro-abaxial aspect 68*f*
preparation and scanning technique 49–51
proximal scutum abnormalities 82–84
proximal sesamoid bones fractures 65, 66–67
schematic organization of 51*f*
septic arthritis 67–68
subchondral bone injury 57–59
superficial digital flexor tendon abnormalities 80–82
synovitis/arthritis 55–57
traumatic arthritis 57–59
fetus. *See also* fetus, colt; fetus, filly
in anterior presentation 390
bi-parietal diameter, 121 days gestation 387*f*
day 50 357*f*
day 51 357*f*
day 48 357*f*
day 60 358*f*
neck 390
180-days-old 395*f*
158-days-old 395*f*
152-days-old 390
110-days-old 395*f*
121 days gestation 387*f*
127-days-old 396*f*
orbital diameter, 211 days gestation 387*f*
218-days-old 395*f*
211 days gestation 386*f*
215-days-old 386*f*
214-days-old 395*f*
244 days old 387*f*, 397*f*
243-days-old 390
279-days-old 388*f*
268 days 391*f*
268-days-old 387*f*
234-days-old 386*f*
236-days-old 389*f*
224-days-old 388*f*
umbilical vein 550
fetus, colt
axial transverse plane of 374*f*
external genitalia. *See* external genitalia
female, mammary gland and teats of 371
genitalia 370
homogenous texture with central vein 380*f*, 381*f*

Vet-ebooks.com

95 days of gestation 377*f*
94 days of gestation 377*f*
115 days of gestation 376*f*
109 days of gestation 379*f*
117 days of gestation 377*f*
113 days of gestation 375*f*
130 days of gestation 380*f*
65 days of gestation 374*f*
fetus, filly 376*f*, 378*f*
135-days-old 396*f*
124-days-old 396*f*
105 days of gestation 378*f*
110 days of gestation 378*f*
134 days of gestation 379*f*
124 days of gestation 379*f*
129 days of gestation 379*f*
122 days of gestation 378*f*
78 days of gestation 375*f*
63 days of gestation 375*f*
FHR reactivity 387–388
fibrin 414, 495*f*
accumulation 485
adhesions 453*f*
peritonitis 459, 461*f*
pleuritis 413*f*
fibularis tertius 225
fluid effusion 214
foals
bladder in 458*f*
chest for thoracic ultrasonography 574
haircoat 573
heart 573
hock 186
liver 452*f*
recumbent 573
umbilical hernia in 556*f*
focal cellulitis 540
focal extensor tendinitis 69*f*
focus 8–9, 9*f*
foot 25
distal interphalangeal joint. *See* distal interphalangeal (DIP) joint
dorsolateral/dorsomedial aspects 27*f*
palmar aspect 26*f*
proximal to coronary band 25–29
transsolar and transcuneal ultrasonography 29–39
ultrasonographic abnormalities 26, 29
fracture(s)
chronic acetabular 238*f*
detection 229
development, stages of 231
"green stick" 230
pelvis, common sites detected *per rectum* 238*f*
rib 412, 412*f*, 413*f*
scapula body 155, 157
stress 229, 243
tuber coxa 233*f*
frame rate 9
free fluid 453*f*
frequency 482
ultrasound waves of 5, 8
fundamental frequencies 9
fungal plaque forms 514

g

gain control 8
gas decomposition 568*f*
gas echoes 562
gastric distention 467*f*
gastric rupture 461*f*
gastrocnemius tendon (GCN) 174
superficial digital flexor tendon and 181*f*
gastrointestinal tract 13, 568–571
cecum 570
duodenal distension 467*f*
duodenitis 467*f*, 570
duodenum 466, 467*f*, 468*f*
esophagus 465–466, 466*f*
jejunum 570, 570*f*
large colon 569
large intestine 473–480
mesenteric rent 571
rectum 480
small colon 570
small intestine 466–473, 469*f*
stomach 466, 467*f*, 570, 571*f*
gelding 292*f*
genioglossus muscles 261
genitalia 370, 372

Vet-ebooks.com

genital tubercle 370, 371
for male and female 373
gestation. *See also* fetus; fetus, colt; fetus, filly
after 150 days 371–372
80 days of 371, 371*f*
55–90 days of 370–371
90–150 days of 371
121 days 387*f*
100 days of 371*f*
211 days 386*f*
277 days 391*f*
212 days 387*f*
gestational age 347
eye volume and 385
resistive index for 397*f*
gestation, first 60 days of. *See also* pregnancy
early embryonic imaging 349–358
endometrial cysts 361–362
transrectal technique 347–349
glandular endometrial cysts 361
glandular parenchyma 516*f*
glans penis 300, 305*f*, 306*f*
glaucoma 485, 500*f*, 504*f*
granulomatous lung disease 417
granulosa cell tumor (GCL) 333–334, 333*f*
gravid uterus 384
"green stick" fractures 230
"ground glass" appearance 419
guttural pouches 514
empyema 518*f*, 519*f*
lateral compartment of 516*f*
medial compartment of 516*f*, 517*f*
tympany 517*f*

h

harmonic waves 9
head:
assessment of structures 262–263, 263*f*
larynx 257–260, 258*f*, 259*f*
salivary glands 262
temporomandibular joint 255–257, 256*f*, 257*f*
tongue 260–262, 261*f*, 262*f*
ultrasonographic assessment 255
ultrasound guided procedures 263–264
healing, assessment of 97–100
heart 409
by echocardiography 409
hemangiosarcoma 420, 453*f*
hemarthrosis 56, 56*f*, 209
hematomas 209, 211, 214, 561*f*, 563*f*
broad ligament 563, 565*f*
mural 563, 566*f*
hemopericardium 415*f*
hemoperitoneum 463*f*, 561
hematoma formation during resolving 561*f*
hemorrhage 203, 208*f*, 339, 415, 486, 564
periparturient 561
perirenal 560
source of 564
hemothorax 414*f*, 415
pleural abscess 415, 415*f*
pyothorax 415, 415*f*
hepatitis 449*f*
hepatoblastoma 452*f*
herniation 419
high suspensory disease. *See* proximal suspensory desmitis
hip joint 235–238, 236*f*
osteoarthritis 237*f*
hippomane 391, 397*f*
hock:
collateral ligaments 173–174
foals 186
intra-arterial perfusion 185–186
lateral digital extensor tendon 179*f*
subcutaneous bursa 180
subcutis 185
tendons and ligaments 173–177
homogenous tissues 3
horizontal tears 218
horses, echocardiography in 426
aortic root rupture 443*f*
aortic valve lesions 433*f*
apical muscular ventricular septal defect 428*f*
chamber dimensions 428
color Doppler in 426*f*
common arterial trunk 431*f*
cor pulmonale 442*f*
diastolic left ventricular function 429

Vet-ebooks.com

dilated cardiomyopathy 441*f*
hemodynamic assessment 429
infective endocarditis 438*f*
left atrial function 429
mitral regurgitation 431*f*–433*f*
myocarditis 439*f*
non-restrictive ventricular septal defect 427*f*
papillary muscle ischemia 442*f*
pericardial effusion 438*f*
restrictive ventricular septal defect 427*f*
systolic left ventricular function 428–429
valvular regurgitation 433–444
humeral tubercles 157–161
hydronephrosis 457*f*
hydroureteronephrosis 457*f*
hyperechogenic fluid 335
hyperechogenic foci 415
hyperechogenic fragments 61
hyperechoic concretions 286
hyperechoic shadow 413
hyperechoic smegma 306*f*
hyperplasia 57
hypervascularity 100
hyphema 495*f*
hypoechogenicity 97, 110
hypoechogenic muscle 89
hypoechoic brachiocephalicus muscle 166

i

iliac artery 545*f*
external 563
plaque in 546*f*
thrombosis of 540, 546*f*
vascular structures 540, 546
ilium:
pelvis 229–230
ultrasonographic assessment of 230*f*
image resolution 5–6, 6*f*
immature callus 230
infective endocarditis 438*f*
inflammatory changes (synovitis) 203
infraspinatus bursa 168*f*
infraspinatus bursitis 167
infraspinatus muscle 166–167, 167*f*, 168*f*
injuries:
cruciate ligament 220
meniscal 215, 218, 220
patellar ligament 204–206, 207*f*
interarticular ligaments 134
intercostal spaces (ICS) 409, 410*f*, 446, 558
internal abscess 462*f*, 463*f*
internal carotid artery 518
internal genitalia 272*f*
stallion 285
transrectal ultrasound evaluation 272
internal jugular vein 540
internal pudendal artery 300
internal reproductive tract
anatomy 271–272
normal ultrasonography 272–286
palpation *per rectum* 272
internal umbilical remnant 555*f*
internal vaginal rings 272
intersesamoidean ligament 72
abnormalities 82–84
desmitis of 65–66
interspinous ligaments 243–245
interstitial pneumonia 411*f*, 419
intertubercular groove. *See* intertubercular sulcus
intertubercular sulcus 157–161
interventricular septum (IVS) 427*f*
intestinal tract 558
intra-arterial perfusion 185–186
intracranial circulation 402–403
intraluminal fluid, septic 566*f*
intraluminal thrombus 542*f*
intra-ocular mass, EOUS 487
intrauterine fluid 335, 343*f*, 353*f*
echogenicity of 335
uterus 564
intrauterine growth restriction (IUGR) 385, 402
intrauterine marbles 339
intravenous catheter 541*f*
inverted uterine horn 566, 567*f*
iris cysts 485, 506*f*
iris prolapse 485
ischiocavernous muscles 300

Vet-ebooks.com

J

Jejunojejunal intussusception 471, 473*f*
jejunum 570, 571
joint 134–136
  capsule 203
  coxofemoral 236*f*
  disease 220
  hip 235–238, 236*f*
  neck 249–254
  surfaces 146
jugular groove 525, 532
  carotid artery 529*f*–530*f*, 532
  esophagus 534, 534*f*, 535*f*, 537
  trachea 532, 533*f*, 534, 534*f*
  ultrasound structures in 529*f*
jugular vein 466*f*, 529*f*–533*f*, 540
  internal and external 540
  lateral thoracic vein 545*f*
  myositis 541*f*
  normal 541*f*
  occlusion 541*f*
  perivascular cellulitis/edema 544*f*
  thrombophlebitis 542*f*
  thrombosis 542*f*, 543*f*
  vascular structures 540
juvenile tendinitis 93, 94*f*

k

keratitis 484, 489*f*, 499*f*
kidneys 446, 455
  normal left 454*f*
  normal right 454*f*
Klebsiella pneumoniae 455*f*

l

large intestine 473–480
larynx 257–260, 258*f*
  anatomy and scanning technique 257–260
  lateral transverse view of 259*f*
  ultrasonographic abnormalities 260
  ventral aspect of 259*f*
lateral carpus 129–130, 130*f*, 131*f*
  premature foal 137*f*
lateral collateral ligament (LCL) 64, 195
  of elbow joint 149–150, 152*f*, 153*f*, 154*f*
  hock 173
lateral deep digital flexor tendon 175, 177, 180
lateral digital extensor tendon (LDET) 90, 129, 130*f*, 179*f*, 186*f*
lateral digital flexor tendon (LDFT) 91
lateral femoral condyle (LFC) 198*f*, 200*f*
lateral femoral epicondyle (LFE) 198*f*
lateral femorotibial joint (LFT) 195, 198*f*, 199*f*
lateral patellar ligament (LPL) 193*f*, 206*f*, 207*f*, 211*f*, 212*f*
lateral region 537, 539
lateral resolution 5, 6*f*
lateral thoracic vein 545*f*
lateral tibial condyle (LTC) 198*f*
lateral trochlear ridge (LTR) 206*f*, 208*f*
  distal aspect 212*f*
Lawsonia intracellularis infection 471, 473*f*
left hemithorax 410
left kidney 446, 558
  normal 454*f*
left testis:
  cranial–caudal view of 311*f*, 313*f*
  lateral view of 311*f*, 312*f*
left ventral colon (LVC) 448*f*, 474*f*
left ventricular outflow tract (LVOT) 424*f*
leiomyomas 343*f*
lens rupture 486, 501*f*
leptosporosis 456*f*
lesions 57, 77, 93
  meniscal 218
  osseous cyst-like 220
ligaments 86–91, 88*f*
  carpus 143
  dorsal sacroiliac 232, 234*f*, 235, 235*f*
  hock 173–177
linear array transducers 384
linear transducers 6, 6*f*, 27*f*, 173
  standoff for 8*f*
lipoma 470*f*, 471*f*
liver 446, 558, 559
  amyloidosis 449*f*
  bile duct stricture 450*f*
  cranioventral abdomen 448*f*
  and duodenum 448*f*
  hepatitis 449*f*

Vet-ebooks.com

normal 447*f*
portal vein 448*f*
local anesthesia 264, 481
local traumatic injuries 103–106
long digital extensor muscle 225
long digital extensor tendinopathy 124*f*
longitudinal tears 218, 219*f*
long lateral collateral ligament (LLCL) 173, 174, 176*f*, 179*f*
long medial collateral ligament (LMCL) 174*f*
long plantar ligament (LPL) 174, 176*f*
desmitis of 175
lumbar facet joints 245–248
lumbar intertransverse joints 240
per rectum, normal 241*f*
lumbar intervertebral articulations (IVAs) 245*f*, 246, 246*f*, 247*f*
lumbosacral joints 238–240
per rectum ultrasonograph 239*f*, 240*f*
lumen 534
lung:
abnormal 411*f*
cardiac notch of 409
normal 410*f*, 411*f*
parenchyma 416*f*, 417, 419
thoracic ultrasonography 410*f*
LV peripheral wall (LVPW) 441*f*
lymphatic cysts 335
lymph nodes 520*f*
laryngeal 522*f*
retropharyngeal 524*f*
lymphosarcoma 420, 453*f*

m

magnetic resonance imaging (MRI) 25
male:
genital tubercle for 373
penis in 370
umbilical cord in 370
mammary gland 377
mandibular salivary gland 518, 519*f*
manica flexoria 70, 71*f*, 72, 74, 82, 82*f*
partial/complete tearing 80
tearing 81*f*, 83*f*
marbles, uterus 339, 342*f*
mare reproductive abnormalities:
cervix 342
ovaries. *See* ovary/ovaries
ultrasound examination 331
uterus 335–342
vagina 342–345
maternal circulation, assessment of 400–401
mature callus 230
mechanical probes 6
mechanical transducers 6
meconium impaction 578*f*
medial carpus 130–131, 131*f*, 133*f*
medial collateral ligament (MCL) 64, 65*f*, 131, 195, 196*f*, 197*f*, 216*f*
hock 173
meniscal injuries 217*f*
medial deep digital flexor tendon 180
medial digital flexor tendon (MDFT) 91
medial femoral condyle (MFC) 196*f*, 197*f*
caudal aspect of 204*f*
medial meniscus 204*f*
subchondral cyst-like lesions of 223*f*
medial femoral epicondyle (MFE) 216*f*
medial femorotibial joint 194–195, 197*f*, 224*f*
medial lens subluxation 498*f*
medial meniscus (MM) 204*f*, 217*f*, 218, 219*f*, 224*f*
chronic degenerative changes in 221*f*
cranial meniscotibial ligaments of 220*f*
medial palmar intercarpal ligament (MPaICL) 134, 135*f*
medial tibial condyle (MTC) 196*f*
medial trochlear ridge (MTR) 192*f*, 210*f*, 211*f*
medial window 91
megaesophagus 534, 536*f*
melanoma 506*f*, 514*f*, 515, 539*f*
melting ulcer 491*f*
meniscal injuries 215, 218, 220
meniscofemoral ligament (mfl) 198*f*
mesenteric abscess 563*f*
mesenteric disruption 561
mesothelioma 419*f*
metacarpal condyle (MC) 59*f*
metacarpophalangeal joint 61, 66, 73
metacarpus (MC3) 51–52, 90
bony injuries 122–126

Vet-ebooks.com

extensor tendons 122
palmar aspect 103*f*
preparation and scanning technique 85–86
scanning protocol for 86*t*
tendinopathy/desmopathy. *See* tendinopathy/desmopathy
tendons and ligaments, appearance of 86–91, 88*f*
ultrasonographic anatomy 86–92, 87*f*
metatarsus (MT3) 51–52. *See also* metacarpus
scanning protocol for 86*t*
metritis 567*f*
micro-convex probes 7
microconvex transducer 25, 27*f*, 39
small footprint 25
microphakia 486, 497*f*
middle carpal joint (MCJ) 128
Middle Cerebral Artery (MCA) 402–403
middle patellar ligament (MiPL) 192, 192*f*, 193*f*, 195*f*, 204, 210, 211*f*
distal third of 209*f*
and trochlea 208*f*
mineralization/ossification 77
of meniscal fragment 218
mirror-image artifact 17
M-mode 4–5, 5*f*, 421, 425*f*, 429, 435*f*
mucus/biofilm 339, 340*f*
multicystic uterus masculinus 295*f*
mural hematoma 563, 566*f*
muscles 537
atrophy 248
brachiocephalic 537
omohyoid 537
sternocephalic 537
sternohyoid and sternothyroid 537
strap 537
swellings in 537
muscular capsule 285
myocarditis 439*f*
myositis, jugular vein 541*f*

n

nasogastric tube 535*f*
navicular bone 27*f*, 30
flexor surface 40*f*
navicular bursa 35*f*
N-butylscopolammonium bromide 323
neck:
abscess 538*f*, 539*f*
bones and joints 249–254
of fetus 390, 390*f*
jugular groove. *See* jugular groove
lateral region 537, 539
muscles 537, 538*f*
muscles of 248
preparation and scanning technique 510
soft tissues 248–249, 248*f*
ultrasound assessment 243
upper cervical region. *See* upper cervical region, neck
negative frequency shift 17–18, 18*f*
neonatal intensive care unit (NICU) 573
neonate/neonatology:
abdominal cavity 576–579
intercostal spaces 573
medical/physical condition 573
patient 573
rib fracture 412*f*
size and lack of body fat 573
thoracic cavity 574–576
upper lung 573
neoplasia 417
neoplastic disease 420
nephritis 455*f*
perirenal edema and 458*f*
nephrolith 455*f*, 456*f*, 457*f*
nephrosplenic entrapment 474*f*
non coronary cusp (NCC) 424*f*
non-pregnant mare:
in diestrus 351
examination of 324
reproductive tract 324
ultrasonographic evaluation of 323
uterine horn 394, 394*f*
uterus 559
non-septic tenosynovitis 74
non-viable pregnancies 359*f*
33 to 39 days gestation 359*f*
24-day gestation 358*f*
normal bladder 579*f*

Vet-ebooks.com

o

oblique distal sesamoidean ligaments (ODSLs) 41–43, 45*f*
oblique transverse transsolar/cuneal ultrasound 34*f*
obturator artery 300
olecranon fossa 149
omohyoid muscle 537
omphalitis 578*f*
omphalophlebitis 578*f*
onion-ring lesion 100
operator error artifacts 11–12
Optical Coherence Tomography (OCT) 491*f*
optic nerve 484
orbital diameters 385–386
orchitis 313, 315*f*
osseous cyst-like lesions 61, 63*f*, 147*f*, 220
osseous lesions 161
osteoarthritis (OA) 29, 30*f*, 204
  of elbow joint 149, 151*f*
  femorotibial joint 220–221
  fetlock 59
  hip joint 237*f*
  of proximal interphalangeal joint 47
osteochondral fragmentation 61–64, 145*f*
osteochondritis dissecans (OCD) 60, 64*f*
osteochondrosis (OC) 59–61, 60, 61*f*, 62*f*, 183, 184*f*, 206, 209
  trochlear ridge 206
osteochondrosis dissecans (OCD) 206
osteomyelitis 184*f*
osteophytes 59, 204
ovarian hematomas 334–335, 335*f*
ovary/ovaries
  accessory corpora lutea on 356*f*
  anovulatory follicles 332–333, 332*f*
  contralateral 333, 334
  with corpus luteum 329*f*
  during early transitional phase 325*f*
  epithelial inclusion cysts 334, 334*f*
  granulosa cell tumor 333–334, 333*f*
  ovarian hematomas 334–335, 335*f*
  parovarian cysts 334, 334*f*
over-strain midsubstance injuries 77, 77*f*
ovulation date 357

p

PAL. *See* palmar/plantar annular ligament
palmar carpus 131–134, 134*f*, 135*f*
palmar foot 26*f*
palmar metacarpophalangeal ligament 65–66
palmar/plantar annular ligament (PAL) 44, 72, 72*f*, 75*f*, 76*f*
  digital flexor tendons sheath 76–77
palmar/plantar P1 fragments 67
palpation 323
  of internal reproduction tract 348*f*
  per rectum 272, 558
  pregnancy diagnosis 347
papillary muscle ischemia 442*f*
paralumbar fossa (PLF) 446
paraphimosis 302, 307*f*
paratendinitis 106, 107*f*
parotidoauricularis muscle 256
parotid salivary gland 510–511, 513*f*, 514, 514*f*
parovarian cysts 334, 334*f*
parrot-beak tears 218
partial CL tears 215
pastern 39–47
  fetlock and 39
  preparation and scanning technique 41
  ultrasonographic abnormalities 42–47
  ultrasonographic anatomy 41–42, 42*f*
patellar fractures 209–210
  cranial aspect of 213*f*
patellar ligament (PL) 191, 194*f*, 210*f*
  injuries 204–206, 207*f*
  lateral 204
  middle 192, 192*f*, 193*f*, 195*f*, 204, 210, 211*f*
patellar luxation 225
patent urachus 555
patient preparation 10–11, 11*f*
peak systolic velocity (PSV) 302
pelvicitis 560, 560*f*
pelvic limb differences 91
pelvic urethra 273*f*–274*f*, 296*f*
  normal stallion 296
pelvis:
  areas of interest in 229

Vet-ebooks.com

dorsal sacroiliac ligaments 232, 234*f*, 235, 235*f*
equipment 229
hip joint 235–238
ilium 229–230
indications 229
lumbar intertransverse joints 240, 241*f*
lumbosacral joints 238–240, 239*f*, 240*f*
per rectum evaluation 238
sacroiliac joint 240
sacrum 240
third trochanter 232, 233*f*, 234*f*
tubera sacrale 230, 230*f*, 231–232, 235*f*
tuber coxa 230, 230*f*, 231–232, 232*f*
tuber ischium 231–232, 232*f*
ultrasound assessment 229
penis:
anatomy 300
blood flow 302
body, proximal part of 303*f*
and cross-sections, diagram of 301*f*
distal part 301*f*, 306*f*, 308*f*
dorsal artery 300, 302*f*, 303*f*
free part 304*f*
glands 306*f*
in male 370
organizing hematoma of 309*f*
pathologies 302–309
ultrasound evaluation 300–302
urethra 302*f*
vascu-larization of 302
percutaneous electrical nerve stimulation (PENS) 263
periarticular injuries 67
pericarditis 426
periosteal new bone formation 144*f*
periostitis 122
periparturient hemorrhage 561
peripheral pulses 388
perirectal abscess 480*f*
perirenal edema 458*f*
perirenal hemorrhage 560, 560*f*
peritoneal cavity 459–463
pathology of 560, 561
peritoneal fluid 459, 559
peritoneum 559
peritonitis 459, 561–562, 562*f*, 563*f*, 564, 567*f*
bacterial 460*f*, 461*f*, 462*f*
exudative 462*f*
with fecal contamination 471*f*
fibrinous 461*f*
fibrin tags 462*f*
intestinal wall in 461*f*
jejunum in 461*f*
neonatal foal with 463*f*
transrectal view of 462*f*
perivascular cellulitis/edema 544*f*
perivascular injection 540
peroneus tertius 177, 179*f*
rupture 177
tendon 225
per rectum 568
evaluation, pelvis 238
palpation 272, 558
per vaginum 568
phased-array probes 7
physics of ultrasound 1–5
B-mode 3–4
echogenicity 3–4
M-mode 4–5
ultrasound waves. *See* ultrasound waves, features of
physis 183, 187*f*
distal tibial 185*f*
septic tibial 185*f*
piezoelectric crystals 2
placental dysfunction 399
pleural abscess 415, 415*f*
pleural effusion 413*f*, 414–415
pleural fluid 560
pleural hemorrhage 412
pleural space 413–414, 414*f*
pleuritis 413–414, 413*f*
fibrinous 413*f*
pleuropneumonia 413*f*, 414*f*
plugged ampullae 286
pneumometra 568
pneumonia 574*f*
pneumopericardium 417
pneumoperitoneum 461*f*, 564

Vet-ebooks.com

pneumothorax 13, 416–417, 416*f*
pneumouterus 567*f*
positive frequency shift 17, 18*f*
post-anesthetic myopathy 155
posterior chambers 483
  fibrin accumulation in 485
posterior lens luxation 499*f*
post foaling complications
  abdominal discomfort in 558
  abdominal viscera, pathology of 563–568
  bladder rupture 562
  common variations 559
  cystitis 562
  diaphragmatic hernia 559–560, 560*f*
  gastrointestinal tract 568–571
  hemoperitoneum 561
  normal anatomy 558–559
  pelvicitis 560, 560*f*
  peritoneal cavity,pathology of 560, 561
  peritonitis 561–562, 562*f*, 563*f*
  prepubic tendon 559
  rectus abdominis 559
  retroperitoneal hemorrhage (perirenal) 560
  ruptured body wall 559
  technique 558
  transabdominal ultrasonography, limitations of 559
  uroperitoneum 562
post mating/breeding induced endometritis (PMIE/PBIE) 335
post-partum lochia 564
Potomac Horse Fever colitis 477*f*
power Doppler 20
  transverse trans-solar 41*f*
pregnancy
  abnormal conceptuses 359
  database 383–384
  day 21 366*f*
  day 29 adjacent to cysts 365*f*
  days 9 to 16 351
  days 17 to 20 351, 353
  days 21 to 28 353
  days 30 to 40 353–354
  days 40 to 60 354, 357–358
  detectable heartbeat 353, 355*f*
  early pregnancy examination 358
  elective feto-placental evaluation 384
  embryonic stage 349
  in equine practice 384
  failure 358–360
  gestational age of 357
  loss and return 360*f*
  loss prior to day 359
  monitoring 383
  non-viable 359*f*
  resorbing 353*f*
pregnancy diagnosis
  detection 347
  first 60 days 347
  palpation 347
  transrectal technique 347–349
pregnant mare serum gonadotrophin (PMSG) 339, 356*f*
preovulatory follicle 328*f*
prepubic tendon 559
preputial tissue 377
priapism (persistent erection) 302
primary tenosynovitis 73–76
prostaglandin, release after twin reduction 367
proximal digital annular ligament (PDAL) 42, 46*f*
proximal digital sheath 70, 70*f*, 75
proximal interphalangeal joint (PIP) 42
  abnormalities 47
  articular cartilage of 47
  lateral axial palmar ligament of 46*f*, 47*f*
  osteoarthritis of 47
proximal scutum (scutum proximale) 52, 72
  abnormalities 82–84
proximal sesamoid bones (PSBs) fractures 65, 66–67
proximal suspensory desmitis 107–113, 109*f*, 110*f*, 111*f*
pubis, fracture of 239*f*
pulmonary abscesses 418
pulmonary atelectasis 417, 417*f*
pulmonary consolidation 416*f*, 417
pulmonary edema 13
pulmonary parenchyma 411*f*, 412, 574*f*

Vet-ebooks.com

perpendicular 411*f*
pulsed wave (PW) Doppler 18–19, 19*f*, 421, 429
pus (ipopion) 485
pyothorax 415, 415*f*

q
quadriceps muscle 191, 213*f*
tears 211, 214*f*
quantitative assessment, of flexor tendon and suspensory ligament size 91–92

r
radial tears 218
radiography 43, 128, 214, 220
raisin heart 428
record-keeping systems 335
rectal ampulla 384
rectal trauma 560
rectum 480
rectus abdominis 559
rectus femoris muscle 214*f*
recurrence 101, 102*f*
reflection 2–3
refraction 3
relative wall thickness (RWT) 428
renal cortex 446
renal dysplasia 456*f*
retained placenta,566, 568, 568*f*
retina 484
retinaculum of the carpus (RetC) 131, 132
retina detachment 487, 502*f*, 503*f*
retrobulbar cellulite 487
retrobulbar diseases 487
retrobulbar space 482
retroperitoneal hemorrhage (perirenal) 560
retropharyngeal lymph nodes 511, 524*f*
abscess 523*f*, 524*f*
reverberation artifacts 12–14, 12*f*, 13*f*, 488, 488*f*
Rhodococcus equi infection 249, 462*f*
rib fractures 412, 412*f*, 413*f*
right coronary cusp (RCC) 424*f*
right dorsal colitis 475, 475*f*, 476*f*
right dorsal colon (RDC) 446, 447*f*, 448*f*
right hemithorax 410–411
right kidney 446, 558
normal 454*f*
right ovary 331
right ventricular outflow tract (RVOT) 424*f*
ring-down artifact 12, 13, 14*f*

s
sabulous cystitis 564*f*
sacroiliac joint 229, 240
caudal aspect of 241*f*
sacrum 240
per rectum 242*f*
salivary duct (Stensen's duct) 511
salivary glands 262
scapula 155–157
fractures 155, 157, 159*f*
scapulohumeral joint (SHJ) 167–172, 169*f*, 170*f*, 171*f*
level 167*f*
normal proximodistal ultrasound scans of 169*f*
scar tissue 563
scatter 3
scintigraphy 57
sclera 484
scoring system 335
scrotal content:
echotexture of 313
epididymis 313
evaluation 311*f*
qualitative evaluation of 313–314
spermatic cord 313
testis 313
vaginal cavity 313, 314
scrotum 310
"seagull's wings" 487
secretion 271
sedation 148, 255
seminal vesiculitis 289*f*, 290, 295
sepsis 104
septic arthritis 67–68, 149, 221, 225
of elbow 150*f*
iatrogenic 224*f*
septic extensor carpi radialis tendon sheath 138*f*
septic intraluminal fluid 566*f*

Vet-ebooks.com

septic pedal osteitis 36*f*
septic synovitis 167, 177
septic tendinitis 105*f*
septic tenosynovitis 73
serosanginous peritoneal fluid 469*f*
Sertoli cell tumor 316*f*
sesamoid bones 90
short lateral collateral ligament (SLCL) 174, 176*f*
short medial collateral ligament (SMCL) 174*f*
shoulder
  normal point of 161*f*
  scanning technique 155
  scapula and supraglenoid tubercle 155–157
  septic synovitis of 167
side-lobe artifact 16–17, 17*f*
slice-thickness artifact 15–16, 16*f*
small intestinal muscular hypertrophy 472*f*
small intestine 466–473, 469*f*
  entrapped 571*f*
  intussusception 577*f*
  lipoma 470*f*, 471*f*
  non-strangulating entrapment of 471*f*
  strangulation 470*f*
  volvulus 577*f*
  volvulus with ventral sedimentation 470*f*
soft tissues
  neck 248–249, 248*f*
  structures 255
  swelling 175
solar corium 33*f*
SonoSite M-Turbo® ultrasound system 348
spectral Doppler 18, 18*f*
sperm accumulators 290
spermatic cord 313
  affected 315*f*
  cross-section of 314*f*
  hyperechoic inconsistencies in 315*f*
  torsion 314*f*, 315*f*
spleen 3, 4*f*, 410, 446, 558
  cholangiohepatitis 450*f*, 451*f*
  hemangiosarcoma 453*f*
  lymphosarcoma 453*f*
  normal 452*f*
  splenic tear 453*f*
spleen–stomach relationship 452*f*, 453*f*, 466*f*
splenic vein 446
spontaneous echo contrast (SEC) 437*f*
spontaneous fetal movement 357
squamous cell carcinoma (SCC) 507*f*
stallion
  internal genitalia 272, 286
  internal reproductive tract 295
  internal vaginal rings 272
  pelvic urethra 272
  penis. *See* penis
  Tennessee Walking Horse 449*f*
  testes size 319
standoff pad 7, 8*f*, 49, 85, 148, 155, 482
sterile ultrasound coupling gel 482
sternocephalic muscle 537
sternothyroid muscles 537
stifle
  abscesses 213*f*
  anatomy of 191–203
  femoropatellar joint. *See* femoropatellar joint
  femorotibial joints. *See* femorotibial joints
  lateral femorotibial joint 195, 198*f*, 199*f*
  medial aspect 214*f*, 219*f*, 225*f*
  medial femoral condyle 196*f*, 197*f*
  medial femorotibial joint 194–195, 195*f*
  preparation and scanning technique 189–191
stomach 465, 466, 571*f*
  cranial aspect of 467*f*
  dorsocaudal displacement 570
  enlarged 576*f*
  gastrointestinal tract 570
  spleen and 466*f*
  tube 467*f*
straight distal sesamoidean ligaments (SDSLs) 41–43, 44*f*
  insertion site of 43*f*
strap muscles 537
Streptococcus equi 514, 523*f*
Streptococcus equi zooepidemicus 340*f*, 345*f*, 455*f*
stress fractures 229, 243
  in racehorses 231*f*
stromal abscesses 484, 489*f*, 490*f*

Vet-ebooks.com

and anterior uveitis 492*f*
stromal corneal lesion 493*f*
Strongylus vulgaris infection 540
stylohyoid bone 514
subacute synovitis 58*f*
subchondral bone 206
defects 67
injury 57–59
subchondral cyst-like lesions 220, 223*f*
subcutaneous bursa 180
subcutis 185
subperiosteal hemorrhage 126*f*
subsolar abscess 35*f*
superficial digital flexor tendon (SDFT) 42, 43, 69, 70, 72, 73, 76, 86, 89, 91, 96*f*, 100, 105*f*, 133*f*, 139*f*, 174, 175
complete rupture of 95
cross-sectional area of 97*f*
digital sheath abnormalities 80–82
and gastrocnemius tendon 181*f*
lateral branch of 80*f*
paratendinitis of 107*f*
proximal metacarpal 96*f*
tendinopathy/desmopathy 93–96, 96*f*
superficial soft tissues 143
supraglenoid tubercle 155–157
fracture 160*f*
supraspinatus fossa 155, 159*f*, 166*f*
supraspinatus muscle 163–166, 166*f*
supraspinous ligament (SSpL) 243–245, 244*f*, 245*f*
surgery 146
suspensory desmopathy 106
suspensory ligament (SL) 89–90, 106
branches 117–118, 118*f*, 119*f*
desmitis of body 113–117, 115*f*, 116*f*
size 91–92
sustentaculum tali (ST) 182*f*, 183*f*, 187*f*
swellings, in muscle 537
synechiae 484
synovial cavity 224*f*
synovial effusion 203
synovial fluid (SF) 177, 187, 254, 257*f*
synovial fossa 149
synovial hypertrophy 57
synovial inflammation 214
synovial membrane 61, 62*f*
synovial plica 52
synoviocoele 75, 75*f*
synovitis 55–57, 177
systolic left ventricular function 428–429

t

tarsal sheath 177*f*, 180–181, 182*f*
tarsocrural joint (TCJ) 174*f*
dorsal aspect 187*f*
dorsomedial pouch of 179*f*
tarsometatarsal joint (TMTJ) 180
tarsus
bony structures 181, 183
collateral ligaments 173–174
dorsal aspect 177, 186*f*
plantar aspect of 174–175
plantaromedial aspect 175–177
synovial structures 177–180
tarsal sheath 180–181
ultrasonography of 173
tears 79–80
caudal horn 218
collateral ligament 215
cranial meniscotibial ligament 215
cranial meniscotibial ligaments (CMTL) 215
longitudinal 218
meniscal 215, 218, 220
splenic 453*f*
uterine 568*f*
vaginal 463*f*
temporomandibular joint (TMJ) 255
abnormal 257*f*
caudolateral ultrasound image 256*f*
in normal adult horse 257*f*
normal anatomy and scanning technique 255–257
ultrasonographic abnormalities 257
tendinitis/desmitis 92, 106
tendinopathy/desmopathy 92–122
assessment of healing 97–100
chronic 100–102, 101*f*
cross-sectional area of 93

Vet-ebooks.com

deep digital flexor tendon 106
general ultrasonographic changes 92–93
local traumatic injuries 103–106, 103*f*
semi-objective assessment of severity 96–97
superficial digital flexor tendon 93–96, 96*f*
tendons 86–91, 88*f*
biceps brachii 158*f*
carpus 143
of deep digital flexor tendon 177
hock 173–177
infraspinatus muscle and 166–167
and long digital extensor muscle 225
peroneus tertius 225
supraspinatus muscle and 163–166
triceps brachii 158*f*
tensocopy 84
testes. *See* testis
testis
cranial–caudal view of 311*f*, 313*f*
height 311, 311*f*
interpretation 317, 319
lateral view 311*f*, 312*f*
length 311
measures 310–313
parenchyma 316*f*
probe type 310
scrotal content. *See* scrotal content
size 314
stallion position and location 310
tunica albuginea of 316*f*
varicocele 315*f*
volume, measurement and interpretation of 314–319
width 311, 313, 313*f*
third trochanter 232, 233*f*, 234*f*
thoracic cavity (TC) 357*f*, 574–576
ventro-lateral aspect of 545*f*
thoracic limb 88–89
thoracic lymphadenopathy 414
thoracic ultrasonography
diaphragm 410, 410*f*, 419*f*
diaphragmatic disruption 419
heart 409
hemothorax 414*f*, 415
increased pulmonary volume 419
interstitial pneumonia 419
left hemithorax 410
limitations of 420
musculature of 409
normal lung 410*f*
pleural effusion 413*f*, 414–415
pleural space, pathology of 413–414
pneumopericardium 417
pneumothorax 416–417
pulmonary abscesses 418, 418*f*
pulmonary appearance 411–412
pulmonary atelectasis 417
pulmonary consolidation 417
right hemithorax 410–411
technique 409
thoracic wall, pathology of 412–413
thorax 13, 13*f*
thrombophlebitis 540, 541*f*
anaerobic infection 543*f*
IV catheter 543*f*
of jugular vein 542*f*, 543*f*
thrombosis, jugular 542*f*
thyroid cartilage (TC) 259, 260*f*
thyroid gland 520, 524*f*, 525
left lobe of 525*f*–527*f*
right lobe of 526*f*
time-gain compensation (TGC) control 8, 9*f*, 15
tissue Doppler imaging (TDI) 421, 429
tissue harmonic imaging (THI) 9–10
"T" ligament 25
tongue 260–262
anatomy and scanning technique 260–261
longitudinal ultrasound image 261*f*
transverse ultrasound image 262*f*
ultrasonographic assessment 261
total testicular volume (TTV) 317, 319*f*
trabeculae:
of corpus cavernosum 304*f*, 308*f*, 309*f*
in corpus spongiosum 308*f*, 309*f*
trace 18
trachea 466*f*, 532, 534
with fluid 534*f*
normal 533*f*
transabdominal ultrasonography 384

Vet-ebooks.com

limitations of 559
transcorneal ultrasound 482
transducer:
frequency 5–6, 6*f*
selection 10
types of 6–7
trans-eyelid scan 483
trans-palpebral ultrasound 482
transrectal ultrasonography (TRUS) 272, 384
transsolar and transcuneal ultrasonography 29–39
transverse facial vein 257
transverse ultrasound scan 29*f*
traumatic arthritis 57–59
triceps brachii muscle 155
on olecranon tuberosity 158*f*
T-type linear probe 310
tubera sacrale 230, 230*f*, 231–232
asymmetry of 235*f*
tuber coxa 230, 230*f*, 231–232, 232*f*
fracture of 233*f*
tuber ischium 231–232, 232*f*
tubular diverticula 271
tunica albuginea 308
turbulent flow 19
twinning. *See also* twins
avoidance 363
ovulation induction products 363
twins
flunixin meglumine 366
management 363
reduction by intracardiac/intra-thoracic injection 384
reduction considerations 363
separating 364
success rate 368
28-day adjacent 367*f*
twin vesicles 364*f*
of different diameters 365*f*
differing sizes 364*f*
separated 364*f*
two-dimensional (2-D) imaging 421
2-D speckle tracking (2DST) 421
typhlitis 479*f*

u

ulnaris lateralis muscle 150, 155, 156*f*, 157*f*
ulnaris lateralis tendon (ULT) 130
ultrasonography 1
ultrasound 226
definition 2
guided procedures, head 263–264
physics 1–5
ultrasound gel 310
ultrasound machine 4
console 5
controls 7–10
depth 8
focus 8–9, 9*f*
frame rate 9
gain control 8
image optimization 7–10
image resolution 5–6, 6*f*
patient preparation 10–11, 11*f*
presets 7–8
time-gain compensation control 8, 9*f*
tissue harmonic imaging 9–10
transducer frequency 5–6, 6*f*
and transducer selection 10
transducer, types of 6–7
ultrasound waves, features of 2–3
absorption 3
acoustic impedance 2–3, 2*t*
reflection 2–3
refraction 3
scatter 3
umbilical arteries 550, 553*f*, 554*f*, 579*f*
umbilical circulation 401
umbilical cord (UC) 356*f*, 373, 376*f*, 396–399
of fetus 217-days-old 399*f*
and hippomane 397*f*
in male 370
at 180 days gestation 397*f*
placental root of 397*f*
234 days gestation 398*f*
umbilical hernia 555, 556*f*, 557, 557*f*
umbilical remnant 548*f*, 550*f*
external 547, 549*f*
internal 555*f*
probe orientation 548*f*

Vet-ebooks.com

umbilical arteries 550, 553*f*
umbilical hernia 555, 556*f*, 557, 557*f*
umbilical vein 547, 550
urachus 550, 555
umbilical vein 547, 550, 551*f*, 552*f*
fetus 550
infection 550
linea alba 551*f*
omphalophlebitis 578*f*
pathology 550, 551*f*
unidentified mass, in upper cervical region 527*f*–528*f*
upper cervical region, neck 510–525
carotid artery 518
laryngeal lymph node 522*f*
left 512*f*
lymph nodes 520, 521*f*–522*f*
mandibular salivary gland 518
parotid salivary gland 510–511, 513*f*, 514, 514*f*
sites and associated structures in 512*f*
thyroid gland 520, 524*f*, 525, 525*f*–527*f*
ultrasound landmarks of 512*f*
unidentified mass 525, 527*f*–528*f*
urachus 550, 555, 578*f*
infection 555
omphalitis 578*f*
patent 555
urethra 300
corpus spongiosum of 302
penis 302*f*
urethralis muscle 271
urethral sinus 300, 307*f*
urinary calculi 460*f*
urine-filled bladder 562
urogenital sinus 271
uroperitoneum 460*f*, 562, 579*f*
urovagina 343–345
uterine arteries (UA) 400
rupture 339
uterine body 331, 340*f*, 348
cross-section of 325*f*
diestrus 324*f*
estrus with edema 324*f*
gentle ballotment of 384
longitudinal ultrasonography 350*f*
lumen of 361*f*
uterine cysts 350
cluster of 351*f*
uterine edema 326, 568*f*
uterine fluid, scoring system for 335
uterine horn 348
cranial aspect 350*f*
in cross-section 341*f*
cross-section of 349*f*
11-day embryonic vesicle in 351*f*
15-day embryonic vesicle in 352*f*
14-day embryonic vesicle in 352*f*
inverted 566, 566*f*
non-pregnant 394, 394*f*
12-day embryonic vesicle in 351*f*
ultrasonography 350*f*
uterine lumen 336*f*, 337*f*, 348*f*
uteroplacental unit 394
uterus 326, 335–342
air in 339, 339*f*
body of 324
broad ligament hematoma, 563, 565*f*
diestrus 329*f*, 335
with edema and normal fluid 326*f*
endometrial cups 339, 341*f*
endometrial cysts 335, 337*f*, 338*f*, 339
good visualization of 324*f*
horn 324*f*
intraluminal hemorrhage 567*f*
intrauterine fluid 335, 343*f*, 564
inverted uterine horn 566, 567*f*
involuting 566*f*
lumen of 324*f*, 325*f*
marbles 339, 342*f*
mucus/biofilm 339, 340*f*
mural hematoma 563, 566*f*
mural laceration, necrosis, and perforation 564
non-pregnant 559
pneumometra 568
post-partum 566
retained placenta 566, 568, 568*f*
uterine artery rupture 339
vaginal fluid 568

Vet-ebooks.com

utriculus masculinus 271
in colliculus masculinus 286
uveitis 485, 490*f*, 492*f*, 496*f*
cataracts and 497*f*

v

vagina 342–345
and cervix 345*f*
vault 345*f*
vaginal cavity 313, 314
fluid (hydrocele) in 318*f*
vaginal fluid 569*f*
uterus 568
vaginal tear 463*f*
valvular regurgitation 433–444
varicocele 315*f*
vasa deferentia 271, 273. *See also* vas deferens
ampullae of 276*f*–280*f*, 294*f*, 295*f*
vascular structures 540
distal limb vasculature 540
iliac arteries and aorta 540, 546
jugular vein. *See* jugular vein
lateral thoracic vein 540
vas deferens. *See also* vasa deferentia
ampulla of 283*f*–284*f*, 289
dilated ampulla of 285*f*
occluded ampulla of 285*f*
terminal portion of 281*f*–282*f*
ventral cervix 344*f*
ventral colon 559
ventrolateral larynx 259
vesicular glands 271
ampulla of 281*f*
enlarged 298
fundus of 288*f*
mucous membrane 271
palpation 272
secretion 280
stallion with seminal vesiculitis 290*f*
terminal portion of 281*f*
ultrasound appearance 280
ultrasound image of 289
veterinary medicine 481
veterinary ultrasonography 1
villonodular synovitis 57
vitreous chamber 484
vitreous inflammation 486
vitreous opacity 486–487

x

xiphoid cartilage 547
xylazine 323

y

yolk sac 350*f*
envelopment of 357

Vet-ebooks.com

WILEY END USER LICENSE AGREEMENT

Go to www.wiley.com/go/eula to access Wiley's ebook EULA.

Vet-ebooks.com